Proceedings

ISES Solar World Congress 2023

Conference of

ISES
International
Solar Energy Society

In cooperation with

isa
INTERNATIONAL
SOLAR
ALLIANCE

Proceedings

Proceedings of the Solar World Congress 2023 in New Delhi, India

International Solar Energy Society
Wiesentalstr 50
79115 Freiburg
Germany

Tel + 49 761 45906 – 0
Fax + 49 761 45906 – 99
Email hq@ises.org
http://www.ises.org

ISBN 978-3-982 0408-9-9

Produced by International Solar Energy Society

Notice

The International Solar Energy Society nor any one of the supporters or sponsors of the SWC 2023 conference make any warranty, expressed or implied, or accepts legal liability or responsibility for the accuracy, completenessor usefulness of any information, apparatus, product, or process disclosed, or represents that its use would not infringe privately on rights of others. The contents of articles express the opinion of the authors and are not necessarily endorsed by the International Solar Energy Society or supporters or sponsors of the conference. The International Solar Energy Society or any one of the supporters or sponsors of the SWC 2023 conference do not necessarily condone the politics, political affiliation and opinions of the authors or their sponsors.

Disclaimer

We cannot assume any liability for the content of external pages. The operators of those linked pages are solely responsible for their content. We make every reasonable effort to ensure that the content of this web site is kept up to date, and that it is accurate and complete. Nevertheless, the possibility of errors cannot be entirely ruled out. We do not give any warranty regarding the timeliness, accuracy or completeness of material published on this web site and disclaim all liability for (material or non-material) loss or damage incurred by third parties arising from the use of content obtained from the website.

Note from Congress Chair Dr. Dave Renné

As Chair of the 2023 ISES Solar World Congress, held in New Delhi, India from October 30 to November 4, I am delighted to present the Congress Proceedings, and to add my message to that of Dr. Ashvini Kumar the Congress Scientific co-Chair, introducing the Proceedings, which can be found below.

ISES Solar World Congresses are held every two years in different venues around the world. In 2023 we were excited to return to India, where we last had a Congress back in 1978 (ISES Congresses were a mere six years old at the time). Our Congresses are designed to bring together stakeholders from all segments of the renewable energy landscape, especially researchers, practitioners, government decision makers, and civil society interested in learning about the latest breakthroughs and trends in solar energy and related technologies. The Congress is structured in such a way to offer researchers in all aspects of renewable energy to present their results in technical sessions while also offering participants the opportunity to learn about the latest trends in renewable energy development from esteemed plenary and keynote speakers.

For Solar World Congress 2023 we were particularly thrilled to have a day of joint activities with the International Solar Alliance (ISA), in conjunction with their annual General Assembly. Dr. Ajay Mathur, Director-General of the ISA, served on the SWC 2023 International Organizing Committee and worked with ISES to put together a joint day of panel discussions related to identifying technologies, policies, and financial tools to accelerate the deployment of renewables in the region and around the world.

The Congress occurred just a few weeks before the United Nations Framework Convention on Climate Change (UNFCCC) held its 28th Conference of the Parties (COP) in Dubai, United Arab Emirates. For nearly 30 years the UNFCCC has convened these annual COPs to bring governments from around the world together to find solutions to the growing climate crisis caused by human activity. For the first time, the nearly 200 countries participating in the climate negotiations agreed to specific language calling out renewable energy as a key to limiting global warming to no more than 1.5 0C above preindustrial levels. The agreement proclaimed a goal of “tripling of renewable energy capacity and doubling energy efficiency improvements by 2030”. Ironically in 2023 the world experienced record warmth, due in part to an active El Nino pattern that became well established by the middle of the year, but also to the continued growth in emissions of greenhouse gases into the atmosphere, due largely to the use of fossil fuels for energy production.

The scientific community’s response to the global climate challenge and especially the confluence of these events in 2023 is reflected well in these Proceedings. Renewable energy technology costs, especially wind and solar, continue to decrease and are now often the most cost-competitive source of new power generation throughout much of the world. Technological advances leading to these reductions continue to be a major focus of renewable energy researchers within academia, research institutes, and even in private enterprises. These Proceedings provide good examples of the results of research and development efforts around the world that will not only help address the challenges put forth in the COP 28 agreement, but also create healthier environments, economic growth, and energy security in communities that fully adopt these technologies over the long term.

I hope you find these Proceedings of value to your own research and development activities. I look forward to seeing you at future Congresses and learning of the continued development and growth of these important technologies and how they address our energy needs and societal issues.

Dr. Dave Renné

SWC 2023 Congress Chair

Note from Dr. Ashvini Kumar (Scientific Commitee)

Taking cognizance of the theme “Moving the world towards 100% renewable energy”, SWC 2023 held in Delhi India provided a platform to the stakeholders around the world including researchers and practitioners to share their piece of research work on technology developments, new breakthroughs, case studies and best practices in solar and renewable energy development.

Overall, the Congress was structured to have technical sessions on carefully selected themes, interspersed with the keynote addresses by the global experts, two specially designed plenary sessions and several invited talks. The list of themes covered quite comprehensively the whole spectrum of elements important for accelerating the dissemination of solar technologies ranging from technology (PV and solar thermal power), solar buildings and neighborhood designs, rural energy supply, circular economy and recycling, system analysis, solar photocatalysis and solar fuel production, and solar resource assessment. Cross-cutting themes like grid integration and sector coupling and perspectives for a 100% renewable energy world were also included.

In all, 153 academic contributions were made comprising 80 oral presentations and 73 posters dotted with 10 keynote addresses by the experts and another 11 speakers during the two plenary sessions. One plenary session was to have a perspective on the India’s growth story in Renewable Energy which is one of the largest programs in the world anchored around the dynamic policy development by the Government and huge participation of the domestic and international investors. The other plenary session gave global overview and developments in the sector by the accomplished leaders.

The key questions which the Congress looked for responses include

a) Ways to enhance economic viability of the PV technology
b) Alternatives to land for installing solar capacities
c) Moving towards 100% solarization

It was noted that the viable alternatives to land have already begun to be implemented in the form of floating solar and agro-voltaics besides roof-tops, road highways and railway tracks. For enhancing solar share, solar hybrids (with wind, hydro, and CSP) have reached initial commercialization; next round of research is progressing on the fast development of storage systems (battery, water pump). Further, development of policy frameworks to incentivize demand side management was recommended to be important. Amongst others, cooling and heating applications including solar thermal were also captured attention, especially for accelerating industrial decarbonization. Disharmony in the spatial distribution of the jobs lost and creation of new jobs due to clean energy transition got the focus.

The PV technology was recognized as a mainstay of capacitating widespread solar infusion into the energy systems of various nations as it has already crossed a level of 1TWH capacity global installations, and even a vision of 75 TWH by 2060 looks possible due to large investments being made in the entire co-system including manufacturing. We are happy to present a compendium of the research papers presented during the Congress.

Dr. Ashvini Kumar

Co-chair of the SWC 2023 Scientific Committee

Committees

Congress Chair

Congress Chair: Dr. Dave Renné | ISES Immediate Past President

International Organizing Committee

Dr. Dave Renné | ISES Immediate Past President
Dr. Ashvini Kumar | Shakti Sustainable Energy Foundation
Assoc. Prof. Caroline Hachem-Vermette | Concordia University
Prof. Michael K.H. Leung | City University of Hong Kong
Dr. Ajay Mathur | Director General International Solar Alliance
Prof. Andreas Häberle | Eastern Switzerland University of Applied Science
Jaideep N. Malaviya | Malaviya Solar Energy Consultancy
Prof. Klaus Vajen | University of Kassel
Robert Youngberg | Sustainable Development International
Prafulla Pathak | President Solar Energy Society of India
Joanna Costello | International Solar Energy Society
Melina Hanhart | International Solar Energy Society
Arabella Liehr | International Solar Energy Society

Scientific Committee

Co- Chairs:

Dr. Ashvini Kumar | Shakti Sustainable Energy Foundation

Assoc. Prof. Caroline Hachem-Vermette | Concordia University

Prof. Michael K.H. Leung | City University of Hong Kong

Scientific Program Theme Chairs:

Prof. Anil Kottantharayil
Prof. Ricardo Rüther
Dr. Gurleen Kaur
Prof. Pradip Dutta
Dr. José González-Aguilar
Prof. Shireesh Kedare
Prof. Uli Jakob
Prof. B K Panigrahi
Dr. Aline Kirsten Vidal de Oliveira
Prof. Ashok Lall
Dr. Debajit Palit
Dr. Atul Raturi
Dr. Ritu Mathur
Dr. O S Sastry
Dr. RD Vashistha
Dr. Managit Sengupta
Prof. Rangan Banerjee
Dr. Paulette Middleton
Prof. Michael K. H. Leung

Scientific Review Committee Members

A Sreekumar
Adam R. Jensen
Adriano Möhlecke
Ahmed Alami Merrouni
Alberto Coronas
Alexander Thür
Alicia Bayon
Aline Cristine Pan
Amin Altamirano
Anand B Rao
Andre Felippe Vieira da Cunha
Andre Nobre
Andrea Charbel
Andrea Frazzica
Andreas Häberle
Anish Modi
Antonia Sonia Diniz
Aron Habte
Atul Kumar
Beccali Marco
Biboum Alain
Birinchi Bora
Bojia Li
Bram Hoex
Brinchi Bora
Carlos Cadena
Cedric Paulus
Chiel Boonstra
Christophe Menezo
Costas Travasaros
Cristof Brunner
Dai Yanjun
Dani Rusirawan
Daniel Macdonald
David Pozo-Vazquez
Deepak Kumar
Derek Baker
Dipti Gupta
Douglas Riffel
Elsabet Nielsen
Esther Rojas
Fabienne Salaberry
Gabriele Lobaccaro
Gilberto Figueiredo
Harald Drück
Hernando Romero Paredes Rubio
Hesan Ziar
Himanshu Tyagi
Isadora Pauli Custódio
Izete Zanesco
Jaideep Malaviya
Jan Remund
Jasim Uddin
Jie Ji
Jinlei Feng
Joachim Göttsche
John Pye
Joyashree Roy
Juan Carlos Muñoz
Kalyan Bhaskar
Karla G. Cedano
Karl-Anders Weiss
Klaus Vajen
Korbinian Kramer
Laltu Chandra
Larry Kazmerski
Lars Broman
Loreto Valenzuela Gutiérrez
Mahesh Suryawanshi
Manaswita Bose
Marcelo Pinho Almeida
Maria João Carvalho
Marília Braga
Mathieu David
Merlinde Kay
Monica Oliphant
Nicolas Lamaison
Olga Vilela
P Mukhopadhyay
Paul Munro
Peter Johnston Director
Philip Ohnewein
Phillippe Blanc
Pramod Borse
Prasad Vaidya
Prasun Das
Priya Jadav
Prodyut R. Chakraborty
Rachid El Bachtiri
Rafael Guedez
Rajan Rawal
Rajat Gupta
Ramon Frederick
Reshma Singh
Robert Foster
Robert Youngberg
Roberto Zilles
S K Samadarshi
Sadhan Mahapatra
Sameer Khandekar
Samuel Lune de Abreu
Santanu Bandyopadhyay
Shawn Martin
Stephan Fischer
Surendra Poonia
Tarak Kandpal
Vidhee Kiran Avashia
Vijay Soni
Viktor Unterberger
Werner Weiss
Wolfgang Streicher
Yanjun Dai
Yit Fatt Yap
Yogi Goswami
Yu Xie

Conference Themes

Electrical Components, Systems and Applications

1. **PV Cell Technologies**
   - c-si photovoltaics, perovskite solar cell; innovative PV, emerging solar cell technologies; other innovations, technologies or applications
2. **Innovative Application of PV Technologies**
   - accelerating agrivoltaics; floating PV; electrical storage; other innovations, technologies or applications

Thermal Components, Systems and Applications

3. **Solar Thermal Power**
   - CSP; thermal storage; other innovations, technologies or applications
4. **Renewable and Efficient Heating and Cooling Systems**
   - renewable heating and cooling; solar energy and heat pumps; innovative industrial process heat; innovative district heating and cooling; thermal storage; other innovations, technologies or applications

Cross Cutting Subjects

5. **Grid Integration and Sector Coupling**
   - smart grids; grid stabilization; storage technology for grid flexibility and stabilization; other innovations, technologies or applications
6. **Solar Buildings and Urban and Neighborhood Design**
   - daylighting; almost zero energy buildings; energetic renovation of buildings; energy supply for neigbourhoods and cities; other innovations, technologies or applications
7. **Rural Energy Supply**
   - solar food processing; solar cooking; solar energy access and applications
8. **System Analysis**
   - system modelling; artificial Intelligence; digitalization
9. **Testing, Certification and Monitoring**
   - electrical systems; thermal systems; other innovations, technologies or applications
10. **Circular Economy, Recycling**
    - towards net -zero manufacturing practices; other innovations, technologies or applications
11. **Solar Resource Assessment and Energy Meteorology**
12. **Perspectives for a 100% Renewable Energy World**
    - renewable energy education; solar energy and climate resilience; workforce development and jobs in renewable energy; solar history; renewable energy strategies, scenarios, financing and policies
13. **Solar Photocatalysis and Solar Fuel Production**
    - green hydrogen; green ammonia; hydrocarbon compounds and others

Partners

In cooperation with

INTERNATIONAL SOLAR ALLIANCE

Knowledge partner

SHAKTI SUSTAINABLE ENERGY FOUNDATION

Country partner

SESI
Solar Energy Society of India
Estd.1978

With support from the UNDP

UNDP

With support from Elsevier

NON SOLUS
ELSEVIER

Supporters

GOVERNMENT OF INDIA
MINISTRY OF NEW AND RENEWABLE ENERGY

NSEFI
MAKING SOLAR ENERGY AFFORDABLE

igef
Indo-German Energy Forum Support Office

SHC
SOLAR HEATING & COOLING PROGRAMME
INTERNATIONAL ENERGY AGENCY

GWNET
Global Women's Network for the Energy Transition

TotalEnergies

SCI
SOLAR COOKERS INTERNATIONAL

SOLAR POWER DEVELOPERS ASSOCIATION

SEIAPI
Sustainable Energy

ABENS

MESol
Rede Brasileira de Mulheres na Energia Solar

ASES SOLAR 2023
Transforming the Energy Landscape for All
August 8-11, 2023
University of Colorado, Boulder

ICLEI
Local Governments for Sustainability

ISREE

WORLD BIOENERGY ASSOCIATION

POWER FOR ALL

CRES

solarthermalworld.org

STFI
SOLAR THERMAL FEDERATION OF INDIA

SOLAR TODAY

SNEC ES+
ENERGY STORAGE CONFERENCE & EXHIBITION

pv magazine group

Renewable Energy India Expo
17th edition
3 4 5 OCTOBER 2024
India Expo Centre, Greater Noida

OFF-GRID Expo + Conference

informa markets

17th Edition
EMEA • ASIA-PAC • LATAM
MICROGRID GLOBAL INNOVATION FORUM
SEPTEMBER 26-27, 2023 • LONDON

Scientific Program

01. PV Cell Technologies

02. Innovative Application of PV Technologies

03. Solar Thermal Power

04. Renewable and Efficient Heating and Cooling Systems

05. Grid Integration and Sector Coupling

06. Solar Buildings, Urban and Neighborhood Design

07. Rural Energy Supply

08. System Analysis

09. Testing, Certification and Monitoring

10. Circular Economy, Recycling

11. Solar Resource Assessment and Energy Meteorology

12. Perspectives for a 100% Renewable Energy World

13. Solar Photocatalysis and Solar Fuel Production

14. Solar Energy Advances: SWC 2023 Select Papers

11. Solar Resource Assessment and Energy Meteorology

12. Perspectives for a 100% Renewable Energy World

01. PV Cell Technologies

Absorption Depth Profile of Silicon Substrate in the Presence of Copper Nanoparticles: A Study on Simulation and Fabrication Thereof

Mohammad Kamal Hossain[1]

[1]Interdisciplinary Research Center for Renewable Energy and Power Systems (IRC-REPS), Research Institute, King Fahd University of Petroleum & Minerals (KFUPM), Dhahran 31261, (Kingdom of Saudi Arabia)

Abstract

Copper nanoparticles have attracted interest in the field of solar cells due to their potential for improving light absorption, plasmonic effects, cost-effectiveness, non-toxicity, and simplicity of production and integration. In this context, simulative prediction of such system facilitates efficient device fabrication. In this work, finite-difference time-domain (FDTD) analysis was carried out to understand the influence of copper nanoparticles within silicon (Si) substrate. An FDTD model, "Copper nanoparticles array as 3×3 on c-Si slab" was developed and absorption depth profiles were extracted at several incident wavelengths of solar spectrum for different interparticle gaps of copper nanoparticle array. It was noted that absorption distribution within Si substrate depended on incident wavelengths of solar spectrum as well as distribution of copper nanoparticles. To realize the results obtained in FDTD simulation, a simple strategy was devised to fabricate copper nanoparticulate using sputtering technique. High resolution field emission scanning electron microscopic (FESEM) images revealed that as-fabricated copper nanoparticles were in the range of 80-100 nm in diameter. FESEM-aided energy dispersion spectroscopy confirmed the elemental composition of the copper nanoparticulate.

Keywords: Copper nanoparticles, FDTD simulation, absorption depth profile, sputtering deposition

1. Introduction

Most of the photovoltaic panels are silicon (Si)-based, although conventional Si-based solar cells are neither cost-effective or efficient enough. However, thin film solar cells, particularly third generation solar cell, have enormous cost-cutting and efficiency-boosting potential (Lee and Ebong, 2017; Abdullah et al., 2019). In this context, down-shifting materials are very promising to convert higher-energy photons such as ultraviolet (UV) photon into lower-energy photons (McKenna and Evans, 2017). The process not only supports the increased photocarriers generation, but also deals with UV protection of the photoactive devices (Gheno et al., 2018). Copper is one of the most commonly utilized materials, as it is simple to acquire both chemically and through physical deposition techniques (Cemin et al., 2016). Copper nanoparticles can improve the light absorption capability of solar cells (Shreya and Varshney, 2021; Jhuang et al., 2021). They can be added to the active layer of a solar cell, such as the bulk heterojunction (BHJ) or the perovskite layer, to boost solar absorption. Copper nanoparticles have plasmonic characteristics that lead to interaction with light at certain wavelengths. This interaction has the potential to increase light trapping and absorption within the solar cell, resulting in higher efficiency (Chen et al., 2021). Copper is a plentiful and relatively inexpensive substance when compared to noble metals such as gold or silver. As a result, copper nanoparticles are an appealing option for improving solar cell performance without considerably raising production costs (Shaikh et al., 2021). Copper is non-toxic, which is advantageous for ecologically friendly solar cell technology. It eliminates worries about the use of harmful compounds in the manufacture of solar cells. Chemical reduction, solvothermal approaches, and solution-based processes can all be used to create copper nanoparticles (Parveen et al., 2016). They can be included into the structure of a solar cell via ink formulations, nanoparticle dispersions, or thin film deposition processes.

10.18086/swc.2023.01.03 Available at http://proceedings.ises.org

In this study, a finite difference time domain model "Copper nanoparticles arrayed as 3×3 on c-Si slab" was used to understand the photon absorption within the Si layer. Although several incident solar spectrum wavelengths were employed throughout the simulations, three specific wavelengths were in focus: one in the near UV (400 nm), one in the visible range (800 nm), and another in the near IR (i.e. 1100 nm). A simple strategy was devised to fabricate copper nanoparticles using sputtering technique followed by further treatment. Topographic and elemental confirmation were carried out using high resolution field emission scanning electron microscope (FESEM) and FESEM-aided energy dispersion spectroscopy (EDS) respectively.

2. Method and experimental

A typical thin film solar cell illustrating possible inclusion of functional nanoparticulate has been shown in Fig. 1a. To realize the concept, it was inevitable to fabricate Cu nanoparticulate as an initial layer. A one step process has been devised in this work as mentioned in Fig. 1b. Fig. 1b represents a freehand schematic demonstrating steps involved in fabricating copper nanoparticulate. Copper target of 2 inch in diameter (99.99% purity) were purchased from ACI alloy, Inc. and used as received without any further treatment. The chamber base pressure and working pressures were kept about 1.7×10-5 torr and 2.8×10-3 torr, respectively in Ar flow rate of 30 SCCM. The deposition power was maintained at 30 W and an in-built thickness monitor was set to 50 nm. Afterward, the deposited films were annealed in a tube furnace (model MTI Corporation OTF-1200X) at 600 °C for 2 hrs with a heating rate of 20 °C/min. This is to be understood that here in this work, an attempt has been taken to fabricate copper nanoparticulate that can be further utilized as initial layer in thin film solar cell design. An FDTD simulation tool (Lumerical Solution, ver 8.6) was utilized to extract absorption depth profiles at different wavelengths of solar spectrum for different interparticle gaps as shown in Fig. 1c. The choice of nanoparticle size in FDTD simulation, i.e. 100 nm in diameter was based on FESEM confirmation. Although several incident wavelengths of solar spectrum were used for interparticle gaps of 0, 1 and 3 nm, three specific wavelengths of solar spectrum 400, 800 and 1100 nm were chosen as demonstrated in the later part of the text.

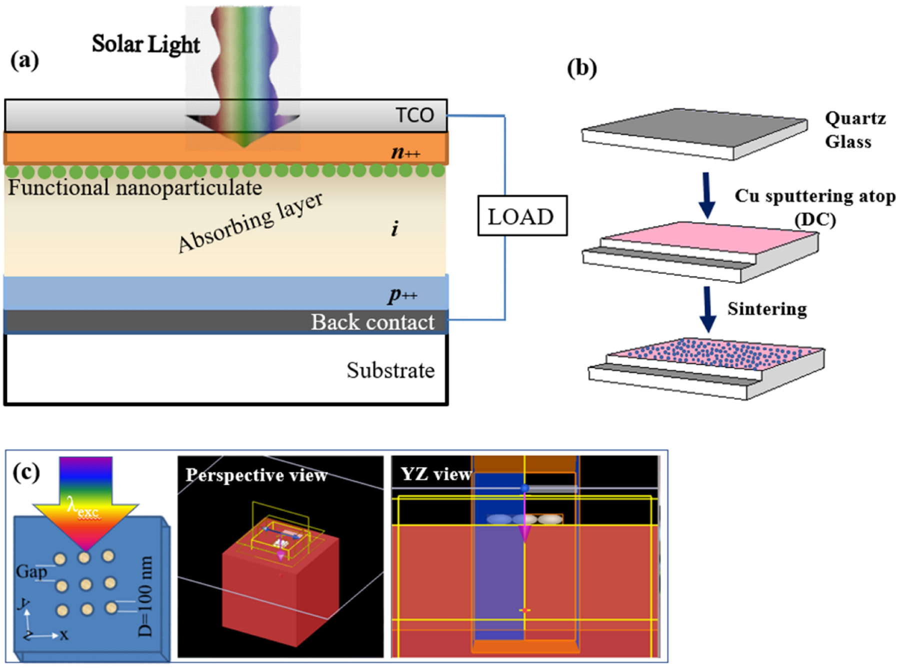

Fig. 1: (a) A tyypical thin film solar cell illustrating possible inclusion of functional nanoparticulate, (b) Free-hand schematic showing the mechanism adopted in this investigation to achieve Cu nanoparticulate to be included within thin film solar cell design and (c) FDTD model used in simulation; left-pane: free-hand schematic, middle-pane: perspective view and right-pane: YZ view showing the position of monitors.

3. Results and discussion

Understanding and adjusting solar cell absorption depth profiles is critical for reaching high conversion efficiencies. Continuous efforts are made to investigate innovative materials, device designs, and light trapping technologies in order to increase light absorption and overall performance of solar cells. The depth at which light is absorbed inside the active layer of a solar cell is referred to as the absorption depth profile. It is a critical factor that influences the overall efficiency and performance of the solar cell. Figure 2a–c show absorption depth profiles of interacting copper nanoparticles array at incident solar wavelengths of 400, 800 and 1100 nm respectively along with maximum and average power. It is noteworthy that at lower incident wavelength of solar spectrum (e.g. 400 nm), underneath Si was found more affected whereas at longer wavelengths such as 800 and 1100 nm lower absorption depth profiles were observed. In this context, zoon-in views of the absorption depth profile within Si were extracted and were shown in corresponding insets. In the case of shorter wavelength such as at 400 nm of solar wavelength, more than half of the active layer that is just below the Cu nanoparticulate was found to be enhanced. However for longer wavelengths such as at 800 and 1100 nm of solar wavelength most of the underneath Si was moderately enhanced. Absorption depth profiles for interparticle gaps of 1 and 3 nm have been extracted at 400, 800 and 1100 nm of incident wavelengths. To the extend, maximum absorption power and average power have been recorded for interparticle gaps of 0, 1 and 3 nm at 400, 800 and 1100 nm of incident wavelengths of solar spectrum.

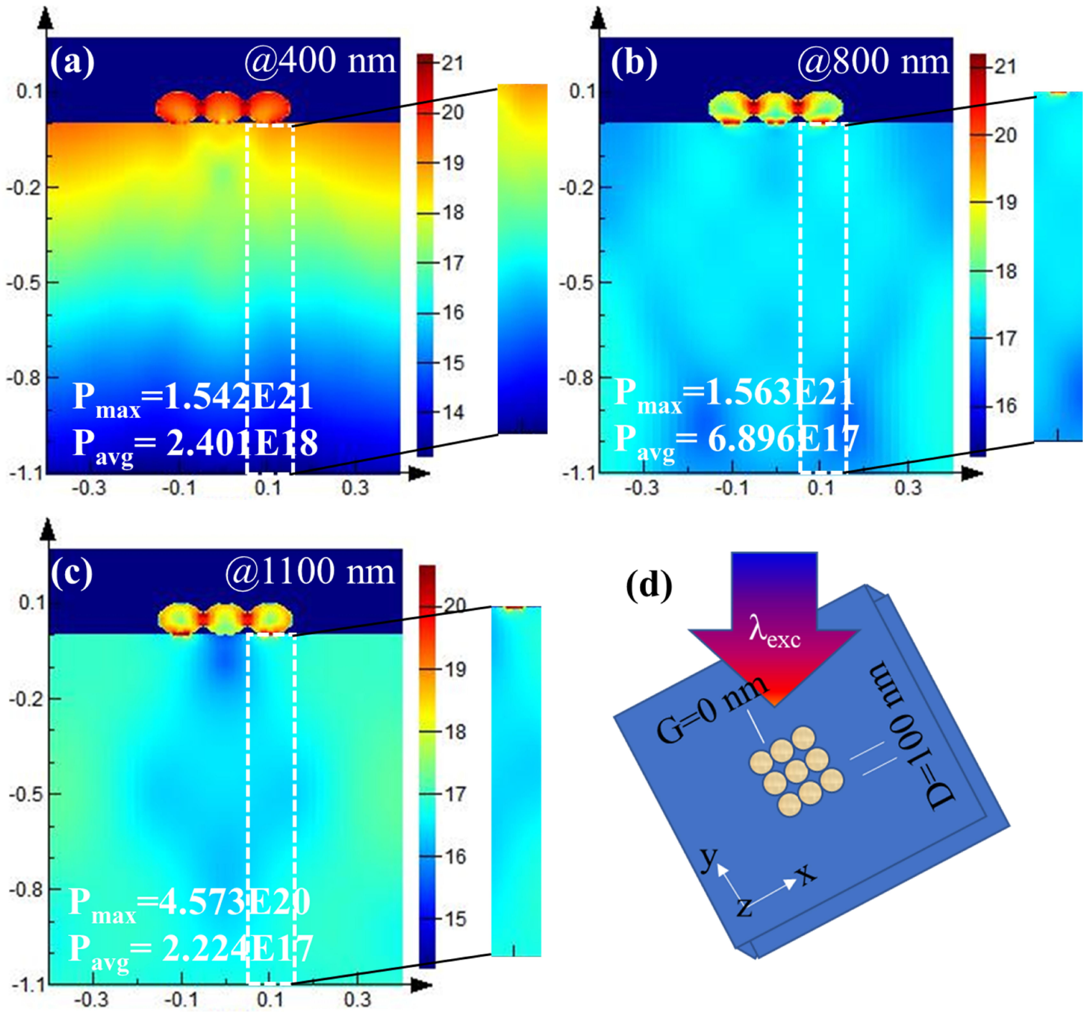

Fig. 2: (a)-(c) Absorption depth profile of interacting copper nanoparticles array at 400, 800 and 1100 nm respectively and (d) free-hand schematic to represent model geometry (not to the scale) used in FDTD simulation. Corresponding color bar represents the absorption intensity in log scale.

Apart from improved absorption and energy quenching, the nanoparticulate interparticle gap has a significant effect on plasmon coupling driven properties. When nanoparticles are close together, the plasmon resonances of surrounding particles may be tuned to meet specific demands. The specific impact is determined on the nanoparticles' size and shape, as well as the interparticle spacing. A decreased interparticle gap results in increased light absorption at shallower depths as shown in Fig. 2a-c.

Figure 3a–c show absorption depth profiles of copper nanoparticles array of 1 nm interparticle gap along with maximum and average power at incident solar wavelengths of 400, 800 and 1100 nm respectively. One can notice that at lower incident wavelength of solar spectrum, underneath Si was found more affected whereas at longer wavelengths such as 800 and 1100 nm lower absorption depth profiles were observed. Similar to interacting Cu nanoparticle array, at shorter wavelength, more than half of the active layer was found to be influenced as displayed in Fig. 3a. However, the majority of the underneath Si was only slightly improved for longer wavelengths, such as at solar wavelengths of 800 and 1100 nm as shown in Fig. 3c and Fig. 3d. In this regards, zoon-in views of the absorption depth profile within Si were extracted and were shown in corresponding insets.

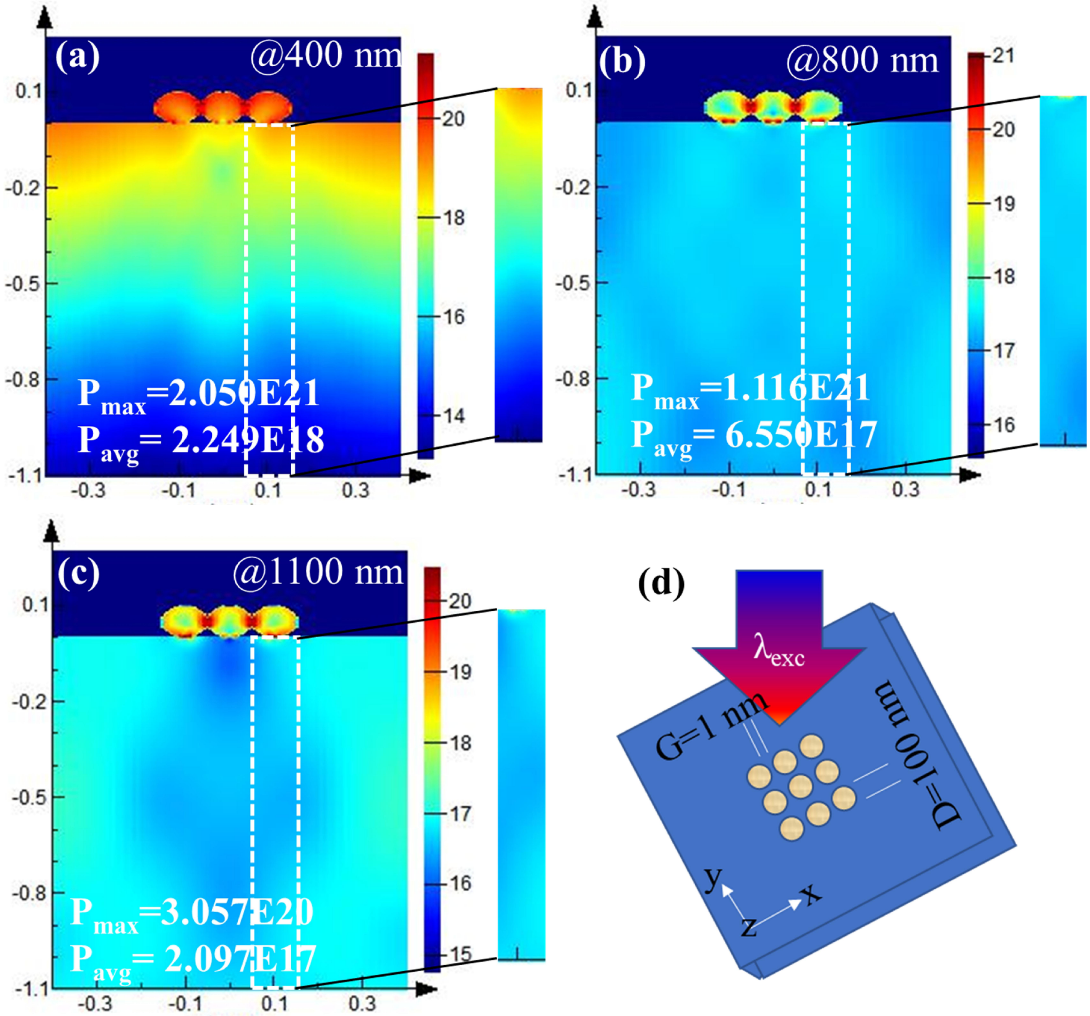

Fig. 3: (a)-(c) Absorption depth profile of copper nanoparticles array of 1 nm interparticle gap at 400, 800 and 1100 nm respectively and (d) free-hand schematic to represent model geometry (not to the scale) used in FDTD simulation. Corresponding color bar represents the absorption intensity in log scale.

In the case of higher interparticle gaps, the absorption depth profile distributions started to change within Si active substrate place to place. Figure 4a–c show absorption depth profiles of copper nanoparticles array of 3 nm interparticle gap along with maximum and average power at incident solar wavelengths of 400, 800 and 1100 nm respectively. At shorter wavelength of solar spectrum, underneath Si was found more or less similar to those obtained at interacting and closely packed Cu nanoparticles array. However, at longer wavelengths such as 800 and 1100 nm lower absorption depth profiles were observed to be spread throughout the underneath layer. Zoon-in views of the absorption depth profile within Si as shown in corresponding insets represent the scenario. The effect of interparticle gap on the absorption depth profile of nanoparticles is a complex phenomenon that depends on the size, shape, and arrangement of the nanoparticles. The interparticle gap can influence the plasmon resonances, leading to changes in the absorption spectrum and depth profile.

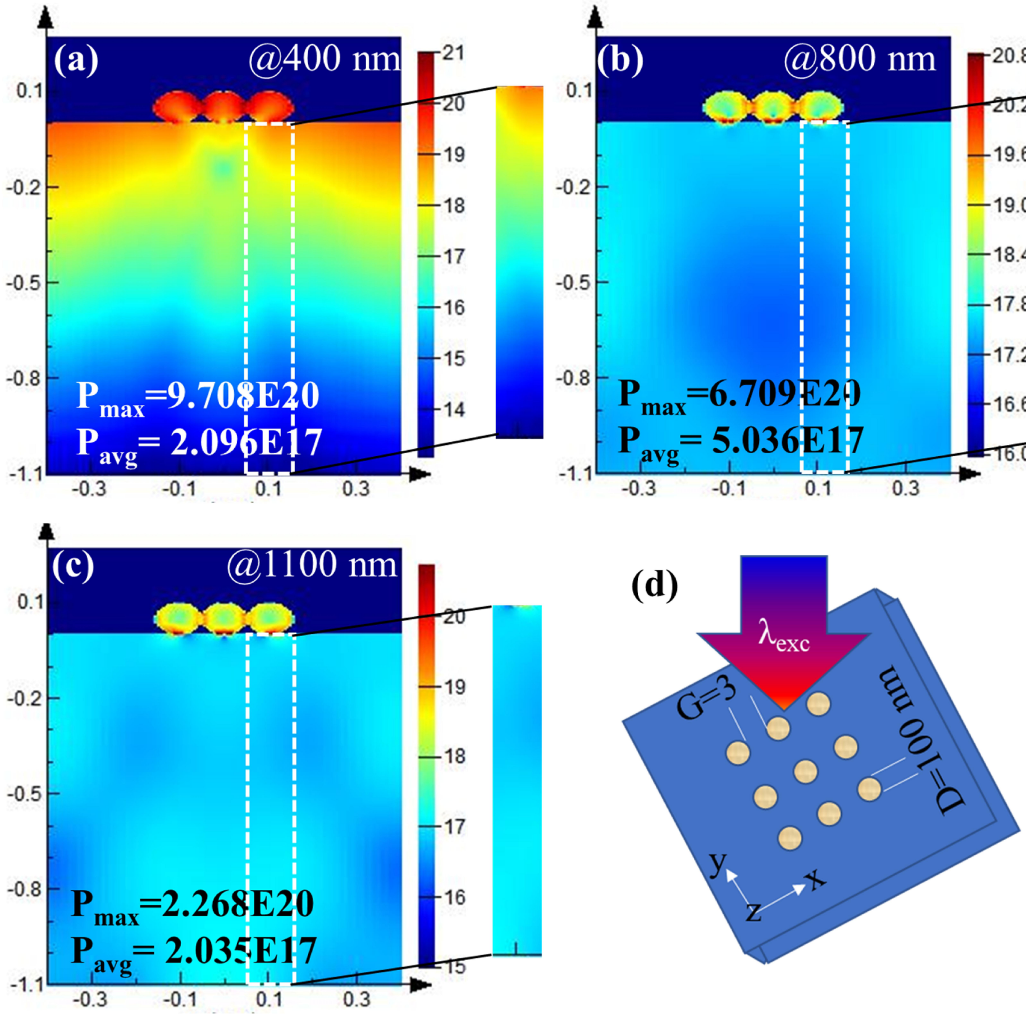

Fig. 4: (a)-(c) Absorption depth profile of copper nanoparticles array of 3 nm interparticle gap at 400, 800 and 1100 nm respectively and (d) free-hand schematic to represent model geometry (not to the scale) used in FDTD simulation. Corresponding color bar represents the absorption intensity in log scale.

An attempt was taken to fabricate copper nanoparticles as shown in Fig. 5a. Such multifunctional layer can be integrated in substrate and superstrate type thin film solar cell as explained in previous study (Hossain and Mukhaimer, 2020). A high resolution FESEM micrograph of copper nanoparticulate was shown in Fig. 5b. Inset (i) of Fig. 2b reconfirmed an average diameter of copper nanoparticles of ca. 80 nm. SEM-aided EDS was carried out to confirm elemental composition of the film as shown in inset (ii) of Fig. 5b.

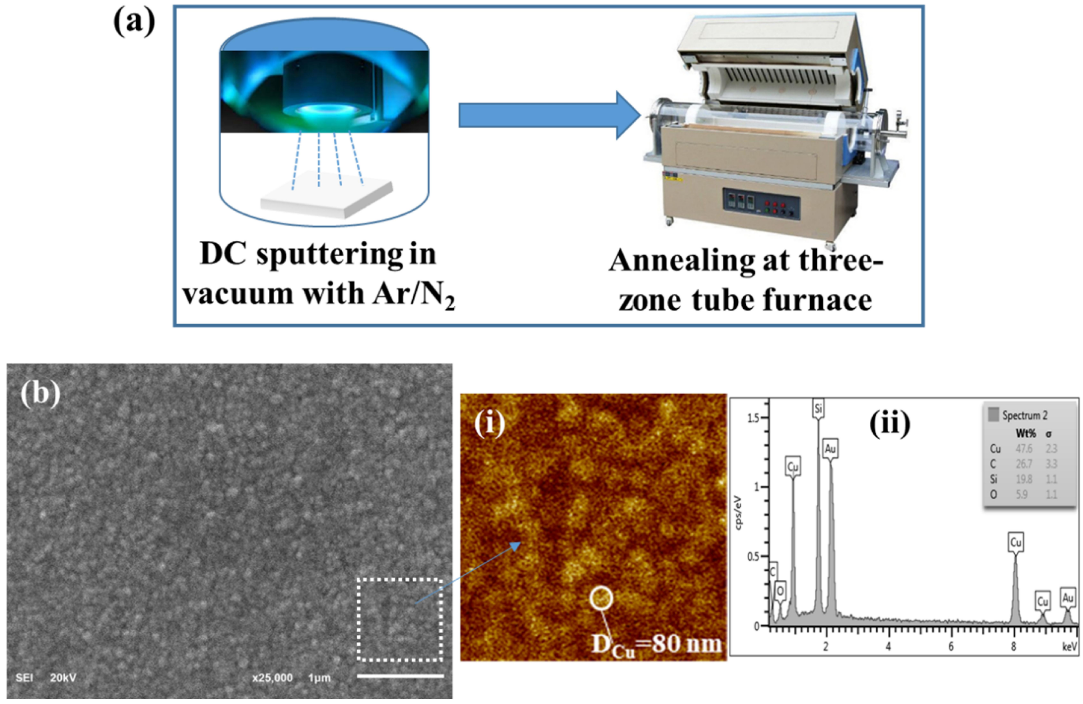

Fig. 5: (a) Free-hand schematic of thin film growth using sputtering technique and subsequent treatment and (b) FESEM micrograph of copper cluster fabricated on glass; inset (i): Zoom-in view of a selected area (1 µm × 1 µm) as marked by the white dashed square in Fig. 2b and inset (ii): SEM-aided EDS measurement of the same nanoparticulate.

4. Conclusion

FDTD simulation for a model “Copper arrays on c-Si slab” showed that absorption profile of the underneath Si subtracted get affected and depend highly on the incident wavelengths of solar spectrum as well as interparticle gaps of copper array. At lower incident wavelength of solar spectrum (e.g. 400 nm), absorption distributions were more intense in Si whereas at longer wavelengths such as 800 and 1100 nm lower absorption depth profiles were observed. When particles are near together, they interact and generate scattering and interference effects. These influences modify the path of light and hence the absorption depth profile distribution. The fact was further demonstrated by varying the interparticle gaps from 0, 1 to 3 nm of the model geometry “Copper arrays on c-Si slab”. To realize the potential of such copper nanoparticles in thin film solar cell, an attempt was taken to fabricate copper nanoparticulate in such a way so that the layer can be utilize further to be considered as an initial layer in thin film solar cell design. FESEM image confirmed the diameter of as-fabricated copper nanoparticles in the range of 80-100 nm.

5. Acknowledgement

Author thanks Interdisciplinary Center for Renewable Energy and Power systems (IRC-REPS), Research Institute, King Fahd university of Petroleum and minerals (KFUPM), Dhahran 31261, Saudi Arabia and acknowledge the support received under IRC-REPS Grant INRE2318.

6. References

Abdullah, M.R., Harun, N.H., Ibrahim, S.N., Wahab, A.A. 2019. Thin film coating of copper nanoparticles with DC magnetron sputtering via physical vapor deposition. In AIP Conference Proceedings (Vol. 2129, No. 1, p. 020120). AIP Publishing LLC.

Cemin, F., Lundin, D., Cammilleri, D., Maroutian, T., Lecoeur, P., Minea, T., 2016.Low electrical resistivity in thin and ultrathin copper layers grown by high power impulse magnetron sputtering. J. Vac. Sci. A 34(5), 051506.

Chen, W.J., Lin, Y.C., Kumar, G., Xie, S.Y., Chen, F.C., 2021. Polymer-capped copper nanoparticles trigger plasmonic field for improving performance of perovskite solar cells. Synthetic Metals, 273, 116675.

Gheno, A., Trigaud, T., Bouclé, J., Audebert, P., Ratier, B., Vedraine, S., 2018. Stability assessments on luminescent down-shifting molecules for UV-protection of perovskite solar cells. Opt. Mater. 75, 781-786.

Hossain, M.K., Mukhaimer, A.W., 2020. Nanoparticles-decorated silicon absorber: Absorption depth profile characteristics within absorbing layer. Sol. Energy, 204, 552-560.

Jhuang, L.S., Kumar, G., Chen, F.C., 2021. Localized surface plasmon resonance of copper nanoparticles improves the performance of quasi-two-dimensional perovskite light-emitting diodes. Dyes and Pigments, 188, 109204.

Lee, T.D., Ebong, A.U., 2017. A review of thin film solar cell technologies and challenges. Renewable Sustainable Energy Rev. 70, 1286-1297.

McKenna, B., Evans, R.C. 2017. Towards efficient spectral converters through materials design for luminescent solar devices. Adv. Mater. 29(28), 1606491.

Parveen, F., Sannakki, B., Mandke, M.V., Pathan, H.M., 2016. Copper nanoparticles: Synthesis methods and its light harvesting performance. Solar Energy Materials and Solar Cells, 144, 371-382.

Shaikh, J.S., Shaikh, N.S., Mishra, Y.K., Kanjanaboos, P., Shewale, P.M., Sabale, S., Praserthdam, S., Lokhande, C.D., 2021. Low-cost Cu-based inorganic hole transporting materials in perovskite solar cells: Recent progress and state-of-art developments. Materials Today Chemistry, 20, 100427.

Shreya, S., Varshney, A. 2021.Solar absorbance enhancement in perovskite solar cells with the inclusion of copper nanoparticles: an architectural study. Optical and Quantum Electronics 53: 1-11.

Analysis of Reverse Stress in Potential Induced Degradation Affected PV Module Under Partial Shading Conditions

Asokan S[1], Vishal E. Puranik[1], Ravi Kumar[1], and Rajesh Gupta[1]

[1]Department of Energy Science and Engineering

Indian Institute of Technology Bombay, Mumbai (India)

Abstract

Potential induced degradation (PID) is a detrimental failure mechanism that has gained greater attention in medium and large-scale photovoltaic (PV) plants in a recent decade. PID reduces shunt resistance and increases the recombination diode's reverse saturation current. As a direct consequence, the efficiency of PID affected module experiences a substantial decline, often leading to module failure well before their expected operational lifespan. Further, when a PID affected cell of a module is partially or entirely shaded, reverse stress is observed across the shaded PID cell, which ultimately affects the module's reliability. This paper presents an analysis of the reverse stress across the shaded cell encountered in PID affected PV module under partial shading conditions. The findings suggest that the high reverse current flows through the PID affected cell under partial shading conditions as compared to partially shaded healthy cell. The reverse stress current across the shaded cell depends on the value of its shunt resistance. By understanding the impact of reverse stress on PID affected modules, further degradation of PV modules can be prevented, improving the performance and overall efficiency of the PV system.

Keywords: Potential induced degradation (PID), Partial shading, Reverse stress, Reliability

1. Introduction

The crystalline silicon (c-Si) solar cell is one of the widespread photovoltaic (PV) technology used worldwide for commercial applications. PV modules are supposed to work in the field for at least 25-30 years. Therefore, ensuring the reliability of photovoltaic systems is a concern for the PV community. However, in the field, PV modules are exposed to a wide range of environmental conditions that can lead to different defects and degradation, which affects the performance and reliability of PV modules (Sharma and Chandel, 2013). Common field defects and degradations reported in PV modules include corrosion, delamination, discoloration, breakages, cracks, hot spots, light induced degradation (LID), light and elevated temperature induced degradation (LeTID) and potential induced degradation (PID) (Roy, Kumar and Gupta, 2019)(Luo *et al.*, 2017). PID is a severe degradation mechanism, observed in medium and large PV system due to high system voltages. It significantly increases module degradation rates and losses in a PV system, making it one of the most critical issues in medium and large-scale PV plants. It can advance rapidly in a PV module during its initial years after installation, with a degradation rate that can be as high as 4% per year (Puranik and Gupta, 2022). PID reduces the shunt resistance (R_{sh}) and increases the reverse saturation current of the recombination diode (Kumar, Puranik and Gupta, 2023). Low shunt resistance significantly impact performance and reliability of PV module, especially under low irradiance or partial shading conditions (Barbato *et al.*, 2014, Braisaz and Radouane, 2014).

Under partial shading condition, reverse current flows through the shunt resistance of the reverse stressed shaded cell. The amount of reverse current depends on the value of the R_{sh}, amount of shading on the cell and the string current in the module (Arekar, Puranik and Gupta, 2021). Partial shading can occur due to surrounding poles, bird droppings, leaves, dirt, building towers, and trees. PV system is highly susceptible to partial shading (Teo *et al.*, 2018). A distinct correlation between the shunt resistance and the slope of the shaded cell's reverse I-V curve has been proposed in the literature (Meyer and Van Dyk, 2005). A bypass diode is used in PV module across a string to prevent highly degraded reverse stress condition i.e., hotspot. Even in the presence of bypass diode, a hotspot condition can occur if the shunt resistance of the shaded cell is sufficiently low. Under such circumstances, the PV cell may attain a temperature that can cause permanent

10.18086/swc.2023.01.01 Available at http://proceedings.ises.org

damage due to hotspot heating. This severely affect the reliability of the module (Rossi *et al.*, 2015). Therefore, it is crucial to investigate PID affected module under partial shading conditions.

This paper aims to investigate the reverse stress conditions across a PID affected cell with different extent of PID under partial shading conditions. In PSpice simulations, reverse stress current, voltage, and power dissipation are calculated at different levels of PID by adjusting the shunt resistance and photogenerated current. Same has been validated using experimentations.

The article is organized as follow: section 2 presents the approach used in this investigation, section 3 presents and discusses the results obtained and finally section 4 concludes the article.

2. Approach

Experimentation, modelling, and simulation were performed to investigate the reverse stress experienced by the PID module under shading. The solar module (Make: Sun solar, 7.5W, mc-Si based on Al- BSF technology) was used for the PID test. Initially, in order to observe existing defects, the module was characterized before the PID generation by using IV characterization and electroluminescence (EL) imaging.

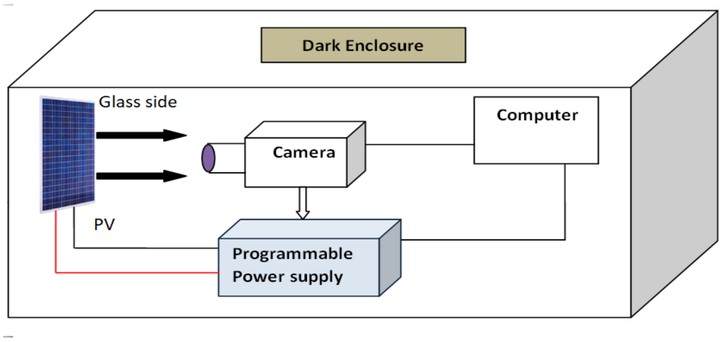

Fig. 1: Electroluminescence (EL) imaging Setup

A solar simulator has been used for the IV analysis part (make: Autosys, Model: SMT-INV 2011SF Class: BAA). The measurements were performed in accordance with standard test conditions (STC) of AM 1.5G, 1000 W/m^2 and 25 °C. It provides the performance parameters i.e., maximum output power (P_{max}), short circuit current (I_{sc}), and open circuit voltage (V_{oc}). Subsequently, for the purpose of localizing and conducting a spatial analysis of cells within PV modules, EL imaging was performed. The EL imaging setup is shown in Fig. 1. In the imaging setup, an EL camera (Make: Greateyes Gmbh) has been used. The system is equipped with a silicon-based charge-coupled device (Si-CCD) having a resolution of 1024×1024 pixels, which proves adequate for the spatial analysis required for the PID test in this study. The camera has been connected to an externally programmed power supply (TDK-Lambda, GEN150–10) for biasing the modules. The EL operation is controlled by a monitoring PC. The entire setup is enclosed within a dark chamber to minimize the impact of stray light, and the chamber's temperature is maintained at a constant 25 °C to ensure consistent measurement conditions. In the absence of light, the PV cell undergoes electrical excitation, with the EL current being less than or equal to the short-circuit current (I_{sc}). As a consequence, the cell emits an EL signal due to band-to-band radiative recombination occurring within the bulk region (Roy and Gupta, 2019).

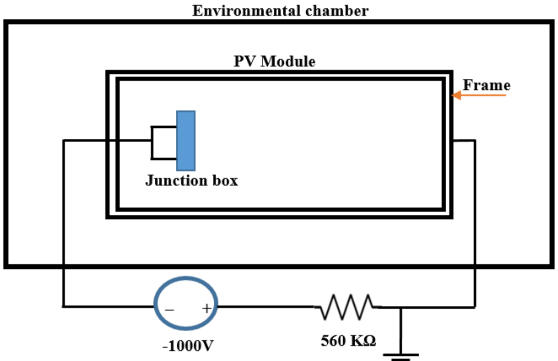

Fig. 2: Schematic diagram of PID test setup

Following the initial phases of IV characterization and EL imaging, an accelerated PID test was conducted in a controlled environmental chamber (Manufactured by REMI Instruments). Under PID testing the modules was subjected PID accelerated testing conditions (-1000 V, 60°C, 85% RH) lasting for 96 hours. PID test setup is shown in Fig. 2. EL images and IV characteristics of the PV module pre and post PID testing are shown in Fig. 3 (a), (b) and (c). Moreover, for a holistic view of the module's performance, a detailed comparison of its parameters before and after the PID test is provided in Tab 1.

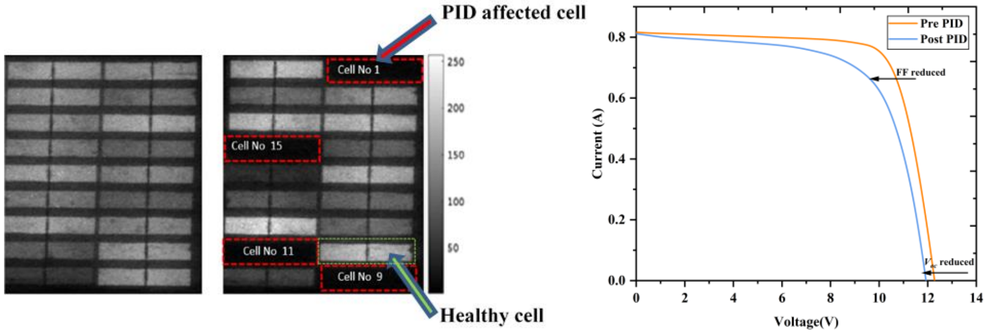

(a) (b) (c)

Fig. 3: EL images of the module (a) pre PID (b) post PID (c) pre and post PID I-V characteristics of the module

Tab.1. Module specifications pre PID and post PID

Status	**(V_{oc})**	**(I_{sc})**	**(P_m)**	**(V_m)**	**(I_m)**	**FF**
pre PID	12.27	0.81	7.54	10.05	0.75	0.76
post PID	11.9	0.81	6.35	9.49	0.67	0.66

From Tab. 1, it can be observed that PID results in a reduction in the fill factor (FF) and open circuit voltage (V_{oc}) of the PV module. The IV characteristics of solar cells, when measured under both dark and illuminated conditions, serve as a crucial tool for evaluating their performance. Therefore, destructive analysis was conducted to perform dark I-V characterization, which enable the extraction of seven parameters of the double diode model (DDM) for each cell. The DDM of a PV cell is generally used for either higher accuracy or modelling shunt-related defects such as PID (Ishaque, Salam and Taheri, 2011), as shown in Fig .3. In this context, the variables are defined as follows: I_{ph} represents the light-generated current, while I_{01}, I_{02}, n_1, and n_2 represent the saturation current and ideality factors of the bulk diode (D_1) and recombination diode (D_2), respectively. R_s and R_{sh} denote the series and shunt resistance of a PV cell.

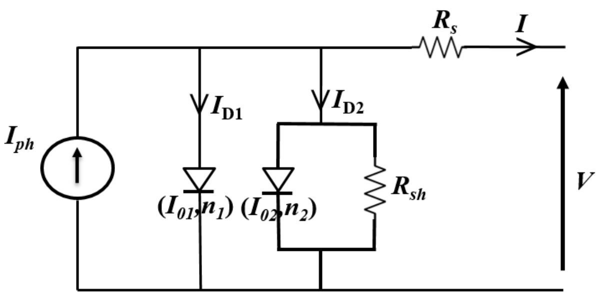

Fig. 4: Double diode model of a PV cell

$$I = I_{ph} - I_{01}\left[\exp\left(\frac{V+IR_S}{n_1 V_t} - 1\right)\right] - I_{02}\left[\exp\left(\frac{V+IR_S}{n_2 V_t} - 1\right)\right] - \frac{V+IR_S}{R_S} \qquad \text{(eq. 1)}$$

Equation 1 shows the current-voltage relation of a PV cell, which contains seven unknown parameters (I_{ph}, I_{01}, I_{02}, n_1, n_2, R_s, R_{sh},), whereas V_t represents the diode thermal voltage. Double diode model simulations have been performed using PSpice, as it is a versatile tool to simulate the electrical and thermal aspects of PV modules (Somasundaran, Sinha and Gupta, 2012). Individual cell power output is determined by PSpice simulations by using parameters extracted using DDM. To confirm cells affected by PID, EL images (Post

PID) are compared with the individual cell power levels. PID-affected cells are identified by their reduced power output, evident from their darker appearance in EL images compared to healthy cells. Using the extracted parameters, impact of shading on both PID-affected and healthy cells are simulated to calculate reverse saturation current, reverse saturation voltage, and power dissipation.

3. Result and Analysis

The power loss of each cell in a PV module is depicted in Fig. 5. It is evident that the PID affect the power output. It is expected that healthy cells or those minimally impacted by PID would exhibit negligible power loss. From Fig. 5, cell no. 12 and cell no. 8 are found to be minimally PID-affected while cell no. 15 and cell no. 11 are found to be highly PID affected cells, showing more significant power losses.

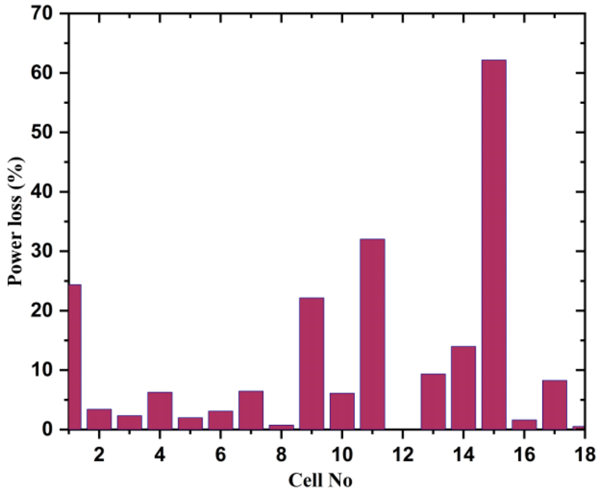

Fig. 5: Cell wise power loss of PID tested PV module

Using the above identified cells, simulations and experiment are carreid out to obtain the reverse stress current, voltage and power dissipation under partial shading condition across the healthy and PID affected.

3.1 Simulation

To analyze the reverse stress across the PID-affected cells, simulations have been performed by changing the R_{sh} and light generated current. Fig. 6(a) illustrates the reverse current, reverse voltage, and power dissipation characteristics of a healthy cell (cell no.12) under varying shading conditions, including complete shading (0 W/m²) and partial shading (200 W/m² and 500 W/m²). For the purpose of comparison, normalised reverse current (Reverse current of R_{sh} of the shaded cell / Current of R_{sh} of healthy cell without shading (nominal value)), normalised reverse voltage (Reverse voltage across R_{sh} of the shaded cell / Voltage across R_{sh} of healthy cell without shading (nominal value)), normalised power dissipation (Power dissipation of R_{sh} of the shaded cell / Power dissipation of R_{sh} of healthy cell without shading (nominal value)) have been considered.

From Fig. 6(a), it is observed that when the healthy cell is completely shaded, the reverse current through the R_{sh} is approximately eight times the nominal value. However, as the cell experiences partial shading (200 W/m² and 500 W/m²), the reverse current begins to decrease. This phenomenon can be attributed to the fact that the healthy cell possesses a substantial resistance. When shaded, the current generated by neighbouring cells starts flowing through the shaded cell, resulting in the observed reverse current in R_{sh}. Although the magnitude of current flowing through the R_{sh} is relatively low, the product of resistance and current leads to significantly elevated power dissipation levels under complete shading conditions. Remarkably, the power dissipation of the shaded cell reaches many times the nominal value when completely shaded. However, as the cell starts receiving irradiance, the reverse current diminishes, subsequently reducing both the normalized voltage and normalized power dissipation. Notably, at 500 W/m², the reverse current, reverse voltage, and power dissipation in the R_{sh} become negligible. To gain further insights, the shading effects on a slightly PID affected cell are investigated. Fig. 6(b) illustrates the shading impact on the reversse stress parameters for the slighlty affected PID cell. Notably, as PID conditions become more severe, the reverse current through the R_{sh} increases.

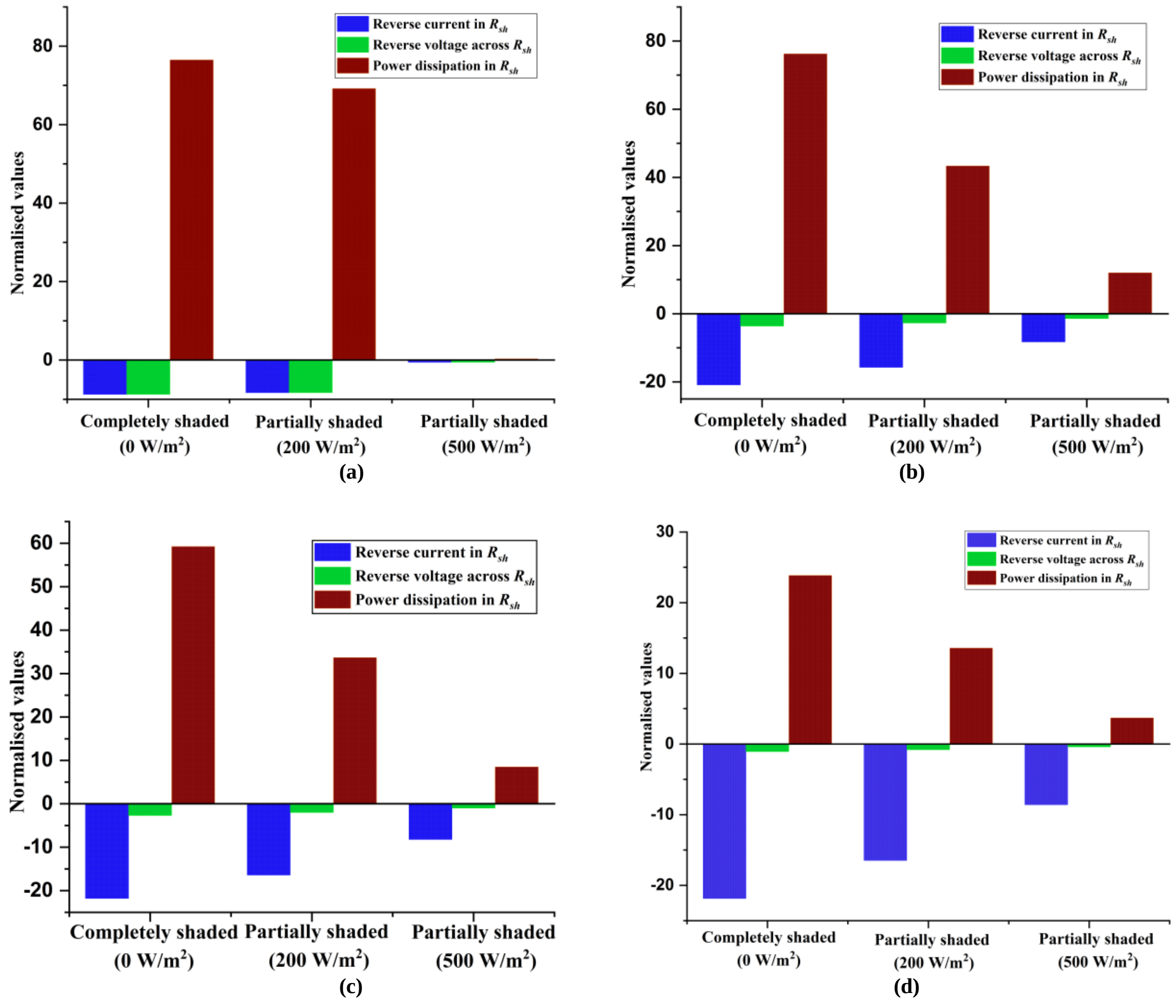

Fig. 6. Variation in reverse current, reverse voltage and power dissipation for (a) Shading on healthy cell, (b) Shading on slightly PID affected cell, (c) Shading on moderately affected PID cell, and (d) Shading on severely affected PID cell.

This phenomenon is attributed to the PID reduction in R_{sh}, causing an elevated current flow through it. Remarkably, the observed current through the R_{sh} is approximately 20 times the nominal value, a significantly higher magnitude compared to shading on a healthy cell. Conversely, the voltage across the R_{sh} experiences a reduction. This decline can be explained by the diminished product of current and resistance. Despite the decrease in voltage, the power dissipation across the shaded cell remains high, comparable to that of a healthy cell. This is because power dissipation is proportional to the square of the current multiplied by the resistance. Furthermore, as shading conditions are reduced, the reverse stresses on the cell also diminish, mirroring the trends observed in shading effects on healthy cells.

To investigate deeper into the effects of shading, a simulation on a moderately PID-affected cell was conducted. Fig. 6(c) provides a visual representation of shading versus normalized values for this moderately PID-affected cell. The observed current through the R_{sh} is approximately 21 times the nominal value, which is notably higher compared to shading on a slightly PID-affected cell. The voltage across the R_{sh} undergoes a reduction due to the decreasing value of R_{sh}. Moreover, as shading conditions decrease, the reverse stresses also decrease, like the trends observed in shading on slightly PID-affected cells. It is evident that the power dissipation in the moderately PID-affected cell is approximately 60 times the nominal value, which is significantly high.

Fig. 6(d) shows the shading effects on a cell severely impacted by PID, which highlights the extreme nature of the PID severity. This very severely PID-affected cell has experienced a complete loss of power due to the extreme severity of PID, resulting in a significant reduction in the R_{sh} value. As a result, there is a substantial surge in the reverse current flowing through the R_{sh}. Notably, Fig. 6(d) demonstrates that the current through the R_{sh} reaches approximately 23 times the nominal value. Simultaneously, the voltage across both the R_{sh} and the cell itself experiences a profound reduction, primarily attributed to the substantial decrease in shunt resistance. As the PID severity intensifies, so does the impact on the cell's electrical characteristics, leading to increasingly adverse effects. It is crucial to highlight that as shading conditions are diminished, the reverse stresses on the cell diminish accordingly; it agrees with the trends observed in shading on severely PID-affected cells. Remarkably, the power dissipation in the severely PID-affected cell decreases to approximately 20 times the nominal value. While this figure remains notably elevated, it represents a significant reduction compared to shading on severely affected PID cells. However, it's essential to emphasize that the high reverse current flowing through R_{sh} can have detrimental consequences for the cell's reliability. When a low R_{sh} cell is shaded, the concentration of high reverse current in a localized area raises the risk of hotspot formation. This underscores the critical importance of addressing and mitigating severe PID effects to preserve the overall reliability and performance of photovoltaic systems.

3.2 Experimental validation:

To validate the simulation results, experimentation has been performed on a PID-affected module. The identified PID cells are shaded by using cardboard, and each cell is accessed through destructive analysis. CRO (Make: Yogowa, Model: DL850E) is connected across each cell, and I-V characterization has been performed.

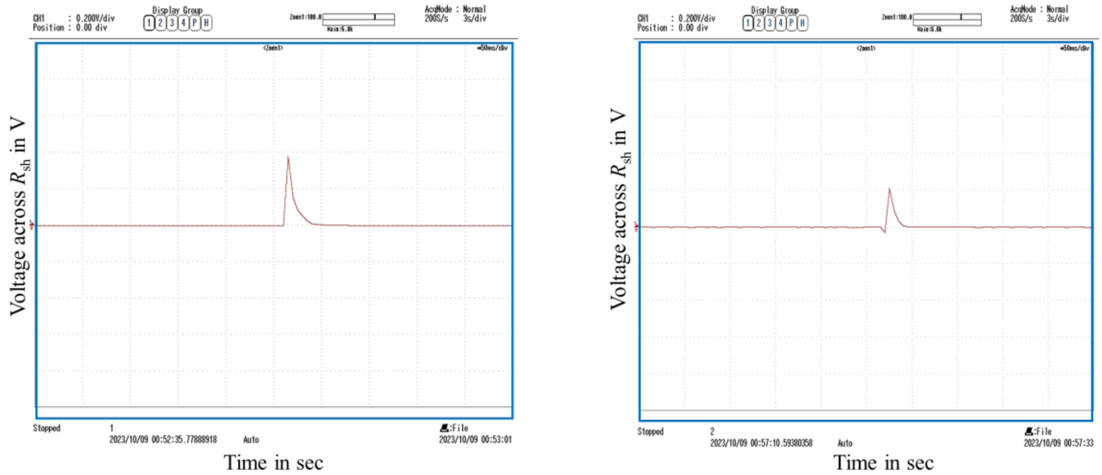

(a) **(b)**

Fig. 7: Voltage across R_{sh} without shading for (a) healthy cell and (b) PID-affected cell

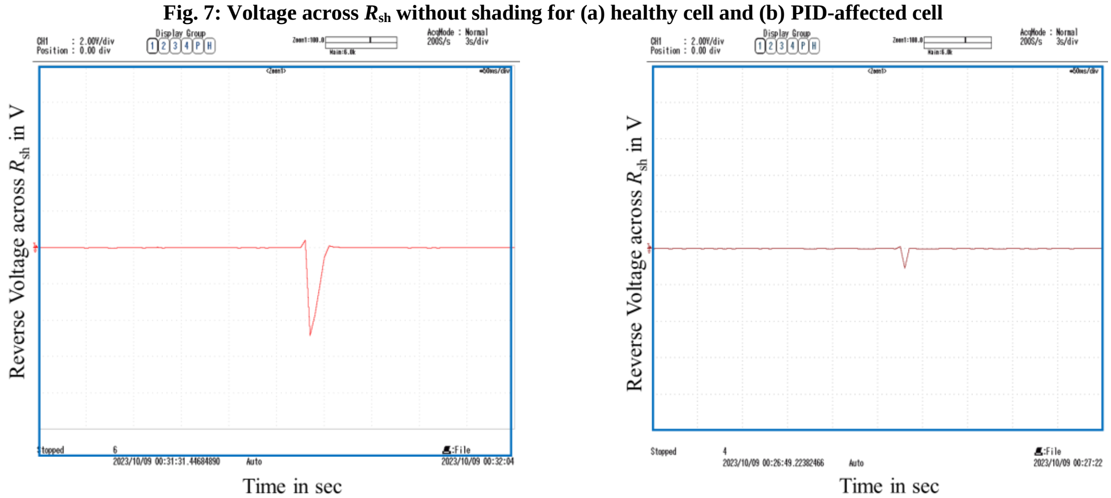

(a) **(b)**

Fig. 8: Reverse voltage across R_{sh} with shading for (a) healthy cell and (b) PID-affected cell

In Fig. 7(a), the voltage across the healthy cell in an unshaded condition is depicted. It is evident that the shunt resistance sinks the current, resulting in a positive voltage across the cell. Similarly, in Fig. 7(b), the voltage across the PID-affected cell without shading is illustrated. Notably, the voltage across the PID-affected cell is lower than that of the healthy cell due to the reduced R_{sh}.

The findings showcased in Fig. 8(a) offer a significant insight into the performance of a healthy cell under shading conditions. From this, the reverse voltage characteristics of a healthy cell when it is fully shaded are observed. Notably, it reveals that the reverse voltage across the healthy cell substantially rises when subjected to shading. This observation serves as a remarkable agreement between the experimental results and the simulated outcomes.

Fig. 8(b) represents the reverse voltage across a severely PID-affected cell when shaded. It can be noted that the reduction in voltage across the R_{sh} for PID affected cell is lower than that of the healthy cell for shaded conditions. This observed reduction in voltage corresponds well with the results obtained from simulation.

4. Conclusion

In this work, impact of PID on reverse stress current, voltage and power dissipation across the partial shaded cell in a PV module is investigated. Reverse stress parameters i.e., current, voltage and power dissipation are calculated for healthy and PID affected PV cells in a PV module using PSpice simulations. The reverse current across the shaded cell increases with PID progression which maximises under completely shaded condition while the reverse voltage and power dissipation across the shaded cell decreases. Reverse voltage trend with PID progression obtained experimentally successully support the simulation results. A high current across the PID affected cell poses a risk of hotspot formation. The value of the reverse current, voltage and power dissipation across the shaded cell depends on the PID severity and amount of shading. The obtained results provide a valuable insights into the behaviour of PID affected PV cells under partial shading conditions.

5. References

Arekar, K., Puranik, V. E. and Gupta, R. (2021) ‘Performance Analysis of PID Affected Crystalline Silicon PV Module under Partial Shading Condition’, *Conference Record of the IEEE Photovoltaic Specialists Conference*, pp. 2415–2420. doi: 10.1109/PVSC43889.2021.9518533.

Barbato, M. *et al.* (2014) ‘Influence of shunt resistance on the performance of an illuminated string of solar cells: Theory, simulation, and experimental analysis’, *IEEE Transactions on Device and Materials Reliability*, 14(4), pp. 942–950. doi: 10.1109/TDMR.2014.2347138.

Braisaz, B. and Radouane, K. (2014) ‘PID results at low irradiances on c-Si modules’, *2014 IEEE 40th Photovoltaic Specialist Conference, PVSC 2014*, pp. 1993–1996. doi: 10.1109/PVSC.2014.6925316.

Guechi, A., Chegaar, M. and Aillerie, M. (2012) ‘Environmental effects on the performance of nanocrystalline silicon solar cells’, *Energy Procedia*, 18(1), pp. 1611–1623. doi: 10.1016/j.egypro.2012.06.001.

Ishaque, K. *et al.* (2011) ‘Modeling and simulation of photovoltaic (PV) system during partial shading based on a two-diode model’, *Simulation Modelling Practice and Theory*, 19(7), pp. 1613–1626. doi: 10.1016/j.simpat.2011.04.005.

Ishaque, K., Salam, Z. and Taheri, H. (2011) ‘Simple, fast and accurate two-diode model for photovoltaic modules’, *Solar Energy Materials and Solar Cells*, 95(2), pp. 586–594. doi: 10.1016/j.solmat.2010.09.023.

Kumar, R., Puranik, V. E. and Gupta, R. (2023) ‘Application of Infrared Thermography for Cell-Level Power Estimation of PID-s Impacted Crystalline Silicon PV Module’, *IEEE Journal of Photovoltaics*, 13(1), pp. 141–149. doi: 10.1109/JPHOTOV.2022.3229485.

Luo, W. *et al.* (2017) ‘Potential-induced degradation in photovoltaic modules: A critical review’, *Energy and Environmental Science*, 10(1), pp. 43–68. doi: 10.1039/c6ee02271e.

Meyer, E. L. and Van Dyk, E. E. (2005) ‘The effect of reduced shunt resistance and shading on photovoltaic module performance’, *Conference Record of the IEEE Photovoltaic Specialists Conference*, pp. 1331–1334. doi: 10.1109/pvsc.2005.1488387.

Puranik, V. E. and Gupta, R. (2021) ‘Novel Quantitative Electroluminescence Method for Detailed Performance Analysis of PID-s Affected Crystalline Silicon PV Module’, *IEEE Journal of Photovoltaics*, 11(6), pp. 1470–1478. doi: 10.1109/JPHOTOV.2021.3108764.

Puranik, V. E. and Gupta, R. (2022) ‘Analysis and insight of electroluminescence imaging in the assessment of potential-induced degradation in crystalline silicon photovoltaic module’, *Engineering Failure Analysis*, 134(October 2021), p. 106027. doi: 10.1016/j.engfailanal.2022.106027.

Rossi, D. *et al.* (2015) ‘Modeling and detection of hotspot in shaded photovoltaic cells’, *IEEE Transactions on Very Large Scale Integration (VLSI) Systems*, 23(6), pp. 1031–1039. doi: 10.1109/TVLSI.2014.2333064.

Roy, S. and Gupta, R. (2019) ‘Non-destructive approach for severity investigation of shunts in crystalline silicon photovoltaic modules by combination of electroluminescence imaging and lock-in thermography’, *Measurement Science and Technology*, 30(4). doi: 10.1088/1361-6501/ab0265.

Roy, S., Kumar, S. and Gupta, R. (2019) ‘Investigation and analysis of finger breakages in commercial crystalline silicon photovoltaic modules under standard thermal cycling test’, *Engineering Failure Analysis*, 101, pp. 309–319. doi: 10.1016/J.ENGFAILANAL.2019.03.031.

Sharma, V. and Chandel, S. S. (2013) ‘Performance and degradation analysis for long term reliability of solar photovoltaic systems: A review’, *Renewable and Sustainable Energy Reviews*, 27, pp. 753–767. doi: 10.1016/j.rser.2013.07.046.

Somasundaran, P., Sinha, A. and Gupta, R. (2012) ‘Simulation and characterization of spatial variation of shunts in industrial solar cells by PSPICE and dark lock-in infrared thermography’, *27th European Photovoltaic Solar Energy Conference and Exhibition*, (September), pp. 744–748.

Teo, J. C. *et al.* (2018) ‘Impact of partial shading on the P-V characteristics and the maximum power of a photovoltaic string’, *Energies*, 11(7). doi: 10.3390/en11071860.

A Detailed Balance Study of Rear Surface of $Cs_3Sb_2Br_9$ Perovskite Solar Cell

Sachchidanand[1], Akash Patnaik[1], Anil Kumar[2], Pankaj Sharma[1,*]

[1] Advanced Semiconductor Materials and Nanoelectronics (ASMAN) Research Group, Indian Institute of Information Technology, Design and Manufacturing, Jabalpur (India)

[2] Department of Electronics and Communication Engineering, PDPM Indian Institute of Information Technology, Design and Manufacturing, Jabalpur (India)

Abstract

An analytical model based on a detailed balance theory has been adopted to obtain the performance limitation of a $Cs_3Sb_2Br_9$-based perovskite solar cell (PSC). Two different structures surrounded by the angular reflection layer at the front along with a perfect mirror and an absorbing substrate at the rear surface, individually, are investigated. The performance analysis of both structures on the cell is done by tuning the angle of incident sunlight. The obtained result highlights an increment of 1.6% in the performance for the perfect mirror-based structure as compared to the other structure. The obtained result signifies a good performance of the $Cs_3Sb_2Br_9$-based PSC for a plane wave (90°). The proposed analytical model and corresponding results can be used as a suitable model for estimating the performance parameters of the PSC for various materials.

Keywords: $Cs_3Sb_2Br_9$, perovskite solar cell, detailed balance model, AM1.5G, absorbing substrate, perfect mirror

1. Introduction

Solar cells (SCs) are the most attractive technology in recent years due to a very vast range of emerging materials that drastically improve the device's performance. For decades, emerging perovskite materials have attracted the solar community for a low-cost device with reliable performance. The recent reports on perovskite-based SCs (PSCs) with the highest efficiency of 26.1% encourage the research community ((NREL), n.d.; Green et al., 2023). Moreover, the large range of perovskite materials and cost-effective fabrication methods like solution-based methods, sol-gel, hot-injection, etc. also support the development of efficient PSCs (Shah et al., 2020). Firstly, Sha et al. proposed a detailed balance model to calculate the efficiency limit of $CH_3NH_3PbI_3$ PSCs and calculated the limit as 31% (Sha et al., 2015). Sun et al. approached a physics-based analytical model of PSCs using a fitting function (Sun et al., 2015). Agarwal et al. proposed a scheme of device engineering to achieve a nearly ideal efficiency of PSC (Agarwal and Nair, 2015). Ren et al. explored the drift-diffusion-based analytical model for obtaining the theoretical limit of PSC (Ren et al., 2017). In the context of a lead-free perovskite, we have designed a $Cs_3Sb_2Br_9$-based PSC and all-perovskite tandem solar cell (TSC), for the first time, to determine the contribution of $Cs_3Sb_2Br_9$ in these devices (Sachchidanand et al., 2023, 2022, 2021). This work presents a detailed balance model-based analytical approach on $Cs_3Sb_2Br_9$-based PSC to study the performance limit of the cell (PSC).

2. Model development

To do an investigation, two different structures are proposed, as shown in Fig. 1. For Fig. 1(a) the optical medium surrounding the photovoltaically active absorbing cell is "air" at the front surface and a perfect reflector mirror at the rear surface. Any solar cell thick enough to be manufactured with the back surface of its

10.18086/swc.2023.01.05 Available at http://proceedings.ises.org

active region accessible to make it a perfect reflector can possibly approach such a device. For Fig. 1(b) the absorbing cell is surrounded by "air" at the front surface and an absorbing substrate at the rear surface. Such a structure emphasises a more practical situation that is highly adopted in fabricating any solar cell. The Assuming only the radiative recombination mechanism exists, under illumination at the steady state condition, photon absorption in the cell must be equal to the photon emission, corrected for the fraction *f* as current in the external circuit.

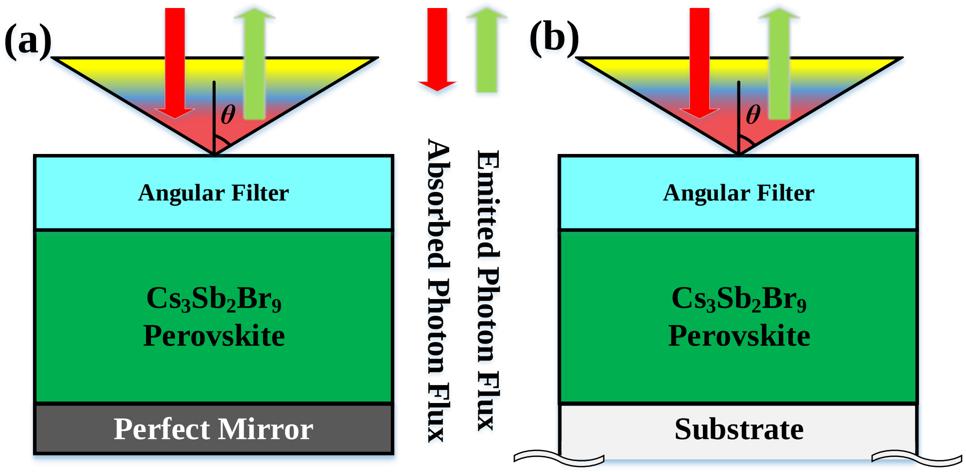

Fig. 1 Schematic of $Cs_3Sb_2Br_9$-based perovskite solar cell (PSC). The structure has a planar top surface along with (a) a perfect mirror, and (b) an absorbing substrate at the rear surface.

$$J_0 exp\left(\frac{qV}{kT}\right) = (1-f)J_L \quad \text{(eq. 1)}$$

The photogenerated current (J_L) after photon absorption can be computed as:

$$J_L = \frac{q}{hc}\int_0^\infty \Gamma(\lambda)a(\lambda)\lambda d\lambda \quad \text{(eq. 2)}$$

where $\Gamma(\lambda)$ is the incident AM1.5G solar spectrum, $a(\lambda)$ is the absorptivity, q is the electron charge, h is the plank constant, and c is the light speed. The leakage current (J_0) owing to carrier loss can be computed as:

$$J_0 = \frac{q}{hc}\int_0^\infty b(\lambda)a(\lambda)\lambda d\lambda \quad \text{(eq. 3)}$$

where $b(\lambda)$ is the black-body emission spectrum of the cell which can be calculated by (Sha et al., 2015) with consideration of the Boltzmann approximation. Moreover, in a detailed balance model, the maximum current that can circulate through the given external circuit is calculated as the difference between the photogenerated current after photon absorption and leakage current owing to photon emission.

$$J(V) = J_0 exp\left(\frac{qV}{kT}\right) - J_L \quad \text{(eq. 4)}$$

Furthermore, the absorptivity expresses in Eqs. (2) and (3) for both structures depends majorly upon the cell's thickness (W), refractive index (n) and angle of incident sunlight (θ) and can be computed as:

$$a(\lambda) = 1 - exp\left(\frac{-\mathrm{m}\alpha(\lambda)W}{cos(\theta_{inc})}\right) \quad \text{(eq. 5)}$$

Here m is an optical path multiplier owing to the rear surface of the cell; m = 2 for the perfect mirror, and m = 1 for the back absorbing substrate at the rear surface of the cell. $\theta_{inc} = cos^{-1}\left(\sqrt{1-n^{-2}sin^2(\theta)}\right)$ is the angle of propagation inside the absorbing cell after suffering from reflection.

The fixed point performance parameters, short-circuit current density (J_{sc}) and open circuit voltage (V_{oc}), can be obtained from Eq. (4) by putting null to either biasing voltage (V) or current density (J) and can be written as:

$$J_{sc} = -J_L \text{ , and } V_{oc} = V_t ln\left(\frac{J_L}{J_0}\right) \quad \text{(eq. 6)}$$

where $V_t = kT/q$ is the thermal voltage. For an efficient PSC, the power conversion efficiency (PCE) expresses the conversion performance of the cell and can be given by:

$$PCE = \frac{max(J \times V)}{P_L} \quad \text{(eq. 7)}$$

where P_L is AM1.5G spectrum having a power density of 100 mW/cm^2.

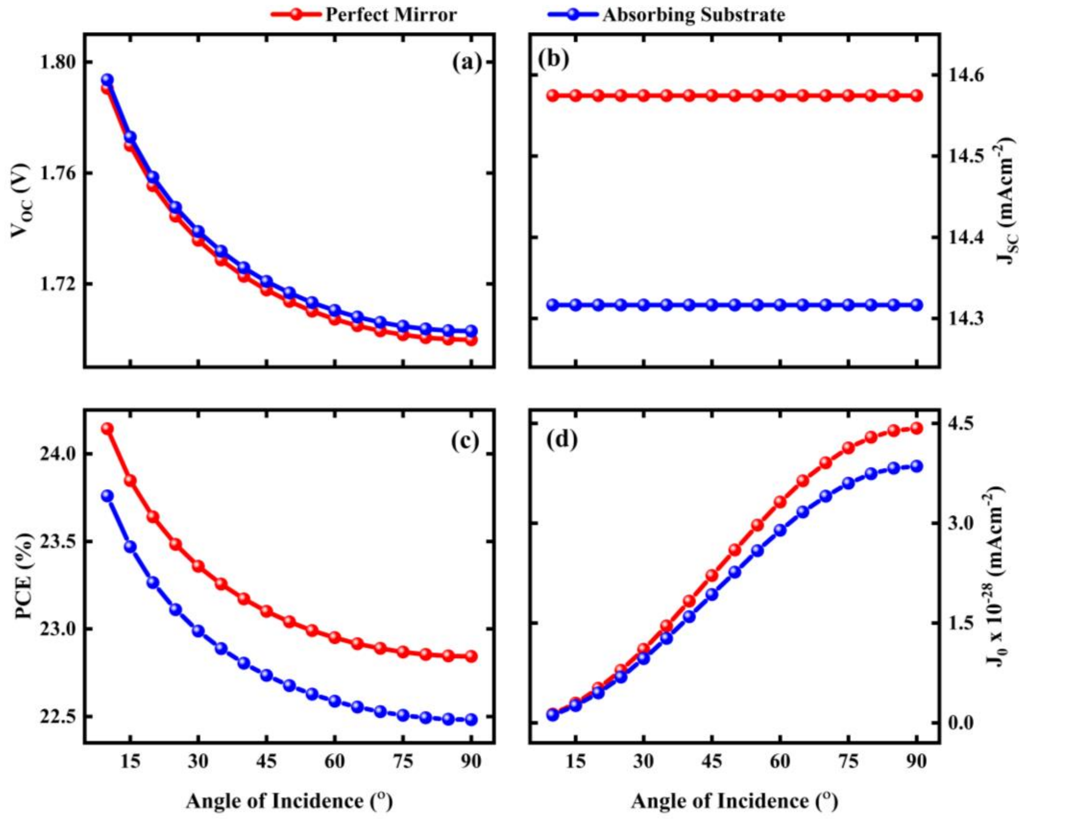

Fig. 2 Performance parameters of both Planar PSCs by varying the incident angle, such as (a) open-circuit voltage (V_{OC}), (b) short-circuit current density (J_{SC}), (c) power conversion efficiency (PCE), and (d) Leakage current density (J_0).

3. Results and discussion

3.1. Influence of rear substrate on the solar incidence angle on structures

In Fig. 2, the influence of solar incidence angle on the performance of the planar structures having perfect mirror and back absorbing substrates is observed. From Fig. 1, the angular restriction layer allows the incident photon to penetrate inside the structure owing an angle of incidence (θ) and bound it‘s emission. The variations in θ between 10º and 90º having stepping of 5º is depicted in Fig. 2 using V_{OC}, J_{SC}, PCE and J_0. As θ increases the V_{OC} decreases and J_0 increases exponentialy with a marginal difference for both structures at θ > 30º. This variation in V_{OC} and J_0 is due to rise in the direct recombination of photon because of a rise in the angle of emission which is the counterpart of θ (Ren et al., 2017). Moreover, as θ gets updated, J_{SC} accounts a fixed value with a 0.61% higher value for the structure having the perfect mirror on the rear side{Fig. 1(a)} instead of that of the back absorbing substrate {Fig. 1(b)}. This fixed J_{SC} may be due to the constant generation of free charge carrier at thermal equilibrium and the difference is due to the different optical path of the free charge carriers in both structures (Sachchidanand et al., 2022; Sun et al., 2015). As PCE is the effective performance of the structure which can be calculated as the ratio of the maximum value of the multiplication of current density J and baised voltage V to the incident solar power (P_L), as in Eq. (7). From Fig. 2(c), as θ changes, the performance of both structures varies which follow the nature of V_{OC} because of fixed J_{SC}. The planar structure having the perfect mirror shows a better outcome in comparison to the planar structure having the back absorbing substrate due to double absorptivity hence better J_{SC}, see Fig. 2(b). Thus, it can be concluded that the $Cs_3Sb_2Br_9$-based PSC having the perfect mirror performed well with a 1.6% higher PCE in comparison to that structure having the back absorbing substrate. Table 1 displayed a performance comparison of $Cs_3Sb_2Br_9$-

based PSC with previous detailed balance-based models and experimental reports.

Tab. 1: Performance comparison of $Cs_3Sb_2Br_9$-based PSC with previous detailed balance-based model and experimental reports

Perovskite	E_g (eV)	Angle of Incidence (°)	PCE (%)	
			Detailed Balance-based Model	Experimental
$MAPbI_3$	1.5	90	28.82 (Sha et al., 2015)	25.50 (Li et al., 2021)
$MAPbBr_3$	2.2	90	19.60 (Shockley and Queisser, 1961)	4.85 (Mehdi et al., 2019)
$Cs_3Sb_2Br_9$	2.0	90	22.84 [This Work]	-

3.2. Impact of solar incidence angle on structures with different front design

An investigation of the performance of the 'Planar Front' and 'Textured Front' based PSC is presented in Fig. 3(a) as the function of θ. In both PSCs, as θ increases, the performance starts decay which may be due to decrease in the absorptivity which increases the recombination of charge carriers in the structure (Rühle, 2016). Moreover, the effect of different absorber's thickness like 800 nm, 1000 nm, and 1200 nm on both PSCs is also depicted in Fig. 3(a). The 'Planar Front' PSC shows a negligible difference by varying the absorber's thickness may be due to double optical path. While the 'Textured Front' PSC shows a difference of 1.15% and 1.83% for the absorber thickness of 1000 nm and, 1200 nm in compared to that of 800 nm, respectively. These marginal differences in the PSC may be due to lesser emission of the incident photon at the higher thicknesses of the absorber. As result, the 'Planar Front' and the 'Textured Front' PSCs reaches a maximum PCE of 22.84% and 22.48%, respectively, at θ of 90° and the absorber thickness of 1000 nm. This may also be due to lower optical path of the charge carriers at the front texturing design in compared to front planar design. It highlights the elevated performance of the 'Planar Front' PSC and concluded the optimum absorber thickness of 1000 nm. The influence of different front design and back substrate at the absorber thickness of 1000 nm is depicted in Fig. 3(b). It shows a maximum performance limit of 24.14% at θ of 10° for the $Cs_3Sb_2Br_9$-based PSC having planar front and back mirror design. Thus for a lead-free inorganic $Cs_3Sb_2Br_9$-based PSC, the maximum performance is achieved for a 'Planar Front' having a back mirror design.

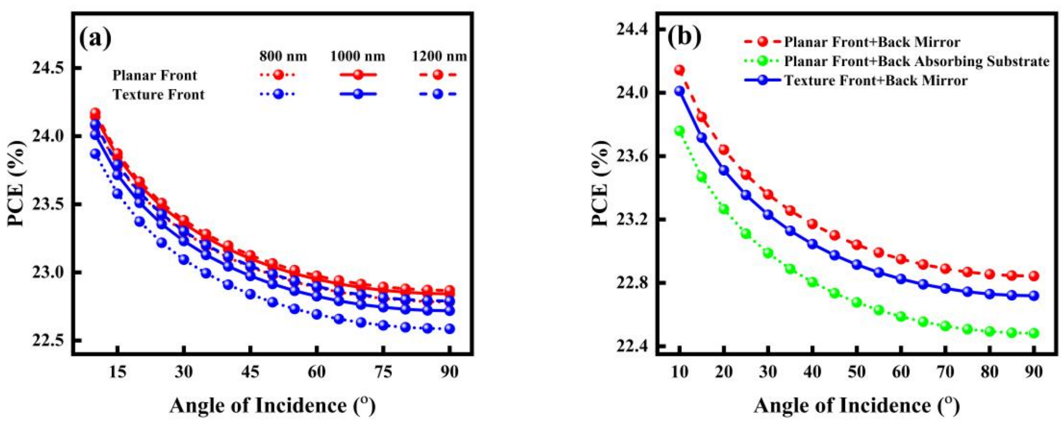

Fig. 3 Variation in the power conversion efficiency (PCE) of (a) the planar and texture front having a back perfect mirror at different thicknesses of 800 nm, 1000 nm, and 1200 nm, and (b) different structures at the thickness of 1000 nm as the function of angle of incidence.

4. Conclusion

A detailed balance model-based analytical approach for the calculation of the performance limit of $Cs_3Sb_2Br_9$-based PSC is investigated. The variation in the performance parameters as the function of the angle of incident sunlight is observed. The obtained result highlights that the perfect mirror-based structure reflected a better performance limited of 22.84% at θ of 90° which is 1.6% higher as compared to the back absorbing structure.

It also signifies that for a good performance of the $Cs_3Sb_2Br_9$-based PSC, a perfect mirror helps to improve the performance by increasing the optical path and lowering the photon emission angle. The discussed analytical model and its corresponding result can be used as a suitable model for estimating the performance-limiting parameters of the PSC for various materials.

5. Acknowledgments

The author would like to thank Dr. Anil Kumar for his keen support in the research and also acknowledge Dr. Pankaj Sharma for providing Faculty Initiation Grant no. IIITDMJ/Dir. Off. /109/2020/11/41. This work is partially supported by DST Science & Engineering Research Board (SERB) project no. SRG/2021/001946.

6. References

(NREL), N.R.E.L., n.d. best-research-cell-efficiencies-rev220126.pdf.

Agarwal, S., Nair, P.R., 2015. Device engineering of perovskite solar cells to achieve near ideal efficiency. Appl. Phys. Lett. 107. https://doi.org/10.1063/1.4931130

Green, M.A., Dunlop, E.D., Siefer, G., Yoshita, M., Kopidakis, N., Bothe, K., Hao, X., 2023. Solar cell efficiency tables (Version 61). Prog. Photovoltaics Res. Appl. 31, 3–16. https://doi.org/10.1002/PIP.3646

Li, D., Zhang, D., Lim, K.S., Hu, Y., Rong, Y., Mei, A., Park, N.G., Han, H., 2021. A Review on Scaling Up Perovskite Solar Cells. Adv. Funct. Mater. 31, 1–27. https://doi.org/10.1002/adfm.202008621

Mehdi, H., Mhamdi, A., Hannachi, R., Bouazizi, A., 2019. MAPbBr3 perovskite solar cells: Via a two-step deposition process. RSC Adv. 9, 12906–12912. https://doi.org/10.1039/c9ra02036e

Ren, X., Wang, Z., Sha, W.E.I., Choy, W.C.H., 2017. Exploring the Way to Approach the Efficiency Limit of Perovskite Solar Cells by Drift-Diffusion Model. ACS Photonics 4, 934–942. https://doi.org/10.1021/acsphotonics.6b01043

Rühle, S., 2016. Tabulated values of the Shockley-Queisser limit for single junction solar cells. Sol. Energy 130, 139–147. https://doi.org/10.1016/j.solener.2016.02.015

Sachchidanand, Garg, V., Kumar, A., Sharma, P., 2021. Numerical simulation of novel lead-free Cs3Sb2Br9 absorber-based highly efficient perovskite solar cell. Opt. Mater. (Amst). 122, 111715. https://doi.org/10.1016/j.optmat.2021.111715

Sachchidanand, Kumar, A., Sharma, P., 2023. Transfer matrix method-based efficiency enhancement of lead-free Cs3Sb2Br9 perovskite solar cell. Sol. Energy 259, 63–71. https://doi.org/10.1016/j.solener.2023.05.014

Sachchidanand, Kumar, A., Sharma, P., 2022. Performance Investigation of Organic/Inorganic Bottom Cell on Lead-Free Cs3Sb2Br9 Based All-Perovskite Tandem Solar Cell. IEEE Trans. Electron Devices 69, 3462–3469. https://doi.org/https://doi.org/10.1109/TED.2022.3167965

Sha, W.E.I., Ren, X., Chen, L., Choy, W.C.H., 2015. The efficiency limit of CH3NH3PbI3 perovskite solar cells. Appl. Phys. Lett. 106. https://doi.org/10.1063/1.4922150

Shah, S.A.A., Sayyad, M.H., Khan, K., Guo, K., Shen, F., Sun, J., Tareen, A.K., Gong, Y., Guo, Z., 2020. Progress towards High-Efficiency and Stable Tin-Based Perovskite Solar Cells. energies Rev. 13, 1–42. https://doi.org/10.3390/en13195092

Shockley, W., Queisser, H.J., 1961. Detailed balance limit of efficiency of p-n junction solar cells. J. Appl. Phys. 32, 510–519. https://doi.org/10.1063/1.1736034

Sun, X., Asadpour, R., Nie, W., Mohite, A.D., Alam, M.A., 2015. A Physics-Based Analytical Model for Perovskite Solar Cells. IEEE J. Photovoltaics 5, 1389–1394. https://doi.org/10.1109/JPHOTOV.2015.2451000

Impact of Microcracks on the Performance of a Crystalline Silicon Photovoltaic Cell

Dibyendu Hazra[1], Roopmati Meena[1], Ravi Kumar[1], and Rajesh Gupta[1]

[1]Department of Energy Science and Engineering

Indian Institute of Technology Bombay, Mumbai (India)

Abstract

Solar cells are susceptible to the formation of microcracks throughout different stages of their lifespan. Microcracks can lead to power loss through different impacting mechanisms, such as enhancing surface recombination or increasing resistive losses, leading to performance loss in solar cells. These operating mechanisms can co-occur in a solar cell, which has yet to be studied in detail. In this work, the impact of different operating mechanisms of microcracks on the electrical performance of a solar cell has been analysed using PSpice simulations. Three scenarios have been considered to assess the effects of microcracks, namely, enhanced surface recombination mode, resistive loss mode, and a combination of both. Simulations have been performed using a distributed diode model of the solar cell for the three most occurring microcrack orientations. The results show that in resistive mode, the power loss is comparatively less for all microcrack orientations. For parallel to busbar microcrack, no resistive power loss is observed, and for diagonal and perpendicular to busbar microcrack, after a certain threshold resistance, the power loss does not increase due to changes in the path of the lateral current flow. The recombinative loss mode results in higher performance loss than the resistive loss mode. Further, depending on the presence of stress factors, performance loss due to a combination of both loss modes leads to higher performance loss, impacting its reliability. This work highlights the possible extent of performance loss due to the different operating mechanisms of microcracks.

Keywords: Microcracks, Recombinations, Resistive loss, Solar cell, Photovoltaics, Power loss

1. Introduction

In the modern world, most of our current power consumption is supplied using fossil fuels, which are non-renewable and not environmentally friendly. Shifting to renewable energy resources like solar, wind, and hydro is necessary to meet the future energy needs of the growing population. Out of the available renewable energy sources, the photovoltaic (PV) industry has developed into one of the fastest-growing technologies in recent decades. This is mainly because the PV modules generally have a comparatively higher lifetime, lower long-term costs and local as well as grid-level energy generation capability. In the last decade, the weighted average of the levelized cost of electricity for commercial-scale solar PV has dropped from 0.381 USD/kWh to 0.057 USD/kWh (IRENA Renewable Cost Database, 2020), making solar energy the most cost-efficient and viable energy source right now. Crystalline silicon (c-Si) PV modules currently dominate the PV market industry due to being the most abundant and well-researched. PV modules operate under harsh environmental conditions, resulting in defects and degradations, significantly impacting the performance of PV modules in the long term. International Technology Roadmap for Photovoltaics (ITRPV) reported a significant reduction in the wafer thickness of solar cells to reduce the cost (ITRPV, 2018). However, thinner wafers lowered the robustness of the solar cell against thermo-mechanical loads, resulting in a higher chance of cell cracking. Microcracks in solar cells are one of the critical forms of defect and degradation in crystalline silicon solar cells, which can propagate, resulting in increased severity and leading to other degradation modes. Microcracks can form due to thermo-mechanical stress in the cells during manufacturing, transportation, and outdoor operating conditions due to temperature variation, hailstorms, snow, wind, etc. Microcracks are invisible to the bare eye as they have a width of less than 30μm (Dhimish *et al.*, 2017). They can be detected through imaging processes such as electroluminescence (EL) imaging. Herein, microcracks appear as dark lines due to reduced EL emission caused by carrier recombination sites created around the microcrack region (Mohammed Niyaz, Meena and

10.18086/swc.2023.01.02 Available at http://proceedings.ises.org

Gupta, 2021). Microcracks do not electrically disconnect cell areas; however, they can interrupt fingers along the length of the microcrack, increasing the series resistance. Dhimish et al. have reported a power loss of up to 20% due to microcracks at the module level (Dhimish *et al.*, 2017). In addition to resistive losses, microcracks may also lead to an increase in surface recombination (Buerhop *et al.*, 2012). Herein, the severity and area of surface recombination vary with the length, width, depth and orientation of the microcracks (Buerhop *et al.*, 2012; Papargyri *et al.*, 2020; Mohammed Niyaz, Meena and Gupta, 2021). While each of the aforementioned loss-incurring modes of microcrack has been studied in isolation, they may co-occur under outdoor field conditions, which needs to be studied further. In this work, the impact of microcracks based on their operating mechanism on electrical performance has been investigated at the cell level using a simulation approach. For the simulations, the distributed diode model of solar cells has been used, where the microcracks are modelled with local parameter variation depending on the position of the microcracks. Diagonal, perpendicular to the busbar and parallel to the busbar orientations of microcracks and three power loss incurring mechanisms due to microcracks have been considered for the simulations.

The further sections of this article are structured as follows. Section 2 describes the three different electrical models used for solar cell modelling. Section 3 depicts the detailed model used in the modelling of microcracks in this paper. In section 4, the simulation results have been discussed, and finally, section 5 concludes this paper.

2. Electrical modelling of solar cells

The modelling and simulation approach is helpful in studying the effects of change in parameters due to microcracks in a solar cell, which is difficult to change experimentally. There are several electrical models for solar cells to accommodate different needs in modelling certain phenomena. The different electrical models for solar are discussed in the following sections.

2.1. Single-diode model of solar cell

The solar cell can be represented by an equivalent circuit using the single diode model (SDM) shown in Fig. 1. In this model, the current source, J_L, represents the light-generated current density due to the illumination of the solar cell. The diode represents the p-n junction in the solar cell. R_S is the series resistance due to a combination of base-emitter and contact resistance between metals and silicon. R_{sh} is the shunt leakage resistance typically due to manufacturing defects.

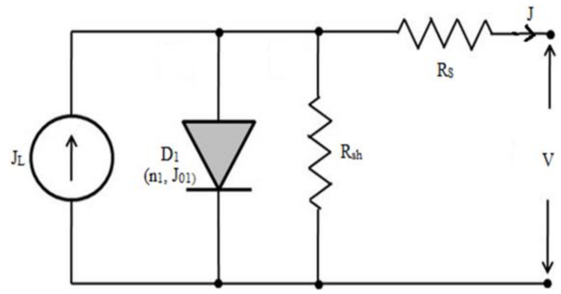

Fig. 1: Solar cell equivalent circuit using single diode model

The current-voltage (*I-V*) characteristics equation of this solar cell equivalent circuit can be written as

$$J = J_L - J_0\{exp[\frac{q(V+JR_S)}{n_1 kT}] - 1\} - \frac{V+JR_S}{R_{sh}} \quad \text{(eq. 1)}$$

Here, n_1 is called the ideality factor, K is the Boltzmann constant, and T is the absolute temperature of the solar cell. In a single-diode model, the value for the ideality factor is taken as constant. In operating conditions, the ideality factor varies as a function of the applied voltage across the solar cell (Kikelj *et al.*, 2021). The ideality factor is close to one when the surface and bulk regions dominate the recombinations in the solar cell. However, when the recombination around the p-n junction dominates, the ideality factor approaches two. To model the junction recombinations, the double diode model is used.

2.2. Double-diode model of solar cell

In the double diode model, a second diode representing junction recombination is added in parallel with the first one. Typically, the ideality factor of the diode is taken as two. The circuit of the double diode model is shown in Fig. 2.

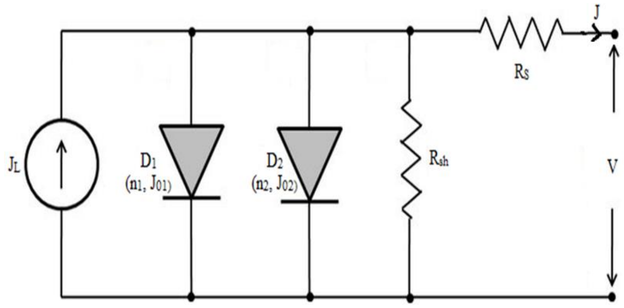

Fig. 2: Double diode model of solar cell

J_L is the light-generated current density, D_1 ($n_1 = 1$, J_{01}) represents the bulk recombination and, D_2 ($n_2 = 2$, J_{02}) represents recombination in the junction, R_s and R_{sh} represent the series resistance and shunt resistance of the solar cell, respectively. The mathematical expression for the double diode model's output current density (J) can be written as given in eq. 2 (PVEducation).

$$J = J_L - J_{01}\{exp[\frac{q(V+JR_S)}{kT}] - 1\} - J_{02}\{exp[\frac{q(V+JR_S)}{2kT}] - 1\} - \frac{V+JR_S}{R_{sh}} \quad \text{(eq. 2)}$$

2.3. Distributed diode model of solar cell

In single and double-diode models, the complete solar cell is taken as a whole and considers uniform effects of all parameters. In reality, there is a non-uniform current generation being different in sites of finger, busbar and emitter sheet. Also, due to the lateral flow of current on the surface of the cell, there is a voltage drop across the length (Zekry and Al-Mazroo, 1996). To consider these effects and the spatial non-uniformity of the solar cell, a 3D model called the distributed diode model is used (Spataru *et al.*, 2015). In the distributed diode model, the solar cell is divided into several small elemental areas, which are modelled by the single or double diode model. Each elemental area consists of a diode, a shunt resistance and a current source connected in parallel. Each neighbouring elementary area is connected with a series resistance. Using this model, anomalies in small parts of the solar cell can be detected easily due to modelling such small elemental areas.

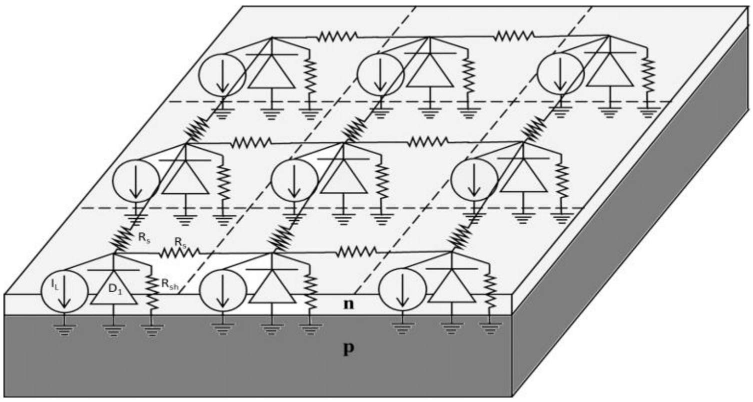

Fig. 3: Distributed diode model approach of solar cells

In Fig. 3, a simple 3x3 distributed diode model is shown, which is extended further in all directions in 3-D to model an entire solar cell. In this work, the distributed diode model has been used to model the microcracks in solar cells. The model used is discussed in the next section.

3. Modelling of microcracks

In the current work, microcracks have been modelled and analyzed for their impact on the performance of solar cells. Microcracks can affect the solar cell parameters in a few ways. An air gap is created on the surface of the cell along the length of the microcrack due to the width and depth of a microcrack. The air gap hinders lateral current flow on the surface, thus increasing the emitter resistance. Recombination sites form on the microcrack location due to dangling bonds. Also, due to higher resistance across the microcrack, the charge carriers are blocked. The blocked charge carriers at the edge of the microcracks increase the recombination around the p-n junction along the microcrack (Van Mölken *et al.*, 2012; Kasewieter *et al.*, 2014). Also, short-circuit paths can form in microcrack locations due to the shorting of the p-n junction due to other material defects around the microcrack location, increasing the shunt resistance. Microcrack and shunt area due to microcrack are directly related, and shunt area increases with the microcrack's length, width and depth (Buerhop *et al.*, 2012; Demant *et al.*, 2016; Dong *et al.*, 2018). These different physical phenomenon affects different solar cell parameters, thus impacting the performance of the solar cell.

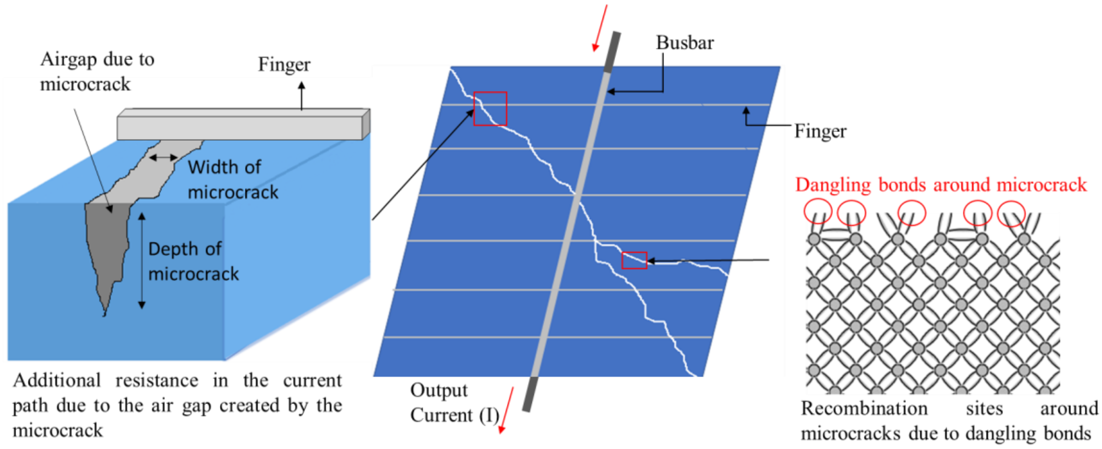

Fig. 4: Schematic of different impact mechanisms of microcrack

In the current study, the spatial characteristics of microcracks have been modelled using the distributed diode model of solar cells. In this model, a grid of 100×100 smaller sub-cells have been created by dividing a healthy solar cell with three busbars. Each sub-cell is modelled using essentially the two-diode model using the combination of a current source (I_L), two diodes (D_1, D_2), and a shunt resistance (R_{sh}) to represent the p-n junction in the solar cell, as illustrated in Fig. 5(a). Distinct sub-cells (as depicted in Fig. 5(b)) are linked through resistive elements such as sheet resistance (R_{sheet}), finger resistance (R_{finger}), and busbar resistance (R_{busbar}), depending on the sub-cell's spatial location. A standard 15.6 cm x 15.6 cm cell is considered for the model, and it is simulated in the PSpice circuit simulator.

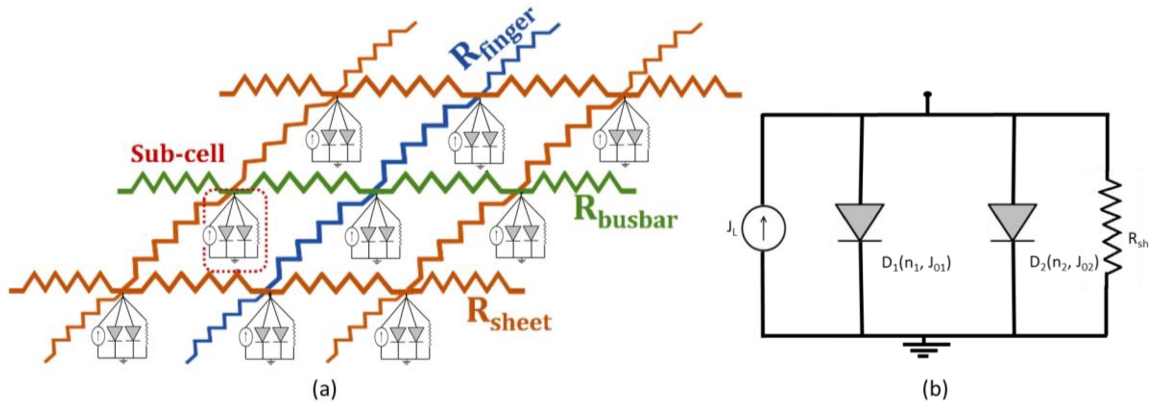

Fig. 5 (a) Distributed diode model using different sub-cells (b) Individual sub-cell

The parameters that are used in the simulations using the above model are depicted in Tab. 1. The parameter values here represent a healthy solar cell. The numerical values for the simulation are taken from Meena et al., where the values have been experimentally obtained (Meena, Niyaz and Gupta, 2023).

Value for each sub-cell is calculated the following way,

$$I_{sc}(\text{node}) = \frac{I_{sc}(\text{experiment})}{Number\ of\ active\ nodes\ in\ the\ circuit} \qquad \text{(eq. 3)}$$

$$I_0(\text{node}) = \frac{I_0(\text{experiment})}{\text{Total number of nodes in the circuit}} \quad \text{(eq. 4)}$$

$$R_{sh}(\text{node}) = R_{sh}(\text{experiment}) \times \text{Total number of nodes in the circuit} \quad \text{(eq. 5)}$$

Tab. 1: Numerical values of different components used in the distributed diode model

Parameter	Value
I_{sc} (A/node)	1.0996×10^{-3}
n_1	1
n_2	2
J_{01} (A/cm^2)	1×10^{-11}
J_{02} (A/cm^2)	1×10^{-9}
R_{sh} (Ω/node)	3.603×10^{5}
R_{sheet} (Ω/cm)	90
R_{finger} (Ω/cm)	2.89×10^{-4}
R_{busbar} (Ω/cm)	2.58×10^{-5}

The resistive components (R_{sheet}, R_{finger}, R_{busbar}) are obtained from the literature Meena et al., where they measured them experimentally. (Meena, Niyaz and Gupta, 2023). To model the microcracks using the distributed diode model, the corresponding parameters have been changed accordingly. Microcracks can affect the performance of the solar cell through three types of mechanisms which affect different model parameters. The three possible mechanisms for power loss due to microcracks are (a) Resistive loss mode, (b) Recombinative loss mode, and (c) a combination of both types of loss modes. Also, the orientation of the microcracks plays a critical role in affecting the power of the solar cell (Kajari-Schröder *et al.*, 2011). Different microcrack orientations can affect the solar cell performance differently. So, the three most commonly occurring orientations of microcracks have been studied. Those three microcrack orientations, namely, (a) diagonal to the busbar, (b) perpendicular to the busbar and (c) parallel to the busbar, are considered for each power loss mode.

3.1. Resistive loss mode

The air gap in the cell, due to the microcrack (Fig. 4), hinders the lateral flow of current on the surface, thus increasing the sheet resistance. To model this, the sheet resistance is increased according to the length, width and depth of the microcrack. Only resistive power loss occurs in this mode as the lateral current must pass through higher sheet resistance or flow in an alternate path, increasing the resistance. To model this type of crack, the sheet resistance values are increased for the corresponding sub-cells through which the microcrack passes for the three different microcrack orientations.

3.2. Recombinative loss mode

Microcracks can increase the recombination of charge carriers in solar cells around it. As microcracks are on the surface of the cell, they can increase the recombination around the p-n junction along the microcrack due to the dangling bond created on the open surface. This can happen without the resistive loss mode. For example, if the microcrack is a scratch on the surface, then the air gap is negligible, and so is the resistive loss. However, due to the enhanced recombination on the microcrack site, it will still affect the performance of the solar cell. In order to model the recombination loss in power due to recombination in the p-n junction due to the microcrack, the reverse saturation current density (J_{02}) of the second diode (D_2 ($n_2 = 2$) is taken as the variable as it directly represents the junction recombination (Van Mölken *et al.*, 2012). Also, as reported in the literature, due to material defects in the microcracked location, the R_{sh} corresponding to the sub-cells decreases, thus affecting the output power. These micro-cracks can also enhance another degradation mode, potential induced degradation (PID), around their location, further increasing the recombination and shunting (Dong *et al.*, 2018). The values for changes in J_{02} and R_{sh} are taken from the literature (Van Mölken *et al.*, 2012; Dong *et al.*, 2018; Kumar, Puranik and Gupta, 2023).

3.3. Combination of resistive and recombinative loss mode

Under outdoor operating conditions, recombinative and resistive microcrack modes operate simultaneously (Mohammed Niyaz, Meena and Gupta, 2021). Herein, the resistive and recombinative loss mode may increase in magnitude depending on the external stress conditions promoting power losses. The performance loss in solar cells due to the simultaneous occurrence of both loss mechanisms is under-researched. To simulate the co-occurrence of both modes, combinations of R_{sheet} values with different J_{02} and R_{sh} values are taken for the three microcrack orientations. The results of the simulations have been discussed in the next section.

4. Results and Discussions

Microcracks with three different loss-impacting mechanisms with three different orientations have been modelled using the distributed diode model, and the circuits are simulated using the PSpice circuit simulator.

4.1. Resistive loss mode

Here, the sheet resistance corresponding to the sub-cells along the microcracks is increased, representing the increase in resistance due to the air gap. The loss in maximum power due to higher sheet resistance for the three orientations of cracks is shown in Fig. 6. It is observed that overall, for all three orientations, the power loss is very low (<1%).

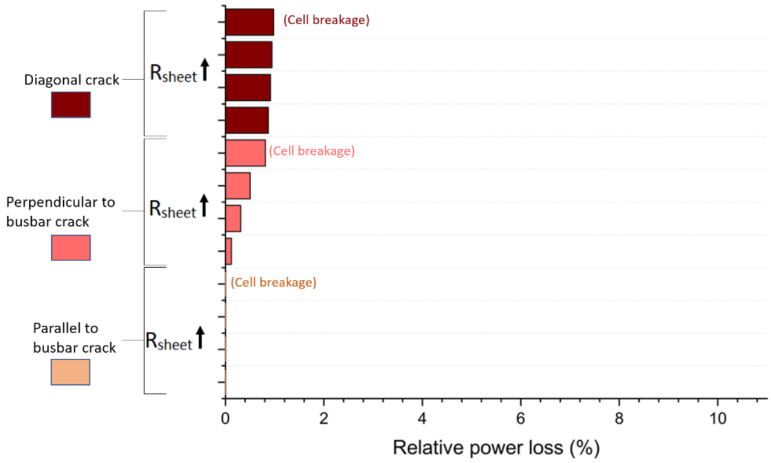

Fig. 6: Power loss due to resistive loss mode for different microcrack orientation

For the diagonal to busbar crack, it is observed that the increase in sheet resistance increases power loss but remains almost constant for higher sheet resistances up to cell breakage. This can be explained as the sheet resistance increases after a certain point, the current finds an alternate path to the nearest finger (Fig. 7), considering that the fingers are not damaged due to the microcrack (Fig. 4). So, after a certain point, increasing the R_{sheet} does not affect the output power of the cell as long as the fingers are not damaged. This also explains the power loss due to the perpendicular to the busbar microcracks, where the microcrack is considered closer to one finger. So, the power output decreases very slightly due to the additional current path introduced, but soon, the lateral current finds the alternative path to the other closest finger; thus, no further decrease in power occurs. For parallel to busbar microcracks, there is no power loss, irrespective of the increase in sheet resistance. This is due to the fact that as long as the finger remains intact, the parallel to busbar cracks do not introduce an additional current path, so the output power is not affected.

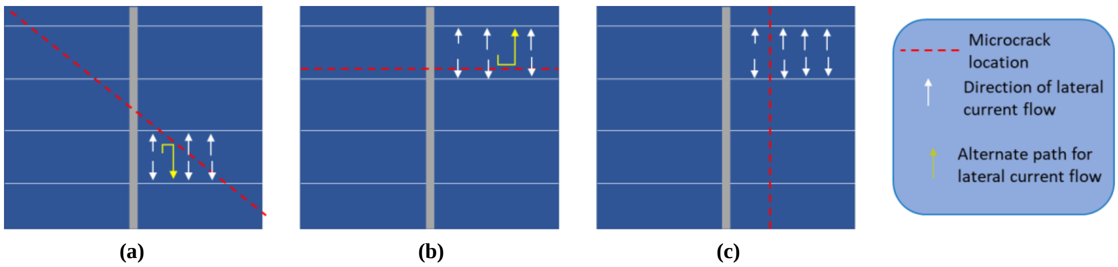

Fig. 7: Lateral current flow directions due to higher sheet resistance for (a) Diagonal, (b) Perpendicular to the busbar, (c) Parallel to the busbar

4.2. Recombinative loss mode

For recombinative loss mode, the relative power loss for different J_{02} values is shown in Fig. 8. The power loss is negligible for low levels of recombination but increases non-linearly with an increase in J_{02}. The slightly higher power loss for the diagonal microcrack can be due to the higher length of the diagonal microcrack.

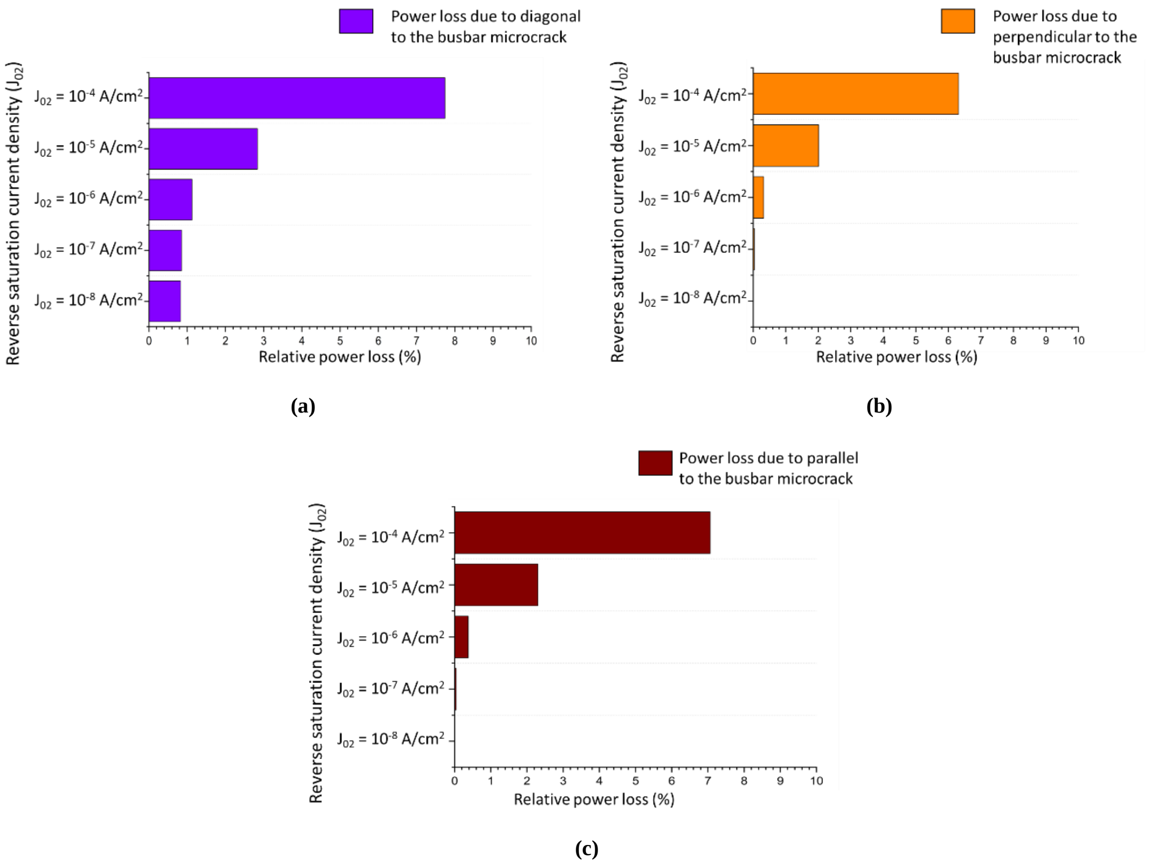

Fig. 8: Power loss due to recombinative loss mode for (a) Diagonal, (b) Perpendicular to the busbar, (c) Parallel to the busbar

The value of J_{02} has been varied from 10^{-8} to 10^{-4} A/cm^2 based on the reported values of change in J_{02} due to recombination losses (Van Mölken *et al.*, 2012; Kumar, Puranik and Gupta, 2023). The recombination around the microcracks can also increase greatly due to possible PID induction around microcracked sites. Maximum power loss of up to 8% is observed due to recombination sites around microcracks for the diagonal to busbar orientation.

4.3. Combination of resistive and recombinative loss mode

The combined effect of both resistive and recombinative losses has been simulated by varying the J_{02} for different R_{sheet} values. The results for diagonal microcracks are shown in Fig. 9(a), 9(b) and 9(c) for different microcrack orientations, respectively.

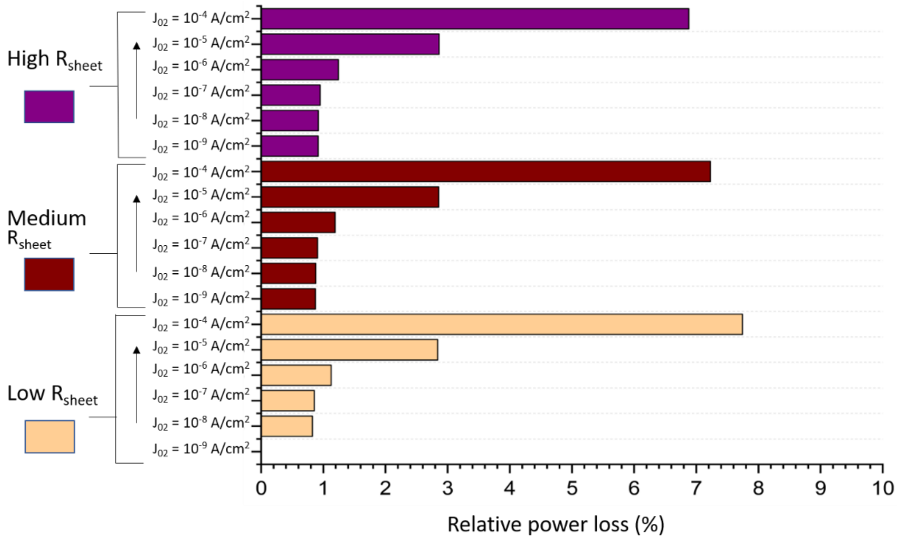

(a)

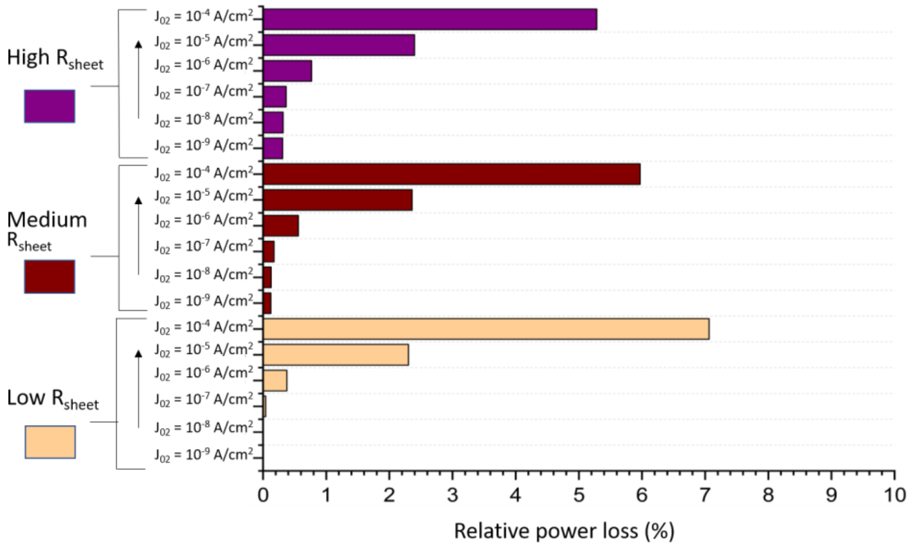

(b)

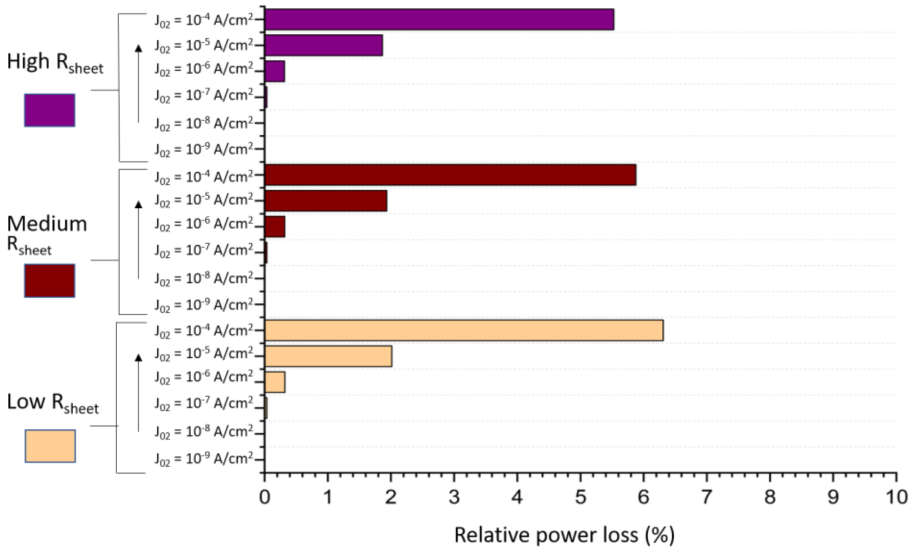

(c)

Fig. 9: Power loss for combination of recombinative and resistive loss mode due to (a) diagonal, (b) perpendicular to the busbar, (c) parallel to the busbar microcrack

It is observed that there are significant power losses due to the combination of both loss modes, the highest loss being for the diagonal microcrack orientation. The power loss for higher J_{02} values decreased with higher R_{sheet} values. The maximum power loss due to the microcrack for all orientations is around 6-8% for the combination of both resistive and recombinative modes. For higher sheet resistance as the lateral current path changes, the recombination of the charge carriers for sub-cells in the path via the microcrack decreases.

5. Conclusion

In this work, the effect of different operating mechanisms of microcrack with three most occurring orientations on the performance of solar cells has been studied using a simulation approach on a distributed diode model. Depending on the electrical parameters affected, the impact of microcracks was classified into resistive mode, recombinative mode and combination of resistive and recombinative mode for power loss. The distributed diode model of solar cells was used to model the spatial impact of power loss incurring modes of microcracks having different orientations. It was observed that for resistive loss mode, power loss increases until a certain threshold value of sheet resistance after which, the power output does not get affected as the lateral flow of current finds an alternate path with less resistance. For recombinative loss mode, the power loss due to recombination in the junction increases non-linearly for high junction recombination. The non-linear increase in power loss is due to the non-linear electrical properties of the diodes, which are mainly affected by the recombination. The combination of both loss-incurring modes affects the output power the most; however, it is not significantly more than the recombinative mode. This spatial impact analysis of microcracks would be helpful to predict the power losses due to microcracks and also their long-term impact on the performance of solar cells.

6. References

Buerhop, C. *et al.* (2012) ‘Reliability of IR-imaging of PV-plants under operating conditions’, *Solar Energy Materials and Solar Cells*, 107, pp. 154–164. Available at: https://doi.org/10.1016/j.solmat.2012.07.011.

Demant, M. *et al.* (2016) ‘Microcracks in Silicon Wafers II: Implications on solar cell characteristics, statistics and physical origin’, *IEEE Journal of Photovoltaics*, 6(1), pp. 136–144. Available at: https://doi.org/10.1109/JPHOTOV.2015.2465172.

Dhimish, M. *et al.* (2017) ‘Effect of micro cracks on photovoltaic output power: Case study based on real time long term data measurements’, *Micro and Nano Letters*, 12(10), pp. 803–807. Available at: https://doi.org/10.1049/mnl.2017.0205.

Dong, N.C. *et al.* (2018) ‘The influence of sodium ions decorated micro-cracks on the evolution of potential induced degradation in p-type crystalline silicon solar cells’, *Solar Energy*, 174, pp. 1–6. Available at: https://doi.org/10.1016/j.solener.2018.08.082.

International technology Roadmap for photovoltaic (ITRPV) ninth edition, Results 2017.” (2018). Available at: http://www.itrpv.net/Reports/Downloads/2018 (Accessed: 20 September 2023).

IRENA Renewable Cost Database (2020) ‘Renewable Power Generation Costs in 2020’, *International Renewable Energy Agency*, pp. 1–160.

Kajari-Schröder, S. *et al.* (2011) ‘Spatial and orientational distribution of cracks in crystalline photovoltaic modules generated by mechanical load tests’, *Solar Energy Materials and Solar Cells*, 95(11), pp. 3054–3059. Available at: https://doi.org/10.1016/j.solmat.2011.06.032.

Kasewieter, J. *et al.* (2014) ‘Cracks in solar cell metallization leading to module power loss under mechanical loads’, *Energy Procedia*, 55, pp. 469–477. Available at: https://doi.org/10.1016/j.egypro.2014.08.011.

Kikelj, M. *et al.* (2021) ‘Spatially resolved electrical modelling of cracks and other inhomogeneities in crystalline silicon solar cells’, *Progress in Photovoltaics: Research and Applications*, 29(1), pp. 124–133. Available at: https://doi.org/10.1002/pip.3348.

Kumar, R., Puranik, V.E. and Gupta, R. (2023) ‘Application of Infrared Thermography for Cell-Level Power Estimation of PID-s Impacted Crystalline Silicon PV Module’, *IEEE Journal of Photovoltaics*, 13(1), pp. 141–149. Available at: https://doi.org/10.1109/JPHOTOV.2022.3229485.

Meena, R., Niyaz, H.M. and Gupta, R. (2023) ‘Investigation and Differentiation of Degradation Modes Affecting Series Resistance in Photovoltaic Cells and Modules’, *IEEE Journal of Photovoltaics*, 13(2), pp.

283–290. Available at: https://doi.org/10.1109/JPHOTOV.2023.3239744.

Mohammed Niyaz, H., Meena, R. and Gupta, R. (2021) ‘Impact of cracks on crystalline silicon photovoltaic modules temperature distribution’, *Solar Energy*, 225, pp. 148–161. Available at: https://doi.org/10.1016/j.solener.2021.07.038.

Van Mölken, J.I. *et al.* (2012) ‘Impact of micro-cracks on the degradation of solar cell performance based on two-diode model parameters’, in *Energy Procedia*. Elsevier Ltd, pp. 167–172. Available at: https://doi.org/10.1016/j.egypro.2012.07.046.

Papargyri, L. *et al.* (2020) ‘Modelling and experimental investigations of microcracks in crystalline silicon photovoltaics: A review’, *Renewable Energy*. Elsevier Ltd, pp. 2387–2408. Available at: https://doi.org/10.1016/j.renene.2019.07.138.

Spataru, S. *et al.* (2015) ‘Quantifying solar cell cracks in photovoltaic modules by electroluminescence imaging’, in *2015 IEEE 42nd Photovoltaic Specialist Conference, PVSC 2015*. Institute of Electrical and Electronics Engineers Inc. Available at: https://doi.org/10.1109/PVSC.2015.7356124.

Stuart Bowden, C.H. (2019) *PVEducation*. Available at: https://www.pveducation.org/pvcdrom/characterisation/double-diode-model (Accessed: 20 September 2023).

Zekry, A. and Al-Mazroo, A.Y. (1996) ‘A distributed SPICE-model of a solar cell’, *IEEE Transactions on Electron Devices*, 43(5), pp. 691–700. Available at: https://doi.org/10.1109/16.491244.

Performance Evaluation and Comparison of Bifacial and Mono-Facial Crystalline Silicon PV Modules and Systems

Anindya S. Parira[1], Dr. Vamsi K. Komarala[2], Dr. Jai Prakash[3], Radhey Shyam[1]

[1]Ministry of New and Renewable Energy, Delhi (India)

[2] Indian Institute of Technology, Delhi (India)

[3] National Institute of Solar Energy, Gurgaon (India)

Abstract

The objective of the study is to evaluate the technical performance of a bifacial PV system & compare it with its mono-facial counterpart in outdoor conditions in India. It is found that the energy generation from the bifacial latitude tilt system is highest, followed by the mono-facial latitude tilt system and then the bifacial vertical tilt system. The quantum of excess energy generation depends on various parameters like ground albedo, GCR, GCH, module tilt angle etc. It is also found in the study that the bifacial gain is over 20% with natural vegetation & grass as the ground reflecting material and it increases further when SS-sheet was used as the ground reflecting material. The simulation study reveals that the LCOE from the bifacial system is comparatively lower than the equivalent mono-facial system when the albedo is 0.2 or above. The higher module cost of the bifacial module compared to its mono-facial counterpart is compensated by the extra energy generated by the bifacial system. The study further reveals that the albedo of the Ladakh region and desert of Rajasthan, India is naturally higher than the normal plain. Thus, these potential sites in India should be targeted for setting up MW-scale bifacial PV plants for higher energy yield and thereby, lower LCOE. Further, bifacial PV vertical systems can also be set up along the bunds of the agricultural land or the side of the national highways.

Keywords: bifacial, mono-facial, solar PV, bifaciality factor, bifacial gain, albedo, GCR, GCH, LCOE

1. Introduction:

In recent years, solar photovoltaic (PV) technology has gained prominence as a conventional energy source. Initially, mono-crystalline silicon (c-Si) PV modules were the dominant technology. Multi-crystalline silicon p-type solar cells with Aluminum Back Surface Field (Al-BSF) technology were widely used until 2015 [1]. However, the PV industry witnessed a shift in 2016 with the production of cost-effective mono-crystalline c-Si wafers. This encouraged the industry to explore innovative solar cell technologies such as Passivated Emitter Rear Contact (PERC), n-type Passivated Emitter Rear Totally-diffused (n-PERT), and heterojunction cells, which had previously only been developed in laboratories. Mono-facial PERC cells, known for their improved cell efficiency exceeding 22.5%, have reached their practical efficiency limit. However, to further increase energy output, the industry is transitioning to bifacial PERC cells. This transition doesn't significantly add to production costs. In the case of bifacial PERC cells, the traditional full-area Aluminum screen print on the rear side of mono-facial PERC cells is replaced with an optimized Aluminum/Silver finger grid, similar to the front side. Bifacial cell and module technology have gained popularity over the years. Bifacial modules harness energy from incident irradiance on both the front and rear sides of the module, resulting in higher energy generation in the field compared to mono-facial counterparts. With advancements in mono-crystalline Si PV cells, improved durability, reliability, and sturdy structures, many module manufacturers are adopting glass-glass panels, making bifacial solar technology an industry preference.

According to Kopecek, R. et al. [2], the global installed capacity of bifacial PV technology reached approximately 20 GW by the end of 2020, with significant installations in China, Chile, Mexico, and the Middle East. This capacity is expected to increase in the coming years. The International Technology Roadmap for Photovoltaic (ITRPV) 2021 suggests that bifacial cells, which accounted for about 30% of the market share in 2020, are projected to increase to approximately 80% in the next decade. Similarly, the market share of bifacial modules, which stood at around 18% in 2020, is forecasted to grow by 55% in the next decade [3]. In

10.18086/swc.2023.01.04 Available at http://proceedings.ises.org

India, despite the dominance of Al-BSF multi-crystalline Si PV cells in the solar PV market, the potential of bifacial technology to produce more energy at nearly the same panel cost as mono-facial counterparts is making bifacial technology an attractive option for achieving lower Levelized Cost of Electricity (LCOE).

Section-1 of the paper presents the introduction of the study and describes the review of literature, Section-2 describes the objectives of the study, Section-3 depicts the methodology adopted to carry out the study, Section-4 illustrates the result and discussion, and Section-5 presents the conclusions and scope of further work.

Various literature on the performance of bifacial PV technology revealed that the daily power generation of the bifacial modules is more than mono-facial counterpart both on sunny and cloudy days. The bifacial gain on cloudy days is even higher than on sunny days due to the higher diffuse irradiance content in the global irradiance. Further, the energy generation of the bifacial system increases with higher ground albedo, tilt angle up to the optimum tilt, and module elevation. In general, it is observed in the literature that the optimum tilt angle of the bPV system is higher than the mPV system under the same external conditions. The optimization of module elevation is also important to trade-off between bifacial gain and system cost.

Wenbo Gu et al. [4] conducted an experimental study on bifacial PV modules under real conditions. They compared the electrical and thermal performance of bifacial modules with mono-facial modules, considering various installation parameters. Bifacial modules were found to produce more power than mono-facial modules due to their ability to collect more irradiance from the rear side. It concluded that higher ground albedo and specific tilt angles favoured bifacial modules. Long-term simulations showed a substantial annual bifacial gain of 14.77%. Suna Xingshu et al. [5] developed a physics-based model for optimizing bifacial solar PV modules on a global scale. Empirical equations derived from the model could estimate bifacial gain based on these parameters, facilitating quick evaluations. The study found that ground-mounted bifacial modules with higher ground albedo coefficients and elevated installations achieved higher bifacial gains, but the balance between gain and installation cost needed optimization.

Stein Joshua S. et al. [6] conducted a study to understand the performance factors of bifacial PV systems. They found that bifacial modules receive more irradiance on their rear surface, making traditional performance models for mono-facial modules inadequate. Factors like module height, tilt angle, azimuth angle, and ground albedo were studied. Results showed that bifacial modules produced more power than mono-facial modules under similar conditions. The annual energy production was highest for south-facing bifacial modules, but the annual bifacial gain was greatest for west-facing vertical modules due to cooler mornings. String-level performance analysis demonstrated varying bifacial gains with different tilt angles. Patel M. Tahir et al. [7] focused on temperature-dependent energy gain in bifacial PV farms on a global scale. They analyzed how temperature affected energy generation, the Levelized Cost of Electricity (LCOE), and compared standalone bifacial modules to solar farms with bifacial modules. Temperature-dependent cell efficiency was considered, and irradiance modelling was integrated for light collection. Bifacial modules, despite collecting more irradiance, could experience lower cell efficiency due to increased temperature. The study revealed that mutual shading in solar farms caused higher cell temperatures and reduced efficiency, particularly in hotter climates, impacting LCOE. They also found that bPV modules with lower temperature coefficients were more efficient and had higher power output. The study compared bifacial gain and LCOE for different module types and optimal elevation considerations.

Liang Tian Shen et al. [8] conducted a review of crystalline silicon bifacial photovoltaic (bPV) performance characterization and simulation. They discussed challenges in establishing standard test conditions for bPV cells/modules. Various methodologies were used to compare bPV and mono-facial PV (mPV) technology, including bifacial gain, equivalent efficiency, and bifacial STC rating. The review also highlighted different techniques for indoor and outdoor characterization of bPV cells and modules, emphasizing the importance of accurate optical modelling for bPV simulations. Additionally, the paper discussed the need for international standards and software tools for precise bPV performance evaluation. NREL [9] presented outcomes from the bifiPV2020 Bifacial Workshop, offering an overview of recent developments in bifacial solar PV technology. The report noted the increasing size of PV wafers and cells, as well as concerns about the long-term durability and reliability of bifacial modules. It highlighted the popularity of glass/glass bPV modules and the emergence of glass/transparent back sheets. The report also mentioned the shift towards n-type bPV technology and the importance of bifacial energy gain (BEG) as a key parameter for comparing bPV and mPV systems. Challenges related to tracking systems, standardization, and modelling were discussed, as well as the need for further research in various areas. Park Hyeonwook et al. [10] conducted an outdoor performance test of bifacial n-type silicon photovoltaic modules in South Korea. They evaluated the performance of bifacial modules and strings compared to mono-facial counterparts under different conditions, including varying ground albedo and the use of tracker systems. The study included indoor measurements under standard test conditions (STC) using mini-modules with different back sheet types. It found that the module with a white back sheet had the highest I_{SC}, while the transparent back sheet bifacial module exhibited high bifaciality factors. The outdoor tests revealed that bifacial modules performed significantly better than mono-facial modules, with higher annual energy yields and bifacial gains, especially in conditions with high-ground albedo. Asgharzadeh Amir et al. [11] conducted a study analyzing the impact of various installation parameters and system size on the energy yield and bifacial gain of photovoltaic (PV) systems. They used RADIANCE simulation software to investigate the effects of module elevation, ground albedo, tilt angle, and system size on PV system performance. The study considered three different system configurations: a single module, a row of five modules, and five rows of five modules. The simulation explored how changing module height, tilt angle, and ground albedo affected the performance throughout the year. Results indicated that the optimum tilt angle for bifacial modules varied with module height and time of year. Carlos D. Rodríguez-Gallegos et al.'s [12] paper, compared the cost-effectiveness of mono-facial and bifacial silicon-based PV modules across 55 locations worldwide. The study evaluated the levelized cost of electricity (LCOE) for various PV system configurations, considering factors like weather conditions, albedo, market conditions, and electrical performance. The research compared LCOE for mono-facial modules with different orientations, bifacial modules with standard orientation (AMO), and bifacial modules with vertical module orientation (VMO). Weather data from ground stations were used to estimate power generation, and cost parameters were adjusted based on the location. The study found that optimizing module orientation reduced LCOE and that mono-facial systems were more cost-effective at lower latitudes, while bifacial systems became more cost-effective at higher latitudes. Bifacial systems with AMO design were shown to deliver more energy in all locations, with increasing bifacial energy gain at higher latitudes. However, for ground albedos between 0.12 and 0.3, bifacial AMO systems were more cost-effective. Bifacial VMO systems became cost-effective at higher latitudes and near the poles, particularly with ground albedos between 0.29 and 0.57 [13], [14], [15].

However, these research studies have limitations. Most of these primarily focused on standalone bifacial modules, which may not reflect real-world installations with multiple modules and strings. Additionally, these studies mostly relied on satellite data from NASA rather than on-site measurements at various locations. Overall, these studies provide valuable insights into the performance, characterization, and challenges of bifacial photovoltaic technology, both indoors and outdoors, and emphasize the need for standardized testing and modelling approaches in the industry. However, some limitations of the study included the unavailability of accurate ground weather data for all locations, insufficient consideration of shading losses, land cost variations, transportation costs, policy and tax differences, and a limited system capacity.

Though many countries have been working on bifacial technology for decades, India is lagging in its development, deployment, and evaluation of performance at local conditions. The present paper aims to evaluate the performance of the bifacial system at latitude tilt & its comparison with the mono-facial system with latitude tilt and bifacial vertical tilt under outdoor conditions in India with estimation of bifacial gain at different albedo conditions, study of module temperature & its effect on energy yield and simulation study of bifacial PV power plant and optimization of various parameters to determine the minimum LCOE. The positive outcomes on the technical and financial fronts of the present study would help in the widespread acceptance and deployment of the bifacial PV technology.

2. Objective:

The primary objective of this research is to conduct a comprehensive technical assessment of bifacial PV (bPV) systems in outdoor conditions within the Indian context. This assessment involves comparing their technical performance with that of mono-facial PV (mPV) systems and determining the Levelized Cost of Electricity (LCOE) across various scenarios relevant to the Indian market.

The specific objectives of this study encompass the following:

- ✓ Energy Generation Comparison: Analyzing and contrasting the energy output between mPV systems and b PV systems at their respective latitude tilt angles. Additionally, it assesses the energy production of bifacial PV systems at vertical tilt orientations.
- ✓ Bifacial Gain Measurement: Investigating the bifacial gain achieved under varying albedo conditions, including scenarios involving natural vegetation, soil, and other reflective materials.
- ✓ Performance Assessment of Vertical Bifacial Systems: Evaluating the performance of vertical bifacial PV systems and comparing it with both mono-facial and bifacial systems employing latitude tilt.
- ✓ Module Temperature Study: Examining the impact of module temperature on energy yield and overall system performance.
- ✓ Simulation Analysis: Conduct in-depth simulation studies on bPV power plants to understand their energy generation characteristics. This analysis will encompass the influence of parameters such as tilt angle, ground albedo, ground coverage ratio (GCR), module elevation above ground level, and other relevant factors. Additionally, the study will involve calculating the minimum LCOE for these systems.

In instant, this research aims to provide a rigorous technical assessment of bPV systems in Indian outdoor conditions, addressing key aspects of their performance and cost-effectiveness.

3. Methodology:

To realize the objectives, this research is structured into different sets of activities in Indoor and Outdoor evaluations, each outlined below in technical detail:

3.1 Indoor Performance Evaluation:

The indoor performance assessment of mono-facial and bifacial modules was carried out. Initially, the indoor measurements of both mono-facial and bifacial modules were conducted. Specifically, four mono-facial modules and six bifacial modules (three for each at latitude tilt and vertical tilt) were randomly selected for indoor testing. The current-voltage (I-V) characteristics of all modules, both mono-facial and bifacial, were measured under Standard Test Conditions (STC) utilizing a single light source solar simulator (Eternalsun Spire) available at the National Institute of Solar Energy (NISE). When one side of the bifacial module was exposed to light, the other side was covered with a black mask to prevent unintended contribution. Subsequently, the bifaciality factor (φ), defined as the minimum of the ratio between the rear side to the front side Isc and Pmax [min (φIsc, φPmax)], was determined. Using the bifaciality factor (φ), the bifacial power gain (BiFi) was calculated by illuminating the front side of the module with an equivalent irradiance (G_E) and noting the corresponding maximum power (Pmax). The equivalent irradiance was selected to achieve rear irradiances (Gri) close to three specific values: 100 W/m^2, 135 W/m^2, and 200 W/m^2. The graph between Pmax and corresponding Gri was plotted. The linear fit of data points passes the y-axis at Pmax, STC. The slope of this graph gives the bifacial power gain (BiFi). Finally, utilizing the bifacial power gain, the maximum power output of the modules was calculated, which represents the sum of the maximum output power of the front surface at STC and two values of rear irradiances, specifically 100 W/m^2 and 200 W/m^2.

3.2 Outdoor Performance Evaluation:

The second phase of the study involves evaluating the performance of mPV and bPV systems under outdoor conditions. The experimental setup consisted of three distinct systems: System-I, a 5 kWp bPV system at latitude tilt; System-II, a 5 kWp bPV system at vertical tilt; and System-III, a 10 kWp mPV system at latitude tilt. These systems were installed at the NISE in Gurgaon, India, and comprised mono-crystalline PERC cells as shown in the Fig. 1.

All three systems were grid-connected via individual grid-interactive inverters. Data regarding daily energy generation and module temperatures were recorded using data loggers. Days with grid-related issues, such as grid unavailability or overvoltage, were excluded from data analysis to focus solely on PV system performance.

The electricity generated by these three systems was compared, and the bifacial gain, representing the increase in energy output from the bifacial system compared to its mono-facial counterpart, was determined. This assessment included scenarios with natural ground cover (vegetation and soil) as well as stainless steel (SS) sheets as ground-reflecting materials.

System-I **System-II** **System-III**

Fig. 1: System-I: bPV system at Latitude Tilt, System-II: bPV system at Vertical Tilt, System-III: mPV system at Latitude Tilt

The study also examined solar power generation and bifacial gain on both sunny and cloudy days. Module temperature and its impact on energy yield were also investigated. Furthermore, the performance of vertically installed bPV systems was compared with bifacial systems at latitude tilt and mono-facial systems at latitude tilt.

3.3 Simulation Study:

Using the National Renewable Energy Laboratory's (NREL) System Advisor Model (SAM), a simulation study was conducted to compare the energy generation capabilities of Systems I, II, and III under identical external conditions. Additionally, the levelized cost of electricity (LCOE) was simulated using SAM to assess the financial feasibility of bifacial technology within the Indian market context.

Finally, a comprehensive study was compiled, covering the indoor performance evaluation of both mono-facial and bifacial modules, the determination of maximum power output from bifacial modules, a comparative analysis of the three systems (System-I, II, and III) considering different ground albedo conditions, the bifacial gain achieved by System-I over its counterpart System-III, a simulation study of a bifacial technology-based PV power plant, and the calculation of its LCOE. The report concludes with key findings and recommendations for further research.

4. Results and Discussion:

Three distinct PV systems (System-I, II, & III) have been installed at NISE Gurgaon, India, employing mono-crystalline Passivated Emitter and Rear Cell (PERC) technology.

4.1 Indoor measurements of mono-facial modules:

To carry out indoor measurements, four mono-facial modules were selected (out of the modules of System-III) randomly. The current-voltage (I-V) characteristics of all four modules were measured under STC using a single light source solar simulator (Eternalsun Spire). The mean and median values of maximum power (Pmax) of mono-facial modules are found to be 352 W and 352.2 W respectively.

4.2 Indoor Measurements of Bifacial Modules:

Similarly, six bifacial modules were randomly chosen for indoor measurement. Current-voltage characteristics for both the front and rear sides of these six modules were recorded under Standard Test Conditions (STC) using a single light source solar. When one side of the module was illuminated, the other side was shielded with a black mask to prevent any unintended contribution from that side.

4.2.1 Determination of Bifaciality Factor at STC:

The performance of the rear side with respect to the front side of the bifacial module is called bifaciality factor (φ). The bifaciality factors of all six modules for different parameters (Isc, Voc and Pmax) were calculated. The average value calculated of φIsc, φPmax and φVoc is 0.82, 0.81 and 0.99 respectively. The minimum of (φIsc, φPmax) is considered as the bifaciality factor. Therefore, the average bifaciality factor considered for the study is 0.81.

4.2.2 Determination of Bifacial Power Gain Driven by Rear Irradiance and Maximum Output Power:

The equivalent irradiance (G_E) method was used to find out the bifacial power gain (BiFi) using a single-side illumination solar simulator. The mean and median values of maximum power for rear irradiance 100 W/m^2 are 384.4W and 384.1W respectively. Similarly, the mean and median values of maximum power for rear irradiance 200 W/m^2 are 410.7 W and 409.9 W respectively.

4.3 Outdoor measurements:

4.3.1 Measurement of bifacial gain with natural vegetation and soil as the ground reflecting material:

The collection of generation data started with natural vegetation and soil as the ground reflecting material with an estimated ground albedo coefficient of 0.25[5]. The module elevation/ground clearance height, measured at the centre of System I and System III at latitude tilt is 1.0 meters and for System II, it is 0.2 meters. All three systems were connected to the grid through individual grid-interactive inverters. During the collection of data, the days with no grid or grid over-voltage were filtered out while aggregating the electricity generation at the system level to differentiate based on PV system performance only.

The electricity fed into the grid from 12-11-2021 till 24-02-2022 (after filtering out the days with partial no grid or grid over-voltage; the effective data is for 54 days) by individual systems (I, II and III) is given in Fig. 2. The generation data from System-III is normalized to 5 kWp equivalent system.

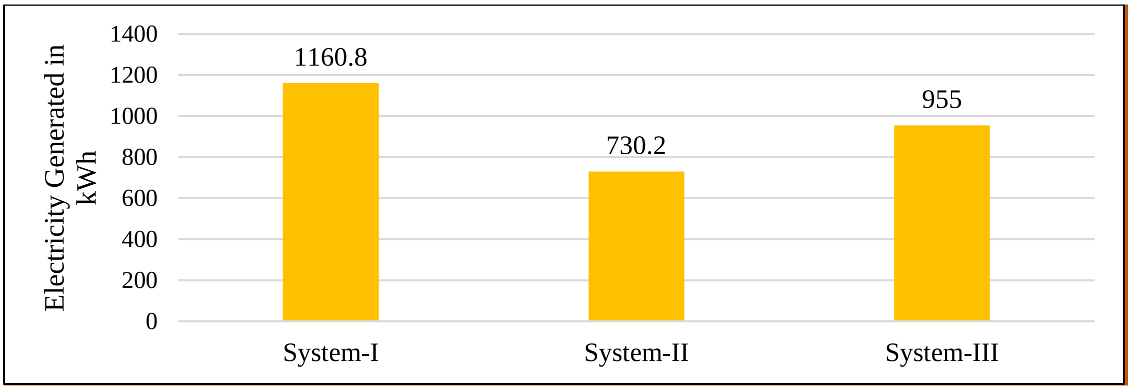

Fig. 2: Electricity fed into the grid by the three systems with natural vegetation and soil as the ground reflecting material

The bifacial gain (%) of the bPV system with latitude tilt (System-I) compared to its mono-facial counterpart (System-III) is calculated. Bifacial Gain = {(Energy generated by bPV system – Energy generated by the mPV system) * 100}/ Energy generated by the mPV system = {(1160.8 – 955) *100}/955 = 21.5%.

This bifacial gain obtained during November, December, January and most of the days of February is clearly due to the additional radiation available due to the natural vegetation and soil as the ground reflecting material which can be converted only by the bifacial modules. The bifacial gain of 21.5% appears to be higher compared to the data in the available literature. This higher gain may be due to higher system elevation and limited system size.

4.3.2 Measurement of bifacial gain with stainless steel (SS) sheet as the ground reflecting material:

System-I

System-II

Fig. 3: System-I with SS-sheet as ground reflecting material, System-II with SS-sheet as ground reflecting material

The same experimental set-up is used to find out the bifacial gain using SS-sheet as the ground reflecting material. The SS-sheet for System I and II was placed on 25-02-2022. The System-III being mono-facial, only natural vegetation and soil are used as the ground reflecting material. The System I and System II are shown in Fig. 3.

The electricity fed into the grid from 25-02-2022 till 20-05-2022, after filtering out the days with partial/no grid or grid over-voltage; the effective data available is for 33 days) by the individual system (I, II and III) is given in Fig. 4. The generation data from System-III is normalized to a 5 kWp equivalent system.

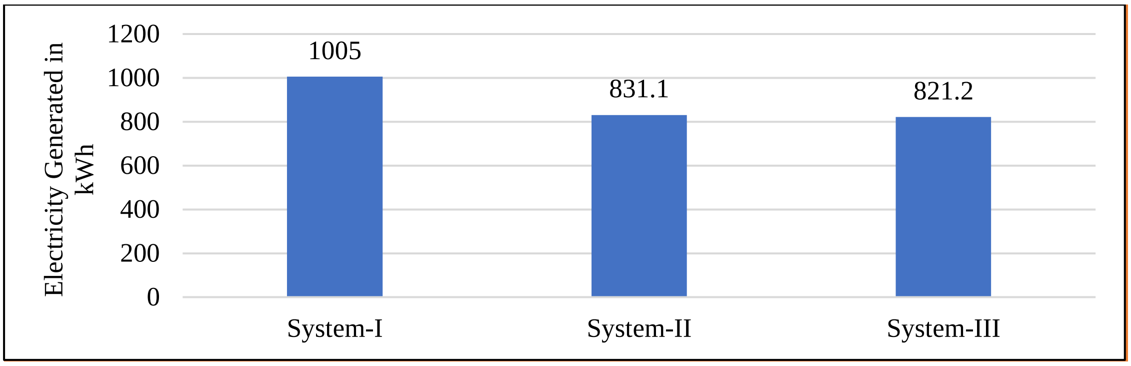

Fig. 4: Electricity fed into the grid by the three systems with SS-sheet as the ground reflecting material

The bifacial gain (%) of the bPV system with latitude tilt (System-I) compared to its mono-facial counterpart (System-III) is calculated. Bifacial Gain = {(Energy generated by bPV system – Energy generated by the mPV system) * 100}/ Energy generated by the mPV system = {(1005 –821.2) *100}/821.2 = 22.4%

This bifacial gain of 22.5% obtained is clearly due to the additional radiation available when SS-sheet is used as the ground reflecting material, which can be converted only by the bifacial modules. The bifacial gain obtained is ~ 1% higher as compared to the bifacial gain obtained (21.5%) when natural vegetation and soil are used as ground reflecting material.

4.3.3 Solar Power Generation and Bifacial Gain on an Arbitrary Sunny Day:

The generation of solar power from all three systems of capacity 5 kWp (the System-III is normalized to 5 kWp equivalent system) on an arbitrary sunny day (02nd Jan. 2022) was considered and depicted in Fig. 5 below.

It was observed that the power generated from System-I is highest followed by power generated from the System-III and then System-II. It was also observed that in the case of System-II, the maximum power output occurs two times a day, once in the morning and another in the evening and the power output was minimal during solar noon. The bifacial gain (%) of the system-I compared to its system-III on that particular day was calculated: {(21.9 – 18.2) *100}/18.2 = 20.3%

4.3.4 Solar Power Generation and Bifacial Gain on an arbitrary cloudy day:

The generation of solar power from the three individual systems of capacity 5 kWp each, throughout an arbitrary cloudy day (28th Dec. 2021) was considered and depicted in Fig. 6.

As expected, the power generated from System-I is highest followed by power generated from System-III and then System-II. The bifacial gain (%) of the system-I to system-III on that day is calculated which is {(3.9 – 3.2) *100}/3.2 = 21.9%.

Thus, the bifacial gain was higher on a cloudy day (21.9%) compared to a sunny day (20.3%). The increase in bifacial gain with the decrease in sky clearness index is due to the increased absorption of diffused radiation by the rear surface since on cloudy days the content of diffuse irradiance in the global irradiance is higher. It also indicates bPV technology is advantageous in fluctuating weather conditions with low irradiance levels. It is also important to mention that the difference in energy generation between a bifacial vertical system and a mono-facial latitude tilt system is less on a cloudy day compared to a sunny day.

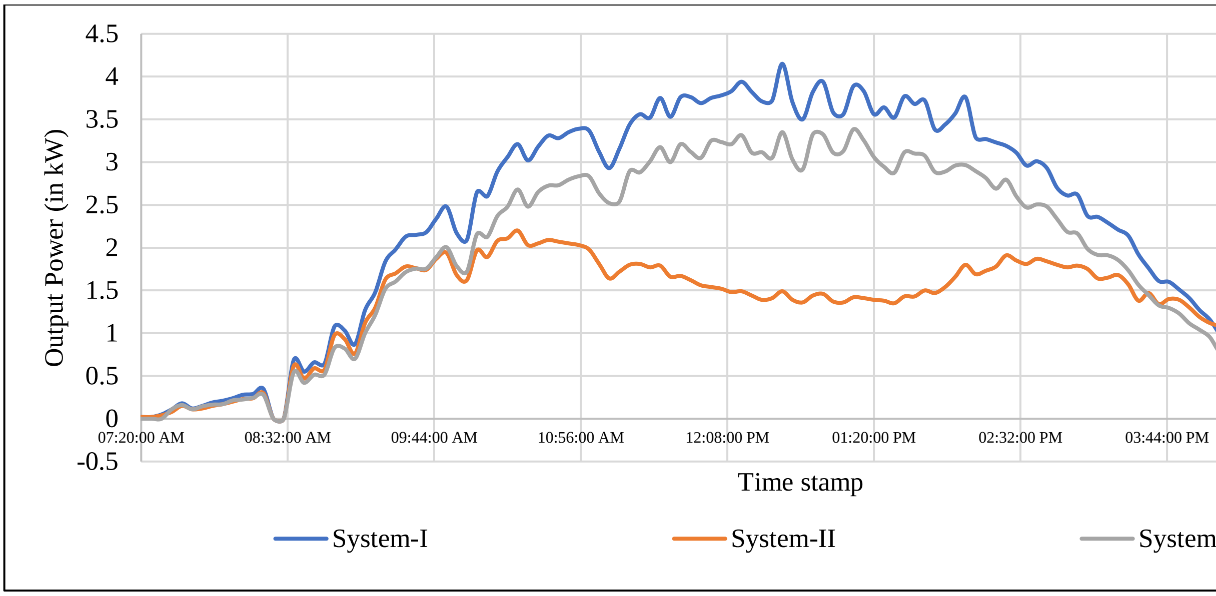

Fig. 5: Solar Power Generation from three systems throughout a sunny day *(02nd Jan. 2022)*

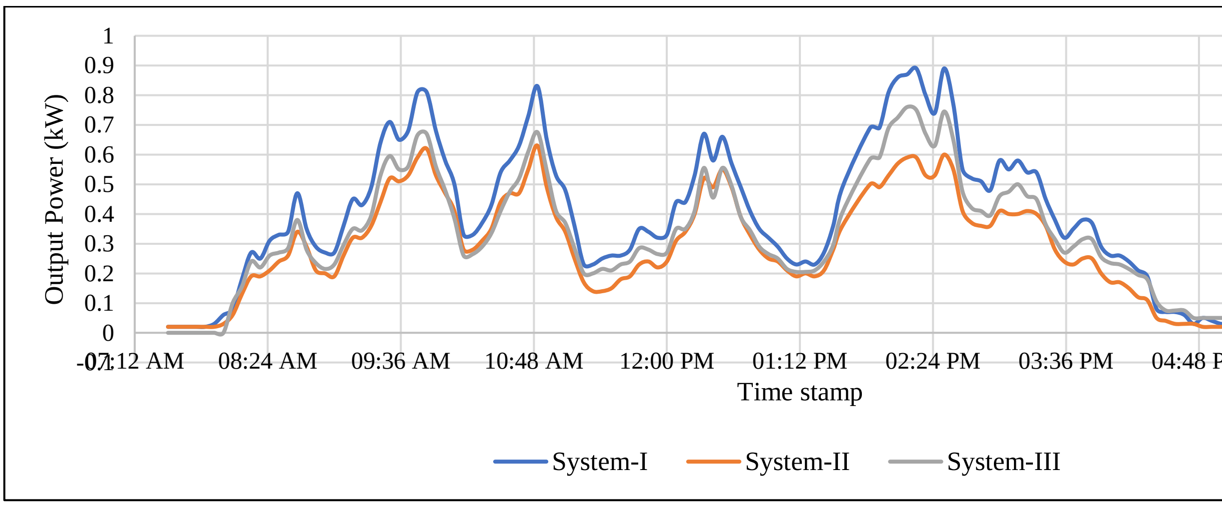

Fig. 6: Solar Power Generation from three systems throughout a cloudy day *(*28th Dec. 2021)

4.3.5 Module temperature study and its impact on energy yield:

Module temperatures of the three systems were measured daily at an interval of 10-minute time stamps. The monthly average temperatures are then determined to study the module temperature variations in various months. The temperature sensors are placed at the rear side of mono-facial and bifacial modules as shown in Fig. 7 (a, b & c) below.

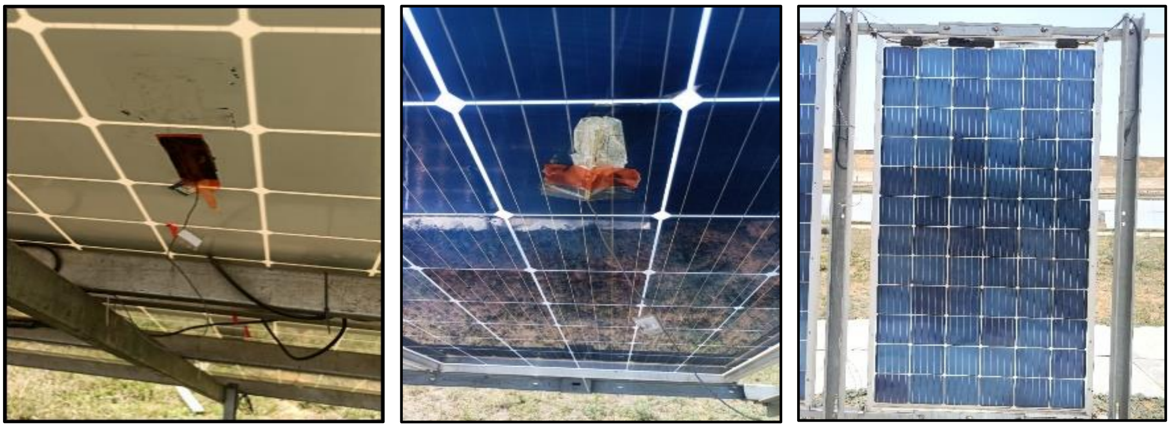

(a) (b) (c)

Fig. 7: (a) mPV module temperature sensor, (b) bPV latitude tilt module temperature sensor, (c) bPV vertical tilt module temperature sensor

In the case of a mono-facial system, two temperature sensors were placed at the rear side of two modules and their average was taken for the study. In the case of the bifacial latitude tilt and vertical tilt system, the temperature sensors were placed at the rear side of one module of each system. The maximum temperatures of the three systems were taken separately for every month of the study (from Nov-2021 to April-2022) and are shown in Fig. 8.

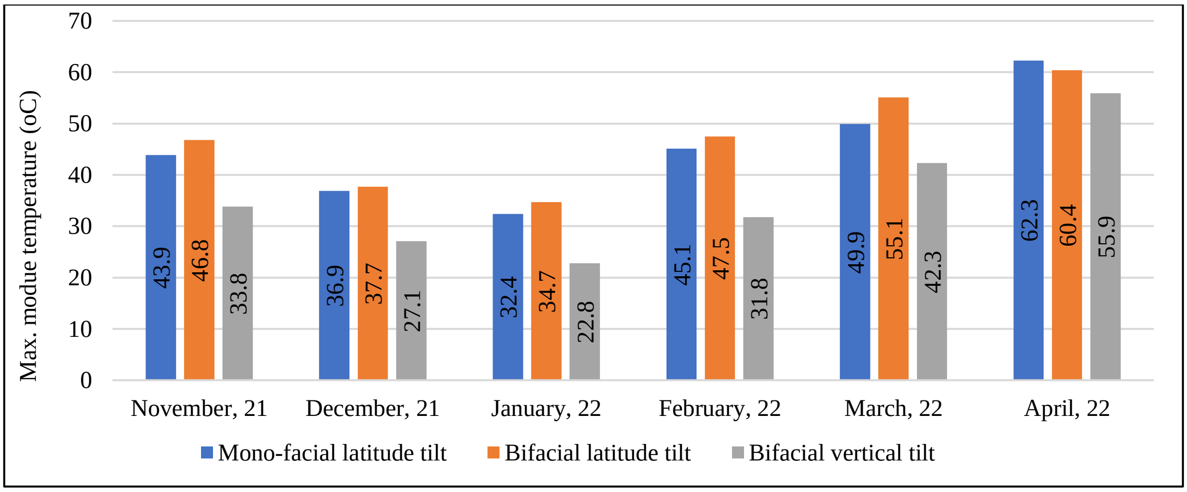

Fig. 8: Maximum module temperatures of three systems in different months

From the above study, it was evident that the module temperature of the bifacial latitude tilt system was comparatively higher (~ 2^0C - 5^0C) than that of the mono-facial latitude tilt system in various months. The higher module temperature of the bifacial latitude tilt system is possibly attributed to the absorption of higher total irradiance compared to the mono-facial latitude tilt system. Absorption of higher total irradiance by the bifacial latitude tilt system results in the generation of more solar electricity and thereby, an average bifacial gain of over 20%.

It was also observed that although the morning and evening temperatures of bifacial vertical modules were higher, the average module temperature of this system (System-II) was lower (~ 10^0C) compared to both bifacial and mono-facial systems with latitude tilt. The less absorption of light in the vertically installed system (around noon time) is the possible reason for the lower temperature in the vertically installed system. The reduction in absorption of incident light for vertical systems also results in a lower generation of solar electricity compared to mono-facial and bifacial systems with latitude tilt.

4.3.6 Performance study of the vertically installed bifacial system:

The energy generation from the vertically installed bPV system (System-II) was comparatively lower than both bPV and mPV systems with standard tilt (System-I & System-III respectively). It was observed that the daily average specific energy yield from System-II is around 37% and 23% lower than System-I and System-III respectively from Nov to Feb when the ground reflecting material is natural vegetation and grass; while it was around 17% lower than System-I and 1.2% higher than System-III during March to mid of May, when the ground reflecting material was SS-sheet. The higher daily specific average energy yield of the bifacial vertical tilt system is due to the change in ground reflecting materials and with the increase in ground reflection (with special preparation), it is possible to achieve similar energy output compared to mPV systems as can be seen in the experimental data with SS sheet.

It was observed that the bifacial modules supplied by the vendor were with standard frame (as in mono-facial modules) as shown in Fig. 9, which was causing significant shading on the rear side especially when the rear side of vertically installed modules were facing the sun. That was a possible reason for the lower energy yield from the vertical bifacial system especially in the second half of the day. Thus, for a vertical bifacial module, it is recommended to use specially designed frames to avoid the shading on the rear side and the module should be with high bifaciality. It was also observed that the daily average maximum module temperature of the bPV vertical system was comparatively lower than both bPV and mPV systems with latitude tilt.

Fig. 9: Standard frame shading the rear side of a bPV module

The bifacial vertical system can be set up along the bunds of the agricultural land or along the side of the national highways. Thus, it can save the cost and hassle of acquiring land for setting up solar PV projects. Even though the energy generation is comparatively lower, a bifacial vertical system is very useful for Agro-PV or PV systems installed along the highways.

4.4 Simulation Study for Levelized Cost of Electricity (LCOE):

The LCOE was simulated for the three systems configurations each having capacity of 1 MW_{dc}. The LCOE calculator of NREL's System Adviser Model was used for the above assessment. The site selected for carrying out the study was Bhadla (27.55^{0}N, 71.95^{0}E), District Jodhpur, Rajasthan. The bifaciality = 0.81, albedo = 0.3, ground coverage ratio = 0.3 and ground clearance height = 0.6 meters have been considered for the calculation of LCOE. The capital cost of the projects has been considered as per the current market trends. The various assumptions made for the study including the land cost for the bPV vertical system were assumed to be zero as vertical plants are generally hosted on the bunds of agricultural fields or along the side of highways. MW-size vertical PV plants are generally not installed on open fields. This is why the system cost of the bifacial vertical system is considered the lowest among the three system configurations. The cost of bifacial module was assumed to be USD cent 0.50/Wp higher than its mono-facial counterpart. Therefore, the system cost including cost of installation is highest for bPV latitude tilt system followed by mPV latitude tilt system and then bPV vertical tilt system.

The LCOE calculator of SAM uses the fixed-charge rate (FCR) method to calculate the project-levelized cost of electricity. The FCR is the revenue required per amount of investment to recover the investment made. After simulation, the results obtained for all three configurations are tabulated in Tab. 1.

Thus, LCOE= {(FCR x Capital Cost + Annual O&M cost)/Annual Electricity Production} + Variable Operating cost (if any)

Tab. 1: Simulated results for LCOE

Results	bPV system with latitude tilt	m PV system with latitude tilt	bPV system with vertical tilt
Annual energy production	18,14,446 kWh	15,85,615 kWh	15,21,172 kWh
Capacity Factor	20.7%	18.1%	17.3%
Energy yield	1,816 kWh/kW	1,587 kWh/kW	1,519 kWh/kW
LCOE (Exchange rate 1 USD= INR 74 during that time)	USD Cent 2.53/unit or INR 1.87/unit	USD Cent 2.86/unit or INR 2.12/unit	USD Cent 2.92/unit or INR 2.16 unit

Bifacial Gain = {(Energy yield from bPV system with latitude tilt - Energy yield from mPV system with latitude tilt)/Energy yield from mPV system with latitude tilt} = {(1816 - 1587)/1587} = ~14%

Thus, it is observed that LCOE is minimum for the bPV system with latitude tilt followed by LCOE for the mPV system with latitude tilt and then the bPV system with vertical tilt. The LCOE for the bPV system with latitude tilt is ~12% lower than the mPV system and the LCOE for the bPV system with vertical tilt is ~ 2% higher than the mono-facial PV system with latitude tilt. Though the LCOE of the bifacial PV with vertical tilt is the highest among the three configurations, it is useful for niche applications like Agro-PV, fencing, noise barriers etc.

Further, the LCOE for bifacial PV systems with latitude tilt depends on various parameters like tilt angle, albedo, ground coverage ratio (GCR), ground clearance height or elevation of the modules from the ground etc.

4.4.1 Optimized parameters for minimum LCOE:

The optimized various parameters for the minimum LCOE of a bPV power plant (1 MWdc) located at Bhadla, District-Jodhpur, Rajasthan are given in Tab. 2 as:

Tab 2: Optimized values of various parameters for minimum LCOE

Various parameters	Optimized value
Sub-array tilt angle	35^0
Ground coverage ratio	0.3
Ground clearance height	1.2 meter
Ground albedo for desert sand	0.3

With the above-optimized parameters, the energy yield and minimum LCOE for 1 MWdc bPV system are given in Tab. 3 as under:

Tab. 3: Energy Yield and Minimum LCOE for 1 MWp optimized system

Various parameters	Value
Annual Energy	18,61,280 kWh
Capacity Utilization Factor	21.3%
Energy Yield	1863 kWh/kW
Performance Ratio	0.82
Levelized Cost of Electricity (1 USD =INR 74)	USD Cent 2.51/kWh or INR 1.857/kWh

5. Conclusions and Scope of Further Work:

The bPV modules and system undoubtedly generate more energy than their mono-facial counterpart. The quantum of excess energy generation depends on various parameters like ground albedo, ground coverage ratio, ground clearance heights, module tilt angle etc. In this study, it is found that the bifacial gain is over 20% with natural vegetation and grass as the ground reflecting material which increases further when SS-sheet is used as the ground reflecting material.

The slightly higher module cost of the bifacial module compared to its mono-facial counterpart is compensated by the extra energy generated by the bifacial system. The simulation study reveals that the LCOE from the bPV system is comparatively lower than the equivalent mPV system when the albedo is 0.3 or above. The albedo of the Ladakh region and desert of Rajasthan is naturally higher than the normal plain as the Ladakh region is covered with snow for most of the time round the year and the desert areas of Rajasthan are covered with sand. Thus, these are the natural potential sites in India for setting up MW-scale bPV plants with higher energy yield and thereby, lower LCOE. Though it is not economically feasible and advisable to change the ground-reflecting material of the entire solar field, it may be possible for a rooftop solar system. The rooftop may be white painted once a year to harness more energy from the bPV rooftop solar systems. Thus, the bifacial modules can also become useful for rooftop solar systems as India has an ambitious target of 40 GW of rooftop solar systems.

The bPV vertical tilt system is also very useful and it has wide applications. Though it generates comparatively lower energy than the mPV latitude tilt system, it can be set up along the bunds of the agricultural land or along the side of the national highways. Thus, it can save the land cost and hassles of acquiring land for setting up solar PV projects. Therefore, a bifacial vertical system is very useful for Agro-PV or PV systems installed along the highways.

6. Acknowledgement:

I convey my sincere thanks to the Indian Institute of Technology Delhi, National Institute of Solar Energy, Gurgaon, & International Solar Alliance for allowing me to carry out the study. Further, the views expressed in the research paper are based on the study conducted and do not represent the views of the organizations.

7. References:

[1]. REN21. Renewable 2021 Global Status Report. Available online: https://www.ren21.net/wp-content/uploads/2019/05/GSR2021_Full_Report.pdf (2021) (accessed on 05-07-2021)

[2]. Kopecek, R. & Libal, J. Bifacial Photovoltaic 2021: Status, Opportunities and Challenges. *Energies,* 14, 2076 (2021) https://doi.org/10.3390/en14082076

[3]. ITRPV 2020. International Technology Roadmap for Photovoltaic (ITRPV) 2020 Results. Available online: *https://itrpv.vdma.org/en/* (2021) (accessed on 05-07-2021)

[4]. Gu, Wenbo & Li, Senji & Liu, Xing & Chen, Zhenwu & Zhang, Xiaochun & Ma, Tao, 2021. "Experimental investigation of the bifacial photovoltaic module under real conditions," Renewable Energy, Elsevier, vol. 173(C), pages 1111-1122. https://doi.org/10.1016/j.renene.2020.12.024

[5]. Sun Xingshu et al. Optimization and performance of bifacial solar modules: A global perspective. *Applied Energy* 212, pp. 1601-1610 (2018) https://doi.org/10.1016/j.apenergy.2017.12.041

[6]. Stein J. S. et al. Outdoor Field Performance from Bifacial Photovoltaic Modules and Systems. *IEEE 44th Photovoltaic Specialist Conference (PVSC)* (2017) https://doi.org/10.1109/PVSC.2017.8366042

[7]. Patel M. T. et al. Temperature-dependent energy gain of bifacial PV farms: A global perspective. *Applied Energy.* 276, 115405 (2020), https://doi.org/10.48550/arXiv.2003.03660

[8]. Liang T. S. et al. A review of crystalline silicon bifacial photovoltaic performance characterization and simulation. J. *Energy & Environmental Science,* Vol.12, Issue 1 (2018), https://doi.org/10.1039/C8EE02184H

[9]. NREL, USA. Technical Report on bifiPV2020 Bifacial Workshop: A Technical Overview. NREL/TP-5K00-77817 (2020), https://www.nrel.gov/docs/fy21osti/77817.pdf

[10]. Park H. et al. Outdoor Performance Test of Bifacial n-type Silicon Photovoltaic Modules. *Sustainability.* 11, 6234 (2019), https://doi.org/10.3390/su11226234

[11]. Asgharzadeh A. et al. Analysis of the Impact of Installation Parameters and System Size on Bifacial Gain and Energy Yield of PV Systems. *IEEE 44th Photovoltaic Specialist Conference (PVSC), pp. 3333-3338* (2017), https://www.osti.gov/servlets/purl/1460255

[12]. Rodríguez-Gallegos C. D. et al. Monofacial vs bifacial Si-based PV modules: Which one is more cost-effective? *Solar Energy.* 176, pp. 412–438 (2018), https://doi.org/10.1016/j.solener.2018.10.012

[13]. Solar World. White Paper on calculating the additional energy yield of a bifacial solar modules. Available online: https://solaren-power.com/pdf/Calculating-Additional-Energy-Yield-Through-Bifacial-Solar-Technology.pdf

[14]. International Energy Agency. Bifacial Photovoltaic Modules and Systems: Experience and Results from International Research and Pilot Applications 2021. Available online: https://iea-pvps.org/wp-content/uploads/2021/04/IEA-PVPS-T13-14_2021-Bifacial-Photovoltaic-Modules-and-Systems-report.pdf (accessed on 08-09-2021)

[15]. National Renewable Energy Laboratory. System Advisor Model (SAM) 2020.11.29. https://sam.nrel.gov/download.html

02. Innovative Application of PV Technologies

Cooking food with a solar PV-powered DC stove

Ashmore Mawire[1] and Oyirwoth P. Abedigamba[2]

[1]North-West University, Material Science, Innovation and Modelling (MaSIM) Research Focus Area, Department of Physics, Mmabatho 2745, Mahikeng, South Africa, *email: ashmore.mawire@nwu.ac.za

[2]Department of Physics, Kyambogo University, P.O. Box 1, Kyambogo, Kampala, Uganda

Abstract

An experimental setup to evaluate a new 12 V DC-powered electrical cooker is presented. The DC cooker is powered by a 450 W solar panel connected to a maximum power point tracking (MPPT) charge controller and a 12 V AGM 100 AH deep cycle battery. The cooking tests are performed when the DC cooker and the pot containing food are placed in a closed-insulating wonderbag cooker to reduce heat losses. Four different food cooking tests are carried out during different times of the day to evaluate the cooking performance of the system. The cooking tests are boiling rice at night, boiling eggs during midday, preparing chicken and turkey stew after midday, and frying chicken late in the afternoon. All foods are well cooked within 90 minutes, and the food that takes the longest time to cook is rice because the energy from the battery is solely used to cook the food. For all tests, the electrical cooking powers are comparable, implying that the system can be used at any time of the day which is better than existing solar cookers which operate optimally only under high solar radiation conditions. There is also no need to include an inverter since the cooker operates in DC mode.

Keywords: Cooking Food; DC Stove; Solar PV

1. Introduction

Solar cookers utilize the sun's energy to cook food and are vital in reducing greenhouse emissions generated by firewood used for cooking in developing countries. The four main types of solar cookers are concentrating solar cookers, box solar cookers, panel solar cookers, and indirect solar cookers. All these types of solar cookers have the disadvantage of not operating properly or very poorly in overcast or cloudy conditions. Concerted efforts to improve the performance of solar cookers for periods with little or no sunshine have been made by integrating them with thermal energy storage (TES) systems (Aramesh et al., 2019; Bhave & Thakare, 2018; Bhave & Kale, 2020; Coccia et al., 2020; Lecuona et al., 2013; Mawire et al., 2022; Omara et al., 2020; Rekha & Sukchai, 2018). However, there might be continuous days of bad weather which makes short-term TES null and void. The only option during continuous bad weather days is to resort to electrical cooking, liquified petroleum gas (LPG), paraffin, firewood, and other polluting fossil fuel-based cooking energy sources.

Instead of relying on these mentioned energy sources, solar photovoltaic (PV) panels can be used. Solar panels can operate during cloudy conditions although not optimally. PV panels can be used with an inverter and battery storage for operating small AC electrical cooking hot plates which increases the cost of the system due to the expensive inverter systems. A possible solution is to operate a DC stove together with a PV panel to reduce the cost. Some researchers have recently reported on an induction DC-powered cooker (Altouni et al., 2002) which requires specialized ferromagnetic cooking pots. Other researchers have investigated different versions of PV cookers with DC-to-DC converters, and storage generally with operating voltages above 12 V (Atmane et al., 2020; Lamkaddem et al., 2022). The 12 V option for a DC cooker removes the need for expensive DC-to-DC converters together with expensive inverters. According to our reviewed literature, a 12 V DC stove which can be powered by a 12 V battery charged with a solar panel has not been reported. In this article, the cooking performance of a new cheap 12 V DC cooking stove that is sold locally online in South Africa from Takealot (Takealot, 2023) is evaluated while being powered by a 450 W solar panel connected to a maximum power point tracking (MPPT) charge controller and a 12 V 100 AH battery. The DC stove and

10.18086/swc.2023.02.06 Available at http://proceedings.ises.org

cooking pot are tested in an insulated wonderbag slow cooker reported by Mawire et al., (2020) to reduce the impact of environmental conditions such as windspeed variability which increases heat losses. According to the knowledge of the authors, no study has ever been reported on a DC cooking stove integrated with a PV panel, charge controller, and battery storage together with an insulated slow cooker (wonderbag). The novel aspect of the study is that cooking is tested under different conditions, and this type of cooking setup will compete with current electrical cookers since cooking is possible any time of the day. Additionally, not only will the system cook food, but the system can also be a multi-purpose device providing energy for other DC appliances such as refrigerators and lights without the need for expensive inverter systems, The system can be used in remote locations without grid connectivity.

2. Experimental method

A photograph of the 12 V DC cooker with four terminals is shown in Fig. 1 (Takealot, 2023). The cooker has two coils indicated by the four terminals in Fig. 1. It implements DC heating at two powers of approximately 200 W and 300W. The heating powers are estimated from the measured resistances of the single coil and the two coils which are 0.8 Ω and 0.6 Ω, respectively. For 200 W, one coil consisting of two terminals (red and black) is connected to the 12 V battery/source. For the 300 W setting, the two red terminals are connected to the positive terminal of the battery/source, and the other two black terminals are connected to the negative terminal of the battery/source. The cooking surface of the DC stove is 16.7 cm in diameter, and its height is 5.5 cm. The total diameter of the cooker is 23 cm.

Fig. 1: A photograph of the 12 V DC cooker used in the experimental test (Takealot, 2023)

Fig. 2 shows a photographic view of the experimental setup. The sun charges the battery via the solar panel, and the charge controller regulates the amount of electrical energy supplied to the DC stove. A 100 AH battery was used to cook multiple meals. With a 100 AH battery, the theoretical energy supplied is 1200 WH which means that it is theoretically possible to cook for 6 H (1200 WH/200 W). The 12 V DC stove is placed in a wonderbag insulating cooker to reduce heat losses during the experimental trials which prevented most convection heat losses because of external windspeed variability. Power to the 12 DC stove is supplied from the charge controller.

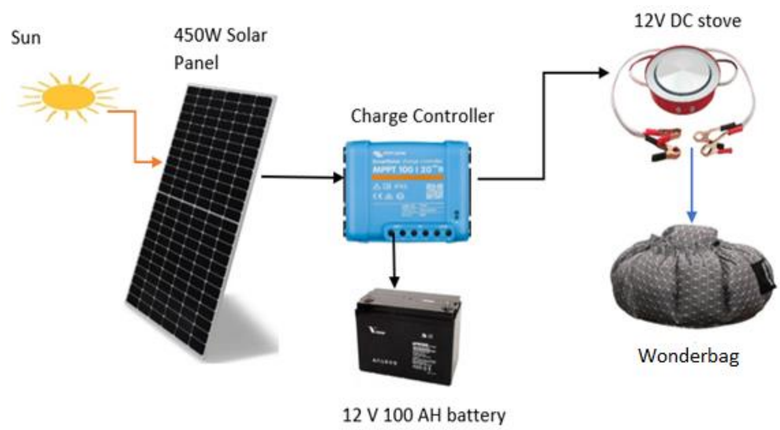

Fig.2: A photographic view of the experimental setup and connections.

Photographs of sections of the experimental setup are shown in Fig. 3. A 450 W solar panel is connected via the charger controller and battery shown in Fig. 3(a). The tilt angle of the panel was 30 º which was chosen based on the balancing the panel to the supporting structure instead of the maximum PV output production. However, the tilt angle falls between 30-45 º for maximum PV output production. The panel experienced a bit of shading, but it was used in the indirect mode to just charge the battery, so this tradeoff was acceptable since the battery was used to cook. A maximum power point tracking (MPPT) charge controller controls the charging of the battery providing maximum power to the DC stove. The maximum operating current of the charge controller is 20 A. Only one coil was used in the cooking tests since the controller could not provide adequate current to run both coils. The output of the charge controller ensured that maximum power was transferred to the DC cooker. Each experimental cooking test was run for a maximum period of 90 minutes. Two multimeters measured the DC voltage and current every five minutes manually to estimate the electrical heating power. Two other multimeters recorded the cooking and ambient temperatures which were manually recorded every five minutes. An RS solar power meter was used to measure the global horizontal irradiance (GHI) every five minutes manually. Ideally, the irradiance on the plane of the array should be measured but only estimated values were used for the GHI since the DC cooker operated in the indirect mode, and only an estimate was required. The experiments were carried out in a closed wonderbag shown in Fig. 3(c) where the DC cooker, the cooking pot, and the food were placed to reduce heat losses. The electrical heating power to the DC stove can be estimated by multiplying the measured current through and voltage across the stove together, and it can be expressed as:

$$P_E = VI, \tag{1}$$

where P_E is the electrical heating power, V is the measured DC voltage and I is the measured current.

Fig. 3: Photographs of the experimental setup showing (a) the PV panel connected to the DC cooker in a wonderbag, (b) the 12 V AGM battery and the MPPT controller, and (c) a closed wonderbag with the DC cooker and the cooking pot with food.

Fig. 4 shows a photograph of the silver stainless steel cooking pot used as a cooking utensil enclosed in the wonderbag. It has an outer diameter of 21cm and a height of 10 cm, making its capacity 3.5 litres

Fig.4: A photograph of the silver stainless steel cooking pot used in the experiments.

The total cost of the system is around R6,000 (USD 314) (Mawire et al., 2024). The PV system seems expensive, but for South African conditions it is reasonably priced considering that the system can be used as a multipurpose system with the capability of cooking, heating, cooling, and lighting applications. Only the cooking application is presented in this paper. Also, quality components and a large charging panel were used to make the price more expensive. The real price could be 50 % lower (USD 157) if a smaller solar panel and cheaper components were used (Mawire et al., 2024). The larger panel enables the charging of the battery faster, and it provides more versatility in terms of operating more DC devices.

3. Results and discussion

Fig. 5 shows experimental results for the cooking tests. The cooking tests were performed from 20-23 March 2023. The first test was boiling 203 g of rice with 500 ml of water at night on 20 March 2023. This was followed by boiling 285 g of eggs in 300 ml of water around midday on 21 March 2023. The third test was after lunchtime (14:25-15:55 hrs) on 21 March 2023, and this involved preparing chicken (280 g) and turkey (233g) stew using 200 ml of water. The last test performed on 23 March 2023 involved frying 425 g of chicken in 134 g of sunflower oil late in the afternoon.

Midday and after-lunch cooking have the highest solar radiation for cooking and charging the battery, thus their electrical cooking powers are slightly higher than the other tests. It is important to note that the cooking tests are terminated when the food has been cooked, thus the electrical cooking powers for all three tests dropped to zero after the food is cooked well. The only cooking test to last for 90 minutes is boiling of rice at night which shows the lowest cooking power since the stored energy from the battery is solely used to cook rice. The cooking powers for all four tests are comparable and fall within 165-210 W implying that food can be cooked efficiently at any time of the day, unlike traditional solar cookers which require high solar radiation conditions. Boiling of eggs is shorter than the other cooking processes since the mass of water used is less. Frying of chicken shows the highest temperatures achieved since sunflower oil with a lower thermal mass is used to fry chicken instead of water. The temperature drop in the frying of chicken at 35 mins is due to the opening of the wonderbag to examine whether the chicken is well-fried. The other drops for frying of chicken and cooking the chicken and turkey stew are due to switching off the power and allowing the food to simmer and cook slowly in the wonderbag to save power. It must also be stated that, unlike traditional cooking, the possibility of burning food regularly is drastically reduced due to the lower cooking power involved. Also, unlike traditional solar cookers, trapped/stored heat inside the wonderbag can be used to extend the cooking period without power thus saving power for cooking purposes.

The overall average thermal efficiencies of the PV cooker ranged between 4-16 % and the water heating efficiencies between 38-57 %. More details of the efficiencies have been reported in our related work (Mawire et al., 2024).

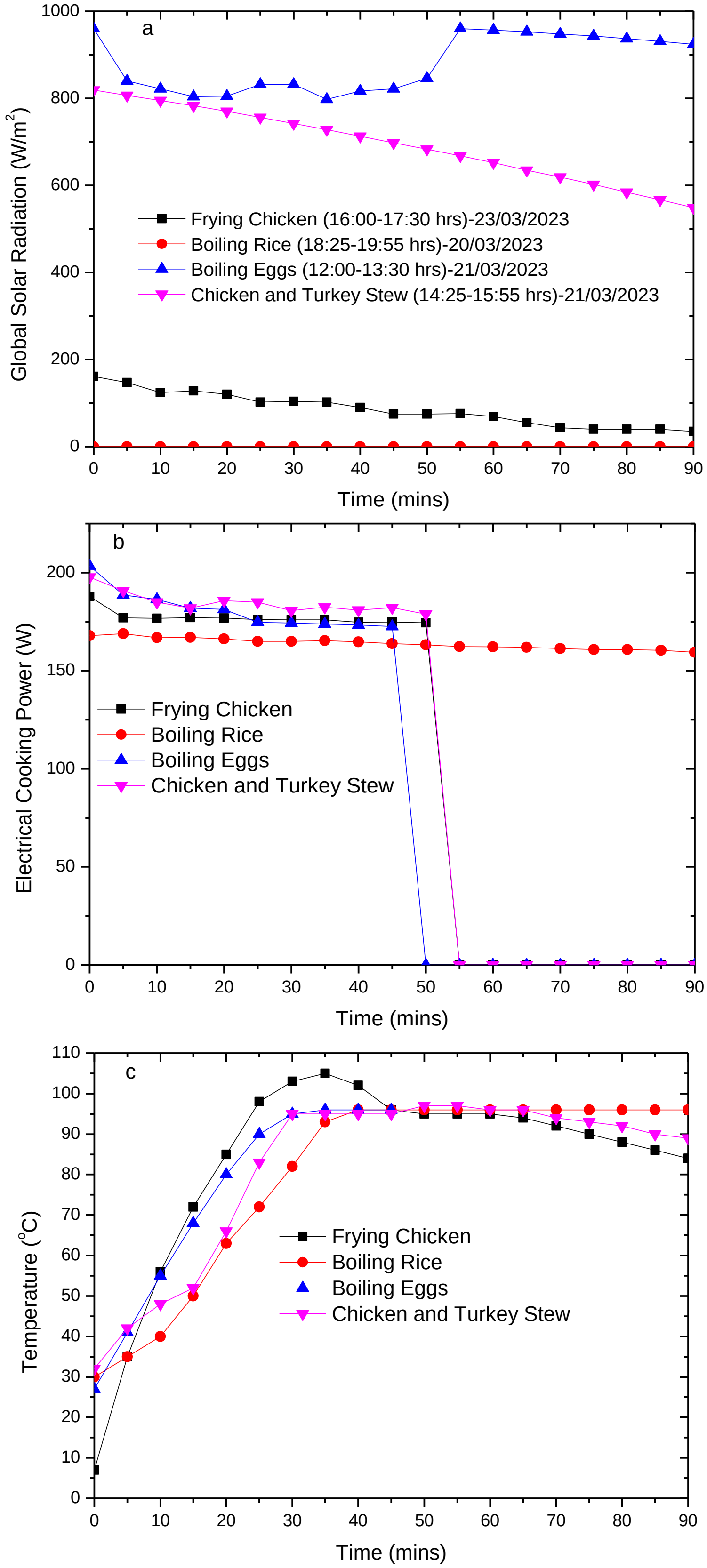

Fig. 5: Experimental cooking results for the four cooking tests showing: (a) the global solar radiation, (b) the electrical cooking power, and (c) the temperature profiles of the cooked food.

Fig.6 shows crispy and well-cooked chicken and chips (fries) using the solar PV-powered DC stove.

Fig. 6: Chicken and chips (fries) cooked using the solar PV-powered DC stove.

4. Conclusion

A new 12 V DC cooking stove powered by a PV panel integrated with battery storage and an MPPT charge controller was experimentally evaluated for cooking different foods under four different conditions. All the cooking tests showed that the cooker can cook food well in 90 minutes or less. For all cooking tests, the electrical cooking powers were comparable, implying that the system can be used at any time of the day which is better than existing solar cookers which operate optimally only under high solar radiation conditions. The cooker also does not require an expensive inverter since it operates in the DC mode. Future work will involve comparing the reported cooker with a parabolic dish cooker which shows the highest cooking temperatures and the fastest cooking speeds under different weather conditions.

5. Acknowledgements

The authors would like to acknowledge the National Research Foundation (NRF) and SASOL for funding to carry out the work under the Sasol-NRF Research Grant (138608)-Development of low-cost standalone solar cookers with thermal energy storage for decentralized communities. We acknowledge that opinions, findings, and conclusions or recommendations expressed in any publication generated by the NRF-supported research are our own and that the NRF accepts no liability whatsoever in this regard.

6. References

Altouni A, Gorjian S, Banakar A. (2022). Development and performance evaluation of a photovoltaic-powered induction cooker (PV-IC): An approach for promoting clean production in rural areas. Cleaner Engineering and Technology 6, 100373.

Aramesh M, Ghalebani M, Kasaeian A, Zamani H, Lorenzini G, Mahian O, Wongwises S. (2019). A review of recent advances in solar cooking technology. Renewable Energy 140, 419-435.

Atmane I., El Moussaoui N., Kassmi K., Deblecker O., Bachiri N. (2021). Development of an innovative cooker (hot plate) with photovoltaic solar energy. Journal of Energy Storage 36, 102399.

Bhave A.G., Thakare K.A. (2018). Development of a solar thermal storage cum cooking device using salt hydrate. Solar Energy 171, 784-789.

Bhave A.G., Kale C.K. (2020). Development of a thermal storage type solar cooker for high-temperature cooking using solar salt. Solar Energy Materials & Solar Cells 208, 110394.

Coccia G., Aquilanti A., Tomassetti S., Comodi G., Nicola G. (2020). Design, realisation, and tests of a portable solar box cooker coupled with an erythritol-based PCM thermal energy storage. Solar Energy 201, 530-540.

Lamkaddem A., EL Moussaoui N.L., Rhiat M., Malek R., Kassmi K., Deblecker O., Bachiri N. (2022). System for powering autonomous solar cookers by batteries. Scientific African 17, e01349.

Lecuona A. Nogueira J.I., Ventas R., R odríguez-Hidalgo M.., Legrand M. (2013). Solar cooker of the portable parabolic type incorporating heat storage based on PCM. Applied Energy 111, 1136-1146.

Mawire A, Lentswe K, Owusu P, Shobo A, Darkwa J, Calautit J, Worall M. (2020). Performance comparison of two solar cooking storage pots combined with wonderbag slow cookers for off-sunshine cooking. Solar Energy 208, 1166-1180.

Mawire A., Lentswe K., Owusu P. (2022). Performance of two solar cooking storage pots using parabolic dish solar concentrators during solar and storage cooking periods with different heating loads. Results in Engineering 13, 100336.

Mawire A., Abedigamba O.P., Worall M. (2024). Experimental comparison of a DC PV cooker and a parabolic dish solar cooker under variable solar radiation conditions. Case Studies in Thermal Engineering 54, 103976.

Omara A.A.M., Abuelnuor, A.A., Mohammed H.A., Habibi D., Younis O. (2020). Improving solar cooker performance using phase change materials: A comprehensive review. Solar Energy 207, 539-563.

Rekha S.M.S., Sukchai S. (2018). Design of Phase Change Material Based Domestic Solar Cooking System for Both Indoor and Outdoor Cooking Applications. Journal of Solar Energy Engineering140, 041010.

Takealot. DC 12V Stove - Hot Plate. https://www.takealot.com/dc-12v-stove-hot-plate/PLID91699937 Website accessed, 5 April 2023.

FLOATING SOLAR – A DEVELOPER PERSPECTIVE

Viktor Dancza

Blue Leaf Energy Asia, Singapore

Abstract

Ground and roof mounted solar PV is well understood and adopted around the world, while placing PV modules on water surfaces may seem experimental. The benefits of floating PV usually cite cooling effect of water, evaporation reduction and reduced pressure on arable land, but general knowledge and publications around this rather niche sector is still holding it back from reaching its full potential. The objective of this work is knowledge sharing from the development perspective, based on real world learnings and potential solutions that are independent from products or country specific challenges. By sharing first-hand experience, the author wishes to contribute not just to FPV development but the broader acceleration of renewable energy uptake.

Keywords: Floating PV, FPV, project development, knowledge sharing, real-world experience

1. Introduction

Although solar photovoltaic (PV) technology is close to 100 years old, floating photovoltaic (FPV) is relatively new. Despite its modest initial uptake, some sources estimate its global potential in the Terawatts (Jin et al, 2023). Cost remains one of the key obstacles, while lack of standardization of products and availability of international design standards further hinder uptake. The lack of experience and understanding of the technology often lead to concerns from local communities and contribute to uncertain permitting timelines. Meanwhile, there is increasing recognition of how FPV can contribute to the overall renewable energy targets, as growing number of suppliers and developers enter this nascent sector (NREL, 2021).

2. Prominent FPV Publications

The first notable publication, that tried to summarize the benefits and challenges of this technology was released in 2019 by The World Bank (The World Bank, 2019), drawing from lessons learned at the world's largest floating solar testbed, which is operated by the Solar Energy Research Institute of Singapore (SERIS, 2016). The second publication of global significance came from international consultant DNV (DNV, 2021). Their document was developed as a joint industry project, with 24 participating companies. A third, albeit lesser-known guideline was also released in 2021, and updated in 2023, but it is only available in Japanese language (NEDO, 2021 and 2023). While all three of these documents are a real treasure trove of general information, they are written from a consultant' perspective and often lack directly applicable, practical advice that project developers need.

3. Site Selection Challenges

3.1. Water body

Projects are more often originated with potential water bodies being offered by their owners, rather than developers choosing the most ideal locations. As such, many of the key considerations like bathymetry, wind speed, wave height, water level fluctuation will become engineering challenges to solve and not a selection criterion. While these are necessary information for design, often they are not readily available and mapping a large lake is very costly; a spending that is not possible at site selection stage. Publicly available data and assumptions are the best compromise in early development stage, while ascertaining the cost of such surveys must be identified and captured in the development expenditure (DEVEX). Furthermore, as many of these parameters change over time, a simple survey cannot measure them, but rather a long-term measurement campaign needs to be considered, which can be incorporated into a pilot system at the eventual project location.

10.18086/swc.2023.02.02 Available at http://proceedings.ises.org

3.2. Land

While focusing on the water body, it is easy to lose sight of the importance of suitable land. As lakeside land parcels are often desirable for leisure or housing purposes, securing them could be costly and challenging. The size of the permanent land needed will be driven by the project size, location of inverters and electrical facilities, while the temporary land for construction and launching the system will be driven by the desired speed of the project deployment. If the permanent land cannot be acquired at the ideal location, there is possibility to shift the facilities further from the shore, by using horizontal directional drilling for example and taking cable under roads or other land parcels. In fact, water level changes (including unforeseen changes due to climate change) may make it a wise choice not to locate electrical facilities directly on the shore. Access for heavy goods vehicles to the lake and the lakeshore properties can further limit site suitability.

3.3. Grid

Connecting floating PV systems to the grid can be achieved through underwater or floating power cables. While the latter is cheaper and easier to maintain, it also blocks the water surface from boats and may not be suitable for larger lakes, where the water body has multiple users. The additional cost and complexity should be considered from early on, both in CAPEX and OPEX terms.

One of the key technical challenges for FPV systems is grounding, earthing and lightning protection require a different approach than GPV, which may raise questions around the security and quality of the power supplied by the plant. While there are recognized methods for lightning protection for PV systems (IEC, 2020), FPV plants are not yet included. Furthermore, deploying thousands of lightning terminals is not just costly, but also not practical and a risk-based approach can be a more practical solution here.

4. Development Challenges

4.1. Cost competitiveness

One of the biggest barriers to FPV is the constant comparison to GPV and the expectations to bring their cost to the same level. At the time of writing this, an approximate USD0.10 /Wp cost difference exists (Frost & Sullivan, 2023) which makes FPV based offtake opportunities less attractive, than their land-based competitors. As closing this gap may not be possible for some time, it might be a more realistic target to work on different offtake options and quantify the additional benefits FPV can bring. Auctions and FIT tariffs have historically distinguished between roof and GPV and in some countries FPV have also become a separate category.

4.2. Experienced workforce

The nascent nature and relatively small size of the FPV market also means, there is a general lack of experienced workforce. This creates two issues; one is the cost premium demanded by the few, experienced companies and the other is the generally available skill level among PV workers. The good news here is the leading FPV technology providers include training and supervision among their services, which once again, makes product selection crucial for the success of the project. As workforce will need to be trained in most cases, this also creates a great opportunity for community engagement through providing local job opportunities and long-term skills in construction and maintenance.

4.3. Community support

Potentially the most crucial and delicate aspect of FPV projects, is convincing the diverse group of stakeholders (e.g. recreational users, fisherfolks, resort owners, residents, farmers, etc.) about the safety and benefit of the project. Their concerns range from the visual impact to water quality, electrical safety, impact to wildlife or their own livelihoods. In many countries obtaining permits will also be dependent on community support, whether directly or indirectly. Appointing a community engagement officer, making frequent trips to the project location, and holding community engagement sessions are all key steps, which need to be factored in both in the project schedule and the cost estimations.

4.4. Accepted standards

At the time of writing this, the only dedicated national (design) standard comes from Singapore (Singapore Standards, 2022), with IEC, NFPA, VDE, BS, etc. are still yet to release their own guidelines. This gap is often filled by drawing experience from the marine industry and ground mount PV systems, but differences remain, which often leads to delays in permitting or doubts by the local community and grid operators.

Certification and globally accepted standardization of product quality, also lags the roof- and ground-mounted PV systems, where well established and understood processes exist. Testing procedures and acceptance criteria are highly arbitrary to each manufacturer, leaving the customers confused and investors nervous. A recognized and respected name in product testing, released their suggested product testing process, but its application remains voluntary (TÜV, 2020).

4.5. Permitting route

One of the most frustrating consequences of working with emerging technologies, is the lack of clear path for obtaining approvals. While land parcels are easily divided and boundaries can be drawn, existing land use can be converted, obtaining rights for lake surface (or part of) is a relatively uncharted territory in many countries. Furthermore, as anchoring and mooring lines are located under water, it is not just the surface of the lake, that requires approvals for development. Drawing from more developed FPV markets and proactively meeting decision makers to suggest solutions, can accelerate discussions and help bring approvals closer.

4.6. Insurability

The relatively small number of operating FPV plants and some famous instances of catastrophes (PV Magazine, 2019; Recharge, 2020; Offshore, 2021), also present a risk for the insurance industry. Many insurance companies may decline to provide a cover, others might limit the scope or charge a very high premium. As project details will not be available in early stage, it is better to go with more conservative assumptions in cost estimations, while also engaging insurance brokers from the start. Contacting financing institutes, who engaged in similar projects in the past, is another good source for identifying supportive insurance providers.

4.7. Environmental concerns

Covering the water surface with PV modules can create both benefits and issues for the local flora and fauna (e.g. reducing evaporation, cooling the water, creating shade, etc). Likewise, existing biodiversity could be beneficial or harmful for the PV plant (e.g. soiling by birds, marine life chewing on cables and mooring lines, etc). The exact requirements for studies, as well as long-term monitoring activities (e.g. water quality, fish stock, etc) vary from country to country, but some form of environmental impact assessment (EIA) should be considered among the project activities in any case. There are many experienced consultants available, who can draw on their international experience, while working with local experts on the ground. Voluntarily conducting such studies could also help with permitting and community approvals, as the study outcome will answer many of these stakeholders' questions and concerns.

5. Conclusions

FPV technology has been around for nearly two decades, but only started to gain global acceptance in the past few years. There are increasing number of industry events and market reports, while the sector is still suffering from skilled-labor shortage, cost competitiveness and lack of knowledge sharing by industry players. As project development is the real test of all theories and guidelines, it is essential for practitioners to share their experience and help this sector reach its potential. Making their voices - and often frustrations - heard, will not only help the growth of the industry, but can also pave the way for more FPV friendly landscape for all stakeholders.

6. References

DNV, 2021. DNV-RP-0584 Design, development and operation of floating solar photovoltaic systems. Available at: https://www.dnv.com/energy/standards-guidelines/dnv-rp-0584-design-development-and-operation-of-floating-solar-photovoltaic-systems.html

Frost & Sullivan, 2023. Technological Advancements in Floating Solar Technologies. Available at: https://www.frost.com/uncategorized/floating-solar-addresses-growing-land-scarcity-issues/

International Electrotechnical Commission, 2022. IEC TR 63227:2020 - Lightning and surge voltage protection for photovoltaic (PV) power supply systems. Available at: https://webstore.iec.ch/publication/64039

Jin, Y., Hu, S., Ziegler, A.D. et al, 2023. Energy production and water savings from floating solar photovoltaics on global reservoirs. Nature Sustainability. https://doi.org/10.1038/s41893-023-01089-6

NEDO, 2021. Guideline for the design and construction of floating PV (FPV) systems. The New Energy and Industrial Technology Development Organization (NEDO) Available at: https://www.nedo.go.jp/content/100939012.pdf

NREL, 2021. Enabling Floating Solar Photovoltaic (FPV) Deployment - Review of Barriers to FPV Deployment in Southeast Asia. Available at: https://www.nrel.gov/docs/fy21osti/76867.pdf

Offshore Energy, Incident severely damages floating solar plant in Albania. Available at: https://www.offshore-energy.biz/incident-severely-damages-floating-solar-plant-in-albania/

PV Magazine, Japan’s largest floating PV plant catches fire after Typhoon Faxai impact. Available at: https://www.pv-magazine.com/2019/09/09/japans-largest-floating-pv-plant-catches-fire-after-typhoon-faxai-impact/

Recharge, Fire hits BP venture's flagship floating solar plant in UK. Available at: https://www.rechargenews.com/transition/fire-hits-bp-ventures-flagship-floating-solar-plant-in-uk/2-1-877293

Singapore Standards, 2022. TR 100:2022 - Floating photovoltaic power plants – Design guidelines and recommendations. Available at: https://www.singaporestandardseshop.sg/Product/SSPdtDetail/a2b5734e-1f94-4bfd-91db-fb3e59fec053

Solar Energy Research Institute of Singapore, 2017, Floating PV R&D and Testbed. Available at: https://www.seris.nus.edu.sg/services/Floating-PV-R&D-and-Testbed.html

TÜV Rheinland, 2020. 2 PfG 2731/02.20 - Requirements for materials used in and construction of floating bodies. Available at: https://www.tuv.com/world/en/floating-pv-certification.html

World Bank, 2019. Where Sun Meets Water, The World Bank, Washington DC.

Modelling and Estimation of Photosynthetically Active Solar Radiation in an Agrivoltaic Plant in New Delhi

Subhra Das
Solar Engineering Department, Amity School of Engineering and Technology, Amity University

Abstract

The objective of the present work is to develop a model to estimate the photosynthetically active radiation (PAR) under a solar photovoltaic panel located in New Delhi. The proposed model utilises only the location parameter along with day of the year and time to predict the instantaneous total and diffuse PAR, monthly average hourly PAR and monthly average daily PAR values. The result is compared with those reported in the literature which shows considerable agreement in the result for the winter, summer and monsoon months for the peak value of PAR. The total PAR varies between 0.5-463W/m^2 and the diffuse PAR varies between 24.8- 125.7W/m^{2}over the year.
Keywords*:* Agro-voltaic, PAR, Decomposition model, Sustainable Agriculture

Introduction

With the proliferation of solar energy generation in India, people have started taking interest in combining farming with solar photovoltaic power generation. The objective of this paper is to estimate the solar radiation under a ground mounted solar photovoltaic plant located in New Delhi and thereby estimate the photosynthetically active solar radiation under the solar panels. Mathematical models are proposed to estimate the instantaneous total and diffuse PAR, monthly average hourly and daily total PAR and monthly average hourly diffuse PAR.

Small and marginalized farmers in India are unable to earn enough money from the agriproducts and are selling off their land and taking up other secure job roles to earn money for their livings. This is leading to loss of agricultural land and loss of skilled manpower (farmers) whose knowledge and skills goes a waste as they move into some other profession. Now, the Government of India has provided a solution to the farmers to increase their revenue from the same piece of land under the KUSUM scheme by combining solar PV power generation with agriculture(Pulipaka et al. 2021). As per the scheme farmers can install solar PV power plant in their agricultural field which can be installed at a height of 3 ft above the ground so that the land can be utilized for farming. Sandbox Solar, founded by Ian Skor, PE, has developed an agri-voltaic software modelling tool to optimize the design of collocated solar PV with crops. Agri-voltaic is seen to be a technology which can increase the revenue of the farmers from the same piece of land over the entire year. There are three different layouts of the AVPs based on the arrangement of solar panels and agricultural area (Pulipaka et al. 2021). The first one is the interspace farming wherein crops are grown in the space between two rows of solar arrays. The second type is farming below the panels which are installed with a tilt angle equal to the latitude and no special arrangement is made for growing crops underneath these panels. Manual cultivation is only possible under these panels. The third type is the farming below elevated structures which are around 3m high (Casares de la Torre et. al. 2022). The elevation enables farmers to use machineries for farming and allow sunlight to uniformly spread over the land area. As per the available literature there are sixteen operational agri-voltaic plants in India (Das 2022) scaling from 1 MW agri-voltaic plant at GPCIL Amrol Gujrat to 7 kW at Junagadh Agricultural University.

The major challenges that one faces while growing crops underneath the solar panels is of the availability of solar radiation. Mathematical relations were derived to calculate the fraction of light that reach the ground under the collector field when collectors are mounted 2m above the ground with row

10.18086/swc.2023.02.03 Available at http://proceedings.ises.org

spacing equal to three times the height of the collectors (Goetzberger et al. 1982).
Trommsdorff et al. 2022 proposed two categories of agri-voltaic plants viz. Category I- Overhead PV with vertical clearance > 2.1 m and Farming under the agri-voltaic system Category II- Interspace PV with vertical clearance < 2.1 m and Farming between the rows of agri-voltaic systems.
Solar radiation is the main source of energy for all natural processes especially photosynthesis and solar PV performance (Oliphant and Stoy, 2018; Norman and Welles, 1983) Analogous to solar PV system, plants use solar radiation in the wavelength of 400-700 nm for photosynthesis. This component of the solar radiation is known as photosynthetically active radiation (PAR). Quantum sensors are utilised for measuring PAR at any site. But it is difficult to have a ground measured PAR data for all sites which can be utilized for decision making for the selection of plants that can be grown in the given site. Ghayas et al. (2022) reported that long term study of PAR for Indian region is not available because of the absence of dedicated sensor network for regular measurement of PAR over Indian regions. They have conducted a study to measure PAR for Delhi for four years starting from 2013 to 2016.These calls for the requirement of models to predict PAR for Indian regions. The present work will focus on developing a model to estimate PAR for New Delhi.
Gardea (2020) presented a review of the empirical models developed by researchers across the globe to estimate PAR. PAR_{total} is estimated using various parameters like global solar radiation, solar elevation angle, clearness index, aerosol optical depth to name a few. Salim et al.(2014) developed a non-reproducible model to estimate PAR at Dehradun, India. Researchers have proposed decomposition models to estimate $PAR_{diffuse}$ as a function of parameters like clearness index, diffuse fraction, solar elevation, PAR_{total} and these models are compared to check their accuracy in estimating $PAR_{diffuse}$ (Lu et al. 2022). Decomposition models are found to be useful in the absence of on-site diffuse measurements. It is used to predict diffuse horizontal irradiance at any arbitrary locations, which can be further utilised to estimate $PAR_{diffuse}$. Lu et al. (2022) compared seven stand-alone decomposition models and an EMOS approach model for global horizontal radiation which is used to estimate PAR.

Proposed Model

In an Agri voltaic system decomposition of photosynthetically active solar radiation into diffuse and direct component is essential because of the shading caused by the solar panels which shows seasonal and diurnal variation. The diffuse and total PAR values are computed using the following steps:

Step 1: Estimate instantaneous extraterrestrial radiation on a horizontal surface having a wavelength between 400- 700nm.

The extraterrestrial radiation on a horizontal surface is given by (Duffie and Beckman,:

$$G_o = G_{sc}\left(1 + 0.033\cos\frac{360n}{365}\right)\cos\theta_z \quad (1)$$

where Gsc = 1367 W/m2 is the solar constant, n is the day of the year and is $\theta_z$the zenith angle. As per the World Radiation Centre spectrum (Duffie & Beckman,) the fraction$f_{0-\lambda}$ of the total energy in the spectrum that lies between wavelengths zero and 400nm is 0.080 and $f_{0-700nm} = 0.469$.
Therefore, the fraction of the total spectrum that lies between 400-700nm is given by:

$$f_{400-700nm} = 0.469 - 0.080 = 0.389 \quad (2)$$

Thus, the extraterrestrial radiation(PAR_{ext}) incident on a horizontal surface having a wavelength between 400-700nm is given by:

$$PAR_{ext} = G_o \times f_{400-700nm} \quad (3)$$

Step 2: Estimate instantaneous Photosynthetically Active Radiation on a horizontal surface on the earth surface.

The fraction of extraterrestrial radiation that reaches the earth surface on completely clear and overcast day at an altitude of up to 300m is denoted by f= a+ b where the parameters a and b depends on altitude of the place and month of the year (Rahman et al. 2013). The values of a and b are tabulated in Table 1.

Tab 1: The values of the parameter a and b for computing the fraction of extraterrestrial radiation reaching the earth surface (Rahman et al. 2013)

For altitude up to 300 m	**January, February, December**	**March, April, May**	**June, July, August**	**September, October, November**
a	0.18	0.21	0.25	0.25
b	0.51	0.49	0.51	0.51

Therefore, the radiation reaching the earth surface on a horizontal plane having a wavelength between 400-700nm is given by:

$$PAR_{total} = f \times PAR_{ext} \tag{4}$$

Step 3: Estimating monthly average hourly PAR on a horizontal surface

The monthly average hourly extraterrestrial radiation on a horizontal surface (kJ/m^{2}h) can be calculated using the following two relations reported in literature Duffie (2013) and Sukhatme (2012) respectively**:**

$$I_{o1} = \frac{12\times3600}{\pi} G_{sc}\left[1 + 0.033\, cos\,\left(\frac{360n}{365}\right)\right] \times \left[\cos\varphi\cos\delta\,(\sin\omega_2 - \sin\omega_1) + \frac{\pi(\omega_2-\omega_1)}{180}\sin\varphi\sin\delta\right] \tag{5}$$

$$I_{o2} = G_{sc}\left[1 + 0.033\, cos\,\left(\frac{360n}{365}\right)\right](sin\,\varphi\, sin\,\delta + cos\,\varphi\, cos\,\delta\, cos\,\omega \tag{6}$$

where G$_{sc}$= 1.367kW/m^2, φ is the latitude of the place, δ is the declination angle, ω is the hour angle and n is the day of the year.

The monthly average hourly PAR on a horizontal surface ($\overline{PAR}_H$) can be calculated using the following relation:

$$\overline{PAR}_{H,j} = f \times I_{oj} \;; j = 1{,}2. \tag{7}$$

Step 4: Estimating monthly average daily PAR on a horizontal surface

The monthly average of daily extraterrestrial radiation$\overline{H}_o$ on horizontal surface (kJ/m^2-day) can be calculated using the relation Duffie (2013):

$$H_o = [24\, I_{sc}(1 + 0.033\cos\left(\frac{360n}{365}\right))\{\omega_s\sin\varphi\sin\delta + \cos\varphi\cos\delta\sin\omega_s\}]/\pi \tag{8}$$

Here ω_s is the sunset hour angle. Klein (1977) determined that the value of H$_o$ is equal to $\overline{H}_o$ on January 17, February 16, March 16, April 15, May 15, June 11, July 17, August 16, September 15, October 15, November 14 and December 10.

The monthly average daily PAR on a horizontal surface can be calculated using the following relation:

$$\overline{PAR}_D = f \times I_{oj} \;; j = 1{,}2. \tag{9}$$

Step 5: Estimate diffuse PAR on a horizontal surface

Lu et al. (2022) calculated PAR$_{diffuse}$ as a function of diffuse fraction and solar elevation angle using decomposition method.

$$k_{d,PAR} = \frac{PAR_{diffuse}}{PAR_{total}} = \frac{[1+0.3(1-k_d{}^2)]k_d}{1+(1-k_d{}^2)cos^2(90-\alpha)\cos^3\alpha} \tag{10}$$

Here k$_d$= DHI/ GHI is the diffuse fraction where DHI and GHI are respectively the diffuse and global horizontal irradiance (W/m^2), and α is solar elevation angle measured in degree. The ASHRAE model can be used to compute DHI and GHI.

Step 6: Estimate the area between the panels which will receive total PAR and diffuse PAR

Estimation of the length of the shadow

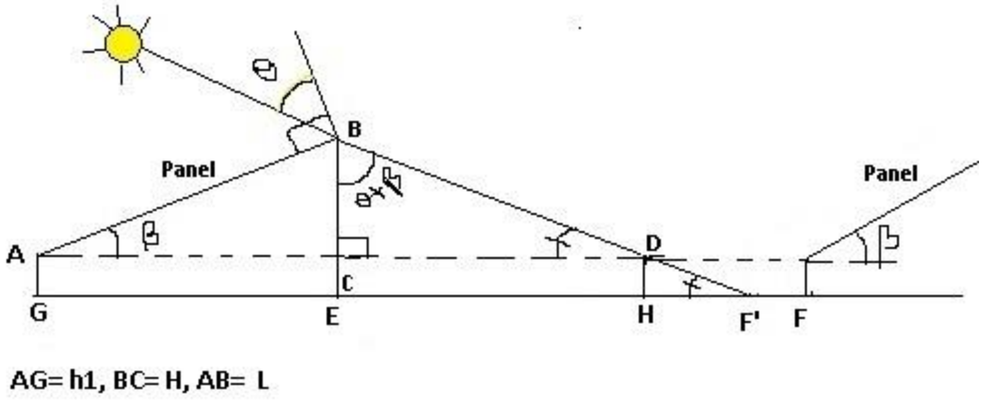

Fig 1: Shadow Analysis

The plants can be grown under the panels (region GE) and in the inter row spacings i.e EF region as shown in Fig1. The region GE is always under shadow but length of the shadow EF' in the EF region changes over the day and shows seasonal variation as well. The distance between two panels EF is calculated based on the day on which the panel will cast the longest shadow i.e. corresponding to the winter solstice.

Form ΔABC we get,

$$AC = AB\cos\beta = L\cos\beta \quad (11)$$

The length of the shadow (D=CD+ HF') that the panel will cast on the ground in the region EF is calculated from ΔBCD. And ΔDHF as

$$CD = L[\sin\beta / \tan(90° - \theta - \beta)] \quad (12)$$

$$HF' = [h_1 / \tan(90° - \theta - \beta)] \quad (13)$$

where L is the length of the panel AB, β is the tilt angle of the panel, θ is the angle of incidence of the beam radiation on the tilted panel at any time of the day and h_1 is the height AG at which the panel is installed. The length of the shadow in the inter row spacings vary over the day and shows seasonal variation.

Thus, on a particular day the plants which are grown under the panel will receive diffuse radiation throughout the day. On the other hand, plants grown in the inter row spacings will receive both beam and diffuse radiation based on the time and day of the year. Beam radiation will be in the region F'F and diffuse radiation will be in the region GF'.

Results and Discussions

In this work, a ground mounted solar PV power plant is stuided which is installed at New Delhi (28°35' N, 77°12'E) having an average of 8.6 h of sunshine hours per day. The dimensions (length x breadth x thickness) of the modules used in the plant is 197.6 x 99.2 x 3.5 cm and are tilted at an angle of 30° with the horizontal. Applying the proposed model, the photosyntheically active solar radiation is estimated for the entire year.

The analytical modelling of Photosynthetically Active Radiation is conducted using the formultaion described above. The instantenous extrateresstrial radiation having a wavelength between 400-700nm (PAR_{ext}) is calculated for the entire year and is shown in Fig 2. It has been observed that the mean PAR_{ext} is 236.4±170 W/m^2 for the entire year. Consequently, PAR_{total} incident on a horizontal surface in New Delhi vary between 0.5- 463 W/m^2 having a mean equal to 172 ±123 W/m^2 for the year.

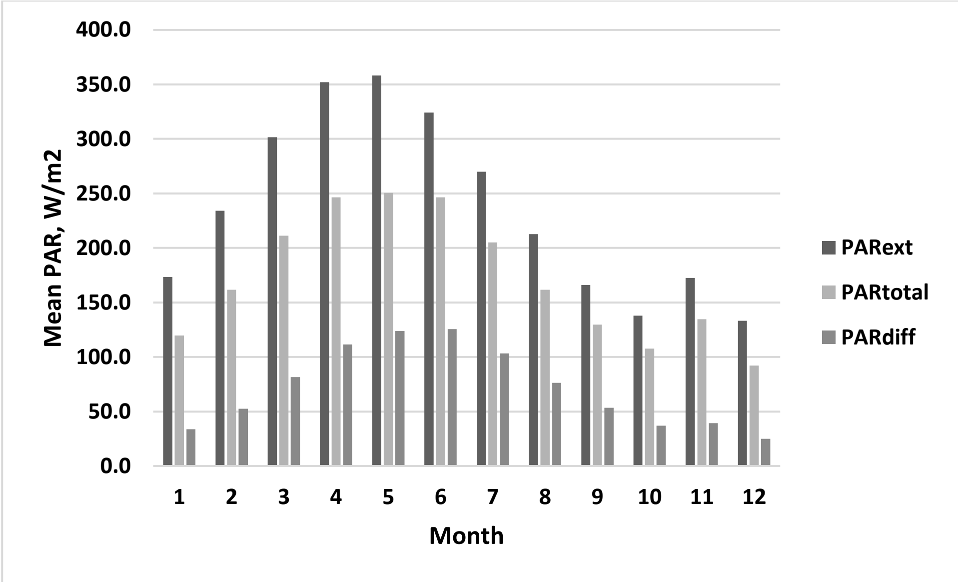

Fig 2: Monthly average of Instanteneous extraterrestrial radiation having a wavelength between 400-700nm, total and diffuse PAR incident on a horizontal surface at New Delhi..

The monthly average hourly PAR is calculated using equations (5-7) on a horizontal surface located in New Delhi and is shown in fig 3. The average, range and standard deviation of these values were calculated for the entire year. It is observed that mean $\overline{PAR}_{H,1}$= 667±175 kJ/m^{2}h, having a range of 397-912 kJ/m^{2}h for the entire year. The PAR values computed using eq.6 gives the mean equal to 604±147 kJ/m^{2}h, having a range of 372- 810 kJ/m^{2}h for the entire year. There is a 8.8% difference in the value of $\overline{PAR}_H$ computed using formula 5 and 6.

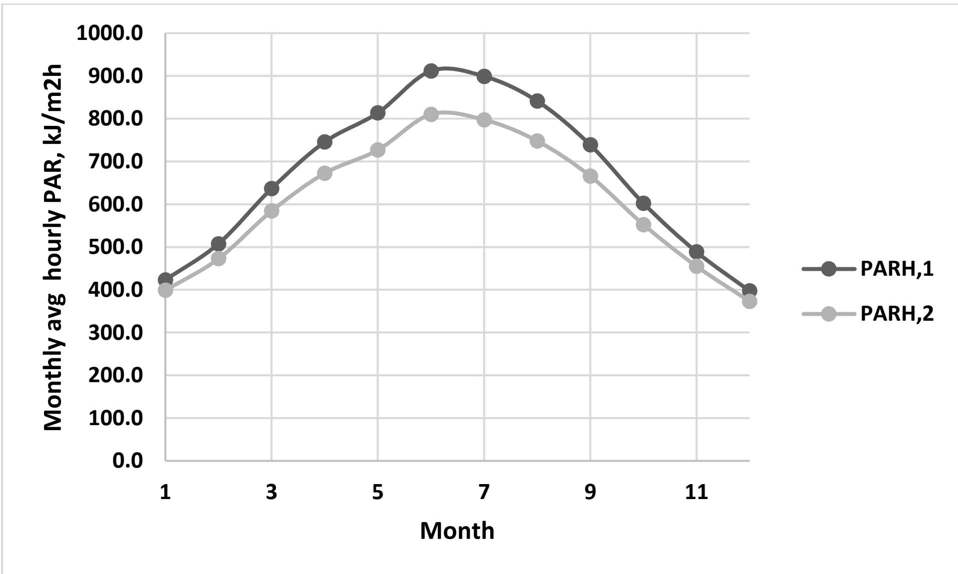

Fig 3: Monthly average hourly photosynthetically active radiation, $\overline{PAR}_{H,j}$ incident on a horizontal surface at New Delhi computed using two different relations for I_o.

Theaverage value of instantaneous diffuse PAR varies between 24- 125W/m^2 for the entire year as shown in fig 2. However, the monthly average hourly diffuse PAR varies from 107-465kJ/m^{2}h and 100-413 kJ/m^{2}h respectively when I_o is computed using eq 5 and 6 as shown in fig 4.

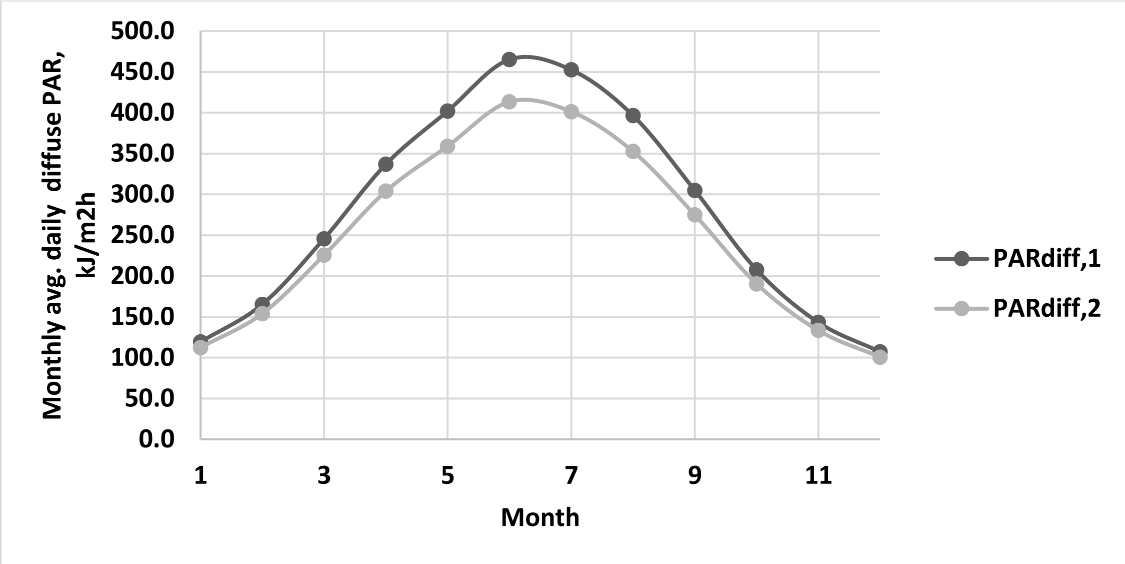

Fig 4: Monthly average hourly diffuse photosynthetically active radiation, $\overline{PAR}_D$ incident on a horizontal surface at New Delhi computed using two different relations for I_o.

It is observed that on an average 47% of interrow spacings between the panels are mostly shaded during the year. However, the shading in the interrow spacings increases during the winter months and hence during this time the plants which are grown in this region will receive majorly $PAR_{diffuse}$. Only during the summer months that 20-30% of the space remains under the shadow and hence plants recives both direct and diffuse component of PAR.

The results obtained is compared with the observed values reported by Ghayas et al. (2022) for the range of the peak PAR values for the winter, summer, monsoon and post monsoon season in New Delhi and presented in Table 2

Tab 2: Comparison of results for peak value of PAR

	Winter		**Summer**		**Monsoon**		**Post monsoon**	
	Propos ed	Ghay as et al. 2022	Propos ed	Ghay as et al. 2022	Propos ed	Ghay as et al. 2022	Propos ed	Ghay as et al. 2022
Min of peak PAR, W/m^2	229.2	101.8	448.5	311.5	324.8	378.4	233.7	214.3
Max of peak PAR, W/m^2	378.3	353.5	463	515.7	459.3	560.5	272.9	477.5
%error, min of peak PAR		-1.25		-0.44		0.14		-0.09
%error, max of peak PAR		-0.07		0.10		0.18		0.43

The percentage error for the minimun value for the peak PAR varies between 9-125% showing a considereable agreement of the result for the monsoon and post monsoom months but there is a positive bias seen in the PAR values for the summer and winter months using the proposed model. Whereas, the percentage error for the maximum peak PAR values ranges between 7-43% having the least error during the winter and maximum error during the post monsoon season.

Conclusions

The proposed model can be utilised to estimate the photosythetcally active solar radiation under a solar photovoltaic power plant for any location. The information regarding the available PAR can be utilised to select the variety of plant that can be grown under the solar PV powerplant. The proposed model shows considerable agreement with the observed maxima of the peak values of PAR during the summer, winter and monsoon season. The model is simple and utilizes only the location, date and time of the day for computing the PAR values.

References

Casares de la Torre F.J., Varo M., Lopez-Luque R., Ramírez-Faza J., Fernandez-Ahumada L.M. (2022). Design and analysis of a tracking / backtracking strategy for PV plants with horizontal trackers after their conversion to agrivoltaic plants. Renewable Energy 187, 537-550.

Das S (2022). Status of Agri-voltaic in India and the Opportunities and Challenges. Book of Proceedings, Agricultural Innovation, Sustainability, Entrepreneurship and Networking (i-FAISEN), July 4th-8th, 2022, pp 71-77, Thailand. Organized by Asian Association of Agricultural Colleges and Universities, Maejo University Thailand.

Duffie J. A. and Beckman W. A. (2013). Solar Engineering of Thermal Processes. 4th ed.John Wiley & Sons, Inc.

Ghayas H., Radhakrishnan S.R, Sehgal V. K, et.al (2022). Measurement and comparison of photosynthetically active radiation by different methods at Delhi. Theoretical and Applied Climatology, 150 (3-4):1-13.

Goetzberger A and Zastrow A. (1982) On the coexistence of solar-energy conversion and plant cultivation. International J Solar Energy 1,55–69.

Grima M, Fernandez E,, et al (1999). Photobioreactors: light regime, mass transfer, and scale up. J. Biotechnol. 70, 231–247 (1999)

Lu M, Zainali S., Stridh B.,et. al (2022) Photosynthetically active radiation decomposition models for agrivoltaic systems applications. Solar Energy 24, 536–549.

Norman, J.M., Welles, J.M., (1983). Radiative transfer in an array of canopies. Agron. J. 75, 481–488. https://doi.org/10.2134/agronj1983.00021962007500030016x.

Oliphant, A.J., Stoy, P.C., (2018). An evaluation of semiempirical models for partitioning photosynthetically active radiation into diffuse and direct beam components. J. Geophys. Res. Biogeosciences 123, 889–901. https://doi.org/10.1002/ 2017JG004370.

Pulipaka S., and Peparthy M (2021). Agrivoltaics in India: Overview of Operational Projects and relevant Policies. Report by National Solar Federation of India and Indo-German Energy Forum Support Office, New Delhi version v1.4.

Rahman M. M, Ahmed A U. et al (2013). Solar energy potential in Bangladesh.Int. Conf. on Mechanical Engineering and Renewable Energy, 24-27 Dec.

Sukhatme S. P., Nayak J. K.(2012). Solar Energy, Principles of collection and storage. 3rd edition, Tata McGraw Hill Education Pvt Ltd

Trommsdorff M. , Gruber S. , Keinath T. et al.(2022) Agrivoltaics: Opportunities for Agri-culture and the Energy Transition. A Guideline for Germany, Fraunhofer Institute for Solar Energy Systems ISE.

Setting up of Optimum Design Parameters for Agrivoltaic Power Plants in Indian Geo-Climatic Conditions

Mr. Dwipen Boruah[1], Mr. Prasun Das[2], Mr. Anurag Priyadarshi[1],

[1]Global Sustainable Energy Solutions India Pvt. Ltd.

[2]The Deutsche Gesellschaft für Internationale Zusammenarbeit GmbH (GiZ)

ABSTRACT

Agrivoltaics is a promising solution for addressing the growing demand for food and energy in the face of climate change, land scarcity, and rising populations. This comprehensive study aims to establish design parameters for agrivoltaic power plants across various geo-climatic regions and soil types in India. The study explores India's major geo-climatic regions and soil types, examining the multiple crops cultivated in these regions and identifying plant characteristics critical for agrivoltaics, such as plant physiology, root penetration, growth pattern, sunlight requirement (Photosynthetically Active Radiation) and Daily Light Integral (DLI) values, plant life, and sowing and harvesting seasons. The research develops a methodological framework and matrix for determining suitable crops for agrivoltaic systems in different geo-climatic regions and soil types.

The research establishes design and installation parameters for agrivoltaic setups, considering geographical and climate conditions, PV modules layout and structure design considering sunlight requirement of plants, foundation type, selection and matching of equipment, cable layout design, system protection requirements, energy yield estimation, installation, operation, and maintenance requirements. Moreover, the study explores the cost impact of various design aspects on agrivoltaic economics, providing valuable insights for stakeholders looking to invest in agrivoltaic power plants. By understanding the influence of design parameters on the overall cost, stakeholders can make informed decisions and optimise the development of agrivoltaic systems.

One of the critical outcomes of this study is the development of a method and matrix to determine the amount of sunlight available in different zones within a solar field segment for different structural configurations in terms of inter-row spacing, height, width and tilt angle. By knowing the available sunlight in different zones during different seasons of the year, appropriate crops/ plants can be selected to grow under these zones based on the minimum sunlight required to produce such plants. The System Advisory Model developed by the National Renewable Energy Laboratory was used to simulate the results in multiple scenarios.

Keywords: Agrivoltaics, photovoltaics, photosynthetically active radiation, daily light integral

---

List of Abbreviations

Abbreviation	**Description**
APV	Agri-Photovoltaics
CUF	Capacity Utilization Factor
DLI	Daily Light Integral
GHI	Global Horizontal Irradiance
HDGI	Hot Dipped Galvanized Iron
ICAR	Indian Council of Agricultural Research
IEC	International Electrotechnical Commission
IP	Ingress Protection

10.18086/swc.2023.02.01 Available at http://proceedings.ises.org

IS	Indian Standards
NREL	National Renewable Energy Laboratory
NSRDB	National Solar Radiation Database
O&M	Operation and Maintenance
PAR	Photosynthetically Active Radiation
PR	Performance Ratio
PV	Photo-Voltaic
SAM	System Advisory Model

List of Units

Units	Description
%	Percentage
^{o}	Degree
^{o}C	Celsius
km	Kilometre
km/hr	Kilometre per hour
kV	Kilovolt
kW	Kilowatt
kWh	Kilowatt Hour
kW_p	Kilo Watt peak
m/s	Meter per second
MW	Megawatt
MW_p	Megawatt peak
W	Watt
W_p	Watt peak

1 Introduction

Renewable energy technologies are crucial in addressing the global need for sustainable energy and environmental conservation. India, a prominent player in this global transition, is undergoing significant changes in its energy landscape. The nation actively diversifies from its traditional, centralised coal-hydro energy supply towards a broader portfolio of renewable energy (RE) sources. As of 2022, India held the 4th position worldwide in total renewable power capacity [1][2][3]. By May 2023, renewable power, including large hydropower, comprised 41.57% of India's total energy capacity, an equivalent of 173.61 GW out of 417.67 GW [4][5]. However, excluding large hydropower, the renewable power capacity accounted for 30.35%, amounting to 126.77 GW of the total renewable energy capacity [4,5]. This progress was spurred by India's ambitious targets to install 175 GW and 450 GW of renewable energy by 2022 and 2030, respectively [6][7].

Agrivoltaics or Agrovoltaics, also known as Agro-photovoltaics, refers to the innovative integration of solar photovoltaic systems and agriculture, which allows for the simultaneous production of food and renewable energy. This approach is significant as it can increase land use efficiency, increase crop yields, and improve the performance of solar panels by providing a cooler microclimate. Notable progress in this field has been made worldwide, with numerous projects and research studies conducted to understand and optimise the combination of solar energy systems and agriculture. In India, agrivoltaics has gained traction as a promising solution to meet the growing demand for food and energy, especially considering the country's vast agricultural land and abundant solar potential.

The critical issue is the delicate balance between land use for food production and energy generation –the food-energy nexus. The concept of agrivoltaics offers a promising solution. Agrivoltaics integrates agricultural practices with solar power production, enabling simultaneous crop growth and solar energy generation on the same plot of land. This synergistic approach could optimise land utilisation, benefiting farmers by enhancing crop growth conditions and offering an additional source of income. While the execution of agrivoltaics demands thoughtful planning to meet agricultural and energy generation needs effectively, it bears substantial potential to boost India's renewable energy capacity without endangering food supplies [8][9][10][11].

With abundant sunlight, expansive agricultural land, and a rapidly growing solar PV sector, India is an ideal candidate for implementing agrivoltaics. However, the nation's diverse geo-climatic conditions and variety of soil types present unique challenges in designing agrivoltaic power plants that can accommodate different crops and optimise energy production. Although still in its nascent stage, India has seen a growing number of agrivoltaic pilot projects in recent years. The National Solar Energy Federation of India (NSEFI), in association with the Indo-German Energy Forum (IGEF), has conducted a study on the current ongoing agrivoltaic projects in India, identifying 21 projects spread across the country [12]. These diverse projects, located in various geographic and socioeconomic contexts, highlight the significant potential of agrivoltaics in advancing India's renewable energy objectives and simultaneously offering substantial advantages to local agriculture. This highlights the necessity for a comprehensive study of the design parameters of agrivoltaic power plants suitable for various regions across India.

India's extensive geographic and climatic diversity contributes to various geo-climatic regions and soil types, each with unique agricultural attributes. Recognising this complexity, the Planning Commission of India, in association with the National Remote Sensing Agency, divided the country into 15 Agro-climatic regions [13]. They stretch from the Western Himalayan Region to the Islands Region, covering all states and union territories, and offering unique agricultural challenges and opportunities. A comprehensive understanding of the interrelation between these geo-climatic zones, soil types, and cultivated crops was established using many resources [14][15]. These resources provided a detailed delineation of India's 15 Agro-climatic zones, soil types, temperature ranges, rainfall, and major crops cultivated in each zone. They also offered an agricultural contingency plan outlining the agricultural profile of each zone.

This paper aims to thoroughly analyse these design parameters in differing geo-climatic and soil conditions. By investigating the factors influencing the design, construction, and operation of agrivoltaic systems, this study aims to identify suitable crop types and best practices for effective agrivoltaic project implementation in India. It is expected that the outcomes of the study will provide valuable insights and guidelines for developing agrivoltaic projects in India with a better understanding of technical design aspects.

The introductory section of this paper provides the growth scenario of solar PV in India and the study's objective. The second section offers critical plant characteristics in terms of height, sunlight requirement, root penetration, plant life and cultivation time and method of sowing and harvesting. The third section discusses agrivoltaic design considerations, which cover the design of the mounting structure, plant layout, and selection of crops based on structure heights and available sunlight. The matrices for selecting crops for different agrivoltaic setups in other geo-climatic regions of India have been presented in this section. The fourth section of this paper offers the aspects of system performance and the cost impact of different design aspects. The conclusion of the study is included in section 5.

2 Critical characteristics of crops for agrivoltaic

2.1 Height

The height of crops is one of the most critical factors for agrivoltaic setup. When crops are cultivated in an agrivoltaic setup, solar panels should not obstruct their growth, and they should not cast any shadow on the solar panels. Cultivated crops should be able to grow well in the space beneath and between the solar arrays/panels, and any possibility of damaging solar modules during sowing and harvesting time should be taken into consideration. It is equally crucial that crops grown in front of the solar arrays should not cast any shadow between 9 a.m. and 4 p.m. (This time should be adjusted based on solar time). Table 1 below provides a classification of typical crops cultivated in India based on typical maximum height [16][17].

Table 1: Classification of crops based on the typical maximum height

Typical maximum height	Typical crops
Less than 50 cm	Herbs: Gucchi (Himalayan Mushroom), Sugar Beet, Carrot, Radish, Cabbage, Cauliflower, Spinach, Black Gram, Sankhpuspi, Groundnut, Lettuce, Cumin, Isabgol etc. Creepers: Watermelon, Zucchini, pumpkin, Ash gourd etc.
Less than 100 cm	Herbs: Aloe vera, Mustard, Ginger, Green Gram, Mungbean, Onion, Kariyatu (Andrographis paniculata), Cow Pea, Parsley, Poppy, Stevia Leaves, Rye, Oats, Chick Pea (Gram or Bengal gram), Mothbean, Cluster Bean, Fenugreek, Mari Gold, Mint Leaves, Brinjal (eggplant), Capsicum, Chilli, Geranium, Coriander, Garlic etc. Shrubs: Tea, Patchouli, Sarpagandha, Berseem Clover, Potato etc.
Less than 150 cm	Herbs: Arrowroot, Asparagus, Soybean, Turmeric, Ashwagandha, Rice, Linseed, Wheat, Elephant Foot (Yam), Tomato etc. Shrubs: Jethimadh, Tobacco etc.
Less than 200 cm	Herbs: Cotton, Fennel, Sesame, Indigo, Maize etc. Shrubs: Raspberry, Senna etc. Climber (controlled): Betel Leaves, Black Pepper, Indian Bean, Long bean, French Bean, Ash gourd (Pusa Urmi), Snake Gourd, Bitter gourd, Bottle Gourd, Blonde cucumber etc. Grass: Citronella, Vetiver etc.
Less than 300 cm	Herbs: Ladies Finger (Okra) Shrubs: Sonamukhi, Pearl millet (Bajra), Guava Hybrid etc. Grass: Hybrid Napier Grass, Lemon Grass etc.
More than 300 cm	Herbs: Banana, Cardamom, Jute etc. Shrubs: Coffee, Castor, Annatto dye, Sunn Hemp etc. Grass: Guinea Grass, Sugarcane etc. Trees: Papaya, Pomegranate, Kiwi, Mango, Pigeon Pea, Sapota (Chiku) etc.

2.2 Sunlight Requirement

All crops need sunlight for photosynthesis, but the amount required can vary significantly. Some crops require full sun, while others can tolerate or even prefer partial shade. In an agrivoltaic system, solar panels can create shaded areas, which can be beneficial for shade-tolerant crops but detrimental for those needing full sun. Table 5 below categorises the crops into four groups based on their DLI requirements: low light (3-6 $mol \cdot m^{-2} \cdot day^{-1}$), medium light (6-12 $mol \cdot m^{-2} \cdot day^{-1}$), high light (12-18 $mol \cdot m^{-2} \cdot day^{-1}$), and very high light (exceeding 18 $mol \cdot m^{-2} \cdot day^{-1}$) crops **Error! Reference source not found.Error! Reference source not found.**.

Table 2: Classification of crops based on sunlight requirement

Typical sunlight requirement	Typical crops
Low light crops Daily light integral (DLI): 3 to 6 ($mol/m^2/day$) Solar Radiation: 0.41 to 0.83 $kWh/m^2/day$	Herbs: Centella asiatica (Brahmi Booti/ Mandukaparni), Himalayan Mushroom (Gucchi), Arrowroot
Medium-light crops Daily light integral (DLI): 6 to 12 ($mol/m^2/day$) Solar Radiation: 0.83 to 1.66 $kWh/m^2/day$	Herbs: Carrot, Cauliflower, Mustard, Parsley, Cow Pea, Radish, Mungbean, Green Gram, Parsley, Cow Pea, Cotton, Vetiver, Okra/ Ladies finger/ Bhindi, Sugar beet, Ginger, Aloe vera, Kariyatu (Andrographis paniculata), Poppy, Asparagus, Soybean, Turmeric, Aswagandha, Cotton, Fennel, Asparagus, Soybean, Turmeric, Jute Shrubs: Peas, Sonamukhi, Sarpagandha, Tea, Patchouli, Jethimadh, Cardamom, Climbers: Black Pepper (climber), Betel Leaves Grass: Guinea Grass, Citronella, Vetiver (grass) Tree: Papaya
High light crops Daily light integral (DLI): 12 to 18 ($mol/m^2/day$) Solar Radiation: 1.66 to 2.48 $kWh/m^2/day$	Herbs: Black Gram, Cabbage, lettuce, Spinach, Onion, Coriander, Rye, Fenugreek, Garlic, Mint, Wheat, Lettuce, Spinach, Onion, Chilli, Eggplant, Stevia Leaves, Coriander, Garlic, Rye, Sesame, Chicory, Sankhpuspi, Groundnut, Isabgol, Cumin, Stevia Leaves, Oats, Chick Pea, Moth bean, Cluster Bean, Fenugreek, Marigold, Mint Leaves Chicory (herb), Brinjal, Capsicum, Elephant foot yam, Linseed, Tomato, Raspberry, Senna, Indigo Shrubs: Potato, Tobacco, Pearl millet (Bajra), Guava Hybrid, Berseem Clover, Senna, Sunn Hemp, Annatto dye, Castor Creeper: Ash gourd Climbers: Snake Gourd, Bitter gourd, Indian Bean, Ash gourd, Long bean, French Bean, Grass: Sugar Cane Tree: Pigeon Pea, Kiwi, Mango, Pigeon pea
Very high-light crops Daily light integral (DLI): More than 18 ($mol/m^2/day$) Solar Radiation: More than 2.48 $kWh/m^2/day$	Herbs: Paddy Rice, Maize, Poppy, Geranium Creepers: Pumpkin, Watermelon, Zucchini Climber: Bottle Gourd, Blonde cucumber

2.3 Root Penetration

The depth and spread of a plant's roots can significantly impact agrivoltaic systems. Crops with deep root systems may not be suitable if underground cables and other infrastructure are present. Moreover, root systems also affect soil erosion and water uptake, which can have implications for the maintenance and efficiency of agrivoltaic systems [16][17].

Table 3: Classification of crops based on root penetration

Typical root depth and spread	Typical crops
Root depth: Less than 50 cm Root spread: Less than 100 cm	Herbs: Centella asiatica (Brahmi Booti/ Mandukaparni), Gucchi (Himalayan Mushroom), Arrowroot, Aloe vera, Ginger, Radish, Fenugreek, Cumin, Mint Leaves, Capsicum, Geranium, Garlic etc. Shrubs: Patchouli, Potato Climber: Betel Leaves
Root depth: Less than 100 cm Root spread: Less than 100 cm	Herbs: Mustard, Green Gram, Mungbean, Kariyatu (Andrographis paniculata), Soybean, Turmeric, Aswagandha, Fennel, Parsley, Sesame, Spinach, Stevia Leaves, Rye, Linseed, Wheat, Indigo, Mari Gold, Brinjal (eggplant), Chilli, Maize Shrubs: Tea, Jethimadh, Peas, Berseem Clover, Raspberry, Tobacco Grass: Citronella grass, Hybrid Napier Grass Climber: Black Pepper, Indian Bean, Long bean, French Bean, Snake Gourd, Bitter gourd, Blonde cucumber, Ash gourd, Bottle Gourd, Creeper: Ash gourd
Root depth: Less than 150 cm Root spread: Less than 100 cm	Herbs: Cow Pea, Cotton, Jute, Chick Pea (Gram or Bengal gram), Cluster Bean, Chicory Shrubs: Sonamukhi, Castor, Sunn Hemp etc. Grass: Vetiver
Root depth: Less than 150 cm Root spread: More than 100 cm	Herb: Banana, Asparagus, Cardamom, Elephant Foot (Yam) Shrubs: Coffee, Senna, Annatto dye, Guava Hybrid Grass: Guinea Grass, Sugarcane Creepers: Pumpkin, Watermelon, Zucchini Tree: Kiwi, Papaya, Pigeon Pea, Sapota (Chiku), Mango,

2.4 Crop life and growing season

The lifespan of the crops and how that aligns with the solar panel lifecycle is another factor to consider. Perennial crops that don't require yearly replanting could benefit an agrivoltaic system. The cropping system (annual or perennial) will influence the design of the agrivoltaic system in terms of panel height, orientation, and arrangement [16][17].

Table 4: Classification of crops based on life cycle

Plant Life	Typical crops
Annual (crops which completes their life cycle within one growing season)	Herbs: Sugar Beet, Mustard, Green Gram, Radish, Mungbean, Kariyatu (Andrographis paniculata), Soybean, Cauliflower, Cow Pea, Cotton, Jute, Lady Finger (Okra), Poppy, Paddy Rice, Sesame, Cabbage, Black Gram, Oats, Chick Pea (Gram or Bengal gram), Linseed, Wheat, Groundnut, Mothbean, Cluster Bean, Fenugreek, Lettuce, Cumin, Isabgol, Mari Gold, Mint Leaves, Tomato, Chilli, Coriander, Garlic, Maize Shrubs: Peas, Berseem Clover, Pearl millet (Bajra), Sunn Hemp, Tobacco Creeper: Watermelon, Zucchini, Pumpkin, Ash gourd Climber: Long bean, French Bean, Ash gourd, Snake Gourd, Bitter gourd, Bottle Gourd, Blonde cucumber
Biennial	Herbs: Carrot, Parsley, Onion, Rye, Indigo

(crops which complete their life cycle in two years)	
Perennial (crops that live for more than two years)	Herbs: Centella asiatica (Brahmi Booti/ Mandukaparni), Gucchi (Himalayan Mushroom), Banana, Arrowroot, Aloe vera, Ginger, Asparagus, Turmeric, Ashwagandha, Cardamom, Fennel, Spinach, Stevia Leaves, Sankhpuspi, Chicory, Elephant Foot (Yam), Brinjal (eggplant), Capsicum, Geranium Shrubs: Coffee, Tea, Patchouli, Sarpagandha, Jethimadh, Sonamukhi, Raspberry, Senna, Castor, Annatto dye, Guava Hybrid, Potato Grass: Guinea Grass, Hybrid Napier Grass, Lemon Grass, Vetiver, Citronella grass, Sugarcane Climbers: Betel leaves, Black pepper, Indian bean Trees: Papaya, Pomegranate, Kiwi, Mango, Pigeon Pea, Sapota (Chiku)

2.5 Method of sowing and harvesting

Sowing and harvesting methods and the tools and equipment used are to be considered in designing agrivoltaic systems. The method of sowing and harvesting and the types of tools and equipment used in these processes are essential to understand to assess if any specific design considerations are required for agrivoltaic systems.

Impact of sowing methods on agrivoltaic design

For methods such as transplanting, agrivoltaic structures should facilitate easy access for workers, necessitating wider pathways between solar panels. Broadcasting demands even panel spacing, with the potential for movable setups to ensure uniform light distribution across the field. The dibbling technique requires the design to be non-obstructive, ensuring precision in seed placement and adequate sunlight penetration. Meanwhile, the drilling method stresses the importance of solar panel alignment to prevent shadowing on the sown rows and provide ample space for the operation and movement of drilling equipment.

Tale 8 below presents sowing methods of different crops cultivated in India [18][19][20][21][22][23][24][25].

Table 5: Classification of crops based on the method of sowing

Method of sowing	Typical crops
Transplanting	Herbs: Centella asiatica (Brahmi Booti/ Mandukaparni), Banana, Arrowroot, Aloe vera, Sugar Beet, Asparagus, Kariyatu (Andrographis paniculata), Aswagandha, Cardamom, Parsley, Onion, Stevia Leaves, Lettuce, Mint Leaves, Elephant Foot (Yam), Brinjal (eggplant), Tomato, Chilli, Geranium Shrubs: Coffee, Tea, Patchouli, Sarpagandha, Jethimadh, Raspberry, Annatto dye, Guava Hybrid, Tobacco Climber: Betel Leaves, Black Pepper Trees: Papaya, Pomegranate, Kiwi, Mango, Sapota (Chiku) Grass: Guinea grass, Lemon grass, Sugarcane
Broadcasting	Herbs: Green Gram, Radish, Fennel, Jute, Poppy, Rice, Sesame, Spinach, Black Gram, Rye, Linseed, Wheat, Indigo, Sankhpuspi, Cluster Bean, Fenugreek, Cumin, Isabgol, Mari Gold, Chicory Shrubs: Sonamukhi, Berseem Clover, Senna, Sunn Hemp Grass: Hybrid Napier Grass, Vetiver
Dibbling	Herbs: Carrot, Ginger, Mung bean, Soybean, Turmeric, Cauliflower, Cotton, Lady Finger (Okra), Cabbage, Chick Pea (Gram or Bengal gram), Capsicum, Coriander, Maize Shrubs: Pearl millet (Bajra), Castor

Method of sowing	Typical crops
	Creeper: Watermelon, Zucchini Climber: Indian Bean, Long bean, French Bean, Snake Gourd, Bitter gourd, Bottle Gourd, Blonde cucumber Tree: Pigeon pea
Drilling	Herbs: Mustard, Cow Pea, Oats, Groundnut, Moth bean, Garlic Shrubs: Peas, Potato Creeper/ Climber: Pumpkin, Ash gourd

Impact of harvesting methods on agrivoltaic design

Harvesting by hand emphasises the need for an agrivoltaic design that supports the free movement of workers around panel structures. When harvesting with hand tools, the design must provide adequate space between the panels to prevent any accidental damage during the use of tools. In contrast, machine harvesting demands a design with even more spacious setups to accommodate large machinery. The structures must also be robust and possibly elevated, ensuring they can withstand potential contact with the machines and provide the necessary clearance.

Tale 6 below presents harvesting methods of different crops cultivated in India [18][19][20][21][22][23][24][25].

Table 6: Classification of crops based on the method of harvesting

Method of harvesting	Typical crops
Harvesting by hand	Herbs: Cardamom, Cow Pea, Cotton, Onion, Cluster Bean, Lettuce, Isabgol, Mari Gold, Chicory, Tomato, Capsicum, Chilli, Coriander, Garlic Shrubs: Tea, Patchouli, Sonamukhi, Peas, Raspberry, Annatto dye, Guava Hybrid Creeper: Ash gourd Climber: Betel Leaves, Black Pepper, French Bean, Ash gourd, Bitter gourd, Bottle Gourd, Cucumber Trees: Papaya, Pomegranate, Kiwi, Mango, Sapota (Chiku)
Harvesting with hand tools	Herbs: Centella asiatica (Brahmi Booti/ Mandukaparni), Gucchi (Himalayan Mushroom), Banana, Arrowroot, Aloe vera, Carrot, Mung bean, Asparagus, Kariyatu (Andrographis paniculata), Soybean, Cauliflower, Fennel, Jute, Lady Finger (Okra), Parsley, Poppy, Rice, Sesame, Cabbage, Spinach, Black Gram, Stevia Leaves, Rye, Oats, Chick Pea (Gram or Bengal gram), Linseed, Wheat, Indigo, Sankhpuspi, Moth bean, Fenugreek, Mint Leaves, Elephant Foot (Yam), Brinjal (eggplant), Geranium, Maize Shrubs: Coffee, Sarpagandha, Berseem Clover, Senna, Pearl millet (Bajra), Castor, Sunn Hemp, Tobacco Climbers: Indian bean, Long bean, Snake gourd Grass: Hybrid Napier Grass, Lemon Grass, Guinea Grass, Vetiver, Citronella grass, Sugar Cane
Harvesting with machines	Herbs: Sugar Beet, Mustard, Ginger, Green Gram, Radish, Turmeric, Ashwagandha, Groundnut, Cumin Shrubs: Jethimadh, Potato

3 Agrivoltaic systems design considerations

There could be two broad approaches to developing agrivoltaic projects:

(1) A brownfield agrivoltaic project – planning for utilisation of existing solar power plant sites for agricultural purposes and selecting crops that will be suitable for the site and can co-exist with the solar power plant without impacting its performance and with no significant changes or investment required.
(2) A greenfield agrivoltaic project – A new site where a PV power plant and agricultural activities are planned together. Such sites may already be used for agricultural purposes and PV power plants are planned to use the land for dual purposes to enhance productivity (agriculture and energy).

For both approaches, as mentioned above, the following fundamental considerations are necessary for designing an agrivoltaic project.

(1) Structure and crop height: Matching crop height to a mounting structure of a PV power plant to avoid hindrance to crop growth and any shadow on the PV modules.
(2) Access to sunlight: Solar fields (placement of PV arrays) and agricultural fields shall be placed so crops get adequate access to sunlight according to their DLI (daily light integral) requirement. As different zones in the solar field site will have different levels of sunlight, crops shall be selected based on minimum DLI requirements and sunlight availability due to shading from PV modules.
(3) Safety of personnel: In solar power plants, PV modules are connected in series, resulting in a DC voltage of 300 V to 1500 V, depending upon the size of the plant and the type of inverters used. The string and array cables carrying such voltage are laid across the solar field and mounting structure. Similarly, the output of PV inverters is around 400 V AC, which will be further stepped up to 11 kV or 33 kV in a utility-scale plant. Exposure to such voltages is hazardous and fatal. In an agrivoltaic setup, in addition to the personnel working for the power plant, other personnel will also be involved in agricultural activities. Therefore, utmost care must be taken in designing electrical safety considerations for agrivoltaic projects.
(4) Safety of power plant and equipment: The life and performance of PV power plant and equipment can be affected due to electrical faults (such as over current/over voltage/arcing), mechanical damage (damage of cables/PV modules/structure) and poor maintenance practice. In an agrivoltaic setup, PV plants will be exposed to multiple agricultural activities during sowing, nursing and harvesting. Depending upon the method of sowing/nursing/harvesting and tools and equipment used for such activities, the risk of mechanical damage is to be assessed and appropriate measures considered in the design for the protection of PV modules, cables and other equipment.
(5) Design optimisation for cost: To achieve the desired return on investment, carrying out a life cycle cost-benefit analysis for agrivoltaic projects, particularly greenfield projects is essential. Based on the priority of expenditure vs. income for the project life cycle, the design approach should be optimised for maximum return on investment.

The following section discusses the design considerations of ground-mounted PV plants in an agrivoltaic setup.

3.1 Mounting structure design considerations

Ground-mounted PV systems are generally installed with fixed structures with a suitable tilt angle facing south (facing north in the southern hemisphere), fixed structures with a provision to change the tilt angle a few times in a year and single-axis tracking systems rotating east to west on a horizontal N-S axis. Two-axis tracking arrays are also employed in selective projects where the structure rotates both the N-S and E-W axis, aligning the PV array to the direct beam angle of the sun throughout the day in all seasons. General guidelines for PV array mounting structures are given in IS/IEC 62548: 2016 Photovoltaic array design requirements and IS/IEC TS: 62738: 2018 Ground-mounted photovoltaic power plants – Design guidelines and recommendations [26][27][28][29].

The following are the essential factors in designing a structure for ground-mounted PV arrays.

- Adequate space between two rows must be kept to avoid shadow.
- Access must be there to reach each module without stepping on it.
- Optimum tilt angle for maximum generation for a fixed tilt structure.
- A minimum tilt of 10º to reduce material accumulation (dust, etc.) on the PV array.
- Use of corrosion-resistant materials suitable for the lifetime of the system.
- Shall be rated for minimum wind loading as per the basic wind speed of the site.
- Design consideration to allow thermal expansion/ contraction of the PV modules as per site conditions.

For an agrivoltaic setup, the following factors should be considered based on the site location and type of crops to be grown in the solar field areas.

3.1.1 Height of the structure

The structure's height is one of the most critical factors for greenfield agrivoltaic projects. Structure height should be selected based on the typical maximum height of the crops and vice versa to avoid any obstruction to the growth of crops and there should not be any shadow on the solar panels from the grown crops. It is also essential to consider if there is any possibility of damaging solar modules during sowing, nursing and harvesting crops due to the lower height of the solar panels. Avoiding shadow from the crops on the solar arrays should be considered from 9 a.m. to 4 p.m. (This time should be adjusted based on solar time). Table 1 in the previous section provides a classification of typical crops cultivated in India based on typical maximum height.

For brownfield agrivoltaic projects, existing PV plants' ground clearance (height of the lowest part of PV modules) is typically kept at 50 cm to 100 cm. For such projects, increasing the height of the structure or rearranging the solar field for agricultural purposes may not be justified for economic reasons. Therefore, the selection of crops according to the maximum typical height and placement of agricultural fields based on the availability of sunlight should be considered. The availability of sunlight and subsequent daily light integral (DLI) for crops at different zones of solar fields is discussed in the next section.

For greenfield agrivoltaic projects, it is crucial to understand whether certain crops must be grown on the site due to local climate, soil or economic reasons. If the choice of crops is limited, the mounting structure for the PV power plant shall be as required for the growth of proposed crops. However, it is worth mentioning that the higher the structure height, the higher the structure cost due to increasing wind loading and weight of the structure materials. Therefore, structure height should be finalised based on overall techno-economic analysis and the power plant's safety in the event of higher wind loading conditions.

Figure 1 below shows different possible heights for equator-facing fixed tilt structures in an agrivoltaic setup. This figure shows two configurations of structure – one with two PV modules in portrait orientation and the other with one PV module in portrait orientation or two in landscape orientation. For both configurations, six different possible heights are considered. Maximum ground clearance is considered 3 m. The availability of sunlight and subsequent daily light integral (DLI) for crops at different zones of solar fields are simulated using the System Advisor Model (SAM) for both configurations at all different heights [25].

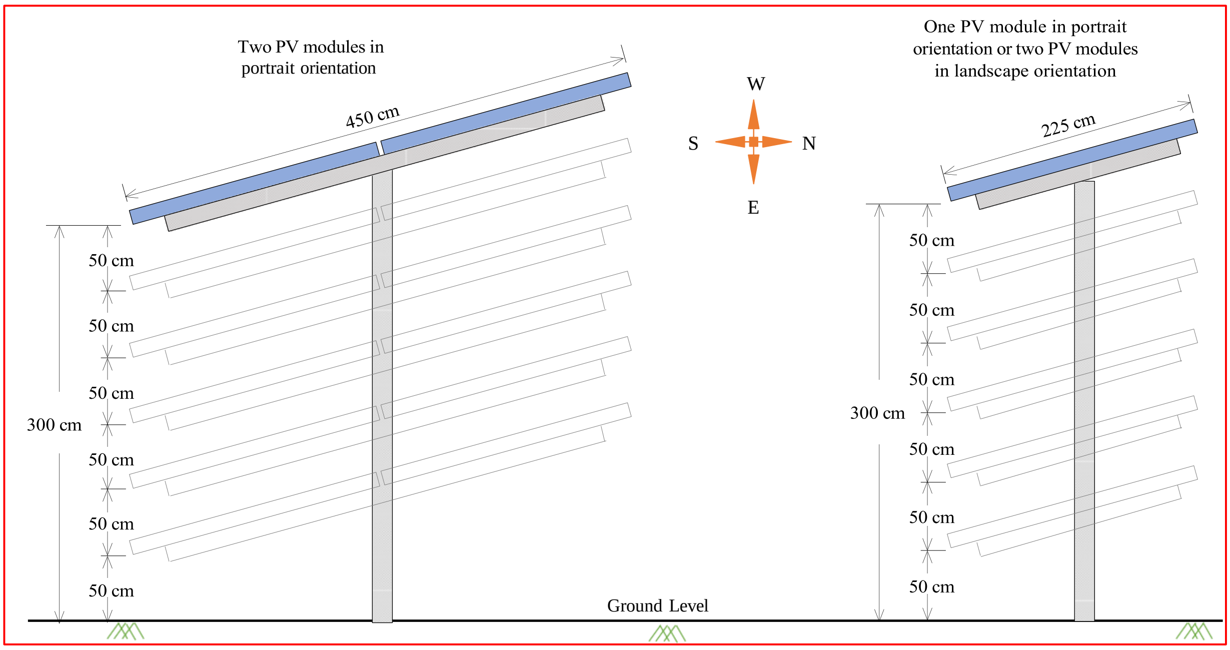

Figure 1: Different possible heights for equator-facing fixed tilt structure in agrivoltaic setup

Similarly, Figure 2 shows an east-west facing single-axis tracker and vertically installed fixed structure. In the single-axis tracking system, one module is installed in portrait orientation and 70 to 80 modules are fixed in one tracker. Two modules can be installed in landscape orientation for a vertically installed fixed structure. Ground clearance is kept between 50 cm to 100 cm for both cases. The availability of sunlight and subsequent daily light integral (DLI) for crops at different zones of solar fields are simulated using the System Advisor Model (SAM) for both configurations at 50 cm ground clearance. The results of the simulations are presented in the next section.

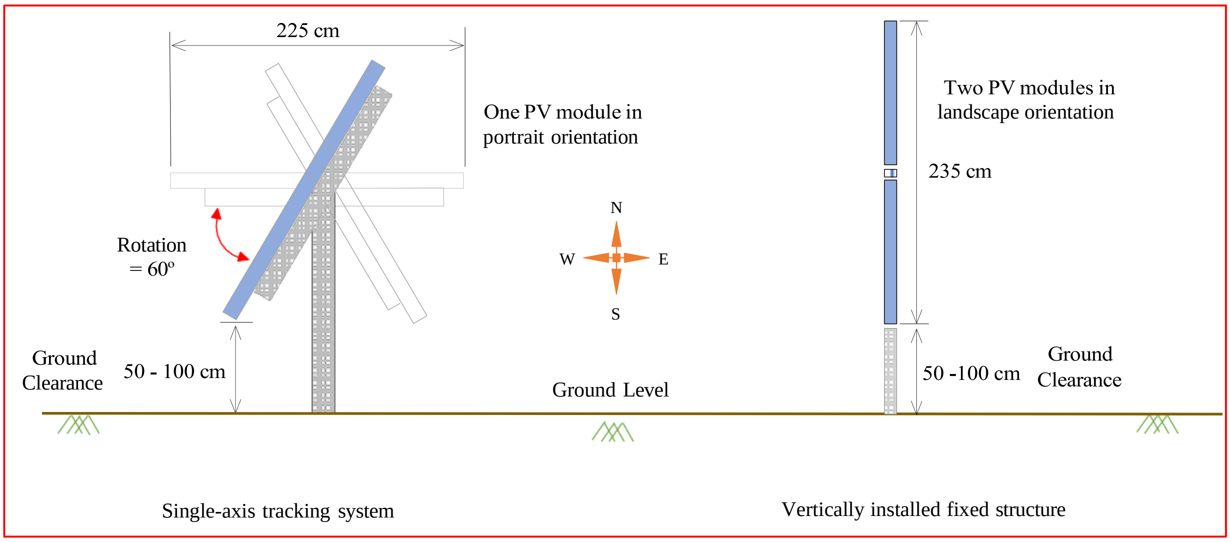

Figure 2: East-West facing single axis tracker and vertically installed fixed structure

3.1.2 Table size and placement of modules

It is recommended not to lay DC cables across roads or pathways in an agrivoltaic setup. Therefore, the table size should be such that it accommodates the modules connected in series (a string). The inverter input voltage and the minimum and maximum temperature of the site determine the number of modules in a string. The same needs to be determined in accordance with IS/IEC 62548: 2016 Photovoltaic array design requirement [26][27]. For a fixed tilt structure, when two modules are installed in portrait orientation, around 20 modules can be installed in one table, and when one module is installed in portrait orientation, around 10 modules can be installed in one table, as presented in Figure 3.

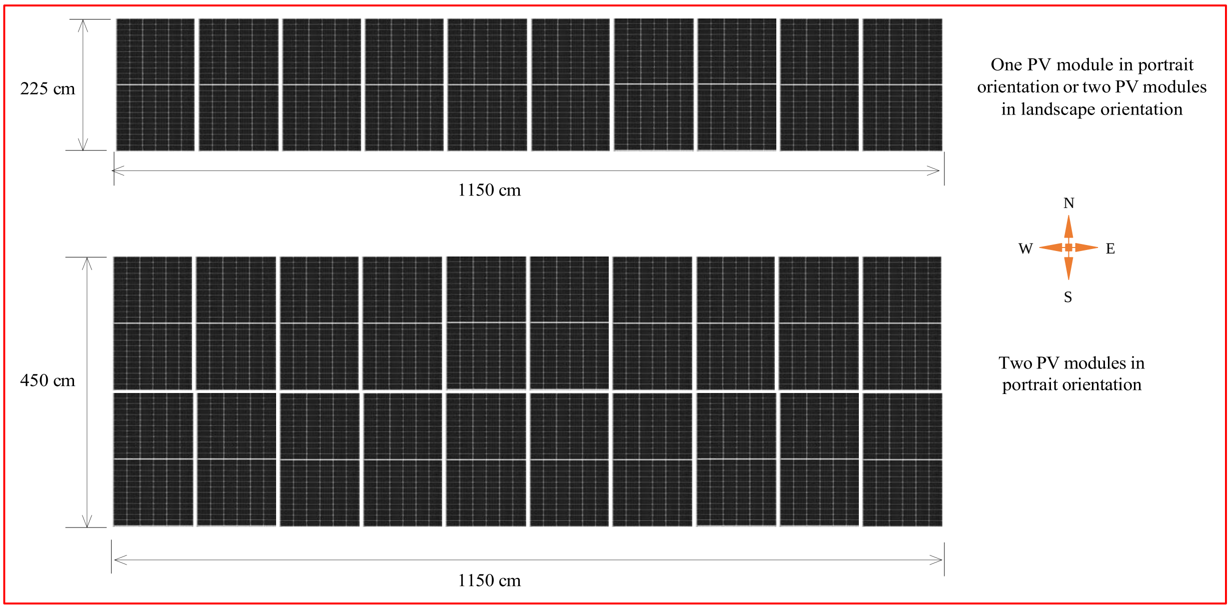

Figure 3: Placement of modules in two different tables in fixed tilt structures

In a single-axis tracking system, one PV module is fixed in portrait orientation and 70 to 80 PV modules are installed per tracker. PV modules will be facing east in the forenoon and west in the afternoon. The axis of the tracker will be in the North-South direction. Similarly, when two bifacial PV modules are installed vertically in landscape orientation. Modules will be facing east and west direction and not more than 2 strings (around modules per string based on the inverter input voltage) shall be used to make one table. These are illustrated in Figure 4 and Figure 5.

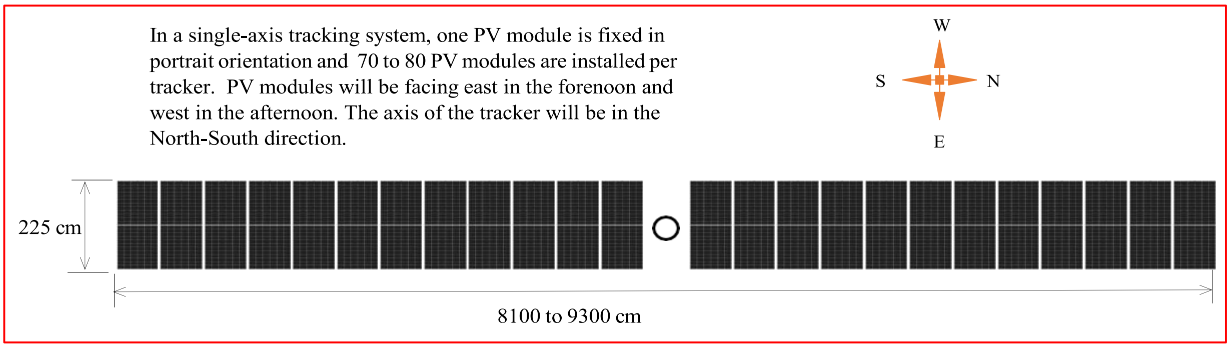

Figure 4: Placement of modules in a single-axis tracking structure

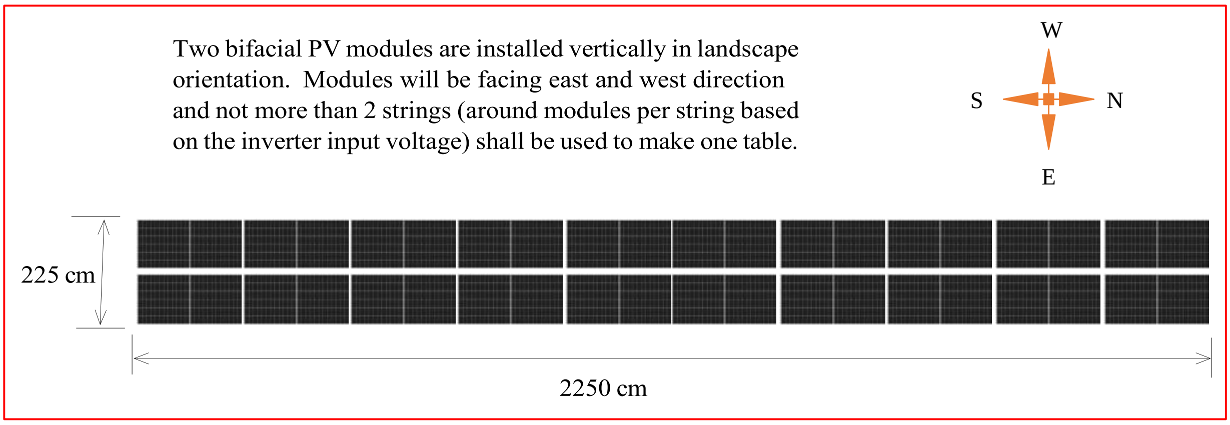

Figure 5: Placement of modules in a vertically installed fixed structure.

3.1.3 The tilt angle of the structure

The PV arrays are mounted on a structure in the following manners:

(1) Equator-facing fixed-tilt arrays
(2) Equator-facing adjustable tilt arrays
(3) East-West facing single-axis tracking arrays
(4) Two-axis tracking arrays

The main objective of choosing a type of structure is to generate maximum energy at a location based on the sun's position and sun movement during the year. However, a decision is made to achieve performance and cost objectives for a particular site.

Fixed tilt arrays are installed at a fixed tilt angle facing south (facing north in the southern hemisphere). The optimum tilt angle for annual energy generation is equal to the latitude angle up to 20º per IS/IEC TS 62738: 2018 Ground mounted photovoltaic power plants design guidelines and recommendations [28][29]. However, a lower tilt angle in the range of 5º to 20º is used to reduce wind loading and the cost of the structure.

When PV modules are installed at a lower tilt (less than 10º), there will be more accumulation of dust or dirt as wind or rain will not efficiently remove specks of dirt. In such cases, rainwater or cleaning water remains accumulated at the bottom of the modules when the module frame does not have drainage slots at the corners. In an agrivoltaic setup, more dust will likely be generated from agricultural activities, particularly during crops' sowing and harvesting time. Therefore, a minimum tilt of 10º and preferably 15º or more should be considered to maximise the self-cleaning of modules.

Equator-facing adjustable tilt arrays are fixed-tilt arrays with a provision to change the tilt angle once or more in a year based on the sun's position. A higher tilt angle is set for the winter months and a lower one for the summer months. This type of system is generally not used in large PV power plants due to increased wind load in the higher tilt position and maintenance cost.

Single-axis tracking arrays are installed on a structure which rotates on a horizontal north-south axis to follow the sun's path from morning to evening. PV modules will face east in the morning and west in the afternoon. The maximum tilt towards east and west with respect to the horizon is 60º.

Two-axis tracking arrays are installed on a structure that rotates PV modules on the north-south and east-west axes, allowing PV modules to always follow the sun during the day. This type of structure is not widely used due to its high cost, higher self-consumption and vulnerability to wind loading.

For an agrivoltaic project in India, tilt angles are recommended for fixed-mounting structures based on the geographical location of the Agro-climatic zones, as presented in Figure 6 and Table 7 below.

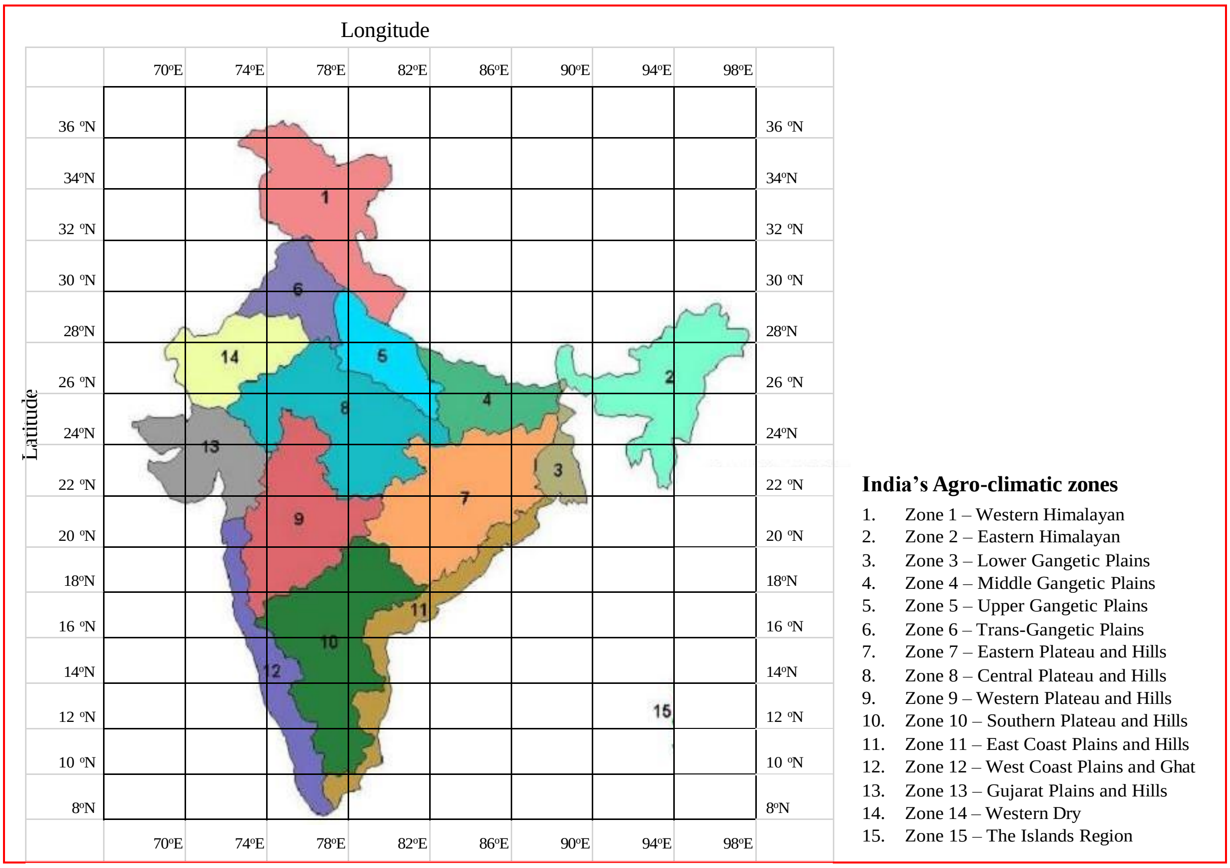

Figure 6: Latitude and Longitude of India's Agro-climatic zones (Indicative)

Table 7: Recommended tilt angle for fixed mounting structures

Geo-climatic regions	Agro-climatic & Geographical regions	Latitude	Recommended Tilt angle
The Himalayan Region	Zone 1: Western Himalayan Region: Jammu and Kashmir, Himachal Pradesh and Uttarakhand	Lat: 27ºE to 37ºE Lon: 73ºN to 81ºN	20º to 30º
	Zone 2: Eastern Himalayan Region: Sikkim, Darjeeling (West Bengal), Assam Hills, Arunachal Pradesh, Nagaland, Manipur, Mizoram, Tripura and Meghalaya	Lat: 22ºE to 29ºE Lon: 84ºN to 98ºN	20º to 25º
The Northern Plains	Zone 3: Lower Gangetic Plains: Eastern Bihar, West Bengal, and Assam valley.	Lat: 22ºE to 28ºE Lon: 87ºN to 95ºN	20º to 25º
	Zone 4: Middle Gangetic Plains: Eastern Uttar Pradesh and Bihar (except Chotanagpur plateau)	Lat: 24ºE to 28ºE Lon: 82ºN to 88ºN	20º to 25º
	Zone 5: Upper Gangetic Plains: Central and western parts of Uttar Pradesh.	Lat: 25ºE to 30ºE Lon: 73ºN to 81ºN	20º to 25º
	Zone 6: Trans-Gangetic Plains: Punjab, Haryana, Delhi, Chandigarh and Ganganagar district of Rajasthan	Lat: 28ºE to 32ºE Lon: 77ºN to 82ºN	20º to 25º

Geo-climatic regions	Agro-climatic & Geographical regions	Latitude	Recommended Tilt angle
The Western Arid Region (Thar Desert)	Zone 14: Western Dry Region: Western Rajasthan west of the Aravallis	Lat: 25ºE to 27ºE Lon: 69ºN to 76ºN	20º to 25º
The Central Highlands	Zone 7: Eastern Plateau and Hills: Chotanagpur plateau Rajmahal hills, Chhattisgarh plains and Dandakaranya.	Lat: 18ºE to 25ºE Lon: 80ºN to 88ºN	15º to 20º
	Zone 8: Central Plateau and Hills: Bundelkhand, Bhander plateau, Baghelkhand, Malwa plateau and Vindhyachal hills.	Lat: 22ºE to 28ºE Lon: 72ºN to 83ºN	20º to 25º
The Deccan Plateau	Zone 9: Western Plateau and Hills: Southern part of the Malwa plateau and Deccan plateau (Maharashtra)	Lat: 17ºE to 25ºE Lon: 73ºN to 80ºN	15º to 20º
	Zone 10: Southern Plateau and Hills: Southern Maharashtra, Karnataka, western Andhra Pradesh and northern Tamil Nadu.	Lat: 10ºE to 20ºE Lon: 74ºN to 82ºN	10º to 20º
The Coastal Plains and Islands	Zone 11: East Coast Plains and Hills: Coromandel and Northern Circar coasts, coasts of Andhra Pradesh and Orissa.	Lat: 9ºE to 22ºE Lon: 76ºN to 88ºN	10º to 20º
	Zone 12: West Coast Plains and Ghat Region: Malabar and Konkan coasts and the Sahyadris	Lat: 8ºE to 21ºE Lon: 72ºN to 77ºN	10º to 20º
	Zone 13: Gujarat Plains and Hills: Kathiawar and fertile valleys of the Mahi and Sabarmati rivers	Lat: 21ºE to 26ºE Lon: 68ºN to 74ºN	15º to 25º
	Zone 15: The Islands Region: Andaman-Nicobar and Lakshadweep	Lat: 10ºE to 16ºE Lon: 70ºN to 95ºN	10º to 15º

3.2 Agrivoltaic plant layout and site planning

For ground-mounted PV power plants, the main criteria and design objectives for layout planning and equipment positioning considered are:

- Field segments are placed such that there is no variation in orientation and tilt angle;
- Obstruction-free access to each PV module installed in the field segment;
- Provision for access to roads for the movement of equipment, goods and personnel;
- Access roads have adequate turning radius for the free movement of vehicles;
- Provision for cable trench and drainage system alongside the road;
- Tables are placed such that DC string cables do not cross any pathway;
- DCCB and inverter should be placed to ensure minimum crossover of DC cables;
- DCCB and inverter stations are placed such that they are easily accessible during the time of operation and maintenance and situations of fault;
- Inverters are installed such that the overall DC cable voltage drop is less than 3%;
- Adequate free areas are kept for the installation of containerised inverter-transformer stations.

In an agrivoltaic setup, the planning of solar and agricultural field segments is equally important.

3.2.1 Planning of solar field segment

Solar fields are planned for optimum utilisation of available area, minimum cable loss, and strategic operation and maintenance of the plant. For large utility-scale power plants, the land parcel is divided into several solar field segments to accommodate 1 MW to 2 MW in each field segment. Table 8 shows the land area required by solar field segments for different structure types. The indicative field segment also includes boundary areas and a road on one side.

Table 8: Land area required by solar field segment for different structure types

Sl. No.	Structure type and table size	Interrow gap (meter)	Field segment capacity	Field segment area (Hectare)
1	Fixed tilt array with 2 x 10 modules per table	4	1 MW_p	1.22
2	Fixed tilt array with 1 x 20 modules per table	4	1 MW_p	1.74
3	Single axis tracking with 80 modules per tracker	4	1 MW_p	1.75
4	Fixed tilt array vertically installed 2 x 10 modules per table	7.6	1 MW_p	1.91

While planning solar field segments, it is essential to consider appropriate interrow gaps to avoid shading. The interrow spacing required to avoid shadow will be variable based on the latitude of the place. Considering the longest shadow on 21st December (after 9:30 am and before 3:30 pm), the maximum gap between two rows for different locations has been determined for different locations as shown in Table 9.

Table 9: Minimum gap requirement between two rows for different locations

Sl. No.	Geo-climatic region and specific Location	Tilt Angle	Minimum gap between two rows (meter)			
			Fixed tilt array with 2 x 10 modules per table	Fixed tilt array with 1 x 20 modules per table	Single axis tracking with 80 modules per tracker	Vertically installed array 2 x 10 modules per table
1	Region 1: Srinagar Lat: 34.08° N	30	4.98	2.49	4.31	4.98
2	Region 2: Delhi Lat: 28.7° N	25	3.5	1.75	3.59	4.14
3	Region 3: Jaisalmer Lat: 26.9° N	25	3.22	1.62	3.30	3.81
4	Region 4: Raipur Lat: 21.25° N	20	2.22	1.11	2.81	3.25
5	Region 5: Ratnagiri Lat: 16.99° N	15	1.47	0.73	2.46	2.84
6	Region 6: Kozhikode Lat: 11.26° N	10	0.73	0.36	1.81	2.09

However, the gap between two rows is not only determined to avoid shadow but also to fulfil the requirement of movement of vehicles/equipment for operation and maintenance and safe access to personnel to carry required tools and materials. A minimum interrow spacing of 4 m is recommended for fixed-tilt mounting systems for maintenance requirements. The tracker manufacturers recommend the centre-to-centre spacing of 6.3 m between two rows for the single-axis tracking systems.

3.2.2 Planning of agricultural field

The following factors must be considered for planning agricultural fields in an agrivoltaic setup.

(1) The maximum typical height of the crops
(2) The minimum daily light integral (DLI) requirement
(3) Typical root penetration/ spread

(4) Plant life and sowing and harvesting time
(5) Method of sowing and harvesting and tools and equipment used
(6) Method of land preparation and tools and equipment used

These critical plant characteristics for agrivoltaic setup have been discussed in the previous section of this paper. Different crops are classified based on typical maximum height (Table 1), minimum DLI requirement (Table 2), typical root penetration (Table 3), plant life and sowing /harvesting time (Table 4) and method of sowing and harvesting (Table 5 & Table 6).

In an agrivoltaic setup, crops can be cultivated within the solar field segment and in open areas, unused areas and boundaries. Most agricultural field segments will be planned around the solar field segment. Therefore, it is essential to understand the availability of sunlight and corresponding DLI in different locations of solar field segments. For planning agricultural field segments in unused open areas and boundaries, shadow analysis must be carried out to avoid shadows from the crop on the solar modules.

System Advisor Model (SAM) developed by the National Renewable Energy Laboratory (NREL) was used to perform simulation modelling for different configurations of agrivoltaic setup across six geo-climatic regions of India to derive available sunlight and corresponding DLI in solar field segments. Region-wise specific locations and different design configurations for performance modelling are presented in Table 10 below.

Table 10: System performance modelling with different design configurations for different locations

Sl. No.	Geo-climatic region and specific Location	Tilt Angle	Number of designs simulated with structure height (ground clearance) variation			
			Fixed tilt array with 2 x 10 modules per table	Fixed tilt array with 1 x 20 modules per table	Single axis tracking with 80 modules per tracker	Vertically installed array 2 x 10 modules per table
1	Region 1: Srinagar Lat: 34.05° N	30	0.5 m to 3 m (six designs)	0.5 m to 3 m (six designs)	-	0.5 m (one design)
2	Region 2: Delhi Lat: 28.65° N	25	0.5 m to 3 m (six designs)	0.5 m to 3 m (six designs)	0.85 m (one design)	-
3	Region 3: Jaisalmer Lat: 26.95° N	25	0.5 m to 3 m (six designs)	0.5 m to 3 m (six designs)	-	-
4	Region 4: Raipur Lat: 21.25° N	20	0.5 m to 3 m (six designs)	0.5 m to 3 m (six designs)	-	-
5	Region 5: Ratnagiri Lat: 16.95° N	15	0.5 m to 3 m (six designs)	0.5 m to 3 m (six designs)	-	-
6	Region 6: Kozhikode Lat: 11.25° N	10	0.5 m to 3 m (six designs)	0.5 m to 3 m (six designs)	0.85 m (one design)	0.50 m (one design)

The System Advisory Model, by default, divides the space between two successive PV array rows into ten evenly distributed zones and provides irradiance values at the midpoint of each of these zones as illustrated in Figure 7 below.

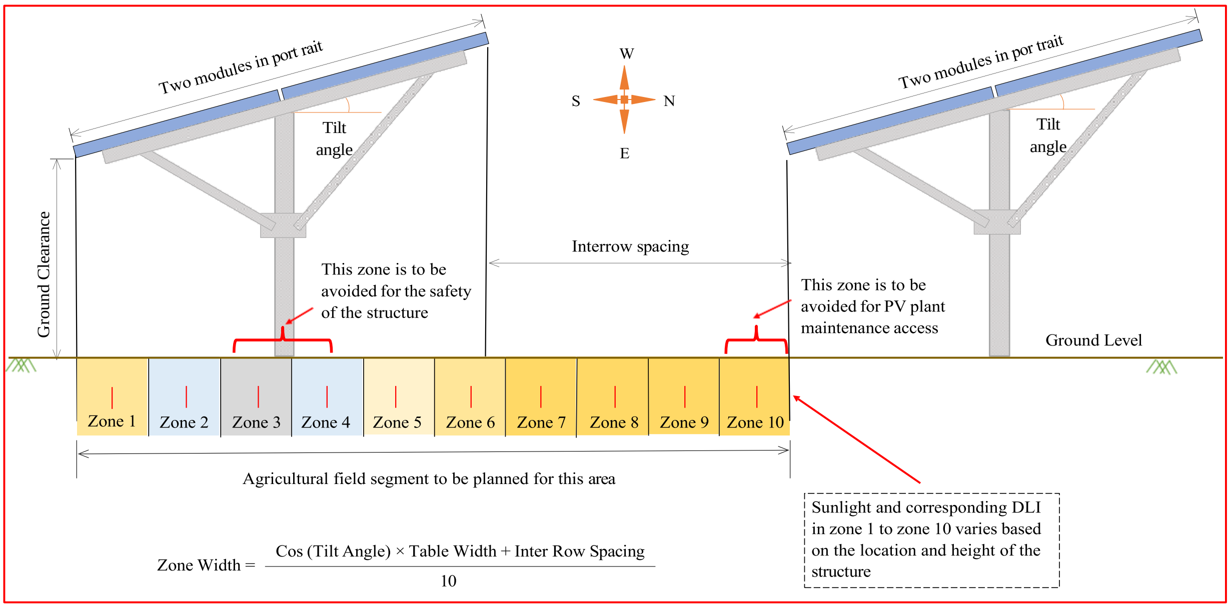

Figure 7: Illustration of fixed tilt array with 20 modules per table with 2 modules in portrait

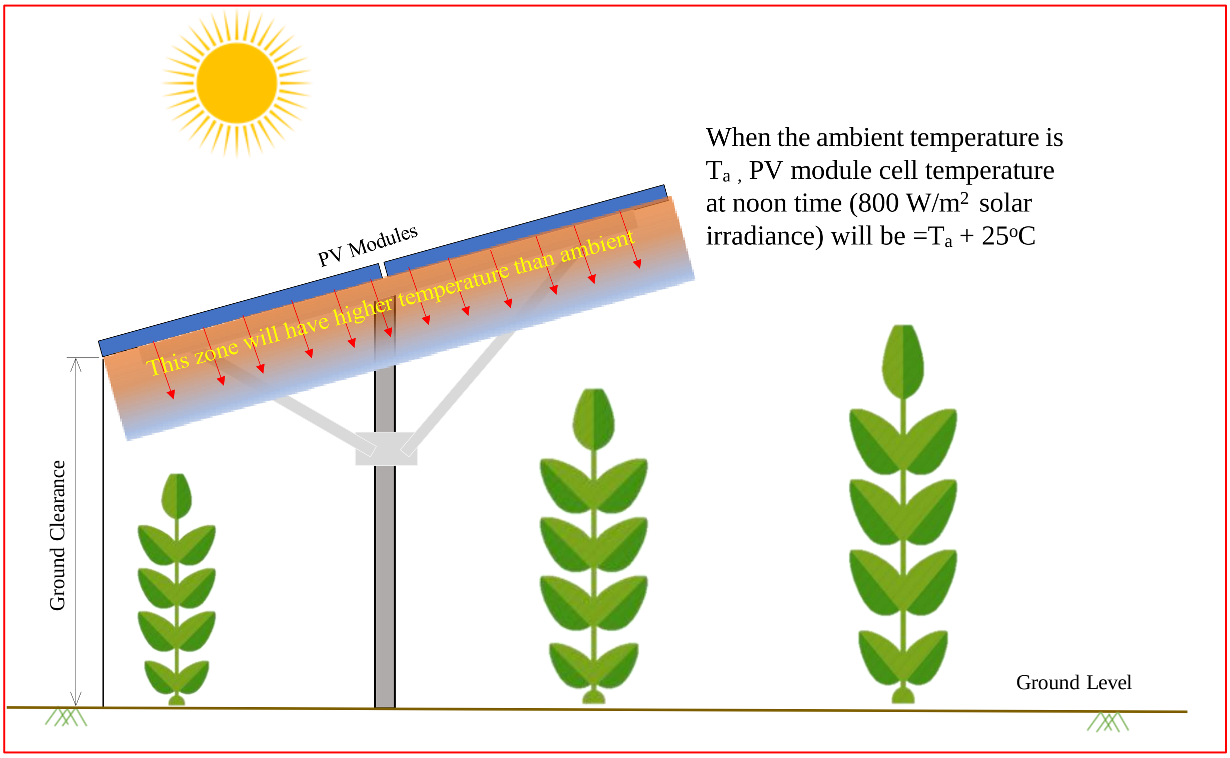

Figure 8: Illustration of temperature difference under PV arrays

The entire area in the solar field segment cannot be used for agricultural activities. The most critical areas to exclude from agricultural activities are – both sides of the structure foundation and the ground above cable trenches. Excluding at least 50 cm on both sides of the foundation/ piles is recommended. Similarly, at least 100 cm exclusion on each side of all major cable trenches is recommended. The roads and drainages will always be kept from any other activities. It is also important to keep a pathway always free on the lower side of the PV array for inspection and maintenance purposes. These provisions are illustrated in Figure 9 and Figure 10 below.

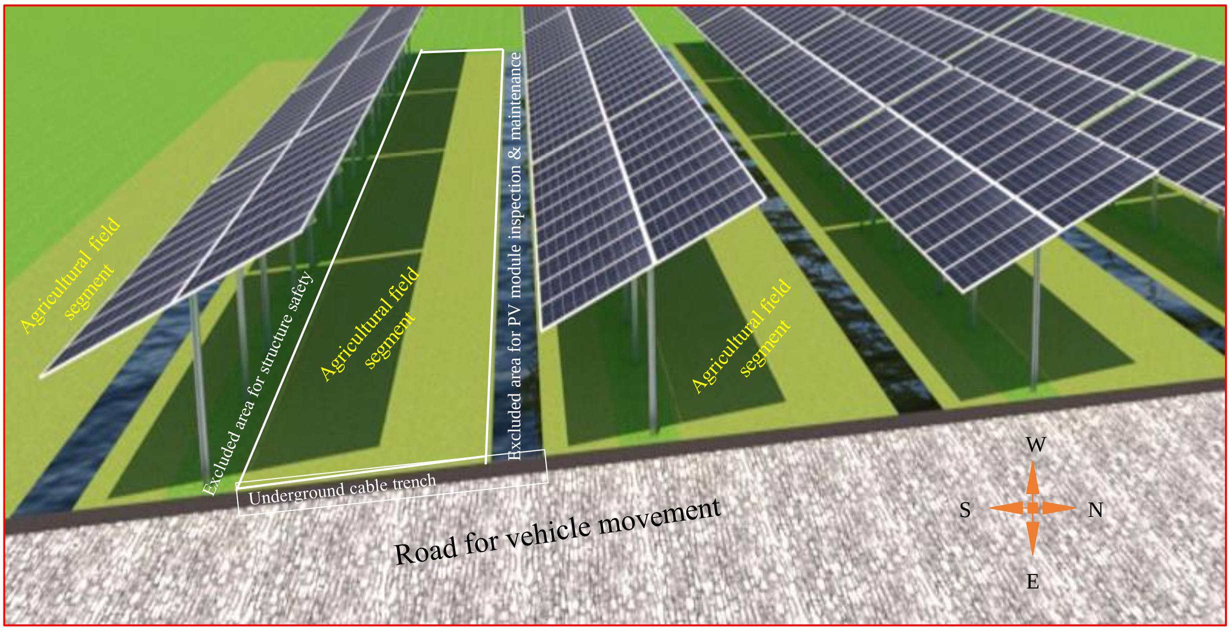

Figure 9: Agricultural field segments and excluded areas in a solar field with fixed tilt array with 2 x 10 modules per table

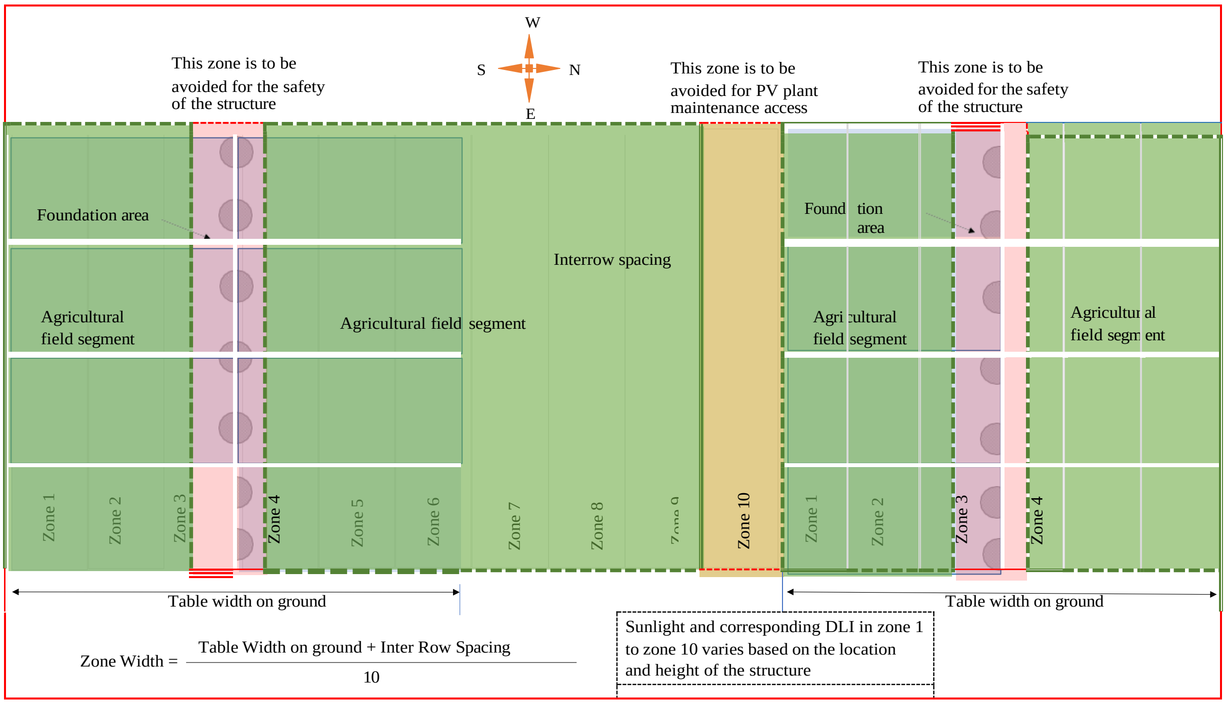

Figure 10: Plan view of agricultural field segments and excluded areas in a solar field with fixed tilt array with 2 x 10 modules per table

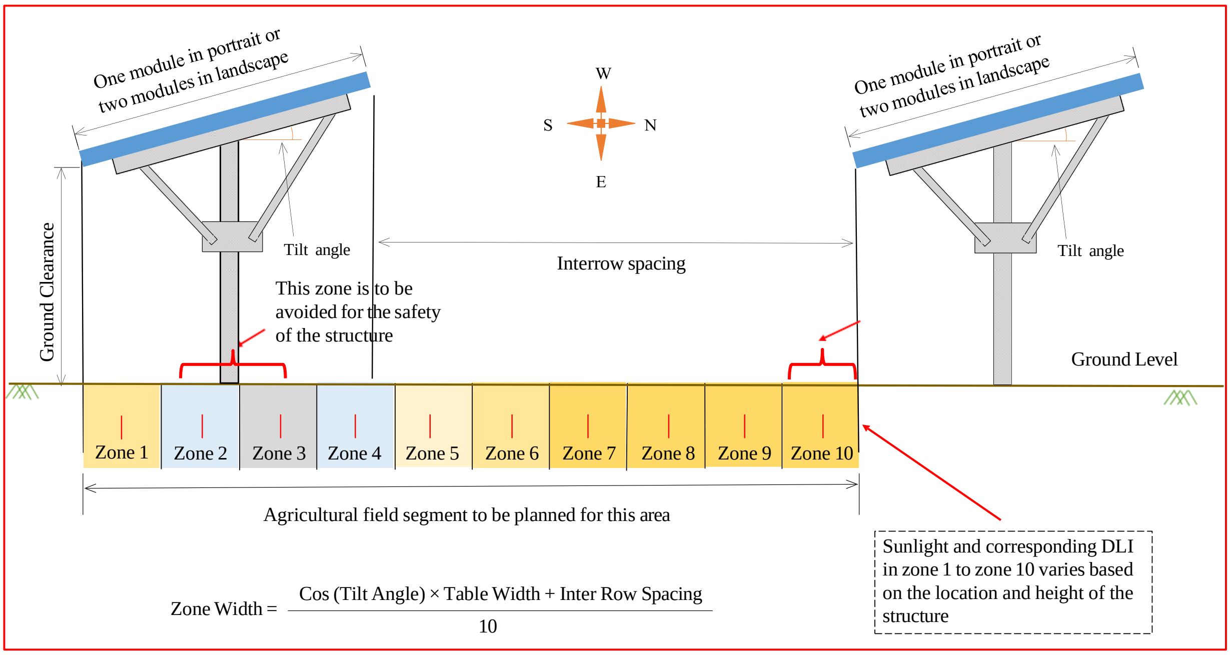

Figure 11: Illustration of fixed tilt array with 20 modules per table, 1 module installed in portrait

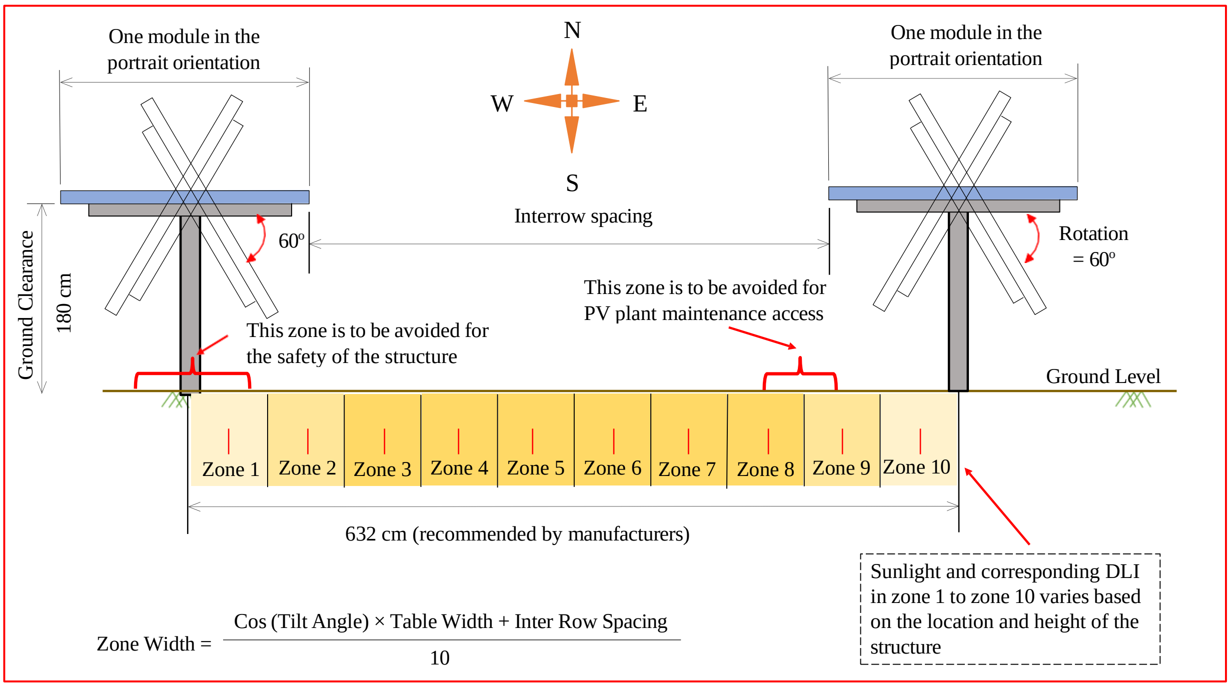

Figure 12: Illustration of single axis tracking system with 80 modules per tracker installed in portrait

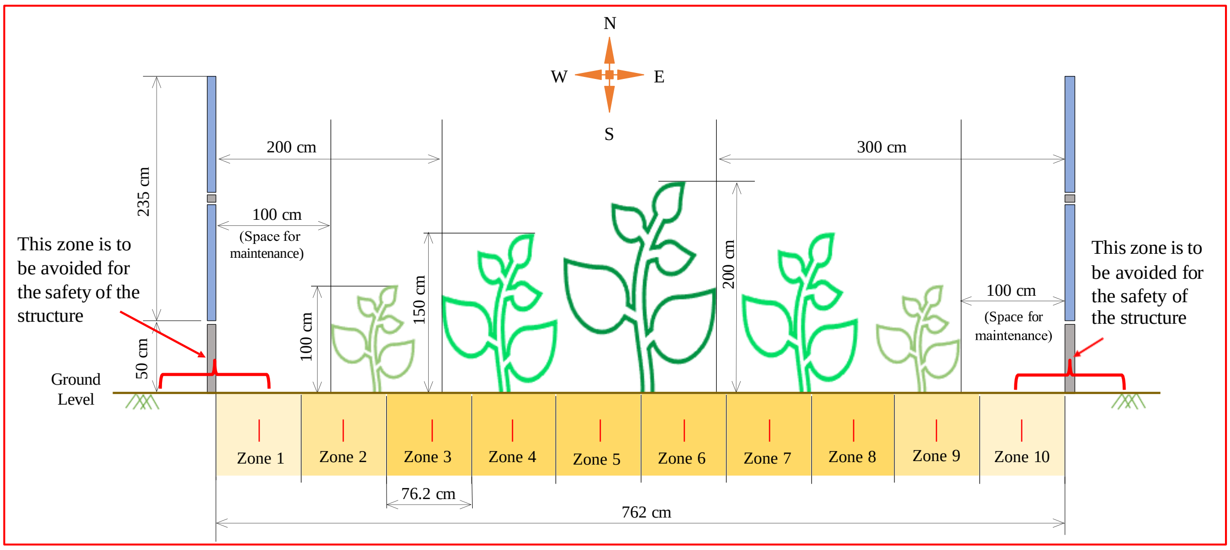

Figure 13: Illustration of a vertical array with 20 modules per table, 2 modules installed in landscape

3.3 Selection of crops based on structure height and available sunlight

The critical characteristics of different crops are presented in the previous section of this paper. In this section, Table 1 presents the typical maximum height, Table 2 presents the minimum DLI requirement, Table 3 presents typical root penetration, Table 4 shows plant life and sowing /harvesting time and Table 5 & Table 6 presents methods of sowing and harvesting of different crops cultivated in different geo-climatic regions. Based on these parameters, a selection index for crops for agrivoltaic projects based on sunlight requirement, growing season & height has been prepared and presented in Table 11.

Performance modelling has been carried out for six geo-climatic regions considering different design parameters such as table size, structure height, tilt angle, fixed tilt arrays, single axis tracker and vertically installed PV arrays, as presented in Table 10. The performance modelling provides the sunlight available within the solar field segments by dividing the space between two successive PV array rows (including the area underneath the PV array) into ten evenly distributed zones. The outcome of the performance modelling is solar radiation available in each zone of the solar field segment hourly for the entire year, total energy generation, specific energy yield and performance ratio of the PV power plant. The hourly solar radiation values have been converted to the daily average monthly and the same has been converted into equivalent DLI. This exercise has been carried out for all six geo-climatic regions for different design configurations. Matrices have been prepared for the selection of crops based on plant height, DLI and cultivation months for all six geo-climatic regions. The selection matrix for Srinagar (Lat: 34.05°N, Lon: 74.85°E, Tilt 30°) is presented in Figure 14 as an example.

.

Ground Clearance		Zone 1	Zone 2	Zone 3	Zone 4	Zone 5	Zone 6	Zone 7	Zone 8	Zone 9	Zone 10	Open Field
Annual (Perennial)	0.5 m	A6 (10)	1	2	4	A6 (8)	A9 (20)	A12 (26)	A12 (29)	A12 (32)	A12 (33)	36
	1.0 m	B9 (16)	B3 (5)	3	4	B6 (8)	B9 (18)	B12 (24)	B12 (28)	B12 (30)	B12 (30)	36
	1.5 m	C12 (19)	C6 (9)	5	4	C6 (7)	C9 (16)	C12 (21)	C12 (25)	C12 (28)	C12 (28)	36
	2.0 m	D12 (19)	D6 (11)	7	6	D6 (7)	D9 (15)	D12 (20)	D12 (24)	D12 (26)	D12 (26)	36
	2.5 m	D12 (20)	D6 (12)	9	8	D6 (8)	D9 (14)	D12 (20)	D12 (23)	D12 (26)	D12 (26)	36
	3.0 m	E12 (21)	E9 (13)	10	9	E6 (9)	E9 (14)	E12 (19)	E12 (22)	E12 (24)	E12 (25)	36
Ground Clearance		Zone 1	Zone 2	Zone 3	Zone 4	Zone 5	Zone 6	Zone 7	Zone 8	Zone 9	Zone 10	Open Field
March - August	0.5 m	A5 (8)	2	3	5	A5 (13)	A11 (34)	A11 (41)	A11 (43)	A11 (43)	A11 (42)	45
	1.0 m	B8 (14)	3	3	5	B5 (12)	B11 (31)	B11 (39)	B11 (42)	B11 (43)	B11 (41)	45
	1.5 m	C11 (19)	C2 (5)	4	6	C5 (11)	C11 (28)	C11 (35)	C11 (39)	C11 (41)	C11 (38)	45
	2.0 m	D11 (22)	D5 (7)	5	6	D5 (10)	D11 (26)	D11 (34)	D11 (37)	D11 (40)	D11 (37)	45
	2.5 m	D11 (26)	D5 (9)	6	7	D5 (10)	D11 (24)	D11 (35)	D11 (38)	D11 (40)	D11 (39)	45
	3.0 m	E11 (28)	E5 (11)	7	7	E5 (10)	E11 (22)	E11 (33)	E11 (37)	E11 (39)	E11 (38)	45
Ground Clearance		Zone 1	Zone 2	Zone 3	Zone 4	Zone 5	Zone 6	Zone 7	Zone 8	Zone 9	Zone 10	Open Field
September - February	0.5 m	A7 (13)	1	2	3	A1 (4)	A1 (5)	A4 (11)	A7 (16)	A10 (21)	A10 (23)	27
	1.0 m	B10 (18)	B4 (7)	2	3	B1 (4)	B1 (5)	B4 (9)	B7 (14)	B7 (18)	B10 (20)	27
	1.5 m	C10 (20)	C4 (13)	5	3	C1 (4)	C1 (5)	C4 (7)	C7 (12)	C7 (15)	C10 (23)	27
	2.0 m	D7 (16)	D7 (15)	10	5	D1 (4)	D1 (4)	D1 (6)	D4 (10)	D7 (13)	D7 (14)	27
	2.5 m	D7 (16)	D7 (15)	12	9	D1 (5)	D1 (5)	D1 (5)	D4 (8)	D4 (11)	D4 (12)	27
	3.0 m	E7 (14)	E7 (14)	12	11	E4 (8)	E1 (5)	E1 (5)	E1 (7)	E4 (10)	E4 (12)	27
				Excluded zones for structure safety							Excluded zones for PV plant maintenance access	

Figure 14: Matrix for selection of crops based on plant height, DLI and cultivation months for Srinagar considering fixed tilt array with 2 x 10 modules per table

How to read this Matrix?

Refer to Table 11: Crop selection index based on sunlight requirement, growing season & height. In this table, a crop can be selected using a two-character index. The first character of the index is represented by an English capital letter A, B, C, D, E and F. The second character of the index is represented by a number 1, 2, 3, 4, 5, 6, 7, 8, 9, 10, 11 and 12. The first index (capital letter) represents the typical maximum height of different crops, i.e. A (less than 50 cm), B (less than 100 cm), C (less than 150 cm), D (less than 200 cm), E (less than 300 cm) and F (more than 300 cm). These are placed in six columns on the right side of the table. The second index (number) represents the typical sunlight (DLI) requirement for the crop and cultivation months. For example, 1, 2, and 3 represent low-light crops that require daily light integral (DLI) of 3 to 6 mol/m²/day or equivalent solar radiation of 0.41 to 0.83 kWh/m^2/day. Number 1 represents crops cultivated during September- February, number 2 represents crops cultivated during March-August, and number 3 represents crops cultivated during all months (perennial).

Now follow Figure 14, where cells are filled with a two-character index and a number within a bracket or with only a number without a two-character index. The number within a bracket or without an index is the DLI value derived from the solar radiation available in a particular zone, at a specified height (ground clearance) of the structure during specified months or yearly. For example, the first cell on the top left is A6 (10), which refers to the Sugar beat in Table 11. This means sugar beet is a medium-light perennial crop with a typical maximum height of less than 50 cm, which can be cultivated in Zone 1 and Zone 5 under a PV array structure having minimum ground clearance of 50 cm.

Table 11: Selection index for crops based on sunlight requirement, growing season & height

Typical sunlight requirement	Cultivation months	INDEX	Typical maximum height of crops				
			Less than 50 cm	Less than 100 cm	Less than 150 cm	Less than 200 cm	Less 300
			A	B	C	D	E
Low light crops Daily light integral (DLI): 3 to 6 (mol/m²/day) Solar Radiation: 0.41 to 0.83 kWh/m^2/day	September - February	1	Centella asiatica (Brahmi Booti/ Mandukaparni) (herb)				
	March - August	2	Himalayan Mushroom (Gucchi) (herb)		Arrowroot (herb)		
	All months (perennial)	3					Coff
Medium-light crops Daily light integral (DLI): 6 to 12 (mol/m²/day) Solar Radiation: 0.83 to 1.66 kWh/m^2/day	September - February	4	Carrot (herb) Cauliflower (herb)	Mustard (herb) Parsley (herb) Cow Pea (herb) Radish (herb)		Peas (shrub)	So (
	March - August	5		Mung bean (herb) Green Gram (herb) Parsley (herb) Cow Pea (herb) Sarpagandha (shrub)		Cotton (herb) Vetiver (herb)	Ok fing (

Typical sunlight requirement	Cultivation months	INDEX	Typical maximum height of crops				
			Less than 50 cm	Less than 100 cm	Less than 150 cm	Less than 200 cm	Less 300
			A	B	C	D	E
	All months (perennial)	6	Sugar beet (herb)	Ginger (herb) Tea (shrub) Aloe vera (herb) Guinea Grass Patchouli (shrub) Kariyatu (Andrographis paniculata) (herb) Poppy (herb)	Asparagus (herb) Soybean (herb) Turmeric (herb) Ashwagandha (herbs) Jethimadh (shrub)	Black Pepper (climber) Betel Leaves (climber) Sunamukhi (shrub) Cardamom (shrub) Citronella (grass) Cotton (herb) Fennel (herb) Vetiver (grass)	As (So (Tu (Ashv (Jet (
High light crops Daily light integral (DLI): 12 to 18 (mol/m²/day) Solar Radiation: 1.66 to 2.48 kWh/m²/day	September - February	7	Black Gram (herb) Cabbage (herb) lettuce (herb) Spinach (herb)	Onion (herb) Rye (herb) Coriander (herb) Fenugreek (herb) Garlic (herb) Potato (shrub) Mint (herb)	Tobacco (shrub) Wheat (herb)	Snake Gourd (climber) Bitter gourd (climber)	
	March - August	8	lettuce (herb) Spinach (herb)	Onion (herb) Chili (herb) Eggplant (herb) Stevia Leaves (herb) Coriander (herb) Garlic (herb) Rye (herb)		Sesame (herb) Snake Gourd (climber) Bitter gourd (climber) Indian Bean (climber) Ash gourd (creeper/ climber)	Pea ((Guav (

Typical sunlight requirement	Cultivation months	INDEX	Typical maximum height of crops				
			Less than 50 cm	Less than 100 cm	Less than 150 cm	Less than 200 cm	Less 300
			A	B	C	D	E
	All months (perennial)	9	Sankhpuspi (herb) Groundnut (herb) Isabgol (herb) Cumin (herb)	Stevia Leaves (herb) Chicory (herb) Oats (herb) Chick Pea (herb) Berseem Clover (shrub) Mothbean (herb) Cluster Bean (herb) Fenugreek (herb) Marigold (herb) Mint Leaves (herb) Chili (herb) Chicory (herb) Brinjal (herb) Capsicum (herb)	Elephant foot yam (Herb) Linseed (Herb) Tomato (Herb)	Rasp Berry (shrub) Senna (shrub) Indigo (herb) Senna (shrub) Long bean (climber) French Bean (climber)	Su (
Very high light crops Daily light integral (DLI): More than 18 ($mol/m^2/day$) Solar Radiation: More than 2.48 $kWh/m^2/day$	September - February	10	Pumpkin (creeper) Watermelon (creeper)		Poppy (herb)	Maize (herb) Bottle Gourd (climber)	
	March - August	11	Pumpkin (creeper) Watermelon (creeper) Zucchini (creeper)		Paddy Rice (herb)	Maize (herb) Blonde cucumber (climber) Bottle Gourd (climber)	
	All months (perennial)	12		Geranium (herb)			

4 Performance evaluation and cost impact

Specific yield and performance ratios (PR) have been derived for different design variations for all six sites using the System Advisor Model (SAM) using solar radiation data from the NREL National Solar Radiation Database. Values of specific yield and PR for all design variations are presented in Table 12. It is noted that the specific yield and performance ratio for fixed tilt arrays with two different table sizes and six different structure heights is the same for a single location. The performance ratio in a specific location is the same for all designs and varies for other locations due to variations of loss in the system due to temperature. Using a single-axis tracking system enhances energy generation by 10% in New Delhi with a capacity utilisation factor (CUF) of 19.95% and 19% in Kozhikode with a CUF of 22.89% compared to fixed tilt arrays. This indicates that using a single-axis tracking system is more beneficial for the locations near the equator. On the other hand, the energy generation of vertically installed bi-facial solar arrays was reduced by 21% in Srinagar (CUF 15.15%) and 40% in Kozhikode (CUF 11.44%). This indicates that vertically installed bi-facial modules perform better in locations away from the equator than near the equator.

The design variations used for the performance evaluation are:

Design 1 – Fixed tilt with a table for 20 modules with two modules installed in portrait (**Figure 7**)
Design 2 – Fixed tilt with a table for 20 modules with 1 module installed in portrait (**Figure 11**)
Design 3 – Single-axis tracker with a tracker table with 80 modules installed in portrait (**Figure 12**)
Design 4 – Vertical bifacial with a table for 20 modules with two modules installed in landscape (**Figure 13**)

Table 12: Specific yield and performance ratio of different designs at different locations in India

Geo-climatic region and design variation	Table size	Row spacing	Tilt Angle	Specific Yield ($kWh/kW_p/y$)	Annual PSH ($kWh/m^2/y$)	PR	CUF
Region 1: Srinagar Design - 1 (Fixed array)	2 × 10	5 m	30°	1680	2024	83%	19.18%
Region 1: Srinagar Design - 2 (Fixed array)	1 × 20	4 m	30°	1680	2024	83%	19.18%
Region 1: Srinagar Design - 4 (Vertical)	2 × 10	7.6 m	90°	1327	1598	83%	15.15%
Region 2: Delhi Design - 1 (Fixed array)	2 × 10	4 m	25°	1589	2037	78%	18.14%
Region 2: Delhi Design - 2 (Fixed array)	1 × 20	4 m	25°	1589	2037	78%	18.14%
Region 2: Delhi Design - 3 (Tracking)	1 × 80	4 m	0°	1748	2241	78%	19.95%
Region 3: Jaisalmer Design - 1 (Fixed array)	2 × 10	4 m	25°	1781	2283	78%	20.33%
Region 3: Jaisalmer Design – 2 (Fixed array)	1 × 20	4 m	25°	1781	2283	78%	20.33%
Region 4: Raipur Design – 1 (Fixed array)	2 × 10	4 m	20°	1682	1998	84%	19.20%
Region 4: Raipur Design – 2 (Fixed array)	1 × 20	4 m	20°	1682	1998	84%	19.20%

Geo-climatic region and design variation	Table size	Row spacing	Tilt Angle	Specific Yield ($kWh/kW_p/y$)	Annual PSH ($kWh/m^2/y$)	PR	CUF
Region 5: Ratnagiri Design - 1 (Fixed array)	2 × 10	4 m	15°	1681	2033	83%	19.19%
Region 5: Ratnagiri Design - 2 (Fixed array)	1 × 20	4 m	15°	1681	2033	83%	19.19%
Region 6: Kozhikode Design - 1 (Fixed array)	2 × 10	4 m	10°	1682	2063	82%	19.20%
Region 6: Kozhikode Design - 2 (Fixed array)	1 × 20	4 m	10°	1682	2063	82%	19.20%
Region 6: Kozhikode Design - 3 (Tracking)	1 × 80	4 m	0°	2005	2445	82%	22.89%
Region 6: Kozhikode Design - 4 (Vertical)	2 × 10	7.6 m	90°	1002	1222	82%	11.44%

4.1 The impact on cost parameters in agrivoltaic projects

The project design approach, selection of equipment site parameters and geographic locations highly influence the cost of developing solar projects. Therefore, the cost of developing solar projects may vary from site to site. Similarly, the cost of developing greenfield agrivoltaic projects is also determined by design approach, selection of equipment site parameters and geographic locations. The level of impact on cost parameters compared to conventional PV projects is presented in Table 13.

Table 13: The level of impact on cost parameters in comparison to conventional PV projects

Sl. No.	Cost parameters	Estimated cost in comparison to conventional PV projects			
		Brownfield agrivoltaic projects	Level of impact on cost	Greenfield agrivoltaic projects	Level of impact on cost
1	Land	None	None	None/High	None/Low
2	PV Modules	None	None	None	None
3	Inverters and inverter housing	None	None	None	None
4	DC side electrical	None	None	None/High	None/Moderate
5	AC system, substation and grid integration	None	None	None	None
6	PV array mounting structure & foundation	None	None	High	Moderate
7	Site development and civil infrastructure	None	None	None	None
8	System protection (over current & overvoltage)	None	None	None	None/Low
9	System safety from mechanical damage	Upgradation	Low	High	Low

Sl. No.	Cost parameters	Estimated cost in comparison to conventional PV projects			
		Brownfield agrivoltaic projects	Level of impact on cost	Greenfield agrivoltaic projects	Level of impact on cost
10	Protection for personnel safety including signages & markings	Upgradation	Low	High	Low
11	Installation cost	None	None	None	None
12	Operation and maintenance	None	None	High	Moderate

5 Conclusion

Agrivoltaics is not a 'one-size-fits-all' solution. With its potential to synergise renewable energy production and agriculture, it calls for careful customisation, considering regional specifics such as geographical locations, climatic and soil conditions, and agricultural practices. This study explores the prospective implementation of agrivoltaics across India's diverse geo-climatic zones, offering valuable insights and technical guidelines. It emphasises the viability of dual land use and integrating energy generation with agricultural production. A detailed analysis of crop suitability, PV array configurations, and region-specific solar irradiance data sheds light on the critical design parameters for optimising agrivoltaic systems.

The design and operation of agrivoltaic systems should factor in crop characteristics such as height, sunlight requirements, root penetration, and growth cycle. These characteristics have been systematically documented in this study. Advanced simulation tools like the ‘System Advisory Model’ demonstrate the interaction between diverse PV designs and the resultant solar irradiance across various regions. These insights facilitate optimal crop selection, paving the path towards achieving the maximum land equivalent ratio.

Performance ratios and specific yields, influenced by PV array configurations and geographical location, have revealed remarkable trends. For instance, in New Delhi and Kozhikode, single-axis tracking systems enhanced energy generation by 10% and 19%, respectively, compared to fixed tilt arrays, indicating a preference for locations closer to the equator. Conversely, energy generation diminished by 21% in Srinagar and 40% in Kozhikode with vertically installed bi-facial solar arrays, suggesting better performance in locations further from the equator.

The cost of developing agrivoltaic projects, akin to conventional solar projects, is contingent on several factors, including project design approach, equipment selection, site parameters, and geographic location. As a result, costs tend to vary from one site to another. While compared to conventional PV plant set-up, there will be a low to moderate increase in cost for agrivoltaic setup based on the design approach. The principal factors that influence agrivoltaic project cost are optimum uses of land for both purposes, PV array mounting structure design for specific crops, DC cables, additional protection required for the safety of personnel and system/equipment and enhanced operation and maintenance activities of PV plant.

In this paper, the methodology employed a two-step process to assess the feasibility of agrivoltaics. Initially, solar irradiation data was simulated under and behind the PV arrays. Subsequently, a thorough evaluation of suitable crops was conducted, considering the global trend of most agrivoltaic plants being extensions of pre-existing PV installations. As an alternative approach, a predetermined list of crops would be prepared, and the PV system could then be designed to optimise available space without compromising agricultural yield. This approach is preferable when cultivated crops hold substantial commercial value and farming is the primary income source. In such cases, the focus is balancing conserving agricultural productivity and enhancing land-use efficiency through PV generation.

Integrating agrivoltaics into India's renewable energy strategy holds significant promise for yielding substantial benefits. This study lays a strong foundation for such a transition, presenting a roadmap for the smooth integration of agricultural productivity and renewable energy generation. The study's outcomes are expected to provide valuable insights and guidelines for developing agrivoltaic projects in India, enriching understanding of the technical design aspects. However, the key to success lies in adopting a region-specific approach and cultivating a continuous learning and adaptation culture. Further research is required on implementing different design approaches and their impact on PV system performance and agriculture production.

6 Acknowledgement

The work described here was part of a study carried out under the Indo-German Energy Forum (IGEF) project, facilitated by the Deutsche Gesellschaft für Internationale Zusammenarbeit (GIZ GmbH)of Deutsche Gesellschaft für Internationale Zusammenarbeit (GIZ GmbH). The project has been funded by the Federal Ministry for Economic Affairs and Climate Action (BMWK) and is being implemented by GIZ GmbH under the Indo-German Energy Program.

7 References

[1] International Renewable Energy Agency. (2022). Renewable capacity statistics 2022.
[2] Ministry of New & Renewable Energy. (2023). Annual report 2022-23. Government of India.
[3] REN21. (2022). Renewables 2022 global status report.
[4] Ministry of New & Renewable Energy. (2023). Programme/scheme-wise cumulative physical progress as on May, 2023. Government of India.
[5] Central Electricity Authority. (2018). Installed capacity report (May 2018). Ministry of Power, Government of India.
[6] Central Electricity Authority. (2023). Installed capacity report (May 2023). Ministry of Power, Government of India.
[7] Garg, V., Gulia, J., Thayillam, A., & Sharma, P. (2022, May 26). Solar Tariffs to Rise by ~21% in the Next 12 Months. JMK Research & Analytics and Institute for Energy Economics and Financial Analysis.
[8] Weselek, A., Ehmann, A., Zikeli, S., Lewandowski, I., Schindele, S., & Högy, P. (2019). Agrophotovoltaic systems: applications, challenges, and opportunities. A review. Agronomy for Sustainable Development, 39, 1-20.
[9] Al Mamun, M. A., Dargusch, P., Wadley, D., Zulkarnain, N. A., & Aziz, A. A. (2022). A review of research on agrivoltaic systems. Renewable and Sustainable Energy Reviews, 161, 112351.
[10] Toledo, C., & Scognamiglio, A. (2021). Agrivoltaic systems design and assessment: A critical review, and a descriptive model towards a sustainable landscape vision (three-dimensional agrivoltaic patterns). Sustainability, 13(12), 6871.
[11] Mahto, R., Sharma, D., John, R., & Putcha, C. (2021). Agrivoltaics: A Climate-Smart Agriculture Approach for Indian Farmers. Land, 10(11), 1277.
[12] National Solar Energy Federation of India. (2023). Agrivoltaics in India: Overview on operational projects and relevant policies (v4.0)
[13] Planning Commission of India. (1988). Agro-climatic regions/zones in India. http://apps.iasri.res.in/agridata/19data/chapter1/db2019tb1_2.pdf
[14] National Bureau of Soil Survey and Land Use Planning, ICAR. (n.d.). Soils of India (Publication No. 94).
[15] Khullar, D. R. (2018). India: A comprehensive geography.
[16] https://www.apnikheti.com/en/pn/home
[17] https://www.ikisan.com/tg-castor-morphology-and-growth.html

[18] Haddad, N. I., Salkini, A. B., Jagatheeswaran, P., & Snobar, B. A. (1988). Methods of harvesting pulse crops. World crops: Cool season food legumes: A global perspective of the problems and prospects for crop improvement in pea, lentil, faba bean and chickpea, 341-350.

[19] Mechanization & Technology Division , Department of Agriculture, Cooperation and Farmers Welfare, Ministry of Agriculture and Farmers Welfare, Government of India. (n.d.). HARVESTING EQUIPMENT. https://farmech.dac.gov.in/FarmerGuide/NE/Harvesting%20Equipments.htm

[20] Agricultural Guide. (April 12, 2023). Broadcasting Method Of Sowing In Agriculture. https://guide2agriculture.com/broadcasting-method-of-sowing-in-agriculture/

[21] M&T Division, Dept. of Agriculture and Cooperation, Min. of Agriculture, Govt. of India (2012) Small agricultural Machinery and implement. https://agricoop.nic.in/sites/default/files/small%20machinery%20-01.03.2012.pdf

[22] Indian Council of Agricultural Research. (2017). AICRP on Farm Implements and Machinery (AICRP-Fim) https://aicrp.icar.gov.in/fim/salient-achievements/sowing-and-planting-equipment/3/

[23] E-krishi shiksha. (2013). Forage Harvesters, hay conditioners. http://ecoursesonline.iasri.res.in/mod/page/view.php?id=125397

[24] Akshar Agro Engineering.(n.d). Groundnut Digger Shaker https://www.aksharagro.in/Groundnut-Digger-Shaker.php

[25] Shaila S. (n.d). List of Agricultural Tools Used for Harvesting https://www.agricultureinindia.net/harvest/agricultural-tools/list-of-agricultural-tools-used-for-harvesting/20531

[26] National Renewable Energy Laboratory. (n.d.). System Advisor Model (SAM). Retrieved May 20, 2023, from https://sam.nrel.gov/

[27] International Electrotechnical Commission. (2016). IEC 62548: Photovoltaic (PV) arrays - Design requirements.

[28] Bureau of Indian Standards. (2016). IS/IEC 62548: Photovoltaic PV Arrays Design Requirements.

[29] International Electrotechnical Commission. (2018). IEC TS 62738: Ground-mounted photovoltaic power plants - Design guidelines and recommendations.

Shading tolerance of Different PV Module Topologies

K Naga Bhavya Jyothi and Narendra Shiradkar

Indian Institute of Technology Bombay, Mumbai (India)

Abstract

This paper analyzes the significance of solar cells interconnection in a module to improve the module shading tolerance. Different PV module configurations are considered in this paper – series, series-parallel and total cross tied. Corresponding PSpice models are developed to simulate the power loss for different module configurations. Simulations are performed for various shading patterns to understand the effect of cells interconnection scheme leading to higher power loss. Shading tolerance with respect to power loss, maximum reverse voltage drop and peak power dissipation in a shaded cell is analyzed and was observed that series configuration is more prone to power losses compared to series-parallel and total cross tied configuration.

Keywords: Partial shading, PV module configuration, solar cell, solar module, series connection, series parallel connection, total cross tied connection

1. Introduction

The demand for electricity has enhanced over the years depleting the resources and also causing harmful effects to the environment due to the release of greenhouse gasses. Among the available resources, solar has been one of the reliable solutions as it is available in abundance and is a natural resource. Wherever sunlight is available, solar panels can be deployed and the electricity can be extracted. This allowed the government to launch schemes leading to massive deployment of PV modules globally including urban environments. However, PV modules installed in urban environments are often subjected to non-uniform irradiation due to partial shading caused by birds, trees, buildings etc. Under non-uniform irradiation conditions, the performance of a PV module is significantly affected as the current generated by the solar cells is proportional to the incident irradiation. In the conventional modules, due to the series configuration, the module current gets limited by the cell that generates the least current. In the presence of bypass diodes, the mismatch in the current generation by different cells would lead to multiple peaks in the power curve. Though maximum power point tracking techniques try to maintain the module at peak power point, there is still some loss incurred due to the module configuration. Also, during partial shading, the cells receiving lower irradiation would develop hotspots and start degrading in the long term. Therefore, partial shading not only affects the PV module performance but also the reliability of the module. This implies that there is a need for mitigating the negative effects of the partial shading by deploying modules that possess high shading tolerance. This is important as it is very difficult to avoid shading in urban environments.

Several researchers are working on developing shade tolerant modules by modifying interconnection between the cells and bypass diodes in the modules. Numerous module topologies are listed in the literature like series-parallel, total cross tied etc. This might necessitate the complexity in the manufacturing process. However, the unavoidable shading from the structures in the surrounding, has a huge negative impact on the solar module peak power output. To understand the need for different configurations (Pannebakker et al., 2017) (Calcabrini et al., 2021), we aim to show the different configurations' shading tolerance with PSpice simulation results.

In this paper, the PSpice models are developed for the three configurations, then the simulations are performed for different shading scenarios. The power loss, reverse voltage and the power dissipation has been considered and compared for different shading layouts to analyze the significance of module configuration and its role in enhancing the module performance.

2. Solar Module Configurations

The interconnection of the cells in the module has a huge potential impact in degrading or improving the module performance. Based on the different interconnection layouts, three different configurations are considered – series connection (SC), series-parallel connection (SP) and total cross tied connection (TCT). The interconnection of the cells in all the three configurations is shown in fig.1. In series connection topology, all the 72 full size cells(6"x6")

10.18086/swc.2023.02.05 Available at http://proceedings.ises.org

are connected in series with three bypass diodes each across 24 cells as illustrated in fig.1(a). The series-parallel configuration has 144 half cut cells with two groups of 72 half cut cells. Each group has 72 half cut cells connected in series and the two groups are connected in parallel with three bypass diodes as shown in fig.1(b). Half cut cells are considered for SP configuration instead of full-size cells as the current would be doubled due to parallel connection of the two groups. Higher currents might be difficult to handle and would also lead to power loss near the connections. Therefore, half cut cells are preferred over full size cells in SP configuration. The other configuration is the total cross tied connection where all neighboring cell junctions are tied as shown in fig.1(c).

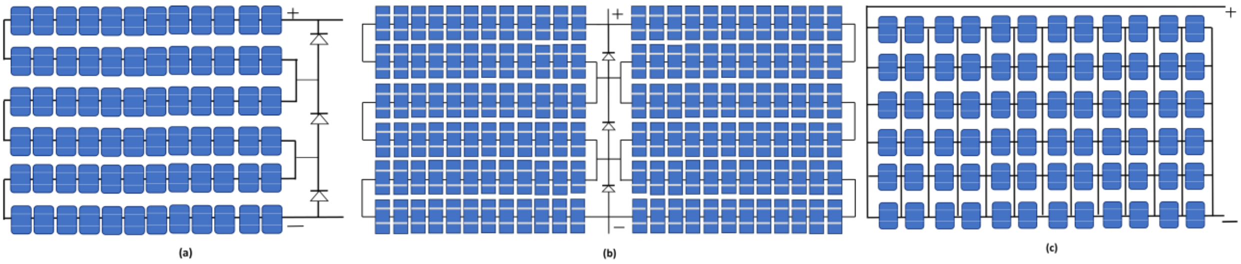

Fig. 1: Solar module topologies (a) series connection (SC) (b) series-parallel connection (SP) (c) total cross tied connection (TCT)

3. Partial Shading Patterns

The partial shading in the urban environment can be of different types. Four shading patterns are considered in this paper- only one cell is shaded, two cells are shaded, a row of cells are shaded, a column of cells are shaded as shown in Fig.2. In this figure, all the shading patterns for the considered topologies are illustrated. Fig.2(a) depicts the situation when only one cell is shaded. For better comparison among the different configurations, two half cut cells are shaded whenever one cell is shaded. In order to analyze the effect of partial shading, when two cells from different sub-strings are shaded, a second shading pattern is considered as shown in Fig.2(b). In this situation, two bypass diodes would be activated in SC and SP configuration. TCT has no bypass diodes. In the presence of building structures or poles, there could be a long horizontal or vertical shading. This is examined by considering row of cells, column of cells as shaded as can be seen in fig.2(c) and fig.2(d). Simulations are performed for all these shading patterns in PSpice to observe the power loss for different configurations

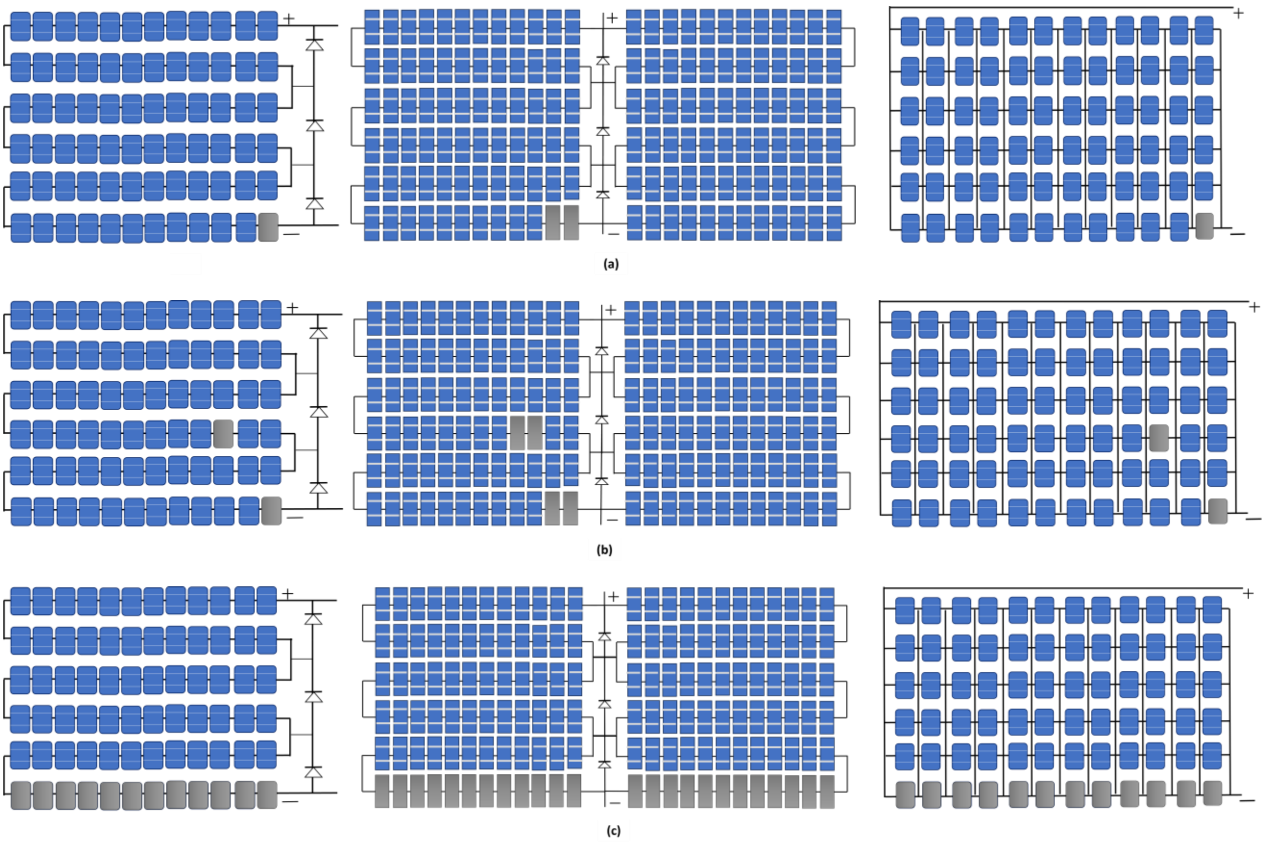

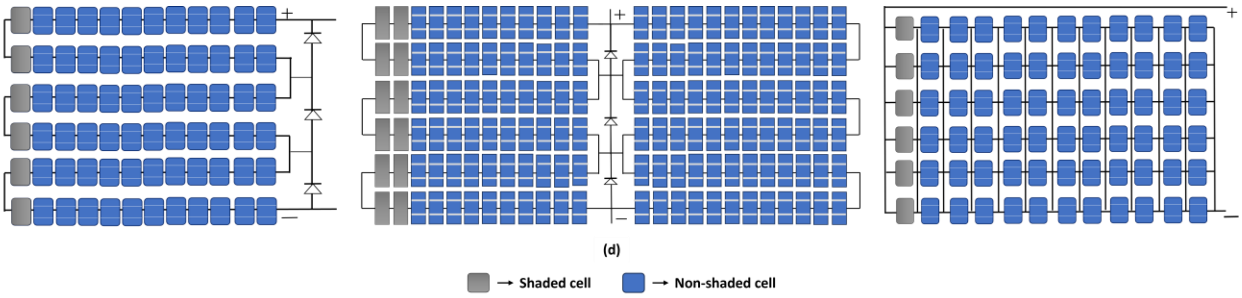

Fig. 2: Solar module topologies (a) one cell shaded (b) two cells shaded (c) a row of cells shaded (d) a column of cells shaded

4. PSpice Simulation Results and Discussion

PSpice models are developed for all the different configurations and shading patterns mentioned in previous sections. In the PSpice models, the non-shaded cells are given 1000W/m^2 and the shaded cells are assigned 500W/m^2 i.e., 50% shading for better analysis based on the amount of shading. The IV and the corresponding PV curves for all the scenarios are illustrated in Fig.3. The bypass diodes of the sub-strings with shaded cells are activated and are indicated by the step in the IV curves. This led to multiple peaks in the PV curves as depicted in fig.3(a) and fig.3(b).

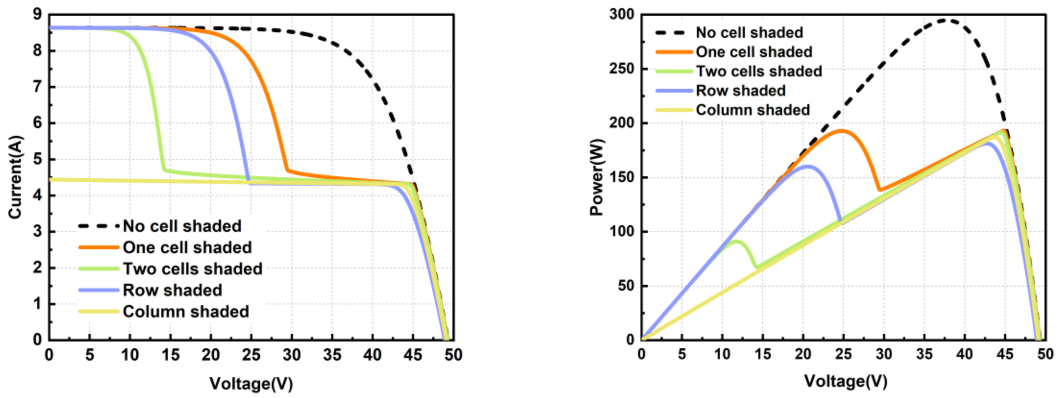

(a)

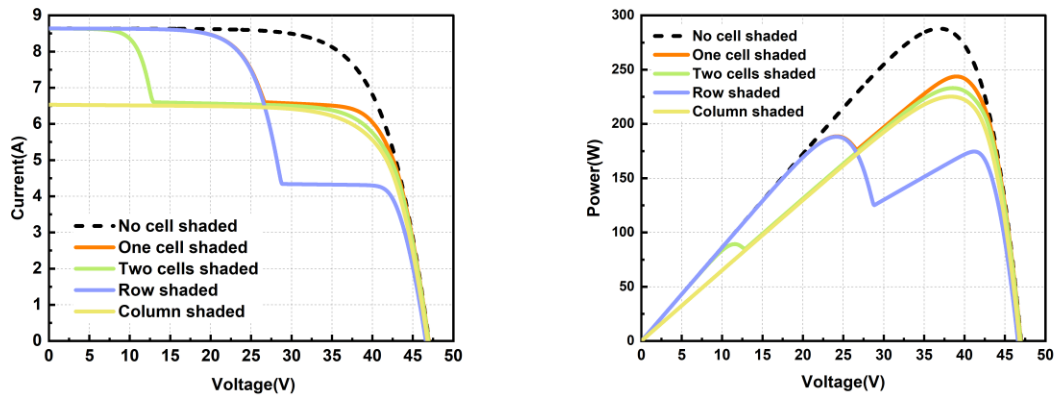

(b)

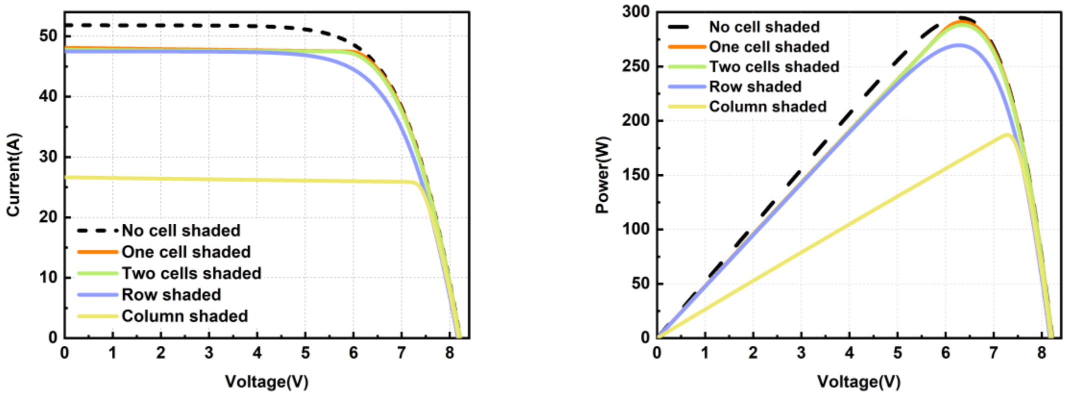

(c)

Fig.3. IV and PV characteristics of the different configurations for all the shading scenarios (a) series (b) series-parallel (c) TCT

Due to the absence of bypass diodes, TCT configuration doesn't show any step in the IV curve(fig3.(c)), thus no multiple peaks observed in the PV curve(fig.3(c)). To analyze the effect of different shading patterns, power loss for each shading pattern is calculated in percentage using eq.1 P_{no_sh} is the peak power generated by the module when no cells are subjected to shading and P_{sh} is the global peak power for a particular shading pattern. P_{sh} is calculated for all the different configurations subjected to different shading patterns.

Power loss(%) = $\frac{P_{no\_sh}-P_{sh}}{P_{no\_sh}}$ x100 (eq.1)

The power loss (%) results for all the scenarios is shown in Fig.4. It can be observed that the loss is more for all scenarios in the series configuration and is lowest is TCT configuration except for the column shading. This implies that TCT configuration modules have high shade tolerance in other shading patterns. However, it is important to note that under column shading, TCT module current is totally limited by the shaded cells as shown in the IV curve in fig.3(c). Since there are no bypass diodes, the total module current would drastically decrease if the column cells are totally shaded. This would lead to huge power loss. Apart from this, under uniform irradiation, TCT module current is also very large which might lead to power losses during the flow of current from cell to cell. Also, the busbars must be able to handle the higher currents which would enhance the complexity in the manufacturing process. Therefore, series-parallel configuration whose power loss is still comparatively less than series configuration can be considered as a better shade tolerant module over series configuration module. However, one disadvantage of SP connection is that, when a whole row of cells are shaded, SP would still result in nearly equal power loss as that of series connection. This is because the non-shaded half cut cells would generate less current than the non-shaded full-size cells.

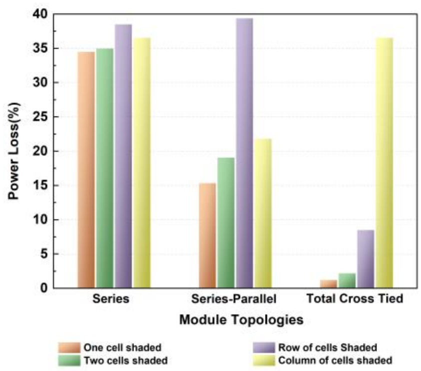

Fig.4. Power loss (%) for both the shading scenarios can be observed for all the three configurations

Along with power loss, the reverse voltage drop across the cells under short circuit condition is also observed for all the scenarios. Basically, the bypass diodes activate to prevent large amounts of reverse voltage across the shaded cells. Under high reverse voltage, the cell would get heated up, developing hotspots leading to permanent damage.

The maximum reverse voltage under short circuit condition for all the configurations subjected to different shading patterns is shown in fig.5. The reverse voltage drop is the highest for series configuration and is the lowest for TCT when all the cells in a row are shaded. Since, voltage across the cells in a column in TCT configuration would be the same, there won't be any negative voltage drop in this condition. Since, the maximum reverse voltage drop would be equal to the number of columns in this configuration, there would be at most 8V reverse voltage drop across a shaded cell which is less than cell breakdown voltage. Therefore, there is no need for bypass diodes in TCT configuration. SP configuration also shows less reverse voltage drop across its cells for this considered shading level and the shading patterns.

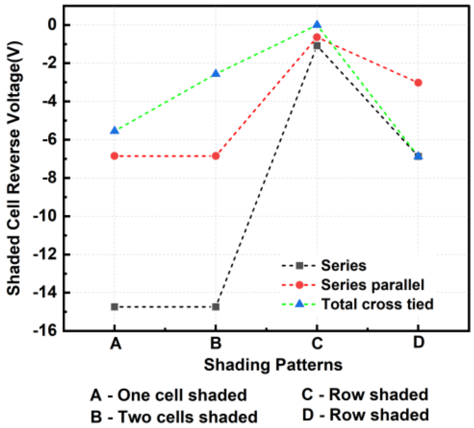

Fig.5. Reverse voltage drop across the shaded cell under short circuit condition for all module configurations subjected to various shading patterns

Though the reverse voltage drops are low, it is important to calculate possible peak power dissipation in the shaded cells. In order to find the peak power dissipation, the module current must be at its peak current (Imp). Thus, the cell must be shaded by an amount to generate Imp current. By following the procedure mentioned in (Jyothi et al., 2022), peak power dissipation for all the scenarios is calculated and plotted in fig.6. Even here, series configuration leads to highest peak power dissipation in its shaded cells. Whereas, SP and TCT configurations show lower peak power dissipations in the shaded cells. But, as already mentioned, the voltage across a column of cells in TCT configuration would be the same. This implies, if a cell in a row is shaded, the non-shaded cells would also be maintained at a negative voltage due to the interconnection scheme. It was observed that the non-shaded cells in this row would still be generating higher current as per the incident irradiation i.e., 8.63A(Isc) for 1000W/m2. This implies, the non-shaded cells in this row would dissipate larger power than the shaded cells. Since, the maximum reverse voltage is less than 8V, the power dissipation would be less than 64W. Though the power dissipation is less, the cells are subjected to high power dissipation though they are not shaded. Considering all the results based on power loss, maximum reverse voltage drop and peak power dissipation, SP would be a better shade tolerant module. TCT also might be a good shade tolerant module, but the complexity in the manufacturing process is more for TCT configuration than SP configuration.

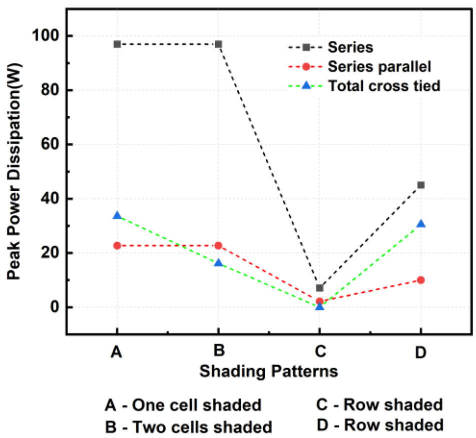

Fig.6. Peak power dissipation over the shaded cells in all module configurations due to various shading patterns

3. Conclusion

In this paper, three different configurations of solar modules are considered whose simulation results are compared to understand the shading tolerance of each configuration. Four shading patterns were considered and the PSpice simulations are performed for all the configurations to analyze the peak power reduction compared to uniform illumination condition. Also, the maximum reverse voltage drop across the shaded cell is observed. Along with this, the maximum power dissipated was obtained through simulations. In comparison, it was noticed that TCT configuration outperforms other configuration with respect to shading tolerance except when a column of cells are shaded. However, there are complexities involved in the manufacturing process due to high module current and also some limitations are observed when a column of cells are shaded leading to huge power loss. Therefore, series-parallel configurations seem to be a better shade tolerant module with lower power loss, maximum reverse voltage drop and peak power dissipation.

4. References

Calcabrini, A., Weegink, R., Manganiello, P., Zeman, M., & Isabella, O. (2021). Simulation study of the electrical yield of various PV module topologies in partially shaded urban scenarios. Solar Energy, 225, 726–733. https://doi.org/https://doi.org/10.1016/j.solener.2021.07.061

K Naga Bhavya Jyothi, Ruchita Korgaonkar, N. S. (2022). Hot-spot Endurance Test for Vehicle Integrated Photovoltaics. 8th World Conference on Photovoltaic Energy Conversion, 1244–1247. https://doi.org/10.4229/WCPEC-82022-4BV.1.62

Pannebakker, B. B., de Waal, A. C., & van Sark, W. G. (2017). Photovoltaics in the shade: one bypass diode per solar cell revisited. Progress in Photovoltaics: Research and Applications, 25(10), 836–849.

Test on bifacial cells utilizing various ground surfaces

Daniela Fontani[1], Paola Sansoni[1] and David Jafrancesco[1], Luca Mercatelli[1]

[1] CNR-National Institute of Optics, Firenze (Italy)

Abstract

The bifacial photovoltaic module (Bifacial PV) is a PV panel that can generate energy from both sides. This work studies different configurations of bifacial photovoltaic fields. Diffusing and retro-reflective (RR) materials are used to exploit the light reflected from the ground. So, the radiation not reaching the modules is minimized. The research includes ray tracing simulations of the possible ground configurations and field measurements on a small-scale system. Field measurements were developed to evaluate the effective contribution of the optimized fields to the production of electricity. The configurations measured in the field are compared in order to evaluate the actual increase in production compared to the classic photovoltaic (PV) module, which has only one active face. The studied configurations allow to increase the obtained peak power of more than 10 %.

Keywords: Bifacial PV, Retro-Reflective (RR) Materials, Ray Tracing Simulations, Field Measurements.

1. Introduction

Bifacial modules are acquiring an ever-greater space within the photovoltaic market and in the strategies of the main manufacturers. The bifacial photovoltaic module (Bifacial PV) is a particular type of panel that manages to generate energy from both sides of the photovoltaic cell, thus increasing production compared to a standard photovoltaic module (PV) (Guerrero-Lemus et al., 2016; Kopecek and Libal, 2021). A comprehensive review was carried out to present a detailed analysis of the thermal and electrical performance of bifacial photovoltaic technology (Gu et al 2020). It has been reported in the literature that the use of bifacial panels can improve the energy yield of power plants by 25-30% (Stein et al., 2021). The increase in production that a double-sided module can guarantee, thanks to the capture of the light reflected from the ground on the rear side, is a highly appreciated advantage in applications involving large ground systems, for which the payback times are still today the most important aspect. For this reason, it is necessary to install components capable of guaranteeing high electricity production and better performance.

A thorough investigation (Rodríguez-Gallegos et al., 2018) into the economic advantages of bifacial solar panels compared to monofacial panels has shown that bifacial panels are generally more cost-effective in areas with high ground reflectivity. Due to their promising efficiency, bifacial panels have been widely deployed in a variety of applications, such as green roofs, agriculture and highways (Sultan Mahmud et al.,2018; Riaz et al., 2021; Katsikogiannis et al., 2021; Baumann et al., 2019). A miniatured test array was set up, as a commercial bifacial PV system using a 3×3 module array, for the systematic measurements of bifacial systems in various mounting conditions (Nussbaumer et al., 2019).

In bifacial modules it is important to consider the albedo of the ground. Albedo, i.e. the fraction of solar radiation reflected by a surface (Frezza et al., 2021), is a well investigated characteristic of the ground that can affect the power output of the bifacial photovoltaic modules. In this framework, the purpose is to identify suitable materials, to be deposited on the ground under and around the modules, in order to reduce the part of radiation not exploited by the modules, which would therefore be lost. In Riedel-Lyngskær et al 2021 the effect of spectral albedo in bifacial photovoltaic performance was analyzed.

In the literature there are articles with tests performed on photovoltaic solar fields that consider soils with grass (Bembe et al., 2018) and standard materials, like white paint (Riedel-Lyngskær et al., 2020) or concrete (Bembe et al., 2018), or discuss tests on roofs always using standard materials (Medium Brown Shingles, White Tiocoat/Swarco Beads, Aluminum Paint) (Sciara et al., 2016). A study was carried out on a commercial solar power plant in Seville,

10.18086/swc.2023.02.04 Available at http://proceedings.ises.org

where different vegetal species were planted in two strings, and the performance of the string was monitored (Rodriguez-Pastor et al., 2023).

The objective of this work is to confirm that the design of a bifacial photovoltaic field optimized for the exploitation of the light reflected from the ground is effective. In Fontani et al 2023, after having identified the materials that optimize the reflection towards the panels, to be deposited on the ground under and around the modules, the best configurations from an optical point of view were studied. In this way the part of radiation which does not impinge on the modules, and which would therefore not be utilized, is minimized. The work considered the following aspects: identification of suitable materials for the optimization of the collected light, optical simulations of the possible configurations, field measurements on a small-scale system. Field measurements were developed to evaluate the effective contribution of the optimized fields to the production of electricity. In this paper, the configurations measured in the field are compared in order to evaluate the actual increase in production compared to the classic photovoltaic (PV) module, which has only one active face.

2. Identification of materials and configurations of the fields

As a first step of the research, materials suitable for increasing the retro-reflected flux from the ground have been identified (Fontani et al., 2023). The retro-reflective panels used were made with a highly reflective white paint, on which glass beads with an average diameter of 200 ÷ 300 µm were applied. The glass particles were dispersed as homogeneously as possible on the upper side of the panel itself. Four panels were realized to be used in the field experiments. A photo of these four panels with retro-reflective materials is shown in Fig. 1.

Fig. 1: The four retroreflective panels used in the measurements.

Furthermore, optical simulations were carried out to identify the best ground configurations in order to maximize the flux received by the bifacial module. From these studies, the most promising solutions resulted from those with a field made of diffusing-Lambertian soil and with a mixed configuration: mainly made up of diffusing-Lambertian soil with a part of the soil, the one behind the photovoltaic mini-modules, with retro-reflecting (RR) materials. A more extensive description of this process of material selection and optical simulation is presented in Fontani et al. (2023).

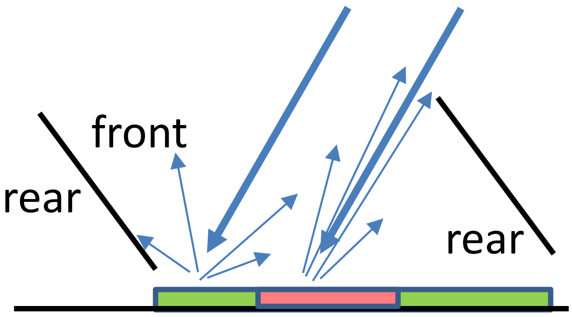

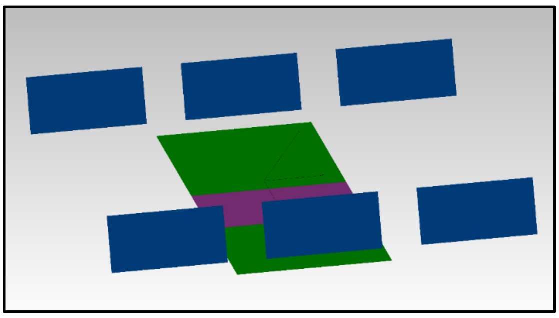

Fig. 2: The proposed mixed solution. Sketch of lateral view (left) and simulation 3D view (right). The green color indicates the ground with diffusing material, while the pink color shows the ground with RR material.

3. Measurements in the field

To verify the results of the simulations, some field measurements were carried out with direct exposure to the sun. Minimodules made up of 4 bifacial photovoltaic cells were used. The three different configurations examined for the field in which the measurements were carried out are:

- **Optimized Mixed field**, with diffusing material and retro-reflecting material,
- **Optimized field with diffusing material**,
- **Non-optimized field** (Reference field).

For the Optimized field with diffusing material and the Optimized Mixed field, several panels with diffusing paint and 4 panels with retro-reflective materials were made to be placed on the ground (Fig. 3).

For each measurement session of the Optimized Fields, the diffusive panels were placed on the ground so as to cover the entire surface. Furthermore, for the measurements with retro-reflective materials a retro-reflective panel was placed in the position foreseen in the simulations. The Non-optimized field measurements were carried out both without intervening on the measurement field, made up of gray stone, and by carrying out a measurement placing on the ground a sheet of black cardboard (Fig. 4).

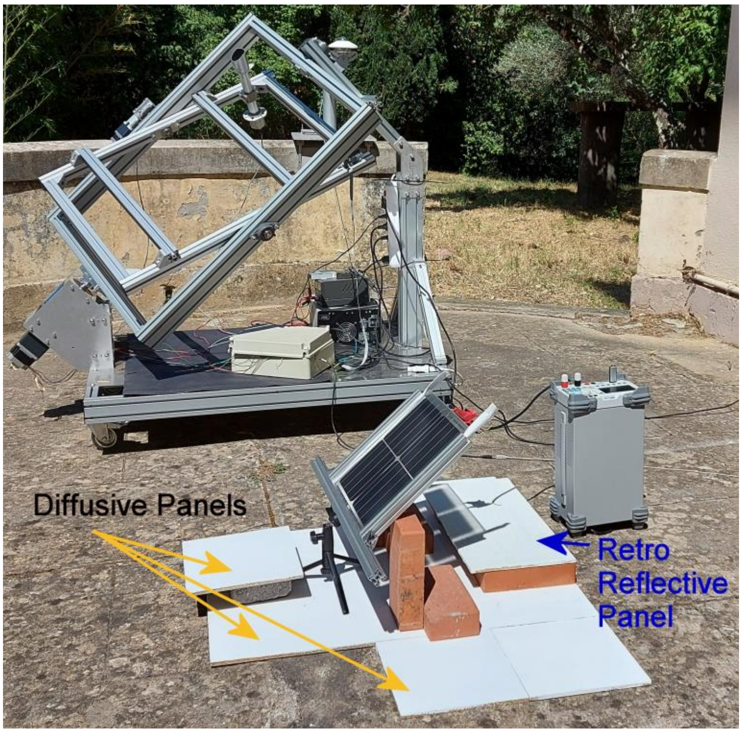

Fig. 3: Set-up of the field for the measurements.

Fig. 4: Set up of the Reference field measurement.

For each measurement session, the data are acquired initially considering only the side exposed to direct radiation (*Front*), obscuring the rear side of the minimodule (*Back*) with a covering. Then the covering was removed so that the minimodule works in a double-sided way (indicated with *Front+Back*). The Front configuration simulates the behavior of a classical PV module and is used for the comparison with the Bifacial configuration (Front+Back).

For each measurement session, the following were acquired: total radiation with a pyranometer and direct radiation with a pyrheliometer; 3 sampling cycles of the voltage-current curve (VI) using a variable load; temperature of the cells at the beginning and at the end of the measurement session; ambient temperature at the beginning and at the end of the measurement session; open circuit voltage (V_{oc}) at the beginning and at the end of the measurement session.

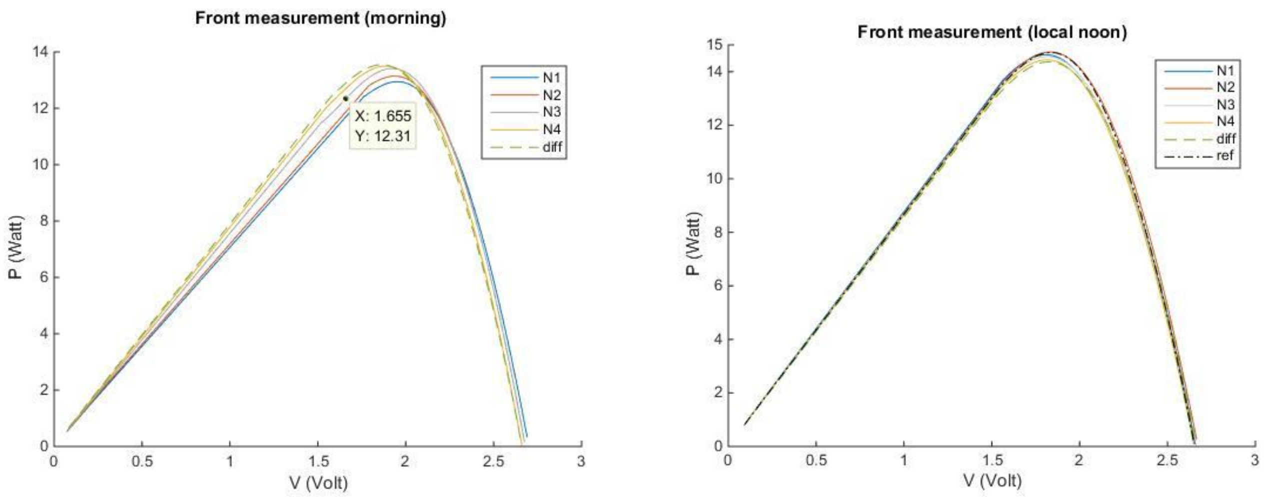

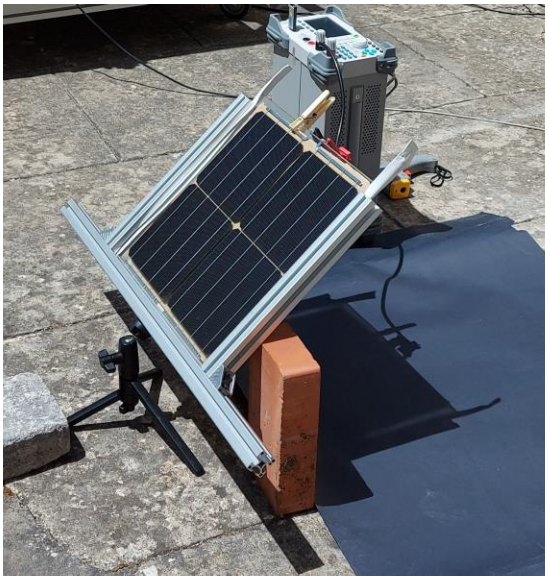

4. Processing of measures

The VI data (voltage-current curve) acquired during the measurement sessions were interpolated to obtain the maximum power (P_{max}) and obtain the short-circuit current value (I_{SC}).

Fig. 5: Power versus Voltage graphs. Left: Front measurements performed in the morning. Right: Front measurement performed around the local noon.

The results of the elaboration for the Front measurement are plotted in the graphs shown in Figure 5. The curves report the values of the calculated power as a function of the voltage values. The curves indicated with N1, N2, N3 and N4 refer to measurements with Optimized Mixed field, obtained by alternating the 4 retro-reflecting panels.

While the curve indicated with "diff" is obtained placing on the ground only diffusive panels. The black curve in the right graph (called "ref") is the reference measurement made using the black panel and the configuration shown in Figure 4.

Table 1 presents the values related to the graphs shown in Figure 5 and reports the data for the Front measurements performed in the morning and around the local noon. V_{oc} is the voltage measured in open circuit configuration, I_{sc} and P_{max} are the results of the interpolations. V_{oc} is express in Volt, the short-circuit current I_{sc} in Ampere and the maximum power P_{max} in Watt.

Table 1: numerical data of the measurements shown in Figure 5.

Field configuration	Morning			Local noon		
	V_{oc}	I_{sc}	P_{max}	V_{oc}	I_{sc}	P_{max}
Optimized Mixed field with panel N1	2,70	7,28	12,94	2,66	8,98	14,63
Optimized Mixed field with panel N2	2,68	7,461	13,14	2,67	8,89	14,73
Optimized Mixed field with panel N3	2,68	7,63	13,41	2,65	8,91	14,56
Optimized Mixed field with panel N4	2,66	7,88	13,50	2,65	8,85	14,44
Optimized field with diffusing material	2,66	8,02	13,55	2,66	8,73	14,37
Reference configuration (non-optimised)				2,65	8,83	14,71

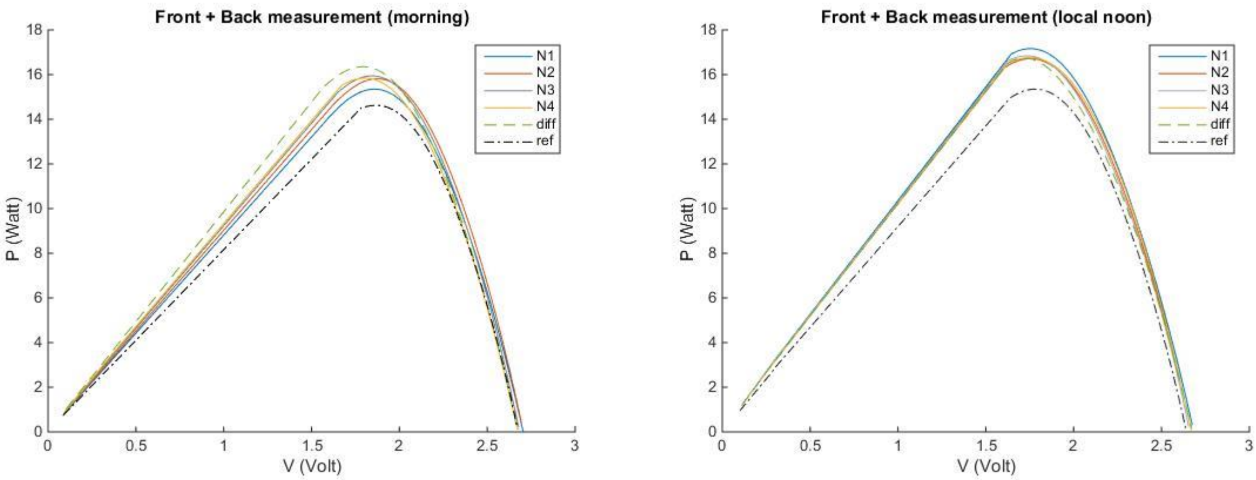

Fig. 6: Power versus Voltage graphs. Left: Front+Back measurements performed in the morning. Right: Front+Back measurement performed around the local noon.

The results of the elaboration for the Front+Back measurement are plotted in the graphs shown in Figure 6. The curves report the values of the calculated power as a function of the voltage values. Similarly, to Figure 5, the graphs indicated with N1, N2, N3 and N4 refer to measurements with Optimized Mixed field obtained by alternating the 4 retro-reflecting panels. While the curve indicated with "diff" is obtained placing on the ground only diffusive panels. The black curve (called "ref") in the right plot of Figure 6 refers to the reference measurement made with the black panel and the configuration shown in Figure 4; while the black curve called "ref" in the left graph is obtained from a measurement in our data base, which was performed without using the black panel, so the ground was made of grey stone. The values related to the Front+Back measurements performed in the morning and around the local noon are reported in Table 2. V_{oc} is the voltage measured in open circuit configuration, I_{sc} and P_{max} are the results of the interpolation. Table 2 also reports the value of the average solar irradiance during the measurement, G_k, this quantity will be used for further elaborations. V_{oc} is expressed in Volt, I_{sc} in Ampere, P_{max} in Watt, G_k in Watt/m^2.

Table 2: numerical data of the measurements shown in Figure 6.

Field configuration	Morning				Local noon			
	V_{oc}	I_{sc}	P_{max}	G_k	V_{oc}	I_{sc}	P_{max}	G_k
Optimized Mixed field with panel N1	2,70	8,95	15,35	853	2,68	10,86	17,16	985

Optimized Mixed field with panel N2	2,70	9,09	15,81	889	2,67	10,74	16,71	970
Optimized Mixed field with panel N3	2,68	9,36	15,94	892	2,66	10,92	16,84	987
Optimized Mixed field with panel N4	2,67	9,60	15,84	909	2,67	10,76	16,75	995
Optimized field with diffusing material	2,67	10,02	16,35	929	2,67	10,71	16,74	978
Reference configuration (non-optimized)	2,67	8,63	14,62	889	2,64	9,70	15,35	967

Since the irradiance value varies during outdoor measurements, for each measurement it was calculated the value of

$$m_k = P_k / G_k \qquad \text{(eq. 1)}$$

where P_k is the maximum power obtained in the interpolation of the k-th measurement, and G_k is the average solar irradiance during the measurement itself.

For each set of measurements, a reference value was chosen, and the following value was calculated:

$$\mu_k = (m_k - m_{ref})/m_{ref} \qquad \text{(eq. 2)}$$

where the subscript "$_k$" refers to the value of the k-th measurement and the subscript "$_{ref}$" to the reference measurement.

Note that for constant irradiance the value of μ_k is equivalent to the quantity ΔP_{kmax}, calculated as:

$$\Delta P_{kmax} = (P_k - P_{ref})/P_{ref} \qquad \text{(eq.3)}$$

The comparisons between the configurations were made based on the ΔP_{kmax} and μ_k values.

5. Comparison of measurements

Comparison 1: comparing the performance of a Bifacial module using different field configurations.

The first comparison is performed in order to understand the improvement given by the optimized grounds with respect to the non-optimized ground. The reference measurement, with non-optimized ground, for the local noon case is the measurement performed at noon with black sheets on the ground (these values are in Table 2). Since the measurement with the black panel is not available for the morning case, the reference data set for the morning has been chosen from our database, selecting a suitable configuration without modification of the ground and with the irradiance nearest to the mean value registered during the morning session (these values are in Table 2).

Table 3: Comparison between the various Bifacial (Front+Back) measurements.

Field configuration	**Morning**		**Local noon**	
	ΔP_{kmax} (%)	μ_K (%)	ΔP_{kmax} (%)	μ_K (%)
Optimized Mixed field with panel N1	4,98%	9,41%	11,82%	9,77%
Optimized Mixed field with panel N2	8,15%	8,15%	8,89%	8,55%
Optimized Mixed field with panel N3	9,04%	8,68%	9,72%	7,50%
Optimized Mixed field with panel N4	8,36%	5,98%	9,16%	6,08%
Average of the 4 mixed fields measurements	*7,63%*	*8,05%*	*9,89%*	*7.98%*
Optimized field with diffusing material	11,86%	7,04%	9,08%	7,85%

Referring to mixed field measurements, since the production process is still at the laboratory level, in Table 3 there is also an average value of the measurements with the 4 retro-reflecting panels. The results show that the process for realizing the Retro Reflective panels needs still to be improved. These results indicate that the use of an optimized ground produces an advantage in the performances during all day, not only for the time where the optimized configuration has been calculated (local noon). The values of μ_k result more stable that ΔP_{kmax} that is influenced by the variations of solar irradiance. The optimal field was obtained for the noon configuration; the values of ΔP_{kmax} for local noon confirm that the average value of the Mixed field is better than the results obtained with ground composed only of diffusing materials, as expected. Meanwhile, the values of the normalized parameter μ_K show a more constant behavior during the day and a better performance for the mixed solution. In fact, the mean values of μ_K for the Retro Reflecting material are greater than the corresponding values obtained with the diffusing materials. While the mean value of the power of the field (ΔP_{kmax}) with Retro Reflective panels is greater than the power with only the diffusive material, but only at the local noon.

Comparison 2: comparing the performance of a standard PV module without optimized ground with a Bifacial Module with optimized ground.

Table 4 illustrates the values of the comparison between the performance of the single-sided cell and the performance of the double-sided cell. The single-sided cell is equivalent to the measurements carried out on the *Front* side only of a double-sided cell. The measurement on the double-sided cell has the contribution of the *Front+Back* sides of the minimodule. The reference measurement (*ref*) used in eq. 3 and eq. 2 for the calculation of ΔP_{kmax} and μ_k corresponds to the *Front* measure with the black cardboard.

In Table 4 the first four values (rows 2-5) refer to measurements with field in mixed configuration obtained by alternating the 4 retro-reflecting panels (indicated with N1-N4). Referring to these measurements, since the production process is still at the laboratory level, in Table 4 (row 6) there is also an average value of the measurements with the 4 retro-reflecting panels. Finally, the measurement in row 7 of Table 4 refers to the configuration with a field composed only of diffusing panels. For each measurement, the table reports the values of ΔP_{kmax} and μ_k calculated with eq. 3 and eq. 2. The last row reports the comparison between PV minimodule and Bifacial PV minimodule, for the reference configuration, which is with the non-optimized field.

Tab. 4: Comparison between the performance of PV minimodule and Bifacial PV minimodule at local noon.

Field configuration	ΔP_{kmax}	μ_k
Optimized Mixed field with panel N1	16,63%	15,21%
Optimized Mixed field with panel N2	13,57%	13,92%
Optimized Mixed field with panel N3	14,44%	12,82%
Optimized Mixed field with panel N4	13,85%	11,34%
Average of the 4 mixed fields measurements	*14,62%*	*13,32%*
Optimized field with diffusing material	13,77%	13,19%
Reference configuration (non-optimised)	4,30%	4,95%

Analyzing the results of Table 4 it can be noticed that both the optimized fields (Optimized Mixed field and Optimized field with diffusing material) give an improvement more than 10% with respect to the PV single face module. The bifacial configuration with non-optimized field gives an improvement of 4,30% for ΔP_{kmax} and of 4,95% for μ_k, so the addition of the optimized field boosts the value of around 10% for ΔP_{kmax} and around 8% for μ_k.

Since the amount of solar irradiance does not change in the raytracing simulations, the value of ΔP_{kmax} and μ_k in the simulations results the same. It is possible to evaluate the maximum amount of ΔP_{kmax} (Fontani et al., 2023), because the power obtained on the receiver does not take into account the angular response of the Bifacial PV minimodule. This means that the expected ΔP_{kmax}, calculated as the ratio between the recovered power of each configuration and the Direct Flux on the panel, was estimated to have a maximum of 17.7% for the Optimized field with diffusing material and 20.3% for the Optimized Mixed field. Hence, the results obtained show that is possible to recover the 2/3 of the power that reaches the back of the Bifacial Panel.

6. Conclusion

The purpose of this work is to find materials and field configurations to optimize the efficiency of the bifacial photovoltaic minimodules through the optimization of the solar field. This article presents an innovative approach trying to maximize the sun power collected by the back side of a bifacial PV module, performing a study on suitable materials and ray tracing simulations.

In a previous work (Fontani et al., 2023) some suitable Retro-Reflective (RR) materials have been studied and realized to minimize the flux lost because it does not reach the rear part of the panel and maximize the recovery of the solar flux. It was found that the optimal RR material is the one with a diameter of microspheres of 200-300 µm regardless of density. For the field optimization, a ray tracing analysis was performed in order to obtain the best configuration considering a real field and the materials examined in the previous study,both diffusive and RR. As result of these simulations the best configuration is a mixed ground with diffusive parts and a RR part. The RR part is located in an area behind the photovoltaic panel. Some tests on a scaled field with a single minimodule were performed in order to verify the effectiveness of the optimizations combining the results of material studies and raytracing simulations. The measurement was executed in the summer season, 2 sets of measurements were performed on the same PV module alternating the 4 RR panels realized and the diffusive one. Moreover, a measurement with a black panel in a grey ground was done as reference for the noon measurement. The comparison between the measurements performed with and without the plywood panels on the ground shows that there is an improvement of the minimodule output when the ground is properly settled.

Comparing the performance of a Bifacial module using different field configurations it can be noticed that the values of μ_k result more stable that ΔP_{kmax} that is influenced by the variations of solar irradiance. The values of ΔP_{kmax} for local noon confirm that the average value of the Mixed field is better than the results obtained with ground composed only of diffusing materials (this result was obtained from the simulations optimizing the field for the local noon). Meanwhile, the values of the normalized parameter μ_κ show a more constant behavior during the day and a constant better performance for the mixed solution.

Comparing the performance of a standard PV module (*Front* measurement) without optimized ground with a Bifacial Module (*Front+Back* measurement) with optimized ground it can be noticed that the bifacial configuration with non-optimized field causes an improvement of 4,30% for ΔP_{kmax} and of 4,95% for μ_k, while the addition of the optimized field boosts the value of around 10% for ΔP_{kmax} and around 8% for μ_k.

Utilizing the data of the raytracing simulation it is possible to affirm that the results obtained show that is possible to recover the 2/3 of the power that reaches the back of the Bifacial Panel.

7. Acknowledgements

The present experimental research was funded by the Italian Ministry of University and Scientific Research (MUR) under the PON Project entitled “BEST4U-Bifacial Efficient Solar Cell Technology with 4-Terminal Architecture for Utility Scale”.

8. References

Baumann, T., Nussbaumer, H., Klenk, M., Dreisiebner, A., Carigiet, F., Baumgartner, F., 2019. Photovoltaic systems with vertically mounted bifacial PV modules in combination with green roofs. Solar Energy 190, 139–146. Issn: 0038092X. doi: 10.1016/j.solener.2019.08.014.

Bembe, M. T., Chowdhury, S. P. D., Meeding, N., Lekhuleni, E. G., Ayanna M. B., Simelane, S., 2018. Effects of Grass and Concrete Reflective Surface on the Performance of Dual Axis Bifacial Solar PV Systems IEEE PES/IAS PowerAfrica 734-738, doi: 10.1109/PowerAfrica.2018.8521143.

Frezza, L., Santoni, F., Piergentili, F., 2022. Sun direction determination improvement by albedo input estimation combining photodiodes and magnetometer, Acta Astronautica, 190, 134-148, doi:10.1016/j.actaastro.2021.09.029.
Fontani, D., Jafrancesco, D., Sansoni, P., Nicolini, A., Di Giuseppe, A., Pazzaglia, A., Castellani, B., Rossi, F., Mercatelli, L. 2023. Field optimization for bifacial modules. Optical Materials, 138, 113715. https://doi.org/10.1016/j.optmat.2023.113715.

Guerrero-Lemus, R., Vega, R., Kim, T., Kimm, A., Shephard, L.E.,2016. Bifacial solar photovoltaics – A technology review, Renewable and Sustainable Energy Reviews 60, 1533-1549 https://doi.org/10.1016/j.rser.2016.03.041.

Gu, W., Ma, T., Ahmed, S. Zhang,Y., Peng,J., 2020. A comprehensive review and outlook of bifacial photovoltaic (bPV) technology, Energy Conversion and Management, 223, 113283, doi:10.1016/j.enconman.2020.113283.

Katsikogiannis, O.A., Ziar, H., Isabella, O., 2022. Integration of bifacial photovoltaics in agrivoltaic systems: A synergistic design approach. Applied Energy 309, 118475. Issn: 03062619. Doi: 10.1016/j.apenergy.2021.118475.

Kopecek, R., Libal, J., 2021. Bifacial Photovoltaics 2021: Status, Opportunities and Challenges. Energies 14, 2076. https://doi.org/10.3390/en14082076.

Nussbaumer, H., Klenk, M., Morf, M., Keller, N., 2019. Energy yield prediction of a bifacial PV system with a miniaturized test array, Sol. Energy. Doi:10.1016/j.solener.2018.12.042

Riaz, M. H., Imran, H., Younas, R., Butt, N.Z., 2021. The optimization of vertical bifacial photovoltaic farms for efficient agrivoltaic systems. Solar Energy 230, 1004–1012. Issn: 0038092X. doi: 10.1016/j.solener.2021.10.051.

Riedel-Lyngskær, N., Poulsen, P.B., Jakobsen, M.L., Nørgaard, P., Vedde, J., 2020. Value of bifacial photovoltaics used with highly reflective ground materials on single-axis trackers and fixed-tilt systems: a Danish case study. IET Renew. Power Gener. 14, 3946-3953. https://doi.org/10.1049/iet-rpg.2020.0580.

Riedel-Lyngskær, N., Ribaconka, M., Pó, M., Thorseth, A., Thorsteinsson, S., Dam-Hansen, C., Jakobsen, M.L., 2022. The effect of spectral albedo in bifacial photovoltaic performance, Solar Energy, 231, 921-935, doi:10.1016/j.solener.2021.12.023.

Rodríguez-Gallegos, C.D., Bieri, M., Gandhi, O., Singh, J.P., Reindl, T., Panda, S.K.,2018. Monofacial vs bifacial Si-based PV modules: Which one is more cost-effective?. Solar Energy 176, 412–438. Issn: 0038092X. doi: 10.1016/j.solener.2018.10.012.

Rodriguez-Pastor, D.A., Ildefonso-Sanchez, A.F., Soltero, V.M., Peralta, M.E., Chacartegui, R., 2023. A new predictive model for the design and evaluation of bifacial photovoltaic plants under the influence of vegetation soils, Journal of Cleaner Production, 385, 135701, doi:10.1016/j.jclepro.2022.135701.

Sciara, S., Suk, S.J., Ford, G., 2016. Characterizing Electrical Output of Bifacial Photovoltaic Modules by Altering Reflective Materials, Journal of Building Construction and Planning Research, 4, 41-55, doi:10.4236/jbcpr.2016.41003.

Stein, J., Reise C., Castro, J., Friesen, G., Maugeri, G., Urrejola, E., Ranta, S., 2021. Bifacial Photovoltaic Modules and Systems: Experience and Results from International Research and Pilot Applications. Sandia National Laboratories (SNL), Apr. 2021. Doi: 10.2172/1779379.

Sultan Mahmud, M., Wazedur Rahman, M., Hossain Lipu, M.S., Al Mamun, A., Annur, T., Mazharul Islam, M., 2018. Solar Highway in Bangladesh Using Bifacial PV. 2018 IEEE international conference on system, computation, automation and networking (ICSCAN), Pondicherry, India, 6-7 July 2018, pp. 1-7, doi: 10.1109/ICSCAN.2018.8541253.

03. Solar Thermal Power

Boundary conditions and Natural temperature decay from experimental data analysis to on-design of a tank for CSP plant

Part 2

Alfredo Angelillo[1], Walter Gaggioli[2], Primo Di Ascenzi[2], Valeria Russo[2]

[1] REEFS2–D.Eng., Oslo (Norway)

[2] ENEA–Italian National Agency for New Technologies, Energy and Sustainable Economic Development, Rome (Italy)

Abstract

Translating real boundary conditions in a simulated 2D environment aids to control the performances of a tank prone to store energy. In particular, the ullage has been investigated along a natural decay of temperature since it is a significant observed heat loss along the dome. Whether the tank is prone to store energy along a stand-by phase, during O&M or even in operation, it can affect the performance, maintenance upgrading plans. Experimental data campaigns conducted since 2004 as well as experimental campaigns between 2020 and 2021 have been used to model a lumped-circuit abstraction to focus on heat losses from the upper dome. Those values have been investigated to find a physical law of tank-insulation aging (Angelillo et al., 2021). Under a set of imposed assumptions, a setup of simulation has been used such aid tools to identify a temperature coefficient to visualize the variations of tank performance. Results of data analysis show the characterizing value for tank aging. Therefore, according to a simulated lumped-circuit scheme in OpenModelica in a previous study, has found out key values for more comprehensive energy 2D simulation. Particularly, the lumped-circuit scheme has been used to find the involved thermocouples and translate this accuracy into a temperature coefficient among others. Hence, a set-up of model has been presented to how control it. The novelty of study is based on the opportunity to match a tank design and monitor it along operational phase in no-adiabatic conditions, namely approximately to real conditions.

Keywords: Lumped-circuit, Tank, Storage, O&M

1. Introduction

During the experimental campaigns programme SFERA III, at PCS ENEA Casaccia-Rome between 2020 and 2021, has been collected data since 2004 about a series of experiments to study components and the processes of CSP technology (W. Gaggioli et al., 2016). In particular, all those data, both numerical and operating records, haven't be used to diagnose specific conditions of the system such as errors, shut down, aging, failures and so on. Therefore, the data cataloguing along the campaign has been central to set-up an experiment with the scope to check the performance of some components. The tank SA.1.01 is perfect for the goal because it belongs the experimental power station since 2004 without significant upgrading or updating.

In this regard, heat losses along the natural decay of temperature affect the internal temperatures if the tank set-up lowers the performances in a no-simulated environment, i.e., no adiabatic boundary conditions. Namely, this piece of information could lead to evaluate the state of tank if the original performance has no reached any more, and when.

According to a previous paper (Angelillo et al., 2021) a modelled solution based on lumped-circuit abstraction under a set of imposed assumptions led to a better equation of temperature decay. Regardless of further purposes of the equation, the aim in this paper is to get clear evidence about the aging of tank using the natural decay of temperature. Hence, a time-elapsed comparisons have been done since 2004, even though the paper present only three examples: 2004 first operation year; 2008 after four years of experiments; 2020-2021 the last experimental campaign.

As matter of fact, the natural decay of temperature in the tank is the only condition it can be observed without considering other causes, i.e., increasing parameters and variables.

10.18086/swc.2023.03.01 Available at http://proceedings.ises.org

Furthermore, the immitted energy has shown to exert influence on molten salt level throughout. The two electric flange immersion heaters and the three welded ones along the tank-skin (F. Fabrizi et al., 2006), expand the molten salt while the density reduces (G. Milozzi et al., 2001, K. Cornwell, 1970); to be specific molten salt level varies accordingly. As result, the natural decay, and the level of molten salt inside of the tank are boundary conditions to validate the comparisons of curves, in the absence of significant variations of atmospheric conditions, *ceteris paribus*. To aim to the goal, in accordance with previous paper (Angelillo et al., 2021) of which is an essential part, heat losses have been identified and quantified consistently with the tank geometry and shapes.

The geometry, which has a significant impact (M. Mehos et al., 2020, A.B. Zavoico, 2001), and other implications of data analysis, were explained a previous paper (Angelillo et al., 2021), as such the temperature trends is studied without adiabatic conditions and omission of the tank surface. Other extra information about manipulation of data and measures taken in advance to obtain reliable results has been discussed in the Method paragraph. Subsequently, the paper has focused on the heat loss via ullage, which visualizes the aging of natural temperature decay in SA.1.01 during almost 20 years.

The heat transient has been compared in accordance with a lumped circuit. The fundamentals of heat and mass transfer in relation to the principles of electrostatics, and more generally for what concerns inductances, resistances and capacitors intended also in AC for some configuration, has been used to aid the right modelling of equations. This has led to a novel type of lumped circuit abstraction being applied with time-dependent initial energy for heat transfer. Thereafter some clarifications have been given in the paragraph Methods as well. In fact, the scheme used in the previous paper (Angelillo et al., 2021) has been expanded, showing the parts that were negligible in the case of natural temperature decay. Naturally, such association between the forms of heat transport, both steady-state and thermal transients, are not new in the field, but here the logic finds a new application for the available automation technology.

The heat transient has been compared in accordance with a lumped circuit, Fig. 1; where the fundamentals of heat and mass transfer have been referred to the principles of electrostatics and AC. Those have been used to aid the right modelling of equations. Also, this has led to a novel type of lumped circuit abstraction being applied with time-dependent initial energy for heat transfer. In fact, the scheme used in the previous paper (Angelillo et al., 2021) has been expanded, showing the parts that were negligible at first instance. Naturally, such association between the forms of heat transport, both steady-state and thermal transients, are not new in the field, but here the logic finds a new application for the available automation technology and software like Modelica. Additional clarifications have been given in the next paragraph Methods.

The final purpose by observing the natural decay of temperatures as well as the level trend of molten salts, and stored energy is to optimize the design of all tanks prone to store energy, also to improve Control System during the charging-discharging phase.

2. Method

The manipulation of data recalled the list in Appendix A, have been based on the tagged component changing over time, the several expedients for the experiments, and the DCS images variations. All data have been controlled by operating written PCS records and sorted on the same comparable parameters for the set problem. That is, the molten salt level inside the tank should have been almost the same with a tolerance of ±100 mm in high; no pump motion; no previous pressurization test; all the electric flange and welded heaters switched off; and already at stabilized temperature of molten salt for those were immersed in, and for those corresponding the ullage above.

According to Fig. 1, the resistivity for the convection $\mathbf{h_{ull\text{-}stl}}$ along the interface between the air – ullage – and steel of skin tank has been assumed to have the higher value, namely the same for both horizontal and upwards (Scott M. Flueckinger et al, 2012). The main reason is based on the sheltered area where the tank is located. This area could easy been assumed to have the same outdoor temperature downwards, horizontal, and upward, hence the same for the free stream condition resistance $\mathbf{R_\infty}$. That is, the heat flow has almost the same ΔT along the ullage. Precisely, the outdoor temperature has matter if we reach lower temperature after freezing phase (W. Gaggioli et al., 2017), or where the oscillations among days and nights could be significant at lower temperature. Generally, outdoor temperature at PCS location in Rome can be assumed as temperature mean of day, i.e., no meaningful diurnal air temperature variation. As consequence, the insulation resistance $\mathbf{R_{iso}}$ from the ullage plus the interface $\mathbf{h_{ull\text{-}stl}}$ is the same along the whole ullage volume.

The molten salt dome followed the same logic downwards, that is to use the higher convection $\mathbf{h_{ms\text{-}stl}}$. In this case, the horizontal one is the higher value than downwards one. As matter of fact, the paper (Angelillo et al., 2021) held about a reliable way to find out a superficial outer tank temperature without having any measurement on the outer skin-tank along the collected data. Thus, obtaining an expression entirely dependent on physical and geometric parameters. Furthermore, the skin-temperature could be intended as quasi-uniform, but the proportion between the molten salt mass and ullage becomes fundamental, both to assume it, and how to determine those temperatures.

$$T_0(\tau, H_{lms}) = \sum\left(\left(\prod_i \frac{T_{TT,max,i}+T_{TT,min,i}}{2}\,\frac{V_{ms,i}}{V_T}\right)^{\frac{1}{i}} + \left(\prod_j \frac{T_{TT,max,j}+T_{TT,min,j}}{2}\,\frac{V_{ull,j}}{V_T}\right)^{\frac{1}{j}}\right)_{,k} \frac{\Delta\tau_k}{\Delta\tau} \qquad \text{(eq.1)}$$

Hence, $T_0(\tau, H_{lms})$ is the initial temperature weighted as a function of the time intervals in which the salt level and the volume of the salts vary. Assumed that, the subscripts $_{\mathbf{ull}}$ refer to ullage, and $_{\mathbf{ms}}$ refer to molten salt volume underneath, the initial temperature depends on the level of molten salt or likewise the ullage above, so the initial skin temperature increases with bigger molten salt volume or decreases with the bigger ullage ones according to the transient. This is the start point for the natural decay of temperatures. Trivially, where the molten salt volume $V_{ms} = 0$, i.e., no molten salt in the tank, the formula calculates the skin-temperature by only the air inside the tank.

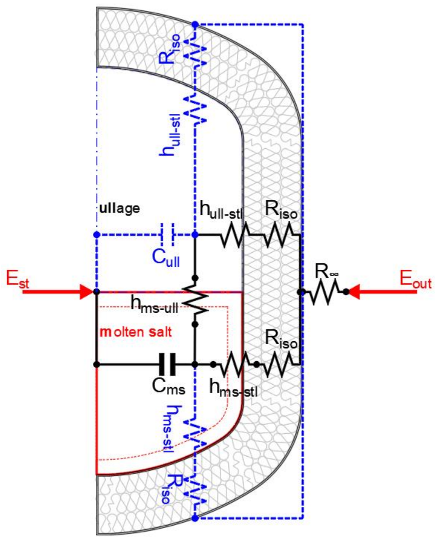

Fig. 1 Extended lumped circuit in use for modelling equation and simulations. The blu dashed lines are the negligible values in consistency with boundary conditions.

On the reporting of the experimental campaigns and historical data, the most consistent way to test statements and assertions is to use the variations between those two volumes in comparable volumes as well as minimizing significant pressure variation. On purpose, the decay temperature trends are based on ullage around 52%.

In accordance with extended lumped circuit in Fig. 1, the ullage capacitor $\mathbf{C_{ull}}$ was neglected in (Angelillo et al., 2021) due to a scale factor between air and molten salts. Indeed, the pressure inside the tank is assumed and it is almost constant, realistically. That is all the physics phenomena are at constant pressure. If so, we can consider taking the variations of the physical parameters of the air at constant pressure. That means two parallel connected capacitors are the sum of capacitors, but where the $\mathbf{C_{ull} \ll C_{ms} : \{C_{ull}+C_{ms}\} \approx C_{ms}}$. Although, it is considered that the heat from the molten salts subsequently releases to the ullage via the interface $\mathbf{h_{ull\text{-}stl}}$ will be a small negligible amount of energy that the air can store.

So, assumed that: $\begin{cases} C_{ms} = c_{p,ms} m_{ms} \\ C_{ull} = c_{p,air} m_{air} \end{cases}$ (eq.2)

in accordance with thermal-physical properties and constitutive correlation, Appendix B, the capacitor $\boldsymbol{C_{ull}}$ is around 0,04% of total amount of loaded energy, simply negligible. As matter of fact, the air has no resilience in accordance with material science. Methodologically, the attention was set on the heat flow and the velocity of heat losses via ullage to define the boundary conditions into the simulated environment.

Firstly, the domes have longer characteristic length that result into a worse form factor and act as disperser. The factor forms for the cylindrical part of PCS SA.1.01 is 2,02 m^{-1}, while only the dome is almost 9,45 m^{-1}. This result stand for 45% of total heat loss by domes. Naturally, the upwards dome is worse than the downwards one. The first is interfaced with air, while the downwards contains molten salts with significant higher specific heat at constant pressure.

Secondly, the interface $\mathbf{h_{ull\text{-}st}}$, as mentioned above, is based on a lower resistivity and higher velocity. Based on the recorded temperature inside the tank and on the skin steel under the isolation layer, that could be guessed, this convection heat transfer coefficient at boundary layer $\boldsymbol{y} = 0$ is (T.L. Bergman et al., 2017):

$$h_{ull-stl} = \frac{-\lambda_{air}(T)\frac{\partial T}{\partial y}\Big|_{y=0}}{T_s - T_{\infty,ull}} \qquad \text{(eq.3)}$$

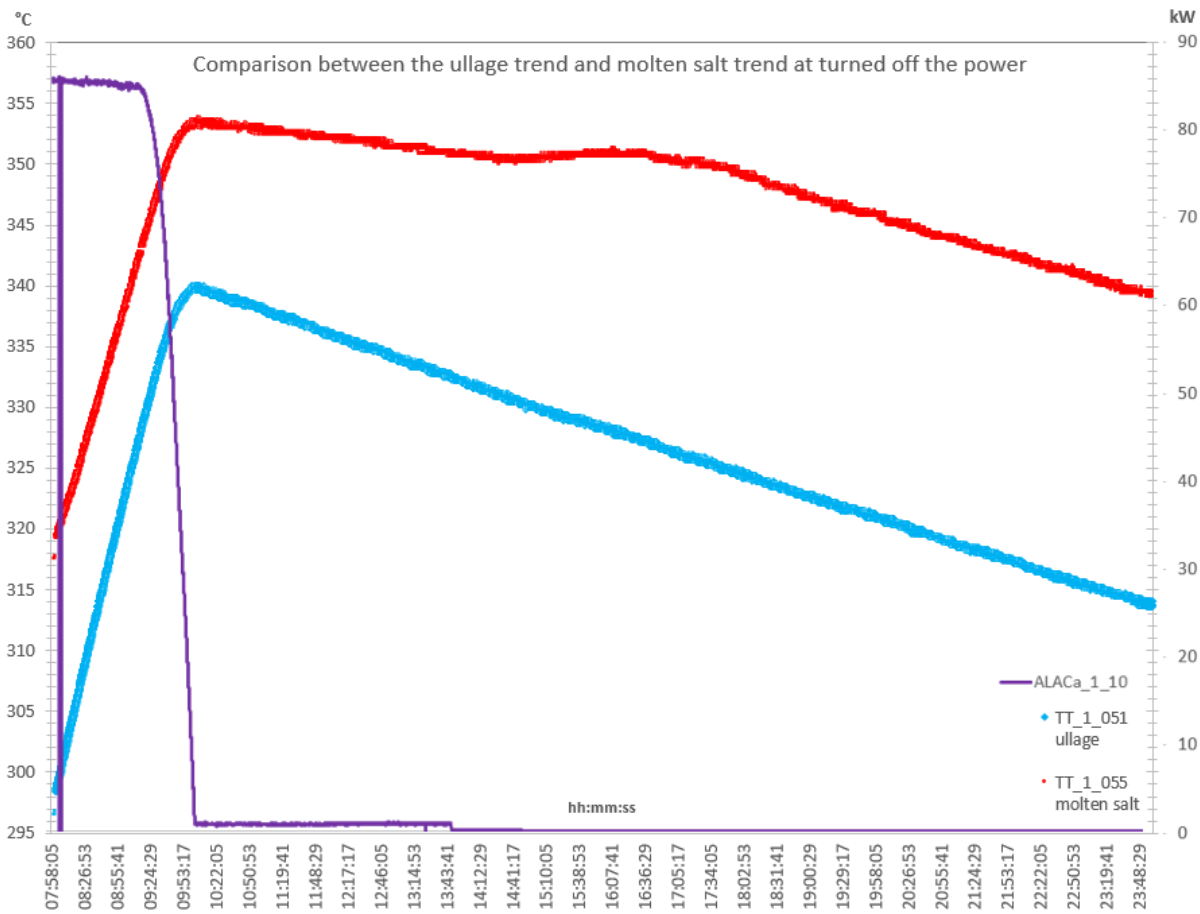

Fig. 2 The immersed thermocouple in molten salt (red line) and in ullage (blue line) compared to power (violet line)

As the distance $\boldsymbol{y}$ between the inner side of tank surface and centre of ullage increases, so the velocity must be consistent to the variations of time related to the variation of temperatures on the surface, that is:

$$\tau_{ull} = \mu(T)\frac{\partial u}{\partial y}\Big|_{y=0} \qquad \text{(eq.4)}$$

The upwards convection transfer coefficient is the one used inside the ullage despite of directions, because the historical trends of air inside the tank have shown a precise curve in comparison to the molten salt; namely an immediate higher heat loss according to downwards convexity of the thermocouple trend, Fig. 2.

This figure (Fig. 2) visualizes the beginning of temperature natural decay where the switched off power sets the trend of ullage temperature to decrease quasi-immediate. That has been verified to match a capacity for air mass around 727 J°C^{-1}m^{-3} *versus* a 47% molten salt mass of the total tank volume, ca. 2,63 MJ°C^{-1}m^{-3}. Therefore, it can be assumed that the ullage heat loss reaches own energy level immediately, and right after it dropped down in comparison to the resilience of molten salt mass, i.e., the first part of red line at switched off power in Fig. 2. The molten salt takes almost 8 hours to reach the decay point inertially, while the ullage has doubled the ΔT in comparison to molten salt trend after 4 hours. Conclusively, in this way the methodology has taken into account the strong correlation between molten salt level, temperature, stored energy and physics parameters.

3. Results

The analysis of data listed in Appendix A has led to identify a way to signal aging, namely the performance of the tank after 17 operating years. The trends in Fig. 3 and Fig. 4 show the comparisons of the curves in the three referenced mentioned years: 2004 first operation year; 2008 after four years of experiments; 2020-2021 the last experimental campaign. In accordance with methodology and the parameters used to evaluate the transient of natural temperature decay, and collected data with same weather conditions, it was avoiding significant swings in temperatures during the long necessary time to reach the freezing point of molten salt volume. Consequentially, the comparisons are based on the same outdoor temperature mean between 10°C and 15°C.

The reference year is 2004, the first operational year for PCS, depicted with orange line in both Fig. 3 and Fig. 4. The mentioned period in 2004 is between 6th and 10th of April with outdoor temperature mean of 12,48°C and ±2,42°C diurnal air temperature variation. The level of molten salt during the same period in NO-operational or stand-by mode conditions was between 1171 mm and 1235 mm within the predetermined ±100 mm tolerance range. The thermocouple TT_1_051 is the highest one installed on SA.1.01 tank and measured the ullage without been affected by other causes. Furthermore, the operational records aided to recognize activity that could have invalidated the result. In Fig. 4 the trend of TT_1_051 shows the most suitable period among the 5 days data, while in Fig. 3 is the same, but shorter in comparison to 2008's data trend. In particular, before beginning of natural decay in 2004, Fig. 4, the trend is affected by two electric flange immersion heaters to reach the set point 320°C, and at the end the power was switched on to hold the molten salt over the freezing point, i.e., around 260°C. Between these two moments, it was recorded a natural decay of temperatures, used here as representative specimen of the recorded data in 2004.

The first comparison is along the 12th of March 2008 between 9:05 and 17:40 o'clock, blue marker in Fig. 3. The outdoor temperature mean was 13,1°C and ±2,9°C diurnal air temperature variation. The referred level of molten salt was 1086 mm and 1114 mm with a deviation of 8,46% compared with the referenced curve. The operational records in 2008 aided to interpret the trend of curve correctly. That date was planned a reparation on central siphon, so the solar field was switched off, hence the natural decay of temperature took place until a pump was reactivated again as shown into Fig. 3. For the comparison, the natural decay in the diagram is settled in the same period of time and temperature difference, thereby it is seen another tangential variation between the two mentioned years.

The second comparison refers to the experimental campaign between 17th and 25th of October 2020, the grey line in Fig. 4. The experimental set-up was to collect data from the tank SA.1.01 after reaching the set-point of 500°C and leave temperature to decay to 300°C, the most common period observed since 2004. The outdoor temperature mean along the week was 15,1°C and ±5,1°C diurnal air temperature variation with a deviation around 9,07%. To avoid significant diurnal air temperature variation, the comparison focused on the daylight part of data, even though it has been confirmed in a time-elapsed observation each 4 years along different days, *ceteris paribus*. As matter of fact, some deviations have been observed with decreasing outdoor temperatures, see Fig. 4, even though a same tangential angle of the curve is in place. As expected, the natural decay in the same period of time, x-axis, and the temperature difference, y-axes, had an even worse inclination in comparison to the ones in 2004, also bigger than 2008 as in Fig. 3 and Fig. 4.

These comparisons have given evidence to pursue that the tank had lowering performances along the years. As result, it is self-evident that the insulation layer is reducing its performance capabilities along its lifespan since the layers in place for 17 years have been the steel tank, the insulation, and the aluminium cladding, and considered that the metal layers have not shown sign of corrosion or deterioration.

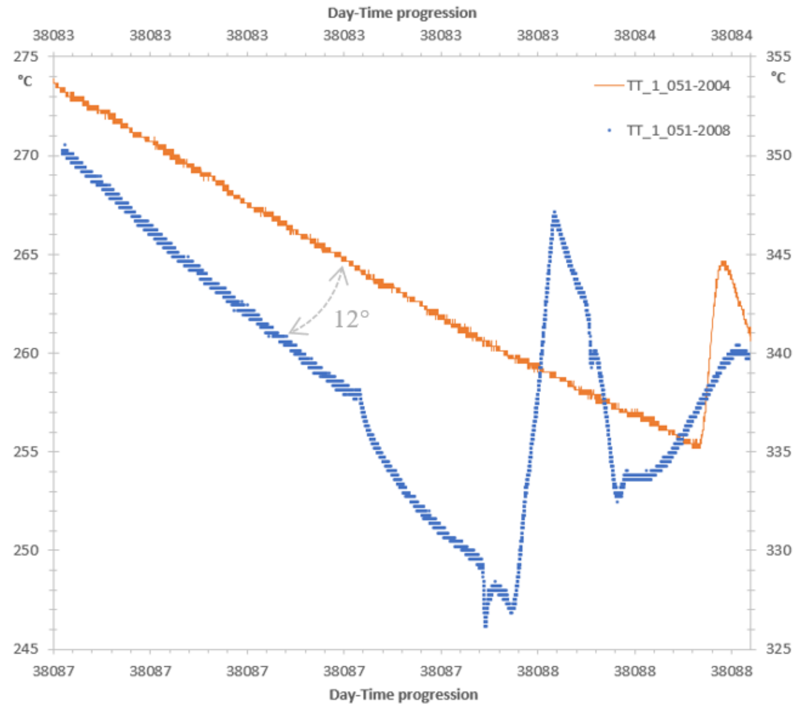

Fig. 3 Comparison between the same thermocouple in two different years, 2004 in orange and 2008 in blue. The curves have a tangential variation of 12°.

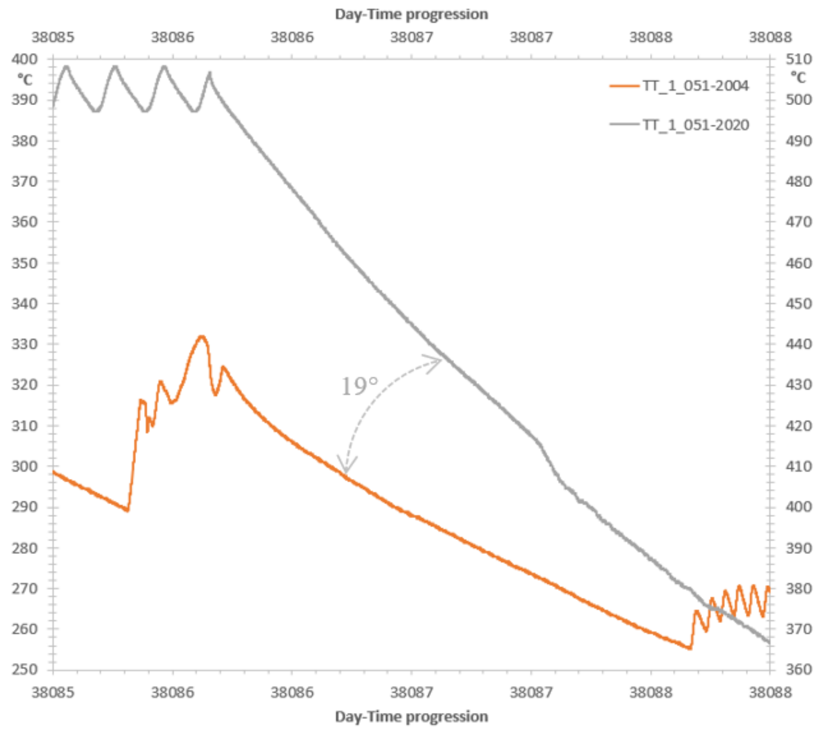

Fig. 4 Comparison between the same thermocouple in two different years, 2004 in orange and 2020 in grey. The curves have a tangential variation of 19°.

4. Simulation Set-up

In this paper, only the simulations that have an interest in terms of thermal losses and the verification of the hypotheses made in non-adiabatic conditions are taken into consideration. In particular, the aim was to verify a modelling of the tank with a set-up of parameters that are consistent with the experimental tests as well as to verify and control the heat loss areas. The same model has used for further insights that will be developed in subsequent papers.

The physical characteristics of the materials in use are indicated in Appendix B, which have been applied in the temperature range 260°C – 500°C. In accordance with the assumptions made in paragraph Method, the steel shell is not taken into consideration, nor is the external radiosity solver, to reduce the need for negligeable calculations.

The simulation area is 2,5*4,0 meters, divided into 4 shaped elements: external environment, molten salts, ullage, and insulation. The boundary conditions of the simulation area are set as Neumann condition, constant heat flux equal to 0°Cm^{-1}. In addition, a condition is set on the vertical plane to the screen to obtain a better performance of the diffusivity step of the Navier-Stockes equations. The focus is on speed, i.e., advection step in the governing equations, to verify the correspondence between the horizontal losses along the tank-wall and those vertical along the ullage as investigated.

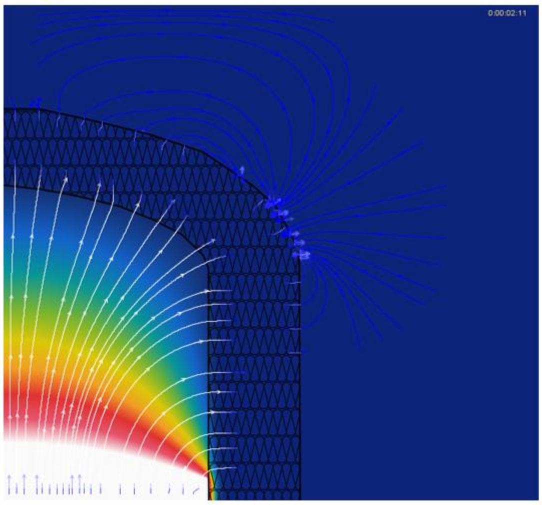

a

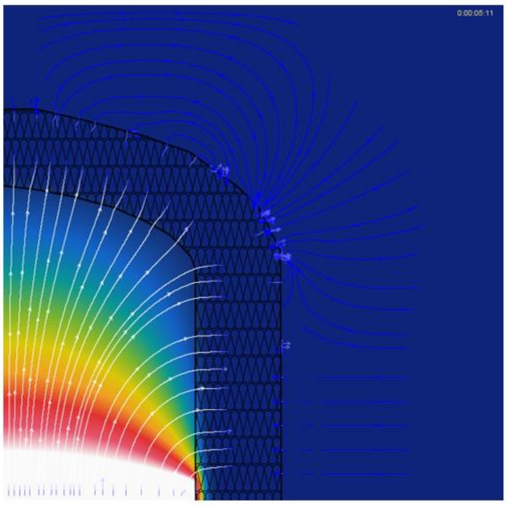

b

Fig. 5 Simulation in free stream convection conditions for outdoor temperatures and ullage dome.

Specifically, since the external temperature is much lower, it has been modelled as a shaped block around the tank with the physical parameters of the air at the average temperature of 12,5°C. This has made it possible to obtain a certain simplification of the calculation without losing results for the heat flux lines. In fact, Fig. 5 a and b show the heat flux lines in the case of free stream convection simulation of ullage side model, where the heat flux lines intersect at a distance similar to the tangents of the iso-heat flux lines in Fig. 6. This allows to consider negligible the body force such as gravity or buoyancy into Navier-Stockes equation **f**, in some circumstances, or indeed to take it as a negligible constant according to air parameter at outdoor temperature. As matter of fact, assumed that the reference Navier-Stock equation is,

$$\frac{\partial \mathrm{v}}{\partial \tau} = \alpha \nabla^2 \mathrm{v} - (\mathrm{v} \cdot \nabla)\mathrm{v} - \nabla p + f, \qquad \text{(eq.5)}$$

the Fig. 5 visualizes the outdoor air in free stream convection condition, dissimilar to Fig. 6 where the outdoor air is modelled as an element with an initial temperature of 12,5°C Fig. 5. The difference lies in the divergence of the part of the Navier-Stockes equations dependent on the advection step which can cause instability especially with increasing external wind speed. However, the set boundary conditions avoid that calculations blow up. Since the tank is placed in a totally sheltered area, this allows to observe no blow up simulation occurred with a very short time step length, but that the heat loss towards the dome of the ullage, Fig. 5a, occurs before the horizontal one of the tank wall, Fig. 5b. The heat flux lines are affected by the absence of diffusivity in the plane orthogonal to the screen of the 2D simulation to increase the advection component in the Navier-Stockes equations. Furthermore, the variation between the boundary conditions for Fig. 5 compared to Fig. 6 do not give significant variations in the output of the heat flux lines, with the exception of the Neumann boundary conditions of simulation area which enclose all the heat flux lines.

Consistent with the data analysed, the simulations Fig. 6 were performed in the aforementioned temperature range corresponding to a constant density, kinematic and dynamic viscosity of the two mediums, varying the properties of the air tank temperatures lower than approximately 226 °C that is, up to an external air temperature of 12,5°C according to measured value. The error for the constant molten salt density along the temperatures mentioned, such as reported in the simulations, has been measured equal to 1,1%.

The simulation of the natural decay of molten salt temperatures, Fig. 6, has a power source with a set-point from 300°C to 260°C. Setting a temperature coefficient of -0,5°C, i.e., it is in agreement to an increase in the decay rate equal to about three times that one actually occurred, considering a step length of 0,025 seconds in comparison to 0,0004°Cs^{-1} detected by experimental data for the reference year 2004.

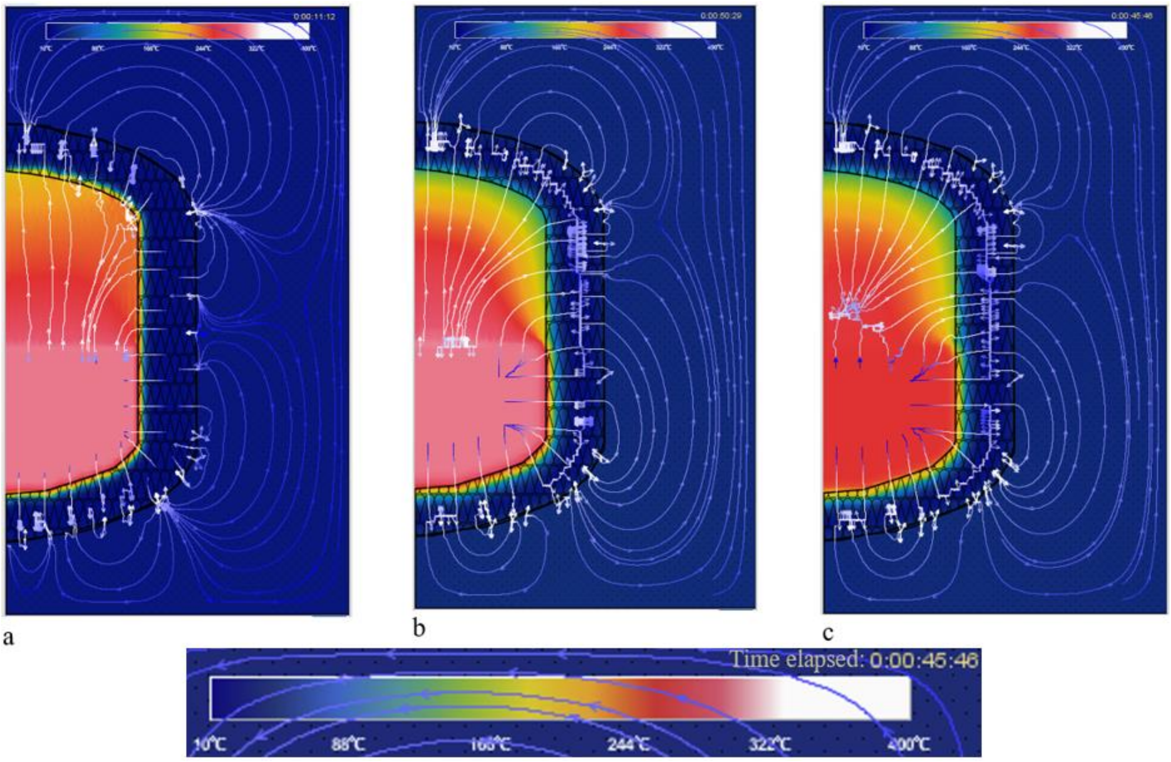

Fig. 6 Simulation in free stream condition inside the ullage with initial outdoor temperature of 12,5°C.

5. Conclusions and Outlook

The transient of temperature decay data could lead to a novel method to control operational and maintenance conditions or to improve the design. This paper has reinforced previous paper (Angelillo et al., 2021) of which is an essential part. Particularly, the heat losses via ullage are of fundamental importance for the analysis of temperature decay because air is lack of resilience capability and has a significantly lower specific heat in comparison to molten salt. Besides the ullage and molten salt volumes mutually influence temperatures and heat losses flow through the tank. To be precise, the ullage has presented a more suitable ability to be compared since the heat, close to the inner tank, becomes conductive without any other causes.

As matter of fact, the lumped-circuit abstraction and 2D visual simulations has been a support to investigate and evaluate key-parameters, such as superficial temperature which are crucial of calculating heat flow. Several simulations have been carried out to set up a reliable model to identify the key parameters with the aim of comparing variations of performance. While the physical parameters could be held constant throughout the lifespan, a temperature coefficient consistent with natural decay of temperatures can be crucial to identify the aging.

Accordingly, the geometry of tank has also been discussed in compliance of the lumped circuit, i.e., electrical capabilities of suited components. In addition to this, the velocity of heat loss from the ullage has been analysed related between convection, temperature, and immediate conduction towards the outer layer. As result, the recorded data of ullage, which depict the heat loss from the inner to the outer side of the tank according to boundary conditions in force, can be compared to evaluate in which size an insulation layer is still capable of performing correctly. To do so, the data over the years must be admissible and comparable. Admissible stands for to be inside a percentage of deviations it doesn't alter results. Comparable means to be defined as equivalent or that can be approximate confidently.

An outlook of lumped-circuit, i.e., the mention Modelica simulation and 2D energy simulation, the variation of the ullage-air in regard to increase or decrease the mass of salts with the heat flow in no-adiabatic conditions will be part of more comprehensive paper.

Finally, this novel study can be used to evaluate the condition in operation of a tank whichever a storage or prone to it, but also it could orient to introduce a new perspective in a project phase in terms of design and quantity of molten salt as storage.

Acknowledgement

We thank ENEA for the support of its scientific and technical staff provided during the accesses SURPF2001170003A and SURPF2201170005 to PCS facility. The access SURPF2001170003A was arranged in the frame of H2020 SFERA-III project activities – European Union's Horizon 2020 G.A. n. 823802 –.

References

A. Angelillo, W. Gaggioli, P. Di Ascenzi, Boundary conditions and Natural temperature decay from experimental data analysis to on-design of a tank for CSP plant – Part 1, ISES Conference Proceedings (2021) Solar World Congress

A.B. Zavoico, Solar power tower design basis document. Sandia National Laboratories. Report no. SAND2001-2100

F. Fabrizi, W. Gaggioli, L. Rinaldi, P. Tarquini, Applicazioni della tecnologia solare termodinamica sviluppata dall'ENEA in impianti di piccola taglia per la produzione di energia elettrica e termica in processi industriali e civili, ATI, 2006

K. Cornwell, The thermal conductivity of molten salts, Department of Mechanical Engineering, Edinburgh, 1970

Mehos, Mark, Hank Price, Robert Cable, David Kearney, Bruce Kelly, Gregory Kolb, and Frederick Morse, Concentrating Solar Power Best Practices Study, Golden, CO: National Renewable Energy Laboratory. NREL/TP-5500-75763, 2020

Miliozzi, G.M. Giannuzzi, P. Tarquini, A. La Barbera, Fluido termovettore: dati di base della miscela di nitrati di sodio e potassio, s.l. 2001 – Doc.ENEA/SOL/RS/2001/07

Scott M. Flueckiger, Suresh V. Garimella, Second-law analysis of molten-salt thermal energy storage in thermoclines, Solar Energy, 86 (2012): 1621-1631

T. L. Bergman, A. S. Lavine, Fundamentals of heat and mass transfer, Wiley, 8th edition 2017

W. Gaggioli, F. Fabrizi, L. Rinaldi, P. Di Ascenzi, Experimental tests about the cooling/freezing of the molten salts in the receiver tubes of a solar power plant with parabolic trough conditions, AIP Conference Proceedings 1850, (2017) 020005.

W. Gaggioli, P. Di Ascenzi, L. Rinaldi, P. Tarquini, F. Fabrizi, Effects assessment of 10 functioning years on the main components of the molten salt PCS experimental facility of ENEA, AIP Conference Proceedings 1734, (2016) 070009

Appendix A

Tab. 1 ENEA experimental data, received and analyzed, in accordance with the PCS operating conditions ongoing recorded on log-book between 2004 and 2022.

Prg.	Date in:	Prg.	Date in:	Prg.	Date in:
1	02.04.2004	14	20.05 to 22.05.2004	27	30.07 to 31.07.2005
2	05.04 to 08.04.2004	15	25.06 to 23.08.2004	28	23.09 to 26.09.2005
3	09.04 to 12.04.2004	16	24.08 to 27.08.2004	29	25.11 to 28.11.2005
4	13.04 to 16.04.2004	17	28.08 to 29.08.2004	30	28.02.2008
5	17.04 to 19.04.2004	18	30.08 to 31.08.2004	31	12.03.2008
6	20.04 to 21.04.2004	19	01.09 to 17.09.2004	32	01.04.2008
7	26.04 to 30.04.2004	20	14.01 to 18.01.2005	33	03.04 to 07.04.2008
8	01.05 to 02.05.2004	21	04.02.2005	34	03.04 to 07.04.2008
9	07.05.2004	22	10.02.2005	35	30.05 to 03.06.2008
10	14.05.2004	23	17.02 to 21.02.2005	36	09.07.2008
11	17.05.2004	24	06.04.2005	37	01.10.2008
12	18.05.2004	25	13.05.2005	38	17.10.2008
13	19.05.2004	26	15.07 to 19.07.2005	39	25.10.2008
40	31.10 to 04.11.2008	45	08.05 to 12.05.2012	50	05.09 to 06.09.2018
41	28.11 to 30.11.2008	46	09.06 to 25.06.2012	51	17.09 to 18.09.2018
42	01.12.2008	47	13.07.2012	52	17.10 to 25.10.2020
43	16.12.2008	48	08.12 to 12.12.2016	53	03.02 to 04.02.2021
44	22.11 to 28.11.2008	49	27.08 to 30.08.2018	54	20.07 to 15.09.2021

Appendix B

Tab. 2 Thermal-physical properties and constitutive correlation to the temperature

Material	Thermal physical property	Equation
Air, *air = ull*	Thermal conductivity, k_{air}	$k_{air} = 0{,}224 + (8{,}02)10^{-4}\,T - (3{,}28)10^{-7}\,T^2 [W\,m^{-1}\,°C^{-1}]$
	Density, ρ_{air}	$\rho_{air} = 2{,}8953 + 0{,}26733\,T + 132{,}45\,T^2 + 0{,}27341\,T^3 [K]\,[kg\,m^{-3}]$
	Specific heat, $c_{p,air}$	$c_{p,air} = 0{,}10 + (1{,}40)10^{-4}\,T + (1{,}01)10^{-7}\,T^2 - (5{,}69)\,10^{-11}\,T^3\,[J\,kg^{-1}°C^{-1}]$
	Viscosity, μ_{air}	$\mu_{air} = [0{,}1726 + (4{,}52)10^{-4}\,T - (1{,}937)10^{-7}\,T^2 + (4{,}185)10^{-11}\,T^3]\,10^{-4}\,[°C]\,[kg\,m^{-1}s^{-1}]$
Stone mineral wool, *iso*	Thermal conductivity, k_{iso}	$k_{iso} = 0{,}106\,[W\,m^{-1}\,K^{-1}]$

	Density, ρ_{iso}	$\rho_{iso} = 100[kg\ m^{-3}]$
	Specific heat, $c_{p,iso}$	$c_{p,iso} = 1030\ [J\ kg^{-1}K^{-1}]$
Molten salt, *ms*	Thermal conductivity, k_{ms}	$k_{ms} = 0{,}443 + 1{,}9 \times 10^{-4}\ T\ [W\ m^{-1}\ °C^{-1}]$
	Density, ρ_{ms}	$\rho_{ms} = 2090 - 0{,}636\ T[°C]\ [kg\ m^{-3}]$
	Specific heat, $c_{p,ms}$	$c_{p,ms} = 1443 - 0{,}172\ T\ [J\ kg^{-1}°C^{-1}]$
	Viscosity, μ_{ms}	$\mu_{ms} = [22{,}714 - 0{,}12\ T + 2{,}281 \times 10^{-4}\ T^2 - 1{,}474\ \times 10^{-7}\ T^3]\ \times 10^{-3}[°C]\ [kg\ m^{-1}s^{-1}]$
Steel, *stl*	Thermal conductivity, k_{stl}	$k_{ms} = 60\ [W\ m^{-1}\ K^{-1}]$
	Density, ρ_{ms}	$\rho_{stl} = 8000[kg\ m^{-3}]$
	Specific heat, $c_{p,stl}$	$c_{p,stl} = 480\ [J\ kg^{-1}K^{-1}]$
Aluminum, *alu*	Hemispherical emissivity	$\varepsilon = 0{,}1\ [-]$

Appendix C

Tab. 3 Acronyms

Acronyms	**Explicit**
ENEA	Energia Nucleare ed Energie Alternative = Nuclear Energy and Alternative Energy
O&M	Operating and Maintenance
PCS	(stazione di) Prova Collettori Solari = Solar Collector Test (station)
CSP	Concentration Solar Power
AC	Alternating Current
DCS	Distributed Control System

Controlled Static Environment Tests on Vacuum-Membrane Solar-Dish Facets for a Low-Cost Vacuum Control System

Duncan S. McGee[1] and Willem G. le Roux[1]

[1] Department of Mechanical and Aeronautical Engineering, University of Pretoria, Pretoria (South Africa)

Abstract

Small-scale vacuum-membrane facets for multi-faceted concentrated solar power (CSP) systems are investigated in this work. These facets are constructed from polymer-based reflective membranes adhered to the rim of cost-effective elliptical television antennas. Focal lengths on each facet can be varied by adjusting membrane depth. Previous studies have indicated that the membrane depth changes due to varying ambient conditions which affects the optical performance of the concentrator. The current work first focused on identifying the main cause of membrane movement using a controlled-environment experimental setup. Secondly, the work focused on how membrane movement could be reduced by utilizing a low-cost focus control system in outdoor experiments. The controlled-environment experimental setup underscored the significant influence of ambient temperature alterations on membrane movement compared to ambient pressure alterations. The outdoor experiment demonstrated substantial membrane movement; however, results showed that a low-cost constant differential pressure focus control system consisting of two 12 V diaphragm air pumps, two BMP280 barometric pressure sensors, and a microcontroller could reduce this movement to being within the targeted minimum limit of ±2 mm. It was found that periodic adjustments may be required to maintain long-term stability.

Keywords: Vacuum-membrane, CSP, Concentrator, Low-Cost, Focus Control System

1. Introduction

The University of Pretoria is actively working on the development of a small-scale concentrated solar power (CSP) system for the generation of electrical power and/or process heat (Roosendaal, et al., 2020; Swanepoel, et al., 2021). Such a system incorporates a multi-faceted solar dish concentrator that employs vacuum-membrane technology, as shown for example in Fig. 1(a). The facets constituting this innovative design are constructed from readily available and cost-effective elliptical television antennas. Over the rim of each facet, a reflective polymer-based membrane is stretched and affixed with adhesive (Roosendaal, et al., 2020). A crucial step involves creating a vacuum within each facet, a process that results in the formation of a near-parabolic shape of the membrane. What makes this system particularly versatile is its ability to accommodate variable focal lengths on each facet within the solar-dish array. This variability arises because the focal length is intrinsically linked to the membrane depth. For instance, investigations conducted by Swanepoel et al. (2020) demonstrated that altering the membrane depth from 25 mm to 5 mm can cause a substantial shift in focal length, ranging from about 2 m to 8 m.

From earlier outdoor experiments involving these facets, it became apparent that changes in the internal facet temperature, largely influenced by prevailing environmental conditions, had a pronounced impact on membrane depth (McGee, et al., 2021). Various interventions aimed at mitigating these depth fluctuations, such as filling the facets with helium or R-134a (refrigerant), or reducing the initial air volume, failed to yield a significant reduction in depth variation when compared to the original air-filled facets. However, promising results emerged from facets equipped with less-tightly pretensioned membranes, hinting at the potential to curtail overall membrane depth variations during typical operational days. Research conducted by Murphy (1987) has indicated that a thin membrane with a small modulus of elasticity and substantial pretension can approximate a nearly perfect parabolic shape. This holds true if vacuum-induced deformations do not push the

10.18086/swc.2023.03.08 Available at http://proceedings.ises.org

membrane beyond its yield point. In contrast, membranes lacking pretension tend to assume shapes closer to spheres rather than the preferred parabolic configuration, which is essential for efficient concentration of solar energy (Murphy & Tuan, 1987).

This ongoing work delves deeper into the vacuum-membrane facets integral to the multi-faceted solar dish concentrator. The objective is to systematically investigate the influence of static environmental conditions on membrane depth. This is achieved by manually manipulating the direct ambient temperature and pressure within a controlled-environment setup. The findings from this investigation promise to be invaluable in the development of an autonomous, cost-effective vacuum control system. Such a system will play a pivotal role in maintaining a consistent membrane depth during the operational phase of the CSP system, thereby enhancing its overall efficiency and performance.

2. Methodology

A controlled-environment enclosure was assembled using 30-mm-thick Medium Density Fibreboard (MDF). It included a removable 3-mm-thick acrylic hatch on the top to allow visibility, and this hatch was securely fastened before adjusting the internal pressure. To prevent movement due to pressure changes, an outer structure was added to reinforce the acrylic hatch, and sections of polystyrene were used for insulation on the inside. Beneath the enclosure, two 1/4-inch solenoid valves were in place, controlled by a microcontroller. These valves could either introduce high-pressure air into the enclosure to raise the internal pressure or enable a vacuum pump with a reservoir to extract air from the enclosure, reducing the internal pressure. Inside the enclosure, a heater with a built-in fan was installed, under the control of a Delta DTA4848 temperature controller. Additionally, a thermocouple was positioned in front of the fan to monitor temperature. At the centre of the enclosure, a vacuum-membrane solar dish facet was mounted. This facet comprised a polymer-based material with an aluminized reflective membrane adhered to the rim of a commercially available satellite television antenna. It was secured within a specially designed frame before closing the enclosure, with the membrane having an initial, evenly distributed pretension of 71 kg. Fig. 1 shows both the external (b) and internal (c) components of the experimental setup within the wind tunnel laboratory at the University of Pretoria, South Africa.

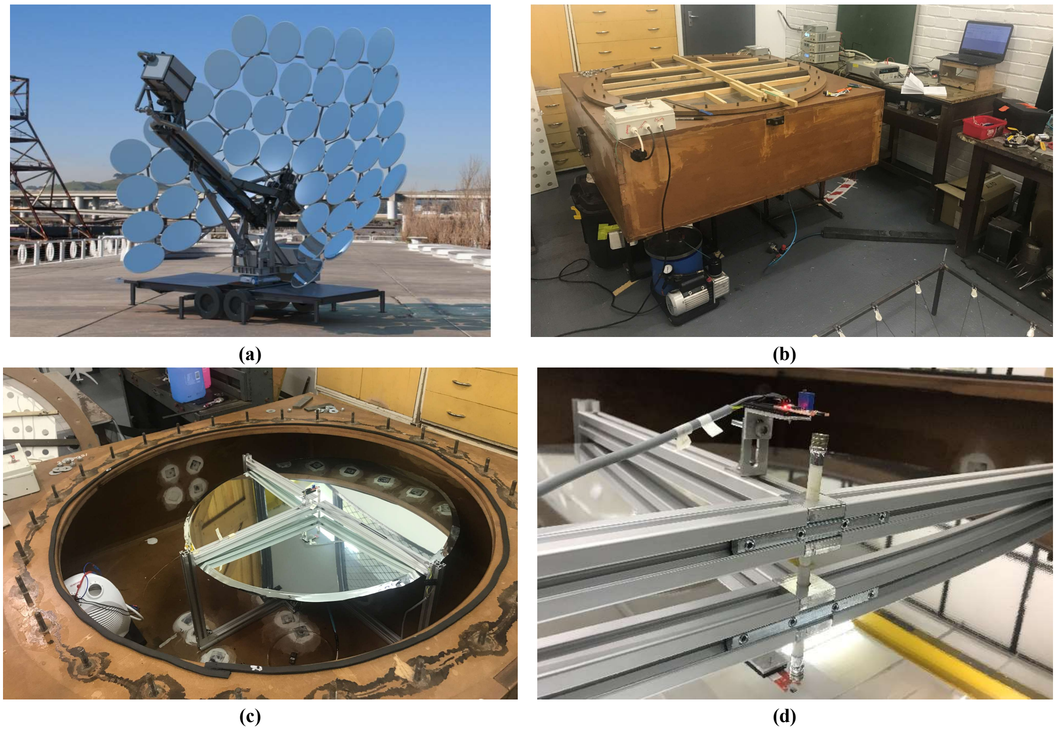

(a) (b) (c) (d)

Fig. 1: (a) Visualization of a CSP system under development, (b) the controlled-environment experimental setup, (c) the inside view of the setup, and (d) the Hall effect module mounted on the support frame at the exact centre of the reflective membrane.

The facet support frame was specifically designed to hold the dish on the factory bracket at the rear of the dish, ensuring that the facet did not make contact with any other part of the support frame. This setup replicated the mounting conditions during the actual operation of the concentrated solar power (CSP) system. The top part of the frame, which extended over the reflective membrane, was precisely aligned with the centre of the facet. At this intersection point, there was an aluminium guide that directed a plastic rod either upward or downward as the membrane expanded or contracted due to changes in the volume of the vacuumed cavity. Located at the opposite end of the plastic rod were three permanent magnets, directly positioned beneath a Hall effect module mounted on the top section of the support frame, as illustrated in Fig. 1(d). The Hall effect module measured the analog signal in volts of the magnetic strength. When the magnets were near the Hall effect sensor, the maximum voltage reading obtained was 4.3 V. As the magnets moved farther away from the sensor due to membrane contraction, the voltage reading decreased. To ensure accuracy, the Hall effect module underwent calibration using a milling machine and Digital Readout (DRO) at 0.5 mm increments, ranging from 0 mm to 25 mm. This calibration resulted in a function that correlated voltage readings to membrane depth in millimetres. To assess measurement repeatability, random voltage readings were recorded at different depths and compared with the original voltage readings, confirming an acceptable repeatability within ±0.0001 V.

In addition to monitoring the facet itself, ambient conditions outside the controlled enclosure were closely observed to understand how the direct ambient conditions of the facet inside the enclosure were altered. This involved measuring ambient temperature using a Type-T thermocouple connected to a data acquisition device (DAQ), as well as monitoring ambient pressure with a BMP280 barometric pressure module linked to an Arduino Uno microcontroller. The differential pressure between the ambient environment and the interior of the enclosure was gauged using an Omega PX277 differential pressure transducer connected to the DAQ. To determine the facet's actual ambient conditions, the differential pressure transducer reading was either added to or subtracted from the barometric sensor reading, depending on whether the enclosure was pressurized or depressurized.

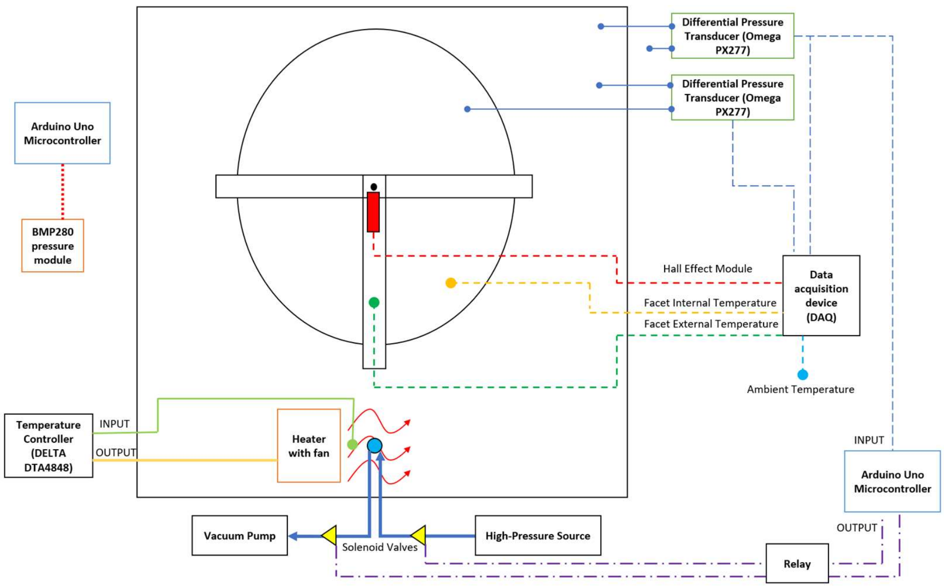

Fig. 2: Schematic of the controlled-environment enclosure experimental setup.

As shown in the schematic shown in Fig. 2, various measurements were taken inside the enclosure and inside the facet. A Type-T thermocouple was positioned on top of the facet support frame as close to the centre of the enclosure as possible. Additionally, the temperature within the facet itself was measured using another Type-T thermocouple, which featured a removable coupling located at the bottom of the facet. To determine the internal pressure of the facet, the differential pressure between its interior and the enclosure was measured with an Omega PX277 differential pressure transducer. All the instrumentation used to measure the facet and enclosure conditions was connected to the DAQ.

2.1 Ambient pressure alteration experiment

Three specific tests were conducted on the facet while it was inside the enclosure, with an initial membrane depth of approximately 10 mm. These tests involved altering the direct ambient pressure on the facet, either decreasing or increasing it and adjusting the direct ambient temperature. For the pressure experiments, the enclosure's hatch was securely bolted shut to ensure an airtight seal. The test commenced with a 20-second period of inactivity until the microcontroller activated a relay module, which in turn opened a solenoid valve connecting the enclosure to either the vacuum pump's reservoir or a high-pressure source. This action resulted in either decreasing or increasing the gauge pressure within the enclosure. The pressure was adjusted until the differential pressure transducer between the enclosure's internal and external environments registered approximately -500 Pa (gauge) or 500 Pa (gauge). At this point, the microcontroller maintained a constant pressure for 20 seconds by manipulating the solenoid valves associated with the vacuum pump or high-pressure source, depending on the necessary adjustment to stabilize the enclosure's pressure. After this 20-second interval, the microcontroller opened only the relevant solenoid valve to either pressurize or depressurize the enclosure back to its initial internal pressure.

2.2 Ambient temperature alteration experiment

For the temperature alteration experiment, the enclosure's hatch was placed on top without being bolted shut to ensure ventilation. This approach was adopted because initial tests had shown that sealing the enclosure tightly led to a drastic increase in internal pressure as the temperature rose, causing leaks and making it impossible to maintain the intended constant pressure. Nevertheless, the ventilation approach still yielded valuable results. The test began with a 5-minute period of inactivity, after which the temperature controller was activated. It initiated the operation of the heater and fan inside the enclosure. The heater (excluding the fan) was cycled on and off repeatedly for 25 minutes until the facet's direct ambient temperature reached approximately 318 K. This control strategy was implemented to prevent excessive heating, particularly on one side of the enclosure where the temperature controller's thermocouple was positioned directly in front of the fan. After the 25-minute period, the heater and fan were switched off, and the test continued to monitor conditions until the temperature returned to a constant room temperature.

2.3 Outdoor experiment

Upon studying the effects of altering static ambient conditions on membrane movement, it was suggested that maintaining a constant differential pressure might eliminate membrane movement throughout an operational day as tested by Schertz, et al. (1991). An outdoor experiment was first conducted without any focus control system to determine how the membrane would move throughout an operating day. Consequently, an outdoor experiment featuring a low-cost focus control system was also conducted on the roof of the Engineering 2 Building at the University of Pretoria, South Africa. Notably, the facet remained stationary on the roof and did not maintain a consistent angle relative to the sun, as would be the case in a CSP system (see Fig. 3).

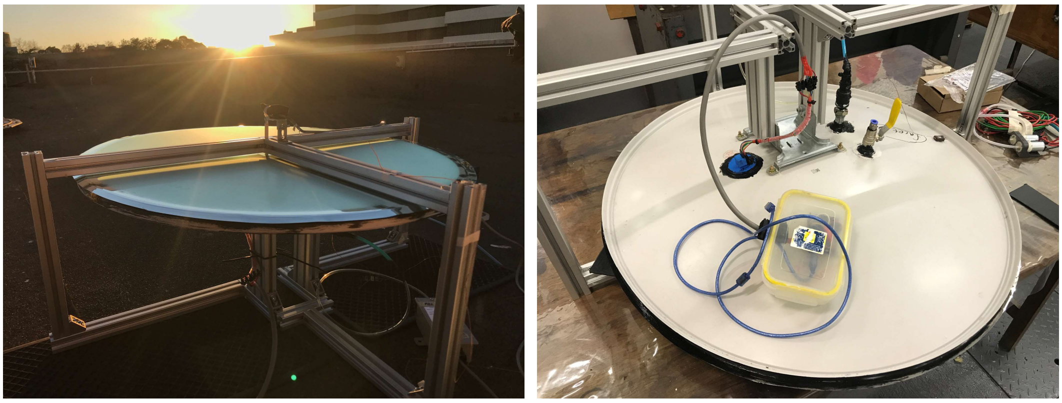

(a) **(b)**

Fig. 3: (a) Outdoor experimental setup and (b) the bottom of the facet with the focus control system components.

To maintain the differential pressure, a low-cost focus control system was employed. This controller utilized cost-effective components, including an Arduino Uno microcontroller, two BMP280 barometric pressure modules for input, and a relay module to manage two 12 V diaphragm air pumps, with one serving as a vacuum pump. Fig. 4 provides a schematic of the focus control system used to maintain the differential pressure while simultaneously monitoring internal and ambient conditions with the DAQ setup mentioned previously. The total cost of this focus control system at the time of the study was 29.34 USD. In a multi-faceted system, where one microcontroller could control multiple facets, costs could be further reduced.

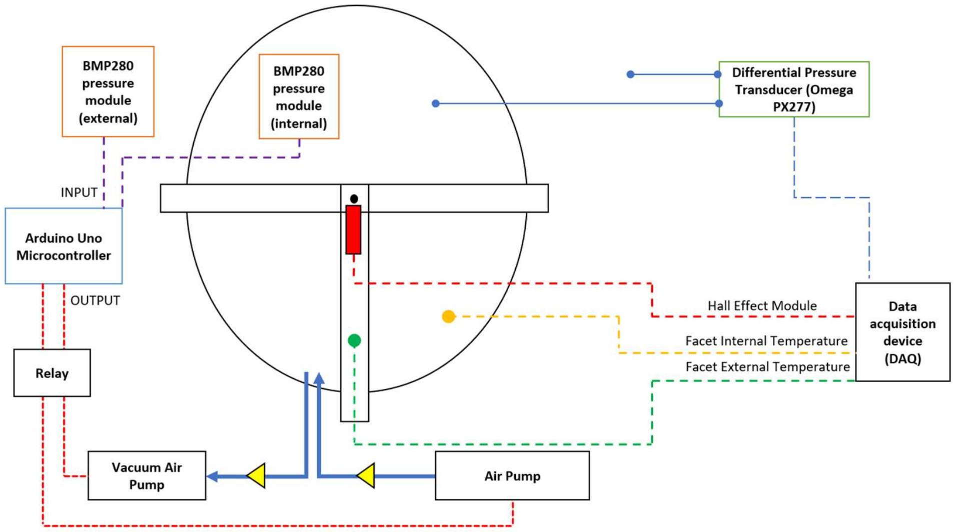

Fig. 4: The schematic of the outdoor experimental setup.

3. Results and discussion

3.1 Ambient pressure alteration experiment

Fig. 5 illustrates the complete test process in which the facet's direct ambient pressure decreased by about 500 Pa. The test exhibited a consistent linear decrease in the direct ambient pressure of the facet, indicating that neither the enclosure nor the top hatch deformed as the pressure changed. The membrane depth also followed a linear pattern, decreasing by approximately 0.8 mm until the facet's direct ambient pressure reached approximately -500 Pa (gauge). This pressure was then maintained as closely as possible for 20 seconds before being returned to its initial level. These isolated linear relationships are further presented in Fig. 6. During the test, it was observed that the facet's direct ambient temperature slightly decreased as the pressure decreased. This observation aligns with the principles of the ideal gas law theory. Additionally, the internal pressure of the facet experienced a slight increase during the period when the direct ambient pressure decreased. This phenomenon can be attributed to the reduction in air particles within the enclosure, exerting less force on the exterior surface of the membrane. Consequently, the remaining air particles inside the facet pushed the membrane slightly upward due to the diminished external force. This effect can be analogously compared to an inflated helium balloon ascending higher in the atmosphere, causing the balloon to expand as atmospheric pressure decreases.

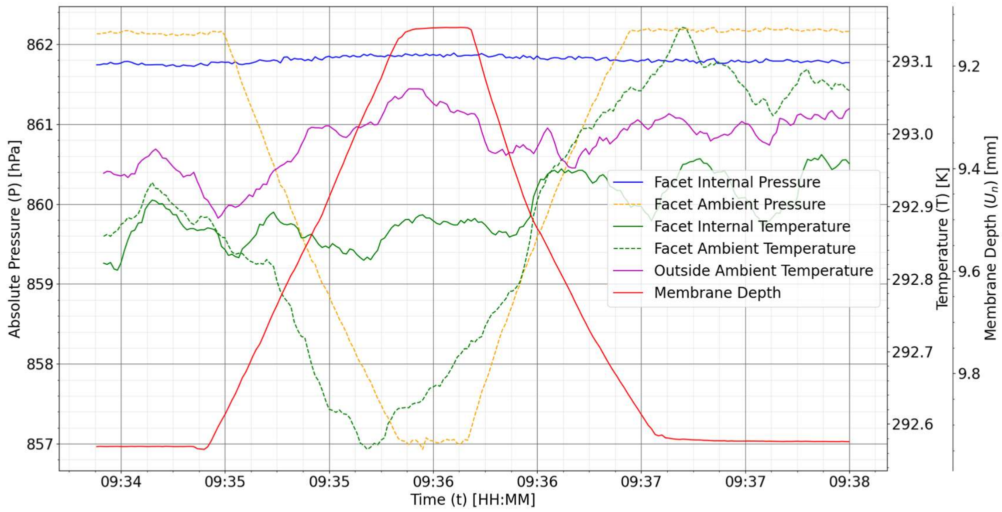

Fig. 5: Decrease in ambient pressure test (4th of June, 2023).

For the isolated pressure decrease and increase periods of the test, it was observed that the membrane depth deviated slightly from its initial position. This variation occurred because the change in direct facet ambient pressure had an impact on both the internal and direct ambient temperature of the facet, thereby influencing the final membrane depth. Nevertheless, this difference was minimal, and a clear linear relationship remained evident. A linear correlation of 0.14 mm/hPa was established between the membrane depth and the ambient pressure of the facet, as illustrated in Fig. 6. This implies that, with minimal temperature changes factored in, the membrane depth will decrease by approximately 0.14 mm for every 1 hPa decrease in ambient pressure.

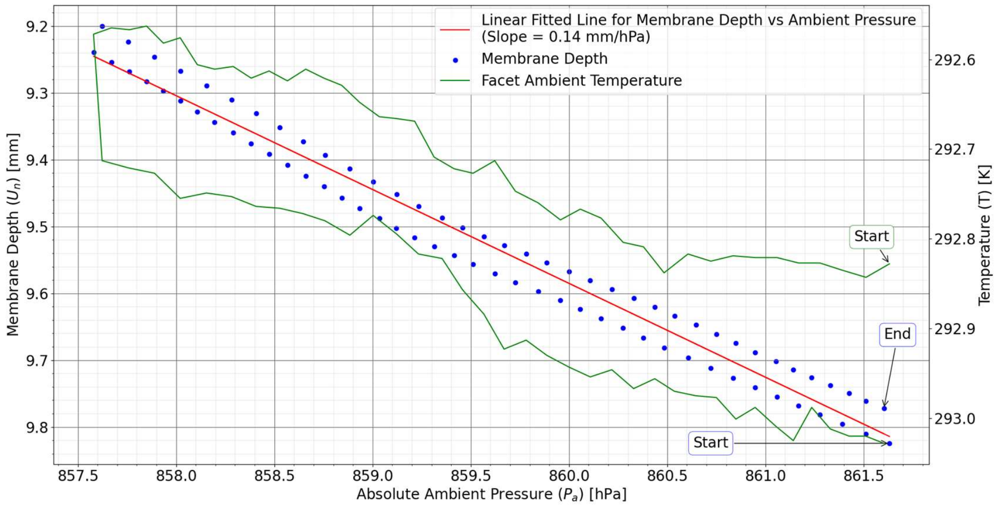

Fig. 6: Membrane depth and internal temperature versus the decreased ambient pressure (4th of June, 2023).

Fig. 7 presents the entire test process in which the facet's direct ambient pressure increased by 500 Pa. The test initially displayed a linear rise in the facet's direct ambient pressure, which later shifted to an exponential increase. This change suggested a slight deformation of the top hatch, although it was not a significant issue as the membrane depth also began to change exponentially during this phase. The membrane depth shifted by a total of approximately 0.7 mm downward until the facet's direct ambient pressure reached approximately 500 Pa (gauge). The pressure was then maintained as consistently as possible for 20 seconds, during which the membrane depth remained constant. Subsequently, the pressure was decreased back to its initial level, exhibiting a linear decrease in pressure and membrane depth. These isolated linear relationships are further presented in Fig. 8. It's noteworthy that the internal pressure of the facet experienced a slight decrease during the period when the direct ambient pressure was increased. This reduction in internal pressure can be attributed to the increase in air particles within the enclosure, which exerted a greater force on the exterior surface of the membrane.

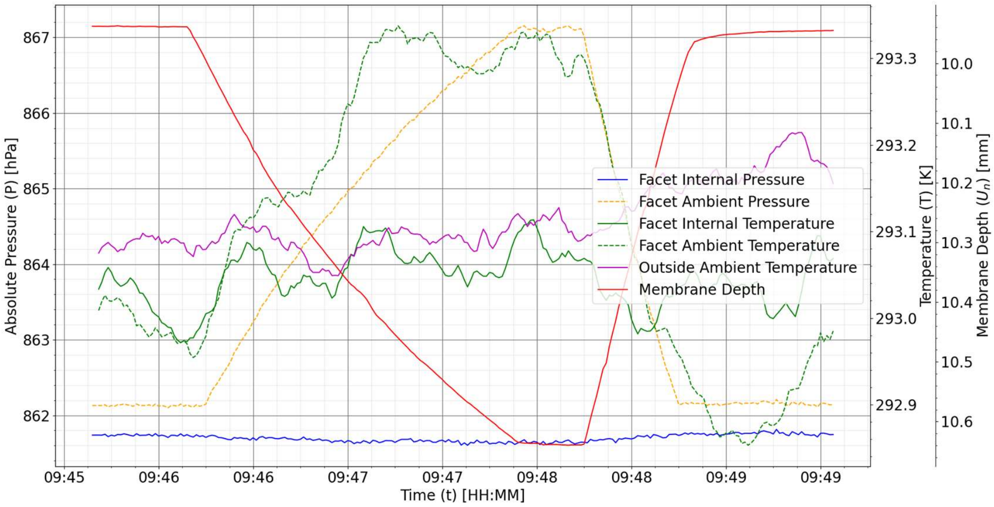

Fig. 7: Increase in ambient pressure test (4th of June, 2023).

For the isolated pressure increase and decrease periods of the test, it was also noted that the membrane depth was slightly off from where it started since the change in direct facet ambient pressure altered the internal and direct ambient temperature of the facet which affected the final membrane depth. However, the difference is minimal, and a clear linear relation is still notable. A linear relation of 0.125 mm/hPa was determined between the membrane depth and ambient pressure of the facet, as shown in Fig. 8. This means that the membrane depth would increase by approximately 0.125 mm if the ambient pressure increased by 1 hPa (with minimal temperature alterations). From this, it is evident that the effect of decreasing or increasing ambient pressure is almost similar since the difference is only about 0.015 mm/hPa (0.075 mm difference over a pressure alteration of 500 Pa). This difference can be due to measuring errors, linear regression errors, or due to the slight differences in temperatures during the two tests.

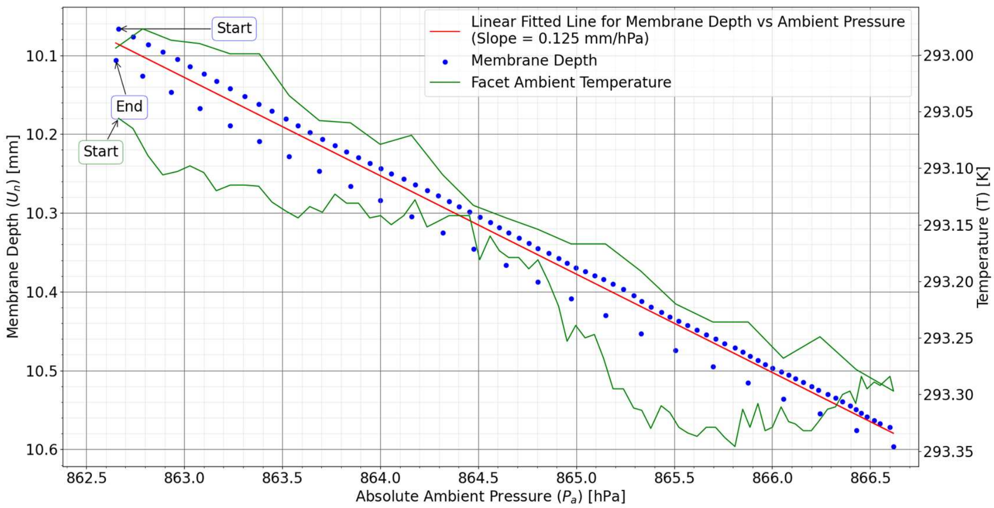

Fig. 8: Membrane depth and internal temperature versus the increased ambient pressure (4th of June, 2023).

3.2 Ambient temperature alteration experiment

Fig. 9 provides an overview of the complete temperature test conducted on the facet. The initial conditions remained constant for the first 5 minutes of the test until the heater and fan were activated. The facet's direct ambient temperature promptly rose to around 318 K, after which only the heater was periodically cycled on and off by the temperature controller, allowing the temperature to oscillate around 317 K. This resulted in the heater toggling frequently for 25 minutes, as depicted in the figure, reflecting temperature fluctuations. These fluctuations, primarily attributed to the heater, were also mirrored in the membrane's movement, indicating that temperature significantly impacts membrane motion. Upon turning on the heater, the facet's direct ambient pressure instantly increased and then gradually decreased throughout the test. During this phase, the membrane depth decreased by approximately 3.4 mm until the internal facet temperature reached 310 K. Both the internal facet temperature and membrane depth exhibited exponential growth with slight fluctuations attributed to the heater. Subsequently, the heater and fan were switched off for the cooling phase of the test, leading to rapid decreases in the facet's direct ambient temperature and pressure, facilitated by the enclosure's ventilation during the test. During the initial minutes of the cooling period, the membrane depth increased rapidly as the conditions surrounding and inside the facet reverted to their initial state.

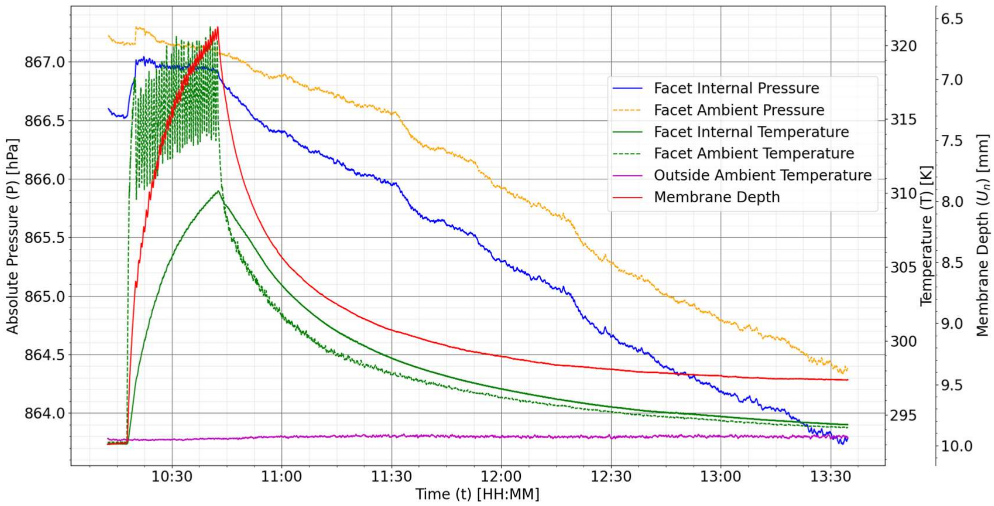

Fig. 9: Increase and decrease in ambient temperature test (11th of June, 2023).

During the heating period of the test, the facet's direct ambient pressure exhibited minor fluctuations within a range of 0.3 hPa, as depicted in Fig. 10. Subsequently, during the cooling period, the direct ambient pressure decreased by approximately 2.7 hPa. This indicates that ambient pressure had a minimal impact on the movement of the membrane depth during this test, contributing only -0.3375 mm to the depth, as per the findings from the earlier ambient pressure tests. The results in Fig. 10 also clearly reveal the influence of the heater cycling on and off, particularly around 317 K. Notably, there is a linear relationship between membrane depth and ambient temperature during the cooling period, spanning from 310 K to 294 K. To enhance clarity, this linear trend is isolated later in Fig. 12 for a detailed view.

Fig. 11 illustrates the behaviour of the facet's internal pressure as it increased exponentially once the internal temperature began to rise. Subsequently, as the heater's fluctuations commenced, the internal pressure exhibited a linear increase until it reached its peak at 310 K. This data showed less fluctuation compared to earlier results because the air inside the facet was not in direct contact with the heater's effects. At the start of the heating period, the membrane depth underwent an exponential decrease until it reached a depth of 8.7 mm. Following this, the depth displayed a linear fluctuation trend until reaching its minimum depth of 6.6 mm. As the ambient temperature decreased during the cooling period, the membrane depth initially increased exponentially until reaching 8.1 mm, after which it followed a linear upward trend until the end of the test. These trends suggest that the exponential patterns are indicative of transient-state heat transfer conditions between the facet and the ambient environment, while the linear trends represent steady-state heat transfer conditions. During real operation, the facet is likely to experience steady-state heat transfer since changes in ambient conditions are not as sudden as the rapid on or off switching of the heater.

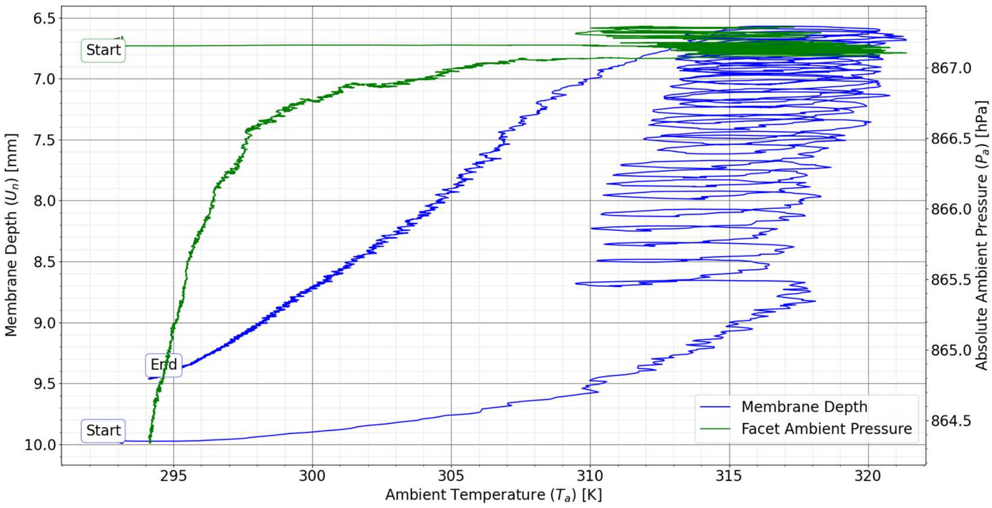

Fig. 10: Membrane depth and ambient pressure versus the ambient temperature (11th of June, 2023).

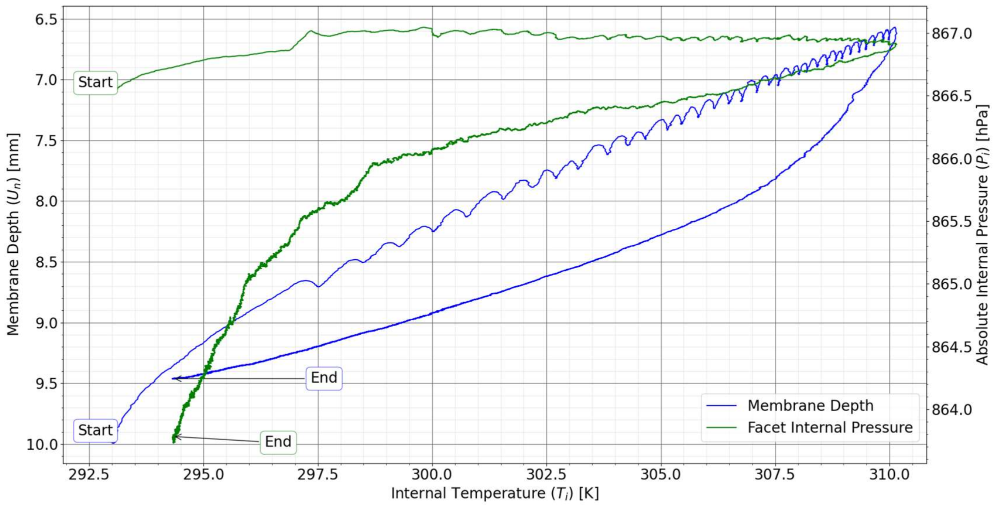

Fig. 11: Membrane depth and internal pressure versus the internal temperature (11th of June, 2023).

Fig. 12 presents the isolated steady-state heat transfer data observed during the temperature test of the facet. During the heating period of the test, a linear relationship was established, indicating that the membrane depth and internal temperature were related at a rate of 0.159 mm/K. Conversely, during the cooling period, another linear relationship was identified, with the membrane depth and internal temperature having a rate of 0.102 mm/K. Additionally, during the cooling period, a linear relationship emerged between the membrane depth and ambient temperature, indicating a rate of 0.133 mm/K. This implies that the membrane depth will increase by approximately 0.133 mm for every 1 K decrease in ambient temperature, assuming minimal pressure alterations.

Based on the findings presented in this section, it is evident that ambient temperature has a more significant influence on membrane movement compared to ambient pressure during an operational day. In the context of a winter's day in Pretoria, South Africa, where ambient conditions can be expected to change by approximately 3 hPa in terms of pressure and about 15 K in terms of temperature, the effect on membrane depth can be estimated. Specifically, the membrane depth is projected to change by approximately 0.398 mm due to variations in ambient pressure and approximately 1.995 mm due to changes in ambient temperature, assuming no dynamic effects from radiation and convection are considered. These estimates underscore the substantial impact of temperature fluctuations on membrane movement in comparison to changes in ambient pressure.

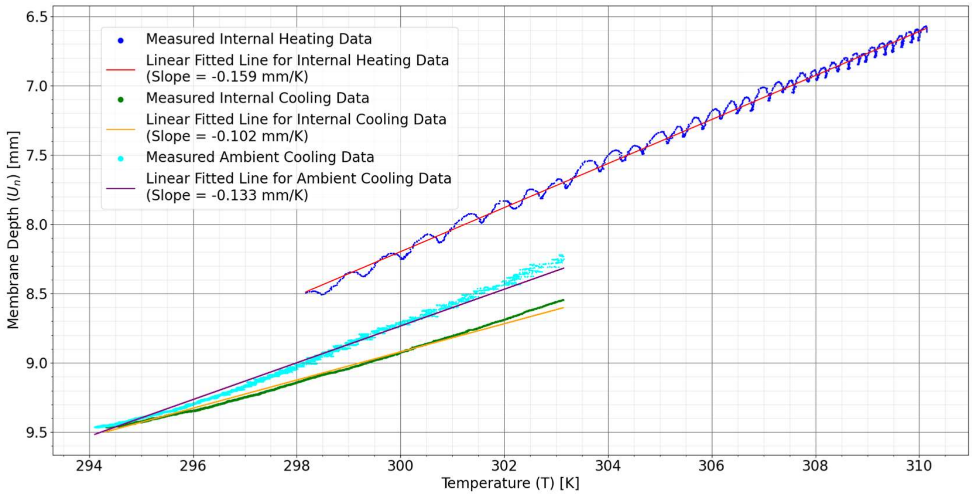

Fig. 12: Isolated linear trends of the membrane depth versus temperature (11th of June, 2023).

3.3 Outdoor experiment.

The outdoor test results, conducted without a focus control system, clearly indicate significant membrane movement, with a maximum depth reduction of 4 mm during an operational day, as demonstrated in Fig. 13. At the shallowest depth of 6 mm, the ambient pressure decreased by about 1.3 hPa and the ambient temperature increased by about 17.5 K. From the controlled-environment enclosure test, the membrane depth decreased by about 2.5 mm due to static ambient conditions, indicating that the remaining 1.5 mm is possibly due to the dynamic ambient conditions. The internal and ambient temperatures closely mirrored each other throughout the day, suggesting the presence of steady-state heat transfer conditions, consistent with the controlled-environment experimental results. It's worth noting that the internal facet temperature had a significant impact on membrane movement, as evidenced by the close resemblance between the profiles (red and green lines), aligning with the findings from the controlled-environment tests.

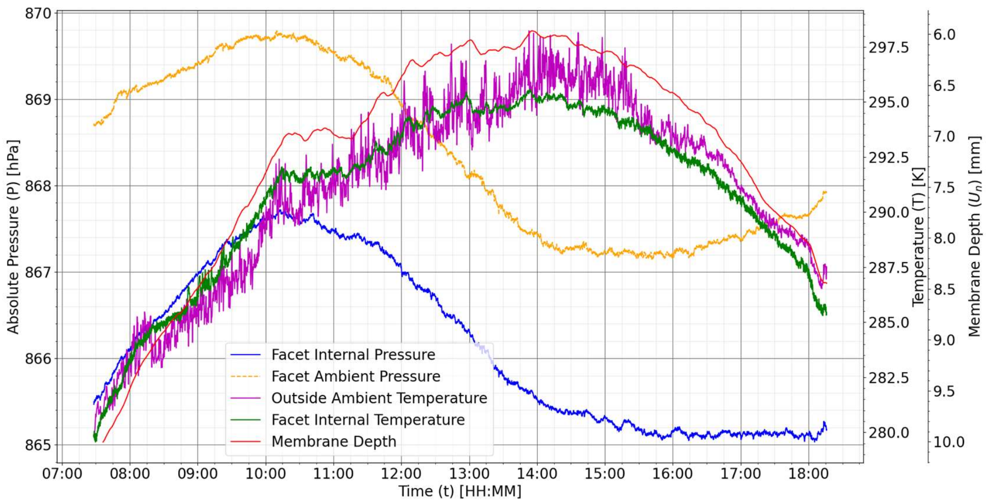

Fig. 13: Outdoor experiment results without a focus control system (1st of July, 2023).

A linear relationship was found between membrane depth and internal temperature, with a relation of 0.277 mm/K (see Fig. 14). This linear trend persisted even as the temperature decreased after reaching its peak at around 295 K. Comparing this result to the controlled-environment test (0.159 mm/K), it's evident that the outdoor relation is 74% higher. This difference is likely due to the influence of radiation and convection effects which are present outdoors, factors which were not considered in the controlled-environment tests. This suggests that static ambient conditions contributed to about 57% of the internal conditions, with the remaining 43% influenced by dynamic effects like radiation and convection.

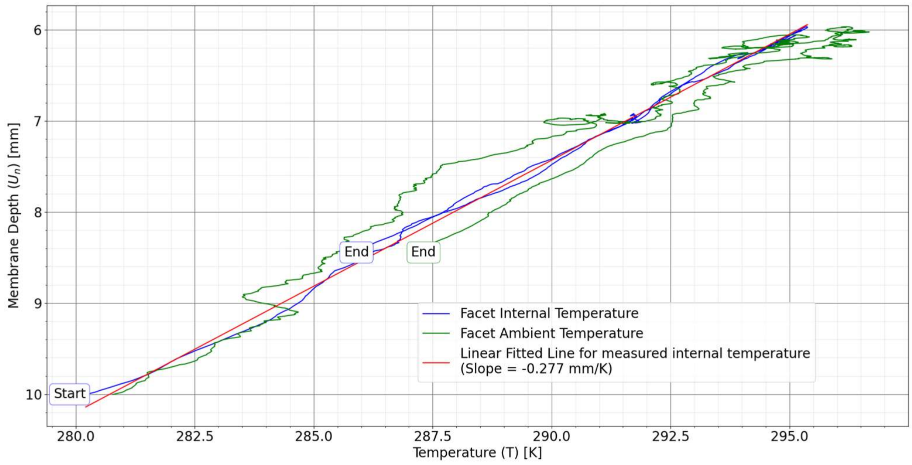

Fig. 14: Membrane depth versus temperature during the outdoor experiment without a focus control system (1st of July, 2023).

In the outdoor test of the controlled facet, which maintained a constant differential pressure utilizing the low-cost focus control system, the membrane movement exhibited a notable reduction compared to the uncontrolled facet throughout an operating day, as illustrated in Fig. 15. The test began with a membrane depth of approximately 11.1 mm at 06:40 and reached a peak value of 12.7 mm around 09:00. Subsequently, the membrane depth gradually decreased to a minimum of 9.6 mm at 18:00. This indicates that the membrane depth experienced increases and decreases of about 1.6 mm and 1.5 mm, respectively. These variations fall within the 2 mm accuracy threshold required for achieving a targeted minimum intercept factor of 90%, as determined by Roosendaal et al. (2021). It's worth noting that Roosendaal et al. emphasized the sensitivity of the intercept factor to negative adjustments, making the observed 1.5 mm change just within the specified limit.

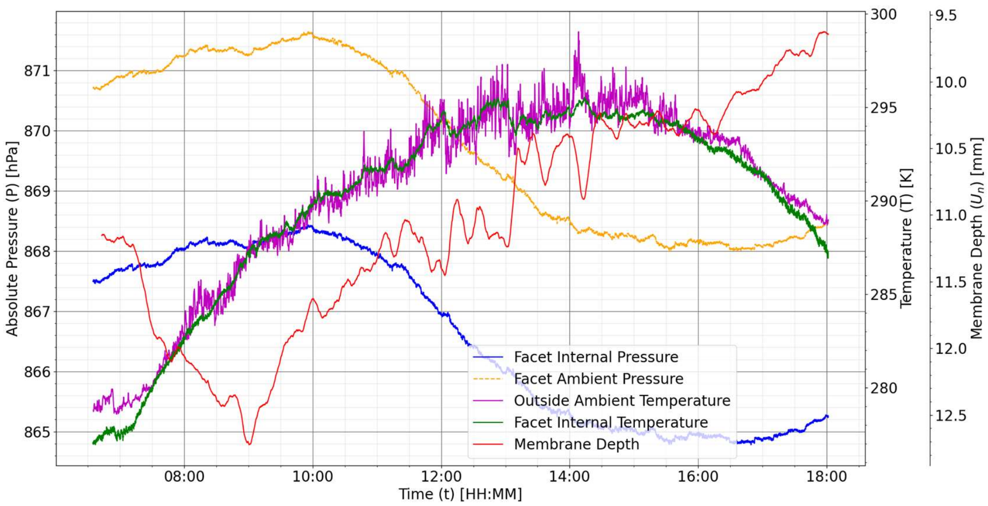

Fig. 15: Outdoor experiment results with constant differential pressure focus control system (3rd of July, 2023).

Maintaining a constant differential pressure for the facet doesn't guarantee long-term operation on a CSP system without adjustments. As seasons change, ambient pressure fluctuates, necessitating periodic control system resets, potentially at the start of each season or even weekly, depending on extended tests. The membrane depth should ideally remain constant when differential pressure is constant. However, the membrane material's stiffness, affected by temperature changes, complicates this ideal scenario. Polymer-based membranes stiffen at lower temperatures and soften at higher ones. This means that relying solely on differential pressure control may not be effective for polymer-based reflective membranes, unlike metal-based membranes like the SKI facet (1991), which are less sensitive to temperature changes.

4. Conclusion and recommendations

In conclusion, this research reveals the relationship between ambient conditions and membrane movement in solar concentrating systems. Controlled ambient pressure experiments demonstrated linear connections between pressure changes and membrane depth, with decreasing and increasing pressure affecting the membrane similarly. However, controlled ambient temperature experiments revealed a more substantial influence on membrane behaviour. Temperature fluctuations had a pronounced impact on membrane movement, with both heating and cooling periods showing linear relationships between temperature changes and membrane depth. Comparing the effects of ambient pressure and temperature, it became clear that temperature fluctuations had a more significant impact during an operational day. Outdoor experiments without a focus control system showcased substantial membrane movement during the day, with significant temperature-dependent effects. In contrast, outdoor tests with a constant differential pressure focus control system exhibited reduced membrane movement, but maintaining constant pressure alone is insufficient for long-term stability. Periodic control system adjustments may be necessary due to seasonal changes, especially for polymer-based reflective membranes, which are sensitive to temperature variations.

Further exploration of the constant differential pressure focus control system is advisable, with a focus on integrating temperature-related effects on membrane stiffness. This can potentially lead to a more significant reduction in overall membrane movement. Additionally, it is recommended to explore an alternative focus control system that continuously monitors membrane depth. This approach would mitigate challenges arising from dynamic pressure effects caused by wind and temperature-induced material stiffness variations. Furthermore, investigating various vacuum-membrane construction methods, including considerations such as pretension, membrane thickness, and facet size, may help further minimize membrane movement.

5. Acknowledgements

The authors express their gratitude to the Renewable Energy Hub and Spokes Program of the Department of Science and Innovation (DSI) for financial support through the UP Solar Thermal Spoke.

6. References

McGee, D.S., Roosendaal, W. & Le Roux, W.G., 2021. Environmental Investigation of Vacuum-Membrane Solar-Dish Facets. (Online), 27th SolarPACES Conference. 27 September – 1 October.

Murphy, L.M., 1987. Moderate Axisymmetric Deformations of Optical Membrane Surfaces. Journal of Solar Energy Engineering, 109(2), pp. 111-120. https://doi.org/10.1115/1.3268187

Murphy, L.M. & Tuan, C., 1987. The formation of optical membrane reflector surfaces using uniform pressure loading (Report: SERI/TR-253-3025), Golden: Solar Energy Research Institute.

Roosendaal, C., Swanepoel, J.K. & Le Roux, W.G., 2020. Performance analysis of a novel solar concentrator using lunar flux mapping techniques. Solar Energy, Volume 206, pp. 200-215. https://doi.org/10.1016/j.solener.2020.05.050

Roosendaal, C., Swanepoel, J.K. & Le Roux, W.G., 2021. Optical modelling of a vacuum-membrane solar dish based on elliptical television antenna. Southern African Sustainable Energy Conference, Stellenbosch, 17–19 November.

Schertz, P.T., E., P., Brown, D.C. & Konnerth III, A., 1991. Facet Development for a Faceted Stretched-Membrane Dish by Solar Kinetics Inc. (Report: SAND91-7009), Albuquerque: Sandia National Laboratories.

Swanepoel, J.K., Le Roux, W.G., Lexmond, A.S. & Meyer, J.P., 2021. Helically coiled solar cavity receiver for micro-scale direct. Applied Thermal Engineering, Volume 185, p. 116427. https://doi.org/10.1016/j.applthermaleng.2020.116427

Swanepoel, J.K., Roosendaal, C. & Le Roux, W.G., 2020. Photogrammetry Analysis of a Vacuum-Membrane Solar Dish Using Elliptical Television Antennas, (Online) 26th SolarPACES Conference, 28 September–2 October. https://doi.org/10.1063/5.0087025

Development of the investigation of solar updraft tower in the city of Erbil to the north of Iraq

Soorkeu A. Atrooshi
University of Kurdistan, Erbil (Iraq)
soorkeu@gmail.com

Abstract

This work is the result of more than ten years of research in solar tower power plant that has led to five international publications in this field. The investigation started with the work on developing a relation between the size of the components, so that when the system is designed, a more feasible outcome can be achieved. In the next stage the collector area limitations were studied and for that purpose the capacity of the collector was reduced to one third and the sides were sealed in a rig that was built for this purpose. The loss of thermal volume due to a smaller collector was compensated in the next stage by introducing thermal concentration with the help of a sun tracking mirror that reflected the solar thermal radiation on the tower base. The work was partially hindered when the School Administration decided to destroy the rig. Fortunately, sufficient data was collected to finish this stage. In the next stage a simulation model was developed to look into the ability of such a device to adapt to alpine terrain which is an attribute of local landscape. The model was verified and used to run a parametric study. The system performance was compatible but lower than the conventional flat configuration. In the final stage a turbine was designed for the system using a different airfoil profile. The model was verified but could not be integrated into the simulation for the whole system. The misgivings of the reverse fan model were outlined when compared to the turbine. The reverse fan model was assembled into the developed sloped collector solar tower model and used to investigate the performance of the overall system. The system was functional with reduced capacity.

Keywords: Solar, Updraft tower, geometry, thermal concentration, sloped collector, turbine

1. Introduction

Historically, Iraq has been largely dependent on fossil fuel for meeting its energy needs. The move towards renewable energy has started but it is caught at a slow pace on a lengthy freeway. Until now hydropower has been the only significant contributor however its role has been affected by the annual precipitation, irrigation, drinking and industrial demands, imposed on dams and reservoirs (Our World in Data, 2022).

An enduring energy source of high potential in the region with extensive effectiveness duration, scoring a minimum of 8 hours at 8 degrees elevation in December and substantial intensity, exceeding 8.5 kWhr/m^2/day in June, is solar energy, Fig (1), (NASA, 2023) and (University of Oregon, 2023). Eight degrees elevation corresponds to 08:00 hrs, marking 49 minutes after sunrise and 16:00 hrs, indicating 53 minutes before sunset, on December 21st which is the shortest day of the year for latitude 36.18 and longitude 44.01 matching the considered location within the limits of the city of Erbil to the North of Iraq. The fact that grid electricity has not been able to meet the load demand has historically pushed the authorities to rely for varying amounts of electricity, according to the time of day and season, on large diesel district generators. They usually reconnect the electricity after grid failure with custom amounts of power, sold in cash per Ampere for as high as 10 to 15 times the public tariffs. Increasing evidence of decentralized solar energy systems on roof tops and more recently centralized public utilities are becoming more mainstream in the Norther region (Gov.krd, 2023).

In solar updraft tower thermal energy is used to stimulate density change and air movement over a turbine, leading to electricity generation. Solar updraft tower also known as solar tower is composed of primarily a solar collector with the specific task to heat the air beneath it. The second component in this system is the tower, usually placed at the center of the collector. The tower is mostly vertical but can be designed to match the surrounding terrain, be divergent or even float in the air (Zhou, 2009). The third component is a modified air turbine, usually placed inside the tower near the base.

Using solar thermal effects to generate air currents and channeling this synthesized wind to pass over a turbine in a controlled environment inside an updraft tower, form a potential alternative worthy of research to support the existing

10.18086/swc.2023.03.03 Available at http://proceedings.ises.org

renewable resources in the region. When considering the main requirements of solar updraft tower power plant against the Iraqi arid climate and type of terrain, including the region to the north of the country where the city of Erbil is, there is sufficient justification for the development of this concept through investigation and experimental work. Solar updraft tower has also been projected as a hybrid system with supportive roles in air purification, water desalination, drying in agriculture and co-generation with photovoltaics (Huang, 2020), (Tawalbeh et al., 2023) and (Xie et al, 2022).

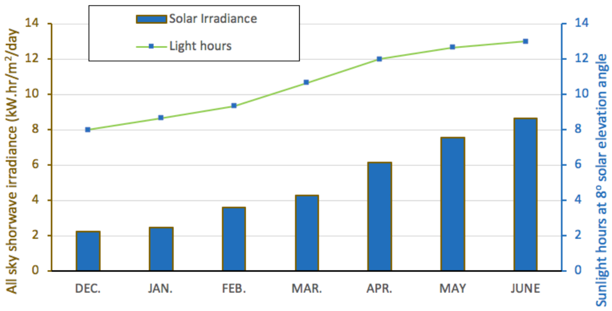

Figure 1: Solar irradiance and sunlight hours for Erbil from Dec. 2021 to June of 2022 at 8 degrees solar elevation

This work is comprised of consecutively reviewing selected literature relating to different aspects of solar chimney, also known as the solar updraft tower. The review connects between research projects in complementing fields of solar updraft tower, planned by the author and performed with research partners and teams. This document is based on five international publications where this researcher has taken over the role of the corresponding author and four academically assessed documents, under his supervision. Throughout this work, there is a candid tendency to refer to the obstacles and challenges. It is an attempt to visualize a more comprehensive reflection of what these endeavors contained. The aim is to motivate researchers to strengthen strive for reaching workable solutions and accredited recognition.

2. Modeling for a geometrical relation

Study of the geometry of the system defied the classical boundaries through adjustment and improvement of mathematical models. In an interesting work, solar tower geometry was investigated using a dimensionless model. The model proved successful with more realistic results for the pressure at the bottom of the tower and air flow enhancement (Okada, 2015). Research on improvement of the dimensional layout of the plant continued on a different note with the development of an unsteady simulation model. This investigation suggested a direct relation between the tower height and the system output represented by the generation efficiency and stability (Li et al., 2016). The relation between the ratio of geometry constraints of the main components was investigated within a merged convective axisymmetric domain. The results suggested a combined approach to estimation of collector and tower variables strongly affected by the ground heat storage (Vieira et al., 2017). In another attempt to reach an optimal geometrical configuration, the collector was slightly tilted in a converging cast. Thermodynamics of air flow was investigated using a turbulence model and CFD simulation. Flow regimes at the tower base were studies with emphasis on the development of pressure, temperature and velocity profiles. It was concluded that the increase of collector slope, convergence angle and radius created noteworthy improvements in performance (Fu, 2019).
Nearly ten years of research in solar updraft tower started with an experimental project and basic conceivable goals. The preliminary experimental work resulted in building the first model and then working on applying improvements in terms of the covering material and establishing a variable collector slope. Unfortunately, the experimental targets set for the model in Fig. (2) were not realized due to financial difficulties in 2014. However, the unfinished experimental work maintained a parallel course with an adjusted proposal looking into modeling and the relation between the geometrical components of the system (Mohammed, 2019).

Figure 2: Different stages of construction for the unfinish model (2) hindered by terminal difficulties. (a) Motion support on the circumference (b) Angle adjustment (c) Lifting mechanism (d) Polycarbonic cover (e) Installation of the cover

A steady state, two-dimensional, axisymmetric model was constructed for the system, working through an incompressible flow with homogenous heating and uniform streams inside the collector and no peripheral currents or temperature gradient in the tower. The properties were fixed except for density which was obtained from the Boussinesque approximation. These assumptions were applied to continuity, momentum, energy and standard turbulent ($k-\epsilon$) model (Ming et al., 2017). Ansys Fluent was used for designing the structure and modeling the flow and heat transfer inside the collector, tower and the absorber layer. After testing a range of different element lengths, a mesh size of 0.9 m (leading to 1,294,321.00 elements) was selected based on the stability of results.
The velocity and temperature results were compared with experimental data from Manzanares (Haaf, 1983) and the obtained Rayleigh numbers were checked against similar works in literature with reasonable agreement (Tahar and Mahfoud, 2013). Over 180 cases were tested within 15 groups to find similar patterns at different collector and tower dimensions so that to suggest the most appropriate matching. Figures (3) and (4) show the relations graphically and can be used to select in between values.

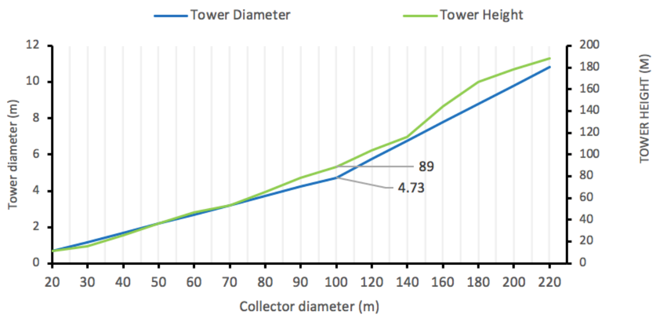

Figure 3: Relation between collector diameter and tower "height and diameter" for optimized performance

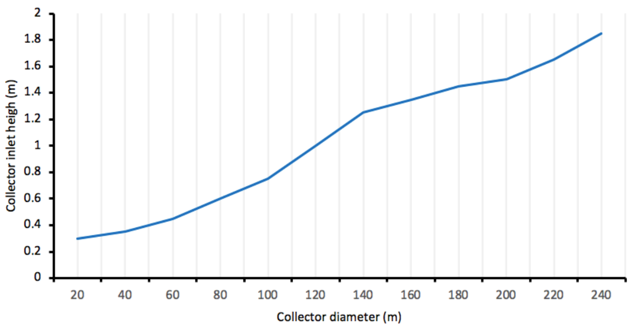

Figure 4: Relation between collector inlet height and collector diameter for optimized performance

3. Experimental work with restricted geometry

Eighty years after Isidoro Cabanyes, the most significant evidence of solar tower principle employed for power generation was up and running in a different part of Spain. The power plant in Manzanares was the living evidence that there is power to be made from solar tower. The next section is prepared as a brief review over the recent experimental works and geometrical modification related to solar tower power plant.
The experimental work found new momentum as researchers attempted to explore the geometry and investigate the effect on the performance. A group of researchers in Fukuoka - Japan constructed and developed a numerical model for a divergent tower and applied a parametric approach to study the divergence angle and tower height. They

suggested a slope of 4 degrees for optimum results working with a tower of 2 m height (Ohya et al., 2016). Looking into it from a different angle, a group of researchers in Edirne – Turkey experimented with a perforated collector of 10 m radius and closed periphery inlet. They called it; transpired solar collector with 35% collector area perforation and a tower height of 16.5 m. Air was allowed to enter the heating space from the collector top. They ran the system in winter and summer and observed higher efficiencies reaching a maxim temperature difference of 18 ºC (Eryener et al., 2017). And in another work, a group of researchers from Tafresh – Iran, measured the thermal performance of three collector configurations in indoors environment, using four artificial sources of thermal energy on a 100:1 scale model of the Spanish rig. The normally sloping (divergent) layout achieved the highest temperature difference and air flow velocity in the system (Mehdipour et al., 2020).

The idea of this work (Khalid and Atrooshi, 2020a) which represents the third generation of development on the original rig geometry was born out of the concern over the land restrictions. However, there were other factors that led to this design such as cost, availability of material, weather effects and funding. Two aspects were considered. One was the collector size and the other; the physical boundaries surrounding the allocated location. An experimental rig was designed and constructed as in Fig. (5) with the collector; one third the size of a normal circular shape. The sides where sealed and air was allowed only from the frontal inlet which was positioned to face south. The tower base was adjusted to accommodate the collector shape and the collector was divided into (16) sections with each section made up of (7) rows. Collector diameter was (19 m) and tower height (7.35 m).

Figure 5: Showing the experimental rig when the collector was shape. (a) Front view of the rig showing the air inlet area (b) Side view showing a sealed side

Temperature readings were collected from (12) sensors connected to a data logger. The sensors were installed along the collector radius, in the transition zone and over the length of the tower as shown in Fig. (6). Additionally, ambient air, ground and collector surface temperatures were also recorded. Airflow inside the tower was measured by a GM8901 anemometer so was the thermal solar radiation using a Hukseflux LP02 pyranometer. Calibration, error estimation and uncertainty analysis were applied to the instruments.

Narrowing collector section towards the tower base and sealing the collector sides against air flow, affected the development of temperature profile and created a gap between the glass and ground. Temperature readings for a typical day are complemented by solar radiation and airflow velocity in Fig. (7). The diagram shows that both temperature and velocity peak simultaneously for this particular geometry and while solar radiation reaches its highest value at mid-day, the highest ambient temperature is reached around two hours later.

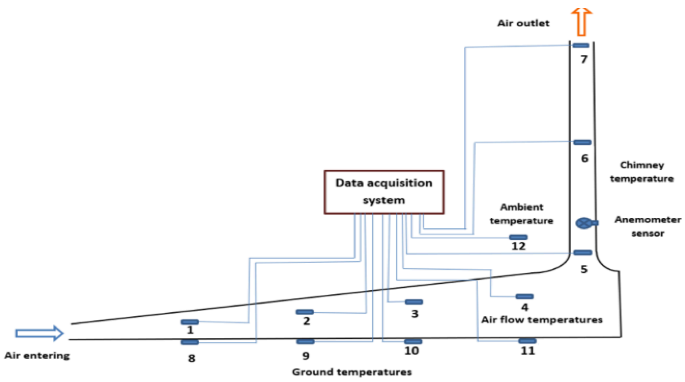

Figure 6: Instrumentation layout for the test rig

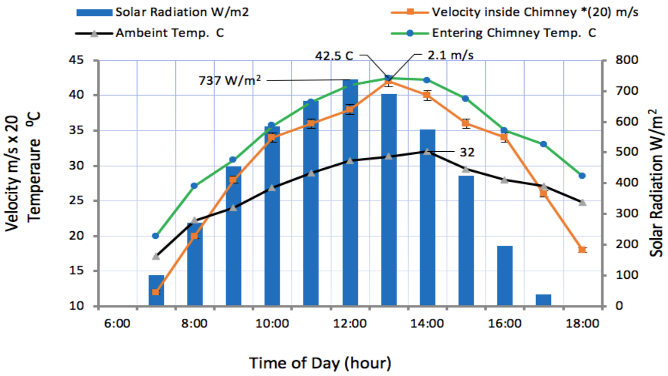

Figure 7: Hourly readings for ambient air temperature, air temperature at tower inlet, solar radiation and airflow velocity for October 7, 2017

4. Solar thermal concentration effect

Regardless of the amount of optimization, any reduction in collector surface area will have implications on the thermal performance of the system. In order to balance this act, the solar exposure intensity on the system should be enhanced through a suitable mechanism. One way for achieving this goal is by introducing solar thermal concentration. There are limited practical examples of such systems but a review over a few recent attempts in this category has been included to outline the progress in this field before describing the development of the concept in Erbil.

Following a very similar goal, solar thermal concentration was channeled by two intensifiers and an air sink, working with a small model. Obtained data was used to verify an assembled simulation model using SIMPLE and RNG turbulence model inside Ansys Fluent. They concluded that the thermal concentration effect benefited the system with improved air flow characteristics (Shahrezan and Imani, 2015). A few years later another group of researchers experimented with solar thermal concentration inside an experimental unit. They used adjustable mirrors to manually reflect solar radiation on the collector surface using a heliostat model. The outcome indicated enhancement in thermal performance and generated higher airflow rates inside the tower (Hussein and Al Sulaimani, 2018).

The motivation for this work (Khidir and Atrooshi, 2020b) came from the need to overcome the thermal incapacity of a collector reduced to one third of its volume as explained in the previous case. It was an experimental investigation involving a tracking reflector supported by a numerical code based on energy conservation equation developed in Matlab. The reflector was a flat mirror 1 x 1.6 m assembled into a tracking mechanism supported by two DC motors for daily and seasonal adjustments, Fig. (8 a, b, c, and d). The reflector was placed to the north of the system in a position to access the base of the tower.

The reflector mirror had a vertical configuration which allowed a small incident angle and the optimum performance was expected in the morning when the cosine of the angle had a large value. As the sun went up in the sky the angle between the vertical to the plane and the sun beam increased leading to dispersion of the reflected beam and difficulty in staying focused on the target. During data collection, bias, systematic and precision errors were used to verify and explain the deviations (Coleman and Steele, 2009).

Once the reflected beam hit the tower base it went through the transparent polycarbonate layer across the confined air and over to the absorber plate. Heat transfer mechanism between the reflector plate and the absorber layer is based on energy balance equations assuming quasi-steady state conditions (Tiwari and Shyam, 2016). The total area was divided into segments with boundary conditions and preliminary assumptions in Matlab.

Figure 8: Different views of the solar concentration system showing the solar reflection. (a) Reflector and the tracking mechanism from the side (b) Reflector front view supported from behind (c) Reflection of solar thermal radiation on the tower base (d) Front view of the system with collector extending towards south

Probably the most significant of these is the temperature rise due to the concentration effect. Fig. (9) shows the role of the concentrator reflector in enhancing the temperature rise at the tower base for January 2018. The highest effect is observed between 09:00 to 13:30 hours. At its peak, the concentration effect created 10.25% increase in the maximum obtainable temperature. Incident angle is the assembly of a number of solar angles, including altitude which refers to the elevation of the sun during the day and azimuth which is the deviation from north-south plane. Air flow inside the modified collector is still dominated by the density gradient driven by the temperature change. However, it is subject to different constrains. Due to the closed sides, the flow of air is more longitudinal than radial. This is similar to a channel flow with frictional effects from four sides. Fig. (10) shows the profile of airflow for typical days in January and April of 2018. The peak velocity is observed at mid-day with a maximum improvement of 22.2% due to the concentration effect.

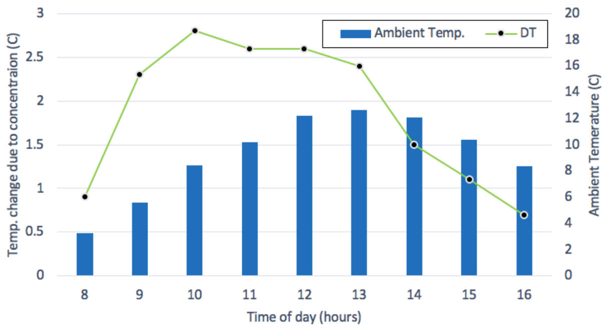

Figure 9: Hourly temperature change at the tower base due to the concentration for a typical day in January

The experimental rig was to continue to provide valuable data for the remaining months of 2018, namely August to December and there was a plan to integrate the assembly of a small turbine into the rig. Unfortunately, on August 18, 2023 this effort was permanently interrupted by the decision of School of Engineering Administration to destroy the rig, Fig. (11). This act ended the experimental journey; however, it did not impede the motivation but on the contrary it became the inspiration for improvement in conveying the scientific message and from then on research relied on modeling and simulation.

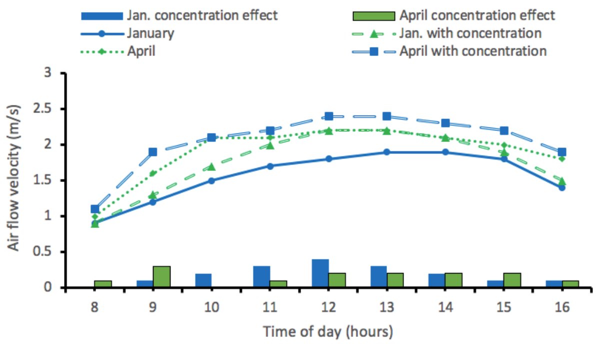

Figure 10: Hourly airflow change at tower base showing the concentration effect for typical days in January and April

Figure 11: Destruction of the experimental rig before the end of the study

5. Adaptation to the landscape with sloped collector

One of the main requirements of any solar tower power plant is a collector of any shape to create the sufficient temperature and density difference at the base of the tower. In locations where the available land is mountainous there are restrictions on construction of large size collectors. One way to overcome this difficulty is by adapting to the existing nature of the land.

The slope of the collector roof was investigated by a group of researchers from Sfax, Tunisia, who used a numerical model in Ansys Fluent and a small experimental solar tower. They studied the effect of changing the collector roof height on the main performance parameters such as temperature, airflow and pressure under local ambient conditions. They concluded that reduction of collector roof height and inlet opening will lead to improvement of outlet power (Ayadi et al., 2017). These results were partially challenged by another investigation that employed a three-dimensional model to look into the tower height and collector slope. The researchers from Telangana, India, concluded that increasing the collector slope leads to enhancement of airflow rate while the temperature inside the collector reduces due to this change (Das and Chandramoh, 2018). Collector slope angle was also investigated by a team of researchers from Algeria. In their research they experimented with the collector entrance slope using a two-dimensional axisymmetric model. They simulated the system performance and concluded that the optimal slope depends on the sloping distance (Kebabsa et al., 2020).

Collector slope may relate to different aspects of the collector shape but so far it has been used extensively to indicate collector roof gradient. In this fourth case, (Weli et al., 2021) the intention was to use the landscape slope as the indicator and run the collector roof slope parallel to it, Fig. (12), to model the natural landscape in the research area. Numerical simulation was developed in Ansys Fluent for steady, three-dimensional, axisymmetric, incompressible flow with Boussinesque approximation for density. Solution of Navier Stokes equations was based on coupling pressure and velocity. Discretization was applied in the process of solving continuity, energy and momentum equations.

The obtained performance figures from this model were comprehensively compared with other works. The noted differences were considered acceptable and validated the developed model for the next stage in which the model was adjusted for the sloped collector geometry. An initial collector slope of (35 degrees) will impose (70 m) reduction in tower height if the overall height of the system is to be kept at (194.5 m) and reduce the horizontal span by (22 m) to (100 m). In this work collector angle was used synonymously with ground slope. Fig. (13) shows the change in tower height and collector horizontal span relative to ground slope angle when overall system height and collector span are kept at (194.6 m) and (244 m) for comparison with the Spanish rig.

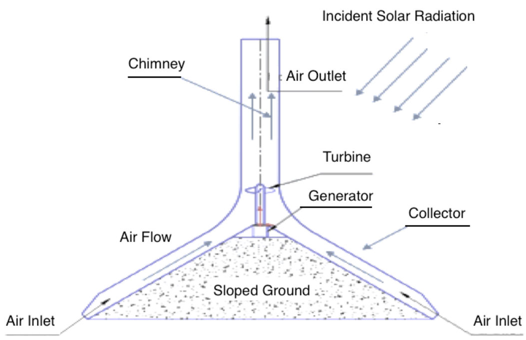

Figure 12: Sloped collector solar tower power plant

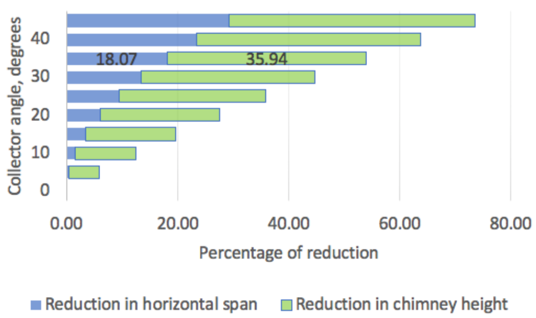

Figure 13: Effect of ground slope angle on system dimensions

In order to investigate the thermal performance of the system it was decided to start with verification of the optimum slope angle for the collector during the period from January to September. The reference point was zero slope at zero surface azimuth angle, facing south. The negative slope referred to inclination on the collector side facing north and the projection of tower shadow was not considered in this work. Solar radiation data from typical days in January, March, July and September at solar noon and different slope angles suggested (35 degrees) as the optimized angle, Fig. (14).

This concluded the requirements for the simulation of the sloped model with dimensions similar in layout to the Spanish rig composed of 1,631,824 nodes and element mesh size of (0.6 m). This model was then used to check the variation of the main performance parameters; temperature, airflow velocity and pressure change along the radial stretch of the sloped collector. The sloped collector solar tower was lagging behind the conventional system by up to 43.14% in airflow velocity and 40.9% in maximum obtainable temperature.

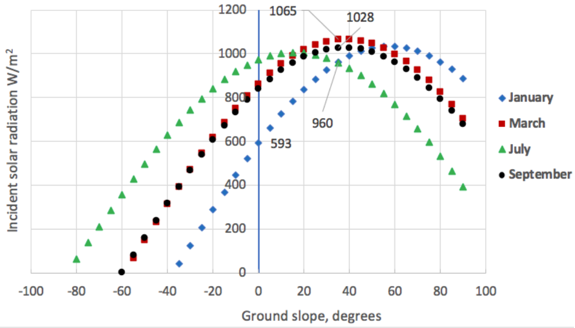

Figure 14: Incident solar radiation during different months of the year at different collector slope angles

6. Development of the turbine effect

Turbine is an essential component in any solar updraft tower system. Without the turbine the arrangement will turn into a natural ventilation system, still very beneficial but not effective for power generation. Turbines in solar towers are different from open access, horizontal or vertical axis wind turbines and the shape, size and position of these turbines have been the subject of research for many years.

The Spanish rig represented the first real manifestation of a turbine inside a solar tower. The confinement inside the tower and the synthesized wind made for a modest upper limit airflow of 9 – 15 m/s but at the same time provided for up to 12.5% higher pressure difference than the conventional wind turbines, allowing for an estimated turbine efficiency of 83% (Haaf et al., 1983). The deployed turbine was positioned at the bottom of the tower and was accessed through guided vanes. The rotor, composed of four adaptable blades was based on glider design with FX W-151-A blades made of composite material, preferably utilizing up to 80% of system overall pressure drop (Schlaich et al., 2005).

The position of the turbine inside the power plant was investigated by a group of researchers from Rize, Turkey. Pressure change which relates directly to the output power of the system was evaluated along the path of airflow. They recommended to use the obtained pressure pattern to find the optimal airflow position and place the turbine there (Cuce et al., 2020). A new design for the turbine inside the updraft tower was studied by a team of researchers who based their approach on the axial flow in the rotor, descending from hydraulic turbine and pump impeller designs. The results revealed that based on this design the system output is less affected by the rotor speed (Zuo et al., 2021). The role of guide vanes was investigated by researchers from India. In this experimental work they compared between the performance the system with and without the vanes. They reported up to 10% improvement when the guide vanes were implemented (Das and Chandramohan, 2022).

In this final case the focus is on the turbine inside the tower (Bakir et al., 2023). The mathematical model for the turbine design was based on blade element momentum theory. The calculation procedure was iterative and aimed to check on design parameter such as chord length, relative flow angle and the twist angle (Manwell and McGowan, 2009). The selected airfoil was NACA 4412, selected for superior performance at low rotational speeds (Yossri et al., 2021). A numerical model was constructed in Matlab. The calculation process was based on assumed values for induction factors leading to local speed ratio. The results were validated in comparison with open-source QBlade software (Marten and Wendler, 2013) and examples from literature including (Khaled et al., 2017).

The above turbine model was assembled to the solar tower simulation model developed in the previous case (Weli et al., 2021) and compared with a number of examples from literature. The developed turbine model proved that optimizing design parameters can indeed allow fruitful results in terms of performance. However, it was not possible to fit this model into the intended sloped collector due to integration and convergence issues. The next available option was to use the reverse fan model. Despite the observed deviations, the reverse fan model was the available option to be employed inside the sloped collector solar tower due to time limit restrictions.

In the concluding sections the performance of the overall sloped collector solar tower power plant was studied. The configuration is as shown in Fig. (12). The sloped collector behaves independently from other settings. The impact of the pressure change imposed by the reverse fan model was tangible for both temperature and velocity, Fig. (15).

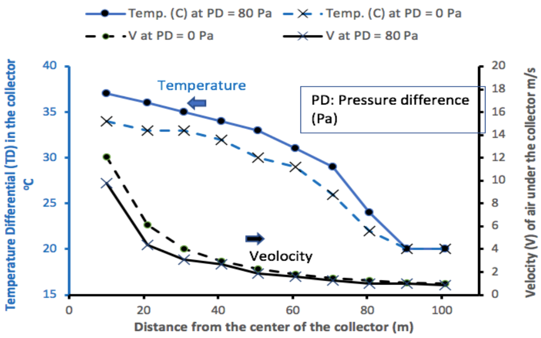

Figure 15: Velocity and temperature change along the radius of sloped collector solar chimney

A maximum temperature difference of nearly (3° C) was imposed by the turbine effect, near the entry to the tower. The pressure reduction due to the turbine effect led to an increase in airflow velocity, peaking near the tower at (12 m/s), almost (2 m/s) higher than when there was no reverse fan effect. The limit for turbine pressure-drop in the sloped collector solar tower power plant was set at (120 Pa), Fig. (16). Beyond this threshold the system became unpredictable. The recommended range of pressure-drop for turbine operation in a plant of this configuration and size is between (80 to 100 Pa).

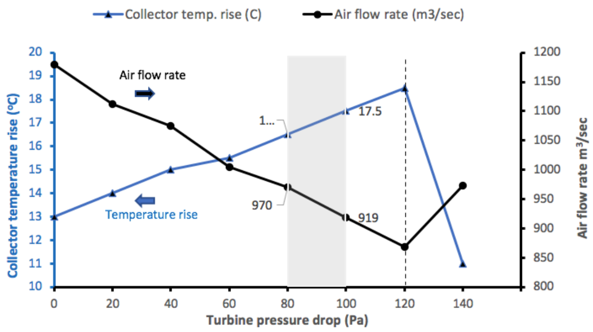

Figure 16: Effect of turbine pressure drop on collector temperature and airflow rate

7. Conclusions

This work reviews the different phases of the dedicated research work on solar tower power plant in the academic scene of the city of Erbil to the North of Iraq. The manuscript trails the achievements of five published articles in relevant international journals. Case one was developed to optimize the meshing of geometry for the different components of the system. Relations were developed to suggest the best match. Case two was experimental and worked on one-third the circular collector size. Performance of the system in terms of temperature, pressure and airflow velocity was of prime value due to the unique shape. Case three was applied to compensate the reduction of the thermal performance of the system with solar concentration. Hourly data were collected for temperature and airflow velocity and the effect of solar angles on temperature rise was recorded. The collection of data was interrupted with the decision of the School Administration to destroy the rig! Experimental work was discontinued indefinitely but modeling was adopted to support the remaining work. In the next case a sloped collector solar tower power plant was modeled with Ansys to look into the adaptation of the collector to the landscape in the research area. The results were compatible but suffered 43.14% in airflow velocity. In the final case the focus was on the turbine and a model was designed starting from the airfoil. A reverse fan configuration was compared with this model and despite its drawbacks it was used to run a parametric study on the sloped collector solar tower system. Both temperature and airflow velocity interacted with the pressure reduction in the turbine scoring (3° C) and (2 m/s) decrease. While the concept of solar updraft tower is still being intensively investigated, bold action is required to deliver it to the next stage.

References

Asnaghi, A. and Ladjevardi, S.M., " Solar chimney power plant performance in Iran", Renewable and Sustainable Energy Reviews, 16 (2012) 3383 – 3390; https://doi.org/10.1016/j.rser.2012.02.017

Ayadi, A., Bouabidi, A., Driss, Z., and Abid, M.S., "Experimental and numerical analysis of the collector roof height effect on the solar chimney performance", Renewable Energy 115(2018) 649 – 662; https://doi.org/10.1016/j.renene.2017.08.099

Cao, F., Zhao, L., Li, H., and Guo, Liejin, "Performance analysis of conventional and sloped solar chimney power plants in China", Applied Thermal Engineering 50 (2013) 528 – 292; https://doi.org/10.1016/j.applthermaleng.2012.06.038

Coleman, H.W., and Steele, W.G., 2009, Experimentation, Validation and Uncertainty Analysis for Engineers, third ed. John Wiley and Sons Inc, New Jersey

Cuce, E., Cuce, P.M., and Sen, H., "A thorough performance assessment of solar chimney power plants: Case study for Manzanares", Cleaner Engineering and Techology 1 (2020)100026; https://doi.org/10.1016/j.clet.2020.100026

Das, P., and Chandramohan, V.P., 2018, "CFD analysis on flow and performance parameters estimation of solar updraft tower (SUT) plant varying its geometrical configurations", Energy Sources, Part A: Recovery, Utilization, and Environmental Effects, Taylor and Francis; https://doi.org/10.1080/15567036.2018.1477881

Das, P., and Chandramohan, V.P., "An experimental study on performance assessment of solar updraft tower power plant with guide vanes", Heat Transfer Engineering, Vol 44 (2023) issue 7: Selected Papers from the 3rd International Conference on Recent Advances in Mechanical Infrastructure, Aug. 6 – 8 2021, Ahmedabad, India; https://doi.org/10.1080/01457632.2022.2079050

Eryener, D., Hollick, J., Kuscu, H., "Thermal performance of a transpired solar collector draft tower", Energy Conversion and Management, 142, (2017) 286 – 295; https://doi.org/10.1016/j.enconman.2017.03.052

Fu, S., "An enhanced heat collector design and numerical simulation for solar chimney power plant", IOP Conference Series: Materials Science and Engineering Vol. 631, Issue 4, 042022, http://doi:10.1088/1757-899X/631/4/042022

Gov.KRD, "Several new power plants installed last year", https://gov.krd/dmi-en/activities/news-and-press-releases/2023/january/several-new-power-plants-installed-last-year/, accessed: January 28, 2023.

Haaf, W., Fredrisch, K, Mayr, G., and Schlaich, J., "Solar chimneys Part I: Principle and construction of the pilot plant in Manzanares", Int. J. Sol. Energy, 2 (1983), pp.3 – 20; https://doi.org/10.1080/01425918308909911

Haaf, W., "Solar chimneys - Part II: Preliminary test results from Manzanares Pilot Plant", Int. Journal of Solar Energy, 1984, Vol. 2, pp. 141 – 161

Haung, M-H., Chen, L., Lei, L., He, P., Cao, J-J, He, Y-L, Feng, Zh-P, and Tao, W-Q, "Experimental and numerical studies for applying hybrid solar chimney and photovoltaic system to the solar-assisted air cleaning system", Applied Energy, 269 (2020), 115150, https://doi.org/10.1016/j.apenergy.2020.115150

Hussein, F.M., and Al Sulaimani, F.A., "Performance analysis of a solar chimney power plant design aided with reflectors, Energy Conversion and Management", 177 (2018) 30 – 42; https://doi.org/10.1016/j.enconman.2018.09.043

Kebabsa, H., Lounici, M.S., Lebbi, M., and Daimallah, A., "Thermo-hydrodynamic behavior of an innovative solar chimney", Renewable Energy, 145 (2020) 2074 – 2090; https://doi.org/10.1016/j.renene.2019.07.121

Khidhir, D.K., and Atrooshi, S.A., "Performance of a solar chimney with a modified collector geometry: A case study from Erbil to the north of Iraq", Journal of Solar Energy Engineering, Feb. **2020a**, 142(1): 011010 (12 pages); https://doi.org/10.1115/1.4044371

Khaled, M., Ibrahim, M.M., El Sayed, H., and Ahmed, A., "Aerodynamic design and blade angle analysis of a small horizontal – axis wind turbine", Am. J. Mod. Energy 3 (2017) 23 – 37; http://dx.doi.org/10.11648/j.ajme.20170302.12

Khidhir, D.K., and Atrooshi, S.A., "Investigation of thermal concentration effect in a modified solar chimney", Solar Energy 206 (**2020b**) 799 – 815; https://doi.org/10.1016/j.solener.2020.06.011

Li, J., Guo, H. and Huang, S., "Power generation quality analysis and geometric optimization for solar chimney power plants", Solar Energy, 139 (2016) 228 – 237, https://doi.org/10.1016/j.solener.2016.09.033

Manwell, J.F., and McGwan, J.G., 2009, Wind Energy Explained, Theory, Design and Application, 2nd ed, John Wiley and Sons Ltd.

Mehdipour, R., Mohammadi, E., Parsa, A.M.B. and Nahalekah, H., " Thermal and exergy assessment of solar chimney performance in various energy absorptions; using indoor experimental setup", Heat Mass Transfer, 57, 417 – 429 (2021); https://doi.org/10.1007/s00231-020-02926-6

Ming, T., Gong, T., de Richter, R.K., Cai, C. and Sherif, S.A., "Numerical analysis of seawater desalination based on a solar chimney power plant", Applied Energy, Vol. 208, 2017, pp 1258-1273, https://doi.org/10.1016/j.apenergy.2017.09.028

Muhammed, H.A., and Atrooshi, S.A., "Modeling solar chimney for geometry optimization", Renewable Energy, 138 (2019) 212 – 223, https://doi.org/10.1016/j.renene.2019.01.068

NASA Power Data Access Viewer, Renewable Energy, https://power.larc.nasa.gov/data-access-viewer/, accessed; January 06, 2023

Ohya, Y., Watak, M., Watanabe, K., and Uchida T., "Laboratory experiment and numerical analysis of a new type of solar tower efficiently generating a thermal updraft", Energies, 2016, 9, 1077; https://doi.org/10.3390/en9121077

Our World in Data, Iraq: Energy country profile, 2022, https://ourworldindata.org/energy/country/iraq, accessed; May 28, 2023

Marten, D., and Wendler, J., QBlade Guidelines V 0.6, 2013; david.marten@tu-berline.de

Schlaich, J., Bergermann, R., Schiel, W., and Weinrebe, G., Weinrebe, "Design of commercial solar updraft tower systems – utilization of solar induced convective flows for power generation", Jornal of Solar Energy Engineering, 2005, Vol. 127 – 124; https://doi.org/10.1115/1.1823493

Shahreza, A.M., and Imani, H., "Experimental and numerical investigation on an innovative solar chimney" Energy Conversion and Management, 95 (2015) 446 – 452; https://doi.org/10.1016/j.enconman.2014.10.051

Tawalbeh, M, Mohammed, S., Alnaqbi, A., Alshehhi, S. and Al-Othman, A., "Analysis for hybrid photovoltaic/solar chimney seawater desalination plant: A CFD simulation in Sharjah, United Arab Emirates", Renewable Energy, Vol. 202, January 2023, pp 667 – 685, https://doi.org/10.1016/j.renene.2022.11.106

Tiwari, G.N., and Shyam A.T., 2016, Handbook of Solar Energy; Theory, Analysis and Applications, Springer Science and Business Media Singapore

University of Oregon, Sun path chart program, "Solar Radiation Monitoring Laboratory", 2023, (http://solardat.uoregon.edu/SunChartProgram.html, accessed; January 07, 2023

Vieira, R.S., Petry, A.P., Rocha, L.A., Isoldi, L.A., and dos Santos, E.D., "Numerical evaluation of a solar chimney geometry for different ground temperatures by means of constructal design", Renewable Energy, 109 (2017) 222 – 234, https://doi.org/10.1016/j.renene.2017.03.007

Weli, R.B., Atrooshi, S.A., and Schwarze, R., "Investigation of the performance parameters of a slped collector solar chimney model – An adaptation for the North of Iraq", Renewable Energy, 176 (2021) 504 – 519; https://doi.org/10.1016/j.renene.2021.05.075

Weli, R.B., Atrooshi, S.A., and Schwarze, R., "Design characteristics and validation of the turbine model – Case of development of turbine effect in sloped collector solar chimney plant", Energy Reports, 9 (2023) 2087 – 2101; https://doi.org/10.1016/j.egyr.2023.01.031

Xie, M., Jia, T., and Dai, Y., "Hybrid photovoltaic/solar chimney power plant combined with agriculture: The transformation of a decommissioned coal-fired power plant", Vol. 191, May 2022, Pages 1 – 16, https://doi.org/10.1016/j.renene.2022.03.148

Yossri, W., Ayed, S.B., Ghommem, M., and Abdelkefi, A., "Computational modeling and optimization of small-scale wind turbines for low-power applications", AIAA 2020 Forum Conference; https://doi.org/10.2514/6.2020-2799

Zhou, X., and Yang, J., "A novel solar thermal power plant with floating chimney stiffened onto a mountainside and potential of the power generation in China's deserts", Heat Transfer Eng. 30(5), 400-407, 2009, https://doi.org/10.1080/01457630802414813

Zuo, L., Dai, P., Yan, Z., Li, C., and Zheng, Y., "Design and optimization of turbine for solar chimney power plant based on lifting design method of axial-flow hydraulic turbine impeller", Renewable Energy 171 (2021) 799 – 811; https://doi.org/10.1016/j.renene.2021.02.121

EXPERIMENTAL ANALYSIS ON A SINGLE TANK ENERGY STORAGE SYSTEM INTEGRATED WITH A COOKING UNIT FOR SOLAR COOKING

Jimmy Chaciga[1*], Denis Okello[1], Ole J. Nydal[2], Karidewa Nyeinga[1]

[1] Department of Physics, Makerere University, Kampala, (Uganda)

[2] Department of Energy and Process Engineering, Norwegian University of Science and Technology (NTNU), Trondheim (Norway)

Abstract

This paper presents the experimental analysis and thermal performance of a single tank energy storage system integrated with a funnel and cooking unit designed, constructed and tested using a funnel system to produce high quality heat front for immediate cooking without mixing thermocline. A prototype was constructed using available suitable materials. It consists of funnel system, heating element, refined sunflower oil and a stainless-steel tank. The funnel was made of metal pipe and a position for a cooking unit to provide immediate cooking. Oil was used as a heat storage medium and a 1.5kW, 220V heater was used to heat it. The heater was switched on during charging and switched off during discharging process. It charged the STESS, fast and effectively to temperatures above 180ºC in 20 minutes highly attributed to system design. There was no mixing of hot and cold oil during the charging and hot heat. An overflow barrier-controlled charging while oil circulated in one way and reversed during the discharge process. The funnel charging energy efficiency was estimated to be 72.5% for the first case of barrier height and 51.9 % in the second barrier level by the funnel technique. About 453.6kJ of energy was consumed in boiling 1.5L of water in 10 minutes while 1.04MJ in boiling 1 kg of dry beans in 2hours. There was 6.23MJ left during charging while cooking and 3.54MJ left after discharging process.

Keywords: Single tank system, Funnel system, Quality heat front, Heat storage.

1. Introduction

Globally, 3 billion people rely on biomass materials for cooking and commercial activities, leading to an estimated four million deaths annually due to household air pollution [1]. While some people use liquid petroleum gas and grid electricity, over 85% of the population in developing countries, particularly in Africa, still rely on biomass energy, causing harmful effects on the environment, health, and climate change [2]. The use of biomass fuels has resulted in significant greenhouse gas emissions, deforestation, conflicts, food shortages, and extreme weather conditions. The cost of LPG fuel and other gasoline has also increased over time. Energy storage systems are most suitable application for indirect solar cooking methods [3-5].

Mawire et al. [6] investigated both vegetable oils (palm oil and refined sunflower) and refined mineral oil (shell thermia B) in South African market as possible heat transfer and thermal energy storage fluids. The study reveals that, refined sunflower had the highest exergy and energy efficiencies followed by palm oil during charging, with values increasing as the thermal gradient increases. Tabu et al. [7] experimentally evaluated the thermal performance of selected oils in Uganda for heat storage system for indirect solar cooking applications. Sunflower oil and Palm oil were selected from the local market and Shell Thermia B, a synthetic oil; energy and exergy analysis were performed to test their suitability as heat transfer and heat storage fluids. Sunflower oil was reported to have higher stratification and stored more

10.18086/swc.2023.03.04 Available at http://proceedings.ises.org

energy. Sunflower, being an edible vegetable oil was then recommended for TES system for cooking and the key properties are summarized on Table 1.

Table 1: Thermophysical properties of refined sunflower oil [7]

Physical quantity	Dependent variable/Value	Unit
Density	$930.62 - 0.65\,T$	kgm^{-3}
Specific heat capacity	$2115.0 + 3.13\,T$	$Jkg^{-1}K^{-1}$
Thermal conductivity	$0.161 + 0.018e^{\left(\frac{-T}{26}\right)}$	$Wm^{-1}K^{-1}$
Flash point temperature	235	℃
Smoke point temperature	350	℃

Mawire et al.[8] experimented the thermal performance of rock pebbles as sensible materials in terms of the axial temperature distribution, total energy stored, the exergy, and the transient charging efficiency. The results indicated that not only the value of the total amount of energy stored is important for the thermal performance of oil-pebble-bed systems but also that the exergy stored and the degree of thermal stratification. The system had no cooking unit integrated. In addition, Kajumba et al. [9] evaluated the performance of TES system integrated with a cooking unit; the cooking unit was made below the heat storage and hot oil from tank was driven by means of gravity for heat extraction. They reported a challenge of depletion of hot oil from the TES tank during cooking since the oil could not be circulated back into the TES tank. Further investigations of designs and technologies were reported by a number of researchers on small scale thermal energy storage system for solar cooking applications by [10]–[13].

Furthermore, Abedigamba et al. [14] reported on the heat of utilization and efficiency values of two selected oils namely; Sunflower oil and Roki oil in Uganda. The results suggest that Roki oil is a potential heat storage material for domestic applications however, the Sunflower oil indicated better heat of utilization characteristics than Roki oil during the tests. Okello et al.

[15] designed and tested a TES System integrated with a cooking unit where the cooking unit was embedded inside the oil TES tank. They demonstrated boiling of beans during charging. However, cooking during discharge was limited by the fact that the hot oil at the top would mix with the cold oil from the bottom. Hence, the quality of the heat front and thermal stratification in the tank was destroyed during discharge cycle

The paper describes a new design for a Thermal Energy Storage (TES) system that is integrated with a funnel and cooking unit. The funnel system was designed to charge a small volume of oil in it quickly to higher temperatures without mixing hot oil a in the single tank, enabling immediate cooking and quality heat front. This funnel can be adjusted to vary the cooking rate and temperature of oil by raising it up and down manually. This was not possible with earlier designs reported in literatures [15]. The TES cooker consists of a single tank system with a funnel inside it and a position for cooking unit. Heating is done using a grid electricity in the funnel, and a small barrier allows hot oil to overflow into the tank after reaching a certain temperature. The hot oil overflows into the bulk tank while the cold oil from the bottom enters the funnel to be heated and process is repeated. The system ensures that there is no mixing of hot and cold oil, maintaining quality heat front for cooking. This single tank system developed as an alternative cooking technology for solar cooking. Experimental tests were conducted to demonstrate and validate the system's effectiveness for solar cooking application.

2. Materials and Methods

2.1. System Design and Experimental Setup

Figure 1 shows the single tank energy storage system integrated with a funnel and cooking unit. The heating chamber consists of a pipe made metal, and on top made in the form of funnel; this is referred to as a funnel top. A heating element positioned at the centre of the funnel system heat the oil inside the tank. Funnel is made adjustable using long screws attached to the funnel top. Refined sunflower oil was used as heat storage medium. The Table 1 presents the dimension of the cooking system constructed and experimentally tested.

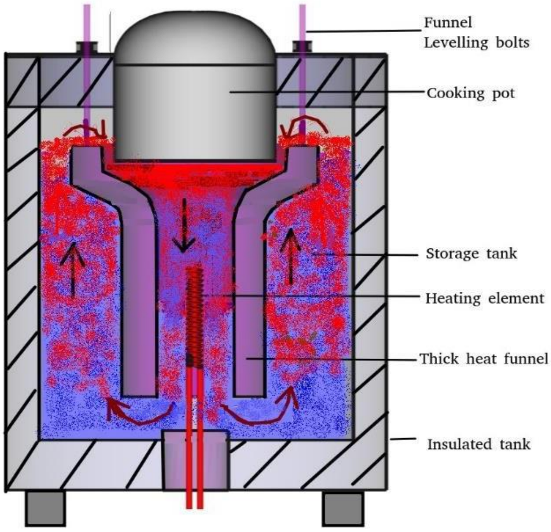

Figure 1(a): Schematic diagram of the system design.

Table 2. The dimensions of the main parts of the single tank heat storage system.

Design components	Internal diameter (m)	Height (m)
Storage tank	0.30	0.40
Cooking pot	0.20	0.10
Funnel top/Cooker	0.20	0.05
Heat funnel	0.07	0.25

Figure 1 shows the schematic diagram of the experimental setup. The heat storage had 18L refined sunflower oil and heat source was supplied by the heating element mounted inside the funnel center. A prototype was constructed and tested on grid; where; during charging; the heating element was switched on to heat the oil meanwhile the heater was switched off during discharging process of the single tank system. A number of thermocouple sensors interfaced with TC 08 data logger and a computer was used to collect data on temperature profile every minute in; the funnel system, heat storage and cooking unit to analyze its performance during charging and cooking -discharge process.

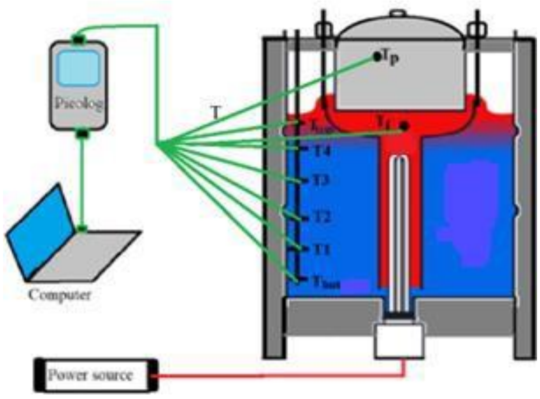

Figure 1(b): Schematic diagram for Experiments and data collection showing the arrangement of thermocouple sensors.

2.2. Experimental Procedure

The prototype of the STHSS was design and constructed: The experimental schematic diagram in Figure 1(b) was setup and a number of thermocouples sensors arranged in the single tank heat storage, funnel system, and cooking pot were connected to TC-08 data logger to measure and record temperature profile every minute. The system was connected to power source and the system was charged while demonstrating cooking and later heat storage was first charged to average temperature of above 180 oC and then discharged through cooking. Cooking tests were made using water boiling tests and boiling of dry beans. Boiling time and energy consumption during cooking was analysed. Figure 2 shows the experimental setup of the system. Five k-type thermocouples were arranged into the storage tank at a distance of 4.0 cm apart. Thermocouple, $Tpot$ was inserted into the cooking pot while , Tf was on top of the funnel and it registers the same temperature as the sensor,$Ttop$. Inside the tank, more thermocouples,

$T1$, $T2$,$T3$, $T4$ and $Tbot$ were arranged as shown in Figure 4 to. The thermocouples were connected to a TC08 Pico-log data logger interfaced with a computer, and configured to measure and record the average temperatures every minute. The storage tank was filled with 18L of refined sunflower oil. To the heating element rated at 1.5 kW, 220V an AC grid power was connected to provide electricity to heat the oil. Thermocouples were inserted at different points in the system.

Figure 2: A) Showing the picture of the experimental setup of single tank system integrated with a cooking unit B) is the positioning of thermocouples and Pico data logger.

2.3. Experimental Procedure

2.3.1. Charging and discharging of the single tank energy storage system

During the charging process, the power to heater was switched on; this results into heating of the oil in the funnel. The volume of oil in the funnel system was about 2.5 L. The heated oil in the funnel becomes less dense, rises and overflows into the storage tank. The temperature profile in the system was monitored and recorded.

The discharging process involves carrying out cooking tests. After the system was charged to the desired temperature, the heater was switched off during the discharge mode, the hot oil flows from the top of the heat storage tank into the funnel where the cooking pot sits. The cooking pot contained either cold water, rice, or bean’s soup. The water or beans was allowed to boil using the energy stored in the system. Boiling of water and beans was repeated several times. In general, the charging and discharging processes were conducted several times during the experiment.

2.3.2. Cooking tests -during charging and discharging

A cooking pot of capacity of 3 L was used to carryout cooking tests. The pot was inserted into top of funnel making good contact with the walls. The bottom of the cooking pot was made in contact with the oil on top of the funnel. Cooking tests were demonstrated during both charging and discharging for boiling 1.5 L of water multiple times and boiling of 1 kg of bean’s soup. Beans are common type of sauce consumed by majority of the families in Uganda. It is also the major sauce in schools, eaten by students almost every day. However, beans require a lot of energy before it is ready for consumption with cooking time of over 2 hours [10]. Therefore, it is very important to test if the single tank heat storage unit is able to cook beans. Figure 6 shows pictures of the experimental setup during cooking test that were demonstrated.

Figure 3. A) Picture shows boiling of 1 kg of dry beans in the cooking pot, B) shows the boiling of 1.5 L of water in the pot.

Cooking during charging was started a few minutes after the heater was switched on; due to the fact that the temperature at the top of the funnel rose faster. Cooking was continued as the tank was being charged. On the other hand, cooking during the discharge process was started after the heating element was switched off. While boiling dry beans, more water had to be added into the pot since dry beans take longer time to get cooked. The temperature profile during cooking processes were recorded. A manual valve has been mounted onto the heat storage tank at the lower bottom to occasionally drain the oil from inside the TES tank out in case of servicing and maintenance of the cooker.

2.4. Thermal performance analysis of the single tank heat storage system

2.4.1 Heating power

During charging, a small volume of oil (about 2.5L) was heated in the funnel using the heating element. The temperature of the oil in the funnel would rise faster. The total energy, $Esup$, supplied in heating the oil in time, t, is determined by Equation (1):

$$Esup = Pt \tag{1}$$

where, P is the rated power of the heating element.

2.4.2 Thermal energy stored in the tank

The total thermal energy, Est, stored in the stratified tank divided into n-segments after charging for a given time, t, is determined by Equation (2):

$$Est = \sum_{j=1}^{n} \rho av cp{,}av Vj \Delta Tj \tag{2}$$

where ρav, is the average density of refined sunflower oil in a segment, $cp{,}av$, is the average specific heat capacity of oil in a segment, Vj is the volume of oil in the jth segment, and ΔTj is the temperature difference in a segment of the stratified tank.

2.4.3 Rate of energy consumption during cooking

The rate of energy, E_W required to boil water of mass, m_W from an initial temperature, T_{ini}, to final temperature, T_w (the boiling point) in time, t, is given by Equation (3):

$$E_w = \frac{(\rho_w V_w) c_{p,w} (T_w - T_{ini})}{t} \tag{3}$$

where, V_w, is the volume of water, ρ_w the density of water, $c_{p,w}$ the specific heat capacity of water. Heat loss to the environment is ignored.

The rate of energy, E_b required to boil beans of a given mass, m_b, is determined by Equation (4) as:

$$E_b = \frac{(m_b c_{p,b} + m_w c_{p,w})(T_{boil} - T_{amb})}{t_1} + \frac{m_w L_v}{t_2} \tag{4}$$

where m_b is the mass of beans, $c_{p,b}$ is the specific heat capacity of beans, m_w is the mass of water, $c_{p,w}$ is the specific heat capacity of water, T_{boil} is the boiling point of water, T_{amb} is the ambient temperature, t_1 refers to time to reach the boiling point, and t_2 is time when the water is at its boiling point as the beans continues to boil. In case of boiling beans, usually more water is added once the water level drops during cooking, therefore, the new times: t_1 and t_2 have to be determined again. We assume the same mass of water. Table 3 provides thermal properties of beans and water used in the study.

Table 3: Summary of Properties of water and dry beans; properties of beans adapted from [12].

Parameter	Value
Density of water, ρ	1000 kgm^{-3}
Specific heat capacity of water, $C_{p,w}$	42000 $Jkg^{-1}K^{-1}$
Specific heat capacity of dry beans, $c_{p,b}$	1800 $Jkg^{-1}K^{-1}$
Moisture content of dry beans	12% w.b

2.4.4 Thermal charging efficiency

The thermal energy charging efficiency, η_{ch},is determined by Expression 6 as:

$$\eta_{ch} = \frac{E_{sto}}{E_{input}} \times 100\ \% \qquad (6)$$

where E_{sto}, is the energy stored in the tank, and E_{input}, is the electrical energy supplied to heat the oil. The charging efficiency was determined for cases where no cooking was done during charging. The heat loss to the environment was ignored in the above computation.

2.4.5 Heat extraction efficiency

The heat extraction is determined during the discharge cycle. It is based on the cooking of food or boiling water using the energy stored in the tank. The heat extraction efficiency, η during cooking is expressed as Equation (7):

$$\eta = \frac{E_{cons.}}{E_{rel.}} \times 100\% \qquad (7)$$

where, E_{cons} is the energy consumed by the food in the cooking pot while E_{rel} is the energy supplied to the cooking pot. However, the energy released by the heat storage, is determined by

$$E_{rel} = E_{cons} + E_{loss} \qquad (8)$$

where; the energy consumed by food (boiling beans and water) is determined using equation (9)

$$E_{cons} = (m_b c_{p,b} + m_w c_{p,w})(T_{boil} - T_{amb}) \qquad (9)$$

While the energy loss during this process is estimated using the expression (10)

$$E_{loss} = (UA)(LMTD) \qquad (10)$$

Where; U is the heat transfer coefficient of material of the tank while, A, is the surface area of the system and $LMTD$ is the log mean temperature difference of oil inside the tank in Kelvin**.**

3. Results and Discussions

3.1 Thermal Charging at the first overflow barrier position

The experimental setup in Figure 6 was used to carry out the charging process. The heat storage tank contained 18 L of refined sunflower oil. About 2.5 L of oil was in the heating chamber. The oil level in the funnel was adjusted to be just at the bottom of the funnel barrier. Figure 4 shows the temperature profiles in the system during charging for about 90 minutes.

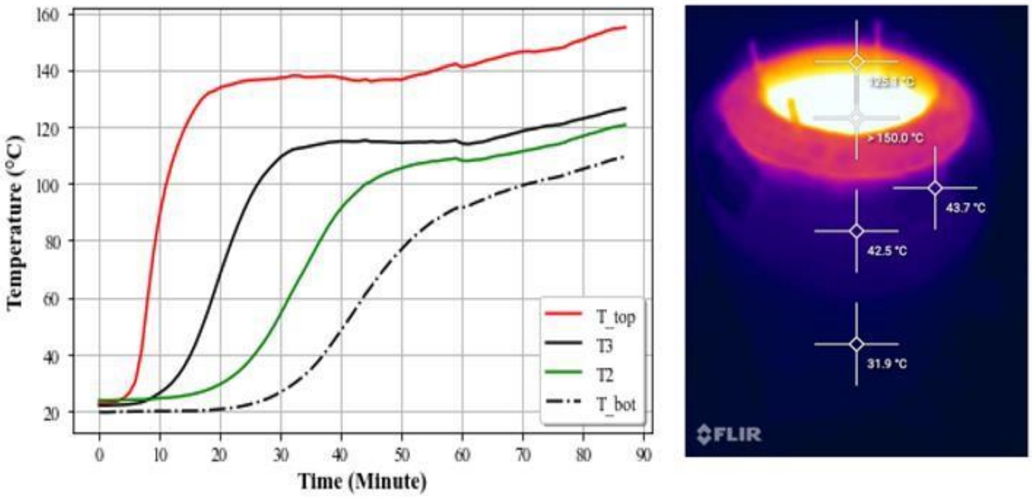

Figure 4. The temperature profile inside the energy storage tank and the funnel; and on the right hand is the thermal image showing heat distribution at the top of the tank and in the cooking unit.

It can be observed from Figure 4 that the temperature at the top of the funnel increased rapidly to about 138 ^oC within 20 minutes. Thereafter, the temperature remained fairly constant for the next 30 minutes despite the continuous heating. After about 1 hour, a slight increase in temperature was observed at the top of the funnel; the maximum temperature attained was about 155 ^oC at the end of the charging process.

The temperature profiles in the storage tank indicates that in the first 10 minutes, the temperatures were close to ambient temperature. Thereafter, the temperature at the top of the tank started to increase, reaching about 134 ^oC in 20 minutes. After additional 10 minutes of charging, the temperature at the top of the tank increased rapidly for the next 20 minutes to about 140 ^oC at the top and reached 115 ^oC in the middle, and then remained fairly constant for about 30 minutes. Further increase in charging, resulted into slight rise in temperature. On the other hand, the temperatures in the middle and bottom of tank remained close to ambient for the first 20 minutes of charging. Thereafter, the temperatures in the middle and bottom of the tank were observed to increase rapidly for the next 30 minutes reaching 110 ^oC and 90 ^oC respectively. Further increase in charging did not cause significant rise in temperature in the tank.

The rapid increase in the temperature at top of the heat funnel is attributed to the fact that a small volume of oil (about 2.5L) was heated in the funnel. Therefore, in about 10 minutes, the temperature at the top of the funnel had reached 100 ^oC. In addition, there was minimum heat conduction through the sides of the funnel into the storage tank during the start of the charging process. The heated oil in the funnel, becomes less dense and therefore, rises into the funnel top and this is replaced by cold oil flowing from the bottom of the tank into the funnel s observed, natural circulation sets in. As the oil is heated further, it rises above the funnel barrier and overflows into the tank. This is the cause for the rise in temperature of the oil at the top of the tank, while the middle and the bottom of the tank remained at ambient temperatures. Due to the overflow of hot oil into the tank, the temperature at the top of the funnel remained fairly constant. As cold oil is circulated from the bottom of the tank into the funnel for heating, the middle and bottom sections are replaced by hot oil flowing from the top and hence the observed increase in temperatures. However, the flow cold oil from the bottom of the tank into the funnel causes a slight decrease in temperature at the top of the tank as observed by the temperature profile after an hour. Thereafter, as heating continues, we observed an increase in temperature.

As heating was continued, the temperatures in the middle and bottom sections are seen to rise although the middle section rises faster. This is attributed to the fact that more hot oil from the funnel overflows into the tank, and the dense and cold oil at the bottom of the tank flows into the funnel. This process is repeated resulting into increase in temperatures in the middle and bottom sections of the tank while at the top of the tank, the temperature tends to flatten. In general, there is high heat distribution at the top of the tank as shown by the thermal image. After 90 minutes of charging, about 4.60 MJ of energy was stored in the storage tank in this case using equation 2.

3.2 Thermal charging – effect of increasing height of the funnel

The temperature of the hot oil at the top of the funnel was about 140 ^{o}C when it started to overflow into the tank. To achieve higher temperatures in the funnel, the levelling screws were used to raise the funnel by 2 cm. This means the height of the barrier for hot oil to overflow into the storage tank was raised by 2 cm above the initial position. The same experimental setup in Figure 2 was used, and Figure 5 shows the temperature profiles in the funnel and tank.

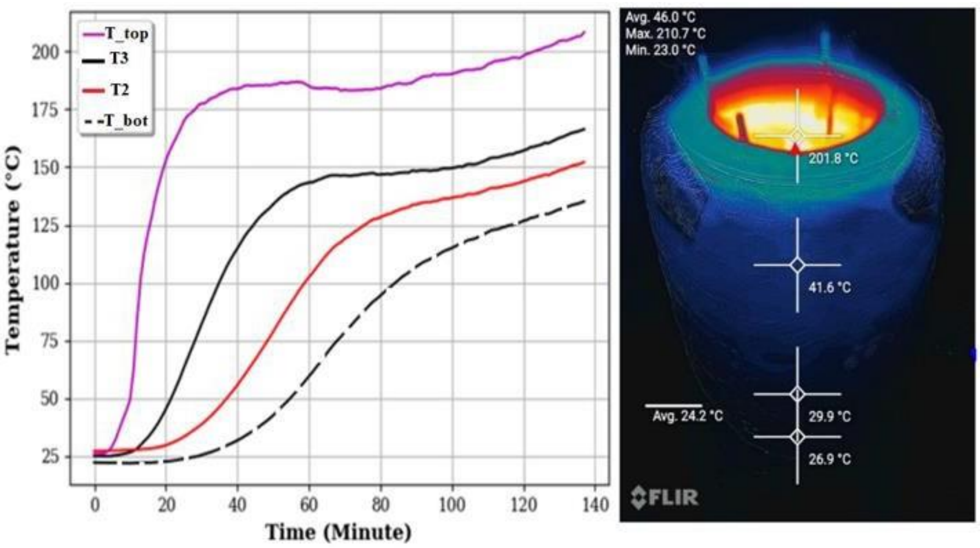

Figure 5. Temperature profiles in the funnel and tank; on the right is the thermal image of the heat distribution in the system. Highest temperature achieved at the top of funnel was above 200 ^{o}C after 2 hours of charging.

It can be observed from Figure 5 that the temperature profiles depict the same trend as shown in Figure 4. As noted, before, there was a rapid increase in temperature at the top of the funnel because of heating a small volume of oil. However, in this experiment, higher temperatures are attained compared to those in Figure 4. A temperature of about 155 oC was attained at the top of the funnel within 20 minutes compared to 135 oC in Figure 4. The highest temperature at the top of the funnel achieved was about 200 oC after 2 hours of charging.

As explained previously, the temperature at the top of the funnel remained fairly constant when the hot oil began to overflow into the storage tank. At this point, the dense, cold oil at the bottom of the tank flows into the funnel where it is heated. The oil becomes less dense and would rise, and overflow into the tank. This process is repeated as heating continuous. The temperature at the top of the tank reached a maximum of about 150 oC and remained fairly constant; while in the middle and the bottom temperatures of about 125 oC and 100 oC were attained.

The observed high temperatures in Figure 5 compared to Figure 4 are due to the raising of the funnel. The increase in the height of the funnel by 2.0 cm resulted into increasing the barrier height before the hot oil could start to overflow into the tank. This means, the oil is heated longer and hence attaining higher temperatures before starting to overflow into the tank. In general, the heating of small volume of oil causes a sharp rise in temperature in short time leading to overflow of hot oil into the tank. Thermal stratification is established in the tank with a sharp thermocline.

Figure 4 and Figure 5. shows the charging of the oil by using the funnel technique and the impact 0f adjusting the funnel barrier height varies the temperature at which hot oil begins to overflow into the tank. The energy stored in the tanks under the above cases were estimated from Figure 4 and Figure 5 where About 4.6 MJ of energy was stored during the first charging and about 5.9 MJ in the second case after raising the funnel height by 2 cm.

3.3 Charging the system while boiling 1 kg beans

The heating element was switched on and as well demonstration of boiling tests was performed on the heat storage. The temperature profile recorded and plot

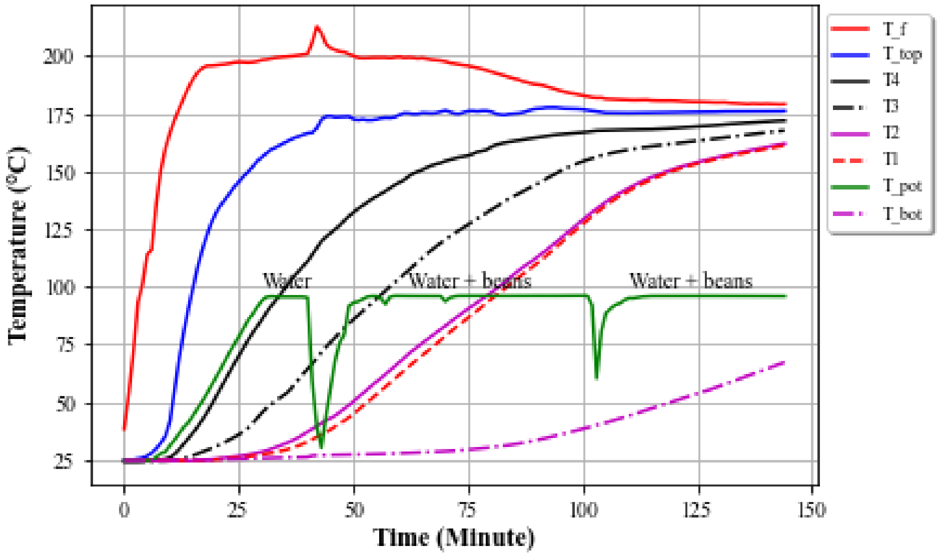

Figure 6. Shows the temperature profile during charging of the system while cooking; boiling of 1.5 litres of water and then boiling 1 kg of beans soup. The beans boiled in about 2 hours and boiling was repeated several times.

Figure 6 shows that the initial 1.5 L of water at 25oC, reached boiling temperature in less than 20 minutes; and boiling was prolonged for further 20 minutes. This is shown by the temperature

$Tpot$ remaining constant, then 1 kg of dry beans was added into the cooking pot. This resulted into the first drop in temperature of the cooking pot after about 40 minutes.

Thereafter, the temperature of cooking pot rose quickly reaching the boiling point in less than 20 minutes. The beans continued to boil at constant temperature T_{pot}. The small drops in temperature of the cooking pot observed between the 50^{th} and 75^{th} minute are associated with opening the lid of the cooking pot to check the status of beans as it boils. After about one hour of boiling beans, a drop in temperature is observed at the cooking pot. This is due to addition of 0.5L of water at room temperature. The temperature of the cooking pot reached to boiling point very fast since a small volume of water was added. The beans boiled for further 40 minutes and it became soft and cooking was stopped. In total it took about 2 hours to boil the dry beans.

The total energy used in boiling of the beans was calculated using Equation (7-9) and it was found to be 3.89MJ. Therefore, the power used in boiling beans within 2 hours is about 3.0 kWh by using equation 3-5. This is a comparable amount of energy consumed in boiling of 1 kg beans when using improved firewood stove reported to be 2.61kWh [14]. The value obtained was slightly higher than that of energy consumed by firewood stove probably due to the calorific energy value in firewood and energy losses. In addition, Kajumba et al. [8] also reported that, it took 2½ hours to boil only ½ kg of dry beans on heat storage. This means that, the current study of single tank system had better performance compared to the previous work reported in literature.

3.4 Discharging process – through Boiling water

in the Figure 7, the cooker was tested by boiling 1.5 L of water obtained at room temperature during the discharge process. The heat storage tank was first charged to about 200 o C, and then, the heater was switched off. Then the first 1.5 L of water was added into the pot and allowed to boil. After boiling of the water, another (1.5L) of water at room temperature was replaced in the pot and the process was repeated several times. Figure 13 shows the temperature during charging and discharge process.

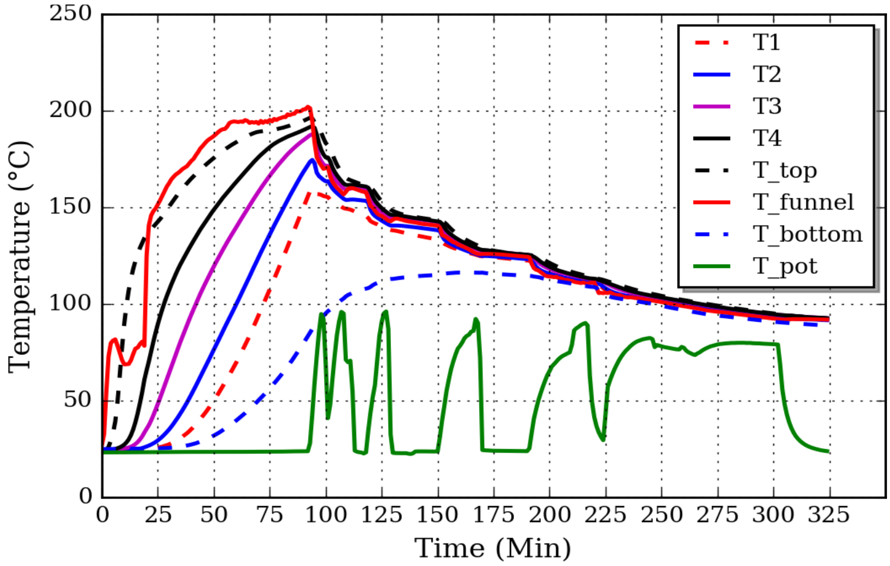

Figure 7. The temperature profiles during charging and discharging cycles of the system; by boiling of 1.5L of water multiple times.

Charging was done for about 80 minutes and the temperatures at the top of the funnel and heat storage tank reached about 200 °C as observed in Figure 7. Then 1.5L of water at room temperature (25 °C) was put into the cooking pot. It took about 8 minutes for the water to boil during the first test and consuming about 447.3kJ by equation 4. The green temperature profile recorded by T_{pot} represents different boiling tests. The second boiling test was done immediately; it took about 10 minutes for the water to boil. The drop in cooking temperature profile in the pot happened when the pot was removed and water at room temperature was added. After the first two tests, there was a delay of about 10 minutes before putting more 1.5L of water to boil. After the third cooking test; boiling of water was done after 30 minutes interval for the next two tests. During this time interval, the temperature for the cooking pot remained constant at about 25 °C. During the final boiling test, the water was left to continue boiling after it had reached its boiling point in 20 minutes. The slight drop in temperature observed during the boiling process was when the top cover on cooking pot was remove. However, the funnel charging energy efficiency was estimated to be 72.5% for the first case of barrier height and 51.9 % in the second barrier level by the funnel technique using equation 6. About 453.6kJ of energy was consumed in boiling 1.5L of water in 10minutes while 1.04MJ in boiling 1 kg of dry beans in 2hours. There was 6.23MJ left during charging while cooking and 3.54MJ left after discharging.

4. Conclusions

The single tank system with funnel charging mechanism was developed tested successfully to charge the energy storage tank to high temperature in a short period without mixing hot oil in the heat storage attributed to the funnel designed. Immediate cooking on the cooker was possible and cooking tests (boiling water and cooking beans) were demonstrated both during charging and discharge process successfully. The funnel maintained quality heat front at both during charging and discharge process. Therefore, an off-grid solar PV system is recommended and suitable to supply power to charge the small volume of oil in this funnel technique for solar cooking.

Data Availability Statement

The data presented in this study are available on request from the author**.**

5. Acknowledgments

The authors are grateful to the Norwegian Agency for Development Cooperation for financial support through NORHED II Project – Energy Technology Network (EnergyNET). EnergyNET is a research collaboration between the Norwegian University of Science and Technology, Makerere University, and African Universities.
The authors appreciate the International Solar Energy Society (ISES, SWC2023) 30th October -4th November Conference 2023, for the invitation and organising the Scientific Event in New Delhi, India.
Conflicts of Interest:
The authors declare no conflict of interest in undertaking this research work and publication.

6. References

S. C. Bhattacharya and P. Abdul Salam, "Low greenhouse gas biomass options for cooking in the developing countries," *Biomass Bioenergy*, vol. 22, no. 4, pp. 305–317, 2002, doi: 10.1016/S0961-9534(02)00008-9.

L. Nkhonjera, T. Bello-Ochende, G. John, and C. K. King'ondu, "A review of thermal energy storage designs, heat storage materials and cooking performance of solar cookers with heat storage," *Renewable and Sustainable Energy Reviews*, vol. 75. Elsevier Ltd, pp. 157–167, 2017. doi: 10.1016/j.rser.2016.10.059.

G. Petrokofsky, W. J. Harvey, L. Petrokofsky, and C. Adongo Ochieng, "The importance of time-saving as a factor in transitioning from woodfuel to modern cooking energy services: A systematic map," *Forests*, vol. 12, no. 9, Sep. 2021, doi: 10.3390/f12091149.

D. Campbell-Lendrum and A. Prüss-Ustün, "Climate change, air pollution and noncommunicable diseases," *Bulletin of the World Health Organization*, vol. 97, no. 2. World Health Organization, pp. 160–161, Feb. 01, 2019. doi: 10.2471/BLT.18.224295.

S. L. Hemstock, M. Charlesworth, and R. D. Singh, "Household Energy Usage, Indoor Air Pollution, and Health," 2019, pp. 1–12. doi: 10.1007/978-3-319-69627-0_82-1.

A. Mawire, "Performance of Sunflower Oil as a sensible heat storage medium for domestic applications," *J Energy Storage*, vol. 5, pp. 1–9, Jun. 2016, doi: 10.1016/j.est.2015.11.002.

B. Tabu, K. Nyeinga, J. Chaciga, and D. Okello, "Thermal Performance of Selected Oils in Uganda for Indirect Solar Domestic Cooking Applications," *Tanzania Journal of Science*, vol. 44, no. 4, pp. 77–90, 2018, [Online]. Available: www.ajol.info/index.php/tjs/

A. Mawire, M. McPherson, and R. R. J. Van Den Heetkamp, "Simulated energy and exergy analyses of the charging of an oil-pebble bed thermal energy storage system for a solar cooker," *Solar Energy Materials and Solar Cells*, vol. 92, no. 12, pp. 1668–1676, 2008, doi: 10.1016/j.solmat.2008.07.019 P. K. Kajumba,

D. Okello, K. Nyeinga, and O. J. Nydal, "Experimental investigation of a cooking unit integrated with thermal energy storage system," *J Energy Storage*, vol. 32, Dec. 2020, doi: 10.1016/j.est.2020.101949.

P. K. Kajumba, K. Nyeinga, D. Okello, and O. J. Nydal, "Assessment of the energy needs for cooking local food in Uganda: a strategy for sizing thermal energy storage with cooker system."

J. Chaciga, N. Karidewa, D. Okello, and B. Tabu, “Construction of a High Temperature (~ 200 °C) Oil Pump for Solar Thermal Energy Storage System for Cooking Applications,” *Tanzania Journal of Science*, vol. 44, no. 4, pp. 21–35, 2018, [Online]. Available: www.ajol.info/index.php/tjs/

D. Okello, C. W. Foong, O. J. Nydal, and E. J. K. Banda, “An experimental investigation on the combined use of phase change material and rock particles for high temperature (∼350 C) heat storage,” *Energy Convers Manag*, vol. 79, pp. 1–8, Mar. 2014, doi: 10.1016/j.enconman.2013.11.039.

O. P. Abedigamba, S. F. Mndeme, A. Mawire, and M. Rukaaya, “Heat Utilization Characteristics of Two Sensible Heat Storage Vegetable Oils for Domestic Applications,” *Sustainability (Switzerland)*, vol. 15, no. 8, Apr. 2023, doi: 10.3390/su15086825.

D. Okello, R. Omony, K. Nyeinga, and J. Chaciga, “Performance Analysis of Thermal Energy Storage System Integrated with a Cooking Unit,” *Energies (Basel)*, vol. 15, no. 23, Dec. 2022, doi: 10.3390/en15239092.

MECS, “The State of Access to Modern Energy Cooking Services,” 2020. Accessed: Aug.03, 2023.[Online] Available: https://documents1.worldbank.org/curated/en/937141600195758792/pdf/The-State-of-Access-to-Modern-Energy-Cooking-Services.pdf

Hybrid Nanofluids for Solar Thermal Process Heating Applications

Satish Upadhyay[1, 2, #], Laltu Chandra[1, 3], Jahar Sarkar[1]
[1]Department of Mechanical Engineering, IIT (BHU) Varanasi (India).
[2] uGDX School of Technology, ATLAS SkillTech University Mumbai, (India).
[3]Department of Sustainable Energy Engineering, IIT Kanpur, (India).
[#]Correspondence: satishupadhyay.rs.mec18@itbhu.ac.in

Abstract

Experiments with turbulent flow of hybrid nano-oils are reported to mitigate the dearth of experimental data for assessing the developed generalized Nusselt number correlation, deduced using separation approach. A controlled, Joule-type, uniform heating condition is adopted for simplicity. The significant findings are (a) the Nusselt number enhanced with the addition of nano-particles, (b) the addition of nanoparticles increases the pressure drop and (c) the assessment of Figure of Merit confirms that the use of hybrid nano-oil is beneficial compared to pure oil, and (d) the generalized Nusselt number correlations are applicable for hybrid nano-oils within the reported uncertainty of ± 15%. Therefore, the experiment is a step towards utilization of hybrid nano-oils as heat transfer fluid for heat transfer applications.

Keywords: Experiment, hybrid nano-oil, Nusselt number, turbulent flow

Introduction

Solar energy is freely available and is widely used for process heating and cooling applications. In Industries, many applications lie in the medium temperature range of 353 – 573 K, discussed by Pranesh et al. (2019). Concentrating Solar Thermal systems can fulfill this demand; in this Parabolic Trough collector is the most mature technology, which is expected to save to save fossil fuel, enhance the system efficiency, and mitigate the emission of greenhouse gases. Such systems require heat transfer fluids (HTFs) to transport the heat generated significantly by reflected solar irradiance to the applications for heating or cooling. (Vignarooban et al., 2015). A parabolic trough collector (PTC) absorber is exposed to peripherally non-uniform concentrated heat flux, and a heat transfer fluid is utilized to recover the generated heat via forced convection. Interestingly, the use of a secondary reflector is one method to reduce the non-uniformity. Tang et al. (2021) discussed how to achieve uniform heat flux distribution by optimizing the design of the secondary reflector of PTC. Various research focused on HTF-like nanofluid and hybrid nanofluid and reported an enhancement in efficiency and Nusselt number. Various Nusselt number correlation, specific to nanofluid, and also the generalized Nusselt number correlation deduced by separation approach is discussed in detailed by Upadhyay et al. (2021, 2022). Krishna et al. (2018) thoroughly reviewed experimental and numerical work utilizing nanofluid in PTC. Literature suggested use of hybrid nanofluid over nanofluid (Tiwari et al., 2021). Thus hybrid nanofluid is selected for experimental work.

The literature review revealed the need for heat transfer experiments with hybrid nano-oil. Therefore, experiments are performed with Therminol VP1 (TVP1) and 1% (V/V) Al_2O_3-CuO-TVP1 hybrid nano-oil subjected to uniform heat flux conditions assuming PTC absorber consisting of secondary reflector to homogenize the solar radiation to get uniform heat flux. The objective is to find experimental heat transfer enhancement with hybrid nano-oil for turbulent flow and assess the generalized Nusselt number correlation developed for an oil-based hybrid nanofluid experimentally. The paper presents the preparation and stability of the oil-based hybrid nanofluid, the developed experimental setup, the heat transfer coefficient, and Nusselt number. To the best of the authors' knowledge, no such detailed experiments with hybrid nano-oil are reported thus far. The details of the experiment setup, the adopted procedure, and the findings are presented subsequently.

1. Experimental setup and procedure

The schematic of the forced convection experimental setup is shown in Figure 1. It comprises a heat transfer fluid tank (HTF tank), pump, bypass valve, flow meter, test section (heated and unheated section), U-tube manometer,

10.18086/swc.2023.03.12 Available at http://proceedings.ises.org

power supply, and chiller. HTF tank stores sufficient fluid, which is supplied as soon as the pump is turned on. Initially, the HTF is heated by an immersion heater placed inside the HTF tank up to the desired inlet fluid temperature (T_{in}) and a chiller is used to maintain the steady operating condition. A one-horsepower pump is used to circulate the HTF through the test section, including the chiller. A bypass valve is installed to control HTF's flow and attain the desired flow rate during the experiment. A turbine-type flow meter is installed to record the flow rate in liters per minute (LPM). The test section comprises a 4 m long, straight, horizontal copper tube depicting a PTC absorber with an external heating element. The test section (copper tube) is divided into two parts, viz. unheated and heated length of 2 m, the outer diameter of the tube is 0.025 m, and the inner diameter of the tube is 0.023 m. Thus, a sufficient length-to-diameter ratio of ~86 is provided to attain the heated copper tube's hydraulically fully developed inflow condition.

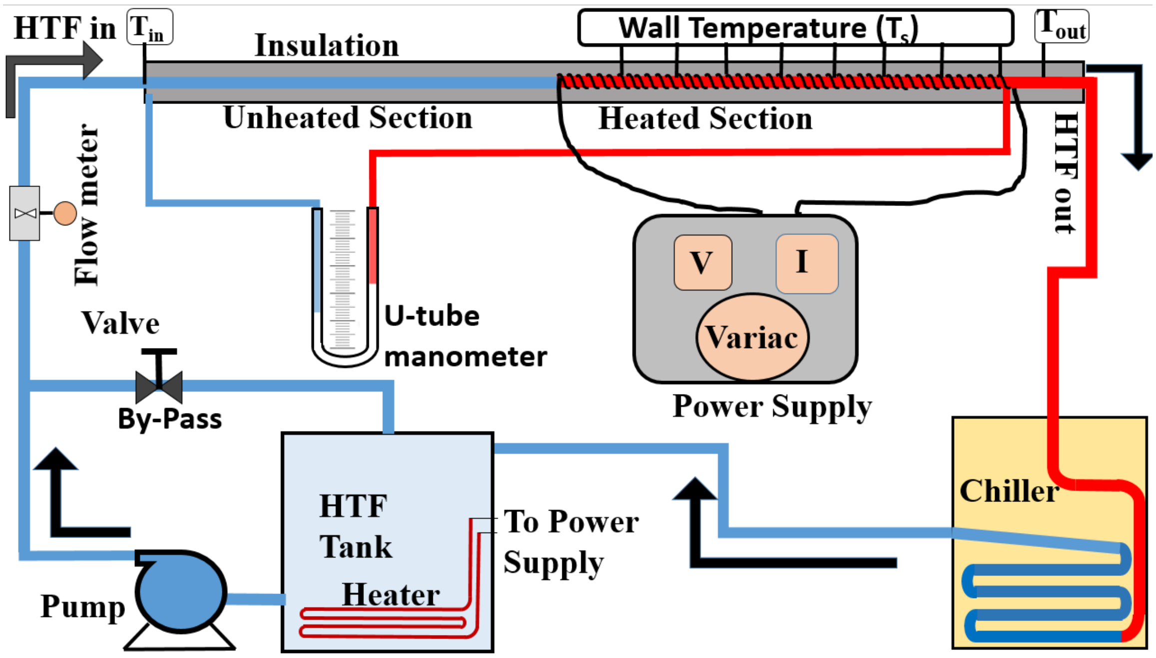

Figure 1. Schematic of the installed experiment setup for the heat transfer with therminol and hybrid nano-oil.

Figure 1 illustrates that K-type thermocouples and a data acquisition (DAQ) system are installed to record the inlet, outlet, and outer wall temperatures. A U-tube manometer is installed to measure the pressure drop across the straight tube using the height of the mercury column. The test section is externally insulated, with sufficient thickness, to mitigate heat losses. It is worth mentioning that the inlet and outlet of the test section are provided with a wire mesh to promote mixing and redistribution of HTF temperature. Therefore, as far as possible, the measured temperatures are interpreted as the bulk mean. The measured parameters, the corresponding instruments, their range, and accuracy details are provided in Table 1.

Table 1. The measured parameters, instruments, and their operating range/accuracy

Parameters	**Instruments**	**Range**	**Accuracy**
Flow rate	Turbine-type flowmeter	10 to 50 LPM	±0.1 LPM
Temperature	K-type thermocouple	20 to 300 ºC	±0.1 ºC
Wattmeter	Wattmeter, Specification: 250 V, 50 Hz, Maximum 10 A	Less than 2.2 KW	±0.25%

A photograph of the installed experimental facility is shown in Figure 2a. The externally insulated, long, straight test section (copper tube), including thermocouples, is wrapped with nichrome wire as a heating element (see Figure 2b). Silicon rubber is provided between the unheated and heated part of the test section to mitigate the heat transfer, as far as possible, during the experiment. K-type thermocouples are installed on the outer wall of the copper tube using a groove of 0.5 and a high-temperature epoxy. Due care is taken to isolate the thermocouple sensor from the heating element by utilizing insulation around the same. The thermocouples are uniformly spaced (25 cm) along the axial direction on the heated section, and some probes are placed along the circumferential direction to record azimuthal variation, if any, for the applied boundary conditions. Several efforts were made to perform the experiments for uniform and non-uniform heat flux distributions along the azimuthal direction. However, achieving a non-uniform heat flux distribution depicting discrete heating conditions was not possible using the installed nichrome wire-wrapped copper tube. The authors finally concluded that the same can be attained, possibly by using an external radiation source, and is of future interest. However, the current experiment provided helpful data for the assessment of the generalized Nusselt number correlation for hybrid nano-oil. The installed, multiple K-type thermocouples at the inlet and outlet near the wire mesh are shown in Figure 2c.

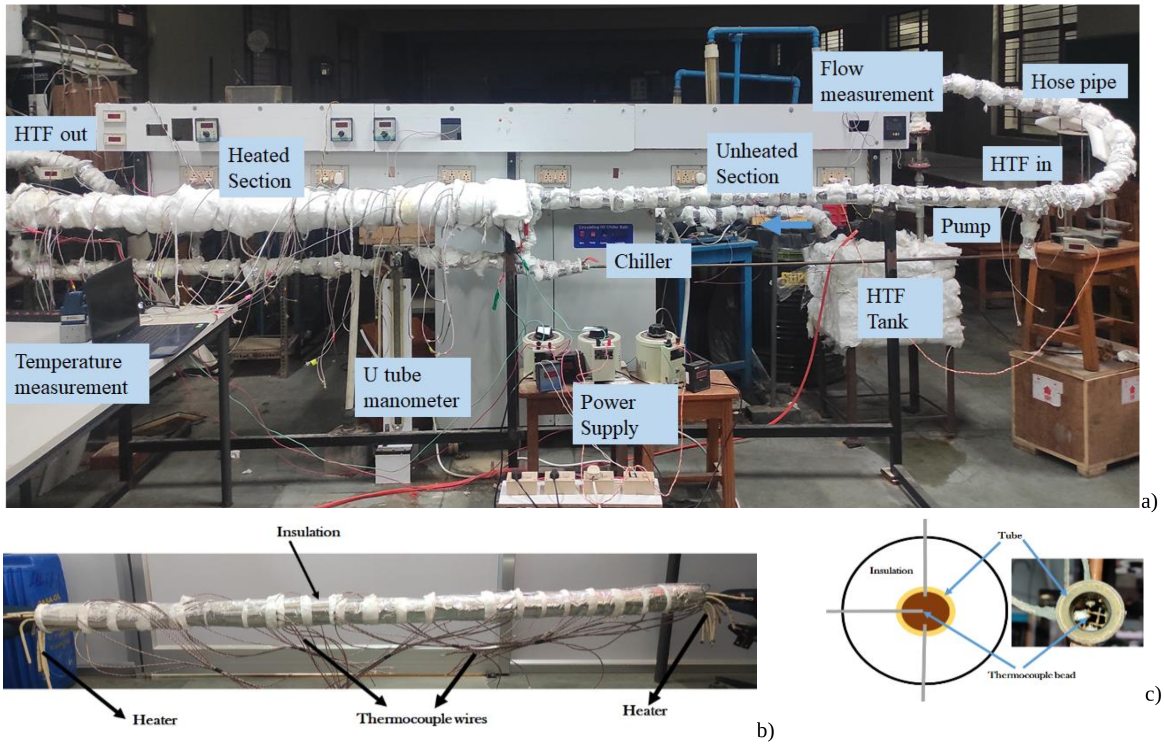

Figure 2. Photograph of a) the installed experimental setup for heat transfer with oil and hybrid nano-oil, b) the installed, externally insulated heating section with thermocouples, and c) the installed thermocouples at the inlet and outlet to measure fluid temperature.

The following step-wise approach is adopted for performing the experiments:

Step 1: The HTF is heated to the desired inlet temperature, and the flow rate is steadily increased to attain the desired flow rate or the corresponding Reynolds number in the range of 7000 - 19000. Subsequently, the flow is allowed to stabilize for some time.

Step 2: The power supply is turned on, and the same is regulated using a variac. This is measured using a wattmeter, and the same is verified using the attached voltmeter and ammeter. This allows external heating of the 2 m long test section.

Step 3: The system is allowed to operate and stabilize. Once the steady state is attained, the flow rate, inlet, outlet, and wall temperatures are recorded.

Following the adopted procedure, the HTF is heated to attain the inlet temperature of 353 K. The flow rate of HTF is maintained at a value between 10 – 26 LPM with an increment of 2 LPM. The first set of experiments is performed with TVP1 oil, and the second set of experiments is performed for 1% (V/V) Al_2O_3-CuO TVP1 hybrid nano-oil. The input power to the 2 m long, straight copper tube is maintained at 3.2 kW for all the experiments. Achieving a higher power was challenging because of safety-related issues in the laboratory. Several parameters are noted for the experiment after attaining a steady state. This was inferred from the test section's measured fluid and solid temperatures. The thermophysical properties of pure oil and hybrid nano-oil are adopted from various literature shown in Table 2. Thus, after calculating the thermophysical properties and using the appropriate equations presented later in the data deduction, the Nusselt number and friction factor are calculated and compared with the standard correlation discussed in section 3.

Table 2. Thermophysical property of Therminol VP1 and hybrid nano-oil.

Material/oil/ nano-oil	Equations/correlations
TVP1 (Mwesigye et al. 2017, Klein, 2017)	$\rho = 1.4386 \times 10^{-3} - 1.8711T + 2.737 \times 10^{-3}T^2 - 2.3793 \times 10^{-6}T^3$ (kg m^{-3}) $c_P = 2.125 \times 10^3 - 11.017T + 0.049862 \times T^2 - 7.7663 \times 10^{-5}T^3 + 4.392 \times 10^{-8}T^4$ (J kg^{-1}K^{-1}) $\lambda = 0.14644 - 2.0353 \times 10^{-5}T - 1.9367 \times 10^{-7}T^2 + 1.0614 \times 10^{-11}T^3$ (W m^{-1}K^{-1}) $\mu = 0.023165 - 0.1476 \times 10^{-3}T + 3.617 \times 10^{-7}T^2 - 3.9844 \times 10^{-10}T^3 + 1.6543 \times 10^{-13}T^4$ Pa.s
Hybrid nanofluid (Upadhyay et al. 2021, Mwesigye et al. 2017, Pak et al. 2013, Xuan et al. 2000)	$\rho_{hnf} = (1-\phi)\rho_{bf} + \phi_1\rho_{np1} + \phi_2\rho_{np2}$ (kg m^{-3}), where $\phi = \phi_1 + \phi_2$ $C_{phnf} = \frac{(1-\phi)\rho_{bf}C_{pbf} + \phi_1\rho_{np1}C_{pnp1} + \phi_2\rho_{np2}C_{pnp2}}{\rho_{hnf}}$ (J kg^{-1}K^{-1}) $\lambda_{nf} = \left[(3\phi-1)k_{np} + (2-3\phi)k_{bf} + \sqrt{\Delta}\right]$ (W m^{-1}K^{-1}) where $\Delta = \left[(3\phi-1)k_{np} + (2-3\phi)k_{bf}\right]^2 + 8k_{np}k_{bf}$ (W^2 m^{-2}K^{-2}) $\lambda_{hnf} = \frac{k_{nf1}\phi_1 + k_{nf2}\phi_2}{\phi}$ (W m^{-1}K^{-1}) $\mu_{hnf} = \mu_{bf}(123\phi^2 + 7.3\phi + 1)$ (Pa s)

2.1. Hybrid nano-oil preparation: Al_2O_3-CuO TVP1

Hybrid nano-oil is prepared by mixing an appropriate fraction of Al_2O_3 and CuO nanoparticles in TVP1. In general, 1g of hybrid nanoparticles comprises 0.8g of Al_2O_3 and 0.2 g of CuO nanoparticles. Thus, to prepare 1% (V/V) of hybrid nanofluid, 395.4 g of Al_2O_3 and 98.84 g of CuO nanoparticles are dispersed in 11 L of TVP1 oil. The high-precision electronic weighing machine (model: SWIL 220, India) is used to measure the weight of nanoparticles and surfactants with a resolution of 0.1 mg. The measured quantity of nanoparticles is mixed in TVP1 with a magnetic stirrer (Tarsons Digital Spinot) for more than 2 hours. Subsequently, for proper dispersion of the hybrid nanoparticles, Sodium Dodecyl Sulfate (SDS) is used Gimeno-Furio at al. (2017). After stirring, the solution is sonicated in the ultrasonicator (Labman Scientific Instruments, India) for more than 2 hours. The steps for hybrid nano-oil preparation are shown in Figure 3. The stability of the prepared hybrid nano-oil is inspected by two methods, viz. a) visual inspection and b) pH Value. The concept of isoelectric point (IEP) is used to test the stability of a hybrid nanofluid by its pH value. The stability of a hybrid nanofluid can be ensured if its pH value is far from the isoelectric point of nanoparticles (Kumar et al., 2019). This is attributed to a large repulsive force between the suspended nanoparticles in the base fluid. For example, the isoelectric point of Alumina nanoparticles is 9.1 (Singh et al., 2005), and that of copper oxide nanoparticles is 10 (Sousa et al., 2013). The pH value is measured by a pH meter (model: CL 54+Toshcon Industries, India). The pH meter is calibrated before measurement, and the measurement is repeated three times. The stability of the hybrid nano-oil is discussed in section 3.1

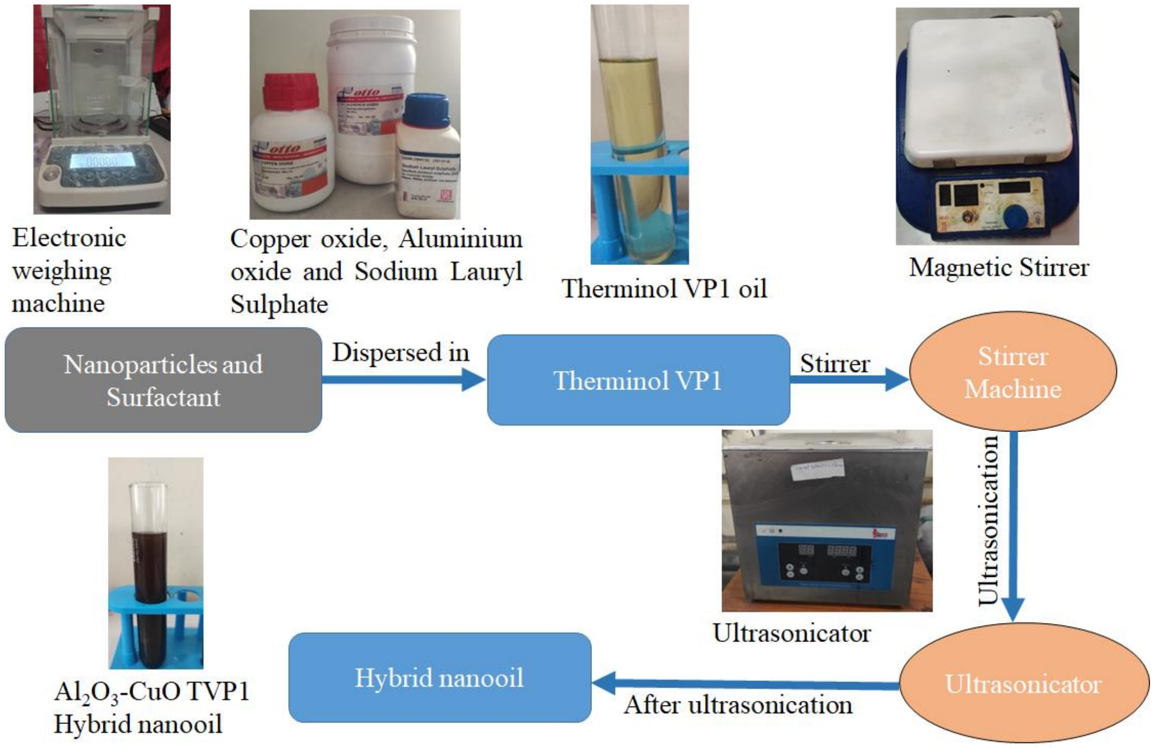

Figure 3. Equipment used and steps for the preparation of hybrid nano-oil.

2.2. Data Deduction

To calculate the Nusselt number and friction factor, the following equations are used:

Rate of electrical heat input: $\dot{Q}_{electrical} = VI$ (eq. 1)

Rate of heat removal by HTF: $\dot{Q}_{absorbed} = \dot{m}c_p(T_{out} - T_{in})$ (eq. 2)

The recorded heat loss rate $\left(\dot{Q}_{electrical} - \dot{Q}_{absorbed}\right)$ is less than 3% of the rate of electrical power input. The surface-area averaged convective heat transfer coefficient is obtained by Newton's law of cooling, as follows:

$$\bar{h} = \frac{\dot{Q}_{absorbed}}{A(T_s - T_b)} \quad \text{(eq. 3)}$$

where $T_s = \frac{\sum_{i=1}^{8} T_{si}}{8}$ K, $T_b = 0.5(T_{in} + T_{out}), A = \pi(D_{in}L)$, T_{in} is the inlet temperature of the fluid, T_{out} is the outlet fluid temperature of the fluid, T_s is the average wall temperature, T_b is the mean bulk fluid temperature, A is the inner surface area of the tube, L is the heated length of the tube, and D_{in} is the inner diameter of the tube.

Experiment-based average Nusselt number and friction factor are calculated as follows:

$$\overline{Nu} = \frac{\bar{h}D_{in}}{k} \quad \text{(eq. 4)}$$

$$f = \frac{\Delta P}{\frac{L}{D_{in}}\left(\frac{\rho V^2}{2}\right)} \quad \text{(eq. 5)}$$

The experimentally calculated Nusselt number is compared with the generalized Nusselt number correlation for hybrid nanofluid and is discussed in results and discussion. The deduced generalized Nusselt number correlation and Figure of Merit (FoM) taken from Upadhyay et al. (2021, 2022) are as follows:

$$Nu_{gen} = \underbrace{1.01\alpha_r^{0.08879}\phi^{0.0542}n^{-0.1482}}_{\eta} \underbrace{\left\{\frac{\frac{f}{8}(Re-1000)Pr}{1+12.7\sqrt{\frac{f}{8}}\left(Pr^{\frac{2}{3}}-1\right)}\right\}}_{\textit{Gnielinski correlation},\ Nu_{bf}} \quad \text{(eq. 6)}$$

$$FoM = \frac{Nu}{CP}, \text{ where } CP = \frac{\Delta P}{0.5\rho V^2}, \quad \text{(eq.7)}$$

2.3. Uncertainty Analysis

The various parameters like dimension, flow rate, temperature, and power input are measured by vernier caliper, turbine flowmeter, k-type thermocouple, and wattmeter, respectively. The uncertainty calculation for the dependent parameters such as Reynolds number, Prandtl number, heat transfer rate, convective heat transfer coefficient, Nusselt number, friction factor, coefficient of pressure, and Figure of Merit are calculated using the following eq. (8) (McClintock et al., 1953).

$$U_z = \left[\left(\frac{\partial Z}{\partial X_1} i_1\right)^2 + \left(\frac{\partial Z}{\partial X_2} i_2\right)^2 + \left(\frac{\partial Z}{\partial X_3} i_3\right)^2 + \ldots\ldots\ldots\ldots + \left(\frac{\partial Z}{\partial X_n} i_n\right)^2\right]^{\frac{1}{2}} \quad \text{(eq. 8)}$$

Where, $i_1, i_2, i_3, \ldots\ldots\ldots, i_n$ are the uncertainties of the independent variables, and Z is a function of the independent variables X_1, X_2, X_3,…, X_n.

Table 3. Uncertainty estimation for different experiment-based parameters

Parameters	**Uncertainty (%)**
Heat transfer rate	±2.8331
Reynolds number	±2.8372
Prandtl number	±3.4641
Convective heat transfer coefficient	±2.8402
Nusselt number	±3.474996
Pressure drop	±2.2362
Coefficient of pressure (*CP*)	±3.0099
Figure of merit (FoM)	±4.6581

2.4. Validation

The experiment-based average Nusselt number for pure TVP1 are compared with the Gnielinski correlation (see figure 4). The measured values are found well within ±10%. With the increasing Reynolds number from 7000 to 19000 the turbulent intensity increases. Consequently, the Nusselt number increases with the increasing Reynolds number, as expected.

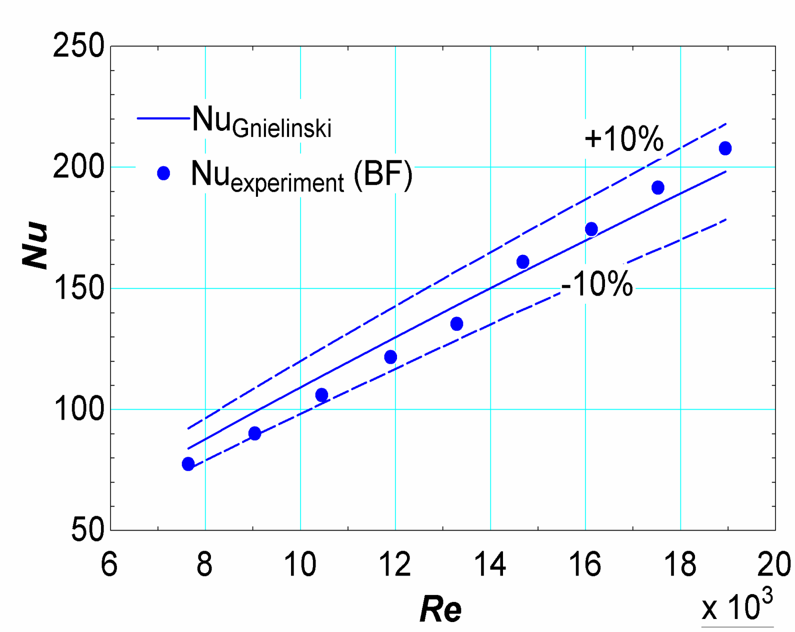

Figure 4. Comparison between the experiment-based Nusselt number and Friction factor with Gnielinski correlation

2. Results and discussion

3.1. Hybrid Nanofluid: Stability

Figure 5 displays the samples of pure TVP1 and Al_2O_3-CuO-TVP1 hybrid nano-oil. The stability of the hybrid nano-oil is assessed through visual inspection. Figure 5b to 5f presents the photograph of hybrid nano-oil that is captured at different time intervals immediately after preparation (day 0) and after one, two, three, and four days of preparation. In particular, until day 2 (Figure 5d), there is no practical visual evidence of nanoparticle sedimentation, indicating that the hybrid nano-oil remains stable during this period. However, after day 2, minor sedimentation becomes evident (see Figure 5d), suggesting some settling of nanoparticles in the fluid. Apart from visual inspection, the stability of the prepared hybrid nano-oil is also inspected by the concept of an isoelectric point (IEP). The IEP of Al_2O_3 is 9.1, and for CuO, it is 10, which are both significantly far away from the measured pH value of 5.1 for the hybrid nano-oil. This difference supports the stability of hybrid nano-oil. Furthermore, the experiments are conducted continuously, meaning that any sedimentation process occurring beyond day 2 is unlikely to affect the experimental outcome significantly. Therefore, the stability of the hybrid nano-oil throughout the experiment is reasonably assured, and the results obtained from the tests remain reliable.

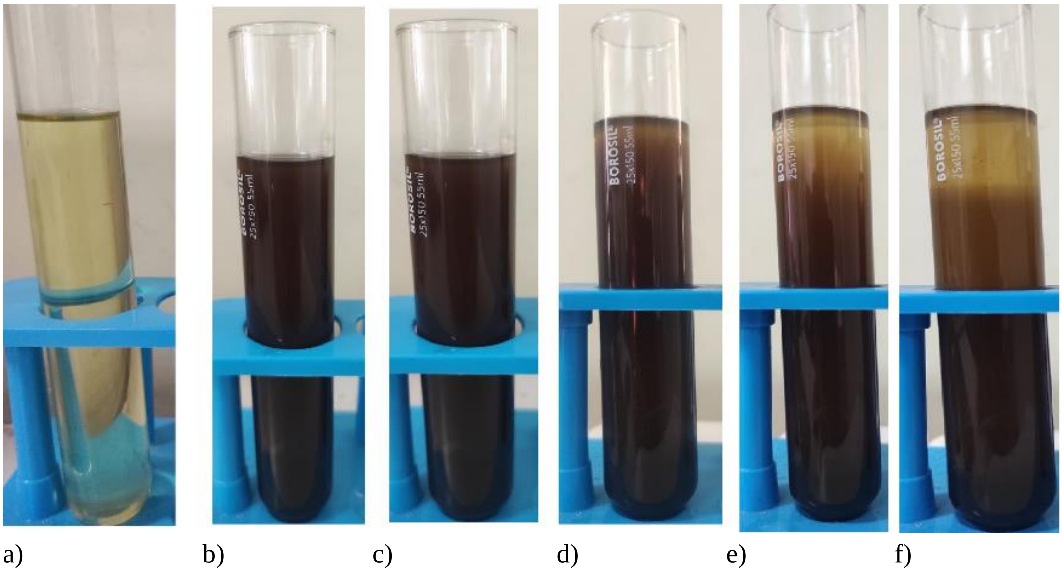

Figure 5. Photograph of a) TVP1, (b)-(f) 1% (V/V) Al_2O_3-CuO-TVP1 hybrid nano-oil after (b) day 0, (c) day 1, (d) day 2, (e) day 3 and (f) day 4.

3.2. Convective Heat Transfer Coefficient and Nusselt Number: Oil and Hybrid Nano-oil.

The experiments are conducted using a carefully prepared 1% (V/V) Al_2O_3-CuO-TVP1 hybrid nano-oil, with flow rates ranging from 10 to 26 LPM, increasing in increments of 2 LPM. The objective is to compare the heat transfer characteristics of pure TVP1 oil and the Al2O3-CuO-TVP1 hybrid nano-oil. Figure 6a illustrates the comparison of experiment-based surface-area averaged heat transfer coefficient for both fluids, while Figure 6b presents a similar comparison for the experimental calculated Nusselt number.

The results demonstrate notable improvements in both the surface-area averaged heat transfer coefficient and Nusselt number when using the hybrid nano-oil compared to pure oil. Specifically, the Nusselt number for the hybrid nano-oil increases by approximately 15% compared to pure oil. This enhancement in heat transfer performance indicates that the use of hybrid nano-oil can significantly improve the thermal efficiency of the system. Consequently, the surface area required for a Parabolic Trough Collector (PTC) absorber, which is the heart of PTC-based concentrated solar thermal system, can be reduced by about 15% for a given temperature difference and input power compared to pure oil. This reduction in surface area is a substantial benefit, as it can lead to cost savings and increased overall system performance for concentrated solar thermal systems. Thus, the use of hybrid nano-oil seems favorable for concentrated solar thermal systems. However, while the heat transfer benefits of the hybrid nano-oil are promising, one question remains: is the pressure drop favorable for the turbulent flow of the hybrid nano-oil? The pressure drop is a critical factor, and it is essential to consider the impact of pressure drop in the turbulent flow of the hybrid nano-oil. This is discussed subsequently.

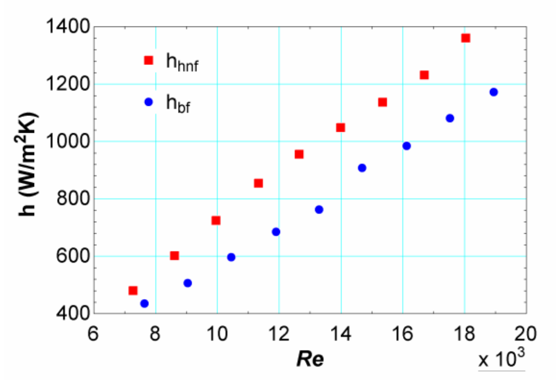

a)

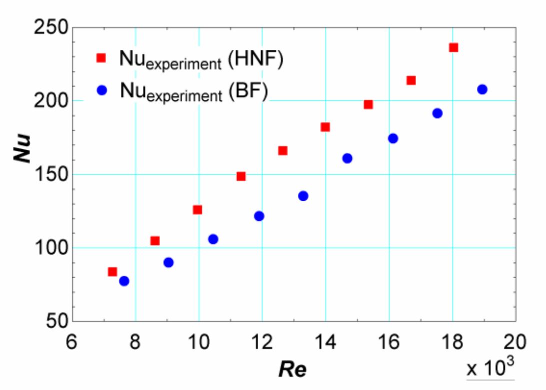

b)

Figure 6. a) Convective heat transfer coefficient and b) Nusselt number for TVP1 and Al_2O_3-CuO-TVP1 hybrid nano-oil.

3.3. Pressure drop: Oil and Hybrid Nano-oil

Figure 7 comprehensively compares the measured pressure drops between pure TVP1 oil and Al_2O_3-CuO-TVP1 hybrid nano-oil. The observations are twofold: (a) the pressure drop increases with the volume flow rate for both pure oil and the hybrid nano-oil, and (b) the turbulent flow of the Al_2O_3-CuO-TVP1 hybrid nano-oil experiences, on average, approximately 12% higher pressure drop compared to TVP1 across the considered volume flow rates. This suggests that using the hybrid nano-oil in the PTC absorber will necessitate a higher pumping power than the pure TVP1, indicating a disadvantage associated with using the hybrid nano-oil in terms of increased energy consumption for fluid circulation.

Despite the drawback of higher pumping power, it is vital to assess if there are any relative benefits in terms of heat transfer performance with the hybrid nano-oil compared to the pressure drop. To address this question, the proposed figure of merit (FoM = *Nu*/*CP*), where *Nu* represents the averaged Nusselt number and *CP* is the coefficient of the pressure of the fluid, is considered. These parameters are discussed subsequently for both pure oil and the hybrid nano-oil.

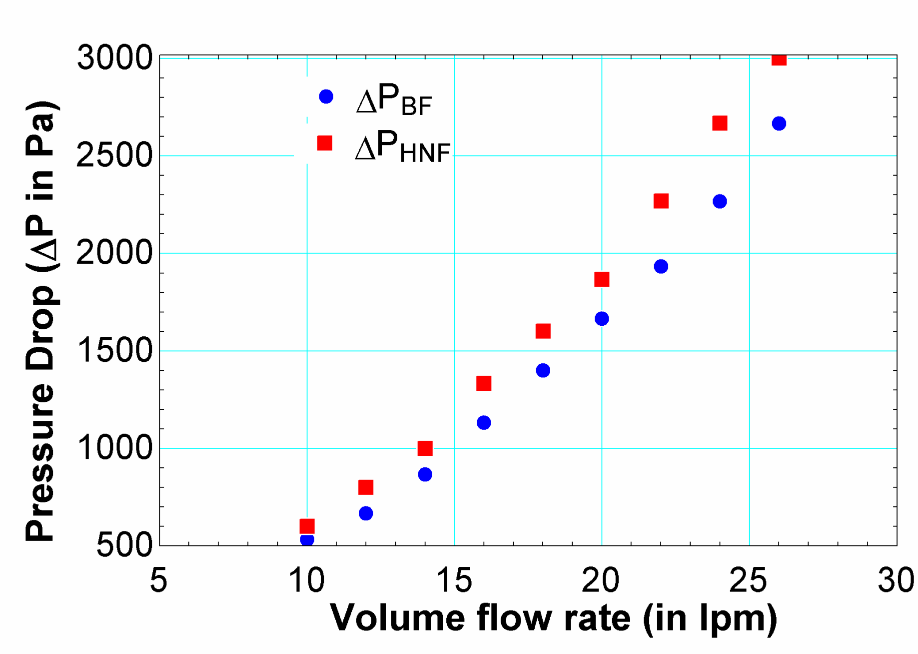

Figure 7. Pressure drop versus volume flow rate for TVP1 and Al_2O_3-CuO-TVP1 hybrid nano-oil.

3.4. Figure of Merit: Oil and Hybrid Nano-oil

A comprehensive analysis of the figure of merit (FoM) has been conducted to evaluate the performance of pure TVP1 oil and the Al_2O_3-CuO-TVP1 hybrid nano-oil for concentrated solar thermal systems. A non-dimensional parameter, viz. ratio of the Nusselt number to the coefficient of pressure ratio (*Nu/CP*), represented by the FoM, is plotted in Figure 8. This analysis aims to evaluate the relative benefits of using the hybrid nano-oil compared to pure oil in concentrated solar thermal systems. The findings from Figure 8 indicate that the experiment-based FoM for the hybrid nano-oil is approximately 5-6% higher than that of pure oil. This significant improvement in the FoM for the hybrid nano-oil implies, despite experiencing a higher pressure drop, that the hybrid nano-oil exhibits a significantly superior Nusselt number compared to the penalty incurred from the increased friction factor. Based on the comprehensive experimental investigation and the analysis of the FoM, it is concluded that the Al_2O_3-CuO-TVP1 hybrid nano-oil can be recommended as the preferred choice for PTC-absorber in comparison to pure TVP1 oil for PTC-based concentrated solar thermal systems.

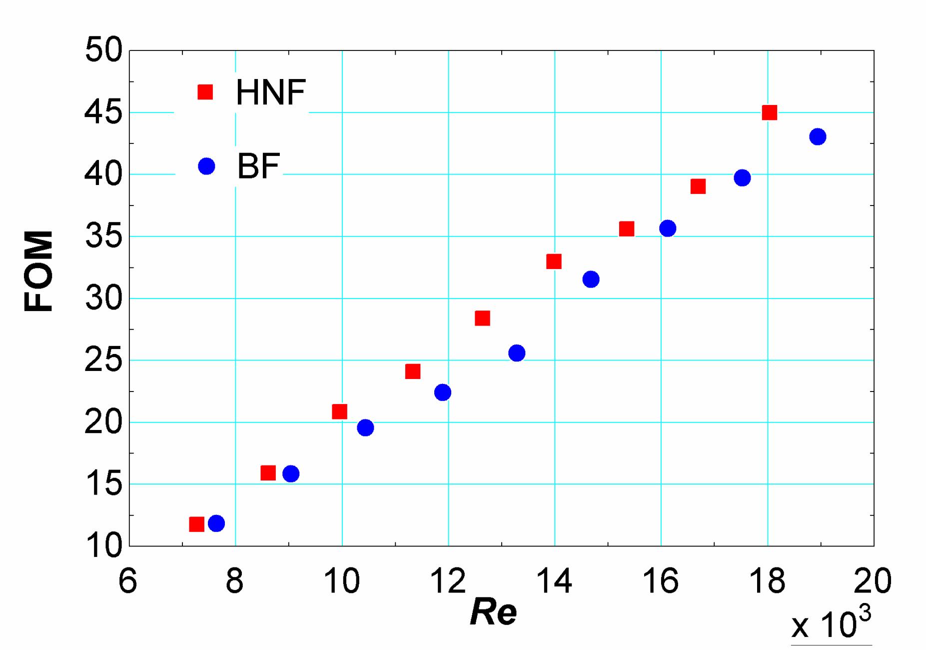

Figure 8. Figure of merit (FOM) versus Reynolds number for hybrid nano-oil 1% (V/V) of Al_2O_3-CuO-TVP1 and pure TVP1 oil.

3.5. Experimental Nusselt number comparison with Generalized Nusselt Number correlation

A thorough comparison between the experimentally determined Nusselt number and the predictions obtained using the generalized Nusselt number correlation (see eq. 6), has been conducted for the hybrid nano-oil under turbulent flow conditions. Figure 9 depicts the results of this comparison, demonstrating that the generalized Nusselt number correlation provides a reasonably good prediction of the experimentally obtained values, well within the proposed margin of ±15%, across the selected Reynolds number range. This in turn, indicates that the generalized Nusselt number correlation is indeed suitable for estimating the convective heat transfer coefficient for turbulent flow of hybrid nano-oil, which will serve as valuable input for the system-lelvel tool to assess the heat transfer with hybrid nano-oil. Therefore, the findings and the reported data will serve as a vehicle for researchers and engineers working on applications involving the turbulent flow of hybrid nano-oil for system design and analyses.

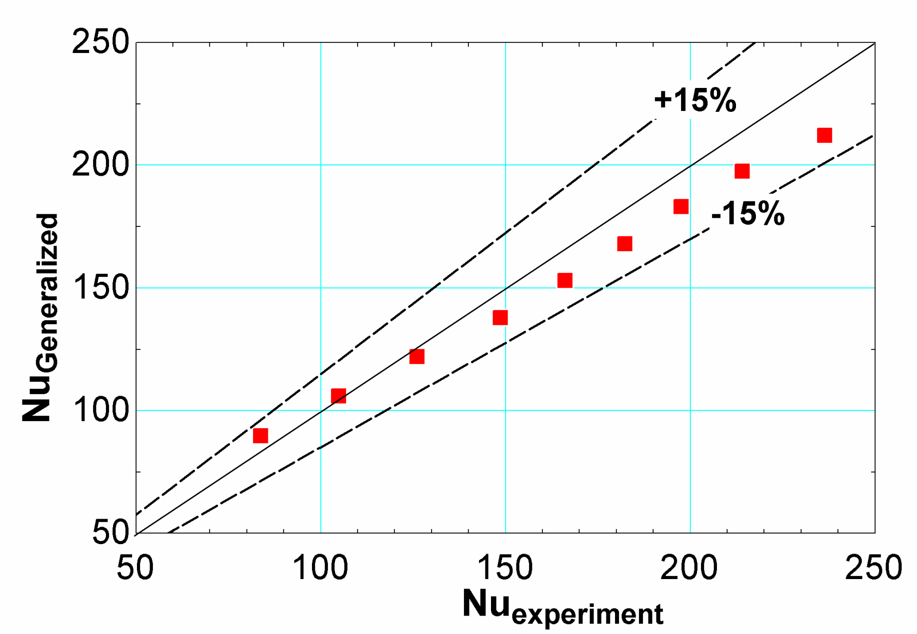

Figure 9. Comparison between experiment-based and generalized Nusselt number for hybrid nano-oil 1% (V/V) of Al_2O_3-CuO-TVP1.

3. Conclusions

This paper reports heat transfer experiments for turbulent flow of pure TVP1 and 1% (V/V) Al_2O_3-CuO-TVP1 hybrid nano-oil. The considered volume flow rates ranging from 10 to 26 LPM lead to Reynolds number in the range 7000 - 19000. The experimental setup involved a specially designed long, straight copper tube subjected to uniform heat flux conditions, simulating a parabolic trough absorber tube with secondary reflectors. The key findings and conclusions from these experiments are as follows:

- The hybrid nano-oil remained stable for up to 2 days, ensuring data reliability.
- Hybrid nano-oil exhibited a 15% improvement in surface area-averaged Nusselt number compared to TVP1, making it more efficient.
- However, hybrid nano-oil caused a 12% higher pressure drop, requiring more pumping power.
- The figure of merit (FoM = Nu/CP) for hybrid nano-oil was 5-6% higher than TVP1, indicating a favorable heat transfer-to-pressure drop ratio.
- It's recommended to use Al_2O_3-CuO-TVP1 hybrid nano-oil in parabolic trough absorbers for enhanced heat transfer and potentially reduced absorber length.
- The generalized Nusselt number correlation accurately predicted experimental values within ±15%, making it useful for analyzing heat transfer in the heated long tube.

Incorporating this correlation into system-level tools can enhance predictive capabilities for applications like the PTC absorber.

4. References

Gimeno-Furio et al., 2017. Stabilization and characterization of a nanofluid based on a eutectic mixture of diphenyl and diphenyl oxide and carbon nanoparticles under high temperature conditions. International Journal of Heat and Mass Transfer. 113, 908–913.

Klein, S. A., 2017. Engineering Equation Solver Professional Verison V10.215. F-chart Software Madison WI.

Krishna et al., 2018. State-of-the-art heat transfer fluids for parabolic trough collector. International Journal of Heat and Mass Transfer. 152, 119541.

Kumar, V., and Sarkar, J., 2019. Numerical and experimental investigations on heat transfer and pressure drop characteristics of Al2O3 -TiO2 hybrid nanofluid in minichannel heat sink with different mixture ratio. Powder Technology. 345, 717–727.

McClintock, F., and Kline, S., 1953. Describing uncertainties in single-sample experiments. Mech. Eng, 75. 3–8.

Mwesigye, A., and Meyer, J. P., 2017. Optimal thermal and thermodynamic performance of a solar parabolic trough receiver with different nanofluids and at different concentration ratios. Applied Energy. 193, 393–413.

Pak, B. C., and Cho, Y. I., 2013. Hydrodynamic and Heat Transfer Study of Dispersed Fluids with Submicron Metallic Oxide. Exp. Heat Transf. A J., Therm. Energy Transp., Storage, Convers. 11, 37–41.

Pranesh et al., 2019. A 50 year review of basic and applied research in compound parabolic concentrating solar thermal collector for domestic and industrial applications. Solar Energy. 187, 293-340.

Singh et al., 2005. Stability of dispersions of colloidal alumina particles in aqueous suspensions. Journal of Colloid Interface Sci. 291, 181–186.

Sousa, V. S., and Teixeira, M. R., 2013. Aggregation kinetics and surface charge of CuO nanoparticles: The influence of pH, ionic strength and humic acids. Environ. Chem., 10, 313–322, 2013.

Tang et al., 2021. A design method for optimizing the secondary reflector of a parabolic trough solar concentrator to achieve uniform heat flux distribution. Energy. 229, 120749.

Tiwari et al., 2021. A review on the application of hybrid nanofluids for parabolic trough collector: Recent progress and outlook. Journal of Cleaner Production. 292, 126031.

Upadhyay et al., 2021. A generalized Nusselt number correlation for nanofluids, and look-up diagrams to select a heat transfer fluid for medium temperature solar thermal applications. Applied Thermal Engineering. 190, 116469.

Upadhyay et al., 2022. Generalized Nusselt Number Correlation for Binary Hybrid Nano-Oils as Heat Transfer Fluid in Solar Thermal Systems. Journal of Heat and Mass Transfer ASME. 144, 1–10.

Vignarooban et al., 2015. Heat transfer fluids for concentrating solar power systems – A review. Applied Energy. 146, 383-396.

Xuan, Y., and Roetzel, W., 2000. Conceptions for heat transfer correlation of nanofluids. International Journal of Heat and Mass Transfer. 43, 3701–3707.

Investigating the Synergistic Effects of Cascaded ST-LHTES Unit and CEG with PCM on Thermal Performance: A Numerical Study

Narender Kumar[1], Chandrashekhar Bhardwaj[1] and Prodyut R. Chakraborty[1*]

[1] Indian Institute of Technology Jodhpur, Rajasthan (India)

[*] Corresponding Author

Abstract

Latent heat based thermal energy storage systems (LHTES) have gained interest for their high energy storage density and isothermal energy charging and discharging. However, challenges such as low thermal conductivity and performance enhancement must be addressed. The promising solution for this is using a cascading of PCMs combined with compressed expanded graphite (CEG). In this study, cascading is considered by employing two phase change materials (PCMs), Lithium Nitrate (PCM 1) and Solar Salt (PCM 2), arranged axially along the heat transfer fluid (HTF) flow direction (Therminol-66). Numerical simulations using ANSYS Fluent 2019 R2 is conducted to investigate the charging dynamics of a 2-D axisymmetric shell and tube LHTES unit. A volume fraction-updating scheme is used to study the melt fraction of PCMs in all cases. Moreover, the proposed model will analyze the exergy efficiency and effectiveness of LHTES.

Keywords: Latent Heat, Compressed Expanded Graphite, Cascading, Charging and Discharging

1. Introduction

With the global pursuit of sustainable alternatives to fossil fuels, the prominence of solar energy is rapidly surging as an increasingly favored option. However, efficient solar energy exploitation requires thermal energy storage (TES) to store surplus energy and supply it during shortages. Among the TES categories, latent heat thermal energy storage (LHTES) is the most suitable due to its high energy storing capacity under nearly isothermal conditions [Khan et al., 2016]. LHTES uses phase change materials (PCMs) that store or release latent heat energy during melting or solidification. However, one of the major constraint that limits its usage corresponds to its lower thermal conductivity which narrows down the rate of heat transfer and hinders their further significance [Wu et al., 2017]. In corresponds to refine the thermal capability, numerous techniques have been implemented to improve thermal conductivity, incorporating metal fins [Kumar and Verma, 2020], diffusing high conductivity nanoparticles [Colla et al., 2017], appending heat pipes [Zhao et al. 2016], PCM embedded in metal foam [Zheng et al., 2018] and compressed expanded graphite (CEG) [Mallow et al., 2016; Mills et al., 2006] to form a composite. Nevertheless, among the aforementioned approaches, incorporating phase change material (PCM) into composite encapsulated graphite (CEG) appears to be the most efficient strategy for enhancing thermal conductivity. This is primarily due to several benefits it offers, such as superior conductivity, enhanced thermal contact, cost-effectiveness, and ease of molding.

One other way to improve thermal performance is to cascade the thermal energy storage (CTES) systems, incorporating multiple phase change materials (PCMs), by ensuring a consistent temperature difference between the PCMs and the heat transfer fluid (HTF) in the direction of flow. To accomplish this, arrange PCMs during the charging process in decreasing order of their melting temperatures. CTES has shown superior storage performance compared to conventional LHTES systems that use a single PCM. Few studies have explored the benefits of cascaded PCM-based thermal energy storage (TES). Farid and Kanzawa (1989) and Farid et al. (1990) introduced the advantages of cascaded PCM TES and demonstrated significant overall performance improvements. Gong and Mujumdar (1996, 1997) study the effect of different PCM melting temperature arrangements with different thermo-physical properties and boundary conditions on charging and discharging processes. The results revealed that the charging-discharging rate improved by 35% for the multiple PCM units compared with the single PCM unit. Wang et al. (1999) proposed arranging multiple PCMs in a parabolic profile to reduce phase change time. Li et al. (2012) studied the exergy analysis of two phase change materials for solar thermal power and found that the melting temperatures of PCM1 and PCM2 have different influences on the overall exergy efficiency. Considering a wide gap in the literature, a numerical model is proposed that investigates the combined effect of cascading and CEG on LHTES.

10.18086/swc.2023.03.05 Available at http://proceedings.ises.org

2. Problem Statement

In the present work, the cycle dynamics of the 2-D axisymmetric shell and tube LHTES unit is investigated numerically. A dual approach is employed to enhance the performance of the storage unit. This involves cascading the LHTES unit and augmenting the effective thermal conductivity of the PCM through the incorporation of CEG while maintaining a constant volume constraint. A cascade of two PCMs is arranged axially along the flow direction of heat transfer fluid (HTF) to ensure the optimal utilization of the storage material. PCMs selected for energy storage are lithium nitrate (melting point: 253 °C) and solar salt which is a binary eutectic mixture of $NaNO_3$ and KNO_3 in the ratio of 60:40 by weight) (melting point: 238 °C). For heat transfer from source to PCM, Therminol-66 is selected as HTF. The arrangement of PCM is such that their melting temperature decreases along the HTF flow direction during charging. Cascading precisely addresses this concern by incorporating a second PCM (lower melting temperature), thereby maintaining the driving potential for heat transfer. An increase in the effective thermal conductivity of the PCM leads to a reduction in total melting time as well as performance enhancement of the LHTES unit. ANSYS Fluent 2019 R2 is used for the simulations, where the volume fraction-updating scheme will estimate the melt fraction of both PCMs. The energy conservation equation is considered diffusion-dominated in the PCM domain (due to the presence of the CEG matrix), while the k-ϵ model is adopted for turbulent flow in the HTF zone. The default energy equation and solidification/melting models available in Fluent solver is switched off; instead, a user defined scalar (UDS) is developed in C++ language for energy equation along with various UDFs for volume fraction updating scheme, anisotropic conductivity in PCM, velocity profile and source terms, and are hooked to ANSYS Fluent 2019 R2 solver.

Four Cases are considered for the study:

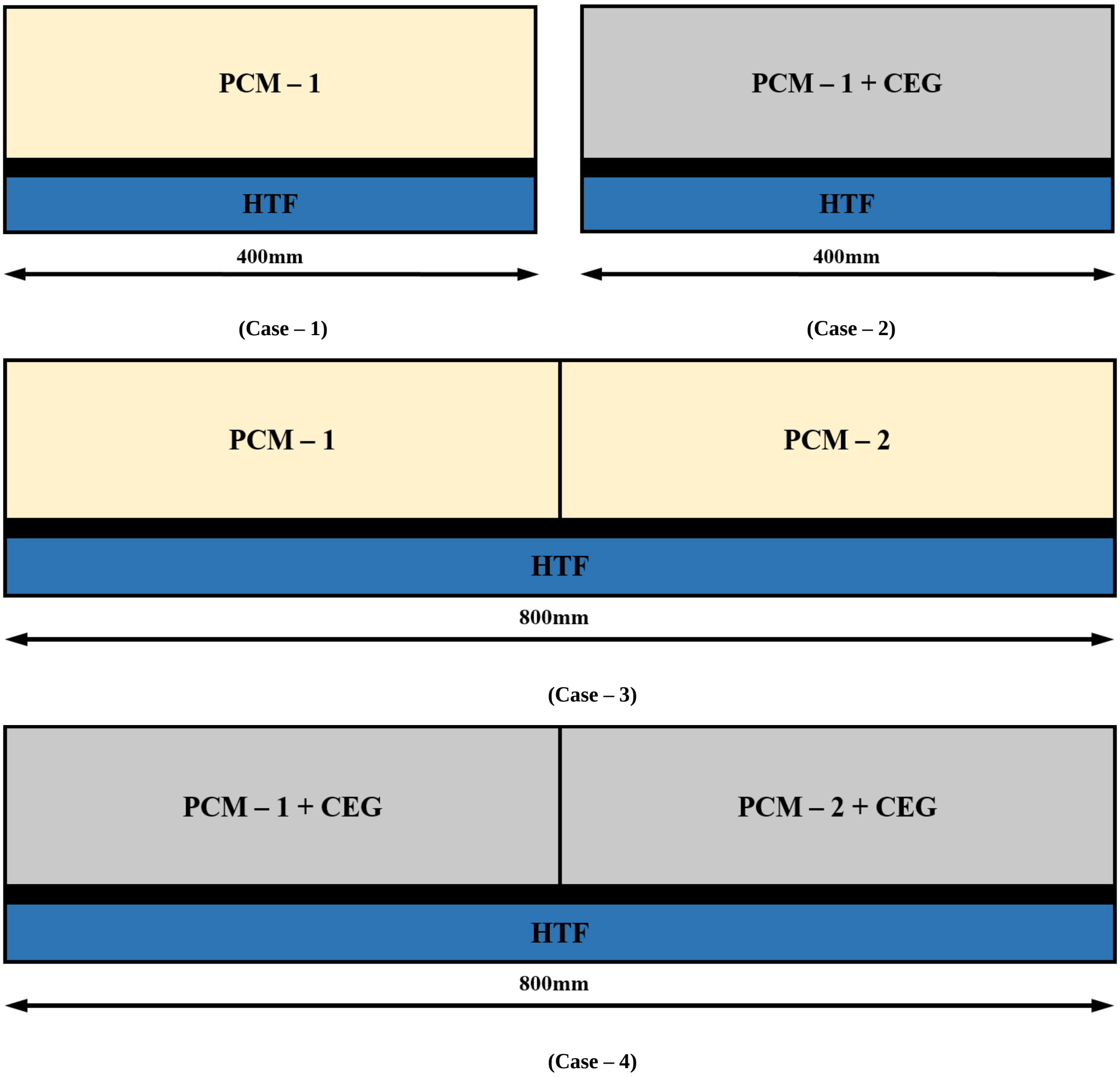

Fig. 1: Axisymmetric shell and tube LHTES unit for all four cases

As seen in Fig. 1, case - 1 and 2 are single PCM storage without CEG and with CEG respectively, and case – 3 and 4 are double cascaded storage unit without and with CEG respectively.

The analysis will be helpful to design LHTES unit for thermal energy storage applications considering volume constraints where multiple enhancement techniques are included simultaneously. The size of the domain is crucial for analysis, being viewed as a specific component within the ST-type latent heat storage unit. This unit comprises 100 tubes, all of the same size, and the shell side is also assumed to be identical to that of the storage unit.

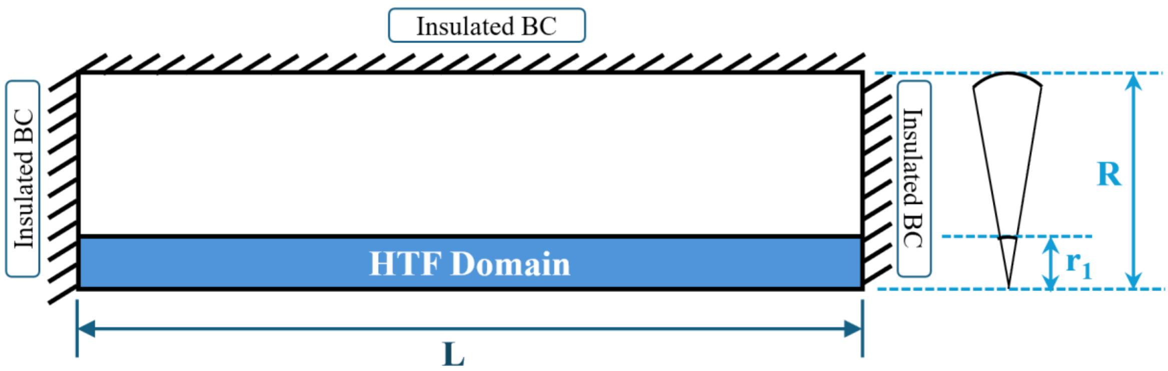

Fig. 2: Boundary conditions of the domain

L = 400 mm, R = 16.86 mm, r_1 = 4.62 mm

Tab. 1: Initial Conditions and Boundary Conditions

	PCM	HTF
Initial Conditions	T(x,r,0) = 237 °C, $[r_1 \leq r \leq R]$	T(x,r,0) = 237 °C , $[0 \leq r \leq r_1]$
Boundary Conditions	$(\frac{dT}{dx})_{(0,r,t)} = 0$, $[r_1 \leq r \leq R]$ $(\frac{dT}{dx})_{(L,r,t)} = 0$, $[r_1 \leq r \leq R]$ $(\frac{dT}{dr})_{(x,R,t)} = 0$, $[0 \leq x \leq L]$	T(0,r,t) = T_in °C, $[0 \leq r \leq r_1]$

Tab. 2: Properties of PCMs

The properties of $LiNO_3$ are sourced from Mohamed et al. (2016), while the properties of Solar Salt are referenced from Iverson et al. (2012) and EG from Xia et al. (2010). All properties are at temperature 30 °C.

PCM	Melting Temperature (°C)	Heat of Fusion(kJ/kg)	Thermal conductivity (W/m-K)	Density (kg/m³)	Specific heat (J/kg-K)	
					Solid	Liquid
$LiNO_3$	253	373	0.51	2380	1688.5465	2015.1447
Solar Salt	238	109.8	0.5	1938.625	1850	1550
EG	-	-	25	270	690	719

Tab. 3: Properties of Therminol-66 (HTF)

Operating Temperature(°C)	Density (kg/m³)	Specific Heat(J/kg-K)	Thermal conductivity (W/m-K)	Dynamicviscosity (N-s/m²)
300	809	2570	0.0946	0.000413

3. Modelling

3.1. Assumptions

- Assuming PCM domain as 2-D axisymmetric.
- Diffusion heat transfer is dominated within the PCM domain.
- The effect of shrinkage in PCM is neglected.
- Axial heat conduction in HTF is neglected and is justified by high L/D ratio of the pipe.

- HTF does not change its phase.
- Materials properties are kept constant.
- Buoyancy (gravity) is not considered.

3.2. Mathematical Modelling

A mathematical model has been developed to investigate the heat transmission and charging characteristics in a horizontal shell and tube LHTES system for single unit and cascading system. The numerical modelling of phase change processes presents challenges due to the intricate interplay of thermal energy transfer between the PCM and HTF domain. Moreover, it is essential to address the nonlinear effects resulting from the absorption or release of substantial latent heat, along with addressing the transient properties arising from the motion of the solid-liquid interface. In the context of multiphase transport phenomena, Bennon and Incropera (1987) introduced a comprehensive conservation equation utilizing a fixed-grid volume averaging technique. The energy conservation equation within the CPCM is expressed as follows:

$$\left(1-g_g\right)(\rho_{PCM}c_{ps})\frac{\partial T}{\partial t} = \nabla.(k\nabla T) - (\rho_{PCM}h_{sl})\frac{\partial g_l}{\partial t} - \rho_{PCM}(c_{pl}-c_{ps})\frac{\partial}{\partial t}[g_l(T-T_m)] - (\rho_g c_{pg} g_g)\frac{\partial T}{\partial t} \qquad \text{(eq. 1)}$$

Where, g, h, k, ρ, and T represents volume fraction, specific enthalpy, thermal conductivity, mass density and temperature respectively. Subscripts g, pcm, s and l stand for graphite, PCM, solid phase and liquid phase present in PCM-Graphite composite. Since shrinkage during slid-liquid phase transition is neglected, $\rho_l = \rho_s = \rho_{PCM} \neq \rho_g$, and the volume averaged density of PCM-Graphite composite is represented as $\rho = g_l\rho_l + g_s\rho_s + g_l\rho_l + g_g\rho_g$. For solid and liquid phases of PCM, and graphite, the specific enthalpies are defined as: $h_s = c_{ps}T$, $h_l = c_{ps}T_m + h_{sl} + c_{pl}(T-T_m)$ and $h_g = c_{pg}T$ respectively. The volume fraction of PCM in the PCM-graphite composite is identical to pore volume fraction in CEF foam and given by $\varepsilon = 1 - g_g = g_l + g_s$. Here we define a field parameter φ_l, defined as $\varphi_l = g_l/\varepsilon$. Here, we define a field parameter φ_l essentially represents the melt fraction () within the pore and varies within the range $0 \leq \varphi_l \geq 1$.

Now, for the HTF in the circular pipe; the 1- D energy conservation equation proposed by Morisson, et al. (2008) is as follows:

$$\rho_f\frac{\partial}{\partial t}\left(c_{pf}T_f\right) + \dot{G}\frac{\partial}{\partial x}\left(c_{pf}T_f\right) = \frac{2}{r}h(T_{wall}-T_f) \qquad \text{(eq. 2)}$$

Where, h is convective heat transfer coefficient between HTF and wall of the pipe (A constant value of 1000 W/(m^{2}K) is assumed, with further elaboration provided by Morisson et al. (2008)), the subscript f is for the heat transfer fluid (HTF), $\dot{G}$ is the mass flux (kg/m^2 s) and r denotes the radius of pipe.

3.3. Energy Analysis

The rate of actual heat transfer $\dot{Q}_{act}$ (W) from HTF to heat storage unit for single and cascaded unit respectively was calculated by the following equation:

In case of single storage unit:

$$\dot{Q}_{act} = \dot{m}_f c_{pf}(T_{in} - T_{out}) \qquad \text{(eq. 3)}$$

In case of double storage (cascaded TES) unit:

$$\dot{Q}_{act} = \dot{m}_f c_{pf}\{(T_{in1} - T_{out1}) - (T_{in2} - T_{out2})\} \qquad \text{(eq. 4)}$$

As the outlet temperature of the first storage is the inlet of the second, (i.e. $T_{out1} = T_{in1}$)

$$\dot{Q}_{act} = \dot{m}_f c_{pf}(T_{in1} - T_{out2}) \qquad \text{(eq. 5)}$$

The rate of maximum heat transfer $\dot{Q}_{max}$ (W) from HTF to heat storage unit was calculated by the following equation:

In case of single storage unit:

$$\dot{Q}_{max} = \dot{m}_f c_{pf}(T_{in} - T_m) \qquad \text{(eq. 6)}$$

In case of double storage (cascaded TES) unit:

$$\dot{Q}_{max} = \dot{m}_f c_{pf}\{(T_{in1} - T_{m1}) - (T_{in2} - T_{m2})\} \qquad \text{(eq. 7)}$$

As the outlet temperature of the first storage is the inlet of the second, (i.e. $T_{in2} = T_{m1}$) therefore we can write:

$$\dot{Q}_{max} = \dot{m}_f c_{pf}(T_{in1} - T_{m2}) \qquad \text{(eq. 8)}$$

The heat transfer analysis of TES is quite similar to that of a heat exchanger, where heat transfers between HTF and PCM. Therefore, the effectiveness of the charging processes in the LHTES can be found as the ratio of the actual heat transfer to the maximum

$$\varepsilon = \frac{\dot{Q}_{act}}{\dot{Q}_{max}} \qquad \text{(eq. 9)}$$

For single PCM unit:

$$\varepsilon = \frac{\dot{m}_f c_{pf}(T_{in} - T_{out})}{\dot{m}_f c_{pf}(T_{in} - T_m)} \qquad \text{(eq. 10)}$$

For double PCM unit:

$$\varepsilon = \frac{\dot{m}_f c_{pf}(T_{in1} - T_{out2})}{\dot{m}_f c_{pf}(T_{in1} - T_{m2})} \qquad \text{(eq. 11)}$$

The actual heat transfer rate is calculated according to the difference in HTF inlet and outlet temperature in both (i.e. single as well as in double PCMs unit) cases. However, the calculation of maximum heat transfer rate assumes that; the HTF outlet temperature approaches towards the minimum temperature of the system (i.e., melting temperature of PCM). In the case of cascading, the minimum melting temperature PCM is placed at the end of the system, which also ensures that the HTF temperature would be minimum. Thus, the effectiveness of the system is calculated by eq. 10 and eq. 11 for the single and cascaded storage unit.

4. Results and Discussion

In the present numerical analysis, four different cases are considered and simulations are performed to obtain melting fraction, isothermal plot, HTF outlet temperature versus time plot, average temperature of PCMs and for the efficiency analysis.

Case 1: Pure Lithium Nitrate ($LiNO_3$) is used as PCM in LHTES.

Case 2: Composite PCM ($LiNO_3$ + 11.11% graphite) is used for thermal energy storage in LHTES.

Case 3: Cascaded system of energy storage; $LiNO_3$ as PCM-1 and Solar salt as PCM-2, are considered for the analysis.

Case 4: Cascaded system of energy storage; PCM-1 ($LiNO_3$ + 11.11% graphite) and PCM-2 (Solar salt + 11.11% graphite) are considered for the analysis.

All the cases were simulated for different HTF inlet conditions (T_{in} = 300, 280, 260 °C).

4.1. Effect of Graphite

Comparison between case-1 & 2 and case-3 & 4 is done after 500 seconds of each case to show the effect of anisotropy in thermal conductivity of PCM composite on charging.

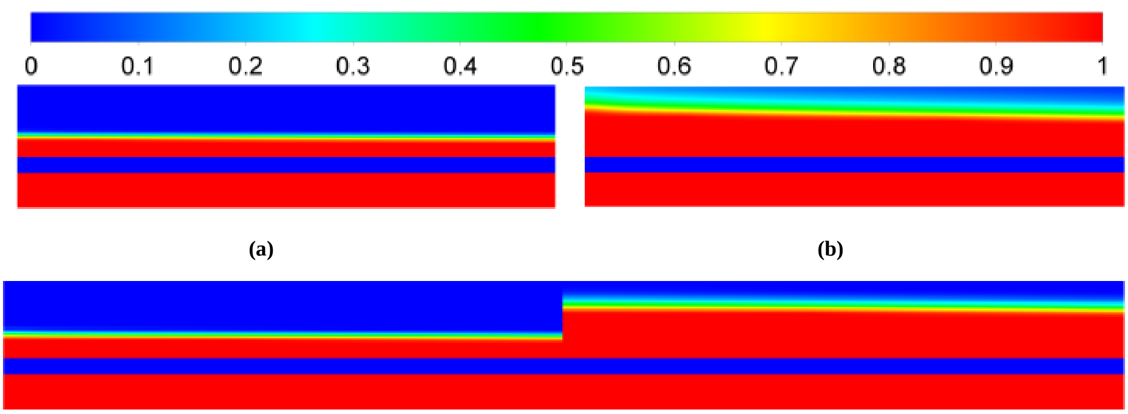

(a) (b)

(c)

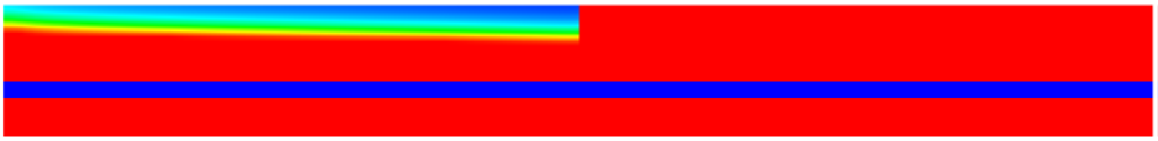

(d)

Fig. 3: Melt contours after 500 seconds; (a) Case-1, (b) Case-2, (c) Case-3 and (d) Case-4

Fig. 3 corresponds to the melt front of the PCM after 500 seconds when the inlet temperature is 300 °C. In Fig. 3 (a, c), PCM is not incorporated with graphite, while in Fig. 3 (b, d) graphite is incorporated in PCM. The incorporation of graphite renders the anisotropic in the PCM domain; from the Fig. 3 (b, d) it is clear that the radial thermal conductivity in the composite is higher as compared to the axial direction thermal conductivity. In addition, the melt fraction is higher for the cases that contain graphite. The single PCM and cascaded LHTES unit, both shows a higher melt rate with graphite. Case-2 shows the significant rise in melt fraction as compare to case-1, and similarly, the same result can be seen between case-3 and case-4. The presence of graphite in the PCM domain significantly increases the composite's thermal conductivity, resulting in an improvement in the melting rate of PCM.

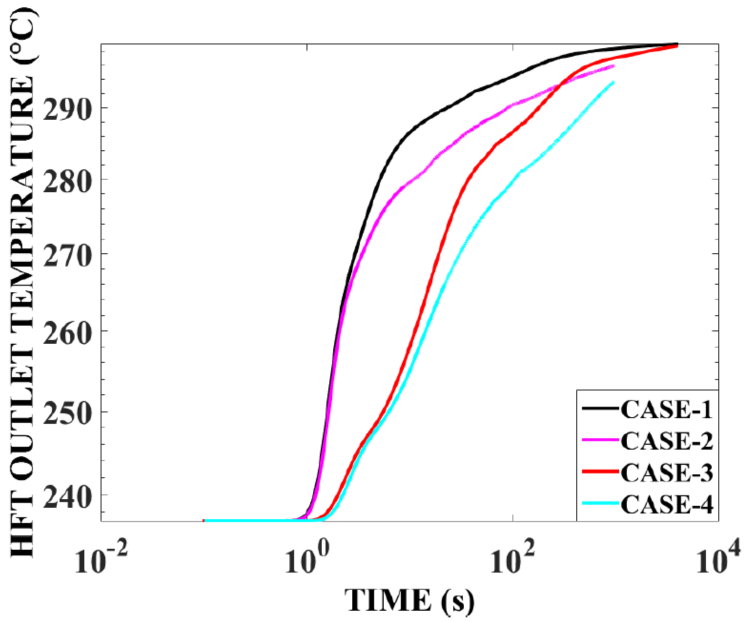

Fig. 4: HTF outlet temperature of different cases

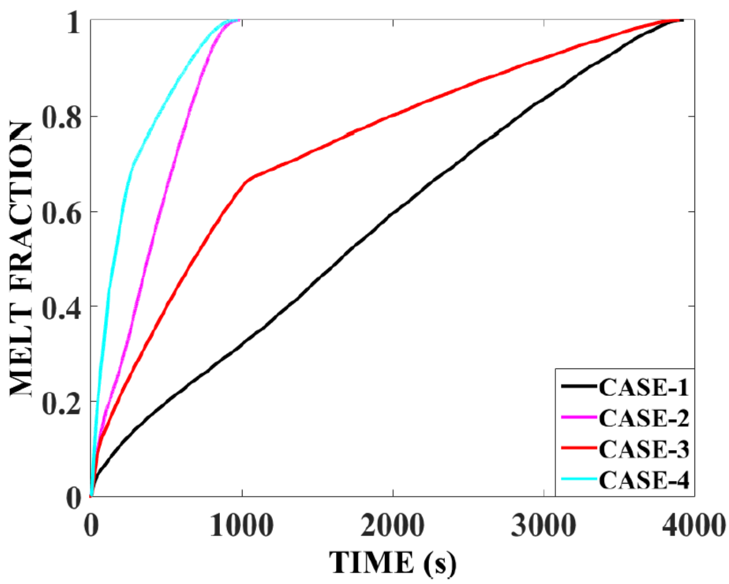

Fig. 5: Melt fraction vs Time

Fig. 4 shows the temperature profile of HTF at the outlet of the pipe with respect to time. It can be observed that the increase of the HTF temperature at the outlet is less in the case of, the enhanced thermal conductivity of the composite, the PCM with graphite. In case-2 and case-4, the HTF outlet temperature is lower as compared to case-1 and case-3, respectively. The lowering in temperature is due to the higher thermal conductivity of the composite PCM, which augment the heat transfer rate from HTF to PCM.
The melting rate of the PCM is also a parameter to measure the performance of the LHTES; a higher melting rate means an enhancement in heat transfer rate, which results in an increase in heat storage rate. Fig. 5 shows the melt-fraction profile of the PCM domain with respect to time. In case-2 and case-4, the melting of PCM is completed before case-1 and case-3, respectively, with a significant marginal of time. This shows the reduction in time to complete the charging process due to incorporation of graphite.

4.2. Effect of Cascading

Comparison between case-1 & 3 and case-2 & 4 is done to show the effect of cascading. Case- 3 and 4 correspond to the cascading of the LHTES, without graphite and with graphite, respectively.

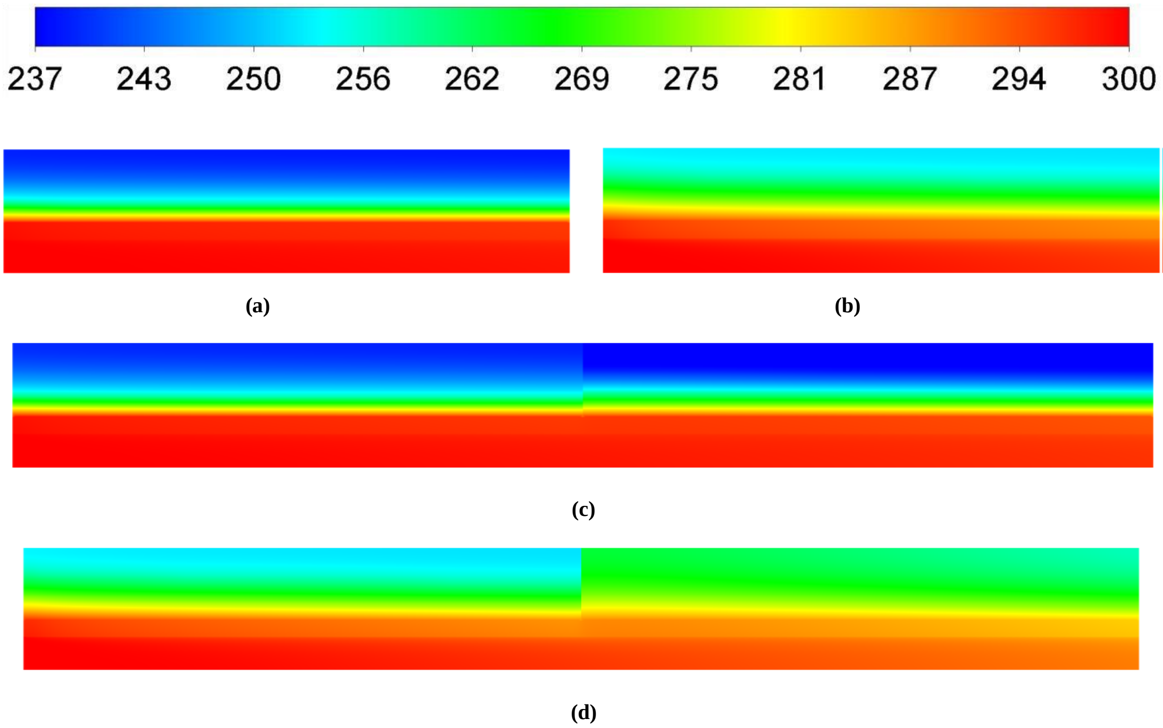

Fig. 6: Temperature contours after 500 seconds; (a) Case-1, (b) Case-2, (c) Case-3 and (d) Case-4

The incorporation of the second storage unit with a low melting temperature of PCM recovers the loss of heat through HTF. The lower melting temperature of the second PCM increases the temperature difference between the HTF and the average temperature of PCM, which results in the augmentation of the driving potential of the heat transfer. Fig. 6 shows the temperature contours of the PCM after 500 seconds when the inlet temperature is 300 °C. Fig. 6 (c, d) represents the cascading results of the part a & b (i.e., case1 and 2), respectively. It can be observed that the temperature contours of the first storage unit of both the cases c and d are almost the same as that of the respective single PCM storage unit cases a & b. This shows the equal temperature rise in storage units, and then the second storage unit additionally accepts the heat from the HTF, which results in a temperature drop of the HTF, consequently the recovery of the heat loss.
In addition to that, in Fig. 3, the melt front of the first storage unit of the part a & c and part b & d are almost alike; this means the melting rate of first storage is the same while the addition of second storage stores the part of the remaining leaving energy. The addition of a second storage unit does not affect the total melting time, as shown in Fig. 5, because the PCM-2 (which has a lower melting temperature) completely melts before PCM-1 as shown in Fig. 7 for case-4 at 300 °C inlet temperature.

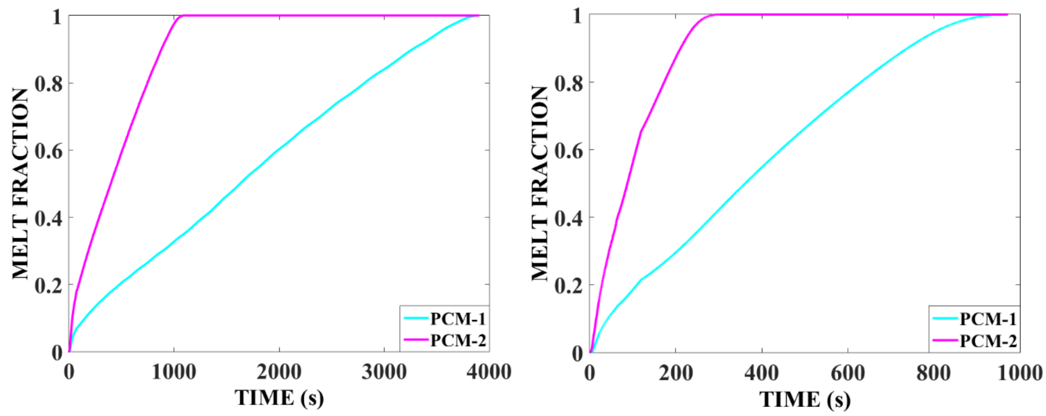

(a) (b)

Fig. 7: Melt fraction vs time; (a) case-3 & (b) case-4

4.3. Effect of Inlet Temperature

In this section, the effect of different inlet temperatures is shown in Fig. 8. The inlet temperature of the HTF mainly increases the charging rate of the LHTES.

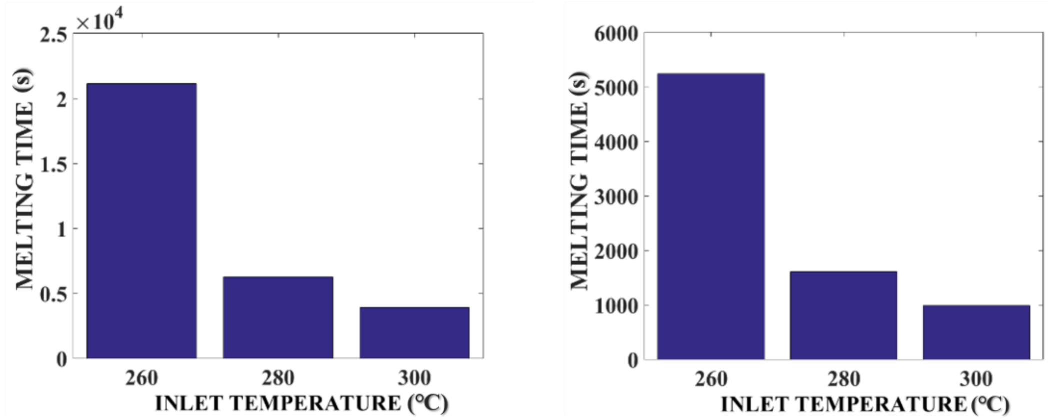

(a) (b)

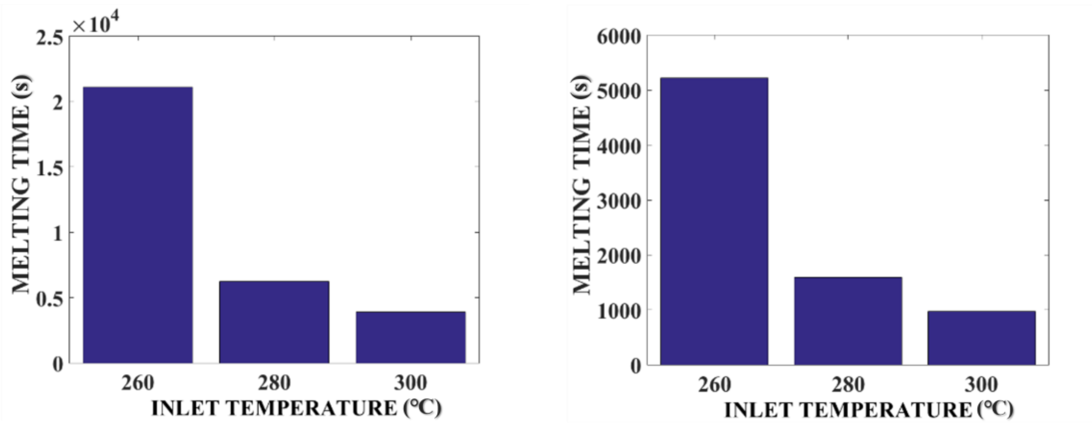

(c) (d)

Fig. 8: Illustration of effect of intel temperature on melting time

Fig. 8 illustrates that high inlet temperature reduces the complete melting time of PCM. The HTF with high inlet temperature enters with greater amount of thermal energy and as the temperature, difference between HTF and PCM is more; the driving potential of heat transfer also more. Thus, the melting time is less in the all the cases for inlet temperature of 300 °C followed by 280 °C and 260 °C.

5. Conclusion

The numerical simulation investigates the charging dynamics of the 2-D axisymmetric shell and tube LHTES unit. In order to enhance the heat transfer rate, which reduces the melting time, graphite is incorporate in PCM, and another LHTES unit is added (cascading) to reduce the thermal energy loss. Cascading is achieved by employing two PCM’s, arranged axially along the flow direction of heat transfer fluid (HTF) which is Therminol-66. PCMs selected for the energy storage are Lithium Nitrate (PCM 1) and Solar salt (PCM 2).
The analysis shows the increase in melting rate due to the enhancement of thermal conductivity of the PCM composite. The anisotropy in the thermal conductivity of composite PCM, as graphite is incorporated, renders the heat transfer in the PCM domain. The thermal conductivity in the radial direction is greater than the axial direction; therefore, the melting rate is more in the radial direction.

The cascading of LHTES reduces the energy loss at the high HTF inlet temperature. However, the cascaded LHTES unit reduces the effectiveness at lower HTF inlet temperature. The lower inlet temperature diminishes the driving potential of heat transfer due to the decrease in temperature difference between HTF and PCM; consequently, the effectiveness of the LHTES decreases.

The inlet temperature significantly affects the charging time of the LHTES. The higher inlet temperature increases the temperature difference between HTF and PCM, which increases the heat transfer potential of the system, consequently, the charging time of the LHTES reduces.

6. References

Bennon, W.D. and Incropera, F.P., 1987. A continuum model for momentum, heat and species transport in binary solid-liquid phase change systems—I. Model formulation. International Journal of Heat and Mass Transfer, 30(10), 2161-2170.

Colla, L., Fedele, L., Mancin, S., Danza, L., Manca, O., 2017. Nano-PCMs for enhanced energy storage and passive cooling applications. Applied Thermal Engineering. 110, 584-589.

Farid, M. M., Kanzawa, A., 1989. Thermal performance of a heat storage module using PCM’s with different melting temperatures: mathematical modeling. Journal of Solar Energy Eng. 111, 152-7.

Farid, M. M., Kim, Y., & Kansawa, A., 1990. Thermal performance of a heat storage module using PCM’s with different melting temperature: experimental. Journal of Solar Energy Eng. 112, 125-31.

Gong, Z. X., & Mujumdar, A. S., 1996. Enhancement of energy charge-discharge rates in composite slabs of different phase change materials. International Journal of Heat and Mass Transfer. 39(4), 725-733.

Gong, Z. X., & Mujumdar, A. S., 1997. Thermodynamic optimization of the thermal process in energy storage using multiple phase change materials. Applied Thermal Engineering. 17(11), 1067-1083.

Iverson, B.D., Broome, S.T., Kruizenga, A.M. & Cordaro, J.G., 2012. Thermal and mechanical properties of nitrate thermal storage salts in the solid-phase. Solar Energy, 86(10), 2897-2911.

Khan, Z., Khan, Z., & Ghafoor, A., 2016. A review of performance enhancement of PCM based latent heat storage system within the context of materials, thermal stability and compatibility. Energy conversion and management. 115, 132-158.

Kumar, R., & Verma, P. 2020. An experimental and numerical study on effect of longitudinal finned tube eccentric configuration on melting behaviour of lauric acid in a horizontal tube-in-shell storage unit. Journal of Energy Storage. 30, 101396.

Lachheb, M., Adili, A., Albouchi, F., Mzali, F. & Nasrallah, S.B., 2016. Thermal properties improvement of lithium nitrate/graphite composite phase change materials. Applied Thermal Engineering, 102, 922-931.

Li, Y. Q., He, Y. L., Wang, Z. F., Xu, C., & Wang, W., 2012. Exergy analysis of two phase change materials storage system for solar thermal power with finite-time thermodynamics. Renewable Energy. 39(1), 447-454.

Mallow, A., Abdelaziz, O., & Graham Jr, S., 2016. Thermal charging study of compressed expanded natural graphite/phase change material composites. Carbon. 109, 495-504.

Mills, A., Farid, M., Selman, J. R., & Al-Hallaj, S., 2006. Thermal conductivity enhancement of phase change materials using a graphite matrix. Applied thermal engineering. 26(14-15), 1652-1661.

Morisson, V., Rady, M., Palomo, E. & Arquis, E., 2008. Thermal energy storage systems for electricity production using solar energy direct steam generation technology. Chemical Engineering and Processing: Process Intensification, 47(3), 499-507.

Wang, J., Chen, G., & Jiang, H., 1999. Theoretical study on a novel phase change process. International journal of energy research. 23(4), 287-294.

Wu, W., Yang, X., Zhang, G., Chen, K., & Wang, S., 2017. Experimental investigation on the thermal performance of heat pipe-assisted phase change material based battery thermal management system. Energy Conversion and Management. 138, 486-492.

Xia, L., Zhang, P., & Wang, R. Z., 2010. Preparation and thermal characterization of expanded graphite/paraffin composite phase change material. Carbon, 48(9), 2538-2548.

Zhao, J., Rao, Z., Liu, C., & Li, Y., 2016. Experiment study of oscillating heat pipe and phase change materials coupled for thermal energy storage and thermal management. International Journal of Heat and Mass Transfer. 99, 252-260.

Zheng, H., Wang, C., Liu, Q., Tian, Z., & Fan, X., 2018. Thermal performance of copper foam/paraffin composite phase change material. Energy conversion and management. 157, 372-381.

Levelized electricity cost reduction of a 1 MWe multi-field solar thermal power plant

[1]Irfan Shaikh and [1]Anish Modi

[1]Department of Energy Science and Engineering, Indian Institute of Technology Bombay, Powai, Mumbai 400076, Maharashtra, India

Abstract

A levelized cost of electricity (LCOE) reduction opportunity for a 1 MWe multi-field solar thermal power plant in Jodhpur, India, without thermal storage has been identified and proposed. To generate useful heat, a multi-field solar thermal power plant utilizes two distinct concentrating solar fields—a parabolic trough collector and a linear Fresnel reflector. Feedwater from the power block in a parabolic trough solar thermal power plant is preheated using the cost-intensive parabolic trough collectors. A linear Fresnel reflector has been included for partial feedwater preheating to improve electricity generation economics. The linear Fresnel reflector solar collector field utilizes a saturated vapour at 250 °C and 40 bar pressure to preheat the incoming feedwater from 46.5 °C to 150 °C before entering the primary preheater. Techno-economic modelling and simulation were conducted using TRNSYS, and the levelized cost of electricity was reduced by 5% compared to the configuration without a feedwater heater.

Keywords: Linear Fresnel reflector, levelized cost of electricity, multi-field, parabolic trough collector

1. Introduction

Solar thermal power plant (STPP) technology has gained popularity worldwide for cleaner electricity generation. This is evident with a noted cumulative increase of six times the global STPP installations in the last decade (Feldman et al., 2021). The weighted average levelized cost of electricity (LCOE) has also come down by 68% over the past ten years, according to the International Renewable Energy Agency (IRENA, 2021). Globally, the most commercially implemented concentrating solar power (CSP) technology is the parabolic trough collector (PTC) that employs heat transfer fluid oil (Therminol VP-1) (Islam et al., 2018). Linear Fresnel reflector (LFR) is categorized as another line-focused CSP technology used to generate direct saturated steam.

Nomenclature

A_{ap}	aperture area of the collector (m^2)
C	cost of the system ($ or $ kWe or $ m^{-2})
CRF	capital recovery factor
d	discount rate
E	net electric energy (kWh)
h	enthalpy (J kg^{-1})
I	direct normal irradiance (W m^{-2})
LCOE	levelized cost of electricity ($ kWh^{-1})
$\dot{m}$	mass flow rate (kg s^{-1})
P	pressure (bar)
$\dot{Q}$	collector useful heat (W)
T	temperature (°C)
U	overall heat transfer coefficient (W m^{-2} K^{-1})

10.18086/swc.2023.03.11 Available at http://proceedings.ises.org

$\dot{W}$	Net electric power (W)
Greek symbols	
η	efficiency
Subscripts	
col	collector
d	design value
i	inlet
l	loss
m	mean
o	outlet
opt	optical

LFR collectors are considered economical in capital investment due to the ease of manufacturing slightly curved mirrors with ground installation and operation and maintenance costs due to simple stationary receivers and pipe joints (Hussain et al., 2017). However, the optical efficiency of the LFR collectors is less compared to PTC due to higher optical losses and tracking errors of the mirrors installed with reference to stationary receivers (Gunther, 2011). Intending to reduce the levelized cost of electricity (LCOE), several researchers have put forth innovative configurations and conducted a techno-economic analysis to compare a PTC and LFR-based STPP for electricity generation. Manzolini et al. (2011) conducted a steady-state design simulation of an STPP utilizing a novel configuration of a PTC solar field and molten salt as heat transfer fluid (HTF) to exploit direct and indirect steam generation. The innovation configuration resulted in a 6.5% cost decrease compared to the base scenario PTC STPP, indicating a potential path to lower LCOE.

Giostri et al. (2012) studied a performance comparison of different PTC STPP with different HTF (Therminol VP-1 and molten salt) with an innovative hybrid direct steam generation (DSG) and different HTF-based STPP. This study has reported that a hybrid DSG–-molten salt STPP increases solar-to-electricity conversion efficiency compared to alternative configurations due to its higher power block efficiency. A techno-economic comparison was conducted by Giostri et al. (2013) between PTC (indirect steam generation) and LFR (a combination of indirect and direct steam generation) configurations. This study concludes that the specific investment cost of the LFR technology must be halved compared to PTC to be cost-competitive. The leading cause is the decreased optical efficiency of the single-field LFR collectors utilized in the DSG process, which lowers the power plant's total efficiency. To realize the cost-benefit of a low-cost LFR collector compared to PTC, a multi-field STPP was proposed under the initiative of the Indian Institute of Technology Bombay and the Ministry of New and Renewable Energy (MNRE), India, in 2009. In the vicinity of New Delhi, India, a 1 MWe multi-field STPP comprising LFR and PTC solar fields and a superheated steam Rankine cycle-operated power block were commissioned and installed (Nayak et al., 2015). Desai and Bandyopadhyay (2015) conducted a techno-economic study featuring design optimization of a 1 MWe multi-field STPP without thermal energy storage for Jodhpur, India, to evaluate the cost-benefits of LCOE. Similar work on techno-economic modelling and analysis was carried out to reduce the LCOE using a solar tower with molten salt thermal energy storage along with a saturated and superheated LFR collector technology with phase change material (PCM) enhanced steam accumulator (Karandikar et al., 2021).

A 1 MWe multi-field (STPP) is made up of a low-cost and low-temperature LFR solar field to generate direct saturated steam, which is then combined with indirectly produced saturated steam before being superheated with a high-cost and high-temperature PTC solar field via Therminol VP - 1 HTF flowing through the steam generators. This combined saturated steam was heated to the turbine inlet temperature by the PTC solar field in the superheater. Earlier configuration from the literature (Desai and Bandyopadhyay, 2015) uses the heat produced by the PTC solar field for pre-heating the feedwater to a saturated water temperature of 250 °C from 46.5 °C before it enters the evaporator. This causes a substantial increase in the heat exchanger area and, therefore, the cost and a corresponding increase in the PTC solar field costs. As shown in Fig.1, a novel multi-field configuration has been proposed in this study to pre-heat the feedwater to 150 °C before it enters the preheater unit of the PTC solar field. Saturated steam at 250 °C would be the source of heat from a low-cost LFR solar field, which will condense to 150 °C using an open feedwater heater (OFWH) at the exit of the steam drum. This reduces the pre-heating heat load of the feedwater at the PTC side, eventually reducing the PTC solar field's collector area and the cost of net annual electricity production.

The present work is based on steady-state design point modelling and simulation of the novel configuration using Engineering Equation Solver (EES) (Klein and Nellis, 2021) and techno-economic modelling, simulation, and analysis using TRNSYS 18.0 (Klein et al., 2018). The results of the models reported in this research were compared to the published literature (Desai and Bandyopadhyay, 2015).

2. Design point modelling and simulation

2.1 Modelling methodology

Fig.1 shows the proposed configuration of the 1 MWe multi-field solar thermal power plant. The STPP is proposed to operate without fossil fuel and thermal energy storage backup. A Rankine cycle power block was used to generate electricity. The power cycle operates at an exit pressure of 0.1 bar and a turbine inlet design pressure of 40 bar. The turbine inlet temperature is set to 350 °C. A water-cooled steam condenser operating at a design pressure of 0.1 bar is employed. PTC and LFR solar fields are the source of heat input to the power block. PTC collector is designed to operate at the maximum operating temperature of 390 °C. The heat from the PTC solar field is transferred indirectly using Therminol VP-1 HTF (Eastman, 2019) oil to water/steam heat exchanger, whereas the heat from the LFR solar field is transferred through direct steam generation.

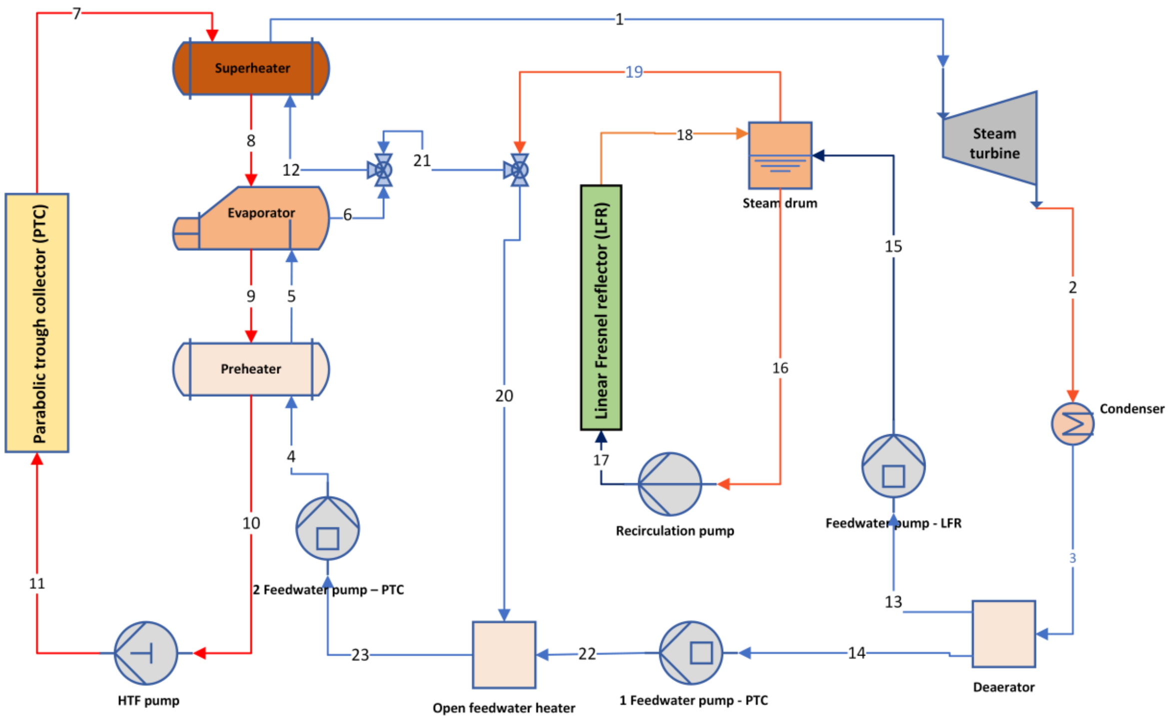

Fig. 1: Multi-field solar thermal power plant with open feedwater heater

During design operation, wet steam is produced with a designed exit vapour quality of 50 % in the LFR solar field receiver tubes. The wet steam is separated in a steam drum near the LFR receiver tube outlet and converted into saturated vapour and liquid. A recirculation pump is employed to return the saturated liquid to the LFR solar field receiver tube's inlet. The saturated vapour from the steam drum is fed to the control valve that allows the designed demanded source steam to the open feedwater heater implemented at the exit of the PTC feedwater pump for the pre-heating of PTC side feedwater. The exit condition of the feedwater heater is set at 150 °C before it is fed to the PTC preheater unit. Feedwater pumps pump the water to the desired operating pressure of 40 bar. The design parameters of the STPP are shown in Table 1. A steady-state design point modelling was carried out using the parameters in Table 1.

The steady-state characteristic equation of both the collector field has been used to evaluate the collector aperture area (Desai and Bandyopadhyay, 2015) given by

$$\eta_{\mathrm{d,col}} = \eta_{\mathrm{opt,col}} - \frac{U_{\mathrm{l,col}} \cdot \Delta T_{\mathrm{col}}}{I_{\mathrm{d}}} \qquad \text{(eq. 1)}$$

where: $\eta_{\mathrm{d,col}}$ = design solar field collector efficiency (%)

$\eta_{\mathrm{opt,col}}$ = design solar collector optical efficiency (%)

$U_{\mathrm{l,col}}$ = solar collector overall heat loss coefficient per unit aperture area, (W m^{-2} K^{-1})

$\Delta T_{\mathrm{col}} = T_{\mathrm{m,col}} - T_{\mathrm{a}}$ = difference of solar collector mean and ambient temperature

$T_{\mathrm{m,col}} = (T_{\mathrm{o,col}} + T_{\mathrm{i,col}})/2$ = mean temperature of the solar collector

I_{d} = design direct normal irradiance (W m^{-2})

Table 1: Design point parameters for a multi-field (PTC+LFR) 1 MWe STPP (Desai and Bandyopadhyay, 2015)

Design parameters	Value
Design direct normal irradiance	555 W m^{-2}
Optical efficiency of LFR	0.65
Optical efficiency of PTC	0.7
Overall heat loss coefficient for PTC and LFR	0.1 W m^{-2} K^{-1}
Isentropic efficiency of the turbine	65 %
Isentropic efficiency of the pumps	60 %
PTC collector outlet temperature	390 °C
Turbine inlet pressure	40 bar
Ambient temperature	30 °C
Heat exchanger pinch temperature difference	10 °C
Condenser pinch temperature difference	5 °C

$$\eta_{\mathrm{d,col}} = \frac{\dot{Q}_{\mathrm{d,col}}}{I_{\mathrm{d}} \cdot A_{\mathrm{ap,col}}} \qquad \text{(eq. 2)}$$

where: $\dot{Q}_{\mathrm{d,col}}$ = collector useful thermal power produced by the collector receiver (MWt)

$A_{\mathrm{ap,col}}$ = collector aperture area (m^2)

To estimate the unknown design parameters such as temperatures, mass flow rates, collector thermal capacities, heat exchanger duty and pump ratings, the energy and mass balance and respective characteristic equations of all the power plant components were solved in EES. The heat exchanger was modelled using the ε-NTU method to estimate the overall heat conductance of the heat exchanger (Patnode, 2006). A parametric study has been performed to evaluate the significance of adding an OFWH on the performance of the multi-field STPP. The following section discusses this parametric study.

2.2 Parametric study

It is intended to integrate OFWH at the exit of the LFR steam drum to preheat the feedwater from 46.5 °C to 150 °C before it enters the actual PTC preheater. The heat supplied to OFWH is through the saturated steam at 250 °C extracted from the LFR steam drum. It requires enlarging the collector aperture area of the LFR solar field to provide the OFWH with adequate heat for preheating the feedwater supplied to the PTC preheater. A parametric study was performed based on the collector aperture area of the PTC and LFR solar fields. An aperture area ratio (AR) has been defined as the ratio of the LFR collector area to that of the PTC aperture area. Fig. 2 shows the effect of increasing the (AR) on the thermal capacity of the power block. It shows that power block thermal capacity increases as the (AR) increases. This is because the power block's thermal capacity tends to rise when the thermal capacity of the OFWH increases. On the other hand, it diminishes as soon as the AR > 1, at which point the PTC thermal capacity has much reduced, lowering the OFWH capacity and the extraction mass flow rate that goes along with it for preheating.

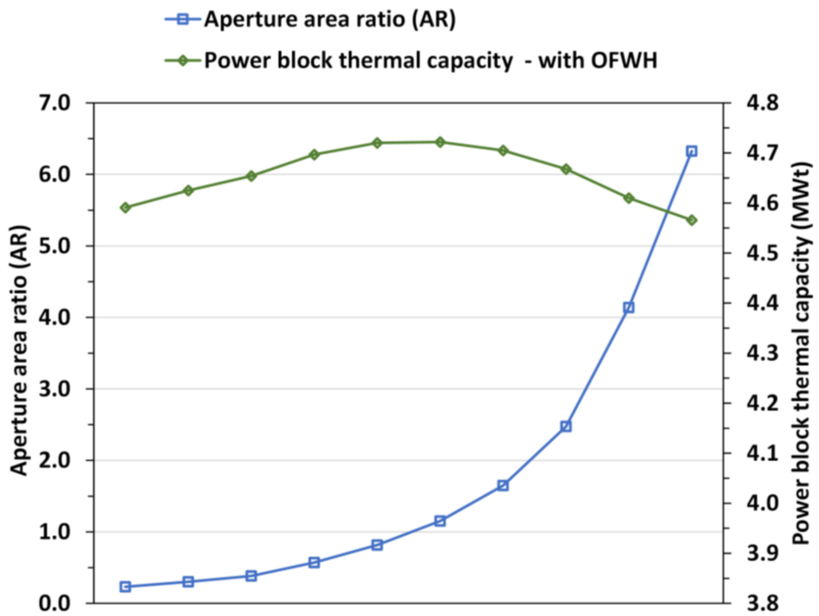

Fig. 2: Effect of increasing aperture area ratio on the power block thermal capacity

This trend has been illustrated in Fig. 3, which shows an increasing trend of the OFWH thermal capacity before AR<1 and a decreasing trend later. This is because when AR < 1, PTC's thermal capacity was more significant than the LFR's, necessitating higher extraction mass flow rates of saturated steam from the LFR solar field to the OFWH. The required extracted mass flow rate to OFWH decreased when LFR thermal capacity exceeded PTC thermal capacity at AR>1, and as a result, its thermal capacity gradually dropped as the LFR collector area increased. The PTC feedwater's design thermal capacity is declining, primarily because it is a function of PTC thermal capacity and falls as AR increases. Thus, the parametric study inferred that design point modelling and simulation must be carried out at the higher AR because it could benefit due to reduced heat exchanger and PTC collector area costs and improve the power generation's economy.

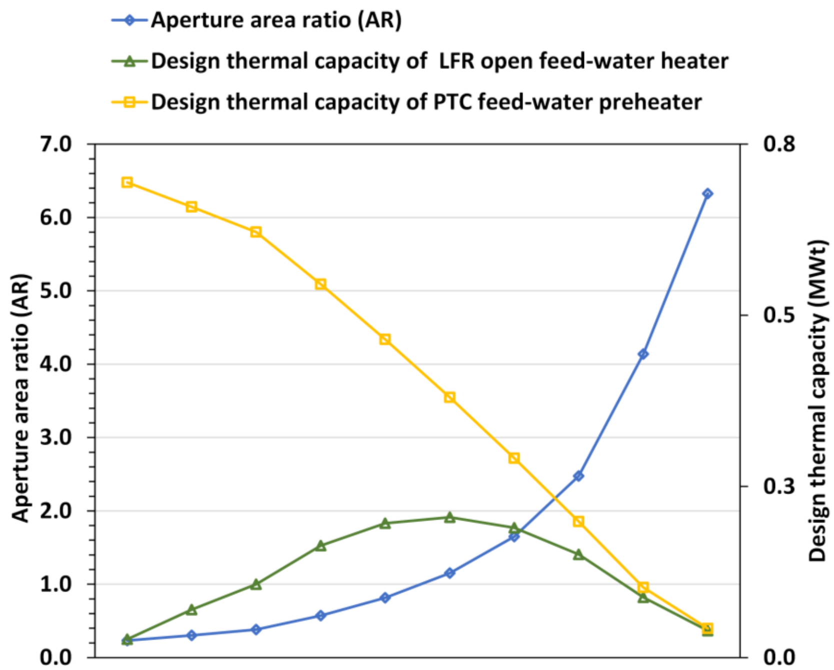

Fig. 3: Effect of increasing aperture area ratio on the OFWH and preheater thermal capacity

Table 2 lists the estimated design parameters of a novel 1 MWe multi-field STPP with open feedwater integrated at the outlet of the LFR steam drum.

Table 2: Calculated design parameters of the 1MWe multi-field STPP

Design parameters	Value
Collector aperture area of PTC	2617 m^2
Collector aperture area of LFR	10832 m^2
HTF mass flow rate through PTC solar field	2.72 kg s^{-1}
Feedwater mass flow rate to PTC – HX	0.22 kg s^{-1}
Feedwater mass flow rate to LFR – steam drum	1.37 kg s^{-1}
Saturated water mass flow rate through LFR	4.28 kg s^{-1}
Saturated steam mass flow rate to open feedwater heater	0.033 kg s^{-1}
PTC thermal rating	0.94 MWt
LFR thermal rating	3.66 MWt
Condenser thermal rating	3.51 MWt
PTC Collector efficiency	64.8 %
LFR Collector efficiency	61.0 %
Power block efficiency	21.6 %
Turbine gross power	1.025 MWe
Overall heat conductance of superheater	8392 W K^{-1}
Overall heat conductance of evaporator	12354 W K^{-1}
Overall heat conductance of preheater	2750 W K^{-1}

The quasi-steady modelling and simulation using TRNSYS 18.0 were carried out using the computed design parameters in Table 2. An off-design simulation in TRNSYS of a multi-field STPP with OFWH was performed to assess annual net power production from the STPP in Jodhpur, India. The steady-state thermodynamic values of a 1 MWe multi-field STPP with OFWH are detailed in Table 3.

Table 3: Steady-state design point state points of a 1 MWe multi-field STPP

State points	P	T	h	s	$\dot{m}$
	[bar]	[°C]	[kJ kg^{-1}]	[kJ kg^{-1} K^{-1}]	[kg s^{-1}]
1	40.0	350.2	3092.0	6.58	1.57
2	0.1	46.0	2437.0	7.69	1.57
3	0.1	46.2	192.6	0.65	1.57
4	40.0	150.2	634.5	1.84	0.23
5	40.0	250.5	1087.0	2.80	0.23
6	40.0	250.5	2801.0	6.07	0.23
7	13.0	390.2	-	-	2.73
8	12.0	322.6	-	-	2.73
9	10.0	260.5	-	-	2.73
10	8.5	243.4	-	-	2.73
11	13.6	243.8	-	-	2.73
12	40.0	250.5	2801.0	6.07	1.57
13	0.1	46.0	192.6	0.65	1.37
14	0.1	46.0	192.6	0.65	0.19
15	40.0	46.9	199.3	0.66	1.37
16	40.0	250.5	1087.0	2.80	4.29
17	45.0	250.8	1088.0	2.80	4.29

18	40.0	250.5	1944.0	4.43	4.29
19	40.0	250.5	2801.0	6.07	1.37
20	40.0	250.5	2801.0	6.07	0.03
21	40.0	250.5	2801.0	6.07	1.34
22	40.0	46.9	199.3	0.66	0.19
23	40.0	150.2	634.5	1.84	0.23

3. Techno-economic modelling and simulation

Techno-economic modelling was carried out using a performance and economic model of various components of the STPP. The performance or off-design modelling of the solar field and power block components was carried out using TRNSYS 18.0 (TRANSSOLAR Energietechnik GmbH, 2017). The model considered the off-design states of the LFR and PTC solar fields by using an incidence angle modifier correction from Morin et al. (2012) and Schenk et al. (2014). A flow following constant pressure and throttle-governed steam turbine has been employed to model the off-design electric power generation. The change in steam mass flow rate and turbine inlet temperature affects the turbine's isentropic efficiency. This change in the isentropic efficiency of the steam turbine due to the change in steam mass rate generation has been considered using an isentropic efficiency equation from the literature (Shang, 2000). Heat exchanger units were modelled using the ε–NTU method using the solar thermal electric component (STEC) library model (Schwarzbözl et al. 2002). Open feedwater heater, condenser, and pump units have been modelled using the thermal energy systems specialist (TESS) library (Thornton et al. 2012). The weather file used for the solar resource input data of direct normal irradiance and ambient temperature with 1-hour time resolution has been used for Jodhpur, India (Ramaswamy et al. 2013).

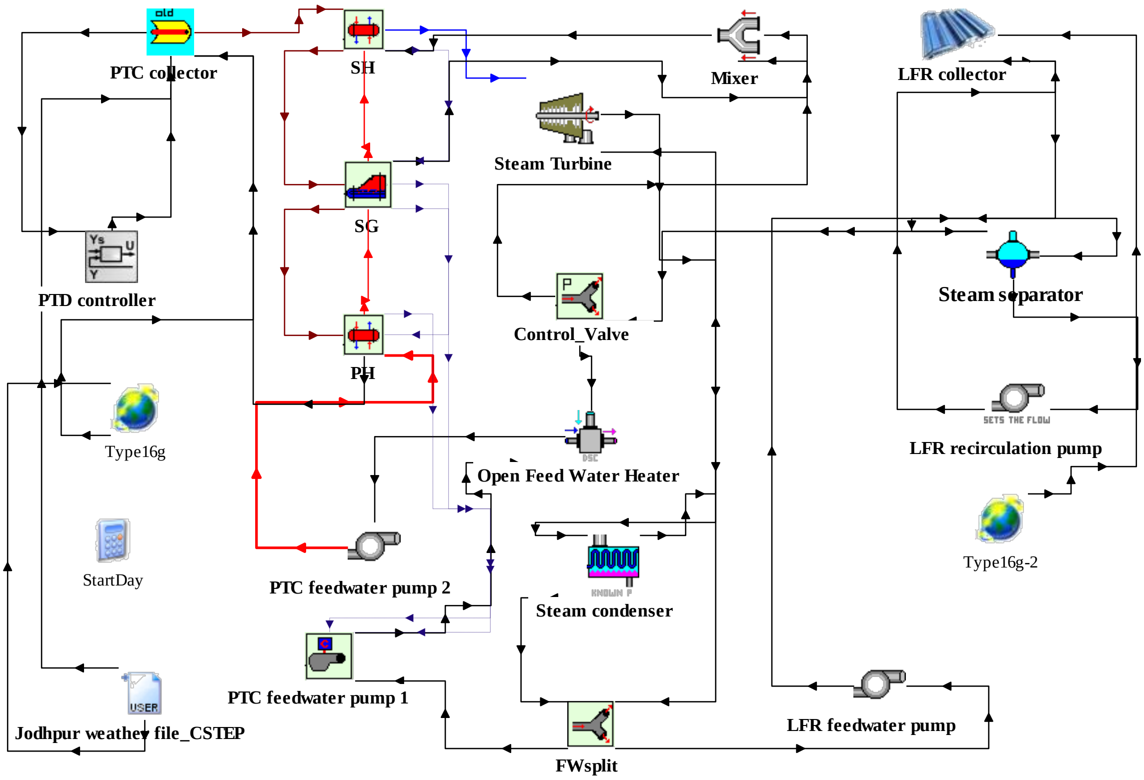

Fig. 4: TRNSYS model of a 1 MWe multi-field STPP with OFWH

Fig. 4 shows a TRNSYS model of a 1 MWe multi-field STPP with OFWH. A PID controller has been used to control the outlet temperature through tracking fraction by defocusing the PTC collector area. A control valve has been used to direct a controlled source steam mass flow rate to the OFWH from the incoming saturated steam at the steam drum outlet. The cost functions for the various components have been taken from the literature (Desai and Bandyopadhyay. 2015). The economic modelling was predicated on a 10% discount rate and a thirty-year plant life. The annual simulation of a techno-economic model results in the STPP producing net amounts of electricity. The annual electricity production was utilized in calculating the plant's LCOE.

$$\mathrm{LCOE} = \frac{\left(C_{\mathrm{equipment}}+C_{\mathrm{misc}}\cdot\dot{W}_{\mathrm{gen,kWe}}+C_{\mathrm{civil}}+C_{\mathrm{land}}\right)\cdot\mathrm{CRF}+\left(C_{\mathrm{O\&M}}\right)}{E_{\mathrm{gen}}} \qquad \text{(eq. 3)}$$

where E_{gen}= Net annual electric energy generation (kWh)

$\dot{W}_{\mathrm{gen,kWe}}$= Net electric power capacity or name-plate capacity (kWe)

C_{civil} and C_{land} = Civil work and land cost ($)

$C_{\mathrm{equipment}}$ = Equipment cost of the power block and solar field system components ($)

C_{misc}= miscellaneous cost ($ kWe^{-1})

$C_{\mathrm{O\&M}}$= operation and maintenance cost ($)

CRF = capital recovery factor = $\frac{d\cdot(1+d)^n}{(1+d)^n-1}$; d = discount rate and n = plant life

4. Results and discussion

Fig. 5 depicts the monthly net electric energy generated by a 1 MWe multi-field STPP with and without an OFWH configuration and the related effective direct normal irradiation (EDNI). The total amount of energy entering a surface per unit area under direct normal irradiation is known as EDNI. It should be noted that the electric energy yield is significantly higher with OFWH than without it for nearly every month of the year. It also demonstrates that the generation of electric energy depends on the EDNI of the location. In October, the Jodhpur location recorded its highest EDNI of 198.1 kWh m-2 month-1, resulting in a net electric generation of 0.24 GWh. Conversely, July marked the lowest electric energy generation, with an EDNI of 93.2 kWh m-2 month-1, responsible for a net electric generation of 0.07 GWh. This results from the monsoon's seasonal influence on the region, constituting a cloud cover.

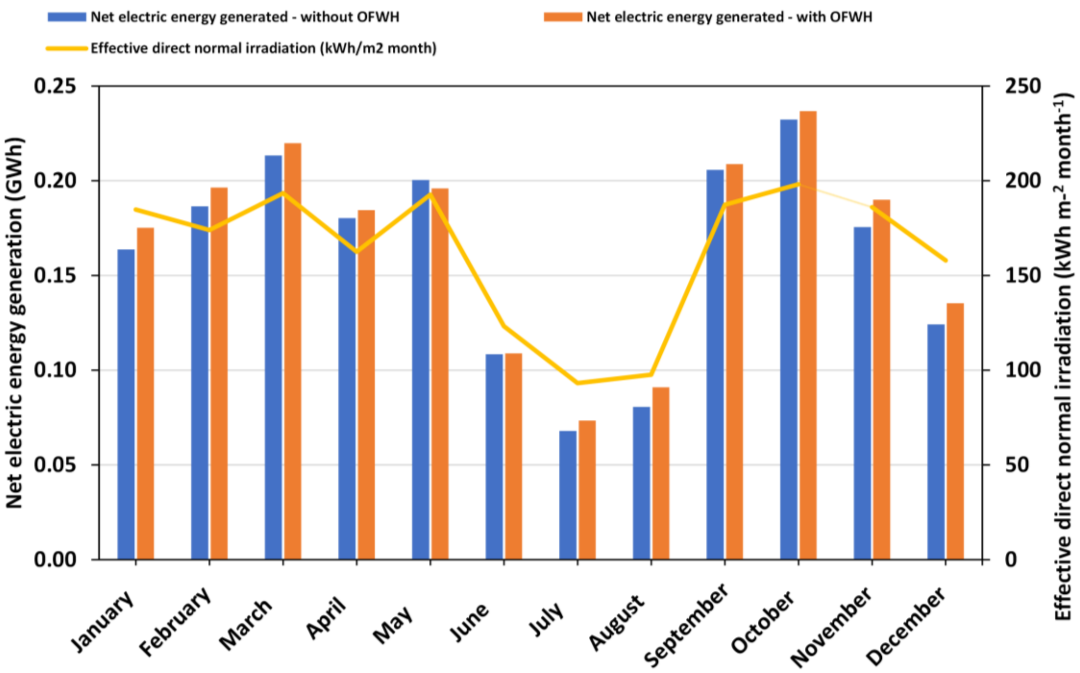

Fig. 5: Monthly net electric energy generation comparison of a 1 MWe multi-field STPP without and with OFWH and the corresponding effective direct normal irradiation

The monthly variations in the LFR collector efficiency of the OFWH and the multi-field configuration performance efficiency are depicted in Fig. 6. It can be seen that LFR collector efficiency for both configurations remains almost the same, irrespective of their design thermal capacity. Nonetheless, the OFWH operated with a nearly constant thermal efficiency from October to April, when the LFR useful heat generation remained high. However, from May to July, the OFWH's thermal performance declined due to insufficient useful heat generation of the LFR solar field; this also impacted the power plant's net electric energy generation, as depicted in Fig. 5. The impact of AR on the STPP's performance and LCOE is highlighted in Table 4. Higher AR tends to reduce the design thermal capacity of the preheater and PTC solar field, reducing the capital cost of the STPP. Furthermore, the design thermal capabilities of the preheater and OFWH are practically the same.

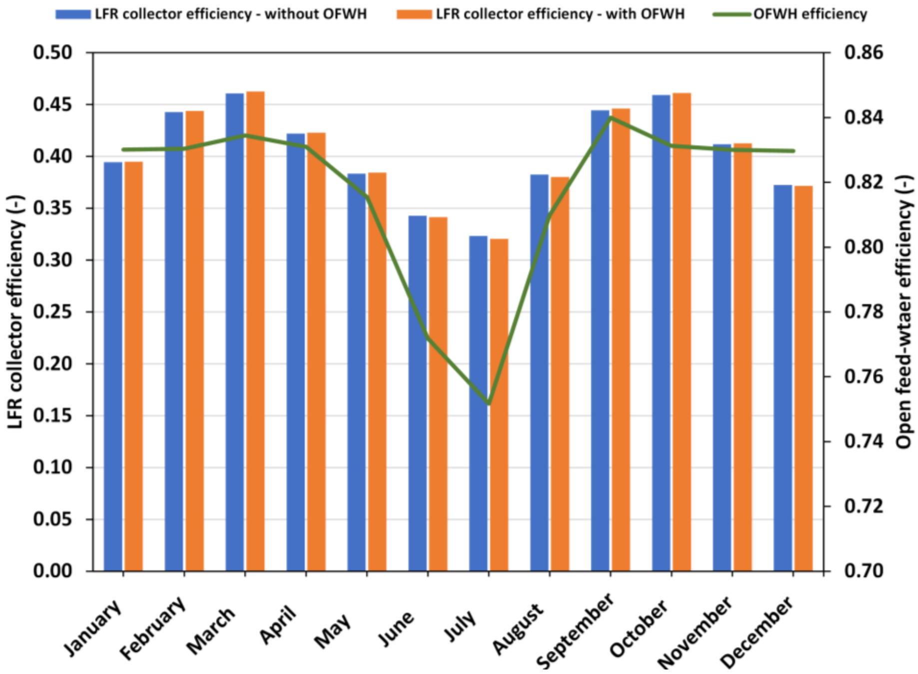

Fig. 6: Monthly variation of LFR collector efficiency of a 1MWe STPP multi-field configuration with and without OFWH and Open feed water heater efficiency

As a result, the OFWH uses less energy for preheating. However, the net electric energy generation is slightly higher at low AR. This is due to the increased gross capacity of the turbine power. All these factors tend to improve the economics of power generation, reducing the LCOE.

Table 4: Performance and LCOE variation at two different aperture area ratios (AR) of a 1 MWe multi-field STPP

Aperture area ratio (AR)	Annual heat energy extracted from OFWH	Annual heat energy transfer from preheater	Annual useful heat energy collected from LFR solar field	Net annual electric energy generated	LCOE
(-)	(GWh)	(GWh)	(GWh)	(GWh)	($/kWh)
1.15	0.57	1.16	5.85	2.12	0.332
4.14	0.21	0.24	8.69	2.02	0.306

In Table 5, the outcomes of a techno-economic analysis are presented, along with a comparison to the configuration that does not incorporate the open feedwater heater for the proposed multi-field configuration. It compares the LCOE obtained for the proposed configuration to the LCOE obtained for a multi-field configuration without an OFWH using the TRNSYS model, the literature model, and a simulation from (Desai and Bandyopadhyay, 2015).

Table 5: Techno-economic comparison of a multi-field STPP with and without open feedwater heater integration

Description	Area of LFR	Area of PTC	Net annual electric energy generated	LCOE
	(m^2)	(m^2)	(GWh)	($ kWh^{-1})
Literature (without open feedwater heater) (Desai and Bandyopadhyay, 2015)	9500	3500	-	0.326
Our model (without an open feedwater heater)	9500	3500	1.94	0.324
Our model (with an open feedwater heater)	10832	2617	2.02	0.306

It was found that the LCOE of the suggested multi-field setup with a feedwater heater is 5.5% lower than the LCOE of the configuration without the open feedwater heater. This is due to lower upfront costs for the PTC collecting area and heat exchanger units and an increased low-cost LFR solar field area.

5. Conclusion

A novel 1 MWe multi-field STPP configuration with open feed water integrated at the LFR steam drum output has been proposed to improve the LCOE of electric energy generation in Jodhpur, India. A techno-economic study was performed for a given configuration, and the LCOE was compared with a multi-field STPP configuration without an open-feed water heater. An aperture area ratio was used in a design parametric study, which revealed that the STPP constructed with larger aperture area ratios helps lower the STPP's capital cost and, thus, the LCOE. Compared to a configuration lacking an open-feed water heater, the novel configuration results in a 5% reduction in the LCOE.

References

Desai, N. B., and Bandyopadhyay, S., 2015. Integration of parabolic trough and linear Fresnel collectors for optimum design of concentrating solar thermal power plant. Clean Technologies and Environmental Policy, 17(7), 1945–1961.

Giostri, A., Binotti, M., Astolfi, M., Silva, P., Macchi, E., Manzolini, G., 2012. Comparison of different solar plants based on parabolic trough technology. Solar Energy. 86(5), 1208–1221.

Giostri, A., Binotti, M., Silva, P., MacChi, E., Manzolini, G., 2013. Comparison of two linear collectors in solar thermal plants: Parabolic trough versus Fresnel. Journal of Solar Energy Engineering, Transactions of the ASME. 135(1), 1–9.

Gunther, M., 2011. Advanced CSP Teaching Materials - Linear Fresnel Technology. Advanced CSP teaching materials.

Islam, M. T., Huda, N., Abdullah, A. B., & Saidur, R., 2018. A comprehensive review of state-of-the-art concentrating solar power (CSP) technologies: Current status and research trends. Renewable and Sustainable Energy Reviews. 91, 987–1018.

Klein, S. A., Duffie, J. A., Mitchell, J. C., Kummer, J. P., Thornton, J. W., Bradley, D. E., Arias, D. A., Beckman, W. A., Duffie, N. A., Braun, J. E., Urban, R. E., Blair, N. J., McDowell, T. P., Duffy, M. J., 2018. TRNSYS 18: A Transient System Simulation Program. Getting Started (Vol. 1).

Manzolini, G., Giostri, A., Saccilotto, C., Silva, P., Macchi, E., 2011. Development of an innovative code for the design of thermodynamic solar power plants part B: Performance assessment of commercial and innovative technologies. Renewable Energy. 36(9), 2465–2473.

Morin, G., Dersch, J., Platzer, W., Eck, M., Häberle, A., 2012. Comparison of Linear Fresnel and Parabolic Trough Collector power plants. *Solar Energy*, *86*(1), 1–12. https://doi.org/10.1016/j.solener.2011.06.020

Nayak, J. K., Kedare, S. B., Banerjee, R., Bandyopadhyay, S., Desai, N. B., Paul, S., Kapila, A., 2015. A 1 MW national solar thermal research cum demonstration facility at Gwalpahari, Haryana, India. In Current Science (Vol. 109, Issue 8, pp. 1445–1457). https://doi.org/10.18520/v109/i8/1445-1457

Ramaswamy, M. A., Suresh, N. S., Rao, B. S., Thirumalai, N. C., 2013. Estimation of Hourly Direct Normal Irradiance(DNI). Center for Study of Science, Technology and Policy (CSTEP).

Schenk, H., Hirsch, T., Feldhoff, J. F., Wittmann, M., 2014. Energetic comparison of linear Fresnel and parabolic trough collector systems. Journal of Solar Energy Engineering, Transactions of the ASME. 136(4), 1–11.

Schwarzbözl, P., Eiden, U., Pitz-Paal, R., & Jones, S., 2002. A TRNSYS Model Library for Solar Thermal Electric Components (STEC). A Reference Manual Release 2.2.

Shang, Z., 2000. Analysis and optimization of total site utility systems, Doctor of Philosophy. Department of Process Integration University. University of Manchester Institute of Science and Technology,UK, (Issue August).

Thornton, J. W., Bradley, D. E., McDowell, T. P., Blair, N. J., Duffy, M. J., LaHam, N. D., Naik, A. V., 2012. TESSLibs 17 - Combined Heat and Power (CHP) / Cogeneration Library Mathematical Reference (Vol. 13).

TRANSSOLAR Energietechnik GmbH., 2017. TRNSYS 18 (Vol. 3).

Modelling of a CPV-T Collector for Combined Heat and Power Generation

Chandan Pandey[1], Mingyang Wu[1], Hasan Yildizhan[1,2], Ivan P. Acosta-Pazmiño[3], C.I. Rivera-Solorio[3], M. Gijon-Rivera[4], Rafael A. García-Ramos[3] and Christos N. Markides[1*]

[1] Clean Energy Processes Laboratory, Department of Chemical Engineering, Imperial College London, London (United Kingdom)

[2] Department of Energy Systems Engineering, Adana Alparslan Türkeş Science and Technology University, Adana 46278, Turkey

[3] Tecnologico de Monterrey, Escuela de Ingeniería y Ciencias, Ave. Eugenio Garza Sada 2501, Monterrey, (Mexico)

[4] Tecnologico de Monterrey, Escuela de Ingeniería y Ciencias, Vía Atlixcáyotl 5718, Puebla, 72453, Puebla, (Mexico)

***Corresponding author: c.markides@imperial.ac.uk**

Abstract

In this work, a coupled optical, electrical and thermal model of a concentrated photovoltaic-thermal (CPV-T) collector with a geometrical concentration ratio of 11 is developed. To estimate the accuracy of the coupled model, this is first validated against data of known collectors in the existing literature. Results show that the model can predict the optical and thermal performance of these collectors with a deviation under 8%. The model is then used to predict the performance of a new collector design. Simulation results reveal that the collector achieves a thermal efficiency of 68% and an electrical efficiency of 14% at a direct normal irradiance of 1000 W/m^2, an ambient temperature of 25 °C, an inlet water temperature of 25 °C and a mass flowrate of 0.01 kg/s. The characteristic thermal and electrical efficiency curves of the collector are also generated. Based on this CPV-T collector design, a prototype is being constructed and tests are being performed in Mexico.

Keywords: Cogeneration; concentrated solar; combined heat and power; hybrid PV-thermal; solar energy

1. Introduction

The simultaneous production of electricity and heat allows for a more efficient solar energy utilization. In particular, concentrated photovoltaic-thermal (CPV-T) collectors can play a significant role in low-carbon energy systems thank to their ability to provide a high-grade thermal energy (>70 °C) (Acosta-Pazmiño et al., 2022). Nevertheless, CPV-T technologies also present certain technical challenges such as a more complex optical design, thermal and electrical management, material selection and durability, safety and reliability along with economic feasibility (Madurai Elavarasan et al., 2022). Addressing these challenges through research, development and innovation is crucial for advancing CPV-T technology, which has led to various numerical and experimental investigations in pursuit of advancements in this technology.

A parabolic trough-based CPV-T collector was developed and studied by Cabral et al. (2021) who reported thermal and electrical efficiencies of 58% and 8%. Karathanassis et al. (2017) designed, developed and tested a CPV-T collector with a rectangular absorber. Their experimental results showed that the collector achieved electrical and thermal efficiencies of 8% and 44%, respectively. Deymi-Dashtebayaz et al. (2022) studied the influence of nanofluids as heat transfer fluids on the electrical and thermal performance of a CPV-T collector, while Demircan et al. (2023) developed a finite volume-based numerical model to estimate the thermal and electrical performance of a CPV-T collector. The model predicted a PV cell temperature of roughly 110 °C at an inlet temperature of the heat transfer fluid (HTF) of 50 °C.

A review of the literature on CPV-T collectors reveals that significant work, both numerical and experimental, has already been done on CPV-T collectors. However, to the best knowledge of the authors, none of the models

10.18086/swc.2023.03.10 Available at http://proceedings.ises.org

presented in the literature feature coupled optical and thermal models in a single design tool. Chandan et al. (2022) used Zemax to estimate the optical flux reaching the absorber of an LCPV-T module, which was then used as input to a CFD model. Similarly, Parthiban et al. (2022) and Barthwal & Rakshit (2022) used the optical software tools Solatrace and Tracepro, respectively, to estimate the optical flux for use in a CFD model. This study aims to develop a coupled optical electrical and thermal model for a CPV-T collector using single modelling tool. The single modelling tool will reduce the errors in the estimation of the performance of the collectors. Results from the developed model are presented in this work.

2. Methodology

2.1. Model description

The main components of the CPV-T collector studied here are an optical concentrator, PV cells and a HTF, as shown in Fig. 1. Since the aim of the present study is to retrofit commercialized parabolic trough-based solar thermal collectors with PV cells, a commercially available parabolic trough with a geometrical concentration ratio of 11 was selected for this work. The aperture width of the collector is 1.1 m and the length of the collector is 3 m. The hybrid receiver is a triangular channel constructed from an aluminum sheet of thickness 0.005 m and an illuminated area of 0.3 m^2. Solar cells are attached on two faces of the triangular channel which are illuminated area of the channel. Cells are attached in such a way that they are thermally in contact with the channel, but electrically insulated. To cool the solar cells and extract useful heat, water is used as the HTF. A cover glass of outer diameter 0.07 m and thickness 0.002 m is used to cover the receiver and trap the long wavelength radiation.

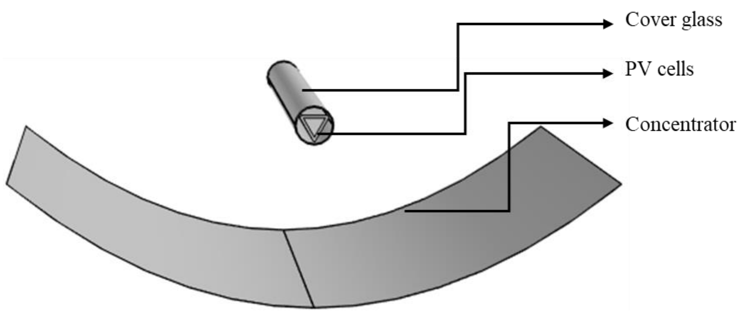

Fig. 1: Simple schematic of the CPV-T collector design investigated in the present work

2.2. Optical and thermal models

An optical model of the concentrator was developed using the COMSOL ray tracing module, allowing us to estimate the flux distribution over the cells. The ray tracing is based on the law of reflection where the angle of incidence is equal to the angle of reflection, following the governing equation given as (Chandan et al., 2022):

$$r_{\mathrm{ref}} = r_{\mathrm{inc}} - 2(n.r_{\mathrm{inc}})n \qquad \text{(eq.1)}$$

where r_{ref} is the reflected ray and r_{inc} is the incident ray.

In the optical model, it was assumed that the reflectivity of the mirror is 90 % (Chandan et al., 2021) and that the transmissivity of the cover glass is 90 %. Further, the absorptivity of the solar cells was assumed to be 88 % (Chandan et al., 2021) in this study.

A 3-D CFD model was developed to estimate the thermal performance of the CPV-T collector. For the estimation of the thermal performance, it is important to couple the optical and thermal models. By implementing ray heating in the model, the flux obtained from the optical model directly becomes the incident flux on the cells. Of the total flux incident on the cells, a part of it is converted to electrical energy and the rest heats the solar cells. Therefore, it is assumed that cells act as a heat-generating source. The heat generated in the solar cells is then transferred to the triangular receiver in bottom direction by conduction which was subsequently dissipated to the cooling fluid via convection. The cells also lose heat over their top surfaces via natural convection and radiation to the surroundings. The convection loss between the solar cells and the cover glass are suppressed by maintaining a vacuum between them. Surface-to-surface radiation between the solar cell and the cover glass and cover glass and sky was considered in this study. On the top surface of the cover glass, convection heat transfer was also considered. The fluid flow inside the triangular channel was assumed to be laminar, as Reynolds number was estimated to be 1100.

With these imposed boundary conditions on the geometry of the collector, the geometrical model was discretised into small elements also referred as mesh. For each element of the discretised geometrical model, mass, momentum and energy balance equations were solved numerically. The mass, momentum and energy balance equations are (Herrando et al., 2019):

$$\rho_{\mathrm{f}} \nabla \cdot v_{\mathrm{f}} = 0 \quad \text{(eq.2)}$$

$$\rho_{\mathrm{f}} v_{\mathrm{f}} \nabla \cdot v_{\mathrm{f}} = -\nabla P + \mu \nabla^2 v_f + \rho_{\mathrm{f}} \mathrm{g} \quad \text{(eq.3)}$$

$$\rho_{\mathrm{f}} c_{\mathrm{p}} v_{\mathrm{f}} \nabla \cdot T_{\mathrm{f}} = \nabla \cdot (k_{\mathrm{f}} \nabla T_{\mathrm{f}}) \quad \text{(eq.4)}$$

where P is the fluid pressure, μ the dynamic viscosity, g the acceleration due to gravity, T_{f} the fluid temperature, k_{f} the thermal conductivity of the fluid, v_{f} the velocity of the fluid, c_{p} is specific heat capacity of water and ρ_{f} the density of the fluid.

2.3. Electrical model

The electrical efficiency of solar cells decreases linearly with the cell temperature. To predict the electrical performance of the cells, the cell temperature was estimated by the CFD model which was then used to estimate the electrical efficiency (Huang et al., 2021; Huang & Markides, 2021; Liang et al., 2022):

$$\eta_{\mathrm{PV}} = \eta_0 (1 - \beta (T_{\mathrm{cell}} - 298\ \mathrm{K})) \quad \text{(eq. 5)}$$

where η_0 is the base efficiency of the cell at standard test conditions (1000 W/m^2, 298 K, AM1.5G spectrum), β the power temperature coefficient, and η_{pv} the efficiency of the cells at an operating temperature of T_{cell}.

2.4. Thermal and electrical performance

The thermal efficiency of the collector is estimated by using the equation below:

$$\eta_{\mathrm{th}} = \frac{\dot{m}.c_{\mathrm{p}}.(T_{\mathrm{fo}} - T_{\mathrm{fi}})}{I.A_{\mathrm{ap}}} \quad \text{(eq. 6)}$$

where η_{th} is the thermal efficiency of the collector, $\dot{m}$ the mass flowrate inside the collector, T_{fo} the outlet water temperature from the collector, T_{fi} the inlet water temperature to the collector, I the incident solar radiation, and A_{ap} the aperture of the concentrator.

The reduced temperature of the collector is given as:

$$T_{\mathrm{r}} = \frac{\left(\frac{T_{\mathrm{fo}} + T_{\mathrm{fi}}}{2}\right) - T_{\mathrm{amb}}}{I} \quad \text{(eq. 7)}$$

where T_{r} is the reduced temperature of the collector, and T_{amb} the ambient temperature. The SI unit of reduced temperature is K.m^2/W.

3. Results and discussion

3.1. Validation of the optical model

The optical model was first validated against the simulation results presented by Hou et al. (2023). For the optical simulation, a parabolic trough concentrator of geometrical concentration ratio of 16.67 as described in the reference was created using COMSOL. 0.5 million rays were allowed to fall on the concentrator which was collected by a flat absorber of width 60 mm. The reflectivity of the concentrator was set to 90% and the absorptivity of the absorber was set to 10%. The simulation considered the Sun as a finite source with a cone angle of 4.65 mRad. The simulation also considered the limb darkening effect to ensure simulation captures actual conditions when tested in outdoor conditions. The result of the optical simulation is shown in the Fig. **2**. The result shows a fairly accurate match between the simulation results of Hou et al. (2023) and the developed optical model in COMSOL with root mean square error under 10%.

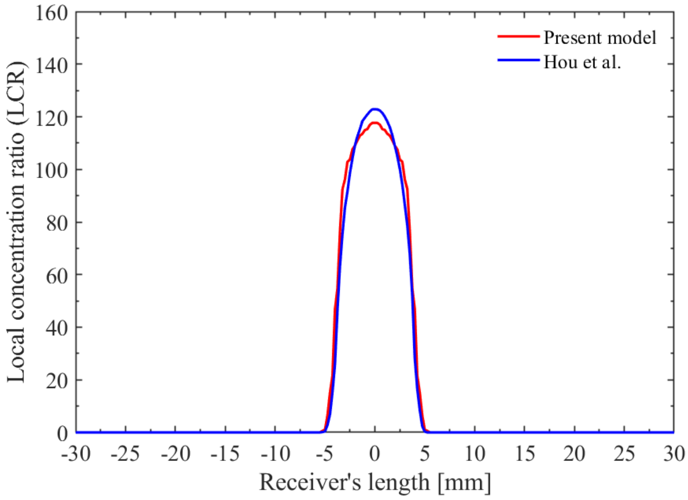

Fig. 2: Comparison of local flux distribution on the absorber

3.2. Thermal model validation

To validate the methodology of coupling the optical model with that of CFD model, work presented by Yousef et al. (2016) was selected. For this, a compound parabolic concentrator (CPC) of geometric concentration ratio 2.66, truncated to 2.4, was selected based on the literature. A PV module of dimension 0.3 m by 0.245 m was placed at the base of the CPC. Underneath the solar cell, a heat exchanger was employed. The heat exchanger was insulated from the back to reduce heat losses. Parameters such as the inlet water temperature, wind speed, insolation and ambient temperature were given as inputs to the model. The optical simulation was used to first calculate the radiation flux reaching the cells as shown in Fig. 3(b). The radiation flux was then coupled to the heat transfer model by ray heating to estimate the cell temperature, outlet water temperature and so on. The temperature distribution profile on the solar cell in shown in Fig. 3(c). The average temperature of the solar cell at different time of the day is shown in Fig. 3(a).

A comparison of results concerning the average cell temperature of the collector are shown in Fig. 3. We observe a good match between the average cell temperature predicted by the model and the experimental results of Yousef et al. (2016) with a root mean square (rms) error under 8%.

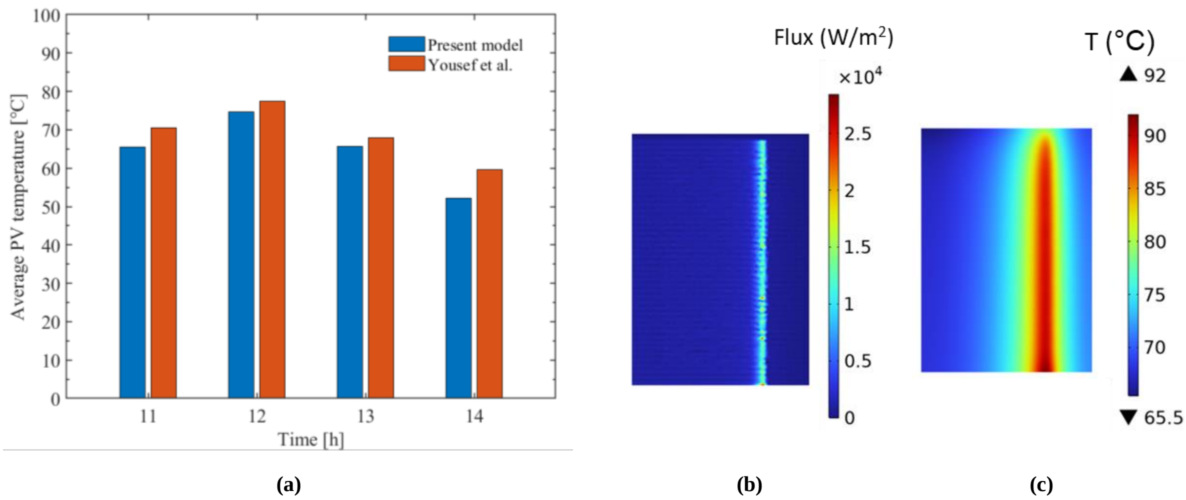

Fig. 3: (a) Comparison of average PV temperature, (b) local flux distribution at 12 pm, and (c) local temperature distribution on the solar cell at 12 pm.

3.3. Optical performance of the CPV-T collector

For the ray tracing of the CPV-T collector, a similar methodology as stated in Section 3.1 was followed. The number of rays falling on the absorber was set to 1 million and the reflectivity of the mirror was set to 90%. The model also included the sun as a finite source suspending a conical disc angle of 4.65 mRad. The total incidence power on the mirror was found to be 3300 W and the total power reaching the absorber was 2550 W. The loss in power was mainly due to transmission losses from the cover glass and reflection losses from the mirror. The overall optical efficiency of the collector was 77%. The raytracing of the CPV-T collector is shown in Fig. 4(a), and the flux distribution on the absorber is shown in Fig. 4(b) whereas the average flux distribution on the absorber is shown in Fig. 4(c). Figure 4(c) shows the average distribution of flux on the triangular absorber when it is unfolded. The actual flux distribution on the CPV-T collector developed at test site in Mexico is shown in Fig. 4(d). The collector developed at Mexico is of same geometry as described in the section 2.1.

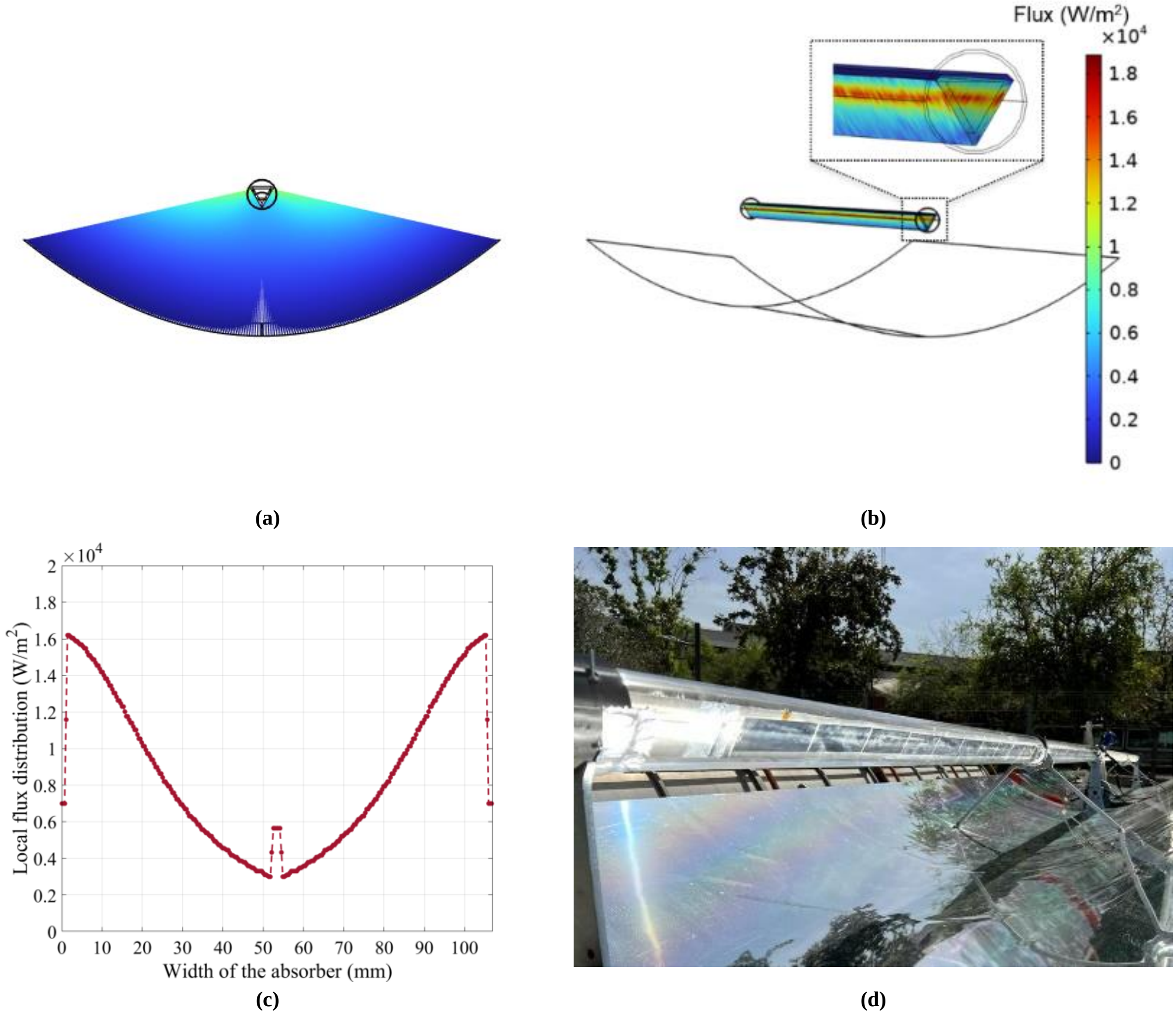

Fig. 4: (a) Ray-tracing simulation for the collector, (b) and (c) simulation results for flux distribution on the PV cells, and (d) actual flux distribution on the test setup in Mexico

3.4. Thermal and electrical performance of the CPV-T collector

To estimate the thermal performance of the collector, the optical simulation results obtained from COMSOL were used as inputs to the thermal model. Specifically, the COMSOL optical model stores the radiation (optical) flux received on the absorber in an accumulator using a variable (*rpb*), which is then used as an input heat flux on the boundary of the receiver for the thermal model. Thus, the exact optical flux profile obtained from the optical simulation was used as input to the model to estimate the thermal performance of the collector. Furthermore, using an incident solar flux of 1000 W/m^2 at an ambient temperature of 25 °C, an inlet water temperature of 25 °C and an inlet velocity of 0.015 m/s (which is the design condition of the parabolic tough collector considered here), results show that the CPV-T collector can deliver hot water at a temperature of 77 °C, a thermal efficiency of 68%, and an electrical efficiency of 14%. The temperature distribution plot of the CPV-T collector is shown in Figure 5.

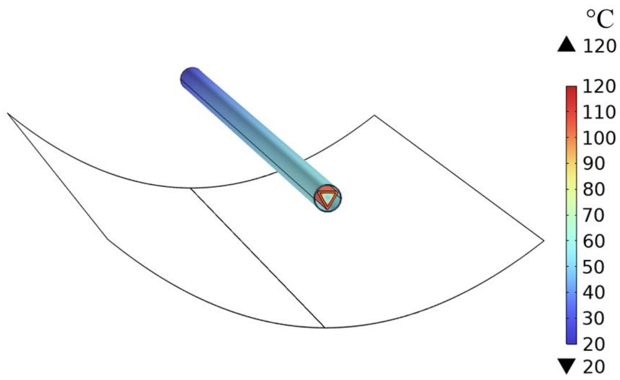

Fig. 5: Temperature distribution over the PV cells for conditions of 1000 W/m², ambient temperature of 25 °C and inlet water temperature of 25 °C and mass flowrate of 0.01 kg/s

Thereafter, characteristic thermal and electrical efficiency curves of the CPV-T collector were plotted as a function of reduced temperature, as shown in Figure 6. For this study, the characteristic curve of the CPV-T collector is plotted by fixing the mass flowrate to be 0.01 kg/s (i.e., inlet velocity of 0.015 m/s) and varying the inlet water temperature in steps of 4 °C. Single characteristic thermal and electrical efficiency plots as a function of reduced temperature within a reasonable range of operating conditions are sufficient to demonstrate the thermal and electrical performance of the collector for different operating condition such as variation of mass flowrate, irradiance, inlet water temperature and ambient temperature. In the present case, the maximum thermal efficiency of the collector when the average temperature of the receiver is close to ambient temperature is observed to be 69%. This essentially means that the collector can achieve maximum thermal efficiency of 69%, electrical efficiency of 16% and rest (15%) are the optical losses from the collector. The simulations are performed for a maximum outlet temperature of 100 °C as operating the collector above 100 °C results in two phase flow which can be taken up in another study. The characteristic thermal and electrical efficiency equations are given below. Equations 8 and 9 are obtained by fitting a polynomial of second order for thermal efficiency and first order for electrical efficiency, respectively. The temperature distribution plot for different inlet water temperature is shown in Fig. 7.

$$\eta_{\mathrm{th}} = -78.2.T_r^2 - 26.4.T_{\mathrm{r}} + 69 \quad \text{(eq. 8)}$$

$$\eta_{\mathrm{el}} = -81.5.T_{\mathrm{r}} + 16.2 \quad \text{(eq. 9)}$$

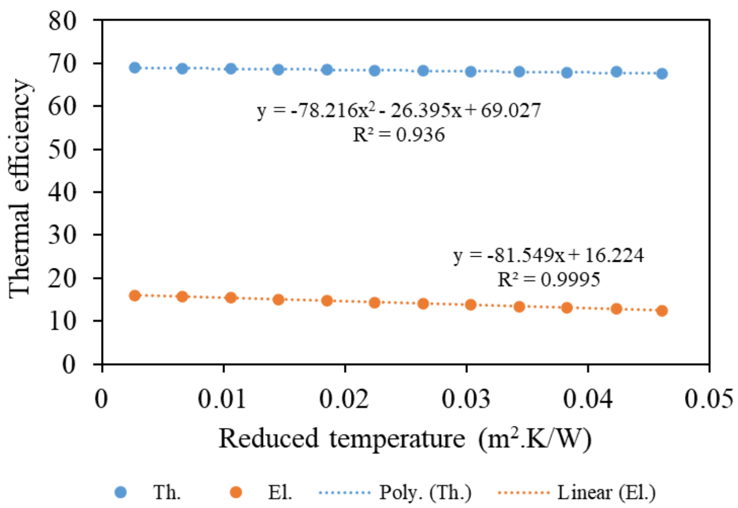

Fig. 6: Characteristic thermal and electrical efficiency curves of the CPV-T collector

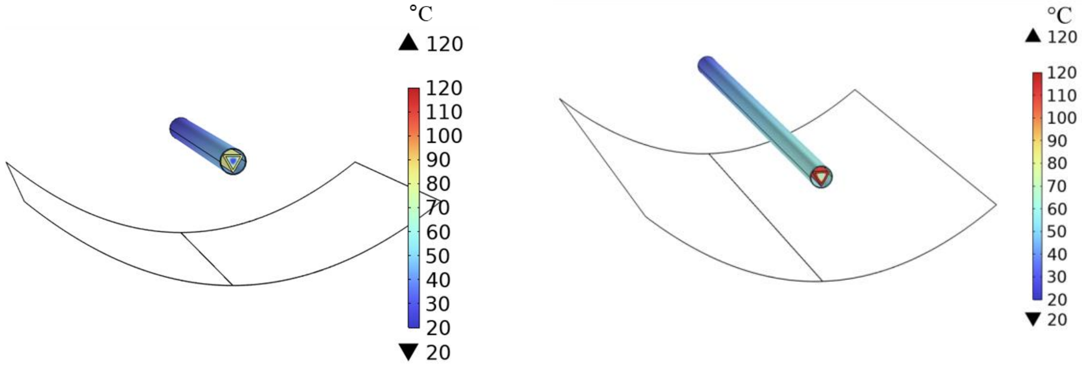

(a) (b)

Fig. 7: Temperature distribution for the CPV-T collector at inlet temperature: (a) 1 °C, and (c) 45 °C

4. Conclusions

A fully coupled optical, electrical and thermal model of a CPV-T collector with a geometrical concentration ratio of 11 was developed. Simulation results revealed that at standard conditions (1000 W/m^2), the total incident power on the aperture of the collector is 3300 W, however, only 2550 W reaches the PV cells, mainly due to optical losses from the mirror and transmission losses from the cover glass. The overall optical efficiency of the collector was 77%. Further, optical simulation results were coupled with a CFD model to estimate the thermal and electrical performance of the collector. Results showed that for an ambient temperature of 25 °C, and an inlet water temperature of 25 °C, the collector can deliver hot water at 77 °C with a thermal efficiency of 68% and an electrical efficiency of 14%. Thereafter, to study the collector's performance in different outdoor conditions, characteristic thermal and electrical efficiency curves as a function of reduced temperature were plotted. The simulations were performed by fixing the heat transfer fluid flowrate and varying its inlet temperature. Results revealed that, the collector can achieve a maximum thermal efficiency of 69% and maximum electrical efficiency of 16%. Based on the investigated design, it is now proposed that passive cooling of the solar cells using spectral splitting will also be explored, while a prototype has been constructed and is being tested in Mexico.

5. Acknowledgments

This work was supported by the UK Engineering and Physical Sciences Research Council (EPSRC) [grant numbers EP/M025012/1, EP/R045518/1, and EP/S032622/1] and an Imperial College London EPSRC Impact Acceleration Account [grant number EP/R511547/1]. The work was also supported by the Royal Society under an International Collaboration Award 2020 [grant number ICA\R1\201302]. The authors would like to thank UK company Solar Flow Ltd. (www.solar-flow.co.uk). Hasan Yildizhan gratefully acknowledges a TÜBİTAK postdoctoral scholarship that supported his visit to Imperial College London. Data supporting this publication can be obtained on request from cep-lab@imperial.ac.uk. For the purpose of Open Access, the authors have applied a CC BY public copyright license to any Author Accepted Manuscript version arising from this submission.

6. References

Acosta-Pazmiño, I. P., Rivera-Solorio, C. I., Gijón-Rivera, M., 2022. Hybridization of a parabolic trough-based thermal plant for industrial heat and power generation. Renewable Energy, 191, 961–973. https://doi.org/10.1016/j.renene.2022.04.074

Barthwal, M., Rakshit, D., 2022. Holistic opto-thermo-electrical analysis of a novel spectral beam splitting-based concentrating photovoltaic thermal system. Journal of Cleaner Production, 379. https://doi.org/10.1016/j.jclepro.2022.134545

Cabral, D., Gomes, J., Hayati, A., Karlsson, B., 2021. Experimental investigation of a CPVT collector coupled with a wedge PVT receiver. Solar Energy, 215, 335–345. https://doi.org/10.1016/j.solener.2020.12.038

Chandan, Baig, H., Tahir, A. ali, Reddy, K. S., Mallick, T. K., Pesala, B., 2022. Performance improvement of a desiccant based cooling system by mitigation of non-uniform illumination on the coupled low concentrating photovoltaic thermal units. Energy Conversion and Management, 257, 115438. https://doi.org/10.1016/j.enconman.2022.115438

Chandan, Dey, S., Iqbal, S. Md., Reddy, K. S., Pesala, B., 2021. Numerical modelling and performance assessment of elongated compound parabolic concentrator based LCPVT system. Renewable Energy, 199–216. https://doi.org/10.1016/j.renene.2020.11.076

Demircan, C., Bayrakçı, H. C., Keçebaş, A., Calise, F., Vicidomini, M., 2023. The effect of temperature distribution on parabolic triangular-based CPVT system performances: Electrical and thermal perspectives. Thermal Science and Engineering Progress, 38, 101664. https://doi.org/10.1016/j.tsep.2023.101664

Deymi-Dashtebayaz, M., Rezapour, M., Farahnak, M., 2022. Modeling of a novel nanofluid-based concentrated photovoltaic thermal system coupled with a heat pump cycle (CPVT-HP). Applied Thermal Engineering, 201, 117765. https://doi.org/10.1016/j.applthermaleng.2021.117765

Herrando, M., Ramos, A., Zabalza, I., Markides, C. N., 2019. A comprehensive assessment of alternative absorber-exchanger designs for hybrid PVT-water collectors. Applied Energy, 235, 1583–1602. https://doi.org/10.1016/j.apenergy.2018.11.024

Hou, Y. tian, Yu, X. hui, Yang, B., Liu, S. shuai, Qi, Y., 2023. Optical performance investigation on flat receiver for parabolic trough solar collector based on the MCRT method. Renewable Energy, 202, 525–536. https://doi.org/10.1016/j.renene.2022.11.109

Huang, G., Markides, C. N., 2021. Spectral-splitting hybrid PV-thermal (PV-T) solar collectors employing semi-transparent solar cells as optical filters. Energy Conversion and Management, 248, 114776. https://doi.org/10.1016/j.enconman.2021.114776

Huang, G., Wang, K., Markides, C. N., 2021. Efficiency limits of concentrating spectral-splitting hybrid photovoltaic-thermal (PV-T) solar collectors and systems. Light: Science and Applications, 10(1), 1–14. https://doi.org/10.1038/s41377-021-00465-1

Karathanassis, I. K., Papanicolaou, E., Belessiotis, V., Bergeles, G. C,. 2017. Design and experimental evaluation of a parabolic-trough concentrating photovoltaic/thermal (CPVT) system with high-efficiency cooling. Renewable Energy, 101, 467–483. https://doi.org/10.1016/j.renene.2016.09.013

Liang, H., Su, R., Huang, W., Cheng, Z., Wang, F., Huang, G., Yang, D., 2022. A novel spectral beam splitting photovoltaic/thermal hybrid system based on semi-transparent solar cell with serrated groove structure for co-generation of electricity and high-grade thermal energy. Energy Conversion and Management, 252, 115049. https://doi.org/10.1016/j.enconman.2021.115049

Madurai Elavarasan, R., Mudgal, V., Selvamanohar, L., Wang, K., Huang, G., Shafiullah, G. M., Markides, C. N., Reddy, K. S., Nadarajah, M., 2022. Pathways toward high-efficiency solar photovoltaic thermal management for electrical, thermal and combined generation applications: A critical review. Energy Conversion and Management, 255, 115278. https://doi.org/10.1016/j.enconman.2022.115278

Parthiban, A., Mallick, T. K., & Reddy, K. S., 2022. Integrated optical-thermal-electrical modeling of compound parabolic concentrator based photovoltaic-thermal system. Energy Conversion and Management, 251, 115009. https://doi.org/10.1016/j.enconman.2021.115009

Yousef, M. S., Abdel Rahman, A. K., Ookawara, S., 2016. Performance investigation of low – Concentration photovoltaic systems under hot and arid conditions: Experimental and numerical results. Energy Conversion and Management, 128, 82–94. https://doi.org/10.1016/j.enconman.2016.09.061

Appendix: Units and Symbols

Table 2: List of symbols

Quantity	Symbol	Unit
Absorptance	α	
Acceleration due to gravity	g	m/s^2
Aperture area	A_{ap}	m^2
Density	ρ	kg/m^3
Dynamic viscocity	μ	Pa.s
Efficiency	η	%
Emittance	ε	
Mass flowrate	$\dot{m}$	kg/s
Pressure	P	Pa
Reduced temperature	T_r	$K.m^2/W$
Reflectance	r	
Shear stress	τ	Pa
Specific heat	c_p	J/ (kg.K)
Temperature	T	K
Temperature coefficienct of power	β	% /K
Thermal conductivity	k	W/(m.K)
Transmittance	τ	
Velocity	v	m/s

Table 3: List of subscripts

Quantity	Symbol
Reflection	ref
Incident	inc
Photovoltaic	pv
Thermal	th
Outlet fluid	fo
Inlet fluid	fi
Aperture	ap
Ambient	amb

Numerical Investigation of Energy Desorption in Dual Metal Hydride Bed based Thermochemical Energy Storage System

Sumeet Kumar Dubey[1], K. Ravi Kumar[1], Vinay Tiwari[2] and Umish Srivastva[2]

[1] Indian Institute of Technology (IIT) Delhi, New Delhi (India)

[2] Indian Oil Corporation R&D Centre, Faridabad, Haryana (India)

Abstract

Among thermal energy storage (TES) systems, thermochemical energy storage (TCES) systems are known for high energy storage density. Metal hydride (MH) based TCES system, due to its good chemical reversibility and higher thermal stability, found suitable for high temperature TES applications. Many studies have reported the improvement in energy storage characteristics with enhancement in the heat transfer phenomenon in dual MH bed systems. The study investigates the discharging characteristics of a dual MH bed system for high temperature thermal energy release process. The dual metal hydride bed system includes a high temperature metal hydride (HTMH) bed, which works as energy storage media operating at high temperatures and a low-temperature metal hydride (LTMH) bed, used as hydrogen storage media. $NaMgH_2F$ is used as HTMH, while Mg_2NiH_4 is used as LTMH. The heat transfer phenomenon, energy discharging characteristics, and hydrogen transfer during thermal energy release from HTMH are studied. The energy desorbed from the MH bed for thermal conductivity 0.5 W/m K, 0.75 W/m K, and 1 W/m K are found as 251.25 kJ, 258.22 kJ, and 260.57 kJ, respectively. Hydrogen absorbed in the HTMH during thermal energy desorption for thermal conductivity 0.5 W/m K, 0.75 W/m K, and 1 W/m K are 6.94 g, 7.13 g, and 7.17 g, respectively. The heat transfer phenomenon in HTMH bed has improved with the increase in thermal conductivity of HTMH, and hence, the heat desorption characteristics also improved. The thermal energy discharging rate from HTMH also increased with the increase in the thermal conductivity of the HTMH bed.

Keywords: Concentrating solar power, Thermochemical energy storage, High temperature thermal energy storage, Dual metal hydride system.

Introduction

Solar energy has a huge potential to fulfill the thermal energy requirement in industrial process heating and solar thermal power generation. However, the utilization of solar energy has challenges, such as its intermittent nature and diurnal variation hindering the usage of solar energy. A thermal energy storage system (TES) can address the abovementioned issues and utilize solar energy effectively. TES systems can be classified as sensible, latent, and thermochemical energy storage systems (Jain et al., 2021). Sensible energy storage system stores/releases heat by changing the temperature of the working media, while the latent energy storage system stores/releases heat by changing the phase of the storage media. Thermochemical storage system stores/releases heat as an endothermic/exothermic chemical reaction, as shown in the chemical reaction below in Equations 1 and 2. With the limitation of low energy storage density of sensible and latent storage, thermochemical energy storage has recently gained attention. TCES systems are also found thermally stable at high temperatures with good cyclic stability. Metal hydride-based thermochemical systems have better reversibility and long cyclic life as compared to other thermochemical energy systems.

$$MH + \Delta H \rightarrow Metal\,(alloy) + Hydrogen \tag{1}$$

$$NaMgH_2F + \Delta H \rightarrow NaF + Mg + H_2 \qquad (\Delta H = 96.8\ kJ/mol\ H_2) \tag{2}$$

In earlier studies on metal hydrides for thermal energy storage, Magnesium (Mg) and its alloys have been extensively studied because of their higher storage capacity, thermal stability, cyclic stability, and lesser cost. Mg-based metal hydrides have been studied to store waste heat for steam generation application. The system stored 9.08 kWh of heat energy at 370 ºC with storage efficiency near 80% (Bogdanović et al., 1995). A Mg hydride system was also studied for cyclic stability at 420 ºC. 19 gm Mg hydride system was operated for 20 cycles without any change in storage density. The heat losses from the system were significant, but the authors expected a reduction in heat loss with an increase in the size of the system (Paskevicius et al., 2015). Numerical analyses of single bed (Mg_2Ni alloy) HTMH have been performed to study heat transfer, energy absorption,

10.18086/swc.2023.03.06 Available at http://proceedings.ises.org

and desorption (sorption) characteristics (Dubey and Kumar, 2022a, 2022b, 2021a, 2021b). Tubular and annular configurations of Mg_2Ni alloy were compared for charging/discharging time and storage density. The desorption of hydrogen from the annular reactor was found to be 70% fast without much variation in energy storage density (Sunku Prasad and Muthukumar, 2023).

Dual metal hydride-based thermal energy storage systems were also investigated for the system's feasibility and performance. $NaMgH_2F$ and $TiCr_{1.6}Mn_{0.2}$ were used as HTMH and LTMH, respectively and an energy storage density of 226 kWh/m^3 was reported (D'Entremont. et al., 2017). Another dual metal hydride system, which used Mg_2FeH_6 as HTMH and Na_3AlH_6 as LTMH, was investigated. The system was found suitable for the temperature range of 450-500 ºC and energy storage density of 132 kWh/m^3 (D'Entremont et al., 2018). The same pair of metal hydrides used fins as extended surfaces and reported an energy storage density of 90 kWh/m^3 and 96% storage efficiency (Sofiene Mellouli et al., 2018). Another study that used Mg_2Ni alloy as HTMH and $LaNi_5$ alloy as LTMH reported 156 kWh/m^3 energy storage density with an energy storage density of 89.4% (Malleswararao et al., 2020).

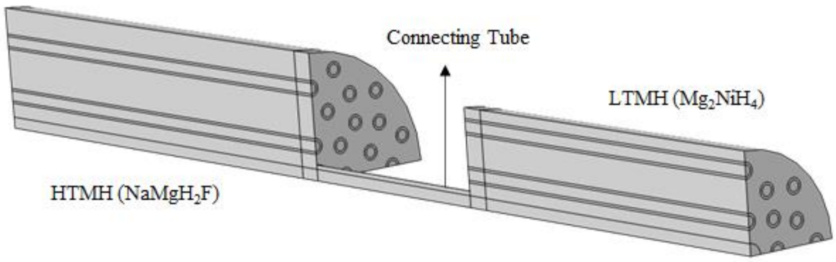

Figure 1: Geometry of coupled metal hydride bed system

This study considers the discharging process of heat at high temperature from a dual metal hydride bed system for performance analysis. $NaMgH_2F$ is used as HTMH, while Mg_2NiH_4 is used as LTMH. One kg of HTMH storage media is considered in a cylindrical shape bed. The HTMH and LTMH beds are embedded with radially distributed axial heat transfer fluid (HTF) tubes and a hydrogen tube at the center coupled by a connecting tube, as shown in Figure 1. Since the HTMH and LTMH are symmetric with respect to the x and y axis, one-fourth of the complete geometry is considered for analysis to minimize the computational time. The LTMH requirement is calculated by considering the quantity of hydrogen released from HTMH.

Mathematical Modelling

This section includes a discussion on the model development in COMSOL Multiphysics. The governing equations, thermochemical properties, assumptions, geometry details, initial values, and boundary conditions used in the model are discussed in detail.

Governing Equation

The mass, momentum, and energy conservation equation used in the numerical analysis are discussed (Dubey and Kumar, 2022b, 2021a; Malleswararao et al., 2020). Equation (3) represents the mass balance equation for hydrogen flowing inside the pores of metal hydride while eq. (4) represents the mass balance equation for the metal hydride fraction. Equation (6) and Equation (7) represent mass balance for HTF (compressed air) and hydrogen flow in tubes.

$$\varepsilon \frac{\partial \rho_g}{\partial t} + \nabla.\left(\rho_g u_g\right) = -S_m \tag{3}$$

$$(1-\varepsilon)\frac{\partial \rho_s}{\partial t} = S_m \tag{4}$$

$$S_m = C_d exp\left(\frac{-E_d}{RT}\right) ln\left(\frac{p}{p_{eq}}\right)(\rho_{sat} - \rho) \tag{5}$$

$$\frac{\partial \rho_g}{\partial t} + \nabla.\left(\rho_g u_g\right) = 0 \tag{6}$$

$$\frac{\partial \rho_a}{\partial t} + \nabla.(\rho_a u_a) = 0 \tag{7}$$

The Brinkman equation represented by equation (8) is used for the momentum balance of hydrogen flow in metal hydride pores. Navier Stokes equation represented by equations (9) and (10) are used for the momentum balance of hydrogen and HTF.

$$\frac{\rho_g}{\varepsilon}\left(\frac{\partial u_g}{\partial t} + u_g.\frac{\nabla u_g}{\varepsilon}\right) = -\nabla p - \frac{\mu_g}{K}u_g - \frac{S_m}{\varepsilon^2}u_g + \nabla.\left[\frac{\mu_g}{\varepsilon}\left(\nabla u_g + \left(\nabla u_g\right)^T\right) - \frac{2\mu_g}{3\varepsilon}\left(\nabla.u_g\right)\right] \tag{8}$$

$$\left(\frac{\partial u_g}{\partial t} + u_g.\frac{\nabla u_g}{\varepsilon}\right) = -\nabla p + \nabla.\left[\mu_g\left(\nabla u_g + \left(\nabla u_g\right)^T\right) - \frac{2\mu_g}{3}\left(\nabla.u_g\right)\right] \tag{9}$$

$$\left(\frac{\partial u_a}{\partial t} + u_a.\frac{\nabla u_a}{\varepsilon}\right) = -\nabla p + \nabla.\left[\mu_a(\nabla u_a + (\nabla u_a)^T) - \frac{2\mu_a}{3}(\nabla.u_a)\right] \tag{10}$$

Energy balance equations for metal hydride , hydrogen and HTF are represented by equation (10), (15), and (16) respectively. Effective thermal properties are calculated by using average volume methods as represented by equation (12) and (13). Energy source term (the volumetric energy absorption rate) is represented by equation (14).

$$\left(\rho c_p\right)_{eff}\frac{\partial T}{\partial t} + \rho c_{pg}\left(u_g.\nabla T\right) = \nabla.\left(\lambda_{eff}\nabla T\right) + S_T \tag{11}$$

$$\lambda_{eff} = \varepsilon\lambda_g + (1-\varepsilon)\lambda_s \tag{12}$$

$$\left(\rho c_p\right)_{eff} = \varepsilon\left(\rho c_p\right)_g + (1-\varepsilon)\left(\rho c_p\right)_s \tag{13}$$

$$S_T = S_m(\Delta h) \tag{14}$$

$$\left(\rho_g c_{pg}\right)\left(\frac{\partial T}{\partial t} + u_g.\nabla T\right) = \nabla.\left(\lambda_g\nabla T\right) \tag{15}$$

$$\left(\rho_a c_{pa}\right)\left(\frac{\partial T}{\partial t} + u_a.\nabla T\right) = \nabla.\left(\lambda_a\nabla T\right) \tag{16}$$

Table 1: Metal hydride properties used in analysis (D'Entremont et al., 2018; Nyamsi and Tolj, 2021; Sheppard et al., 2014)

Properties	HTMH	LTMH
Reaction rate constant (1/s)	120000 (desorption)	175 (desorption)
Activation energy (kJ/mol)	102.5 (desorption)	52.2 (desorption)
Enthalpy of reaction (kJ/mol)	96.8	64.5
Entropy of reaction (J/mol K)	138	122.2
Specific heat capacity (kJ/kg K)	0.419	0.697
Gravimetric storage density (wt%)	2.5	3.6
Unsaturated density (kg/m^3)	1390	3200
Saturated density (kg/m^3)	1424.75	3315.2
Thermal conductivity (W/m K)	0.5	0.2

Assumptions

The assumptions considered in the numerical investigation are listed below.

- H_2 is assumed as an ideal gas.
- Thermal equilibrium between H_2 and MH are considered.
- The MH material is homogenous and isotropic.
- The effect of radiation inside the MH bed is not considered.
- The thermal properties of MH, H_2, and HTF are considered constant.
- The heat transfer between MH bed and surrounding is neglected.

Geometrical Parameters

The dimensions of the different domains of the dual metal hydride bed system considered in the numerical modeling are listed in Table 2. The diameter and height of the LTMH and HTMH bed, along with the dimensions of heat transfer fluid tubes and hydrogen supply tube, are listed below.

Table 2: Geometrical parameter of computational domain

Parameter	HTMH	LTMH
MH bed diameter (cm)	10.4	7.9
MH bed height (cm)	20.8	15.8
Diameter of H_2 tube (cm)	0.95	0.95
HTF tube inner diameter (cm)	0.44	0.44
HTF tube outer diameter (cm)	0.64	0.64
Number of HTF tubes	44	24

Initial Values

The initial values of different domains considered in the analysis are listed in Table 3 below.

Table 3: Initial values of different domains of HTMH and LTMH

Domain	$NaMgH_2F$ (HTMH)	Mg_2NiH_4 (LTMH)
Temperature of MH bed and HTF (°C)	550	386.6
Pressure of MH bed (bar)	11.61	18.84
Temperature of H_2 (°C)	25	25
Pressure of H_2 (bar)	1	1
Pressure of HTF (bar)	1	1
Density of MH bed (kg/m^3)	1390	3315.2

Thermodynamic cycle

The thermodynamic cycle of the MH bed for energy absorption and energy release process is shown in Figure 2. The energy release process takes place at point D where hydrogen movement is shown by dashed blue line from point A to D. The temperature of point D is 550ºC and due to the pressure difference between point A and D the movement of hydrogen takes place.

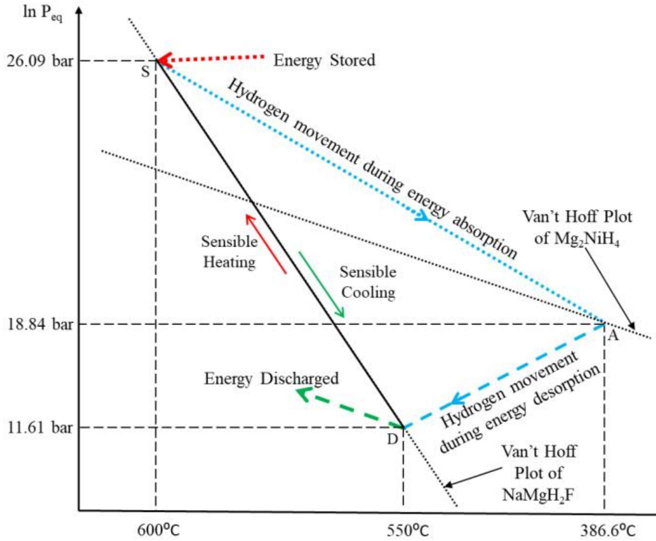

Figure 2: Thermodynamic cycle for dual MH bed TES system

Results and discussion

The study performed on the dual metal hydride bed system includes heat transfer analysis and energy desorption characteristics for variation of thermal conductivity of HTMH bed. Heat transfer analysis includes the study of temperature variation in the MH bed for different thermal conductivity of HTMH. The energy desorption characteristics include the evaluation of the quantity of energy released from the HTMH bed, the desorption rate, and the quantity of hydrogen absorbed in the HTMH bed.

During energy release from the HTMH bed, the average temperature of HTMH increases initially because of the exothermic reaction and the metal hydride bed releases more than 60% of thermal energy within 2000 seconds for all three cases of thermal conductivity. Figure 3 represents the variation of average metal hydride bed temperature with time for three different cases of thermal conductivity. With the increase in thermal conductivity of the MH bed, heat transfer from the MH bed is found to be improving and the MH bed temperature quickly attains the equilibrium temperature. The saturation fraction represents the fraction of thermal energy in the MH bed. The value of saturation fraction 1 means the MH bed is completely saturated with the thermal energy and no heat absorption will occur. The zero value of saturation fraction represents an empty MH bed. Figure 4 represents the saturation curve of the HTMH bed with time for different thermal conductivities. Due to effective heat transfer with higher thermal conductivity value, the metal hydride bed releases heat faster.

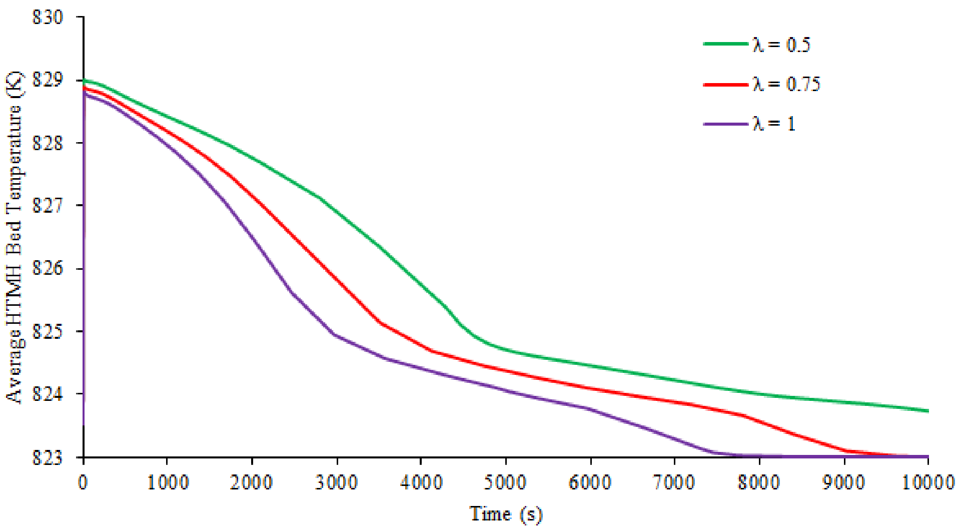

Figure 3: Average MH bed temperature variation of HTMH bed with time

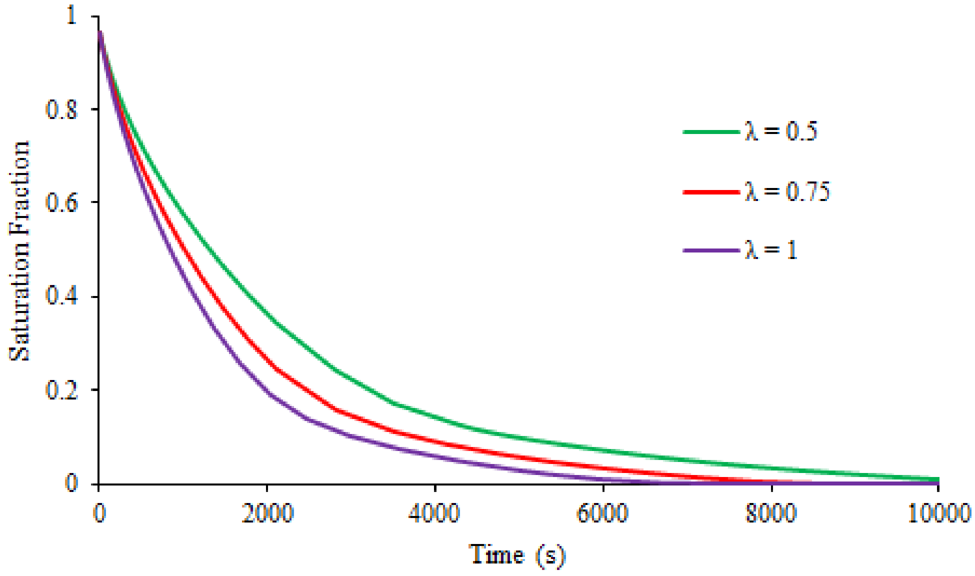

Figure 4: Saturation fraction variation of HTMH bed with time

Table 4 represents the saturation fraction value of the HTMH bed at different instants for three different thermal conductivity cases considered for analysis. The energy fraction available in HTMH bed at 500 s for 0.5 W/m K, 0.75 W/m K, and 1 W/m K thermal conductivity is found as 0.72, 0.67, and 0.64, respectively. Similarly, at 4000 s, the values are 0.14, 0.09, and 0.05, respectively. It shows that the energy release rate increases with the increase in thermal conductivity of the HTMH bed.

Table 4: Saturation fraction for different thermal conductivity at different instants during energy desorption

Time (s)	Saturation Fraction (HTMH)		
	0.5 (W/m K)	**0.75 (W/m K)**	**1.0 (W/m K)**
500	0.720686	0.677386	0.641221
1000	0.573917	0.502201	0.443264
2000	0.361458	0.264213	0.196231
3000	0.222463	0.145327	0.101345
4000	0.141797	0.090014	0.058569

The temperature contours and density contours for the energy release process at different instant is shown in Figure 5 and 6. The legend on the left in Figures 5 and 6 indicates the values for HTMH, while the right one indicates LTMH values. The cross-sectional temperature of HTMH is more uniform for high thermal conductivity. Due to improvement in heat transfer for higher thermal conductivity, the increase in temperature of HTMH bed is lesser and thus, the reaction kinetic is better in control rather than uncontrolled reaction due to higher temperature.

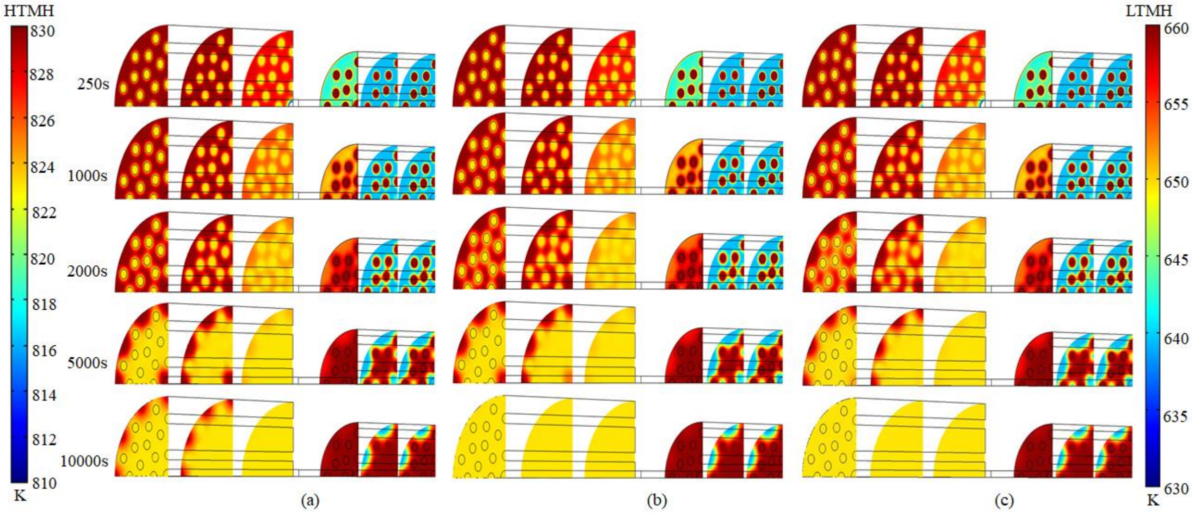

Figure 5: Temperature contours of dual MH bed for different thermal conductivity (a) 0.5, (b) 0.75, and (c) 1 W/m K

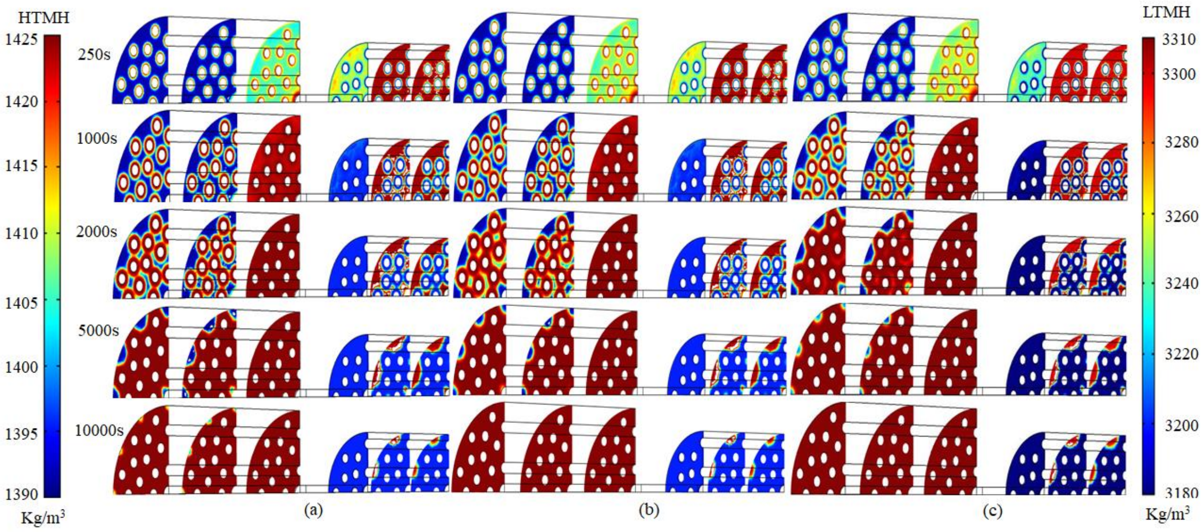

Figure 6: Density contours of dual MH bed for different thermal conductivity (a) 0.5, (b) 0.75, and (c) 1 W/m K

The energy released from the HTMH bed is found to increase with the thermal conductivity of the HTMH bed. The thermal energy release for 0.5 W/m K, 0.75 W/m K, and 1 W/m K thermal conductivity is found to be 251.25 kJ, 258.22 kJ, and 260.57 kJ, respectively. The quantity of hydrogen absorbed in the HTMH bed during energy release for 0.5 W/m K, 0.75 W/m K, and 1 W/m K thermal conductivity are found as 6.94 g, 7.13 g, and 7.17 g, respectively.

Conclusions

The heat transfer improvement due to an increase in the thermal conductivity of HTMH has shown better energy desorption characteristics. The key takeaways of the analysis are as follows:

- The increased thermal conductivity of the metal hydride bed leads to improved heat transfer rate from the HTMH bed.
- The release rate of energy has increased with the increase in the thermal conductivity of the HTMH bed.
- The energy release from the MH bed was found minimum for thermal conductivity 0.5 W/m K i.e., 251.25 kJ, and maximum for 1 W/m K i.e., 260.57 kJ.
- Hydrogen absorbed in the HTMH for thermal conductivity 0.5 W/m K, 0.75 W/m K, and 1 W/m K are 6.94 g, 7.13 g, and 7.17 g, respectively.

Acknowledgments

The authors are thankful to the Science and Engineering Research Board (SERB), Department of Science and Technology (DST), Government of India for awarding "Prime Minister Fellowship for Doctoral Research" to Mr. Sumeet Kumar Dubey in collaboration with Indian Oil Corporation Limited, Research and Development Centre and kind support from Confederation of Indian Industry (CII).

References

Bogdanović, B., Ritter, A., Spliethoff, B., Straßburger, K., 1995. A process steam generator based on the high temperature magnesium hydride/magnesium heat storage system. International Journal of Hydrogen Energy 20, 811–822. https://doi.org/10.1016/0360-3199(95)00012-3

D'Entremont., A., Corgnale, C., Sulic, M., Hardy, B., Zidan, R., Motyka, T., 2017. Modeling of a thermal energy storage system based on coupled metal hydrides (magnesium iron – sodium alanate) for concentrating solar power plants. International Journal of Hydrogen Energy 42, 22518–22529. https://doi.org/10.1016/j.ijhydene.2017.04.231

D'Entremont, A., Corgnale, C., Hardy, B., Zidan, R., 2018. Simulation of high temperature thermal energy storage system based on coupled metal hydrides for solar driven steam power plants. International Journal of Hydrogen Energy 43, 817–830. https://doi.org/10.1016/j.ijhydene.2017.11.100

Dubey, S.K., Kumar, K.R., 2022a. Charging and discharging analysis of thermal energy using magnesium nickel hydride based thermochemical energy storage system. Sustainable Energy Technologies and Assessments 52, 101994. https://doi.org/10.1016/j.seta.2022.101994

Dubey, S.K., Kumar, K.R., 2022b. Numerical investigation of energy desorption from magnesium nickel hydride based thermal energy storage system. Journal of Energy Systems 6, 165–175. https://doi.org/10.30521/jes.952627

Dubey, S.K., Kumar, K.R., 2021a. Numerical investigation of energy desorption from magnesium nickel hydride based thermal energy storage, in: 9th Eur. Conf. Ren. Energy Sys. Istanbul, Turkey, pp. 457–462.

Dubey, S.K., Kumar, K.R., 2021b. Numerical Investigation of Thermal Energy Storage using Magnesium Nickel Hydride, in: 26th National and 4th International ISHMT-ASTFE Heat and Mass Transfer Conference. pp. 577–583. https://doi.org/10.1615/IHMTC-2021.870

Jain, S., Dubey, S.K., Kumar, K.R., Rakshit, D., 2021. Thermal Energy Storage for Solar Energy, in: Fundamentals and Innovations in Solar Energy. pp. 167–215. https://doi.org/10.1007/978-981-33-6456-1_9

Malleswararao, K., N, A., Srinivasa Murthy, S., Dutta, P., 2020. Performance prediction of a coupled metal hydride based thermal energy storage system. International Journal of Hydrogen Energy 45, 16239–16253. https://doi.org/10.1016/j.ijhydene.2020.03.251

Nyamsi, S.N., Tolj, I., 2021. The impact of active and passive thermal management on the energy storage efficiency of metal hydride pairs based heat storage. Energies 14. https://doi.org/10.3390/en14113006

Paskevicius, M., Sheppard, D.A., Williamson, K., Buckley, C.E., 2015. Metal hydride thermal heat storage prototype for concentrating solar thermal power. Energy 88, 469–477. https://doi.org/10.1016/j.energy.2015.05.068

Sheppard, D.A., Corgnale, C., Hardy, B., Motyka, T., Zidan, R., Paskevicius, M., Buckley, C.E., 2014. Hydriding characteristics of NaMgH2F with preliminary technical and cost evaluation of magnesium-based metal hydride materials for concentrating solar power thermal storage. RSC Advances 4, 26552–26562. https://doi.org/10.1039/c4ra01682c

Sofiene Mellouli, Askri, F., Edacherian, A., Alqahtani, T., Algarni, S., Abdelmajid, J., Phelan, P., 2018. Performance analysis of a thermal energy storage based on paired metal hydrides for concentrating solar power plants. Applied Thermal Engineering 144, 1017–1029. https://doi.org/.1037//0033-2909.I26.1.78

Sunku Prasad, J., Muthukumar, P., 2023. Design of metal hydride reactor for medium temperature thermochemical energy storage applications. Thermal Science and Engineering Progress 37, 101570. https://doi.org/10.1016/j.tsep.2022.101570

Numerical study of novel air-based PVT designs validated using standardized testing approach.

Giorgos Aspetakis[1], Qian Wang[1,2]

[1] Department of Civil and Architectural Engineering, KTH Royal Institute of Technology, Teknikringen 78, Stockholm, 114 28, Sweden

[2] Uponor AB, Hackstavägen 1, Västerås, 721 32, Sweden

Abstract

The study focuses on the simulation of a novel Air-Based Photovoltaic Thermal (PVT) prototype, experimentally investigated according to ISO 9806, specifically for collectors generating thermal and electrical energy. Experimental studies are carried out to validate a benchmark Computational Fluid Dynamics (CFD) simulation model in a previous study. The same setup shall be used to explore new thermal enhancement designs of the prototype. The aim of the model is on the one hand to assess the thermal performance enhancement of multiple newly developed inserts/baffles. The results indicate the optimal design selections for next-step experimental prototypes. The secondary objective is to assess the feasibilities of the PVT prototype for operational characteristics at different climate conditions. Insights are provided regarding the reliability, workflow and overall methodology of validating CFD models by testing through an international standardized process. Outlines for system-level modelling are presented as well.

Keywords: PVT, simulation, experimental, validation

1. Introduction

Building integrated PVT solutions have shown promising potential for covering thermal and electrical demand in residential applications. However, the efficiency of photovoltaic cells drops linearly with temperature (Skoplaki and Palyvos, 2009). Cooling PV modules effectively enhances their electrical efficiency and prolongs their operational lifetime (Dwivedi et al., 2020). Decentralized on-site renewable energy generation in forms of both thermal and electrical energy is vital for the transition to a carbon free society. PVTs can assist in facilitating sustainable growth worldwide and are strongly linked to the UN's Sustainable development goals 7 and 11 which focus on clean, affordable energy production and sustainable cities respectively.

By cooling PV modules, PVT systems can maintain increased electrical efficiency and generate thermal energy. Waste heat from the PV surface causes a temperature rise of the cooling medium which can subsequently be harnessed. Air based systems, frequently overlooked, are examined in this study. Such systems require testing and experimental studies to validate for numerical simulations and/or to evaluate real-life performance. To develop thermally efficient designs, Computational Fluid Dynamic (CFD) models can evaluate the performance of different insert arrangements, in only a fraction of time and effort of a fully-fledged outdoor testing sequence. Therefore, to uphold credible results, a validation process has already taken place.

Scaling up solutions is equally important for the wide-adoptions of PVT technology. The feasibility of scaled up configurations can be estimated by utilizing simulations of PVT systems, for example, CFD or analytic numerical ones, without experimentally testing each individual case. To further strength the replicability and scalability, standardized testing approaches were utilized. Current literature investigated various designs, yet few studies carry out validations based on standard approach.

Testing in regions with low solar potential, such as the Nordic countries, is of also of great interest, with limited studies available. In the current study, validation data are obtained from standardized testing of a blank channel PVT collector located in Sweden.

The test methods described in the ISO 9806:2017 (*ISO 9806:2017 Solar energy — Solar thermal collectors — Test methods*, 2017) standard are applied for certifying solar thermal collectors, including a dedicated part for thermal performance evaluation. The enhanced thermal performance of a newly developed PVT configuration, with a blank

10.18086/swc.2023.03.02 Available at http://proceedings.ises.org

air-channel, has been selected following the ISO 9806 testing procedure. The intent of this study is to present reliable designs, which have been developed using validated CFD models. More specifically, the aim is to determine the necessary requirements for successful CFD simulation of Air-based PVT collectors. These are incorporated in general guidelines for researchers and engineers that might have ISO test report.

2. Methods

2.1 Experimental testing

ISO 9806:2017 (ISO 9806:2017 Solar energy — Solar thermal collectors — Test methods, 2017) was followed for testing the thermal performance of the PVT prototype. A subsection is addressed to co-generating collectors. PVTs can therefore be tested with the same methods as solar air heaters, at the electrical maximum power point of the solar cells. More specifically, the prototype fits under the categories of air-heating collectors and Wind or Infrared Sensitive Collector (WISC), because the cooling medium utilized is air and the absorber surface, in this case the PV modules, are exposed to the ambient with no glazing.

An experimental testing rig located in in central Sweden was built for measurements. On a fixed angle base, situated on ground level a prototype PVT system was installed, consisting of PV panel, cooling channel underneath panel, air ducts, air fan unit and measurement instruments. The open-to-ambient configuration without air preconditioning, described in the standard, was implemented, shown in Figure 1. Ambient air is circulated through a blank channel under the PV surface through negative pressure. The standard requires temperature measurements with a maximum uncertainty of 0.2 K, thus Pt-100 RTD sensors were selected. For flow measurements, it was stressed that the sensor should not utilize thermal measurement methods. Therefore a configuration of a differential pressure transducer coupled with a Pitot tube was set up, from which the volume flow is calculated. The same pressure transducer was utilized to measure the pressure drop of the PVT

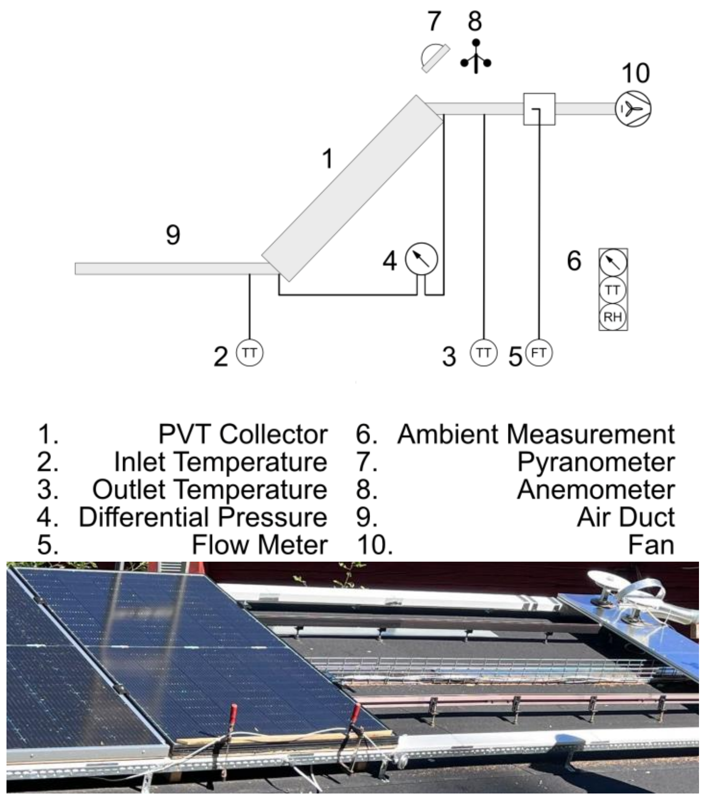

Fig. 1: Open-to-ambient setup with listed sensors and photo of the installation.

prototype. Two pyranometers were installed parallel to the PVT surface for global and diffuse irradiance monitoring, respectively. Alongside those, a cup anemometer was placed for measuring the wind parallel to the surface, in order to assess its effect on performance. Maximum Power Point Tracking (MPPT) was achieved through an inverter connected to the electrical output of the panel, measuring simultaneously the power output in real time. All data flows were directed to a central datalogger system. An example of measured data is presented in Figure 2, in which shows the inlet and outlet temperatures of the collector for a typical summer day.

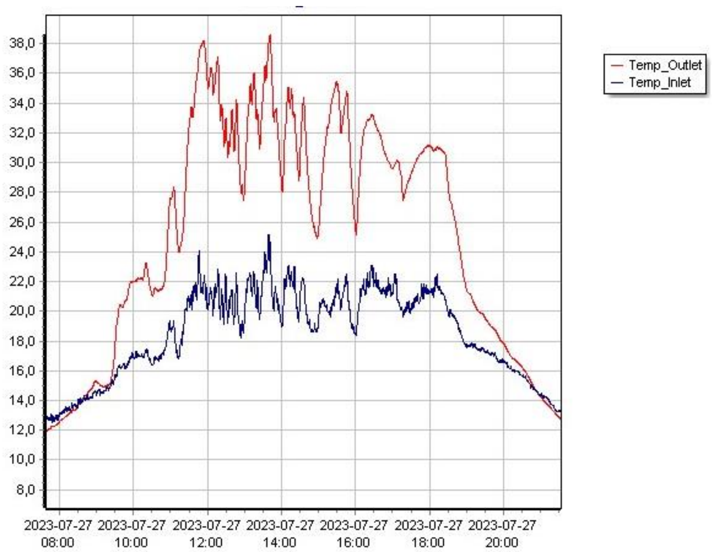

Fig. 2: Temperature of collector inlet and outlet for a typical summer day.

Table 1 presents the specifications of testing instruments measuring instruments along with their accuracy ranges. As per the standard, irradiance levels are always higher than 700 W/m^2 and near normal incidence angles were tested.

Tab. 1: Measuring instruments utilized in the experiment, detailing measurement location, type of sensor, brand and accuracy.

Measurement	Location	Type	Sensor	Accuracy
Temperature	Inlet Flow/Ambient	Pt-100 RTD	JUMO Etemp	±(0,1+0,0017 * T) K
	Outlet Flow			
Mass flow	Outlet Flow	Diff. Pressure+ Pitot Tube	KIMO CP212-HO-R	±0.5% of reading ± 2 Pa
Irradiance	Parallel to PV Surface	Pyranometer	Kipp & Zonen CM11	±2%
PV Electrical	PV Output	Inverter	In-house built	±1%
Windspeed	Parallel to PV Surface	Cup Anemometer	Thies Clima WT	±0.5 m/s
Datalogger	-	-	Campbell CR1000X	±(0.04% of reading + offset)

Validation of simulation models in Sola Air Heaters and PVT technologies typically requires the characterization of thermodynamic and hydraulic performance, which respectively necessitate the calculation of the Nusselt number (Nu) and friction factor for different Reynolds numbers (Re). Thus, measurements are taken at multiple flowrates and consequently at different Re values. The standard testing requires measurements at 3 mass flow rates. In this testing instance, these are expanded to 5 in order to incorporate the validation process in the standardized testing sequence. Effectively, two functions are served with one testing routine. Testing blocks had a duration 20 minutes allowing for stabilization of monitored values.

2.2 Calculations

For calculating thermal power output, measured physical quantities of the airflow are used. The temperature rise of the airflow underneath the PV surface caused by the exposure to solar irradiance is described below,

$$q_{col} = \dot{m}C_p(T_{out} - T_{in}) \qquad \text{(eq. 1)}$$

The heat transfer to the working fluid through convection is

$$q_{conv} = h(\bar{T}_{sur} - T_b) \qquad \text{(eq. 2)}$$

Where T_{sur} is the average surface temperature and

$$T_b = \frac{T_{out}+T_{in}}{2} \qquad \text{(eq. 3)}$$

which corresponds to the power output of the collector. Thus

$$q_{col} = q_{conv} \rightarrow h = \frac{\dot{m}C_p(T_{out}-T_{in})}{(\bar{T}_{sur}-\frac{T_{out}+T_{in}}{2})} \qquad \text{(eq. 4)}$$

The Nusselt number describes the ratio of convective to conductive heat transfer at a boundary in a fluid in the following way

$$Nu = \frac{hD_H}{k} \qquad \text{(eq. 5)}$$

And the friction factor f is a dimensionless number characterizing the energy needed to overcome the induced pressure drop.

$$f = \frac{(\Delta P/L)D_H}{2\rho U^2} \qquad \text{(eq. 6)}$$

The needed variables are measured and calculated from the testing, at different mass flow rates that lead to different Reynolds numbers:

$$Re = \frac{UD_H}{\nu} \qquad \text{(eq. 7)}$$

Where

$$D_H = \frac{4\times Area}{Wetted\ Perimeter} \qquad \text{(eq. 8)}$$

is the hydraulic diameter.

2.3 Simulation

ANSYS Fluent was applied for numerical calculations. Li et al. investigated the performance of various turbulence models in transpired collector applications and showed that the K-epsilon RNG turbulence model delivered the highest accuracy and consistency, with low computational demand. In this study, given the highly similarity of the heat transfer in PVT collectors and transpired collectors, this particular turbulence model was selected. Turbulent intensity was assumed to be around 5%. The interior walls of the collector are considered are set to no-slip condition and adiabatic due to the insulation installed. Since the heat transfer between surface and airflow needs to be investigated, the thermal boundary layer must be solved, requiring thus a value of $y^+=1$. The mesh has therefore been constructed accordingly and is shown in Figure 3.

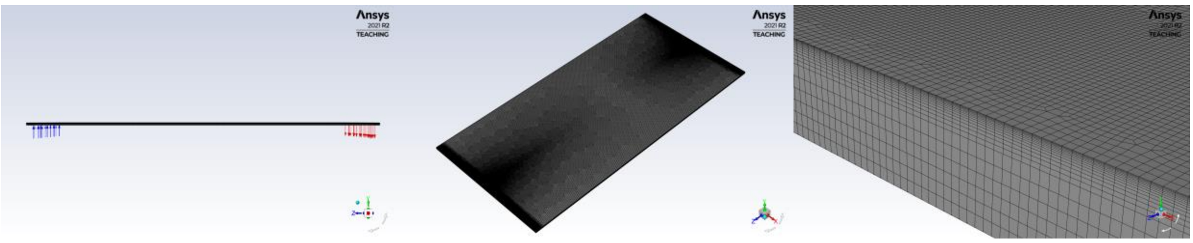

Fig. 3: Mesh of the CFD model, additionally showing applied inflation and inlet/outlet boundary.

To ensure the validity of the results, convergence criteria were set to 10e-6, and for the energy equation 10e-9. The boundary conditions were set according to experimental values. These include: irradiance, inlet temperature equal to ambient, flowrate, surface temperature. At the inlet a mass flow inlet was set, pressure outflow at the exit. At the wall surfaces, adiabatic heat flux boundary conditions were set. For the PV surface the following heat balance holds:

$$q = \alpha G - \varepsilon\sigma(T_{sur}^4 - T_\infty^4) - h(T_{sur} - T_a) - {}^{P}/_{A} \qquad \text{(eq. 9)}$$

Where α is the absorptance, ε emittance, σ Stefan-Boltzmann constant, h the heat transfer coefficient and P the electrical power generated. The terms in respective order represent the heat transferred to the airflow, absorbed solar irradiance, radiation losses, convection losses and electrical power generated. A diagram of the heat balance is shown in Fig 4.

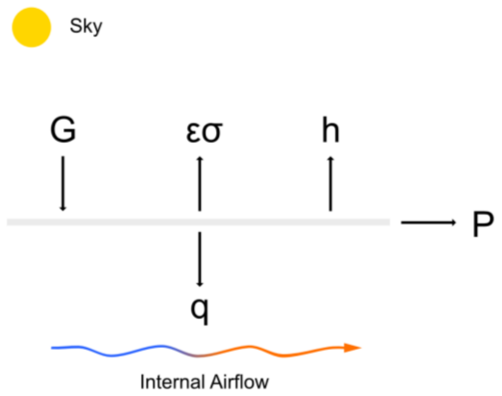

Fig. 4: Illustration of heat transfer at the PV surface boundary.

For the convection, the correlations for the heat transfer coefficient of solar collector cover glass developed by (Watmuff et al.,1977) have been utilized.

$$h_{glass} = 2.8 + 3u_{wind} \qquad \text{(eq. 10)}$$

The radiation temperature was calculated in a similar study (Kim et al., 2020) and is derived from:

$$T_\infty = 0.00552T_a^{1.5} \qquad \text{(eq. 11)}$$

Thus a mixed boundary condition can be used. Table 2 describes the different boundary conditions set in the simulation model.

Tab. 2: Location and Source of Boundary Conditions

Test Data Source	CFD Boundary Condition	Location
Irradiance G	Heat flux	PV Surface
Ambient Temp	Inlet Temperature	Inlet
Flowrate	Mass flow inlet	Inlet
-	Pressure Outflow	Outlet
-	Adiabatic	Walls

3. Results and Discussions

A comparison of test and simulated average outlet temperature is shown in Fig 5. Good agreement between results is achieved. Particularly, mean absolute error (MAE) is calculated 0.25 °C and normalized root square mean error (NRMSD) at 1.07%. Outlet temperature drops with higher mass flows. A slight increase is observed at 0.03 kg/s due to elevated irradiance levels at the time of testing, as shown in Fig. 5.

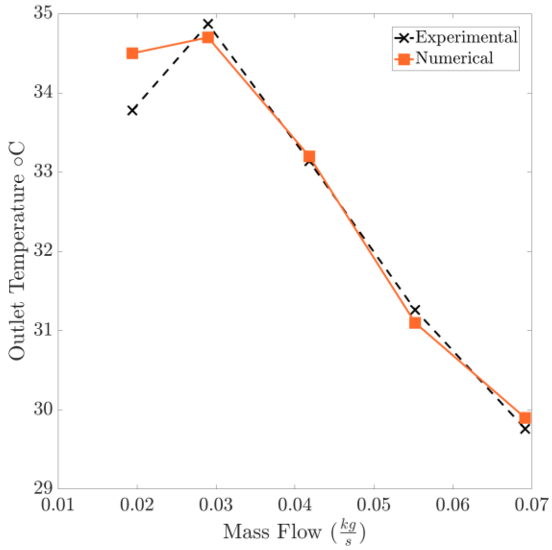

Fig. 5: Experimental and numerical outlet Temperature for different mass flows.

In Figure 6, the comparison of test and simulated thermal output is presented and displays acceptable agreement. MAE is equal to 8.44 W and NRMSD to 7.7%. Heat generated rises with mass flow rate. Although outlet temperature has decreased, a greater amount of air has been heated which translates to higher heat output. However, to achieve higher mass

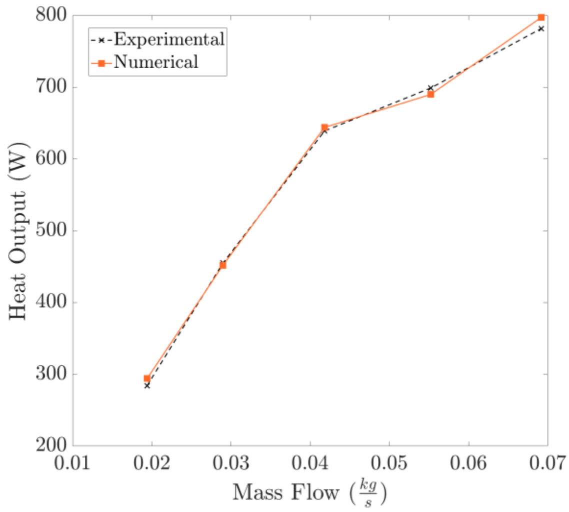

Fig. 6: Experimental and numerical thermal output for different mass flows

flows, blowers are required to compensate with higher pressure drops. The correlation is illustrated in Figure 7 where pressure drops measured and simulated are displayed. As expected, pressure drop increases with mass flow. Good agreement is observed, with higher mass flows containing relatively larger error. MAE was calculated at 1.38 Pa and NRMSD 17.1%. This might be due to the effect of minor losses and entrance effects which are under a quadratic correlation to the velocity of the flow, notably 90° turns and change of hydraulic diameter.

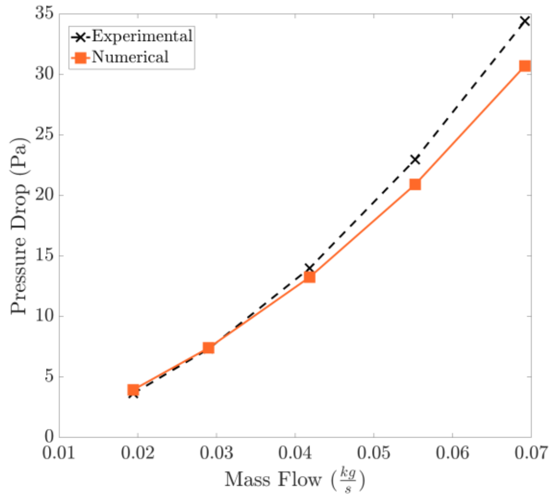

Fig. 7: Experimental and numerical pressure drop for different mass flows.

The Nusselt no. for different Reynolds no. values are displayed in Figure 8. Nu increases as the flow becomes more turbulent, as expected. Yet it remains relatively low, indicating that room for improvement exists. Various techniques have been developed on this front, most notably thermal inserts or modified absorber surfaces. As introduced, those add friction to the flow causing greater pressure drops. This effect is expressed by the friction factor *f*, presented in Figure 9. These values are expected to rise when thermal inserts are added. Designs that cause lower friction increase play an essential role in this application.

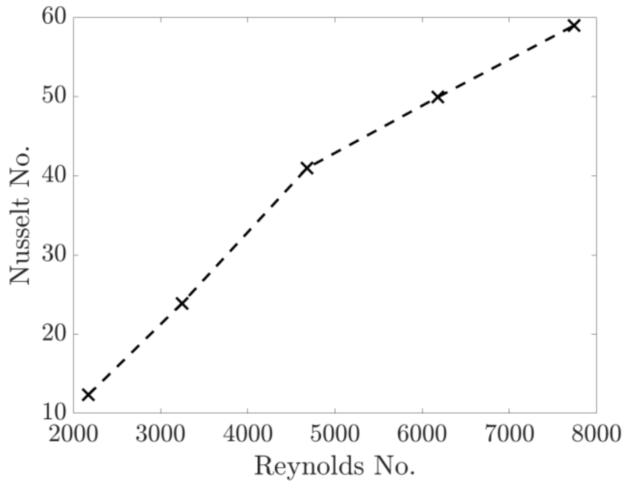

Fig. 8: Numerical Nusselt no. for different Reynolds no.

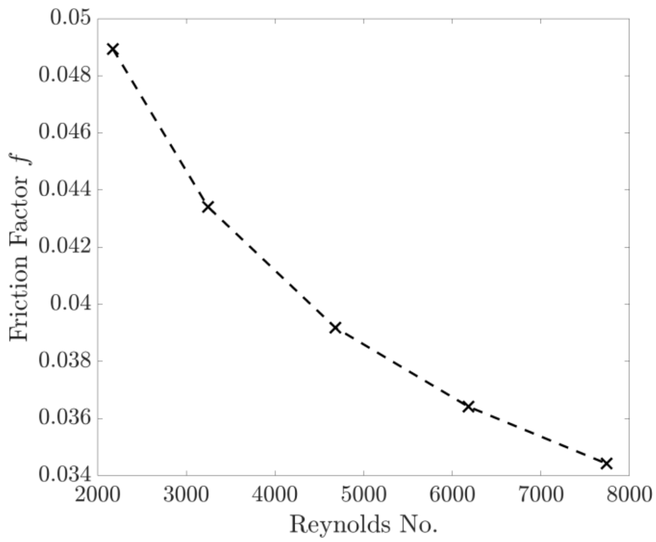

Fig. 9: Numerical Friction Factor f for different Reynolds no.

The results of the CFD simulation agree with test measurements, both in terms of thermal and pressure aspects, indicating that the CFD model can be considered valid for future investigations, having been validated by field testing. Thus, measurements according to ISO 9806 are adequate for constructing a CFD model of the collector. The necessary inputs can be derived from the ISO 9806 thermal performance report, an example shown in Figure 10. This, combined with corresponding schematics or drawings enables the modelling of collectors that have already been tested using the standardized method of ISO 9806, without performing other measurements. In essence, the measurements performed in the ISO 9806 are adequate for creating and validating a CFD simulation model of the investigated collector. Avoiding the reiteration of testing for older collectors saves a significant amount of time and resources.

Data point	$\dot{m}_i$	G''	ϑ_a	u	$K_b(\theta_T, \theta_L)$	$\eta_{hem,\dot{m}_i}$	$b_{u,\dot{m}_i}$	$\dot{Q}$	Standard deviation
	kg/h	W/m^2	°C	m/s	—	—	s/m	W	W
1									
2									
...									
27									

Fig. 10: Thermal performance report of the ISO 9806 standard, with the utilized parameters highlighted.

Research with streamlined modelling process is better able to explore additional modifications. These potentially lead to the development of new heat transfer enhancements that are suitable either for solar air heating or PVT technologies such as absorber geometries or thermal inserts. The main finding of the current study indicates that CFD modelling sourced with ISO 9806 performance data is a feasible practice.

4. Conclusion

The ISO 9806 standard was followed for the experimental testing of a PVT collector. Based on the measurements, a computational fluid dynamics model was devised. Agreement of experimental and numerical results indicates correct validation of the model. It was noted that the data measured was sufficient to determine the correct boundary conditions needed for the numerical analysis. Thus, investigators in possession of a ISO 9806 thermal performance report and schematics of the collector geometry, are able to successfully simulate thermal collectors or PVTs. As such, novel performance enhancing methods can be further explored with extensive design variations at the early design stage.

5. Acknowledgments

The authors gratefully acknowledge the financial support from the Swedish Energy Agency (grant number: 52488-1).

6. References

Dwivedi, P., Sudhakar, K., Soni, A., Solomin, E., Kirpichnikova, I., 2020. Advanced cooling techniques of P.V. modules: A state of art. Case Studies in Thermal Engineering 21. https://doi.org/10.1016/j.csite.2020.100674

ISO 9806:2017 Solar energy — Solar thermal collectors — Test methods, 2017. International Organization for Standardization, Geneva, Switzerland.

Kim, Y., Lee, K., Yang, L., Entchev, E., Kang, E., Lee, E., 2020. Validation and Numerical Sensitivity Study of Air Baffle Photovoltaic-Thermal Module. Energies 2020, Vol. 13, Page 1990 https://doi.org/10.3390/EN13081990

Li, S., Karava, P., Savory, E., Lin, W.E., 2013. Airflow and thermal analysis of flat and corrugated unglazed transpired solar collectors. Solar Energy 91, 297–315. https://doi.org/10.1016/J.SOLENER.2013.01.028

Skoplaki, E., Palyvos, J.A., 2009. On the temperature dependence of photovoltaic module electrical performance: A review of efficiency/power correlations. Solar Energy 83, 614–624. https://doi.org/10.1016/J.SOLENER.2008.10.008

Watmuff, J., Charters, W., Proctor, D., 1977. Solar and wind induced external coefficients - Solar collectors. Cooperation Mediterraneenne pour l'Energie Solaire, 56

NOMENCLATURE AND SYMBOLS

Quantity	Symbol	Unit
Heat transfer coefficient	h	W m^{-2} K^{-1}
Thermal conductivity	k	W m^{-1} K^{-1}
Hydraulic diameter	D_H	m
Pressure drop	ΔP	Pa
Density	ρ	kg m^{-3}
Flow velocity	U	m s^{-1}
Friction Factor	f	
Reynolds No.	Re	
Nusselt No.	Nu	
Irradiance	G	W m^{-2}
Emittance	ε	
Absorptance	α	
Stefan-Boltzmann constant	σ	W m^{-2} K^{-4}
Heat flux	q	W m^{-2}
Mass flow rate	$\dot{m}$	kg s^{-1}
Specific heat	c	J kg^{-1} K^{-1}
Kinematic viscosity	ν	m^2 s^{-1}
Mean Absolute Error	MAE	
Normalized Root Mean Square Error	$NRMSE$	

Performance assessment of double Slope Solar Still with Pebbles & Cooling water jacket for performance enhancement

Ashutosh Mishra[1] and Ravi Kumar Sharma[2,*]
[1] Pluss Advanced Technologies Ltd., Haryana, India
[2]Department of Mechanical Engineering, Manipal University Jaipur, Rajasthan, India

Abstract

The unavailability of fresh drinking water can sometimes compel people to drink unclean water which causes illnesses and other health issues. This research work aims to develop & study a cost-efficient desalination technique employing thermal energy of solar irradiance. This device popularly known as passive solar still has been studied for a district in Jaipur, India for three solar still configurations i.e., 1) Conventional double slope solar still; 2) Still incorporating Pebbles as naturally available energy storage material & 3) cooling water jacket for glass cover for higher clean water production. Along with the experimental work, Energy & Exergy efficiency calculations were also performed for the entire system. In this study it has been concluded that the double slope solar still incorporating water cooling jacket for glass cover resulted in highest water production, Energy & exergy efficiency followed by still with Pebbles & conventional solar still. The total water yield for the above configurations being 1.9, 2.3 and 2.9 Liters respectively.

Keywords: Solar Desalination, Solar Thermal Power, cost efficient, Double Slope Solar Still, Energy Storage Material.

1. Introduction

Clean water is one of the basic necessities of different lifeforms to survive on the planet. In fact, scarcity of water also affects food, livestock management, industries etc. The demand for this resource has escalated over time due to the increase in population & growth in different sectors like agriculture & industries. Often direct use of this resource is not advisable due to the presence of harmful organisms or high TDS. Out of the various methods available such as reverse osmosis, fossil fuel based thermal desalination etc., most of these are highly energy intensive and expensive (Kariman et al., 2023). Hence a need for an alternative solution is generated for production of clean water at very low cost following a simple process.

Passive Solar Desalination technique using a solar still is a promising solution as it is cheap & follows a simple process of evaporation and condensation utilizing solar thermal power. Solar still is a simple device that can be used to convert saline, brackish water into potable water (Tarazona-Romero et al., 2022) . The construction of a solar still comprises of a basin containing brackish water covered with a transparent media such as glass (Murugavel et al., 2010). The solar irradiance when passing through transparent cover, is absorbed by water & basin which increases the temperature of brackish water inside the still due to greenhouse effect. This gives water enough thermal energy to evaporate in a saturated state at a slow rate leaving behind the impurities and rising towards Transparent cover. Once encountering the inner side of cover, due to temperature difference between water vapor and glass cover, the water vapor condenses on the inner side of glass cover. This condensed water then flows along the inner surface of glass cover due to gravity and is collected in a collection tank via a drainage channel. This clean water can be used directly without the need for any further treatment. An important point to keep in mind is that this type of setup can be easily fabricated using locally available materials without the need for any fabrication expertise.

In India, many areas of Gujarat, Rajasthan & Haryana have been facing a problem of freshwater scarcity. Luckily these areas are blessed with ample solar irradiance which can be utilized to desalinate salty ground water. Findings of one such study conducted by (Khanna et al., 2008) for Chui, a remote village of Rajasthan reported that people

10.18086/swc.2023.03.09 Available at http://proceedings.ises.org

of this village have been facing a lot of difficulty getting a fresh water source. A water sample testing done at Guru Kripa Test House; district of Ajmer revealed that quality of drinking water is not appropriate. The author's findings also indicate that the local people of this village were optimistically looking for a low-cost water purification device which can fulfill the basic water demands. Conventional desalination methods such as reverse osmosis, multistage flash and electro-dialysis are expensive and use conventional energy sources which negatively pollute the environment. Application of solar stills in India stands a good chance of success due to availability of both solar irradiance and need for fresh water at low cost.

Some of the known development cases of Solar distillation in India include installation of first solar based distillation plant by Central Salt and Marine Chemical Research Institute (CSMCRI) in Bhavnagar to supply drinking water in Awania village and Chhachi lighthouse in 1978 (Natu et al., 1979). This facility consists of 90 stills each having an evaporation surface area of 20.74 m^2. With a production capacity of 5000L per day. After regular use of desalinated water, residents of this village understood the quality difference between desalinated water & water available in ponds/wells. Although Solar still are of great advantage they also require regular cleaning due to accumulation of salts which settle down during desalination process. Also, the production capacity of such systems is very low hence such systems are generally uneconomical for mass adoption. Recently a lot of work has been carried out to enhance the water yield of a solar still.

It has been established that air or water flow over still cover enhances the productivity of still. This is because when cover temperature drops, it creates higher temperature difference between saturated water & condensing surface (Dimri et al., 2008, Dutt et al., 1993). Efforts were made to understand the effect of cover slope angle on still productivity, it was realized that for locations with latitude higher than 20°, single-sloped stills were found preferable whereas for lower latitudes, double-sloped stills facing north and south directions and having a cover inclination equal to the latitude angle received near normal sun rays throughout the year (Murugavel et al., 2008). Studies for brine depth for still suggested that higher outputs and efficiencies occur at lower depths of brine (Badran, 2007, Tiwari & Tiwari, 2007). (Kalidasa Murugavel et al., 2008, Tripathi & Tiwari, 2005) reported that productivity of still is inversely proportional to brine depths for daytime but for nighttime the reverse is true. This inverse effect was attributed to the energy storage effects of brine during nighttime. The productivity of solar stills can also be enhanced by utilizing phase change materials. (Ayoub & Malaeb, 2012) in their work have integrated a thin layer of stearic acid beneath basin as Phase change material. During the day, PCM charges up and release this same energy during night, hence extending the evaporation duration even in night until next day morning. Although daytime productivity of still dropped a little but overall productivity for entire duration of working increased significantly.

The objective of the present work is to fabricate and analyze a cost-efficient double slope solar still utilizing naturally available pebbles as sensible heat storage material and water jacket for cooling of glass cover to enhance yield of potable water. All three different configurations have been studied for their water output for a water depth of 2cm in basin. An additional attempt has been made to analyze theoretical energy and exergy efficiency of all still configurations. The obtained results have then been compared. Energy & Exergy values have been determined for temperature values starting from 08:00 hr. to 17:00 hr. While the total water output has been determined for a period of 24hrs, entire duration of operation.

2. Location, Materials and Method

As various designs have been explored by researchers for solar still optimization and analysis, for the present work, a single basin double slope solar still is fabricated for the investigation of all the proposed configurations. As many previous research works are based on methods which generally increase the unit cost of water yield. The solar still configurations selected for this study are such that it keeps the unit cost of water yield very low while enhancing the yield greatly.

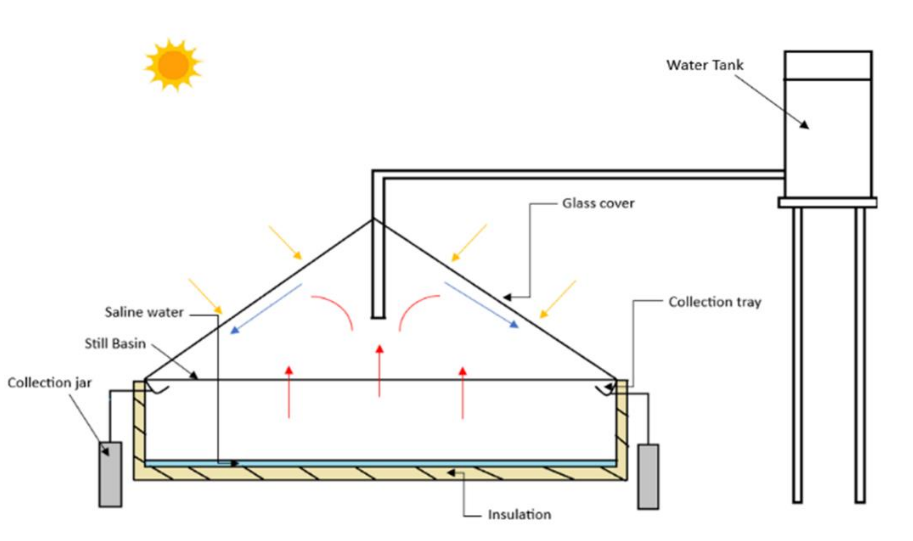

Figure 1: Schematic diagram of Double Slope, single basin passive solar still showing working mechanism.

The schematic diagram shown in Fig.1 showcases the solar still design and its working mechanism. Generally, such systems consist of common components such as basin, transparent cover such as glass, collection tray, collection tanks and refill tank to maintain saline water level in basin. The working mechanism of this system is such that upon the incidence of solar irradiation onto the transparent cover, the irradiance gets transmitted to the basin. This increases the internal temp of solar still due to which the water molecules at the surface, start to show slower rates of evaporation. The water vapor produced flows and get accumulated on to the inner surface of glass cover where vapor loses its latent heat of vaporization and gets converted to liquid which then flows along the inner surface of glass cover to collection tray and then to collection tank for use. Saline water treated in such a manner can be used directly without any requirement of further treatment.

Figure 2: A photograph of double-slope, passive solar still (MUJ, Jaipur, India)

The orientation of solar still is in a manner that tilted glass covers face north-south direction (vertical side glasses face east-west direction) so that both the glass covers receive similar irradiance. Also, the basin liner was painted black for maximum absorption of solar irradiance. As not many studies are available for the Indian state of Rajasthan, the experimental work has been performed for a district of Jaipur, Rajasthan (India). The designed solar still is presently operational and maintained by the Department of Mechanical Engineering at Manipal University, Jaipur. The climatic and operational parameters considered for this study are for Jaipur (26.8439° N, 75.5652° E) as mentioned in the Table. 3, 4 &5.

Table 3: Climatic specifications for double slope solar still.

Time	G_s **(W/m^2)**
08:00	352
09:00	569
10:00	730
11:00	852
12:00	922
13:00	925
14:00	861
15:00	738
16:00	558
17:00	358

Table 4: passive solar still materials specification.

Component	**Material**
Transparent cover	Glass
Basin	Aluminum, (grade- 6082)
Insulation	Glass wool
Collection tray	PVC
Tanks	10 L, HDPE container
Stands	Mild steel
Energy storage material	Pebbles
Thermocouples	K-type

Table 5: Design specifications of passive solar still.

Parameter	**Value**
Glass cover tilt angle from horizontal, θ	45°
Glass cover thickness	0.003 m
Basin dimension	0.9 m × 0.9 m × 0.2 m
Area of basin, A_b	0.81 m^2
Thickness of basin	0.003 m
Insulation thickness	0.01 m
Thermal conductivity of insulation material (Hung Anh & Pásztory, 2021)	0.03 W/m-K
Depth of brine in basin, d	0.02 m
Latent heat of vaporization, h_{fg} (Ranjan et al., 2016)	2260 × 10^3 J/Kg

For the research work proposed in this article, the assumptions considered for energy and exergy analysis are as mentioned below:

(i) The double slop solar still with ‘θ’ tilt angle (with horizontal) operates in a quasi-static (steady) state.
(ii) Incident solar irradiance is uniform throughout the transparent cover.
(iii) No temperature gradients across any component of solar still (except glass cover) and saline water.

(iv) Material composition is uniform throughout for all components of still.
(v) Solar still is water and vapor leak proof.
(vi) Heat transfer coefficient being temperature dependent.
(vii) Temperature difference in inner and outer glass cover temperature ($T_{gi} \neq T_{go}$).
(viii) Heat leakages have been neglected.
(ix) Saline water level is maintained in still at a constant level throughout the experiment.
(x) Saline water properties considered are like water for simplification of calculations.
(xi) Phenomena of reflection and absorption of solar irradiance due to glass cover have been neglected.

The solar still configurations under study for the present work are 1) conventional solar still, 2) solar still with pebbles and 3) solar still with cooling water jacket for glass cover. The conventional solar still consists of common parts like basin glass cover, tank etc. as described previously. This is the most common design, and its results will be used as datum values for comparison. The second configuration of solar still incorporates pebbles (as thermal energy storage material). While these pebbles are naturally available and very cheap, the role of pebbles here is to act as thermal energy storage medium to extend the time-period for desalination. Utilization of pebbles also keeps the cost of production very low. The third configuration utilizes a cooling water jacket to lower the glass cover temperature.

3. Expression for theoretical productivity, energetic and exegetic efficiency of solar still.

A very important aspect of any solar-based system is its efficiency. With lower system efficiencies, lower amounts of distillate are produced for any solar still. Energy analysis is often employed to study the system energy efficiency which also helps in determination of distillate output (Ranjan et al., 2016). A drawback of this approach is that as energy analysis is based on the first law of thermodynamics, it only gives an estimate of the qualitative aspects of the system. To have a thorough understanding of the system losses, exergy analysis is performed (Singh et al., 2000). Being based on the second law of thermodynamics, this tool gives true estimate of system losses along with its location. The principles of energy and exergy can be utilized to fabricate effective solar stills with reduced irreversibility's hence giving highest distillate output per unit cost of production (Vaithilingam et al., 2021). As there are not many papers available utilizing exergy technique for passive solar still. An attempt has been made to utilize these complementary thermodynamic tools and validate the different configurations of double slope solar still proposed in this work.

Given below is the expression for hourly distillate output (m_d) for passive solar still (Kg/m^2-h) (Aghaei Zoori et al., 2013, Yousef et al., 2017):

$$\mathrm{m_d} = \frac{\mathrm{h_{e,w-g}} \times (\mathrm{T_w} - \mathrm{T_{gi}})}{\mathrm{h_{fg}}} \times 3600 \qquad \text{(eq. 1)}$$

Here $h_{e,w-g}$ (W/m^2-K) is the evaporative heat transfer coefficient between inner glass cover and saline water and h_{fg} (J/Kg) is the latent heat of vaporization of water.

The expression for thermal energy efficiency on hourly basis of passive solar still can be regarded as the ratio of energy available in distillate output to input solar irradiance (Aghaei Zoori et al., 2013, Yousef et al., 2017)

$$\eta_{en} = \frac{m_d \times h_{fg}}{G \times 3600} \qquad \text{(eq. 2)}$$

Where, m_d is the hourly distillate output (Kg/m^2-h) and G is global solar irradiance (W/m^2).

The exergy efficiency of a solar still can be regarded as the ratio of desired solar still output exergy to input exergy efficiency single slope solar still (Kumar & Tiwari, 2011, Yousef et al., 2017)

$$\eta_{ex} = \frac{E_{x_{e,w-g}}}{E_{x_{sun}}} \qquad \text{(eq. 3)}$$

While the equations for $E_{x_{e,w-g}}$ and $E_{x_{sun}}$ are as follows:

$$E_{x_{e,w-g}} = h_{e,w-g} \times A_b \times (T_w - T_{g_i}) \times \left(1 - \frac{T_a+273}{T_w+273}\right) \quad \text{(eq. 4)}$$

$$E_{x_{sun}} = A_g \times G_s \times [1 + \frac{1}{3}\left(\frac{T_a+273}{6000}\right)^4 - \frac{4}{3}\left(\frac{T_a+273}{6000}\right)] \quad \text{(eq.5)}$$

4. Results and discussion

The focus of investigation for this study is to analyze the performance of the double slope solar still for three distinct configurations. Hourly variation of the solar irradiance for the test site is as shown in Fig. 3. It can be interpreted from the data that during the first half of the day, the solar irradiance gradually increases reaching the maximum value of 925 W/m^2 at 13:00 hr. and after which it gradually decreases. Although for the present study the solar still was operational for an entire duration of 24 hr., solar irradiance and temperature data were captured for the time interval of 08:00 hr. to 17:00 hr.

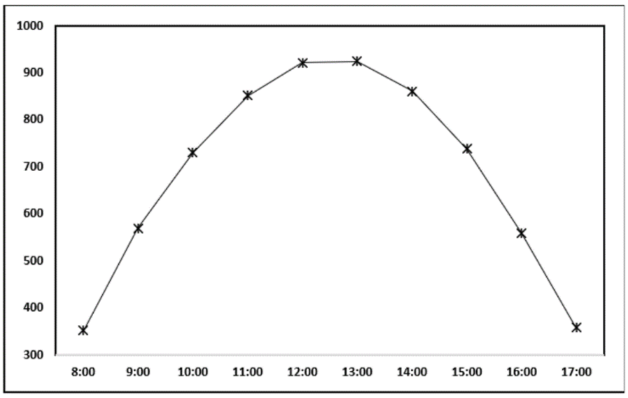

Figure 3: Hourly variation solar irradiance.

From Fig. 4 it can be understood that even though energy and exergy graphs are following the same trend, the efficiency of energy is comparatively much higher than efficiency of exergy. This can be attributed to the fact that saline water's temperature is much lower than sun's temp which is about 6000K. Also, it gives clear indication of the possibility of presence of irreversibility's in different components of the system. It can also be understood from the data that the slope of the characteristic curve is generally positive which is due to temperature dependent properties of the system. The above findings are also in good agreement with the results published in (Kumar & Tiwari, 2011, Ranjan et al., 2016, Yousef et al., 2017).

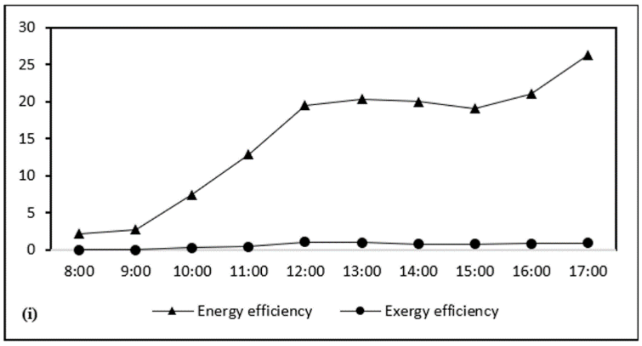

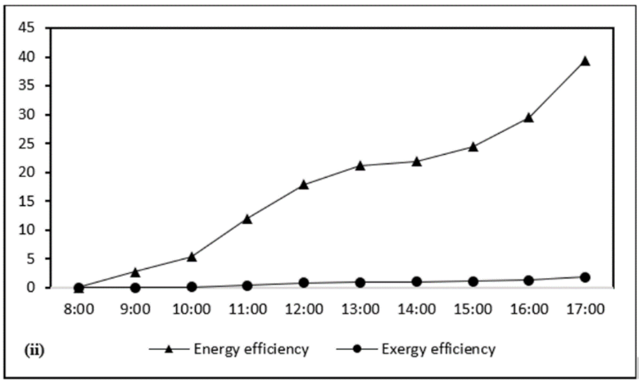

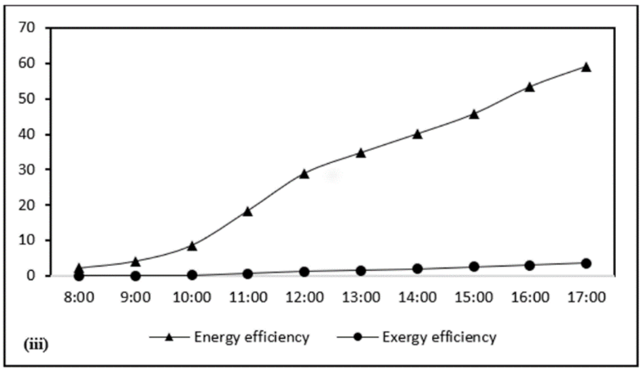

Figure 4: Hourly variation of energy and exergy efficiency for (i) Conventional solar still, (ii) Pebbles based solar still and (iii) solar still with cooling cover.

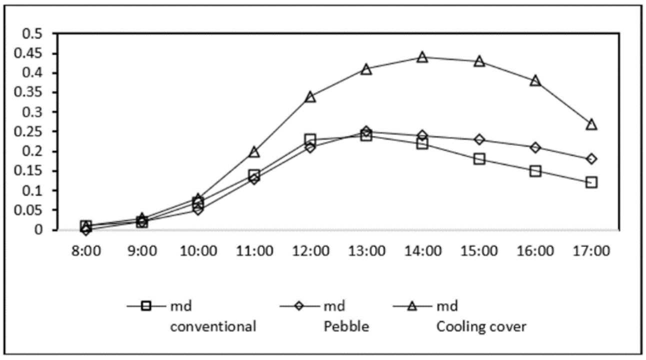

Figure 5: hourly variation of solar still productivity.

The data in Fig. 5 shows the hourly variation of water yield for the three configurations of double slope solar still. It can be understood that initially in comparison to conventional solar still design, the productivity of pebble based solar still is generally lower. This can be attributed to the fact that in the first half of the day, solar thermal energy is being utilized by both the saline water as well as pebbles. It was after 13:00 hr. that once pebbles have stored enough thermal energy; the remaining energy was supplied to saline water. Also, during the end of the day, productivity of pebbles-based system is higher than conventional system due to the utilization of thermal energy stored in pebbles. Application of pebbles lead to prolonged duration of desalination of saline water. For the case of cooling cover, as established in several research works (Ranjan et al., 2016) higher temperature difference between inner glass cover and saline water, leads to higher water yield and exergy efficiency. It is evident from the data that application of cooling cover for solar still enhances hourly productivity significantly. The joint effect of colling cover and solar irradiance greatly enhances productivity. Glass cover being regarded as a solar still component with highest exergy efficiency (Ranjan et al., 2016), any modification in its temperature leads to immediate change in the results. The Overall water yield for the conventional still, pebble based still and still with water cooling jacket for glass cover was recorded as 1.9, 2.3 and 2.9 Liter respectively.

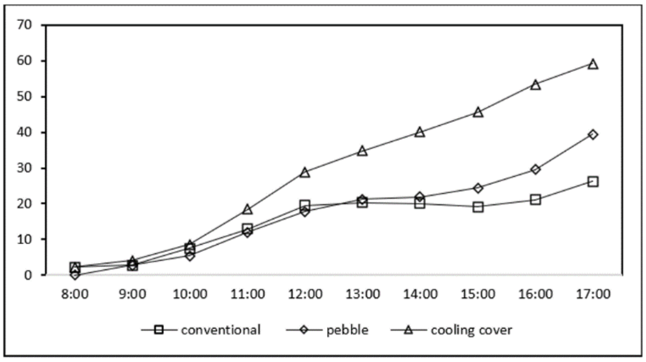

Figure 6: Energy efficiency for conventional, pebble and Cooling cover configuration of still.

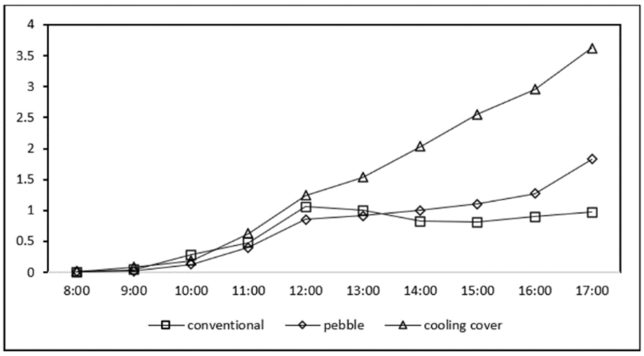

Figure 7: Exergy efficiency for conventional, pebble and Cooling cover configuration of still.

The findings of this study also include the energy and exergy comparison for all the configurations. Fig. 6 &7 shows a comparison of energy and exergy efficiency of solar still for all the three configurations. It is clear from that that energy and exergy efficiency of the system for all configurations are generally tracing a positive trend which can also be seen in the work done by (Kumar & Tiwari, 2011, Ranjan et al., 2016). Analysis of the present study suggests that before 13:00 hr., the efficiency of solar still with cooling cover is highest followed by conventional solar still and then solar still with pebbles. However, after 13:00hr., the order of energy and exergy efficiency is such that it is highest for still with cooling cover followed by still with pebbles and then conventional solar still. The increase in the efficiency of solar still pebbles after 13:00 hr. is because the pebbles have been thermally charged enough and the complete solar irradiance is being supplied to solar still while pebbles maintain the temperature of water even after sun sets leading to prolonged desalination.

5. Conclusions and recommendations

A single basin, double slope solar still is fabricated and tested for different configurations. The main aim of this work being to improve solar still productivity, energy and exergy efficiency without increasing the cost of production. Namely three configurations were selected i.e., conventional still, still with pebbles for thermal energy storage and still with cooling water jacket for reducing the glass cover temperature. From the study it was determined that the solar still configuration with cooling water jacket for glass cover proved to be the highest performing solar still amongst all the configurations. While this configuration has a productivity of 2.9 L/day, productivity for still with pebbles and conventional solar still has come out to be 2.3 and 1.9 respectively. It can also be seen that the energy and exergy efficiency of still with cooling cover is higher than the remaining two configurations. The reasoning behind this can be understood as by lowering the glass cover temperature, higher temperature difference is created between water vapor and inner glass cover leading to higher productivity for the same basin area. It has also been understood that for solar still the exergy efficiency is much lower than energy efficiency, a fact which is also confirmed by various researchers in the field. So, the research work undertaken by the authors has yielded some satisfactory results in terms of improvement in productivity, energy and exergy efficiency. Though an attempt has been made by the authors of this article to improve upon the productivity of solar still. It is well understood that more collaborative efforts are needed in this area of research to help make this an economical product for practical use and mass adoption.

6. Nomenclature:

A_b	Area of basin (m^2)
A_g	Area of Glass cover (m^2)
d	Depth of brine (m)
$E_{x_{e,w-g}}$	Output exergy for solar still (W)
$E_{x_{sun}}$	Input exergy for solar still (W)
G_s	Solar Irradiance (W/m^2)
$h_{e,w-g}$	Evaporative heat transfer coefficient between water and glass cover (W/m^2-K)
h_{fg}	Latent heat of vaporization (J/Kg)
m_d	Solar still productivity (L/h)
T_a	Ambient temperature (˚ C)
T_{g_i}	Temperature of inner glass cover (˚ C)
T_w	Temperature of saline water in basin (˚ C)
η_{en}	Energy efficiency
η_{ex}	Exergy efficiency

7. Acknowledgments

Authors would like to thank and acknowledge the support and guidance provided by the Department of Mechanical engineering, Manipal University Jaipur, Rajasthan (India).

8. Citation / References

Aghaei Zoori, H., Farshchi Tabrizi, F., Sarhaddi, F., & Heshmatnezhad, F. (2013). Comparison between energy and exergy efficiencies in a weir type cascade solar still. *Desalination*, *325*, 113–121. https://doi.org/10.1016/j.desal.2013.07.004

Ayoub, G. M., & Malaeb, L. (2012). Developments in Solar Still Desalination Systems: A Critical Review. *Critical Reviews in Environmental Science and Technology*, *42*(19), 2078–2112. https://doi.org/10.1080/10643389.2011.574104

Badran, O. O. (2007). Experimental study of the enhancement parameters on a single slope solar still productivity. *Desalination*, *209*(1–3), 136–143. https://doi.org/10.1016/j.desal.2007.04.022

Hung Anh, L. D., & Pásztory, Z. (2021). An overview of factors influencing thermal conductivity of building insulation materials. *Journal of Building Engineering*, *44*, 102604. https://doi.org/10.1016/j.jobe.2021.102604

Kalidasa Murugavel, K., Chockalingam, Kn. K. S. K., & Srithar, K. (2008). Progresses in improving the effectiveness of the single basin passive solar still. *Desalination*, *220*(1–3), 677–686. https://doi.org/10.1016/j.desal.2007.01.062

Kariman, H., Shafieian, A., & Khiadani, M. (2023). Small scale desalination technologies: A comprehensive review. *Desalination*, *567*, 116985. https://doi.org/10.1016/j.desal.2023.116985

Khanna, R. K., Rathore, R. S., & Sharma, C. (2008). Solar still an appropriate technology for potable water need of remote villages of desert state of India - Rajasthan. *Desalination*, *220*(1–3), 645–653. https://doi.org/10.1016/j.desal.2007.01.060

Kumar, S., & Tiwari, G. N. (2011). Analytical expression for instantaneous exergy efficiency of a shallow basin passive solar still. *International Journal of Thermal Sciences*, *50*(12), 2543–2549. https://doi.org/10.1016/j.ijthermalsci.2011.06.015

Murugavel, K. K., Sivakumar, S., Ahamed, J. R., Chockalingam, K. K. S. K., & Srithar, K. (2010). Single basin double slope solar still with minimum basin depth and energy storing materials. *Applied Energy*, *87*(2), 514–523. https://doi.org/10.1016/j.apenergy.2009.07.023

Natu, G. L., Goghari, H. O., & Gomkale, S. D. (1979). Solar distillation plant at awania, Gujarat, India. *Desalination*, *31*(1–3), 435–441. https://doi.org/10.1016/S0011-9164(00)88548-3

Ranjan, K. R., Kaushik, S. C., & Panwar, N. L. (2016). Energy and exergy analysis of passive solar distillation systems. *International Journal of Low-Carbon Technologies*, *11*(2), 211–221. https://doi.org/10.1093/ijlct/ctt069

Singh, N., Kaushik, S. C., & Misra, R. D. (2000). Exergetic analysis of a solar thermal power system. *Renewable Energy*, *19*(1–2), 135–143. https://doi.org/10.1016/S0960-1481(99)00027-0

Tarazona-Romero, B. E., Campos-Celador, A., & Maldonado-Muñoz, Y. A. (2022). Can solar desalination be small and beautiful? A critical review of existing technology under the appropriate technology paradigm. *Energy Research & Social Science*, *88*, 102510. https://doi.org/10.1016/j.erss.2022.102510

Tiwari, A. Kr., & Tiwari, G. N. (2007). Thermal modeling based on solar fraction and experimental study of the annual and seasonal performance of a single slope passive solar still: The effect of water depths. *Desalination*, *207*(1–3), 184–204. https://doi.org/10.1016/j.desal.2006.07.011

Tripathi, R., & Tiwari, G. N. (2005). Effect of water depth on internal heat and mass transfer for active solar distillation. *Desalination*, *173*(2), 187–200. https://doi.org/10.1016/j.desal.2004.08.032

Vaithilingam, S., Gopal, S. T., Srinivasan, S. K., Manokar, A. M., Sathyamurthy, R., Esakkimuthu, G. S., Kumar, R., & Sharifpur, M. (2021). An extensive review on thermodynamic aspect based solar desalination techniques. *Journal of Thermal Analysis and Calorimetry*, *145*(3), 1103–1119. https://doi.org/10.1007/s10973-020-10269-x

Yousef, M. S., Hassan, H., Ahmed, M., & Ookawara, S. (2017). Energy and exergy analysis of single slope passive solar still under Egyptian climate conditions. *Energy Procedia*, *141*, 18–23. https://doi.org/10.1016/j.egypro.2017.11.005

Thermo-Optical modeling of hyperbolic cavity receiver of 40 m^2 parabolic dish collector

Pradipta Mandal, Abhinav Rajan, K. S. Reddy*

Heat Transfer and Thermal Power Laboratory, Department of Mechanical Engineering,
Indian Institute of Technology Madras, Chennai 600036, India

Abstract

Thermo-optical modeling of a solar cavity receiver, hyperbolic in shape, including a secondary reflector applicable for solar parabolic dish collector (PDC), is carried out in this article. The combined receiver and secondary reflector geometry constitute the hyperbolic shape. This investigation aims to optimize the receiver geometrically and optically, then to estimate the heat transfer rate from the receiver surface owing to natural convection and radiation of the optimized receiver under parameters that influence the PDC system performance. The commercial optical software tool ASAP® 2013 is used for optical simulation. The optical simulation includes the investigation of the performance of the receiver for varying cavity height h_1 and secondary height h_2 at a constant diameter of the cavity aperture of d = 0.5 m. The effects of cavity absorptivity (86-94%) and reflectivity of the secondary (86-94%) on optical performance are also studied. The optimal value of optical efficiency found is 91.72% for the mounting height of 4.21 m when h_1= 0.75 m and h_2 = 0.25 m. With ANSYS® Fluent 2020 R1, the receiver's 0°, 30°, 60°, and 90° orientations or angle of tilt θ are modeled thermally. A thorough analysis comparing the various turbulence models has been presented.

Keywords: Parabolic dish collector, Cavity receiver, Optical simulation, Thermal simulation, Geometrical concentration ratio, Secondary trumpet

---

* Corresponding author. E-mail address: ksreddy@iitm.ac.in (K.S. Reddy)

10.18086/swc.2023.03.07 Available at http://proceedings.ises.org

1 Introduction

Since fossil fuels are exhaustible and responsible for polluting the environment, technologies for converting solar energy into thermal energy are becoming more and more popular. The solar parabolic dish system is one concentrating solar power (CSP) technology that shows promise for effective solar-thermal energy conversion. The essential elements of a Parabolic Dish Collector (PDC) system, a point-focused technology, include the concentrator, receiver, dual-axis tracking system, and supporting structure. The cavity's geometry is essential and affects the system's overall performance.

Many researchers have analyzed heat loss for cavity receivers of various shapes, such as cylindrical, hemispherical, conical, etc. Pavlovic et al. (2018) compared conical with spiral-shaped receivers experimentally. Bellos et al. (2019) have examined various cavity receiver forms from both the optical and thermal points of perspective. Their results indicate that the cylindrical-conical design geometry is the ideal one. Taumoefolau et al. (2004) conducted experiments at different inclination angles and aperture-to-cavity diameter ratios to ascertain the heat lost via free convection from dish cavity geometry form. Johnston (1998) measured and defined a 20 m^2 dish's focal zone experimentally. Daabo et al. (2016a) focused on the distribution of flux and optical performance for various receiver shapes, such as conical, spherical, and cylindrical ones. Si-Quan et al. (2019) evaluated the optical performance (88.9%) of a spherically shaped cavity receiver using the Monte Carlo Ray Tracing (MCRT) method. An additional and workable strategy to amplify the efficiency of the solar energy-to-thermal energy transformation process is to minimize the radiation heat loss from a receiver and optimize the receiver's geometry and shape. It has been demonstrated by Ngo et al. (2015) that heat loss from natural convection can be minimized by plate fins fastened to a cavity. The wind speed, direction, and receiver inclination significantly affect heat loss. López et al. (2020) reported the thermal performances of flat and cavity-type receivers for industrial applications. Reddy et al. (2016) have investigated the effect of different operating wind velocities and directions on heat loss for modified cavity receivers tiled at different angles. Craig et al. (2020) analyzed the heat loss from a tubular receiver. Using thorough ray tracing simulations, Hernández et al. (2012) designed a unique type of receiver and optimized with a large rim angle of 90°. The dimensions of cylindrical, conical, and spherical cavities are compared and optimized.

A parabolic dish with a second-stage optical feature can improve the concentration ratio at a fixed interception factor. Making use of a secondary reflector for increasing the concentration level can be beneficial if the first reflector has a significant error and a high required temperature (Jaffe and Poon, 1981). Wang et al. (2020) investigated the improvement in the performance of cavity receiver geometry with spilled skirts using hyperbolic trumpet, compound parabolic concentrator (CPC), and conical as secondary. The MCRT is used to assess the cavity receivers' efficacy using heat transfer models. Reddy and Kumar (2009) developed a computer model for the modified cavity receiver that considers radiation and evaluates the convection-owned heat loss with reflectors that have conical-type, CPC-type, and trumpet-type forms. The authors reported that the solar receiver with the hyperbolic trumpet as secondary performed better than the receiver with CPC and conical.

One of the critical elements in transforming solar energy into thermal is designing the receiver with a suitable geometry. The shape and angle of the cavity's tilt affect the total performance, which impacts heat loss. The current study improves the concentration ratio by attaching a hyperbolic secondary concentrator, which raises the receiver's surface temperature and enhances system performance overall. This paper offers a detailed investigation using optical-coupled-thermal modeling of a parabolic dish concentrator's hyperbolic cavity-type receiver.

2 System configuration

The PDC of aperture 40 m^2 and receiver analyzed in this work are illustrated in Fig. 1. The receiver geometry is produced in SolidWorks 2019. The maximum concentration is achieved for the rim angle ϕ of 45° (Bopche and Kumar, 2019). Therefore ϕ = 45° is taken in this analysis, for which, the focal length f is calculated to be 4.31 m. The hyperbolic profile is created by both the cavity and trumpet secondary, which are attached. The geometry on which optimization is performed has aperture diameter d = 0.5 m and dimeter-to-total height ratio d/h = 1. The total height h of the geometry is the sum of the cavity height (h_1) and the secondary reflector height h_2; h_1 and h_2 are equal. The absorptivity α_{rec} of receiver surface, reflectivity (ρ_{sec}) of the secondary as well as mounting height L are optimised. The concentrator surface is thought to feature a glass mirror and an iron-silver coating. The position of the receiver is on the PDC's focal plane. The ideal installation height L is attained by vertical movement of the receiver from the base of the concentrator.

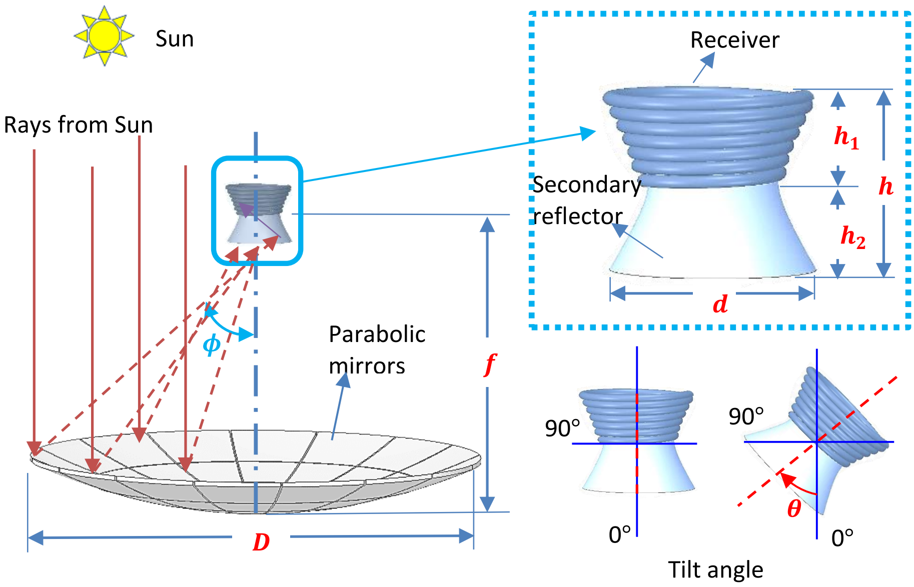

Fig. 1. Dish-receiver system.

As shown in Fig. 1, sunlight falls in a parallel beam across the entire dish area, focusing on the secondary. This is the initial focus phase, and the parabolic dish is appropriately referred to as a primary concentrator. The concentrated ray is then reflected once more onto the cavity from the secondary, which absorbs solar radiation as the second step of concentration.

3 Optical model

The optical model for analyzing the receiver is built using the commercial tool ASAP® 2013 and simulated using the technique of Monte Carlo Ray Tracing (MCRT). The direct normal irradiance (DNI) of 800 W/m^2 impinges on the dish aperture. The reflectivity ρ_{dish} of the dish surface and the secondary reflector ρ_{sec} are 92% and 94%, respectively. The absorptivity α_{rec} value of 94% is assigned to the surface of the cavity. The heat absorbed over the inside surface is considered to calculate the absorbed heat and, ultimately, the optical efficiency. To dimensionally optimize, a parametric simulation of the receiver is done by changing h_1 when d and h_2 are constant and then changing h_2 when d and h_2 are maintained at a constant value. Due to the change in h_1 and h_2, the total height h changes. This leads to a variation of d/h as 0.5, 1, and 1.5.

The sun is defined as an extended source. The source is modeled as an emitting disk. The emitting disk simulates a simple Lambertian surface emitter with elliptical boundaries and a divergence half angle of 0°, which refers to the collimated beam. The source model in ASAP is characterized by randomness.

The relation for focal length f, which is the length between the collector base and its focal point, in terms D and ϕ, is given as follows:

$$f = \frac{D}{4\,tan\,(\frac{\varphi}{2})} \tag{eq. 1}$$

The current optical simulation assumes perfect optics, implying that different optical errors (errors due to sun shape, tracking, specularity, and slope) are considered negligible (Daabo et al., 2016b).

The solar irradiation captured by the collector aperture Q_{dish} is obtained as (Bellos et al., 2019):

$$Q_{dish} = A_{dish} \times DNI \tag{eq. 2}$$

where, A_{dish} is the collector aperture area.

Then, optical efficiency ($\eta_{optical}$) is defined as the fraction of the radiative energy falling over the collector's aperture surface that is ultimately absorbed by the receiver surface (Q_{rec}) and it is expressed as:

$$\eta_{optical} = \frac{Q_{rec}}{Q_{dish}} \quad \text{(eq. 3)}$$

3.1 Ray sensitivity test and validation

One million have been chosen for simulation after the ray sensitivity test because there is practically no change in optical efficiency as the ray count number crosses one million. The ray tracing is demonstrated in Fig. 2(a). The validity of the present optical model is established against the experiment data of Johnston (1998). Here, the author reported the distribution of radiant flux at the PDC system's focal region, which has an aperture area of 20 m^2. A 0.5 m diameter circular copper target was positioned at the focal region. The flux distribution estimated using the present model is compared with that of the literature and is depicted in Fig. 2(b). Further, the model utilized to calculate the total power at the receiver is also validated against the published data literature (Daabo et al., 2016a). The maximum difference in total power results is 7.73%.

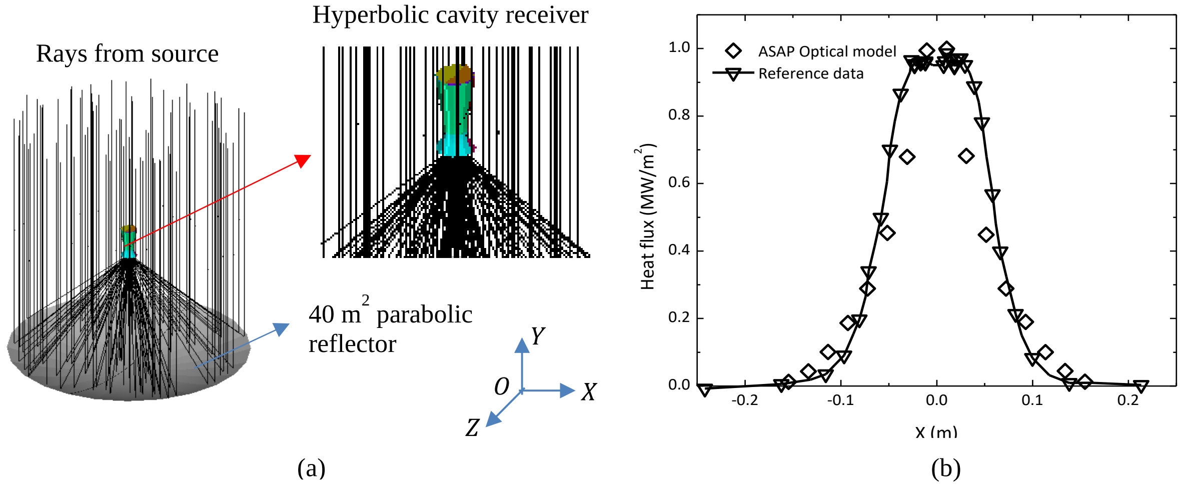

Fig. 2. (a) Ray tracing of solar PDC (b) Validation of flux intensity distribution between against experimental data (Johnston, 1998).

4 Thermal model

4.1 Governing equation

The continuity, momentum, and energy equations regulating laminar natural convection are solved successively (eqs. 4-6):

Continuity equation: $$\nabla V_{vel} = 0 \quad \text{(eq. 4)}$$

Momentum equation: $$V_{vel}\nabla V_{vel} = X - \frac{\nabla p}{\rho_f} + \nu\nabla^2 V_{vel} \quad \text{(eq. 5)}$$

Energy equation: $$\nabla(k_s \nabla T) = 0 \quad \text{(eq. 6)}$$

where ∇ is the Laplace operator, V_{vel} denotes velocity (m/s), p represents pressure (Pa), T indicates temperature (K), ν denotes kinematic viscosity (m^2/s), k_s is thermal conductivity (W/m.K) and X is body force (N/m^3).

The thermal model involves the following assumptions: (1) no wind velocity exists. (2) The receiver surface temperature equals the fluid temperature. (3) The tubular coil of the receiver is so closely packed that it forms a continuous and smooth surface.

The surrounding air is taken to be an ideal, incompressible gas. Density of the air ρ_f is specified using this assumption as:

$$\rho_f = \frac{P_{op}}{RT/M_w} \quad \text{(eq. 7)}$$

where, P_{op} is the operating pressure and M_w is the molecular weight. P_{op} is constant and does not depend on the local relative pressure field value.

The steady-state equations are solved with the Fluent solver. A non-Boussinesq approximation is used to solve the momentum equations. It is appropriate to use the Boussinesq approximation if $\beta(T_w - T_\infty) \ll 1$, where β is the coefficient of thermal expansion, T_w and T_∞ are receiver wall temperature and the ambiance temperature. Because of the secondary, the wall surface receivers are subjected to significant heat flux and reach high surface temperatures. It is, therefore, anticipated that the non-Boussinesq model will be more suitable than the Boussinesq model.

The surface-to-surface (S2S) radiation model is used to calculate surface radiation. Reflected flux refers to the radiant flux coming from the environment, which is interpreted as the radiation that exits all the other surfaces. The eqs. (8-10) below represent the energy that gets reflected from the surface i (Reddy and Sendhil Kumar, 2009):

$$q_{out,i} = \varepsilon_i \sigma T_i^4 + (1 - \alpha_i) q_{in,i} \qquad \text{(eq. 8)}$$

$q_{in,i}$ is represented in terms of $q_{out,j}$ as

$$q_{out,i} = \varepsilon_i \sigma T_i^4 + (1 - \alpha_i) \sum_{j=1}^{N} F_{ij} q_{out,j} \qquad \text{(eq. 9)}$$

The above equation can also be expressed as:

$$J_i = E_i + (1 - \alpha_i) \sum_{j=1}^{N} F_{ij} J_j \qquad \text{(eq.10)}$$

where, J_i is the radiosity (W/m^2), F_{ij} is the shape factor from surface i to j, $\sigma = 5.67 \times 10^{-8}$ W/m^2.K^4 denotes the Stefan-Boltzmann constant, E_i is emissive power at surface i (W/m^2), and N is the number of radiative surfaces.

4.2 Model selection and validation

The validity of the thermal model is supported by the experimental findings in the literature (Taumoefolau et al., 2004), as shown in Fig.3(a). According to this research, natural convection losses from cavity-type receivers were studied using an electrically heated receiver. The analysis was conducted at angles ranging from -90° (aperture facing upward) to 90° (aperture facing downward), and temperatures between 450°C and 650°C were examined. Computational predictions of convection losses from the cavity were made for the angles from 0° to 90°. A reasonable variation exists between the experiment's outcomes and those from the current model. Moreover, the chosen model has also been contrasted with other models, such as laminar, SST $k - \omega$, and realizable $k - \omega$. Fig.3(b) presents a comparison of the acquired data. The laminar model is found to have significantly good prediction.

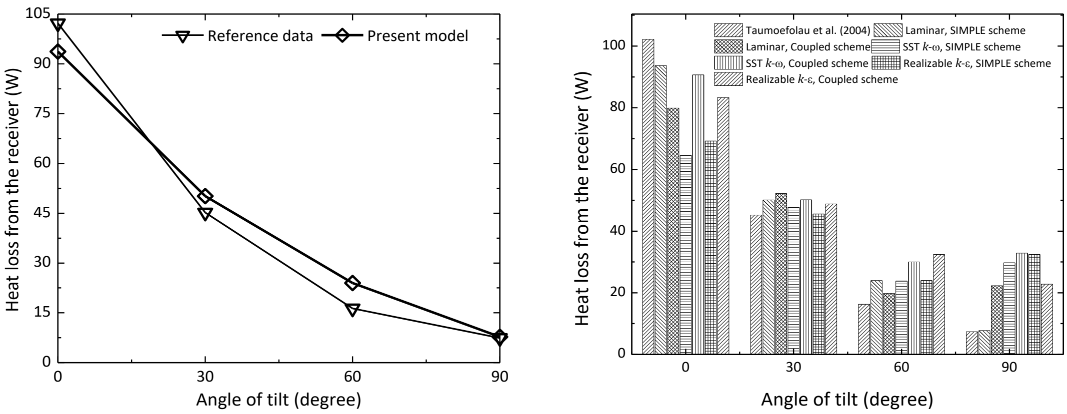

(a) (b)

Fig. 3. (a) Validation of thermal model with experiment (b) comparison of different turbulent models with various schemes for pressure-velocity coupling.

4.3 Numerical procedure

The geometry was divided into eleven parts following the ray tracing analysis to obtain more precise results for the radiative flux. The optical simulation is used to retrieve each element's absorbed heat data. These values have been applied at each element's inner surface as boundary conditions for a constant heat flux. After that, ANSYS® Fluent

2020 R1 is used to import the model geometry and mesh the problem. The receiver is situated inside the suitably sized cylindrical domain. A cylindrical enclosure was selected, and its size was increased so that its impact on thermo-fluidic analysis became negligible and had no discernable influence on the heat transfer rate. A steady-state model and a pressure-based solver are employed in the thermal model. For numerical analysis, the tilt angle has been changed from 0° to 90°, with 0° representing the receiver's upright position.

4.4 Grid sensitivity test and implemented boundary conditions

The inside surfaces of the receiver are subjected to constant heating because they are continuously exposed to solar radiation. As a result, boundary conditions of constant heat flux (radiative flux) values, as determined by optical simulation, have been applied to the cavity's interior wall. It is presumed that ceramic wool insulation covers the outside surface to stop heat transfer to the surrounding air. Thus, the external cavity surface is subjected to the adiabatic boundary conditions. The hyperbolic receiver can be considered surrounded by an unbounded atmosphere. As a result, the domain's pressure inlet is designated as the border condition. It is believed that the surrounding air is a perfect, incompressible gas. The properties of air are modeled as polynomial temperature functions applicable from 300 K to 1000 K. Due to the intricate shape of the receiver, the governing equations (eqs. 4-6) are discretized using an unstructured polyhedral mesh. The air inside the cavity is the working fluid. The Semi-Implicit Method for Pressure Linked Equations (SIMPLE) scheme is employed to couple the pressure and velocity terms. The continuity, momentum, and energy equations were set to 10^{-3}, 10^{-3}, and 10^{-6} as convergence residuals, respectively. The grid independence test involves systematically increasing the number of cells and decreasing cell sizes to ensure the heat loss from the internal region of the cavity is accurately captured without discrepancies as the grid resolution increases. The mesh with 583,533 cells is determined to be the optimal size for meeting accuracy requirements. Fig. 4 shows the volume mesh of the domain and the receiver.

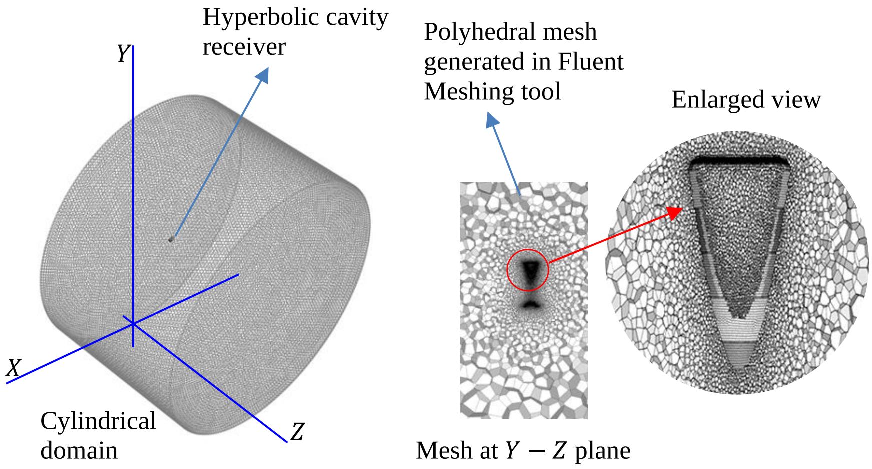

Fig. 4. Meshing of computational domain and receiver.

5 Results and discussion

The cavity receiver, hyperbolic in shape, that has an attached secondary for a 40 m^2 PDC system, is optically optimized by parametric optical modeling. Subsequently, a thermal simulation is performed to determine the area-weighted average temperature and heat loss via convection and radiation. This section includes the effect of diameter-to-height ratio, absorptivity, reflectivity, and inclination.

5.1 Effects of cavity height (h_1) and secondary height (h_2)

The optical efficiency of the system varies with position. Specifically, only h_2 is systematically adjusted, leading to changes in h. Additionally, the diameter of the circular aperture remains constant at all points of interest. The optical efficiency is assessed for various mounting positions ranging from 4.21 to 4.41 m, with increments or decrements of 0.05 m across different d/h ratios. It is evident from Fig. 5(a) that the maximum optical efficiency occurs at $L = 4.21$ m when $h_1 = 0.75$ m and $d/h = 0.5$. This occurs because raising the secondary height enables greater radiation for the second-stage concentration. Fig. 5(b) shows that when h_2= 0.75 m, the optical efficiency hits the highest value. Therefore, increasing the secondary height leads to improved receiver performance at a greater mounting height.

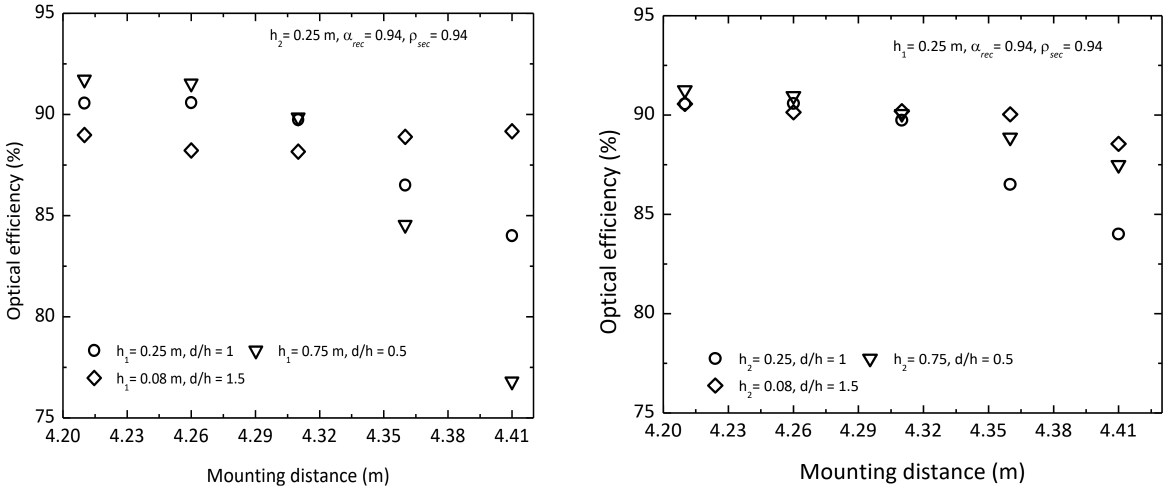

(a) (b)

Fig. 5. Variation of optical efficiency with mounting height at different (a) cavity heights (h_1) and (b) secondary height (h_2).

5.2 Variation of optical performance with wall absorptivity (α_{rec}) and secondary reflectivity (ρ_{sec})

Fig. 6(a) illustrates how optical performance varies with mounting height for different absorptivity values. A range of absorptivity α_{rec} = 86-94% has been examined to study parametrically. The reflectivity value is held constant at ρ_{sec} = 94%. From Fig. 6(a), it's clear that optical efficiency decreases as mounting height increases but increases with higher absorptivity. In other words, higher absorptivity leads to higher optical efficiency. Fig. 6(b) shows how optical efficiency changes with mounting height for various reflectivity values. The range of reflectivity values considered for the analysis is ρ_{sec} = 86-94%. The absorptivity value is held constant at α_{rec} = 94%. It is noted that optical efficiency decreases as mounting height increases. Unlike absorptivity, optical efficiency decreases with higher reflectivity values. Additionally, a comparison of the optical performance of the current receiver with existing studies is presented in Table 1.

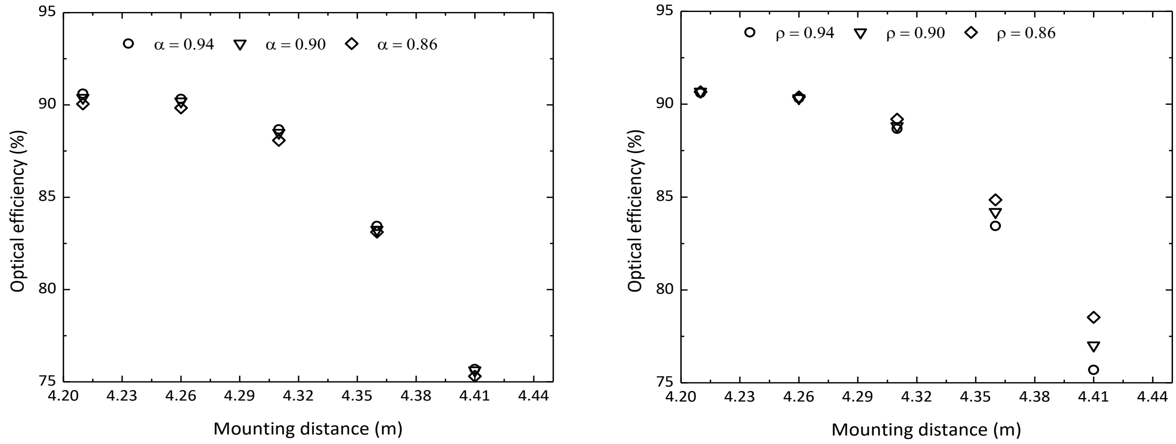

(a) (b)

Fig. 6. Variation of optical efficiency with mounting height for different (a) receiver wall absorptivity (α_{rec}) and (b) reflectivity of secondary (ρ_{sec}).

Table 1 Comparative tabulation of the optical performance of the proposed receiver.

References	Receiver geometry	Maximum optical efficiency (%)
Daabo et al. (2016b)	Conical	75.3
Bellos et al. (2019)	Cylindrical	81.34
	Rectangular	80.11
	Spherical	78.78
	Conical	80.96
Hassan et al. (2021)	Cylindrical	80
Si-Quan et al. (2019)	Spherical	88.9
Proposed receiver	Hyperbolic cavity receiver with secondary	91.72

5.3 Effect of tilt angle (θ) of receiver

Fig. 7(a) and (b) illustrate the relationship between the rate of heat loss from radiation and free convection with the tilt angle for an emissivity (ε) from 0.2 to 1.0. The convective heat loss rises with the receiver tilt. However, because of the numerical model's constant heat flux boundary conditions, radiation heat loss shows the opposite trend. The convective heat loss rises with tilt angle while radiative heat loss decreases. The stagnant zone diminishes, and the convection zone expands as the tilt changes from 0° to 90°. Hot air within the secondary reflector and cavity decreases progressively as the tilt changes from 0° to 90° (Rajan and Reddy, 2021). As the receiver's tilt angle varies from 0° to 90°, the stagnation zone of the receiver gradually decreases. At a tilt of 0°, the stagnant zone occupies most of the space within the cavity receiver. Therefore, the convective heat loss rate rises as the tilt increases.

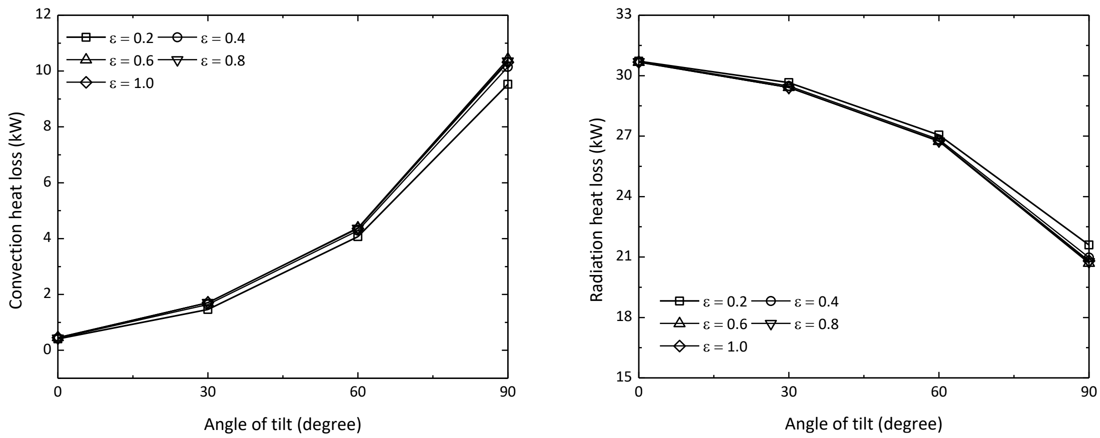

(a) (b)

Fig. 7. Effect of tilt on heat loss (a) via convection (b) radiation.

6 Conclusions

The study is conducted on a 40 m^2 PDC system's hyperbolic cavity receiver, employing ray tracing alongside a thermal model. The receiver's comprehensive optical simulation was carried out using the Monte Carlo Ray Tracing (MCRT) method. The optical modeling is conducted for receivers with different d/h values (0.5−1.5), along with secondary reflectors of varying heights (h_2= 0.08-0.75 m). The highest optical efficiency observed is 91.72% when d/h is 0.5 at a mounting height of 4.21 m. Subsequently, the performance is evaluated for different receiver absorptivity values (0.86-0.94) and secondary reflectivity values (86-94%). With α_{rec} = 94% and ρ_{sec} = 86%, the receiver exhibited optimal performance at a mounting height of 4.21 m. The thermal simulation indicates that convection heat transfer increases as the angle of tilt θ is changed from 0° to 90°, while radiation heat transfer decreases within the emissivity range of ε = 0.2-1.0.

References

Bellos, E., Bousi, E., Tzivanidis, C., Pavlovic, S., 2019. Optical and thermal analysis of different cavity receiver designs for solar dish concentrators. Energy Convers. Manag. X 2, 100013. https://doi.org/10.1016/J.ECMX.2019.100013

Bopche, S.B., Kumar, S., 2019. Experimental investigations on thermal performance characteristics of a solar cavity receiver. Int. J. Energy Environ. Eng. 10, 463–481. https://doi.org/10.1007/s40095-019-00321-4

Craig, K.J., Slootweg, M., Le Roux, W.G., Wolff, T.M., Meyer, J.P., 2020. Using CFD and ray tracing to estimate the heat losses of a tubular cavity dish receiver for different inclination angles. Sol. Energy 211, 1137–1158. https://doi.org/10.1016/j.solener.2020.10.054

Daabo, A.M., Mahmoud, S., Al-Dadah, R.K., 2016a. The optical efficiency of three different geometries of a small scale cavity receiver for concentrated solar applications. Appl. Energy 179, 1081–1096. https://doi.org/10.1016/j.apenergy.2016.07.064

Daabo, A.M., Mahmoud, S., Al-Dadah, R.K., 2016b. The effect of receiver geometry on the optical performance of a small-scale solar cavity receiver for parabolic dish applications. Energy 114, 513–525. https://doi.org/10.1016/J.ENERGY.2016.08.025

Hassan, A., Quanfang, C., Abbas, S., Lu, W., Youming, L., 2021. An experimental investigation on thermal and optical analysis of cylindrical and conical cavity copper tube receivers design for solar dish concentrator. Renew. Energy 179, 1849–1864. https://doi.org/10.1016/j.renene.2021.07.145

Jaffe, L.D., Poon, P.T., 1981. Secondary Concentrators for Parabolic Dish Solar Thermal Power Systems. Proc. Intersoc. Energy Convers. Eng. Conf. 2, 1752–1758.

Johnston, G., 1998. Focal region measurements of the 20 m2 tiled dish at the Australian National University. Sol. Energy 63, 117–124. https://doi.org/10.1016/S0038-092X(98)00041-3

López, O., Baños, A., Arenas, A., 2020. On the thermal performance of flat and cavity receivers for a parabolic dish concentrator and low/medium temperatures. Sol. Energy 199, 911–923. https://doi.org/10.1016/J.SOLENER.2019.07.056

Ngo, L.C., Bello-Ochende, T., Meyer, J.P., 2015. Numerical modelling and optimisation of natural convection heat loss suppression in a solar cavity receiver with plate fins. Renew. Energy 74, 95–105. https://doi.org/10.1016/j.renene.2014.07.047

Pavlovic, S., Loni, R., Bellos, E., Vasiljević, D., Najafi, G., Kasaeian, A., 2018. Comparative study of spiral and conical cavity receivers for a solar dish collector. Energy Convers. Manag. 178, 111–122. https://doi.org/10.1016/J.ENCONMAN.2018.10.030

Rajan, A., Reddy, K.S., 2021. Estimation of convective heat losses from conical cavity receiver of solar parabolic dish collector under wind conditions and receiver orientations. E3S Web Conf. 313, 11001. https://doi.org/10.1051/e3sconf/202131311001

Reddy, K.S., Sendhil Kumar, N., 2009. Convection and surface radiation heat losses from modified cavity receiver of solar parabolic dish collector with two-stage concentration. Heat Mass Transf. und Stoffuebertragung 45, 363–373. https://doi.org/10.1007/S00231-008-0440-2

Reddy, K.S., Veershetty, G., Srihari Vikram, T., 2016. Effect of wind speed and direction on convective heat losses from solar parabolic dish modified cavity receiver. Sol. Energy 131, 183–198. https://doi.org/10.1016/j.solener.2016.02.039

Si-Quan, Z., Xin-Feng, L., Liu, D., Qing-Song, M., 2019. A numerical study on optical and thermodynamic characteristics of a spherical cavity receiver. Appl. Therm. Eng. 149, 11–21. https://doi.org/10.1016/j.applthermaleng.2018.10.030

Taumoefolau, T., Paitoonsurikarn, S., Hughes, G., Lovegrove, K., 2004. Experimental investigation of natural convection heat loss from a model solar concentrator cavity receiver. J. Sol. Energy Eng. Trans. ASME. https://doi.org/10.1115/1.1687403

Wang, S., Asselineau, C.-A., Wang, Y., Pye, J., Coventry, J., 2020. Performance enhancement of cavity receivers with spillage skirts and secondary reflectors in concentrated solar dish and tower systems. Sol. Energy 208, 708–727. https://doi.org/10.1016/j.solener.2020.08.008

04. Renewable and Efficient Heating and Cooling Systems

Advanced Modelling of Solar Energy Based Ice Storage Systems

Vivek J. Glasswala[1], Dr. Andy Gradel[1], Tushar Sharma[1], Dr. Daniel Carbonell[2], Prof. Dr. Tobias Plessing[1]

[1] Institute for Hydrogen and Energy Technology of Hochschule Hof, Hof (Germany)

[2] SPF Institute for Solar Technology, Rapperswil (Switzerland)

Abstract

Storage of fluctuating renewable energy sources is of elementary importance for decarbonizing the energy system. Ice storage systems can be used for this purpose in industrial cooling applications. For an accurate process design, an existing model was extended, improved in accuracy, and integrated into a complete system simulation. The simulation was used to numerically calculate the key performance indicators on all relevant processes of the storage tank, i.e. sensible cooling and heating, freezing and melting. The numerical model was validated with experimental results for a storage tank of 10 m^3 operating under real conditions using ice-on-coil heat exchangers coupled with the ground. The model predicted the ice fraction, heating capacity, average storage temperature as well as the output temperature of the heat transfer fluid with an accuracy above 98 % for the processes of melting and sensible heating.

Keywords: Ice Storage, Industrial Cooling, numerical modelling, TRNSYS simulation

1 Introduction

In order to reach a carbon neutral sustainable future, the energy supply system needs to be integrated with renewable resources. Apart from the residential cooling applications, sectors such as dairy, brewery, bakery, and food production also have a cooling demand with the temperature range from 0°C to 10°C. Using the renewable energy sources for such demands shows potential in cost and carbon emission reduction. However, fluctuating and unpredicted behavior of renewable alternatives such as solar or wind energy require energy storage systems. A promising solution to this challenge is the integration of thermal energy storage (TES) with the renewable resources. One example of such a system integration is the usage of an ice storage tank combined with a chiller. The chiller operated by electrical energy from a photovoltaics system can convert electrical energy into thermal energy, which can be used directly for the cooling demand or can be stored further into an ice storage. One of the advantages of such a system is the effective load shifting during the peak demand.

Since these systems are non trivial, a complete system simulation is necessary before designing a real system. There have been many studies conducted to check the performance of the ice storage with different heat exchanger geometries such as capillary mat (CM) and flat plate (FP) (Carbonell et al., 2017). In order to achieve an accurate process design, numerical models of such systems are available to forecast the effectiveness and energy saving potential. For this research process, a numerical model for ice storage namely Type 861 with the coiled heat exchanger geometry available in the TRNSYS has been considered. A complete system simulation was conducted to check the key performance indicators of an ice storage as well as to validate the model with the data collected from an experimental setup.

1.1 Ice Storage

Earlier in the history of the ice storage, industries such as breweries, dairies, and meat production with huge cooling requirement for product storage, collected and stored the ice from rivers during the winter season in so-called ice cellars, rather than using the machine made ice bars (Goeke, 2021). The modern version of ice cellars are figuratively ice storage tanks. The ice storage consists of heat exchanger, storage material, and the reservoir. Since the heat transfer occurs only between the surface of the heat exchanger and storage material,

10.18086/swc.2023.04.06 Available at http://proceedings.ises.org

most clever arrangement with the highest possible surface area is necessary. Some modern versions of the ice storages are shown in the Fig. 1.

Fig. 1: (a) Cylindrical Ice storage with helical coil heat exchanger geometry from Viessmann Werke (on left) (b) Cuboidal Ice storage with U-type capillary mat heat exchanger from Clina (on right)

Ice storage technology is most widely applied example of latent thermal heat storage (LTES). The incorporation of LTES into practical application depends largely on the phase transformation capability of the thermal storage material. Due to the ability to undergo phase transformation under the isothermal conditions, the materials would freeze at constant temperature when cooled below the melting point. This unique phenomenon provides the storage material with the name *"Phase Changing Material (PCM)"*. Most significant object of latent heat storage is the possibility to store a large amount of energy within a small temperature range (Kalaisalvam and Parameshwaram, 2014).

The latent and sensible energy storage is explained (Kalaisalvam and Parameshwaram, 2014) by the mathematical description of the estimated enthalpy of fusion:

$$2.5RT_m < \Delta h_{m,mol} < 5RT_m \qquad \text{(eq. 1)}$$

Where T_m is the melting temperature, $h_{m,mol}$ is the molar heat of fusion, and R is the molar gas constant.

When the PCM is heated from the initial temperature T_1 to the melting temperature T_m and further to the temperature T_2, the heat stored in the material is:

$$Q_{Total} = Q_{sensible,solid} + Q_{latent} + Q_{sensible,fluid} \qquad \text{(eq. 2)}$$

$$Q_{Total} = m \cdot c_{p,\mathrm{solid}}(T_m - T_1) + m \cdot \Delta h_m + m \cdot c_{p,\mathrm{fluid}}(T_2 - T_m) \qquad \text{(eq. 3)}$$

Ice thermal energy storage systems (ITES) are used in many fields. For a regenerative-fed cooling application of above 0 °C, ice storage can be used as the low cost latent heat storage. The design parameters for ITES systems depend on a wide variety of variables, such as volume, mode of operation, type of heat exchanger, and loading and unloading characteristics for better performance during cooling demand. For an accurate process design, it is essential to have the simulation models as accurate as possible, because a wrong design can endanger the productivity of the respective industries or can consume more unnecessary fossil resources from the backup solutions. This research process targets the total simulation including modeling and validation of combined mathematical model available for ice storage (Type 861) described in Carbonell et al. (2018) with the ground model (Type 709) described in Carbonell et al. (2016) as boundary condition in TRNSYS using the real conditions and available data from the small experiment setup. The process includes the validation of melting and heating behavior of this particular mathematical model.

2 Research Process

In order to run a simulation, certain data are required to define various properties, boundary conditions and input fields. These environmental parameters allow us to observe and understand the effects of each parameter on the performance of the system. This helps to define the system more accurately in the simulation program and to identify the completeness of the mathematical model. These data can be obtained either from the manufacturers or from the sensors installed in the test rig. Data such as the dimensional characteristics of the component, maximum and minimum operating temperatures, maximum volume, etc. are available in the respective operating manuals. On the other hand, the real-time operating data are recorded during the test from the sensor measurements.

For the validation of the performance of the ice storage, a reference test bench for the heat pump with ice storage was considered. This has been designed and set up in the energy laboratory of the Münchberg campus of Hof University of Applied Sciences.

2.1 Test bench and experiment

The basis for this research process was laid in a previous research project, which aimed to design and construct two types of heat pump systems to research and develop the solution to the ever increasing energy demand (Kätzel, 2015). The energy concept shown in Fig. 2 was used to develop the solar heat pump system with ice storage in the laboratory. As shown in Fig. 1, ice storage with spiral heat exchanger by Viessmann consists of a tank with built-in heat exchanger and distributor, which is buried in the garden and usually filled with untreated tap water. Solar air absorbers installed on the roof supply the heat extracted from the ambient air and solar radiation to the tank.

Fig. 2 illustrates the experiment setup available in the lab consisting of an ice storage tank with two different heat exchangers for the extraction and regeneration purpose. The primary circuit is connected to a heat pump that extracts heat from the water in the ice storage via coils through the cooled brine. This is also known as the extraction heat exchanger. The secondary circuit, which connects the solar air absorber with the ice storage tank, is called the regeneration circuit as it transfers the heat collected by the solar air absorber to regenerate the cold energy stored in the form of ice.

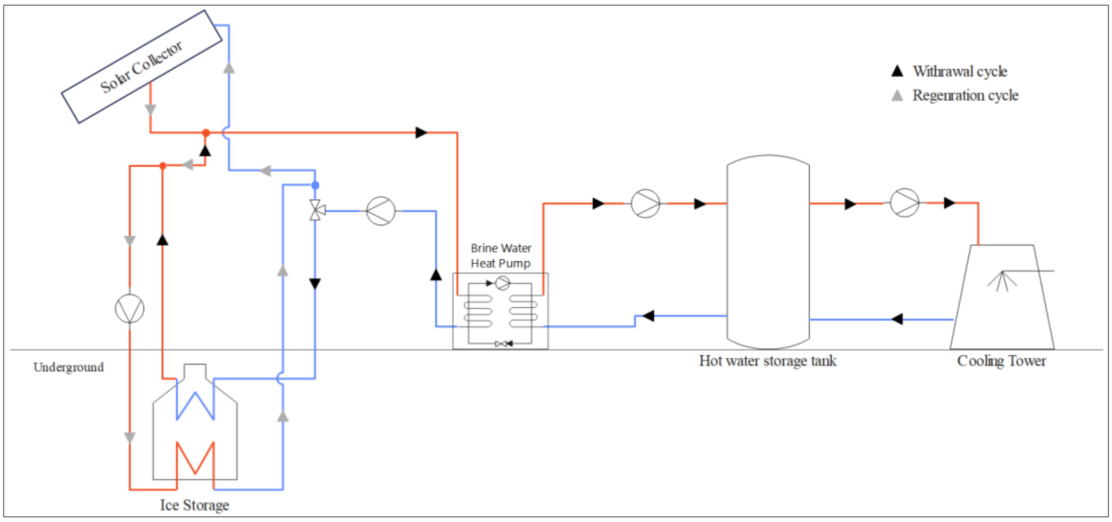

Fig. 2: Hydraulic schema of the test bench

The test bench consists of following main components:

- Brine/Water Heat Pump
- Ice Storage (Buried Underground)
- Solar Air Absorber
- Buffer Tank (Heating Circuit)
- Buffer Tank (Process Water)
- Control System

Depending on the active heat exchanger, all four processes mentioned above can be divided into the following two circuits:

- *Extraction/Withdrawal process*: During the withdrawal process, the heat energy is extracted from the PCM, resulting in cooling and eventually freezing of the PCM. Cooling and Icing/Freezing cycle – Highlighted by black arrows in Fig. 2.

- *Regeneration process*: During the regeneration process, the heat energy is released to the PCM, causing the PCM to melt and eventually heat up. Melting and Heating cycle – Highlighted by grey arrows in Fig. 2.

The challenge of this research process is to test the heating and cooling performance of the ice storage tank with coil heat exchanger. From various literature studies, there were few findings on the validation of ice storage with coil heat exchanger. In terms of a broader perspective, the Type 861 model was validated with capillary mats heat exchangers (Carbonell et al., 2018) and flat plates (Carbonell et al., 2017) and a similar model was validated with one year of monitoring data coupled with the ground using a de-icing ice storage concept (Carbonell et. al, 2016). However, the model lacked validation for ice-on-coil heat exchangers typically used in commercial applications. This validation process will lay base for more accurate predictions for component sizing according to the cooling and heating load profile of an industry.

The continuous experiment was conducted during summertime from *May 30, 2022 to June 18, 2022*. Sensor data were collected at minute intervals and converted into a *CSV* file format. Furthermore, the UA values are responsible for limiting the maximum power input and output to as well as from the water. Since all the phase occurring in the ice storage have different physical dynamics, the complete testing process is divided into four sequences namely,

- Cooling
- Freezing
- Melting
- Heating

Data recorded for each minute of total 20-day experiment helps to increase the accuracy of the validation and provides continuous data without interruption. In order to prepare the data for simulation input files and to simplify the display and behavior of the ice reservoir, the recorded data were also divided into four separate sequences described above.

When validating an ice storage system, the heat exchange rate between the heat exchanger and the PCM as well as the behavior of the PCM in the container are decisive factors. The heat transfer via the heat exchanger can theoretically be calculated by the mass flow through the extraction or regeneration heat exchanger and the temperature difference at the inlet and outlet of the corresponding heat exchanger coil as shown in equation 4.

$$\dot{Q} = \dot{m} C_p \left(T_{brine,out} - T_{brine,in}\right) \qquad \text{(eq. 4)}$$

The calculation of the ice fraction in the ice storage is performed with help of ultrasonic sensor. The ultrasonic sensor provides signals in mA, which is then converted into distance during the calibration process. Calibration was performed in the lab by fixing the ultrasonic sensor in still position and moving a flat plate in the reciprocating action to record the change in sensor value depending upon the distance between sensor tip and the flat plate.

After the calibration of the ultrasonic sensor, the ice fraction is calculated through following equation:

$$M_{fr} = \frac{A_{storage} \cdot \rho_{ice} \cdot \rho_w}{\rho_{ice} - \rho_w} \cdot \frac{(G_n - G_0)}{M_0} \cdot 100 \qquad \text{(eq. 6)}$$

Here, G_0 is the distance calculated from the initial signal from the ultrasonic sensor and G_n is given by:

$$G_n = \frac{U_n - b}{m \cdot 100} \qquad \text{(eq. 7)}$$

Where U being the sensor signal in mA.

2.2 Simulation

As mentioned above, the sensor data collected from different positions of the experiment test bench are utilized in the TRNSYS energy simulation software to create the most accurate digital test bench environment possible and to compare the simulation results with real measured values. A similar type of approach was performed in a previous study at the institute comparing two different heat exchanger geometries namely capillary mat and flat plate (Sharma et al., 2020).

One of the advancements during the research process was the correction of Nusselt number calculation in order to increase the accuracy of heat transfer in the numerical model of the coiled heat exchanger. The new implemented Nusselt number calculation is:

$$Nu = 8.14 * \left(1.98 + \frac{1.8 * D_h}{2 * r_{avg.coil}}\right) \qquad \text{(eq. 8)}$$

Where, D_h is the hydraulic diameter of the heat exchanger pipe and $r_{avg.coil}$ is the average radius of the unevenly distributed coil geometry of the heat exchanger. All the required dimensional parameter of ice storage as well as of the heat exchanger is defined in the simulation as an input. Certain number of control volumes are also defined for the water on the ice storage in order to consider the thermal conduction between the water layers and the thermal stratification due to the water density gradient at different temperature. Before conducting an experiment, the initial storage temperature from two temperature sensors submerged in the ice storage at 1.5 m and 2.5 m was recorded to provide an initial condition to the simulation. For the context of this research, the ice storage is buried in the ground, which represents the system boundary.

Type 861 stands for the mathematical model of the ice storage and Type 709 for the boundary conditions of the storage buried in the ground, which have to be defined in the simulation. As in reality, both components are interconnected, thus the heat transfer between the concrete wall of ice storage and the soil as well as between the atmosphere and the soil should also take place in the simulation. Because of this coupling, the temperature of the soil in different layers will vary.

Fig. 3 shows the geometry and location values of the ice storage buried underground with the necessary sensors to collect the ground temperature as well as the storage temperature data.

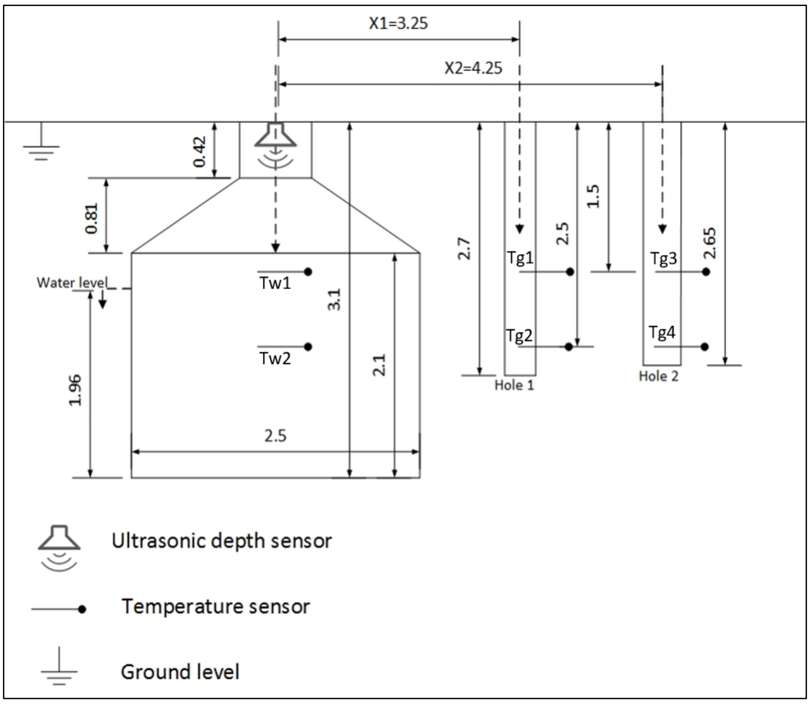

Fig. 3: Dimensional properties and sensor positions of the ice storage buried underground

The coupling between Type 861 and Type 709 was performed using the case study conducted by Carbonell et al., (2016). Considering Fig. 3, the total ground zone has the width of 4.90 m in X-direction and the depth of 5.63 m in negative Y-direction from the top left corner for this particular case. X-direction indicates the horizontal area taken into the consideration from the middle of the ice storage, where ultrasonic sensor has been installed, whereas negative Y-direction indicates depth and thus the vertical values from the ultrasonic sensor in respect to depth. The physical ground surface is then divided into 3-zones and 7-zones in X and in negative Y-direction respectively based on the property of the material. Zones in the X-direction consist PCM, concrete wall of the ice storage, and ground. Whereas as zones in the negative Y-direction consist PCM, concrete wall of the ice storage, and different beddings materials of the ground on which the reservoir foundation has been laid. Type 709 requires the initial ground temperature data at different depth of the ground.

However, as shown in Fig. 3, there are only four ground temperature sensors "TgX " available at 1.5 m and 2.5 m depth at 3.25 m and 4.25 m in X-direction respectively in the test bench. In order to provide more continuous temperature data of ground at different nodal points and control volumes, a depth dependent simple harmonic function was derived.

The soil temperature vary according to the different soil parameters and water content of the soil. From the study in Droulia et al. (2018) and in Máraquez et al. (2016), a depth and time dependent ground temperature behavior was derived and fitted using following approximate equation as a function of time:

$$T_{soil}(z,t) = T_m - T_p e^{-z\sqrt{\frac{\omega}{2\alpha}}} cos\left(\omega t - \varphi - z\sqrt{\frac{\omega}{2\alpha}}\right) \quad \text{(eq. 9)}$$

Where,

T_m= Annual average temperature of soil in the stable layer (°C)

T_p = Amplitude (°C); the peak deviation of the function from zero. In this case the annual amplitude of the monthly average temperature cycle in the place

t = Time coordinate (s). Starting time is set to zero (t=0), meaning it begins from 1 January at 0 s. In special case where the average temperature of the ground of particular month is required, Simulation start time and end time can be set in the Matlab or Scilab model.

ω = Angular frequency (rad s^{-1}); $\omega = 2\pi/T$ is the period of sinusoidal. In this case annual temperature cycle $T = 365 * 3600 * 24$ s

φ = Phase (rad). When φ is non-zero, the entire waveform appears to be shifted in time by the amount φ/ω seconds. A negative value represents a delay, and a positive value represents an advance.

z = The depth in ground (m)

α = The ground thermal diffusivity (m s^{-2}) given by:

$$\alpha = \frac{k}{\rho C} \quad \text{(eq. 10)}$$

ρ = Average soil density (kg m^{-3})

C = Specific heat capacity of soil (J kg^{-1} K^{-1})

k = Thermal conductivity of soil (W m^{-1} K^{-1})

Based on the equation, the mean temperature T_m and the amplitude of the surface temperature T_p were used as fitting parameters, which were in the acceptance range as can be seen in Table 1. The aim was to keep the difference between the measured value with sensor and the calculated value with equation 9 of the soil temperature as small as possible.

Tab. 1: Temperature measurements from the ground sensor and from ground-temperature estimation model

Process and Day	Sensors	Z – Depth m	T_{sensor} °C	$T_{g,Estimated}$ °C
Melting	T0	0	19.50	19.69
(Active Melting)	TG1	1.5	13.10	13.57
166th	TG2	2.5	10.72	11.23
	TG3	1.5	13.57	13.57
	TG4	2.5	11.29	11.23
Heating	T0	0	19.01	19.96
(Active Heating)	TG1	1.5	13.75	13.84
169th	TG2	2.5	11.00	11.45
	TG3	1.5	14.27	13.84
	TG4	2.5	11.42	11.45

Fig. 4 shows the graphical representation of the comparison between the measured temperature data from the sensors on the 166th day of the year and the calculated data from the Ground-Temperature-Estimation model on that particular day. The results obtained from the calculation were utilized to create the initial file, which was then specified as the initial boundary condition of the soil.

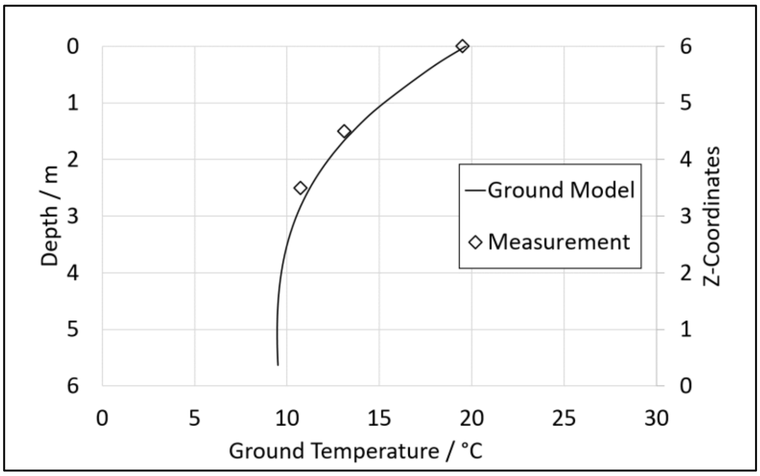

Fig. 4: Illustration of the comparison between the measured temperature data from the sensors and ground-temperature estimation model

From the hydraulics shown in Fig. 2, a simulation model is established using the following components in the TRNSYS:

Tab. 2 Essential component list for simulation model building in TRNSYS

Type	Description	Name
-	Equations and Constants	Equation Block
9	Generic Data Files – Skip Lines to Start – Free Format	Type 9c
25	Printer – No units printed to output file	Type 25f
46	Printegrator – Formatted – Monthly Periods	Type 46f
709	Ground Model	Type 709
861	Ice Storage model with ice-on heat exchangers	Type 861

3 Results and Validation

Once the boundary conditions for each critical component were established, the simulation was performed for melting and heating cycle. The printed file containing the simulation results was then prepared and plotted in Excel for better visualization.

3.1 Melting and Heating:

Once the ice percentage in the ice storage was reached at 80%, melting and heating of PCM was carried out. Melting in this case is considered until the mass of ice is zero and leads to the sensible heating of the PCM. As to be seen in the Fig. 5, the heating capacity follows the negative trend for this research process. The cooling capacity is referred as the positive value since the sole purpose of the ice storage is to deliver the cooling power. The sinusoidal behavior of the *Heating Capacity* as well as of the *Brine Outlet Temperature* as to be seen in the Fig. 5 and Fig. 6 respectively is due to the dependency of regeneration cycle on the solar absorber. Due to the available solar radiation during the daytime, the temperature level in the regeneration heat exchanger reaches its maximum. However, during the nighttime a sudden drop has been observed in the average temperature of the storage and only in the experiment during the melting cycle. It is because the Type 861 is not programmed to record the below zero value of the temperature of the PCM. During the melting cycle, ice on heat exchanger will first start to melt which then slowly transfer the heat from one layer of ice to another. Since there is no external heating energy available from the sun in the nighttime, the PCM far away from the heat exchanger wall still has the lower temperature values compared to the PCM closer to the wall. Due to this, there is a heat exchange in the PCM layers in all direction to reach the thermal equilibrium in the ice storage.

As the Type 861 does not record the below zero temperature value of the PCM, it does not show this behavior in the simulation. However, once that limitation is over, the model also follows the same behavior during the heating cycle as to be seen in Fig. 5. It also shows that the heating capacity of the ice storage in the experiment is similar to the results from the simulation conducted during melting and heating process. Considering the 0.50 °C average storage temperature as the beginning of heating, it begins roughly after 410th relative hour of the simulation. However, in the experiment, it begins quite early. It is because there are only two temperature sensors submerged in the PCM to record the temperature values and to calculate the average temperature of ice storage. They are installed near the heat exchanger wall, which affects the accuracy.

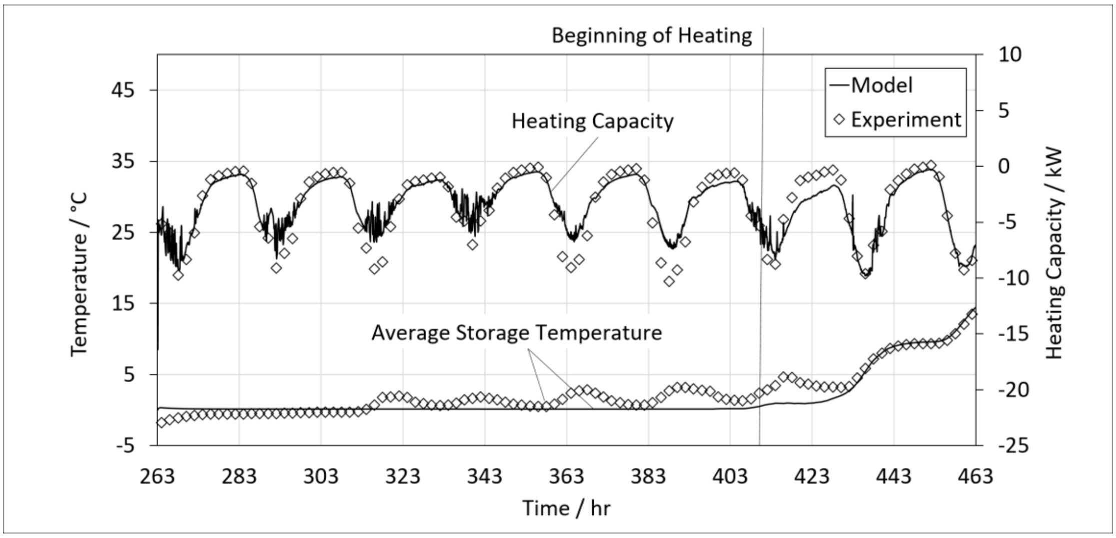

Fig. 5: Comparison of heating capacity and average storage temperature of ice storage during melting and heating process

In addition, there were no major discrepancies between the temperature estimated from the ground model and the data collected from sensors as shown in Fig. 6. As shown in Fig. 7, the initial ice fraction was defined at the 80% in the simulation to match the exact condition in the ice storage respective to storage temperature and the ice percentage calculated in from the ultrasonic sensor data available from the experiment.

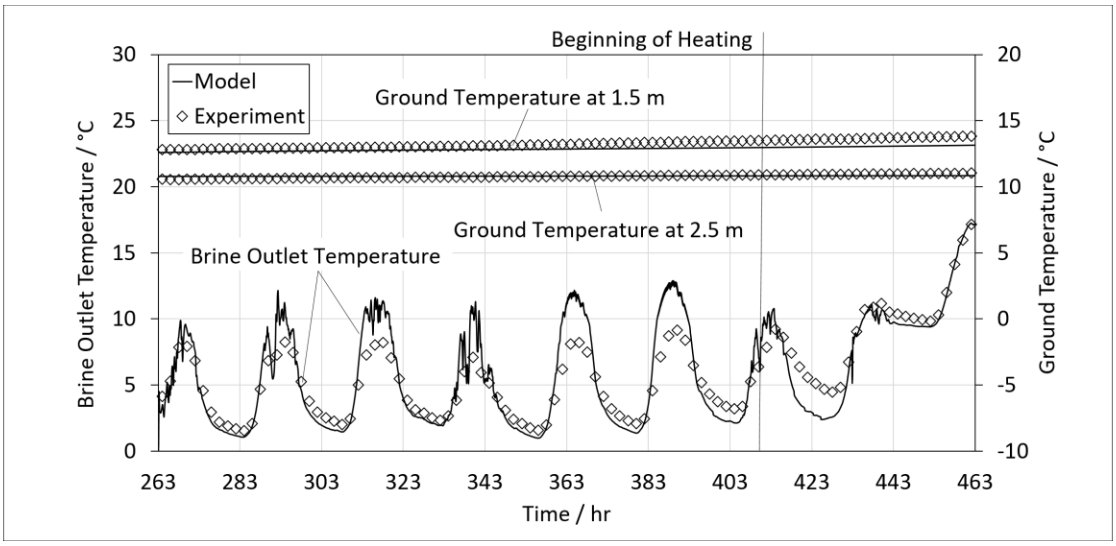

Fig. 6: Comparison of brine outlet temperature of ice storage and ground temperature during melting and heating process

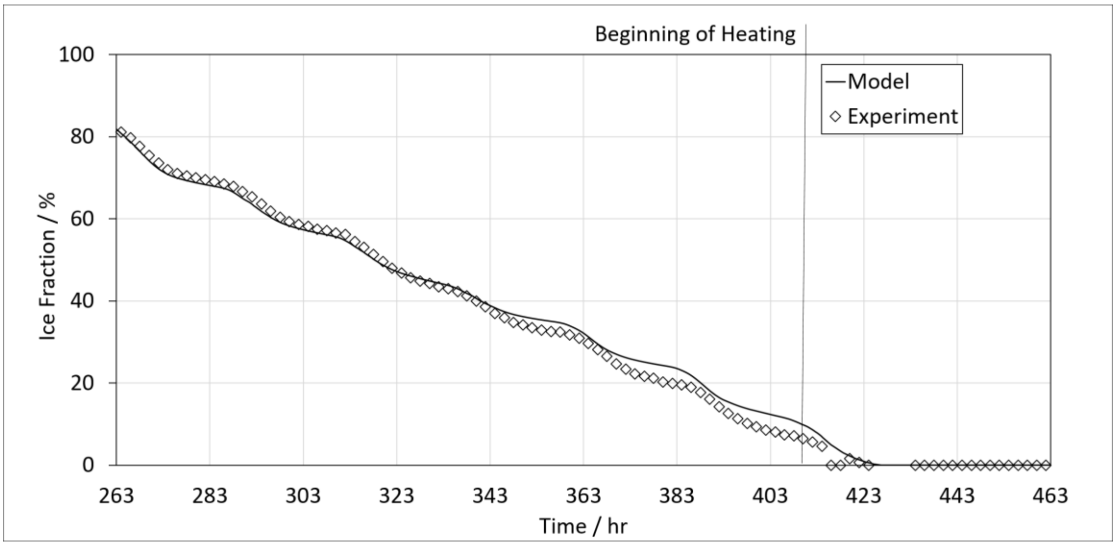

Fig. 7: Comparison of ice fraction in ice storage during the melting and heating process

4 Discussion

Using the standard root mean square average method for both experiment and simulation, the accuracy of each behavior is defined. The result data shows almost 99 % accuracy in ice fraction prediction following by 97 % accuracy in estimating the ground temperature from the recorded data. On an average, the heating capacity shows 86 % accuracy whereas brine outlet temperature and the average storage temperature achieves 94 % accuracy averagely during the whole sequence.

5 Acknowledgement

We thank the Hans Viessmann Technologie Stiftung and the Viessmann Climate Solutions SE for the financial support and we thank the Bavarian State Ministry for Science and Arts for the financial support under the project *KaWaTech*. We also thank the European regional development funds [EFRE] for financial support under the project *Grüne Technologie Werkstatt [GTW]* in cooperation with Genes Kältetechnik GmbH.

6 Reference

Carbonell, D., Philippen, D., Haller, M., Brunold S., 2016. Modeling of an ice storage buried in Modeling of an ice storage buried in the ground for solar heating applications - Validations with one year of monitored data from a pilot plant. Solar Energy: Journal of the international solar energy society 125, 398-414. https://doi.org/10.1016/j.solener.2015.12.009

Carbonell, D., Battaglia, M., Phillipen, D., Haller, M., 2017. Ice-Ex: Heat exchanger analysis for ice storage in solar and heat pump applications. Final report by Institute für Solartechnik SPF. https://doi.org/10.5281/zenodo.5596601

Carbonell, D., Battaglia, M., Phillipen, D., Haller, M., 2018. Numerical and experimental evaluation office storages with ice on capillary mat heat exchanger for solar-ice systems. International Journal of Refrigeration 88, 383-401. https://doi.org/10.1016/j.ijrefrig.2018.02.007

Droulia, F., Lykoudis, S., Tsiros, I., Alvertos, N., Akylas, E., Garofalakis, I., 2008. Ground temperature estimation using simplified analytical and semi-empirical approaches. Solar Energy 83, 211-219. https://doi.org/10.1016/j.solener.2008.07.013

Goeke, J., 2021. Thermische Energiespeicher in der Gebäudetechnik: Sensible Speicher, Latente Speicher, Systemintegration. Springer Nature, Germany. https://doi.org/10.1007/978-3-658-34510-5

Kalaisevam, S., Parameshwaram, R., 2014. Thermal Energy Storage Technologies and Sustainability. Elsevier Inc., London.

Kätzel, A., 2015. Masterarbeit: Planung und Aufbau eines Wärmepumpen-Prüfstandes mit einem Eisspeicher als Primärquelle. Hochscule Hof, Hof Germany.

Máraquez, J.M.A., Bohórquez, M.À.M., Melgar, S.G., 2016. Ground Thermal Diffusivity Calculation by Direct Soil Temperature Measurement – Application to very Low Enthalpy Geothermal Energy Systems. Sensors (Basel) 16(3), 306. https://doi.org/10.3390/s16030306

Sharma, T., Prof. Dr. rer. Honke, R., and Prof. Dr.-Ing. Plessing, T., 2020. Comparison of system performance of different types of Ice-battery for cooling application in industries. TFRE2020: International Conference on Recent Trends in Development of Thermo-fluid and Renewable Energy, NIT Arunachal Pradesh, India, 26-28 November. https://doi.org/10.1007/978-981-16-3497-0_46

Analysis of Thermo-Mechanical Stresses and Strains for a Novel Design of Insulating Glass Flat-Plate Collector

Thorsten Summ[1], Brian Sturm[1], Christian Scherer[2], Christoph Trinkl[1], and Wilfried Zörner[1]

[1] Institute of new Energy Systems, Technische Hochschule Ingolstadt, Ingolstadt (Germany)

[2] H.B. Fuller Deutschland GmbH | Kömmerling Chemische Fabrik GmbH, Pirmasens (Germany)

Abstract

Insulating glass flat-plate collectors have been investigated more intensively during the last decade as this innovative design approach promises to lower heat generation cost for solar thermal applications. The latest investigations in that field indicate that high temperatures and mechanical stresses may affect durability and stability of the collector sealings that are required for an efficient operation of the solar thermal module. A novel design was proposed recently that has not yet been studied regarding its thermo-mechanical loads, stresses, and strains. The objective of this study was to determine typical load profiles for such collectors and – through finite element analysis – determine stresses and strains on the collector sealings. An answer should be given as to whether the novel design improves the thermo-mechanical resilience of the collector and whether the chosen design can withstand typical load conditions for solar district heating. The results show that stagnation is likely to cause gas leakages but unlikely to cause mechanical failure of the collector. Furthermore, it was shown that thermo-mechanical loads during normal operation are uncritical, which is why the novel insulating glass flat-plate collector design is considered superior over the previous. Although a lifetime of 20 to 25 years is very likely to be achieved for the collector, we strongly suggest avoiding stagnation for the collector to avoid gas leakage and resulting decrease in thermal performance.

Keywords: thermo-mechanical analysis, stress, strain, finite element analysis, insulating glass, solar thermal, flat-plate collector, durability

1. Introduction

One recent approach to obtain more cost-effective solar thermal components and systems is to establish the insulating glass flat-plate collector (IGFPC). This novel collector design features low production and system cost while offering comparable thermal performance as conventional flat-plate collectors. This makes it particularly promising for solar district heating (SDH) applications. Since 2014, investigations on IGFPCs were carried out from several research institutions and are still ongoing. So far, their work mainly focused on thermal performance and thermal losses, thermomechanical stresses, durability, production techniques and estimated collector costs.

Simulation studies (Leibbrandt and Schabbach, 2015; Riess et al., 2016), indoor (Giovannetti et al., 2014; Riess, 2017) and outdoor (Giovannetti and Kirchner, 2015; Summ et al., 2023) performance tests showed that the thermal efficiency of these modules is comparable to conventional flat-plate collectors. This is mainly due to the inert gas argon which can be filled inside the enclosed cavity of the collector. This gas surrounds the absorber, has lower thermal conductivities than air, and hence reduces the convective losses of the collector.

However, durability analyses (Giovannetti and Kirchner, 2015) have shown that the insulating glass module sealings experience high thermal and mechanical loads which represent a challenge to maintain collector durability over a longer period of time. Throughout the years, several designs have been developed that impose different thermo-mechanical loads on the sealings. Whereas a pure glass collector design (Leibbrandt and Schabbach, 2015) suffers from low thermal conductivities in the absorbing element, a design setup where the absorber is bonded to the glass (Riess et al., 2015) leads to large absorber deflections causing damage to the coating or significant reductions in thermal performance (Riess et al., 2014; Riess, 2017).

Further experimental research suggests that the argon concentration significantly affects the thermal performance of the modules once the argon concentration inside the collector drops below 50 % (Summ et al., 2023). As the argon gas cost is negligible compared to the overall production cost, the target for collector producers is to achieve the highest possible concentration during production and maintain a value above 50 % during the collector lifetime of 20-25 years. This will lead to IGFPCs with both long-term durability and high performance, but also implies that the

10.18086/swc.2023.04.14 Available at http://proceedings.ises.org

sealings must withstand all imposed thermomechanical stresses and strains.

The most recently proposed collector design (Summ et al., 2020) uses a roll-bond absorber that is placed between the glass front and back pane as seen in Fig. 1. This IGFPC design proved to be the so far most efficient one (Summ et al., 2023). The inlet and outlet connectors were chosen to be fed through the rear glass to reduce the thermo-mechanical loads on the sealings. First lab tests on small scale samples (Summ et al., 2021) have indicated that the temperature loads are within an acceptable range for the collector operation.

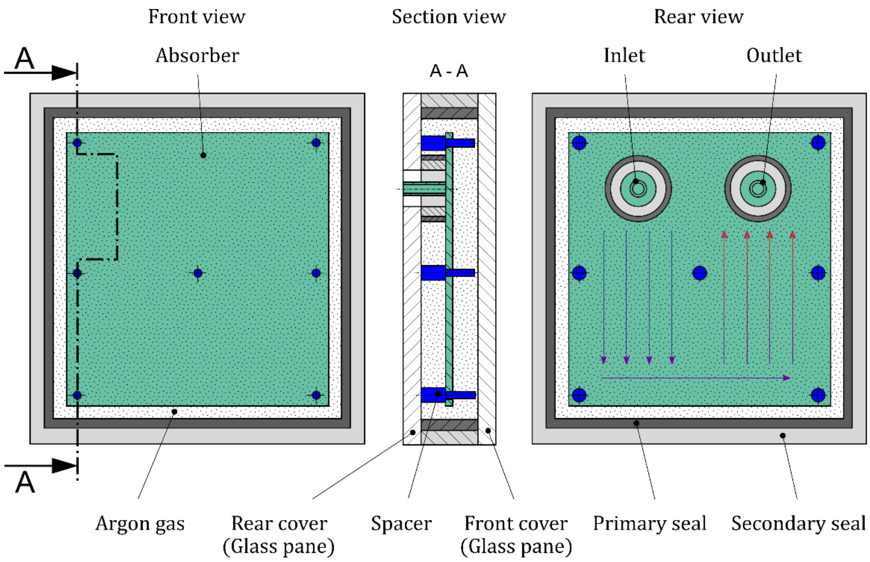

Fig. 1: Simplified sketch of the chosen insulating glass flat-plate collector design.

However, the mechanical loads and thermally induced stresses have not yet been investigated for this collector setup. The most relevant part of the collector sealing is at the inlet and outlet connectors, where the absorber is in direct contact with the sealing material. No evidence is provided whether this design improves the thermo-mechanical resilience of the collector and in that way contributes to an improvement for durability of IGFPCs. The aim of this research is to close this gap by conducting thermo-mechanical simulations and calculate the stresses and strains on the sealing material. The resulting novel outcomes of the presented study are:

- Typical operational states and resulting load conditions for IGFPCs,
- Stresses and Strains of IGFPC sealings for the so-far most efficient design.

2. Methodology

For this study, a three-stage methodological approach was chosen consisting of load analysis, thermo-mechanical finite element simulation and the analysis of stresses and strains from the simulation studies. An overview of the required inputs, methods and outcomes is given in Fig. 2. Weather data was used to determine the environmental conditions which apply to the collector for a selected site. Then, both numerical and experimental data regarding the solar thermal system behavior were taken to derive the external thermal and mechanical loads. From full-year datasets, a load profile on the collector sealings was computed using the finite element model. The results were used to compute the stresses and strains for the critical collector component – the sealings at the inlet and outlet connector.

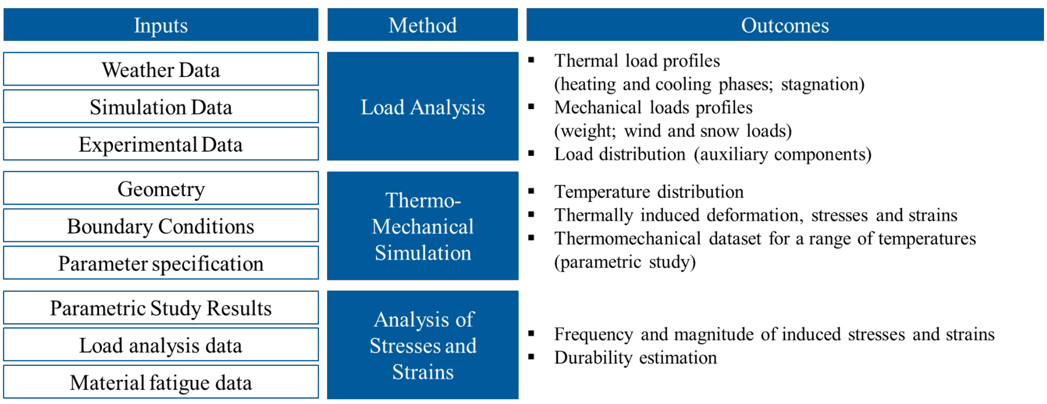

Fig. 2: Inputs, methods and outcomes chosen for this study.

2.1 Load Analysis

The loads that act on the solar thermal collectors is composed of thermal, mechanical, and thermo-mechanical loads. Thermal loads are mainly a result from the collector operation but can be distinguished into "normal" operation and the case of stagnation (e.g. when pumps fail and no heat can be dissipated from the collectors). The mechanical loads on the collector consist of its own weight, wind loads, and snow loads.

The collectors were designed for solar district heating application and for this, wind and snow load categories according to DIN EN 1991-1-3 (Deutsches Institut für Normung, 2023) and DIN EN 1991-1-4 (Deutsches Institut für Normung, 2010) were considered to define the requirements on mechanical strength. For wind load, category 4 was selected and for snow, category 3 was chosen. The sealings at the edges of the collectors correspond to the same as for insulating glass units. These were designed and validated over decades from the insulating glass industry to withstand wind/snow loads. The uncertain part for IGFPCs are therefore the sealings at the inlet and outlet connector.

However, the position of the collector inlets and outlets is near to the edges which leads to low bending loads on their sealings. Furthermore, the normal forces due to wind/snow are intercepted via the spacer elements (c.f. Fig. 1, blue parts) at the front and transferred towards the back glass pane. Therefore, wind and snow loads were considered as negligible for the inlet and outlet connector sealings.

The remaining loads of relevance for the collector sealings represent temperature loads and thermo-mechanical loads. Temperature loads on the edge sealings of the collector are moderate compared to the loads at the inlet and outlet connector. For the latter, the absorber is in direct contact with the sealing leading to the maximum temperatures at this location. Thermally induced stresses on the sealings are also significantly higher there (Riess et al., 2014). It is therefore crucial to know the collector temperature during the operation of the system.

A real solar thermal reference system was chosen for the load analysis to obtain realistic assumptions regarding the operating conditions of IGFPCs. The system is a local district heating plant in Upper Franconia, Germany characterized by a combination of 5 biomass boilers, solar thermal flat-plate collectors, and a combined heat and power generator and a gas boiler. The grid is operated with a flow temperature of 80 °C and a return temperature of 55 °C. Fig. 3 shows the schematic diagram of the system.

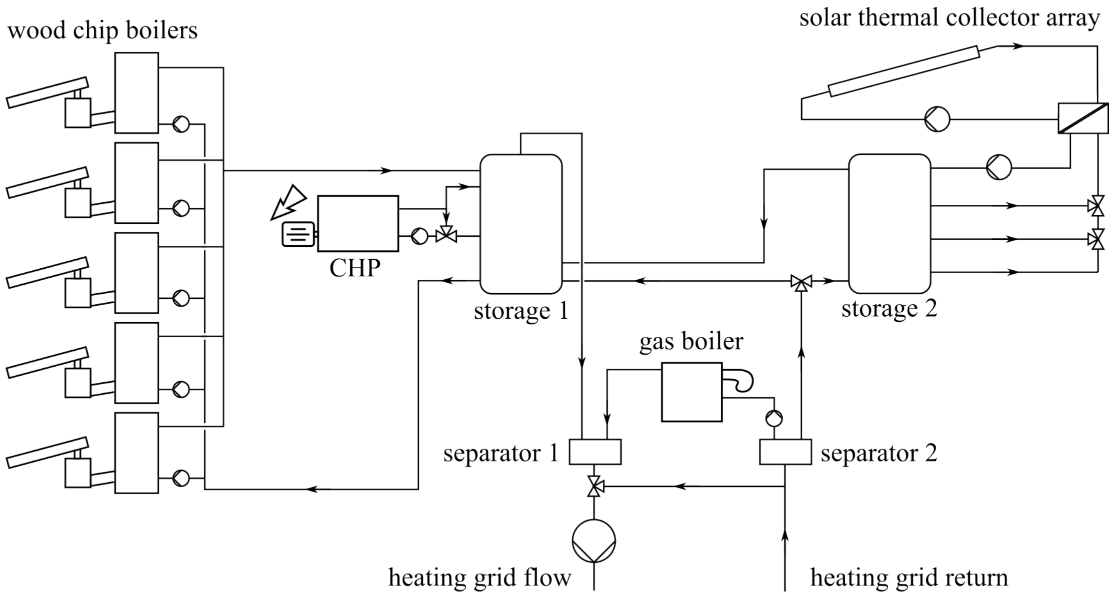

Fig. 3: Schematic diagram of the district heating system.

The base load heat generators for the district heating supply are 5 wood chip boilers with 155 kW each. They are connected to a central buffer storage 1 with a size of 20 m³. The combined heat and power system with 50 kW_{el} and 80 kW_{th} is controlled according to feed-in availabilities for the electrical grid and also connected to the buffer storage 1. The gas boiler with 450 kW is used for peak load operation. It is connected via two separators and can feed directly into the grid. The solar thermal system with 190 kW is integrated into the district heating system via a solar buffer storage 2 with a size of 20 m³. Both storages are connected in series and storage 2 can be bypassed using a 3-way-valve at the return of the heating grid. In this way, solar gains can be stored independently from the operation and temperature levels from the grid.

For this study, the solar thermal system was analyzed to obtain typical operating temperatures that will be relevant for the IGFPC operation in a district heating system. Since the higher outlet temperature is more relevant/critical for the sealing durability than the inlet temperature, the measured outlet temperature of the collector array was taken as a reference for the loads. The results of this analysis are presented in section 3.1.

2.2 Thermo-Mechanical Simulation

To compute the temperature distribution of the collector components and their induced mechanical reaction, a finite element model was created using the software ANSYS Mechanical 2022 R2 (ANSYS, Inc., 2022). Fig. 4 shows the 3D model used for the simulation. The assembly consists of 5 main components. As the collector is symmetric along its vertical principal axis, symmetry conditions were applied and the geometry was cut in half. Furthermore, the lower part of the collector – in higher distance from the inlet and outlet connectors – are not of interest and were cut off. Hence, a quarter of the collector geometry was sufficient to analyze.

The absorber of the IGFPCs described in section 1 consists of three separate sheets that are connected with each other. After applying symmetry, just an outer (1) and inner (2) sheet are left. Both are connected by an intermediate piece (5) that also contains the outlet connector geometry. This piece connects the absorber with the two sealings and the surrounding rear glass pane (4). As shown in Fig. 1, the two sealings are divided into primary and secondary sealing. Being connected to the back pane, the primary sealing provides gas-tightness, and the secondary sealing provides mechanical strength. The absorber thus sealed is protected from external environmental influences, such as rain or dust, and achieves a high degree of stability. The spacers (3), which connect the absorber with the glass pane, prevent relative motion in normal direction during thermal expansion and mechanical loads. The spacers are firmly connected to the individual absorbers and can move relative to the glass pane surface. This allows the absorber and spacers to expand when temperature increases/decreases.

For discretization of the model, a finite element mesh was created using a global mesh size of 1.5 mm and a spherical refinement region (diameter of 160 mm) with a local mesh size of 1 mm. The glass was the only component with a larger mesh size of 7 mm, but also refined as shown in Fig. 5. Tetrahedron elements with a cell node count of 847,368 and element count of 3,230,313 were used for the analysis.

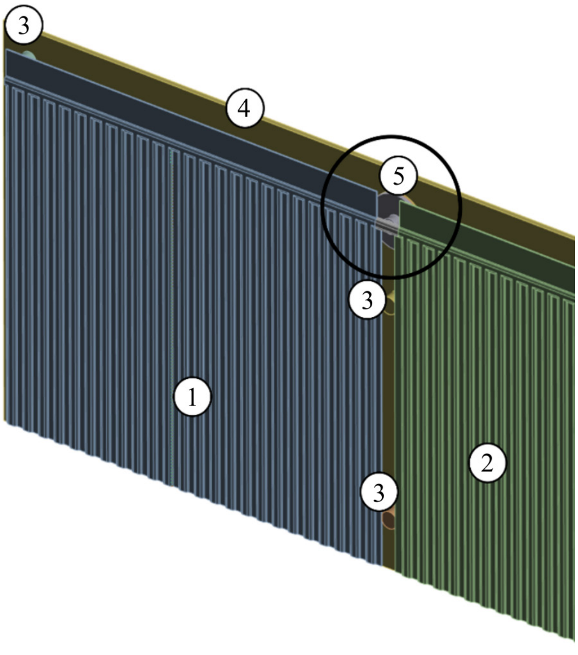

Fig. 4: Geometry of the IGFPC. The circle indicated the refinement region used for mesh generation.

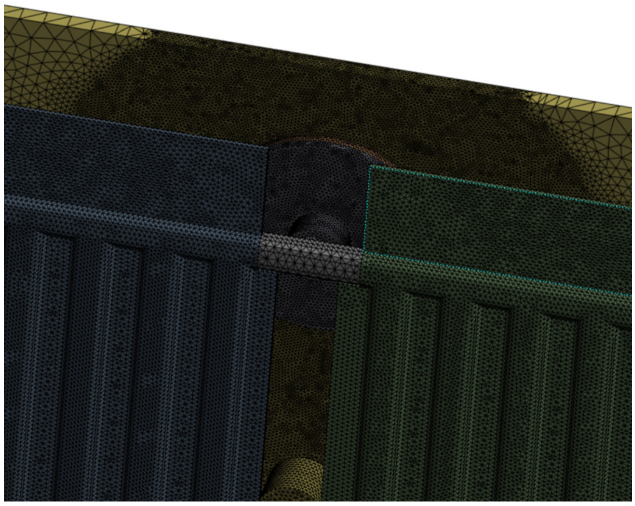

Fig. 5: Meshed geometry of the IGFPC. The refinement surrounding the outlet connector is shown.

The element size around the outlet connector is shown as a magnified view in Fig. 6. The mesh transition between multiple components was selected in such a way, that a conform mesh was generated. This enhances the computation quality, particularly in the regions where high temperature and deformation gradients are expected such as the contact area between outlet connector and primary/secondary sealing. Fig. 7 shows the distribution of element quality and the number of elements with a certain quality level in a histogram. The average element quality was 82 % and exist in the refinement area surrounding the outlet connector.

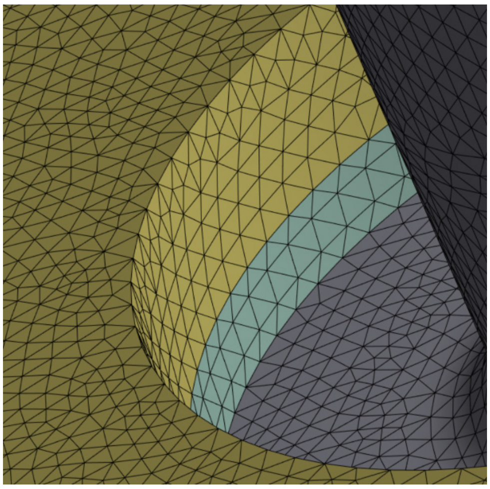

Fig. 6: Meshed geometry around the outlet connector. The transition between multiple components shows that a conform mesh was generated.

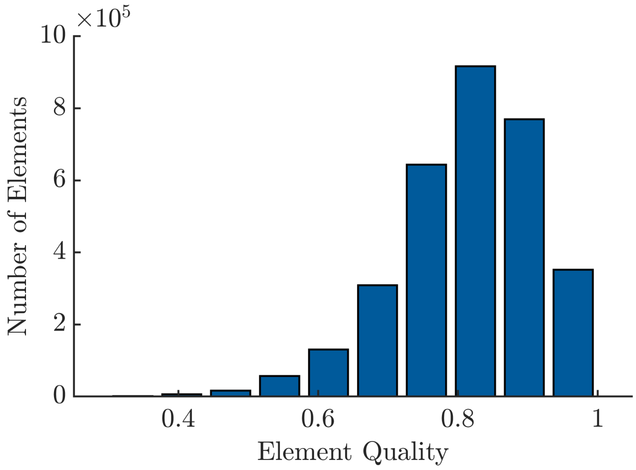

Fig. 7: Element quality histogram. The average element quality was 82 %, which corresponds to the quality range which the most elements had.

As the material properties for the sealing materials are non-linear, the analysis was a non-linear thermo-mechanical simulation. In the case of polyisobutylene, the material exhibits nonlinear behavior due to its viscoelastic properties. Under load, polyisobutylene deforms both elastically and plastically. This means that there is some elastic recovery after unloading, but there is also permanent plastic deformation. This complex behavior results in a nonlinear stress-strain relation. Silicone rubber is considered an ideally elastic (hyperelastic) material that can be described by so-called Mooney-Rivlin parameters. The non-linear material had to be treated confidentially and therefore cannot be disclosed in this paper. The remaining materials were considered to be linearelastic and therefore can be purely described by Young's modulus and Poisson's ratio. Tab. 1 shows the selected material properties for the simulation study.

Tab. 1: Selected material properties for the thermo-mechanical simulation analysis.

Component	**Material**	**Density** in kg/m^3	**Young's modulus** in MPa	**Poisson's Ratio** -	**Thermal expansion** 1/K	**Heat conductivity** in W/(mK)
Absorber	EN AW 1050A	2700	70000	0.30	2.35 E-05	215
Connector	EN AW 6060	2700	70000	0.32	2.34 E-05	210
Glass pane	Float glass	2500	70000	0.23	8.50 E-06	0.76
Primary Seal	Polyisobutylene	1220	N/A	0.50	4.00 E-05	0.76
Secondary Seal	Silicone rubber	1370	N/A	0.50	27.5 E-05	0.18
Spacer	Polytetrafluoroethylene	2180	700	0.40	12.5 E-05	0.25

For the simulation, the following assumptions and simplifications were considered:

- Gravitational acceleration does not act on the components;
- No fluid domains are present;
- The absorber has a homogeneous and constant temperature;
- There is no convective loss from absorber or connector to the inter-pane gas cavity;
- The sealings at the collector edges are not considered;
- The front glass is not considered, but the rear glass with convective losses towards the ambient air.

The load profiles and characteristics obtained from the analysis described in section 2.1 were applied as temperature boundary conditions for the thermo-mechanical simulation. To reduce complexity of the model, the inter-pane cavity containing the argon gas was not included to the model. We assumed that the gas temperature inside the collector is equal to the absorber temperature, although for a real case, the gas will show significantly lower temperatures. A steady-state analysis was chosen for the analysis computing the equilibrium states for different temperature levels.

The boundary conditions that were chosen for the analysis are listed in Tab. 2. All contacts affecting the sealings were chosen as type 'bonded' because the special primary and secondary sealings (HelioSeal and HelioBond) not only adhere to the surface of the adjacent materials but also establish a chemical bond between them. The contact between absorber and connector is a soldered junction and therefore bonded as well. A frictionless contact between the spacers and the glass is considered, as polytetrafluoroethylene is known for its low friction properties and the normal forces occurring in the simulations are negligible. To avoid rigid body movements, one of the short edges at the symmetry plane of the glass was chosen to have a fixed position.

Tab. 2: Boundary conditions chosen for the simulation study.

Type	Affected component	Property	Value
Symmetry	Glass pane – Absorber inner edge	Symmetrical	-
Contact	Absorber – Connector	Bonded	-
Contact	Primary Sealing – Secondary Sealing	Bonded	-
Contact	Sealings – Connector	Bonded	-
Contact	Sealings – Glass pane	Bonded	-
Contact	Spacer – Absorber	Bonded	-
Contact	Spacer – Glass pane	Frictionless	-
Temperature	Absorber sheets	Constant per simulation	Variable for set of simulations
Temperature	All components	Constant for initial step	20 °C
Convection	Glass pane rear side Connector outer surface (backside)	Constant heat transfer coefficient	3 W/(m²K)
Movement	Glass (edge)	Translation | Rotation	**0 | 0**

The simulation model was used to perform a parametric study regarding various temperature levels. Temperatures, elastoplastic deformation, stresses and strains were then evaluated for the analysis.

2.3 Analysis of Stresses and Strains

The thermo-mechanical simulation was subdivided into a static thermal analysis and a static mechanical analysis. Temperature values were used as an input parameter for the subsequent mechanical simulation. This process was conducted several times to obtain multiple thermo-mechanical results in a temperature range which is representing the load conditions of the solar thermal system. Just like the measured temperatures of the collector array during a whole year, the results were used to derive deformation and strain profiles for the whole year.

For the viscoelastic material (primary sealing), the stress strain relation was computed by the following equation:

$$\boldsymbol{\sigma} = \int_0^t 2G(t-\tau)\frac{d\boldsymbol{e}}{d\tau}d\tau + \boldsymbol{I}\int_0^t K(t-\tau)\frac{d\boldsymbol{\Delta}}{d\tau}d\tau \qquad \text{(eq. 1)}$$

where:

$\boldsymbol{\sigma}$:	Cauchy stress tensor
t:	Current (pseudophyiscal) time
$G(t)$:	shear relaxation kernel function
τ:	past time
$\boldsymbol{e}$:	deviatoric strain tensor
$\boldsymbol{I}$:	unit tensor
$K(t)$:	bulk relaxation kernel function
$\boldsymbol{\Delta}$:	volumetric strain tensor

Since the simulation is a steady-state simulation where the physical time is not representative, the stresses were not evaluated for the thermo-mechanical assessment of the collector primary sealing. The strains in eq. 1, however, are representative and were therefore analyzed for the viscoelastic material (primary sealing).

For the hyperelastic material (secondary sealing), the stress strain relation was computed using the so-called Mooney-Rivlin model (Mooney, 1940; Rivlin, 1948) with two parameters. It is determined by the following equation:

$$\boldsymbol{\sigma} = \frac{1}{J}\boldsymbol{F}\,2\frac{\partial W}{\partial(\boldsymbol{F^T F})}\boldsymbol{F^T} \quad \text{(eq. 2)} \quad \text{with} \quad W = c_{10}(\bar{I_1} - 3) + c_{01}(\bar{I_2} - 3) + \frac{1}{d}(J-1)^2 \quad \text{and} \quad J = \det(\boldsymbol{F})$$

where:

$\boldsymbol{F}$:	deformation gradient tensor
W:	strain-energy function per unit undeformed volume
c_{10}:	Mooney-Rivlin material constant
c_{01}:	Mooney-Rivlin material constant
d:	Mooney-Rivlin material constant
$\bar{I_1}, \bar{I_2}, \bar{I_3}$:	principal strains (invariants) of the Cauchy-Green deformation tensor $\boldsymbol{C} = \boldsymbol{F^T F}$

In this case, the stresses are time independent and therefore were evaluated during postprocessing. These results were interpreted further to provide further insights to the durability of the sealings and therefore the collector.

3. Results and Discussion

3.1 Load Analysis

The results of the load analysis were needed both as inputs for the simulation, and to assess the sealing durability after the parametric study. Fig. 8 shows the measured outlet temperature of the collector field during the year 2022. The solar thermal system is active mainly in the months February until November. In the other winter months, the flow temperature may be sufficient to charge storage 2 but undercuts the requirement of 80 °C for the grid. The controllers of the systems are set to maintain a constant feed-in temperature into storage 2 of approximately 90 °C. Despite this target value, a higher peak collector temperature occurred on May 19th 11:20 until 11:35 h with 130°C. Another peak with 128 °C was measured for 5 minutes on May 17th. All remaining peak temperatures in the diagram were below 115 °C. Reasons for this significant overshoot in temperature may be instabilities of the system while controlling the pumps and valves. An entire stagnation of the solar system has not occurred. As long as the solar pump does not fail, stagnation is very unlikely as the thermal power of the solar system is only covering a small share of the total heat demand even in summer operation. Nevertheless, a peak of 130 °C was selected as a maximum temperature for the sealing during normal operation in this investigation.

The annual duration line in Fig. 9 shows the number of hours at which specific temperature levels occurred. This confirms that the number of temperature peaks above 100 °C are present for a limited time of approximately 150 hours per year (1.7 %). For around 575 hours per year (6.6 %), the solar thermal system provides heat in temperature levels that can directly be fed into the grid (> 80 °C) The remaining energy can be fed to storage 2 to increase the grid return temperature. This is particularly the case for 55 °C < T_{out} < 80 °C and yields another 647 hours (7.4 %) where the collector provides solar heat to the system. Consequently, for approximately 7,538 hours in a year (86,1 %) the collector temperature is predominantly affected by the ambient temperature. This analysis of temperature levels for a full-year dataset has therefore shown that short peak temperatures up to 130 °C can occur for a short period of time during a year, and the design temperature for the sealings in normal operation should be considered as approximately 100 °C.

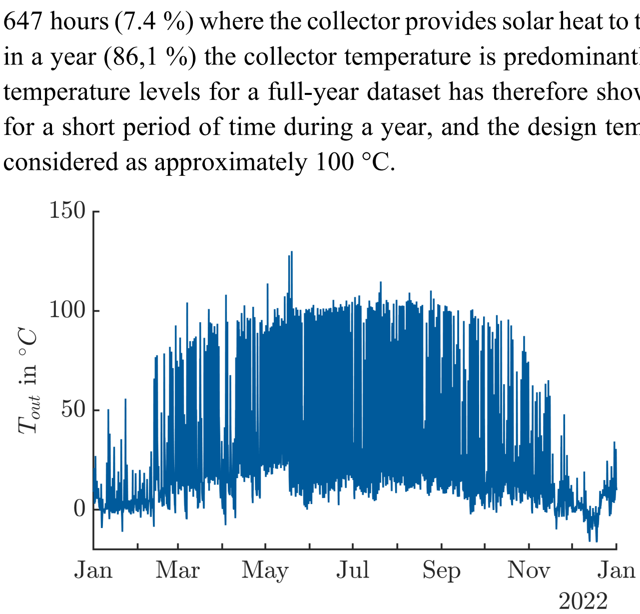

Fig. 8: Measured outlet temperature of the collector field during the year 2022.

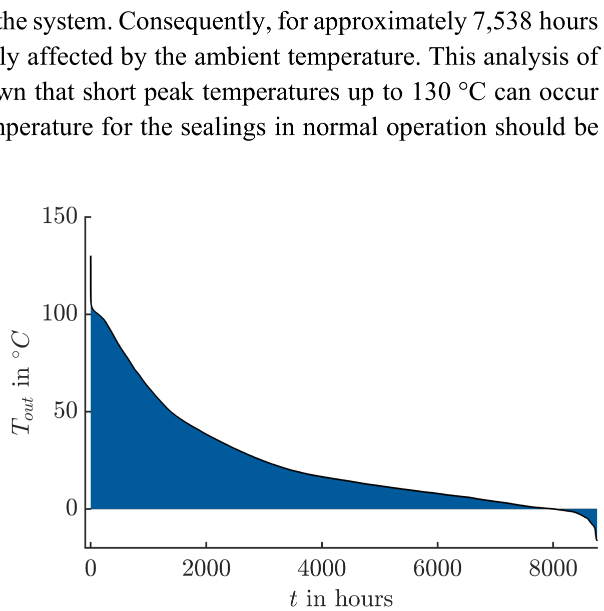

Fig. 9: Annual duration line of collector outlet temperature in the range from 0 to 8760 hours.

In cases where pumps fail or where the solar thermal system is oversized, the heat provided by the collectors cannot be dissipated. This leads to stagnation of the collector. For the analysis, the maximum temperature is calculated using the following equation from the DIN EN ISO 9806 test standard (Deutsches Institut für Normung e. V., 2018).

$$T_{stg} = 1.2\left(T_a + \frac{-a_1+\sqrt{a_1^2+4\eta_0 a_2 G}}{2a_2}\right). \quad \text{(eq. 3)}$$

The stagnation temperature is therefore dependent on the global irradiance G, the ambient temperature T_a, the optical efficiency η_0 of the collector, and its linear (a_1) and quadratic (a_2) thermal loss coefficient. From the latest performance measurements for the respective IGFPCs (Summ et al., 2023) we obtained $\eta_0 = 0.8408$, $a_1 = 3.909$, and $a_2 = 0.01361$. In deviation from the ISO 9806 test standard, we assumed $G = 1225\ \mathrm{Wm^{-2}}$ for considering a more conservative case for regions with very high solar irradiance. Using these parameters for eq. 3, the stagnation temperature of the collector was computed as 236 °C. This maximum temperature was then used to compute the thermo-mechanical reaction of the collector components using the simulation model.

3.2 Thermo-Mechanical Simulation and Analysis of Stresses and Strains

As described in section 2.2, the simulation model first computes the temperature distribution given the thermo-mechanical load conditions described in Tab. 2. The temperature distribution is then used as an input for the mechanical simulation.

3.2.1 Case 1 – Stagnation Temperature

The area of interest is the geometry around the outlet connector. Fig. 10 shows the temperature distribution of the collector in this region. Due to its high thermal conductivity and since its thermal losses inside the collector were neglected, the absorber conducts heat through the connector at high temperatures. The surface of the outlet connector at the back side and the rear surface of the glazing are the only considered heat sinks in the model. As thermal losses at the connector within the collector were neglected, the heat fluxes through the sealings are much more dominant as if these losses were considered and therefore are likely to be overestimated in the model. The glass and its convective heat transfer have a significant cooling effect despite its low thermal conductivity compared to the absorber. As a result, the zone in which the glass experiences significant temperature loads has a size of approximately four times the inner diameter of the sealing.

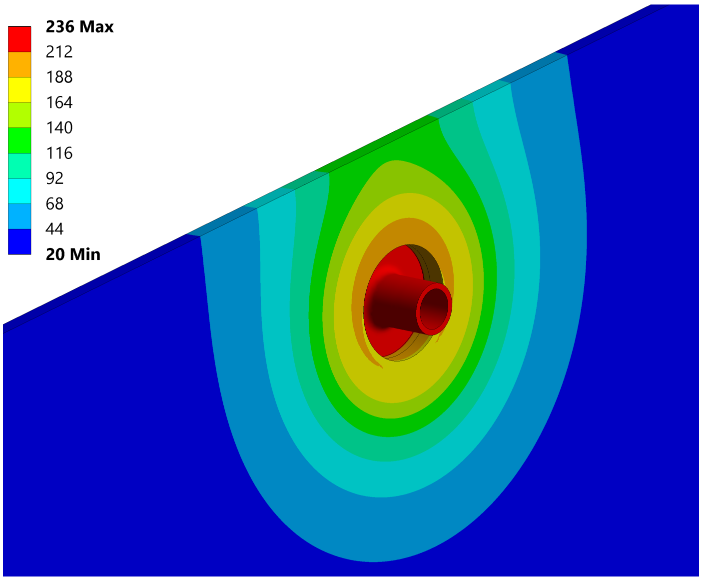

Fig. 10: Temperature distribution (in °C) around the outlet connector in the case of stagnation. The rear side of the collector is shown to indicate the temperature gradients present close to the sealings.

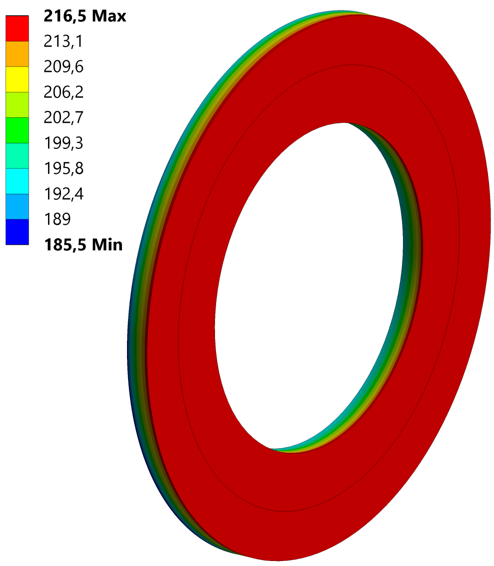

Fig. 11: Temperature distribution (in °C) of the primary and secondary sealings of the outlet connector.

Nevertheless, the convective heat transfer condition at the connector has a cooling effect on the contact area between absorber and sealing. The maximum temperature at this contact surface was observed with 216.5 °C. Fig. 11 shows the temperature distribution within the sealing (undeformed state). On the one hand, the sealings help to reduce thermal bridges from absorber to the ambient by their low thermal conductivity, which is beneficial for the collector efficiency. On the other hand, the sealing temperatures are high consequently. The minimum sealing temperature during stagnation was observed with 185.5 °C and the average temperature with 201.6 °C. As the extreme case of stagnation occurs in the event of a system failure, it is difficult to estimate for how long these temperatures will prevail in the collector. This depends for example on how fast the failure of pumps can be resolved, whether there are clouds during the day or whether there is precipitation. The temperature will also change depending on the solar azimuth and zenith angle. Nevertheless, we expect this extreme temperature may prevail in an unfavorable case for up to 6 to 8 hours on 2 or 3 consecutive days.

The sealing material was designed to withstand constant temperatures up to 130 °C. It can withstand higher temperatures for short-term loads but a definite criterion of failure at temperatures exceeding 130 °C are not given by the manufacturer. At those high temperatures, some ingredients of the sealing may degrade and cause changes to the sealing's thermo-mechanical properties. High-temperature stabilizers will decompose gradually which leads to an increase of the stiffness of the materials. Therefore, the sealings have a reduced ability to compensate for deformations which may lead to leakages. The longer, the material is exposed to excessively high temperatures, the more its flexibility will be reduced and the more likely it is that leakages will occur. The exact time when a leak will occur, is not quantifiable as it depends on a variety of parameters with high degrees of uncertainty such as imperfections during the application of the sealing or unfavorable previous load conditions that are unknown. As a result, there remains a threat for the efficiency of the IGFPCs when it is exposed for too long in the stagnation condition. In contrast, the mechanical stability of the secondary sealing which is required for a reliable operation of the collectors should not be affected by the temperature loads.

The results of the mechanical analysis are shown in Fig. 12. Deformation is magnified by a factor of 6 to visualize the direction in which the components move. As expected, the fixation of the absorber at the two connectors leads to a bending load on the absorber and the sealings. The maximum deformation (displacement) occurred at the absorber edge furthest away from the symmetry plane and was 4.3 mm. This part is not displayed as it has no effect on the sealings. The total deformation of the sealings is significantly smaller.

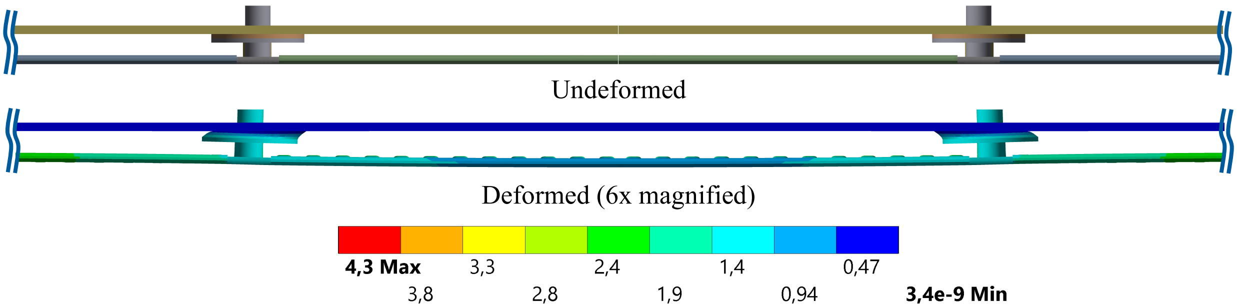

Fig. 12: Comparison of undeformed and deformed (in mm) collector geometry from the top view. The outer left and outer right part of the geometry is not displayed.

In Fig. 13 and Fig. 14 the deformation and mechanical strain of the sealings is shown. For the stagnation case, maximum deformation is 1.4 mm and the corresponding strain 0.501 mm/mm. Using eq. 2, the maximum stress for the secondary sealing was determined as 0.659 MPa. The maximum strains occur at the side facing away from the symmetry plane. For the primary sealing it is 0.439 mm/mm and occurs sparsely in a small region. The average strain is 0.241 mm/mm. For the secondary sealing, the average strain is 0.236 mm/mm and the maximum 0.501 mm/mm.

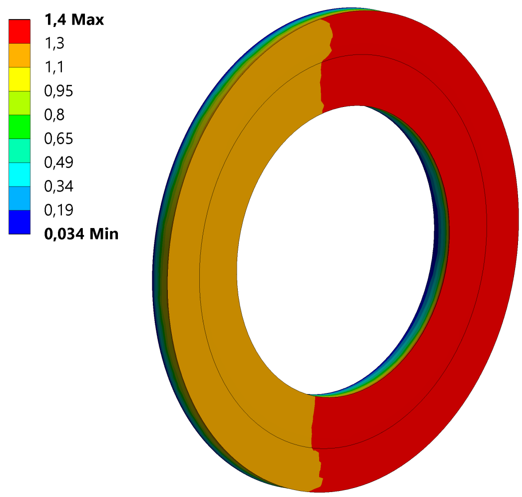

Fig. 13: Deformation (in mm) of the primary and secondary sealings of the inlet/outlet connector.

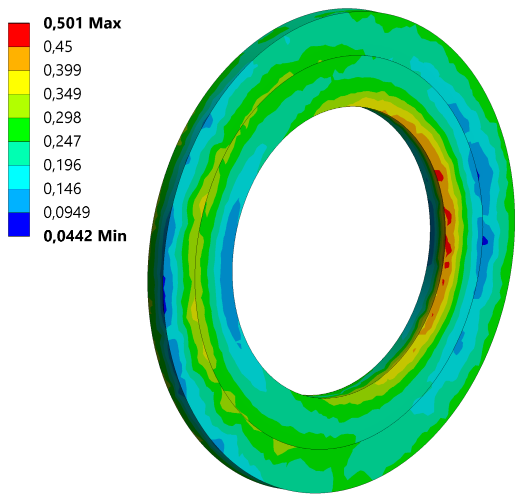

Fig. 14: Strain (in mm/mm) of the primary and secondary sealings of the inlet/outlet connector.

The difference between maximum and average values as well as the sparse presence of peak values within a small part of the sealing indicate, that the sealings may cope with the extreme load conditions for a short period of time.

According to experience from the manufacturer, the maximum strain that the sealings can withstand is approximately 20 % for continuous and 30 % for short term load. Hence, the case of stagnation can be considered as critical (both in terms of temperature and strain) for the lifetime of the sealings. This does affect the efficiency of the modules (gas-tightness) but not its basic functionality (mechanical integrity).

3.2.2 Case 2 – Full-year Load Condition and Parametric Study

To determine the load conditions on the sealings for normal operation during a year, a parametric study was performed for different absorber temperature levels T_{out} ranging from 20 °C to 200 °C. The resulting sealing temperatures, strains, and stress (secondary sealing only) are shown in Tab. 3.

Tab. 3: Simulation results (maximum values) from the parametric study for different absorber temperature levels.

T_{out} °C	T_{pri} °C	T_{sec} °C	ε_{pri} mm/mm	ε_{sec} mm/mm	σ_{sec} MPa
20.0	20.0	20.0	0.004	0.004	0.007
30.0	29.1	29.1	0.017	0.019	0.032
45.0	42.7	42.7	0.045	0.051	0.084
60.0	56.3	56.4	0.075	0.084	0.134
80.0	74.5	74.6	0.119	0.128	0.202
100.0	92.6	92.8	0.162	0.175	0.268
130.0	119.9	120.1	0.227	0.245	0.361
150.0	138.0	138.3	0.269	0.293	0.422
200.0	183.4	183.7	0.370	0.413	0.565

This data was then used to map absorber temperatures to resulting strains in the sealings using linear interpolation (between values listed in Tab. 3) and extrapolation (values below 20 °C). The assembly temperature of the collector was assumed as 20 °C and therefore the stresses and strains that occur for this temperature are numerical noise. For those lower temperatures T_{out}^{-}< 20 °C, the relation $T_{out} = |T_{out}^{-} - 20| + 20$ was used to map temperatures to the strains. In this way, a full-year load curve on the sealings was calculated. These load curves are shown in Fig. 15 and Fig. 16. The figures show that the strains for primary and secondary sealings are well within the limits (0.30 mm/mm for primary and 0.20 for secondary sealing) that the manufacturer of the material defines as the permissible range of application.

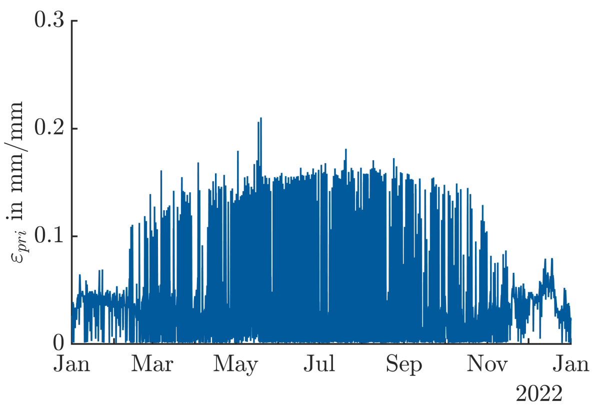

Fig. 15: Time course of the strains (simulated) in the primary sealing for the measured collector temperature loads.

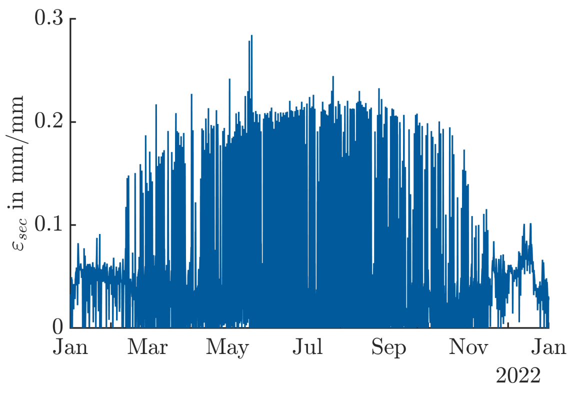

Fig. 16: Time course of the strains (simulated) in the secondary sealing for the measured collector temperature loads.

4. Conclusions

The results of this study have shown, that during stagnation, the thermo-mechanical loads are a critical aspect for the sealings of the insulating glass collector design. This extreme load may affect the efficiency of the modules (gas-tightness) but not its basic functionality (mechanical integrity), which is why the chosen novel design of the collector represents an improvement with respect to collector durability. This advantageous effect was confirmed by results from the loads during normal operation. In that case, the sealing strains and stresses remained within the proposed permissible operating range despite a presumed overestimation of temperatures caused by a series of conservative assumptions. This strongly suggests that the design is durable for its intended use and insulating glass collectors can remain gas-tight for a lifetime of 20 to 25 years. The mechanical results furthermore indicate that absorber deflections are much less critical as compared to previous designs from Riess et al. confirming that the novel design is superior. Finally, we strongly suggest avoiding stagnation for insulating glass collectors by suitable measures such as applying thermochromic coatings to the absorber or emergency generators/batteries with pumps to protect the sealings from overheating. This will help to avoid potential leakages affecting the performance and therefore techno-economic feasibility of the solar thermal system.

Acknowledgments

This work was supported by the Federal Ministry of Economic Affairs and Climate Action of the Federal Republic of Germany within the 7th Energy Research Program under the project “flexLAC” [03ETW015-A].

References

ANSYS, Inc., 2022. ANSYS Mechanical 2022 R2. Software build date: Friday, 27.05.2022 08:55:00, Canonsburg.

Deutsches Institut für Normung, 2010. DIN EN 1991-1-4, Eurocode 1: Einwirkungen auf Tragwerke - Teil 1-4: Allgemeine Einwirkungen - Windlasten. Eurocode 1: Actions on structures - Part 1-4: General actions - Wind actionsloads. Beuth Verlag GmbH, Berlin. Accessed 28 August 2023, 2, 41, 38 Seiten.

Deutsches Institut für Normung, 2023. DIN EN 1991-1-3, Eurocode 1: Einwirkungen auf Tragwerke. Teil 1-3, Allgemeine Einwirkungen - Schneelasten. Eurocode 1: actions on structures. Part 1-3, General actions - snow loads, 1991st ed. ‚Beuth Verlag GmbH, Berlin. Accessed 28 August 2023, 2, 41, 38 Seiten.

Deutsches Institut für Normung e. V., 2018. Solarenergie - Thermische Sonnenkollektoren - Prüfverfahren (ISO 9806:2017); Deutsche Fassung EN ISO 9806:2017. Beuth Verlag GmbH, Berlin.

Giovannetti, F., Kirchner, M., 2015. Performance and Reliability of Insulated Glass Collector Prototypes, in: Proceedings of the EuroSun 2014 Conference, Freiburg, Germany, pp. 355–361. DOI: 10.18086/eurosun.2014.16.07.

Giovannetti, F., Kirchner, M., Kliem, F., Hoeltje, T., 2014. Development of an Insulated Glass Solar Thermal Collector. Energy Procedia 48, 58–66. DOI: 10.1016/j.egypro.2014.02.008.

Leibbrandt, P., Schabbach, T., 2015. Numerical Investigation on Heat Transfer, Fluid Distribution and Solid Stress to a New Type of Solar Flat Plate Collector, in: Proceedings of the EuroSun 2014 Conference, Freiburg, Germany, pp. 1–10. DOI: 10.18086/eurosun.2014.16.13.

Mooney, M., 1940. A Theory of Large Elastic Deformation. Journal of Applied Physics 11 (9), 582–592. DOI: 10.1063/1.1712836.

Riess, H., 2017. Simulation, testing and design of a fully adhesive bonded flat plate solar collector for highly automated production. Ph.D. Thesis. De Montfort University Leicester. https://dora.dmu.ac.uk/bitstream/handle/2086/15041/e-thesis%20submission%20Hermann%20Riess.pdf.

Riess, H., Brandmayr, S., Zörner, W., 2015. A Novel Production Technique for Flat Plate Solar Collectors with a Fully Adhesive Edge Bond, in: Proceedings of the EuroSun 2014 Conference, Freiburg, Germany, pp. 1–9. DOI: 10.18086/eurosun.2014.16.19.

Riess, H., Brandmayr, S., Zörner, W., Greenough, R.M., 2014. Analysis of the Mechanical Behaviour of an All-round Fully Adhesive Supported Absorber. Energy Procedia 48, 201–211. DOI: 10.1016/j.egypro.2014.02.025.

Riess, H., Klärner, M., Zörner, W., Greenough, R., 2016. Thermal Simulation and Efficiency of a Hermetically Sealed Flat Plate Collector with a Fully Adhesive Edge Bond, in: Proceedings of the ISES EuroSun 2016 Conference, Freiburg, Germany, pp. 1100–1113. DOI: 10.18086/eurosun.2016.07.07.

Rivlin, R.S., 1948. Large elastic deformations of isotropic materials IV. further developments of the general theory. Phil. Trans. R. Soc. Lond. A 241 (835), 379–397. DOI: 10.1098/rsta.1948.0024.

Summ, T., Ehrenwirth, M., Trinkl, C., Zörner, W., 2020. Entwicklung eines Großflächenkollektors in Isolierglasbauweise für den Einsatz in Wärmenetzen, in: Online-Symposium Solarthermie und innovative Wärmesysteme. Tagungsunterlagen, pp. 435–448.

Summ, T., Ehrenwirth, M., Trinkl, C., Zörner, W., Pischow, K., Greenough, R., Oyinlola, M., 2023. Effect of argon concentration on thermal efficiency of gas-filled insulating glass flat-plate collectors. Applied Thermal Engineering, 120657. DOI: 10.1016/j.applthermaleng.2023.120657.

Summ, T., Scherer, C., Ehrenwirth, M., Trinkl, C., Zörner, W., 2021. Messtechnische Untersuchung von Kleinmustern eines Isolierglaskollektors anhand von Temperaturbelastungstests, in: Tagungsunterlagen. Online-Symposium Solarthermie und innovative Wärmesysteme. Tagungsunterlagen. Conexio GmbH, Pforzheim, pp. 401–408.

ANNUAL COOLING PERFORMANC PREDICTION OF AN ADSORPTION CHILLER APPLIED SYSTEM BASED ON A NUMERICAL MODEL

Fang He[1], Hong Z. Liu[1], Katsunori Nagano[1] and Junya Togawa[2]

[1] Hokkaido University, Sapporo (Japan)

[2] Nihon Netsugen System, Tokyo (Japan)

Abstract

This study focuses on the annual cooling performance prediction of the Adsorption Chiller (AC). A three-dimensional numerical calculation program was built in our previous study for the parameter analysis of the AC, and the results were applied to develop an approximate function of COP and SCP, thus the performance calculation period of the AC can be reduced obviously and the annual prediction based on the continuous temperature condition was available. Then this approximate function was employed to describe the performance of the AC, which provide cooling capacity for a system numerical model. The real cooling load data of a building and the climate data from March 2022 to February 2023 were applied. This model was proved to work well for the annual cooling performance prediction. Moreover, the performance of this AC was evaluated for its practical application.

Keywords: Adsorption Chiller (AC), Annual cooling performance prediction, Numerical model

1. Introduction

With the development of the global economic, the thermal comfort requirement has increased in the development countries (Pan Q.W. and Wang R.Z., 2018). The traditional compression-type air conditioners market booming is expected, however, problems such as CO_2 emissions and ozone layer depletion need to be addressed (Lu Z.S. and Wang R.Z., 2013). The adsorption chiller (AC), which is one of the thermally driven heat pumps, is considered an attractive solution. An AC can provide cooling capacity by the low-grade heat sources from 60 to 80 ◦C (Sapienza A. et al., 2011), e.g., factory exhaust or hot water from a solar water heater (Akahira A. et al., 2004)(Pan Q.W. and Wang R.Z., 2017) (Sapienza A. et al., 2011). AC is an environmentally friendly technology for its natural refrigerants such as water and ammonia. However, some disadvantages of AC hamper its popularization. The coefficient of performance (COP) is near 0.5 (J. Romero R. et al., 2001)(Jung-Yang San and Tsai Fu-Kang, 2014), which is lower than other types of thermally driven ACs (J. Romero R. et al., 2001)(Manu S. and Chandrashekar T.K., 2016)(Srikhirin P. et al., 2001). The initial cost of the AC is expensive due to its exorbitant adsorbent material (He F. et al., 2022). In addition, the more compact entire AC body is necessary. These disadvantages result in popularization barrier of AC.

In order to overcome these disadvantages mentioned above, a kind of composite material, which called Wakkanai Siliceous Shale (WSS) impregnated with 20 wt. % of LiCl, was proposed by our team (Nakabayashi S. et al., 2011). Several experiments applied this composite material as adsorbent have been conducted to investigate the cooling performance of composite material AC (He F. et al., 2022) (Liu H. et al., 2011)(Togawa J. et al., 2020). It was proved to be a competitive adsorbent material compared with other adsorbent due to its relatively high performance and acceptable price (He F. et al., 2020)(Togawa J. et al., 2020). Then the numerical model has been built for the performance prediction of the AC (He F. et al., 2023)(Seol S.H. et al., 2020). On the other hand, the annual performance prediction of AC system by the numerical model is unavailable due to its large amount of calculation time. The performance prediction speed at each condition need improvement.

In this study, author propose approximate functions to achieve the fast calculation of AC cooling performance.

10.18086/swc.2023.04.04 Available at http://proceedings.ises.org

The numerical model built in our previous study is applied to calculate several representative COP and Specific Cooling Power (SCP)(He F. et al., 2023). The approximately functions are fitted based on the representative of COP and SCP and proved to be creditable. Then a model of AC system, in which the AC is employed to provide cooling capacity, is established for the annual cooling performance prediction. A municipal government office building of Japan is chosen as the target building. The annual cooling load of this building in period from March 2022 to February 2023 is picked up and introduced to this AC system. The area of the solar collector, hot water volume coefficient and the adsorbent weight are evaluated for the optimization as the parameters, and the cover rate and payback year are introduced as the evaluation indices. The results indicate the possibility of using AC to provide cooling capacity, and the minimum payback years in different cover rates are calculated.

2. Methodology

2.1. AC system

In this study, a numerical model was built for the annual cooling performance prediction, as shown in **Fig.1**. The AC system consists of the AC, the solar collector with the hot water tank, and the cooling tower. The target building annual cooling load of a prediction period is introduced to the AC system to determine the cooling capacity. The annual climate data of the same period is download from the weather bureau home page. Based on the annual radiation data, temperature of the hot water boiled by the solar collector can be calculated. The produced hot water is stored in the hot water tank and applied as the regeneration hot water of the AC. Meanwhile the temperature of the cooling water produced by the cooling water is calculated based on the annual temperature and humidity. The cooling water is flowed into the AC for the sorption and condensation process. According to the temperature of the hot water, cooling water and the cooling load, cycle period of the AC is controlled to increase COP while the enough cooling capacity is provided. In addition, the compress type air-conditioner is employed to provide extra cooling capacity while AC can't cover all the cooling load.

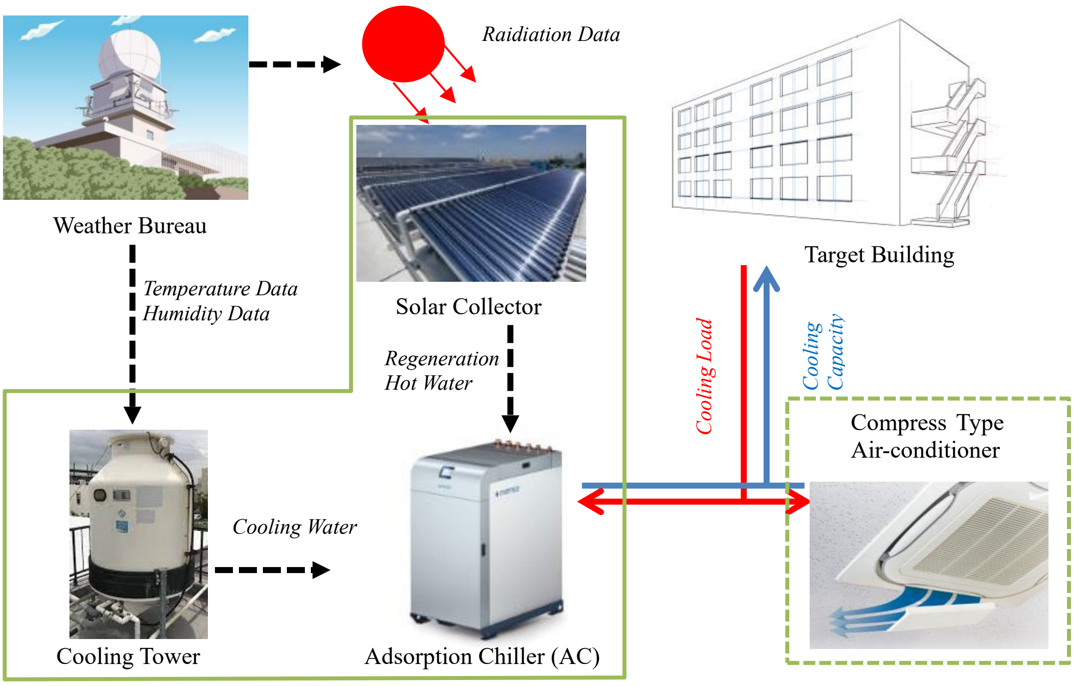

Fig. 1: Schematic of the AC system

2.2. Target building and prediction period

Target building is a municipal government office building, which is in Kamizaki City, Fukuoka province, Japan. The prediction period is from March 2022 to February 2023. The cooling load is recorded every minute, it is exchanged and expressed every hour, as shown in **Fig.2**.

The location of the target building is on south of Japan, which is humid subtropical climate. The cooling load

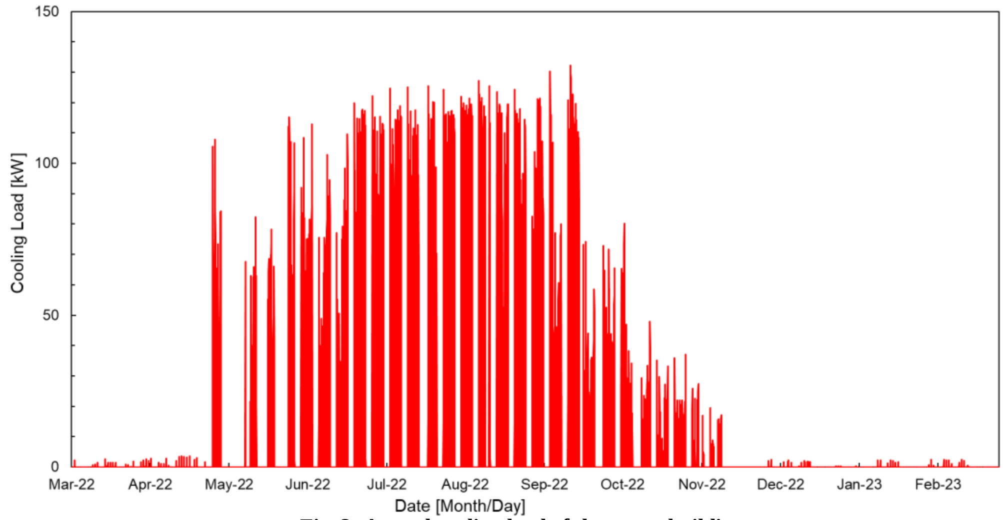

Fig. 2: Annual cooling load of the target building

can be clearly observed from end of April to middle of October. The highest cooling load approach 130 kW, however, the cooling load is generally up to 120 kW. It influences the designing of the AC capacity.

2.3. Numerical model

2.3.1. Performance functions of AC

Then approximate functions of AC performance are established. The 3-dimensional numerical model built in our previous study is employed to determine the representative COP and SCP (He F. et al., 2023). The calculation conditions are shown in **Tab.1**. In this study, AC is only used for the space cooling, hence the evaporation temperature is set at constant 15 °C instead of the dehumidification temperature 7 °C.

Tab. 1: Calculation conditions for the representative COP and SCP

	Regeneration Temperature [°C]	Sorption/Condensation Temperature [°C]	Evaporation Temperature [°C]	Cycle Period [min]
Range	55-80	25-40	15	2-30
Interval	5	5	Constant	2

$$Q_{\mathrm{c}} = (\boldsymbol{a}_1 \times T_{\mathrm{reg}} + \boldsymbol{a}_2 \times {T_{\mathrm{sor}}}^{\boldsymbol{a}_3}) \times \arctan(\boldsymbol{a}_4 \times t_{\mathrm{cyc}}) \quad \text{(eq. 1)}$$

$$Q_{\mathrm{reg}} = (\boldsymbol{b}_1 \times T_{\mathrm{reg}} + \boldsymbol{b}_2 \times {T_{\mathrm{sor}}}^{\boldsymbol{b}_3}) \times \arctan\left(\boldsymbol{b}_4 \times t_{\mathrm{cyc}}\right) + \boldsymbol{b}_5(T_{\mathrm{reg}} - T_{\mathrm{sor}}) \times H_{\mathrm{sensible}} \quad \text{(eq. 2)}$$

Tab. 2: Parameters of the approximate functions

	1	2	3	4	5
a	4.831×10	-7.080	1.640	2.360×10^{-2}	-
b	7.492×10	-1.674×10	1.524	2.184×10^{-2}	4.367×10^{-1}

Based on the calculation results, the approximate functions are fitted, as shown in **eq.(1)** and **(2)**. The parameters of the approximate functions are listed in **Tab.2**. Then the accumulated cooling/regeneration amounts of the calculation results and the approximate functions prediction are shown in **Fig.3**. The line is the approximate functions and the cycle mark is the calculation results. The approximate functions fit the

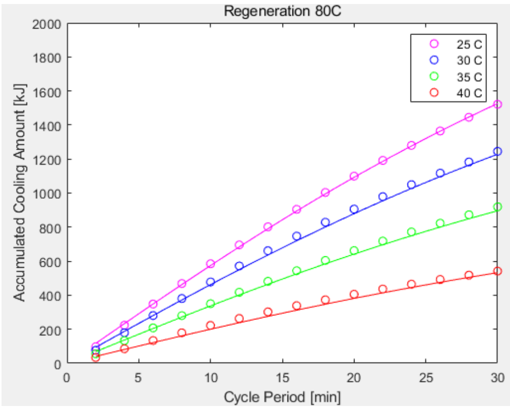

(a): Accumualted cooling amount at regeneration temperature of 80℃

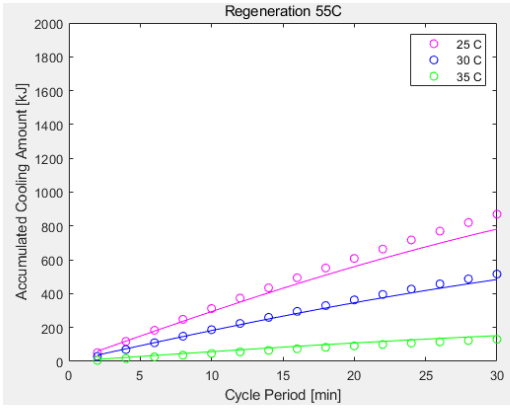

(b): Accumualted cooling amount at regeneration temperature of 55℃

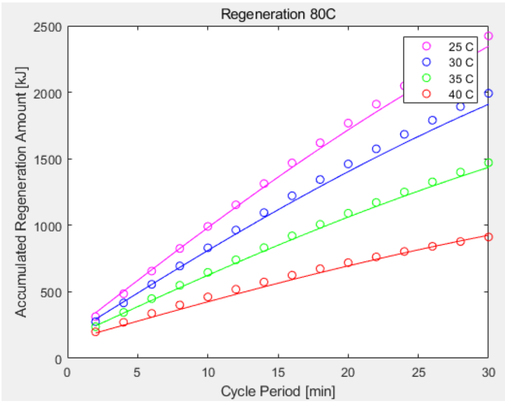

(c): Accumualted regeneration amount at regeneration temperature of 80℃

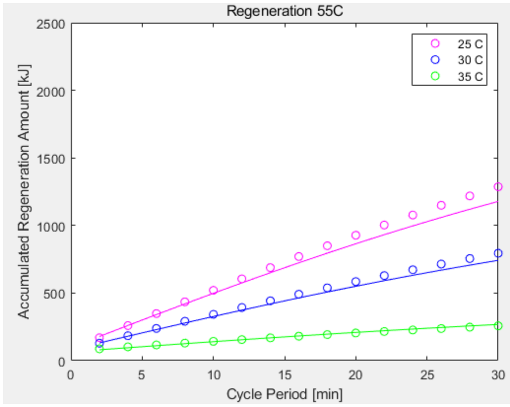

(d): Accumualted regeneration amount at regeneration temperature of 55℃

Fig. 3: Comparison of the calculated results and the approximate functions prediction

calculation results well at regeneration temperature of 80 ℃ for both of the accumulated cooling/regeneration amount. For the cases that the regeneration temperature is 55 ℃, the error between the approximate functions and the calculated results occurred while the cooling temperature decrease to 25 ℃. In this study, the AC system is mainly used in summer, thus this part of error is considered to be acceptable and this approximate function fit the calculation results very well in all the field.

2.3.2. Annual climate data

The annual climate data during March 2022 to February 2023 is down from the home page of the weather bureau. The annual dry bulb temperature and the annual solar radiation are shown in **Fig.4.(a)** and **Fig.4.(b)**, respectively.

2.3.3. Solar collector and cooling tower

The solar collector is applied to produce the hot water. The hot water temperature can be expressed by **eq.(3)**. According to the solar radiation data of **Fig.4.(b)** in section 2.3.2, the hot water can be heated in the solar collector, as the first part on the right side of the equation shows. Meanwhile, the heat loss between the boiled water and the ambient environment is expressed by the second part on the right side of the equation. The boiled water is stored in the hot water tank, the heat loss between the hot water tank and the ambient environment is determined as the third part on the right side of the equation. In addition, the fourth part is the regeneration capacity. In addition, the hot water temperature is limited to lower than 90 ℃ to avoid boiling.

$$c_{\mathrm{w}}\frac{dT_{\mathrm{w}}}{dt} = \eta A_{\mathrm{SC}}E - F_{\mathrm{L}}A_{\mathrm{SC}}(T_{\mathrm{w}} - T_{\mathrm{drybulb}}) - 6.48(T_{\mathrm{w}} - T_{\mathrm{drybulb}})V_{\mathrm{w}} - \dot{Q}_{\mathrm{reg}} \qquad \text{(eq. 3)}$$

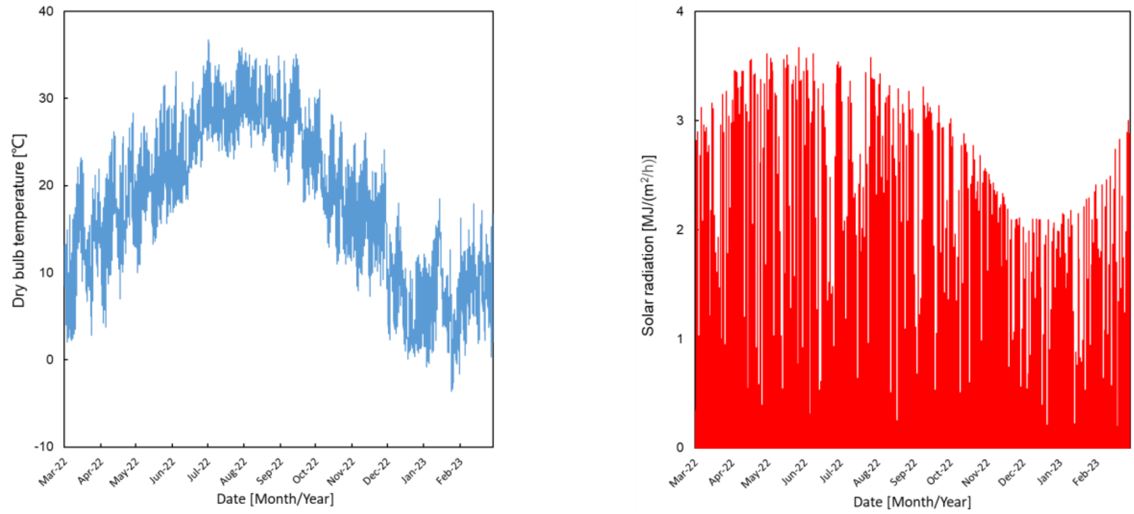

(a): Annual dry bulb temperature (b): Annual solar radiation

Fig. 4: Annual climate data

$$en_{\text{drybulb}} = 1.006 \times T_{\text{drybulb}} + (1.805 \times T_{\text{drybulb}} + 2501) \times RH \quad \text{(eq. 4)}$$

$$en_{\text{wetbulb}} = 1.006 \times T_{\text{wetbulb}} + (1.805 \times T_{\text{wetbulb}} + 2501) \times RH \quad \text{(eq. 5)}$$

$$C = en_{\text{drybulb}} - en_{\text{wetbulb}} - (\frac{T_{\text{drybulb}}}{1000} - RH) \times 4.2 \times T_{\text{wetbulb}} \quad \text{(eq. 6)}$$

$$T_{\text{ct-out}} = T_{\text{sor-out}} - (0.648 \times T_{\text{sor-out}} - 0.439 \times T_{\text{wetbulb}} + 0.316 \times C - 10.142) - (0.648 \times T_{\text{sor-out}} - 0.439 \times T_{\text{wetbulb}} + 0.316 \times C - 10.142) \times 0.39 \times \rho_{\text{w}} \times \dot{m} \quad \text{(eq. 7)}$$

Based on the annual climate data of the dry bulb temperature, the wet bulb temperature and the relative humidity, the temperature from the cooling tower is calculated by **eq.(4)-(7)**.

2.4. Evaluation indices

In this study, coefficient of performance (COP) and specific cooling power (SCP) are applied to investigate the cooling performance of the AC. Based on the approximate function predictions of **eq.(1)** and **eq.(2)**, COP and SCP can be expressed by **eq.(8)**. and **eq.(9)**.

$$\text{COP} = \frac{Q_{\text{c}}}{Q_{\text{reg}}} \quad \text{(eq. 8)}$$

$$\text{SCP} = \frac{Q_{\text{c}}}{m_{\text{adsorbent}} t_{\text{cyc}}} \quad \text{(eq. 9)}$$

In this study, the cover rate (*CR*) and the payback year are introduced to evaluate the practicality of this AC system. The cover rate is calculated by **eq.(10)**, which is the ratio of the annual average cooling capacity provided by AC system versus the annual average cooling load of target building. High cover rate indicates sufficient cooling capacity.

$$CR = \frac{Q_{\text{annual average cooling capacity}}}{Q_{\text{annual average cooling load}}} \quad \text{(eq. 10)}$$

Payback year (PY) is determined by **eq.(11)**. $Cost_{ac,in}$ is the initial cost of the AC and $Cost_{com,in}$ is the initial cost of the compress type air-conditioner, their calculation equations are **eq.(13)** and **eq.(14)**, respectively. The electricity reduction is calculated by **eq.(15)**. Thus, the initial cost and running cost of the AC system are compared with those of the compress type air-conditioner to calculate the payback year. In addition, the introduction grant from the government can be expected due to the renewable energy application. The payback year with the 2/3 of grant is expressed by **eq.(12)**. All the coefficients noticed in **eqs.(11)-(15)** are listed in **Tab.3**.

$$PY = \frac{Cost_{\mathrm{ac,ini}} - Cost_{\mathrm{com,ini}}}{Electricity\ Reduction \times (Price_{\mathrm{ele}} + Emission_{\mathrm{co2}} \times Price_{\mathrm{co2}})} \quad \text{(eq. 11)}$$

$$PY_{\mathrm{Grant}} = \frac{Cost_{\mathrm{ac,ini}} + Cost_{\mathrm{SC}} + Cost_{\mathrm{HT}} \times (1 - \frac{2}{3}) - Cost_{\mathrm{com,ini}}}{Electricity\ Reduction \times (Price_{\mathrm{ele}} + Emission_{\mathrm{co2}} \times Price_{\mathrm{co2}})} \quad \text{(eq. 12)}$$

$$Cost_{\mathrm{ac,in}} = m_{\mathrm{adsorbent}} \times \mathrm{SCP_{max}} \times Coe_{\mathrm{AC}} + A_{\mathrm{SC}} \times Coe_{\mathrm{SC}} + A_{\mathrm{SC}} \times Coe_{\mathrm{Vol}} \times Coe_{\mathrm{HT}} \quad \text{(eq. 13)}$$

$$Cost_{\mathrm{com,in}} = m_{\mathrm{adsorbent}} \times \mathrm{SCP_{max}} \times Coe_{\mathrm{com}} \quad \text{(eq. 14)}$$

$$Electricity\ Reduction = \frac{Accumulated\ annual\ cooling\ capacity}{\mathrm{COP_{com}}} \quad \text{(eq. 15)}$$

Tab. 3: Coefficients of indice

Coe_{AC} [JPY/kW]	Coe_{SC} [JPY/m^2]	Coe_{HT} [JPY/L]	Coe_{com} [JPY/kW]	$Price_{ele}$ [JPY/kWh]	$Price_{co2}$ [JPY/kg]	$Emission_{co2}$ [kg/kWh]	COP_{com} [-]
182500	15000	400	50000	43.14	8.263	0.299	3.5

3. Results and discussion

3.1. Annual performance prediction

The cooling performance and the payback year of the AC system compared with the compress type air-conditioners are influenced by the adsorbent weight, the solar collector area and the hot water tank volume coefficient. Firstly, they are fixed as shown in **Tab.4.**

Tab. 4: Coefficients of indice

Parameter	$m_{adsorbent}$ [kg]	Coe_{Vol} [L/m^2]	A_{SC} [m^2]
Volume	240	100	1200

The results of annual performance prediction are shown in **Fig.5**. The annual cooling load/capacity are shown in **Fig.5.(a)**. Most of the cooling load can be covered by the cooling capacity in May, October and November. However, the cooling capacity provided by the AC system is obviously insufficient during the summer. The annual regeneration and sorption temperature are shown in **Fig.5.(b)**. The annual cooling temperature transient is as regular as the annual dry bulb temperature transient is shown in **Fig.4.(a)**. The regeneration temperature is down to 50 ℃ for several times at the same period the cooling capacity can’t cover the cooling load. It indicates the insufficiency of the solar collector area and the hot water tank volume. The accumulated cooling load and capacity per month are summarized in **Fig.5.(c)**. Obviously, the monthly cooling capacities can’t cover the cooling load from June to September. Annual COP and SCP transients are shown in **Fig.5.(d)**. Annual COP is kept around 0.65 generally and decreased to 0.4 sometimes, meanwhile annual SCP is changed from 0.05 kW/kg – 0.45 kW/kg. In this case, the CR of this case is 85.89 % based on the data of **Fig.5.(c)**. The payback year PY and PY_{grant} are 104.7 years and 34.9 years, respectively. Annual electricity consumption amount of 17420.2 kWh, which equivalent 7.58 ton of CO_2 emissions. The AC system is proved to be effective

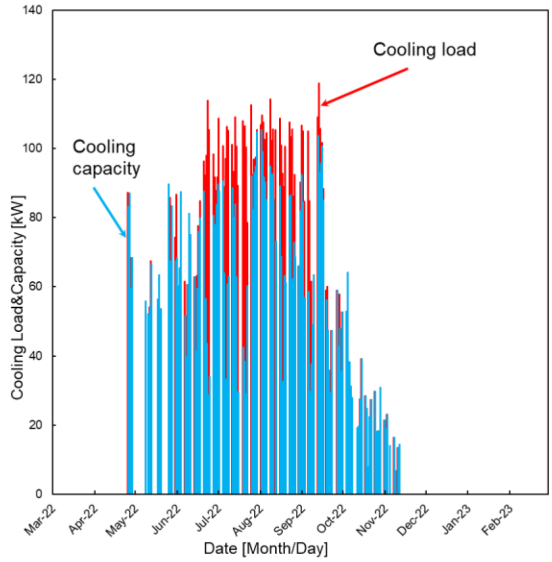

(a): Annual cooling load/capacity

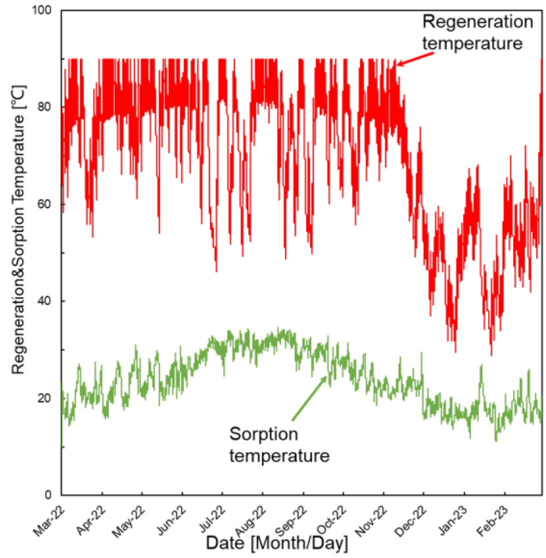

(b): Annual regeneration/sorption temperature

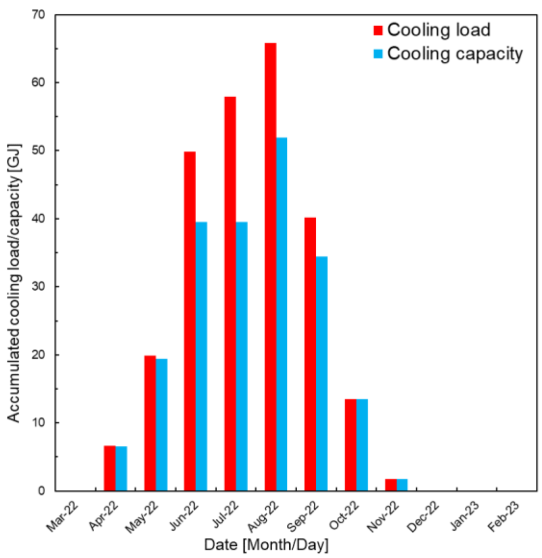

(b): Accumulated cooling load/capacity

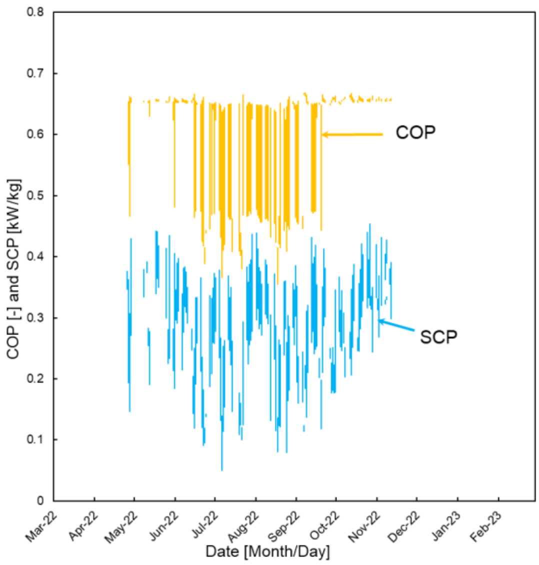

(d): Annual COP and SCP

Fig. 5: Annual climate data

to reduce the electricity consumption and CO_2 emissions.

This entire annual cooling performance prediction need about 40 second to calculate. It is much faster compared with the previous 3-dimentional model, which takes more than 1 hour for a set of temperature and cycle period conditions.

3.2. Parameter study

3.2.1. Adsorbent

The adsorbent weight of the AC is studied to evaluate the cooling performance of the AC system. Coe_{Vol} and A_{SC} are fix as shown in **Tab.4**, meanwhile $m_{\mathrm{adsorbent}}$ is changed from 20 kg to 480 kg at interval of 20 kg.

The prediction results are shown in **Fig.6(a)**. With the increase of the adsorbent weight, the cover rate shows a quick increasing up to 98.34 %. The more adsorbent applied in the AC, the bigger capacity can be provided by the AC to cover the cooling load. The *PY* is reduced to 100.0 years while the adsorbent weight increases to 280 kg, meanwhile the PY_{grant} is reduced to 33.3 years. Then the *PY* is stable around 100 years and the PY_{grant} is stable around 35 years. **Fig.6(a)** express the annual average COP and SCP. COP increase and became stable while the $m_{\mathrm{adsorbent}}$ increase up to 260 kg, meanwhile SCP decrease to less than 0.3 kW/kg. Obviously, too little

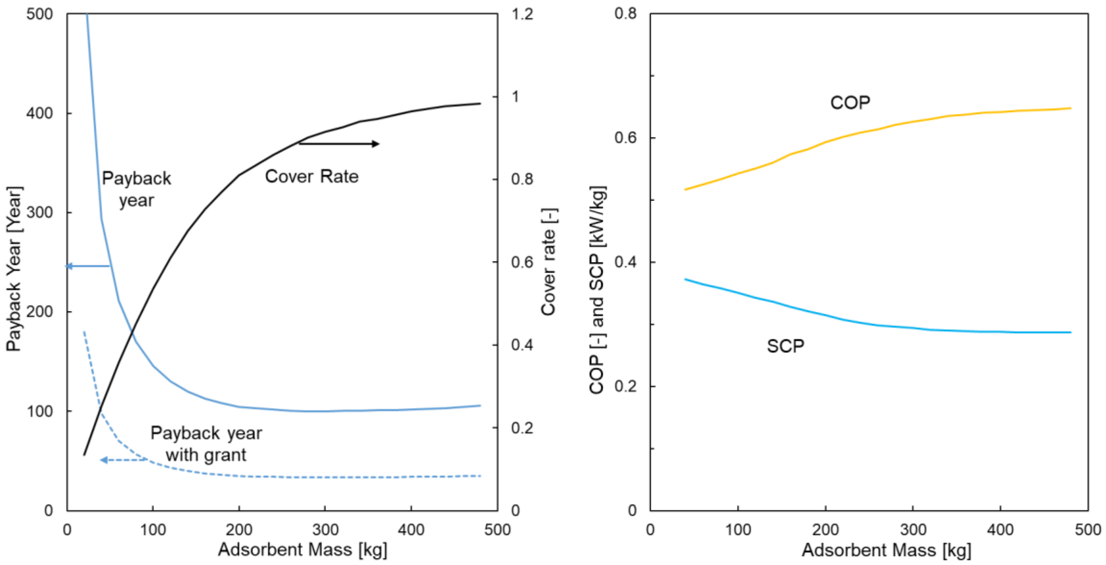

(a): Payback year and cover rate
(b): Annual average COP and SCP

Fig. 6: Prediction results versus the adsorbent weight

adsorbent can't provide enough cooling capacity, at least 280 kg of adsorbent is necessary to improve CR and reduce payback year.

3.2.2. Hot water tank volume coefficient

The boiled hot water needs to be stored into the hot water tank. The larger hot water tank contributes to keep AC at a high regeneration temperature to provide high cooling performance. The volume of the hot water tank relative to the solar collector area, the Coe_{Vol} is changed from 20 L/m^2 to 200 L/m^2 at interval of 20 L/m^2. The $m_{\mathrm{adsorbent}}$ and the A_{SC} are fix as shown in **Tab.4**.

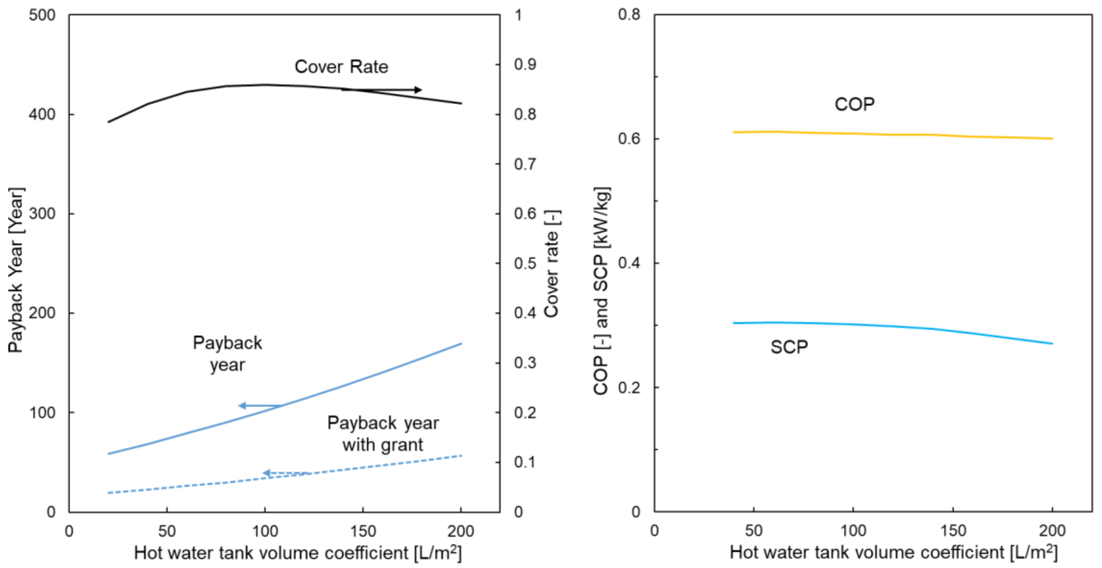

(a): Payback year and cover rate
(b): Annual average COP and SCP

Fig. 7: Prediction results versus the adsorbent weight

As shown in **Fig.7(a)**. The CR is stable from 80 % - 85 % with slight fluctuation, it indicates that CR is unsensitive to the Coe_{Vol}. However, PY and PY_{grant} are increase with the increasing of the Coe_{Vol}. Obviously, small is a smart strategy to reduce the cost while a relatively high CR is kept. The highest CR of 85.89 % can be obtained while Coe_{Vol} of 100 L/m^2 is taken, meanwhile PY and PY_{grant} are 101.9 years and 34.0 years, respectively.

The annual average COP and SCP are shown in **Fig.7(b)**. Mildly decrease of both COP and SCP can be observed with the Coe_{Vol} grow larger than 100 L/m^2. The excess hot water tank volume results in larger heat loss that can't be covered by the solar collector. For the case that Coe_{Vol} is 100 L/m^2, COP and SCP are 0.61 and 0.3 kW/kg, respectively.

3.2.3. Solar collector area

Then the solar collector area A_{SC} is change from 50 m^2 to 2400 m^2 at interval of 50 m^2 while $m_{adsorbent}$ and the Coe_{Vol} is fix as shown in **Tab.4**. The prediction results are shown in **Fig.8**.

CR improve rapid and over 80 % while with the A_{SC} increase up to 850 m^2, then *CR* approaches 92 % slowly. The *PY* and PY_{grant} are reduced down to 68.0 years and 22.7 years respectively while the A_{SC} is 500 m^2. The insufficiency of the solar collector area leads to this result. Both *PY* and PY_{grant} start to rebound for the cases that A_{SC} is bigger 500 m^2. Thus, more than 500 m^2 is necessary in this study.

As shown in **Fig.8(b)**, the annual average SCP keep mildly increasing with the A_{SC} increasing. The larger A_{SC} contributes larger heat capacity for the regeneration heat to increase the annual average SCP, especially in cases that the heat load is extremely high to drop the temperature of the stored hot water. On the other hand, the annual average COP is almost constant around 0.6.

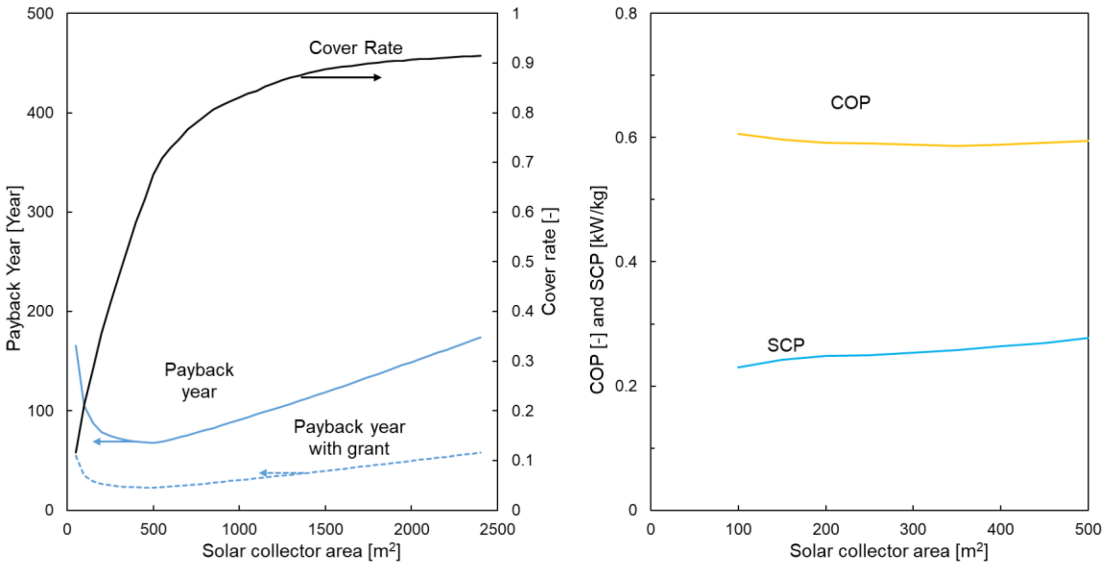

(a): Payback year and cover rate **(b): Annual average COP and SCP**

Fig. 8: Prediction results versus the adsorbent weight

3.4. System optimization

All the parameters of A_{SC}, $m_{adsorbent}$ and Coe_{Vol} are optimized in this section.

The ranges of the A_{SC}, $m_{adsorbent}$ and Coe_{Vol} are set as they're changed in the sections above to to obtain the shortest payback year with grant. In addition, the lowest *CRs* are limited as the extra conditions. The results are shown in **Tab.5**.

Without the limitation of *CR*, the smallest PY_{grant} of 7.6 years and *PY* of 54.1 years are achieved, relatively. It is an acceptable period for the commercial produce. Though *CR* of AC system is only 50.05 %, the AC system can be combined with other air-conditioner to provide sufficient cooling capacity for the factory and office building due to their large cooling capacity requirement. A_{SC} and $m_{adsorbent}$ are 250 m^2 300 kg respectively, it contributes compaction of the AC system. The 20 L/m^2 of Coe_{Vol} proved that the large hot water tank volume is not necessary.

On the other hand, only one domestic air-conditioner is introduced for every family, thus the lower limitation of *CR* is 80 %. While A_{SC}, $m_{adsorbent}$ and Coe_{Vol} are 600 m^2, 460 kg and 20 L/m^2 respectively, the *CR* of 80.39 % can be obtained. The PY_{grant} increased up to 9.6 years and the *PY* increase up to 58.5 years, which are still acceptable. Compared with the case that *CR* is 50.05 %, annual average COP is improved up to 0.64 from 0.61

Tab. 5: Optimization results

Coverate	**50.05 %**	**60.74 %**	**70.81 %**	**80.39 %**	**90.28 %**
$m_{adsorbent}$ [kg]	300	380	360	460	460
Coe_{Vol} [L/m^2]	20	20	20	20	40
A_{SC} [m^2]	250	300	450	600	900
Annual average COP [-]	0.61	0.63	0.63	0.64	0.64
Annual average SCP [kW/kg]	0.28	0.28	0.29	0.29	0.29
Annual electricity consumption reduction [kWh]	10150.1	12318.9	14360.9	16304.8	18309.4
Annual CO_2 emmision reduction [ton]	4.415	5.359	6.247	7.093	7.965
PY	54.1	55.8	51.31	58.5	69.5
PY_{grant}	7.6	7.7	8.3	9.6	14.3

and SCP is improved up to 0.29 kW/kg from 0.28 kW/kg. The annual electricity consumption of 16304.8 kWh, which equivalent to 7.093 tons of CO_2 emission, can be reduced.

In order to improve *CR* up to 90.28 %, A_{SC} and Coe_{Vol} need to be increased to 900 m^2 and 40 L/m^2, respectively. It results in higher initial cost, the PY_{grant} increase up about 50 % to 14.3 years. However, the annual electricity consumption and its equivalent of the CO_2 emission only improved about 12.3 %, the improvement of the annual average COP and SCP are ignorable. This strategy can be applied to some large-scale and long-term projects with abundant financial support, such as the government building.

4. Conclusion

This study focuses on the annual cooling performance prediction of the (AC). A numerical model of AC system was established for the annual cooling performance prediction and parameter study. The following conclusion were obtained.

- The well-fit approximate functions of COP and SCP were built, they were applied for the rapid COP and SCP calculation.
- A numerical model of AC system was established for the annual cooling performance prediction and parameter study.
- Both A_{SC} and $m_{adsorbent}$ can be determined to achieve the smallest PY_{grant}, however, the PY_{grant} is unsensitive to the Coe_{Vol}.
- PY_{grant} are 7.6 years, 7.7 years, 8.3 years, 9.6 years and 14.3 years while *CR* are 50.05 %, 60.07 %, 70.81 %, 80.39 % and 90.28 %, respectively.

5. References

Akahira A., Alam K.C.A., Hamamoto Y., Akisawa A., Kashiwagi T.. Mass recovery adsorption refrigeration cycle - improving cooling capacity. Refrigeration 2004;27:225–34.

He F., Nagano K., Togawa J.. Experimental study and development of a low-cost 1kW adsorption chiller using composite adsorbent based on natural mesoporous material. Energy 2020;209:118365.

He F., Nagano K, Seol S.H, Togawa J. Thermal performance improvement of AHPusing corrugated heat exchanger by dip-coating method with mass recovery.Energy 2022;239:122418.

He F., Nagano K., Togawa J.. Performance prediction of an adsorption chiller combined with heat recovery and mass recovery by a three-dimensional model. Energy 2023;277:127541.

J. Romero R., Rivera W., Gracia J., Best R.. Theoretical comparison of performance of an absorption heat pump system for cooling and heating operating with an aqueous ternary hydroxide and water/lithium bromide. Appl Therm Eng 2001;21:1137–47.

Jung-Yang San, Tsai Fu-Kang. Testing of a lab-scale four-bed adsorption heat pump. Appl Therm Eng 2014;70:274–81.

Lu Z.S., Wang R.Z.. Performance improvement by mass-heat recovery of an innovative adsorption air-conditioner driven by 50-80 ℃ hot water. Appl Therm. Eng 2013;55:113 – 20.

Liu H., Nagano K., Morita A., Togawa J., Nakamura M.. Experimental testing of a smallsorption air cooler using composite material made from natural siliceous shale andchloride. Appl Therm Eng 2015;82:68–81.

Manu S., Chandrashekar T.K.. A simulation study on performance evaluation of single-stage LiBr–H2O vapor absorption heat pump for chip cooling. Sustain Build Environ 2016;5:370–86.

Nakabayashi S., Nagano K., Nakamura M., Togawa J., Kurokawa A.. Improvement ofwater vapor adsorption ability of natural mesoporous material by impregnatingwith chloride salts for development of a new desiccant filter. Adsorption 2011;17:675–86.

Pan Q.W., Wang R.Z.. Experimental study on operating features of heat and massrecovery processes in adsorption refrigeration. Energy 2017;135:361–9.

Pan Q.W., Wang R.Z.. Study on operation strategy of a silica gel-water adsorption chiller in solar cooling application. Sol Energy 2018;172:24–31.

Srikhirin P., Ahpornratana S., Chungpaibulpatana S.. A review of absorption refrigeration technologies. Renew Sustain Energy Rev 2001;5:343–72.

Sapienza A., Santamaria S., Frazzica A., Freni A.. Influence of the management strategy and operating conditions on the performance of an adsorption chiller. Energy 2011;36:5532–8.

Seol S.H., Nagano K., Togawa J.. Modeling of adsorption heat pump system based onexperimental estimation of heat and mass transfer coefficients. Appl Therm Eng2020;171:115089.

Togawa J., Kurokawa A., Nagano K.. Water sorption property and cooling performance using natural mesoporous siliceous shale impregnated with LiCl for adsorption heat pump. Appl Therm Eng 2020;173:115241.

Appendix: Units and Symbols

Tab. 6: Nomenclature

Quantity	Symbol	Unit
Area	A	m^2
Constant coefficient	$\boldsymbol{a}_n$, $\boldsymbol{b}_n$, n =1,2,3,4,5	
Specific heat	c	kJ kg^{-1} K^{-1}
Irradiance	E	kW m^{-2}
Emission coefficient	*Emission*	kg kWh^{-1}
Specific enthalphy	*en*	kJ kg^{-1}
Heat loss coefficient	F_L	kW m^{-2} K^{-1}
Sensible heat	$H_{sensible}$	kJ kg^{-1}
Mass	m	kg
Mass flow rate	$\dot{m}$	kg s^{-1}
Price of CO_2 emmsion	$Price_{co2}$	JPY kWh^{-1}
Price of electricity	$Price_{ele}$	JPY kWh^{-1}
Heat	Q	kJ
Heat flow rate	$\dot{Q}$	W
Relative humidy	RH	
Temperature	T	K
Time	t,	s

Tab. 7: Greek Symbols

Quantity	Symbol	Unit
Density	ρ	kg m^{-3}
Efficiency	η	

Tab. 8: Subscripts

Quantity	Symbol
Regeneration	Reg
Sorption	Sor
Cycle Perido	cyc
Water	w
Solar collector	SC
Dry bulb	drybulb
Wet bulb	wetbulb
Cooling tower outlet	ct-out
Sorption adsorber outlet	sor-out
Adsorption chiller	ac
Initial cost	ini
Compress type air-conditioner	com
Electricity	ele
CO_2	co2
Volume	Vol
Hot water tank	HT
Maximum	Max
Spectral	λ

ASSESSING THE FEASIBILITY AND ECONOMIC VIABILITY OF SOLAR CPC FOR ABSORPTION COOLING SYSTEM IN DIVERSE INDIAN CLIMATE ZONES

Aditi Garg, Bahni Ray and Sanjeev Jain

Department of Mechanical Engineering, Indian Institute of Technology Delhi, New Delhi (India)

Abstract

The present work analyzes the feasibility of a solar absorption cooling system in the Indian context. A compound parabolic collector (CPC) is used with a single-effect vapour absorption chiller to meet a building cooling load. The thermal economic and environmental performance analysis is carried out for four cities in different climate zones of the country using TRNSYS software. The effect of parameters like solar collector area, storage volume, and collector slope have been observed on the solar fraction (SF), auxiliary heat energy consumption, collector useful energy gain, payback period (PBP), and levelized cost of cooling (LCOC). The optimized values of the parameters have been decided based on the payback period and solar fraction.

Keywords: TRNSYS, Solar cooling, CPC, economic analysis, absorption chiller

1. Introduction

India, geographically positioned between 8°4' north to 37°6' north, boasts a wide range of climates, encompassing hot and dry, warm and humid, moderate, cold, and composite regions. As the country experiences rising temperatures, the demand for space cooling is set to surge, further burdening the power grid. While India has made substantial progress in harnessing renewable resources, there remains untapped potential for further exploration. Solar energy, in particular, has gained considerable momentum in various applications, including solar cooling. Solar cooling is one of the most promising technologies as it may lead to a decrease in electricity consumption in summer and has great compatibility between source supply and load demand.

Among the various options available for solar cooling technologies, the vapor absorption cooling system stands out as a popular option, primarily because of its high efficiency and the successful commercialization of absorption chillers (Xu and Wang, 2017). Absorption chillers demonstrate superior coefficient of performance (COP) values compared to other solar cooling technologies, typically ranging from 0.6 to 0.8 for single-stage chillers and from 0.9 to 1.3 for two-stage chillers. Two common solution pairs used as refrigerant-sorbent in absorption chillers are ammonia-water and water-lithium bromide. Ammonia-water systems can achieve evaporator temperatures below 0 °C, while water-lithium bromide systems can reach temperatures as low as 4 °C.

The operating temperature for single-stage absorption systems can be provided by solar collectors such as flat plate collectors (FPC), evacuated tube collectors (ETC), and compound parabolic collectors (CPC). Among them, CPC can provide a low concentration in the range of 2-10 and operate in the medium temperature range of 100 ⁰C -120 ⁰C. It provides an advantage over non-concentrating collectors like flat plate collectors (FPC) and evacuated tube collectors (ETC) by providing concentration and an advantage over concentrating collectors like a parabolic trough and parabolic dish by their ability to collect both direct and diffuse radiations without employing tracking system. Due to this, it has gained worldwide attention in the last few decades for its use in multiple applications, including solar absorption cooling.

A lot of research has been done on solar absorption cooling integrated with different types of collectors throughout the world. Various companies have installed solar cooling setups in various institutions for space-cooling applications. There are various factors that influence the technical feasibility of these systems, such as the availability of required solar radiation, cost of components, electricity and fuel costs, water, and land availability. Apart from the technical feasibility of the solar cooling system, it must be economically attractive for the developers and investors to fund the system. The useful lifetime period of these systems is 20 years to 25 years. The government also occasionally launches various policies and subsidies to encourage the development of these non-conventional energy systems and reduce the load on the power grid. Environmental assessment is also carried out to determine how much carbon footprint reduction occurs by employing these technologies. Many experimental and simulation studies have been carried out to investigate and improve the performance of solar vapour absorption cooling systems. The simulation studies have mostly been carried out using Transient System Simulation (TRNSYS) software for modelling and simulating the absorption cooling system with different solar collectors. Many studies have analysed the effects of solar collector area, storage tank volume, boiler set point, collector mass flow rate, and solar collector

10.18086/swc.2023.04.05 Available at http://proceedings.ises.org

slope on the thermal, economic, and environmental performance of the solar cooling system and have suggested optimized values of the parameters.

Florides et al. (2002) explored the performance of different types of solar collectors, such as FPC, CPC, and ETC, for an absorption cooling system for residential cooling in Nicosia, Cyprus, using TRNSYS. Assilzadeh et al. (2005) modeled and simulated a single-effect LiBr-water absorption system with ETC for Kuala Lumpur, Malaysia. Hang et al. (2011) analyzed the performance of ETC based absorption cooling system for Los Angeles, California, and concluded that the cost of carbon footprint reduction is the key indicator for the sizing and overall performance of the system. Al-Alili et al. (2012) studied the feasibility of ETC based ammonia water-driven solar cooling system for Abu Dhabi. They suggested a specific collector area and specific tank size with regard to chiller capacity and compared the electrical consumption with vapor compression cooling systems. Xu and Wang (2017) carried out the analysis of CPC-based absorption cooling systems with single-effect, double-effect, and variable-effect absorption chillers for Miami. The performance of variable effect was found to be better, followed by single-effect and double-effect chillers. Sokhansefat et al. (2017) modelled and simulated an existing ETC-based absorption cooling system installed in Tehran, Iraq. A parametric analysis was conducted, and optimized parameters were obtained, which resulted in the enhancement of solar fraction by 28%. Bellos and Tzivanidis (2017) conducted simulation studies for ETC-based absorption cooling systems for ten locations worldwide. Different sets of collector area and storage tank volumes were investigated in order to obtain optimised values for achieving minimised levelized cost of cooling.

Khan et al. (2018) developed and analysed two configurations for solar vapour absorption systems for FPC and ETC for Islamabad in Pakistan. The system performance of two configurations, along with the two collectors, were compared for solar fraction, collector efficiency, and primary energy savings for different collector slopes, collector areas, and storage tank volumes. Altun and Kilic (2020) modelled and analysed an absorption cooling system for FPC and ETC for six cities located in Turkey for various parameters, and solar fraction, levelized cost of cooling, and payback period were plotted for optimum values of parameters.

In the Indian context, few studies have also been conducted to study the potential of solar absorption cooling in some cities. Uttham et al. (2016) analysed the performance of an absorption cooling system with ETC for an office building in Gandhinagar, Gujarat, India. The study also explored optimising parameters such as storage tank volume, collector area, and collector slope. Muye et al. (2016) investigated the performance of ammonia–water absorption power and cooling systems with CPC and biomass auxiliary heater for Chennai (India) and Seville (Spain). The scroll expander was utilised for power generation. The study concluded that increasing the absorber temperature is advantageous for power production while raising the evaporator temperature is detrimental to cold production. Additionally, elevating the condenser temperature is unfavourable for both outputs, with Seville demonstrating better system performance but Chennai achieving a higher solar fraction. Narayanan (2017) conducted a techno-economic analysis for an absorption cooling system with ETC for an office building in Chennai. It was found that the proposed solar absorption cooling system would achieve a full payback after 15.5 years, in contrast to a traditional air conditioner unit. Further, it was noted that this payback period could vary depending on the local climate and cooling demand. Gogoi and Saikia (2019) analysed the performance of a combined solar-powered organic Rankine cycle and absorption cooling system using a parabolic trough collector (PTC) for four months in Jodhpur, India. Five different working fluids were compared for the Rankine cycle. The absorption cooling system performance was compared at two generator temperatures. Sharma et al. (2023) conducted thermal and economic analysis for a solar absorption cooling system using CPC for milk chilling application for an experimental prototype in Jaipur, India. The levelized cost of energy, simple payback period, and discounted payback period were estimated as 0.177 $/kWh, 12.4 years, and 19.7 years.

Despite the growing market presence of solar cooling installations by various Indian companies, there is a notable lack of comprehensive research in this domain, particularly regarding the Indian context. Given that cooling requirements often outweigh heating loads in the Indian climate, solar cooling technologies are of paramount importance. This study aims to bridge this research gap by investigating the feasibility of utilizing CPC-based solar absorption cooling in four major Indian cities: New Delhi, Chennai, Bengaluru, and Ahmedabad. These cities are strategically chosen to represent diverse climate zones within the country. This analysis not only focuses on assessing the thermal performance of the system but also examines the economic viability and environmental analysis of implementing solar cooling systems in these regions.

2. Methodology Overview

2.1 Description of solar cooling system configuration

A solar cooling system has been made in TRNSYS to meet a design cooling load of 100 kW, as shown in Fig. 1. The picture of the solar cooling system for the analysis is shown in Fig.2. Compound parabolic collectors (CPC) have been used with a single-effect vapour absorption chiller to meet the cooling demand using solar energy. The hot water generated by the solar collector is stored in the storage tank and used to power the absorption chiller. An auxiliary boiler is placed between the storage tank and the absorption chiller to ensure the water temperature stays at the desired level. This heater is used when the water temperature falls below the desired temperature. The absorption chiller generates chilled water, which is utilized to meet the building cooling requirements. TMY data is obtained from the Meteonorm database of the TRNSYS library. The system is run in the summer season in India, typically from 1st April to 30th September, for 12 working hours. The same cooling load has been analyzed for all cities to compare the system's feasibility for the location. The building hourly cooling load has been generated using a building load generator component in TRNSYS. The details of the single-effect vapour absorption chiller are mentioned in Table 1. A chiller with a capacity of 125 kW is found to be suitable to meet the peak load. The set point of hot water temperature is considered to be 115 ºC. The flow rates for hot, chilled, and cooling water are calculated as per the details mentioned in TRNSYS documentation.

Table 1 Chiller Specifications

Parameter	**Value**	**Units**
Rated chiller capacity	125	kW
Rated chiller COP	0.7	-
Chilled water temperature (inlet/outlet)	12.22/6.67	°C
Chilled water flow rate	4.297	kg/s
Hot water temperature (inlet/outlet)	115/105	°C
Hot water flow rate	3.4094	kg/s
Cooling water temperature (inlet/outlet)	29.44/32.22	°C
Cooling water flow rate	21.02	kg/s
Electrical power	2	kW

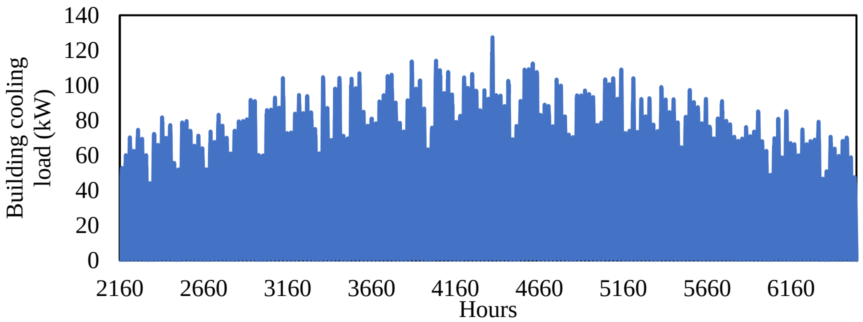

Fig. 1 Building cooling load for the period from 1st April to 30th Sep (2160 to 6552 hours)

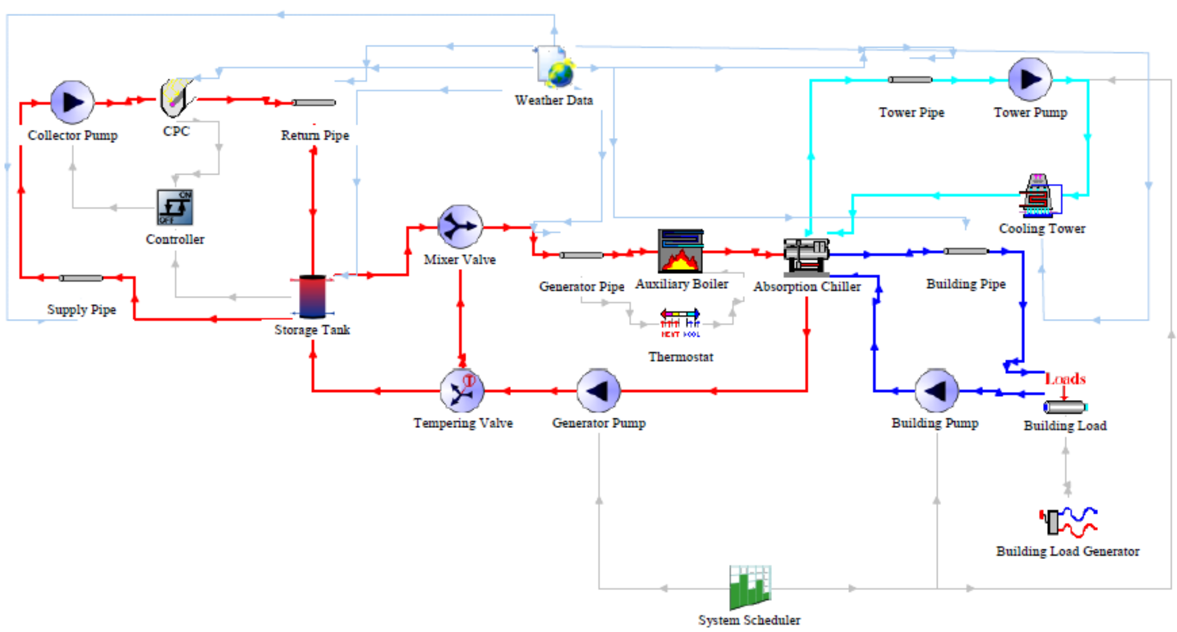

Fig. 2 Solar absorption cooling system model in TRNSYS

2.2 Modelling of system in TRNSYS

The solar absorption cooling system has been modelled in TRNSYS software (v18). The system can be divided into two subsystems: solar collector system and absorption cooling system. The solar collector system includes solar collectors, storage tank, controllers, and collector pumps. The absorption cooling system includes an absorption chiller, pumps, auxiliary heater, controllers, valves, cooling tower, and building cooling load. The various components used are discussed in the subsequent sections. Fig. 2 shows the picture of the solar cooling system modelled in TRNSYS. The model of the system has been developed considering the following assumptions taken from the literature:

- Heat losses are only considered within the storage tank, with no consideration for heat losses in the pipelines and valves.
- Flow mixing within the storage tank is assumed to be adiabatic and perfectly mixed.
- Thermal properties of water are assumed to remain constant throughout the analysis.
- Potential effects of water boiling or freezing within the solar loop are not factored into the calculations.
- Thermal storage tank is oriented vertically to promote thermal stratification.

2.2.1 Weather Data

The weather data has been obtained using the component Type 15-6, which uses a typical meteorological year 2 (TMY-2) data file. This data file provides the solar radiation, dry bulb temperature, and other weather conditions for New Delhi, India. The diffuse solar radiation on the tilted surface has been calculated using the Perez model. This component also takes the values of the slope and azimuth angle for the collector considered. The weather data is taken from 1st April to 30th September (2160h to 6552h), and the simulation time step is taken as 5 minutes.

2.2.2 Solar Collector

The collector was designed using the compound parabolic collector (CPC) model found in the TRNSYS library (TYPE 74). This particular TYPE necessitates multiple inputs for an efficient collector model, including collector area, fluid-specific heat, overall heat loss coefficient, orientation, optical and geometrical parameters. Table 2 contains detailed information on the collector's specifications.

Table 2 Specifications of solar collector

Parameter	Value	Units
Fluid specific heat	4.19	kJ/kg.K
Collector fin efficiency factor	0.85	-
Overall heat loss coefficient	0.833	W/m^2.K
Wall reflectivity	0.9	-
Half-acceptance angle	30	º
Truncation ratio	0.7	-
Axis orientation	1	-
Absorptance of absorber plate	0.85	-
Number of covers	1	-
Index of refraction of cover	1.526	-
Extinction coeff. thickness product	0.0026	-

2.2.2 Storage tank

The storage tank has been modelled using the component TYPE 4a. It is segmented into ten equal-volume segments, each fully mixed, to introduce thermal stratification. The inlets and outlets of the tank are at a fixed position. The hot fluid flows into the tank's upper portion, while the cold fluid enters from the lower section.

2.2.3 Auxiliary heater

A steam boiler is used to provide auxiliary heating for the system and is modelled using Type 700. In this model, the boiler efficiency and the combustion efficiency are supplied as inputs to the model. This component (Type700) assumes that device efficiency is not a function of inlet conditions. It is connected to a thermostat (Type 108), which checks the incoming fluid temperature, and if it is less than the chiller hot water set point temperature, it turns on the auxiliary heater else it remains switched off.

2.2.4 Absorption Chiller

The vapour absorption chiller has been modelled using Type 107. It considers a single effect hot water driven LiBr-H_2O based water-cooled vapour absorption chiller. An external file is utilized to provide performance data for this absorption chiller. This external file contains data points representing the fraction of nominal capacity and the fraction of design energy input for various sets of fractions of design energy load, chilled water setpoint temperature, inlet cooling water temperature, and inlet hot water temperature. This data file is available in the software database. The chiller's specifications can be found in Table 1. Additionally, the electrical power required to operate the chiller's pumps is determined based on information sourced from THERMAX company's absorption chiller brochures.

2.2.5 Cooling Tower

A closed-circuit cooling tower has been modelled using the component Type 510. It provides cooling water to remove heat from the absorber and condenser of the absorption chiller. This cooling tower cools a liquid stream by evaporating water from the outside of coils containing the working fluid. The working fluid is completely isolated from the air and water in this type of system.

2.2.6 Other components

The fluid flow rates in the various loops in the system are operated using single-speed pumps (Type 114). The pump in the collector circuit is operated by the control signals of the differential controller (Type 2b). This controller switches on the pump when the collector outlet temperature exceeds the outlet temperature at the bottom of the storage tank by 3 ºC and switches off if this difference is less than 0.5 ºC (Al-Alili et al., 2012). Pipes are modelled by Type 31 and are sized with at least enough volume to handle the flow during one timestep. The tempering valve (type 11b) compares the temperature of the hot water returning from the chiller with the outlet temperature of the hot water at the top of the tank. If the returning hot water temperature exceeds the tank outlet temperature, the valve bypasses the full flow directly toward the auxiliary heater; otherwise, it is sent to the storage tank. The flow mixer (Type 11h) only facilitates the flow either from the tempering valve or the storage tank. The system's operational schedule is managed by a forcing function component (Type 14h) and is considered for 12 hours daily, from 7 am to 7 pm. Finally, the results are obtained using a plotter (Type 65d) and a printegrator (Type 46a).

2.2.7 Building load

The building load profile for the given system is generated using a synthetic building load generator component (Type 686) in TRNSYS. This component generates hourly cooling loads by employing user-defined parameters for peak cooling design load. It incorporates sinusoidal functions that adjust for seasonal fluctuations, time-of-day variations, and differences between weekdays and weekends. This modeling approach rapidly generates realistic loads, circumventing the labour-intensive process of modeling a real building.

For this study, we consider a peak cooling design load of 100 kW for the building. The actual load may exceed this value due to factors such as noise, multiplier, and offset parameters.

The generated building load profile is characterized as the cooling load for component Type 682. This component essentially imposes the load on the chilled water flowing through it and computes the resulting conditions of the outlet chilled water. Conceptually, it serves as an interface between the building load and the working fluid within an HVAC system.

2.3 Thermal analysis of solar cooling system

The thermal performance of the solar cooling system is evaluated using solar fraction (SF), which is defined as the amount of useful energy gain by the solar collector (E_u) to the total energy required for water heating for the absorption chiller, which includes both useful energy gain by collector (E_u) and auxiliary heat provided by the boiler (E_{aux}) as mentioned in eq. 1. The design parameters such as solar collector area, storage tank volume, and collector slope are varied to study their effect on solar fraction.

$$SF = \frac{E_u}{E_u + E_{aux}} \qquad \text{(eq. 1)}$$

2.4 Economical analysis of solar cooling system

The value of any energy system must ultimately be judged based on its economy. The total cost of the system includes capital cost, installation cost, maintenance, and operating costs. The capital and installation costs are one-time costs that need to be paid once in the useful lifetime of the solar cooling system. In contrast, maintenance and operating costs are periodical costs that must be paid annually. Capital Cost (C.C) is the total cost of all the components used in the system. The installation cost (I.C) is the cost incurred in installing and integrating the system, assuming 25 % system installation and 20 % system integration cost of the capital cost (Eicker and Pietruschka, 2009). The sum of capital cost and installation cost is the total initial investment cost (C_o) required to set up the solar cooling system. The capital cost and installation cost (C.C and I.C) must be converted to equivalent annualised investment cost (C_{o_annual}) as they are a one-time cost and must be added to yearly operation and maintenance costs. The expressions for all the costs are given from eq. (2)-(5). The details of economic parameters are specified in Table 3.

$$\mathrm{C.C} = C_{SC}A_{SC} + C_{ST}V_{ST} + C_{ABS}Q_{ABS} + C_{CT}Q_{CT} \qquad \text{(eq. 2)}$$

$$\mathrm{I.C} = 0.45\ \mathrm{C.C} \qquad \text{(eq. 3)}$$

$$C_O = \mathrm{C.C} + \mathrm{I.C} \qquad \text{(eq.4)}$$

$$C_{o\_annual} = C_O\left(\frac{d(1+d)^N}{(1+d)^N - 1}\right) \qquad \text{(eq.5)}$$

Table 3 Components costs

Components	Value	Unit	Ref.
Solar collector cost (C_{SC})	12000	INR/m^2	Pranesh et al. (2019)
Storage tank (C_{ST})	60000	INR/m^3	Sharma et al. (2023)
Absorption chiller (C_{ABS})	60000	INR/TR	Utham et al (2016)
Cooling tower (C_{ST})	1400	INR/ TR	Sharma et al. (2023)
Market discount rate (d)	6	%	Sharma et al. (2023)
Investment lifetime (N)	25	Years	Sharma et al. (2023)
Fuel inflation rate (FIR)	5	%	Jha et al. (2022)
Fuel cost (C_{FUEL})	5.010	INR/ kWh	Global Petrol Prices (2023)
Electricity cost (C_{ELE})	10.08 (New Delhi)	INR/ kWh	Gill et al. (2017)

Maintenance Cost ($M.C_{annual}$) is the cost incurred in maintaining and repairing the system, and it is considered to be 2% of the total initial investment cost (Co) (Eicker and Pietruschka, 2009, Hang et al., 2012). The operating cost ($O.C_{annual}$) is the cost incurred in total electric power consumption of the system and natural gas consumption by the auxiliary heater (Hang and Ming, 2012). The operating cost for the first year ($O.C_{first\ year}$) is the sum of the total fuel consumption cost in the auxiliary heater and the electricity consumption cost of the total system. Finally, the total annualised cost (T.A.C) is calculated as the sum of all annualised equivalent costs. The expressions for the costs are given from Eq. (6)-(8).

$$\mathrm{M.C}_{annual} = 0.02C_o \qquad \text{(eq.6)}$$

$$\mathrm{O.C}_{annual} = \mathrm{O.C}_{first\ year}\left(\frac{1-\left(\frac{1+FIR}{1+d}\right)^N}{(d-FIR)}\right)\left(\frac{d(1+d)^N}{(1+d)^N-1}\right) \qquad \text{(eq.7)}$$

$$\mathrm{T.A.C} = C_{o\_annual} + \mathrm{M.C}_{annual} + \mathrm{O.C}_{annual} \qquad \text{(eq.8)}$$

The payback period (PBP) and the levelized cost of cooling (LCOC) are two economic indicators that analyses the economic performance of the system. The payback period is defined as the time needed for cumulative fuel savings to be equal to the total initial investment in the system. It must be less than the useful lifetime of the system (N) for the system to be economically viable. PBP is of two types: Simple PBP and Discounted PBP. Simple PBP considers only the market discount rate, while discounted PBP considers the time value of money by incorporating both the market discount rate and inflation rate and is more realistic. Levelized cost of cooling (LCOC) is the unit cost of cooling provided by the cooling system. The expressions for the economic indicators are given from Eq. (9)-(11).

$$\text{Simple PBP} = \frac{\ln\left(1+\frac{C_o.d}{E_U C_{Fuel}}\right)}{\ln(1+d)} \qquad \text{(eq.9)}$$

$$\text{Discounted PBP} = \frac{\ln\left(1+\frac{C_o.(FIR-d)}{E_u C_{Fuel_{first\ year}}}\right)}{\ln\left(\frac{1+FIR}{1+d}\right)} \qquad \text{(eq.10)}$$

$$\mathrm{LCOC} = \frac{\text{Total annual cost (TAC)}}{\text{Total cooling energy generated annually (Ecool)}} \qquad \text{(eq.11)}$$

2.5 Environmental analysis of solar cooling system

The environmental analysis of the solar cooling system is based on the amount of carbon dioxide emission avoided by using VAS instead of VCS. The carbon dioxide emitted (CDE_{VAS}) during the operating phase of the VAS solar cooling system is calculated as the sum of emissions due to natural gas combustion in the auxiliary heater (CD_{ENG}) and emissions due to the electrical consumption by the chiller (CDE_{ELE}) as given by eq. (12). The carbon dioxide emission factor for electricity (EF_{ELE}) is considered as 0.81 kg/ kWh (Bhawan and Puram, 2022), and the carbon dioxide emission factor for natural gas is taken as (EF_{NG}) is considered as 0.2 kg/ kWh (Balghouthi et al., 2012). The electrical energy consumption (E_{ELE_VAS}) and thermal energy provided by natural gas (E_{NG}) are multiplied by their respective emission factors (EF), as shown in eq.(13)-(14). An electrical chiller (or VCS) of equivalent capacity for COP of 2.4 for the same building cooling load and ambient conditions is considered, and carbon dioxide emission due to electrical consumption by this chiller (CDE_{VCS}) is calculated by eq. (15). The difference between the carbon dioxide emissions of VAS and VCS is amount of carbon dioxide emissions avoided ($CDE_{avoided}$) given by eq. (16).

$$\mathrm{CDE_{VAS}} = \mathrm{CDE_{ELE}} + \mathrm{CDE_{NG}} \quad \text{(eq. 12)}$$

$$\mathrm{CDE_{ELE}} = \mathrm{E_{ELE\_VAS}} \times \mathrm{EF_{ELE}} \quad \text{(eq. 13)}$$

$$\mathrm{CDE_{NG}} = \mathrm{E_{NG}} \times \mathrm{EF_{NG}} \quad \text{(eq. 14)}$$

$$\mathrm{CDE_{VCS}} = \mathrm{E_{ELE_{VCS}}} \times \mathrm{EF_{ELE}} \quad \text{(eq. 15)}$$

$$\mathrm{CDE_{avoided}} = \mathrm{CDE_{VCS}} - \mathrm{CDE_{VAS}} \quad \text{(eq. 16)}$$

3. Results and Discussion

This section presents the results of the parametric analysis for the modelled solar cooling system. The simulations were carried out with a time step of 5 min from 1st April to 30th Sep (2160h to 6552h). The parameters considered for the analysis are solar collector area, collector slope, and storage tank volume. The solar collector area varies from 100 m^2 to 1000 m^2 with a step size of 100 m^2, collector slope from 0° to 30° with a 5° step size, and storage tank specific volume ratio from 0.02 m^3/m^2 to 0.1 m^3/m^2 with a step size of 0.02 m^3/m^2. Four cities have been chosen to represent four different climate zones of the country, as tabulated in Table 4. It can be noted that the four cities have similar values of incident horizontal solar radiation received but have different climatic zones.

Table 4 List of cities considered

Climate zone	Cities	Total horizontal solar radiation (kWh/m^2)
Hot & dry	Ahmedabad	1077.37
Warm & humid	Chennai	1073.71
Moderate	Bengaluru	1023.23
Composite	New Delhi	1118.79

3.1 Collector area

The solar collector area is an important parameter for optimizing the solar cooling system. The solar collector area is varied from 100 m^2 to 1000 m^2 with a step size of 100 m^2. Fig. 3 shows the variation of collector useful energy gain, auxiliary heat energy consumption, and solar fraction with collector area, keeping collector slope and storage tank volume fixed. It is observed that collector useful energy gain and solar fraction increase with collector area while the auxiliary heat energy consumption decreases. The increment in solar fraction decreases with the collector area and eventually leads to the fact that after a certain value of collector area, solar fraction will become constant. It is noted that after a collector area of 400 m^2, the auxiliary energy starts becoming lesser than the useful energy gain, indicating that at least a minimum of 400 m^2 is required to meet the cooling load. The solar fraction becomes 47% at an area of 400 m^2. So, the system must have enough capacity to provide at least half of the required heat through the solar collector system. Fig. 4 shows the effect of the collector area on LCOC and PBP.

LCOC initially decreases with the collector area and then starts increasing, while PBP is found to decrease with the collector area. The change in PBP decreases as the collector area increases, so greater areas have no significant economic advantage. Also, the discounted PBP is higher than the simple payback period as it incorporates the time value of money. The discounted PBP becomes economically feasible after the collector area greater than 400 m^2 for the PBP is 23 years. Fig.5 shows the variation of carbon dioxide emissions (CDE) of the vapour absorption system (VAS) with collector area and compares it with a conventional vapour compression system (VCS) and also shows how much CDE is avoided if VAS replaces the VCS system. The CDE of VAS decreases with the collector as the amount of auxiliary energy required decreases with the collector area. However, the change in CDE avoided decreases as the collector area increases because of the slow increase of solar fraction.

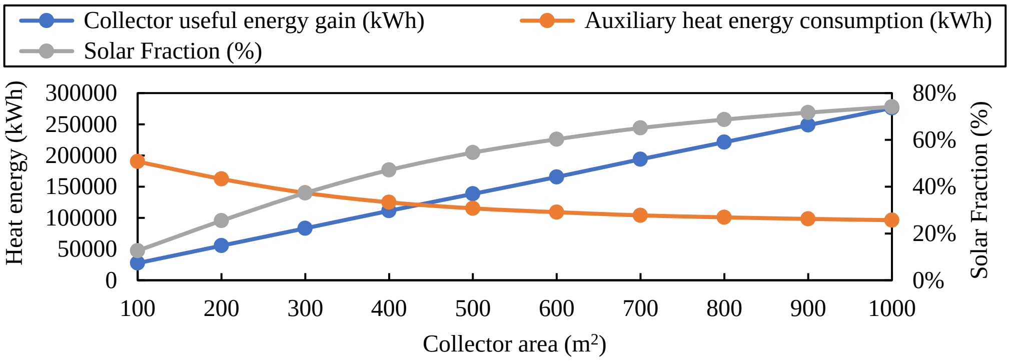

Fig. 3 Variation of collector useful energy gain, auxiliary heat energy consumption, and solar fraction with collector area

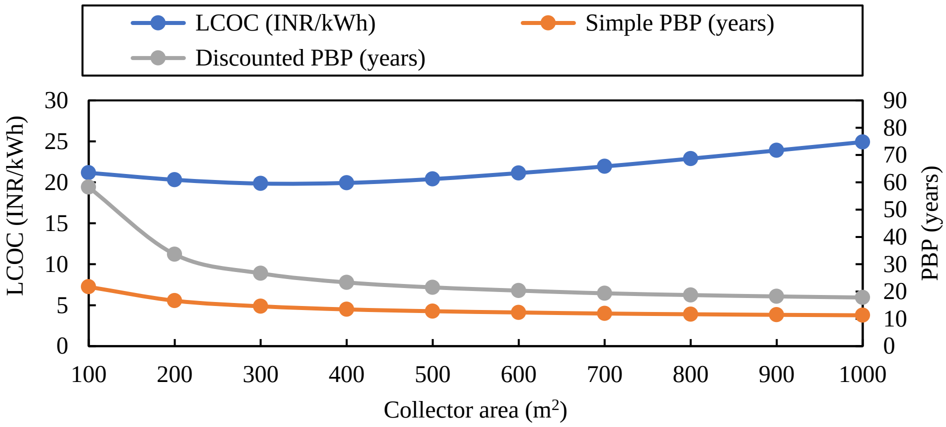

Fig.4 Variation of LCOC, simple and discounted PBP with collector area

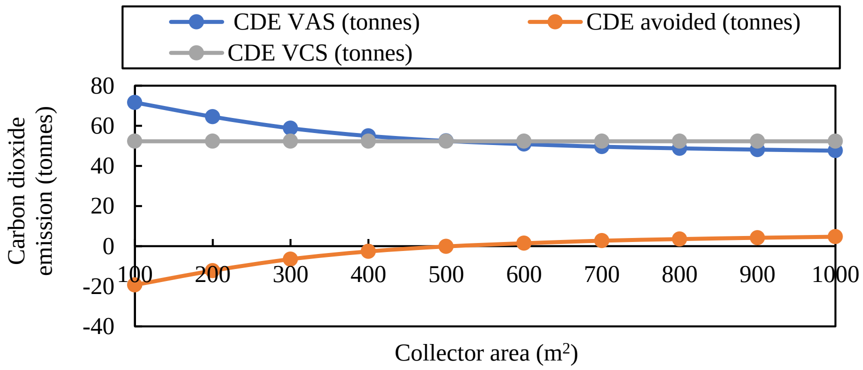

Fig.5 Variation of carbon dioxide emissions with collector area

3.2 Collector slope

Fig.6 shows the variation of collector useful energy gain, auxiliary heat energy consumption, and solar fraction with collector slope, keeping collector area and storage tank volume fixed. The collectors are assumed to be south-facing by keeping their azimuth angle 0º. The solar fraction and collector useful energy gain increases and becomes maximum at 10º, then decreases with the collector slope. The auxiliary heat energy consumption decreases, becomes minimum, and then increases. The solar fraction at the collector slope of 10º is more than 6% than at the location's latitude (28º). Fig. 7 shows the effect of the collector slope on LCOC and PBP, and it can be observed that the collector slope has an insignificant influence on these economic parameters, and they achieve minimum values at 10º as well. The CDE does not change much with the slope and increases after the slope is greater than 20º (Fig.8). This indicates that the collector slope can be optimised based on the thermal analysis as it does not have a considerable impact on economic and environmental analysis.

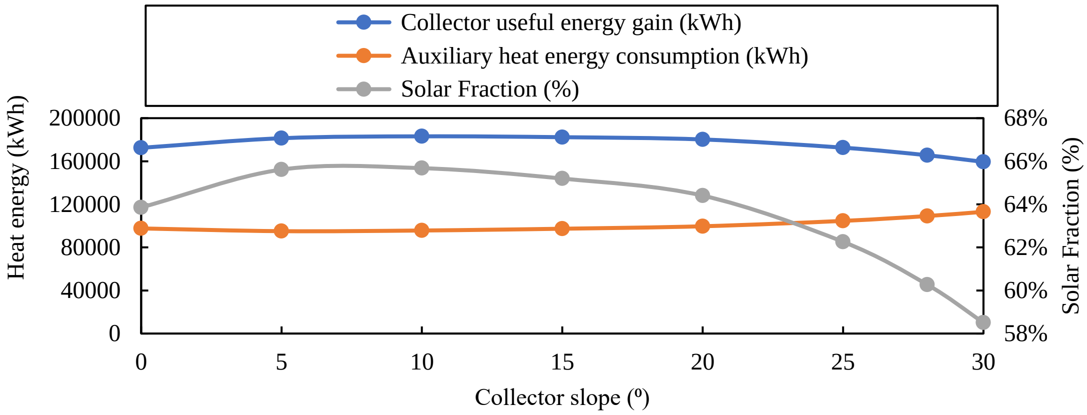

Fig. 6 Variation of collector useful energy gain, auxiliary heat energy consumption, and solar fraction with collector slope

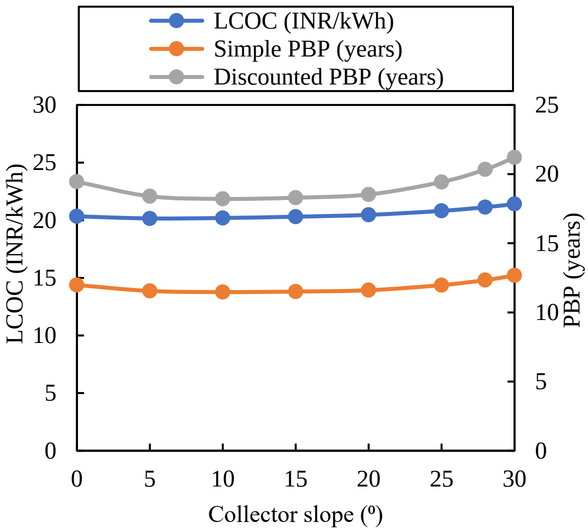

Fig. 7 Variation of LCOC, simple and discounted PBP with collector slope

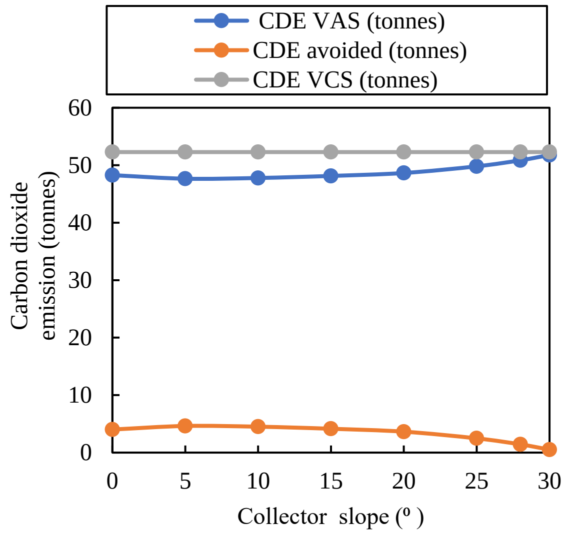

Fig. 8 Variation of carbon dioxide emissions (CDE) with collector slope

3.3 Storage tank specific volume ratio (STSVR)

The storage tank specific volume ratio (STSVR) is varied from 0.02 to 0.1 m^3/m^2 of solar collector area for a step size of 0.02 m^3/m^2 (Hang et al., 2011). Fig. 9 shows the variation of solar fraction with storage tank specific volume ratio (STSVR) for different collector areas. The solar fraction decreases with STSVR for a given collector area, indicating that storage tank volume does not significantly affect the system's thermal performance for small collector areas. The solar fraction increases with collector area as there is a proportional increase in storage tank volume. A few runs for STSVR of 0.01 and collector areas of 1100 m^2 and 1200 m^2 were also done. It was observed that for an area greater than 1000 sq.m, solar fraction increases from the ratio of 0.01 to 0.02 and then decreases. For all areas, the change in solar fraction is less when the ratio varies from 0.01 to 0.02 than the other ratios. There seems to be no advantage when the ratio is more than 0.02

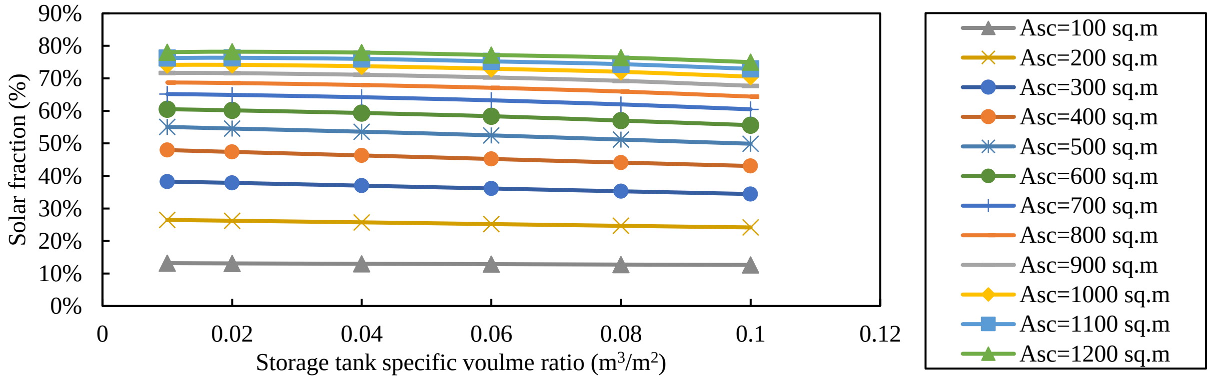

Fig. 9 Variation of solar fraction with storage tank specific volume ratios (STSVR) for different collector areas.

Fig. 10 and Fig. 11 show the effect of storage tank-specific volume ratio on LCOC and PBP. These economic parameters increase with STSVR as the collector area and storage tank volume contribute majorly to the initial investment cost. In Fig.11, many ratios give PBP greater than 25 years, which makes them economically unfeasible. The carbon dioxide emissions by the absorption system are shown in Fig. 12, increasing with the ratio for a given area due to an increase in auxiliary heat energy consumption.

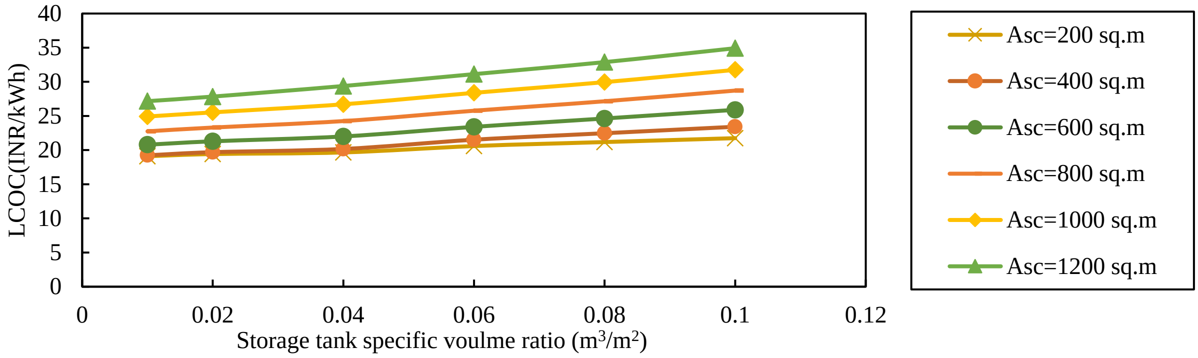

Fig. 10 Variation of LCOC with storage tank specific volume ratios (STSVR) for different collector areas

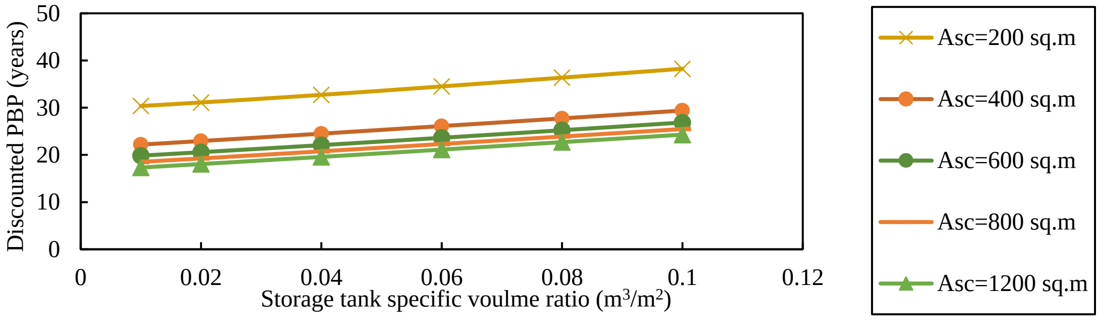

Fig. 11 Variation of PBP with storage tank specific volume ratios (STSVR) for different collector areas

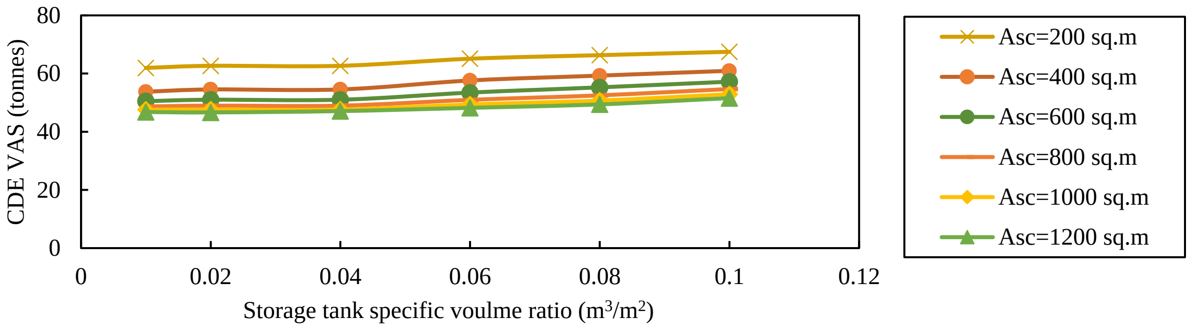

Fig. 12 Variation of CDE associated with solar vapour absorption system with storage tank specific volume ratios (STSVR) for different collector areas.

3.4 Optimisation of parameters

The collector area has a major impact on thermal, economic, and environmental analysis, while the effect of the collector slope is limited to thermal analysis. The storage tank-specific volume ratio does not significantly affect the thermal analysis, and increasing it has no economic advantage for a given collector area. So, from the preceding section, the optimum storage tank-specific volume ratio is considered 0.02 for further analysis. The collector slope is optimised based on a maximum solar fraction, as shown in Fig. 13, for a fixed collector area.

Fig.14 shows the variation of the payback period with the collector area for the four cities considered for the optimised collector slope. The payback period decreases with the collector area; after a particular value, the change in PBP is insignificant to the increase in the collector area. So, that value for the collector area is considered an optimized area. The list of optimized parameters has been tabulated in Table 5.

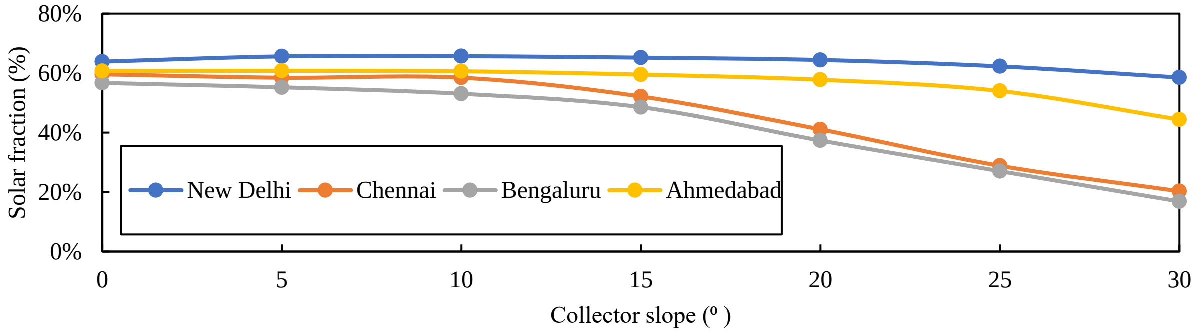

Fig. 13 Variation of solar fraction with collector slope for different cities for a fixed collector area and storage tank specific volume ratio

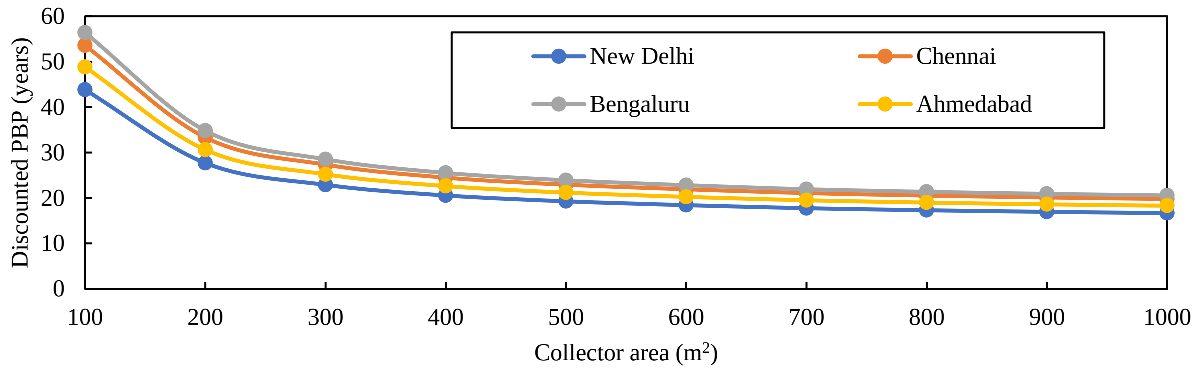

Fig. 14 Variation of PBP with collector area for different cities for optimised collector slope and storage tank specific volume ratio

Table 5 List of optimized results for four cities

Cities	Total horizontal solar radiation (kWh/m²)	Electricity tariff (INR/kWh)	Collector area (m²)	Storage volume (m³)	Collector slope (°)	TAC (INR)	SF (%)	Discounted PBP (years)	LCOC (INR/kWh)	CDE VAS (tonnes)
Ahmedabad	1077.3	6.47	600	12	5	2900938	60.8	20.25	20.06	50.92
Bengaluru	1023.2	6.62	700	14	0	3120266	61.4	21.93	21.58	51.35
Chennai	1073.7	10.29	700	14	0	3185328	64.5	21.09	22.03	48.91
New Delhi	1118.7	10.08	600	12	10	2945037	65.5	18.43	20.37	47.96

Fig. 13 shows that cities in south India (Bengaluru and Chennai) have maximum solar fraction at a collector slope of 0 º as they lie in the tropical region, and in the summer season, the solar radiations are directly falling in the tropics. The optimised parameters mentioned in Table 5 show that these two cities also have similar payback periods (PBP) and levelized cost of cooling (LCOC). The solar fraction (SF) is highest in New Delhi due to higher incident solar radiation, resulting in lower auxiliary heat energy consumption and reduced carbon dioxide emissions (CDE). The payback period (PBP) increasing in the order of New Delhi, Ahmedabad, Chennai, and Bengaluru is analogous to the decreasing incident solar radiation available in the cities. New Delhi exhibits better thermal, economic, and environmental performance, making it the most feasible and economically viable option among the cities (highest SF, lowest PBP, and lowest CDE) for the given parameters. The optimized parameters leading to a payback period (PBP) and levelized cost of cooling (LCOC) ranging from 18.43 to 21.93 years and 20.06 to 22.03 INR/kWh, respectively, exhibit resemblance to the numbers (19.7 years, 0.177$/kWh) determined by Sharma et al. (2023) for Jaipur city in India. The provision of subsidies on the investment cost for developing the solar absorption cooling system will further increase their potential for being developed in various cities and reduce the strain on the country's power grid. The natural gas fuel can be replaced with cheaper alternatives such as sugar cane bagasse, rice husk, or other biomass options to reduce the auxiliary fuel operating cost.

4. Conclusions

In this study, the thermal, economic, and environmental performance of a solar cooling system based on a vapour absorption system (VAS) using a solar compound parabolic collector (CPC) has been analysed for various climatic zones in India. A parametric study is carried out to understand the effect of solar collector area, storage tank specific volume ratio, and solar collector slope on solar fraction, collector useful energy gain, auxiliary heat energy consumption, payback period, levelized cost of cooling, and carbon dioxide emission. The system has been modelled in TRNSYS software. The conclusions of the work are mentioned below.

a) Collector area has a major impact on thermal, economic, and environmental analysis of solar absorption cooling systems.
b) The impact of the collector slope is confined to thermal analysis and demonstrated limited influence on economic and environmental aspects.
c) An increase in storage tank specific volume ratio (STSVR) for a fixed area does not significantly affect the solar fraction (SF). It affects economic and environmental analyses as auxiliary boiler energy consumption increases with increased storage tank volume.
d) The discounted payback period is higher than the simple payback period by 38% to 62% when the collector area varies from 100 m^2 to 1000 m^2 for the fixed value of collector slope and STSVR.
e) The parametric optimisation has been based on solar fraction for the collector slope and the discounted payback period for the solar collector area.

5. References

Al-Alili, A., Islam, M. D., Kubo, I., Hwang, Y., & Radermacher, R. (2012). Modeling of a solar powered absorption cycle for Abu Dhabi. Applied Energy, 93, 160–167.

Altun, A. F., & Kilic, M. (2020). Economic feasibility analysis with the parametric dynamic simulation of a single effect solar absorption cooling system for various climatic regions in Turkey. Renewable Energy, 152, 75–93.

Assilzadeh, F., Kalogirou, S. A., Ali, Y., & Sopian, K. (2005). Simulation and optimization of a LiBr solar absorption cooling system with evacuated tube collectors. Renewable Energy, 30(8), 1141–1159.

Balghouthi, M., Chahbani, M. H., & Guizani, A. (2012). Investigation of a solar cooling installation in Tunisia. Applied Energy, 98, 138–148.

Bellos, E., & Tzivanidis, C. (2017). Energetic and financial analysis of solar cooling systems with single effect absorption chiller in various climates. Applied Thermal Engineering, 126, 809–821.

Bhawan, S., & Puram, R. K. (2022). CO2 Baseline Database for the Indian Power Sector User Guide Government of India Ministry of Power Central Electricity Authority.

Eicker, U., & Pietruschka, D. (2009). Design and performance of solar powered absorption cooling systems in office buildings. Energy and Buildings, 41(1), 81–91.

Florides, G. A., Kalogirou, S. A., Tassou, S. A., & Wrobel, L. C. (2002). Modelling and simulation of an absorption solar cooling system for Cyprus. Solar Energy, Vol. 72, No. 1, pp. 43–51.

Gill, B., Saluja, S., & Palit, D. (2017). Electricity Pricing and the Willingness to Pay for Electricity in India: Current Understanding and the Way Forward. New Delhi: The Energy and Resources Institute (TERI).

Global Petrol Prices (2023). Global Petrol Prices. [WWW Document]. URL https://www.globalpetrolprices.com/ (accessed 08.01.2023)

Gogoi, T. K., & Saikia, S. (2019). Performance analysis of a solar heat driven organic Rankine cycle and absorption cooling system. Thermal Science and Engineering Progress, 13, 100372.

Hang, Y., Qu Ming, M., & Zhao, F. (2011). Economical and environmental assessment of an optimized solar cooling system for a medium-sized benchmark office building in Los Angeles, California. Renewable Energy, 36(2), 648–658.

Jha, I. S., Shri, Goyal, A., & Singh, P. K. (2022). Determination of levellised generic tariff for FY 2022-23 under Regulation 8 of the Central Electricity Regulatory Commission Regulations, 2020. Central Electricity Regulatory Commission, New Delhi.

Khan, M.S.A., Badar, A.W., Talha, T., Khan, M.W., & Butt, F.S. (2018) Configuration based modeling and performance analysis of single effect solar absorption cooling system in TRNSYS, Energy Conversion and Management, 157, 351e363.

Muye, J., Ayou, D. S., Saravanan, R., & Coronas, A. (2016). Performance study of a solar absorption power-cooling system. Applied Thermal Engineering, 97, 59–67.

Narayanan, M. (2017). Techno-economic analysis of solar absorption cooling for commercial buildings in India. International Journal of Renewable Energy Development, 6(3), 253–262.

Pranesh, V., Velraj, R., Christopher, S., & Kumaresan, V. (2019). A 50-year review of basic and applied research in compound parabolic concentrating solar thermal collector for domestic and industrial applications, Solar Energy, Volume 187, Pages 293-340.

Sharma, D. K., Sharma, D., & Ali, A. H. H. (2023). Optimization and thermo-economic performance of a solar-powered vapor absorption cooling system integrated with sensible thermal energy storage. Energy Conversion and Management: X, 20, 104400.

Sokhansefat, T., Mohammadi, D., Kasaeian, A., & Mahmoudi, A. R. (2017). Simulation and parametric study of a 5-ton solar absorption cooling system in Tehran. Energy Conversion and Management, 148, 339–351.

Utham, G., Agravat, S. M., Jani, B., & Bhutka, J. (2016). Modelling, Transient Simulation and Economic Analysis of Solar Thermal Based Air Conditioning System in Gujarat. Smart Grid and Renewable Energy, 07(08), 233–246.

Xu, Z. Y., & Wang, R. Z. (2017). Comparison of CPC driven solar absorption cooling systems with single, double, and variable effect absorption chillers. Solar Energy, 158, 511–519.

Building optimization combined with solar heating and cooling in Nepal

Michael Strobel[1,2], Uli Jakob[1,2], Manuel Ostheimer[1,3], Daniel Neyer[1,3]

[1] Universtität Innsbruck, Unit of energy efficient building, Innsbruck (Austria)

[2] Dr. Jakob energy research GmbH & Co. KG, Weinstadt (Germany)

[3] Neyer Brainworks GmbH, Bludenz (Austria)

Abstract

To meet future heating and cooling needs in buildings, energy efficiency is required at both the technical level of a system and at the building energy efficiency level, followed by the integration of renewable energy. The BEEN project (Building Energy Efficiency in Nepal) aims to establish energy-efficient construction in Nepal, taking into account the country's climatic and topological characteristics. As Nepal's building stock expands rapidly due to economic and population growth, the country has one of the highest urbanization rates in the world. Therefore, the project is active in various areas, such as developing passive design guidelines, manuals and training programs for experts and policy makers, as well as providing technical support to several building case studies. The presented study links improving the energy efficiency of buildings with their coverage by solar heating and cooling systems. Two buildings are used as case studies, one is an office building in a warm climate in Rupandehi district and the other is a hotel building in a cold climate at high altitude in Mustang district. It turns out that a combination of different measures can reduce the total cooling demand by 75% and the sensible heating demand by 98% and increase interior comfort.

Keywords: Building optimization, solar heating, solar cooling, energy efficiency, Passive House

1. Introduction

July 2023 was by far the hottest month ever recorded, with a global average 1.5 °C above the long-term average for July between 1850 and 1900 (Copernicus 2023). This increases the global demand for space cooling and the need for cool and comfortable indoor air conditions. Energy consumption related to building operation already 30 % (International Energy Agency 2023) of the worldwide energy consumption. 20% of global electricity consumption is dedicated to the operation of air conditioners and fans (Dean et al. 2018) Driving factor for the future space cooling demand is the increase of more extreme and longer lasting heat waves alongside the global warming, the growing world population which runs with a growing rate urbanization and the economic development especially of developing countries in Asia and Africa, such as Indonesia and Nigeria. Developing countries are often located in the Sunbelt region between the 20th and 40th latitude on the Northern and Southern hemisphere, where the climate already causes space cooling demand. The economic development causes an increase in individual buying power causing higher number in sales of cooling equipment. The rapid urbanization worldwide connected to dense urban construction also causes the increased and intense occurrence of Urban Heat Islands (UHI), again causing heat stress to counteract via mechanical cooling. All these reasons already caused a tripling in energy consumption for space cooling from 1990 to 2020 (Dean et al. 2018). A projection for the increasing demand for space cooling demand in Nepal is presented in a paper related to the IEA SHC Task 65 (Bonomolo et al. 2023). This projections is based on the methodology of the Cooling Demand Market Index (CDMI) developed in 2023 by Strobel et al. (Strobel et al. 2023). In addition, the building stock worldwide is rising as well. Even though the development of global warming leads in general to an increase of cooling demand and a decrease in heating demand, the space heating sector must be decarbonized in order to meet the goals to minimise the climate change.

A promising way to face these difficulties is the optimization of the building quality to reduce the cooling and heating demand as well as the load in the first place. This optimization includes the correct combination of single measures

10.18086/swc.2023.04.13 Available at http://proceedings.ises.org

for a building in relation to its climate and its use. In the second place, the final energy demand must be supplied in a most efficient and preferably renewable way. A minimization of the non-renewable primary energy consumption and greenhouse gas (GHG) emissions is the target of the technical systems.

The EU funded project Building Energy Efficiency in Nepal (BEEN) takes both of these topics into account, with a greater focus on the building optimization (BEEN 2023). Its target is to establish national guidelines and best communicate practices in Nepal to reduce the GHG emissions for space heating and cooling and to increase the thermal comfort of buildings. Stakeholder groups involve architects, engineers, construction companies, suppliers as well as local municipalities. Nepal has a variety of different climates, from tropical climate with dry season in the border region to India to alpine climates in the Himalayas. This inhomogeneity in climates is a challenge to establish basic guidelines. Thus, individual building studies are required to demonstrate and analyse options to optimize buildings with different backgrounds.

To disseminate and promote the integration of efficient solar solutions for heating and cooling is the fundament of International Energy Agency (IEA) Solar Heating and Cooling (SHC) Task 65.

2. Materials and Methods

2.1. Building energy demand

The focus of this study is the analyses of building energy performance via the Passive House Planning Package (PHPP), developed by the Austrian base Passive House Institute. Two different already existing buildings in two different climate zones with different use are studied and simulated. The building in the warmer climate located in Butwal, Rupandehi district in Nepal, is home the local regional municipality administration with office-use. The other building is a hotel located in Muktinath, Mustang district, sits in a cold climate at 3,760 m elevation. The two buildings are 3D modelled using SketchUp to picture the correct dimensions of the building and the shading effect of the environment, such as neighbouring buildings. Both buildings are optimized in the simulation software to identify measures and their impact on the energy performance.

2.2. Solar system design

The study includes the energy supply analysis via solar energy. The study is based on a monthly approach and solutions for the individual needs. The solar system design partly originates from PHPP solar heating tool. This tool is able to take different solar thermal collectors into consideration. However, this tool is primarily used to receive initial data of monthly solar heat per area, given in kWh/m². Instead, an individual methodology was set up to design the system.

3. Calculation

This chapter provides description of the building models and the simulation boundary conditions of both the building constructions as well as information on the simulation itself.

3.1. Building models

The 3D models are created using SketchUp software with the designPH plug-in. Using this approach, the design and the information of size and number of individual surfaces to picture each building is generated.

The office building in Butwal is characterized by a square ground plot with an also square courtyard. It is surrounded by close standing neighbouring building in the south and trees and area of different use in the north. In the East and West is open space. To consider the shading effect, the neighbouring building is represented as shading surfaces in the model. The characteristics of the façade are also represented in the model to considering the shading effect of overhangs and balconies.

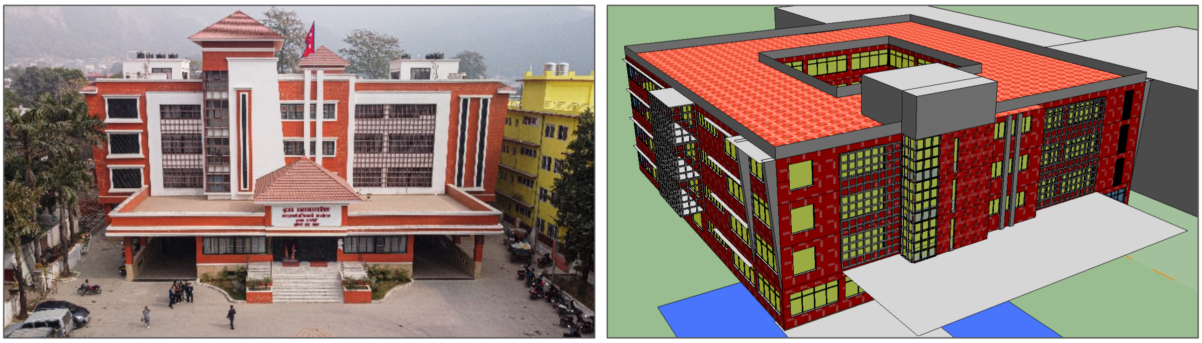

(a) (b)

Figure 1: Comparison of existing building in Butwal (a) and the 3D model (b) representation using SketchUp 2017. Source: (a) (CP Khanal 2023).

The hotel in Muktinath is characterized by its short façade to the street, its relatively narrow ground plan and its stepped roof. The construction based on stone masonry in between RCC pillars is also represented in the model. The open staircase and public place leading to the upper hotel rooms leads to an increase of surface exposed to the ambient. A further characteristic is its closed courtyard with glazed roof. This generates an open space of three levels. On the 3rd floor, there is a closed terrace facing the street with a RCI roof. Figure 2 shows and outside view and an inside view of the existing building and the 3D model in SketchUp.

(a) (b) (c)

Figure 2: External view of the Hotel (a), internal view of the closed courtyard (b) and the 3D model (c) representation using SketchUp 2017.

3.2. Building simulation fundamentals

The building physical characteristics of the buildings are taken from the construction plans and the users. Both buildings are designed in RCC skeleton construction. In Butwal, the wall slabs are filled with bricks and the entire surface is covered with cladding. The wall slabs in Muktinath are different from those in Butwal. Due to the remote location of the site, locally available natural stone masonry is used in the construction on site. In both cases, there is no insulation in the building envelope. A detailed overview of the used construction types and materials can be found in the Appendix.

4. Results

4.1. Building energy demand

The energy demand differs between the two buildings due to their climates and the results are presented are presented for each case separately. The results for base case and the result of combined individual measures are presented for each case.

In the Butwal base case, representing the current state of the building, the sensible cooling energy demand accounts for 190.4 kWh/m²a while the latent cooling energy demand account for 54.6 kWh/m²a. Figure 3 shows the comparison of heat gains which equals in total the sensible cooling energy demand. Additionally, energy is required for dehumidification, pictured in the latent cooling energy demand. This energy is required in the wet season from June to September, whereas sensible cooling energy demand peaks from April to June. The vast majority of heat gains is based on the direct solar heat gains through the windows, followed by internal heat gains. The maximum sensible cooling load in the base case accounts for 61.4 W/m².

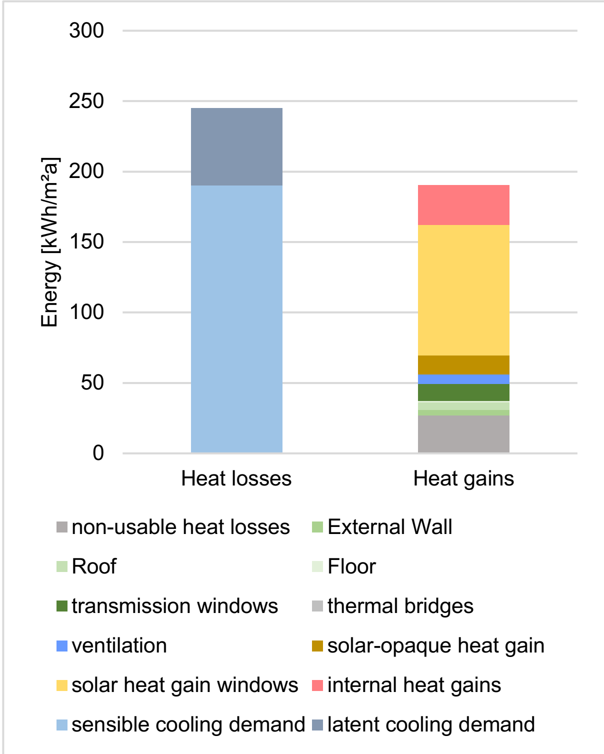

Figure 3: Cooling energy heat balance, comparing sensible cooling energy demand to heat gains.

In total, 28 single measures were implemented individually and assessed based on their impact on the total cooling energy demand. The list includes insulation on wall and roof, window glazing quality, window frame quality, flexible and fixed shading devices, absorption characteristics of the envelope, reduced infiltration and consideration of a ventilation system with heat recovery. The reduction in total cooling energy demand ranges from very little with changes of less than 1% for change in absorption quality in the envelope, over 8-10% due to insulation or window frame improvement to up to about 25% with changes quality of window glazing and reduced direct solar heat gains. Most applied measures cause a reduction of about 7% in total cooling reduction. The measures also differ in addressing only sensible cooling energy demand or both. The reduction in cooling load lies in the same range and shows linear relation to the reduction in cooling energy demand.

The study on combined measures includes 7 steps of single measures. The first step to version A includes a reduction of cooling set-point temperature form 26 °C to 25 °C due to the requirement of PH certification requirements. An improvement in window glazing using an argon filled triple glazing in version B (g-value = 0.35, U_g-value = 0.34 W/m²K) and window frame quality in version C (U_f = 0.64 W/m²K). These two passive measures combined cause a reduction in sensible cooling demand by nearly 100.0 kWh/m²a to version A. In Version D, the external flexible shading elements with a g-value of 0.1 are integrated. This again causes a reduction in sensible cooling demand due to reduced solar energy gains. Version E furthermore considers a 15 cm insulation on both roof and wall. Version E features a reduced sensible cooling demand of 63.7 kWh/m²a and a latent cooling demand of unchanged 54.6 kWh/m²a. Version F includes a reduced infiltration with an improvement of n_{50} from 7 1/h to 0.6 1/h and the final version G regards a central ventilation system with heat recovery of 80%. The combined measures lead to reduction of 66% in total cooling energy demand to a value of 46.2 kWh/m²a for sensible and 10.2 kWh/m²a for latent, achieving the compliance with the passive house requirements which are set at 81 kWh/m²a in total. The maximum cooling load was reduced from 61.6 W/m² to 9.6 W/m².

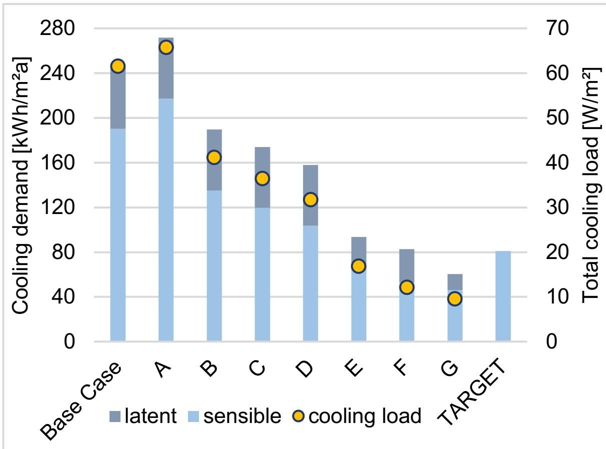

Figure 4: Step-wise reduction of cooling energy demand and load through cumulative integration of optimization measures.

The hotel building in Muktinath, Mustang, is characterized by an envelope of low-insulating properties and an inconsistent thermal separation between in- and outdoors. This results in a poor energy performance of the building and extraordinary high heating demand of 509.6 kWh/m²a. Losses through the building envelope, such as external walls or roofs, make up 84% of the total losses. The external walls alone are responsible for 50% of losses. Heating is required all year, with peaks especially in December and January. The solar gains are quite constant through the year. The building is affected by shading effects from mountains in the East and South and intensely affected by the directly neighbouring building, also located in the East. The greatest losses per area is present in the windows, followed by roof and external walls.

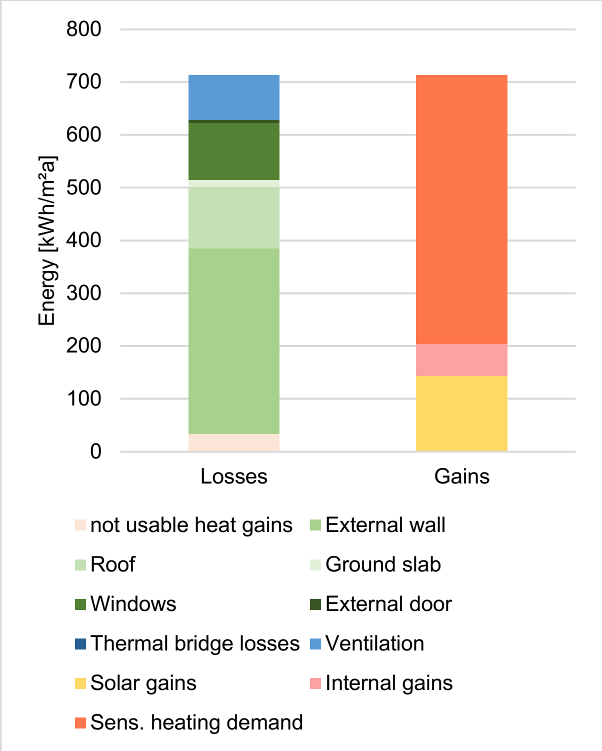

Figure 5: Heating energy balance comparing heat gains and losses of the hotel building in Muktinath, Mustang

An investigation of in total 30 measures revealed that insulation and improvement of window components reduce the heating demand between 8% and 10%. Most impact is identified in insulating the external wall, reducing the cooling demand from 54% (for 5cm insulation) up to 60% (for 20cm insulation). The least impact with a reduction of less than 4% was identified in the single insulation of the CGI roof and the change in window frame quality only. An integration of a central ventilation system with heat recovery between 75% and 90% efficiency brought a heating demand reduction of 4% to 5%.

The hotel is in Mustang offers a wide range in ways to optimize the building. First to mention is the external wall and the CGI roof. A step-wise optimization study is carried out on the hotel building. Figure 6 shows the results of this study presenting the specific annual heating demand and the heating load per version. The base case shows the results as it is. Version A includes an optimization of the insulating the RCC roof, whereas B includes furthermore insulating the CGI roof. In both cases, a 20 cm insulation with $\lambda = 0.03$ W/mK. In version C, the demand and load drop significantly when 20 cm insulation is also applied to the total external wall

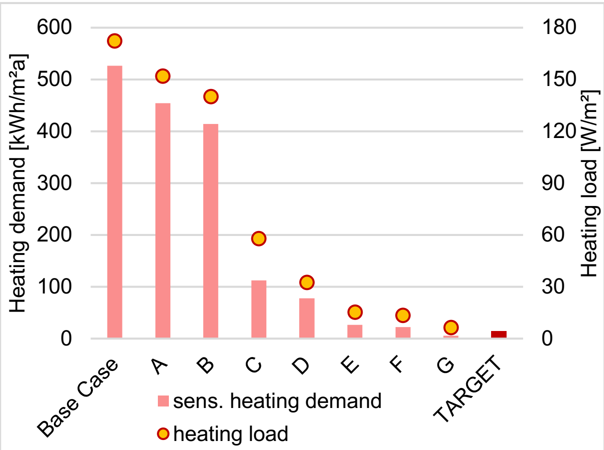

Figure 6: Step-wise reduction of annual heating demand and heating load due to building optimization measures.

4.2. Solar system design

The systems are separately designed for each case. For both cases, the sensible energy demand for both improved cases have been considered. For the basic calculation of solar and collector efficiency, the solar thermal system tool in the PHPP was used. In both cases, installation is considered on the buildings' roofs. Evacuated tube collectors (ETC) are used for solar thermal heat generation.

The office building in Butwal is characterized by highest cooling demand in summer times, from April to September. Figure 7 shows the monthly sum of solar radiation per m² for different slopes of surface facing the equator. A slope of 30° results in highest annual solar radiation of the five presented slopes, accounting for 1,673 kWh/m²a. A low slope results in highest solar radiation in summer times. The shading effect of surrounding mountains in Mustang region affect the solar radiation in winter times, minimizing the difference of solar radiation for different slopes. Considering the peak demand for cooling in summer times, a low slope of 10° is identified as most promising for the application of solar cooling in Butwal.

The hotel building in Muktinath was heat demand for heating purpose as well as for domestic hot water. Thus, the energy demands peaks in winter time and is lowest in summer time. However, the minimum is 19% below monthly average and maximum is 41% above it. This represents a relatively low variation between the monthly heat demands.

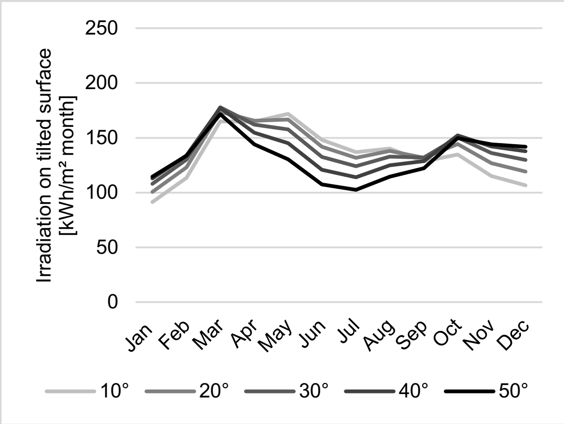

Figure 7: Monthly solar radiation per m² for different slopes of surface for Butwal location.

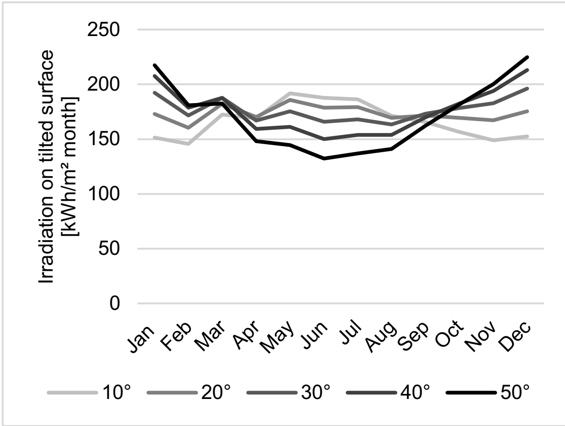

Figure 8: Monthly solar radiation per m² for different slopes of surface for Muktinath location.

A first quick analysis was made using the PHPP solar calculator for DHW. Figure 8 shows the monthly solar radiation per m² in kWh according to the slope of surface, facing the equator. The higher the slope, the is the higher is the solar radiation in from October to March. Thus, a set-up of collectors facing south with a slope of 50° result in most promising the heat demand schedule of the hotel building.

The systems differ in their form of final energy to provide to the user. This study considers following characteristics, as given in Table 1.

Table 1: Boundary conditions for solar thermal heating and cooling systems

Case	Boundary description	Value
Butwal	Shading influence (no shading = 100%)	85%
Muktinath	Shading influence (no shading = 100%)	70%
Both	Solar thermal system efficiency (no losses = 100%)	85%
Both	Heat/ cold dissipation system efficiency (no losses = 100%)	90%
Butwal	Collector outlet temperature	90 °C
Muktinath	Collector outlet temperature	50 °C
Butwal	COP of absorption chiller (constant)	0.65

The system set ups do take into consideration, that the collectors have a shading effect on each other, energy losses already occur on the solar thermal collector side and additionally on the heat respectively cold dissipation side. The effect of shading is different for the cases, as the collectors in Muktinath are more upstanding (50° slope) compared to the ones in Butwal (10° slope). Thus, the collectors in Muktinath suffer from more shading. Furthermore, the collector outlet temperature is different between the two case studies. While at Muktinath, the ETCs must provide heat at 50 °C for DHW and heating purpose, the collectors at Butwal must reach higher temperature. Reason is that an absorption chiller is considered to operate in the warm climate in Butwal to supply cooling to the user. Therefore, heat at 90 °C must be provided to the absorption chiller. It's coefficient of performance (COP) is defined as constantly 0.65. This COP is based on nominal value for absorption chillers (Kohlenbach et al. 2013). The ETC efficiency is varying between the months, taking the thermal losses of the collector to the ambient into account. For Butwal, the efficiency ranges from 10.6% in January to 31.5% in May and June. For Muktinath, the efficiency is higher due to a lower collector outlet temperature. It ranges from 37.5% in January to 44.1% in July.

The collector field is situated at each case on the roof of the building. The total roof area of the Butwal office building accounts for 1,378 m² and the one for the Muktinath hotel building for 207 m². Considering a distance to the roof top of 1 m, around 1,000 m² in Butwal and 110 m² across three roof areas in Muktinath are left. These areas are considered for solar thermal installation.

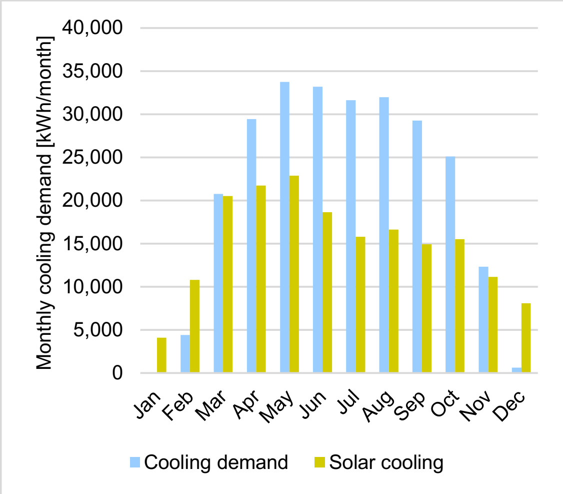

Figure 9: Comparison of monthly sensible cooling demand of the building and monthly generated solar cooling

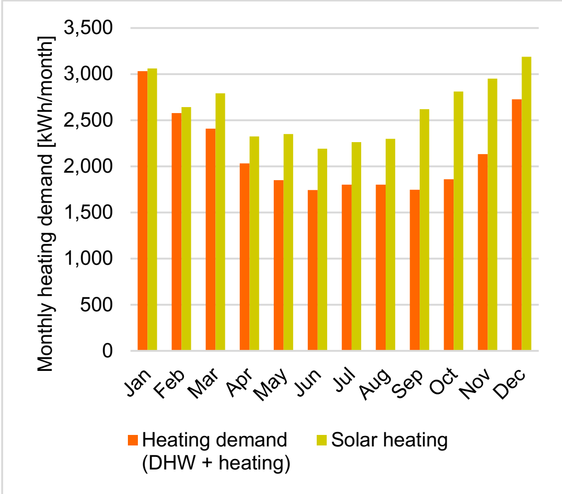

Figure 10: Comparison of monthly heating demand (DHW + space heating) of the hotel in Muktinath and the monthly generated solar heating.

Figure 9 shows the monthly demand in sensible cooling the cooling energy generated through solar cooling system. From November to March the cooling demand by ne fully covered by the solar cooling system. In the months from May to October the demand cannot be fully covered by the solar thermal cooling system only. This requires an additional cooling system to cover the peak loads. However, the annual demand can be covered by 64.5% (not including monthly surplus cooling energy).

The total heating demand of the Muktinath hotel is presented in Figure 10 and compared to the solar heating energy. A solar collector plant of 70 m² is enough to cover the heat demand of the total building throughout the complete year.

5. Conclusion

This study presents the analysis of both building optimization and solar heating and cooling technologies for two differently used buildings in a warm, respectively cold climate. It is demonstrated that through a combination of different measures, that the total cooling demand can be reduced by 75% and the sensible heating demand by 98% and indoor comfort can be increased.

Furthermore, a solar heating/ cooling system located on a building's roof can be provide a majority or even full demand for space cooling, respectively space heating and DHW energy need. A solar cooling with a collector field on the building's roof can cover 70% of the cooling demand in Butwal. The heat demand of the hotel in cold climate can be fully covered with a solar heating system with collectors on the roof. Solar solutions are beneficial at every climate, the system design however must match the demand.

6. Acknowledgement

This research received funding under Building Energy Efficiency in Nepal (BEEN) project by European Commission under the SWITCH-Asia-promoting sustainable consumption and production program, contract number ACA/2021/428-648.

7 Literature

BEEN (2023): Project Homepage. Available at https://been.minergynepal.com/, accessed 31.08.2023.

Bonomolo, M.; Jakob, U.; Neyer, D.; Strobel, M.; Vasta, S. (2023): Integration of Solar Cooling Systems in Buildings in Sunbelt Region: An Overview. In: Buildings, 13 (9), p. 2169. https://doi.org/10.3390/buildings13092169.

Copernicus (2023): Monthly Climate Bulletin. July 2023, the warmest month in Earth's recent history. Available at https://climate.copernicus.eu/july-2023-warmest-month-earths-recent-history, accessed 31.08.2023.

CP Khanal (2023): Pciture: Butwal Sub-Metropolitan city office. Available at https://maps.app.goo.gl/76QkyBnVXBBNceF39, accessed 05.09.2023.

Dean, B.; Dulac, J.; Morgan, T.; Remme, U. (2018): The Future of Cooling. Opportunities for energy-efficient air conditioning. International Energy Agency. Available at www.iea.org.

International Energy Agency (2023): Buildings. Available at https://www.iea.org/energy-system/buildings, accessed 31.08.2023.

Kohlenbach, P.; Besana, F.; Jakob, U.; Luca, M. de; Moser, H.; Podesser, E.; Reinholdt; Lars; Henning, H.-M.; Koller, T.; Eichhorn, A. (2013): Heat driven cooling technologies: closed cycles. In: : Solar cooling handbook. A guide to solar assisted cooling and dehumidification processes. Wien: Ambra V. ISBN: 978-3-99043-438-3, pp. 87–116.

Strobel, M.; Jakob, U.; Streicher, W.; Neyer, D. (2023): Spatial Distribution of Future Demand for Space Cooling Applications and Potential of Solar Thermal Cooling Systems. In: Sustainability, 15 (12), p. 9486. https://doi.org/10.3390/su15129486.

8 Appendix

Table 2: List of abbreviations

Abbreviation	Description
PH	Passive House
PHI	Passive House Institute
PHPP	Passive House Planning Package
RCC	Reinforced Cement Concrete
CGI	Corrugated Galvanized Iron
ETC	Evacuated Tube Collector
DHW	Domestic Hot Water

Table 3: Description of construction types for the office-use building in Butwal, warm climate.

Number	Type	Description (inside to outside)	U-value [W/m²K]
B01	Ext. wall	10 mm brick cladding 13 mm cement plaster 230 mm brick wall 13 mm cement plaster 10 mm wall putty 10 mm brick cladding	1.95
B03	Ext. window glazing	Single glazed window (g-value = 0.83)	5.72
B04	Ext. window frame	50 mm wooden frame	5.0
B05	Ext. roof	150 mm RCC 13 mm screed mortar 10 mm ceramic tiles	3.10

Table 4: Description of construction types for the hotel building in Muktinath, cold climate.

Number	Type	Description (inside to outside)	U-value [W/m²K]
M01	Ext. wall (I)	200 mm stoned masonry 22 mm plaster	3.86
M02	Ext. wall (II)	300 mm RCC	2.78
M03	Ext. window glazing	Single glazed window (g-value = 0.83)	5.72
	Ext. window frame	50 mm wooden frame	5.0
M04	Ext. roof (I)	CGI plate	20.1
M05	Ext. roof (II)	150 mm RCC	1.58

Table 5: Description of simulation boundaries applied to both buildings.

Boundary description	Value
Heating set-point temperature	20 °C
Cooling set-point temperature base case	26 °C
Cooling set-point temperature PH requirements	25 °C
Fresh air requirement	30 m³/hPerson

Comparison of PV and PVT Energy Yield for Low-Temperature Process Heat: a Case Study

Alan Pino[1,2], F. Javier Pino[2], and José Guerra[2]

[1] AICIA - Andalusian Association for Research and Industrial Cooperation, Seville, Spain

[2] Department of Energy Engineering, University of Seville, Seville, Spain

Abstract

Solar energy's integration for industrial decarbonization remains in its early stages. Limited cases of its use in brewing processes are found within medium to large breweries. Brewing, requiring low-temperature heat and cold, suits a solar-assisted polygeneration system well. Unlike larger breweries, microbreweries commonly lack steam boilers, often using gas burners or electric resistors for heat and small vapor-compression chillers for cold. A proposed solution involves a hybrid photovoltaic-thermal (PVT) system preheating brewing water and generating electricity, curbing CO_2 emissions. Research assessed PV and PVT systems' energy output atop a Spanish microbrewery using real load profiles and simulations in TRNSYS. Results indicate the PVT system covering up to 17% to 30% of electric consumption and 20% to 35% of heat demand, for a Central Europe and a Mediterranean location. Notably, the PVT system outperforms PV by 8% to 31% in energy yield, accounting for electricity and useful heat. Despite its energy advantages, the current market conditions render the PVT system less cost-effective than PV systems due to high initial investment and maintenance costs. Recommendations for enhancing its cost-effectiveness are proposed to stimulate further research in this area.

Keywords: SHIP, PVT, microbrewery, solar industrial heat, cogeneration

1. Introduction

Hybrid photovoltaic-thermal (PVT) solar collectors prove advantageous for cogeneration, particularly in situations with limited space, as they occupy less area compared to separate PV and thermal systems. This makes them a viable choice for industries constrained by roof space. Additionally, PVT solar collectors demonstrate the capability to yield higher energy outputs than separated PV and solar thermal systems. Consequently, they emerge as an appealing solution for small-scale industries such as the microbrewery under which require both heat and electricity. However, their operational temperature upper limit for the fluid circuit remains low, typically below 70°C, thus narrowing down their potential applications in contrast to solar thermal collectors. Therefore, therefore it is possible to use the low-grade heat as heat source for heat pumps, what allows higher efficiency and performance (Coca-Ortegón et al., 2023; Herrando et al., 2023). However, the economic assessment it vital to decide if this configuration is cost-effective. On the other hand, the low-grade heat can be used directly to preheat a fluid for an industrial process. Various PVT technologies exist with different cooling approaches, currently at varying stages of development (Ghazy et al., 2022). Among these, flat-plate collector types with water or air as cooling fluids stand as the most prevalent options.

In the last 20 years, the rise of microbreweries, i.e., producing under 5,000 hL annually, has been consistent, indicating ongoing market growth (Garavaglia & Swinnen, 2017). In the US, microbreweries surged from 1,596 in 2009 (Brewers Association, 2015) to 8,895 in 2021 (Brewers Association, 2022). Similarly, in Europe, they grew from 3,020 in 2011 to 8,937 in 2020 (The Brewers of Europe, 2021). Brewing demands high energy, especially in small-scale setups with higher specific energy consumption and increased energy costs. Thus, integrating solar energy seems a cost-effective fit for small breweries and microbreweries.

Roughly fifteen solar heat plants for industrial processes (SHIP) have been established to supply heat to breweries and cider makers (AEE INTEC, 2023). Primarily situated in Central Europe, notably in Germany (Schmitt et al., 2012) and Austria (Mauthner et al., 2014), these plants received partial subsidies. In September

10.18086/swc.2023.04.11 Available at http://proceedings.ises.org

2023, a 30 MWth SHIP plant (the largest of Europe), was inaugurated in Seville, supplying up to 60% of the annual heat demand for the Heineken brewery (Engie España, 2023). However, high upfront and upkeep expenses often deter clients from adopting solar thermal solutions without subsidies. In contrast, breweries, including microbreweries, have installed over 100 photovoltaic (PV) systems due to lower initial costs and simpler maintenance (van der Linden & Wolf, 2019). Likely underreported, the actual number of PV systems in breweries surpasses reported figures. While relatively low compared to total breweries, the inclination towards PV adoption is anticipated to persist. No literature references PVT system integration in breweries.

The present research assesses the energy output of three PVT system sizes in contrasting climates: Malaga, Spain, and Stuttgart, Germany, and compared these results with ones obtained for standard PV systems. A PVT system could potentially decrease heat demands by raising initial water temperatures, cut grid electricity usage through self-generation, and reduce the electric peaks due to use of heat storage (only possible including a thermal storage tank). Employing a TRNSYS simulation model the energy demand and the PVT and PV systems’ energy yield is obtained. Finally, from the results of the energy assessment an economic analysis is performed, considering real energy expenses for these small industries and the market prices of components and installation for system analysis.

2. Methodology

The study's methodology involves simulating the heat, cold, and electricity requirements for brewing, computing the energy needed to meet these demands, evaluating energy generation from PV and PVT systems, and conducting an economic assessment concerning payback periods and return on investment. TRNSYS 18 (Klein et al., 2017) calculates brewing energy needs and models PV/PVT system performance using local weather data, system parameters, and component specifics. In this case recommendations to model and simulate SHIP systems to reduce uncertainty in the results have been taken into account (Cardemil et al., 2022). The economic analysis relies on MS Excel for assessment.

2.1. Base Case and PV and PVT integration

The brewery components' energy interactions are simulated in TRNSYS 18, employing a model validated with a Jerez de la Frontera microbrewery's data (Pino et al., 2023). The case study brewery relies solely on electricity, even for process heat (immersed electric heaters: resistors). The analysis includes two locations: Malaga and Stuttgart (Table 1). The brewery produces 650 L batches three times per week, totaling 1000 hL yearly. Brewing days drive higher energy use; continuous electric demand maintains fermenter and maturer temperatures via an air-water chiller and a 1.3 m^3 cold storage tank. An ACHP system maintains a constant 20°C for beer conditioning throughout the year.

Tab. 1: Main climate characteristics and electric rates for the two locations.

PV	Malaga	Stuttgart
Global Horizontal Irradiation (GHI), kWh/m^2	1832	1088
Direct Normal Irradiation (DNI), kWh/m^2	2001	880
Ambient temperature range, °C	1 to 41	-13 to 32
Average ambient temperature, °C	18	9
Temperature of the water from the, °C	16.7 -28	6.1 - 14
Electricity Price, cent€/kWh (S1/2023)	20.5	29.1

Figure 1 illustrates the yearly energy requirement and electrical usage for the Malaga base case, without solar energy (left). Notably, the most substantial energy usage involves heating water/wort before boiling. The right diagram depicts the hourly electricity demand for one sample week in May. It can be observed the amount of electric energy employed for process heat (for both heating water and boiling) in yellow bars. This causes peaks of electricity demand from the grid.

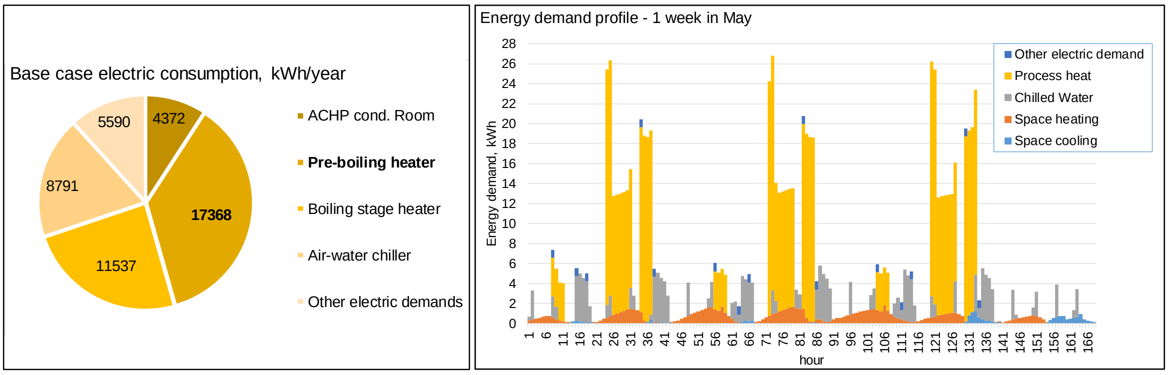

Fig. 1: Base case energy demand (left) and hourly electric consumption for a sample week in May disaggregated by component (right) for Malaga.

2.2. PV and PVT specifications

The proposed PV system aims to connect to the main network using an on-grid inverter to inject excess electricity into the grid. Similarly, the PVT system offers this grid surplus option via an inverter but also integrates a pump, hydronic elements, and a stainless steel thermal storage tank (1.5 m^3 volume, U-value: 0.3 W/m^2K). This tank supplies pre-heated water to the brewing process, a critical ingredient without a return stream. The mains supply the production water, treated to eliminate elements that might impact beer flavors. Figure 2 illustrates the PVT system's integration scheme, with the electric output (yellow) linked to an inverter and the thermal circuit connected to the storage tank (blue: cold water, orange: hot water). It also displays the temperature levels for heat (Qh) and cold (Qc) provided by the various components. The detailed components' specification and performance can be consulted in the simulation tool reference (Pino et al., 2023).

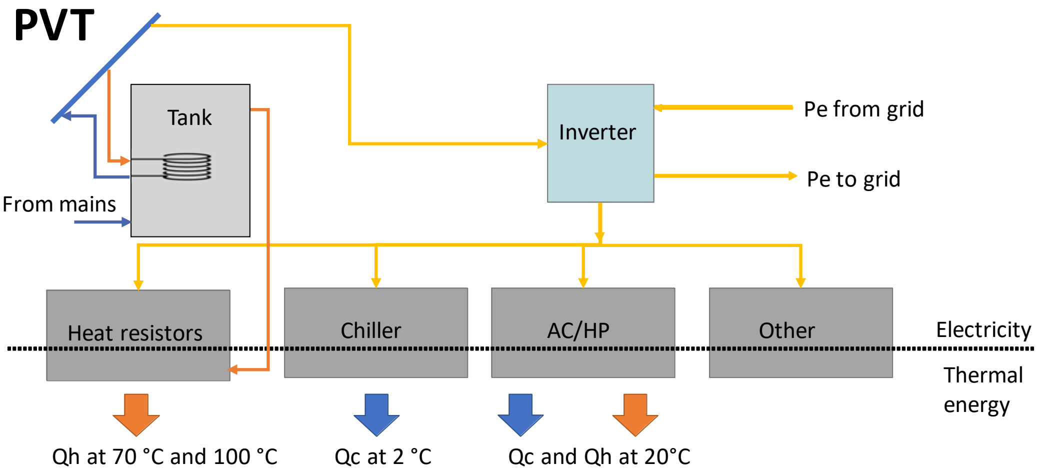

Fig. 2: Schematic diagram of electric and thermal integration of the PVT system in the brewery.

The PV and PVT systems' performance relies on mathematical models within TRNSYS's component library. Type 94a represents the PV module, specifically the Sunrise Solartech SR-M660260, while Type 50 models the PVT module selected for this study: PVT ENDEF390 W. Table 2 details specifications for both modules, with the PVT module having an electric datasheet (Endef Solar Solutions, 2023) and a Solar Keymark certificate for thermal performance (AENOR Internacional S.A.U., 2022). The grid-connected PV inverter is modeled using the Sandia Performance Model (King et al., 2007).

Tab. 2: Specifications for selected PV and PVT modules.

Parameter	PV	PVT	Unit
Nominal power (Pmax)	260	390	Wp
Nominal voltage (Vmp)	30.4	38.5	V
Maximum current (Imax)	8.6	10.13	A
Open-circuit voltage (Voc)	37.4	46.3	V
Short-circuit current (Isc)	9.2	10.87	A
Module efficiency	16.02	19.9	%
Power temperature coefficient	-0.495	-0.27	%/K
Gross area	1.623	1.96	m2
Flow rate for testing	-	0.023	Kg/(sm^2)
a0	-	0.36	-
a1	-	8.71	W/(m^{2}K)
a2	-	0.048	W/(m^{2}K^2)
IAM (50°)	-	0.84	-
Standard stagnation temperature	-	79	°C

2.3. Energy price and system costs

In Spain and Germany, the electricity that regulated users observe in their billing receipt is separated into a fixed term and a variable term. The fixed term represents mainly the cost for the contracted power, whilst the variable term represents the cost of the energy consumed. Since under the scope of this study the contracted power is not varied, only the variable term will vary with self-generated electricity. In addition, a net-billing scheme where the energy injected to the grid is payed as 40% of the energy purchased from the grid is assumed. The electricity rates employed in this study are 0.205 €/kWh for Spain (energigreen, 2023) and 0.291 €/kWh for Germany (Destatis, n.d.), based on the average electric price for regulated user in the small-scale industry (>15 kW contracted power and <50 MWh annual consumption) for the first semester.

Prices for the PV and PVT systems' components were gathered from benchmark sources [16] and direct supplier quotes in Spain. Table 3 presents the detailed costs utilized in this analysis. To facilitate comparison, the PV cost per unit capacity (€/Wp) is a common format, similarly applied to specify the PVT values. The Balance of the System (BoS) for the PVT setup encompasses the pump, pipes, expansion tank, and electric components.

Tab. 3: Specific cost of the PV and PVT components.

	Item	Specific cost	Unit
Photovoltaic (PV)	PV Module	0.4	€/W_{DC}
	Inverter	0.2	€/W_{DC}
	BoS equipment	0.2	€/W_{DC}
	Installation labor	0.3	€/W_{DC}
	Total PV system cost	**1.1**	**€/W_{DC}**
Photovoltaic-thermal (PVT)	PVT Module	0.82	€/W_{DC}
	Inverter	0.2	€/W_{DC}
	BoS equipment (elec. + hydraulic)	1.33	€/W_{DC}
	Installation labor	0.7	€/W_{DC}
	Total PVT system cost	**3.05**	**€/W_{DC}**
	Storage tank with HX	2000	€/m^3

Hence, the calculated total costs for the proposed systems stand between 5,500 € for the 5 kWp PV system and 16,500 € for the 15 kWp version. As for the complete PVT system, encompassing the 1.5 m^3 thermal storage, the total cost ranges between 18,259 € for the 5 kWp and 48,778 € for the 15 kWp size. The study assumes a 3% discount rate over a 25-year period.

3. Results and discussion

The simulation results show promising solar energy yields. As expected, due to the higher solar resource in Malaga, the energy yield for Malaga is higher than for Stuttgart, in all comparable configurations studied (e.g., 5 kW PV in Malaga vs 5 kW PV in Stuttgart). In addition, PVT systems provide added valuable heat, reducing initial brewing heat needs, when compared with a PV system of the same size at the same location. Table 4 details energy values (electricity and thermal) for both locations and the six systems studied (three PV, three PVT). Assessing total useful energy (electricity + heat), in Malaga a 5 kW PVT system outperforms a regular PV by 29%, while in Stuttgart, it is 31% higher. For a 15 kWp PVT system, Malaga yields 11% more than regular PV, and Stuttgart shows an 8% increase.

Tab. 4: Annual energy figures for the PV and PVT systems in both locations.

<table>
<tr><th rowspan="2"></th><th colspan="9">Annual energy values, kWh</th></tr>
<tr><th>Pre-boiling heat</th><th>Boiling heat</th><th>Total Heat</th><th>Total elect. consum-ption</th><th>PV genera-tion</th><th>PV electricity self-consumed</th><th>PV elect. sold</th><th>Useful heat from tank</th><th>Total solar energy (elec. + heat)</th></tr>
<tr><td colspan="10">Malaga</td></tr>
<tr><td>Base case</td><td rowspan="4">17368</td><td rowspan="7">11537</td><td rowspan="4">28905</td><td rowspan="4">47656</td><td>0</td><td>0</td><td>0</td><td>0</td><td>0</td></tr>
<tr><td>PV 5 kW</td><td>9381</td><td>7889</td><td>1492</td><td>0</td><td>9381</td></tr>
<tr><td>PV 10 kW</td><td>18761</td><td>11686</td><td>7075</td><td>0</td><td>18761</td></tr>
<tr><td>PV 15 kW</td><td>28142</td><td>13643</td><td>14499</td><td>0</td><td>28143</td></tr>
<tr><td>PVT 5 kW</td><td>14223</td><td>25760</td><td>44512</td><td>8839</td><td>7480</td><td>1359</td><td>3231</td><td>12069</td></tr>
<tr><td>PVT 10 kW</td><td>13431</td><td>24969</td><td>43725</td><td>17727</td><td>11072</td><td>6655</td><td>4042</td><td>21769</td></tr>
<tr><td>PVT 15 kW</td><td>12943</td><td>24481</td><td>43241</td><td>26640</td><td>12860</td><td>13779</td><td>4543</td><td>31183</td></tr>
<tr><td colspan="10">Stuttgart</td></tr>
<tr><td>Base case</td><td rowspan="4">20967</td><td rowspan="7">11555</td><td rowspan="4">32523</td><td rowspan="4">59596</td><td>0</td><td>0</td><td>0</td><td>0</td><td>0</td></tr>
<tr><td>PV 5 kW</td><td>5661</td><td>5068</td><td>593</td><td>0</td><td>5661</td></tr>
<tr><td>PV 10 kW</td><td>11323</td><td>8480</td><td>2843</td><td>0</td><td>11323</td></tr>
<tr><td>PV 15 kW</td><td>16984</td><td>10832</td><td>6152</td><td>0</td><td>16984</td></tr>
<tr><td>PVT 5 kW</td><td>18522</td><td>30077</td><td>57153</td><td>4920</td><td>4430</td><td>490</td><td>2512</td><td>7432</td></tr>
<tr><td>PVT 10 kW</td><td>17913</td><td>29468</td><td>56544</td><td>9865</td><td>7467</td><td>2398</td><td>3137</td><td>13002</td></tr>
<tr><td>PVT 15 kW</td><td>17557</td><td>29112</td><td>56187</td><td>14824</td><td>9587</td><td>5237</td><td>3502</td><td>18326</td></tr>
</table>

Considering the self-consumed electricity and not the net-billing valued, the PVT system covers between 17% and 30% of the total electric demand in Malaga, depending on the size. For Stuttgart this ranges vary from 8% to 17%. In the case of heat demand, 23% to 35% can be cover with the PVT in Malaga, and between 14% and 20% in Stuttgart. These results infer that the 15 kW PVT system is oversized for the demand. Stuttgart's lower PV generation is partially compensated the PVT system's enhanced yield due to lower mains water temperatures, boosting solar thermal efficiency. For instance, when comparing a 5 kW PVT system in Malaga and in Stuttgart (Table 5), the former yield 80% more electricity than the latter, but only a 29% more useful heat, regardless that the annual GHI is 68% higher in Malaga than in Stuttgart.

Tab. 5: Comparison of PVT electric and heat performance for a 5 kW system in Malaga and Stuttgart.

Annual GHI ratio	PV generation ratio	Useful heat from tank ratio
$\frac{GHI_{Malaga}}{GHI_{Stuttgart}} = \frac{1832}{1088} = 1.68$	$\frac{PVgen_{Malaga,5kW}}{PVgen_{Stuttgart,5kW}} = \frac{8839}{4920} = 1.80$	$\frac{Qu_{Malaga,5kW}}{Qu_{Stuttgart,5kW}} = \frac{3231}{2512} = 1.29$

When the economic figures are analyzed, the findings appear less favorable for PVT. The substantial investment in the PVT system, notably in the BoS, labor, and the thermal storage tank, renders it less cost-efficient than a regular PV system, under the economic parameters assumed in this assessment. Figure 3 illustrates the cumulated cash flow for both PV and PVT systems with capacities of 5 kWp, 10 kWp, and 15 kWp for Malaga (left) and Stuttgart (right). In all cases the PV systems prove profitable for both locations, with low payback periods (under 5 years). The similarity between the results of Malaga and Stuttgart is caused by the lower solar radiation in Stuttgart is nearly compensated by the higher electricity rates than in Malaga (0.291 vs 0.205 €/kWh, respectively). Moreover, the higher investment in PVT systems leads to higher payback periods, ranging from 12 to 20 years for the 5 kW and15 kW systems in Malaga, respectively. In Stuttgart the payback periods are slightly longer, 14 years for the 5 kW system and 22 years for the 15 kW system. Regarding net present value (NPV) for PV the largest system will lead to the higher profit in both location, whilst for PVT system the two smaller systems (5 and 10 kW) will lead to the higher profit. Nevertheless, when comparing same-sizes PV and PVT systems for each location, the PV system will always offer higher NPV than the PVT.

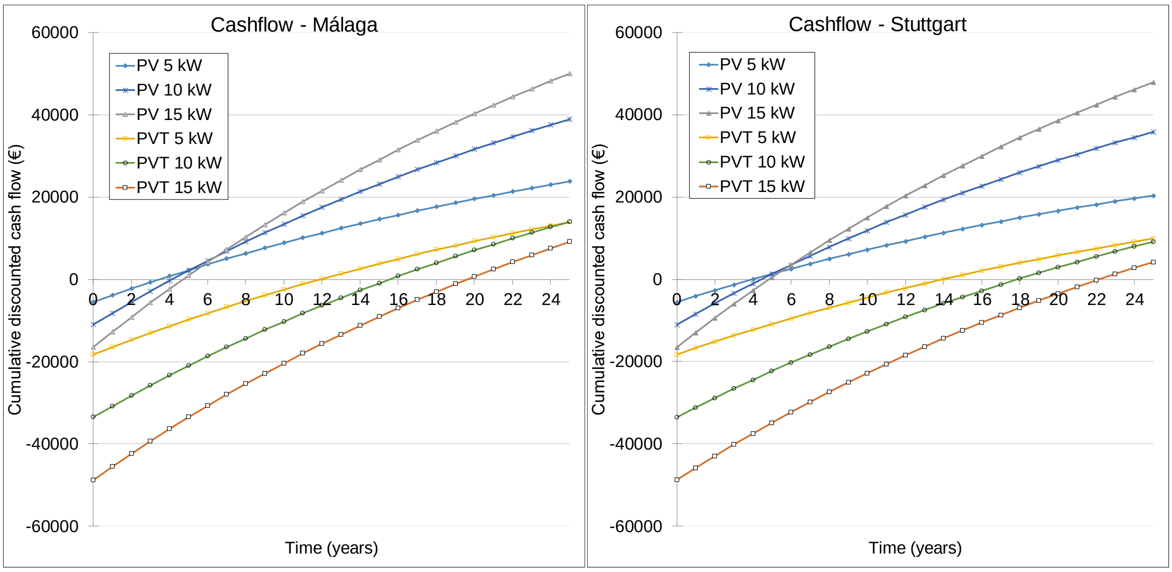

Fig. 3: Cumulated cash flows for the different PV and PVT systems in Malaga and Stuttgart.

4. Conclusions

The comprehensive yield of PVT systems, comprising heat and electricity, surpasses the electricity output of PV systems of comparable sizes. The 5 kWp PVT system yields 29% more in Malaga and 31% more in Stuttgart compared to PV. Similarly, the 10 kWp PVT system outperforms PV by 16% in Malaga and 15% in Stuttgart; while the 15 kWp PVT system outperforms PV by 11% in Malaga and 8% in Stuttgart. Therefore, it is recommended to avoid oversizing the PVT system, especially with a load profile highly variable as in batch processes, since the thermal energy benefits over regular PV are decreasing with larger systems due to lower utilization of the heat. Further sensitivity studies should be performed with different thermal storage sizes. When only electric generation is considered, the PVT model selected performs worse than the PV of same size due to the higher operation temperature, which impacts in the cell efficiency.

The drawback of PVT systems lies in their high investment and operation/maintenance costs. The initial investment for PVT, excluding thermal storage, is nearly three times that of a standard PV system. Normalizing by electric capacity reveals a cost of 1.1 €/kWp for PV versus 3.05 €/kWp for PVT. Operation and maintenance costs for PVT systems significantly impact economic analyses due to movable components (e.g., pumps) and hydronic elements.

Economic analysis shows PVT systems in Malaga and Stuttgart lead to lower long-term profit (NPV) and higher payback period that a regular PV of comparable size. A conclusion in this regard is that, although having energy storage behind-the-meter reduces the grid stress by clipping load peaks, under the current electric market conditions it adds no economic value for the user. Manufacturers and developers should focus on reducing additional balance of system costs to foster PVT system proliferation despite advanced technology and contained module costs.

Future research aims to explore alternative hydraulic integration schemes for PVT systems to cut costs in thermal storage and hydronics. In addition, collaboration with actual breweries is vital to understand their requirements due to material restrictions for food and beverage production. Finally, implementing active control of PV-generated energy, especially with electric or thermal storage, could optimize system economic performance by leveraging time-of-use electric rates.

5. Acknowledgements

The authors would like to thank ENDEF for providing economic and performance data of their PVT collectors.

6. References

AEE INTEC. (2023). *Solar Heat for Industrial Processes (SHIP) Plants Database*. http://ship-plants.info/

AENOR Internacional S.A.U. (2022). *Solar Keymark Certificate - ECOVOLT HiE-S395VG* (Issue 1).

Brewers Association. (2015, March). *2014 Craft Beer Data Infographic*. https://www.brewersassociation.org /association-news/2014-craft-beer-data-infographic/

Brewers Association. (2022). *Annual Report 2021*. https://www.brewersassociation.org/annual-report-2021/

Cardemil, J. M., Calderón-vásquez, I., Pino, A., Starke, A., Wolde, I., Felbol, C., L Lemos, L. F., Bonini, V., Arias, I., Iñigo-labairu, J., Dersch, J., & Escobar, R. (2022). Assessing the Uncertainties of Simulation Approaches for Solar Thermal Systems Coupled to Industrial Processes. *Energies*, *15*(9), 3333.

Coca-Ortegón, A., Simón-Allué, R., Guedea, I., Brun, G., & Villén, R. (2023). *Operational performance of trigeneration PVT-assisted HP system*. https://doi.org/10.1016/j.enbuild.2023.113383

Destatis. (n.d.). *(German) Statistisches Bundesamt Deutschland - GENESIS-Online: Ergebnis 61243-0005*. Retrieved November 15, 2023, from https://www-genesis.destatis.de/genesis/online?sequenz=tabelleErgebnis &selectionname=61243-0005&language=de#abreadcrumb

Endef Solar Solutions. (2023). *ecovolt datasheet*. https://endef.com/wp-content/uploads/2021/07/ecovolt-390W-ficha-tecnica.pdf

energigreen. (2023). *Oferta Electricidad*. https://ofertaelectricidad.energigreen.com/ofertaelectricidad

Engie España. (2023). *(Spanish) Heineken y Engie apuestan por la energía solar térmica*. https://www.engie.es/heineken-construccion-primera-planta-termosolar-de-la-industria-espanola/

Garavaglia, C., & Swinnen, J. (2017). Economic perspectives on craft beer: A revolution in the global beer industry. In *Economic Perspectives on Craft Beer: A Revolution in the Global Beer Industry*.

Ghazy, M., Ibrahim, E. M. M., Mohamed, A. S. A., & Askalany, A. A. (2022). Cooling technologies for enhancing photovoltaic–thermal (PVT) performance: a state of the art. In *International Journal of Energy and Environmental Engineering* (Vol. 13, Issue 4). Springer Berlin Heidelberg.

Herrando, M., Coca-Ortegón, A., Guedea, I., & Fueyo, N. (2023). *Experimental validation of a solar system based on hybrid photovoltaic-thermal collectors and a reversible heat pump for the energy provision in non-residential buildings*. https://doi.org/10.1016/j.rser.2023.113233

King, D. L., Gonzalez, S., Galbraith, G. M., & Boyson, W. E. (2007). *SANDIA REPORT Performance Model* *for Grid-Connected Photovoltaic Inverters*. http://www.ntis.gov/help/ordermethods.asp?loc=7-4-0#online

Klein, S. A., Beckman, A., Mitchell, W., & Duffie, A. (2017). *TRNSYS 18: A Transient System Simulation Program* (No. 18). Solar Energy Laboratory, University of Wisconsin. http://sel.me.wisc.edu/trnsys

Mauthner, F., Hubmann, M., Brunner, C., & Fink, C. (2014). Manufacture of malt and beer with low temperature solar process heat. *Energy Procedia*, *48*, 1188–1193.

Pino, A., Pino, F. J., & Guerra, J. (2023). Integration of solar energy in Small-scale Industries: Application to microbreweries. *Sustainable Energy Technologies and Assessments*, *57*, 103276. https://doi.org /10.1016/j.seta.2023.103276

Schmitt, B., Lauterbach, C., Dittmar, M., & Vajen, K. (2012). Guideline for the utilization of solar heat in breweries. *Proceedings Eurosun Rijeka, Kroatien*, 8.

The Brewers of Europe. (2021). *European Beer Trends: Statistic Report - 2020 Edition*.

van der Linden, T., & Wolf, A. (2019). *Top 100 Solar-Powered Beer Breweries*. Solarplaza International BV. https://www.solarplaza.com/channels/top-10s/12072/top-100-solar-powered-beer-breweries/

Control sequence prioritising ceiling fan operation over air conditioners using machine learning for thermal comfort

Amanda Thounajam[1], Manis Kumar Konsam[1], Prasad Vaidya[1], Gopikrishna A[1], Uthej Dalavai[1], and Yashima Jain[2]

1. Indian Institute for Human Settlements, Bangalore (India)
2. Lawrence Berkeley National Laboratory, Berkeley (USA)

Abstract

This paper proposes and tests the implementation of a sustainable cooling approach that uses a machine learning model to predict operative temperatures, and an automated control sequence that prioritises ceiling fans over air conditioners. The robustness of the machine learning model (MLM) is tested by comparing its prediction with that of a straight-line model (SLM) using the metrics of Mean Bias Error (MBE) and Root Mean Squared Error (RMSE). This comparison is done across several rooms to see how each prediction method performs when the conditions are different from those of the original room where the model was trained. A control sequence has been developed where the MLM's prediction of Operative Temperature (OT) is used to adjust the adaptive thermal comfort band for increased air speed delivered by the ceiling fans to maintain acceptable OT. This control sequence is tested over a two-week period in two different buildings by comparing it with a constant air temperature setpoint (24ºC).

Analysis of the data showed that the MLM is more consistent with lower errors than the SLM across a variety of rooms. Compared to the constant air temperature setpoint control, the OT control sequence showed improved comfort reported by 70 occupants in the study and a cooling electrical energy savings of over 90% during the test conditions.

Keywords: sustainable cooling, ceiling fans, adaptative comfort, air speed, machine learning, AI, control sequence

1. Introduction

Per capita annual electricity consumption for space cooling in India is only at 69 kWh compared to the global average of 272 kWh (IEA, 2018). With global warming, rising temperatures will increase India's cooling energy requirement and more people will need access to cooling. The India Cooling Action Plan calls for synergistic actions to provide sustainable space cooling that is affordable. Much of the new construction is planned for air-conditioning (AC) and the existing building stock is increasingly retrofitted with AC systems. India thus has a large stock of buildings that are operated in spatial or temporal mixed mode (Brager, G., 2006). Mixed mode buildings present a significant opportunity for energy savings while providing exceptional levels of comfort to occupants (Angelopoulos, C., Cook, M., Spentzou, E., & Shukla, Y., 2018). "Mixed mode" in space conditioning blends natural ventilation from operable windows with mechanical systems for air distribution and cooling, optimizing natural ventilation during periods of the day or year when it is feasible or desirable (Brager & Borgeson, 2007). The adaptive comfort model for mixed mode operation can be a promising approach to the cooling energy challenge. However, adaptive models use indoor operative temperature (OT), which requires the measurement of air temperature, air velocity, and globe temperature in a space. Collecting real-time and long-term data for these is difficult. On a previous work we showed a method that uses machine learning to predict operative temperature with minimum measurement equipment (De, A., Thounaojam, A., Vaidya, P., Sinha, D., & Raveendran, S. M., 2020). While that work demonstrated that the RMSE of prediction of OT was less than 0.09ºC, the testing was limited to the room that the MLM was trained on. To use this approach for developing a control sequence that can be used more widely, it is important that the MLM provides acceptable prediction of OT across a range of rooms. This paper tests the MLM in the following ways:

The OT prediction of the MLM is compared with that of a SLM in 3 additional rooms that have different thermal characteristics.

The OT prediction of the MLM is tested further to see if training the MLM in a specific room with different thermal condition improves its prediction.

Then, the MLM approach is used to develop a control sequence for the India Model or Adaptive Comfort (IMAC).

10.18086/swc.2023.04.16 Available at http://proceedings.ises.org

Using the IMAC and the Corrective Power of ceiling fans, the control sequence prioritises ceiling fan operation over AC. to minimise or eliminate the use of ACs and reduce energy consumption. The control sequence is tested in two different rooms; one, in a passively designed building with an insulated envelope, and another, in a typical uninsulated building, tested for these conditions:

- Base case of 24°C (AC set-point suggested by the Bureau of Energy Efficiency, India) with no ceiling fans operating.
- Ceiling fan prioritised control sequence

The aim of this research is to provide energy efficient and comfortable cooling while maintaining thermal comfort of the occupants. We demonstrate the robustness of the MLM, and we summarise the development, implementation and testing a control sequence, which prioritizes the use of ceiling fans over ACs. We use fan and AC products available in the market.

The significant contributions of this work are to demonstrate that OT predicted in real time with ML can be used in a control sequence that automates the prioritisation of ceiling fans, and that in tropical conditions such as those prevailing in India, occupants report higher levels of comfort with ceiling-fan induced air movement and higher temperature set points. The findings of this study point to a method of space cooling that takes full advantage of the IMAC and can be an affordable and sustainable cooling approach.

2. Literature Review

Earlier standards of thermal comfort were formed around static thermal comfort models that were applied universally, but they relied on air conditioning to maintain thermal comfort of occupants (de Dear, & Brager, 1997). A location specific adaptive comfort model for India, which includes the building's ventilation type (naturally ventilated, AC, or mixed mode) was developed by Manu et al., to help in maintaining thermal comfort of occupants but also helps in reducing energy consumption (de Dear, et. al., 2016 and ASHRAE, 2017). It allows buildings to operate within a broader range of indoor operative temperatures.

ASHRAE Standard 55 included an elevated air speed comfort zone method, which allows us to define limits for comfort for indoor operative temperature for increased air speed in the space, when other parameters like met value and clo value are held constant. In the 2017 version of the ASHRAE Standard 55, the upper limit of airspeed was increased to 1.6 m/s. Angelopoulos et al., (2018) used a simulation approach to assess a variety of control algorithms and showed that mixed mode controls with adaptive comfort models provide flexibility of use, improved thermal comfort, and energy savings of about 40% in Indian cities.

Another study by Fanger and Toftum (2002) showed that occupants in warmer countries who have adapted to high temperatures prefer warmer temperatures, especially in naturally ventilated buildings where the outdoor temperature has significant influence on the indoor comfort parameter. Candido & de Dear (2012), also state that occupants who feel hot prefer more air movement, while Zhai et al. (2017) concluded that the provision of air movement is more important than temperature control in such warm environments.

Ceiling fans are an efficient adaptive comfort strategy to induce air movement, improve comfort, and have a corrective power index (CP) of -1K to -7K, when the air speed is as high as 1 m/s and the ambient temperature is as high as 33°C (Zhang, Arens, & Zhai, 2015). Corrective power is defined by ASHRAE 55 as the ability of a PCS to correct the thermal sensation of a person towards comfort zone. It is expressed as the difference in operative temperatures between two instances, where equal thermal sensation is achieved, one with PCS and one without PCS (ASHRAE, 2020). Raftery, Miller, & Zhang, (2020) and Raftery et. al., (2021) conducted a thermal comfort study in California showed a CP of over 4ºK in 10 buildings with air conditioners, where ceiling fans with air movement provided comfort at 26.7°C while only air conditioning provided comfort at 22.2°C. In another study conducted in the tropics, ceiling fans provided comfort up to 27°C, but if given a preference the occupants preferred to have minimal air conditioning along with the ceiling fans to attain comfort (Lipczynska, Schiavon, & Graham, 2018). A study by Bongers et al., (2022) in Australia also found that use of ceiling fans can increase the temperature limit at which the air conditioning needs to be switched on. The study reports annual energy savings up to 76%. A thermal comfort tool by the Center for Built Environment (CBE) shows that the upper limit of the comfort model shifts further upwards in response to increased airspeed in the space (Tartarini, Schiavon, Cheung, & Hoyt, 2020). In our earlier work, we used the tool to obtain the upward shift for several conditions and developed an equation to apply the effect of air speed on the IMAC band (De et. al., 2020).

3. Methodology

3.1 Developing the Machine Learning Model (MLM)

As described in De 2022, for a 400 m^2 building in Bangalore, with a naturally ventilated room that houses workstations, a calibrated thermal model was developed. The model was then used to develop 10 scenarios consisting of different building characteristics and building operations. The simulations of these 10 scenarios provided 87,600 data points for hourly results consisting on outdoor conditions, indoor air temperature, indoor humidity, and indoor OT. Using a train-test ratio of 0.75-0.25 (75% data used for training and 25% data used for testing), a random forest algorithm was trained to give a machine learning model (MLM) that predicted OT based on a combination of indoor air temperature and outdoor conditions that could be measured by a weather station.

3.2 Testing the robustness of the MLM

While this MLM predicted OT with errors (RMSE and MBE) in an acceptable range for the workstation room (Room 1), we needed to test the robustness of the MLM to predict OT for other rooms with different thermal characteristics. If the MLM predicted the OT for other rooms with errors in acceptable ranges, the model would be considered robust. The ASHRAE method for low airspeed uses a simple average of the indoor air temperature (Ta) and the mean radiant temperature (MRT) to calculate OT, which is essentially a linear relationship between Ta and OT (ASHRAE, 2017). Using the data for Room1, we developed a straight line model (SLM) for Room1 where a linear equation predicted the OT based on the Ta. Prediction errors were compared between the SLM and the MLM across 3 additional rooms (Rooms 2, 3, and 4). See Table 1 for a summary of the differences between Rooms 1, 2, 3, and 4. All rooms are located in Bangalore.

Table 1: Summary of differences in rooms used for testing

Item/Room	Room 1	Room 2	Room 3	Room 4
MLM Training	Trained in this room	Non trained in this room	Non trained in this room	Non trained in this room
Room Function	Offices	Offices	Offices	Conference
Room Area (m^2)	35	30	18	17
Building Type	Office, passive design	Office, business-as-usual design	Office, business-as-usual design	Office, business-as-usual design
Floor	Ground Floor	First Floor	Second Floor	Third Floor
Wall construction and U value (W/m^2K)	Rammed earth wall with 50 mm insulation and stone cladding 0.54	Uninsulated brick wall with plaster 2.4	Uninsulated brick wall with plaster 2.4	Uninsulated brick wall with plaster 2.4
Windows facing	West	South	North and East	North
WWR (%)	27	53	41	18
Exterior shading	Overhangs	Trees only	None	Overhangs
Window U value (W/m^2K)	2.68	4.4	4.4	4.4
Internal loads (W/m^2)	35	9.2	5.8	12.5

Figure 1: Images of Rooms 1, 2, 3, and 4, clockwise from top left.

3.3 Developing and testing of the control sequence for ceiling fan prioritisation

Two conference room spaces in Bangalore were selected for the study. One was in a passively designed, insulated office building, and the other was in a business-as-usual, uninsulated office building. Both rooms had split AC units and were operated in mixed mode. Brushless direct current (BLDC) smart fans were installed in both rooms. Indoor environmental quality (IEQ) boxes were installed in both rooms to collect air temperature and relative humidity data. Outdoor weather parameters are collected with a weather station on the buildings. Energy meters were installed to collect energy consumption data for the AC and the ceiling fans. Infrared (IR) blasters were installed to control the ceiling fans and the AC units. See figure 2.

Figure 2. Images of the hardware installed in each room (a) BLDC ceiling fan, (b) IEQ box, (c)IR blaster, (d) energy meters.

The control sequence uses the IMAC for determining the thermal comfort band. Based on the National Building Code 2016, Volume 2, the 90% acceptability range for mixed-mode buildings band is calculated as

$$IMAC\_upper = ((0.28 \text{ x outdoor temperature}) + 17.87) + 3.46 \quad \text{(eq. 1)}$$

$$IMAC\_lower = ((0.28 \text{ x outdoor temperature}) + 17.87) - 3.46 \quad \text{(eq. 2)}$$

Where IMAC_upper, and IMAC_lower are the upper and lower limits respectively, of the thermal comfort band. *The IMAC_upper is used as the threshold for determining comfort.*

The OT prediction ML model runs every minute using the data from the IEQ box and the weather station. The predicted OT is compared with the upper limit of the thermal comfort band. To determine the upward shift of the upper limit of the band when air speed is introduced as a variable in the space, we use the equation determined by De et al., (2022)

$$y = -1.39x^2 + 4.92x - 1.38 \quad \text{(eq. 3)}$$

Where y is the shift in the upper limit of the band (OT) and x is the air velocity.

Average of the air speeds measured where the users are seated in the space is noted as the spatial average air speed of the space. The air speed at each user's location is also measured at the heights of 0.6 m and 1.1 m from the floor level (Gao et. al., 2017). This gave us pre-calculated the airspeeds achieved for each fan speed setting in the room. The shift of the extended upper limit (extended_IMAC_upper) of the comfort band is calculated using the airspeed achieved at each setting and equation 3 (also see figure 3).

- If the predicted OT is lower than IMAC_upper, the control sequence keeps the ceiling fan and AC off.
- If the predicted OT is higher than IMAC_upper, but lower than the extended_IMAC_upper, the control sequence turns on the ceiling fan to the appropriate airpspeed but keeps the AC off.
- If the predicted OT is higher than the extended_IMAC_upper for the highest fan speed setting, the fan is switched on at the highest speed to use its full potential and the AC is switched on with the highest set-point possible. This setpoint is calculated in the following steps:
  1. By using the OT formula from ISO 7726-1998, MRT in the space was calculated by using the predicted OT value.

$$T_{mrt} = \left[\frac{(T_g+273.15)^4+1.1\times10^8\times V_a^{0.6}}{e\times D^{0.4}(T_g-T_a)}\right]^{0.25} - 273.15 \qquad \text{(eq. 4)}$$

$[Where\ T_{mrt} = mean\ radiant\ temperature,\ T_g = globe\ temperature,\ \ V_a = air\ velocity, D = diameter\ of\ the\ black\ ball\ (0.04m\ for\ ping\ pong - ball), T_a = air\ temperature,\ \ e = emissivity\ (0.95\ for\ black - globe)]$

$$T_o = \frac{T_a(\sqrt{10V_a})+T_{mrt}}{(1+\sqrt{10V_a})} \qquad \text{(eq. 5)}$$

$[Where\ T_o = operative\ temperature, T_{mrt} = mean\ radiant\ temperature,\ T_g = globe\ temperature,\ \ V_a = air\ velocity,, T_a = air\ temperature\ ]$

  2. Then the air temperature in the space is calculated using the same formula since MRT and the desired OT values are known.

$$T_a = \frac{T_o(1+\sqrt{10V_a})-T_{mrt}}{(\sqrt{10V_a})} \qquad \text{(eq. 6)}$$

  3. The calculated air temperature is sent as set-point temperature to the AC.

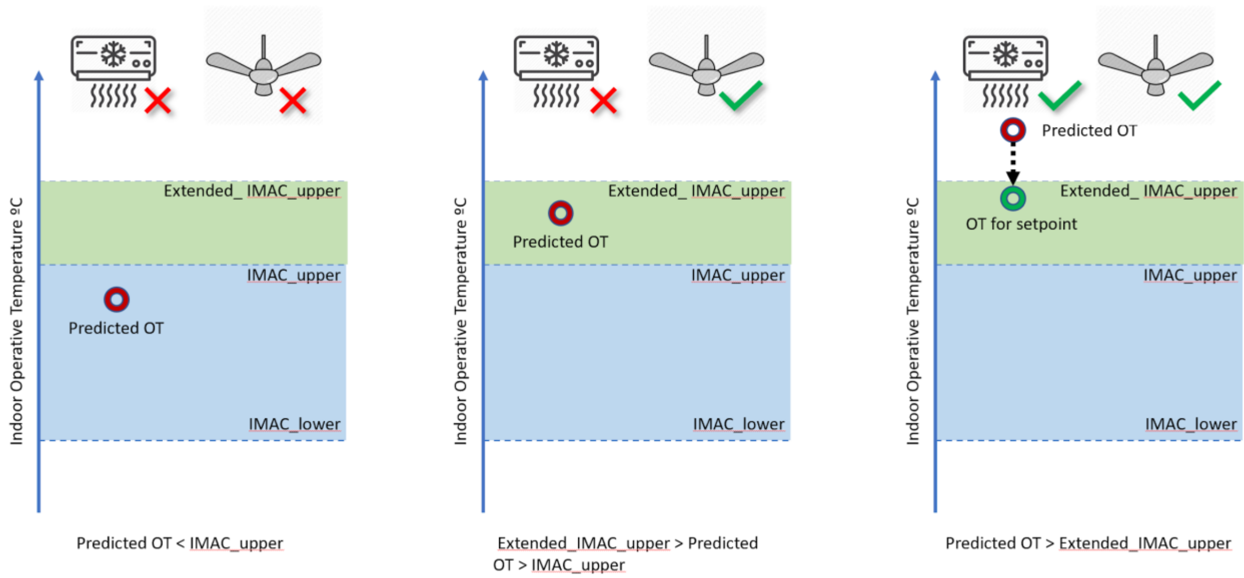

Figure 3: Three scenarios for the control sequence

For the thermal comfort study and energy testing, a total of 70 respondents participated in the study. Data was collected about age, gender, height, and weight, history of their space cooling adaptations and preferences, recent physical activity and documentation of the clothing that they were wearing.

The respondents were exposed to 3 different conditions for 30 minutes each, with 5 minute break outside the test room between the 3 conditions. The conditions were: condition 1 - room maintained at a constant 24ºC setpoint without ceiling fans; condition 2 - room maintained at IMAC band neutral temperature without ceiling fans, and; condition 3 - room comfort maintained using the proposed control sequence. The study was carried out between 14th March, and 28th of March. Energy used by the air conditioners and ceiling fans was recorded by the meters.

Figure 4: Thermal comfort study in progress

4. Results

4.1 Developing the Machine Learning Model (MLM)

The testing of the Machine Learning algorithm to predict OT for a seven-day period with hourly data resulted in an RMSE = 4% and MBE = 3%. The accuracy was found to be 96.77 %.

4.2 Testing the robustness of the MLM

The SLM based on the data of Room 1 yielded the following results with its equation (see figure 5).

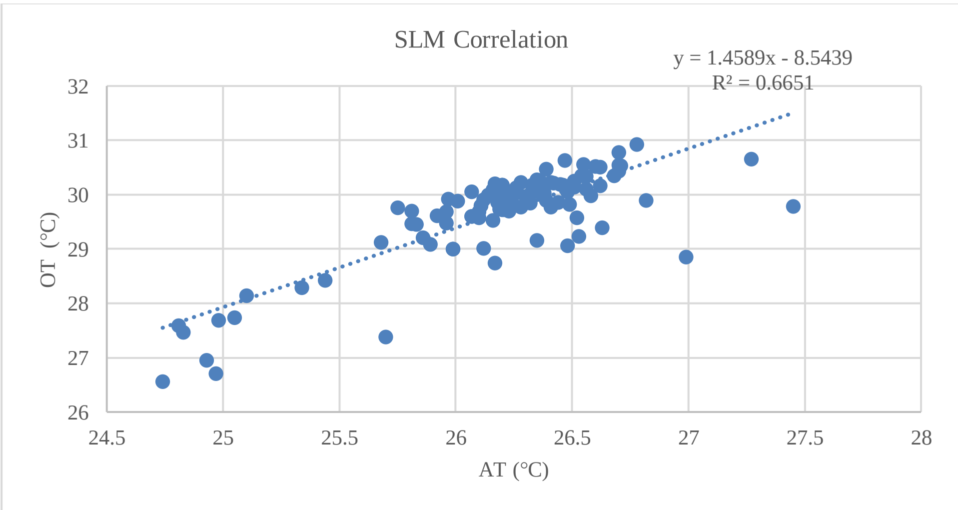

Figure 5: Straight Line Method correlation between OT and AT

Figure 6 shows the comparison of the SLM with the MLM for Room 1, where both models were trained. For this room, the SLM has lower error than the MLM with an RMSE = 1% and MBE = 1%.

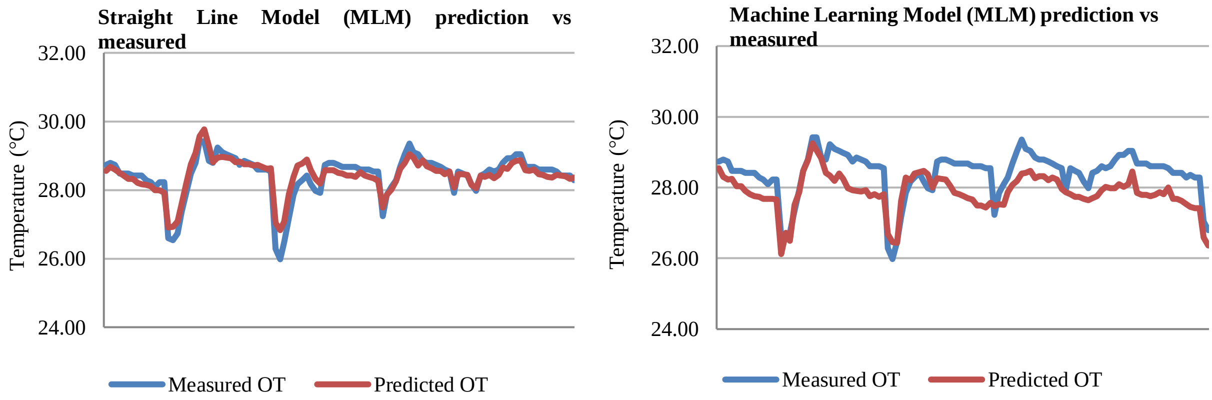

Figure 6: Predicted OT, comparison between SLM and MLM

However, when the errors are compared for the SLM and MLM across rooms 1, 2, 3, and 4 (see figure 7), we can see that the MLM although trained on Room1, provides consistently low errors compared to the SLM. Both the MBE and the RMSE increase significantly for Rooms 2 and 3.

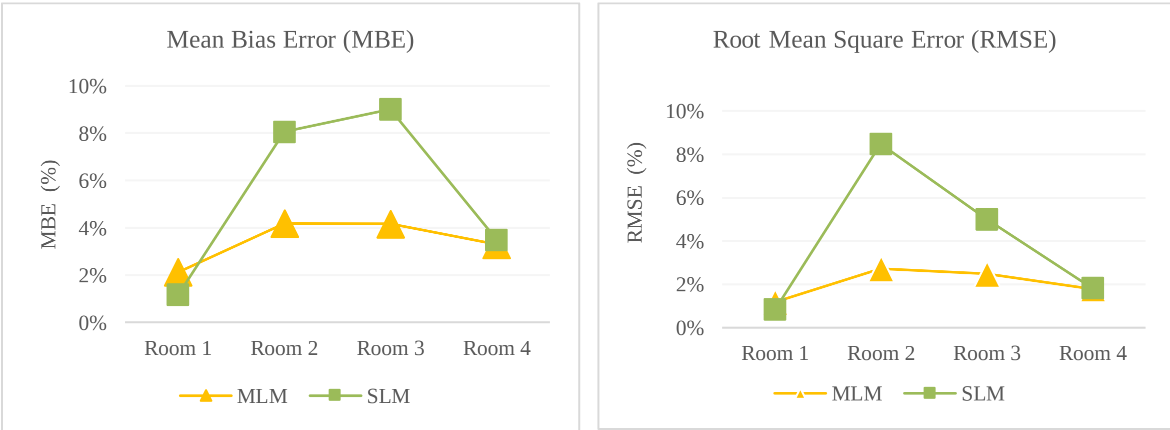

Figure 7: MBE and RMSE comparison between SLM and MLM for different rooms

Knowing that the MLM was more robust for predicting OT in rooms that it was not trained in, it was also important to see how much improvement the MLM prediction would have, if it were custom trained for a room. Figure 8, shows that the RMSE improves from 3% (non-custom trained) to 1% (custom trained), while the MBE improves from 4% (non-custom trained) to 2% (custom trained), a reduction by 2 percentage points on each error metric.

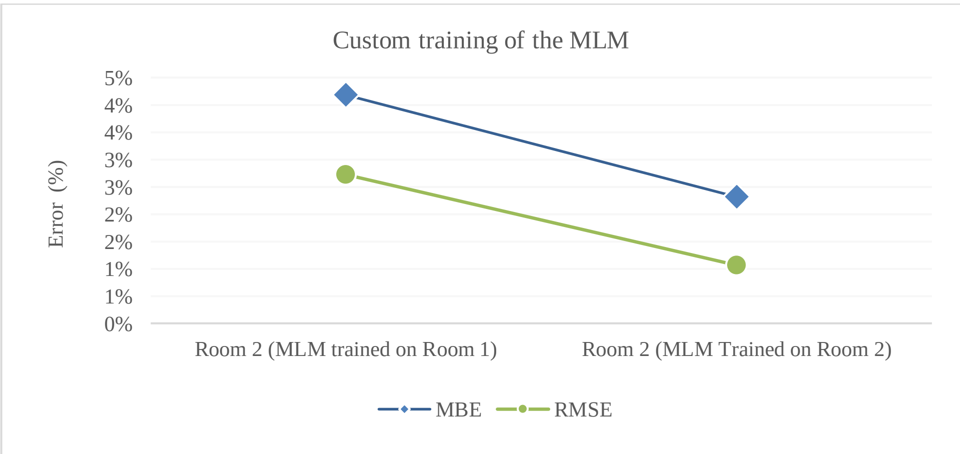

Figure 8: Impact of training the MLM on individual room (custom training)

4.3 Developing and testing of the control sequence for ceiling fan prioritisation

About 60% of the respondents were in the age group of 20 to 39 years and the gender ratio was almost equal. Most of the respondents were involved in sedentary activities before their sessions in the study. 98% of the respondents answered that they use ceiling fans for space conditioning in their residence, followed by operable windows and usage of curtains/blinds. But in their workplaces ceiling fans were used by 68% of the participants, operable windows and air conditioners were used by about 49% of the participants. As a method for space conditioning, ceiling fans were preferred by 49%, operable windows by 35%, and ACs preferred by only 15% of the respondents.

During the two-week testing of the control sequence, the outdoor dry bulb temperature was in the range of 29 °C to 35°C. During the study period, the IMAC neutral temperature setpoint was calculated at 24ºC. This resulted in identical setpoints for condition 1 and condition 2, and the results for thermal comfort and energy for those conditions are very similar. Therefore, the thermal comfort and energy analyses results below only show condition 1 and condition 3.

About 77% of the respondents reported being comfortable in condition 3, i.e. fan prioritized control sequence condition compared to about 69% in the other condition of the study (see figure 9, left hand graph).

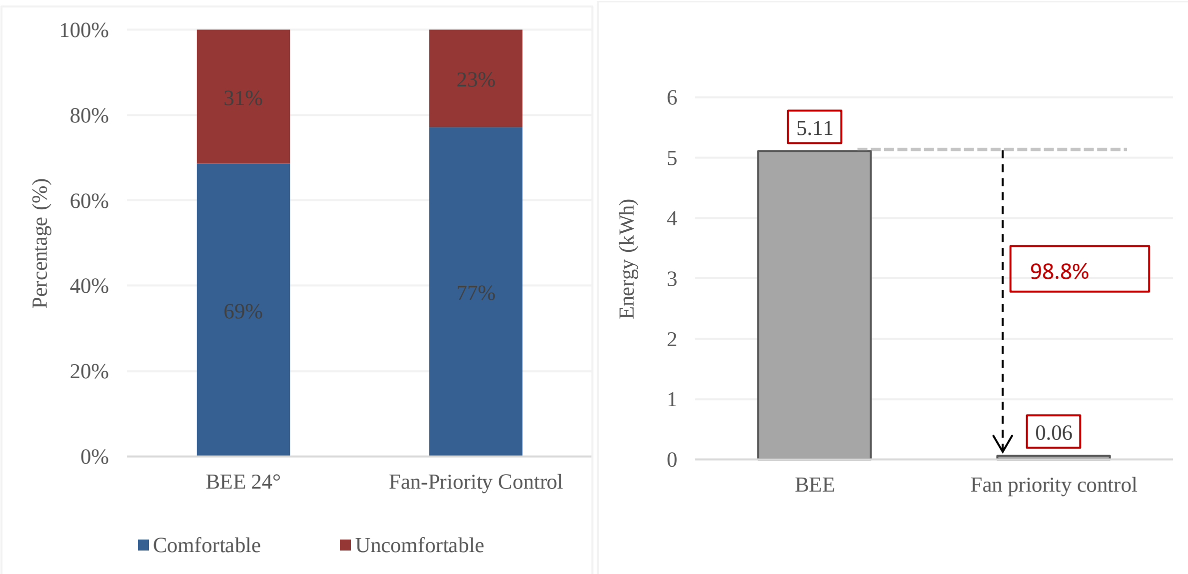

Figure 9: Results of thermal comfort left (left) and energy measurements (right) during the testing of the control sequence

The respondents were also asked whether the airspeeds they experienced were acceptable to them. When the ceiling fan was off, 83% found this unacceptable. Since the fans did not come on at settings of 1, 2 and 6 (FS1,FS 2, FS6) during the study, the data on these are not available. The airspeed of 0.4 m/s was acceptable to 89% of the respondents. The acceptability decreases when the air speed is 0.53 m/s and 0.65 m/s (see figure 10).

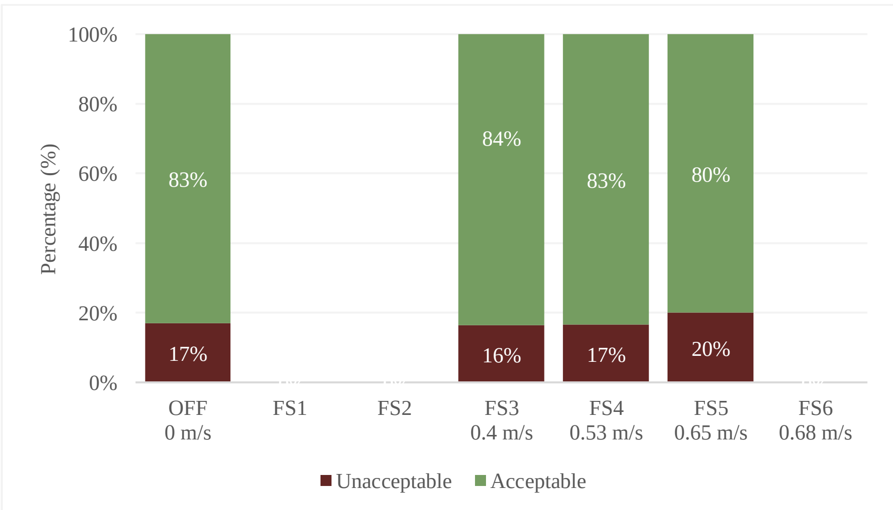

Figure 10: Results of fan-speed setting preference survey during the testing of the control sequence

Electrical Energy consumption for each scenario was determined by calculating the difference in electrical energy meter readings at the beginning and end of the respective scenario. It is observed that under the BEE 24°C baseline, a total of 5.11 kWh was consumed across all sessions, whereas the fan prioritized control sequence showed a consumption of 0.06 kWh, resulting in 98.8% reduction in cooling energy usage (refer to figure 9, right-hand graph). It is important to note that the outdoor dry bulb temperature ranged between 29°C and 34°C during the study. According to the thermal comfort survey that was done (refer to Figure 10), there was a decrease of 1% in unacceptable preference when transitioning from fan mode OFF to Fan mode ON at Fan-speed setting 3 (FS3), and an increase of 4% from Fan-speed setting 3 (FS3) to Fan-speed setting 5 (FS5). Due to this small incremental difference in unacceptable fan-speed setting preference, it is inconclusive to determine whether increasing fan-speed settings makes people more uncomfortable.

In the room in the business-as-usual (BAU) building, cooling energy savings were at 98.6%, while in the passively designed building, savings were 100%. The 100% savings in the passive building can be attributed to the fact that due tot he passive features, the indoor temperature generally remained within the comfort range. In the rare instances when it exceeded this range, it never went above the extended_IMAC_upper. As a result, the ceiling fan was activated only on a few occasions, and the AC unit remained unused in this building. The low energy consumption of the BLDC fans was not recorded in the passive building because of the least count display of the energy meters.

In the BAU building, although the outdoor temperature often exceeded the IMAC_upper, it generally remained below the extended_IMAC_upper. This led to frequent activation of the ceiling fans. Throughout the study in the BAU building, the air conditioner was turned on for a total of only 5 minutes during condition 3. During that event the AC setpoint was 30ºC. Consequently, the energy savings during this 5-minute interval, compared to the BEE 24ºC condition, reached 82%. This demonstrates the significant potential for energy savings with a ceiling fan prioritized control sequence. It is important that this approach is further tested under conditions with higher outdoor temperatures, where the AC is likely to be used more frequently.

5. Conclusion

This paper demonstrates the use of a machine learning model (MLM) for predicting operative temperature as a scalable approach to providing comfort based on the adaptive model of the National Building Code of India. The analysis has shown that the MLM is robust enough to predict temperatures in rooms that the model was not trained in. The MLM does this consistently with low errors compared to a straight line (correlation) model (SLM) across a range of rooms varying in thermal characteristics. While custom training on the MLM for a specific room reduced the RMSE and MB by 2 percentage points, a custom training approach is not scalable.

In this study, a control sequence was developed that employs the corrective power of ceiling fans to adjust the upper threshold of the adaptive thermal comfort band, taking into consideration the airspeed of the fan to raise the AC temperature set-point within the room. The control sequence places a priority on utilizing ceiling fans and was tested in two conference rooms in 2 different buildings. The results of the testing reveal that 77% of the respondents reported feeling comfortable in the space when the fan-prioritized control sequence was employed, as opposed to only 69% for the constant setpoint of 24ºC. Additionally, the fan-prioritized control sequence achieved 98.8% reduction in cooling energy consumption during the study period, even in the face of outdoor temperatures ranging from 29ºC to 34ºC.

These substantial cooling energy savings, coupled with the observation that ceiling fans were sufficient to provide comfort without the use of air conditioners on multiple occasions throughout the study, underscore the potential of ceiling fan-prioritized controls, or even just ceiling fans for cooling, as a pathway to affordable and sustainable cooling.

The key contributions of this study are:

- While existing controls are mostly based on air temperature because OT is difficult to measure in real time, this work uses a novel method to predict OT in a space and uses ceiling fans as an affordable cooling solution, resulting in significant cooling energy savings.
- While most studies performed on ceiling fans focus on giving control to occupants, this work automates the fan and AC controls with increased air speeds to make this approach appropriate for office and institutional buildings.

6. References

Angelopoulos, C., Cook, M., Spentzou, E., & Shukla, Y. (2018). Energy saving potential of different setpoint control algorithms in mixed-mode buildings.

ASHRAE. (2020). ANSI/ASHRAE Standard 55-2020. *ASHRAE Standards*. www.ashrae.org

ASHRAE. (2017). ANSI/ASHRAE Standard 55-2017. ASHRAE Standards. www.ashrae.org

Brager, G., & Borgeson, S. (2007). Summary Report: Control Strategies For Mixed-Mode Buildings. www.cbe.berkeley.edu

Bongers, C., Jay, O., Capon, A., Perkins Centre, C., McBain, A. B., Rey-Lescure, O., Jay, O., Malik, A., Bongers, C., McBain, B., Rey-Lescure, O., de Dear, R., Capon, A., & Lenzen, M. (2022). The potential for indoor fans to change air conditioning use while maintaining human thermal comfort during hot weather: an analysis of energy demand and associated greenhouse gas emissions. In Articles Lancet Planet Health. www.thelancet.com/

Brager, G. (2006). Mixed-mode cooling. UC Berkeley: Center for the Built Environment. Retrieved from https://escholarship.org/uc/item/3bb8x7b8

Candido, C., & de Dear, R. (2012). From thermal boredom to thermal pleasure: a brief literature review. Ambiente Construído, 12(1), 81–90. https://doi.org/10.1590/s1678-86212012000100006

De, A., Thounaojam, A., Vaidya, P., Sinha, D., & Raveendran, S. M. (2020). Predicting Operative Temperature with Machine Learning.

de Dear, R., & Brager, G. S. (1997). Developing an Adaptive Model of Thermal Comfort and Preference-Final Report on RP-884. Challenging lease agreements in Australia: quantifying the effects of higher temperature set points on offices workers' productivity and thermal comfort. View project comfortA-A better understanding of thermal Alliesthesia and thermal Adaptation for correctly predicting dynamic thermal comfort View project. In Macquarie Research Ltd., Center for Environmental Design Research. https://www.researchgate.net/publication/269097185

Fanger, P. O., & Toftum, J. (2002). Extension of the PMV model to non-air-conditioned buildings in warm climates. Energy and Buildings.

Gao, Y., Zhang, H., Arens, E., Present, E., Ning, B., Zhai, Y., Pantelic, J., Luo, M., Zhao, L., Raftery, P., & Liu, S. (2017). Ceiling fan air speeds around desks and office partitions. Building and Environment, 124, 412–440. https://doi.org/10.1016/j.buildenv.2017.08.029

IEA. (2018). World Energy Outlook 2018. International Energy Agency. www.iea.org/weo

Lipczynska, A., Schiavon, S., & Graham, L. T. (2018). Thermal comfort and self-reported productivity in an office with ceiling fans in the tropics. Building and Environment, 135, 202–212. https://doi.org/10.1016/j.buildenv.2018.03.013

Manu, S., Shukla, Y., Rawal, R., Thomas, L. E., & de Dear, R. (2016). Field studies of thermal comfort across multiple climate zones for the subcontinent: India Model for Adaptive Comfort (IMAC). Building and Environment, 98, 55–70. https://doi.org/10.1016/j.buildenv.2015.12.019

Miller, D., Raftery, P., Nakajima, M., Salo, S., Graham, L. T., Peffer, T., Delgado, M., Zhang, H., Brager, G., Douglass-Jaimes, D., Paliaga, G., Cohn, S., Greene, M., & Brooks, A. (2021). Cooling energy savings and occupant feedback in a two year retrofit evaluation of 99 automated ceiling fans staged with air conditioning. Energy and Buildings, 251. https://doi.org/10.1016/j.enbuild.2021.111319

Ozone Cell Ministry of Environment, "INDIA COOLING ACTION PLAN," MOEFCC, 2019.

Raftery, P., Miller, D., & Zhang, H. (2020). UC Berkeley Indoor Environmental Quality (IEQ) Title Integrating Smart Ceiling Fans and Communicating Thermostats to Provide Energy-Efficient Comfort Permalink https://escholarship.org/uc/item/91z0m3xw Publication Date. In Open Access Journals from the University of California. https://escholarship.org/uc/item/91z0m3xw

Tartarini, F., Schiavon, S., Cheung, T., & Hoyt, T. (2020). CBE Thermal Comfort Tool: Online tool for thermal comfort calculations and visualizations. SoftwareX, 12. https://doi.org/10.1016/j.softx.2020.100563

Zhai, Y., Arens, E., Elsworth, K., & Zhang, H. (2017). Selecting Air Speeds for Cooling at Sedentary and Non-Sedentary Office Activity Levels. Building and Environment. http://www.elsevier.com/open-access/userlicense/1.0/

Zhang, H., Arens, E., & Zhai, Y. (2015). A review of the corrective power of personal comfort systems in non-neutral ambient environments. Building and Environment, 91, 15–41. https://doi.org/10.1016/j.buildenv.2015.03.013

Experiences from the first short-term pit thermal energy storage

Ioannis Sifnaios and Adam R. Jensen

Department of Civil and Mechanical Engineering, Technical University of Denmark, Kgs. Lyngby (Denmark)

Abstract

Pit thermal energy storage (PTES) is a promising low-cost storage technology used in connection with district heating. PTES systems have historically been coupled with solar district heating systems and used as seasonal heat storage. However, in January 2023, the first PTES operating as short-term heat storage started operating in Høje Taastrup, Denmark. Unlike existing PTES, this storage is not connected to a solar heating system but directly to the district heating grid and has a storage cycle of around two weeks. This paper presents lessons learned and the first results from the construction and operation of the Høje Taastrup PTES.

Keywords: heat storage, large-scale energy storage, district heating, PTES

1. Introduction

The pit thermal energy storage (PTES) technology has been developed and demonstrated in combination with large solar collector fields in Denmark (Soerensen and From, 2011). In principle, a PTES is a large water reservoir lined with a watertight polymer liner (to prevent water from leaking to the ground) and covered with a floating insulating lid (to reduce heat losses). The PTES technology's main benefit is its simplicity and low material usage, which has enabled construction costs below 27 €/m^3 (Schmidt et al., 2018). However, since PTES is not yet a mature technology, the storage efficiencies of the existing systems range from 60% to 90% (Sifnaios et al., 2023a). So far, PTES systems have only been used for seasonal heat storage, enabling district heating networks to achieve solar fractions higher than 40% (Sveinbjörnsson et al., 2017).

In 2023, the first PTES used for short-term heat storage started operation in Høje Taastrup, Denmark. The pre-feasibility study showed that the optimal operation of the PTES was as a short-term heat storage (storage duration 1-2 weeks) and not as a traditional seasonal storage. Unlike the existing PTES systems, the PTES in Høje Taastrup is charged directly from the district heating network and is not connected to a solar thermal collector field. This way, various heat sources can be used to charge the storage, adding a large degree of flexibility to the district heating system. For example, in times of surplus renewable electricity, heat pumps or electric boilers can be used to charge the storage, and the heat can then be discharged at a later point. The storage also enables more optimal operation of combined heat and power (CHP) plants and utilization of larger amounts of waste heat.

Due to the short-term storage operation, the top water layer of the PTES will, in practice, have an almost constant temperature of 90 °C. However, the polymer liners used in the existing storages could not be guaranteed for such conditions. For this reason, a new liner was developed and installed, which can withstand temperatures of 95 °C for 50 years. This paper presents experiences from the construction stages and initial results from the operation of the PTES in Høje Taastrup.

2. The storage construction

The construction of the PTES in Høje Taastrup started in April 2020 and was completed in December 2022. Typically, the construction period is approximately one year; however, a crack in the liner in February 2021, believed to be caused by the freezing ambient conditions, delayed the construction.

The storage volume is 70,000 m^3, and the operating temperatures are approximately 45 – 90 °C. Fig. 1 shows photos from the start of the excavation and the liner installation. It should be noted that in the image showing the liner installation, the geotextile can also be identified (bright, white-colored liner), which is placed under the bottom liner and provides drainage and cushioning to the liner. Fig. 2 shows the installation of the diffusers and the final lid installation. Note that the black liner in Fig. 2 covering the PTES is a protective liner placed

10.18086/swc.2023.04.12 Available at http://proceedings.ises.org

on the PTES during the water-filling phase to prevent dirt from entering the PTES and minimize corrosion. It should also be mentioned that this is the first PTES where the diffusers were placed close to the edge of the storage. Traditionally, the diffusers were located in the middle of the PTES. However, placing them at one end of the storage makes the installation easier and cheaper since less piping is required.

Fig. 1: Excavation (left) and liner installation (right).

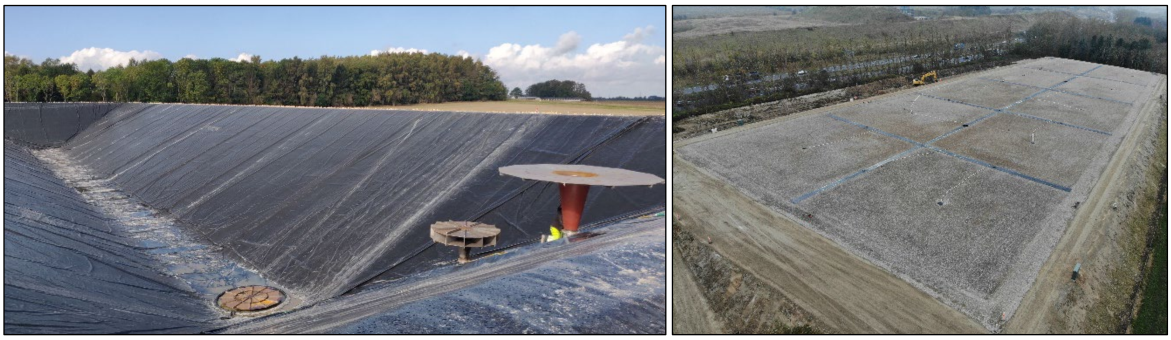

Fig. 2: Diffuser installation (left) and completed lid (right).

2.1. Liner

The liner is an essential part of the PTES since it prevents water from leaking into the ground. Additionally, a liner is installed between the top water surface and the floating insulation lid to prevent water from entering the lid. Commercial PTES have so far all used polymer liners. Specifically in Denmark, all existing PTES have been constructed with a welded high-density polyethylene (HDPE) liner to ensure water tightness. The main reason for choosing polymer liners is their low cost and easy installation (Sifnaios, 2023).

The main drawback of polymer liners is that they degrade when exposed to high temperatures, thus limiting the storage's lifetime. Additionally, polymer liners are not completely water-tight; therefore, some water diffuses into the ground and lid construction.

For the PTES in Høje Taastrup, a new 2.5 mm thick polypropylene (PP) liner was used, which is expected to last 50 years at a temperature of 95 °C. Apart from the longer lifetime, the PP liner was approximately 120,000 € cheaper compared to HDPE alternatives and equally easy to install and weld. The PP liner was found to have approximately four times higher water permeability compared to the HDPE alternatives; however, this was not considered a problem (at least for the sides and bottom of the storage).

Unfortunately, the installed PP liner cracked in February 2021 during the water-filling of the PTES. This incident was a result of the following reasons:

- there was low ambient temperature (below freezing), which made the PP liner brittle
- wooden rods were used to hold the protective liner in place, and in some cases, they had pierced through the PP liner on the embankment
- the weight of the water created extra tension on the PP liner

After inspection, it was decided that the liner was irreparable. Thus, the PTES was emptied of water, and the PP liner was replaced with an improved version, which included additives to withstand temperatures below freezing. In the past, liner manufacturers focused on developing materials that could withstand high temperatures; however, this incident revealed the need for liners to withstand low temperatures.

2.2. Lid construction

The floating insulating lid is the only component that minimizes heat losses to the ambient and is the most expensive component of the PTES. Flexible insulation materials are usually used in lid constructions for the lid to be able to bend due to the thermal expansion of the water.

So far, two different insulation materials have been used, namely Nomalén (NMC Termonova, 2011) and Light Expanded Clay Aggregate (LECA). Nomalén insulation is sold as mats made of cross-linked polyethylene foam, while LECA is small, expanded clay pebbles. Nomalén has been used in the PTES in Marstal and Dronninglund, whereas LECA has been used in Gram, Vojens, and Toftlund (Sifnaios et al., 2021).

Although seasonal PTES connected to solar thermal plants are considered to have a technology readiness level (TRL) of 8, there are still issues related to the lid that have a significant impact on their performance and lifetime, such as:

- degradation of the insulation performance due to exposure to high temperatures and moisture for long periods
- difficulty in removing rainwater from the lid's surface

To overcome these challenges, the company Aalborg CSP has developed a new modular lid (see Fig. 3), with an expected lifetime of a minimum of 25 years (Aalborg CSP, 2020). This lid has been installed in the Høje Taastrup PTES and in Marstal and Dronninglund. Different types of insulation with varying insulating properties and temperature resistance were used to ensure the lid's durability at high temperatures. A high-temperature resistant version of Nomalén was placed close to the storage water surface, and an extruded polystyrene insulation (XPS) was placed on top. Additionally, the lid was divided into multiple modules for more efficient rainwater handling (see Fig. 2). A slope was created towards the center of each module using varying levels of pebbles, and a pump was located at the center to remove the rainwater.

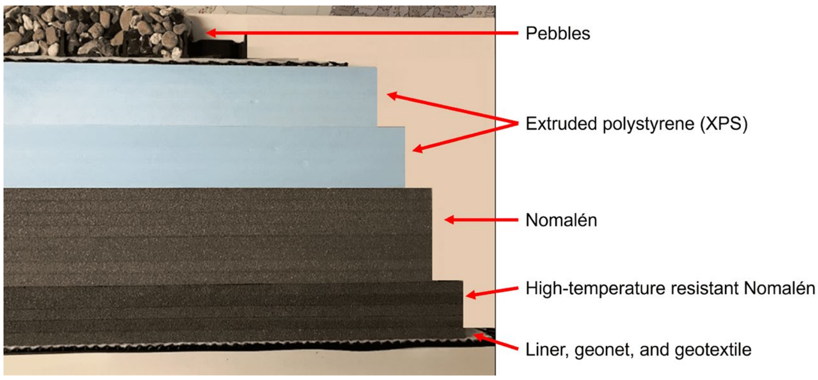

Fig. 3: The new version of the Nomalén lid used in Dronninglund, Marstal, and Høje Taastrup, constructed by the company Aalborg CSP (Sifnaios, 2023).

3. Monitoring program

In order to monitor the operation and performance of the PTES in Høje Taastrup, a number of sensors were installed (see Fig. 4). The monitoring program included the following parameters:

- The storage temperature is measured using four temperature strings, each having 14 PT100 sensors. Two strings are placed at the east end of the PTES and two at the west end.
- Several sensors have been placed between the insulation layers in the lid measuring temperature, humidity, and heat flux.
- The ground temperature is measured using a temperature string having 10 PT100 sensors. The

temperature is measured until a depth of 15 m from the top of the embankment.

- The moisture and thermal conductivity of the ground is measured at a depth of 1 m from the top of the embankment.
- A weather station is used to measure the ambient air temperature, humidity, and wind speed.
- The storage water level is measured in a small well adjacent to the PTES using a guided radar and a hydrostatic sensor.

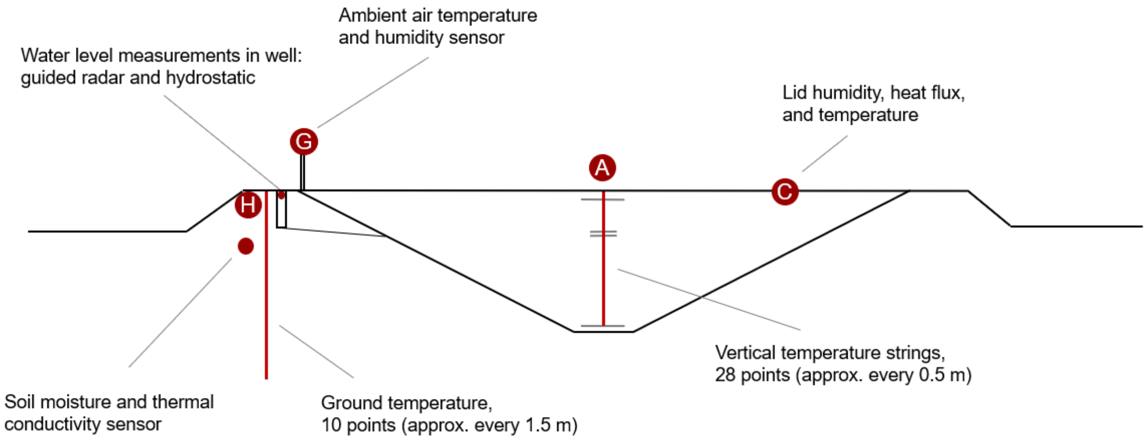

Fig. 4: Schematic of the storage monitoring equipment and measurement points.

4. Storage operation and performance

The temperature of the water layers in the PTES since the start of its operation is presented in Fig. 5. It can be observed that the storage did not operate much during June and July due to the low heat demand during this period. Apart from the summer and a few periods of deep discharge, the water temperature at the top of the PTES was close to 90 °C. However, it should be noted that although the PTES is operational, its operation is still not completely automized, and a number of tests are run frequently. Thus, the presented results should be considered preliminary and may not be indicative of long-term performance.

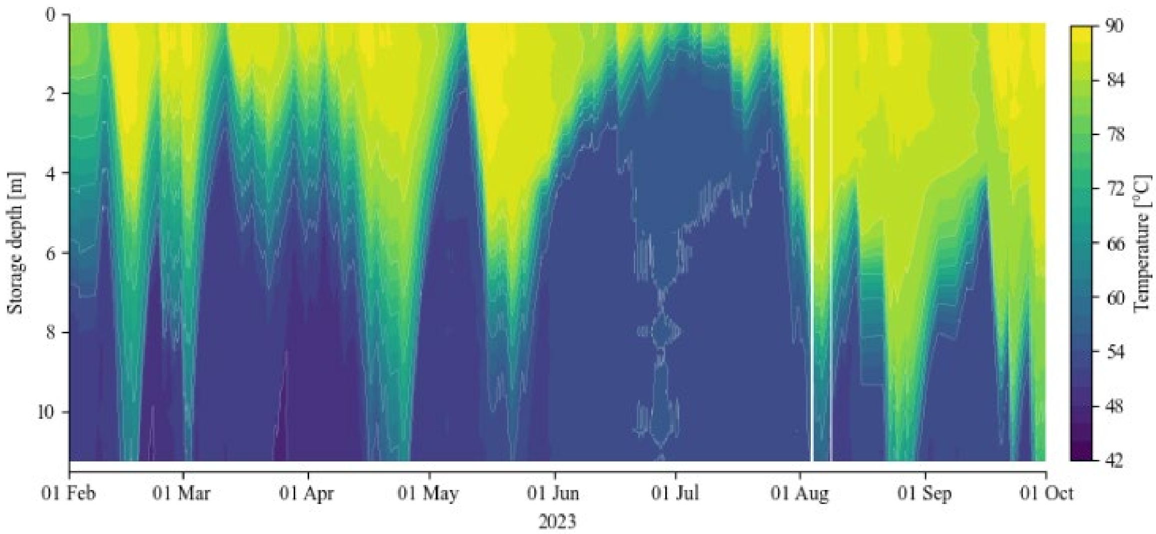

Fig. 5: Water temperature in the PTES.

The weekly charged and discharged heat from the PTES is illustrated in Fig. 6, along with the storage energy content. It should be noted that the PTES maximum capacity was estimated at 3600 MWh (assuming a temperature operating range of 45-90 °C, a constant water density of 980 kg/m^3, and a constant specific heat of 4.18 kJ/kg K). Consequently, it may be observed that the storage was fully charged for the first time in April 2023, while approximately 1000 MWh were charged or discharged most weeks, demonstrating the short-term operation of the storage. Fig. 6 verifies the minimal operation of the PTES in June and July 2023.

The mean monthly efficiency of the PTES during the entire operation period was 84%. However, this value is expected to increase as the heat losses toward the ground become less and less with time. A recent study by Sifnaios et al. showed that the heat losses for a short-term PTES stabilize after approximately eight years (Sifnaios et al., 2023b). Again, it should be emphasized that these results are preliminary, and a more extended monitoring period is required to obtain more representative results of the storage operation during its lifetime.

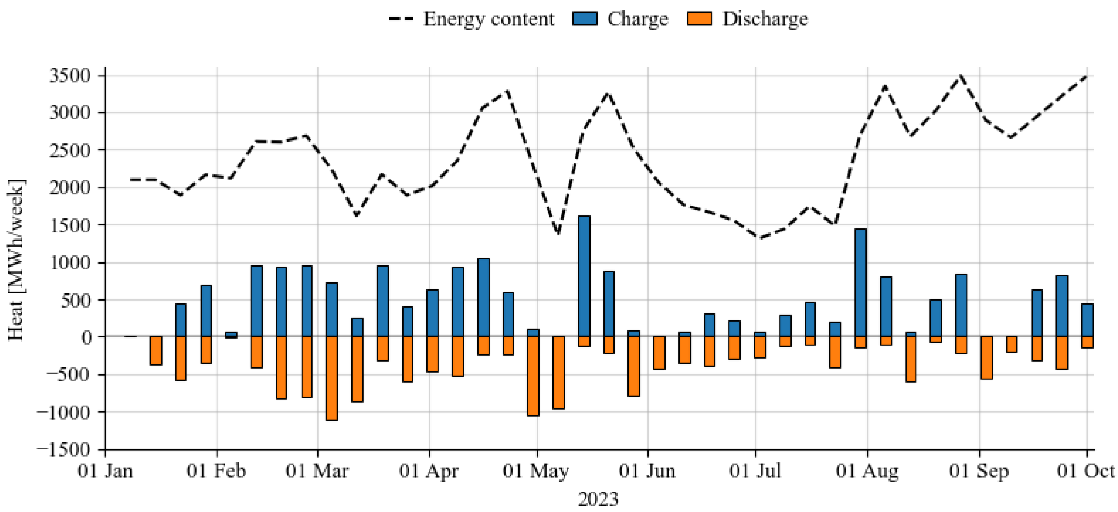

Fig. 6: Weekly charged and discharged energy and storage energy content.

Since the PTES in Høje Taastrup was the first to have the diffusers installed at one end of the storage (instead of the middle), the investigation of stratification was of significant interest. Fig. 7 illustrates the temperature difference between the storage temperature measured at the east and west ends of the PTES. It may be observed that there was a deviation smaller than 1 K between the two ends of the storage, indicating a horizontal uniformity of temperatures. Thus, this design choice can be recommended for future storages.

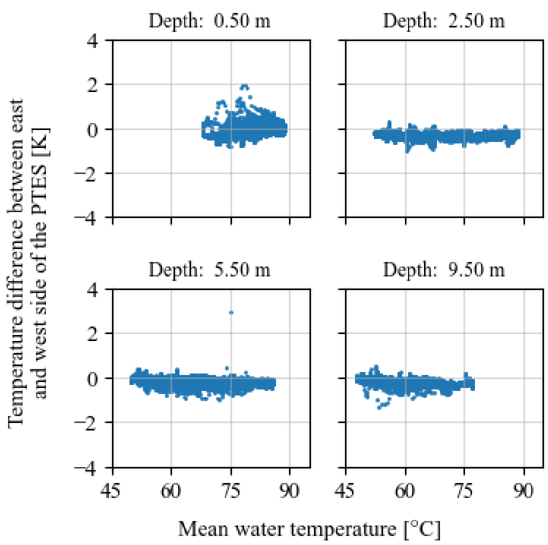

Fig. 7: Temperature difference between the east and west sides of the PTES.

In order to further investigate the stratification in the PTES, the stratification coefficient (*St*) was calculated, as introduced by Wu and Bannerot (1987). In order to calculate this indicator, the storage is divided into discrete layers corresponding to the position of the installed temperature sensors. It is also assumed that each layer has a uniform temperature. This coefficient gives information about the stratification of a storage by comparing the temperature of each water layer with the weighted average storage temperature. A high value indicates a good degree of stratification, whereas a value of zero indicates that the storage has a uniform temperature. However, it should be noted that this coefficient has no physical meaning, but it can be used to compare two different storage systems or different storage operations. The expression developed by Wu and Bannerot (1987), is presented below:

$$St = \sum_{n=1}^{N} \frac{m_i \cdot \left(T_i - T_{avg}\right)^2}{m_{total}} \qquad \text{(eq. 1)}$$

where T_i is the temperature and m_i is the mass of the i'th layer, T_{avg} is the average storage temperature, and m_{total} is the total mass of the storage system.

The *St* for the PTES in Høje Taastrup is presented in Fig. 8. The range of *St* was 0-260 K^2, with a mean value of 160 K^2. For comparison, the range of the stratification coefficient in Dronninglund was 0-500 K^2 with an average value of 154 K^2. For more details on the stratification in the PTES in Dronninglund, the reader is referred to (Sifnaios et al., 2022).

Since the PTES in Høje Taastrup is used as a short-term (i.e., it is charged and discharged several times throughout the year), it is expected to have a higher degree of mixing and, thus, a lower degree of stratification. This is verified by the lower maximum value of *St* for Høje Taastrup compared to Dronninglund. Nevertheless, the mean value of *St* for the PTES in Høje Taastrup is slightly higher, indicating that despite the short-term operation that induced higher mixing, the placement of diffusers in one end of the storage seems to perform well.

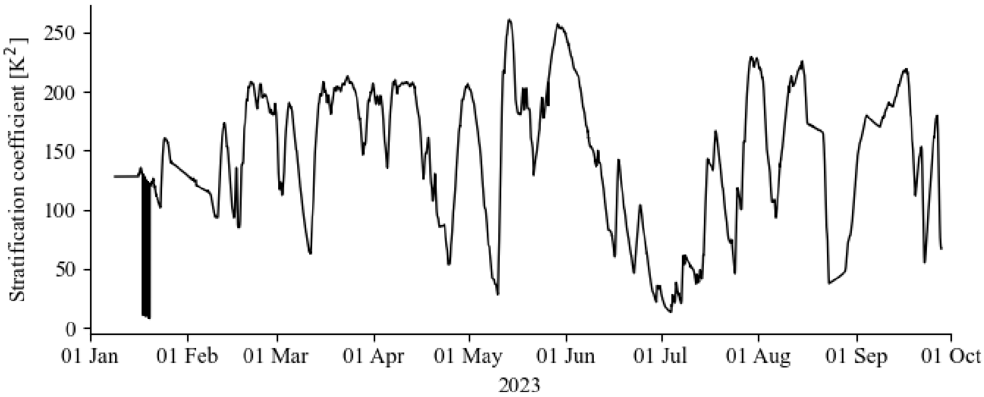

Fig. 8: Stratification coefficient.

Fig. 9 illustrates the ground temperature around the PTES. It should be noted that the ground temperature sensors were installed at the end of July, so a shorter monitoring period is available. However, it is still evident that the ground temperature slowly increases due to the storage operation, particularly close to the surface, where the highest storage temperatures occur.

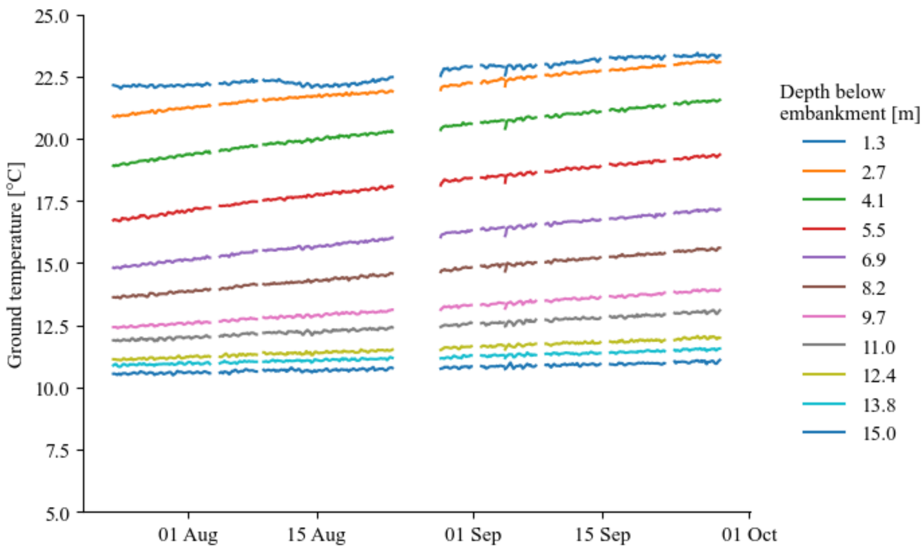

Fig. 9: Ground temperatures around the PTES.

Last, Fig. 10 presents the lid heat fluxes as measured by heat flux sensors installed between the insulation layers in the lid. Similar to the ground temperature, the lid heat flux sensors were installed at the end of July 2023. Although the heat flux is measured in two different locations in the lid, there seemed to be good agreement between the two measurements. Overall, the measured heat flux is in accordance with the theoretical estimation of heat flux based on the thermal characteristics of insulation. This indicates that the lid performs well.

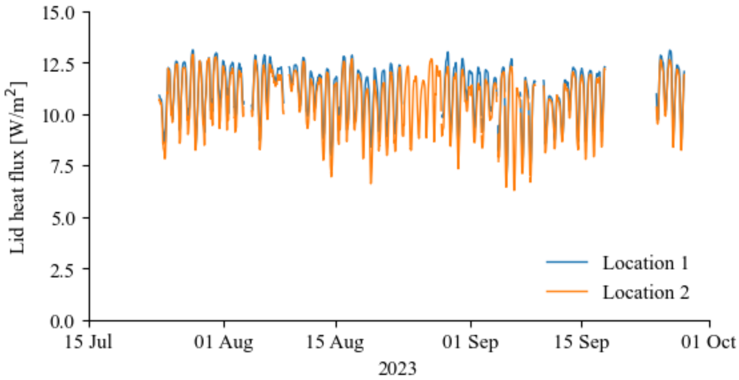

Fig. 10: Lid heat flux measured at two locations on the lid.

5. Conclusions

This study presented experiences from the construction stages and preliminary results from the operation of the PTES in Høje Taastrup, which is the first PTES operated as a short-term heat storage. In general, not many conclusions can be drawn since the storage operates for less than a year. However, the results indicate that installing the diffusers close to the edge of the PTES seems possible without compromising stratification. Overall, the PTES operates as expected, indicating that PTES can be used not only as seasonal storage systems but also as short-term.

6. Acknowledgements

This study was funded by the Danish Energy Agency through EUDP grant no. 64018-0134 (FLEX-TES) and 64020-2036 (IEA ECES Annex 39 Large Thermal Energy Storages for District Heating).

7. References

Aalborg CSP, 2020. Aalborg CSP receives order for lid solution for Integrated Pit Thermal Energy Storage (PTES) System [WWW Document]. URL https://web.archive.org/web/20210417200554/https://www.aalborgcsp.cn/index.php?id=321&tx_news_pi1%5Bnews%5D=775&tx_news_pi1%5Bcontroller%5D=News&tx_news_pi1%5Baction%5D=detail&cHash=6d7aff98a878e1d08d5ecd7f38e4fdbb (accessed 5.4.22).

NMC Termonova, 2011. Nomalen 28N [WWW Document]. URL https://web.archive.org/web/20220426161150/https://azupcs365certviewer.azurewebsites.net/api/GetSDB?env=se&articleNr=550984 (accessed 4.20.22).

Schmidt, T., Pauschinger, T., Sørensen, P.A., Snijders, A., Djebbar, R., Boulter, R., Thornton, J., 2018. Design Aspects for Large-scale Pit and Aquifer Thermal Energy Storage for District Heating and Cooling. Energy Procedia 149, 585–594. https://doi.org/10.1016/j.egypro.2018.08.223

Sifnaios, I., 2023. Investigations of pit thermal energy storages in district heating systems. Technical University of Denmark. https://doi.org/10.11581/DTU.00000291

Sifnaios, I., Dragsted, J., Jensen, A.R., 2021. Thermal inspection of water pit heat storages using drones, in: Proceedings - ISES Solar World Congress 2021. pp. 925–931. https://doi.org/10.18086/swc.2021.35.02

Sifnaios, I., Gauthier, G., Trier, D., Fan, J., Jensen, A.R., 2023a. Dronninglund water pit thermal energy storage dataset. Sol. Energy 251, 68–76. https://doi.org/10.1016/j.solener.2022.12.046

Sifnaios, I., Jensen, A.R., Furbo, S., Fan, J., 2023b. Heat losses in water pit thermal energy storage systems in the presence of groundwater. Appl. Therm. Eng. 235, 121382. https://doi.org/10.1016/j.applthermaleng.2023.121382

Sifnaios, I., Jensen, A.R., Furbo, S., Fan, J., 2022. Performance comparison of two water pit thermal energy storage (PTES) systems using energy, exergy, and stratification indicators. J. Energy Storage 52, 104947. https://doi.org/10.1016/j.est.2022.104947

Soerensen, P.A., From, N., 2011. High solar fraction with pit heat storages, in: 30th ISES Biennial Solar World Congress 2011, SWC 2011. pp. 3020–3030. https://doi.org/10.18086/swc.2011.21.07

Sveinbjörnsson, D., Laurberg Jensen, L., Trier, D., Ben Hassine, I., Jobard, X., 2017. Large Storage Systems for DHC Networks.

Wu, L., Bannerot, R.B., 1987. An experimental study of the effect of water extraction on thermal stratification in storage, in: Proceedings of the 1987 ASME-JSME-JSES Solar Energy Conference, Honolulu. pp. 445–451.

In-situ monitoring of a PVT-heat pump system with ground sources used for heating and cooling applications

Krishna Prasad Timilsina, Bharat Chhugani and Peter Pärisch

Institute for Solar Energy Research Hamelin (ISFH), Germany

Abstract

Photovoltaic-thermal (PVT) collectors are regarded as a potential key technology for climate-neutral energy supply in buildings due to their feature of cogenerating thermal and electrical energy. This paper analyses the performance of a demo plant consisting of uncovered (WISC) PVT collectors in a system configuration, with a brine-to-water heat pump and ground sources i.e., borehole and horizontal ground heat exchangers, used for heating and cooling purposes in a non-residential building. The seasonal performance factor of the system before storage (SPF_{bSt}) for the monitored year 2022 was 3.3 in the heating mode and 4.1 in the cooling mode. PVT collectors proved to be an essential source in the system, covering around a quarter of the heating demands and around 35 % of the cooling demands through nocturnal cooling. In addition, 56 % of the solar heat produced by PVT collectors was used for the regeneration of the ground sources. In this demo site, the solar regeneration enabled the sizing of relatively smaller ground sources during the design phase. Furthermore, the thermal parameters of the PVT collectors are identified with the monitoring data according to the quasi-dynamic test (QDT) mathematical model based on ISO 9806. On average, the typical heat loss coefficient defined specifically for nocturnal cooling per m² PVT estimated from the monitoring data was 21 W/K.

Keywords: PVT collectors, heat pump, monitoring, heating, cooling, quasi-dynamic test method, thermal parameters

1. Introduction

A major challenge for the shift from conventional to renewable energy sources is the transition of heating and cooling systems in buildings to renewables. In 2021, renewables accounted for only 22.9 % of European heating and cooling consumption, and natural gas alone covered 34.3 % of the continent's heating demand (Eurostat 2023). In Germany, only 15.4 % of the energy consumed for heating and cooling of buildings came from renewable sources in 2021 which increased to 17.4 % in 2022 (Umwelt Bundesamt, 2023). Due to the high dependence on natural gas and its imminent insecurity of supply, there is an urgent need for Western European nations to explore alternative solutions for heat supply (Eurostat 2023). As one of the main CO_2 emitters, the building sector must be efficiently integrated with renewable energy technologies to meet the emission targets. In this context, research and applications of solar photovoltaic-thermal (PVT) collectors have significantly increased due to their benefits of gaining electrical and thermal yields from the same aperture area. Therefore, PVT collector-based heat pump systems are considered to play a pivotal role in achieving the emission and energy efficiency targets in building sectors. In 2022, the uncovered PVT collectors had 87 % of the market share due to relatively favourable subsidy schemes (Weiss and Spörk-Dür, 2023). Due to the convective and radiative heat transfer potential of the uncovered PVT collectors, they can also be used for passive cooling of buildings during the night. In order to analyse the performance and efficiency of the installed systems, they need to be monitored under real operating conditions.

This paper is based on the results of the ongoing project "integraTE", which focuses on PVT systems and aims to increase market penetration of technically and economically attractive energy supply through PVT collector-heat pump systems in the building sector. One of the work packages of the project is the monitoring of 10 demo plants consisting of PVT as a single or additional heat source for the heat pump. The case study presented in this paper is focused on a non-residential building, serving as one of the demo plants, wherein a heat pump system is employed to fulfil both heating and cooling requirements. The main aim of this study is to evaluate the heat pump and system efficiency and to analyse the performance of PVT collectors under various operating

10.18086/swc.2023.04.02 Available at http://proceedings.ises.org

and environmental conditions. Furthermore, the thermal performance parameters of the PVT collectors based on ISO 9806:2013 (ISO 9806, 2013) have also been calculated from the monitoring data and compared with the parameters obtained from the laboratory tests conducted as defined in the standard.

2. System Description

Fig 1 illustrates the simplified schematic layout of the monitored system. The solid lines in the figure represent the flow pipes and the broken lines indicate the return pipes. The orange coloured lines indicate pipes transporting fluid with lower temperatures i.e. at heat pump sources or cooling circuits. Conversely, the red lines denote the pipes carrying fluid with higher temperatures i.e. sink side of the heat pump. The fluid flowing in the lines prior to the heat exchanger (HEX) depicted in the diagram is a mixture of brine and water, whereas the green lines beyond the heat exchanger represent the water-based heating and cooling circuits. The system comprises uncovered PVT collectors, borehole heat exchangers (BHE) and horizontal ground heat exchangers (HGHE) serving as sources for a brine-to-water heat pump. The description of these components is shown in Tab 1.

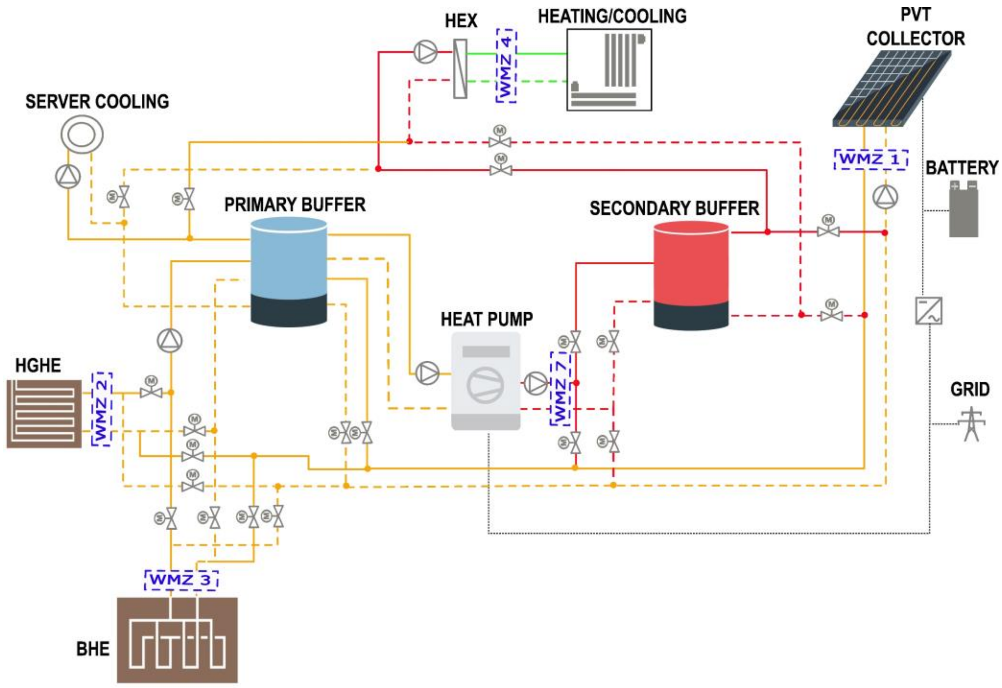

Fig. 1: Simplified hydraulic schematic diagram of the monitored system

Tab. 1: Description of heat sources and heat pump

PVT modules type	Uncovered (WISC) with aluminium heat exchanger on the rear side, see Fig. 2(b)
PVT collectors (thermal)	Area: 230 m²
PV electrical capacity (PV+PVT)	Type: Monocrystalline PV Area: 325 m^2 Power: 61 kWp
Heat pump	Type: Brine-water (B0/W35) Heating capacity: 58.6 kW Cooling capacity: 46.3 kW COP: 4.8
Borehole heat exchangers	6 x boreholes à 100 m depth
Horizontal ground heat exchangers	Area: 360 m^2 (two layers)

The storage system consists of two buffer tanks each 3000 l, one on the source side of the heat pump (primary buffer) and the other on its sink side (secondary buffer). The secondary buffer serves as a distribution tank for the heat supply whereas the primary buffer supplies the heat provided by PVT collectors, BHE and HGHE to the heat pump. Additionally, the primary buffer operates as a distribution tank for server and space cooling of the buildings. The demo plant consists of four buildings: the main building (i.e. office building) and three ancillary buildings, which are used as seminar rooms and for exhibitions or external events. The distribution system delivers the heat from secondary buffer storage to all the aforementioned buildings through a brazed plate heat exchanger (HEX in Fig. 1). The designed supply and return temperatures to the heat exchanger for heating mode are 47 °C and 42 °C respectively. Similarly, for the cooling mode, the respective design supply and return temperatures are 14 °C and 19 °C. The electricity produced by the PV modules is either supplied to the heat pump, fed to the grid or used to charge the batteries and supply electricity to the buildings.

Further information on the system is listed below:

- Location of project: Hannover, Germany
- Year of construction/renovation: 1999 / 2020
- Heated living area: 1803 m^2
- Building heating/cooling load: 58.6 kW / 54 kW
- Method of heating: radiator, floor heating, convectors
- Simulated yearly heat demand: 84,907 kWh
- Simulated yearly cooling demand: 47,694 kWh

3. Monitoring

The monitoring system is equipped with devices and sensors for measuring weather conditions, and the heat and electricity consumed or produced within the system. Each device and sensor independently exports event-driven data to the database i.e. the data is logged exclusively when there is a change in specific sensor readings. Therefore, each sensor has its own time-series data, which has to be merged before analysis.

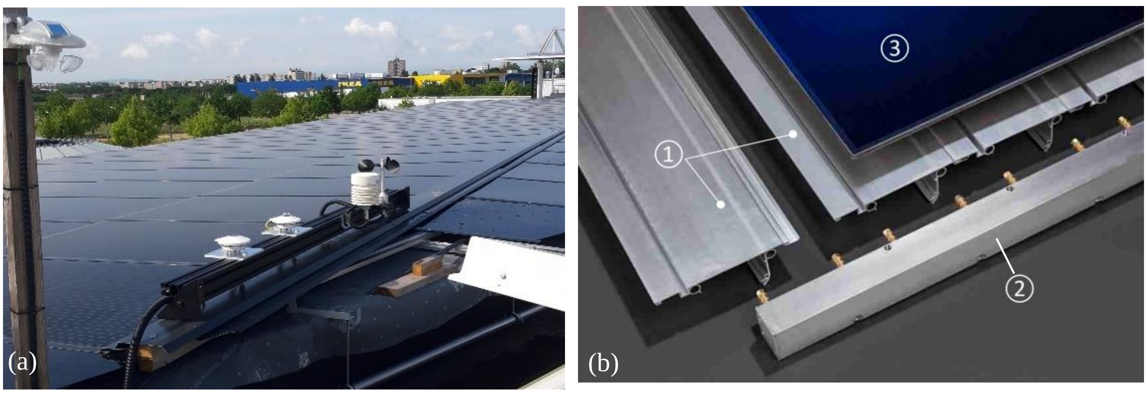

Fig. 2:(a) Weather station installed at PV-PVT field and (b) PVT-module (1. Extruded aluminium profiles, 2. Manifold, 3. PV-module)

Fig. 2(a) shows the weather station installed at the PVT collector field on the roof of the main building. It consists of a transmitter with PT100 temperature sensors and humidity sensors to measure ambient temperature and relative humidity. Additionally, it incorporates a pyranometer to measure solar irradiance, a pyrgeometer to measure longwave irradiance and a wind transmitter to measure wind speed. A total of seven bidirectional heat flow meters are installed to monitor the heat flow at PVT, HGHE, BHE, heat pump condenser and distribution circuits. The heat flow meters installed in the brine loops, i.e. PVT collector, BHE, HGHE and heat pump sink side are based on ultrasonic volume flow sensors and PT500 temperature sensors for flow and return temperatures. Three heat flow meters in the distribution systems based on ultrasonic volume flow sensors and PT100 temperature sensors are installed to record the flow and return temperature of the heating/cooling circuits of three different buildings. The positions of the five main heat flow meters used to create the energy balance of the system are shown in Fig. 1 as “WMZ”. An electricity meter monitors the total electricity consumption of the heat pump, including the circulation pumps on the source and sink sides. Also, the electricity generated from both the PVT collectors and the PV modules is recorded at three different inverters. The electricity consumed by the circulation pumps for the ground sources and the PVT collectors is also recorded. Three PT1000 temperature sensors are used to monitor the temperature of the ground at different depths (5 m, 25 m, and 50 m) for BHE and a temperature sensor records the temperature of the HGHE field at 1.5 m depth.

4. Operation Modes

In the data, an operation mode is assigned to each instance (1 minute) based on the operation status (on/off) of heat sources, heat sinks and the heat pump. The energy flow at any instance is determined based on the operation mode active at that particular occasion. As shown in Fig. 3(left), in heating operation modes, heat sources like PVT, BHE and HGHE supply heat to the primary buffer storage, which is finally delivered to the heat pump evaporator based on the heating requirement at the secondary buffer. The heat pump condenser supplies heat to charge the secondary buffer storage tank which acts as a distribution tank for supplying heat to the buildings. Additionally, in regeneration modes, solar heat from PVT collectors is stored in either BHE or HGHE.

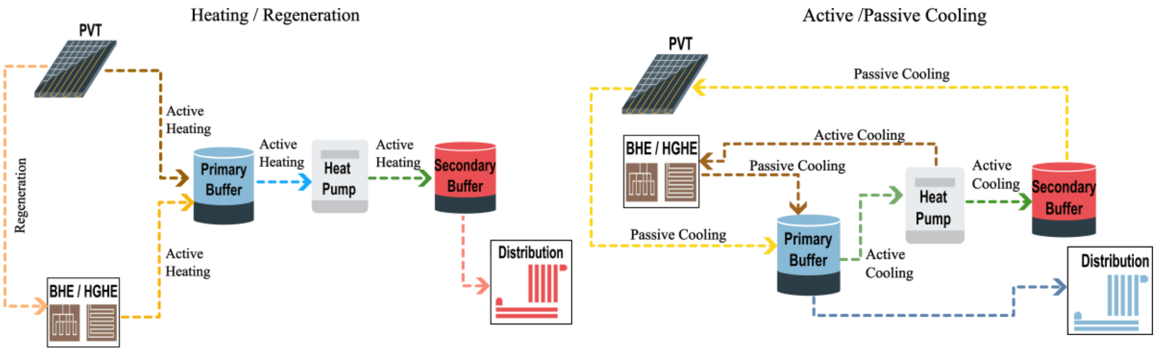

Fig. 3: Operation modes of the system

As shown in Fig. 3(right) cooling modes are divided into active and passive cooling based on the use of the heat pump during cooling operation. Active cooling refers to the cooling modes where the primary buffer storage is cooled through the evaporator of the heat pump where the heat from primary buffer storage is transferred either to the secondary buffer storage or to the ground sources. On the other hand, passive cooling refers to cooling operations without heat pump usage. During passive cooling with BHE and HGHE, the primary buffer is cooled with the aid of circulation pumps when the ground temperatures are on sufficiently lower levels. The PVT collectors cool the secondary buffer through nocturnal passive cooling in summer.

The reference temperatures are compared to enable each operating mode. If the regulatory conditions are met, the operating mode is activated. The system chooses the operation modes according to the following priority order: passive cooling, active cooling, active heating and secondary buffer cooling/regeneration. This priority order is used to decide which mode should be active at a certain instance. The heat pump controller receives a heating or cooling request from the higher-level control. Depending on the requirement, the heat pump monitors primary or secondary storage tanks and keeps them within the defined temperature limits.

5. KPIs for heat pump and system efficiency

To determine the efficiency of the heat pump and the system for heating and cooling modes separately, seasonal performance factors (SPF) for various system boundaries are defined. The SPF is the indicator of the efficiency of the system over a season (or a year). It is the ratio of the useful thermal energy (heating or cooling) supplied by the system to the electrical energy used by the system. Therefore, the SPF of the system during cooling operation differs from that of heating as the useful energy in the cooling mode is obtained from the source side of the heat pump. For the monitored system, the $SPF_{bSt,H}$ as specified in eq. 1 is the ratio of the amounts of heat supplied to the secondary buffer by the heat pump ($\dot{Q}_{HP}$), divided by the electrical energy consumed within the boundary i.e. before storage (Malenković et al., 2013). The electrical power consumed by the heat pump compressor as well as the internal circulation pumps and controls is denoted by $\dot{E}_{HP}$ and $\dot{E}_{Pumps}$ is the electricity consumed by circulation pumps for ground sources and PVT collectors within the system boundary.

Eq. 2 is used to calculate the seasonal performance factor for cooling $SPF_{bSt,C}$ which is the ratio of the total cooling energy delivered to the primary buffer, to the associated electricity consumption (Gehlin and Spitler, 2022; Malenković et al., 2013). The cooling energy delivered to the primary buffer from the heat pump evaporator during active cooling modes is denoted by $\dot{Q}_{Evap}$, and $\dot{Q}_{Passive}$ indicates the heat removed from the primary buffer by HGHE, BHE and PVT without the heat pump operation through passive cooling. To determine the efficiency of the heat pump over a certain period, the coefficient of performance $SPF_{HP,H}$ given in eq. 3 is used, which relates the corresponding integrated amounts of heat supplied, and electricity consumed. Accordingly, eq. 4 is used to calculate the heat pump's coefficient of performance during active cooling i.e. $SPF_{HP,C}$.

$$SPF_{bSt,H} = \frac{\int \dot{Q}_{HP}\, dt}{\int (\dot{E}_{HP} + \dot{E}_{Pumps})\, dt} \qquad \text{(eq. 1)}$$

$$SPF_{bSt,C} = \frac{\int (\dot{Q}_{Evap} + \dot{Q}_{Passive})\, dt}{\int (\dot{E}_{HP} + \dot{E}_{Pumps})\, dt} \qquad \text{(eq. 2)}$$

$$SPF_{HP,H} = \frac{\int \dot{Q}_{HP}\; dt}{\int \dot{E}_{HP}\; dt} \qquad \text{(eq. 3)}$$

$$SPF_{HP,C} = \frac{\int \dot{Q}_{Evap}\; dt}{\int \dot{E}_{HP}\; dt} \qquad \text{(eq. 4)}$$

6. Results

6.1. Performance during heating modes

The complete monitoring of the system has been ongoing since January 2022 and all the findings presented in the work are based on the data collected in the year 2022. During the analysis of the system, a separate energy balance is established for heating and cooling modes. Fig. 4 shows the monthly energy balance and the performance factors (PF) during the heating operation. The energy quantities Q_{PVT}, Q_{BHE} and Q_{HGHE} denote the respective thermal energy contributions from the PVT collectors, BHE and HGHE to the heat pump evaporator. In 2022, the PVT collectors supplied 14,384 kWh of thermal energy to the primary buffer, which is about 24 % of the total heat accumulated in the primary buffer and utilized as a heat pump source. The major heat source for the heat pump system was the BHE field, contributing to 46 % of the total heat, while the HGHE field covered 8 % of the heat delivered to the primary buffer.

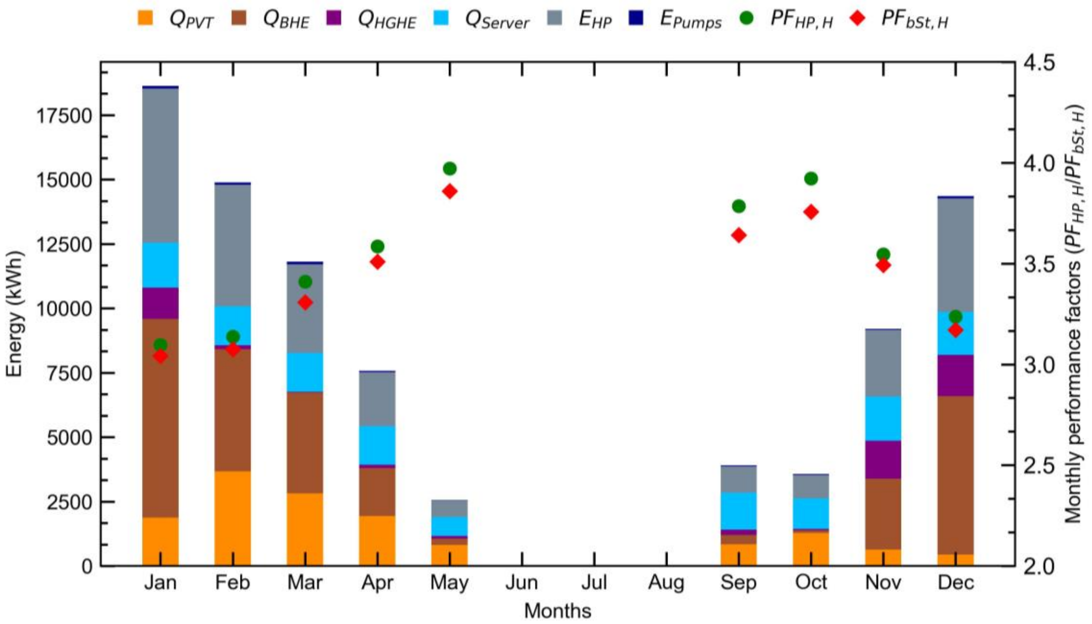

Fig. 4: Monthly energy balance and performance factor for heating modes of operation

The heat accumulated in the primary buffer due to server cooling is also included in Fig. 4 as Q_{Server}. The amount of server cooling was determined from the difference in energy balance at the heat pump, as there is no heat flow meter installed in the server cooling circuit. Throughout the year, the heat gains through server cooling accounted for 22 % of the energy flowing into the primary buffer. During the heating season, the heat pump condenser delivered a cumulative thermal energy output of 85,935 kWh to the secondary buffer storage with a corresponding electricity consumption of 25,788 kWh. The seasonal performance factor of the heat pump $SPF_{HP,H}$ was 3.33. The electricity consumption of the circulation pumps on the source and sink side of the heat pump is measured together with the electricity consumption of the heat pump (E_{HP}). This could be one of the reasons for relatively lower $SPF_{HP,H}$ in the context of similarly configured systems. The annual heat supplied to the buildings via the heat exchanger in the distribution system amounted to 85,590 kWh, equivalent to 47.5 kWh/(m^2·a). This heat delivery matched very well the simulated annual heat demand determined by the planner with the tool TRNSYS, i.e. 84,909 kWh. The seasonal performance factor of the system before storage during heating periods i.e. $SPF_{bSt,H}$, for the year 2022 was 3.3. The circulation pump on the heat pump sink side was running during the heating periods due to a control fault, although the heat pump was not operating. This resulted in increased electricity consumption and could be one of the reasons for the lower system efficiency during heating periods. The simultaneous heating and cooling with multiple sources and the complexity of the system make it difficult to identify the specific reason for the lower system efficiency.

6.2. Performance during Cooling

Fig. 5(a) presents the monthly performance factors and energy balance observed at the heat pump condenser during the active cooling of the primary buffer (cold storage). From mid-May to the end of August 2022, the system was solely used for cooling. The seasonal performance factor of the heat pump in cooling mode ($SPF_{HP,C}$) was 4.08. When including cooling gains through passive cooling and the electrical consumption of the circulation pumps, $SPF_{bSt,C}$ resulted to 4.14. Due to the inclusion of passive cooling of the primary buffer through BHE and HGHE, the $SPF_{bSt,C}$ is slightly higher than the heat pump's coefficient of performance. The higher performance factors observed during active cooling (compared to the heating modes) can be attributed to the lower supply temperatures of the heat pump (see Fig. 5(b)). During the active cooling mode, 17,819 kWh of heat was extracted from the primary buffer from May to October. The excess heat from the primary buffer was transferred through the heat pump condenser either to the ground ($Q_{BHE,reg}$, $Q_{HGHE,reg}$) or to the secondary buffer, which is then cooled by the PVT collectors through passive night cooling ($Q_{PVT,C}$). A total of 13,552 kWh of heat was injected into the ground during active cooling operation (approx. 95 % to the BHE field and 5 % to the HGHE field). In addition, only 377 kWh of heat from the cold storage was fed into the ground through passive cooling of the primary buffer. In total, 35 % of the heat in the primary buffer is dissipated by the PVT collectors and the remaining 65 % by the ground sources (BHE and HGHE). The waste heat during active cooling with ground sources accounted for around 44 % of the heat injected into the ground.

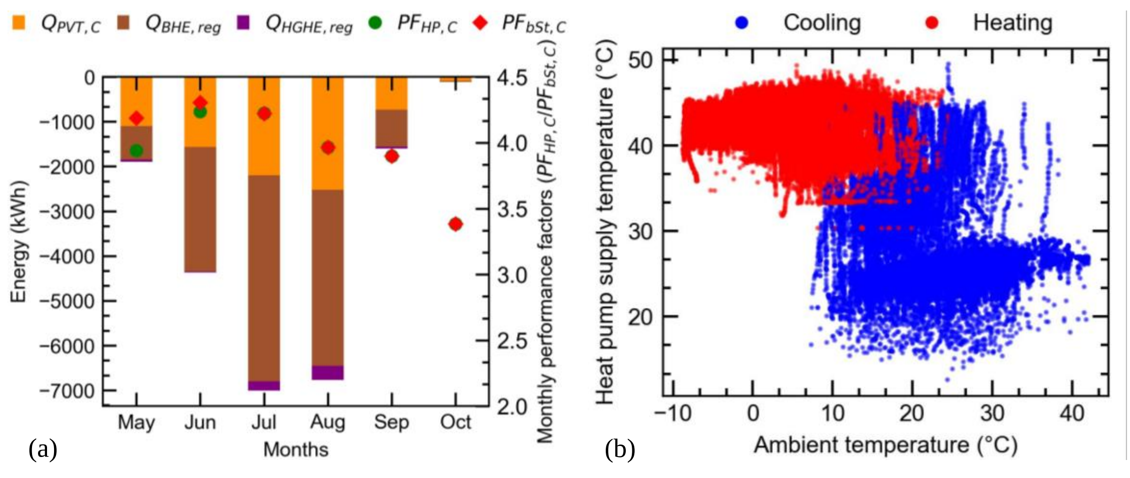

Fig. 5: (a) Monthly energy balance and performance factors during cooling modes (b) Heat pump supply temperature as a function of ambient temperature (minute resolution)

Fig. 5(b) illustrates two distinct supply temperature ranges observed during the heat pump's operation. The data points with the supply temperatures between 35 °C and 48 °C (red cluster) represent the instances when the heat pump is used for heating. The other instances when the heat pump supply temperatures range from

15 °C to 45 °C (blue cluster) refer to the active cooling modes. Upon closer analysis, it was found that most of the concentrated points between 18 to 28 °C refer to active cooling with the ground sources. The remaining points refer to active cooling with the secondary buffer i.e. the instances where the secondary buffer is charged with the excess heat from the primary buffer. At the end of a typical summer day with cooling demands, the secondary buffer ends the day warm with temperatures up to 45 °C and at night, the PVT collectors cool it to temperatures as low as 15 °C. The ambient temperature during heating varied from -8 °C to 25 °C. And during cooling, the ambient temperature was between 10 °C to 42 °C. During higher ambient temperatures, particularly during summer days, the waste heat was directed to the ground as buffer cooling with PVT collectors is not possible for operating conditions with an inlet temperature lower than the ambient temperature. The higher values of the ambient temperatures could be due to the installation of the temperature sensors on the PVT field.

6.3. Energy balance at PVT collectors

Fig. 6 displays the comprehensive overview of monthly thermal energy supplied by the PVT collectors for heating ($Q_{PVT,HP}$), regeneration ($Q_{Regeneration}$) and cooling ($Q_{Nightcooling}$). The thermal yield of the PVT collectors increased from 1,946 kWh in January to 8,461 kWh in April. Despite the PVT collectors' inherent capacity to capture more solar thermal energy during summer months, the actual positive thermal yield remained relatively low due to simultaneous cooling requirements and no heat demand, i.e. domestic hot water preparation. From mid-May to the end of August, the PVT collectors were only used for cooling, releasing 8,404 kWh of heat from the secondary buffer to the surrounding environment via passive nocturnal cooling. Also, in September, the PVT collectors released 701 kWh of heat to the ambient air in addition to the heating and regeneration. The regeneration of the ground with PVT collectors increased from 30 kWh in January to 6,517 kWh in April. To sustain lower ground temperatures essential for cooling, the solar regeneration was intentionally halted from mid-May to the end of August. The ground regeneration restarted at the end of August with the end of the cooling season. In 2022, a total of 56 % of the solar heat was used for ground regeneration. Approximately, 70 % of this energy was injected into the BHE field and the remaining 30 % into the HGHE field. According to the planner, this advantage of regeneration through PVT collectors allowed the planning of shorter borehole lengths. Furthermore, combining PVT with ground sources in this type of system also helps to prevent dropping ground temperatures in the long term.

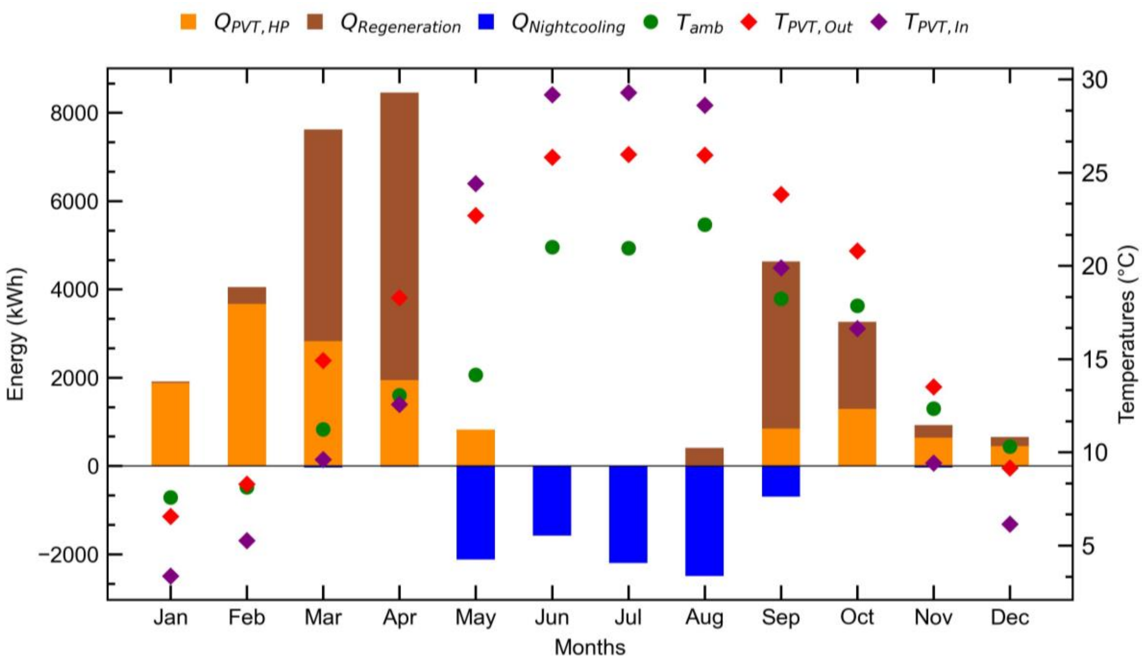

Fig. 6: PVT energy balance and system temperatures

In addition, Fig. 6 illustrates the comparison of the monthly average inlet and outlet temperatures of the PVT collector field ($T_{PVT,In}$ and $T_{PVT,Out}$) and the ambient temperature (T_{amb}). During the winter months (i.e. November to February) which correspond to the heating period, the outlet temperatures are on average 3.2 K higher than the inlet temperature. During the regeneration periods, i.e. in March and April, the difference is relatively higher, with an average of 5.5 K. In the summer months (i.e. May to August), when the PVT collectors were primarily used for passive night cooling to cool the secondary buffer, the inlet temperatures are on average 2.8 K higher than the outlet temperatures. From September onwards, the PVT collectors are used again for heating and regeneration, with an average temperature difference of 3.8 K. In winter and transition seasons, when the ambient temperatures were higher than the inlet temperatures, the PVT collectors gained additional heat from the environment. These observations highlight the dynamic temperature variations and seasonal performance of the PVT collector system.

Fig. 7(a) shows ambient temperature as a function of the sky temperature during the cooling modes using PVT collectors. The sky temperature was indirectly calculated using the longwave irradiance measured by a pyrgeometer. The temperature difference between the ambient air and the sky during these instances was up to 20 K with an average of 11 K. Due to higher fluid temperatures coming from the secondary buffer storage and relatively lower ambient and sky temperature conditions, the night radiative cooling potential of PVT collectors during cooling mode is significant.

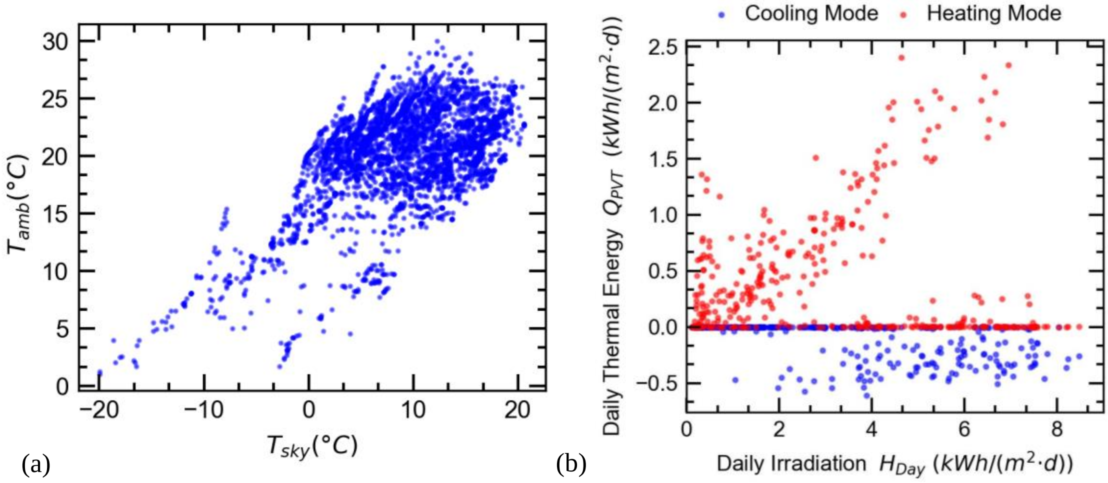

Fig. 7: (a) Sky temperature vs. ambient temperature during cooling with PVT collectors (5-minute resolution); (b) Daily thermal energy as a function of irradiation

6.4. Irradiation and thermal energy yield of PVT collectors

Fig. 7(b) shows the daily heating (positive) and cooling (negative) thermal energies of the PVT collectors compared to the total daily irradiation. The graph indicates that despite a substantial daily solar irradiance of more than 2 $kWh/(m^2 \cdot d)$, there were numerous days when the positive thermal energy of the PVT collectors was zero or close to zero. This occurred due to one of two scenarios: either the collectors were not operational on these days or were exclusively used for cooling. The blue dots with negative thermal energy represent the days when collectors were used for passive night cooling of the secondary buffer. The significant observation here is the presence of positive thermal energy of up to 1.4 $kWh/(m^2 \cdot d)$ at lower solar irradiation (below 1 $kWh/(m^2 \cdot d)$). This phenomenon underlines the PVT collector's ability to extract thermal energy from the surrounding air, effectively functioning as an environmental heat exchanger when the ambient temperatures are higher than the inlet temperature of the collectors. This capability is attributed to the fact that the rear side of the collector is exposed to the external environment, as illustrated in Fig. 2(b). To determine how efficiently the PVT collectors, convert the incident irradiance into energy, the utilization rate is calculated for both the thermal and the electrical parts. The solar thermal utilization rate is defined as the ratio of the generated energy (heat) to the available energy (irradiation). With solar irradiation of greater than 1 $kWh/(m^2 \cdot d)$, the solar thermal utilization rate of the PVT collector ranged from 23 % to 70 % with an average of approx. 40 %. Determination of the utilization rate is not plausible for lower irradiation levels, as the heat is not solely derived from irradiation but also absorbed from the surrounding environment, making the calculation less straightforward.

The annual specific heat yield of the PVT collectors was 152 $kWh/(m^2 \cdot a)$. In addition, the specific annual cooling energy yield of PVT collectors was 40 $kWh/(m^2 \cdot a)$. The use of geothermal sources for cooling in summer limited the permissible increase in ground temperatures, which restricted the regeneration potential of PVT collectors. For this reason, PVT collectors were not used on warm and sunny summer days, which significantly lowered the annual heat yield. In previous investigations involving systems configured for energy supply in single-family houses, which incorporated PVT and BHE as heat sources for heat pumps, comparatively higher thermal energy yields ranging from 330 to 450 kWh/($m^2 \cdot a$) were reported (Helmling et al., 2022). Furthermore, in a non-residential building investigated in a project in Switzerland, the heat yield was 440 kWh/($m^2 \cdot a$) (Zenhäusern et al., 2017). The reason for the higher heat yields of the PVT collectors in these systems compared to the system investigated in this paper is that the PVT collectors were additionally used for hot water production and regeneration of the ground in summer.

6.5. PVT-Collector thermal performance parameters based on ISO 9806

The standard thermal performance parameters calculated using the quasi-dynamic test (QDT) method based on ISO 9806 (2013) are already available for the PVT collector discussed in this paper (Brötje et al., 2018). However, it is important to note that these parameters may vary under real operation due to the different installation, operating and environmental conditions. In our specific case, the test parameters do not reflect the collector's operation without solar irradiance for heating the primary buffer as well as its use during summer nights for cooling. The goal of the work was to determine the PVT collector parameters using yearly data from in-situ monitoring and to evaluate the performance of the PVT collectors under real conditions, installed on a flat roof with a substructure.

The data was first resampled to a five-minute interval as the collector field was large and averaging the data would better characterize the inlet and outlet temperature of the collector field. Valid data points were then selected to characterize the transient behaviour of the PVT collectors by eliminating probable outliers. According to the QDT mathematical model based on ISO 9806 given in eq. 5, the coefficients were determined using robust nonlinear least-squares fitting in Python, but considering both daytime and nighttime data. The older version of ISO 9806 was used to enable comparison of the parameters obtained from the monitoring data with the existing parameters from collector testing. The uncertainty of measurements was not considered in the calculations.

$$\dot{q}_{th} = \boldsymbol{\eta_{0,hem}} \cdot G_{hem} - \boldsymbol{c_1} \cdot (\vartheta_m - \vartheta_a) - \boldsymbol{c_2} \cdot (\vartheta_m - \vartheta_a)^2 - \boldsymbol{c_3} \cdot u \cdot (\vartheta_m - \vartheta_a) + \boldsymbol{c_4} \cdot (E_L - \sigma T_a^4) - \boldsymbol{c_5} \cdot \frac{d\vartheta_m}{dt} - \boldsymbol{c_6} \cdot u \cdot G_{hem} \qquad \text{(eq. 5)}$$

$$c_4 = \eta_{0,hem} \cdot \frac{\varepsilon}{\alpha} \qquad \text{(eq. 6)}$$

$$c_6 = \eta_{0,hem} \cdot b_u \qquad \text{(eq. 7)}$$

The standard QDT model needed to be modified as shown in eq. 5 since the direct and diffuse radiation were not measured separately and only the global hemispherical irradiance (G_{hem}) was available for the monitoring data. The terms $\eta_{0,b} \cdot K_b(\theta) \cdot G_b + \eta_{0,b} \cdot K_d \cdot G_d$ in the standard QDT model are therefore replaced by $\eta_{0,hem} \cdot G_{hem}$ with the consideration that the IAMs (Incidence Angle Modifiers) K_d and K_d are one. To apply this modification, only incidence angles below 60° were applied for the calculation of the zero-loss efficiency $\eta_{0,hem}$. The collector parameters are identified iteratively in two steps. In the first step, the initial guess of $\eta_{0,hem}$ is kept constant and all the other parameters are calculated. In the second step, the parameters calculated in the first step are kept constant and the data with incidence angles below 60° is used to calculate the $\eta_{0,hem}$. In the next iteration, the calculated $\eta_{0,hem}$ is used as an updated constant for the first step and the iterations continue until the optimized parameters are obtained. To reduce the correlation between the parameters $\eta_{0,hem}$, c_4 and c_6, the relationships given in eq. 6 and eq. 7 are used based on the literature (Brötje et al., 2018). The parameter b_u refers to collector efficiency coefficient used to estimate wind dependence of zero-loss efficiency for uncovered collectors. The effective thermal capacity c_5 is kept constant as it is a material property and it is very complex to characterize it with the monitoring data. The parameter c_2 is also set to zero as it resulted in a negative value during the fitting and is also expected to be zero for these types of collectors. The statistical accuracy of the fitting is checked by the calculation of T-ratio as explained in ISO 9806 standard as the ratio of the resulting optimal value for the parameter to the standard error associated with the parameter fitting. The minimum T-ratio for each parameter to be accepted as statistically significant according to the standard is 3 and, in this case, the T-ratio for all the calculated parameters are greater than 35.

Tab. 2 shows a comparison between the collector coefficients obtained from monitoring data and the collector coefficients from the laboratory tests at ISFH. The heat loss coefficients, especially c_1 and c_3 exhibit the most substantial deviations compared to other parameters: the heat loss coefficient c_1 is 25 % lower and the wind dependence of heat loss coefficient c_3 is 18 % lower than the test results. The overall heat transfer coefficient (U-Value = $c_1 + c_3 \cdot u$), calculated for the wind speed of 1.3 m/s is 14.45 W/m²·K for the test parameters and 11.46 W/m²·K for the monitoring parameters i.e. 20 % lower for the monitoring parameters.

Tab. 2: PVT Collector thermal performance parameters according to ISO 9806:2013 for monitoring and test data

Parameter	Description	Monitoring	Test
$\eta_{0,hem}$	Peak collector (zero-loss) efficiency for total radiation (-)	0.66	0.62
c_1	Heat loss coefficient (W/m²·K)	9.64	12.24
c_2	Temperature dependence of heat loss coefficient (W/m²·K²)	0	0.06
c_3	Wind speed dependence of heat loss coefficient (J/m³·K)	1.40	1.7
c_4	Sky temperature (longwave radiation) dependence of heat loss coefficient	0.57	0.57
c_5	Effective thermal capacity (kJ/m²·K)	47.9	47.9
c_6	Wind speed dependence of the zero-loss efficiency (s/m)	0.04	0.03

During the tests at ISFH, the PVT field of 13.8 m² was installed parallel to a test roof with a 38° slope with the collector facing south. Whereas the collector field in the demo site is 17 times larger and installed on a horizontal roof with an inclination of 4.5° facing three different directions (east, south and north). The findings based on the previous investigations on the other PVT fields by Giovannetti et al. (2019) demonstrated the dependency of heat loss coefficients on installation conditions and the dimension of the field. Depending on the direction of the wind, a part of the PVT collector field could have higher exposure to wind than the other due to the inclination on a horizontal surface. However, this can only be confirmed with a detailed measurement of wind direction and wind speed at various positions of the collector field. Additionally, the different inclination of the collectors and the relatively smaller gaps between the substructure and the PVT-panels can obstruct active airflow on the rear side of the collector field, potentially contributing to the observed reduction in the U-value. The heat transfer on the rear side of the field is also less efficient compared to that in the laboratory tests. The zero-loss efficiency for total radiation is slightly higher compared to the test. The heat loss parameter c_6, is greater than the test values. The mass flow rate during the laboratory tests was between 40-53 kg/(m²·h), whereas the mass flow rate for the demo plant varied from 5-40 kg/(m²·h). The difference in mass flow rate and the mathematical model ($\eta_{0,hem}$ instead of $\eta_{0,b}$) could be the reason for the variation of the zero-loss coefficient and its wind dependence parameter.

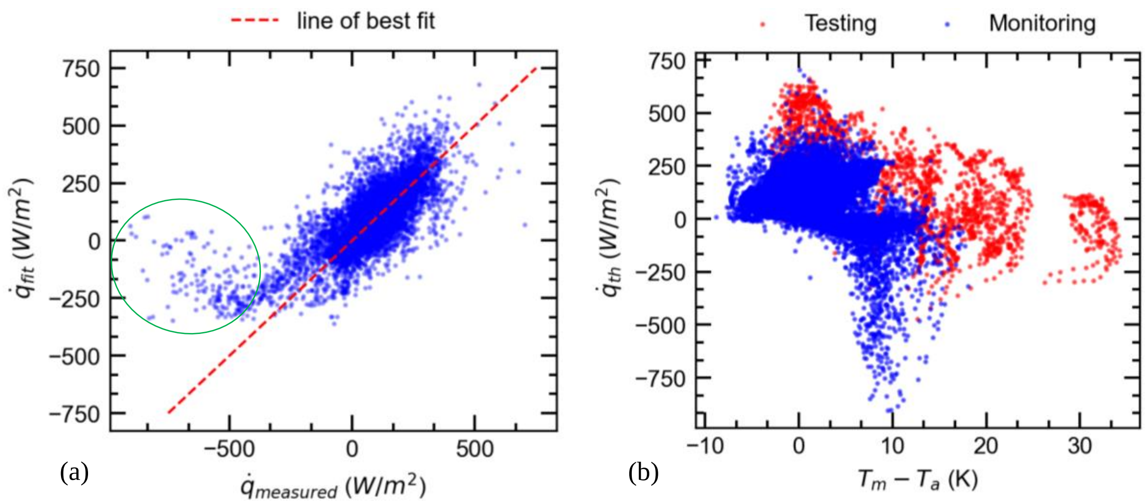

Fig. 8: (a) Comparison between measured and fitted specific thermal power of the PVT collectors for monitoring data, (b) Measured specific thermal power as a function of $T_m - T_a$ for testing and monitoring

Fig. 8(a) illustrates a reasonable fit between the measured and modelled specific thermal power for most instances. However, for $\dot{q}_{measured}$ below -500 W/m² (the cluster marked within the green boundary), the heat losses are underestimated. These data points correspond to the $\dot{q}_{th}$ below -500 W/m² denoted by blue dots in Fig. 8(b) and represent the data during the beginning of buffer cooling mode during summer nights. Compared to other operation modes, during these periods, the inlet temperature was higher (average of 31 °C), the average outlet temperature was 15 °C, ambient temperatures were moderate (average of 15 °C) and the average sky temperatures were 3.5 °C (minimum of -10 °C). These conditions indicate that the radiative heat losses dominate during those instances and higher values of c_4 can be expected. The use of eq. 6 for the calculation of c_4 could have led to an underestimation of the result as it is related to zero-loss efficiency. Our calculation shows that radiative heat losses accounted for at least 48 % of the total cooling achieved and the rest was covered by convective heat losses. However, these ratios serve as an initial approximation and could not be validated with the test results as the tests were not carried out during the night. Furthermore, to quantify the cooling potential of PVT collectors at night, the data during night cooling are considered to calculate a typical value for the heat loss coefficient. This typical heat loss coefficient, which is calculated as the ratio of measured specific thermal power ($\dot{q}_{th}$) and the temperature difference ($T_m - T_a$) for the night cooling, is 21 W/m²·K. However, this value depends on and varies with ambient conditions like wind speed, ambient temperature and sky temperatures. In Fig. 8(b), the data points representing the test sequences with higher operating temperatures i.e. $T_m - T_a$ of more than 15 K up to 35 K (inlet temperatures up to 58 °C) do not exist in the monitoring data.

Tab. 2 shows the error estimates while calculating the collector thermal power using the two different parameter sets to fit the measured data. The column "Testing" refers to the error estimates calculated using the test parameters to estimate the fitted specific thermal power ($\dot{q}_{th,fit}$). Whereas the column "Monitoring" displays the corresponding error estimates based on the parameters identified from the monitoring data. Except for a very small deviation in RMSE, the error estimates show that the parameters obtained from the monitoring data provide comparatively better estimates for the specific thermal power ($\dot{q}_{th,fit}$). So, we can conclude that for the monitoring data, the identified parameters provide better accuracy.

Tab. 3: Comparison of accuracy of collector coefficients from testing and monitoring

Error Estimate	Equation	Testing	Monitoring
Root Mean Squared Error (RMSE)	$\sqrt{\frac{1}{N}\sum_{i=1}^{N}\left(\dot{q}_{th,measured} - \dot{q}_{th,fit}\right)^2}$	80.5 W/m²	80.9 W/m²
Mean Absolute Error (MAE)	$\frac{1}{N}\sum_{i=1}^{N}\left\|\dot{q}_{th,measured} - \dot{q}_{th,fit}\right\|$	51 W/m²	48 W/m²
R-Squared (R^2)	$1 - \frac{\sum_{i=1}^{N}\left(\dot{q}_{th,measured} - \dot{q}_{th,fit}\right)^2}{\sum_{i=1}^{N}\left(\dot{q}_{th,measured} - \dot{q}_{th,measured,Mean}\right)^2}$	0.52	0.59

7. Conclusions

This paper presents a case study of a PVT-heat pump system for heating and cooling operations in a non-residential building, with an emphasis on the thermal performance of PVT collectors. The system exhibited a moderate level of efficiency compared to other systems with similar configurations studied within the same project. For the heating period, the seasonal performance factor $SPF_{bSt,H}$ was 3.3 and for the cooling period, $SPF_{bSt,C}$ was 4.1. The PVT collectors made a significant contribution to the system, supplying 24 % of the heat and 35 % of the cooling energy to the primary buffer. In particular, for commercial buildings with limited roof space, PVT collectors demonstrated the advantage of providing electricity, cooling and heating in the same area. Overall, PVT collectors proved to offer greater flexibility for geothermal heat pump systems supporting both heating and cooling operations, as well as regenerating the ground during transition seasons. However, in terms of efficiency, this system configuration appears to be relatively inefficient and additional analysis is required to further clarify the system performance.

In addition, the collector coefficients of the QDT model defined by ISO 9806:2013 were calculated using monitoring data and then compared with existing parameters from standardized tests. The deviation in parameters could be attributed to two main aspects: the difference in environment and installation conditions and the difference in operation mode. The new set of parameters provided a better fit to the QDT mathematical model. The inclusion of night data related to the passive cooling operation is particularly relevant for the uncovered (WISC) PVT collectors without rear-side insulation like the one described in this paper. However, there is currently no such standardized framework for the inclusion of such data during the parameter identification, which is very important for the representation of the performance of the WISC PVT collectors for operation in periods without solar irradiation. Therefore, the collector parameters obtained in this paper can be used to describe the performance of the specific PVT collectors for heating as well as cooling under real operating and installation conditions. However, they cannot be used to define the performance of the collectors under standard testing conditions and to compare them with the other PVT collectors. Standard test sequences for nighttime testing need to be defined for the identification of an additional parameter set that represents the performance of PVT collectors at night i.e. during night cooling and heat gains from the environment.

8. Acknowledgements

The presented work and the results are part of the research project “integraTE - 03EGB0023”, funded by the Federal Ministry of Economics and Climate Protection (BMWK) and the state of Lower Saxony and carried out with Fraunhofer-ISE and IGTE of Stuttgart University. Furthermore, we would like to thank our industry partners nD-System GmbH, Architektur- und TGA-Planungsbüro Carsten Grobe, PA-ID Prozess GmbH, TripleSolar BV, SunMaxx PVT GmbH, Consolar Solare Energiesysteme GmbH and Splus2 GmbH for their support. The responsibility for the content of this publication lies solely with the authors.

9. References

Brötje, S., Kirchner, M., Schabbach, T. and Giovannetti, F., 2018. Performance Assessment of a Photovoltaic-Thermal Roof with Modular Heat Exchanger, EuroSun 2018 Conference Proceedings, Rapperswil, Switzerland, International Solar Energy Society. DOI: 10.18086/eurosun2018.02.10.

Eurostat, 2023. Shedding light on energy in the EU. Interactive publication, Luxemburg, Eurostat [Online]. DOI: 10.2785/405482.

Gehlin, S. and Spitler, J. D., 2022. Annex 52 - IEA HPT - Long-term performance monitoring of GSHP systems for commercial, institutional, and multi-family buildings, Final report, Heat Pump Centre, Borås, Sweden. DOI: 10.23697/XSBR-XN83.

ISO 9806, 2013. Solar energy — Solar thermal collectors — Test methods, ISO.

Malenković, I., Pärisch, P., Eicher, S., Bony, J. and Hartl, M., 2013. Definition of Main System Boundaries and Performance Figures for Reporting on SHP Systems: Deliverable B1, IEA Solar Heating & Cooling Programme.

Helmling, S., H., Langner, R. and Geimer, K., 2022. Betriebsanalyse von 5 PVT-Wärmepumpensystemen auf Basis von Feldmessdaten über 12 Monate im Rahmen des Projektes integraTE, Tagungsunterlagen: 32. Symposium Solarthermie und regenerative Wärmesysteme, Bad Staffelstein, Germany, 138–152.

Umwelt Bundesamt (2023) Energieverbrauch für fossile und erneuerbare Wärme [Online]. Available at https://www.umweltbundesamt.de/daten/energie/energieverbrauch-fuer-fossile-erneuerbare-waerme accessed 27 July 2023.

Weiss, W. and Spörk-Dür, M., 2023. Solar Heat Worldwide: Global Market Development and Trends 2022, Detailed Market Figures 2021, IEA Solar Heating & Cooling Programme. DOI: 10.18777/ieashc-shw-2022-0001.

Zenhäusern, D., Bamberger, E. and Baggenstos, A., 2017. Energiesysteme mit Photovoltaisch-Thermischen Solarkollektoren, Schlussbericht PVT Wrap-Up, Institut für Solartechnik SPF, HSR Hochschule für Technik Rapperswil, Switzerland.

Giovannetti, F., Lampe, C., Kirchner, M., Littwin, M., Asenbeck, S. and Stephan, F., 2019. Experimental investigations on Photovoltaic-Thermal arrays designed for the use as heat pump source, Santiago, Chile, ISES SWC 2019.

Investigation of a solar cooling and process heat system in hot climates for steam, heat and cold supply in industry

Uli Jakob[1] and Michael Strobel[1]

[1] Dr. Jakob energy research GmbH & Co. KG, Weinstadt (Germany)

Abstract

This paper analyses a solar cooling system including a hybrid heat pump (HHP) and concentrating Fresnel collector plant of 400 m^2 for industrial purpose at four different locations in hot climates (Barcelona in Spain, Johannesburg in South Africa, Mexico-City in Mexico and Cairo in Egypt). The HHP consists of adsorption chillers (AdC) and compressions chillers (CC) connected in series. This design combines the benefits of both technologies, as the solar thermally driven AdCs work in most efficient temperature levels and the CCs only provides the remaining cooling load. The TRNSYS simulation concluded that the operation in Johannesburg shows best performance in total numbers, accounting more than 160 MWh/a solar yield, as well as the steadiest provision of cold throughout the year. The AdCs in the system cause a significant increase of the electrical Energy Efficiency Ratio (EER_{el}) of the CCs by up to 20 %. Furthermore, a connected steam network at the industrial sites serves as heat storage to provide stored solar heat even at night-time. That means that the solar thermally driven chillers have the potential to operate even in night times, resulting in most efficient operation thanks to lower ambient air temperatures. The COP_{th} of the AdC is between 0.45 and 0.50 for Johannesburg and Mexico-City. The increased efficiency of the CCs and solar generated cooling capacity cause a reduction in electricity consumption. This again leads to potential savings of CO_2 emissions. The calculated savings for Johannesburg account more than 50 t/a. The conclusion of the paper is, that the investigated solar cooling system shows best energetic and technical performance for applications in South Africa.

Keywords: Solar cooling, solar process heat, solar steam generation, hybrid heat pump, adsorption chiller, heat rejection, energy analysis, TRNSYS, steam network simulation

1. Introduction

Energy saving and energy efficiency actions are crucial to lower the world's greenhouse gas (GHG) emissions. More than 20 % of direct GHG emissions can be traced back onto the industrial sector. By attributing further emissions from electricity and heat production this share increases to 31 % GHG emissions in total (Pachauri and Meyer, 2014). Renewable energy, in fact solar energy, shows a potential of 5.6 EJ/a in 2050 (UNIDO, 2010) in industrial process heat. Here, the food sector has the major share with 46 %. Currently, the share of Renewable Energies (RE) in the food sector accounts only about 4 %, which is used almost completely in process heat (Eurostat, 2018). However, electricity is second most consumed energy source in food industry with 34 %. Generation of cold here is again the most required form of usage accounting 31 %, see Figure 1. In total, supply of cold accounts 11 % of energy consumption in the food industry (Monforti-Ferrario et. al, 2015). This share differs significantly from one product to another. At this point, the use of solar cooling promises savings in both GHG emissions and primary energy consumption. Concentrating solar systems generating steam are capable to function as a heat source for both process heat and process cooling and show great possibilities of application in the food industry. This paper analyses such a system, in particular with regard to its cooling performance and its possible use in a global context.

10.18086/swc.2023.04.08 Available at http://proceedings.ises.org

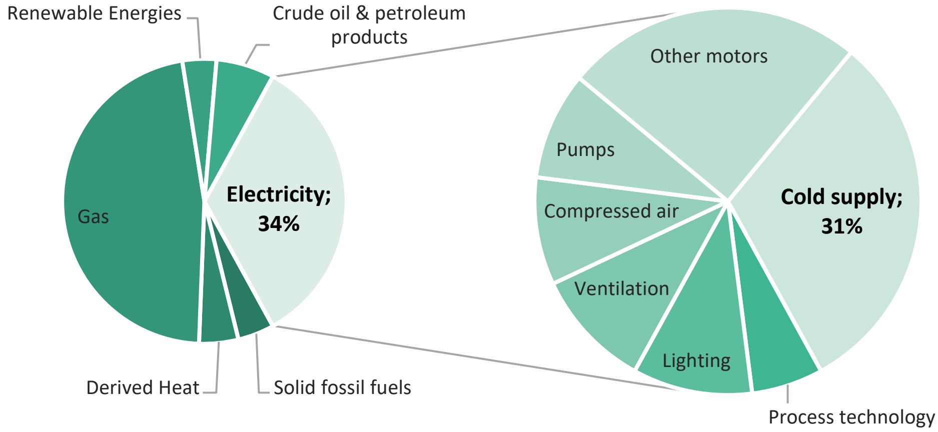

Figure 1: Distribution of total energy consumption and electricity consumption in the food industry. Adapted from (Eurostat, 2018) and (Monforti-Ferrario et. al, 2015) (Source: JER)

2. Weather data analysis

The analysis explores four different locations on three different continents: Europe, Africa and North America. The locations are the cities of Barcelona (Spain), Cairo (Egypt), Johannesburg (South Africa) and Mexico-City (Mexico). A preliminary analysis of the weather conditions for each city is conducted. Each location represents dry weather with hot summers and mild winters, as the temperature ranges show in Figure 2. In addition to the hot temperatures, the chosen global locations have good conditions in terms of Global Horizontal Irradiation (GHI).

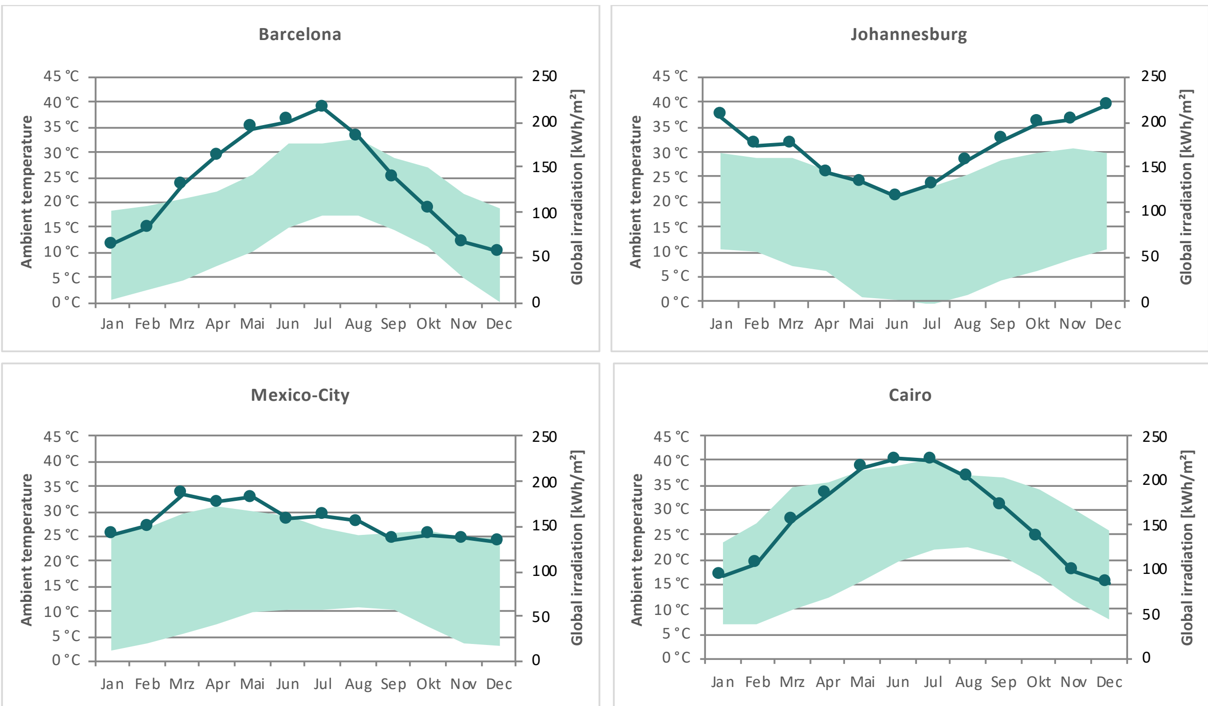

Figure 2: Investigated weather data (ambient air temperature range and global irradiance) for the four global locations.

Mexico-City is the location closest to the equator, followed by Johannesburg, then Cairo and the city farthest away from the equator is Barcelona. The relationship of the locations in context to the distance to the equator can also be seen in the range of the GHI over the year, as the range of the GHI in Barcelona is the most diverse and the GHI in Mexico-City is the steadiest over the year. The yearly sum of GHI is in Johannesburg the highest with 2,036 kWh/m²a and the lowest in Barcelona with 1,600 kWh/m²a. Cairo and Mexico-City show here a similar sum of 1,898 kWh/m²a and 1,859 kWh/m²a, respectively.

Taking into account the temperature levels, Cairo shows the hottest temperature with a maximum of 40 °C, which is up to 10 K higher than in Mexico-City and Johannesburg or about 8 K higher than in Barcelona. Furthermore, as Johannesburg is the only location of the four investigated ones, located on the Southern hemisphere, so it is the only one with higher GHI and higher temperatures from September to March, whereas especially Cairo and Barcelona show high temperature ranges and GHI from April to September. Table 1 also shows the annual direct normal irradiation (DNI) per location.

Table 1: Comparison of annual DNI for the four global locations.

Barcelona	Johannesburg	Mexico-City	Cairo
1,737 kWh/m^2a	2,130 kWh/m^2a	2,055 kWh/m^2a	2,039 kWh/m^2a

3. Investigated solar cooling system

3.1 Design approach

The investigated solar cooling system follows basically the design of the HyCool project using innovative hybrid chillers (Frazzica et. al, 2020). The system will provide both heat and cold for industrial purposes. Several unique features, such as concentrating solar collectors, steam generation, latent heat storage, adsorption chiller, compression chiller, as well as steam, hot water and chilled water circuits are combined within the system, what makes the system so innovative. The schematic design of the system, using two Fresnel collector fields and providing finally both heat and cold, is shown in Figure 3.

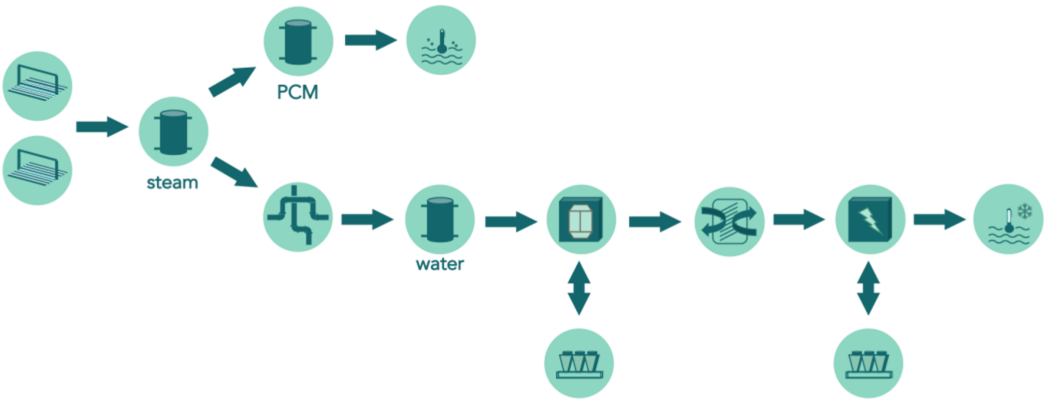

Figure 3: Schematic design of the solar cooling system. (Source: JER)

It contains two fields of concentrating Fresnel collectors providing steam at 25 bar. The steam then will be forwarded to a steam drum, with a 0.5 m^3 volume, separating liquid elements from the gaseous steam. The first solar generated steam of the day is forwarded to a latent heat storage using phase change material (PCM) for industrial heat usage at night-time. Once the storage is fully charged, the system switches to supply the local already existing industrial steam network. The steam network, operating at a pressure level of 20 bar, which supplies heat to a hot water storage. This storage serves as heat source for the thermally driven chillers. The so called HHP storage tank has a volume of 5 m^3. The core of the system is the energy efficient combination of adsorption chillers and compression chillers. Designed in a series connection, the adsorption chillers pre-cool the return flow of the chilled water-glycol mixture, in order that the conventional compression chillers must provide less cooling capacity and thus save electricity accompanied by GHG emissions. However, the chilling cycle is divided into two cycles. The compression chillers is placed directly in the chilling cycle circulating the water-glycol mixture, whereas the adsorption chillers serve a chilled-water cycle which is connected via a heat exchanger to the glycol-water mixture cycle.

Two adsorption chillers are designed with a cooling capacity $\dot{Q}_{chill}$ of 32 kW each under nominal conditions. These chillers are operated with heat from the HHP storage tank with hot water of 85 to 90 °C. The adsorption chillers work in a discontinuous process, resulting in a non-steady chilled water temperature level. The design of the system takes into account, that adsorption chillers show best performance and efficiency when they work with chilled water temperatures at a moderate level. Thus, the AdCs cool the chilled water in a first step from 12 °C down to 8 to 12 °C. The cooling capacity of the AdCs is affected by the provided heat level, the heat rejection and chilled water temperature. In a second step, then the CCs cool down the chilled water to 5 °C to reach in a steady way the targeted process temperature.

Another design approach for the solar cooling system with an HPP, using a cascade configuration of the AdC and CC, was investigated in detail for industrial applications below 0° C in Spain and showed an EER_{el} of 7-8 at ambient air temperature of 36-37°C (Jakob, et. al, 2018).

3.2 Modelling and simulation of the system

The system described was modelled with the simulation program TRNSYS 17. The subject of the simulation is to display the energetic performance throughout the year and to calculate the annual cooling yield. Therefore, emphasis was put on including all components affecting the thermal and energetic performance of the system, such as pressure conditions, specific storage and beyond. Since the focus is on the analysis of possible location and weather-related differences, the mass flows and further processing of steam, hot and chilled water is of great importance.

Table 2: Overview of used TRNSYS types referring to their role in the system simulation.

Component	Type
Concentrating solar collector	Type 1288
Evaporator	Type 1998
Adsorption chiller	Type 820
Compression chiller	Type 666
Evaporation water tank	Type 534
Storage representing PCM storage	Type 60c
HHP storage	Type 60t
Virtual storage (steam network)	Type 60c
Heat exchanger	Type 91
Glycol tank	Type 4e
Pumps	Type 3b

Within the simulation model, the concentrating Fresnel collectors are modelled using Type 1288 in order to calculate the transferred solar energy for heating the heat transfer fluid with its properties. Since Type 1288 doesn't have the potential to work with a fluid in two phases, including its evaporation from liquid to gaseous, the evaporation of the fluid must be modelled separately. Type 1998 is used for this purpose, which is a steam evaporator that calculates the evaporation rate including the resulting mass flows on steam side as outlet and feed water in relation to the entered pressure level and the associated enthalpy of evaporation. The collector model therefore doesn't consider the evaporation temperature, but supplies heat to the collector fluid, which in a further step evaporates the fluid, in this case water, in relation to the supplied heat. At the pressure level of 25 bar, the evaporation enthalpy is 1,860 kJ/kg. According to this calculation method, superheating of the steam is not taken into account. Since the pressure level and thus the resulting evaporation temperature are fixed, the mass flow varies depending on the solar irradiation and the solar collector output. However, before the thermal energy is fed to the evaporator, the evaporation water tank with a volume of 0.5 m^3 is heated up with the collector fluid. Thus, the combination of tank and evaporator simulates the steam drum.

From there on, only the steam mass flow is considered. The first 200 kWh of steam are supplied to the storage tank by the steam evaporator type 1998. At night, the storage tank is discharged from 1 a.m. so that the stored heat can also be used at night. The design of the storage tank and the further use of the heat is not part of the detailed investigation of the performance of the solar cooling system. However, the piping to the storage tank is taken into account as steam condenses within the piping due to heat losses from the piping. This condensate is fed to the Type 1998 as feed water.

Once the storage tank is charged, the rest of the solar generated steam is fed into the existing steam network of the industrial plant. This steam network is actually considered as a virtual storage. This storage carries the solar generated steam and provides heat to the HHP storage tank until it reaches a maximum temperature of 96 °C to avoid boiling. In fact, the virtual storage tank transfers as much heat to the HHP storage tank as solar heat was generated. The loading capacity is therefore limited to the accumulated solar heat that is available.

Type 820 is used for the water/silica gel adsorption chillers. Thanks to the HHP storage tank, heat is supplied to the AdC at a constant temperature between 90 and 95 °C. Under nominal conditions, the AdC has an output of 32 kW cooling capacity. The design of the CCs is based on the data of the Multichiller MCL 78-3 E with a cooling capacity of 50 kW and an EER_{el} of 3.21. For reasons of simplification, the type of heat rejection is constant for each simulated location. The heat rejection inlet temperature of the chillers is set to 5 K above the ambient air temperature. The adsorption chiller Type 820 simulates the operation of a two-chamber adsorption chiller, including internal evaporator and condenser. Thus, both the process of desorption and adsorption are considered. In fact, this requires a simulation in equivalent time steps. In detail, the duration of each cycle, the time of the thermal regeneration of the sorption material and the duration of the exchange of the cycle process must be specified. Since the duration for the exchange is the shortest (10 seconds), this defines the minimum time step of the entire simulation. This short time step combined with the duration of the investigated system simulation results in a data set of 3,153,600 per unit.

Table 3: Characteristics of used heat transfer fluids.

Heat transfer fluid	Density	Spec. heat capacity	Application
Water	1,000 kg/m^3	4.19 kJ/kgK	heat supply AdC, chilling cycle AdC
Glycol 34	1,045 kg/m^3	3.67 kJ/kgK	heat rejection cycle AdC, heat rejection cycle CC
Glycol 50	1,085 kg/m^3	3.27 kJ/kgK	chilling cycle, CC

The entire chilling process focuses on cooling down the heat transfer fluid, a water glycol mixture with 50 % glycol, in the chilling cycle to a target temperature of 5 °C. The heat rejection cycles of both AdC and CC runs with Glycol 34. Both the density and the specific heat capacity are adapted following the specifications in Table 3. The chilled fluid is stored in the glycol tank with a storage volume of 5 m^3. Since the simulation aims to use the generated solar energy whenever and for as long as possible, the mass flow of the chilling cycle runs continuous. This means, that the CCs also run permanently. Since the investigation of the system performance only focuses on the solar performance, the permanent operation of the chilling cycles doesn't affect the entire investigation. However, the return flow temperature of the chilled fluid is fixed at 14 °C. In connection with the assumed mass flow of 20,000 kg/h glycol mixture, the permanent cooling capacity demand is 127.2 kW. This definition was based on the fact, that the four CCs, each with a cooling capacity of 50 kW, are able to provide the desired cooling capacity without the support of the solar thermally driven AdCs. In addition, since the cooling demand can vary greatly, no detailed study of the use of the chilled fluid has been made. In fact, this limit improves the scalability and comparability of the individual simulation results.

Figure 4 shows the entire simulation deck in TRNSYS 17. The simulation can be understood from the upper left corner to the lower right corner. To make the system easier to understand, cold fluid flows in a cycle are shown in blue and hot flows in red. Heat rejection cycles are shown in green.

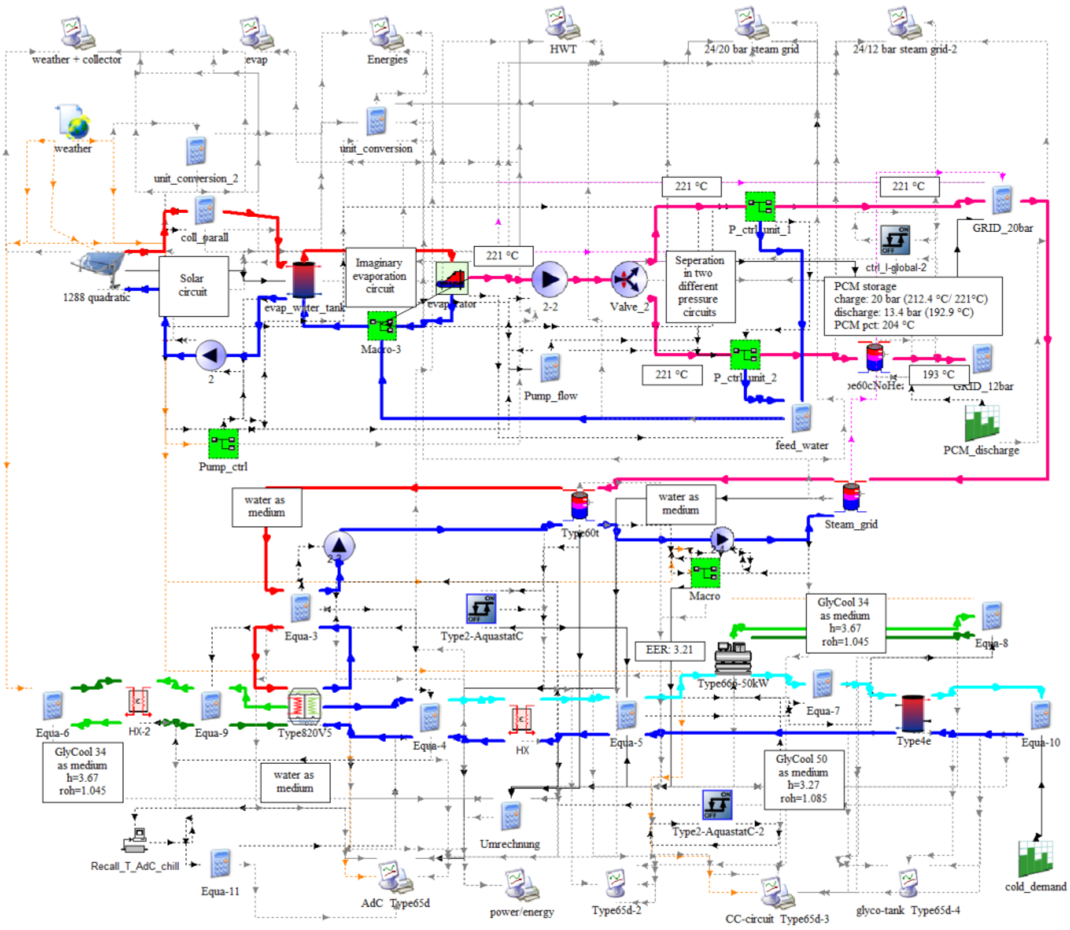

Figure 4: TRNSYS deck of the solar cooling HHP system. (Source: JER)

A detailed analysis of the hydraulics and the pressure conditions in the system as well as the design of the heat exchanger was not carried out. It is expected that these aspects will not results in differences in the performance of the HPP system at different locations. In addition, the power consumption for the various components in the system is also not part of the performance study.

4. Results

First, the weather data conditions were analyzed, secondly the results of the four TRNSYS simulations and finally an assessment of relevant Key Performance Indicators (KPIs) for each location. The results of the simulations are evaluated with regards to EER_{el} and Global Warming Potential (GWP).

According to the weather data, Johannesburg shows the best boundary conditions for the performance of the solar cooling system. The temperature profile reaches the lowest temperatures of all the locations examined. Both sets of weather data for Mexico-City and Cairo have a similar GHI, a similar irradiation, but Cairo shows the highest ambient air temperature of all locations, which anticipates a reduction in the cooling capacity of the chillers. Barcelona has the greatest variance in solar irradiation over the course of the year and also the lowest GHI of the four investigated locations, which means that the lowest solar yield with the lowest cooling yield can be expected.

4.1 Daily analysis

The analysis of the course of a day basically shows the influences and process of solar thermal energy in the simulation. The trends in the Figure 5 show a 48-hour period for December 21 and 22 for the Johannesburg location, including the summer solstice. It shows the performance curves of the solar collector system, the PCM storage loading and the cooling capacity of both AdCs. First, the solar collector system generates heat, which is further distributed to the evaporator in the TRNSYS simulation deck to generate steam. The evaporation water tank (steam drum) is then preheated and the loading of the PCM storage begins. The loading process then takes a little over an hour. The loading curve runs below the solar collector curve, since the PCM storage trend only represents the steam capacity produced. As soon as the PCM storage is fully loaded with 200 kWh, the loading process stops. The capacity of the solar collectors increases during the day and drops briefly at noon. This drop is caused by the design of the concentrating Fresnel collector field, which is oriented in a north-south direction. In fact, in good weather conditions, the solar concentrating collectors provide heat for the system for eleven hours.

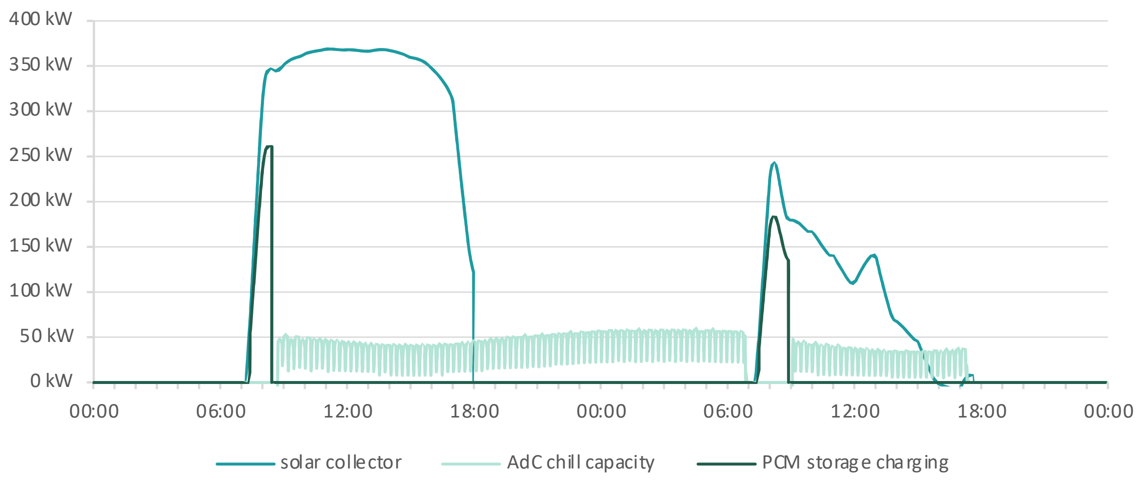

Figure 5: System performance trend for 48 hours.

The operation of the AdCs starts as soon as the PCM storage is fully loaded. The two AdCs then run until shortly before the next solar heat generation the next morning. This shows the effects of storing the solar generated steam in the steam network of the industrial site, which makes it possible to run the chillers at night as well. Moreover, the chillers run more efficiently at night, which can be seen in the higher cooling capacity output. At night, the ambient air temperature is lower than during the day, which affects the heat rejection temperature of the dry cooler. As already explained, the heat supply of the AdC is designed for a constant supply of heat. The next day, the conditions for the solar yield of the collectors are not optimal, since the solar irradiation is not as high during the day and it decreases further during the day. But it can be clearly seen that the PCM storage is fully charged by 10 a.m. After that, the solar thermal output is only used to operate the adsorption chillers. Since the solar irradiation doesn't provide heat as on the first day, the AdCs stop operating before 6 p.m.

4.2 Monthly and annual analysis

Figure 6 shows the monthly sum of the solar collector yield, the heat supplied to the AdCs and finally the sum of the cooling capacity generated by the AdCs. The performance of the systems correlates well with the weather analysis, in fact with the trends of the solar irradiation. The monthly solar yield of the concentrating collector field reaches a maximum of 50 MWh or even more in each investigated location. The overall maximum of the solar yield across all location is found in January in Johannesburg with 53.9 MWh.

Figure 6: Monthly system performance results for Barcelona, Johannesburg, Mexico-City and Cairo.

According to the system design, the yield shown above includes preheating of the water to the evaporation temperature and subsequent boiling. The heat supplied shown in the four graphs is similar to the steam distributed to the "virtual steam network". The last bar provides information about the actual cooling performance of the AdCs. All year round, Johannesburg has the very best performance as it is the only location where the cooling capacity never drops below 10 MWh per month. In terms of yield, Johannesburg is the best location, followed by Mexico City. Cairo hardly shows a greater yield than Barcelona, where solar cooling has little to no effect in the winter months (0.1 MWh).

Comparing the total amount of cold generated over the year in Figure 7, Johannesburg has by far the best performance with 162.0 MWh. Compared to Mexico City, an additional 45 MWh of cold can be generated for the Johannesburg location in South Africa. The performance of the systems for the Barcelona and Cairo locations shows a similar annual cooling capacity: 90.2 MWh in Barcelona and 87.4 MWh in Cairo. Although Cairo has more solar irradiation and higher solar yield compared to Barcelona, the chilling process is less productive and less efficient. The weather in Cairo is the hottest of all weather data sets examined. As the heat rejection process of the chillers depends largely on the ambient air temperature, the heat rejection temperature is higher than at other locations. This leads to a reduction in the COP of the chillers.

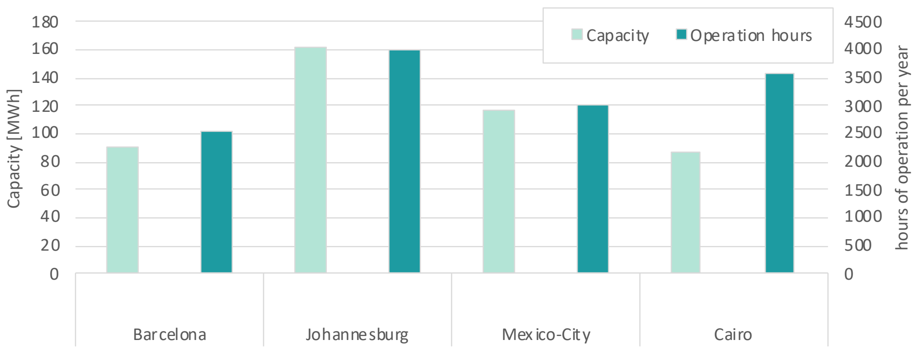

Figure 7: Comparison of annual capacity and operation hours for the four locations.

4.3 Efficiency analysis

Figure 8 shows a comparison of the monthly COP based on the heat supplied to the AdC and the resulting cooling capacity. What is striking is that Cairo has the lowest and therefore worst COP over the course of the year. Due to the high ambient air temperature, the heat rejection temperature affects the COP of the chiller. Mexico-City and Johannesburg show a very similar trend between 0.45 and 0.5. For the Barcelona location, the COP in the first six months is between 0.4 and 0.5. Only in December the COP falls extremely to 0.25. However, it should be mentioned that the cooling yield in this month is only 0.1 MWh.

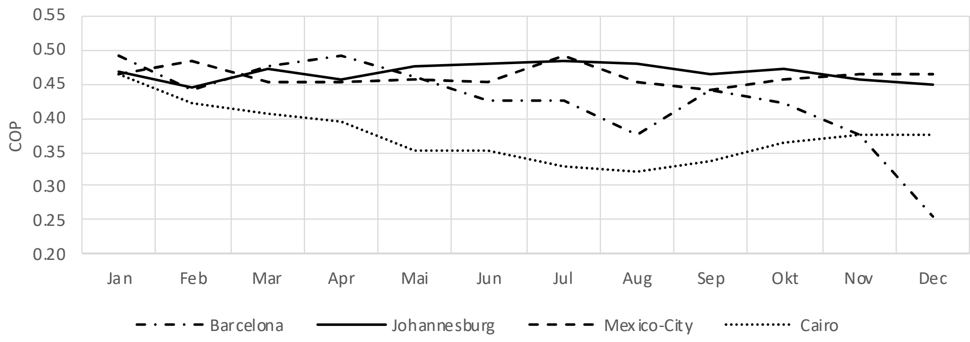

Figure 8: Comparison of annual COP trend per month of AdC**.**

The previously analyzed COP refers to the performance of the AdC, while the EER_{el} refers to the performance of the CC, respectfully to the combination of CC and AdC. The EER_{el} is a technical KPI. It evaluates the chillers' performance and compares the thermal energy output with the electrical energy supplied. As described above, the given EER_{el} of the CC is set to 3.21.

Figure 9 shows the EER_{el} for the Johannesburg location depending on the ambient air temperature. The maximum temperature for the location is slightly above 30 °C. The diagram compares the EER_{el}, which only takes into account thermal output energy of the CC, with the second EERel, which also takes into account the thermal output energy of the AdC. Thanks to the AdC, the CC allows a higher heat rejection temperature and therefore uses less electricity. Thus, the solar cooling system leads to an improvement of the EER_{el} in the system. The diagram shows two main things. On the one hand, the EER_{el} increases as the ambient air temperature decreases. In the case under consideration, the maximum EER_{el} of the CC reaches a value of 7.2. On the other hand, the diagram shows that the EER_{el} increase to higher values by including the AdC. The cooler the ambient air temperature, the greater the change in EER_{el}.

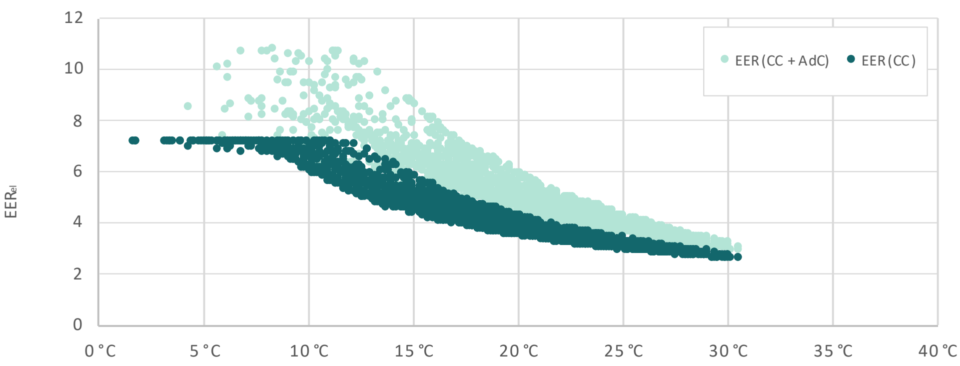

Figure 9: Display of EER_{el} in respect of ambient air temperature for Johannesburg.

Table 4 compares the results of the EER_{el} analysis for each location. The solar cooling system brings best results for the Johannesburg location. The table below also shows that for Egypt, not only the COP of the AdC has the worst performance, but also the EER_{el} of the CC.

Table 4: Comparison of EER_{el} per location for ambient air temperature of 25 °C and above

Location	**EER_{el} (CC)**	**EER_{el} (CC&AdC)**	**Upgrade**
Barelona	2.85	3.25	+14 %
Johannesburg	2.95	3.54	+ 20 %
Mexico-City	2.95	3.54	+ 20 %
Cairo	2.54	2.81	+ 11 %

4.4 Ecological analysis

The other KPI to be analyzed is the potential savings in CO_2 emissions. The potential saving in CO_2 emissions is based on the saved electrical energy consumption of the CCs through the integration of solar cooling. The electricity consumption again is affected by the EER_{el} of the CCs. The EER_{el} varies from one location to another and depends, among other things, but above all, on the ambient air temperature. In addition, the specific CO_2 emissions per kWh electricity vary between the four locations examined. The specific emissions are shown in Table 5. The table contains the OCED average CO_2 factor for comparison purposes. Spain has the lowest CO_2 emissions per kWh_{el} at 247 g/kWh. In contrast, South Africa has the highest CO_2 emissions factor of 926 g/kWh due to the high share of coal (88%) in electricity generation (IEA, 2019). The emission factors of Mexico and Egypt lie between those of Spain and South Africa.

Table 5: Comparison of CO_2 emissions per electric kWh by country.

Country	Spec. electricity-based CO_2-emissions
OECD (OECD, 2022)	432 g/kWh
Spain (2013) (OECD, 2022)	247 g/kWh
South Africa (2013) (OECD, 2022)	926 g/kWh
Mexico (2013) (OECD, 2022)	506 g/kWh
Egypt (2016) (Abdallah et. al, 2017)	630 g/kWh

The saved CO_2 emissions are calculated by dividing the annual cooling capacity by the specific EER_{el} and then multiplying by the individual CO_2 factor. The result of this calculation is shown in Figure 10. The use of solar thermal cooling systems in Johannesburg offers by far the greatest potential for saving CO_2 emissions. The reason for this result lies in two aspects: the Johannesburg location has the best production of cooling capacity and has the highest CO_2 emission per kWh_{el}.

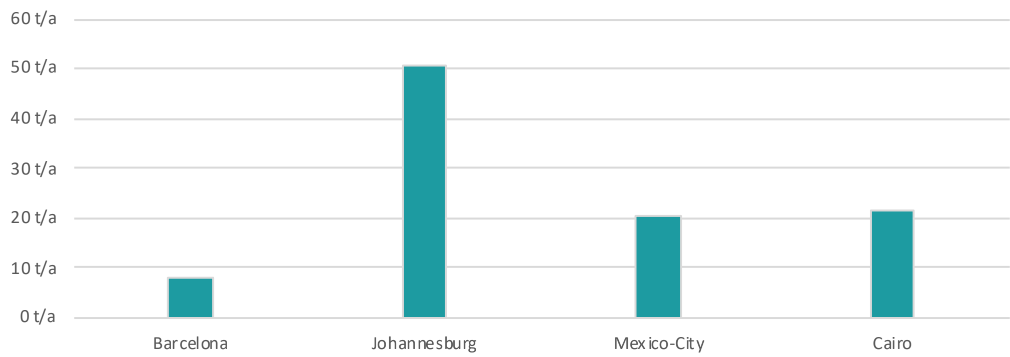

Figure 10: Comparison of potential CO_2 savings.

5. Conclusion

In this work, a solar cooling system for industrial purposes was described and analyzed. Such an innovative system goes beyond the state of the art in industrial heating and cooling supply. Solar systems require a uniform design that meets the requirements of the area of application and of course the climatic and solar conditions of the location. Compared to traditional industrial heating/cooling systems, solar systems tend to be more investment intensive, but are characterized by low operating costs because they are independent of fossil fuels and use solar energy as the primary energy source. For safety reasons in construction site operations, backup systems are still recommended. The technical installation also primarily requires know-how and experts as well as shipping the products. This can be a limitation when it comes to processes in remote areas or developing countries.

The system was simulated in the simulation program TRNSYS 17 to analyze the systems' performance for four locations: Barcelona in Spain, Johannesburg in South Africa, Mexico-City in Mexico and Cairo in Egypt. The weather data analysis showed that Johannesburg has the highest solar radiation, followed by Mexico-City and Cairo. Barcelona has the lowest solar radiation. After analyzing weather data, Johannesburg appears to be the most promising location for industrial solar cooling systems.

The simulation results proved that the most productive, efficient and highest yield results were achieved for the Johannesburg location. The Cairo location has the worst performance due to the highest ambient air temperatures of all four locations. This means that only the combination of ambient air temperature and solar radiation allows conclusions to be drawn about the solar cooling system. A closer look at the AdC's COP_{th} showed that Egypt in particular, but also Spain, have the lowest COP, while the COP for Mexico and South Africa are rather constant throughout the year between 0.45 and 0.50. By integrating solar thermal collectors and thermally driven sorption chillers to the system, the EER_{el} of conventional compression chillers improves by up to 20 %. The environmental analysis came to the conclusion that, with 50 t CO_2 per year, the greatest potential for saving CO_2 emissions lies in South Africa. Mexico and Egypt show a similar result, while Spain already uses renewable energy sources for electricity generation where the potential is therefore the lowest.

Finally, the simulation results and the results of the two analyzed KPI come to the same conclusion: the investigated solar cooling system for industrial purpose examined performs best in Johannesburg, South Africa. In addition, high ambient air temperatures in Cairo reduce the efficiency so much, that even with a higher solar thermal yield, the chiller cooling capacity is lower than in Barcelona.

6. References

Abdallah, L. and El-Shennawy, T., 2017. Evaluation of CO_2 emissions form electricity generation in Egypt: Present Status and Projections to 2030.

Eurostat, 2018. Energy balance sheets 2016 DATA: 2018 edition.

Frazzica, A. et. al, 2020. Renewable Heating and Cooling Solutions for Buildings and Industry. Proceedings, 65, 16; DOI: 10.3390/proceedings2020065016.

IEA, 2019. Data and statistics. Available online: https://www.iea.org/data-and-statistics/data-tables?country=SOUTHAFRIC&energy=Electricity&year=2019 (accessed on 26 November 2022).

Jakob, U. and Kiedaisch, F., 2019. Analysis of a solar hybrid cooling system for industrial applications. Proceedings of ISES Solar World Congress 2019; DOI:10.18086/swc.2019.55.07.

Monforti-Ferrario, F., Dallemand, J.-F., Pinedo Pascua, I., Motola, V., Banja, M., Scarlat, N., Medarac, H., Castellazzi, L., Labanca, N., Bertoldi, P., Pennington, D., Goralczyk, M., Schau, E. M., Saouter, E., Sala, S., Notarnicola, B., Tassielli, G., Renzulli, P., 2015. Energy use in the EU food sector: State of play and opportunities for improvement. European Commission: Institute for Energy and Transport and Institute for Environment and Sustainability.

OECD, 2022. Compare your country. Available online: https://www2.compareyourcountry.org/climate-policies?cr=oecd&lg=en&page=2&visited=1# (accessed on 26 November 2022).

Pachauri, R.K. and Meyer, L.A. (eds.), 2014. Climate Change 2014: Synthesis Report. Contribution of Working Groups I, II and III to the Fifth Assessment Report of the Intergovernmental Panel on Climate Change IPCC, Geneva, Switzerland, 151 pp.

UNIDO, 2010. Renewable Energy in Industrial Applications – An assessment of the 2050 potential.

LONG-TERM PERFORMANCE ANALYSIS OF ICE THERMAL COLD STORAGE WITH PHOTOVOLTAIC-POWERED DC REFRIGERATION SYSTEM FOR MILK COOLING THROUGH COMPUTATIONAL MODEL

Fikadu G. Bodena[1,*], Ole J. Nydal[2], Trygve M. Eikevik[2], and Demiss A. Amibe[1]

[1] School of Mechanical and Industrial Engineering, Addis Ababa Institute of Technology, Addis Ababa University, Addis Ababa (Ethiopia)

[2] Department of Energy and Process Engineering, Norwegian University of Science and Technology (NTNU), Trondheim (Norway)

Abstract

Pastoral communities in Africa depend on animal husbandry and milk production for their subsistence. Even though large quantities of milk are produced by pastoralists and small-scale dairy farms, the milk is either left to be spoilt or excessively consumed due to the absence of power for refrigeration. To address the problem, standalone PV-powered milk refrigeration system with ice thermal storage is proposed. The ice thermal storage replaces the battery for nighttime cooling. Sizing cold thermal storage for milking cooling using charging and discharging techniques with computational models is rarely investigated. Hence, this work focuses on the development of a transient computational model for performance analysis and prediction of the annual performance of a milk cooling system with DC refrigeration integrated with ice thermal storage powered by PV system. The simulations conducted using the MATLAB computational model were used to determine the thickness and mass of ice thermal storage to cool 50 liters of milk between 2-4 ºC for more than a day. A minimum of 0.061m ice thickness and 31kg mass of ice is required.

Keywords: Milk cooling, PV, Cold thermal storage, Charging, and discharging

1. Introduction

Since nearly one-third of the world's food production is spoilt, food preservation has become crucial for tackling world hunger (Hu et al., 2021). This issue is more prevalent in low-income nations, particularly those in East Africa. Dairy remains to be the most easily spoilt food product. Moreover, utilizing raw milk is causing a health crisis in developing countries as refrigerating milk with power from the grid is not a viable option mainly because of inaccessibility and limited infrastructure. Dairy production relies heavily on refrigeration, which reduces losses due to the deterioration of milk and improves milk quality (Sidney et al., 2021). Several developing countries are researching effective ways to keep milk preserved for at least 24 hours (De Blas et al., 2003).

Better and more affordable chilling technologies can help rural and pastoral communities in tropical regions grow economically by making milk reach the market without perishing. Hence, it is necessary to look into alternative energy sources that have the right cooling technology to preserve milk. One suitable solution is the use of PV-based solar power system. Although solar energy from the sun is sporadic, a solar energy system can be used to address the issue from the bottom up. Solar PV systems with rechargeable batteries were initially proposed as a substitute. (Kasera et al., 2021) investigated the performance of a vapor-compression-based milk refrigerator powered by solar photovoltaic modules. The system comprised of a variable-speed R290 DC compressor, solar PV panels, and batteries. (El-Bahloul et al., 2015) examined the operation of a 50-liter portable refrigerator, a solar-driven DC motor vapor compression refrigerator with a PV module, and a battery with or without PCM thermal energy storage. The results showed that this technology can be utilized to transport post-harvest crops in hot, arid environments.

10.18086/swc.2023.04.01 Available at http://proceedings.ises.org

Even though a lot of different researchers worked on utilizing solar batteries as one alternative energy storage for agricultural products and milk storage, the operational expenses of such systems are high and the energy conversion efficiency is low. Therefore, looking for other storage alternatives for use in rural and pastoral communities, where there is high milk production and located far away from the grid, is substantial. A cost-effective method for preserving milk and ensuring its safety for longer than a day is replacing the batteries with ice thermal energy storage. Ice thermal storage is a thermal latent heat storage system that potentially reduces cost and environmental pollution by shifting power demand from on- to off-peak hours. In comparison to sensible heat thermal energy storage, latent heat thermal storage systems provide substantial energy storage density and give the advantage of energy release or absorption with steady temperature control (Ezan et al., 2011). Water is the preferred phase change material (PCM) in this study due to its high latent heat of fusion and low cost. Producing and utilizing ice in static or dynamic modes are two alternatives (Ghaith & Onur Dag, 2022). In static mode, ice is produced and used in the same location during charge and discharge, while in dynamic mode, ice is produced during charging and transferred to another space for discharge (Asgharian & Baniasadi, 2019). In this study, latent thermal storage and static modes of ice utilization for milk cooling were used to reduce cooling costs and ensure good energy density. Regarding ice thermal storage, research has been conducted in this area for use as a replacement for solar batteries for a variety of applications. Some that are relevant researches are highlighted in this study. (Xu et al., 2018) found that all solar energy converted by the panels can be preserved in ice. The outcomes of the experimental studies show that it is feasible to store components utilizing ice thermal storage instead of battery banks. (Asgharian & Baniasadi, 2019) uses numerical models and spherical capsules to optimize an ice reserve system. Analysis indicates that utilizing two heat transfer fluid inlets minimizes charging time and improves efficiency by 37%. (Xie & Yuan, 2014) study focuses on a novel thin-layer ring structure and allows a numerical model to foresee ice formation in a thermal storage system. Following this, increasing ring thickness could improve the accumulation of ice rate. (Abhishek et al., 2019) conducted experimental and numerical modeling to look at the charging and discharging performance of an ice-on-coil latent thermal energy storage tank (LTES). The study found that thermal stratification in molten phase change materials significantly impacts charging and discharging performance.

(Xu & Li, 2022) investigated the feasibility of low-cost ice thermal storage as part of replacing battery banks for energy storage. Solar irradiance and compressor fluctuations were looked at under four different operating scenarios with a 3 HP residential air conditioning system. (Ghaith & Onur Dag, 2022) explored the possible use of ice storage and solar-powered cooling systems for space cooling in residential and commercial structures. With peak cooling loads of 70 kW and 366 kW, respectively, and PV panel installation areas of 240 m^2 and 400 m^2, the system was tested on two Abu Dhabi office towers and a residence in Dubai, which significantly decreased annual energy usage in the office building by 38%, with savings of around 140,160 kWh and a 40% reduction in CO_2 emissions.

(Kahraman, 2002) explored the energy-saving draft beverage coolers by applying numerical simulation and experimental validation of an ice bank and adopting a glycol solution as an alternative refrigerant to sustain stable inner pipe temperatures.
The development of PV-powered cold storage with a vapor compression refrigeration system (VCR) promotes the rapidly growing cold chain logistics industry, particularly fueled by the demand for agricultural fresh products (Hu et al., 2021). An experimental investigation of the ice thermal storage employed in milk refrigeration from rapid pasteurization-induced milk chilling has been carried out using an external ice-on-coil producing and ice melting increased rapidly, as the cooling load was higher, with outlet water temperature below 0.8°C in all discharging experiments (Grozdek et al.,

2010). (Han et al., 2021) proposed a photovoltaic direct-driven DC compressor ice storage air-conditioning system, improving refrigeration efficiency. In the investigation, as the thickness of the ice layer rises, the evaporator's thermal conductivity declines. (Hu et al., 2021) developed a PV-driven cold storage system with ice thermal storage, with PV capacity of 5.4 kW at a maximum cumulative solar insolation of 20.41 MJ/m^2, with a maximum daily cumulative ice mass of 144.10 kg, thereby providing a competitive alternative for chain logistics services and can be eased with the ice thermal storage system, which can maintain ice storage temperatures within 5°C for 11 hours. (Marques et al., 2014) look at the development and performance of a thermal storage refrigerator, emphasizing the numerical modeling and validation through experimentation carried out with the guidance of a working prototype refrigerator fitted with a PCM. The findings prove that embedding a 5mm PCM slab allows for 3-5 hours of uninterrupted use without an additional power supply.

To determine the precise quantity of ice needed for cooling the milk for more than a day and the quantity of energy necessary, the system should be sized using the proper technique. An ice thermal energy storage system's yearly electricity consumption and overheads can be reduced by 25% to 32% by optimal design (Sanaye & Khakpaay, 2022). Although there are several studies on ice thermal storage, a handful of them trace sizing through proper techniques that determine the amount of ice needed for charging and discharging, helping to avoid over- and under-sizing of the necessary amount of ice that is needed for milk chilling at night.
This study investigates the sizing of cold thermal storage for milk cooling, employing charging and discharging techniques using computational models and predicting the performance of the system.

2. Methodology

The ice thermal storage that is going to be traced and obtained through the refrigeration cycle mainly harvests power from a PV array and is driven by a DC compressor, as indicated in Fig.1. During the day, PV arrays transform solar energy into DC electricity, which is used to drive the DC compressor. The refrigeration effect is obtained through the use of R134a refrigerant in the vapor compression refrigeration(VCR) system, and as the temperature of the refrigerant in the evaporator is low, the heat is absorbed from the water, and ice begins to form in the ice storage tank when the water temperature of the thermal storage reaches 0°C.

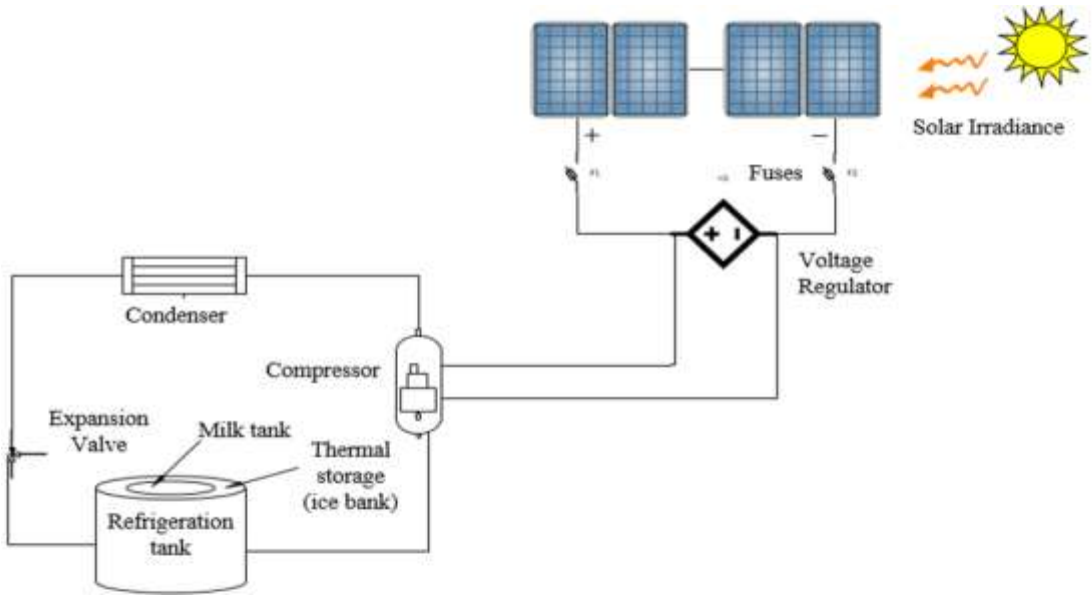

Fig. 1: overall description of ice thermal storage

The system consists of a concentric cylinder, where milk is placed in the inner cylinder, surrounded by a water jacket in the annular space. The evaporator helical coils are placed in the inner wall of the outer cylinder as shown in Fig. 2. During the day, an ice layer forms around the evaporator copper tube, and from the outer cylinder inward, ice slurries are used for night cooling.

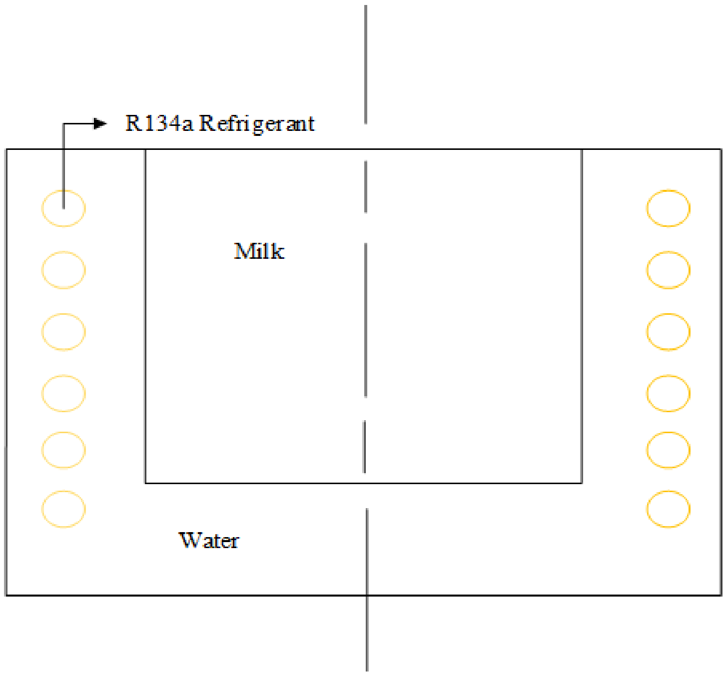

Fig. 2: Concentric ice thermal storage and milk tank

To determine the optimal mass of ice needed, temperature distribution in the water jacket and phase change with increase or decrease of ice thickness due to solidification or melting as a function of the cooling rate of the evaporator obtained from power input to DC variable speed compressor based on power generated by PV panel as per incident solar radiation is required. Such types of problems are usually solved by finite methods using moving boundaries and mesh (solid-liquid interface) or the enthalpy method with a fixed mesh. In this study, the fixed mesh technique and the enthalpy method are used.

The assumptions in the formulation of the computational model are the following:

- The heat transfer from the evaporator through ice/water to the milk tank is considered substantially one-dimensional in the radial direction.

- The charging process for ice is performed by heat transfer from the water to the evaporator in the concentric tank.
- As the water is cooled by the refrigerant in the evaporator coils, the ice thickness increases radially from the evaporator inward during charging as long as the cooling rate of the evaporator is greater than the cooling rate of the milk.
- When the cooling supplied by the evaporator decreases or becomes null in the evening and night, the ice melts, absorbing heat to overcome heat losses and maintain the milk temperature at 2-4 ^{O}C, as shown in Fig.3.

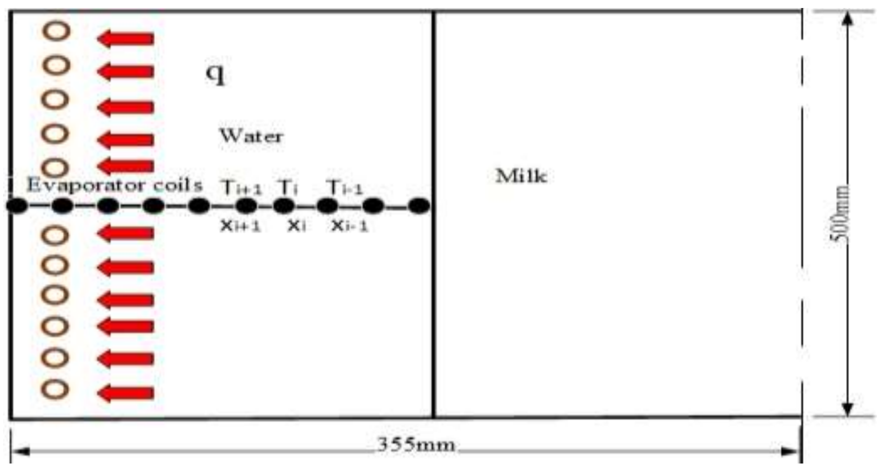

Fig. 3: Charging of ice with the nodal distribution and discharging of ice with the heat transferred from milk.

3. Numerical modeling of ice thermal storage

Ice thermal storage used in this study for milk cooling was modeled using the one-dimensional (1D) enthalpy method. As the heat transfer is predominantly in the radial direction, one-dimensional transient heat conduction equation is used to describe heat transfer during solidification and melting.

$$\rho c \frac{\partial T}{\partial t} = \frac{k}{r}\frac{\partial T}{\partial r} + k\frac{\partial^2 T}{\partial r^2} \quad \text{(Eq.1)}$$

Where ρ and c are density and heat capacity

The ice thickness is computed from the solid-liquid interface condition balance at the interface (Marques et al., 2014).

$$\rho_s L_f \frac{dr_i}{dt} = k_s \frac{\partial T_s(r_i,t)}{\partial r} - k_L \frac{\partial T_L(r_i,t)}{\partial r} \quad \text{(Eq. 2)}$$

Where k_s is solid thermal conductivity, k_L is liquid thermal conductivity, T_s and T_L are solid and liquid temperature.

For the water node at the milk tank boundary during charging as well as discharging, the following boundary condition is applied.

$$-k\frac{\partial T}{\partial r} = h(\ T - T_m) \quad \text{(Eq. 3)}$$

Where T_m is milk temperature.

The explicit finite difference method is used to discretize the above equation in the ice slab for solving the nodal temperature in the liquid and solid domain at the new time step by taking three adjacent nodes. The interior node temperature for the ice/water region is obtained as follows using the appropriate thermophysical properties.

$$T_i^{\ n+1} = \frac{\alpha \Delta t}{2\, r\, \Delta r}\left(T_{i+1}^{\ n} - T_{i-1}^{\ n}\right) + \frac{\alpha \Delta t}{\Delta r^2}\left(T_{i+1}^{\ n} + T_{i-1}^{\ n}\right) + \left(1 - 2\frac{\alpha \Delta t}{\Delta r^2}\right) T_i^{\ n} \quad \text{(Eq. 4)}$$

For the boundary node at the side of the evaporator, the heat flux of cooling from the evaporator has to be considered.

$$T_i^{\ n+1} = \frac{2\alpha \Delta t}{\Delta r^2}\left(T_{i+1}^{\ n} - \frac{\Delta r\, q}{k}\right) + \left(1 - 2\frac{\alpha \Delta t}{\Delta r^2}\right) T_i^{\ n} \quad \text{(Eq.5)}$$

Where q is the heat flux supplied by the evaporator on the outer cylinder surface.

$$q = \frac{\dot{Q}_{evap}}{\pi D\ H} \quad \text{(Eq.6)}$$

Where D and H are the diameter and height of thermal storage.

For the node of the water jacket at the milk tank side during charging without milk or in case of no heat transfer

$$T_{i,j}^{\ n+1} = \frac{2\alpha \Delta t}{\Delta r^2}\left(T_{i-1,j}^{\ n}\right) + \left(1 - 2\frac{\alpha \Delta t}{\Delta r^2}\right) T_i^{\ n} \quad \text{(Eq. 7)}$$

For the water node at the milk boundary during charging as well as discharging

$$T_i^{n+1} = (T_{i-1}{}^n) + \left(\frac{h\Delta r}{k}\right) \, (T_m - T_{i,j}{}^n) \qquad \text{(Eq. 8)}$$

Where $k = k_w$ $\rho = \rho_w$ $c = c_w$ for $T > 0.1^oC$ and $k = k_{ice}$ $\rho = \rho_{ice}$ $c = c_{ice}$ $T < -0.1^oC$

It is assumed that phase change will occur at $-0.1\ ^oC < T < 0.1^oC$, and the thermal conductivity and density are taken as an average of water and ice. However, the heat capacity is calculated from the latent heat of fusion as follows for the assumed phase transition interval, which is, in this case, 0.2 ^oC.

$$c = \frac{Q_L}{\Delta T} = h \qquad \text{(Eq. 9)}$$

The thickness of ice is obtained by interpolation, finding the radial length from the outer radius location of 0^oC at every time step.

4. Result and discussion

The simulation was carried out by using the climate of Semera, Ethiopia, and PV panel of 600 W, and milk tank of 50 liters for representative average days of months of the year, and ice/ water temperatures during charging and discharging, ice thickness, and milk temperature drops after pasteurization were determined.

4.1. Charging and discharging temperature of ice thermal storage

In this study, the water and ice mixture are utilized to cool the milk to the required temperature. During the day, water is charged from an immersed copper coil evaporator that contains an R134a refrigerant that brings the water's temperature to the required level of -1°C. Charged ice thermal storage starts draining once the compressor is off, raising the temperature of the water inside of thermal storage by a maximum of 2°C in 24 hours. The charging and discharging temperature of the ice thermal storage as shown in Fig. 4 of the average months of the year indicated that the maximum temperature of water inside of thermal storage was 2^oC at the end of the 24-hour length for all representative months.

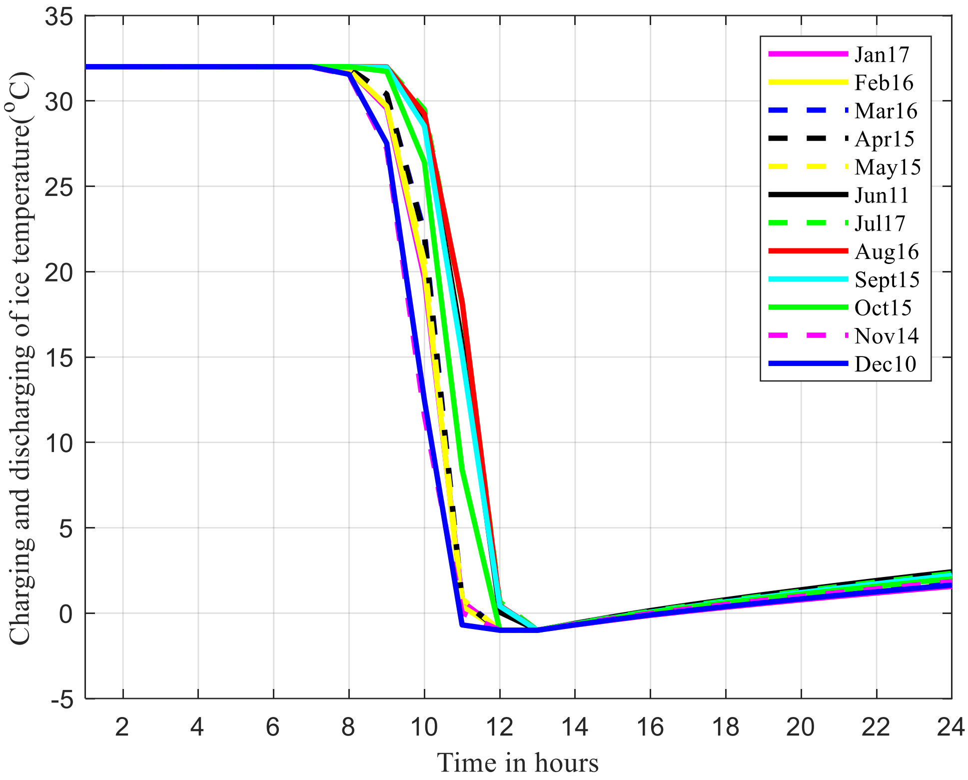

Fig. 4: charging and discharging ice water temperature in an average month of the year

4.2. Ice slab growth and melting in thermal storage

Whenever the solar PV harvests, the variable speed compressor runs, and as the temperature of the water reaches 0ºC around the immersed evaporative coil, the ice slab starts forming. The maximum ice slab thickness obtained from the simulation indicated about 0.074m and the minimum ice slab is about 0.061m in the average month of years during the charging as indicated in Fig.5 below.

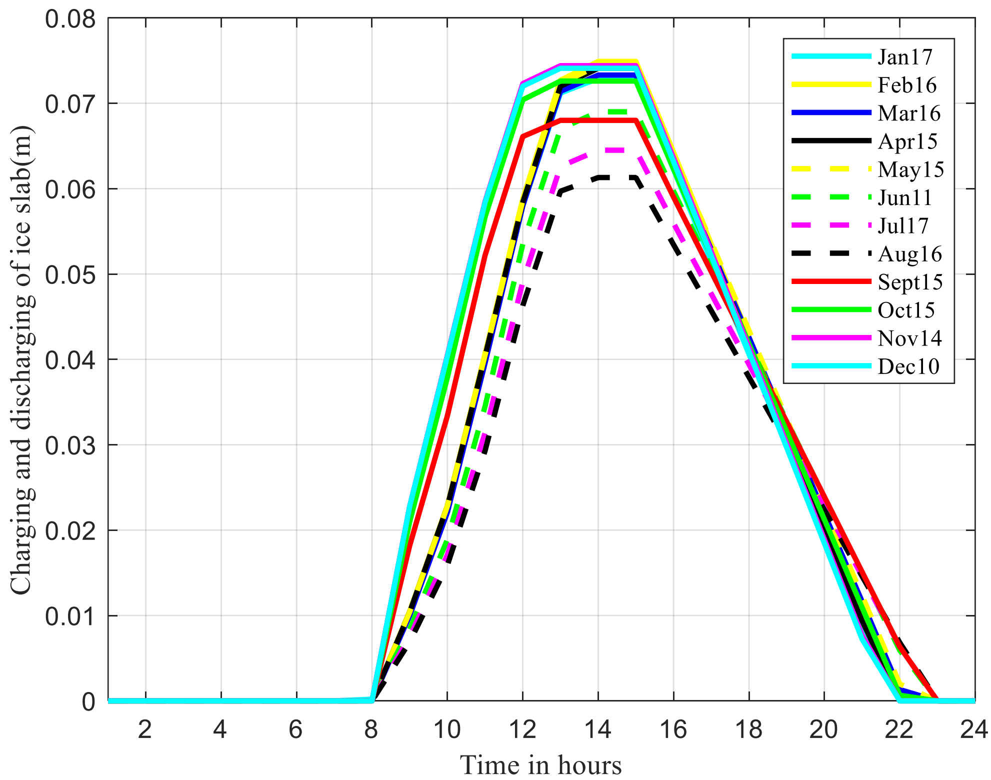

Fig. 5: Charging and discharging temperature and ice thickness of ice thermal storage for average months of a year.

4.3. Mass ice growth and melting

As the ice slab grew, the amount of ice mass required to cool the milk for the given 24 hours was identified. Similarly, as the ice slab started melting, the amount of mass of ice around the evaporative coil discharged. Fig.6 asserted that the maximum amount of ice was about 37 kg and the minimum amount was about 31kg in the average month of the year, respectively.

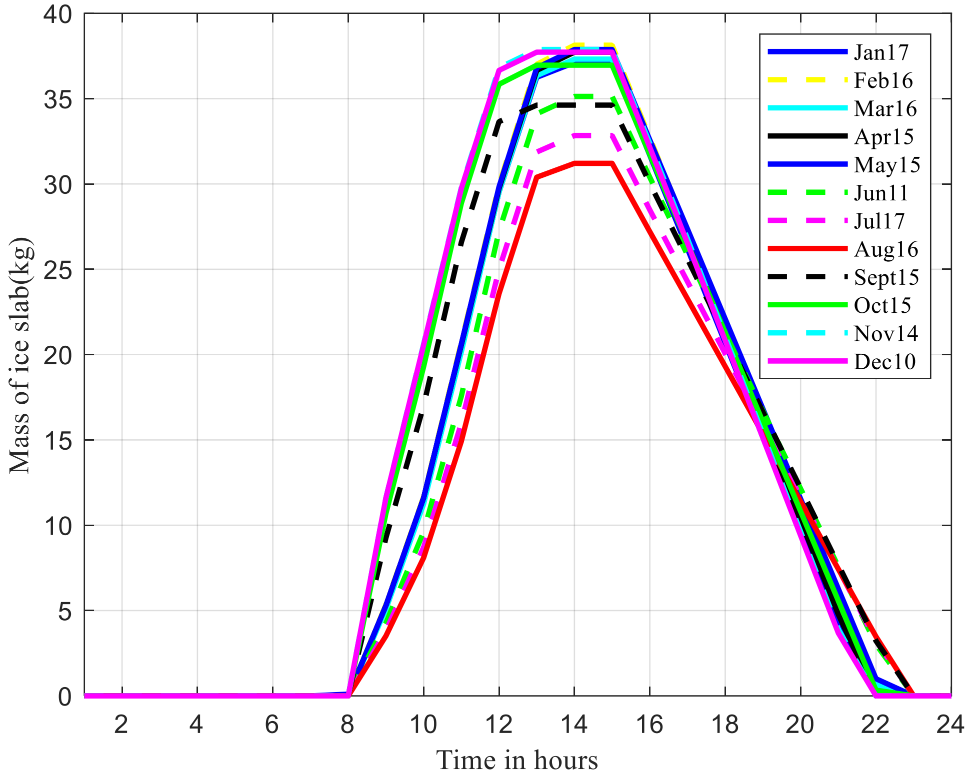

Fig. 6: Mass of ice charging and discharging in average months of the year

4.4. Milk Cooling Temperature

In this study, milk can be pasteurized using an evacuated-tube solar collector, an insulated storage tank, a circulation pump, and a control system. The method involves allowing hot water from a solar water heater to flow through a helical coil heat exchanger that is enclosed by milk in the pasteurization tank. This process ensures that the milk is heated to the required pasteurization temperature. The pasteurization tank has a capacity of 50 liters and requires a 1 m^2 area of evacuated tube solar collector to maintain the temperature of the pasteurized milk from 32°C to above 65°C. As indicated in Figure 7, the maximum temperature for milk pasteurization was 82°C in November and the minimum was 69°C in August. Once the milk reaches the required pasteurized temperature, it is transferred or flows to the milk-chilling tank and it can be cooled to temperatures of 2°C in less than 4 hours for all representative months of the year.

.

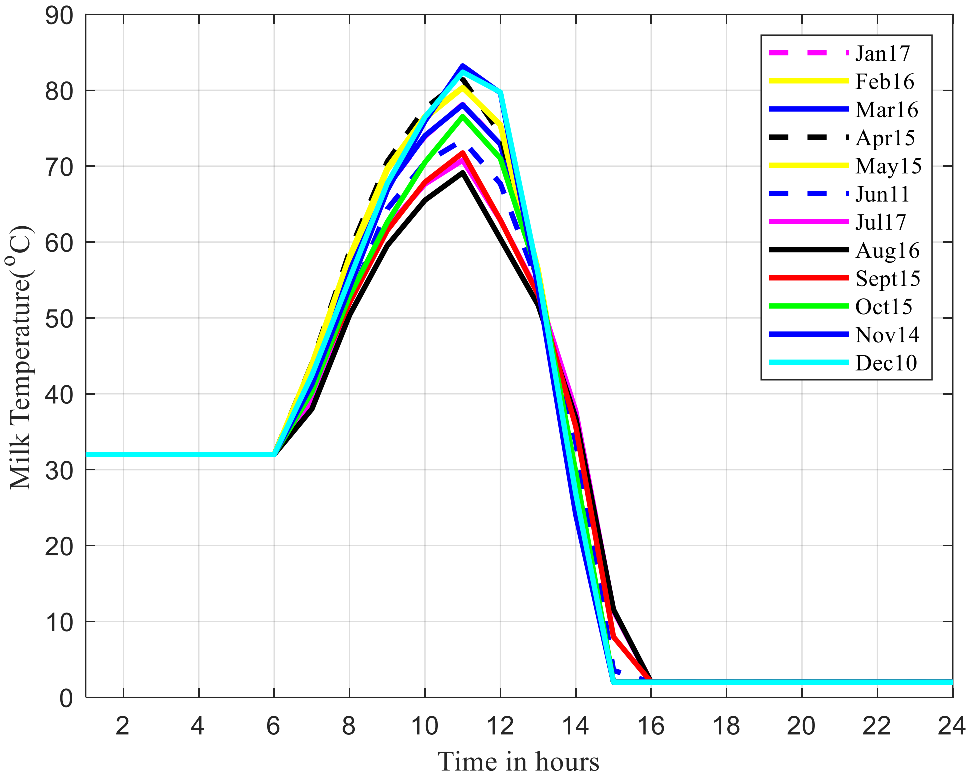

Fig. 7: Milk cooling temperature utilizing ice thermal storage for average months of a year.

5. Conclusion

Ice thickness and temperature during charging and discharging are computed using explicit transient heat conduction, and transient one-dimensional heat flow. Pasteurized milk is refrigerated to the required temperature in less than four hours utilizing ice as a backup. A minimum thickness of 0.061m and 31kg of ice is needed to keep 50 liters of pasteurized milk between 2 and 4^{o}C for more than a day.

6. Acknowledgments

We sincerely thank the Norad Energy Net Project for funding this effort. The materials that are being presented here are a portion of the entire project and should not be viewed as a project output.

7. References

Abhishek, A., Kumar, B., Kim, M. H., Lee, Y. T., Chung, J. D., Kim, S. T., Kim, T., Lee, C., & Lee, K. 2019. Comparison of the performance of ice-on-coil LTES tanks with horizontal and vertical tubes. Energy and Buildings.183, 45–53.

Asgharian, H., & Baniasadi, E. 2019. Experimental and numerical analyses of a cooling energy storage system using spherical capsules. Applied Thermal Engineering. 149, 909–923.

De Blas, M., Appelbaum, J., Torres, J. L., García, A., Prieto, E., & Illanes, R. 2003. A Refrigeration Facility for Milk Cooling Powered by Photovoltaic Solar Energy. Progress in Photovoltaics: Research and Applications. 11(7), 467–479.

El-Bahloul, A. A. M., Ali, A. H. H., & Ookawara, S. 2015. Performance and Sizing of Solar Driven DC Motor Vapor Compression Refrigerator with Thermal Storage in Hot Arid Remote Areas. Energy Procedia.70, 634–643.

Ezan, M. A., Ozdogan, M., & Erek, A. 2011. Experimental study on charging and discharging periods of water in a latent heat storage unit. International Journal of Thermal Sciences. 50(11), 2205–2219.

Ghaith, F. A., & Onur Dag, R. 2022. Performance and feasibility of utilizing solar-powered ice storage system for space cooling applications. Energy Conversion and Management. 16, 100319.

Han, K., Ji, J., Cai, J., Gao, Y., Zhang, F., Uddin, M. M., & Song, Z. 2021. Experimental and numerical investigation on a novel photovoltaic direct-driven ice storage air-conditioning system. *Renewable Energy*.*172*, 514–528.

Hu, C., Li, M., Wang, Y., Li, G., Ma, X., Du, W., Zhou, X., & Zhang, Y. 2021. Preliminary investigation on pilot-scale photovoltaic-driven cold storage with ice thermal storage based on vapor compression refrigeration cycle. Sustainable Energy Technologies and Assessments. 45.

Kahraman, R. 2002. Numerical and experimental investigation of melting of ice involving natural convection. International Journal of Energy Research. 26(4), 347–354.

Kasera, S., Nayak, R., & Chandra Bhaduri, S. 2021. Performance analysis of solar milk refrigerator using energy efficient R290. Case Studies in Thermal Engineering. 24, 100855.

Marques, A. C., Davies, G. F., Maidment, G. G., Evans, J. A., & Wood, I. D. 2014. Novel design and performance enhancement of domestic refrigerators with thermal storage. Applied Thermal Engineering.63(2), 511–519.

Sanaye, S., & Khakpaay, N. 2022. Innovative combined optimization and modified maximum rectangle method for equipment sizing and operational strategy of an integrated system with cold thermal storage. Energy Reports. 8, 137–160.

Sidney, S., Kim, S. C., Dhasan, M. L., & Prabakaran, R. 2021. A novel solar-powered milk cooling refrigeration unit with cold thermal energy storage for rural applications. Environmental Science and Pollution Research. 29,16346–16370

Xie, J., & Yuan, C. 2014. Numerical study of thin layer ring on improving the ice formation of building thermal storage system. Applied Thermal Engineering. 69, 46–54.

Xu, Y., & Li, M. 2022. Impact of instantaneous solar irradiance on refrigeration characteristics of household PCM storage air conditioning directly driven by distributed photovoltaic energy. Energy Science and Engineering. 10(3), 752–771.

Xu, Y., Li, M., Luo, X., Ma, X., Wang, Y., Li, G., & Hassanien, R. H. E. 2018. Experimental investigation of solar photovoltaic operated ice thermal storage air-conditioning system. International Journal of Refrigeration. 86, 258–272.

Performance evaluation of PVT-TEC air collector through the characteristic curve

Ajay Pratap Singh[a], Sumit Tiwari[a,*], Harender[a]

[a]Department of Mechanical Engineering, Shiv Nadar Institution of Eminence, Deemed to be University, Dadri, 201314, India

*Corresponding author: E-mail address: tiwsumit@hotmail.com (Tel. +91 8586985510; fax:+911126591251)

ABSTRACT

This paper deals with developing an analytical equation for the TEC combined with a PVT air collector. The PVT-TEC air collector produces thermal and electrical energy. The integration of TEC on the bottom side of the PV panel reduces the temperature of the PV cell, and then the system's overall efficiency is increased. For the analysis of the air collector, the input variables, namely solar irradiance and atmospheric temperature, have been taken for April month at Shiv Nadar Institution of Eminence (SNIOE), Gautam Buddha Nagar, India. The air collector has been modelled using MATLAB 2022a to find the temperature of PV cell, TEC, and collector outlet temperatures. After finding all temperatures, we can calculate the PVT-TEC air collector's overall electrical, thermal, and exergy efficiency. The results show how a characteristic curve varies with the thermal, electrical, and exergy efficiency. The η_{el} and $\eta_{eq,th}$ was found to be 11.77 – 14.17 % and 42.21 – 48.18 %, respectively. Further, the overall exergy varied from 12.24 – 14.62 %.

Keywords: *Thermoelectric cooler (TEC), Photovoltaic thermal (PVT), Air collector*

1. Introduction

Energy is the most essential key in daily life. The excessive use of fossil fuels for generating energy increases greenhouse gas emissions and affects the climate. Renewable energy is a promoting source of generating energy. Sun energy, wind energy, and geothermal energy are the alternative sources for producing electrical and thermal energy. Solar energy is particularly sustainable and eco-friendly energy (Tiwari et al., 2018).

Photovoltaic (PV) cells are commonly adopted for alternative energy, which can be used for different purposes. Generally, PV cells are insignificant due to almost 80% of heat being reflected back to the atmosphere (Nazri et al., 2019). Thus, PVT systems exist, which can generate energy in thermal and electrical forms. Electrical power can be used in remote areas where electricity is scarce, and thermal energy can be used for space applications. PVT collector combines a PV panel, absorber sheet, air duct and some heat extracting unit (Nazri et al., 2018).

(Tiwari et al., 2016) did mathematical modelling for PVT air collector. The finding was that the PVT collector generates both high and low-grade energy. Furthermore, the PVT air collector produces a reasonable amount of thermal energy. (Dimri et al., 2017) proposed a model for the TEC-integrated PVT air collector and compared his results with the PV-TEC air collector. The result showed that when compared to the PV-TEC air collector, the PVT-TEC air collector's overall electrical efficiency was 4.72 percent higher. (Singh et al., 2022) developed a mathematical model for the PVT-TEC air collector and analysed the solar cell transmissivity effect on the air collector's performance. The average thermal energy and η_{el} were 32.4 W and 14.3%, respectively.

(Naderi et al., 2021) developed PCM and TEG-integrated photovoltaic systems. The outcome was that the electrical efficiency was increased by 1.38% compared to the standard PV with the integration of PCM and TEG on the PV module. (Agrawal et al., 2023) fabricated an experimental setup for a PVT air collector with rectangular fins. In this experimental setup, a rectangular fin is inserted on the back side of the PV module to increase the heat exchange from the PV panel. The electrical and useful heat per year was found to be 1186 kW and 121 kW, respectively.

10.18086/swc.2023.04.15 Available at http://proceedings.ises.org

(Singh et al., 2023) developed an experimental setup for a PVT-TEG air collector integrated dryer. The setup generated the thermal and electrical energy for drying the grapes. The PV panel and η_{th} of the air collector were found to be 14.07% and 48.5%, respectively. (Gupta et al., 2022) proposed a PVT air collector integrated dryer for drying star fruit. The air collector systems' energy and exergy efficiency in FCD and NCD mode were 69.27%, 43.58% and 31.12%, 17.89%, respectively. (Çiftçi et al., 2021) did a computational and experimental study of vertical PVT air collector integrated solar dryer. Fins were placed over the absorber plate in this experimental setup to improve heat transfer. The average η_{th} of PVT collector with fin and without fin was found to be 54.2% and 51.2%, respectively.

In this paper, we have analysed the characteristic curve for PVT-TEC air collector's thermal and electrical efficiency performance.

2. Explanation of PVT-TEC air collector

The PVT-TEC air collector combines a PV panel, TEC, and air duct. Solar energy strikes the PV module, which photonic energy converts into electrical energy. TEC is located just on the bottom side of the PV panel; in TEC, only indirect energy will come from the bottom side of PV panel. Then, using the Seebeck effect, the temperature difference between the TEC ends generates electrical energy. The air duct is located just on the bottom side of the TEC to extract energy in thermal form for use in space heating. The fan is provided to drive the airflow, which has a capacity of (12 V, 0.2 A). The schematic figure of PVT-TEC air collector is given in Fig. 1.

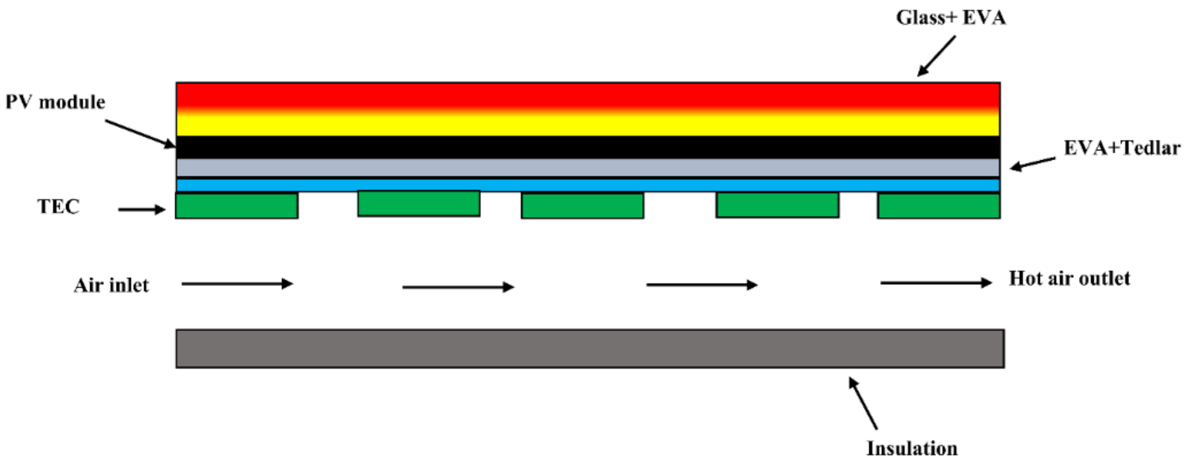

Fig.1. Schematic diagram of PVT-TEC air collector

3. Methodology

The methodology is given below.

- The I_t and T_a are input parameters have been taken from Shiv Nadar Institution of Eminence India for April 2023.
- For finding the solar cell, TEC, and collector temperature, MATLAB 2022a, have been used.
- After finding all temperatures, we can obtain overall electrical efficiency, overall thermal and exergy efficiency.

3.1 Thermal modelling of air collector

The assumptions are as follows.

- PV panel is an opaque type.
- TEC and bottom side of the PV panel consider the same temperature.
- The PVT-TEC air collector is in steady state.

The energy equation for PVT-TEC system is given below.

PV module,

$$I_t\alpha_c\tau_g bdx = h_t(T_C - T_{tec,t})\, bdx + U_{t,c-a}\,(T_C - T_a)bdx + \eta_c\tau_g I_t bdx \quad \text{(eq.1)}$$

Tedlar,

$$h_t(T_c - T_{tec,t})bdx = U_{b,c-f}(T_{tec,t} - T_f)(1 - \beta_{tec})bdx + U_{tec}(T_{tec,t} - T_{tec,b})\beta_{tec}\, bdx \quad \text{(eq. 2)}$$

TEC,

$$U_{tec}\,(T_{tec,t} - T_{tec,b})\beta_{tec}\, bdx = h_{tf}\,(T_{tec,b} - T_f)\,\beta_{tec}\, bdx + \eta_{tec}\, U_{tec}\,(T_{tec,t} - T_{tec,b})\beta_{tec} bdx \quad \text{(eq. 3)}$$

Air duct,

$$h_{tf}\,(T_{tec,b} - T_f)\beta_{tec} bdx + U_{b,c-f}\,(T_{tec,t} - T_f)(1 - \beta_{tec})\, bdx = U_{b-a}(T_f - T_a)bdx + \dot{m}_f\, C_f\, \frac{dT_f}{dx}\, dx \quad \text{(eq.4)}$$

Module efficiency (Skoplaki and Palyvos, 2009)

$$\eta_m = \eta_o\,[1 - \beta_o(T_c - T_o)] \quad \text{(eq.5)}$$

Overall electrical energy (Dimri et al., 2018)

$$E_{el} = \eta_m I_t\, A_m + \eta_{tec} U_{tec}(T_{tec,t} - T_{tec,b})\beta_{tec} A_m \quad \text{(eq.6)}$$

Overall electrical efficiency

$$\eta_{el} = \frac{E_{el}}{I_t A_m} \quad \text{(eq.7)}$$

Thermal efficiency

$$\eta_{th} = \frac{\dot{m}_f\, C_f\,(T_{fo} - T_{fi})}{I_t A_m} \quad \text{(eq.8)}$$

Equivalence thermal efficiency (Tiwari, 2017)

$$\eta_{eq,th} = \eta_{th} + \frac{\eta_{el}}{0.38} \quad \text{(eq.9)}$$

Exergy efficiency (Tiwari and Tiwari, 2016)

$$\eta_{th,ex} = \frac{\dot{Q}_{th,ex}}{[(I_t A_m)(1 - \left(\frac{4}{3}\right)\frac{(T_a+273)}{6000} + \left(\frac{1}{3}\right)\left(\frac{T_a+273}{6000}\right)^4)]} \quad \text{(eq.10)}$$

Total exergy efficiency (Tiwari and Shyam, n.d.)

$$\eta_{eq,ex} = \eta_{th,ex} + \eta_{el} \quad \text{(eq.11)}$$

The different design and heat transfer coefficient parameters are given in the appendix for finding the air collector's solar cell, TEC and outlet temperature.

The methodology is given in a flow chart to better understand the overall approach used for calculating the different results of the system.

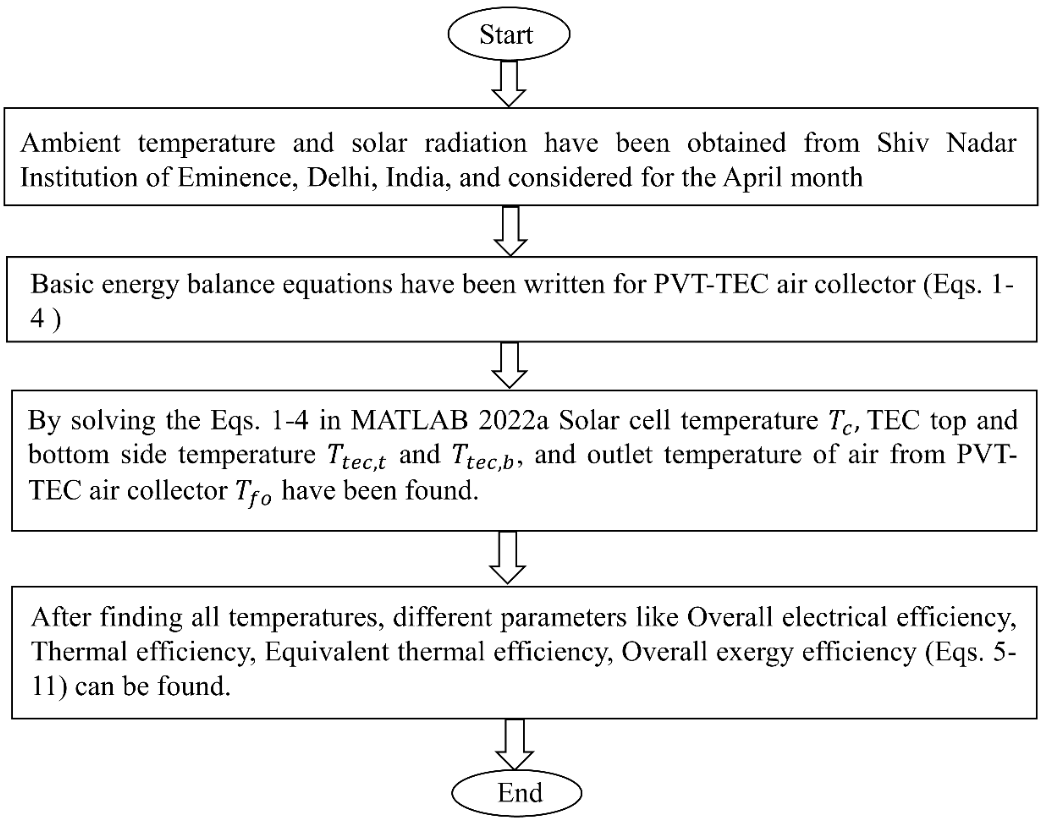

4. Results and discussion

Figure 2. represents the input parameters that have been taken from SNIOE, Gautam Buddha Nagar, India for April month. I_t and T_a are the input parameters.

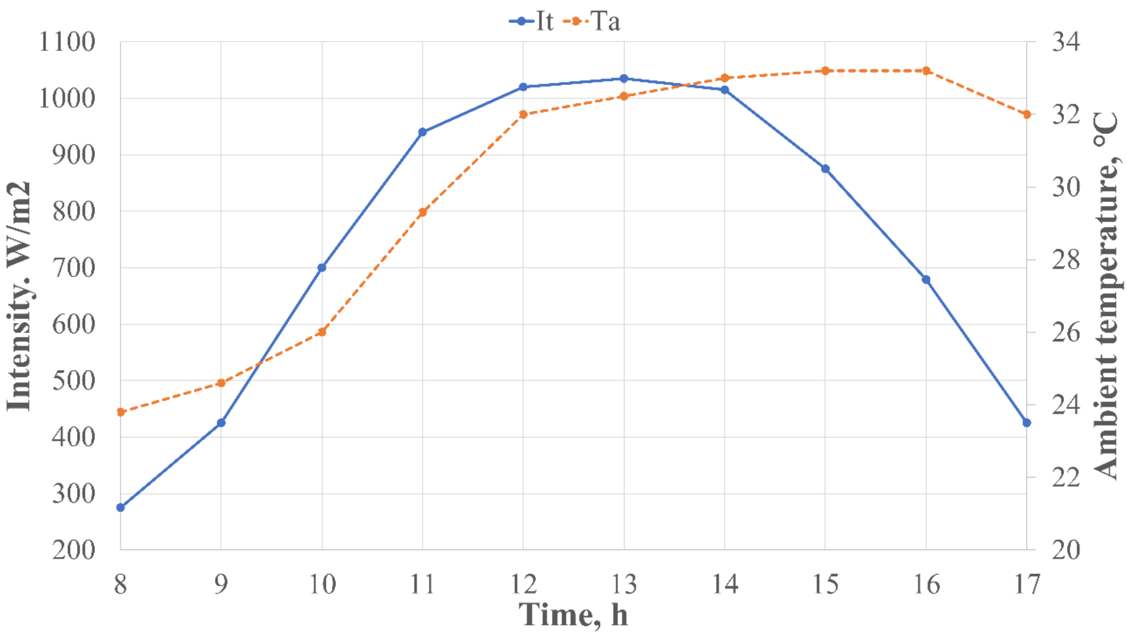

Fig. 2. Hourly variation of I_t and T_a

Figure 3. shows the changes in solar cell, TEC and air collector outlet temperature. The figure shows that the temperature of solar cells is greatest, followed by TEC and air collector outlet temperature. This is because

cells absorb photonic energy from the sun, indirect energy from the bottom side comes to TEC, heat from the bottom side of TEC, and air temperature increases.

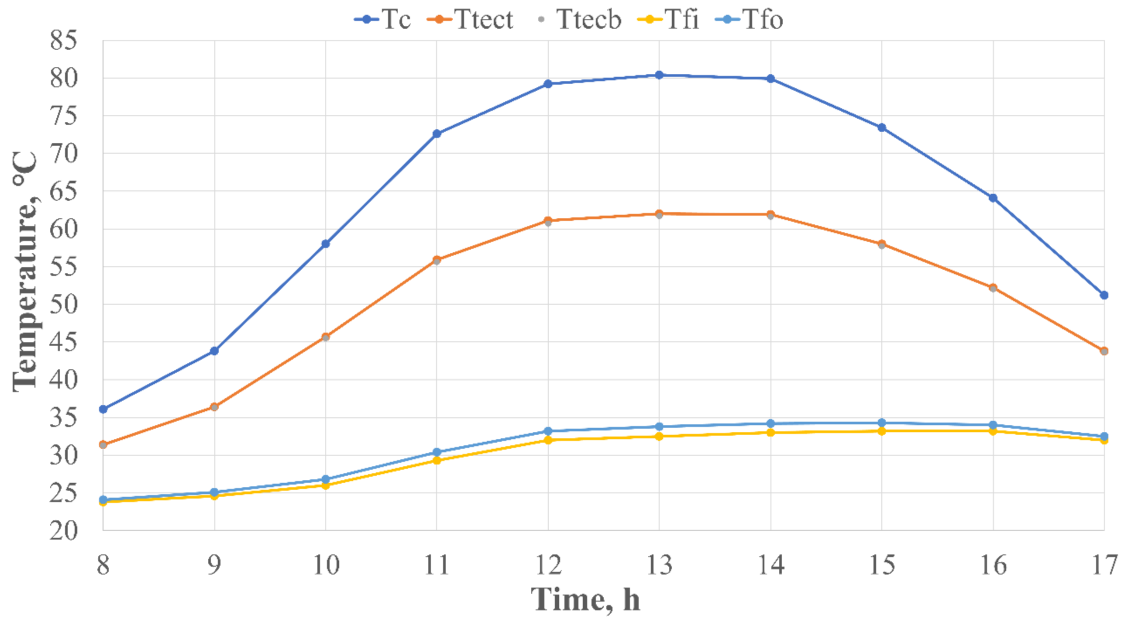

Fig. 3. Hourly changes of T_c , TEC and T_{fo} temperature on air collector

Figure 4 depicts the characteristics curve for η_{el}. The overall efficiency is a summation of the PV module and TEC efficiency. The overall electrical efficiency varies from 11.77 – 14.17 %. The overall electrical efficiency after fan operation varied from 11.35-12.68 % because some electrical power was consumed to operate the fan. The figure shows that with an increment the temperature of solar cell, its efficiency decreases with a negative slope. The higher temperature of solar cells drops the overall efficiency because charged electrons collide in the PV module.

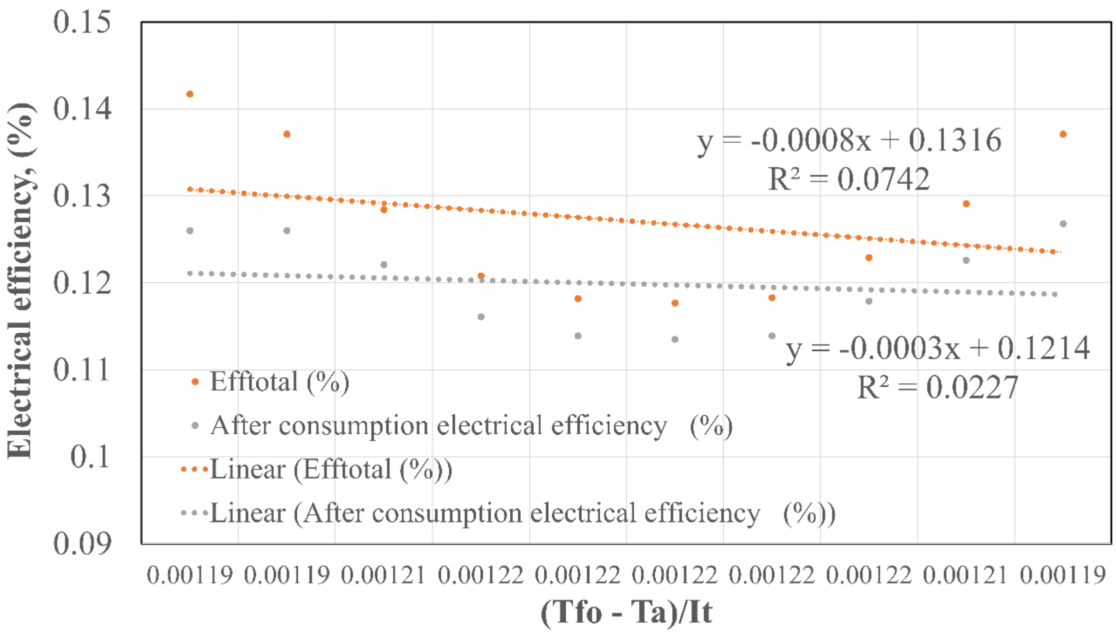

Fig.4. Characteristics curve for η_{el} in air collector

Figure 5 depicts the characteristic curve for η_{th}. The thermal efficiency varies from 10.9 – 11.25%. The figure reveals that the slope of thermal efficiency is positive. The reason behind that heat is being transferred from the back surface of the TEC, which is increasing the air temperature at the collector's outlet.

Figure 6 depicts the characteristic curve for $\eta_{eq,th}$. The overall (equivalence) thermal efficiency varies from 42.21 – 48.18 %. The graph itself reveals that the slope of overall thermal efficiency is negative. The reason behind this is that the overall thermal efficiency is the combination of thermal and electrical efficiency, and this η_{el} has more effect on overall efficiency, and we found a negative slope in overall thermal efficiency.

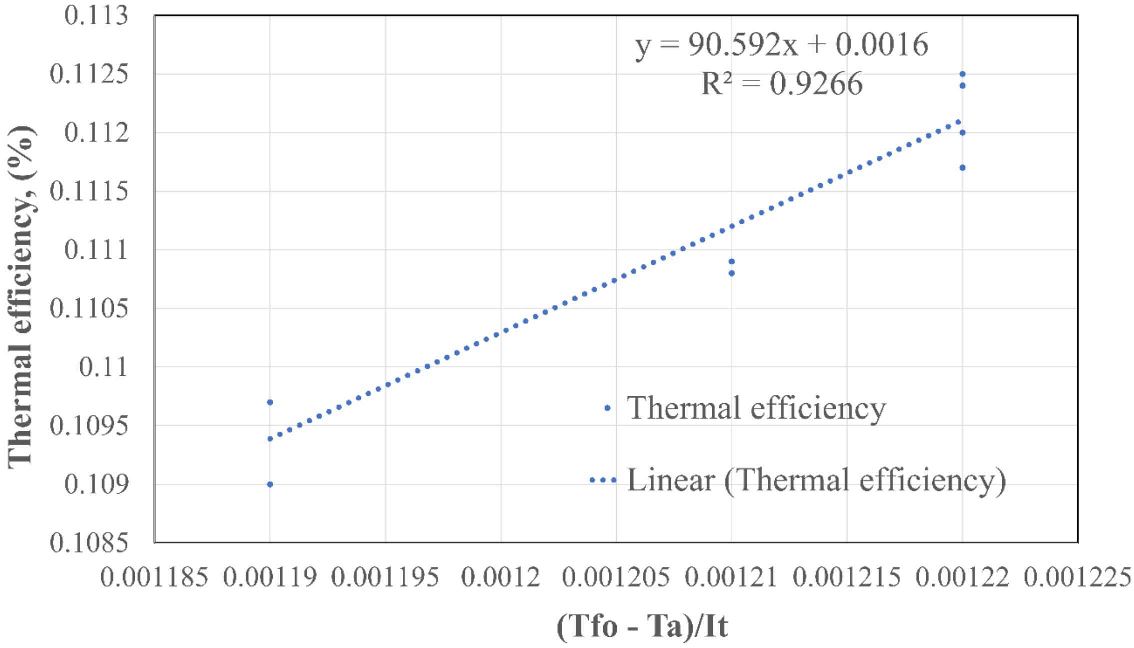

Fig.5. Characteristics curve for η_{th} in air collector

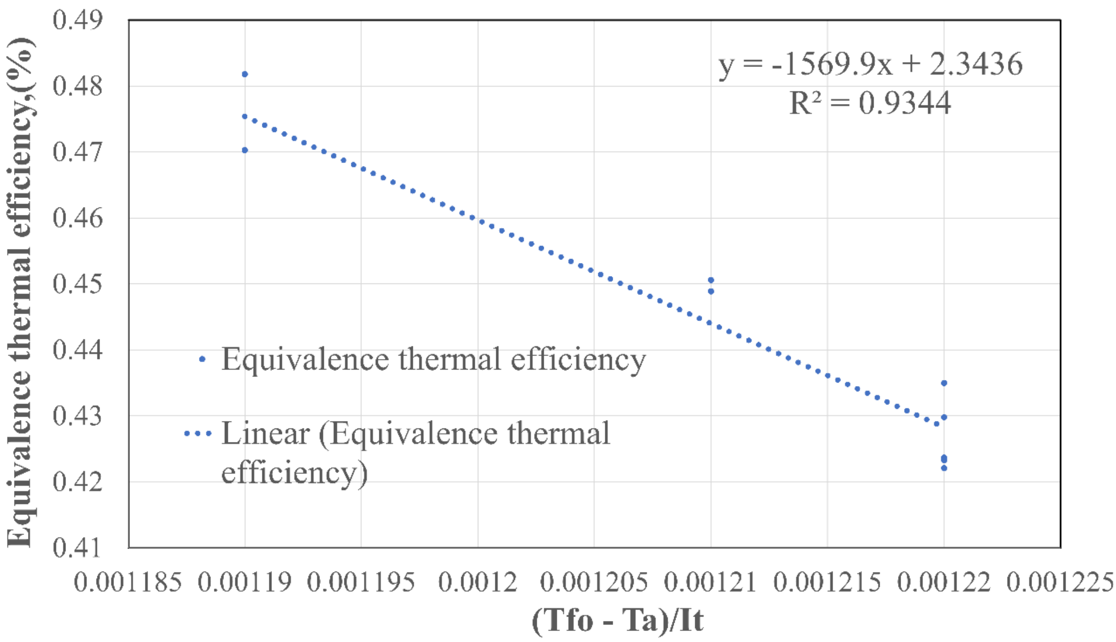

Fig.6. Characteristics curve for $\eta_{eq,th}$ in air collector

Figure 7 depicts the characteristic curve for $\eta_{eq,ex}$. The $\eta_{eq,ex}$ varies from 12.24 – 14.62 %. The overall exergy is a high-grade energy that is the addition of overall electrical energy and exergy. The overall exergy efficiency slope is also negative due to the overall electrical efficiency slope.

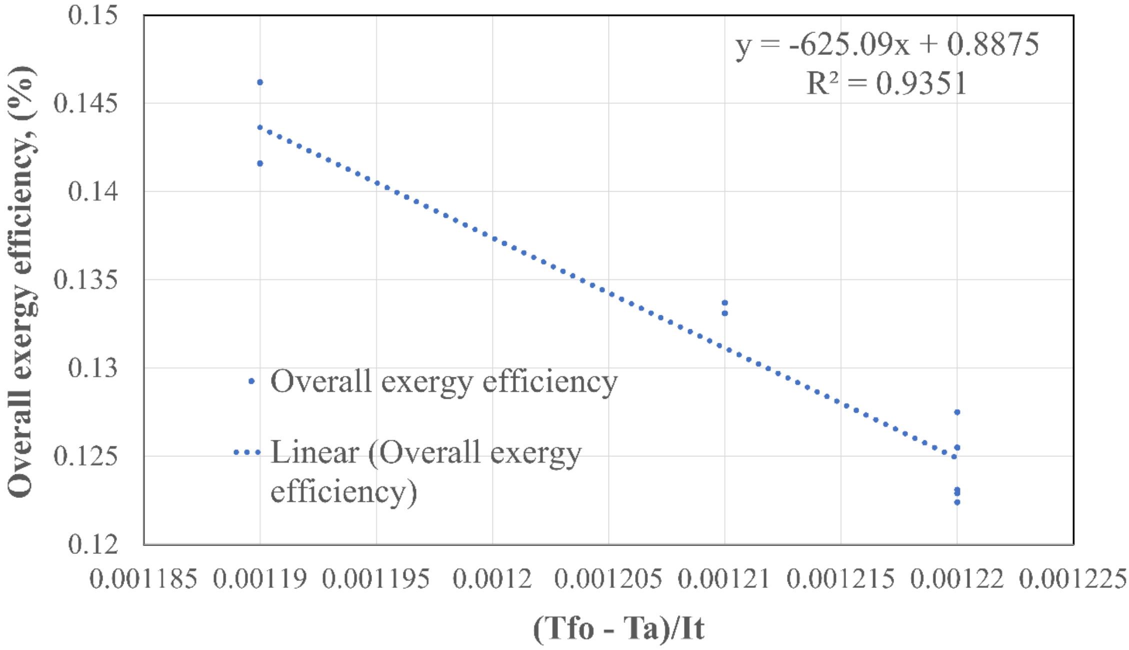

Fig.7. Characteristics curve for Overall exergy efficiency for PVT-TEC air collector

5. Conclusion

The conclusion is as follows.

- The η_{el} and $\eta_{eq,th}$ were 11.77 – 14.17 % and 42.21 – 48.18 %, respectively.
- The $\eta_{eq,ex}$ was found to be 12.24 – 14.62 %.
- TEC generates electrical energy, decreases the solar cell's temperature, and increases the system's overall efficiency.

6. Acknowledgment

We acknowledge the use of computational software for the research provided by SNIOE, Gautam Buddha Nagar, India.

References

Agrawal, Y., Mishra, A., Gautam, A., Phaldessai, G., Singh Yadav, A., Vyas, M., 2023. Performance analysis of photovoltaic thermal air collector having rectangular fins, in: Materials Today: Proceedings. Elsevier Ltd, pp. 6–15. https://doi.org/10.1016/j.matpr.2023.03.787

Çiftçi, E., Khanlari, A., Sözen, A., Aytaç, İ., Tuncer, A.D., 2021. Energy and exergy analysis of a photovoltaic thermal (PVT) system used in solar dryer: A numerical and experimental investigation. Renew Energy 180, 410–423. https://doi.org/10.1016/j.renene.2021.08.081

Dimri, N., Tiwari, A., Tiwari, G.N., 2018. Effect of thermoelectric cooler (TEC) integrated at the base of opaque photovoltaic (PV) module to enhance an overall electrical efficiency. Solar Energy 166, 159–170. https://doi.org/10.1016/j.solener.2018.03.030

Dimri, N., Tiwari, A., Tiwari, G.N., 2017. Thermal modelling of semitransparent photovoltaic thermal (PVT) with thermoelectric cooler (TEC) collector. Energy Convers Manag 146, 68–77. https://doi.org/10.1016/j.enconman.2017.05.017

Gupta, A., Das, B., Biswas, A., Mondol, J.D., 2022. Sustainability and 4E analysis of novel solar photovoltaic-thermal solar dryer under forced and natural convection drying. Renew Energy 188, 1008–1021. https://doi.org/10.1016/j.renene.2022.02.090

Naderi, M., Ziapour, B.M., Gendeshmin, M.Y., 2021. Improvement of photocells by the integration of phase change materials and thermoelectric generators (PV-PCM-TEG) and study on the ability to generate electricity around the clock. J Energy Storage 36. https://doi.org/10.1016/j.est.2021.102384

Nazri, N.S., Fudholi, A., Bakhtyar, B., Yen, C.H., Ibrahim, A., Ruslan, M.H., Mat, S., Sopian, K., 2018. Energy economic analysis of photovoltaic-thermal-thermoelectric (PVT-TE) air collectors. Renewable and Sustainable Energy Reviews. https://doi.org/10.1016/j.rser.2018.04.061

Nazri, N.S., Fudholi, A., Mustafa, W., Yen, C.H., Mohammad, M., Ruslan, M.H., Sopian, K., 2019. Exergy and improvement potential of hybrid photovoltaic thermal/thermoelectric (PVT/TE) air collector. Renewable and Sustainable Energy Reviews 111, 132–144. https://doi.org/10.1016/j.rser.2019.03.024

Singh, A.P., Gupta, A., Biswas, A., Das, B., 2023. Experimental study of a novel photovoltaic-thermal-thermoelectric generator-based solar dryer for grapes drying. Int J Green Energy. https://doi.org/10.1080/15435075.2023.2244046

Singh, A.P., Tiwari, S., Sahdev, R.K., Harender, Tiwari, P., 2022. Effect of transmissivity on PV module glass for PVT-TEC air collector, in: Proceedings - 2022 International Conference on Computational Modelling, Simulation and Optimization, ICCMSO 2022. Institute of Electrical and Electronics Engineers Inc., pp. 401–406. https://doi.org/10.1109/ICCMSO58359.2022.00083

Skoplaki, E., Palyvos, J.A., 2009. On the temperature dependence of photovoltaic module electrical performance: A review of efficiency/power correlations. Solar Energy 83, 614–624. https://doi.org/10.1016/j.solener.2008.10.008

Tiwari, G., 2017. Performance Evaluation of PVT Mixed Mode Dryer with Load Condition. Journal of Fundamentals of Renewable Energy and Applications 04. https://doi.org/10.4172/2090-4541.1000141

Tiwari, G.N., Shyam, A.T., n.d. Energy Systems in Electrical Engineering Handbook of Solar Energy Theory, Analysis and Applications.

Tiwari, S., Agrawal, S., Tiwari, G.N., 2018. PVT air collector integrated greenhouse dryers. Renewable and Sustainable Energy Reviews. https://doi.org/10.1016/j.rser.2018.03.043

Tiwari, S., Tiwari, G.N., 2016. Exergoeconomic analysis of photovoltaic-thermal (PVT) mixed mode greenhouse solar dryer. Energy 114, 155–164. https://doi.org/10.1016/j.energy.2016.07.132

Tiwari, S., Tiwari, G.N., Al-Helal, I.M., 2016. Development and recent trends in greenhouse dryer: A review. Renewable and Sustainable Energy Reviews. https://doi.org/10.1016/j.rser.2016.07.070

Nomenclature

Quantity	**Symbol**	**Unit**
PV module area	A_m	m^{-2}
Collector breadth	b	m
Air specific heat	C_f	Jkg^{-1} K^{-1}
Overall electrical energy	E_{el}	W
PV module electrical energy	E_{PV}	W
TEC electrical energy TEC	E_{tec}	W
Heat transfer coefficient due to wind velocity	h_i	W$m^{-2}K^{-1}$
Outside heat transfer coefficient	h_o	W$m^{-2}K^{-1}$
Tedlar heat transfer coefficient	h_t	W$m^{-2}K^{-1}$
TEC to fluid heat transfer coefficient	h_{tf}	W$m^{-2}K^{-1}$

Global solar radiation	I_t	$\mathrm{W}m^{-2}$
Fluid thermal conductivity	K_f	$\mathrm{W}m^{-1}K^{-1}$
Glass thermal conductivity	K_g	$\mathrm{W}m^{-1}K^{-1}$
Insulation thermal conductivity	K_i	$\mathrm{W}m^{-1}K^{-1}$
Tedlar thermal conductivity	K_t	$\mathrm{W}m^{-1}K^{-1}$
TEC thermal conductivity	K_{tec}	$\mathrm{W}m^{-1}K^{-1}$
Length of collector	L	m
Fluid thickness in duct	L_f	m
Thickness of glass	L_g	m
Insulating material thickness	L_i	m
Tedlar thickness	L_t	m
TEC module thickness	L_{tec}	m
Air mass flow rate	$\dot{m}_f$	$\mathrm{kg}s^{-1}$
Thermal energy gain	$\dot{Q}_{th}$	W
Equivalent thermal exergy	$\dot{Q}_{eq,ex}$	W
Atmospheric temperature	T_a	℃
Standard Solar cell temperature	T_0	℃
Solar cell temperature	T_c	℃
Temperature of fluid	T_f	℃
Inlet fluid temperature	T_{fi}	℃
Outlet fluid temperature	T_{fo}	℃
Temperature of TEC top end	$T_{tec,t}$	℃
TEC bottom end temperature	$T_{tec,b}$	℃
Heat transfer coefficient from top of solar cell to ambient	$U_{t,c-a}$	$\mathrm{W}m^{-2}K^{-1}$
Overall heat transfer coefficient from tedlar to fluid	$U_{b,c-f}$	$\mathrm{W}m^{-2}K^{-1}$
TEC heat transfer coefficient	U_{tec}	$\mathrm{W}m^{-2}K^{-1}$
Heat transfer coefficient from insulation to ambient	U_{b-a}	$\mathrm{W}m^{-2}K^{-1}$
Solar cell absorptivity	α_c	
Standard temperature coefficient	β_0	
Packing factor of TEC	β_{tec}	
Transmissivity of glass	τ_g	
Efficiency of solar cell	η_m	
Standard Solar cell efficiency	η_0	
Efficiency of TEC	η_{tec}	
Overall electrical efficiency	η_{el}	
Thermal efficiency	η_{th}	
Equivalent thermal efficiency	$\eta_{eq,th}$	
Equivalent exergy efficiency	$\eta_{eq,ex}$	

Combine form of absorptivity and transmittivity	$(\alpha\tau)_{eff}$	
Velocity of air in ambient	v	ms^{-1}
Prandtl number	Pr	
Photovoltaic thermal	PVT	
Thermoelectric cooler	TEC	
Phase change material	PCM	
Thermoelectric generator	TEG	
Forced convection dryer	FCD	
Natural convection dryer	NCD	

Appendix I

Some Parameters

$(\alpha\tau)_{eff} = \tau_g\,(\alpha_c - \eta_c)$

$U_{t,c-a} = \left[\frac{L_g}{K_g} + \frac{1}{h_o}\right]^{-1}$

$U_{b,c-f} = \left[\frac{L_t}{K_t} + \frac{1}{h_i}\right]^{-1}$

$h_t = \frac{K_t}{L_t}$

$U_{b-a} = \left[\frac{L_i}{K_i} + \frac{1}{h_i}\right]^{-1}$

$h_i = 2.8 + 3\,v$

$h_o = 5.7 + 3.8\,\mathrm{v}$

$h_{tf} = \frac{K_f}{L}\,Nu$

$Re = \frac{V\,L}{\nu}$

$Nu = 0.332\,Re^{0.5}\,Pr^{0.33}$

Appendix II

Design parameters

A_m=0.5471 m^2	L= 1.077 m
b = 0.508 m	L_f = 0.01 m
C_f = 1005 $Jkg^{-1}\,K^{-1}$	L_g =0.003 m
K_f = 0.02622 $Wm^{-1}K^{-1}$	L_i =0.100 m
K_g =0.816 $Wm^{-1}K^{-1}$	L_t =0.005 m
K_i = 0.166 $Wm^{-1}K^{-1}$	L_{tec} =0.004 m
K_t = 0.033 $Wm^{-1}K^{-1}$	$\dot{m}_f$ =0.05 kgs^{-1}
K_{tec} =1.82 $Wm^{-1}K^{-1}$	T_a= 25 °C
V = 2 ms^{-1}	β_{tec} = 0.4324
η_{tec} = 0.08	η_o = 0.15

Photovoltaic-Thermal (PVT) collectors as monovalent or bivalent heat sources for heat pumps in new multi-family houses

Bharat Chhugani, Christoph Büttner, Peter Pärisch, Federico Giovannetti

Institute for Solar Energy Research Hamelin (ISFH), Emmerthal (Germany)

Abstract

Photovoltaic-thermal (PVT) collector combines a solar thermal collector and a photovoltaic module in a single component, generating power and heat from the same area simultaneously. Hence PVT can be a crucial technology for the future energy supply of buildings. The paper presents a simulative study of PVT as source in heat pump systems for heat supply in multi-family houses. Results show that combining PVT collectors with borehole heat exchangers (BHE) offers the possibility of reducing and even eliminating BHE while achieving a high performance. The heat pump with a combination of PVT (80 m²) with one BHE with 150 m achieves a seasonal performance factor $SPF_{bSt}^{(Grid)}$ of 3.76. Additionally, the results confirm the good performance of PVT as a single heat source. Compared to PV with air-source heat pump, a PVT heat pump with 80 m² accomplishes $SPF_{bSt}^{(Grid)}$ of 3.45, whereas the maximum $SPF_{bSt}^{(Grid)}$ of PV (80 m²) to air source heat pump is 3.12.

Keywords: Photovoltaic-Thermal (PVT) collector, heat pump system, TRNSYS Simulation, multi-family house

1. Introduction

The energy supply for heating and cooling represents almost 50 % of the EU's total gross final energy consumption (Eurostat 2023). Renewable energy covered 22.9 % of the European heating and cooling consumption, and natural gas alone covered 34.3 % of the heating demand. Not only with a view to the climate goals and the necessary reduction of CO_2 emissions but the current political situation in Europe and gas supplies strongly encourage to accelerate more into renewable energy, especially in the heating sector. For this purpose, heat pump (HP) systems offer a promising opportunity to replace conventional fossil fuel-based heating systems for space heating and domestic hot water (oil and gas boilers).

In Europe, the residential heat pump market has been steadily increasing for several years in most countries. Heat pumps are most common in new single-family houses, while the heat pump market share in multi-family buildings (MFHs) remains low. An important barrier to heat pump integration in MFHs is the difficult access to a suitable heat source. The majority of multi-family buildings are located in cities with high densities. Hence, access to geothermal sources for heat pumps could be complicated because the place to drill boreholes is missing, and air-source heat pumps are challenging to integrate because of the noise and efficiency issues. Photovoltaic-thermal (PVT) collectors represent a promising alternative as a single or additional heat source for brine-water heat pumps and have been receiving increasing attention both in research projects and on the market in the last years. PVT collectors convert solar radiation into useful heat and electricity; hence, higher solar energy is harvested with the same collector area. Therefore, PVT can maximize the fraction of local renewable energy source utilization.

The ongoing project "integraTE" investigates PVT collectors with heat pumps and tries to increase market awareness of this technically attractive energy supply system for the building sector. The project aims at carrying out detailed simulative investigations of different system configurations and monitoring of ten demonstration plants, e.g. (Timilsina et al. 2023). The simulation results of various energy supply concepts for a single-family house and monitoring results of one of the demo plants are presented (Chhugani et al. 2023).

This paper aims to investigate PVT as a monovalent or bivalent heat source for heat pumps for new multi-family houses. One of the focuses of the study is to find out to what extent the BHE length can be reduced or entirely eliminated by using PVTs. Because in a new multi-family house normally requires 3 or 4 (total length of 300 m to 400 m) borehole heat exchangers (BHE). One of the case studies presented by Bockelmann (2021) on performance monitoring of ground source heat pump systems in two multi-family houses, where each MFH has 450 m boreholes length for the efficient heat pump operation.

Hence first goal of this paper is to combine BHE and PVT together as heat pump source to solve the problem of

10.18086/swc.2023.04.03 Available at http://proceedings.ises.org

available space for drilling boreholes in cities/locations with high building densities. The second goal of the paper is to compare PVT with brine-water heat pump to PV with air-water heat pump systems. For the performance evaluation, two metrics have been used, which are CO_2-emissions and seasonal performance factors (SPF) and explained in equations 1 to 3.

2. Boundary conditions, system components and methodology

To investigate the behavior of the PVT heat pump system in a multi-family house (MFH), transient system simulations have been carried out using the software TRNSYS v17.0028 for the German location Wuerzburg. The detailed boundary conditions of the building and required components are explained in the following sections.

2.1 Building

The simulated MFH building has 4 floors, each featuring 2 flats with 84 m² living space. The south and north façades are equipped with windows. This multi-family house corresponds to the German building standard - KfW55 (KfW-Bankengruppe 2020), with a heating demand of approx. 21.1 MWh/a (specific 31 kWh/(m²·a)) and domestic hot water demand of approx. 6.7 MWh/a (specific 10 kWh/(m²·a)). The MFH was modeled as part of the ongoing BMWK-funded research project “Solar-VHF” and the detailed building description is presented in (Frick et al. 2021).

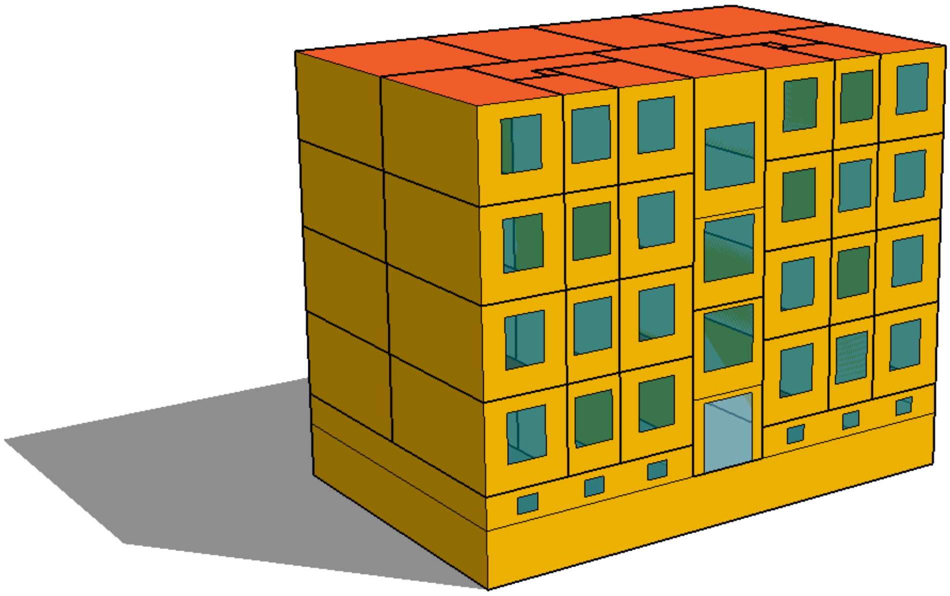

Fig. 1: Multi-story residential building containing 8 flats on 4 floors, each flat with 84 m² living space

The building features a two-pipes network for the heat distribution, which consists of one pair of pipes carrying heating water (flow and return) for both floor heating and domestic hot water. Each apartment in the building has a heat interface units (HIU). The supply temperature from the buffer storage tank to the HIU is maintained constant at 50 °C throughout the year to fulfill the domestic hot water demand.

The simplified hydraulic schematic of one of the simulated heating systems (PVT - heat pump system) is presented in Fig. 2. The system consists of a brine-water-heat pump, a borehole heat exchanger, PVT collectors, buffer storage, riser pipes, heat interface units in each apartment, a floor heating system (flow and return temperature 35/32 °C), a single-room air handling unit with heat recovery in each room except corridor, and external shading devices on all windows. The heat pump uses either PVT or the borehole heat exchanger (BHE) as a heat source. PVT additionally regenerate the BHE in the summer and can therefore reduce the BHE length.

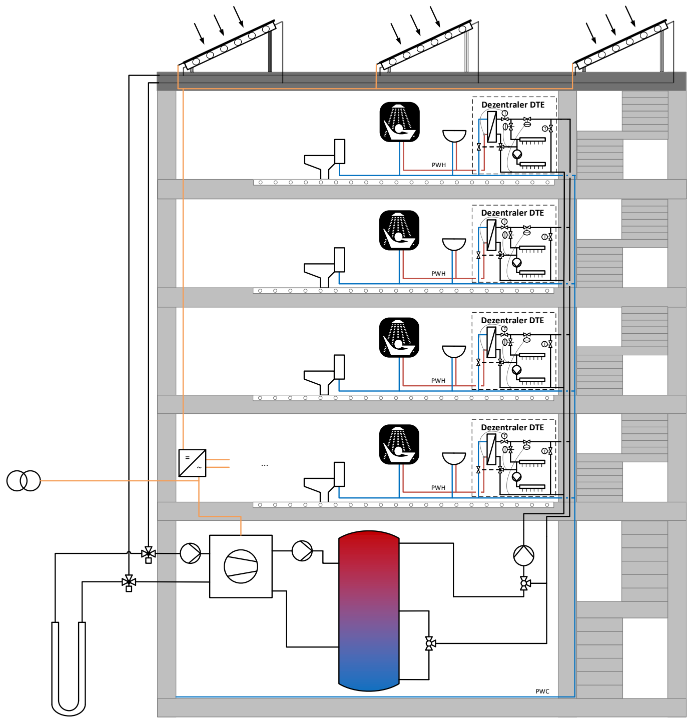

Fig. 2: Simplified hydraulic schematic of investigated multi-family house (MFH) integrated with PVT - heat pump systems

2.2 Brine water heat pump

The modulating brine-water heat pump with a thermal capacity of 12.46 kW and a COP of 4.13 at B0/W35 has been used in the study. This heat pump is suitable for integration with PVT collectors as well as geothermal sources as it can operate down to a minimum inlet source temperature of -15 °C up to 35 °C on the evaporator side.

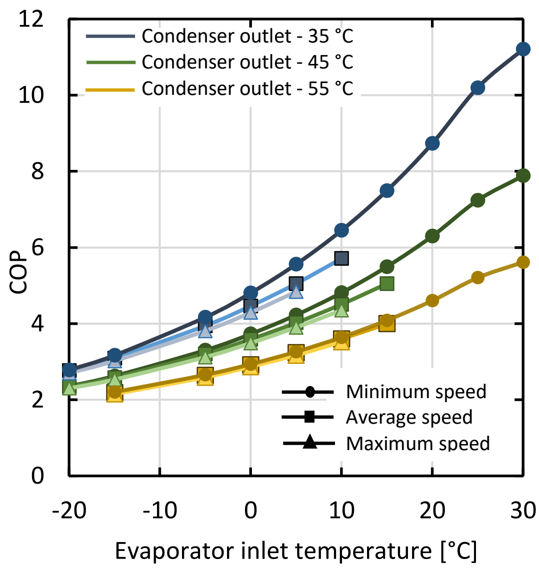

Fig. 3: Coefficient of performance of the heat pump used for the simulations at different evaporator inlet temperatures (x-axis) and condenser outlet temperatures (blue 35 °C, green 45 °C, yellow 55 °C) for three different compressor speeds

However, for the investigation in the paper, the heat pump is only used up to an inlet source temperature of -10 °C. If the source temperature falls below the minimum source inlet temperature, the integrated auxiliary heater (15 kW) in the heat pump takes over the charging of the storage tank as a bivalent alternative operation.

A study presented by Chhugani et al. (2020) confirms that changing the bivalence point from -10 °C to -15 °C, achieves 20 to 25 % higher Seasonal performance factors (SPF). The reason for not using the heat pump at very low evaporator inlet temperatures (i.e., -15 °C) for this investigation on MFH is that the heat pump's thermal power is insufficient to meet the building's thermal energy demand at very low inlet temperatures. This can be solved by using a heat pump with higher thermal power at lower evaporator temperatures or using bivalence parallel operation, where an auxiliary heater supports the partial thermal energy demand of the building. This strategy would also improve the system's efficiency; however, this is not investigated in this paper.

For compressor protection, as in actual heat pump operation, the heat pump has a minimal pause time of 15 min. The characteristics data of the heat pump is presented in the Fig. 3.

The TRNSYS type 401 developed by Afjei and Wetter (1997) is used to model the heat pump. This type can simulate different heat pumps, such as air-source and brine-water. The heat pump model is based on biquadratic polynomials for condenser and compressor power calculated from the heat pump characteristic data obtained from experiments. The modulation is modeled with three instances of type 401 in parallel and linear interpolation, as proposed by Hüsing and Pärisch (2020).

2.3 Photovoltaic - Thermal (PVT) collectors

An uncovered/WISC PVT collector with a finned air heat exchanger on the back side has been used in the investigation. The thermal parameters of the collector presented in Tab. 1 were determined by means of outdoor tests (Giovannetti et al. 2019) and validated for TRNSYS simulations (Chhugani et al. 2020). The electrical data of the PVT module is shown in Tab. 2. In the investigations, PVT Modules are facing south with tilt angle of 45 °.

Tab 1: Thermal PVT parameter sets (MPP-related)

	η_0 [-]	c_1 [W/(m²·K)]	c_3 [J/(m³·K)]	c_4 [-]	c_5 [kJ/(m²·K)]	c_6 [s/m]
PVT (WISC) with fins	0.532	19.08	3.69	0.434	26.05	0.067

Tab 2: Electrical PV parameter at Standard Test Conditions (STC)

	P_{mpp} [Wp]	A [m²]	η_{el} [-]	V_{mpp} [V]	I_{mpp} [A]	V_{oc} [V]	I_{sc} [A]	TC [%/K]
PV module	340	30	17.5	37.6	9.05	48.0	9.45	-0.39

In the bivalent heat source configurations, PVT is used solely if the PVT collector temperature is 5 K higher than BHE. Otherwise, only BHE is used as long as the BHE is available, because for the frost protection, inlet temperature of BHE has been restricted at -3 °C, after that only PVT is used until the bivalence point of heat pump is reached. On sunny days, BHE is regenerated with PVT heat, when the heat pump is not running and PVT temperature are higher than BHE. Once the BHE temperature reaches 25°C, regeneration is stopped and PVT heat is not used and rest produced heat from PVT is wasted.

2.4 Borehole heat exchanger (BHE)

The study investigates BHE as a single heat pump source or a combination with PVT. BHE and PVT are connected in parallel, and the higher temperature source is chosen when the HP is running. The reason for these simulations is the high efficiency and the opportunity to shorten the required length of BHE by regeneration of the ground in the summer through PVT. For the simulation, up to 150 m deep BHE was simulated. However, the length of BHE is under-dimensioned for multi-family houses (MFH) because the goal here is to investigate the possibility of BHE length reduction by integrating PVT collectors. TRNSYS Type 451 is used to model the BHE, which was validated through the experimental system at ISFH for TRNSYS simulation (Pärisch et al. 2015). The simulation with a borehole heat exchanger runs for two years, and the second year’s simulated result is evaluated and presented here in the paper.

2.5 Air source heat pump

The air-source heat pump of the reference system has a thermal heating capacity of 14.9 kW and a COP of 3.65 at A2/W35, including defrosting losses. TRNSYS type 401 (Afjei and Wetter M. 1997) is also used for the air-source heat pump simulations with the built-in COP-reduction for defrosting. Additionally, the air-source heat pump modeling considers other electrical stand-by losses and thermal losses due to the frosting processes of the air heat exchanger outdoor unit. These losses are simplified in type 401 by a modified Gauss function representing the percentage reduction in COP as a function of the outdoor temperature, and the method is explained (Afjei and Wetter 1997). The COP reduction function of the simulated heat pump in this paper is derived according to experimental investigations from ISFH and presented for different relative humidity levels in (Chhugani et al. 2023). Moreover, as in a real system, de-icing with reverse operation can occur every 30 to 60 minutes on winter days. At that time, the heat pump can no longer supply energy to the building, which is to be compensated with a bigger storage volume and a higher thermal capacity. However, this intermittent operation cannot be simulated with type 401.

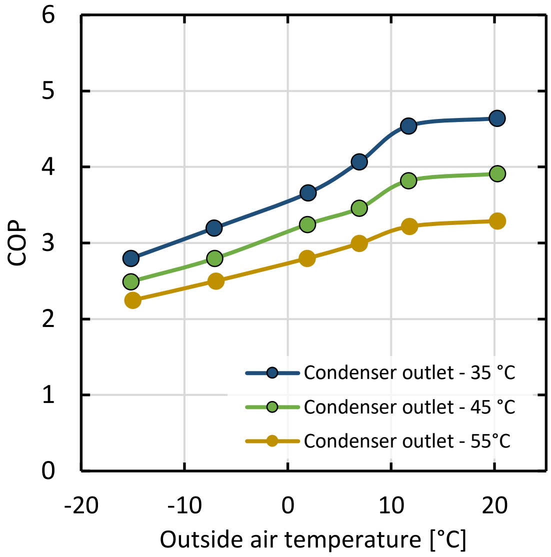

Fig. 4: Air source heat pump coefficient of performance for different air temperatures (x-axis) and condenser outlet temperatures (35 °C, 45 °C, 55 °C) with defrosting losses

2.6 Key performance indicators (KPIs)

The heat supply systems presented in the paper are evaluated and analysed based on two key performance indicators (KPIs). Firstly, the CO_2 emissions of the systems are calculated as the sum of the energy consumption values (electricity) and multiplied by the corresponding emission factors according to the German Building Energy Act (GEG) as shown in equation 1.

$$CO_{2,Emissions} = Final\ energy\ consumption\ (Electricity) \cdot x_{CO_2} \qquad \text{(eq. 1)}$$

Where the CO_2- emission factor (x_{CO_2}) of grid-taken electricity is 0.56 kg CO_2-equiv. for kWh, and self-consumed PVT/PV electricity is considered to have zero emission.

As second KPI, seasonal performance factors (SPF) are used to evaluate the system. The SPF_{bSt} (before storage) is the ratio of heat supplied to the buffer storage by the heat pump Q_{HP} and the auxiliary heating Q_{Backup} divided by the electrical energy consumed within this system boundary. $\dot{E}_{HP}$ is electrical energy of the heat pump compressor, $\dot{E}_{Pumps}$ is pumps energy and $\dot{E}_{Backup}$ is auxiliary heater electrical energy consumption. On the other hand, the $SPF_{bSt}^{(Grid)}$ describes the self-consumed PVT/PV electricity in the same system boundary. This means that the generated electrical power by PVT/PV is used simultaneously for the electrical consumption of the heating system (simulation time-step = 1 min), and the surplus PVT electricity is fed into the grid since there is no battery. Ultimately, this metric only considers the electrical energy drawn from the grid. Here, the household electricity profile is not covered in the consumption.

$$SPF_{bSt} = \frac{\int (\dot{Q}_{HP} + \dot{Q}_{Backup})\, dt}{\int (\dot{E}_{HP} + \dot{E}_{Backup} + \dot{E}_{Pumps})\, dt} \qquad \text{(eq.2)}$$

$$SPF_{bSt}^{(Grid)} = \frac{\int (\dot{Q}_{HP} + \dot{Q}_{Backup})\, dt}{\int_{>0} \left(\dot{E}_{HP} + \dot{E}_{Backup} + \dot{E}_{Pumps} - \dot{E}_{PVT/PV\ el\_Self}\right) dt} \qquad \text{(eq. 3)}$$

3. Results and discussion

Fig. 5 illustrates the seasonal performance factors (SPF) of the simulated systems. Here, simulation results are shown for combinations of different PVT areas (20 – 80 m²) with different BHE depths (1 - 150 m) as a heat source for the heat pump. Different colors in the graph show different ranges of $SPF_{bSt}^{(Grid)}$ for different PVT with BHE combinations, i.e., 60 m² PVT with BHE of 120 m, achieves $SPF_{bSt}^{(Grid)}$ of 3.46 (Range between 3.25 – 3.50). Similarly, the SPFs for further PVT - BHE combinations can be evaluated from Fig. 5.

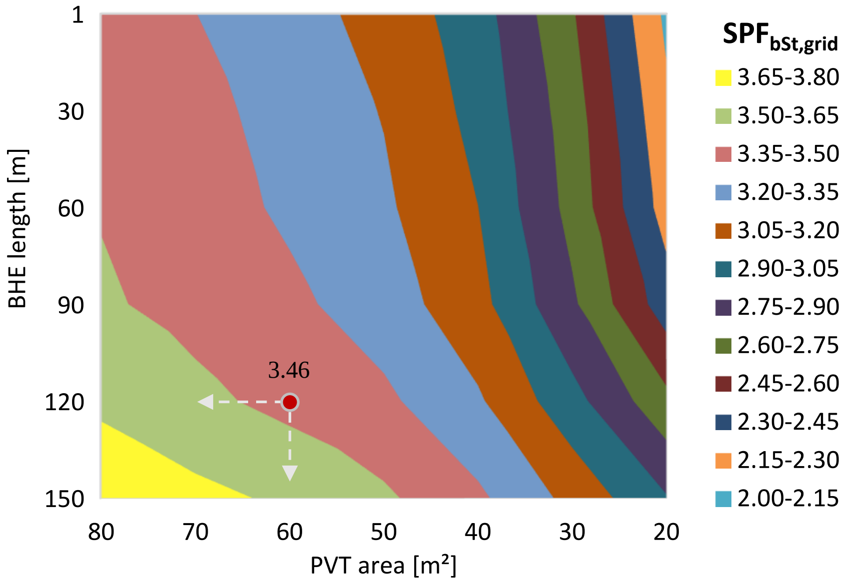

Fig. 5: SPF ranges of different PVT areas with BHE combination for heat pump systems, where the x-axis shows the PVT area and the y-axis indicates different borehole heat exchanger (BHE) lengths

Here, it is crucial to understand that the PVT combination with BHE opens the possibility of reducing BHE length without significantly affecting system efficiency. This aspect becomes economically more relevant for larger systems with two or more boreholes. On the other hand, ground regeneration via PVT heat generally ensures a sustainable system operation and can compensate for planning uncertainty even for small BHE installations.

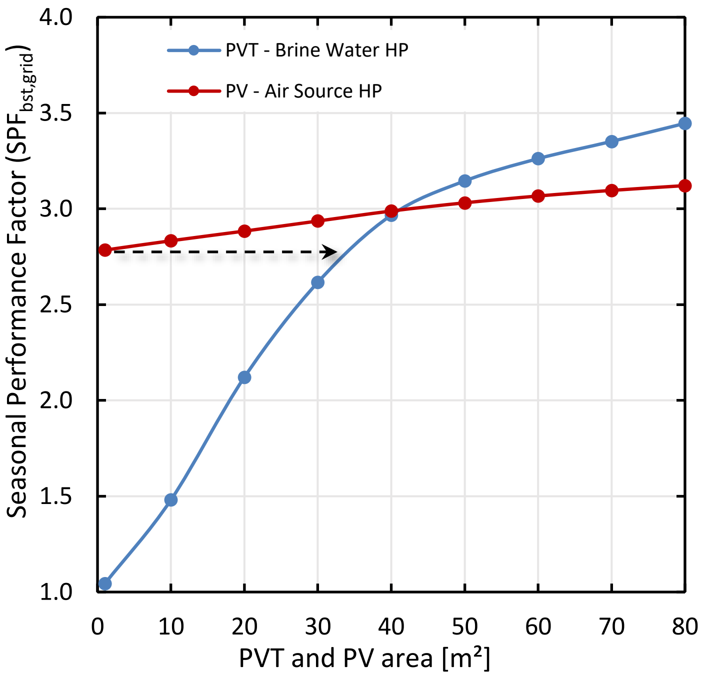

Fig. 6: SPF ranges of different PVT areas with brine-water heat pumps in comparison with different PV areas with air-source heat pump

Fig. 6 illustrates $SPF_{bSt}^{(Grid)}$ of the PV-assisted air-source heat pump and PVT with brine-water heat pump depending on the different PV or PVT areas. Here, the brine-water heat pumps use PVT as the only heat source. As Fig. 6 shows, the SPF rises gradually depending on the PVT collector area. With 80 m² PVT heat pump, the achieved SPF is 3.45, whereas the maximum accomplished SPF with 80 m² PV to air source heat pump is 3.12.

As indicated with black arrow in Fig. 6 that a minimum of ~35 m² PVT collector area is required for the brine-water heat pump source to reach similar SPF as PV with air-source heat pumps. With 40 m² PVT and PV area, both systems show similar efficiency, with larger areas PVT with brine-water heat pump system shows better performance than PV with air-source heat pump systems.

Fig. 7 shows the CO_2-equivalent of different simulated PVT - BHE combinations with heat pumps. As shown in the graph, the most efficient in terms of the lowest amount of CO_2 emissions (4.35 tons) is produced by 80 m² PVT and 150 m deep BHE with heat pumps. Small PVT areas of less than up to 20 m², combined with any BHE depths (here only up to 150 m deep), emit more CO_2 emissions than PV to air-source heat pumps. However, if a higher PVT area is added to the brine-water heat pump system (higher than 40m² PVT), then all the brine-water heat pump systems (only PVTs or combination of PVTs - BHE) are more efficient than PV to air-source heat pumps.

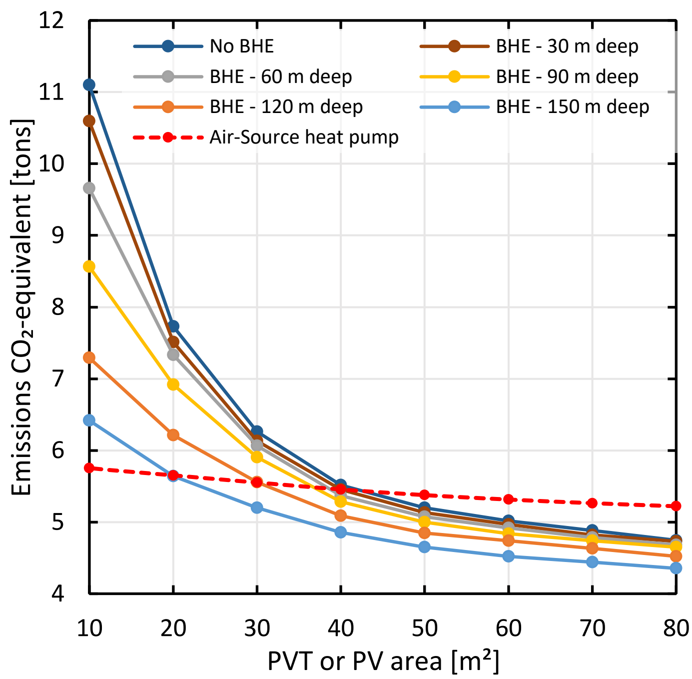

Fig. 7: CO_2-emissions for different PVT areas with BHE combination for heat pump systems for the multi-family house (MFH)

However, it can also be observed from the graph that the PVT combinations with smaller BHEs significantly reduce the CO_2 emissions, in some cases, such as only PVT (80 m²) with heat pumps can open the option to eliminate complete BHE without significantly emitting extra emissions.

4. Conclusion

The ongoing research project "integraTE" aims to comprehensively assess PVT with heat pump systems and increase market awareness of this new technology for the building energy supply sector. Detailed simulative investigation in the project generates information and allows understanding of the performance of these systems for the use in multi-family houses.

The following points summarize the essential findings of the simulations:

- PVT (80 m²) with borehole heat exchangers (BHE 150 m) to heat pump achieves a SPF of 3.76.
- PVT 35 m² collector area is required as the heat source for the brine-water heat pump to reach similar SPF as only air-source heat pumps.

- With PVT (80 m²) brine-water heat pump achieves SPF of 3.45, whereas PV (80 m²) to air source heat pump reaches maximum SPF of 3.12.

Summing up, direct coupling of PVT collectors with heat pumps as a single source (thermal side) achieves good system efficiency and represents a promising alternative to PV with air-source and geothermal heat pumps for the MFH. In the PVT-BHE configuration, PVT can favorably supply the heat to the heat pump directly or regenerate the ground source. As mentioned in the section 1, for the efficient heat pump operation with only borehole heat exchangers (BHE), three or four boreholes are required for multi-family houses. Integration of PVT plays here an important role, especially with larger installations like here in multi-family houses, where smaller dimensioning of BHE is possible. As presented in this paper that one BHE combination with PVTs can be very attractive and can be sufficient for efficient heat pump operation. Additionally, the solar regeneration via PVT enables a sustainable operation of the BHE field by avoiding long-term cooling effects.

5. Acknowledgments

The presented work and results are part of the research project “integraTE” (reference number: 03EGB0023) funded by the German Federal Ministry for Economic Affairs and Climate Action (BMWK) and supported by the Lower Saxony Ministry of Science and Culture. Furthermore, we thank our partners Fraunhofer ISE, IGTE of University Stuttgart and Solrico for the collaboration. Further thanks go to nD-Systeme, PA-ID, Architektur- und TGA-Planungsbüro Carsten Grobe, SunMaxx, Splus2, TripleSolar, and Consolar - Solare Energiesysteme for their financial support. The authors are grateful for the support and are responsible for the content of the publication.

6. References

Afjei, T.; Wetter M. (Hg.), 1997. Type 401, TRNSYS Compressor heat pump including frost and cycle losses, version 1.1. Available online at https://trnsys.de/download/en/ts_type_401_en.pdf.

Bockelmann, F., 2021. IEA HPT Annex 52 - Long-term performance monitoring of GSHP systems for commercial, institutional and multi- family buildings. Case study report for KON, Germany. Multi-family-house with borehole heat exchanger. DOI: 10.23697/19WQ-WN21.

Chhugani, B., Pärisch, P., Helmling, S., Giovannetti, F., 2023. Comparison of PVT - heat pump systems with reference systems for the energy supply of a single-family house. In: Solar Energy Advances 3, 100031. DOI: 10.1016/j.seja.2022.100031.

Chhugani, B., Pärisch, P., Kirchner, M., Littwin, M., Giovannetti, F., Lampe, C., 2020. Model Validation and Performance Assessment of Unglazed Photovoltaic-Thermal Collectors with Heat Pump Systems. EuroSun: 13th International Conference on Solar Energy for Buildings and Industry, Online. DOI: 10.18086/eurosun.2020.05.13.

Eurostat, 2023. Shedding light on energy in the EU. Interactive publication. DOI: 10.2785/405482.

Frick, E., Büttner, C., Kirchner, M., Giovannetti, F., 2021. Solar Thermal, Rear-Ventilated Facades as Heat Pump Sources in Multi-Story Buildings. Solar World Congress, Online. DOI: 10.18086/swc.2021.43.01.

GEG. Gesetzes zur Vereinheitlichung des Energieeinsparrechts für Gebäude und Änderung weiterer Gesetze, Artikel 1, Gesetz zur Einsparung von Energie und zur Nutzung erneuerbarer Energien zur Wärme- und Kälteerzeugung in Gebäuden (Gebäudeenergiegesetz - GEG) Bundesgesetzblatt Jahrgang 2020 Teil I Nr. 37, ausgegeben am 13. August.2020.

Giovannetti, F., Lampe, C., Kirchner, M., Littwin, M., Asenbeck, S., Fischer, S., 2019. Experimental Investigations on Photovoltaic-Thermal Arrays Designed for the Use as Heat Pump Source. Solar World Congress: IEA SHC International Conference on Solar Heating and Cooling for Buildings and Industry, Santiago. DOI: 10.18086/swc.2019.05.03.

Hüsing, F., Pärisch, P., 2020. Modelling of Inverter Heat Pumps in TRNSYS. EuroSun: 13th International Conference on Solar Energy for Buildings and Industry, Online. DOI: 10.18086/eurosun.2020.04.08.

KfW-Bankengruppe, 2020. Anlage zum Merkblatt: Energieeffizient Bauen. Technische Mindestanforderungen und ergänzende Informationen für den Neubau eines KfW-Effizienzhauses.

Pärisch, P., Mercker, O., Oberdorfer, P., Bertram, E., Tepe, R., Rockendorf, G., 2015. Short-term experiments with borehole heat exchangers and model validation in TRNSYS. In: Renewable Energy 74, 471-477. DOI: 10.1016/j.renene.2014.07.052.

Timilsina, K. P., Chhugani, B., Pärisch, P., 2023. In-Situ-Monitoring eines Wärmepumpensystems mit PVT-Kollektoren und Erdwärmequellen für Heizung und Kühlung. 34th Symposium Solarthermie und Innovative Wärmesysteme, Kloster Banz, Bad Staffelstein.

Solar Cooling for the Sunbelt Regions – Results from Task 65 activities

Uli Jakob[1], Salvatore Vasta[2], Wolfgang Weiss[3] Daniel Neyer[4,5], and Paul Kohlenbach[6]

[1] Dr. Jakob energy research GmbH & Co. KG, Weinstadt (Germany)

[2] CNR - ITAE, Messina (Italy)

[3] ergsol Inc., Portland/OR (USA)

[4] Neyer Brainworks GmbH, Bludenz (Austria)

[5] University of Innsbruck, Innsbruck (Austria)

[6] Berliner Hochschule für Technik, Berlin (Germany)

Abstract

The energy demand for air-conditioning is growing faster than any other energy consumption in buildings. The main share of the projected growth for space cooling comes from emerging economies and will more than triple by 2050 to 6,000 TWh/a globally (IEA, 2018). Therefore, the IEA SHC Task 65 "Solar Cooling for the Sunbelt Regions", started in July 2020, is focusing on innovations for affordable, safe and reliable Solar Cooling systems for the Sunbelt regions. The innovation is the adaptation of existing concepts/technologies to the Sunbelt regions using solar energy, either solar thermal or solar PV. The importance of the topic is reflected in the high number of experts participating in IEA SHC Task 65, especially as 50% of the Task experts come from industry and SMEs. This paper presents the Task 65 results of the different activities carried out in last 3 years and highlights the ongoing research projects.

Keywords: Solar thermal cooling, PV cooling, Sunbelt regions, IEA SHC Task 65

1. Introduction

Global energy demand is growing, although its growth rate is less than in the past. Nevertheless, by 2040 an increase of 30% is projected by OECD (2017). Nowadays air-conditioning accounts for nearly 20% of the total electricity demand in buildings worldwide and is growing faster than any other consumption in buildings (IEA, 2018). The undisputed rationales for the increase are global economic and population growth and thus rising standards of living. Growth in the demand of cooling is especially driven by countries with high temperatures. Three emerging countries (India, China, Indonesia) contribute to more than half of the annual growth rates. Additionally, the efficiency of the air-conditioners varies considerably. The most common systems run at half of the available efficiency. If measures are not taken to counteract this increase, the space cooling demand could triple by 2050.

Nowadays e.g. in India, 30% of total energy consumption in buildings is used for space cooling which reaches 60% of the summer peak load. This is already stretching the capacity of the Indian national electricity supply dramatically (Patwardhan et al., 2012). In other countries peak load through air conditioning reaches >70% in hot days (IEA, 2018). Moreover, in the countries of the Association of Southeast Asian Nations (ASEAN) the electricity consumption increased 7.5 times from 1990 to 2017 (IEA, 2019). With the increase in demand comes the increase in the cost of electricity and summer blackouts, which have been attributed to the large number of conventional air conditioning systems running on electricity.

As the number of traditional vapor compression chillers grow so do greenhouse gas emissions, both from direct leakage of high GWP refrigerant, such as HFCs, and from indirect emissions related to fossil fuel derived electricity consumption. Solar air-conditioning is intuitively a good combination, because the demand for air-conditioning correlates quite well with the availability of the sun. The hotter and sunnier the day, the more air-conditioning is required. Interest in solar air-conditioning has grown steadily over the last years. The latest numbers of worldwide installations in 2023 showed nearly 2,000 systems (IEA SHC, 2023). Solar air-conditioning can be achieved by either driving a vapor compression air-conditioner with electricity produced by solar photovoltaic cells or by solar thermal heat to run a thermally driven sorption chiller.

10.18086/swc.2023.04.09 Available at http://proceedings.ises.org

2. Adaptation of solar cooling technologies

The knowhow capitalised in OECD countries (Europe, US, Australia, etc.) on solar cooling technology (both thermal and PV) is already very great, but very few efforts have been made to adapt and transfer this knowhow to Sunbelt countries such as Africa, MENA, Asian countries, which are all dynamic emerging economies They are also part of the global increase in demand for air conditioning (AC), where solar cooling could play an important role, as these are all highly irradiated regions of the world.

Therefore, the present Task 65 focus on innovations for affordable, safe and reliable cooling systems for the sunbelt regions worldwide (sunny and hot climates, between the 20th and 40th degrees of latitude in the northern and southern hemisphere). It covers the small to large size segment of cooling and air conditioning (between 2 kW and 5,000 kW). The implementation/adaptation of components and systems for the different boundary conditions is forced by cooperation with industry and with support of target countries like India and UAE through Mission Innovation (MI) Innovation Community on “Affordable Heating and Cooling of Buildings” (MI IC7, 2023).

3. Objectives of IEA SHC Task 65

The key objective of IEA SHC Task 65 is to adapt, verify and promote solar cooling as an affordable and reliable solution in the rising cooling demand across Sunbelt countries. The existing technologies need to be adapted to the specific boundaries and analysed and optimized in terms of investment and operating cost and their environmental impact (e.g. solar fraction) as well as compared and benchmarked on a unified level against reference technologies on a life cycle cost bases. Solar cooling should become a reliable part of the future cooling supply in Sunbelt regions. After completion of the IEA SHC Task 65 the following should be achieved:

- Support the development of solar cooling technologies on component and system level adapted for the boundary conditions of Sunbelt (tropical, arid, etc.) that are affordable, safe and reliable in the medium to large scale (2 kW-5,000 kW) capacities
- Adapt existing technology, economic and financial analyses tools to assess and compare economic and financial viability of different cooling options with a life-cycle cost-benefit analyses (LCCBA) model.
- Apply the LCCBA framework to assess case studies and use cases from subtasks A and B to draw conclusions and recommendations for solar cooling technology and market development and policy design.
- Pre-assess ‘bankability’ of solar cooling investments with financial KPIs.
- Find boundary conditions (technical/economic) under which solar cooling is competitive against fossil driven systems and different renewable solutions.
- Establish a technical and economic data base to provide a standardized assessment of demo (or simulated) use-cases.
- Accelerate the market creation and development through communication and dissemination activities.

4. Latest results of the Subtasks

4.1 Subtask A – Adaptation

The Sunbelt Regions encompass a wide range of climates, from hot and arid deserts to humid subtropical zones. Designing effective solar cooling systems in these regions requires a comprehensive understanding of the prevailing climatic conditions. Designing solar cooling systems for Sunbelt regions requires a holistic approach that considers a wide range of climatic factors. By tailoring systems to these conditions and promoting sustainable practices, the region can harness its abundant solar resources for efficient and eco-friendly cooling solutions. The following sections report the results that have been achieved in Subtask A within the Activities already completed (October 2023).

<u>A1: Climatic Conditions & Applications</u>

Generally, the suitability of (solar) cooling systems and the specific applications thereof are highly contingent on the geographical location. To establish region-specific prerequisites for solar cooling systems, leveraging geographical data is a logical approach. This necessitates the utilization of a Geographic Information System (GIS), which possesses the capability to acquire, store, validate, and visualize data associated with Earth's surface coordinates. Most pertinent geographical data essential for this purpose can readily be sourced from various outlets, including solar radiation statistics, climate records, population demographics, and more.

In the initial phase (Activity A1) of this project, GIS software was employed to amalgamate geographical data in a manner conducive to ascertaining localized reference conditions for solar cooling systems within Sunbelt regions. Moreover, this methodology can be adapted to generate insights into potential deployment sites and the feasibility of specific solar cooling systems. Supplementing this approach with data such as population density and purchasing power lays the groundwork for prospective market studies focusing on particular products or technologies. Consequently, prospective sites can be pinpointed, and economic variables can be factored into the identification of both current and future markets.

The data sources used in this study consist of multiple layers, with each layer containing data on specific topics or numerical values. These data layers are extensive, comprising 145 million grid cells and having a size of approximately 1.5 gigabytes each. The analysis took into account various conditions and sources, including geographic areas requiring cooling (spanning latitudes between 48°N and 44°S), different solar irradiances (DNI, GHI, DIF) and photovoltaic power potential (PVOUT), population density and settlement levels, climate zones based on the Köppen–Geiger climate classification system, water availability, assessment of market risk through Environmental Social Governance (ESG) factors, and considerations of Purchasing Power Parity (PPP) and Gross Domestic Product (GDP). These data sources and conditions played a crucial role in conducting the comprehensive analysis (Figure 1).

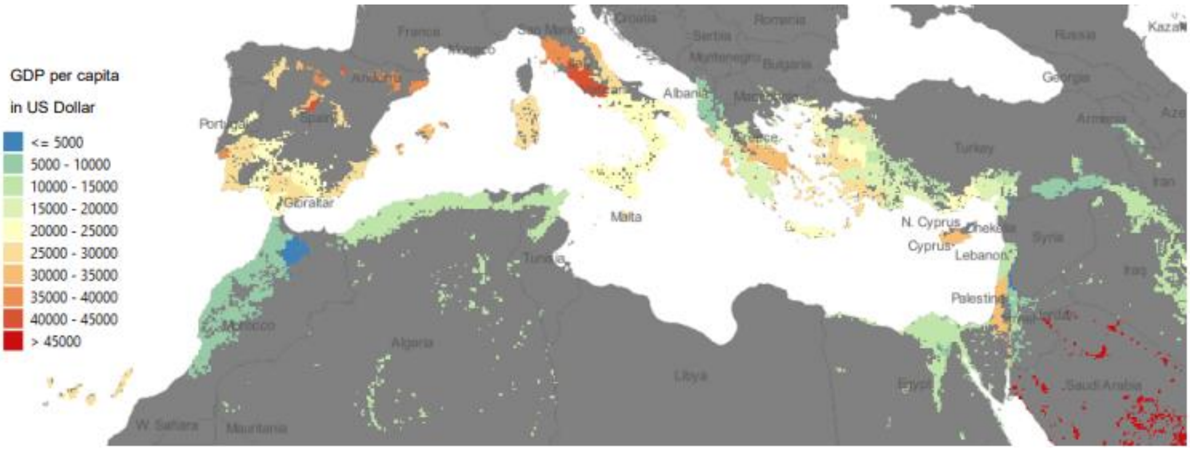

Fig. 1: A world map cut-out focusing on the Mediterranean region was used to identify the potential for a specific Solar Cooling System in building cooling applications. The analysis was conducted on a 10km raster grid, taking into account the Gross Domestic Product (GDP) levels. A detailed high-resolution map is provided in the annex for reference (Source: ZAE Bayern, 2022).

The prospects for further investigation and improvement of the methodology encompass refining the method to provide specific regional or country-level insights for better result quality, conducting a more precise analysis of industrial areas and population distribution to identify clusters of large buildings showcasing cooling network potential, incorporating additional data sources like cooling degree days and energy prices to increase the significance of results by considering economic factors, expanding the study to encompass various building types (residential, commercial, hospital, university, etc.) to enhance its overall value in assessing cooling network potential, applying the methodology's principles to other renewable energy technologies for heating and electricity supply, and exploring the development of interactive web-based maps for improved user exploration, providing flexibility in presenting information according to specific needs and details. These considerations outline potential directions for refining and extending the methodology in future research and applications.

Further details can be found in the published A1 final report (Gurtner et. al, 2023).

<u>A2: Adapted Components</u>

The Sunbelt regions feature diverse climates with critical factors like temperature, humidity, and dust presence. These factors affect the design and performance of solar cooling systems. Reliable data on these conditions is essential for selecting or adapting components to specific markets. Documenting available components is crucial for promoting solar cooling. Activity A2 focuses on documenting components, including collectors (photovoltaic, thermal, etc.), storage units, chillers, and heat rejection systems. This documentation combines climatic conditions and typical applications for effective technical adaptation. It considers the Köppen climate classification to qualitatively assess systems and components in the involved countries.

After a double-stage survey and data collection, a monitoring procedure for Solar Heating and Cooling (SHC) systems was developed in Task 38 Solar Air-Conditioning and Refrigeration. The goal is to adapt it to various SHC system types designed for space heating, cooling, and DHW production. The procedure evaluates performance, estimates primary energy savings compared to conventional systems, and enables comparisons between SHC systems. It helps identify best practices based on climate, building features, and usage conditions. The procedure uses an Excel file for calculations, including primary energy ratio (PER), electrical coefficient of performance, solar heat management efficiency, and fractional savings compared to conventional systems. Key Performance Indicators (KPIs) are defined, and conventional/reference systems are established in collaboration with experts. The Excel file has three levels, each offering different levels of detail and complexity for monitoring systems.

General system data is entered, including location, size, technologies, and major SHC components. The procedure adapts to the monitored system and lists the monitored energy flows based on available sensors. The procedure's three levels provide varying levels of information, depending on sensor availability and system complexity. This scheme was developed considering Task 38 Solar Air-Conditioning and Refrigeration's research.

This study analyzes various components used in solar cooling technologies and their relationships with factors like solar collector type, climatic zone, application, and adapted components (Beccali, 2022). Solar cooling has the potential to effectively decarbonize energy use related to cooling in the Sunbelt regions. With rising cooling demands in these areas, selecting the right components and analyzing existing projects can enhance its impact. The study examines 32 projects from 18 Sunbelt countries, considering their demographic distribution. The Köppen-Geiger climate classification is used to categorize climate zones, crucial for choosing cooling systems and solar collectors. The majority of projects are in hot desert and hot semi-arid climates. About 50% of projects are in the implementation phase, 18% are operational, and 25% are in the concept phase. Evacuated tube collectors are popular in simulations, while flat plate and Fresnel collectors are common in implemented projects. Solar cooling systems are often installed in public buildings (34%) and domestic buildings (25%), with potential applications in food preservation and process industries.

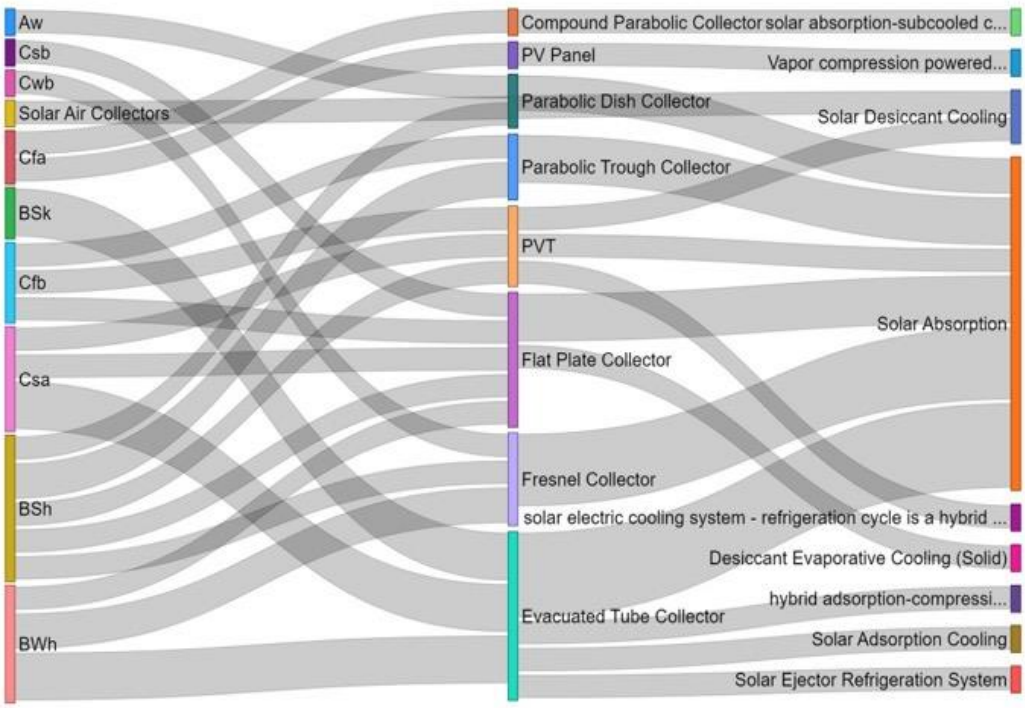

Fig. 2: Representation of weather profile with solar collector and solar cooling technology used

For example, the results showed that heat storage tanks, along with auxiliary heating systems, play a vital role in meeting cooling requirements during periods of minimal or zero solar radiation, particularly at night. The cooling demands in public buildings like offices and educational institutions are primarily concentrated during daytime hours, leading to a reduced need for these components. In contrast, for domestic applications such as villa houses, multi-family buildings, and process industries, cooling needs may extend throughout the entire day. Cold backup components, including vapor compression systems, are employed to extend the cooling capacity even when the solar cooling system is not active.

Furthermore, the Sankey diagram shown in Figure 2 provides valuable insights into the relationship between climate classifications, the types of solar collectors used, and the choice of solar cooling systems. Noteworthy observations from this analysis include:

1. In regions characterized by hot desert climates (BWh), Fresnel and evacuated tube collectors are often preferred for harnessing solar energy.

2. For areas with Hot summer-Mediterranean (Csa) and Tropical and subtropical steppe (BSk) climates, evacuated tube collectors are commonly chosen.

3. Solar absorption cooling emerges as the most prevalent solar cooling technology, followed by PV-assisted cooling and ejector cooling.

This analysis offers valuable guidance for selecting components and systems based on the specific climate zone of a project.

A4: Building and process optimization potential

The primary objective of Activity A4 was to assess the potential of energy-efficient buildings and processes in Sunbelt regions, both for new and existing structures. This involved studying other related projects and examining the integration of solar cooling into retrofitted HVAC systems. Integrating solar cooling into existing HVAC systems can be complex, especially concerning refrigerants and cold distribution methods. The aim was to identify the best technical solutions from both technical and economic perspectives. However, not all the planned analyses yielded useful data, leading to adjustments in the workflow. Some research projects and IEA Energy in Buildings and Communities Programme (EBC) projects were reviewed, but it was found that there are limited recent projects focusing on the application of solar cooling systems in buildings. Nevertheless, the information gathered can serve as a foundation for assessing the potential energy savings achievable through the implementation of solar cooling systems.

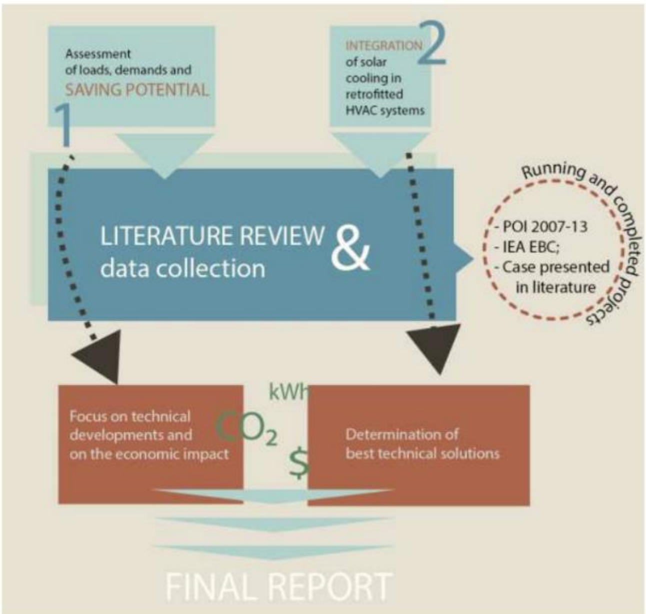

Fig. 3: Flow-chart of the data gathering and processing

The initial phase of Activity A4 involves collecting and analyzing data from various buildings to assess the potential for energy-efficient building processes in Sunbelt regions (Figure 3). This assessment pertains to both new constructions and existing structures. One particular challenge addressed in this study is the integration of solar cooling into pre-existing HVAC systems. This integration presents hurdles related to refrigerants and cold distribution. Additionally, the study explores the application of cold delivery systems to reduce drafts in air-based systems and improve thermal comfort within buildings. The data used in this analysis are sourced from the POI projects and selected completed IEA EBC projects.

In cases where the required data were note available through the primary data collection efforts, a comprehensive analysis of relevant literature was conducted. This approach effectively filled in the missing data gaps. By reviewing existing research papers, reports, and studies relevant to the field, valuable insights and information that enriched the research findings were accessed. This literature-based data acquisition approach is a standard practice in research, ensuring the completeness and credibility of the study.

The literature review revealed that space cooling significantly contributes to the energy consumption of the building sector, accounting for approximately 16% of the final energy consumption in 2021. Furthermore, projections indicate that global electricity usage for space cooling could triple from 2020 to 2050. This trend is particularly prominent in rapidly developing countries like India and Indonesia, which experience cooling-intensive climates. To address these challenges, efforts have focused on providing efficient and environmentally friendly cooling solutions grounded in three fundamental principles: building energy efficiency, system energy efficiency, and renewable primary energy supply. Combining these principles results in cost-effective and sustainable cooling solutions that enhance user comfort and mitigate greenhouse gas emissions, benefiting the environment and climate.

The outcomes of this study underscore the multifaceted nature of achieving energy efficiency in Sunbelt regions, especially concerning solar cooling and building processes (Bonomolo et. al, 2023a). These findings emphasize the importance of robust data analysis, considering a range of factors that impact energy consumption and cooling demands in different building contexts.

Looking ahead, future activities should concentrate on addressing the challenges posed by varying building characteristics, materials, orientations, and occupant behavior. Moreover, there is a need to develop standardized assessment methods to effectively compare the performance of different solar cooling systems. Economic considerations and the economic impact of these systems should also be a priority in future research. Furthermore, the introduction of the Cooling Demand Market Index (CDMI) highlights the growing importance of cooling demand globally (Strobel et. al, 2023), particularly in developing countries experiencing economic growth and climate change. Future work should delve deeper into understanding and mitigating the rising cooling demand in Sunbelt regions to ensure sustainable and energy-efficient solutions.

Further details can be found in the published A4 final report (Bonomolo et. al, 2023b).

4.2 Subtask B – Demonstration

Although solar cooling has a long history, first examples were built in the 1990s, a real market couldn’t be established anywhere. Roughly 2,000 solar (thermal) cooling systems exist worldwide. Most of them can be declared as customized, early-stage systems. PV supported cooling developed in the recent years, whereas PV is often only attached to a common electrical driven system and real control and optimized support (or increase of self-consumption) is rather seldom. Several technical and mostly economic reasons are still preventing solar cooling from a wider market uptake. Besides these barriers, the most important approach for introducing these technologies in the Sunbelt is a wide range of demonstrations. It must be assured that solar cooling is seen as a technically reliable, economically viable, and smart solution. The future perspective in Sunbelt countries through the adaptation of components and systems need to be proven by monitored best practice examples for all kind of system configurations and applications. Achievements for Subtask B to date (October 2023).

B1/A2: Show cases on system and component level

A collection of findings examines the constituent elements employed in different solar cooling technologies and their relationships with various variables, including type of solar collector, climate zone, application, and the components integrated into the systems. Solar cooling stands as a promising and efficient means of contributing to decarbonization efforts in nations within the Sunbelt region. Considering the expected increase in cooling needs within these nations, there is a substantial opportunity to identify the best components and conduct comprehensive evaluations of existing/ongoing projects. This approach would expand its scope and amplify its overall influence significantly. The research encompasses 32 studies conducted in 18 countries located in the Sunbelt region. Figure 4 illustrates the demographic distribution of these projects.

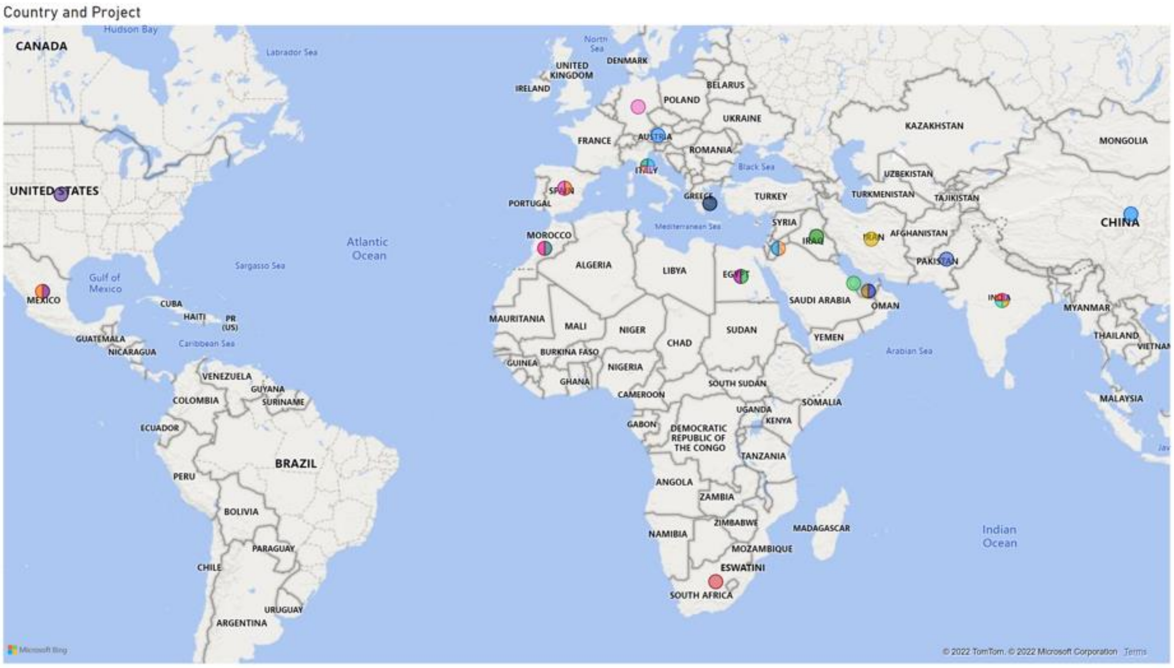

Fig. 4: Case studies located in the Sunbelt region

Project Typology: The studies conducted addressed a diverse range of project types. Among these, 50% of the projects are presently in the implementation phase, while 18% are in operation and have attained established outcomes. 25% of these studies involve conceptual projects examined for implementation through simulation tools like TRNSYS, Python, Matlab, and other mathematical modeling techniques. These tools serve as effective methods to assess system performance before actual implementation. Additionally, the survey includes published works featuring laboratory experiments and simulations validated by real-time building energy usage. This approach ensures a comprehensive and varied analysis.

Solar Collector Types: Solar Cooling uses a range of solar energy harnessing devices. Among these, evacuated tube collectors are utilized in 30% of the analyzed projects, while both flat plate collectors and Fresnel collectors are equally prominent at 17% each. The research also indicates that Fresnel collectors and flat plate collectors are the most commonly chosen options in executed projects, whereas evacuated tubes are predominant in simulation projects. Examining the distribution of different solar collectors across various temperature profiles provides valuable insights into their suitability for different scenarios. Evacuated tube collectors find extensive application across three distinct climate regions: BSk (Cold semi-arid), BWh (Hot desert climates), and Csa (Hot-summer Mediterranean climate). Similarly, flat plate collectors are suitable for a range of five different profiles, spanning from Hot Desert (BWh) to Warm-summer Mediterranean climates (Csb).

Solar Cooling Applications: In the majority of the examined cases, solar cooling systems are installed in public buildings (34%), including offices, schools, and university buildings, enabling direct utilization of solar energy during daytime hours. Domestic buildings (25%) appear to be the next most studied due to prevalent requirements for improved indoor comfort in the Sunbelt region. It is also noted that these systems have promising potential applications in sectors such as food preservation and process industries.

B2: Design guidelines

A detailed questionnaire has been meticulously crafted to cover aspects of solar cooling components, design considerations, sizing, and other sub-systems like heat rejection units and cold distribution systems. This questionnaire was distributed to active participants in the task, and their responses have been collected. Data has been gathered from 10 case studies, detailing component capacities and sizing procedures and covered in activity B1. In activity B2, case studies are presented to illustrate the performance of solar cooling systems under varying boundary conditions. Three distinct case studies, each with its unique scope and attributes, are elaborated upon. The summary is as follows:

Industrial Cooling Potential: Industrial cooling holds significant promise for solar cooling applications. These systems can achieve a high solar fraction, leading to a considerable reduction in CO_2 emissions compared to conventional electricity-driven chillers.

Solar PV and Vapor Compression Chillers: The integration of Solar PV with vapor compression chillers is examined as an emerging solution for decarbonizing cooling systems. A comparative analysis involving different load and weather profiles, suggests that solar PV cooling can result in a lower levelized cost of cooling compared to solar thermal. The study underscores the significance of thermal storage and the effectiveness of lower temperatures in solar thermal collectors for cost competitiveness.

Hybrid Electrical and Thermal Chillers: This study is based on the HyCool project. The focus is on combining electrical and thermal chillers. Both simulation and real-world outcomes demonstrate a significant decrease in electricity consumption when utilizing the topping cycle of the absorption chiller. Progress in policies and economies of scale is expected to boost the cost-effectiveness of these innovative methods.

In conclusion, these case studies underscore the transformative potential of cooling solutions. As technology advances and policies evolve, the adoption of such systems will play a pivotal role in shaping a greener and more energy-efficient cooling future.

B5: Lessons learned (technical and non-technical)

Activity B5 involved identifying and documenting lessons learned, both technical and non-technical, with the purpose of creating a summary for dissemination in Subtask D. The primary objective was to collect trustworthy data and gain valuable insights from various stakeholders. A survey was conducted to gather information on stakeholder's requirements, expectations, and specific circumstances that may prompt the utilization of solar cooling. The primary objective of the survey was to identify crucial factors influencing the adoption of solar cooling technologies across different applications and regions. The gathered information was then analysed to better comprehend the challenges, needs, and desires of the stakeholders involved.

The results obtained from the questionnaire showed that solar cooling technologies are highly valued and important, but their market transformation requires collaboration across various sectors. Engaging with stakeholders, including government agencies, industry players, research institutions, and consumers, is crucial for creating a supportive ecosystem for solar cooling. GIS software aids in effective planning and deployment, while technical training programs build capacity and expertise in the industry. Demonstrating the technical and economic viability of solar cooling and reducing reliance on the electrical grid can promote adoption. A multi-faceted strategy involving awareness-raising, market acceptance, and accelerated penetration can make solar cooling a sustainable solution for cooling needs. This approach contributes to climate change mitigation, economic growth, and energy security.

4.3 Subtask C – Assessment and Tools

The concurrent technical, economic and financial assessment of solar cooling options is of high importance in each stage of the life cycle of a project, starting with comparison of different technology options and pre-design, detailed planning, optimizing of operation but also for policy design with proven concepts. In all life cycle phases, it is crucial to have corresponding tools that deliver the necessary information and key performance indicators for the different stakeholder. The KPIs need to take into consideration economic, financial, social and environmental issues as well as other 'Multiple Benefits'. Tools and their specific outputs permit to provide guidance on optimized system design and implementation and show the level of quality of both the most critical components and systems. The following results have been achieved in Subtask C so far (October 2023).

C1: Design tools and models

The work involved reviewing and adapting tools and models for technical and financial assessment and design for solar cooling and the project phases from pre-feasibility to simulation to monitoring. The focus is the documentation of the tools and their specific application to provide measured data for validating the tools and the adaptation of selected ones for Sunbelt countries.

Three approaches are used to evaluate tools used worldwide and this IEA SHC Task. First, a (i) generic literature research in Web of Science (WoS), (ii) interviews and questionnaires among the IEA SHC Task Expert, and (iii) interactive questionnaires during Task expert meetings.

A total of 1,216 documents were identified as a result of the search in WoS. The query search string used is ALL=("solar cooling" OR "solar refrigeration"), and the index dates covered are 1990/01/01-2021/06/30. A network visualization diagram was generated in VOSviewer. A query search string ("solar cooling") ("design") AND ("software") in the topic field produced 38 documents.

The initial data gathered provide a general idea of which components are being used and which software is being implemented. Based on the information provided by the task participants, the following software are currently being implemented in their applications/research: Matlab, Meteonorm + Excel tool, TRNSYS, EES, and Phyton. This is also reflected in the third evaluation of tools.

Conclusion: Modelling and assessing the technical and economic behavior of solar cooling plants is essential in all design phases up to implementation and optimization. Different tools are used, from sophisticated dynamic simulation models to simple spreadsheet calculations. Companies and their experts often develop their own for their specific components and systems. Generic publicly available models can be found for almost all applications, especially simulation tools. The configuration and data sheets for the entire tool depend on the approach and are often difficult to find.

Further details can be found in the published C1 final report (Daborer-Prado et. al, 2023).

C2: Database for technical and economic assessment

The elaboration of the database and collection of technical (e.g. standard reference systems, etc.) and economic data (energy prices for electricity, natural gas, etc.) for different components (Investment, maintenance, lifetime, etc.) and for the different sunbelt countries (based on subtask B demo cases) is ongoing and is the basis for the following assessments of the various solar cooling concepts. The data base includes future scenarios for technical and economic boundaries (e.g. efficiency of conventional chillers, energy prices) to provide the base and a solid framework for the sensitivity analyses and future scenarios. The database elaboration is also including review of existing useful information of IEA knowledge (e.g. IEA SHC Task 54, and others).

C3: Assessment mechanism

This activity is combined with B3 activity, the review of existing tools (other IEA SHC Task 53, …) and methods for technical (e.g. Solar Performance Factor, etc.) and economic (e.g. Levelized Cost of Heating/Cooling, etc.) provides the bases to select the necessary KPIs for different project phases and stakeholders. A selection of one tool/platform will be forced to be used by this Task, the adaptation of methods and integration of the database (activity C2) are the core activities. The focus is to provide the corresponding methods for the analyses and creation of assessments for certain stakeholders.

4.4 Subtask D – Dissemination

A wide penetration of solar cooling in Sunbelt countries is not only depending on the accomplishment of technical barriers. Non-technical barriers often have a critical role. Financing, policy advise, and dissemination/communication of success stories are among the important activities to overcome also non-technical barriers. The focus is on the implementation of target specific promotion activities based on the collected results, upgrade of material for dissemination for external communication, the implementation of knowledge transfer measures towards the technical stakeholders, the development of instruments and their provision for policy makers. At the time of writing (October 2023), the following results have been achieved in subtask D.

D1: Task65 website and publications

A website included into the IEA SHC portal has been created, see https://task65.iea-shc.org/. It firstly presents the Task purpose and activities and secondly the Task results. It also lists all Task participants and observers. Finally, in the future the website will also host an online best practice collection webpage, presenting the system concepts, state of the art of cooling markets, the main lessons learned and the entire technical and economic KPIs. After the end of the Task the website will become an archive of the Task's collective work results.

Several publications about Task 65 and the experts work related to the different activities have been published: EuroSun 2020, FotoVolt 10/2021, SWC 2021, APSRC 2021, ISEC 2022, EuroSun 2022, APSRC 2022, s@ccess 2023, ICR 2023, SWC 2023). For a comprehensive list please visit https://task65.iea-shc.org/news.

D2: Policy advise and financing models

The work in Activity D2b is ongoing. A list of the most relevant business and financing models that could be used for solar cooling systems has been compiled. A clear distinction has to be made between business models and third-party financing – these terms are often mixed up. Third party financing (TPF) can be part of a business model, but the latter goes well beyond financing. Some examples of ESCO (energy service company) models have existed in the solar thermal sector for a long time. Scottsdale's Desert Mountain High School in Arizona, USA, was one of the first clients to profit from a cooling energy supply contract (Epp, 2014). In 2014 SOLID from Austria financed and installed a 3.4 MW cooling system and signed a 20-year cooling energy supply contract with the school (Figure 5).

Fig. 5: Solar roof for Scottsdale's Desert Mountain High School in Arizona, USA (Source: SOLID, 2014)

Another example is a special purpose vehicle, where a separate legal company is established, which plans, builds, finances and operates the energy production units and signs all the relevant documents such as EPC contracts, O&M agreements or loan contracts. The first solar thermal specialists are already using this model successfully - for example NewHeat in France. The company created an SPV already in 2018 to finance and operate a package of solar industrial and district heat projects (Epp, 2017). Solar fields from the Netherlands also founded an SPV recently for the 37 MW district heating plant under construction in Groningen (Epp, 2022).

Given the special situation in some sunbelt countries with weaker economies, another model can be recommended: the utility-based on-bill repayment model. On-bill repayment is widely used in the United States for energy-saving measures or heating upgrades in the residential sector. Here, the asset including the re-financing agreement can be sold with the house if the owners have to move.

D5: Workshops conducted

The following national and industry workshops as well as SHC Solar Academy trainings have been conducted so far by the Task 65 experts:

- SHC Solar Academy Training for CCREEE, Nov 10th 2020 (online)
- National Workshop for China, Dec 5th 2020 (online)
- National Workshop for Austria, March 24th 2021 (online)
- Industry Workshop Task 65 + HPT Annex 53, Mar 25th 2021 (online)
- SHC Solar Academy Training for SOLTRAIN / SACREEE, Nov. 8th-9th 2021 (Stellenbosch, South Africa)
- Industry Workshop Task 65 & sol.e.h2., Dec. 2nd 2021 (online)
- ISES SHC Solar Academy Webinar Task 65, Oct. 25th + 27th 2022 (online)
- Industry Workshop Task 65 + HPT Annex 53, March 24th 2023 (Innsbruck, Austria / hybrid)
- SHC Solar Academy Training for SOLTRAIN / ECREEE, Oct. 10th-11th 2023 (Praia, Cape Verde)

5. Trends and outlook

One of the main trends in the upcoming years will be that more and more hybrid system solutions of all kinds in the field of solar cooling will come onto the market. They will offer high CO_2 savings also in small to medium cooling capacity ranges with good economic efficiency at the same time. Furthermore, in the area of medium-temperature systems (solar collector temperatures around 160-180 °C) and double-effect absorption chillers, there will be solutions with better efficiency and profitability, since they will have smaller solar fields and lower heat rejection capacities to achieve an investment advantage of up to 40% compared to conventional solar cooling systems.

However, one of the significant challenges of solar cooling lies in the intermittent nature of solar energy availability.

Moreover, quite often in emerging countries the reliability of public grids face challenges and load shedding often appears, such as in South Africa. Especially when focusing on industrial applications including agri-food, manufacturing industry and tourism, the reliability and availability of renewable solutions and its economic impact compared to conventional backups is key.

As the world seeks sustainable alternatives to conventional energy sources, solar cooling has emerged as a promising solution also for industrial applications. Solar thermal energy combined with waste heat recovery and innovative thermal storage concepts (starting from sensible heat, but extending storage solutions to latent heat, using Phase Change Materials (PCM) and thermochemical solutions) is a promising solution to meet cooling demands at a minimum environmental impact. These three key areas are future topics that solar cooling systems leverage the abundant and renewable energy provided by the sun to meet both the heating and cooling needs of industrial processes. This sustainable energy is then utilized to power sorption and hybrid-based systems, which offer efficient cooling capabilities for industrial environments.

6. Acknowledgments

This work has partially received funding from the German Federal Ministry for Economic Affairs and Energy (BMWi / PtJ) under grant agreement No. FKZ 03ETW024B (SorptionTakeOff).

The funding of Austrian's participation of IEA SHC Task 65 (FFG no. 883011) through the Austrian Research Promotion Agency (FFG), the program "research cooperation international energy agency" and the Federal Ministry on Climate Action, Environment, Energy, Mobility Innovation and technology is gratefully acknowledged.

7. References

Beccali, M., Vasta, S., Weiss, W., Baby, B.A., Bonomolo, M., 2022. Adapted components and showcases on solar cooling systems in sunbelt region. EuroSun 2022 Proceedings. DOI: 10.18086/eurosun.2022.06.02.

Bonomolo, M., Jakob, U., Neyer, D., Strobel, M., Vasta, S., 2023a. Integration of solar cooling systems in buildings in Sunbelt region: an overview. In Buildings 2023, 13 (9), p. 2169. DOI: 10.3390/buildings13092169.

Bonomolo, M., Strobel, M., Vasta, S., Jakob, U., Neyer, D., 2023b. Building and process optimization potential. IEA SHC Task 65 Report D-A4. DOI: 10.18777/ieashc-task65-2023-0003.

Daborer-Prado, N., Neyer, D., Aye, L., Jakob, U., 2023. Design tools and models. IEA SHC Task 65 Report D-C1. DOI: 10.18777/ieashc-task65-2023-0004.

Epp, B., 2014. SOLID operates 3.4 MW_{th} cooling system as ESCO in Arizona. Solarthermalworld.org, last accessed 25.10.2023, https://solarthermalworld.org/news/usa-solid-operates-34-mwth-cooling-system-esco-arizona/.

Epp, B., 2017. French independent heat supplier: Optimise and de-risk all contracts. Solarthermalworld.org, last accessed 25.10.2023, https://solarthermalworld.org/news/french-independent-heat-supplier-optimise-and-de-risk-all-contracts/.

Epp, B., 2022. 37 MW solar district heating plant in the Netherlands with outstanding features. Solarthermalworld.org, last accessed 25.10.2023, https://solarthermalworld.org/news/37-mw-solar-district-heating-plant-in-the-netherlands-with-outstanding-features/.

Gurtner, R., Schmetzer, T., Riepl, M., 2023. Climatic conditions and applications. IEA SHC Task 65 Report D-A1. DOI: 10.18777/ieashc-task65-2023-0002.

IEA, 2018. The Future of Cooling. Opportunities for energy efficient air conditioning. IEA Publications, International Energy Agency.

IEA, 2019. The Future of Cooling in Southeast Asia. IEA Publications, International Energy Agency.

IEA SHC, 2023. Solar Heat Worldwide – Global Market Development and Trends in 2022 – Detailed Market Figures 2021, Edition 2023. IEA SHC Publications, International Energy Agency.

MI IC7, 2023. Innovation community on affordable heating and cooling of buildings (IC7). Mission Innovation Initiative, last accessed 25.10.2023, http://mission-innovation.net/platform/innovation-community-ic7/.

OECD, 2017. World Energy Outlook 2017. Paris: OECD Publishing. https://ebookcentral.proquest.com/lib/gbv/detail.action?docID=5160837.

Patwardhan, A.P., et al., 2012. Global Energy Assessment (GEA). International Institute for Applied Systems Analysis. Cambridge: Cambridge University Press.

Strobel, M.; Jakob, U.; Streicher, W.; Neyer, D., 2023. Spatial Distribution of Future Demand for Space Cooling Applications and Potential of Solar Thermal Cooling Systems. In Sustainability 2023, 15 (12), p. 9486. DOI: 10.3390/su15129486.

Study on the Thermohydraulic Performance of Double Pass Solar Air Heater

Ankush Hedau* and S. K. Singal

Department of Hydro and Renewable Energy, Indian Institute of Technology Roorkee (India)

*Corresponding author: ankush.hedau@gmail.com

Abstract

Experimental and numerical investigations are conducted in this study to optimize different turbulence models and thermohydraulic performance of double pass solar air heater (DPSAH) under different Reynolds numbers (*Re*) of 3000 to 19000. The DPSAH was investigated using five different turbulence models: SST-k-ω, standard k-ω, realizable k-ε, RNG k-ε, and standard k-ε. Using the RNG k-ε turbulence model, the experimental results are found in close agreement with the numerical results, with an average absolute deviation of 2.6% for the Nusselt number (*Nu*) and an average absolute deviation of 0.4% for friction factor (*f*). In comparison to single pass solar air heater (SPSAH), the DPSAH enhanced the values of the Nusselt number (*Nu*) from 1.13 to 1.89 and increased the values of friction factor (*f*) from 2.69 to 3.5 for a considered range of *Re*. The maximum thermohydraulic performance parameter (THPP) over the SPSAH was obtained as 1.25, which corresponds to *Re* of 19000.

Keywords: Thermohydraulic performance, solar energy, computational fluid dynamics, friction factor, Nusselt number

1. Introduction

Energy consumption is increasing day by day throughout the world due to rising population, technological advancements, and economic developments. Moreover, the major portion of energy consumption is met by the non-renewable sources of energy such as coal, natural gas and petroleum oil, causing an increase the global warming and greenhouse gas emissions. It is essential to utilize renewable energy sources (solar energy, biomass energy, geothermal energy, and wind energy) in order to reduce the impact of global warming and greenhouse gas emissions. Solar energy is found to be the highest potential renewable energy source that fulfils the world's energy requirement. Solar air heater (SAH) is a device which harnesses solar energy for a wide range of low-temperature purposes, including drying, natural ventilation and greenhouse heating. There are two primary components of the SAH. These two components are the absorb plate and the glass cover. As a heat transfer medium, the SAH utilizes air to transfer heat.

In SAH, the main drawback is the low heat transfer between the absorber plate and the air. This is because of the thermal boundary layer formation along the length of the absorber plate. In order to increase the heat transfer, the absorber plate's surface area must be increased in contact with the air. Further, the SAH is categorized according to the number of passages as either double pass or single pass. Moreover, SAH with double pass is more effective than SAH with a single pass due to its large heat contact surface area (Hernández and Quiñonez 2013; Kabeel et al. 2017). The various authors conducted experimental and numerical investigations on the double pass solar air heater (DPSAH) and single pass solar air heater (SPSAH), which are discussed in the following paragraphs.

An extensive literature review was presented by Alam and Kim (2017) on different methods of improving the performance of a DPSAH. The results concluded that the performance was enhanced with DPSAH because of increased heat transfer surface area, turbulence intensity, and reduced thermal losses. The thermal performance of DPSAH was found to be greater than that of SPSAH. The comparative analysis of the SPSAH and DPSAH filled with porous media in the lower passage was experimentally presented by Kareem et al. (2013). It was observed that the thermal performance of SAH increases with increasing number of passes. The maximum

10.18086/swc.2023.04.07 Available at http://proceedings.ises.org

thermal efficiency of the SPSAH and DPSAH was achieved to be 52% and 70 %, respectively. Hernández and Quiñonez (2013) examined the thermal behaviour of parallel and counter-flow DPSAH. They developed various mathematical expressions to evaluate the heat transfer coefficients and heat transfer removal factor of the SAHs. The double pass counter flow had higher temperature rise compared to double pass parallel flow.

Gill et al. (2012) studied the thermal performance of single-glazed and double-glazed SAHs. It is seen that double-glazed SAH has higher stagnation temperatures and thermal efficiency. The double-glazed SAH is more cost-effective in terms of air outlet temperatures and thermal efficiency than a single-glazed SAH. The thermal performance of SPSAHs was numerically analyzed by Yadav and Bhogoria (2013) using five different turbulence models: SST-k-ω, standard k-ω, realizable k-ε, RNG k-ε, and standard k-ε. The RNG k-ε turbulence proved the best turbulence model to validate with the Dittus-Boelter equation and Blassius equation. Kumar (2017) numerically analyzed the thermohydraulic performance of V-corrugated SAHs with an RNG k-ε turbulence model. It was concluded that V corrugated SAH has better thermohydraulic performance than smooth flat plate SAHs.

From an extensive literature review, it has been concluded that counter-flow DPSAHs have better outlet temperatures and thermal efficiency than SPSAHs. However, no study has been conducted on a DPSAH with different turbulence model. The thermohydraulic performance of DPSAHs has not yet been reported. Accordingly, an experimental and numerical investigation is conducted in order to examine the thermohydraulic performance of DPSAH having five different turbulence models (SST-k-ω, standard k-ω, realizable k-ε, RNG k-ε, and standard k-ε).

2. Numerical approach

Computational fluid dynamics (CFD) is a method of analyzing fluid flow and heat transfer in DPSAHs. In the present study, the numerical analysis is conducted on DPSAH with ANSYS Fluent 2020 R_2. The numerical approach is explained in the following subsections.

2.1. Computational model

ANSYS design modeler was used to develop the computational model of DPSAH, which has dimensions of 35 mm height, 1000 mm length, and 350 mm width. The computational domain consists of lower and upper passages, each with a height of 35 mm. However, 50 mm air circulation gap was provided near the U-turn passage to divert air from the lower passageway to upper passageway and to minimize the pressure loss. The dimension of computational domain is shown in Fig. 1.

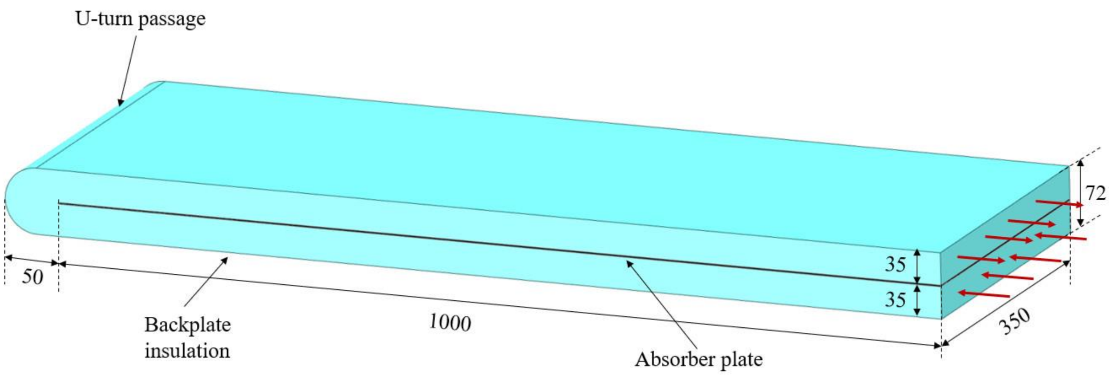

Fig. 1: Three-dimensional computational domain of double pass solar air heater (DPSAH) (All dimensions are in mm)

Assumptions considered during CFD analysis: (i) Flow is steady, incompressible, 3-dimensional, turbulent and fully developed (ii) The air outlet pressure should equal the gauge pressure (iii) The properties of the absorbing plate and air are kept constant (iv) Heat transfer due to radiation is negligible as solar radiation of 880 Wm^{-2} is uniformly distributed across the absorber plate (v)The sidewall and bottom plate are considered insulated.

2.2. Meshing

Heat transfer and fluid flow were analyzed by dividing the computational model into number of elements and cells using a grid generation method. The meshing of DPSAH is shown in Fig. 2. A uniform and fine grid was created with the meshing module in Ansys 2020 R_2. The smoothing was high for creating a uniform grid. Fine and uniform meshing were used for accurate flow simulation. Grid-independence test (GIT) was performed with an RNG k-ε turbulence model to accommodate small deviation in friction factor (*f*) and Nusselt number (*Nu*). The elements varied between 369026 and 3959280 for Reynolds number (*Re*) of 5000, as shown in Tab. 1. The number of elements increased until *Nu* and *f* deviations were less than 1%. The optimum number of nodes and elements for the grid independence test were found to be 2488827 and 2300638, respectively.

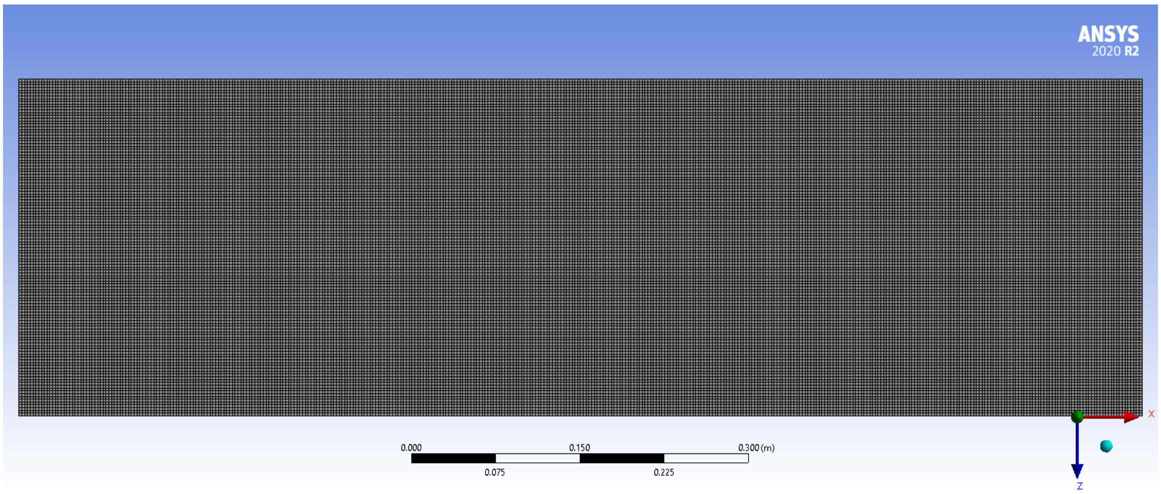

Fig. 2: Meshing of the absorber plate of DPSAH.

Tab. 1: Grid independence test of DPSAH for *Re* of 5000

Element size	**No. of nodes**	**No. of elements**	***Nu***	***f***	**% Variations in *Nu***	**% Variations in *f***
0.0035	425169	369026	18.34	0.0327		
0.003	684982	608800	19.37	0.0321	5.32	1.97
0.0027	863500	771502	20.20	0.0323	4.11	0.54
0.0024	1283028	1166286	20.92	0.0320	3.44	0.87
0.0021	1895184	1739881	21.69	0.0323	2.55	0.84
0.0019	2488827	2300638	21.90	0.0321	0.96	0.58
0.0018	2951088	2740804	22.11	0.0320	0.95	0.26
0.0017	3503538	3268496	22.31	0.0318	0.90	0.56

2.3. Governing equation

To analyze the fluid flow and heat transfer of DPSAH, three governing equations, namely the energy equation, continuity equation and Navier-Stokes equation, were applied. The finite volume method (FVM) solves these governing equations for steady-state regimes. This system was governed by the following 3D equations in Cartesian coordinates:

Continuity equation (Mass conservation equation)

$$\frac{\partial(\rho u_j)}{\partial x_j} = 0 \qquad \text{(eq. 1)}$$

Navier-Stokes equation (Momentum conservation equation)

$$\frac{\partial}{\partial x_i}(\rho u_i u_j) = -\frac{\partial P}{\partial x_i} + \frac{\partial}{\partial x_j}\left[\mu\left(\frac{\partial(\rho u_i)}{\partial x_i} + \frac{\partial(\rho u_j)}{\partial x_j}\right)\right] + \frac{\partial}{\partial x_j}\left[-\overline{\rho u'_i u'_j}\right] \qquad \text{(eq. 2)}$$

Energy conservation equation

$$\frac{\partial}{\partial x_i}\left(\rho u_j T\right) - \frac{\partial}{\partial x_j}\left[\left(\Gamma + \Gamma_t\right)\frac{\partial T}{\partial x_j}\right] = 0 \qquad \text{(eq. 3)}$$

The governing equations were solved in the present study with the help of boundary conditions mentioned in Tab. 2.

Tab. 2. Boundary conditions

Boundary zone	Zone condition	Zone type	Values
Inlet	Velocity inlets	Fully developed	1.23 to 4.67 ms^{-1} (3000 to 19000)
Outlet	Pressure outlets	Fully developed	101.3 kPa (Atm.)
Absorber plate	Wall	No slip	880 Wm^{-2}
Side and bottom wall	Wall	No slip	Insulated

2.4. Turbulence model and solution method

The double-precision pressure-based solver was used for predicting accurate flow simulations. A least square-based method was used to perform the spatial discretization. To simulate fluid flow and heat transfer behaviour, second-order upwind scheme was used to account for continuity, pressure, momentum, turbulence dissipation rate, turbulent kinetic energy and energy equation. The SIMPLE algorithm was selected for solving governing equations based on the conservation laws and boundary conditions. The convergence criteria selected for continuity equation was 10^{-3}, and for the momentum and energy equation was 10^{-6}. The numerical investigation of DPSAH was carried out on five different turbulence models such as realizable k-ε, RNG k-ε, standard k-ε, SST-k-ω and standard k-ω turbulence model.

In order to validate the turbulence model of DPSAH, the experimental testing rig is designed and manufactured, which is discussed in the next section.

3. Experimental Study

3.1. Details of the experimental approach

The experimental testing rig consists of four parts: rectangular duct, solar simulator, data acquisition system and air circulating unit, as illustrated in Fig. 3.

The solar simulator was designed and manufactured with dimensions of 1600 mm×400 mm and consists of 24 halogen tubes, four dimmers, and an iron frame. The solar simulator was powered by variac to produce solar radiation of 1000 Wm^{-2}. The solarimeter measures the intensity of solar radiation in order to maintain a uniform solar radiation of 1000 Wm^{-2} throughout the glass cover.

There are three sections along the length of air duct: the entry section, the test section and the exit section. For the flow to be fully developed inside the duct, the entry and exit sections were kept at 550mm in length, as per the ASHRAE standard (Standard 1986). To increase the absorption of incoming solar radiations, aluminium was used as the absorbing plate, which was covered with a black paint coat. A lower passage of 35 mm was provided between the backplate and absorber plate, and upper passage of 35 mm between the absorber plate and glass cover. The glass cover thickness of 4 mm, having transmissivity of 0.88 and absorptivity of 0.1, was used.

To reduce the conduction and convective losses to the atmosphere, three different insulation materials were provided at the sidewalls and bottom wall of the rectangular duct. The first insulation layer was provided by the plywood thickness of 12 mm to reduce the conduction losses. The plywood was covered by glass wool of thickness of 6 mm. The glass wool was covered by thermocol with thickness of 12 mm to minimize the heat losses to the surroundings. The centrifugal blower powered by a motor rating of 2 kW,230V running at 2880 rpm was used to suck the air from the atmosphere and direct the air from the lower passageway to upper passageway.

The 52 T-type thermocouples were calibrated by Fluke 9142. With the help of two data loggers (midi LOGGER GL800), temperature data was recorded from thermocouples attached to the inlet and outlet sections, as well as the heating surface of the absorber plate. The U-tube manometer and the orifice plate were used for measuring the mass flow rate of the air, and the control valve was used for controlling the mass flow rate of the air. The digital manometer was used to measure the pressure difference of the rectangular duct.

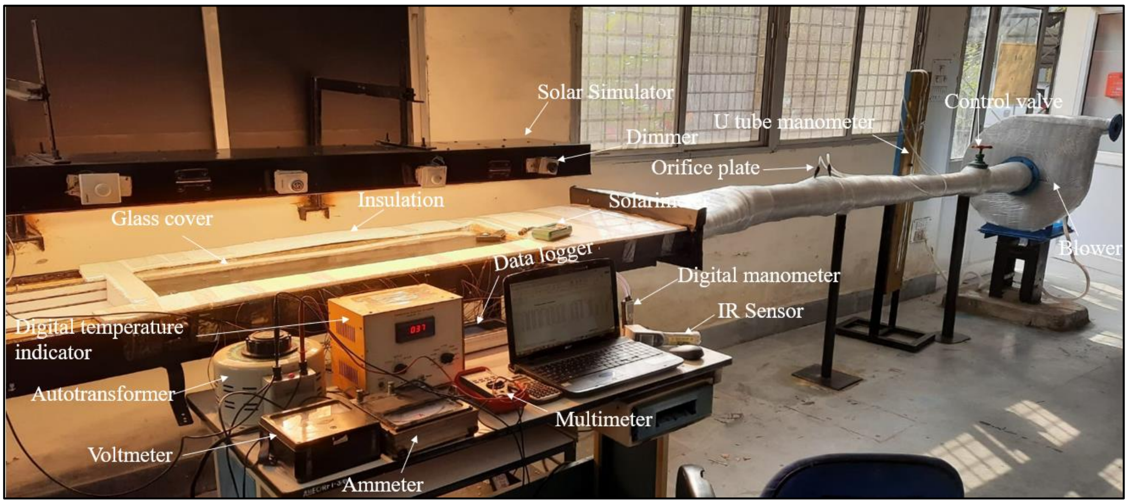

Fig. 3: Experimental test rig of DPSAH

3.2. Data collection

The following parameters were recorded under the steady state conditions.

- Pressure difference across the orifice plate (ΔP).
- Lower and upper absorber plate temperatures (T_{pm})
- Temperatures of inlet air (T_{in}) were recorded at inlet of the lower passage.
- Temperatures of the outlet air (T_{out}) were recorded at outlet of the upper passage.
- Pressure difference inside the duct $(\Delta P)_d$.

The various mathematical formulations were used to calculate the values of friction factor (f), Nusselt number (Nu), and THPP of DPSAH, which are discussed in the following subsections.

3.3. Data reduction

Using the value of pressure difference across the orifice plate (ΔP), airflow inside duct is calculated as follows:

$$\dot{m} = C_d \times A_o \times \left[\frac{2 \times \rho_a \times (\Delta P)}{1 - \beta^4}\right]^{0.5} \quad \text{(eq. 4)}$$

Where C_d is the orifice plate discharge coefficient, A_o is the orifice area, and β is the ratio of the orifice meter radius to orifice pipe the radius.

The air velocity (V) is calculated as follows:

$$V = \frac{\dot{m}}{\rho_a \times W \times H} \quad \text{(eq. 5)}$$

The value of Re is determined as follows:

$$Re = \frac{\rho_a \times V \times D_h}{\mu} \quad \text{(eq. 6)}$$

Where D_h represent equivalent diameter and is calculated as:

$$D_h = \frac{4\,(W \times H)}{2\,(W + H)} \quad \text{(eq. 7)}$$

The air heat gain (Q_u) is mathematically determined as follows:

$$Q_u = \dot{m} \times C_{pa} \times (T_{out} - T_{in}) \quad \text{(eq. 8)}$$

The convective coefficient (h) is determined by equating value of Q_u to the convective heat transfer rate (Q_{conv}), as follows.

$$h = \frac{Q_u}{A_p(T_{pm} - T_{am})} \quad \text{(eq. 9)}$$

T_{pm} and T_{am} are the mean weighted average temperature of the absorber plate and air, respectively.

The value of Nu is determined as follows (Kays 1985).

$$Nu = \frac{h \times D_h}{k} \quad \text{(eq. 10)}$$

The value of f is determined as follows (Brown 2002).

$$f = \frac{(\Delta P)_d D_h}{2\rho_a L V^2} \quad \text{(eq. 11)}$$

Using the thermohydraulic performance parameter (THPP), the optimal value of DPSAH is determined as follows (Webb and Eckert 1972).

$$\text{THPP}= \left(\frac{Nu}{Nu_s}\right) \Big/ \left(\frac{f}{f_s}\right)^{1/3} \quad \text{(eq. 12)}$$

3.4. Validation of experimental results

The experimental setup was designed and constructed to determine the accuracy of the experimental results of SPSAH. The values of Nu_s and f_s of SPSAH were validated with the Dittus-Boelter and Blasius equations, respectively. The Dittus-Boelter equation and Blasius equation correlations are expressed as follows.

Dittus-Boelter correlation (Kays 1985),

$$Nu_s = 0.023(Re)^{4/5}\,(Pr)^{0.4} \quad \text{(eq. 13)}$$

Blasius correlation (BHATTI 1987),

$$f_s = 0.085(Re)^{-\frac{1}{4}} \quad \text{(eq. 14)}$$

The experimental validation of Nusselt number (Nu_s) and friction factor (f_s) with empirical correlations is shown in Fig. 4. It is seen that the experimental results of SPSAH are found to be in good agreement with the empirical correlations developed for the value of Nu_s and f_s. The mean absolute percentage error was found as 1.4% for the value of Nu_s and 6.8% for the value of f_s.

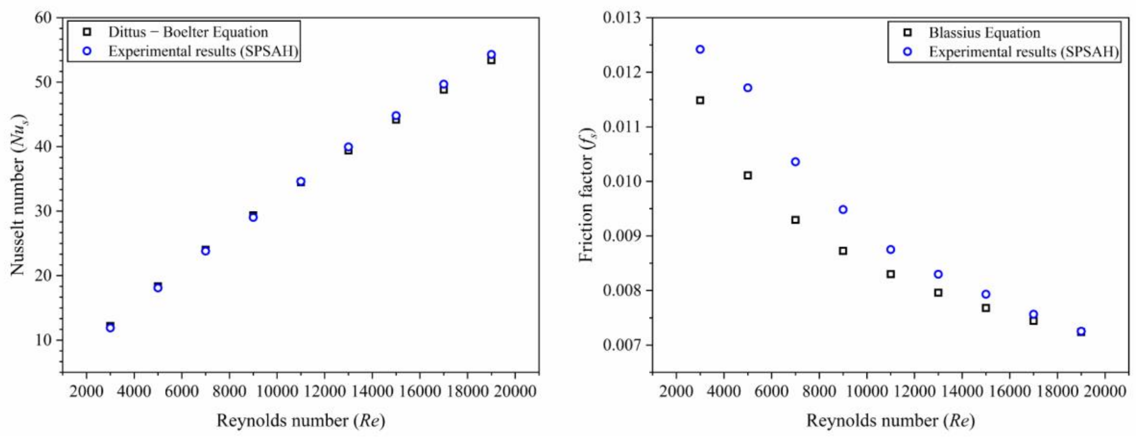

Fig. 4: Experimental validation of the Nu_s and f_s for the single pass solar air heater (SPSAH)

In order to optimize the turbulence models for the DPSAH, an experimental setup was developed following the experimental validation of SPSAH. The thermohydraulic performance parameter is further analyzed in comparison with the SPSAH.

4. Result and Discussions

In the present study, the optimization of different turbulence models and thermohydraulic performance of DPSAH is carried out for *Re* varied from 3000 to 19000 and is discussed below sub-sections.

4.1. Optimization of turbulence model of DPSAH.

The numerical results of smooth plate DPSAH with different turbulence models are compared to the experimental results for the values of *Nu* and *f*. The optimization of turbulence models is carried out for the value of *Re* from 3000 to 19000.

The variation in *Nu* with *Re* for different turbulence models and experimental results is presented in Fig. 5. It is found that the RNG k-ε turbulence model with enhanced wall treatment gives the least mean absolute percentage error (MAPE) of 2.6 % in *Nu* for the range of *Re* considered. This is due to the RNG k-ε turbulence model predicts the average absorber plate temperature to be close to the experimental results, as shown in Tab. 3. The static temperature contours corresponding to the different turbulence model at *Re* of 7000 are shown in Fig. 6. From the temperature contours, it can be concluded that the RNG k-ε model exhibits almost the same temperature distribution as the realizable K-e and standard k-ε models. Moreover, the realizable k-ε turbulence model and standard K-e turbulence model with enhanced wall treatment have more deviation in *Nu* at a low value of *Re*, and deviation has decreased with an increase in *Re*, and the corresponding MAPE is found as 4.1% and 4.8%, respectively. The k-ε turbulence model gives the closest results to the experimental results because it considers two more transport equation: turbulence dissipation rate (ε) and kinetic energy (k).

In comparison to experimental results, the standard k-ω turbulence model and SST- k-ω turbulence model gives more deviation in *Nu* at a low value of *Re*, and the deviation increases as the value of *Re* increases. The corresponding MAPE is found to be 8.6% and 11%, respectively. The reason for this is that k-ω predicts an absorber plate temperature that is higher than the experimental results, resulting in a large deviation in *Nu*.

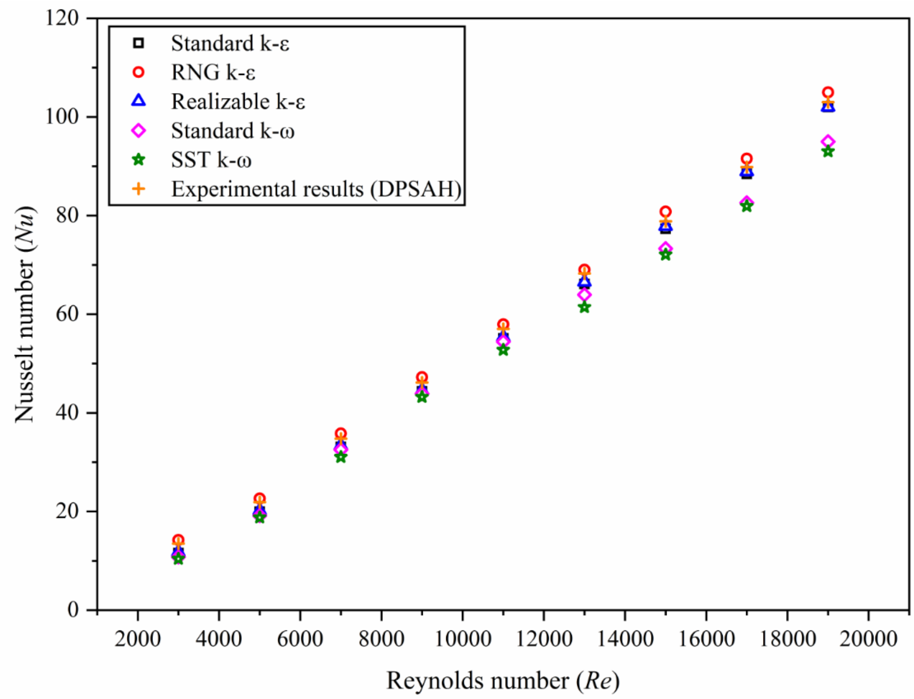

Fig. 5: Variation of *Nu* with *Re* of DPSAH with different turbulence models

Tab. 3: Average absorber temperature (T_{pm}) corresponding to the different turbulence models.

Turbulence model	Standard k-ε	RNG k-ε	Realizable k-ε	Standard k-ω	SST- k-ω	Experimental Results
T_{pm} (K) at Re=3000	397.88	393.57	395.98	398.51	398.70	390.52
T_{pm} (K) at Re=5000	377.09	374.18	376.88	379.01	379.00	370.75
T_{pm} (K) at Re=7000	360.28	358.35	360.12	361.28	362.34	354.95
T_{pm} (K) at Re=9000	350.70	349.16	350.64	351.03	351.83	345.88
T_{pm} (K) at Re=11000	343.90	342.65	343.82	344.73	345.22	339.35
T_{pm} (K) at Re=13000	338.65	337.60	338.54	339.62	340.53	334.15
T_{pm} (K) at Re=15000	334.57	333.56	334.43	335.85	336.24	330.34
T_{pm} (K) at Re=17000	331.24	330.48	331.11	332.70	332.81	327.11
T_{pm} (K) at Re=19000	328.54	327.97	328.47	329.01	330.39	324.55

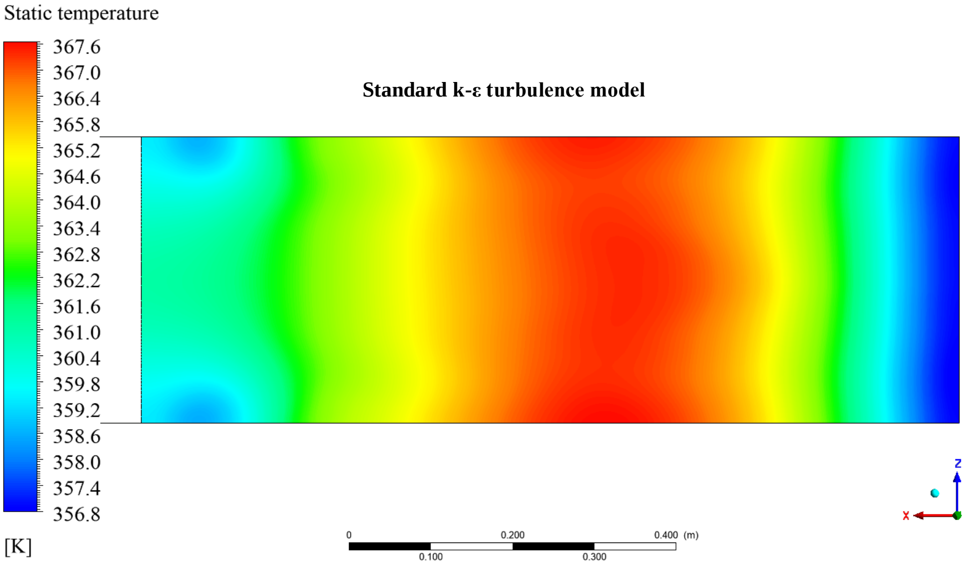

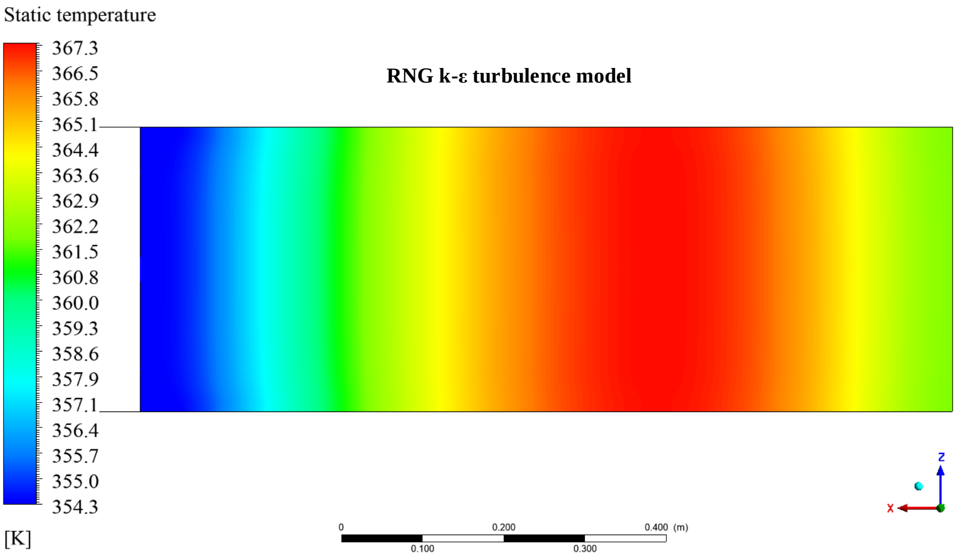

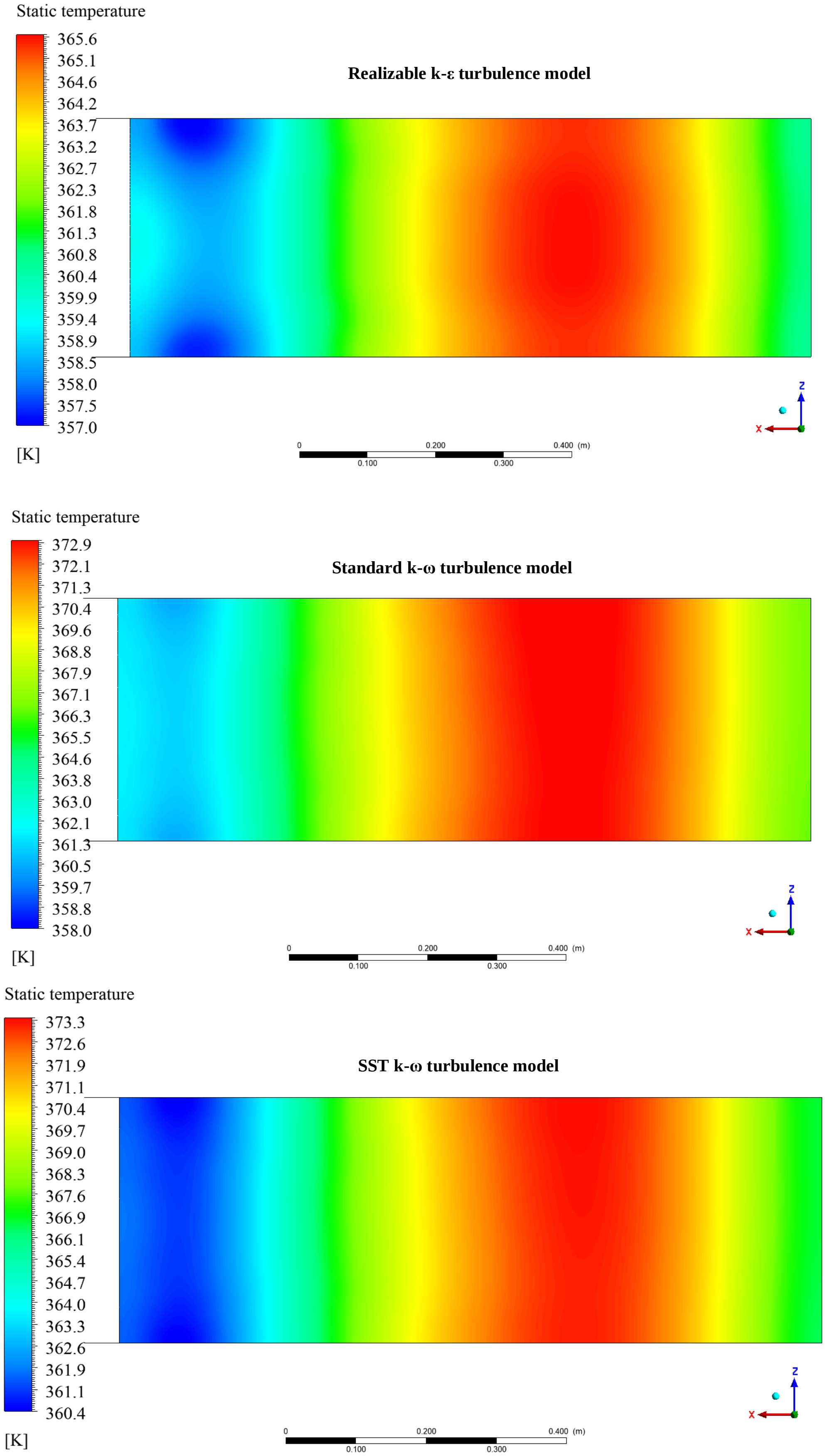

Fig. 6: Static temperature contours corresponding to the different turbulence model at *Re* of 7000

The variation in *f* with *Re* for different turbulence models and experimental results is presented in Fig. 7. For the considered range of *Re*, the RNG k-ε turbulence model with enhanced wall treatment is found in close agreement to experimental results with MAPE of 0.4%. Furthermore, the standard k-ω model, SST- k-ω model, standard k-ε model and realizable k-ε model are also validated with experimental results with MAPE of 0.8%, 2%, 2.1% and 3.9%, respectively. The results showed that the friction factor (*f*) accuracy is much better than the Nusselt number (*Nu*). The reason is that the values of *Nu* deal with various factors, such as uncertainties in the boundary conditions, heat transfer mechanisms, or inherent complexities within the system. In contrast, the friction factor (*f*) of a rectangular duct depends only on flow behaviour.

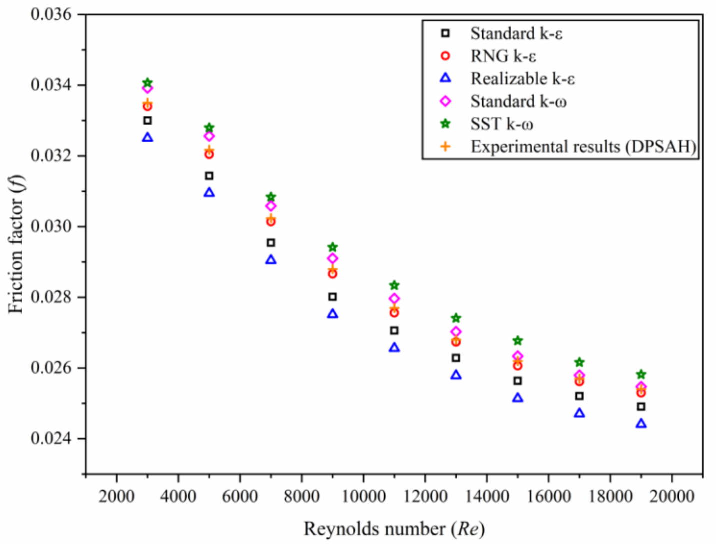

Fig. 7. Variation in *f* with *Re* of the DPSAH under different turbulence models

4.2. Thermohydraulic performance

The variation of friction factor increment (f/f_s), Nusselt number enhancement (Nu/Nu_s), and THPP with *Re* of a DPSAH is shown in Fig. 8. It is found that the values of *f/fs*, Nu/Nu_s, and THPP increase with increasing value of *Re*. Compared to SPSAH, the DPSAH increased Nu/Nu_s from 1.13 to 1.89 and f/f_s from 2.69 to 3.5 over the range of *Re*. The thermo-hydraulic performance parameter (THPP), as defined in eq. 12, is used to determine the optimum performance of DPSAH. The results showed that the THPP is less than 1 for values of *Re* below 6500, which is not advantageous. It is due to the high value of f/f_s in comparison to Nu/Nu_s. Further, with an increase in *Re* from 6500 to 19000, the THPP value also increases. This happens because heat contact surface area increases with increasing values of *Re*. As a result, the outlet temperature of the DPSAH is increased over that of the SPSAH, thereby increasing the effective heat gain and the THPP, as shown in Fig. 9. The maximum value of the THPP over the SPSAH was determined as 1.25, which corresponds to *Re* of 19000.

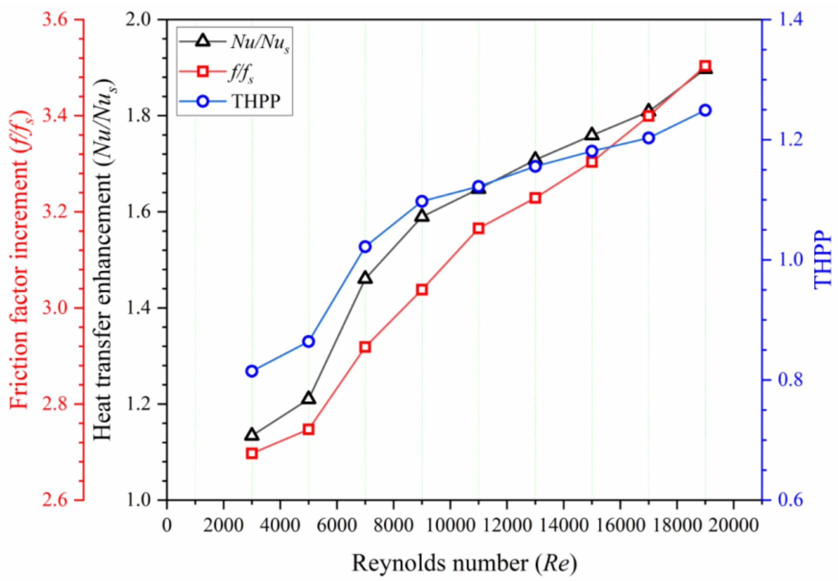

Fig. 8: Variation of Nu/Nu_s, f/f_s and THPP with *Re*

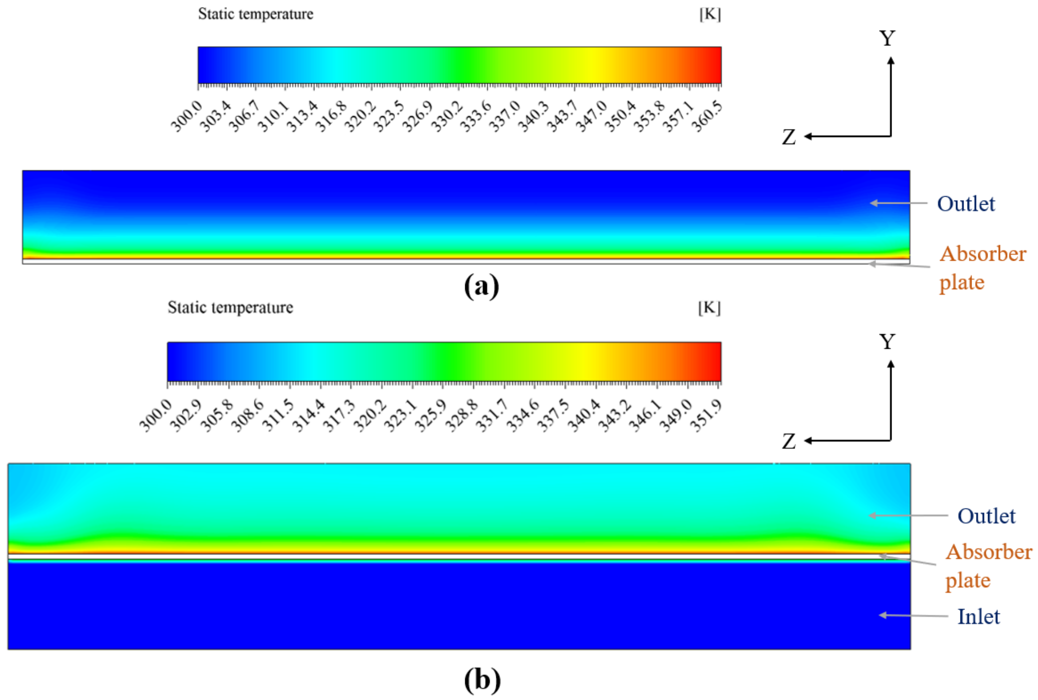

Fig. 9. Static temperature contours corresponding to Re of 7000 for (a) SPSAH and (b) DPSAH.

4.3. Performance comparison with previous research data

The present study analyzes the thermohydraulic performance of DPSAH over SPSAH. The maximum value of THPP is determined as 1.25 at *Re* of 19000. An attempt has been made to compare the THPP value with the previous studies, as presented in Tab. 4. The smooth DPSAH increases the THPP value by 10.4%, 15.2% and 1.6% over the discrete D-shaped ribs (Dutt et al. 2023), transverse wire ribs (Gupta, Solanki, and Saini 1997) and two truncated ribs (Sharma and Kalamkar 2017), respectively.

Tab. 4. Comparison of the results of this study with those of previous studies

References	Investigated geometry	$(Nu/Nu_s)_{max}$	$(f/f_s)_{max}$	THPP
Dutt et al. (2023)	Discrete D-shaped ribs	1.41	2.09	1.12
Gupta et al. (1997)	Transverse wire ribs	-	-	1.06
Sharma and Kalamkar (2017)	Two truncated ribs are placed with total truncation of 10% (10 mm) on one side	1.78	7.4	1.23
Present study	Smooth double pass solar air heater (DPSAH)	1.89	3.5	1.25

5. Conclusions

In this study, different turbulence models and thermohydraulic performance of a DPSAH are optimized for various values of *Re* from 3000 to 19000. Following is a summary of the major findings of the study:

- For the considered range of *Re*, the RNG k-ε turbulence model with enhanced wall treatment is found in close agreement to experimental results with MAPE of 2.6% for Nusselt number (*Nu*) and MAPE of 0.4% for friction factor (*f*).
- The standard k-ω model, SST- k-ω model, standard k-ε model and realizable k-ε model are also validated with experimental results of Nusselt number (*Nu*) with MAPE of 8.6%, 11%, 4.8% and 4.1%, respectively.
- Similarly, standard k-ω model, SST- k-ω model, standard k-ε model and realizable k-ε model are also validated with experimental results of friction factor (*f*) with MAPE of 0.8%, 2%, 2.1% and 3.9%, respectively.

- For the range of *Re*, the DPSAH enhanced the values of Nu/Nu_s from 1.13 to 1.89 and increased the values of f/f_s from 2.69 to 3.5 in comparison to SPSAH.
- The maximum thermohydraulic performance parameter (THPP) over the SPSAH was obtained as 1.25, which corresponds to *Re* of 19000.

6. Acknowledgement

The authors are grateful to the Ministry of Education (MoE), Government of India, for providing financial support in the form of fellowship for the research work. We also acknowledge the National Supercomputing Mission (NSM) for providing computing resources of 'PARAM Ganga' at IIT Roorkee, which is implemented by C-DAC and supported by the Ministry of Electronics and Information Technology (MeitY) and Department of Science and Technology (DST), Government of India.

7. References

Alam, T., Man H.K., 2017. Performance improvement of double-pass solar air heater – A state of art of review. Renew. Sust. Energ. Rev. 79, 779–793.

Bhatti M. S., Shah, M.S., 1987. Turbulent and transition flow convective heat transfer in ducts, in: Kakac, S., Shah, R.K., Aung, W. (Eds.), Handbook of single-phase convective heat transfer, Wiley., New York, pp. 32

Brown, G 2002. The history of the darcy-weisbach equation for pipe flow resistance. *Proceedings of the Environmental and Water Resources History*, United States, 3-7 November.

Dutt, N., Hedau, A.J., Kumar, A., Awasthi, M.K., 2023. Thermo-hydraulic performance of solar air heater having discrete D-shaped ribs as artificial roughness. Environ. Sci. Pollut. Res. 1, 1–22.

Gill, R. S., Singh, S., Singh, P.P., 2012. Low cost solar air heater. Energy Convers. Manag. 57, 131–142.

Gupta, D., Solanki, S.C., Saini, J. S., 1997. Thermohydraulic performance of solar air heaters with roughened absorber plates. Sol Energy. 61, 33–42.

Hernández, A.L., and Quiñonez, J.E., 2013. Analytical models of thermal performance of solar air heaters of double-parallel flow and double-pass counter flow. Renew. Energy. 55, 380–391.

Kabeel, A. E., Hamed, M.H., Omara, Z. M., Kandeal, A.W., 2017. Solar air heaters: Design configurations, improvement methods and applications – A detailed review. Renew. Sust. Energ. Rev. 70, 1189–1206.

Kareem, M. W., Habib, K., Sulaiman, S. A., 2013. Comparative study of single pass collector and double pass solar collector filled with porous media. J. Asian Sci. Res. 6, 445–455.

Kays W. M., Perkins, H. C., 1985. Forced convection, internal flow in ducts, in: Rohsenow, W.M., Hartnett, J.P., Ganic, E.N. (Eds.) Handbook of Heat Transfer Fundamentals, Second ed. Mac-Graw Hill, New York.

Kumar, A., Shinde, S.M., Gholap, A., Vyavahare, M.P., Gangarde, R., Mete, V.B., 2017. Performance of solar air heaters with corrugated absorber plate-A CFD approach. Int. J. Innov. Res. Adv. Stud. 4, 76–86.

Sharma, S.K., Kalamkar, V.R., 2017. Experimental and numerical investigation of forced convective heat transfer in solar air heater with thin ribs. Sol Energy. 147, 277–291.

ASHRAE Standard., 1986. Methods of testing to determine the thermal performance of solar collectors, in: Engen, B.W. (Eds.), American Society of Heating, Refrigerating and Air-Conditioning Engineers. Atlanta, pp. 1-42.

Webb, R. L., Eckert, R.G., 1972. Application of rough surfaces to heat exchanger design. Int. J. Heat Mass Transf. 15, 1647–1658.

Yadav, A.S., Bhagoria, J. L., 2013. Heat transfer and fluid flow analysis of solar air heater: A review of CFD approach. Renew. Sust. Energ. Rev. 23, 60–79.

IEA. 2021. Electricity Sector – Analysis - IEA. https://www.iea.org/reports/electricity-sector (May 15, 2023).

05. Grid Integration and Sector Coupling

Congestion Management in High Solar PV Penetrated Distribution System using Smart Charging of Electric Vehicles

Payal V. Dahiwale[1], Zakir H. Rather[1], and Indradip Mitra[2]

[1] Indian Institute of Technology Bombay, Mumbai (India)

[2] Deutsche Gesellschaft für Internationale Zusammenarbeit (GIZ) GmbH, New Delhi (India)

Abstract

Electric-powered vehicles are introduced as a sustainable transportation solution in an evolving road transportation sector. The uncontrolled charging of electric vehicles (EVs) results in negative impacts, such as system overloading, congestion, increased power losses, and voltage stability issues in the distribution system. On the other hand, high penetration of solar PV generation leads to network congestion, overloading, voltage instability, and power quality, in addition to its intermittent power generation. However, smart charging of EVs offers high controllability, so the negative impacts on the distribution system in the presence of high penetration of solar PV can be mitigated by controlled EV charging. In this work, the smart charging of electric vehicles is developed to mitigate the congestion issue in high solar PV penetrated distribution systems. The charging control of EVs in grid-to-vehicle (G2V) charging mode is considered with the objective of network power loss minimization to manage network congestion. The objective function is formulated as a mixed integer non-linear programming (MINLP) optimization problem. Modified IEEE 33 bus system is considered for simulation with different percentage penetration of solar PV and EVs. The result shows that the smart charging of EVs minimizes network power loss while managing network congestion.

Keywords: Congestion management, electric vehicle, network power loss, smart charging, solar PV

1. Introduction

The alarming concern of global warming is motivating sustainable development in fossil fuel-dominated sectors, i.e., the energy and transportation sectors. The developing energy sector promotes sustainable energy solutions like solar PV, wind energy, biofuels, etc., to reduce and decelerate the impact of global warming. Solar PV technology has evolved as a cost-effective renewable energy generation technology. Hence, the integration of solar PV is increasing in the electrical system. The high penetration of solar PV generation in the distribution system can lead to increased power loss, reverse power flow, voltage rise, network congestion, voltage imbalance, reactive power fluctuation, deteriorated power quality, and protection issues (Uzum et al., 2021). Further, network limit violations in the distribution system result in network congestion that prevents additional power flow through the lines (Lo and Ansari, 2012; Zhao et al., 2019). The issue of network congestion and increased network losses in the presence of high solar PV penetration is addressed in this work using controllable electric vehicle loads. However, the increased penetration of EVs through uncontrolled charging leads to technical impacts such as system overloading, congestion, increased power loss, voltage instability, etc. Apart from the above-mentioned disadvantages, electric vehicle charging through power electronics converters offers higher charging controllability. Smart charging of electric vehicles in high solar PV penetrated distribution systems is implemented in this work to address the issue of network congestion and power loss. In solar PV integrated distribution systems, smart charging of EVs can reduce the charging cost and leverage the positive impact in terms of reduced emissions from vehicle and power generation plants.

Centralized and hierarchical methods are prominently used for network congestion management in the presence of renewable generations. A rolling horizon-based look-ahead stochastic dynamic programming algorithm is implemented in (Caramanis and Foster, 2009) to reduce the charging cost of EV charging and the cost associated with regulatory services in the presence of network congestion. The objective function such as

10.18086/swc.2023.05.01 Available at http://proceedings.ises.org

charging cost minimization with line constraints, is formulated as convex optimization to manage the network congestion. The line loading constraint in the optimization problem ensures the power flow below the rated value and schedules the EV charging accordingly (Hu et al., 2014). EV fleet operators can better manage network congestion with a high capacity for charging and discharging power (Hu et al., 2015). A game theory-based congestion management considering charging and discharging prices is developed using the Greedy game approach (Haq et al., 2022). The objective of minimizing the change in the charging power is adopted to reduce network congestion. The robust optimization for minimizing consumer charging cost and peak-to-average is developed considering the flexible loads to mitigate the network congestion due to increased network loading (Khan et al., 2023). Reactive power support, battery energy management system, and curtailment of peak load are studied in (Shabbir et al., 2022) for congestion management in the distribution system. The objective functions of social welfare maximization and load-shedding minimization are used for congestion management in distribution networks (Reddy, 2017; Schermeyer et. al, 2018).

Solar PV integrated into the distribution system deteriorates the voltage profile and causes voltage rise exceeding the tolerance band of $\pm 5\%$. This voltage rise issue can be more adverse in the case of a weakly loaded distribution network, where the restricted power flow in the network due to the voltage limit violation leads to network congestion. Therefore, this paper addresses the issue arising from solar PV, i.e., network congestion, to reduce the impacts of solar PV integration in the distribution network. This work utilizes electric vehicles as the controllable load for managing network congestion.

The contributions of this paper are summarized as below:

1. The optimization framework using mixed integer non-linear programming (MINLP) for congestion management with network power loss reduction as an objective is developed using smart charging of EVs in distribution system with high solar PV penetration. This framework considers the bus voltage limit for minimizing network congestion. EV charging constraints such as maximum charger capacity limit and charging/discharging SoC limits are considered to maintain the charging requirements of EV users.
2. This work establishes the relation between the solar PV hosting capacity and the EV integration capacity of the distribution system. This study shows that in the presence of smart charging of EVs, the solar PV hosting capacity of the distribution system will increase. Whereas, with increased solar PV penetration, more EVs can be integrated into the distribution system.

The paper is structured as Section II discusses the proposed problem formulation for congestion management in distribution networks, and the result & discussion in Section III, followed by the conclusion.

2. Problem Formulation

This paper focuses on network congestion issues arising due to the integration of solar PVs in the distribution system. To mitigate this, a network loss minimization problem with bus voltage limits is formulated. The proposed congestion management and network power loss reduction problem in a distribution system is formulated as a MINLP problem. The objective function of network loss minimization is defined as the summation of the network power loss in the distribution system. The mathematical formulation of the objective function for power loss minimization is defined as a function of line resistance and branch current as given in (eq. 1). Here, t is the time slot, and T denotes the total number of time slots in a day considering 15-minute interval. The constraints in the distribution system are bus voltage limits, which are considered for congestion management. In this formulation, EV charging power is considered as a decision variable in the congestion management framework. The necessary information of arrival and departure time of the EV, maximum charging power, departure SoC level, and charging/discharging limits are considered as constraints for optimization problem. The proposed optimization framework for congestion management is developed for a day-ahead scenario.

$$min \sum_{t=1}^{T} \sum_{(i,j)\in M} R_{ij} \times I_{ij,t}^{2} \qquad \text{(eq. 1)}$$

The branch power flow model in the distribution system is shown in Fig. 1. Here, $(i,j) \in M$, which represents the line between bus i and j, where M represents a set of lines in the distribution system. The line resistance is R_{ij}, and $I_{ij,t}$ is the current flowing through bus i and j at time slot t. The active and reactive power balance equations are mentioned in (eq. 2) and (eq. 3). It establishes the relation between incoming power at the bus ($P_{ij,t}$ and $Q_{ij,t}$), load power ($P_{L,t}$ and $Q_{L,t}$), losses in the line, and the outgoing power from the bus at each time slot t. $P_{ij,t}$ and $Q_{ij,t}$ are active and reactive power flow; $P_{L,t}$ and $Q_{L,t}$ denoted active and reactive load power. The nodal voltage $(v_{j,t})$ and branch current $(I_{ij,t})$ at time slot t are given in equation (eq. 4) and (eq. 5). The voltage constraint with $\pm$ 5% tolerance is considered as an inequality constraint, mentioned in (eq. 6).

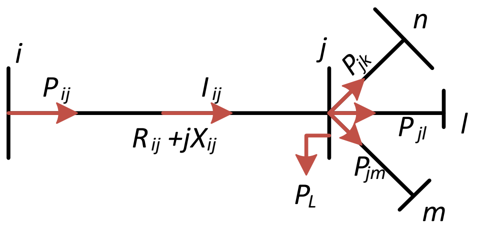

Fig. 1: Branch power flow model in a distribution system

$$P_{L,t} = P_{ij,t} - R_{ij} \times I_{ij,t}^2 - \sum_{k\in C:\{n,l,m\}} P_{jk,t} \quad \text{(eq. 2)}$$

$$Q_{L,t} = Q_{ij,t} - X_{ij} \times I_{ij,t}^2 - \sum_{k\in C:\{n,l,m\}} Q_{jk,t} \quad \text{(eq. 3)}$$

$$v_{j,t} = v_{i,t} - 2\left(R_{ij}P_{ij,t} + X_{ij}Q_{ij,t}\right) + \left(R_{ij}^2 - X_{ij}^2\right) \times I_{ij,t}^2 \quad \text{(eq. 4)}$$

$$I_{ij,t} = \frac{P_{ij,t}^2 + Q_{ij,t}^2}{v_{j,t}} \quad \text{(eq. 5)}$$

$$0.95 \leq v_{j,t} \leq 1.05 \quad \text{(eq. 6)}$$

The constraints for maintaining EV charging requirements are modeled as equality to ensure the desired SoC at the time of departure. It is given in (eq. 7), where the SoC update formula is mentioned in (eq. 8) as a function of arrival SOC, battery rating, charging power, and charging time.

$$SoC_{nm}^{T_d} = SoC_{nm}^{F} \quad \text{(eq. 7)}$$

$$SoC^t = SoC^{t-1} + \frac{P_{nm}^t \, \Delta t}{B^c} \quad \text{(eq. 8)}$$

$$P_{min} \leq P_{nm}^t \leq P_{max} \quad \text{(eq. 9)}$$

SoC_{nm}^F is the final SoC of n^{th} vehicle at bus m where $SoC_{nm}^{T_d}$ is desired SoC departure of EV. t denotes the time slot, B^c is battery capacity and P_{nm}^t is the charging power at t instant for n^{th} EV. P_{max} and P_{min} are the maximum and minimum limits of charging power. The charging power constraint is given in (eq. 9).

3. Results and Discussion

In the presence of solar PV scenarios and lightly loaded distribution network conditions, overvoltage at the distribution system can lead to network congestion. Therefore, to address the overvoltage-driven network congestion/PV generation curtailment, electric vehicles are utilized under a controllable charging scenario, where the power withdrawal by the EVs is controlled such that the voltages can be kept within the tolerance limit of ±5%. Hence, as discussed in Section II, the MINLP optimization method is proposed to analyze the use of controlled EV charging to address PV penetration impact on the distribution system. The modified IEEE 33 bus distribution system with solar PV penetration (shown in Fig. 2) is considered in this work for implementation of the proposed MINLP optimization framework for congestion management.

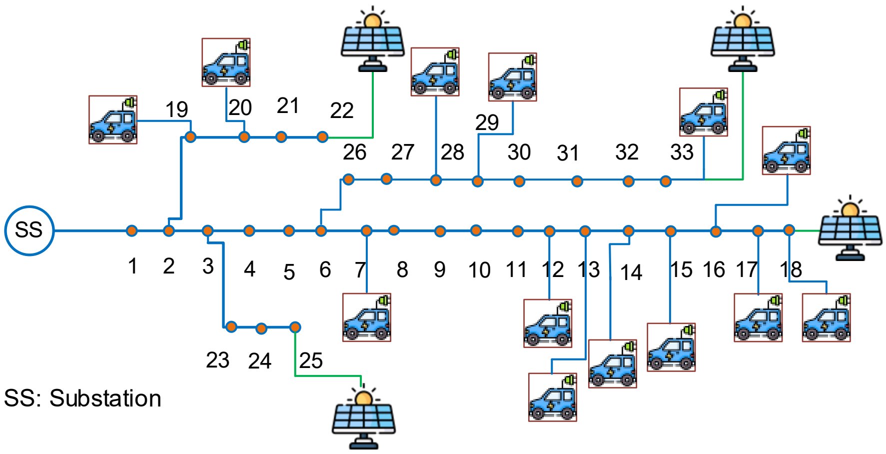

Fig. 2: Modified IEEE 33 distribution network with EV and solar PV integration

The test network considers 130 EVs with 40 kWh battery capacity and a 6.6 kW charger rating (Dahiwale and Rather, 2023). The arrival and departure times of EVs follow the normal probability distribution (Cao Chong et al., 2016). To understand the congestion in the distribution network, the load profile for IEEE 33 bus system is taken from (Dolatabadi et al., 2021) with a peak load of 3.9 MW. As shown in Fig. 2, the solar PV generators are placed at bus 18, bus 22, bus 25, and bus 33 (Dolatabadi et al., 2021). To realize overvoltage scenario due to solar PV integration in a lightly loaded condition, the system is simulated with 50% of peak load condition, and this scenario is considered as a base case. Various PV penetration levels of 100%, 150%, and 200% are considered in this study to simulate the network congestion in the distribution system. Under high solar PV penetration levels and lightly loaded distribution system, congestion is observed in the system due to voltage limit violation as shown in Fig. 3. The acceptable voltage range considered in this study are 0.95 pu and 1.05 pu. From Fig. 3, it can be observed that the voltage values are not maintained within the limit under different PV penetration levels of 100% (i.e., 4 MW) and above.

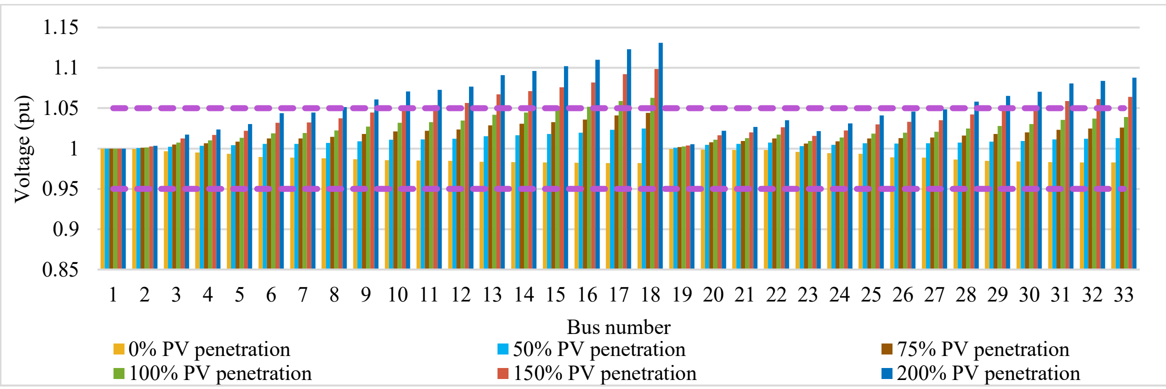

Fig. 3: Voltage profile of IEEE 33 bus distribution system with different solar PV penetration

Fig. 4 shows the power loss profile of the network under different PV penetration levels, and it can be observed that the network losses increased with increasing PV penetration. The system losses are increased because of the surplus PV generation in the system. It is noticeable from the results that the system losses follow the solar PV generation profile.

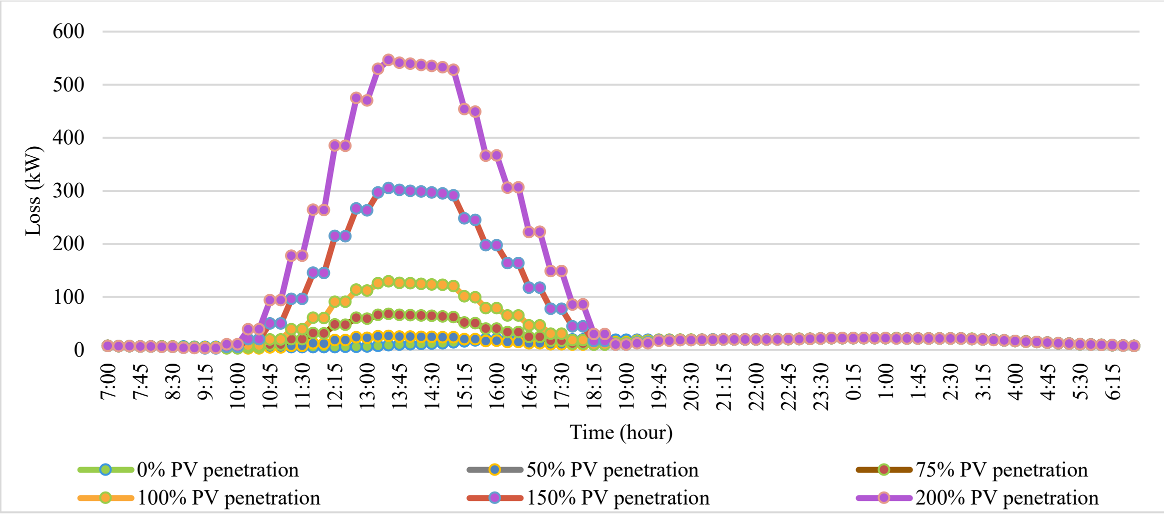

Fig. 4: System loss profile of IEEE 33 bus distribution system with different solar PV penetration

The relationship between grid power, solar PV generation, and system losses is shown in Fig. 5. The grid power is inversely proportional to solar PV generation. In contrast, the system losses are exponentially proportional to the PV generation. Fig. 5 shows that at 200% PV penetration, the grid power and losses have high values compared to the 150% PV penetration scenario followed by 100% PV penetration. The negative value of grid power indicates the reverse power flow from the distribution system to the grid due to surplus solar PV power.

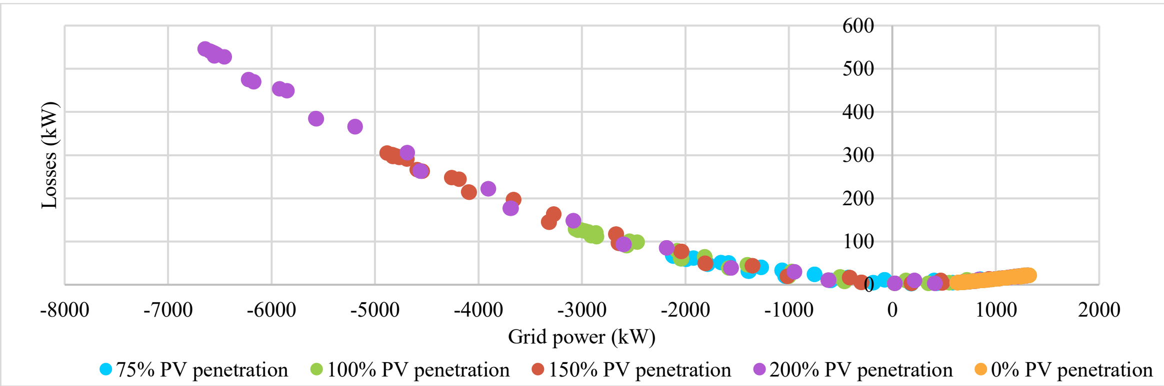

Fig. 5: Relation between Grid power and system losses at different solar PV penetration levels

Electric vehicles as controllable loads are adopted in this study to mitigate the voltage rise issue in the presence of solar PV penetration. In this work, EV charging methods such as dumb charging and controlled charging of EVs are considered for congestion management in the distribution system. The results of dumb charging and controlled charging of EVs are presented in Fig. 6. It is observed that the dumb charging of EVs cannot mitigate the voltage rise issue. Therefore, a controlled EV charging is adopted in this study by considering charging power as a decision variable, as mentioned in the optimization problem in Section II. Fig. 6 shows that the voltage in the presence of dumb charging is slightly reduced compared to the base case scenario with 150% PV penetration. Dumb charging cannot maintain the network voltages within the limits. In contrast, the proposed optimization-based controlled charging maintains the voltage within the bound of ±5%, as depicted in Fig. 6.

The losses in the different charging cases are given in Fig. 7, which indicates the significant reduction in the network losses with the proposed EV charging strategy. Fig. 7 shows that in the case of PV penetration in the system without EVs, the network losses are highest, whereas, in the case of dumb charging, the network losses reduce significantly for a charging duration only and do not guarantee the reduced losses through the day. The proposed optimized charging reduces the overall network losses in a day, as shown in Fig. 7

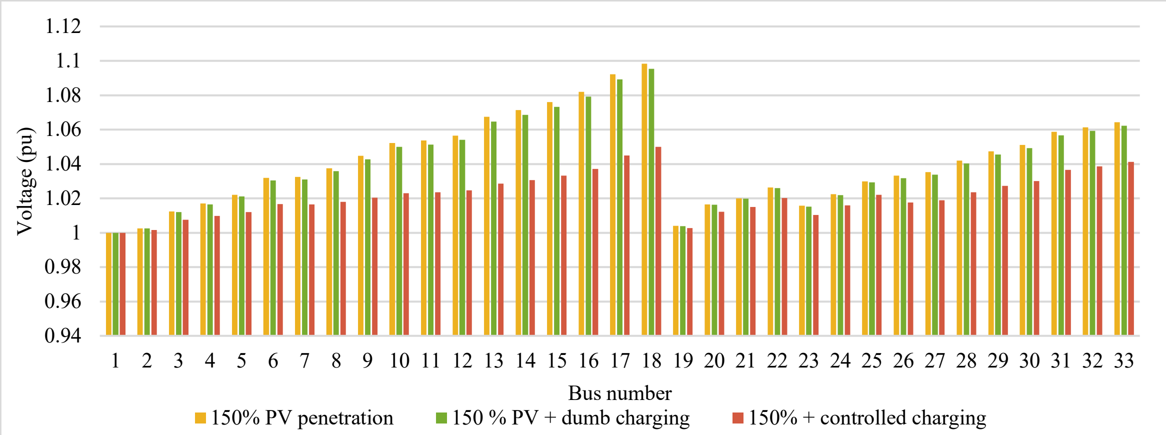

Fig. 6: Voltage profile of IEEE 33 bus distribution system with 150% PV penetration with dumb and proposed controlled charging

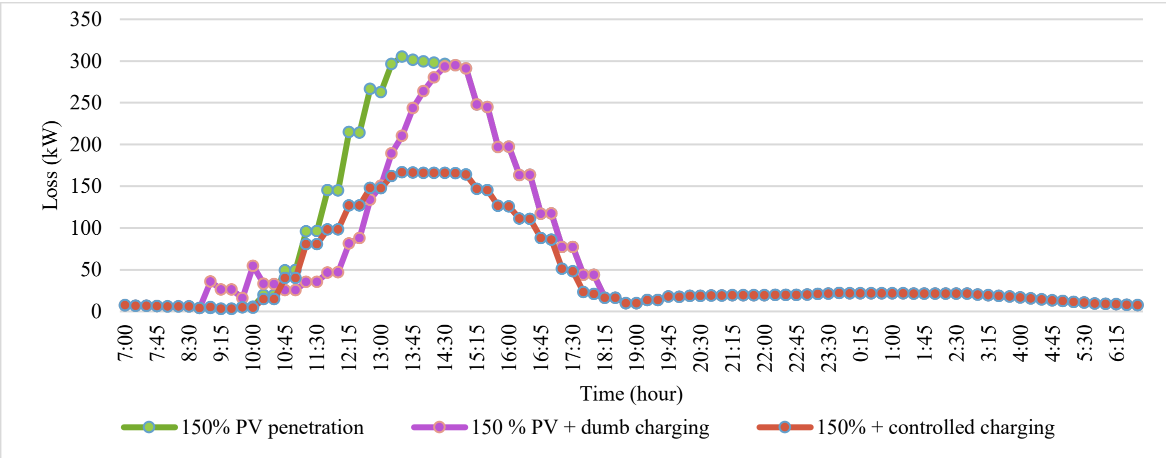

Fig. 7: System loss profile of IEEE 33 bus distribution system with 150% PV penetration with dumb and proposed controlled charging

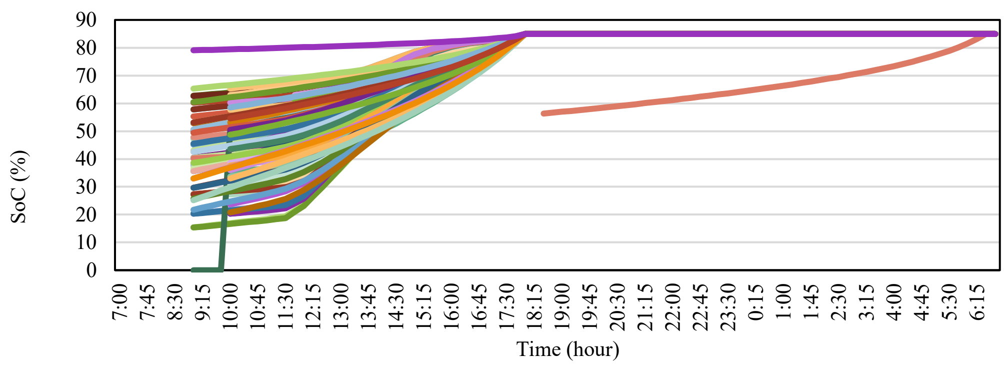

Fig. 8: SoC profile of EVs integrated in the distribution system under proposed controlled charging and 150% solar PV penetration

The SoC profiles of the EVs in the case of 150% PV penetration with controlled EV charging are given in Fig. 8. It shows that each EV has different charging curves, and with distinct charging profile's slope, each EV has a different charging trajectory to reach the desired SoC. The voltage and loss profiles for different PV penetration levels are given in Fig. 9 to Fig. 12. Fig. 9 and Fig. 11 show that at 100% and 150% PV penetration levels, the system voltage is maintained within the voltage limits under the proposed EV charging optimization.

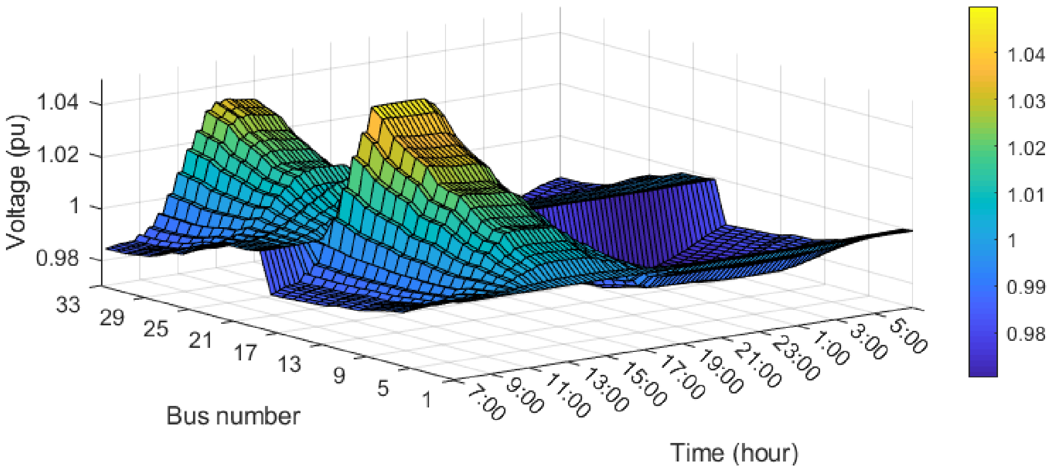

Fig. 9: Voltage profile of IEEE 33 bus distribution system under proposed controlled charging and 100% solar PV penetration

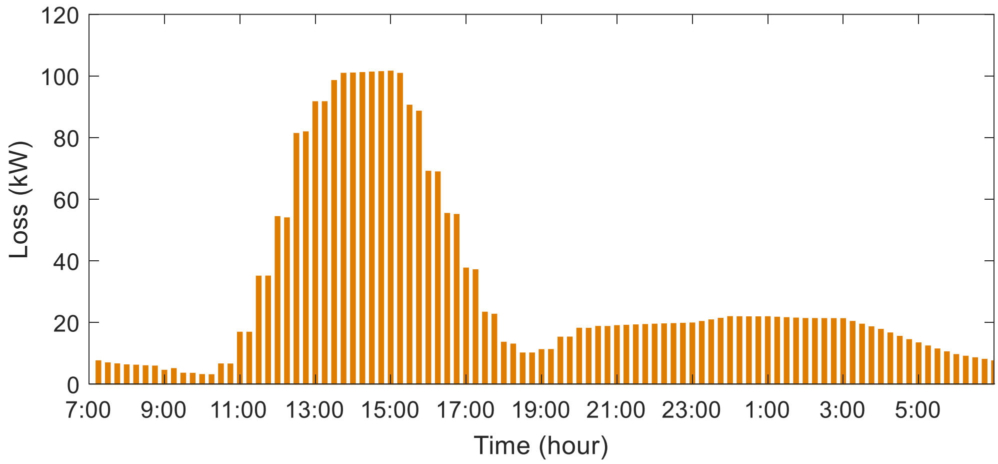

Fig. 10: Loss profile of IEEE 33 bus distribution system under proposed controlled charging and 100% solar PV penetration

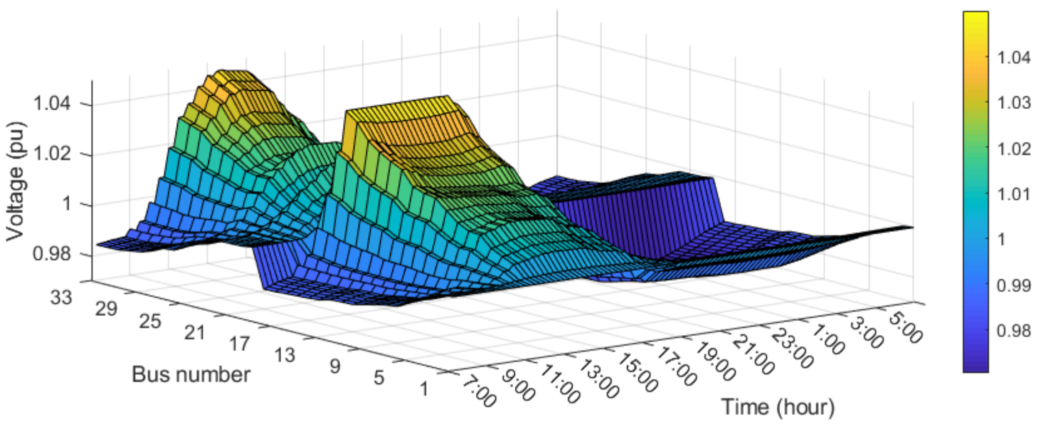

Fig. 11: Voltage profile of IEEE 33 bus distribution system under proposed controlled charging and 150% solar PV penetration

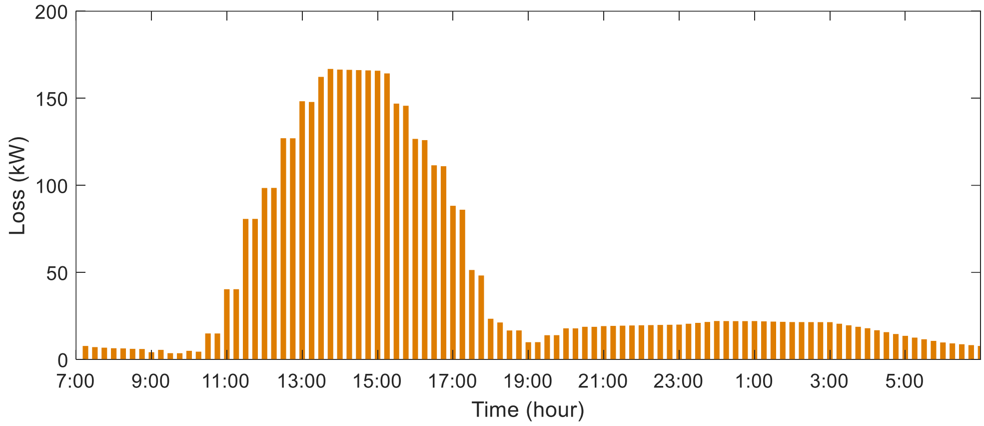

Fig. 12: Loss profile of IEEE 33 bus distribution system under proposed controlled charging and 150% solar PV penetration

Fig. 13 shows the comparative energy loss of the 33 bus system under different PV penetration levels. Energy loss (in MWh) in a day for 100%, 150%, and 200% PV penetration is provided in Fig. 13. The comparative energy losses without EVs, EVs with dumb charging, and EVs with control charging are shown in Fig. 13. It is inferred from the results that the energy losses are highest in the case of PV penetration without EVs. The energy losses are reduced with EV integration through dumb charging but cannot reach the optimal value. The controlled EV charging with the proposed optimization reduces the network losses and achieves the lowest energy losses compared to other cases.

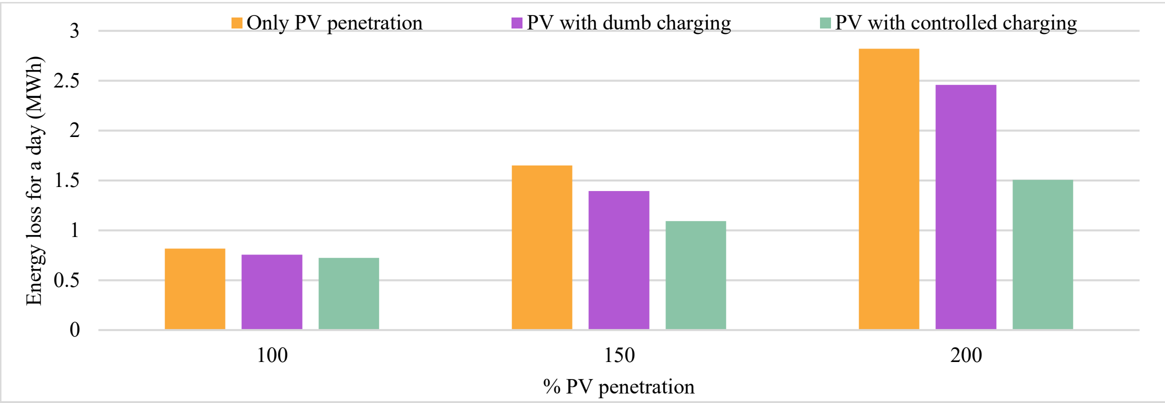

Fig. 13: Comparative energy loss of the test network under different solar PV loading and charging scenarios

The results show that controllable EVs can be used to incorporate PV penetration in the system without causing network congestion. Whereas, with increasing PV penetration, the percentage of controllable EVs should also need to be increased. The increased PV percentage in the network requires additional EV loads to cater the surplus PV generation. In this study, the 0.7MW of EV load, i.e., 17.5% EV load, can offer a PV hosting capacity of 100%, whereas the same EV percentage cannot host 200 % PV penetration in the system. To manage the higher percentage of feasible PV penetration, a higher percentage of EV loads are required. The increased EV penetration, i.e., 2.8MW EV load, offers a PV hosting capacity of 150%. Similarly, to host a 200% PV in the system, an aggregated EV load of 5.6MW is required. It depicts that the increase in the percentage of EVs as a controllable load increases the solar PV hosting capacity of the network.

4. Conclusion

The solar PV integration with a lightly loaded distribution system can cause network voltage rise, line overloading, and increased losses. The PV penetration in the distribution system causes network congestion due to network constraint violations such as line thermal constraint and voltage constraint. In this study, network losses and voltage are considered to reduce network congestion in the presence of solar PV penetration. To address it, a mixed integer non-linear programming (MINLP) optimization is formulated for network loss minimization. The proposed formulation considers network constraints such as active and reactive power balance, voltage constraints, and EV-related constraints such as SoC constraints and charging power constraints. The proposed method is implemented on a modified IEEE 33 bus network. Results show that EV integration through dumb charging in the distribution system reduces network losses but cannot provide an optimal solution to network congestion. The proposed optimization-based EV charging approach provides an optimal solution for network loss reduction and also maintains the voltage profile within limits. Thus, the proposed formulation manages the network congestion. It also indicates that the EVs are effectively utilized as controllable loads while achieving the desired SoC level at the end of the charging session. The analysis shows that the percentage of controlled EV charging load in the system and solar PV hosting capacity holds a direct relationship.

5. Acknowledgments

This work was supported by the India-EU collaborative project SUSTENANCE funded by the Department of Science and Technology (DST) on the Indian side and the European Commission on the EU side.

6. References

Cao Chong, Luting Wang, and Bo Chen, 2016. Mitigation of the Impact of High Plug-in Electric Vehicle Penetration on Residential Distribution Grid Using Smart Charging Strategies. *Energies* 9(12): 1024.

Caramanis, Michael, and Justin M. Foster, 2009. Management of Electric Vehicle Charging to Mitigate Renewable Generation Intermittency and Distribution Network Congestion. in *Proceedings of the 48h IEEE Conference on Decision and Control (CDC) Held Jointly with 2009 28th Chinese Control Conference*, 4717–22.

Dahiwale, Payal Vyankat, and Zakir H. Rather, 2023. Centralized Multi-Objective Framework for Smart EV Charging in Distribution System. In *2023 IEEE PES Conference on Innovative Smart Grid Technologies - Middle East (ISGT Middle East)*, 1–5.

Dolatabadi, Sarineh Hacopian, Maedeh Ghorbanian, Pierluigi Siano, and Nikos D. Hatziargyriou, 2021. An Enhanced IEEE 33 Bus Benchmark Test System for Distribution System Studies. *IEEE Transactions on Power Systems* 36(3): 2565–72.

Haq, Faheem Ul, Pratyasa Bhui, and Kotakonda Chakravarthi, 2022. Real Time Congestion Management Using Plug in Electric Vehicles (PEV's): A Game Theoretic Approach. *IEEE Access* 10: 42029–43.

Hu, Junjie et al., 2015. A Multi-Agent System for Distribution Grid Congestion Management with Electric Vehicles'. *Engineering Applications of Artificial Intelligence* 38: 45–58.

Hu, Junjie, Shi You, Morten Lind, and Jacob Østergaard, 2014. Coordinated Charging of Electric Vehicles for Congestion Prevention in the Distribution Grid. *IEEE Transactions on Smart Grid* 5(2): 703–11.

Khan, Omniyah Gul M, Amr Youssef, Magdy Salama, and Ehab El-Saadany, 2023. Robust Multi-Objective Congestion Management in Distribution Network. *IEEE Transactions on Power Systems* 38(4): 3568–79.

Lo, Chun-Hao, and Nirwan Ansari, 2012. Alleviating Solar Energy Congestion in the Distribution Grid via Smart Metering Communications. *IEEE Transactions on Parallel and Distributed Systems* 23(9): 1607–20.

Reddy, S. Surender, 2017. Multi-Objective Based Congestion Management Using Generation Rescheduling and Load Shedding. *IEEE Transactions on Power Systems* 32(2): 852–63.

Schermeyer, Hans, Claudio Vergara, and Wolf Fichtner, 2018. Renewable Energy Curtailment: A Case Study on Today's and Tomorrow's Congestion Management. *Energy Policy* 112: 427–36.

Shabbir, Noman et al., 2022. Congestion Control Strategies for Increased Renewable Penetration of Photovoltaic in LV Distribution Networks. *Energy Reports* 8: 217–23.

Uzum, Busra, Ahmet Onen, Hany M. Hasanien, and S. M. Muyeen, 2021. Rooftop Solar PV Penetration Impacts on Distribution Network and Further Growth Factors—A Comprehensive Review. *Electronics* 10(1): 55.

Zhao, Jinli et al., 2019. Congestion Management Method of Low-Voltage Active Distribution Networks Based on Distribution Locational Marginal Price. *IEEE Access* 7: 32240–55.

A set of study cases for the massive integration of solar renewables in non-interconnected areas

Mathieu David[1], Mirhado Nahary Andriamandroso[1], Peter Behrensdorff Poulsen[2], Jean Castaing-Lasvignottes[1], Nicolaos Cutululis[3], Kaushik Das[3], Chloé Durif-Aboukali[1], Johann Francou[1], Philippe Lauret[1], Josselin Le Gal La Salle[1], Elke Lorenz[4], Olivier Marc[1], David Melgar[4] and Sergiu Spataru[2]

[1] PIMENT, University of La Reunion, Saint-Denis (Reunion)

[2] Department of Electrical and Photonics Engineering, Technical University of Denmark, Roskilde (Denmark)

[3] Department of Wind and Energy Systems, Technical University of Denmark, Roskilde (Denmark)

[4] Fraunhofer Institute for Solar Energy Systems ISE, Freiburg (Germany)

Abstract

The massive integration of solar renewable energies is challenging in non-interconnected areas such as remote islands or isolated regions. Indeed, their power grid, which cannot rely on the support of larger electricity networks, is more vulnerable to the inherent variability of the solar resource and grid failures, such as sudden breakdown of production units or transmission lines. The TwInSolar project, funded by the European Commission, aims to provide support and solutions to overcome the problems faced by island territories not connected to continental electricity grids. As a part of this project, four study cases are presented to the scientific community, each highlighting specific issues observed at different scales on the island of La Reunion. This article aims to provide a detailed description of the four selected systems, the corresponding challenges, and the data available.

Keywords: Solar energy, non-interconnected area, standalone microgrid, grid-connected microgrid, utility scale PV, insular power grid

1. Introduction

Non-interconnected areas encompass all the power grids that are non-connected to the continental grids, like remote rural communities, entire regions of developing countries or islands. The island of La Reunion, situated in the south-west part of the Indian Ocean, is a good example of a non-interconnected area. Decarbonization and energy self-sufficiency of the non-interconnected energy systems require the use of locally available renewable resources (Erdinc et al., 2015). In many cases, such as island territories in the tropical zone, the sun is the most abundant resource. Moreover, solar systems, like photovoltaic (PV) or domestic solar hot water (DSHW) are mature technologies that produce the cheapest energy in the world (IRENA, 2022). The massive integration of solar energy is, therefore one of the possible ways to achieve the objectives of decarbonization and energy autonomy of these regions.

However, the electricity networks of remote areas are more sensitive than continental grids, and new challenges arise from the massive integration of solar energy. Indeed, due to their small size (thereby impacting power system strength typically represented by system inertia and short circuit power) and limited capacity of power reserves, non-interconnected grids are more vulnerable to unexpected events such as generation ramps, forecast uncertainties commonly observed with variable renewables (i.e., solar and wind) or system failures (e.g., power plant breakdown). Moreover, these isolated grids cannot rely on a larger interconnected grid to balance their lack or excess of generation. On the other hand, solar renewables like PV systems are connected to the grid

10.18086/swc.2023.05.02 Available at http://proceedings.ises.org

through power electronics that must comply with the appropriate standards. For instance, in La Reunion, PV inverters must comply with the DIN VDE 0126-1-1 (VDE, 2013), which defines frequency and voltage bands for normal operation. Out of these ranges, the inverter must automatically shut down the power generation. For an isolated electricity network, it is more challenging to maintain the frequency and the voltage within these ranges in case of severe failure. In such conditions, PV systems could likely stop their production and increase the risk of a grid blackout. Consequently, the massive integration of solar energy in these specific grids presents new challenges that are likely to be faced by continental grids in the future.

The goal of this paper is to highlight the challenges currently experienced by non-interconnected areas, which already have a high share of solar production, through the description of four study cases selected within the framework of the European project TwInSolar ("Twinsolar," 2023). The study cases, located in La Reunion and illustrated in Fig. 1, are representatives of issues observed at different scales. In addition, data related to each study-case are made available to the scientific community.

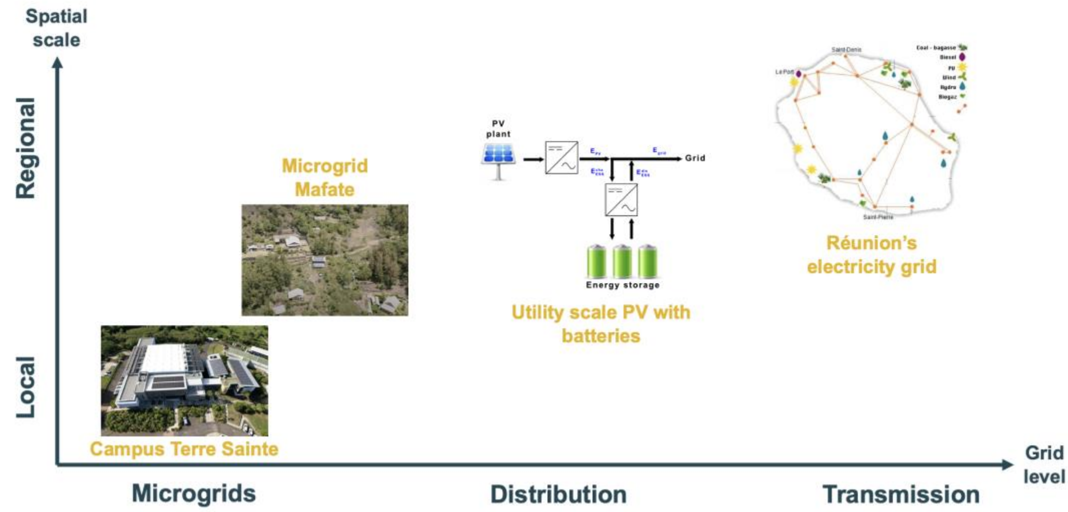

Fig. 1: Positioning of the four study cases selected to highlight the challenges that face non-interconnected island of La Reunion with the massive integration of solar energy.

2. A standalone microgrid

The first case study is a standalone microgrid located in the isolated Mafate cirque, in the heart of a UNESCO World Heritage national park. This micro-region of Reunion has neither roads nor power lines. The small villages in that area are only accessible on foot or by helicopter and must produce their energy locally. Since the 2000s, buildings in Mafate have been mainly powered by standalone PV systems with lead-acid batteries. The first installed photovoltaic systems have recently reached the end of their life. In this context, local authorities have decided to develop isolated microgrids to reduce their replacement costs, facilitate maintenance, and develop a new economic model. These new microgrids connect several houses to a single PV plant equipped with batteries.

Fig. 2: Aerial view (Francou 2022) and repartition of electric load of the remote microgrid located in the Mafate cirque, La Reunion

The proposed study case, illustrated in Fig. 1, has three rural accommodations, a single PV plant of 7kWp, and lead-acid batteries with a capacity of 140kWh (Calogine et al., 2019; Francou et al., 2019). The houses have no heating or cooling. The residents use wood-fire and gas cylinders for cooking and thermal solar panels provide domestic hot water. Thus, the electrical microgrid powers fridges, freezers, multimedia devices (TV, mobile phone, computers), lighting and DIY tools. As presented in Table 1, the fridges and freezers are the main loads of the microgrid. The washing machines also account for a significant share of the load with approximately half of their consumption occurring outside the sunshine hours.

Table 1: Main operation indicators of the remote microgrid of Mafate derived from 1-min records between May 2020 and May 2021

Operation indicators	Average	Min	Max
Power demand (kW)	0.29	0.001	3.28
Daily load (kWh)	5.73	2.57	10.24
Daily plan of array irradiance (kWh/m^2)	5.26	1.29	7.54
Estimated daily PV production (kWh)	29.44	7.25	42.25
Actual daily PV production (kWh)	12.25	7.94	19.96
System daily efficiency (%)	46.7	21.0	83.5
Estimated storage state of charge – SOC (%)	98.1	92.3	100

The system design, based on current practices in design offices, minimizes the risks of electricity shortages and does not consider the possibility of involving users in the operation of the microgrid. Consequently, the battery and power converters are strongly oversized, and the resulting Levelized Cost of Energy (LCOE) is exceptionally high. As shown in Table 1, from May 2020 to May 2021 and considering the average daily energy demand, the capacity of the storage correspond to more than 20 days of electricity supply without sun. One can also observed that the estimated state of charge (SOC) of the storage never fall below 92%. The strong overestimation of the sizes of the components (i.e. ESS and power converters) results in a very low energy storage and distribution efficiency ranging between 21.0% and 83.5% on a daily scale.

The main challenge is to achieve a cost-effective design and to engage the users in the management of the microgrid. Indeed, optimal sizing of the PV plant and the ESS (Energy Storage Systems) leads to a more reasonable investment cost (Francou et al., 2022). Moreover, efficient demand-side management could be achieved with a better involvement of the users. For this study case, a human interface fed by an Energy Management System (EMS) has been tested to improve the simultaneity between the PV generation and the load (Abbezzot et al., 2022).

The microgrid has been fully instrumented and monitored with a sample time step of 1 minute from 2019 to 2022, the duration of the project “Microréseau Mafate” granted by the European Regional Development Funds and the Région Réunion (Francou et al., 2019). First, a weather station installed on the PV plant shelter recorded the main weather parameters (i.e., global horizontal and plan of array solar irradiance, temperature, humidity, wind, and rain). Second, a data acquisition system associated with the PV plant measured the PV production, the total power demand, and the battery state (current, voltage, and state of charge). Finally, five energy meters per house monitored the main types of loads (fridge, washing machine, lights, etc.). One year of anonymized data, from May 2020 to May 2021, are freely accessible on zenodo (Calogine et al., 2023).

3. A grid-connected microgrid

The second system is the university Campus of Terre Sainte, which can be considered a grid-connected microgrid. The campus is located in Saint-Pierre, on the southern coastal part of the island. The climate is hot and humid during the wet season (Nov. to Apr.) and cooler with trade winds during the dry season (Apr. to Nov.). The annual solar potential of the site reaches 2000 kWh.m^{-2} on a horizontal surface, making it an ideal location for using solar renewables. The campus hosts approximately 12,500 m^2 of floor area for the university building, a student residence with 244 rooms, and a restaurant. Fig. 3 gives an overview of the campus and installed PV capacity. The Faculty of medicine, which was commissioned in September 2023, is not currently included in the scope of the microgrid for the moment because we do not have any data.

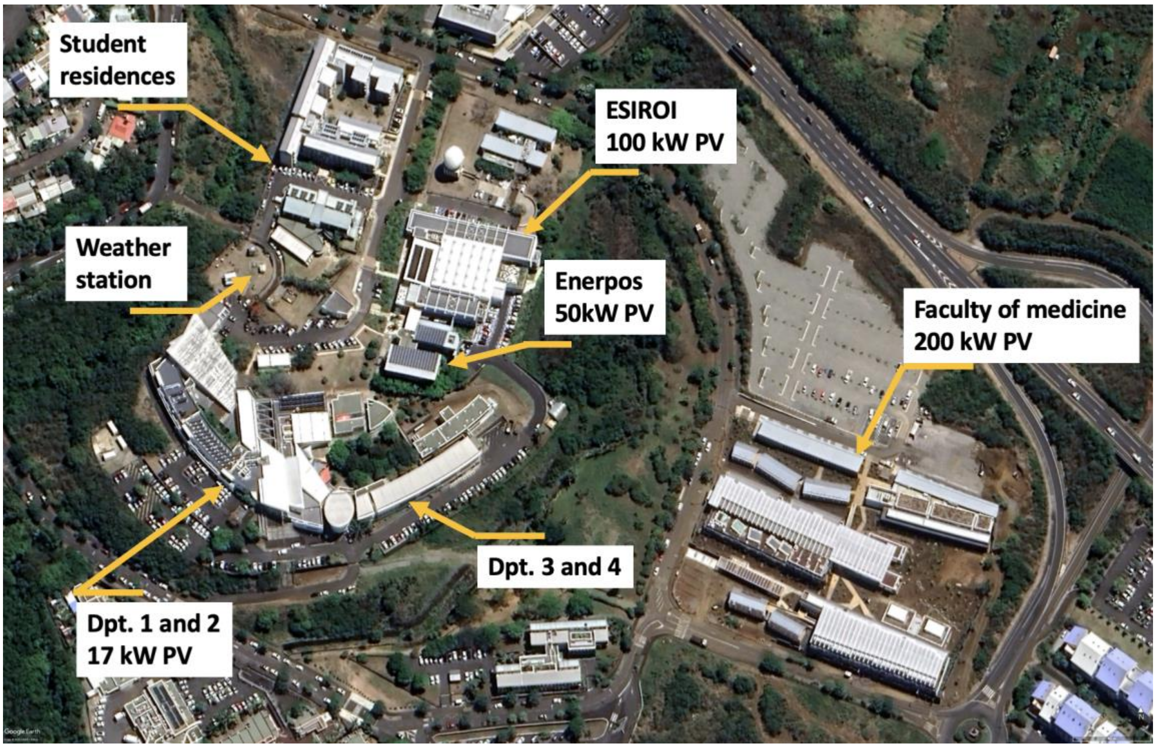

Fig. 3: Overview of the university campus of Terre Sainte, La Reunion

Table 2 below gives more details on the existing buildings. The student residences are already equipped with solar hot water (DWH) that supplies more than 80% of the energy needed for showers and cooking. The university buildings currently host 165,8 kWp of PV on their roofs (the additional 200 kWp of the faculty of medicine will come soon) and the microgrid has an electrical self-sufficiency of nearly 16%. The last generation of university buildings built on the campus (Enerpos and ESIROI) are NetZero Energy Buildings (Lenoir and Garde, 2012). Their annual electricity demand is balanced by the Building Integrated PV installed on their roofs. For instance, the ENERPOS building produces approximately five times its electricity consumption on a yearly basis. With approximately 50% of the area being air-conditioned, cooling is the main load of the microgrid. With the building plans and the online software Helioscope, we estimated the additional PV capacity that could be installed on the available roofs (last column of Table 2). Considering existing systems and the potential for new systems, we could install more than 1 MWp of photovoltaics on the campus and produce more than 1.5 times the annual electricity consumption.

Table 2: Key figures of the university campus of Terre Sainte, La Reunion

Building name	Commissioning Year	Floor area (m^2)	Energy demand 2021 (kWh)	Installed PV (kWp)	Potential additional PV (kWp)
Dpt. 1 and 2	1998	5,006	273,432	17	373.4
Dpt. 3 and 4	2006	2,171	228,309	-	223.0
Enerpos	2008	979	15,710	48.8	46.9
SEAS-OI	2012	597	34,178	-	72,0
ESIROI	2020	3,885	260,160	100	127,9
Student residences	2008 and 2019	6,110	373,060	-	173,0
	Total	**18,748**	**1,184,759**	**165.8**	**1,016.2**

Fig. 4 gives a detailed view of the current load profile of the ESIROI building, where each type of load is monitored. The main load, even if that building is very well designed, is the cooling (purple and orange areas). With a significant difference in the cooling demand, the building load profile differs strongly between summer and winter. The increase of electric vehicles (EV) results in a significant share of the load coming from EV charging (dark green area). The overall shape of the load profile, also representative of the total campus load, shows that energy demand occurs primarily during daylight hours. Therefore, powering the microgrid with solar energy seems to be a good solution to increase its self-sufficiency. However, with a relatively important share of demand occurring at night, a solution based solely on solar energy will have its limitations.

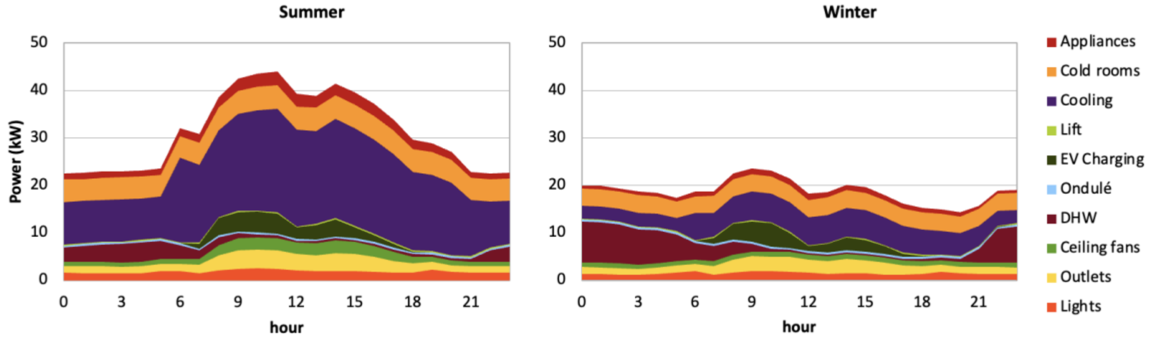

Fig. 4: Average daily profile of electricity demand by type of use of the ESIROI building for summer (Nov. to Apr.) and winter (Apr. to Nov.)

Fig. 5 presents the results of a simplified model of the current microgrid, considering a PV production based on the observed performance ratio of existing systems and actual electricity demand. The model computes the self-sufficiency of the microgrid for an increasing installed PV capacity. As expected, without flexibility means, like ESS or demand side management, the self-sufficiency hardly overtake a limit of 50%. The dotted lines highlight the current situation (blue line), a virtual NetZEB microgrid (green line) and a PV system covering all the available roofs (red line).

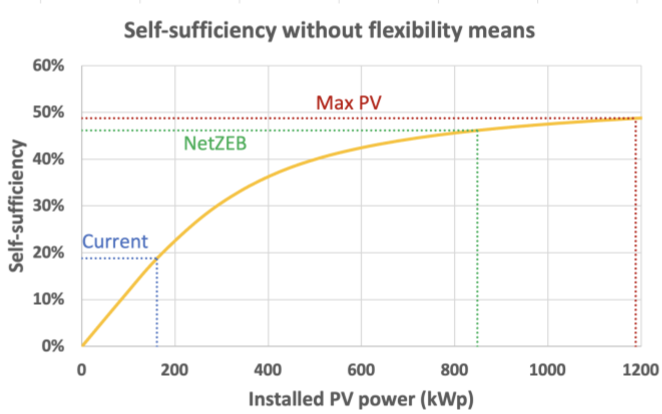

Fig. 5: Simulated self-sufficiency for an increasing installed PV capacity and no flexibility means

Therefore, reducing operation costs and carbon emissions of the whole microgrid requires optimizing the operation and size of a system, which integrates flexibility means like an ESS, to enable increasing the self-sufficiency from solar generation beyond 50%. More precisely, the TwInSolar project aims for 80% self-sufficiency from solar. The main issue is not to install new PV capacity but to achieve a techno-economic optimum to reduce the operation cost of the microgrid. Complementary approaches have already been tested to reach this goal: a combination of PV with compressed air energy storage (Castaing-Lasvignottes et al., 2016; Simpore et al., 2019) and a predictive Energy Management System (EMS) fed by probabilistic solar forecasts and load forecasts (Ramahatana et al., 2022). But these works were restricted to the Enerpos building. The next step is to extend the approach to the whole microgrid.

The campus is fully instrumented to monitor weather and electrical parameters with at least a 10-min time step. First, the university maintains its own complete weather station equipped with advanced solar irradiation sensors (global, diffuse, and direct irradiance on a solar tracker). Second, the electricity demand is recorded for each building separately and for the most recent constructions, the main types of loads (i.e., cooling, lights, ceiling fans, etc.) are also monitored. Finally, the production of the different PV plants is also recorded. A set of consolidated data with a 10-min granularity for two consecutive years, 2021 and 2022, is publicly available on the TwInSolar website in the deliverables section (“Twinsolar,” 2023).

4. Utility scale PV systems with energy storage

In order to reduce the uncertainty associated with their production and consequently improve the stability of the main grid, the latest generation of large-scale photovoltaic farms installed in La Reunion must be coupled with an energy storage system (ESS). In 2021, 19 utility-scale PV plants, for a total of 30 MWp, were operated jointly with energy storage (Reunion Island Energy Observatory (OER), 2022). Tab. 2 gives three examples of these atypical systems installed in La Reunion, with their main characteristics. These PV farms comply with the technical specifications required by a series of calls for tenders launched by the government starting from 2011 for the non-interconnected French areas. The operators of these solar power plants must provide a production schedule one day in advance and risk penalties if they do not respect it. Two different ways of planning the production have been proposed:

- the generation of a trapezium-shaped power profile during the daytime (Ministère de l'Ecologie, de l'Energie, du Développement Durable et de la Mer, 2011),
- a free power profile during the daytime and the possibility of producing a constant power during peak hours (i.e., 7:00 p.m. to 9:00 p.m.) with a better selling price (Ministère de l'Ecologie, de l'Energie, du Développement Durable et de la Mer, 2015).

Tab. 2: Examples of utility scale PV systems with energy storage installed in La Reunion

Name (commissioning year)	Operator	PV capacity	ESS capacity	Operation type	Source
Stade de l'Est (2020)	Albioma	1.25 MWp	1,33 MWh	Free daily profile and evening peak	(Albioma, 2023)
Aéroport Saint-Pierre Pierrefonds (2023)	TotalEnergies	7,7 MWp	10 MWh	Free daily profile and evening peak	(TotalEnergies, 2023)
Les Cèdres (2015)	Akuo	9 MWp	9 MWh	Trapezium-shape daily profile	(Akuo, 2023)

We will focus in this work only on the second type of injection profile, which favors the injection of power at peak hours. The left side of Fig. 6 illustrates the profile shape the operator must deliver to the Distribution System Operator (DSO) one day in advance. This profile and delivery times must respect a series of complex rules. Here, we will give a brief overview of the main requirements. The reader can access the detailed technical specifications here (Ministère de l'Ecologie, de l'Energie, du Développement Durable et de la Mer, 2015). The plant operator must transmit the generation profile of the next day to the DSO at 4:00 PM the day before. 4 redeclarations are possible at 4:00 AM, 10:00AM and 2:00 PM on the day of production. To avoid severe ramps during the daytime, the slope of the announced profile must be less than 0.6% per minute of peak power. Deviations ($Deviation = Actual\ injeted\ power - Announced\ power\ profile$

(eq. 1) from the announced profile, which exceed a power tolerance of $\pm$5% of the installed peak power, lead to penalties calculated as follows: a positive deviation (i.e., overproduction) is not purchased and a negative deviation (i.e., underproduction) results in a penalty given by $Penalty = Feed\ in\ tariff \times \left[\frac{Deviation^2}{Peak\ power} - 0.1 \times Deviation - 0.0075 \times Peak\ power\right]$ (eq. 2. The right side of Fig. 6 illustrates the value of the penalties for deviations ranging from -500 kW to 500 kW for a PV farm of 1 MWp and a feed-in tariff of 215 €/MWh, which corresponds to the average feed-in tariff of the installations awarded by the call of tender launched in 2015 (CRE, 2015). To encourage production during the peak hours, the feed-in tariff was raised by 200 €/MWh.

$$Deviation = Actual\ injeted\ power - Announced\ power\ profile \quad \text{(eq. 1)}$$

$$Penalty = Feed\ in\ tariff \times \left[\frac{Deviation^2}{Peak\ power} - 0.1 \times Deviation - 0.0075 \times Peak\ power\right] \quad \text{(eq. 2)}$$

The rules for the penalties are surprising. Indeed, for a simular absolute value of the deviation, you lose more money when you overproduce (positive deviation) than when you underproduce (negative deviation). No penatly jump appears when leaving the 5% tolerance band for negative deviations, as defined by equation 2. For positive deviation, the penalty corresponds to a shortfall because the DSO will not buy your excess of production. The slope is the feed-in tariff and a jump appears because you are not penalized within the 5% tolerance band.

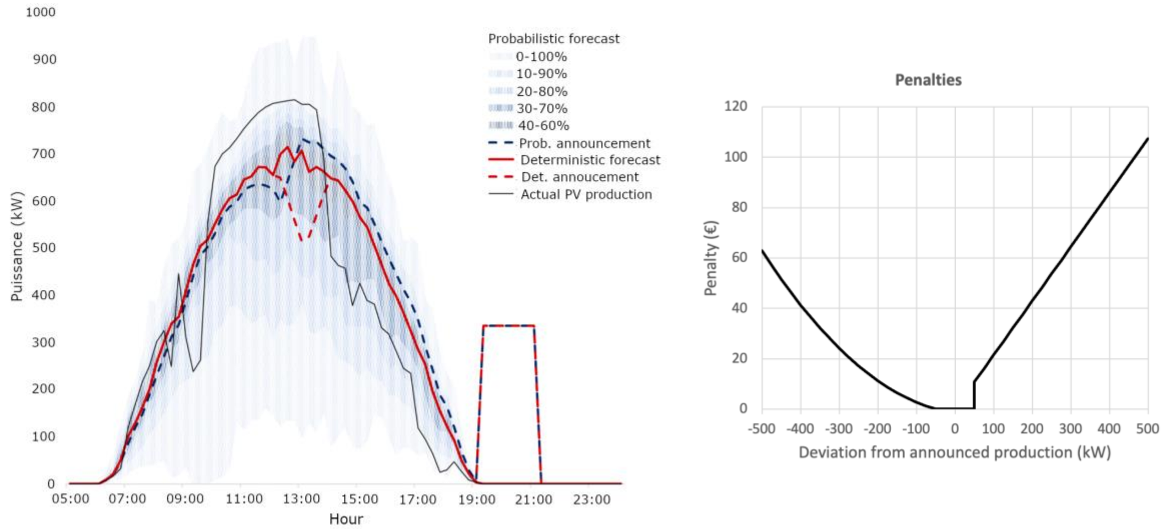

Fig. 6: At the left, one day of deterministic (red line) and probabilistic (grey intervals) forecast, the corresponding announced injection profiles (dashed lines) and the actual PV output power (black line) of 1 MWp PV plant situated in the coastal part of La Reunion. At the right, the penalties resulting from deviation from the announced production profile for a feed-in tariff of 215 €/MWh.

Therefore, the predictive schedule of these plants should reduce penalties while increasing the amount of energy injected into the grid. For instance, to maximize the revenue, a possible strategy is to charge the ESS at 100% during the daytime and to discharge it during peak hours. The main challenge for these specific PV farms and their operators is to select sound solar forecasts and integrate them into the system's EMS (David et al., 2021). Indeed, the quality of a forecast can be evaluated by a large set of indicators, such as the Mean Bias Error (MBE), the Root Mean Square Error (RMSE), the Mean Absolute Error (MAE) for the deterministic forecast (Yang et al., 2020) and the Continuous Rank Probability Score (CRPS), or the Ingnorance Score for probabilistic forecast (Lauret et al., 2019). However, improving these evaluation metrics does not mandatorily correspond to better revenue for the user.

For this study case, the operation data, such as the PV production and the ESS state of charge, are not publicly available because they belong to private operators. However, it is easy to find the main technical characteristics of the PV plants and the ESS on the Internet (see Tab. 2: Examples of utility scale PV systems with energy storage installed in La Reunion. Finally, the technical specifications cited above fully describe the technical and financial rules used to run these PV plants and simulate the EMS. Time series of PV production and forecasts can be simulated through CorRES tool (Koivisto et al., 2019).

5. The power grid of the island of La Reunion

With approximately 400,000 electricity consumers and a wide variety of means of production, the electricity network of La Reunion Island is not a small isolated power grid. Moreover, the distance between La Reunion and the nearest continental grids is so long that interconnection is not possible. This intermediate-size electricity grid, often called non-interconnected, faces different issues than stand-alone microgrids. Therefore, it will prefigure the challenges of continental grids with a high share of intermittent renewable energies such as PV and wind power. In 2021, as illustrated in Fig. 7 andFig. 8, the total installed capacity was 931.8 MW and the annual electricity production was close to 3,000 GWh. The same year, with an installed capacity of 223.6 MW (24% of the total installed capacity), the PV produced 8.7% of the electricity mix (Reunion Island Energy Observatory (OER), 2022). With such a high penetration rate of intermittent renewables and to guarantee the grid stability, the French government fixed a regulatory limit of a maximum of 35% of the total produced power coming from variable renewable energies (VRE) such as PV and wind. Beyond this limit, the local DSO considers that the high penetration rate of renewable energy systems connected via power electronics such as inverters results in an unacceptable risk. Indeed, the inverters must operate within the frequency and voltage bands defined by the DIN VDE 0126-1-1 (VDE, 2013) and, in case of severe failure on the grid, they could stop their production if the frequency or the voltage drop suddenly. With the current conversion to biomass of coal and diesel power plants, the electricity generation will be 100% renewable by 2024 (Ministère de la transition écologique, 2022). However, most of the required biomass (i.e., wood pellets and biofuel) will be imported and this conversion will unfortunately perpetuate the high energy dependency of the island.

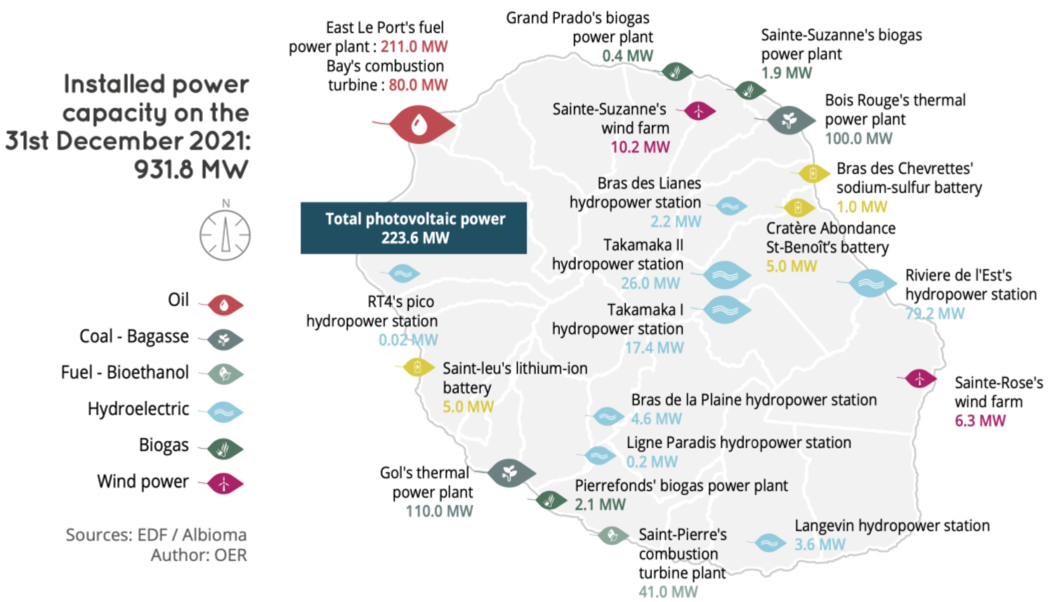

Fig. 7: Schematic diagram of La Reunion's electricity grid in 2021 (Reunion Island Energy Observatory (OER), 2022)

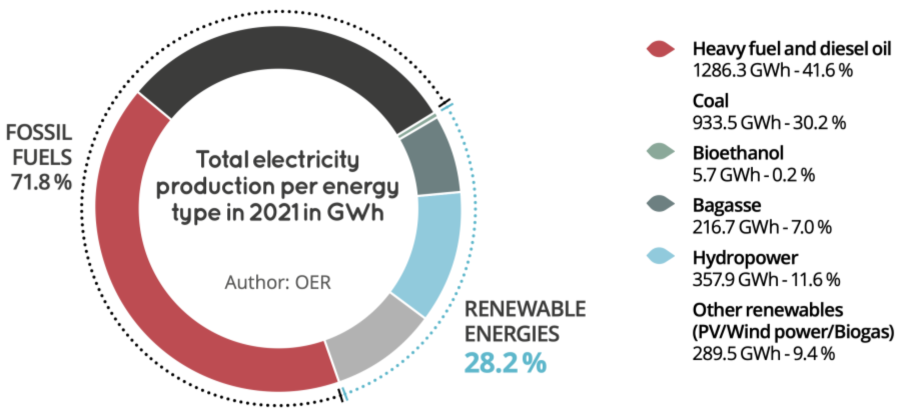

Fig. 8: Electricity production mix of La Reunion in 2021 (Reunion Island Energy Observatory (OER), 2022)

To better understand the current operation of the electricity network, Fig. 9 shows 3 days of hourly electricity production for summer and winter. Coal/bagasse[1] power plants and diesel generators are the historical baseload power plants of La Reunion. Hydropower plants and combustion turbines are the most flexible production means. They are mainly used for peak shaving and power reserve. However, due to the volcanic nature of the soils, large dams are not feasible. As a consequence, hydropower plants have relatively low energy capacity. In summer (left side of Fig. 9), two peaks in electricity consumption appear. The first occurs in the middle of the day due the important cooling demand of the buildings. The second is the classic evening peak caused by residential electricty demand. Solar generation and baseload power plants meet daytime demand. At the same

[1] Bagasse is the sugar cane straw remaining after juice extraction. It's a residue from sugar factories.

time, hydropower offsets fluctuations in demand and solar production. In the evening, fast and expensive combustion turbines are used in combination with hydropower to meet peak demand. In rare cases, such as February 5, 2021, when there is not enough hydropower available at the end of the day, the DSO increases production from coal/bagasse plants. In winter (right side of Fig. 9), air conditioning demand is low and therefore electricity demand is lower than in summer with the exception of the evening peak which remains similar. The latter is managed as in summer with a combination of hydroelectricity, combustion turbines and baseload power plants. However, during the day in winter, we see that power reductions of coal/bagasse plants, which are the least reactive means, compensate for significant solar production. Thus, rapid means such as hydroelectricity are not the only ones to be used to integrate solar production into the electricity mix of La Reunion. A last important point is highlighted in the bottom part of Fig. 9. In summer as in winter, the power limitation of 35% of the total power coming from VRE is frequently reached in the middle of the day. Above this threshold, the DSO must curtail PV production to avoid important risk for the stability of the electricty network.

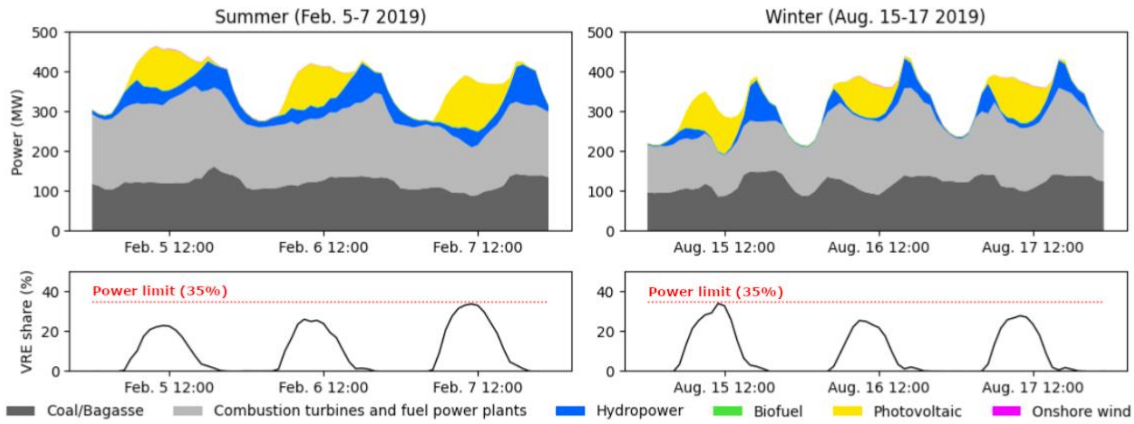

Fig. 9: Hourly profiles of electricity production in La Reunion by type of generation means (top) and associated power fraction from variable renewable energies (bottom) for 3 typical days of summer and winter 2021

As the sun is the first local renewable resource, the self-sufficiency goal for La Reunion requires continuing the installation of PV systems to achieve massive integration of solar renewable energies. To reach a 100% renewable with local resource, a prospective study done by the French energy agency ADEME highlights that the future energy mix of La Reunion will be higly dominated by solar technologies (BISCAGLIA et al., 2018). Moreover, the French government, in agreement with the local authorities, plans a strong increase of the PV with a doubling of the installed capacity by 2028 (Ministère de la transition écologique, 2022). If 100% PV electric production with a affordable Levelized Cost of Energy (LCOE) is achievable (Perez et al., 2023), a important capacity of ESS is needed. However, these works have not solved the issues related to grid stability when sudden production fluctuations are observed or when a severe failure occurs. Therefore, the main challenges to achieve a massive integration of solar renewable energies into the electricity network are PV generation and demand forecasting, ESS and smart management of the production means.

The local DSO, EDF Réunion, recently created a website bringing together a lot of data concerning the island's electricity network (EDF, 2023). These freely accessible data provide a detailed description of the means of production, transport lines and main transformers. Additionally, the web portal also provides hourly records of electricity production by type of generation means (see Fig. 9) and costs from 2016. This dataset provides a useful tool for studying the massive integration of solar energy into a medium-sized non-interconnected power grid.

6. Conclusion

The decarbonization of electricity production and more broadly the energy autonomy of non-interconnected territories like Reunion Island require the massive integration of solar energy in the near future. While solar technologies, such as PV and solar DHW, are mature, the variable nature of the solar resource and their connection to the electrical grid with power electronics raise new scientific challenges to achieve this goal. This work details 4 study cases that highlight these challenges at different scales: an isolated microgrid, a grid-connected microgrid, utility-scale photovoltaic plants equipped with ESS and the electricity network of the island of La Reunion. All these case studies come with freely accessible data allowing the scientific community to study possible alternative solutions to significantly increase the share of solar power in the production mix.

Concerning the case of the standlone microgrid of Mafate located in the isolated cirque of Mafate, in the heart of a national park classified as a UNESCO world heritage site, the sizing of the components of the system (i.e. PV farm, ESS and power converters) should result from user requirements, the potential of demand management measures and the detailed analysis of simulated production profiles. The current design, carried out according to the usual practices of a design office, did not take such a strategy into account. Therefore, the installed system is highly oversized and the LCOE is exceptionally high. Data collected from the microgrid can be used to refine the design process and achieve an affordable energy price.

The second case study is a university campus, located in Saint-Pierre on the southern coastal part of the island, comprising university buildings, student residences and a restaurant. Approximately 50% of the floor area of university buildings is air-conditioned and the cooling demand is the main load of the microgrid. The most recent campus buildings are bioclimatic, energy efficient, and have rooftop PV systems, aiming for a net zero energy balance between consumption and production on an annual scale. In 2021, the whole campus's electricity self-sufficiency was approximately 16%. The next step is increasing the self-sufficiency of the whole microgrid, with a target of 80%, while reducing operating costs. The data recorded over the last few years allows a detailed analysis of loads and PV productions, necessary to achieve cost-effective integration of solar systems.

Since 2013, large-scale PV systems must include an ESS and their operators have to provide a power supply schedule one day in advance. Penalties are applied for the difference between the actual supply and the delivery schedule provided to the authorities. In 2021, 19 utility-scale PV plants, for a total of 30 MWp, were operated jointly with energy storage. The operation of these hybrid systems requires high-quality forecasts of photovoltaic production and efficient EMS to generate forecast schedules for energy injection into the network. The goal is to maximize the direct injection of solar energy into the grid while minimizing penalties due to deviations from schedule.

The last study case is the La Reunion’s electricity network. With around 400,000 electricity consumers, a wide diversity of production means and no possibility of cable connection with continental networks, this electricity grid is an example of a non-interconnected system. To achieve energy autonomy for the Island, the massive integration of solar energy, already underway, seems to be the most suitable solution. However, due to the high variability of solar production and the current specifications of the power electronics used to convert PV production, the massive integration of solar energy in an non-interconnected system raises new issues to guarantee supply security and grid stability. Highlighted by the data provided by the DSO, the main challenges to achieve the massive integration of solar renewable energies are the demand and PV production forecast, ESS and smart management of production means.

7. Acknowledgements

This research received support from the TwInSolar project funded by the European Union’s Horizon Europe research and innovation program grant number 101076447. The authors would also like to thank EDF La Réunion and the University of La Reunion who share open access data allowing the scientific community to carry out research on the study cases presented in this article.

8. References

Abbezzot, C., Francou, J., Calogine, D., 2022. Demand side management applied to a stand-alone microgrid. Int. J. Smart Grid Clean Energy 127–134. https://doi.org/10.12720/sgce.11.4.127-134

Akuo, 2023. Les Cèdres [WWW Document]. CÈDRES. URL https://akuocoop.com/fr/projets/5-les-cedres (accessed 10.8.23).

Albioma, 2023. Stade de l’Est [WWW Document]. Albioma. URL https://www.albioma.com/implantation/la-reunion/stade-de-lest (accessed 10.8.23).

BISCAGLIA, S., CHOTARD, D., DARBOT, A., MAIRET, N., BABONNEAU, F., HAURIE, A., 2018. Vers l'autonomie énergétique en zone non interconnectée à la Réunion.

Calogine, D., Chau, O., Lauret, P., 2019. A fractional derivative approach to modelling a smart grid-off cluster of houses in an isolated area. J. Appl. Numer. Optim. 1. https://doi.org/10.23952/jano.1.2019.3.11

Calogine, D., Francou, J., Abbezzot, C., Tovondahiniriko, F., 2023. Data in experimental stand-alone microgrid. https://doi.org/10.5281/ZENODO.8186302

Castaing-Lasvignottes, J., David, M., Simpore, S., Marc, O., Garde, F., 2016. Simuling a Compressed Air Energy Storage For a Net Zero Energy Building in Tropics. Int. J. Thermodyn. 19, 130. https://doi.org/10.5541/ijot.5000153492

CRE, 2015. Rapport de synthèse AO CREE 2015 ZNI [WWW Document]. URL https://www.cre.fr/media/Fichiers/publications/appelsoffres/rapport-ao-pv-100-zni (accessed 10.7.23).

David, M., Boland, J., Cirocco, L., Lauret, P., Voyant, C., 2021. Value of deterministic day-ahead forecasts of PV generation in PV + Storage operation for the Australian electricity market. Sol. Energy 224, 672–684. https://doi.org/10.1016/j.solener.2021.06.011

EDF, 2023. Open Data EDF Réunion [WWW Document]. Open Data EDF La Réun. URL https://opendata-reunion.edf.fr/ (accessed 10.9.23).

Erdinc, O., Paterakis, N.G., Catalão, J.P.S., 2015. Overview of insular power systems under increasing penetration of renewable energy sources: Opportunities and challenges. Renew. Sustain. Energy Rev. 52, 333–346. https://doi.org/10.1016/j.rser.2015.07.104

Francou, J., Abbezzot, C., Rasoavonjy, P., Calogine, D., 2022. An Islanded Microgrid Design: A Case Study. Presented at the 6th Hybrid Power Systems Workshop, Madeira, p. 6.

Francou, J., Calogine, D., Chau, O., Ramiarinjanahary, O., Tovondahiniriko, F., Rasoavonjy, P., 2019. "Micro Reseau Mafate" project, Smart grid development by experimenting an off-grid micro-grid, in: Proceedings of the Eleventh International Conference in High-Energy Physics. Presented at the HEPMAD 19, Antananarivo, Madagascar.

IRENA, 2022. Renewable Power Generation Costs in 2022. Abu Dhabi, UAE.

Koivisto, M., Das, K., Guo, F., Sørensen, P., Nuño, E., Cutululis, N., Maule, P., 2019. Using time series simulation tools for assessing the effects of variable renewable energy generation on power and energy systems. WIREs Energy Environ. 8, 329. https://doi.org/10.1002/wene.329

Lauret, P., David, M., Pinson, P., 2019. Verification of solar irradiance probabilistic forecasts. Sol. Energy 194, 254–271. https://doi.org/10.1016/j.solener.2019.10.041

Lenoir, A., Garde, F., 2012. Tropical NZEB. High Perform. Build. J. 43–55.

Ministère de la transition écologique, 2022. Décret n° 2022-575 du 20 avril 2022 relatif à la programmation pluriannuelle de l'énergie de La Réunion, 2022-575.

Ministère de l'Ecologie, de l'Energie, du Développement Durable et de la Mer, 2015. Cahier des charges de l'appel d'offres portant sur la réalisation et l'exploitation d'installations de production d'électricité à partir de techniques de conversion du rayonnement solaire d'une puissance supérieure à 100 kWc et situées dans les zones non interconnectées. J. Off. Union Eur.

Ministère de l'Ecologie, de l'Energie, du Développement Durable et de la Mer, 2011. Cahier des charges de l'appel d'offre portant sur la réalisation et l'exploitation d'installation de production d'électricité à partir de l'énergie solaire d'une puissance supérieure à 250 kWc. J. Off. Union Eur.

Perez, R., Perez, M., Remund, J., Rabago, K., Putman, M., Pierro, M., Prina, M.G., Cornaro, C., Moser, D., Schlemmer, J., Dise, J., Hoff, T., Swierc, A., Kellin, P., Boland, J., Tapachès, E., David, M., Lauret, P., van Eldik, R., van Sark, W., Lopez-Lorente, J., Makrides, G., Georghiou, G.E., 2023. Firm Power generation (No. IEA-PVPS T16-04:2023). International Energy Agency.

Ramahatana, F., Le Gal La Salle, J., Lauret, P., David, M., 2022. A more efficient microgrid operation through the integration of probabilistic solar forecasts. Sustain. Energy Grids Netw. 100783. https://doi.org/10.1016/j.segan.2022.100783

Reunion Island Energy Observatory (OER), 2022. Energy balance Reunion Island, Key figures 2021.

Simpore, S., Garde, F., David, M., Marc, O., Castaing-Lasvignottes, J., 2019. Sensitivity analysis and optimization of a compressed air energy storage (CAES) system powered by a photovoltaic plant to supply a building. Procedia Manuf. 35, 137–142. https://doi.org/10.1016/j.promfg.2019.05.016

TotalEnergies, 2023. Sur l'aéroport de Pierrefonds à La Réunion, TotalEnergies inaugure la première centrale photovoltaïque aéroportuaire française [WWW Document]. Total. Renouvelables. URL https://renouvelables.totalenergies.fr/fr/node/1241 (accessed 10.8.23).

Twinsolar [WWW Document], 2023. . Improv. Res. Innov. Achieve Massive Integr. Sol. Renew. URL https://twinsolar.eu/en/ (accessed 10.5.23).

VDE, 2013. DIN VDE V 0126-1-1 Automatic disconnection device between a generator and the public low-voltage grid.

Yang, D., Alessandrini, S., Antonanzas, J., Antonanzas-Torres, F., Badescu, V., Beyer, H.G., Blaga, R., Boland, J., Bright, J.M., Coimbra, C.F.M., David, M., Frimane, Â., Gueymard, C.A., Hong, T., Kay, M.J., Killinger, S., Kleissl, J., Lauret, P., Lorenz, E., van der Meer, D., Paulescu, M., Perez, R., Perpiñán-Lamigueiro, O., Peters, I.M., Reikard, G., Renné, D., Saint-Drenan, Y.-M., Shuai, Y., Urraca, R., Verbois, H., Vignola, F., Voyant, C., Zhang, J., 2020. Verification of deterministic solar forecasts. Sol. Energy 210, S0038092X20303947. https://doi.org/10.1016/j.solener.2020.04.019

06. Solar Buildings, Urban and Neighborhood Design

Characterization and parametrization of a photovoltaic-thermal façade in the context of Building Information Modeling

Wael Mandow[1], Maik Kirchner[1], Federico Giovannetti[1], Fabian Edenhofner[2], Theresa Maier[3]

[1]Institute for Solar Energy Research in Hamelin (ISFH), Hameln (Germany)

[2]ICoM, RWTH Aachen University, Aachen (Germany)

[3]Albert.ing GmbH, Frankfurt am Main (Germany)

Abstract

The use of Building Information Modeling (BIM) for special applications like solar energy as well as for the operation stage of the building process is not yet established and still under development. The paper addresses both topics and presents a methodology for using BIM to monitor a solar façade consisting of novel photovoltaic-thermal (PVT) modules intended for building integration. For this purpose, a digital twin of a real laboratory with its PVT façade was developed in a common data environment (CDE). Main goal of the work is to use the BIM platform to identify possible malfunctions of the façade and to ensure an efficient system operation. For a correct parameterization in the BIM environment as well as for the analysis of the deviation between the usually available laboratory performance data and the behavior under real conditions, we perform a detailed experimental characterization of both the PVT module and the whole PVT façade. Results, critical aspects and future developments are discussed.

Keywords: Building Information Modeling (BIM), building integration, photovoltaics, solar thermal collectors, photovoltaic-thermal collectors, monitoring

1. Introduction

To reduce CO_2 emissions in the building sector, a significant increase in the use of available renewable energies such as solar energy is required, both in existing and new buildings. The combination of photovoltaic-thermal collectors and heat pumps can significantly contribute to this goal. For this purpose, the façade offers a promising untapped potential and design synergies arising from building integration can additionally lead to cost savings and aesthetical advantages compared to common installations. However, as part of the building envelope, a PVT façade must meet several requirements not only with regard to energy but also to building physics and aesthetics.

In the frame of a current research project, a new type of PVT façade is being planned, constructed and measured. The central task is to model the façade using the BIM method in order to analyze and improve its use over its entire life cycle. As a holistic approach, the BIM method is suitable, among other things, for applications in the field of technical building equipment as well as for the analysis of energy supply systems. Early BIM-based planning of a building energy supply system also brings advantages with regard to the use of renewable energy sources such as solar energy. For the operational phase, the BIM method can be used to monitor, for example, the expected thermal or electrical yield of a system. However, there are still fundamental limitations to the specific use of the BIM method in the solar energy field. The available BIM-based object models of solar energy components such as photovoltaic (PV) and solar thermal (ST) are neither uniformly nor fully parameterized for common application scenarios. For photovoltaic thermal collectors, no specific object model exists to date. In addition, the BIM method has so far been used primarily for the planning process.

In this paper, the use of BIM for monitoring the innovative PVT façade is methodically presented. For this purpose, a BIM model of an existing real laboratory with its PVT façade was developed at the Institute for Solar Energy Research in Hamelin (ISFH). Based on this, a digital twin for monitoring in a common data environment was created. This is intended to illustrate the ability to display measured thermal and electrical yields and compare them to target data. This can allow a rapid identification and solution of possible malfunctions thus ensuring an efficient system operation. The BIM parameterization of the PVT collector is based on a previous work (Mandow et al., 2022a). For a correct parameterization in the BIM environment as well as for the analysis of the difference between the usually available laboratory data and the real application, we performed a detailed experimental

10.18086/swc.2023.06.07 Available at http://proceedings.ises.org

characterization of the PVT module as well as of the whole PVT façade.

2. Building Information Modeling method

Building Information Modeling has established itself as one of the generic terms for digitization in the value chain of designing, building and operating structures. With the BIM method, all lifecycle-relevant information of a building can be recorded, managed and exchanged centrally, model-based, digitally and consistently (VDI 2552, 2020). This enables optimal transparent communication between the parties involved in the various construction project phases (architects, planners, installers, operators, etc.). Fig 1 shows this relationship graphically.

All building-relevant data are stored in a Common Data Environment (CDE), and are thus accessible to all project participants at any time. Computer-aided filtering and evaluation - combined with visualization - helps to focus and control project-related activities.

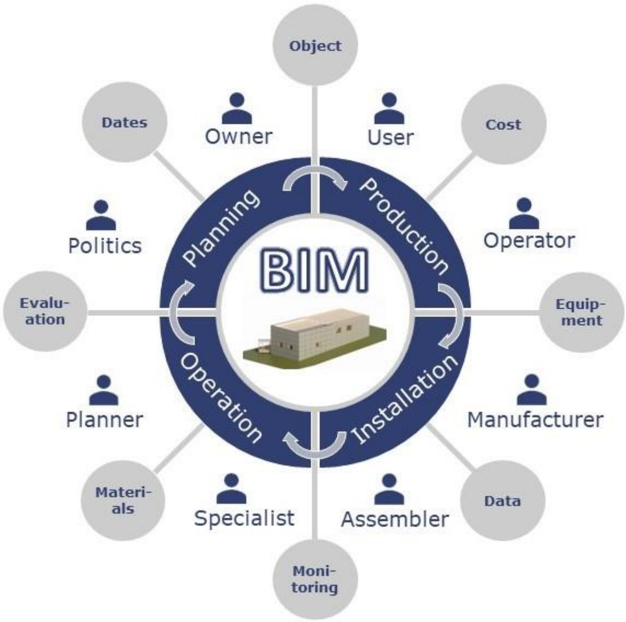

Fig 1: Building Information Modeling, central information management based on models

Building Information Modeling, as a holistic method, holds benefits in all life cycle phases of a structure. Currently, this method is particularly used in the planning phase, but its application in the operational phase also offers great potential. In Germany for the implementation of the BIM method in national projects, the two BIM strategies “Masterplan BIM for Federal Buildings” (BMI, 2021) and “Masterplan BIM for Federal Highways” (BMDV, 2021) recommend initially implementing BIM use cases in the planning phase. The successful use of the BIM method in planning for the generation of the corresponding BIM models is directly related to its use in the subsequent life cycle phases. The data generated over the life cycle of a structure can be continuously aggregated in the BIM model and thus provide an optimal basis for an operation as well as maintenance management of a structure.

There are already comprehensive BIM-based approaches and software products for the application to conventional structures and especially for their planning phase. The application of the method in the field of solar energy is still under development and is a current research topic. There is still considerable potential for development both in the planning and especially in the operation of photovoltaic and solar thermal plants (Mandow et al., 2022b).

In the planning phase, for example, the use of BIM enables solar energy to be considered as part of the energy supply system at an early stage of the integral planning of the building. Furthermore, BIM modeling allows the building to be modeled with its surroundings, which makes it possible to predict the solar energy yield more correctly, by considering any module shading.

To facilitate the planning and modeling process, product manufacturers can make their products available to the general public as BIM objects. On browser-based databases such as BIMobject (BIMobject, 2023), Bimetica (Bimetica, 2023), on the National BIM Library (NBS, 2023), which is widely used in the UK, and on the Autocad/Revit portal for BIM-Apps MEPcontent (MEPcontent, 2023), BIM objects of photovoltaic and solar thermal modules with information on geometry and semantic properties already exist. However, the available parameterization is unsuitable for application scenarios in the field of energy simulation due to lack of some crucial properties like some performance parameters or inconsistent naming.

With regard to semantics, manufacturer information about warranty and maintenance of the actual physical objects can be integrated into their digital images and thus contribute to better operation. By coupling measurement technology and the BIM model, a digital twin of a solar plant can be generated. Within such a BIM-based monitoring approach for the operation of solar plants, the actual measurement data can be compared with target data. The target data can be determined from the available design data or manufacturer specifications by means of appropriate simulation programs. In the event of a deviation above a predefined critical value in the monitoring data, a possible malfunction (e.g. a defective photovoltaic module or solar thermal collector) can be detected at an early stage, communicated to the operator via the BIM platform (CDE) and, if necessary, a repair or replacement can follow. In case of any repair or replacement, the BIM model is updated to show the actual as-built condition. In the case of disassembly, the preparation of cost and work plan analogously to the first installation can be facilitated by the BIM-based approach. Existing information on the recyclability of the dismantled components can also be stored in the BIM model of the project. In principle, all lifecycle-relevant information of a construction project can be stored in a BIM model.

There are a number of proprietary and vendor-neutral approaches for the data management of BIM models. The Industry Foundation Classes (IFC) represents a manufacturer-neutral standard for the data exchange of building information models, which is established as an international standard (DIN EN ISO 16739, 2021). The use of the IFC standard enables the collaboration in BIM projects between different stakeholders and any different software products. This data schema is developed by buildingSMART (buildingSMART, 2023), an international competence network for digital design, construction and operation of buildings. The main task of the non-profit organization is the further development and standardization of the open exchange of information in BIM projects as well as the definition and standardization of corresponding work processes and interfaces.

A BIM-based approach for monitoring a façade-integrated PVT system (BIPVT system) is presented in the coming chapters.

3. BIM use case: yield monitoring

The "yield monitoring" use case is located in the operation life cycle phase of a BIPV(T) system. By combining the BIM model with live monitoring data, a digital twin of the PVT façade is created. For the representation of the digital twin, a suitable BIM platform is developed, which meets the requirements for digital twins of BIPV(T) systems.

The digital representation of the BIPV(T) system, its surroundings and the given location by geo-referencing the BIM model provide essential geometric and meteorological information. In addition, stored semantic information, such as the thermal as well as electrical efficiency of the modules, can be easily retrieved and used for the calculation of the target data for the monitoring. Information on the surface conditions of the structure and the surrounding area can be used directly for the determination of any shading by ray tracing and for the yield analysis.

Fig 2 shows the BIM model of the BIPVT façade (real lab) at the SolarTec building at ISFH modeled in the authoring software Autodesk Revit. Furthermore, Fig 2 shows the basic hierarchy in a building project in the IFC standard and a schematic representation of a PVT module as an object of the IFC class "IfcSolarDevice" together with an extract of possible information (buildingSMART, 2023).

For processing the presented BIM use case, the BIM model must be parameterized with corresponding information so that the calculation of the expected target data (e.g. electrical or thermal yield) can be performed using current weather data. For this purpose, a PVT module was electrically and thermally characterized in the ISFH laboratory. The entire façade was being characterized in field according to quasi-dynamic test method (DIN EN ISO 9806, 2017).

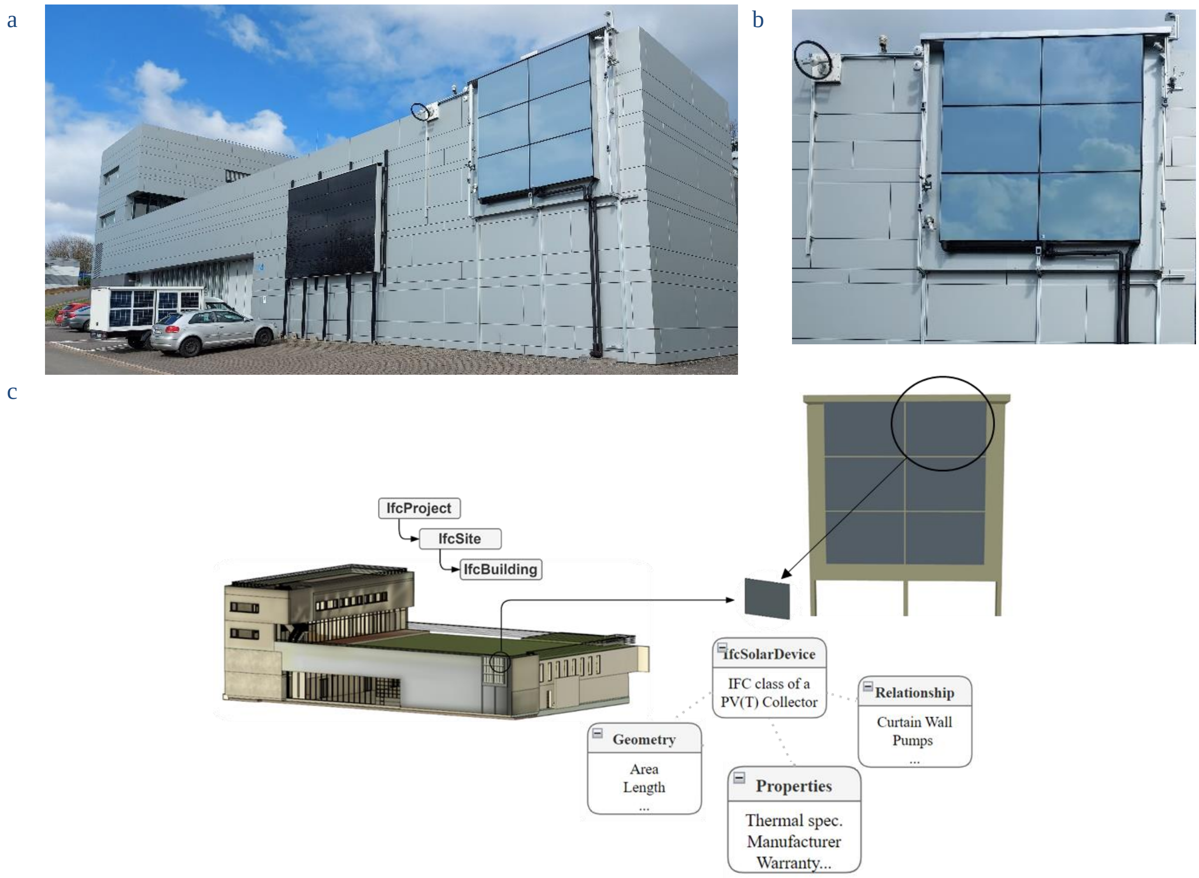

Fig 2: BIM model (digital twin) of the building with the PVT façade at ISFH, a: real building, b: PVT façade, c: BIM model of the building and the PVT façade with schematic explanation of the IFC structure of the PVT façade

4. Module characterization

The PV module used was specifically designed for building integration. It is a light gray, frameless and 1095 x 1620 mm large glass-glass module, where the PV cells are not visible due to the translucent cover glass. Back rails are glued to the back of the c-Si PV module, with which the PV module is clamped onto an aluminum heat exchanger. Fig 3 shows the PVT façade module in detail.

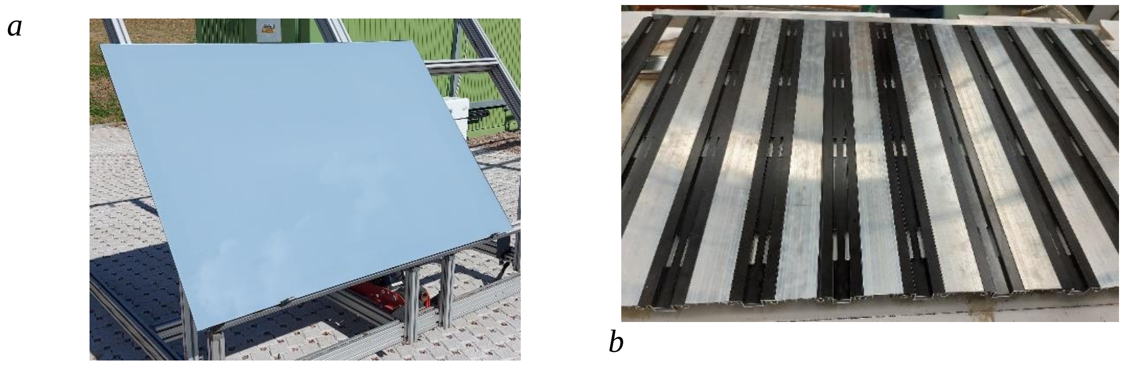

Fig 3: The innovative PVT façade module, a: PV module, b: Aluminum heat exchanger

The PVT façade module was measured at ISFH in the solar simulator of our laboratory according to the Standard (DIN EN ISO 9806, 2017) for uncovered collectors (WISC), both with maximum electrical load (MPP operation) and with open electrical circuit (OC operation). Fig 4 shows the module -installed on an insulated white plate - at a tilt angle of 90° in the solar simulator. The distance between the installed module and the white plate was 50 mm, and the investigation was carried out for two cases: PVT façade collector with closed and open-air gap, as a rear-ventilated façade. Due to the installation situation in the test and on the basis of previous experience with similar building integrated solar modules (Frick et al. 2022), a higher air flow velocity is expected on the back side of the ventilated single module compared to the flow velocity in the air gap of a real façade. This has a strong influence on the efficiency parameters of the module, which is why the PVT module was also measured with a closed air gap. The mass flow rate of the fluid (water) was set to a constant value of 130 kg/h (0.02 kg/s), the indoor air temperature and sky temperature were set to 25 °C and the irradiation (G) to 960 W/m².

Fig 4: Laboratory measurement of the PVT collector as a façade collector in the solar simulator according to DIN EN ISO 9806

The thermal power output is determined according to the following model for uncovered fluid collectors under steady-state conditions described in the (DIN EN ISO 9806, 2017):

$$\dot{Q} = A_G(\eta_{0,hem}G_{hem} - a_1(\vartheta_m - \vartheta_a) - a_2(\vartheta_m - \vartheta_a)^2 - a_3u'(\vartheta_m - \vartheta_a) + a_4(E_L - \sigma T_a{}^4) - a_6u'G_{hem} - a_7u'(E_L - \sigma T_a{}^4) - a_8(\vartheta_m - \vartheta_a)^4) \quad \text{eq 1}$$

The calculated collector parameters are listed in Tab. 1 (for the symbols s. Annex).

Tab. 1: Collector parameters according to DIN EN ISO 9806 (2017)

Installation mode	Operating mode	Collector parameters				
		$\eta_{0,hem}$ -	a_1 W/m²·K	a_3 J/m²·K	a_4* -	a_6 s/m
With air gap	MPP	0.436	15.32	6.01	0.53	0.063
Without air gap	MPP	0.434	9.24	1.63	0.54	0.043
With air gap	OC	0.487	15.48	5.98	0.53	0.066
without air gap	OC	0.495	9.44	1.23	0.54	0.049

*a_4 is calculated according to the following equation:

$$a_4 = \eta_{0,hem}\frac{\varepsilon}{\alpha} \quad \text{eq 2}$$

Whereas α is the solar absorption grad of the module which was measured (α=0.769). Fig 5 and Fig 6 show the thermal efficiency determined from measured data as a function of wind velocity, temperature difference between heat transfer medium and ambient air, and the air gap for both MPP and OC operation mode. The investigation shows the impact of the different installation on the results.

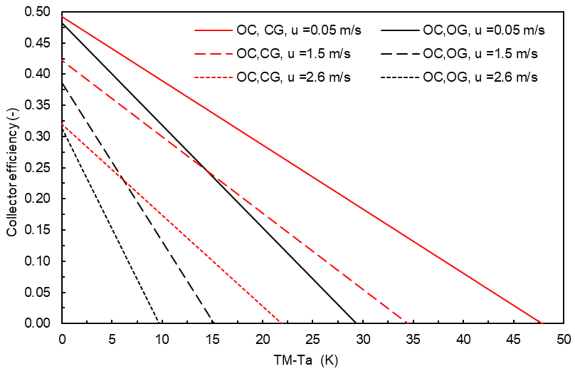

Fig 5: Thermal efficiency of the PVT façade collector according to DIN EN ISO 9806 with (OG) and without 50 mm air gap (CG) in OC mode

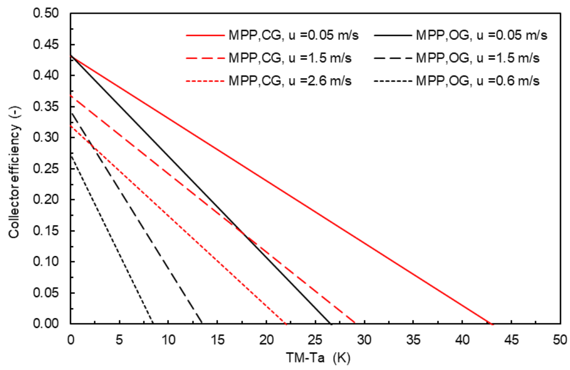

Fig 6: Thermal efficiency of the PVT façade collector according to DIN EN ISO 9806 with (OG) and without 50 mm air gap (CG) in MPP operation mode

5. Façade characterisation

The use of the BIM method in the operational phase for monitoring the façade-integrated PVT (in this case a ventilated curtain wall) as well as the general use of the BIM method for solar components is investigated as real laboratory in an experimental building (SolarTec) at the ISFH. The BIM model is parameterized based on the thermal, electrical and building physics characterization (U-value) of the façade. For the use case "Yield monitoring" the PVT façade was equipped with high-quality measurement sensors to record and analyze the thermal and electrical yield.

The façade consists of 6 PVT modules with a total area of 10.6 m². The PV modules are connected in two strings with 3 modules each in series. The PVT modules are hooked to the heat exchanger using the back rails shown in Fig 3. The heat exchanger is in turn suspended from transverse support rails by means of hooks. The support rails are attached to the wall with Isolink connectors (Schöck Bauteile GmbH, 2023). The special connectors serve to minimize the thermal bridge between the PVT façade and the building. A 50 mm air gap is formed between the PVT façade and the wall insulation. The PVT façade is installed on an existing façade. In order to investigate the thermal interaction between the PVT façade and the building, a heating system was implemented between the wall and the PVT façade to emulate indoor temperature. A heat flow plate was installed to measure the heat flow density between the PVT façade and the building. The surface temperature of PV front and back side as well as of the heat exchanger are measured by temperature sensors (PT-100). The temperature and relative humidity of the air is measured in the upper and lower part of the air gap.

As meteorological data, the hemispherical irradiation, the diffuse irradiation, the long-wave irradiation in the façade plain, the wind speed and direction, the ambient temperature, as well as air pressure and the relative humidity are measured. Fig 7 shows the measurement concept of the PVT façade. In addition, the temperature and mass flow of the heat transfer medium (water-Tyfocor mixture) at the PVT façade inlet as well as the temperature at the façade outlet are measured. To detect shading (possibly caused by surrounding trees), five silicon irradiance sensors were placed at different heights at the edge of the façade. The latter mentioned sensors are used for yield monitoring and comparison with the values of the simulation.

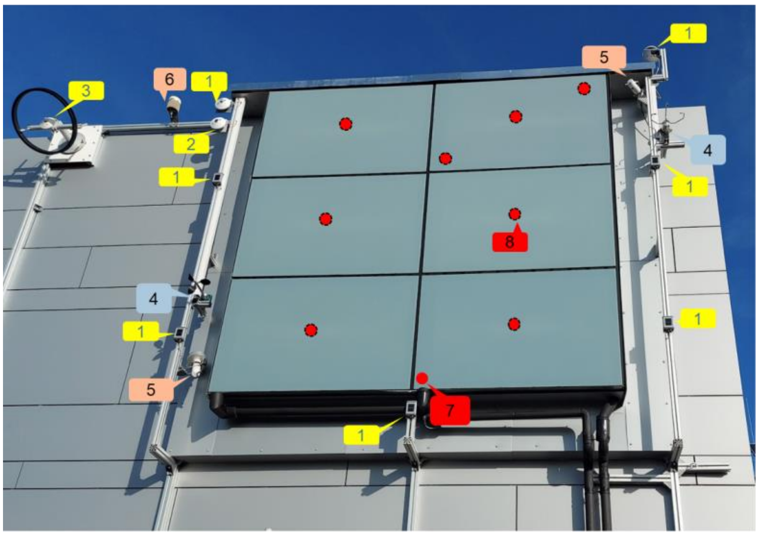

Sensors meteorological data
1-Global radiation (horizontal and vertical)
2-IR radiation
3-Diffuse radiation
4-Wind speed & direction
5-Ambient air temperature
6-Ambient air humidity & pressure

Sensors PVT façade
7-Surface temperature (PV front side)
8-Surface temperature (PV back side)
-Surface temperature (heat excahnger)
-Temperature and humidity in the air gap
-wind speed in the air gap
-heat flow plate
-Surface temperature (back side heating)
-Temperature and mass flow rate of the fluid

Fig 7: The PVT façade at the ISFH SolarTec building with its measurement concept, azimuth: -5°, location: Hamelin

The measurement started in November 2022. The PVT façade is characterized by means of quasi-dynamic test method according to the Standard (DIN EN ISO 9806, 2017) for liquid collectors described by the following equation:

$$\begin{aligned}\dot{Q} = A_G(\eta_{0,b}K_b(\Theta_L,\Theta_T)G_b + \eta_{0,b}K_dG_d - a_1(\vartheta_m-\vartheta_a) - a_2(\vartheta_m-\vartheta_a)^2 - a_3u'(\vartheta_m-\vartheta_a) \\ + a_4(E_L-\sigma T_a{}^4) - a_5\left(\frac{d\vartheta_m}{dt}\right) - a_6u'G - a_7u'(E_L-\sigma T_a{}^4) - a_8(\vartheta_m-\vartheta_a)^4)\end{aligned} \qquad \textbf{eq 3}$$

The calculated PVT façade parameters are listed in Tab. 2.

Tab. 2: PVT façade parameters by means of quasi-dynamic test method according to DIN EN ISO 9806 (2017)

$\eta_{0,b}$	$K_b(b_0)$	K_d	a_1	a_3	a_4	a_5	a_6
-	-	-	W/(m²·K)	J/(m³·K)	-	J/(m²·K)	s/m
0.48	0.036	0.99	9.99	0.508	0.54*	56736	0.0321

*a_4 is calculated according to eq 2

The outdoor thermal efficiency is significantly higher than the indoor one due to higher thermal capacity effect (field comparing to one module) and the solar spectrum as well as the long-wave thermal radiation in the laboratory are different from the solar and sky radiation in the field. The heat loss coefficient a_1 is lower in the field measurement than in the laboratory measurement with air gap (see Tab. 1), thus confirming our expectations and experiences with previous investigations.

Fig 8 shows an example of a daily measurement curve on a sunny day in March 2023. The hemispherical irradiance (G) reaches a maximum of 900 W/m². The temperature of the heat transfer medium at the inlet of the PVT façade (T_{in}) was set to 6 °C. The ambient air temperature (T_a) increases from 0 °C and reaches a maximum of 8 °C at 14:34 o'clock and decreases thereafter. The specific thermal power (q_dot exp) tends to run analogously to the global radiation and reaches a maximum of 315 W/m² (max. temperature increase of the heat transfer medium is about T_e-T_{in} = 7.6 K). Electrically, the PVT façade achieves a maximum specific power ($P_{ele\ exp}$) of about 82 W/m².

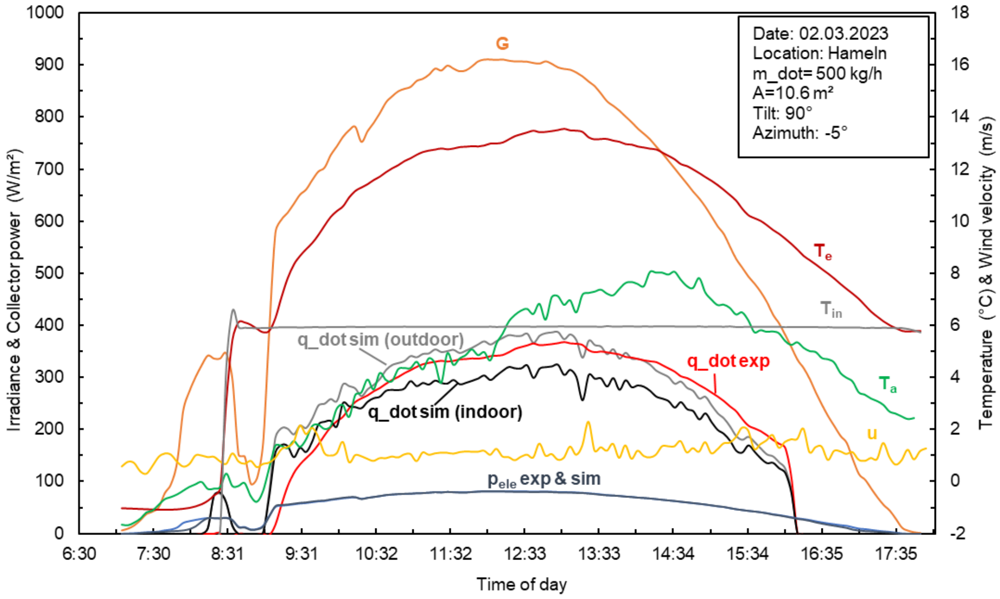

Fig 8: A daily measurement and simulated curve of the PVT façade at ISFH

In order to monitor the measured electrical and thermal yield, the characteristic values from the laboratory measurement on the one hand and the determined characteristic values of the PVT façade on the other hand are used for parameterization. Fig 8 shows the respective calculated thermal yields, whereas: q_dot sim (indoor)is based on the laboratory characterisation according to (eq 1) and q_dot sim (outdoor) on the field characterisation according to quasi-dynamic method (eq 3).

For q_dot sim (indoor), the collector coefficients for the closed air gap case and in MPP mode (see Tab. 1) were used, which better reproduce the behavior of the real façade. The simulated thermal yield depicts the measured one with a deviation that is mostly less than 20% (measurement uncertainty of q_dot is about 5%). The deviation can be due to the following reasons:

- In the field, the measurement of the wind velocity shows a high variation over the façade area and the position of the sensor used can have a strong impact on the results (Frick et al. 2022). The maximum velocity was used in the calculation of the simulated thermal yield.
- The laboratory measurement is done with artificial wind, which characteristics (turbulence, direction, homogeneity) differ from those of the real wind in the field measurements. As a result, there is a significant influence on the heat transfer between the collector and the environment (Frick et al. 2022).
- Installation situation is different (dimension of modules and façade as well as edge effects).
- The solar spectrum as well as the long-wave thermal radiation in the laboratory are different from the solar and sky radiation in the field.

By using the second approach, the simulated thermal yield q_dot sim (outdoor) shows as expected a better agreement with the measurement. From 10:20 onwards the deviation is below 15% and from noon onwards it is significantly lower than 10%. The deviation could be significantly reduced especially due to the more precise determination of the wind velocity.

For monitoring the thermal yield with the BIM method, the first approach can be implemented with manageable effort (laboratory characterization), because the parameters are either available from data sheets or can be determined with a standard test procedure in the lab. Both possibilities are much easier than a field measurement. However, the deviation is significantly larger compared to the use of field measurement parameters and this aspect should be considered for the further development of the method.

Analogously to the thermal yield, the electrical efficiency measured in the laboratory according to standard conditions (STC) is used to monitor the electrical yield. Fig 8 shows that the simulated electrical yield represents the measured electrical yield with high accuracy. The deviation is less than 3%. It should be mentioned that the dependence of the simulated electrical yield on the module temperature is not considered.

The measured data (thermal as well as electrical yield and global radiation) are linked in the CDE with a time resolution of 5 min to the BIM model as described in the next sections. For the BIM-based monitoring approach, the selected sensors listed in Tab. 3 were used if the target data are determined according to eq 1.

Tab. 3: Sensors for the BIM-based monitoring concept

1	Pyranometer (G)	**5**	Coriolis (m_dot)
2	Pyrgeometer (IR)	**6**	Anemometer (u)
3	PT-100 (T_{in})	**7**	Ambient air temperature sensor (T_a)
4	PT-100 (T_e)		

6. CDE as a central basis for yield monitoring and other use cases

The CDE serves as a central communication and collaboration platform in a BIM project (so-called single source of truth). The main functions of a CDE are information exchange, collaboration, visualization and quality assurance. The CDE is used to exchange BIM models, documents, and collaboration assets, with various open data formats, such as IFC, to ensure successful project delivery regardless of the software products used by the stakeholders. For the operational phase the browser-based CDE allows users to visualize retrieved monitoring data in real time (dynamically). Deviations from target data (in our case thermal and electrical yield) can be detected and the failure of specific components (in our case a PVT module) can be diagnosed automatically. In case of a failure, the faulty component can be located easily and visualized by the 3D representation of the system (in our case the PVT-façade).

The possibilities of using a CDE as a platform in projects with PVT façades and their monitoring are manifold. As shown in Fig 9, a CDE (in this case Squirrel CDE developed by the project partner albert.ing) displays and links the component objects and their semantic properties of an IFC model. For the considered yield monitoring, a CDE mockup was created, which allows the import of target and measured data of PVT systems. The measured data include global radiation, specific thermal as well as electrical yield (see Fig 8). The determination of the target data is listed under 5.

The platform highlights deviations of the actual yields from the predicted values that exceed a predefined tolerance threshold. If this occurs, the corresponding PVT string is colored red to enable clear evaluability and thus ensure practicable operation of the PVT façade, otherwise the corresponding PVT string is colored green (as shown in Fig 9). The maximum permitted deviation between actual and target data is exemplarily selected in the representation in order to illustrate the BIM-based method for monitoring.

If one or more strings are colored red, the person responsible for the system operation is contacted and informed automatically. If maintenance is necessary, all required data such as warranty, manufacturer and installation data are available in the CDE. After repair or replacement, the correspondent data have to be updated. Other BIM model-based use cases can be processed in a similar way.

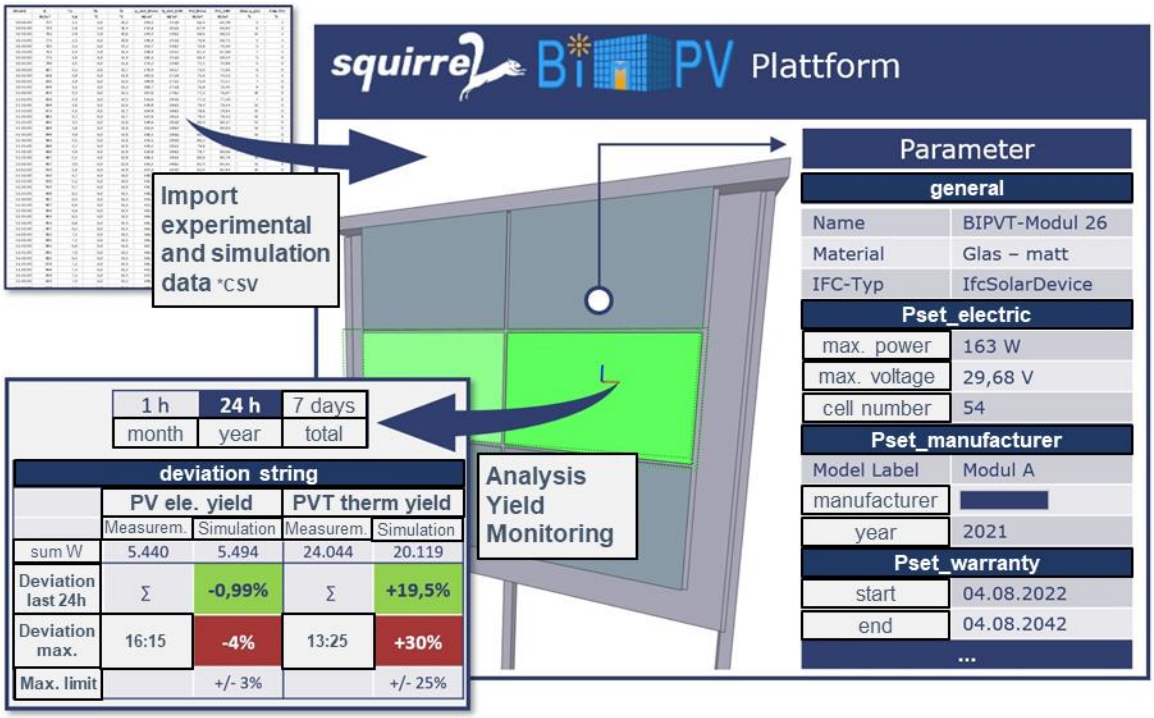

Fig 9: BIM-based monitoring concept of a PVT façade

7. Summary and outlook

Building Information Modeling is a not yet well-established but very promising method for the planning, construction and operation of buildings (building envelope, technical building equipment, etc.). It generally improves collaboration and data exchange between the stakeholders involved in the entire construction process and can be fundamentally applied to all life cycle phases of a building. With regard to the energy supply system, its application can reduce errors due to data loss, manual data transfer, traditional communication methods or model duplication, thus saving time and costs. However, there are still many limitations to its use, especially for solar components and systems. The available models of PV or ST are neither consistent nor fully parameterized. To date, there are no object models for PVT. In addition, the use of the BIM method has so far mainly been limited to the planning process due to its complexity.

In order to use the BIM method in the operational phase to monitor a PVT façade, a BIM model of the existing plant was developed in Autodesk Revit BIM authoring software. The BIM model was further used to create a digital twin on a BIM platform (CDE). The CDE not only stores all necessary data of the PVT façade, but also allows the display and evaluation of the measured thermal as well as electrical yield. It also compares the measured data with the target data, which is based on performance parameters of the module and measured weather data. If the deviation between the measured and simulated data is higher than allowed, the affected PVT string is marked in red. In this case, the responsible person is requested to check the strings and possibly repair or replace defective components.

Within the scope of the project, the first steps for the representation of solar components as BIM models as well as for the methodical linking with the BIM platform both for the planning and for the operation of the façade have been developed so far. For a practical application, the following crucial questions remain to be answered:

- Is the data from available laboratory measurements sufficient for parameterization and especially for BIM-based monitoring of building-integrated solar systems, or is operating data required as target data for this purpose?
- Which minimum measurement equipment is required for successful BIM-based monitoring of a PVT façade to make the concept feasible and economical?

- Which deviation tolerance in terms of target data and uncertainty of measured data is plausible?
- Which time resolution of the actual data is plausible for BIM-based monitoring?

In answering these central questions, one can draw on the existing, extensive know-how of monitoring and fault detection in the field of solar thermal systems like (Pärisch and Vanoli, 2007)and (Schmelzer et al. 2021).

8. Acknowledgments

The joint project "Retrospective BIM approach for life cycle optimized integration of BIPV systems into the building envelope" (BIMPV, FKZ 03EN1010B), on which this publication is based, is funded by the German Federal Ministry of Economics and Climate Protection, following a decision of the German Parliament, and by the State of Lower Saxony. The authors would like to express their sincere thanks for the support. The responsibility for the content of this publication lies solely with the authors.

9. References

Bimetica, 2023. Bimetica. Online available at https://bimetica.com/resultado-busqueda.php?lang=de, last access on 09.10.2023

BIMobject, 2023. Online available at https://www.bimobject.com/de, last access on 20.10.2023.

buildingSMART, 2023. The International Home of BIM. Online available at https://www.buildingsmart.org/, last access on 09.10.2023.

buildingSMART, 2023. IfcSolarDevice schema by BuildingSMART. Online available at https://standards.buildingsmart.org/IFC/RELEASE/IFC4/ADD2_TC1/HTML/schema/ifcelectricaldomain/lexical/ifcsolardevice.htm, last access on 09.10.2023.

DIN EN ISO 16739, 2021. Industry Foundation Classes (IFC) for data sharing in the construction and facility management industries - Part 1: Data schema, German version.

DIN EN ISO 9806, 2017. Solar energy - Solar thermal collectors - Test methods, German Version.

BMI, 2021. Masterplan BIM für Bundesbauten.

BMDV, 2021. Masterplan für die Digitalisierung im Bundesfernstraßenbau.

Frick, E., Kirchner, M., Büttner, C., Wehmeier, T., Giovannetti, F., 2022. Dynamische Charakterisierung solarthermisch aktiver Fassaden als Quelle für Wärmepumpensysteme. Proceedings of the Symposium "Solarthermie und innovative Wärmesysteme", 03.-05. Mai 2022, Bad Staffelstein, Germany, Conexio-PSE GmbH.

Mandow, W., Edenhofner, F., Maier, T., Giovannetti, F., 2022a. Building Information Modeling for solar energy systems. Proceeding of the ISES Eurosun Conference 2022, DOI: 10.18086/eurosun.2022.16.07.

Mandow, W., Edenhofner, F., Maier, T., Giovannetti, F., 2022b. Building Information Modeling (BIM) für die Abbildung solarer Komponenten. Proceedings of the Symposium "Solarthermie und innovative Wärmesysteme", 03.-05. Mai 2022, Bad Staffelstein, Germany, Conexio-PSE GmbH.

MEPcontent, 2023. MEPcontent. Online available at https://www.mepcontent.com/de/bim-files/, last updated on 05.04.2023, last access on 09.10.2023.

NBS, 2023. National BIM Library. Online available at https://www.nationalbimlibrary.com/en/what-is-nbs-national-bim-library/, last access on 09.10.2023.

Paerisch, P., Vanoli K., 2006. Quality assurance of solar thermal systems with the ISFH- Input/Output-Procedure. Proceedings of the 6th ISES EuroSun Conference, Glasgow.

Schmelzer, C., Georgii, M., Kussy, O., Sauer, C.,Orozaliev, J.,Vajen, K., Lang, S. et al., 2021. Entwicklung eines einheitlichen Verfahrens und eines anschaulichen Indikators zur Feststellung der Funktionsfähigkeit thermischer Solaranlagen für Trinkwarmwasserbereitung und kombinierte Heizungsunterstützung. Final Report of the German project "SolarCheck", reference no. 325870A/B.

Schöck Bauteile GmbH, 2023. Schöck Bauteile GmbH. online available at https://www.schoeck.com/de/home, last access on 09.10.2023.

VDI 2552, 2020. Building information modeling Fundamentals.

Appendix: Units and Symbols

Quantity	Symbol	Unit
A_G	*Gross Area of collector*	m²
a_1	*Heat loss coefficient*	$W/(m^2K)$
a_2	*Temperature dependence of the heat loss coefficient*	$W/(m^2K^2)$
a_3	*Wind speed dependence of the heat loss coefficient*	$J/(m^3K)$
a_4	*Sky temperature dependence of the heat loss coefficient*	-
a_5	*Effective thermal capacity*	$J/(m^2K)$
a_6	*Wind speed dependence of the zero loss efficiency*	s/m
a_7	*Wind speed dependence of IR radiation exchange*	$W/(m^2K^4)$
a_8	*Radiation losses*	$W/(m^2K^4)$
G	*Hemispherical solar irradiance*	W/m²
G_{hem}	*Hemispherical solar irradiance*	W/m²
G_b	*Direct solar irradiance (beam irradiance)*	W/m²
G_d	*Diffuse solar irradiance*	W/m²
Kb	*Incidence angle modifier for direct solar irradiance*	-
Kd	*Incidence angle modifier for diffuse solar radiation*	-
Qth	*Thermal power output*	W
q_dot	*Specific thermal power output*	W/m²
m_dot	*Mass flow rate*	kg/h
u	*Surrounding air speed*	m/s
$\eta 0,b$	*Peak collector efficiency based on beam irradiance G_b*	-
$\eta 0,hem$	*Peak collector efficiency based on hemispherical irradiance G_{hem}*	-
ϑa	*Measured ambient air temperature*	°C
ϑm	*Mean temperature of heat transfer fluid*	°C
ε	*Hemispherical emittance*	-
α	*Solar absorptance*	-

DEVELOPMENT AND COMPARATIVE ANALYSIS OF A BOTTOM-UP HEAT DEMAND MODELLING TOOL WITH EXISTING HEAT DEMAND ESTIMATION METHODS FOR GERMANY

Gokarna Dhungel, Theresa Reinhardt, Christoph Schmidt, Viktor Wesselak and Thomas Schabbach

Institut für Regenerative Energietechnik, Nordhausen University of Applied Sciences, 99734 Nordhausen, Germany

Abstract

Demand modelling is an integral part of energy system modelling and the accuracy of an energy model depends highly on the precise value of demand. Taking into account the limited number of open-source heating demand modelling tools available, this paper aims to present a new bottom-up simplified heating demand modelling tool that can create heating curves of high resolutions for any geographical locations and different building types. The tool is a physical model of demand modelling based on general heat balance equations for buildings. A comparative analysis of the outputs obtained from this tool with existing open-source heat demand modelling tools is then carried out. The results of the simulation shows that the heating duration curves obtained are very comparable to the outputs from the BDEW heating profiles that are considered to be the standard heating load profiles for Germany. On the other hand, the output from VDI 4655 that uses a generalized method and input parameters deviates the most, both in terms of peak demand and heating curve.

Keywords: demand modelling, open-source, bottom-up, heating demand, physical model, demandlib, demand.ninja, vdi 4655

1. Introduction

With increase in the renewable share in energy supply system, the energy supply system is growing more complex. Some of the reasons for the complexity account to intermittent nature of energy supply from renewable energy sources such as PV and wind. Moreover, the concept of sector coupling adds to making energy models more complex. Implementing sector-coupled heating systems with more renewable sources like wind and solar contributing in the heating sector demands for the heating profiles with higher spatial and temporal resolutions. Regarding that factor, the traditional ways of estimating heating demand may have limitations in building efficient energy models. There are several tools and methods that are used for creating heating profiles for buildings. EnergyPlus (U.S Department of Energy, 2020), TRNSYS (TRNSYS Software, 2019), IDA (eQUA AB, 2019) etc. are some of the popular tools used for building energy simulation that also includes the heating demand modelling. All the tools mentioned above are, however, not open-source and thus have limitation in contributing to scientific research. There are very less number of open-source tools dedicated particularly to creating total heating demand and heating profiles with high temporal resolutions. Some of the open-source tools widely used in Germany for demand modelling and used for comparison with the physical model are described in the section below.

The aim of this study is to develop a simplified heating demand modelling tool based on physical demand modelling method using python programming language and compare the tool with some open-source demand modelling tools used predominantly in Germany. A standard building from TABULA Typology (TABULA Project Team, 2012) and the weather data of Nordhausen city of the year 2019 is used for the simulation. The hourly demand and the monthly heating demand is estimated using all the tools that form the basis of comparison.

The tools that are used for the comparison are briefly described below.

10.18086/swc.2023.06.05 Available at http://proceedings.ises.org

1.1. Demandlib

Demandlib (oemof Developer Group, 2016) is an open-source, python-based demand modelling tool that can be used to create heat and electricity load profiles. It utilizes the standard load profiles from BDEW (German Association of Energy and Water Industries) (Meier et al., 1999) to create heating and electricity demand curve by taking the annual energy demand as input. Since the standard load profiles are valid for the context of Germany only, it cannot give precise results to model energy demand outside Germany. It can be used to model the demand in residential as well as commercial buildings.

1.2. VDI 4655

VDI is an abbreviation of 'Verein Deutscher Ingenieure' that translates to Association of German Engineers. VDI 4655 (VDI, 2021) is a guideline that can be used to create reference heat, power and domestic hot water load profiles for residential buildings in Germany. The model uses the weather data from German weather service to differentiate the days of the year into 10 different day types based on the temperature, cloudiness, working or non-working day type and seasons. Each of these 10 day types have a specific energy curve that can be distributed to the days of a whole year to create a yearly load profile with daily resolution. In addition, this approach uses a subdivision of Germany into 15 different climate zones and is capable of producing load profiles for places in Germany only.

1.3. Demand.ninja

Demand.ninja (Staffel et al., 2023) is an open-source grey-box model that models hourly demand for heating and cooling energy and uses the heating degree-days method, which is calculated using building-adjusted internal temperature (BAIT) parameters that describe the building and its occupant's characteristics. The demand obtained using the degree day method is, however, later converted into profiles of high resolution by incorporating the weather variables and other statistical parameters. It also has a graphical user interface where one can input the selected input parameters to create a heating profile for any place globally. The input parameter are however limited and there is not much room for modelling individual buildings, rather a representative demand for a region can be obtained. The tool is a very recent addition in the pre-existing renewables.ninja tool (Pfenninger and Staffel, 2016; Staffel and Pfenninger, 2016), which is used to generate hourly solar and wind generation profiles.

The proposed tool will be able to create demand curves for any locations based on the input data fed. An overview of the existing tools and the proposed tool is shown in table 1.

Tab. 1: Overview of considered modelling tools

Tool	Modelling Approach	Resolution	Building Types	Application
Demandlib	Top-down	15 min	All	Germany
VDI 4655	Top-down	hourly	Residential	Germany
Demand.ninja	Bottom-up	hourly	All	No restriction
Proposed tool	Bottom-up	Up to 1 min	All	No restriction

2. Methodology

The physical model of heating demand is developed based on the following heat balance equation for buildings (Wesselak et al., 2017).

$$Q_H(h) = Q_T(h) + Q_V(h) - Q_S(h) - Q_I(h) \; for \; T_a(h) < T_{BP} \qquad \text{(eq. 1)}$$

where,

$Q_H(h)$ = heating demand (for temporal resolution h)

$Q_T(h)$ = transmission (fabric) heat losses

$Q_V(h)$ = ventilation losses

$Q_S(h)$ = solar gains

$Q_I(h)$ = internal gains

T_a = ambient temperature

T_{BP} = balance point temperature

The individual heating losses and gains depend on several other factors, which are described below in brief.

2.1. Transmission heat losses

Transmission heat loss is the amount of heat that is lost from a room through various components such as walls, windows, roof etc. and is calculated using the following equation.

$$Q_T = H_T \,.\, (T_i - T_a) \qquad \text{(eq. 2)}$$

$$H_T = F_{x,i} \,.\, U_i \,.\, A_i \qquad \text{(eq. 3)}$$

where, T_i represents the required internal temperature in the building and the terms F, U and A represent the correction factors, the u values and the area respectively.

2.2. Ventilation heat losses

Transmission heat loss is the amount of heat lost through ventilation (opening of windows and doors and other openings) and is calculated using the equation below.

$$Q_V = H_V \,.\, (T_i - T_a) \qquad \text{(eq. 4)}$$

$$H_V = \mathrm{n} \,.\, 0.34 \,.\, V_L \qquad \text{(eq. 5)}$$

where, the terms n and V represent the airflow rate and the effective volume that is heated.

2.3. Solar heat gains

It is the total amount of heat gained due to the energy gained from the solar irradiation falling on the object. The solar gain is dependent on the factors like g value and area of the windows, and the amount of irradiation entering inside through the windows.

$$Q_s = 0.567 \,.\, g_F \,.\, A_{F,i} \,.\, G_{T,i} \qquad \text{(eq. 6)}$$

2.4. Internal heat gains

Internal heat gains account to the amount of heat produced inside the building because of the internal conditions such as due to the heat gains from electrical appliances and the heat produced by the people living inside. For simplicity, the hourly electricity demand of the object is taken as the internal heat gain in the model.

The balance point temperature (T_{BP}) is the ambient temperature above which the building requires no heating. The value of the balance point temperature in this simulation is taken as 15 °C.

For simplicity, the thermal energy stored in various objects of the building is neglected in this model by setting the thermal capacity to zero. The equation 1 is used to develop a model in python programming language to calculate the corresponding heating profiles. The heating profiles obtained from this model are then compared with the profiles form other methods of heating load determination.

Based on the equations presented above, it is evident that several input parameters are required to create a heating demand profile for a building. Comparison of the heating profile obtained from different tools is not always a simple task, since different tools take different parameters and methods into consideration. For the comparison purpose, to maintain uniformity, the dimensions of a single family house built within the construction period 2002 to 2009 in Germany is taken from the TABULA Web tool (TABULA Project Team, 2012). The weather data is taken from the renewables ninja website (Staffel and Pfenninger, 2016; Pfenninger and Staffel, 2016) for the year 2019 for all cases. The following table presents the input parameters considered to model a heating demand using the proposed physical model.

Tab. 2: Input parameters used for the heating demand modelling using the proposed tool

Parameters	Unit	Value
Total Floor area	m^2	147
Height	m	2.5
Window area north	m^2	3.1
Window area east	m^2	3.9
Window area south	m^2	19.3
Window area west	m^2	3.9
Window area roof	m^2	0
Envelope area	m^2	219
Ground floor area	m^2	80
u value wall	W/m^2K	0.3
u value window	W/m^2K	1.4
u value roof	W/m^2K	0.25
u value floor	W/m^2K	0.28
air flow rate	1/h	0.5
Required temperature	°C	20
Balance point temperature	°C	15
Night setback temperature	°C	15
gF	-	0.486

3. Results and Discussion

The heating demand is estimated for the reference building using the simplified physical model with the input parameters described in section 2. The total amount of heating energy required to heat the reference building is obtained as 12.504 MWh that corresponds to around 85 kWh / m^2. The total heating demand obtained from the physical model is fed into the other tools to create a heating curve using each tool. The results from all the four tools used for comparison are shown in figure 1. It is apparent from the figure that the profiles have a fair daily and seasonal variation for the first three tools whereas the output from the VDI 4655 tool shows comparatively lesser variation.

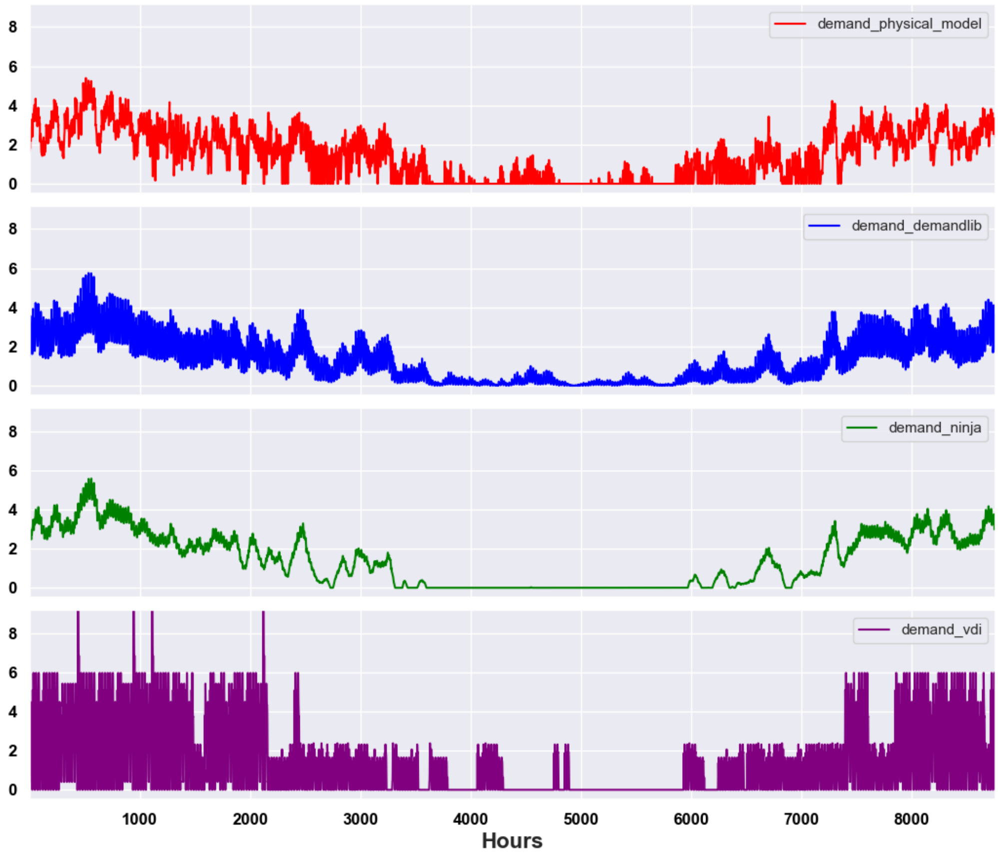

Fig. 1: Hourly heating demand curve generated using the four modelling tools

Figure 2 shows the yearly load duration curve of the demand profiles obtained using the four tools. On comparison of the duration curves, it can be seen that the duration curves for the physical model and the demandlib are comparable except for the rightmost part of the curve i.e. for the lowest heat demand hours. The physical model assumes that the heating demand for the hours with temperature greater than 15 °C is zero whereas the demandlib has non-zero demand estimation throughout the year. Greatest deviation in the profile is seen in the output of VDI 4655 where the peak demand is about 65 % greater than the other three cases and both the hourly curve and load duration curve shows a large difference compared to other three tools.

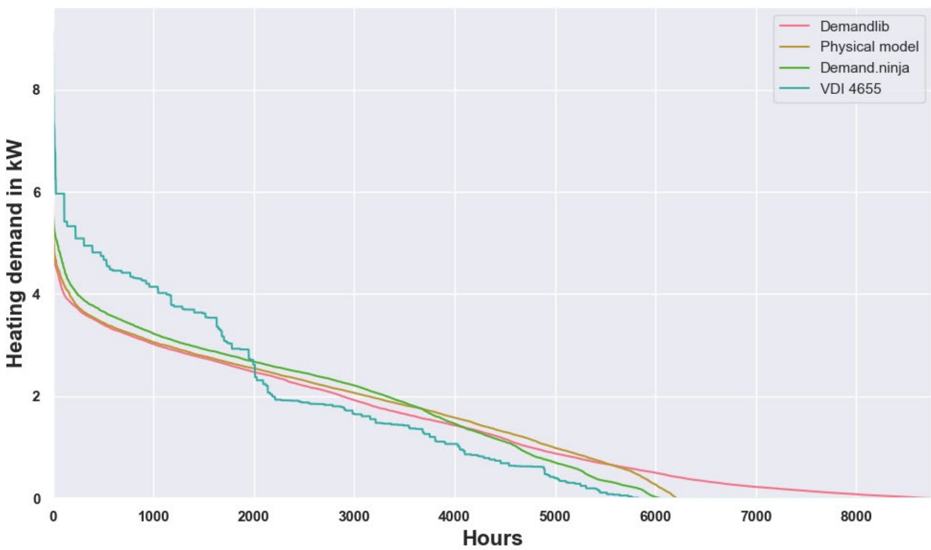

Fig. 2: Load duration curves of the hourly heating demand obtained from the four tools

Table 3 depicts the peak heating demand obtained using each tool. It can be seen that the peak demand obtained using the physical model, demandlib and the demand.ninja tool are almost equal whereas the peak demand obtained using the VDI method largely deviates from the other tool.

Tab. 3: Peak demand values obtained using each modelling tool

Tool	Peak demand (kW)
Physical model	5.39
Demandlib	5.75
Demand.ninja	5.57
VDI 4655	9.15

The aggregated monthly heating demand obtained using each of the four tools is represented in figure 3. It is apparent from the figure that the monthly demand obtained using the proposed tool are consistent with the demand data obtained from the demandlib tool.

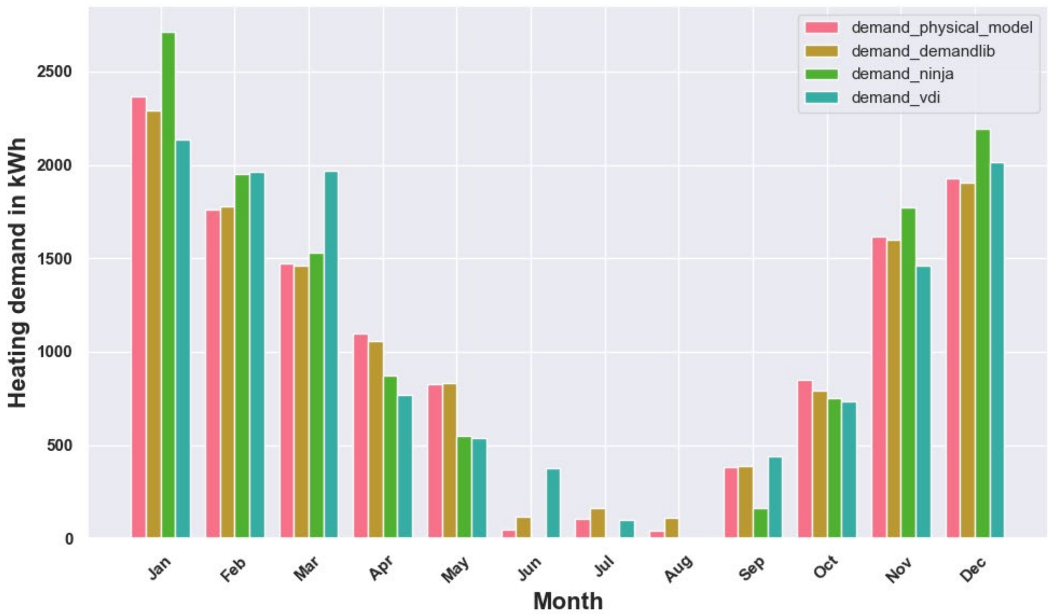

Fig. 3: Bar plot showing the monthly demand data for each of the modelling tools

4. Conclusion

In this study, we have presented a simplified heating demand modelling tool using the physical demand modelling method that gives the total heating demand as well as an hourly heating curve for any type of buildings using some building characteristics and weather data as input parameters. We have then compared the outputs of the tool to some of the existing open-source tools used to create demand curves in Germany. The advantages of the tools to the existing tools are its simplicity and flexibility to create demand profiles using given input parameters. The tool, however, has limitations and is open for further development. Some of the possibilities that can be implemented are the consideration of the thermal capacity of various objects within the buildings and a detailed modelling of the internal heat gains using occupancy factor. These parameters are not modelled in the existing tool. They may have a greater impact while modelling buildings with very low specific heating demand. The results from the comparison shows that the methods like VDI 4655 that uses conventional methods for demand estimation may deviate largely in estimating demand curves and must be used with additional consideration for precise heating demand estimation. The proposed tool gives demand estimation comparable to the standard heating demand profile used in Germany.

Acknowledgements

This work was a part of the project KLIMA-N (KLIMA Netzwerk für mehr Nachhaltigkeit in Thüringen – Climate network for more sustainability in Thuringia), funded by the Bundesministerium für Bildung und Forschung, BMBF (Federal Ministry of Education and Research, Germany).

References

oemof Developer Group, 2016. The oemof demandlib (oemof.demandlib). Zenodo. https://doi.org/10.5281/zenodo.438786, (accessed on 12 April 2023)

TABULA Project Team, 2012. Typology Approach for Building Stock Energy Assessment. Main Results of the TABULA project, Darmstadt

VDI (Verein Deutscher Ingenieure), 2021. Reference load profiles of residential buildings for power, heat and domestic hot water as well as reference generation profiles for photovoltaic plants.

Wesselak, V., Schabbach, T., Fischer, J., Link, T., 2017. Handbuch Regenerative Energietechnik. third ed.; Berlin: Springer Vieweg; 2017. ISBN 978-3-662-53072-6. doi: 10.1007/978-3-662-53073-3.

Meier, H., Fünfgeld, C., Adam, T., Schieferdecker, B., 1999 Repräsentative VDEW-Lastprofile, Frankfurt am Main. Available online: https://www.bdew.de/media/documents/1999_Repraesentative-VDEW-Lastprofile.pdf (accessed on 12 April 2023)

U.S. Department of Energy. (2020). EnergyPlus. https://energyplus.net/

TRNSYS Software. (2019). TRNSYS. https://www.trnsys.com/

eQUA AB. (2019). IDA Indoor Climate and Energy. https://www.equa.se/en/ida-ice

Staffell, I., Pfenninger, S. & Johnson, N., 2023. A global model of hourly space heating and cooling demand at multiple spatial scales. Nat Energy. https://doi.org/10.1038/s41560-023-01341-5

Pfenninger, S. and Staffell, I., 2016. Long-term patterns of European PV output using 30 years of validated hourly reanalysis and satellite data. Energy 114, pp. 1251-1265. doi: 10.1016/j.energy.2016.08.060 www.renewables.ninja

Staffell, I. and Pfenninger, S., 2016. Using Bias-Corrected Reanalysis to Simulate Current and Future Wind Power Output. Energy 114, pp. 1224-1239. doi: 10.1016/j.energy.2016.08.068

EFFECT OF BUILDING FORM ON DAYLIGHT AND ENERGY EFFICIENCY FOR EDUCATIONAL BUILDING IN COMPOSITE CLIMATE

Pushpendra Chaturvedi, Dr. Nand Kumar, Dr. Ravita Lamba, Pushkar Nachan

Malaviya National Institute of Technology, Jaipur, India

Abstract

Adequate daylight design with balanced energy consumption is the prime concern of architectural principles, especially in educational buildings. It not only reduces the building's operational energy demand but also enhances pupils' learning productivity and reduces mental stress by maintaining a healthy indoor environment. This paper presents a parametric simulation approach using the Rhinoceros' Grasshopper tool to investigate the visual comfort and energy efficiency of a school building situated in the semi-arid composite climate of Jaipur (India). Useful Daylight Illuminance (UDI), Daylight Autonomy (DA), Uniformity Ratio, Average Lux, Cooling Energy Demand (CED), and Heating Energy Demand (HED) are assessed as performance indicators with nine different building forms in each orientation. The building forms include single and double line I shapes, L, U, square, hexagonal, rectangle, H, and circle shapes, and their effectiveness on building visual and energy performance has been investigated. This research demonstrates that optimal building form enhances the UDI and uniformity ratio by 35.83% and 293%, respectively, and reduces cooling and heating energy demand by 22.82% and 23.93%, respectively. This analysis provides decision-making support for architects and engineers for building form design in the early design stage to ensure visual and energy performance.

Keywords: Visual comfort, Cooling and heating energy demand, Building form, Rhinoceros' Grasshopper

1. Introduction

School is a very imperative educational space where students spend 50% of their time to sharing information, learning, and interacting with tutors [1]. Creating a healthy indoor environment is a crucial aspect of architectural design principles [2]. Numerous past studies demonstrate how comfort (visual and thermal) levels in surroundings have a significant impact on learning [3]. Better daylight in school helps to create a pleasant learning environment, promotes better health, and provides significant energy savings [4]. Therefore, the provision of daylight in educational spaces is internationally recognized. Moreover, it is the most crucial design challenge in architecture. Visual comfort is the subjective sensation of contentment with the visual system that defines the occupant's perceived satisfaction with lighting conditions, levels, and views in the occupied space for performing specific tasks [5]. Visual comfort is affected by various factors, such as environmental, human, and physiological. The environmental factors are mapped as illumination level, glare, colours, and uniform distribution of light. The human factor includes exposure time, susceptibility to glare, and age. The physiology factor encompasses motivational and transient adaptations [6–7]. There are several indexes available to evaluate the many aspects that influence visual comfort, including the amount of daylight, consistency, quality, and glare of the light. The assessment criteria to measure daylight is the quantity of natural light. Meanwhile, various metrics are available to quantify the daylight. To assess the quantity of daylight, illuminance, daylight

10.18086/swc.2023.06.03 Available at http://proceedings.ises.org

factor (DF), daylight autonomy (DA), useful daylight illuminance (UDI), continuous daylight autonomy, intensity of visual comfort, etc. are available. Besides, illuminance uniformity was used to measure the uniform distribution of daylight in the space [8-10]. Many past studies were available that focused on the investigation of daylight by exploring various envelope design variables through simulation and parametric optimizations. Szentesia et al. (2022) investigate the provision of a uniform distribution of daylight in the classroom building. This research illustrates that the integration of light shelves and skylights enhances the uniformity ratio of daylight [11]. Mushtha et al. (2019) examined daylight factor, glare, and cooling load for the 15 existing school buildings and found that most of the buildings failed to achieve a sufficient luminous level inside the space. Therefore, it is the cause of higher energy demand [12]. Mohammad and Zahra (2016) illustrate that the placement of a lighting shelf at an optimized angle can reduce the glare in the space and enhance the work plane area by 2-40%. It also reveals that southern façade glazing with the integration of a light shelf can reduce the lighting load by 60% in arid climates [13]. Aniela (2020) shows that the orientation of the classroom has a significant impact on operational energy demand. This research investigates the effect of daylight on lighting energy demand with the placement of lighting sensors. It reveals that an optimum orientation of building spaces can achieve 28% energy savings [14]. Mohamed et al. (2022) examined the effect of automatic shading strategies on the indoor thermal visual environment of school buildings [15]. Khaoula et al. (2021) investigate the effect of envelope design, including wall, glass, window-to-wall ratio, and shading, on energy consumption, daylight, and thermal comfort. This research was evaluated by parametric optimization using the Rhinoceroses' Grasshopper tool [16]. Although exploring all the previous literature reviews, the authors identified a lack of research available that extensively examines the effect of various building forms on daylight and energy consumption. Therefore, this work focused on the effects of various building forms that are typically used in architectural design and their significant impact on daylight and energy consumption. Visual comfort and cooling energy demand might have a contradictory relationship in tropical climates. However, enhancing the daylight by envelope, opening, orientation, and building geometry does not give a guarantee of thermal performance because of the penetration of heat inside the building space. To maintain the indoor thermal environment occupant required to run the air-conditioning. Meanwhile, it increases the cooling energy demand. Therefore, this research focused on identifying the optimal building form that is suitable to maintain the trade-off between daylight and cooling consumption in education buildings. The novelty of this study is to investigate the impact of building geometry on various daylight matrices along with cooling energy demand for education building. Moreover, the methodology of this research was applied to the existing allocated site of a school building. In this research, the authors developed nine different building forms such as single I, double I, L, U, square, hexagonal, rectangle, H, and circle shapes, with equal buildup area and volume in a Rhinoceroses tool. Grasshopper was used to investigate the performance objectives such as daylight and energy demand. Useful Daylight Illuminance (UDI), Daylight Autonomy (DA), Uniformity Ratio, and Average Lux were used as performance indices for daylight, and for the determination of energy demand, Cooling Energy Demand (CED), and Heating Energy Demand (HED) were taken into account. This research demonstrates that optimal building form enhances the daylight and reduces the energy demand.

2. Methodology

This section presents the methodological approach used for this research. It comprises into three sequential approaches, as shown in Fig. 1. Step 1 shows the development of different building forms; the second step illustrates the assign the building performance objectives as daylight and energy consumption; and finally, the third step reveals the results and outcomes.

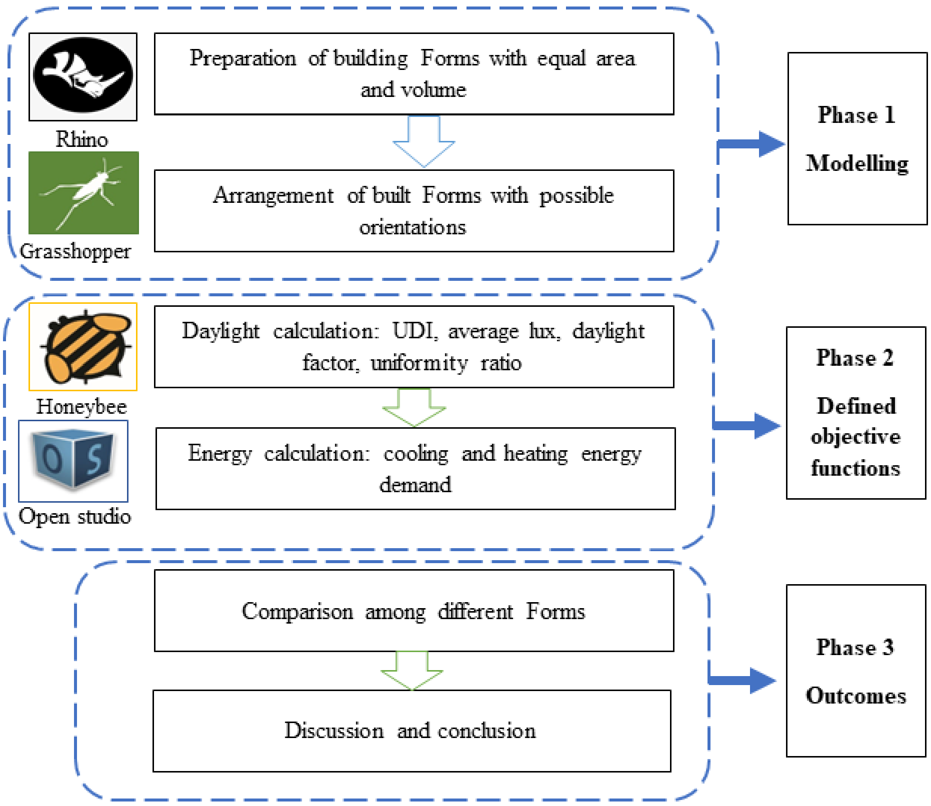

Fig. 1: Methodological hierarchy for simulation

3. Building model

A 3D Rhinoceroses software was used for the modeling. A working site allotted for a school building was assumed for the analysis, which is shown in Fig. 2. It is situated in the composite semi-arid (Köppen climate classification: Bsh) climate zone of Jaipur, India. Jaipur has extremely hot summer (45°C) and cold winter (4°C) temperatures [17]. Therefore, building form has a very crucial role in thermal comfort and energy consumption. In this work, different building forms were created with equal area and volume. Fig. 3 shows the possible building forms created in the Rhino tool. Furthermore, the Grasshopper plugin was used coupled with Rhino for simulation. The created building form was arranged in the possible building orientations as depicted in Fig. 4.

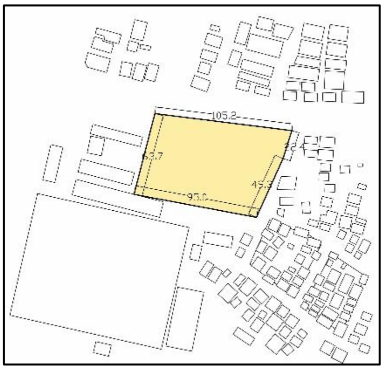

Fig. 2: Site plan for school building

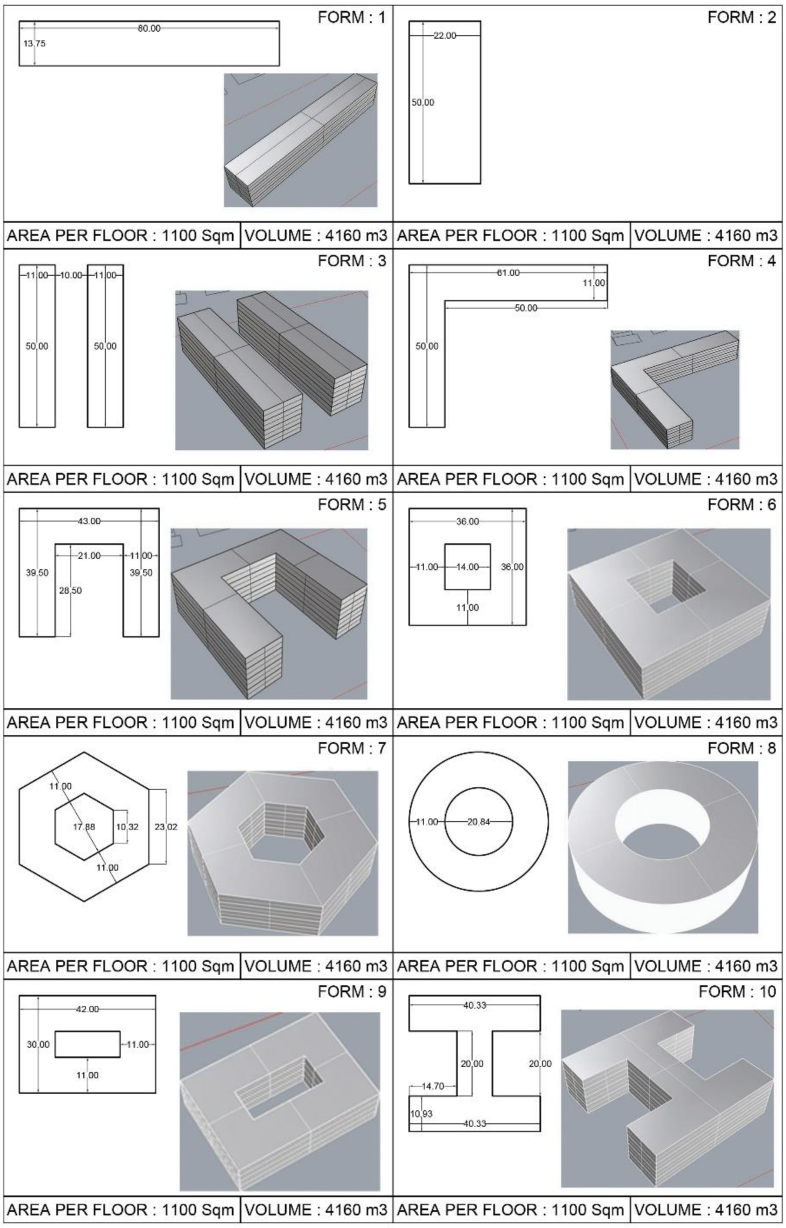

Fig. 3: Different building forms with area and volume

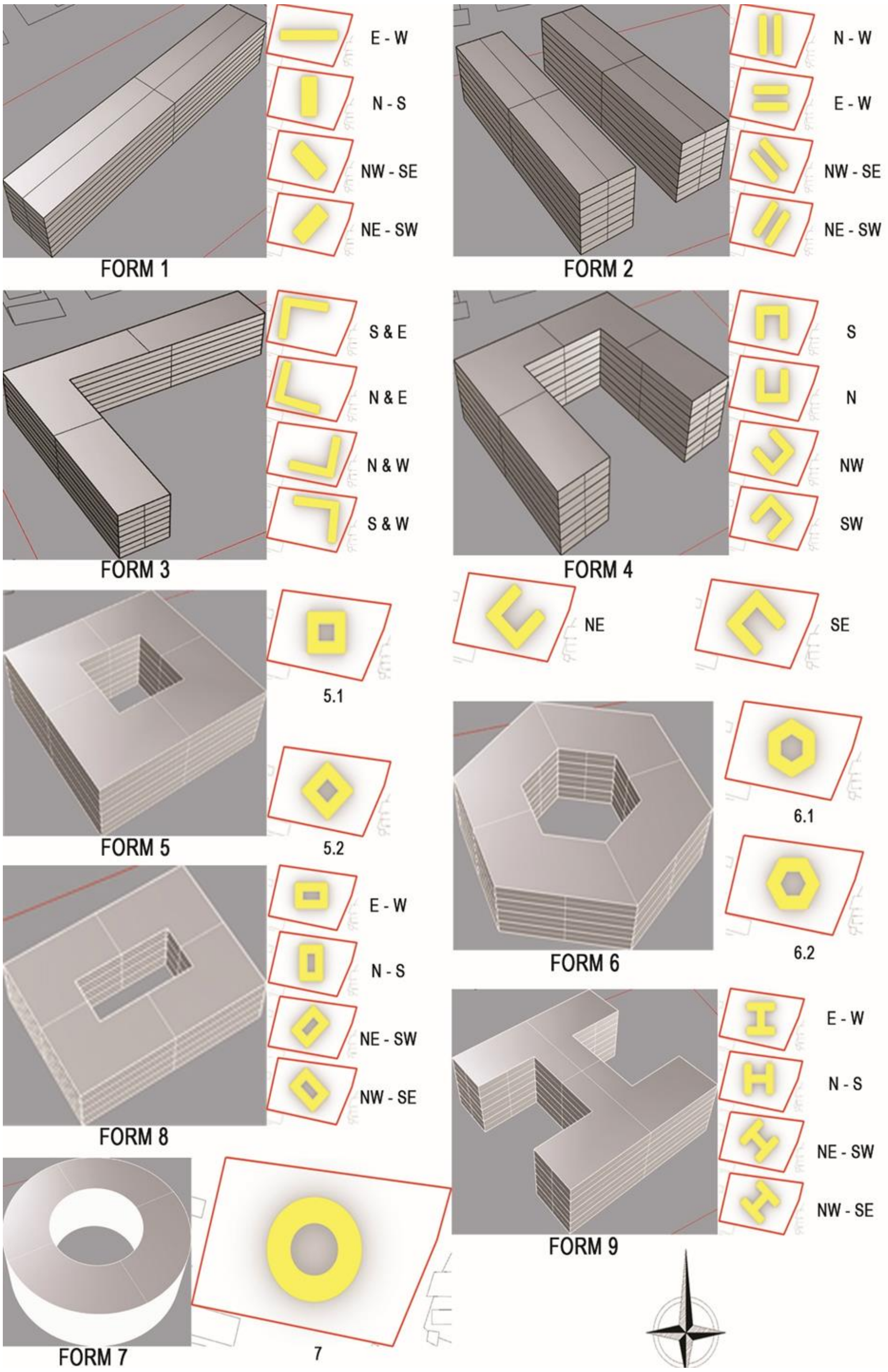

Fig. 4: Different possible orientations for simulation

4. Performance Objectives

In this research, two objectives with different indices were used for simulation. Assessing the quantity of daylight, average lux, useful daylight illuminance (UDI), daylight autonomy (DA), and uniformity ratio were calculated. For the energy calculation, cooling and heating were taken into account.

4.1. Lux

It is the unit of illuminance; it is defined as the amount of light falling on the surface called illuminance. It is used to create a local and short-term metric that evaluates the amount of light using a one-tailed criterion. [18]. Different illuminance threshold was defined for different types of buildings and kinds of use of spaces. In this research minimum 500 average lux level at a work plane height of 0.8 meter was taken into account as a threshold criterion.

4.2. Useful daylight illuminance (UDI)

It is defined as the fraction of time during which horizontal illuminance falls in the indoor space within a defined range. The lower and upper thresholds of illuminance are split into three bins to analyze the period of daylight availability. Upper bins (<2000 lux) show the overflow of daylight, which might be the cause of glare and visual discomfort. Lower bins illustrate the time period when the illuminance range (>100 lux) that is too dark. And intermediate bins (100–2000 lux) show the appropriate amount of daylight that comes into indoor space for the defined time period. [19].

4.3. Daylight autonomy (DA)

It is a long-term, one-tailed, and local index that measures the quantity of daylight that is present at a specific location during times when the area is inhabited. It is described as the proportion of occupied hours during the year when the lone daylight source meets a minimal illuminance threshold. [20].

4.4. Uniformity ratio

Visual comfort is related to both the amount and distribution of light in an area. The ratio of the minimal illuminance value to the average illuminance on the specified plane at the specified time moment is known as the illuminance uniformity (U_0) of the specified plane. Eq. 1 was used to calculate the uniformity ratio [21]. Many studies show that the range of uniformity ratio is between 0.30-0.70 as per space and building typology.

$$U_0 = \frac{E_{min}}{E_{average}} \qquad \text{(eq.1)}$$

4.5. Energy demand

Energy demand defined as the amount of operational energy (kWh) is required for an entire period of a year. In this research, the energy performance index (EPI) was calculated for cooling and heating energy [22]. It is the ratio of total annual energy demand and the built-up are of buildings in sq.m. as shown in Eq. 2.

$$EPI\ (kWh/\ sq.m./\ yr.)\ = \frac{Annual\ energy\ consumption\ (kWh)}{Total\ build{-}up\ area\ (sq.m.)} \qquad \text{(eq. 2)}$$

5. Result and discussion

After modeling in Grasshopper, the Radiance and Open Studio simulation engines were used to perform the daylight and energy simulations, respectively. Daylight was calculated at a work plane (table) height of 0.8 m, and lighting sensors were placed in a 2x2 meter grid matrix. An EPW format of the weather file for Jaipur city was imported into Grasshopper to investigate the defined performance objectives. The weather file contains the weather data including dry bulb temperature, wet bulb temperature, due point temperature, humidity, solar radiation (direct and diffused), global horizontal illuminance, wind velocity, and wind direction. Fig. 5 shows the most important weather data profile that has a significant impact on daylight and cooling energy demand. Fig 5 (a) illustrates the day bulb and wet bulb temperature, 5 (b) shows the humidity and 5 (c) shows the global horizontal illuminance (GHR), direct normal radiation (DNR), and direct radiation (DR).

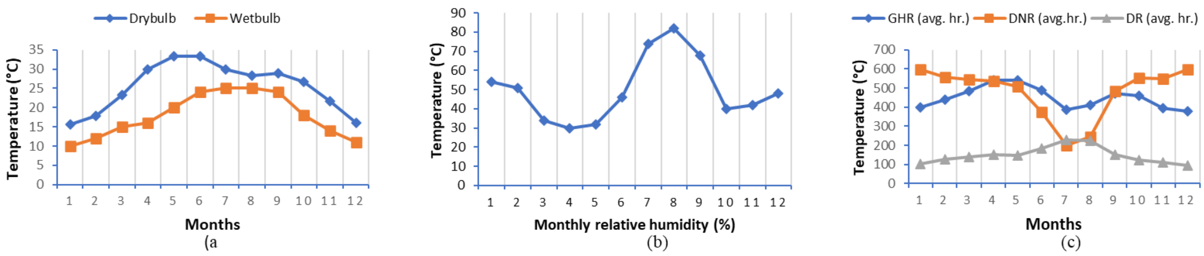

Fig. 5: Typical weather data profile of Jaipur city

The reflectance of the wall, ceiling, and floor was taken as 50%, 70%, and 20%, respectively, as per the energy conservation building code (ECBC) [23]. The calculation of energy demand (cooling or heating) and daylight was conducted for building operational time between 9 a.m. to 5 p.m. as per ECBC. A standard HVAC system type was used as the system configuration. It is an air-load HVAC system in EnergyPlus, which is most suitable in the early design stage considering the calculation time and cost [24]. The cooling set point of 26 °C and heating set point of 18 °C were the most suitable HVAC set point for energy efficiency point of view in tropical climates. The cooling and heating set points are taken as 26 °C and 18 °C, respectively [25]. The occupancy rate and their schedule, infiltration, and other constraints were set as per Indian standards. The ECBC and NBC standards were taken for choosing the setting of schedules during the simulation. Thermal conductivity of wall material 2.41 W/m^{2}K (burnt clay brick) and 3.62 W/m^{2}K (RCC slab) for roofing was taken into account for simulation. Table 1 presents the simulation results of daylight and energy consumption for each building form in different possible orientations. The result demonstrates that the I-shaped building in east-west orientation has higher lux and UDI levels. Because maximum daylight penetration comes from this side. Therefore, in this orientation, the uniform distribution of daylight is also enhanced compared to other orientations. L-shape building form in southwest facing was responsible for higher cooling energy demand. However, in peak summer, the sun's position between 12 p.m. and 3 p.m. is at the top of the building. Therefore, maximum heat comes from the building envelope through conduction and convection. Meanwhile, it enhances the building's cooling energy demand to maintain the indoor thermal environment. H-shaped and hexagonal building forms perform moderately in daylight and energy demand due to their compact building forms.

Table 1 Simulated results for daylight and energy demand

Form	Orientation	UDI	DA	Average Lux	Uniformity Ratio	Cooling Energy Demand	Heating Energy Demand
Single line I-shape	E - W	80.82	94.96	1734.26	22.62	113	18.26
	N - S	75.79	65.67	2254.97	6.86	113.22	18.26
	NE - SW	76.15	65.73	2273.86	9.77	109.4	18.13
	NW - SE	74.88	64.49	1549.37	11.67	111.04	18.71
Double line- I shape	E - W	80.02	86.26	1848.4	29.25	122.65	22.18
	N - S	68.63	96.83	4435.2	10.61	124.55	21.49
	NE - SW	77.51	95.85	3968.27	16.80	126.53	21.85
	NW - SE	78.22	95.36	1981.31	27.02	120.43	22.81
L- shape	S & E Elongation	62.96	98.16	4121.79	15.13	130.34	21.9
	N & W Elongation	59.13	98.51	4410.54	14.21	132.87	21.5
	N & E Elongation	66.26	97.8	4039.66	14.12	134.22	21.56
	S & W Elongation	63.2	97.74	4151.92	14.23	134.77	21.39
U- Shape	South	63.89	97.46	4742.38	10.72	132.72	21.25
	North	64.42	97.5	4516.95	10.59	132.29	21.35
	NW	67.6	97.41	3367.31	14.98	132.03	21.6
	SW	66.59	97.35	3533.33	13.74	132.17	21.48
	NE	68.47	94.98	4231.82	12.04	132.36	21.12
	SE	68.19	94.96	3265.83	14.60	132.14	21.5
Square Shape	1	79.97	83.31	2529.51	18.32	124.78	20.76
	2	79.39	84.12	2663.9	16.95	122.34	20.55
Hexagonal shape	1	68.45	96.7	3931.5	12.02	117.82	21.69
	2	70.94	90.4	3702.55	13.67	118.36	22.47
Rectangle shape	1	68.53	85.24	1862.25	22.75	120.59	20.98
H-Shape	E - W	79.77	94.01	2286.23	17.46	123.14	19.54
	N - S	79.78	94.41	2658.98	15.86	121.74	19.78
	NE - SW	80.3	82.39	2540.95	17.37	120.49	19.64
	NW - SE	79.44	81.85	2363.1	18.19	119.54	19.46
Circle Shape	E - W	70.42	96.63	3384.4	11.48	121.97	21.37
	N - S	73.22	91.09	3608.68	10.21	120.6	20.66
	NW - SE	70.09	96.64	3158.009	12.65	121.84	20.78
	NE - SW	66.34	96.83	4085.9	9.23	122.36	21.35

6. Conclusion

This research purposes is a decision-making approach for building form design in the composite climate of Jaipur, India. An education building site was taken into account for the analysis, and different possible building forms were created and simulated in different directions. A Rhinoceros tool coupled with Grasshopper was used to investigate daylight (average lux, UDI, DA, and uniformity ratio) and energy consumption (cooling and heating). The results reveal that single and double I-shaped buildings situated in east-west orientation were found to be the most suitable for daylight, and northwest-to-southeast longitude buildings had good performance in energy consumption. U and L-shaped buildings had the worst performance in daylight and energy consumption. It also demonstrates that optimum building form design can enhance the UDI and uniformity ratio by 35.83% and 293%, respectively, and reduce cooling and heating energy demand by 22.82% and 23.93%, respectively. The future work can be extended by optimizing the visual comfort, thermal comfort along energy consumption in the realistic education building and investigating the effectiveness of optimal solutions on occupant productivity.

7. References

1. Fazidah Hanim, H., Zafuan, H., & Amani, F. (2015). Environmental psychology: an analy-sis on lighting efficiency of the architecture studio in UiTM Perak/Fazidah Hanim Husain, Zafuan Husri and Farhah Amani.
2. De Luca F, Sepúlveda A, Varjas T. Multi-performance optimization of static shading devices for glare, daylight, view and energy consideration. Building and Environment. 2022 Jun 1;217:109110.
3. Edwards L, Torcellini P. Literature review of the effects of natural light on building occupants.
4. Küller R, Lindsten C. Health and behavior of children in classrooms with and without windows. Journal of environmental psychology. 1992 Dec 1;12(4):305-17.
5. Costanzo, V., Evola, G., & Marletta, L. (2017). A review of daylighting strategies in schools: state of the art and expected future trends. Buildings, 7(2), 41.
6. Cabeza LF, Chàfer M. Technological options and strategies towards zero energy buildings contributing to climate change mitigation: A systematic review. Energy and Buildings. 2020 Jul 15;219:110009.
7. Lan L, Wood KL, Yuen C. A holistic design approach for residential net-zero energy buildings: A case study in Singapore. Sustainable Cities and Society. 2019 Oct 1;50:101672.
8. Yoon Y, Moon JW, Kim S. Development of annual daylight simulation algorithms for prediction of indoor daylight illuminance. Energy and Buildings. 2016 Apr 15;118:1-7.
9. Kontadakis A, Tsangrassoulis A, Doulos L, Zerefos S. A review of light shelf designs for daylit environments. Sustainability. 2017 Dec 29;10(1):71.
10. Carlucci S, Causone F, De Rosa F, Pagliano L. A review of indices for assessing visual comfort with a view to their use in optimization processes to support building integrated design. Renewable and sustainable energy reviews. 2015 Jul 1;47:1016-33.

11. Szentesi-Nejur S, De Luca F, Flamand K. Simulation based daylight uniformity optimizations for elementary school projects in Quebec province. InProceedings of the 40th eCAADe Conference 2022 Sep (pp. 13-16).
12. Mushtaha E, Eiz H, Janbih L, Rifai RE. Analyzing and Improving Natural Daylight in Educational Buildings Using Skylights, Victoria International School of Sharjah as a Case Study. InIOP Conference Series: Earth and Environmental Science 2019 Nov 1 (Vol. 385, No. 1, p. 012013). IOP Publishing.
13. Moazzeni MH, Ghiabaklou Z. Investigating the influence of light shelf geometry parameters on daylight performance and visual comfort, a case study of educational space in Tehran, Iran. Buildings. 2016 Jul 13;6(3):26.
14. Kaminska A. Impact of Building Orientation on Daylight Availability and Energy Savings Potential in an Academic Classroom. Energies. 2020 Sep 19;13(18):4916.
15. Mahmoud RM, Abdallah AS. Assessment of outdoor shading strategies to improve outdoor thermal comfort in school courtyards in hot and arid climates. Sustainable Cities and Society. 2022 Nov 1;86:104147.
16. Lakhdari K, Sriti L, Painter B. Parametric optimization of daylight, thermal and energy performance of middle school classrooms, case of hot and dry regions. Building and Environment. 2021 Oct 15;204:108173.
17. Tewari P, Mathur S, Mathur J, Kumar S, Loftness V. Field study on indoor thermal comfort of office buildings using evaporative cooling in the composite climate of India. Energy and Buildings. 2019 Sep 15;199:145-63.
18. Bardhan R, Debnath R. Towards daylight inclusive bye-law: Daylight as an energy saving route for affordable housing in India. Energy for sustainable development. 2016 Oct 1;34:1-9.
19. Fang Y, Cho S. Design optimization of building geometry and fenestration for daylighting and energy performance. Solar Energy. 2019 Oct 1;191:7-18.
20. Costanzo V, Evola G, Marletta L. A review of daylighting strategies in schools: state of the art and expected future trends. Buildings. 2017 May 13;7(2):41.
21. British Standards Institution. Light and Lighting-Lighting of Work Places: Indoor Work Places. BSI; 2011.
22. Gupta G, Mathur S, Mathur J, Nayak BK. Comparison of energy-efficiency benchmarking methodologies for residential buildings. Energy and Buildings. 2023 Apr 15;285:112920.
23. Energy Conservation Building Code FAQs ECBC 2017: Bureau of Energy Efficiency (beeindia.gov.in).
24. Zhang A, Bokel R, van den Dobbelsteen A, Sun Y, Huang Q, Zhang Q. Optimization of thermal and daylight performance of school buildings based on a multi-objective genetic algorithm in the cold climate of China. Energy and Buildings. 2017 Mar 15;139:371-84.
25. Wu H, Zhang T. Multi-objective optimization of energy, visual, and thermal performance for building envelopes in China's hot summer and cold winter climate zone. Journal of Building Engineering. 2022 Nov 1;59:105034.

Enabling solar shading for power generation

Stefan Wilker[1], Robert Weitlaner[2], David Sengl[3], Stephan Moser[2], Tobias Schneider[2], Alireza Estaji[1], Gerald Lukasser[2], Manuel Trampert[3]

[1] TU Wien, Institute of Computer Technology, Vienna (Austria)

[2] HELLA Sonnen- und Wetterschutztechnik GmbH, InnovationLAB, Abfaltersbach (Austria)

[3] University of Applied Sciences Technikum Wien, Vienna (Austria)

Abstract

Controls of solar shadings are commonly rudimentary in focusing only on daylight control or overheating protection. But the interests in the transparent facade are collidingly multiobjective. Heat losses and gains, view to the exterior, daylight penetration and glare are a few of them. Adding photovoltaics to these objectives bears the potential to leverage the energy bill of a building to net positive. On the other side it brings a major conflict to the overall objective of indoor environment quality, as the best yield is created with blinds always in closed position. Solar shading systems with photovoltaic require a malleable, lightweight, robust and economical technology with good performance and durability. This work proposes an integrating control system for PV enabled venetian blinds to find an optimum between overall energy performance and user comfort. Furthermore, an outlook is given on the use of artificial intelligence to find the aforementioned optimum with different control strategies and PV technologies.

Keywords: photovoltaic, shading, indoor environment quality, energy efficiency, positive energy districts

1. Introduction

As climate change is progressing and the goal of limiting the increase of the average temperature to 2°C has to be reached according to the Paris Agreement of the United Nations, 2015, Positive-Energy-Districts (PED) are getting more important with the increasing urbanisation and dense neighbourhoods. To reach the Positive-Energy Standard, building complexes must produce more energy during the year than they consume. This requirement makes it quite tricky for urban buildings with more than 3 to 4 floors, so for the sake of fairness, the approach has been adopted where dense neighbourhoods get a 'surplus' for efficient use of land and, conversely, loosely built-up neighbourhoods have to produce more. (Schneider et al., 2023).

In general, to achieve a positive energy balance, it is essential to increase energy efficiency and produce as much renewable energy onsite as possible. As the roof is often predetermined for different uses, e.g., urban gardening or other activities, it is necessary to go for innovative solutions like façade integrated- or shading-integrated PV solutions to reach the plus standard.

In this work, the impact of solar shading (e.g., venetian blinds) with PV and AI controls is calculated using a Viennese building complex to test the benefits of such blinds.

2. Angular Characteristic of PV enabled slats

Solar shading slats (e.g. venetian blinds) are used to control solar heat gains in heating and cooling periods and to provide a well daylight and glare free indoor environment. This is often a conflict between fully closing the transparent façade and letting daylight in or opening the shading while causing glare. A conventional venetian blind has a pronounced angular characteristic. A key angular feature is the so-called cut-off tilt angle to block direct insolation depending on the current solar profile angle. Depending on the solar position and the tilt angle the resulting solar heat gain coefficient (SHGC) has a high variance from 0.18 to 0.07 for a 30° elevated sun and tilt angles from 25° (measured from the horizontal position) to 65° for a silverish lamella. The daylight transmittance, given as $t_{v,dir-hem}$, decreases correspondingly from 0.25 to 0.09 (Fig 1.a).

10.18086/swc.2023.06.11 Available at http://proceedings.ises.org

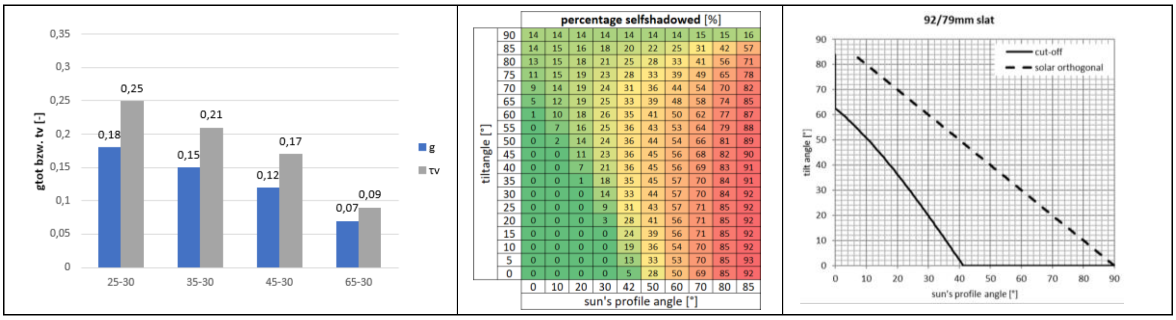

tiltangle [°]	0	10	20	30	42	50	60	70	80	85
90	14	14	14	14	14	14	14	15	15	16
85	14	15	16	18	20	22	25	31	42	57
80	13	15	18	21	25	28	33	41	56	71
75	11	15	19	23	28	33	39	49	65	78
70	9	14	19	24	31	36	44	54	70	82
65	5	12	19	25	33	39	48	58	74	85
60	1	10	18	26	35	41	50	62	77	87
55	0	7	16	25	36	43	53	64	79	88
50	0	2	14	24	36	44	54	66	81	89
45	0	0	11	23	36	45	56	68	82	90
40	0	0	7	21	36	45	56	69	83	91
35	0	0	1	18	35	45	57	70	84	91
30	0	0	0	14	33	44	57	70	84	92
25	0	0	0	9	31	43	57	71	85	92
20	0	0	0	3	28	41	56	71	85	92
15	0	0	0	0	24	39	56	71	85	92
10	0	0	0	0	19	36	54	70	85	92
5	0	0	0	0	13	33	53	70	85	93
0	0	0	0	0	5	28	50	69	85	92

Fig. 1: (a) SHGC and visual direct hemispherical transmittance for two different sun profile angles at four different tilt angles. (b) self-shaded percentage, (c) cut-off and solar-1-axis-orthogonal tilt angle.

Enabling slats with PV adds another conflicting objective to the space of tilt solutions. The kinematic of the venetian blinds geometry results in a critical self-shadowing characteristic, i.e., the slats are very likely to shade each other when in cut-off or 1-axis-solar-orthogonal tilt function (Fig 1.b and c). Working on an hourly closed loop Tilt vs. Power optimizer, it turns out that the slats are often more tilted than would be necessary for cutting off the solar beam. Therefore, the PV yield of different lamella angles has been tested to check the self-shading coefficient. As seen in Figure 2, while in the cut-off control, each angle has been used to track the sun, in the power optimizer control, mainly angles between 40° to 90° have been used. Also, during the summer months of the cut-off control, the angle was mainly at 0°, which means that the lamella was horizontal, as the sun Zenit was too high for other angles.

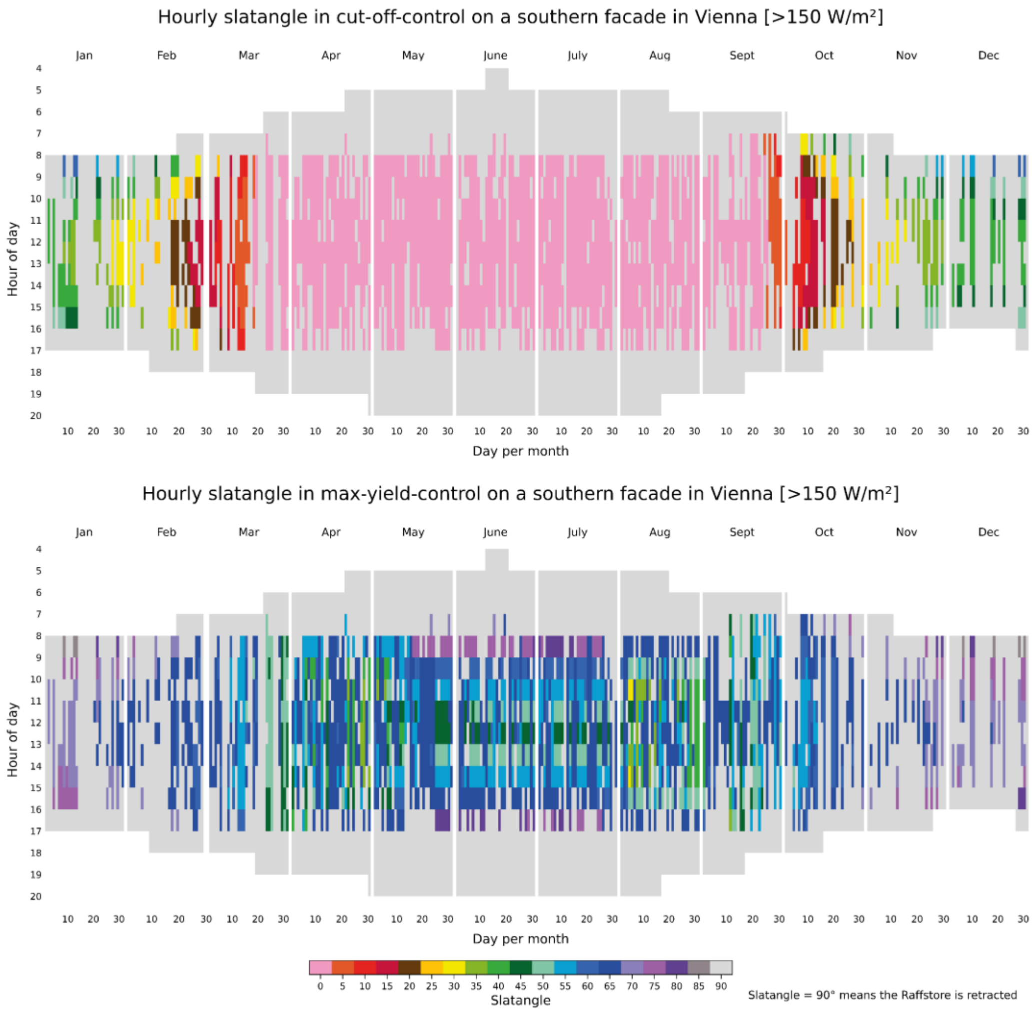

Figure 2: Optimal angles for cut-off control (top) and angles for tilt vs. power optimizer control (bottom).

Applying these angles to the lamella with integrated PV systems, the PV yield differs according to the control logic, as seen in Figure 3. While in the cut-off strategy during summer, the yield is relatively low due to the self-shading of the lamellas, in the power optimizer control, the yield remains constant during the year. Even though the angles do not change much during the yearly prognosis of the power optimizer, the yield is much higher than in the cut-off strategy. Therefore, the boundaries between the two control logics can be set as a requirement for the implemented AI to reach values between the cut-off and the power optimizer, as PV production and cooling demand should be used for the optimization.

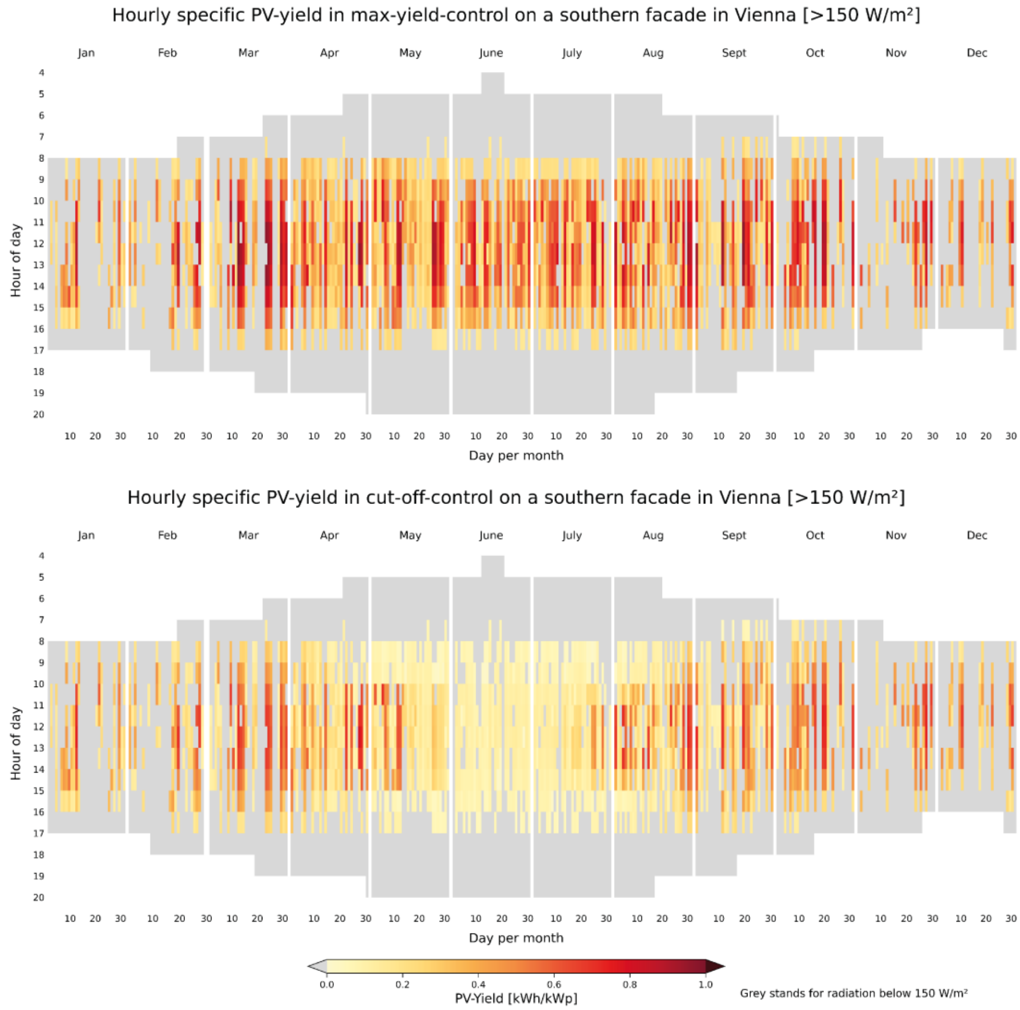

Figure 3: PV-yield for tilt vs. power optimizer control (top) and PV-yield for cut-off control (bottom).

The annual yield of the PV model in PVSites on slats (active when facade irradiance exceeds 150 W/m²), on balcony and 1-axis tracking single modules shows high variation from 422 to 727 kWh/kWp/a and a total generation of 146 kWh to 336 kWh for a 1.5x1.5 m² window respective balcony (Tab. 1).

Tab. 1: PV performance in an Austrian City, south-facing slats with 0.7 active PV surface, covering a 1.5x1.5m2 window, and a 1.5x1.5 m² balcony PV stand-alone module.

Yield	Cut-Off - Venetian Blind	Max-Yield - Venetian Blind	Balcony PV
kWh/kWp/a	422	727	678
on 1.5x1.5m² kWh/a	146	251	336

Different modules were inspected to test the efficiency of the control logic and PV-integrated shading to check the most suitable option for implementation. Therefore, tests with the modules of different angles and temperatures were made whereby the modules were heated up by the solar radiation from 20 °C to 50 °C. When reaching the highest temperature, the tilt angle of the PV system was changed, and the measurement started again. The angle was set from 0° (horizontal) to 80° (nearly vertical) and was heated up by a solar approximating light source in two-meter horizontal distance and a height difference of one meter, as shown in Figure 4. As a light source, a HL313.01 radiation matrix was used. This matrix is no standardized light source for standard testing conditions as it has a higher spectral energy in red. As the efficiency has not been measured in standardized conditions, it is not to compare with the actual module efficiency but more likely a value for comparison between different modules, which was used during the project PowerShade (Stadt der Zukunft, 2020).

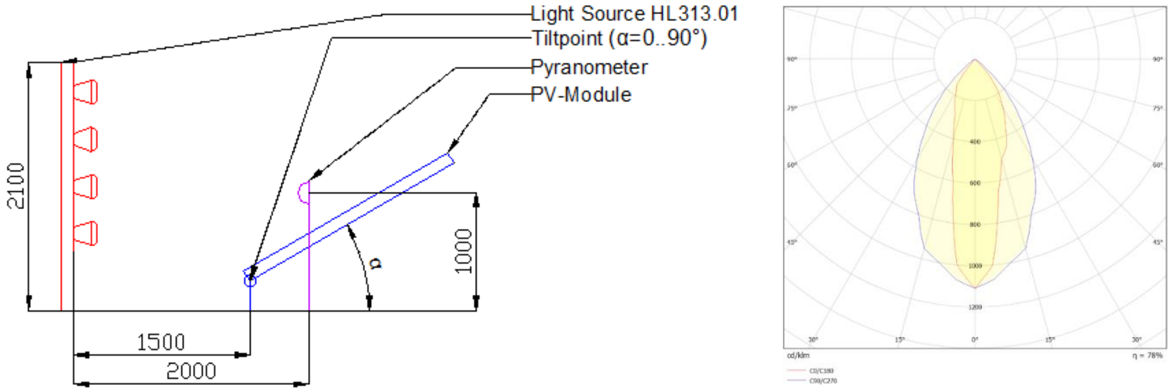

Fig. 4: Measurement setup (left) and light source radiation spectrum (right)

This setup has measured six different modules according to their efficiency decrease by changing the angle and the temperature. A comparison of the different modules is shown in Figure 5. The module names and manufacturer were anonymized, and only the first letter and the module technology were used for comparison.

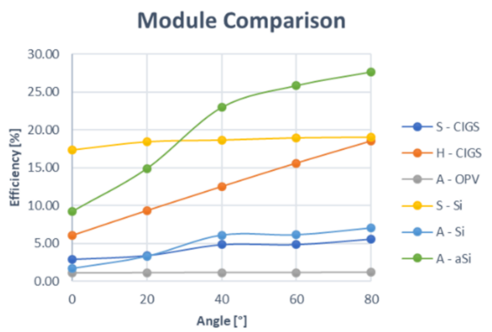

	S - Si			
	Temperature [°C]			
Angle [°]	20	30	40	50
0	0.91	0.83	0.79	0.69
20	0.97	0.89	0.85	0.75
40	0.98	0.90	0.88	0.78
60	1.00	0.92	0.88	0.78
80	1.00	0.94	0.87	0.78

Fig. 5: Efficiency degradation of different modules (left) and normalized correlation between angle and temperature of the chosen module (right)

In the case of this project, Module S – Si was defined as the most suitable option as it only has a minor angular degradation of a maximum of 10% and only a 30% reduction of the efficiency influenced by the temperature. Other modules were more sensitive to these two parameters, and therefore, not as suitable for the measurements or had lower efficiencies in general.

As shown, the maximum efficiency of the S – Si module reached about 19% at 80° inclination and 20 °C temperature. It is also shown that the module is mainly influenced by the temperature and only a little by the angle of inclination; only the angles between 0 to 40° have nearly an impact on 10% of the efficiency losses. This fits the power optimization control of Figure 2, as the control primarily uses angles between 40 to 90° to reach the highest generation efficiency.

State-of-the-art control systems of solar shadings are ignoring or insufficiently considering these angular characteristics. Advanced, deterministic methods include raytracing methods (Bueno 2016) to handle the angular behaviour and add thermal and optical data of the building, its rooms, and its surroundings for evaluating heating/cooling demands and indoor environmental quality. However, they are susceptible to uncertainties in a building's description. Our proposed methodology tackles these uncertainties. With the AI training model, the module's characteristics can be implemented in the simulation, and therefore, the control logic of the lamella angle can be changed accordingly. For example, with the selected module S – Si, the control logic can prioritize indoor comfort more. With other modules like the CIGS the angle of the lamella has a significant impact on the PV yield, and therefore, the AI has to decide whether to prioritize the production or the indoor comfort.

3. Simulation

By simulating the coupling between the building and the shading system, the connection between the cooling demand and production of the system gets clearer. For the simulation, the TRNSYS18 is used. The simulation is based on a living lab office with four workspaces. After the simulation and validating the increase and decrease of the according values, a coupling between TRNSYS18 and the Reinforcement Learning (RL) is established by including Type277 and enabling a Message Queuing Telemetry Transport (MQTT) connection between the two components. Type277 hereby couples the Outputs that TRNSYS needs for the simulation and the Inputs that TRNSYS generates by calculating each timestep via MQTT with the RL. The structure of the simulation and the parameters used are shown in Figure 6.

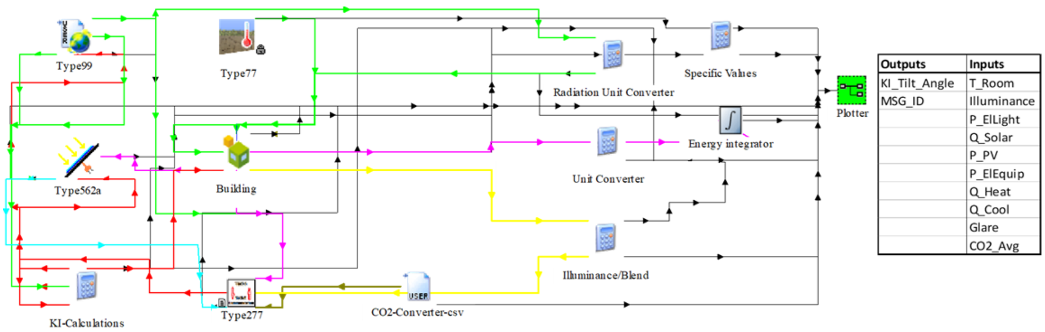

Fig. 6: TRNSYS18 simulation and used parameters

This MQTT connection was established to collect monitoring data from the testbed and compare them to the simulation results in order to validate the simulation. This methodology has also been used in other projects as, for example in the KI4HVACs (FFG, 2022) research project to compare natural environments with the training data of the AI. The implementation of the PV system on the lamella is shown in Figure 7, whereas two different modules, S – Si and S – CIGS, have been applied to the lamella to check the angle depending on yield.

Fig. 7: Application of the PV-Modules on the Testbed (left) and detail of the S – CIGS Module (right)

As the angle dependency of the modules was different, but only one lamella angle was able to be controlled, the AI was trained using the S – Si module. To validate the simulation results, the testbed has been monitored and compared to the simulation results. The measured weather data was implemented to TRNSYS via an established MQTT connection, the simulation for each timestep was done and results were compared (Tab. 2).

Tab. 2: Standard Deviation between measured and simulated values

	T_Amb [°C]	Angle [°]	T_Room [°C]	Illuminance [lx]	Glare [-]	I_Beam [W]	P_PV [W]
Standard deviation	0.8	4.0	3.0	371	0.06	28.1	2.7

The standard deviation was calculated by comparing the squared differences between the measured value in the testbed and the simulated value. The first two values, outdoor Temperature (T_Amb) and the angle, refer to Data provided by the monitored testbed. Therefore, the data of T_Amb only differs from the measured values by 2.1%. The deviation from the angle is reasonable, as the monitored data provides angles in 1° steps, but the simulation can only deal with 5° steps. Therefore, this Data deviates by nearly 9% from the original data. The room temperature (T_Room), Blend (i.e., glare), and illuminance were calculated by the simulation and fit with a mean deviation of a maximum of 36% at the illuminance. This is also reasonable, as the structure of the building, its storage capacity, and the sensor location are not exactly replicated in the simulation to make it more universal.

Therefore, the measured data from the illuminance may differ a lot. The beam Radiation (I_Beam) deviates by 2.4%, which is neglectable as TRNSYS deals with the sun elevation according to the time of day, meaning that the location and sun position are fitting for the simulation. This deviation and approximations for the PV lead to higher deviations in the PV production (P_PV) of 17.7%. Still, when checking the graphs in Figure 8, the course of the values is the same, and therefore the simulation can be used to teach the RL, as it will still be learning the exact building behaviour in the monitoring phase. Based on the experimental and simulation results, by ignoring all effective parameters and just focusing on maximizing PV production, setting a fixed lamella angle in our experiments of 50 and 60 degrees will provide acceptable PV outputs.

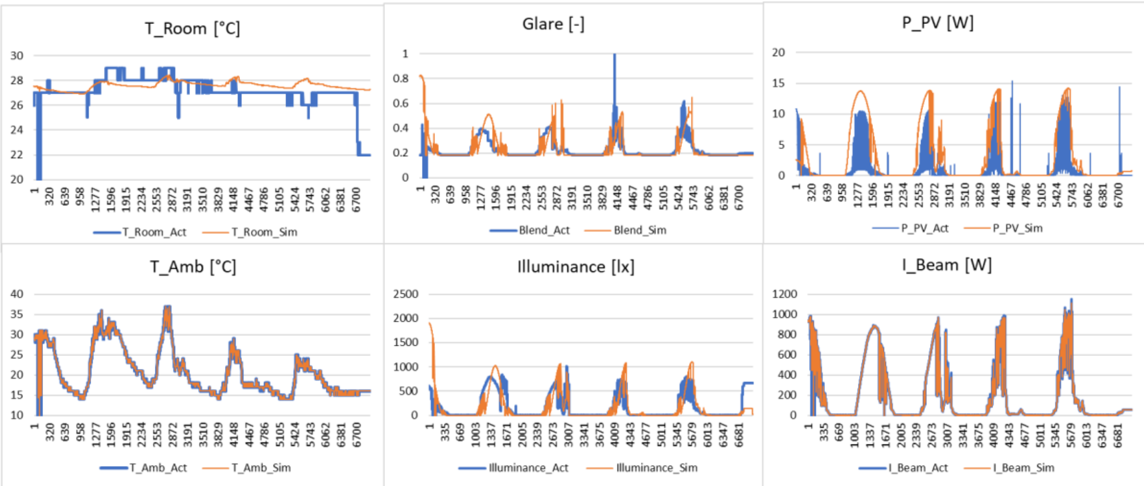

Fig. 8: Comparison of the timeseries of measured and simulated values

4. PED calculation

With the simulation results and the angular characteristics of the PV-shading system PED calculations have been made. Simulation tests have been made in order to test the efficiency increase between the cut-off strategy, the power optimization control and the AI control. The comparison was made by simulating the month June with TRNSYS and comparing the results between the cut-off and the AI control logic. In Figure 9, the comparison between the two control logics is shown.

By comparing the control logic in the middle, it is shown, that mostly the AI has higher production than the cut-off regulation. Only during the morning and evening hours the optimization control has vast differences, which decreases the efficiency by far. This may result due to the prioritized parameters of the AI, which focused on increasing the PV yield and reducing the demand for the building. Therefore, in the evening hours, the AI tried to gain as much direct energy from sunlight as possible and produce PV-power. During the course of one month, the production increased by nearly 1000 kJ (about 0.3 kWh), which resulted in an efficiency increase of 0.9% per Window (3 m²). This value is between the values shown in Table 1, which was set as a requirement for the optimization. It increases the system's overall production compared to the cut-off strategy and, therefore, could be sufficient to reach the PED status in dense districts.

To check the impact on dense buildings, the PV production increase has been implemented in the PED-calculation of a Viennese building block which is located in an outer district of Vienna and has a Floor Space Index (FSI – gross floor area divided by the area of the property) of 4.6 (Schöfmann et al., 2023). In regards to the definition by Schneider et al. (2023), this means that the building needs to produce less than the consumption to reach the positive energy standard. Due to the high density of the district still, rooftop PV is not sufficient enough to cover the demand of the building, and parts of the facades and balconies also have to

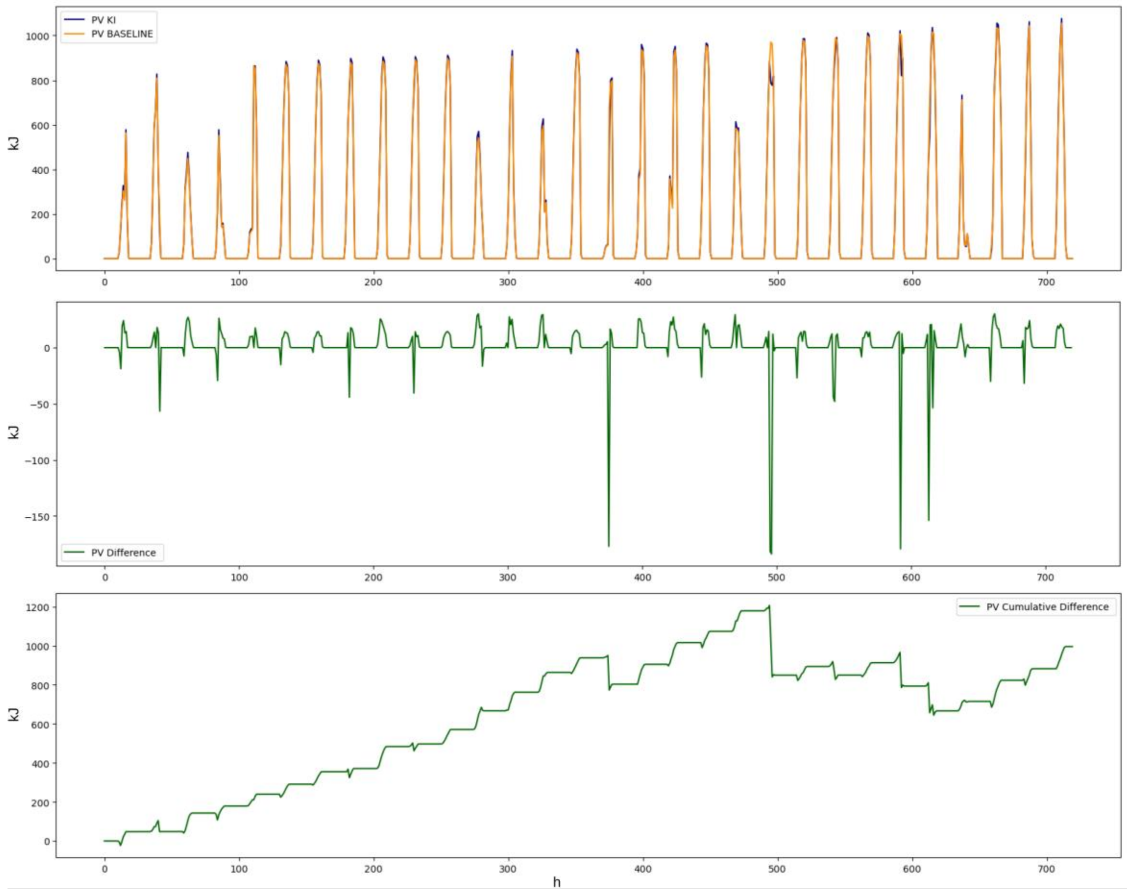

Fig. 9: Increased efficiency for regulation by comparing the cut-off with the AI control

be covered with PV-Systems. As shown in Table 1, the production of balcony PV-Systems is somewhere between the cut-off and the PV-max control logic of venetian blinds. Therefore, according to Schöfmann et al. (2023), the PED-Standard calculation has been made again by changing the balcony PV to shading systems with max-yield control logic. The power production of the PV has been calculated by scaling the maximum output of 1000 kJ/h per 3 m² (92 W/m²), as shown in Figure 9, to the window area of the buildings in south, east and west orientation from the 8th to the 3rd floor and calculating the power production with the Program PVSites. Other windows were not calculated as the shading by other buildings would be too high for economically viable production. The darker the color of the façade of each building in Figure 10, the lower the total irradiation on the surface. Therefore, the total usable window area was calculated with 1690 m² and resulted in a total PV installation of 155 kWp. In contrast, no canopy PV can be installed additionally due to the shading of the windows beneath them.

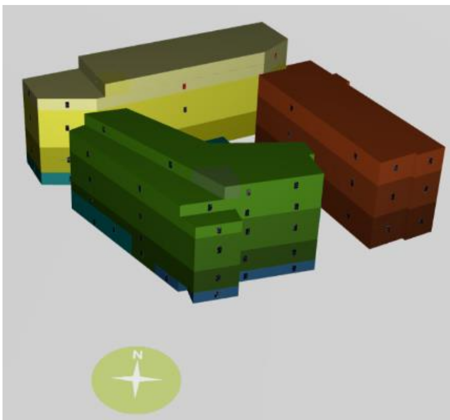

Fig. 10: Suitable areas for PV-Shading systems in the Viennese Demo District (Schöfmann et al., 2023)

This change not only influences the power production of the PV system but also decreases the cooling demand of the building as the solar gains through windows are reduced by the shading system. This results in lower demand

and higher PV production, which again positively impacts the positive energy balance. Table 3 shows the total PV installation on each surface of the building and the positive energy balance based on the net floor area (NFA).

Tab. 3: PED calculation for different control scenarios

Value	Zukunftsquartier 2.0	PowerShade Cut-Off	PowerShade Max-Yield	PowerShade AI
Rooftop PV [kWp]	482.6	482.6	482.6	482.6
Canopy PV [kWp]	68.4	-	-	-
Pergola PV [kWp]	19.5	19.5	19.5	19.5
Balcony PV [kWp]	11.5	-	-	-
Shading PV [kWp]	-	155.0	155.0	155.0
Total PV [kWp]	582.0	657.1	657.1	657.1
Total PV Production [kWh/m$^2_{NFA}$a]	19.4	19.2	20.7	19.5
Primary Energy Demand [kWh/m$^2_{NFA}$a]	38.0	37.5	36.5	37.3
Primary Energy Export [kWh/m$^2_{NFA}$a]	2.7	2.2	2.9	2.3
Density Surplus [kWh/m$^2_{NFA}$a]	40.7			
PED-Balance [kWh/m$^2_{NFA}$a]	5.3	5.4	7.1	5.7

Even though the Cut-Off, Max-Yield, and AI concepts have the same amount of PV installed, they result in different balances. Whereas the production of the Cut-Off during the year is the lowest of the four concepts compared, the max yield has the highest production. This is also shown in Table 1, even if the gap is lower than expected.

The Primary Energy Demand for the three concepts has its peak with the balcony PV as the benefit of the shading system is the reduced cooling energy by reducing the solar thermal gains through summer. Again, the Max-Yield concept is the most sufficient due to the lowest demand. By comparing the Export, it can be seen that now the balcony PV has a higher output than the AI, as the highest energy production is reached during midday when the lowest demand is, and therefore, the energy can be fed to the grid.

All four concepts reach the PED-Standard, but due to the decreased demand and the increased production of the shading system with PV, the three PowerShade-Concepts reach higher values in the PED-balance.

5. Results

Today's paradigm proposes enabling every reasonable surface with PV for transforming buildings to net energy positive. We elaborated the angular effects of a PV-enabled venetian blind, put that data into a dynamic building model of TRNSYS, and coupled it with a reinforcement learning method to enhance the multi-objective search for solutions to the conflicting multi-objective problem of shading, transparent façade, indoor environment, and PV generation. Besides and still open for further research and modeling are the economic constraints for this PV application. We showed that the produced energy, the solar gains, and the indoor comfort are highly variable to different control schemes. We showed that the quality of the TRNSYS model is sufficient. While reducing the objectives to only PV generation, the TRNSYS/RL model shows that the tilt angle needs to be varied between 50 and 60° and not more.

By comparing different concepts of PV installation on a Viennese building complex, it is shown that the PV-implemented shading has higher efficiencies for a positive energy balance due to the reduction of the cooling demand and the efficient usage of sunlight during the day. When comparing the installed power with the balance, it is seen that while the installed power is increased by 12%, the production is only increased by 7%. This means that the balcony and canopy production is more efficient than the shading element. However, by considering the energy demand of the building by checking the PED-Balance, it is a gain of 34% regarding the max-yield control and 8% at the AI control. Another benefit of the AI is the increased comfort due to natural light and glare protection. In order to make a statement about the rentability of the system, an economic analysis has to be made to check whether the increased production covers the higher investment costs.

6. Acknowledgments

The research presented in this paper has been conducted in the scope of the R&D project PowerShade in the research program Stadt der Zukunft (City of Tomorrow), 6.th call 2018" with funding received and gratefully acknowledged under FFG grant no. 877185. Stadt der Zukunft (City of Tomorrow) is a research and technology programme of the FederalMinistry for Climate Action, Environment, Energy, Mobility, Innovation and Technology, Republic of Austria (BMVIT). It has commissioned the Austrian Research Promotion Agency (FFG) together with Austria Wirtschaftsservice GmbH and the Austrian Society for Environment and Technology (ÖGUT) to deliver this programme.

Further research on the AI controls is carried out in the KI4HVACs project (No 888448), which is being funded under the 7th call of the energy research program of the Austrian Research Promotion Agency (FFG) and the Climate and Energy Fund.

7. References

Bueno, Bruno, 2016, A web-based simulation platform for the energy, daylight and glare evaluation of fenestration systems, Radiance Workshop 2016. Available at: https://www.radiance-online.org/community/workshops/2016-padua/presentations/212-Bueno-FenerWebPort.pdf. Access on 12.05.2023

FFG, 2020. PowerShade - Entwicklung strom-generierender Beschattungslösungen für energieflexible Gebäude im urbanen Raum. [Development of energy-generating shading solutions for energy-flexible buildings in the urban context.] Available at: https://nachhaltigwirtschaften.at/de/sdz/projekte/power-shade.php. Accessed on 09.10.2023

FFG, 2022. KI4HVACS - Energieeffizienzoptimierung von HLK-Systemen durch prädiktiver Algorithmen und Modellbildung mittels maschinellem Lernen. [Energy efficiency optimization of HVAC systems using predictive algorithms and machine learning models.] Available at: https://projekte.ffg.at/projekt/4174829. Accessed on 06.10.2023

Schneider S., Zelger T., Sengl D. & Baptista J., 2023. A Quantitative Positive Energy District Definition with Contextual Targets. Available at: https://www.mdpi.com/2075-5309/13/5/1210. Access on 04.05.2023

Schöfmann, P., Forstinger V., Zelger T., Schneider S., Leibold J., Bell D., Schindler M., Mlinaric I., Hackl L., Wimmer F., Holzer O. & Weißböck L., 2023. Zukunftsquartier 2.0 - Replizierbare, thermisch und elektrisch netzdienliche Konzeption von (Plus-Energie-) Quartieren im dichten urbanen Kontext. [Future Districts 2.0 - Replicable, thermally and electrically grid-supporting design of (positive-energy) neighborhoods in dense urban contexts.] Available at: https://nachhaltigwirtschaften.at/resources/sdz_pdf/schriftenreihe-2023-33-zukunftsquartier-2-0.pdf. Accessed on 05.10.2023

Enhanced Non-Imaging Solar Concentrator for a Small Scale Drying in Buildings

Atul A. Sagade[1], Rodrigo Palma-Behnke[2,3], Edgar Estupiñan[1], Lorena Cornejo Ponce[1]

[1]Departamento de Ingeniería Mecánica, Universidad de Tarapacá, Arica (Chile)

[2] Energy Center, FCFM, University of Chile, Santiago (Chile)

[3]Dept. of Electrical Engineering, FCFM, University of Chile, Santiago (Chile)

Abstract

Building energy conservation technologies and developing green buildings have been essential priorities in the last decade. Building integrated clean cooking and heating systems using the Sun's energy can play a vital role in green buildings for several applications. This paper reveals the improved design of the prototype of non- imaging solar concentrator, named as BISC and its possible use for clean drying in buildings. The small prototype of the BISC is experimented under field conditions utilizing simplified thermal analysis for its performance.

The results show that the BISC able to achieve a temperature in the range of 59-74 °C, in the open drying operation. It ensures the potential for highly possible use in green buildings for drying with close drying operation, and other heating applications, such as cooking.

Keywords: sustainable development goals, green buildings and energy, Building integrated solar thermal technologies, solar drying, Renewable heating.

1. Introduction

Many building-integrated solar thermal collector systems (here onward denoted as BISTS) for heating have been reported in the past literature and have been popular from a long time (Morse, 1881; Fuschillo, 1975; Pierce, 1977). Diverse designs of concentrating BISTS were developed, which includes, roof integrated mini- parabolic solar collectors (Petrakis et al., 2009), Fresnel lens concentrator for cooling (Chemisana et al., 2013), and vertical heliostats (González-Pardo et al.,2014), and roof integrated two-stage solar concentrators (Bushra et al., 2022). Sultana et al., 2012 investigated concentrating semi-transparent BISTS in a novel rooftop solar micro-concentrating collector. Ratismith et al. 2014 proposed and compared (Ratismith et al. 2017) a tilted-tough collector arrangement with its orientation inwards at a 15° angle for heating application. The whole-day experimental results of the tilted-tough collector show an increase in efficiency of about 20% and could achieve apparent stagnation temperatures around ~ 180 °C, applicable for industrial process heat applications.

However, past literature significantly on BISTS lacks information about building-integrated solar dryers, even though the building-integrated solar thermal collectors showed good potential for heating and other applications but have not often been used for solar drying. On the contrary, solar drying has been one of the most favored fields of research for decades worldwide, and extensive literature is available on this topic. Interestingly and surprisingly, the investigators and designers of existing solar dryer designs did not keep an eye on their potential for large-scale building integration. There may be several reasons which could lead to the limited availability of literature and potential research gaps related to building integration of the solar dryers and can be enlisted as i) lack of interest and negligence of urban planners, building architects, and engineers as a potential technology for building energy conservation; ii) non-availability of appropriate designs of simple yet efficient building integrated solar dryers (hereafter denoted as BISD); iii) lack of attention, interest, and negligence by the research community to develop BISDs and their potential for low-

10.18086/swc.2023.06.09 Available at http://proceedings.ises.org

cost retrofitting, iv) very limited, rather unavailability of studies on the economics of BISDs v) lack of information about appropriate test methods, and thermal performance parameters available for performance evaluation of BISDs and their usefulness and appropriateness in testing BISDs, vi) lack of information about BISDs temperature attainment at a particular latitude(s) due to changes in solar geometry and weather conditions, even though building integrated solar thermal systems have the potential to reach intermediate to high temperatures (Bergmann and Weiß, 2002; Ratismith et al. 2017), vii) lack of appropriate design of BISDs for a particular latitude leading to apprehensions about their selection.

From the literature on building integrated solar thermal technologies; and most recent and existing designs of solar dryers (Sagade et al., 2022, 2023, Saxena et al. 2023), one can identify and understand the above-enlisted research gaps. Therefore, it is necessary to address them appropriately by presenting new and innovative designs for building integrated solar dryers. Hence, the present work aims to bridge the above-indicated research gap and demonstrate a prototype design of a non-tracking and non-imaging solar concentrator-based building integrated solar thermal dryer (BISD).

Thus, the novelty of the present work is i) design and build a primary prototype of the non-imaging and non-tracking compound parabolic solar concentrator-based BISD, ii) field experimentation of the BISD to demonstrate its usefulness, iii) determination of the thermal performance of the proposed BISD.

2. Materials and design of BISD

The BISD is an extended use of Building integrated solar thermal collector (BISTC) for drying application, which was previously used for cooking application (Sagade et al., 2023). However, detailed description is being avoided. The requirement of temperatures for drying process are relatively lower (~70 to 75 C). Therefore, the main change in the design of BISTC is removal of portable reflector used by Sagade at al. 2023. The reason for this design change is to i) reduced the temperatures in the absorber zone, which is used for drying process and ii) assess the heating performance ability of BISTC without portable reflector. Fig. 1a and 1b shows the photographs of test setup and BISD with drying material, respectively. and specifications are enlisted in Table 1.

Sr. no.	Component of BISD	Parameter
1.	waterproof plywood box	0.54 m (length) × 0.352 m (width) × 0.213 m (depth)
2.	dimensions of CPC are	0.46 m width, 0.35 m length, and 0.21 m depth,
3.	a rectangular absorber surface of CPC	0.23 m (width) × 0.35 m (length)
4.	Anodized aluminum reflectors used in CPC (ALANOD ® GmbH and Co.KG, Germany; Grade 320G)	Reflectivity = 0.86, thickness =0.3 mm
5.	The aperture and absorbing areas of CPC	0.161 m^2
6.	Absorbing area of CPC	0.08 m^2
7.	Effective inclined aperture area of CPC considering trapezoidal wall area	0.4 m^2
8.	The geometric concentration ratio (C_{gcr}) of BISD	2.012.
9.	Top and bottom lengths of the trapezoidal wall	1.08 m (top length); 0.54 m (bottom length)

BISD consists of a non-imaging compound parabolic concentrator (CPC) made of a galvanized iron sheet of 2 mm thickness is fitted in a plywood box. Anodized aluminum reflectors are glued over the galvanized iron surface of CPC, which acts as a reflecting surface of CPC. The building-integrated trapezoidal wall of the BISD is made of waterproof plywood and attached to one of the edges of a box, as shown in Fig. 1a. This allows handling the change in Sun elevation angle due to the Sun's motion over the given experimental day and season. This building-integrated trapezoidal wall is screwed with a anodized aluminum reflector, as mentioned above (See Fig. 1a), and acts as a booster reflector for the BISD. the heat absorbing area of CPC is coated with matt black paint.

The BISD was tested in a fixed position without providing any tracking. For this purpose, a trapezoidal wall faces south throughout the experiment at a location. However, the present work does not present any suggestions or guidelines about the architectural integration of the BISD.

Fig. 1a: Photograph of test setup for BISD

Fig.1b: Photograph of BISD with drying material (Sliced tomatoes)

3. Experiment and thermal analysis equations

Solar drying of the tomatoes has been done using BISD in the present work and drying performance is evaluated on the basis of the amount of moisture removed and the moisture removal rate from the drying material only. A black cloth is used to spread the drying products in the heat absorbing zone of BISD. The drying products (sliced tomatoes) of ~ 500g in the heat absorbing zone allowed to heat up under clear sun conditions without tracking of BISD, as indicated in Section 2. The solar flux falling on the CPC reflector and trapezoidal wall gets reflected in the heating zone of the BISD and food prodcut absorbs the heat. Thus, the temperature of heating zone rises slowly and gradually and moisure removal starts gradually.

A class 2 thermopile-type pyranometer (Dynalab, India) measures the total solar radiation (G_T) on the plane perpendicular to the beam radiation. The ambient air (T_a) and glycerin temperatures (T_{gly}) were measured using J-type temperature sensors. The wind sensor (Dynalab, India) measures the wind velocity at the experimental location. The windshield reduces the wind's impact during the experimentation. All the measuring instruments were connected to the data logger (UniLog, India), which records the experimental parameters every 90s.

The BISD was tested for its thermal performance in the window of ± 120 minutes of the solar noon to establish the primaty opto-thermal performance at the experimental location, SERL (17.66° N, 75.32° E) under ambient conditions as ($\bar{G_T}$) ≥ 700 W/m^2; 20˚C ≤ ($\bar{T_a}$) ≤ 40˚C and wind speed ≤ 1.5 m/s. However, the proposed BISD design may be applicable to the locations of latitude 0 to ± 23.5° around the globe, but such a study will be part of future work and not part of present investigations.

3.1 Thermal performance equations

3.1.1 Determination of moisture content for the solar drying cycle

Eq. 1 (Sethi et al. 2018) depicts the percentage of moisture content removed from the food products in BISD

$$Moisture\ content, (\mathrm{m}_{wc}) = \frac{m_{di}-m_{df}}{m_{di}} \times 100\ (\%) \qquad (1)$$

where, m_{di} and m_{df} are the weight of food product before dehydration (kg), and after dehydration (kg), respectively.

3.1.2 Dehydration rate of the drying material for the drying cycle:

Eq. 2 (Sengar and Kurchania, 2005) expresses the dehydration rate of the drying material

$$Dehydration\ rate = \frac{m_{wc}}{\Delta t}\ \text{(kg/minute)} \qquad (2)$$

where, Δt is the time required for the drying .

3.1.3 Efficiency of the drying process in BISD

Eq. 3 (Andharia et al., 2022) shows the drying efficiency of BISD

$$\eta_D = \frac{Quantity\ of\ heat\ used\ in\ evaporating\ moisture}{solar\ flux\ incident\ on\ the\ BISD}$$

$$\eta_D = \frac{m_{wc} h_{fg}}{G_T A_p \Delta t} \quad (\%) \qquad (3)$$

where, hfg is the latent heat of evaporating moisture is 2260 kJ/kg·K (Andharia et al., 2022))

4.Results and discussions

4.1 Drying performance of BISD

The present work establishes a proof of concept of the possible use of BISD using a prototype model and assess the performance at a temperature attainment in the drying process using non-tracking BISD. Fig. 2 depicts the variation of the different parameters observed for three (3) experimental days. In the drying cycle, on each experimental day, food products have the highest moisture content at the start of the test; thus, the reduction in moisture content is high at the initial phases and reduces gradually with drying time. BISD attains the temperatures in the range of 59-74 °C and can effectively dry a 500g of food products in the window of solar noon. The drying process removes a significant amount of moisture from the drying stuff. BISD removes ~95 to 96 % of moisture on different experimental days at a location during window of the solar noon. The use of cotton cloth below the drying products absorbs the considerable moisture and avoids the overheating and burning of the drying products. Obviously, drying is more efficient when the solar radiation is bright under clear weather.

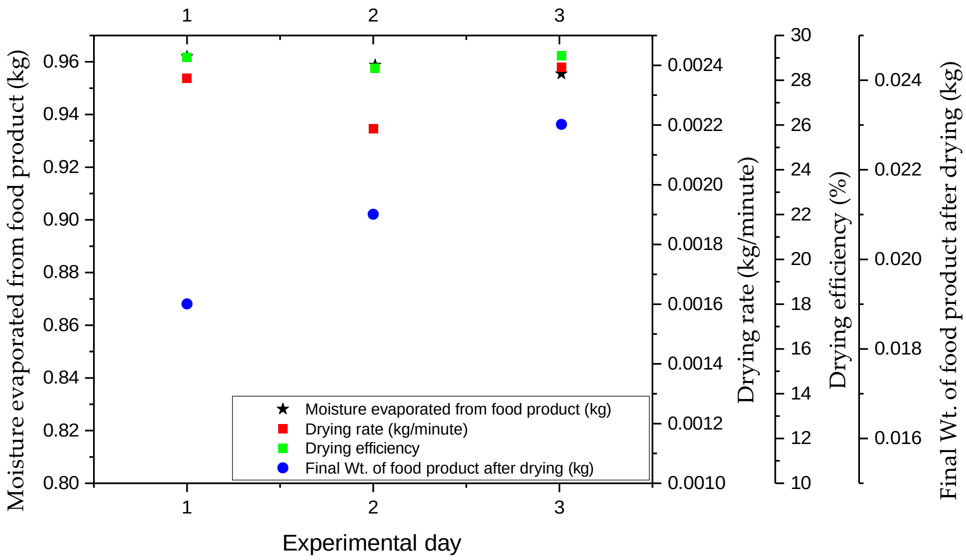

Fig. 2: Variation of experimental parameter for the drying process

Thus, the drying rate of the food products depends on solar radiation and the air temperature in the BISD's heating zone and is proportional to them. The drying rate of food products varies from 0.00218 to 0.00238 kg/minute on different experimental days. According to the variation of the ambient conditions, the dehydrating time was between 200-219 minutes. The higher the solar flux, higher is the drying rate of food products and maximum is reduction in the moisture content of the food product. Hence, at the end of the experiment on any typical day, the drying rate of food products slowed down and reached the apparent stagnation state where further moisture removal may not be possible.

Table 2: BISD's performance in the dehydration process

Day	$(\bar{G})$ (W/m^2)	$(\bar{T_a})$ (°C)	Initial Wt. of food product (kg)	Final Wt. of food product after drying (kg)	Moisture evaporated from food product (kg)	Drying time (minutes)	Drying rate (kg/minute)	Drying efficiency (%)
1	918	35.2	0.5	0.019	0.962	204	0.00235	29.02
2	869	36.8	0.5	0.021	0.958	219	0.00218	28.44
3	932	38.4	0.5	0.023	0.954	200	0.00238	28.91

The drying efficiency of the BISD is around of 29 % for all the three experiments at a location. Table 2 depicts the parameters used and determined for the drying process using BISD. Therefore, the reproducibility of the results confirms the usefulness of BISD as a potential design for small scale solar drying in buildings to avoid wastage of perishable food items. It also enables to preserve them by drying for later use.

5.Conclusions

The present work shows the proof of concept of non-tracking and non-imaging building integrated solar dryer. The major conclusions of the present investigations are summarized below

1. BISD removes ~95 to 96 % of moisture and cotton cloth enables to absorbs the considerable moisture and avoids the overheating and burning of the drying products.
2. The drying rate of food products varies from 0.00218 to 0.00238 kg/minute on different

experimental days.
3. The drying efficiency of the BISD is around of 29 % for all the three experiments at a location.
4. The present proof of concept of the BISD may be adapted for solar drying of different food products in decentralized energy sector with a possibility of their realistic integration in the buildings.
5. The reproducibility of the results confirms the usefulness of BISD for small scale solar drying in buildings.
6. Multiple use of the building integrated non-imaging and non-tracking CPC based solar concentrating collector is possible for at least two applications of cooking and drying the food products and can be extended for other several heating applications.

6.References

[1] Morse ES, Warming and Ventilating Apartments by the Sun's Rays Patent No. 246,626. 1881.

[2] Bergmann I, Weiß W. Fassadenintegration von thermischen Sonnenkollektoren ohne Hinterlüftung. Systemtechnische und bauphysikalische Grundlagen für die Fassadenintegration von thermischen Sonnenkollektoren ohne Hinterlüftung. Berichte aus der Energie- und Umweltforschung. AEE Intec; Arbeitsgemeinschaft ERNEUERBARE ENERGIE; Institut für Nachhaltige Technologien, Gleisdorf. 2002.

[3] Petrakis M, Barakos G, Kaplanis S. Roof integrated mini-parabolic solar collectors. Comparison between simulation and experimental results. TOEFJ 2009;2 (1):71–81.

[4] Chemisana D, López-Villada J, Coronas A, Rosell JI, Lodi C. Building integration of concentrating systems for solar cooling applications. Appl Therm Eng 2013;50:1472–9. https://doi.org/10.1016/j.applthermaleng.2011.12.005.

[5] González-Pardo A, Rodríguez A, González-Aguilar J, Romero M. Analysis of solar shading caused by building-integrated Vertical Heliostat Fields. Energy Build 2014;76:199–210. https://doi.org/10.1016/j.enbuild.2014.02.009.

[6] Bushra N, Hartmann T, Constantin Ungureanu L. A method for global potential assessment of roof integrated two-stage solar concentrators (TSSCs) at district scale. Appl Energy 2022;326:120018. https://doi.org/10.1016/j.apenergy.2022.120018.

[7] Sultana T, Morrison GL, Rosengarten G. Thermal performance of a novel rooftop solar micro-concentrating collector. Solar Energy 2012;86:1992–2000. https://doi.org/10.1016/j.solener.2012.04.002.

[8] Ratismith W, Inthongkhum A, Briggs J. Two non-tracking solar collectors: Design criteria and performance analysis. Appl Energy 2014;131:201–10. https://doi.org/10.1016/j.apenergy.2014.06.030.

[9] Ratismith W, Favre Y, Canaff M, Briggs J. A non-tracking concentrating collector for solar thermal applications. Appl Energy 2017;200:39–46. https://doi.org/10.1016/j.apenergy.2017.05.044.

[10] Fuschillo, N., 1975. Semi-transparent solar collector window systems. Solar Energy 17, 159–165. https://doi.org/10.1016/0038-092X(75)90054-7

[11] Pierce, N. T. (1977). Massachusetts Institute of Technology US4143640 A

[12] Sagade, A.A., Palma-Behnke, R., 2023. Experimental feasibility study of multipurpose low-cost solar thermal device for different applications including inactivation of SARS CoV-2. Sustain. Energy Technol. Assess. 56, 103034 https://doi.org/10.1016/J.SETA.2023.103034.

[13] Sagade, A.A., Palma-Behnke, R., 2022. Novel design of the solar disinfectant closet (device) for inactivation of COVID-19 virus. p. 060005. https://doi.org/10.1063/5.0085676.

[14] Sagade, A.A., Sagade, N.A., Belgasim, B., Tawfik, M.A., Kulkarni, S., Shukla, S.K., 2023. Building integrated innovative non-imaging concentrating solar collector for clean cooking under low sun elevation. Sustain. Energy Technol. Assess. 57, 103234 https://doi.org/10.1016/j.seta.2023.103234.

[15] Saxena, A., Cuce, E., Singh, D.B., Sethi, M., Cuce, P.M., Sagade, A.A., Kumar, A., 2023. Experimental studies of latent heat storage based solar air heater for space heating: a comparative analysis. J. Build. Eng. 69, 106282 https://doi.org/10.1016/j.jobe.2023.106282

HOW TO ACHIEVE OPTIMAL DELIVERY OF ENERGY SERVICES FOR INFORMAL SETTLEMENTS? A METHODOLOGY

Rebekka Besner[1], Kedar Mehta[1] and Wilfried Zörner[1]

[1] Institute of new Energy Systems (InES), Technische Hochschule Ingolstadt (THI), 85049 Ingolstadt, Germany

Abstract

The energy situation in informal settlements of Sub-Sahara Africa is often poor. The electricity sector is commonly characterized by unreliable, unaffordable, illegal, or dangerous supply. Energy for cooking and lighting is predominantly based on fossil fuels. One solution to improve the energy supply in informal settlements is the implementation of an Energy Hub. This system can support both individuals and local businesses by providing energy related services. Energy Hubs can offer a variety of different services. Since the structures in the respective informal settlements differ, the services offered should be oriented and selected individually according to the local needs and livelihood of the population. To obtain a properly dimensioned concept tailored to the respective use case, potential services should be classified and evaluated in advance. In this work, a methodology is being developed to find and prioritise driving factors (parameters) that can classify and evaluate the energy services for the use in an Energy Hub. Based on literature and on-site research, eight parameters were identified and prioritised with the help of an expert survey. A clear ranking of the eight parameters was established with the technical and economical parameters scoring high. A graphical comparison of services based on the parameters concludes the work.

Keywords: Energy Services, Energy Hub, Informal Settlements, Sub Sahara Africa, Likert Scala, Evaluation Parameters

1. Introduction

The energy sector in countries of Sub-Sahara Africa (SSA) is in constant transition. Access to electricity has increased by 22 % over the last 20 years (World Bank Group 2023). In particular, the rise in the installation of renewable energy (RE) based off-grid systems helped to improve living conditions in remote and rural regions (Babayomi et al. 2023). In urban areas, the electrification rate is considerably higher than in rural regions (IEA et al. 2023) because the national grid can be expanded more cost-effectively due to the high density of buildings and the

Fig. 1: Exemplary Street in an informal settlement

10.18086/swc.2023.06.02 Available at http://proceedings.ises.org

associated density of customers. The grid stability, on the other hand, still has potential for improvement compared to European standards (African Development Bank Group 2021; The World Bank Group 2023). Statistics show an almost universal electrification rate for urban areas in several countries of SSA, with more than 95 % in Kenya, Togo, Mali and Rwanda (World Bank Group 2023). However, there are still areas in cities that suffer from poor energy infrastructure and supply. These specific quarters are inhabited especially by the lower strata of society and are referred to as slum regions and informal settlements (ISs) (Mensah 2022; Butera et al. 2015; Cheseto N. Moses 2013). Fig. 1 shows a typical street in an exemplary IS with insufficient basic infrastructure. There are no paved roads, street lighting or running water systems for all residents. Although electrical lines are visible, they are often illegal and thus not laid by the national utility.

Within recent decades, slum upgrading programs have been launched (Anderson and Mwelu 2013). These aim at an area-wide reconstruction and improvement of the infrastructure. However, the implementation of the programms require a high financial outlay and, due to the dense development, considerable structural changes as well as efforts for the residents in the entire settlement. A successful upgrading also facilitates the installation of legal electricity infrastructure due to more structured access to the respective buildings. At the same time, slum upgrading programs face many challenges: The high financial investments, the illegal status of the residents and their consequently low political relevance, power structures formed outside the legal framework, such as cartels (Ndukui 2013). Also due to the high number of ISs, the infrastructure and reality of life in many ISs will not be possible to be improved across the board in the foreseeable future.

The energy supply in ISs is mainly based on fossil fuels, such as candles for lighting or charcoal, kerosene or gas for cooking (Okore et al. 2022). The residents suffer from energy poverty due to their low economic power (Broto et al. 2015). High levels of crime such as theft and vandalism on the one hand and little ability for political participation by residents on the other reinforce a mutual mistrust between the population and authorities as well as the national energy suppliers (Butera et al. 2015). In some countries, national electricity suppliers have withdrawn from ISs by dismantling transformers, leaving the area dark on the short-term and causing supply to be offered by illegal organizations like cartels on the long-term (Mgwali 2022; Kimatu 2021). Due to the high electrification rate in urban areas, this population group always lives close to the national grid, but at the same time cannot benefit from it (Dumitrescu et al. 2020). If they are connected by illegal suppliers, the supply is often characterized by frequent fluctuations and power cuts, dangerous, illegal connections, and often unaffordable tariffs (Broto et al. 2015; Christley et al. 2021). At the same time, the high solar irradiation prevailing in most cities in SSA leads to a large potential for RE, especially solar energy. There are several technological possibilities to improve the energy supply. Besides the option for grid expansion, there are also potential on RE based technologies, e.g., Mini-Grids, SHS or centralized solar kiosks (Besner et al. 2023). One potential solution to improve the energy supply in ISs is Energy Hubs, as shown exemplarily in Fig. 2. This is a compact, centralized off-grid system based on RE generation (generally up to a project size of 35 kW), especially consisting of the combination of photovoltaic (PV) and battery energy storage systems (BESS) (Besner et al. 2023).

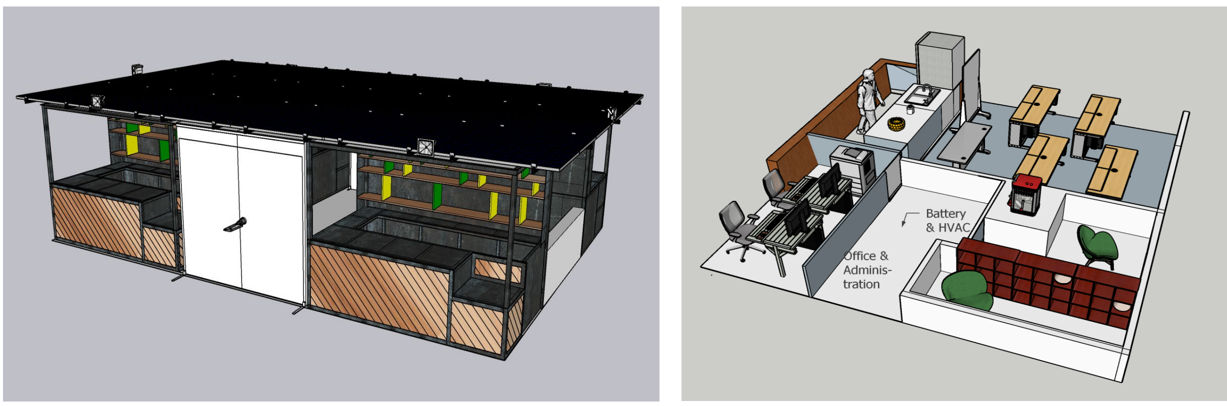

Fig. 2: Exemplary design of an Energy Hub from the outside (left) and inside (right) using the software SketchUp (Trimble Inc. 2023)

The concept is similar to that of a solar kiosk as Tavernier and Rakotoniaina (2016) discuss and can find an answer to the energy related challenges of ISs. If appropriate precautions are taken, the compact design can offer protection and minimise the risk of theft and vandalism. When deploying the Energy Hub, no settlement upgrading is necessary, as only a free, accessible space is required. The services that the Energy Hub can offer are intended to improve the living standards of the local population, as well as to support local businesses. Businesses that depend on electricity for their operations can obtain a space in the Energy Hub and benefit from the Hub's sustainable, reliable electricity supply. Therefore, the Energy Hub can support local businesses by providing electricity for their energy needs, enabling productive use of energy (PUE). At the same time, the Energy Hub pursues the goal of improving educational opportunities within the communities by offering training. The energy services can be used and obtained flexibly according to the users' needs and (financial) possibilities. In the best case, the local population can be involved in the operation of the system, and thereby capacity building is achieved. This can be realized by selecting a group of respected people with experience in selling, trading or offering services, who will take care of the Hub's operation. Theoretically, the mentioned concept can be used in ISs. However, as each IS having individual structures and their resident's individual energy related needs, it is challenging for external stakeholders, such as researchers, authorities, or investors, to analyse which services the Energy Hub should be offering in the respective different ISs. Hence, there is a need to derive the driving factors (parameters) which can evaluate potential energy services for the implementation of Energy Hubs in ISs to improve energy services. However, there is a gap in the research and no scientific information is available about fundamental information that is necessary for Energy Hub designing and implementation. Therefore, the presented study raises two main research questions to contribute to the knowledge:

- How can the energy services that will be offered within the Energy Hub, be evaluated, and subsequently chosen?
- What are the key determining factors (parameters) that can be used to assess the energy services to be provided within the Energy Hub?

Central off-grid systems have been around for several years. However, some concepts did not pass the pilot phase. Most of these systems are implemented in rural and remote areas (Tavernier and Rakotoniaina 2016; Urban and Maphalala 2019; Eales and Unyolo 2018; Frame et al. 2019; Batagarawa and Dodo 2022; THE PULSE Rwanda Ltd. 2022). As there is often no electricity supply in those regions, services which offer basic energy related needs are chosen. Frame et al. (2019) used as market assessment in rural Malawi the offering of a survey to households and businesses with 17 services under consideration. These were up for potential selection for use in the system. The authors inquired from households the willingness to pay for specific services and from businesses their estimation of the success, i.e., number of customers and probability of profit. While this approach is excellent for specific locations, a holistic evaluation of services and the possibility of transferability to other sites is not given. Other solutions, e.g., the operators of THE PULSE Rwanda Ltd. (2022), which offer a network rural PV-centers, are due to their alignment as a business operation less transparent in the methodology of how the range of services has been determined. In urban areas, the situation of energy supply is more diverse (Karekezi et al. 2008). The services offered in an Energy Hub in ISs must be adapted locally to the acute challenges and needs, which requires greater complexity in their selection. If transferability to other ISs within SSA is wished to be achieved, an extensive collaboration with the community of the respective settlement needs to be ensured. The methodology developed in this work for the assessment of different services helps to solve this challenge by proposing a thorough analysis of parameters which helps to evaluate respective energy services.

2. Methodology

The work of this study is divided into five steps. An overview of these steps is given in Fig. 3.

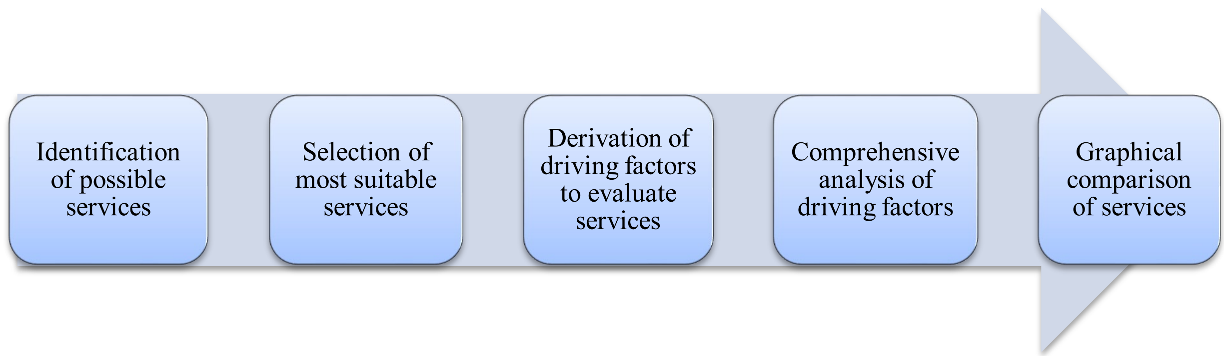

Fig. 3: The individual steps of the work of the underlying study

As a first step, possible energy services which the Energy Hub can offer need to be identified. Literature values as well as research activities are used as a basis for the analysis. During the research in two potential locations, ISs in Nairobi ("Kingstone", Mukuru), Kenya and Maputo ("Hulene B"), Mozambique, quantitative and qualitative data was collected. The quantitative analysis consists of a comprehensive survey of the energy practices and needs, the social and economic conditions and the existing infrastructure of the local population using a pre-developed questionnaire. Both, local businesses (83 in Kingstone, 58 in Hulene B) and households (390 in Kingstone, 229 in

Hulene B) were survey participants. The qualitative data collection involved individual interviews with local businesses and residents as well as the analysis of the utilized electrical appliances in the businesses of the neighborhood. The appliances electrical properties were measured with the help of a current clamp and their usage behavior was questioned to get an impression of potential use cases for the Energy Hub. The possible services are identified based on the already existing businesses in the local area. Furthermore, the question of which businesses and services are lacking within the community was used as an indicator for additional potential services for the Energy Hub.

Since an Energy Hub has limited capacity, confined available space, and a customer clientele with limited economic power, certain energy related services are not eligible for use. For example, providing charging stations for e-mobility may be inappropriate for Hubs in ISs due to the poor road infrastructural conditions and low economic strengths of the residents. Neither can electrically powered vehicles travel to the ISs and thus to the Energy Hub site, nor do their residents have sufficient financial resources to afford this type of vehicle. With this knowledge, the services can be narrowed down and subsequently evaluated. The evaluation is implemented by the introduction of driving factors (parameters). These parameters were derived during the above-mentioned qualitative and quantitative research. In particular, the site visits to ISs contributed to selection, as parameters were chosen in response to local challenges. To obtain verification and validation of the parameters, they are prioritized with the help of an expert survey. For selection and ranking of the parameters according to their relevance, experts from Europe and SSA, who are familiar with the concept of the Energy Hub, were contacted and survey results were obtained. The survey consists of two parts: In the first part, the experts are asked how important they consider the eight pre-selected parameters. Therefore, the Likert scale is being utilized (Susan Jamieson 2023). The scale ranged in five steps from "Very important", "Important", "Neutral" and "Slightly important" to "Not important". The fixed answer options are given a numerical score. Thus, the choice "very important" corresponds to five points, "important" to four points, "neutral" to three points, "slightly important" to two points and "not important" to one point. The coloring indicates analogously a high score in green and a low score in red. The second part allows the participants of the survey to identify other parameters that may be of relevance. Twelve experts were contacted, and ten experts took part in the survey. This results in an expert response rate of 83 %.

The fifth step of the methodology represents the final step, the graphical classification of the services with the aim of obtaining an overview of different options as quickly as possible. For this purpose, the services are evaluated by the parameters, put into a graphical diagram based on their scoring. If the preference of the future planner of an Energy Hub lies in two specific parameters, a graphical comparison of services within the two parameters can quickly help in the decision-making process of selecting services for the Hub.

3. Results

The following section is divided in the six steps. The first five sections deal with the results of the respective methodological step, which were introduced in Figure 3. Section 3.6 presents the limitation of the study.

3.1 Identification of possible services

The mentioned field visits, the quantitative research in combination with the review of literature helped to identify a number of 40 services. The quantitative surveys included interviews with households and businesses in two ISs in Kenya ("Kingstone", located in the capital city Nairobi) and Mozambique ("Hulene B", located in the capital city Maputo). The survey covered the realities of life from household size to financial situation, i.e., income and expenditure, the status quo of energy supply, needs and wishes in the scope of energy infrastructure, information on digitalization, hygiene, and sanitation supply structure as well as missing services in the community. The businesses were asked whether their service suffers from the current energy supply and whether they see a potential for business development when improving the energy supply. Qualitative interviews were conducted with business owners in the respective ISs, their energy needs and challenges with the existing energy supply were discussed. Various services were identified during visits to the settlements, through said surveys and interviews. These identified services with their corresponding field are being presented in Tab. 1. They range from basic infrastructural services, such as the provision of showers or restrooms, to the offer for existing services, such as a place for a tailor, to the option of providing a cinema.

3.2 Selection of most suitable services

The during section 3.1 identified services need to be analyzed according to their suitability for offering in the Energy Hub. Tab. 1 shows the for the use in the Energy Hub accepted services, highlighted in green, and services which can be merged into one generic load profile, in lighter green. The second part of the table, highlighted in red, displays the services, which cannot be considered for use in the Energy Hub and are being excluded. The exclusion used to determine which services would not be suitable for the Energy Hub is based on four main criteria and is being presented in the column "Remarks". These are, primarily, the space that a service occupies ("Too much space needs"), secondly the maximum power and energy that a service requires ("Power needs are too high"), thirdly, whether the service has a focus on energy provision or business activities at all ("No focus on electricity"), and fourth, if the service was mentioned or seen during the fieldtrips more than once ("No demand seen during research").

Tab. 1: Overview of services identified, divided into services accepted and excluded for implementation in the Energy Hub

Accepted identified services	Accepted services to be summed up to one Load Profile "Generic shop"
Tailor, Barber, Salon, Laundry, Copyshop, Wi-Fi, Grain Milling, Education and Training Centre, Juice pressing, Popcorn Sale, Fridge, Freezer, Cold room, Phone charging station, Lights charging station, Outside lighting	Hardware-Shop, Electronics (repair) Shop, Ice cream sale, Chips sale, Milk or Yogurt sale, Supermarket, Grocery, Chemist
Excluded services	**Remarks**
Shoe Making, Soap Production, Entertainment for children, Community Cooking Activities, Clean cooking, Clean water, Hot Water Provision, Shower	No focus on electricity
Emergency, Hospital, Car Wash, Garage	No focus on electricity Too much space needs
Urban Farming, Waste Management, Recycling	Too much space needs
Bakery	Power needs are too high Too much space needs
Welding, Air-Conditioning	Power needs are too high
Incubators for poultry farming, Oil pressing	No demand seen during research

Due to the dense building construction in ISs, space is an extremely scarce commodity. During a visit to the research area, three open spaces were identified, although only one was found to be a usable open space within the center of the Settlement. This amounts to approximately 50 m^2. While a hospital or emergency room requires a reliable power supply, these activities cannot be accommodated by an Energy Hub for a variety of reasons, most notably space constraints and focus of training and support of businesses. A small pharmacy-shop, on the other hand, could be offered within the Energy Hub. Further services, e.g., the implementation of a waste management facility, also cannot be included due to space restrictions. This is accompanied by the limitation by the second criterion, required power or energy. Due to the limited area, the maximum possible PV power that can be installed on the roof of the Energy Hub is also constrained. In addition, to minimize the cost of the Energy Hub, large power must be avoided to decrease the need for greater battery power and capacity. As an example, a bakery that has to operate an oven with a power of several kilowatts for a few hours before sunrise cannot be implemented in the Energy Hub. The car wash is on the one hand irrelevant due to the lack of accessibility for cars, on the other hand this service needs too much space and thirdly the focus for energy provision is missing. Although the provision of clean water for drinking, cooking, or showering is considered to be of extremely high relevance, the direct focus of these offers is not on the provision of energy-related services. Similarly, the options soap and shoe production need more manual than electrical support, so the reason for sorting out is also considered the focus. A fourth exclusion criterion is the frequency of mentions of the potential service during the research activities. If the service was mentioned only once and not identified again during the on-site visits or the surveys, this service is classified as non-relevant and excluded for further use. The services of hardware or electronics sales store, sale of chips, sale of milk, yogurt or ice cream, chemist, supermarket and grocery store are combined in one service, as their applications and thus their load profiles do not differ significantly. This generalized service is being referred to as the “generic shop”. This includes the equipment lamps, fan, an optional radio and a refrigerator or freezer. Collaborative cooking activities can still be conducted if space permits, but there are no additional necessary arrangements to be made on the part of the Energy Hub design to accommodate the activities. Therefore, no extra service is created for it.

3.3 Derivation of driving factors to evaluate services

In total, eight parameters for evaluation of the pre-selected services have been identified based on limitations and challenges, observed during the field visits, and mentioned quantitative and qualitative research as well as expert discussions. Three criteria played an important role in the selection of the parameters: The Technical, the Economic and the Social dimension. The first criterion analyzes whether the service can be used in the Energy Hub from a technical point of view. This essential criterion led to the selection of the following three parameters: Energy storage requirements, space and electricity required by the service. The second criterion analyses, whether it makes sense from an economic perspective to offer this service. Therefore, the criteria of potential for return of investment (RoI), cost of a service and number of necessary employees were chosen. And the third criterion has to do with the social aspect, especially the acceptance of the Energy Hub by the local community. This involves determining how many residents can benefit from the respective service. Furthermore, the type of operation is examined, i.e., whether a service can potentially be organized or operated by the community itself, or whether this must be undertaken by private individuals. Fig. 4 shows the parameters, which were derived and are suitable for evaluating services which could be offered within the Energy Hub. The parameters are divided into the three preselected criteria of technical feasibility (marked in green), economic properties (marked in blue) and social suitability (marked in purple).

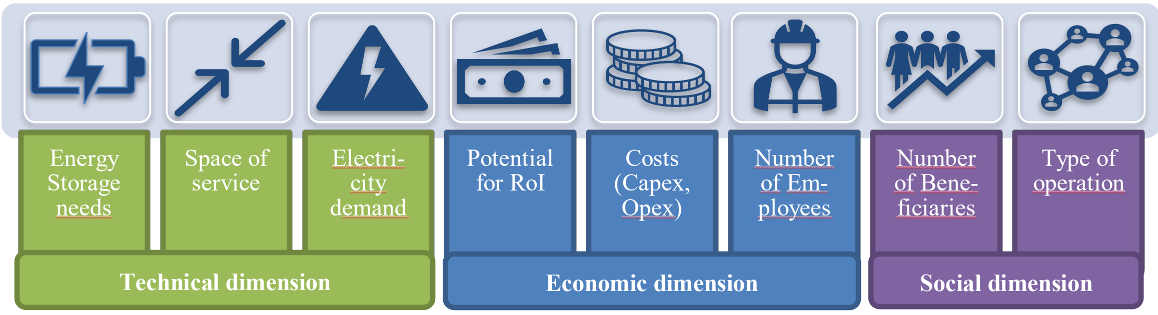

Fig. 4: Derived parameters for evaluating energy services that can be implemented in the Energy Hub

When selecting parameters for evaluation of energy services, attention should be paid to quantifiability, relevance and practicability. Parameters such as “Social Impact” are difficult to quantify, so measuring the "Number of Beneficiaries" is more applicable. Given the limited space available in ISs, a preliminary estimate of the required PV and Energy Hub area per service is relevant. Therefore, the parameter "Available Space" is about assessing how much space the energy service requires within the Energy Hub in meter (e.g., refrigerator around 1.2 x 0.6 m with additional space for door opening). At the same time, a planner must know how much energy and thus PV area is needed (“Electricity demand”), which is quantified in kWp. The parameter “Energy Storage needs” is measured in kWh of battery storage demand per day. The calculation of the RoI (“Potential for RoI”) is in general based on many individual, region-specific, market-dependent prices and variables. Since an analysis of the services based on their RoI is not universally possible due to the varying prices in different countries, a tendency in the form of a ranking is given. This is accompanied by the "cost of a service" parameter, which is used to calculate capital and operating costs. In this case, too, the positions are very dependent on the respective potential location and place of use of the Energy Hub and thus of the service offered. The parameter “type of operation” is analyzing whether a service can be operated by a private person or the community. A typical example of a service run by individuals is the operation of a barber shop. In contrast, a training center is suitable to be organized by several people of the community.

3.4 Comprehensive analysis of driving factors

In the following section, the response of the expert survey is analyzed. When the above introduced methodology is being applied to the response data, the parameters evaluation results in Tab. 2. The table shows the individual ranking proposed by the experts in detail. The individual results are being summed up within their parameter group (“Sum”). To gain a comprehensive, more generalised evaluation, the results are being weighted (“Weighting”). The maximum possible rating of importance is 50 points (equalling a weighting of “1”), which is achieved if each expert considered a criterion to be highly important. With the importance value of 42 of the parameter “Energy Storage Needs”, a total weighting of 84 % is being scored. The resulting ranking of the parameters is displayed in the last row (“Ranking”).

Tab. 2: Results of the evaluation of the pre-selected parameters with coloring from "Highly important" (green) to "Not important" (red)

Parameter / Response	Energy Storage Needs	Space of Service	Electricity Demand	Potential for RoI	Costs of Service	Number of Employees	Number of Beneficiaries	Type of Operation
n = 1	4	5	5	3	5	4	4	5
n = 2	4	5	5	5	4	2	5	4
n = 3	4	5	5	5	4	2	4	2
n = 4	4	5	4	4	3	3	5	5
n = 5	4	5	4	5	4	4	4	2
n = 6	4	5	5	4	5	3	5	5
n = 7	5	5	5	5	4	5	4	4
n = 8	5	5	5	4	5	5	5	4
n = 9	4	5	4	4	3	1	4	5
n = 10	4	3	5	5	4	3	4	5
Sum	**42**	**48**	**47**	**44**	**41**	**32**	**44**	**41**
Weighting	**0.84**	**0.96**	**0.94**	**0.88**	**0.82**	**0.64**	**0.88**	**0.82**
Ranking	**4**	**1**	**2**	**3**	**5**	**6**	**3**	**5**

The highest importance is attributed to the parameter "**Space requirement of the Service**" (Ranking "1"). The services should therefore be evaluated according to their respective space requirements. It can be concluded from the results that a significant challenge in ISs concerns the limited space availability. It is relevant to know how much space a Training Centre with three, five, ten or fifteen seats requires. At the same time, a router (Wi-Fi service) can be hung on the wall and does not require any floor space. The second important parameter, the "**Electricity Demand**" of a certain service, is also related to the first mentioned ("space requirement") parameter. The area of free space, which is covered by the PV system, is limited. Since the Energy Hub is a building and island system with a central rooftop PV, the energy that can potentially be generated with the system is also bounded.

From the experts' point of view, the parameter of whether a service has the "**Potential for RoI**" is the important criterion from the economic perspective. The assessment of services on the basis of this parameter, however, is as already mentioned in section 3.3, more difficult, as both the costs of the services and the income generated by the service differ from country to country.

The **"Number of Beneficiaries"** is considered to be the most important social criterion. Since the Hub is a product that is tailored to a specific community, as many as possible within the community should also benefit from it. Accordingly, services should be examined to determine the extent to which they meet this criterion. One service that could benefit many residents is the charging station for cell phones. A large part of the local population owns mobile phones. In the event of prolonged blackouts or a shutdown of the electricity supply, several community members can use the charging service at the same time. Although the training center imparts knowledge to a limited number of people, in the best case this can lead to many profiteers through the multiplication effect - by passing on this knowledge on to neighbors or family members.

"**Energy Storage Needs**" are not considered very relevant compared to other technical parameters. The storage needs depend on the selection of the different services: security lighting that shines during the night requires more storage than a service that is only open during sunshine hours. However, based on different preferences and local conditions, potential Energy Hub operators could define the availability of their system. As BESS account for a large part of the investment costs in an off-grid system, the capacity of BESS can be reduced in the design of an Energy Hub if, for example, the available funding is limited. The decrease in BESS capacity generally leads to lower system availability. A balance has to be found between the available financial resources, the selected services, the local preferences of the local population and the desired system availability. This can be done regardless of the services chosen, so assessing services based on their individual need for BESS capacity is considered less relevant.

The parameter **"Cost of Service"** is similarly found as less important. When evaluating energy services, the experts identified the RoI as more relevant, since the share of cost of the Energy Hub itself, with its building structure, energy generation and BESS is higher than the services themselves, which is represented by the capital and operational costs for the respective appliances. Furthermore, depending on the financing structure, loans can be granted in various amounts, whereby the total amount, which is influenced by individual services to a minor extent, is less decisive than the potential to repay the loan with interest. Capital and operating costs are input variables of the RoI parameter, which is why the parameter for cost itself is evaluated as less relevant. It is important to consider the costs in particular, since the amount of revenue of the respective service is determined by them.

The evaluation of a service based on the type of possible **"Type of Operation"** is also rated as rather unimportant. The question of whether a service is more suitable for operation by a private individual or by the community is less relevant since the operation of all services can be carried out by both the community and private individuals if organized systematically and respectively. Furthermore, the form of operation depends on many factors, especially the composition of the community, the wishes of the community or the commitment of individuals. The conception of the Energy Hub as well as the selection of services will be designed according to the local operator.

Analogously, the parameter **"Number of Employees"** is classified as less relevant, as the number of staff per service differs depending on the size of the service (for example, for the use five planned shavers for a barbershop more staff needs to be hired then if two shavers are in operation), the opening hours and the type of operator of the Hub.

Suggestions about other possible parameters were also mentioned by the experts. Suggestions were "Safety", "Ownership" and "Accessibility" for customers. These three valuable suggestions are taken into account for the layout of the entire Hub but are not considered necessary for the evaluation of individual services. "Ownership" is being also represented by the "Type of Operation" and will be involved further in the choice of a business model. "Sustainability beyond the donor support period" as well as "affordability of prices for customers" are also important aspects which needs consideration when looking at the big picture of developing the Hub. Another expert cites "urgency and prioritization by the community." This is made possible with the mandatory involvement of the community when initiating a possible building of the Hub.

3.5 Graphical Comparison of services according to diverse parameters

In order to achieve a fast evaluation of different services, this can be implemented by a clear comparison with the help of graphs. In this way, services can be compared on the basis of two parameters. Fig. 5 shows an example comparison of eleven randomly selected services based on the parameters "Space requirements" and "Beneficiaries of service" without detailed axis labeling.

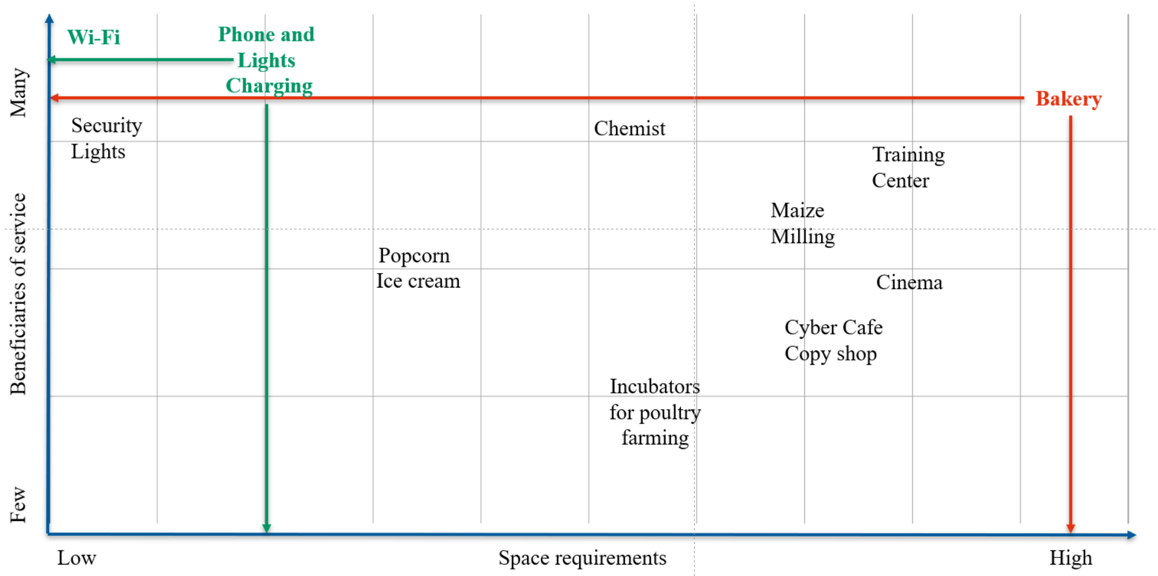

Fig. 5: Exemplary graphical representation of the evaluation of different services based on two parameters

The green-marked area represents services that are particularly suitable for use in the Hub, as it benefits many residents while requiring little space. Similarly, the services in the red-hatched area are less suitable because the necessary space exceeds the scope of the Energy Hub concept. Wi-Fi should be public - and thus available from theoretically everyone in the neighborhood if they are in the vicinity of the Energy Hub. The bakery and pharmacy products can also be purchased by everyone. The cell phone charging service is available to a relatively large number of people, since at least 30 people can use the service in parallel. There are a maximum of two workstations in the cyber cafe or coffee shop, which is why relatively fewer people can use the service here per day. Incubators can only be used by residents who own chickens and have the capacity for operation growth, which significantly limits the number of beneficiaries. Although in theory ice cream and popcorn is also available to everyone, for many it is not an essential, everyday product, which makes the profiteers decrease per day. The Training Centre also has a limited number of courts and training times per day. However, there is room for several people at the same time and the multiplication effect already mentioned increases the number of beneficiaries. The grain mill can only be used by a limited number of customers due to the limited capacity of the mill. From interviews with three millers in the research area of "Kingstone" in Nairobi, a number of customers of up to 25 people per day could be identified (Besner 2022).

3.6 Limitations of the study

No claim is made for completeness in the underlying work. A selection of parameters had to be made and their number chosen in such a way that the analysis is feasible in terms of time and resources while at the same time comprehensively taking all relevant aspects into account. The experts belong to one of two different fields. They are from the area of social sciences or have a technical background. Care was taken to ensure a balanced proportion of experts with the two respective backgrounds. Although the parameter ratings have been selected based on quantifiable criteria (as described in section 3.3), for example, space requirements are described in terms of m^2 definable, the services themselves must often be based on empirical values or with the help of supported assumptions. A comprehensive evaluation of the services exceeds the scope given for this paper, which is why this work concludes with the possible graphical comparison of various services based on two different parameters. The outstanding comprehensive evaluation of the individual services on the basis of the parameters defined in the context of this paper will be carried out in future work.

4. Conclusion

Efforts to ensure a modern, clean, and sustainable energy supply for all must be steadily pursued. In some areas, such as ISs of SSA, the common approach of grid extension or the use of a Mini-Grid is often not possible due to various challenges and local conditions. One solution that can help improve the local energy supply in ISs is the utilization of so-called Energy Hubs. These are a renewable energy based off-grid system with PV and battery energy storage technology, which can support the local community by providing electricity for energy services and PUE. If Energy Hubs are to be set up in several informal locations in SSA, the services that the Hub will offer needs to be tailored to local needs. While there are comparable projects, the choice of services provided by these concepts has not yet been discussed in the literature. Since there are a large number of possible services at the same time and they cannot all be offered in an Energy Hub at the same time, a selection of services must be made. In order to be able to tailor these services to local needs, the services must be evaluated in advance on the basis of various parameters. Therefore, the first step is to identify the services that an Energy Hub can be able to offer. To achieve transferability and adaptability, parameters must be found to analyze, prioritize, and narrow down these services according to suitability and characteristics. The eight within this work derived parameters can describe services extensively. To make an optimised service selection, the chosen parameters are evaluated and prioritized with an expert survey. The most important parameter is to evaluate the services based on their space requirements. Also extremely important, and related to the space requirements, is to identify the amount of energy or electricity needed for each service. In addition to the lack of space for the Energy Hub building, there is the analogous limitation for the PV area provided on the Energy Hub. The two technically justified parameters are followed by an economic parameter: The potential for a service to achieve a return of investment. From a sociological point of view, another indicator is important: the number of those who benefit from the use of the service. In contrast, the experts do not consider the number of employees required and whether the services should be operated by the community or by private individuals to be quite important.

Acknowledgments

We thank the experts who voluntarily and anonymously participated in the survey. This work has been funded by the German Federal Ministry for Education and Research (BMBF) under the grant number 01DG21015A and is part of the project "SEED – Sustainable Energy Education Districts for Informal Settlements".

References

African Development Bank Group (2021): Electricity Regulatory Index. for Africa 2021. Côte d'Ivoire. Available online at https://africa-energy-portal.org/sites/default/files/2021-12/08122021%20ERI%20report%202021.pdf, checked on 9/1/2023.

Anderson, Mark; Mwelu, Keziah (2013): Kenyan Slum Upgrading Programs: KISIP & KENSUP. Available online at https://www.muungano.net/s/2013_KENYAN_SLUM_UPGRADING_PROGRAMS_ANDERSON_MWELU.pdf, checked on 7/28/2022.

Babayomi, Oluleke O.; Olubayo, Babatunde; Denwigwe, Iheanacho H.; Somefun, Tobiloba E.; Adedoja, Oluwaseye Samson; Somefun, Comfort T. et al. (2023): A review of renewable off-grid mini-grids in Sub-Saharan Africa. In *Front. Energy Res.* 10, Article 1089025. DOI: 10.3389/fenrg.2022.1089025.

Batagarawa, Amina; Dodo, Yakubu Aminu (2022): Proposed Solar Kiosk for COVID-19 and Other Infectious Disease Screening in Nigeria. In Ali Sayigh (Ed.): Sustainable Energy Development and Innovation. Selected Papers from the World Renewable Energy Congress (WREC) 2020. 1st ed. 2022. Cham: Springer International Publishing; Imprint Springer (Innovative Renewable Energy), pp. 765–771. Available online at https://doi.org/10.1007/978-3-030-76221-6_84, checked on 8/20/2023.

Besner, Rebekka (2022): Living situation of a miller in the informal settlement of Kingstone. Kingstone, Viwandani, Mukuru, Nairobi, Kenya. Personal Exchange.

Besner, Rebekka; Mehta, Kedar; Zörner, Wilfried (2023): How to Enhance Energy Services in Informal Settlements? Qualitative Comparison of Renewable Energy Solutions. In *Energies* 16 (12), p. 4687. DOI: 10.3390/en16124687.

Broto, Vanesa Castán; Stevens, Lucy; Salazar, Diana (Eds.) (2015): Energy access and urban poverty. Energy and everyday life in an informal settlement in Maputo, Mozambique. Rugby, Warwickshire, UK: Practical Action Publishing (Poor people's energy briefing, 4). Available online at https://practicalactionpublishing.com/pdfjs/web/viewer.html?file=https://practicalactionpublishing.com/pdf/book/2649/9781780449296_01694089209.pdf, checked on 9/7/2023.

Butera, F. M.; Adhikari, R. S.; Caputo, P.; Facchini, A. (2015): The challenge of energy in informal settlements. A review of the literature for Latin America and Africa. In *Analysis of Energy Consumption and Energy Efficiency in Informal Settlements of Developing Countries*, pp. 1–32. Available online at https://www.enelx.com/content/dam/enel-found/topic-download/The%20challenge%20of%20Energy%20in%20Informal%20settlements.pdf, checked on 9/7/2023.

Cheseto N. Moses (2013): Challenges in planning for electricity infrastructure in informal settlements: Case of Kosovo Village, Mathare Valley -Nairobi. Master Thesis. University of Nairobi, Nairobi. Department of Urban and Regional Planning. Available online at http://erepository.uonbi.ac.ke/handle/11295/56433, checked on 8/17/2021.

Christley, Emily; Ljungberg, Hanna; Ackom, Emmanuel; Fuso Nerini, Francesco (2021): Sustainable energy for slums? Using the Sustainable Development Goals to guide energy access efforts in a Kenyan informal settlement. In *Energy Research & Social Science* 79, p. 102176. DOI: 10.1016/j.erss.2021.102176.

Dumitrescu, Raluca; Groh, Sebastian; Philipp, Daniel; Hirschhausen, Christian von (2020): Swarm Electrification: From Solar Home Systems to the National Grid and Back Again? In Oktoviano Gandhi, Dipti Srinivasan (Eds.): Sustainable Energy Solutions for Remote Areas in the Tropics. 1st ed. 2020. Cham: Springer International Publishing; Imprint Springer (Springer eBook Collection), pp. 63–80. Available online at https://doi.org/10.1007/978-3-030-41952-3_4, checked on 5/2/2023.

Eales, Aran; Unyolo, Berias (2018): Renewable Energy Mini-grids in Malawi : Status, Barriers and Opportunities. University of Strathclyde. Glasgow. Available online at https://strathprints.strath.ac.uk/64868/.

Frame, Damien; Dauenhauer, Peter; Eales, Aran; Galloway, Stuart (2019): Experiences from Deploying Solar PV Energy Businesses in Rural Malawi. Available online at https://www.researchgate.net/publication/334480570_Experiences_from_Deploying_Solar_PV_Energy_Businesses_in_Rural_Malawi.

IEA; IRENA; UNSD; World Bank; WHO (2023): Tracking SDG7: The Energy Progress Report 2023. World Bank. Washington DC (Creative Commons Attribution—NonCommercial 3.0 IGO (CC BY-NC 3.0 IGO).). Available online at https://trackingsdg7.esmap.org/data/files/download-documents/sdg7-report2023-full_report.pdf, checked on 7/11/2023.

Karekezi, Stephen; Kimani, John; Onguru, Oscar (2008): Energy access among the urban poor in Kenya. In *Energy for Sustainable Development* 12 (4), pp. 38–48. DOI: 10.1016/S0973-0826(09)60006-5.

Kimatu, Sammy (2021): Mukuru slum in darkness after Kenya Power removes transformer. In *Nation Media Group*, 6/24/2021. Available online at https://nation.africa/kenya/counties/nairobi/mukuru-slum-in-darkness-after-kenya-power-removes-transformer-3449602, checked on 12/16/2022.

Mensah, James Kwame (2022): Electricity and informal settlements: Towards achieving SDG 7 in developing countries. In *Energy Research & Social Science* 93, p. 102844. DOI: 10.1016/j.erss.2022.102844.

Mgwali, Thabisile (2022): City Power pounces on illegal connections in informal settlement near Ruimsig. In *Roodepoort Record*, 6/6/2022. Available online at https://roodepoortrecord.co.za/2022/06/06/city-power-pounces-on-illegal-connections-or-city-power-pounces-on-illegal-connections-in-informal-settlement-near-ruimsig/, checked on 4/4/2023.

Ndukui, Chege Ezekiel (2013): CHALLENGES OF SLUM UPGRADING FOR URBAN INFORMAL SETTLEMENTS; CASE OF SOWETO EAST VILLAGE IN KIBERA INFORMAL SETTLEMENTS, CITY OF NAIROBI. University of Nairobi (REG. NO: B42/82146/2012). Available online at https://www.google.com/url?sa=t&rct=j&q=&esrc=s&source=web&cd=&cad=rja&uact=8&ved=2ahUKEwjrtrO1-YOBAxVdS_EDHSmyBsYQFnoECA4QAQ&url=http%3A%2F%2Ferepository.uonbi.ac.ke%2Fbitstream%2Fhandle%2F11295%2F58641%2FFull%2520Text.pdf%3Fsequence%3D3&usg=AOvVaw04D-GrBUM-DRYTTwSoz5ht&opi=89978449.

Okore, M. LutherK.; Koske, James; Letema, Sammy (2022): Household-based determinants of cooking and heating fuel mixes in informal settlements of Kisumu City, Kenya. In *Energy for Sustainable Development* 71, pp. 64–72. DOI: 10.1016/j.esd.2022.09.002.

Susan Jamieson (2023): Likert scale | Social Science Surveys & Applications. Encyclopedia Britannica. Available online at https://www.britannica.com/biography/Rensis-Likert, updated on 8/7/2023, checked on 8/7/2023.

Tavernier, Louis; Rakotoniaina, Samy (2016): Review of energy kiosk development projects. In *Field Actions Science Report* (Special Issue 15), pp. 66–67. Available online at https://journals.openedition.org/factsreports/4165, checked on 8/31/2021.

THE PULSE Rwanda Ltd. (2022): What is THE PULSE. THE PULSE Rwanda Ltd. Rwanda. Available online at https://the-pulse.africa/about/, updated on 8/17/2022, checked on 10/5/2022.

The World Bank Group (2023): Doing Business | DataBank. System average interruption frequency index (SAIFI) (DB16-20 methodology) (IC.ELC.SAIF.XD.DB1619). Washington, D.C. Available online at https://databank.worldbank.org/reports.aspx?source=3001&series=IC.ELC.SAIF.XD.DB1619, updated on 8/22/2023, checked on 8/22/2023.

Trimble Inc. (2023): SketchUp 2023. Available online at https://www.sketchup.com/.

Urban, Boris; Maphalala, Jabu (2019): Solar turtle: searching for the game changer. In *EEMCS* 9 (2), pp. 1–20. DOI: 10.1108/EEMCS-02-2019-0032.

World Bank Group (2023): Access to electricity (% of population) - Sub-Saharan Africa | Data. Available online at https://data.worldbank.org/indicator/EG.ELC.ACCS.ZS?locations=ZG, checked on 8/22/2023.

Importance of Model Level of Detail and Level of Information in Non-image Forming Simulations: A Case Study on Real-life Office

Jaka Potočnik[1], Luka Pajek[1] and Mitja Košir[1]

[1] Faculty of Civil and Geodetic Engineering, University of Ljubljana, Ljubljana (Slovenia)

Abstract

Complex multispectral simulations and measurements of the luminous environment are required to assess daylight's Non-Image Forming (NIF) effect accurately. In the study, a cellular office located in Ljubljana, Slovenia, was modelled at different levels of detail (LOD) and levels of information (LOI) to determine their impact on the accuracy of the simulation results compared to the experimental measurements of illuminance and spectral irradiance at the vertical plane under clear sky conditions. The difference between simulations and experiments was evaluated through Relative Melanopic Efficacy error, comparing median values and IQR, and performing a pairwise statistical analysis with the Mann-Whitney test. The results were analysed on the level of the entire room, individually investigated measuring points and four view directions. The results showed that the simulation model's LOD and LOI significantly influence the error between simulated and experimental results. Furthermore, it was demonstrated that lower error was achieved for the measuring point further away from the window and view directions either pointed towards the window or to the surfaces with spectrally neutral materials (i.e. white wall). Generally, a model with high LOD and medium LOI is recommended for representative NIF simulations.

Keywords: NIF-effects, level of detail, level of information, daylight, circadian lighting, office

1. Introduction

It is generally accepted that to accurately evaluate the potential of Non-Image Forming effects (NIF) – effects of light which influence the rhythm of our circadian systems (Touitou et al., 2017) and consequentially also our moods, behaviour and alertness (Bellia and Fragliasso, 2021), one has to measure or simulate the luminous environment using intricate instruments or use complex multispectral simulations (Maskarenj et al., 2022). By default, these methodologies are inherently more time-consuming. For example, measurements of the circadian environment require spectrally distinctive measuring equipment (i.e., spectrometers). Furthermore, to achieve a spectrally discerning ability to predict the NIF environment, the simulation software (e.g., ALFA (LLC Sollemma, 2023)) has to utilise multiple parallel RADIANCE (RADSITE, 2012) raytracing algorithms which are computationally and timely consuming (Gkaintatzi-Masouti et al., 2021) and under assumptions that the material properties of the indoor luminous environment are correctly determined. Therefore, the primary goal of this study is to determine to what extent the information embedded in the simulation model expressed as the level of detail – LOD and the level of information – LOI affect the accuracy of the simulation results in comparison to the real-life measurements conducted in a small cellular office located in Ljubljana, Slovenia.

2. Methodology

2.1 Experiment

A real-life office at the Faculty of Civil and Geodetic Engineering in Ljubljana (46.05° N, 14.49° E) has been chosen as a case study. The selected cellular office is a typical office at the faculty, located on the 4th floor, and has dimensions of 5.00 m x 2.60 m (depth x width), with a floor-to-ceiling height of 2.40 m (Figure 1). The office has one window with dimensions of 1.20 m x 1.60 m (width x height) and is oriented towards the SE. The office was emptied of any redundant stationery, books, and chairs. All other furniture was left in the room to give the room a certain level of complexity, which would be appropriate to be modelled with simulation models (Figure 1). The benchmark experiment of the office was executed on the 24th of February 2022 under clear sky conditions at 30-minute measurement intervals from 11:00 until 13:30 local solar time.

10.18086/swc.2023.06.08 Available at http://proceedings.ises.org

The interior luminous conditions were measured with a custom rig (Figure 1), which emulated an average sitting occupant with a corneal height of 1.20 m. The rig simultaneously measured illuminance and spectral irradiance at the vertical plane (corneal height). FLA 603-VL4, V(λ) calibrated lux-meters (Almemo, 2023) with absolute error ±1 lx were used for illuminance measurements and calibrated concave slit grating spectrometer StellarNet BLACK-Comet (StellarNet, 2023) equipped with 180° cosine receptor at 1.5 nm resolution for the entire visual spectrum (380-780 nm) was used for measurement of spectral composition of daylight. The horizontal illuminance was also measured at a plane of 0.85 m above floor level. Exterior luminous conditions were simultaneously monitored on the faculty's roof with an external measuring rig (Figure 1), measuring global illuminance and global spectral irradiance during the experiments. Measurements were done at two preselected points in the office (L1 and L2, see Figure 1) for four cardinal view directions (0° – oriented towards the window, 90°– oriented towards the wall, 180° – oriented towards the door, 270° – oriented towards the cabinets), simulating various gaze directions of a hypothetical office occupant.

Fig. 1: Floorplan of the studied office (top-left), representing the equipment used for measurements (top-right). Picture of the office measured in the experiment (middle). Interpretation of LOD for the studied office (bottom).

2.2 Simulation

The digital models of the office were defined in the Rhinoceros software, while the simulations were executed with a plugin software for calculating circadian environment ALFA. The first step in establishing appropriate simulation geometry was determining the corresponding LODs and LOIs of the models. Both were considered in implementing geometry models intended for simulations to analyse luminous environments. Therefore, based on the already established LOD for BIM, we have defined a specific interpretation of LOD for luminous environments (EN 17412-1, 2020). Hence, the standard definitions were appropriated for the particularity of the requirements of the study of luminous environments. In total, 4 LOD levels, i.e. 100, 200, 300 and 500 (see Figure 1 and Table 1) and 3 LOI levels, i.e. minimum (LOImin), medium (LOImed) and maximum (LOImax), were used for the study. LOImin represents a spectrally neutral material environment, LOImed represents materials selected with visual matching from the ALFA library, and LOImax represents actual materials measured with a spectrophotometer.

Tab. 1: Description of the LOD used in the modelling (see also Figure 1).

LOD100	LOD200	LOD300	LOD500
Shoebox model, maximum level of geometry abstraction No furniture.	Defined wall thickness, defined window with simple frames, simple walls, segmentation in walls excluded, and added doors. No furniture.	Detailed walls, windows, doors, generic furniture (e.g. generic wardrobes, simple generic tables, chairs).	Detailed walls, windows, doors. Actual geometry of furniture in the office.

The simulations were performed with ALFA for the same conditions as the measurements (clear sky, half-hour steps, 24th of February, 11:00–13:30 local solar time). Analogously to the experiment, four view directions were simulated for each analysis point (L1 and L2), matching positions from the experiment. Simulations were executed for each possible combination of LOI and LOD. Experiment and simulation results were compared using the Relative Melanopic Efficacy – RME (Potočnik and Košir, 2020) factor, the quotient between photopic lx and equivalent melanopic lx, which enabled expression of the accuracy of the simulation procedure regardless of absolute irradiance. RME_{error} was calculated using the following equation:

$$RME_{error} = \frac{RME_{experiment} - RME_{simulation}}{RME_{experiment}} \times 100\% \qquad \text{(eq. 1)}$$

Hence, the negative values of RME_{error} indicate that the software overestimates the RMEs, while positive RME_{error} suggests that the simulation underestimates the RME compared to the experimental results.

3. Results

The results will be presented in 3 subsections. The first subsection will give the general impression of the impact of LOD and LOI on the accuracy of the simulations. The second and third subsections will delve deeper into the interpretation of errors occurring when categorising the results by the position in space and view direction.

3.1 Accuracy of simulations in relation to LOD and LOI

The results shown in Figure 2 demonstrate considerable differences in the error between LOI and LOD combinations compared to the experiment. As shown in Figure 2, the lowest median RME_{error} when evaluating the simulation results from the standpoint of LOD is calculated for the LOD100 (-4.05 %), while the highest RME_{error} is calculated for LOD300 (5.37 %). Additionally, we can observe that as the level of detail increases (LOD), the variation in the data error decreases (drop in IQR from 16.41 pp at LOD100 to 12.13 pp at LOD500). We could argue that the LOD500 model is the most reliable among the studied geometric models with the lowest IQR and second lowest median RME_{error} (3.65 %). To assess the statistical significance of variations in geometric between LOD100 to LOD200, LOD200 to LOD300 and LOD300 to LOD500, a pairwise statistical analysis with the Mann-Whitney test for non-parametric comparison of medians was executed. This analysis revealed that we cannot reject the hypothesis that the medians from LOD100 to LOD200 do not differ ($p = 0.36$). On the contrary, statistically significant different medians between pairwise comparisons of LOD200 and LOD300 ($p < 0.001$) and of LOD300 and LOD500 ($p < 0.05$) have been identified. In other words, these results suggest a statistically significant effect of changing the level of detail in the model except for the case of increasing the LOD from 100 to 200.

When we compare the results from the standpoint of LOI, as shown in the a) plot of Figure 2, the highest median RME_{error} is detected with the lowest level of detail LOImin (-6.04 %) and the lowest median RME_{error} is detected with the highest level of detail LOImax (0.69 %). The lowest IQR was calculated with LOImed (13.42 pp) and the highest with LOImax (20.72 pp). Pairwise Mann-Whitney test comparison revealed a statistically significant difference in means between pairs: LOImin and LOImed ($p < 0.001$), LOImed and LOImax ($p < 0.001$), and LOImin and LOImax ($p < 0.05$). Hence, the results indicate a statistically significant effect of LOI on the RME_{error}.

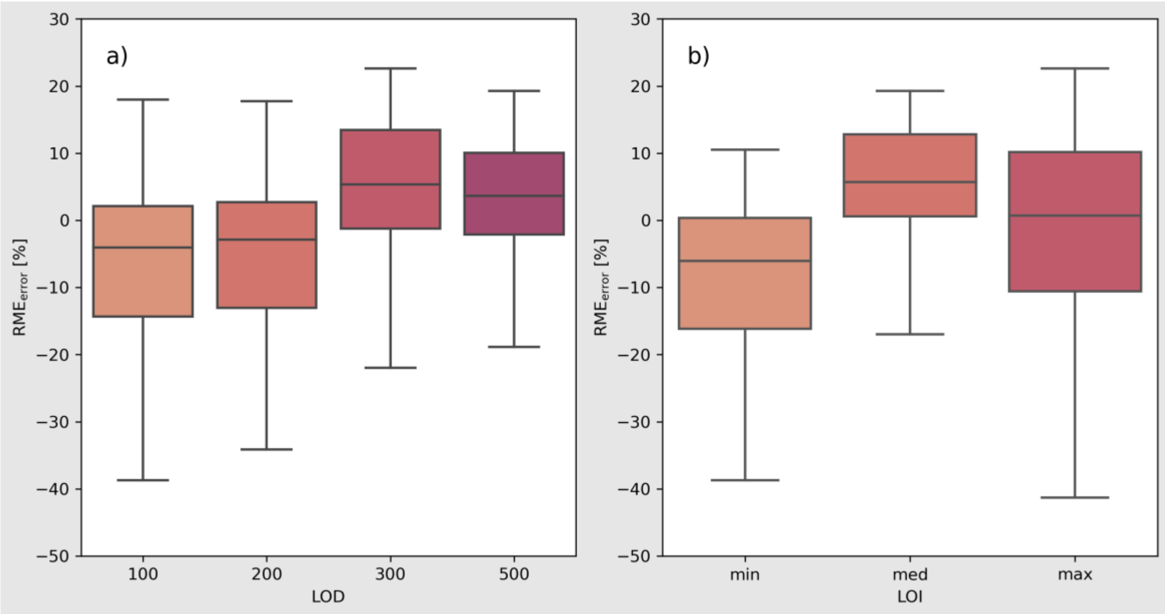

Fig. 2: RME_{error} between experiment and each simulation combination based on LOD classification (left plot) and LOI classification of results, on 24th of February, 11:00–13:30.

3.2 Accuracy of simulations in relation to LOD and LOI by measurement points

The investigated office was analysed from two measurement points. The L0 measurement point is closer to the window and is influenced more by direct daylight. In contrast, the L1 point is more influenced by the reflected light of diffuse/reflective surfaces of the office. Therefore, we were interested in investigating the results when categorised by point of measurement. In plot a) of Figure 3, we show the results of our analysis of the data grouped by measuring points, which reveal a lower median RME_{error} (-2.61 %) and smaller IQR of 14.66 pp for the point L1 (point further away from the window). Contrary to L0, which expresses underestimation of RME, specifically a median RME_{error} of 5.36 % with a larger IQR of 16.43 pp. Mann-Whitney comparison of medians reveals a significant difference ($p < 0.001$) between observed points, which means that the position in the space has a statistically significant influence on the accuracy of the result. Therefore, we can say that when observing all cases by points, the simulation results for the L1 point tend to be slightly more accurate than the ones for the L0 point.

To further investigate the results, we split the data for LOD and LOI (Figure 3, plots b) and c)). When results are categorised according to LOD, the smallest median RME_{error} for point L0 is identified with LOD100 (-0.13 %). In contrast, LOD500 expressed the slightest error (0.38 %) and IQR (8.84 pp) among results for L1. The largest median RME_{error} of 13.14 % was observed with LOD300, and the smallest IQR is expressed with results at LOD500 for point L0 (Figure 3, plot b)). Analogously to the results presented in Figure 2, when observing the results from the viewpoint of LOI, we can observe the lowest median RME_{error} for the LOImin (-1.45 %) and the lowest median RME_{error} (-2.89 %) for the L1 point with the simulation where LOImax materials were used. The lowest IQR for L0 (5.94 pp) and L1 (5.29 pp) points were identified for the LOImed case.

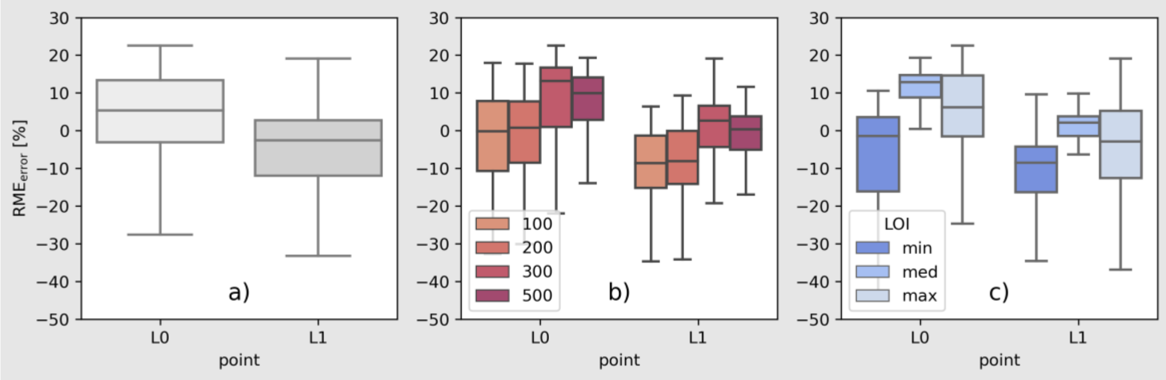

Fig. 3: RME_{error} between experiment and simulations according to the investigated points in the office (plot a), by point and LOD (plot b), by point and LOI (plot c).

3.3 Accuracy of simulations in relation to LOD and LOI view direction

The observed office was relatively small. However, it featured a varied selection of views, where view direction 0° was pointed towards the window opening and a big bookshelf. View directions 90° and 180° were characterised by a white wall with low furniture, and view direction 270° was pointed toward the large floor-to-ceiling cabinets. Thus, we were interested in exploring the relationship between RME_{error} and the investigated views. Plot a) of Figure 4 presents the RME_{error} calculated according to the view direction. The lowest median RME_{error} (0.44 %) and IQR (8.23 pp) were calculated for the 90° view. A similarly slight variation in results expressed in IQR of 10.43 pp was calculated for view direction 0°, which is the view 90 ° characterised by plenty of daylight and a low amount of detail. On the contrary, by increasing the amount of detail in the views, the IQR increases, resulting in the highest IQR (30.9 pp) and the most prominent RME_{error} (-19.51 %) of views at 270°. However, when looked at in depth from the standpoints of LOD (plot b) in Figure 4) and LOI (plot c) in Figure 4) we can argue that this high variance in results is due to the complexity of the views (i.e. a high portion of visible cabinets, floors, walls, ceilings etc.). Furthermore, combinations like LOImax and LOD100 (plot d) in Figure 4) resulted in a high median RME_{error} of -28.79 %. In comparison, the combination of LOImax and LOD500 resulted in distinctively lower median RME_{error} (6.43 %) and almost negligible IQR (4.83 pp). As shown in plot d) in Figure 4, similar is valid for combinations of LOD500 and LOImed, LOD300 and LOImed, and LOD300 and LOImax. Conversely, combinations involving LOD500 and LOImin (median RME_{error} of -29.17 %) and LOD300 and LOImin (median RME_{error} of -30.70 %) result in significantly reduced prominent overestimation of RME compared to the experimental values.

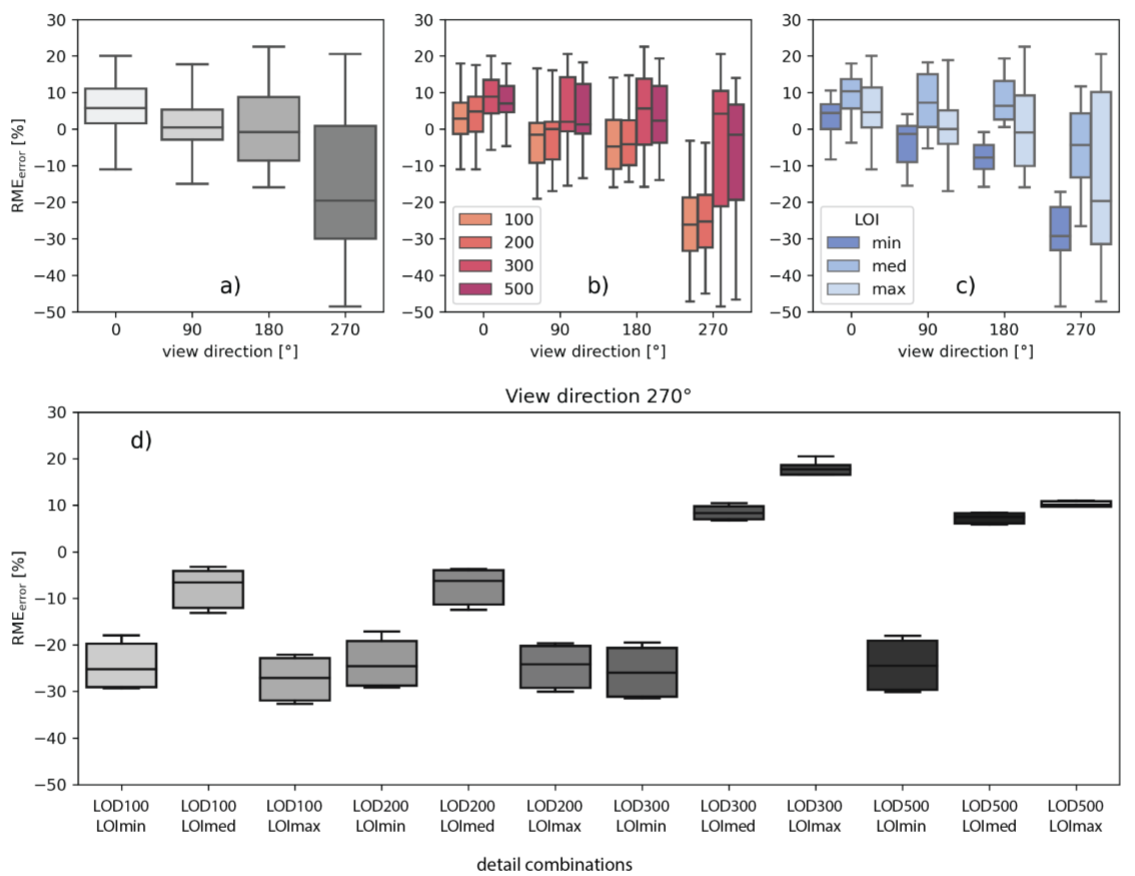

Fig. 4: RME_{error} between experiment and simulations according to the view direction (plot a), by view direction and LOD (plot b), by view direction and LOI (plot c). RME_{error} for the view direction 270° by LOI and LOD combinations (plot d).

4. Discussion and Conclusion

This study has investigated if and to what extent the level of detail (LOD) and the level of information (LOI) of a digital model for luminance environment simulations can affect the accuracy of results compared to the experiment on an example of a cellular office. The study's results have clearly shown that both LOD and LOI in the case of the investigated cell office under clear sky conditions significantly affected the simulation results. The rise of information in LOD caused a lower IQR and neutralised the overestimation of RME of the models without modelled furniture (i.e. LOD100 and LOD200). An increase in the information about materials lowered the median RME_{error}. However, on the other hand, the increase in the LOI also resulted in a higher IQR of simulation results. By itself, this might seem counterintuitive. However, comparing different LOD and LOI combinations for the view direction 270° has shown that the best performance will be identified with configurations where both LOD and LOI of the model are high (LOD300 or above and LOImed or above). Furthermore, significant differences in simulation accuracy were found between the two investigated spatial points and various view directions. The slightest errors were identified for the point further from the window (i.e. L0) and views directed towards the window (i.e. view 0°). On the other hand, the most prominent errors were found for the point closer to the window (i.e. point L1) and the views directed towards the wooden cabinets (i.e. view 270°).

As stated in the introduction, the simulation procedures for Non-image-forming effects of light are usually quite time-consuming, especially if the simulated materials are also measured by a spectrophotometer, which is expensive and often unavailable to everyone. Thus, we could argue that achieving a high LOD of the model is essential for the best results under clear-sky conditions. Later, the high LOD model can be reasonably combined with materials chosen from the simulation tool's library using visual matching. To be able to generalise these findings, the limitations of this study would need to be addressed through additional work. The study was executed only for one day and one type of weather conditions. Evaluation under overcast skies might mitigate the error due to the influence of direct sunlight. The office chosen was relatively small; a study of a bigger space is needed to see if the same LOD relationship is also valid for larger rooms. The simulation errors in the study were investigated solely through RME. Further insight might be gained by evaluating the differences between simulated and experimental spectral distribution curves.

5. Acknowledgements

The research presented in this paper results from a project funded by the Slovenian Research and Innovation Agency (project No. J2 – 3036). The authors further acknowledge the financial support from the Slovenian Research and Innovation Agency (research core funding No. P2 – 0158).

6. References

Almemo, 2023. Ahlborn measuring equipment. https://www.ahlborn.com/en/almemo (accessed 8.30.23)

Bellia, L., Fragliasso, F., 2021. Good Places to Live and Sleep Well: A Literature Review about the Role of Architecture in Determining Non-Visual Effects of Light. International Journal of Environmental Research and Public Health 2021, Vol. 18, Page 1002 18, 1002. https://doi.org/10.3390/IJERPH18031002

EN 174121:2020, 2020. Building Information Modelling — Level of Information Need.

Gkaintatzi-Masouti, M., van Duijnhoven, J., Aarts, M.P.J., 2021. Review of spectral lighting simulation tools for non-image- forming effects of light. J Phys Conf Ser 2042, 012122. https://doi.org/10.1088/1742-6596/2042/1/012122

LLC Sollemma, 2023. ALFA - Adaptive Lighting for Alertness https://www.solemma.com/Alfa.html (accessed 10.30.20).

Maskarenj, M., Deroisy, B., Altomonte, S., 2022. A new tool and workflow for the simulation of the non-image forming effects of light. Energy Build 262, 112012. https://doi.org/10.1016/J.ENBUILD.2022.112012

Potočnik, J., Košir, M., 2020. Influence of commercial glazing and wall colours on the resulting non-visual daylight conditions of an office. Build Environ 171, 106627. https://doi.org/10.1016/j.buildenv.2019.106627

RADSITE, 2017. Radiance. A validated Lighting Simulation Tool. https://www.radiance-online.org/ (accessed 8.30.23)

StellarNet, 2023. StellarNet Black Comet UV-VIS Concave Grating Spectrometer. https://www.stellarnet.us/spectrometers/black-comet-uv-vis-concave-grating-spectrometers/(accessed 8.30.23)

Touitou, Y., Reinberg, A., Touitou, D., 2017. Association between light at night, melatonin secretion, sleep deprivation, and the internal clock: Health impacts and mechanisms of circadian disruption. Life Sci. https://doi.org/10.1016/j.lfs.2017.02.008

Influence of the natural wind speed on the performance of solar thermal façades

Edward Frick[1], Maik Kirchner[1] and Federico Giovannetti[1]

[1] Institute for Solar Energy Research in Hamelin (ISFH), Emmerthal (Germany)

Abstract

The solar thermal activation of the building envelope offers untapped potential for novel solutions based on renewable energy in multi-story buildings. Activated façades designed as uncovered collectors are particularly suitable for the support of heat pump-based supply systems as they can gain heat from both solar energy and ambient air thus achieving high yields at low temperatures. The characterisation of such façades requires the modelling of the thermal performance in dependence of the wind speed. The wind speed in front of the façade is influenced by various factors such as the surroundings, the microclimate, thermal effects as well as the size of the façade. In order to model the wind dependency more accurately than in standard tests for solar thermal collectors, we carried out detailed wind field measurements on a 26 m² large active metal façade. The measurements showed that the flow behaviour in front of the façade is strongly affected by the wind direction. For wind directions parallel to the façade, we observed an almost linear velocity gradient in the vertical direction, while for wind directions perpendicular to the façade we reported a homogeneous distribution. The comparison of the measurements to wind data recorded by a nearby weather station suggests a scaling factor of 0.3 to 0.6. Based on our experimental results we performed an adjusted efficiency measurement of the metal façade and compared the yearly energy output calculated with both parameter sets. The difference is remarkable in low temperature ranges relevant for heat pump applications (i.e. 7.5% at 0°C) but negligible for operation temperatures above 10°C.

Keywords: solar thermal façades, building envelope, solar collector measurement, WISC, multi-story residential buildings, building integrated solar thermal

1. Introduction

In order to achieve net zero greenhouse gas emissions in the building sector, a significant increase of carbon-neutral heat generation technologies is required in both new and existing buildings. For this purpose, the energetic use of the building envelope is a meaningful measure, particularly for multi-story residential buildings due to their large ratio of available façade to roof area. Here, building integrated solar thermal systems can offer promising solutions with a high architectural quality (Maurer et al., 2017; Munari-Probst and Roecker, 2007). The combined use of solar thermal activated façades and heat pumps offers synergy effects such as the additional supply of environmental heat by the façades due to the low temperatures in the heat pumps evaporator (Frick et al., 2021). In particular, uncovered systems benefit from the better thermal coupling to the ambient air. Furthermore, the combination with geothermal heat pumps enables a regeneration of the ground source via the activated façades, which allows a more sustainable operation and a size-reduction of the required borehole heat exchanger field (Weiland et al., 2022; Hadorn, 2015).

Activated façades designed as uncovered solar collectors show a high dependency of the thermal performance on the wind speed due to the lack of a transparent glazing. The knowledge of this dependency is necessary to carry out performance and yield calculations and to properly dimension the heat supply system. For instance, the influence of the wind speed on the heat losses is characterized during collector performance measurements according to DIN EN ISO 9806 (2017) by determining the collector coefficients a_3 and a_6. During the measurements the wind speed is measured at one or more positions, usually outside of the collector surface area. The measured wind speed, however, can only reflect the actual wind flow velocities over the collector surface to a limited extent. Especially under natural weather conditions and with large collector arrays, the

10.18086/swc.2023.06.06 Available at http://proceedings.ises.org

wind field is usually highly inhomogeneous and is influenced by the surroundings, the collector surface itself and the microclimate (Simon et al., 2020). By using wind generators for the performance measurements, the resulting wind field shows different flow characteristics than the natural wind, which impacts the heat transfer between the collector surface and the ambient air. Furthermore, with large vertical facades at temperatures much higher than air temperature, the flow velocity field is overlapped by the upwards flow caused by natural convection, which is most noticeable at low wind speeds. Therefore, for large façades an estimation of the real mean wind speed over the façade and a proper positioning of the wind sensors are necessary to correctly assess its performance.

For the calculation of annual yields, location-based weather data is generally used. The wind speed is usually measured in undisturbed areas at a height of approximately 10 m (Burch and Casey, 2009). For a realistic estimation of the collector performance, the reduction of the wind speed at the collector level should be considered. For roof-installed solar thermal systems various approaches for the adjustment of the meteorological wind speed already exist: Haller et. al (2013) suggest a scaling factor of 0.5, while Burch and Casey (2009) suggest factors from 0.3 to 1, depending of the site and the height of the building. Other approaches for the calculation of wind speeds in different heights and depending on the site are the use of a logarithmic velocity profile in the atmospheric boundary layer as explained by Troen and Petersen (1990) as well as Hau (2017).

In order to obtain information about the actual wind flow velocities in front of large solar thermally active façades, we carried out wind field measurements on a test façade. After a description of the experimental setup, the paper presents and discuss the results. Furthermore, we analyzed the correlations between the wind velocities, which were measured at different positions inside and outside of the collector area, and compared them to the measurements from a nearby weather station. At last, we evaluated the performance measurement and correspondent yield calculations for the façade with the adjusted wind speed and compared them to the results based on standard procedures.

2. Experimental setup

The wind field measurements were carried out on a solar thermally active metal façade on a test stand at the Institute for Solar Energy Research in Hamelin, Germany. The test stand consists of a south-facing free-standing concrete wall with a size of 10 x 6 m² (width x height) and enables the parallel operation of two thermally active façades, each with an approximate area of 25 m². The façades are connected to hydraulic modules that allow the control of the mass flow and the inlet temperature of both façades. Moreover, the rear-side of the concrete wall is equipped with an electrical surface heating to emulate a constant interior wall temperature of a building. This measure enables the analysis of the impact of the activation on the heat flux through the wall under realistic conditions.

The test stand features an extensive measurement equipment to record the meteorological data and quantities of the façade prototypes. The meteorological station consists of two pyranometers for the measurement of the hemispherical solar irradiance in the façade plane and the horizontal plane, a pyranometer with a shadow ring for the diffuse irradiance, a pyrgeometer for the long-wave-irradiance and various sensors for measuring the ambient temperature and humidity.

To record the wind speed, three ultrasonic anemometers (MESA Systemtechnik) were installed at different positions parallel to the façade surface, which track the vertical and horizontal components of the airflow velocity in the plane in front of the façade. These were placed outside of the thermally activated area with a distance between the façade surface and the sensor of approximately 12 cm.

To characterize the façade, we used PT100-temperature immersion sensors to record the inlet and outlet temperature, PT100 surface temperature sensors for measuring the façade absorber temperatures, Coriolis flow sensors for determining the mass flow and heat flux panels to detect the heat flow through the wall structure. The façade as well as the test stand are described in more detail in (Frick et al., 2022).

Two different large-scale solar thermal activated façades were installed on the test wall: A double glazed glass façade with an active area of 22 m² and an uncovered metal façade with an active area of 26 m². Both façades feature a standard rear-ventilated design with a mineral wool insulation of 180 mm (thermal conductivity of

0.035 W m^{-1} K^{-1}, ROCKWOOL Fixrock 035 VS) and a ventilation gap of 60 mm (metal façade) and 45 mm (insulation glass façade). The solar thermal activation was achieved by the application of heat exchangers on the rear-side of the claddings in the ventilation gap. In case of the metal façade, the heat exchangers were fixed with clamping profiles and threaded bolts (Frick et al., 2021). In case of the glass façade an adhesive layer was used for the connection. Fig. 1 shows the façade test stand with the installed thermally activated façades as well as the measured meteorological quantities.

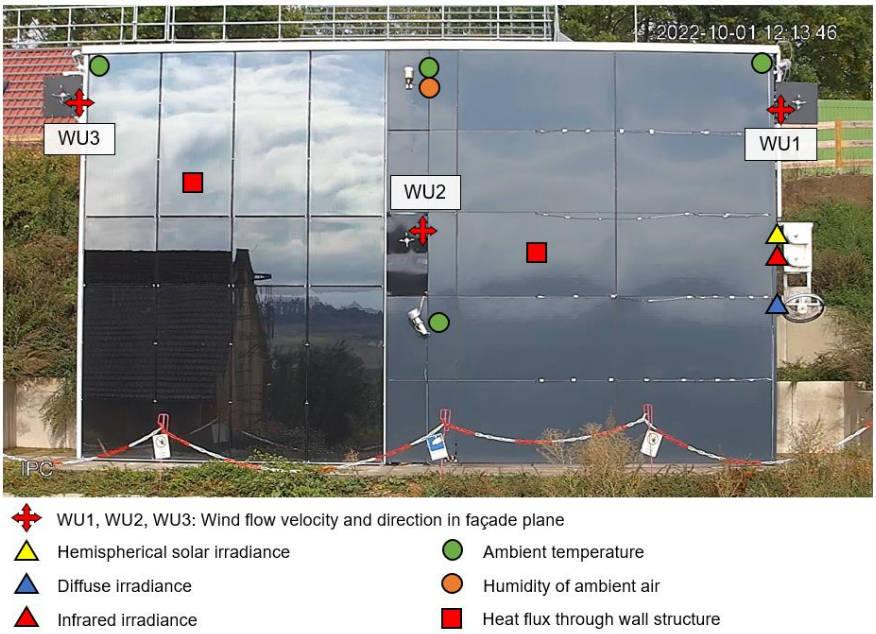

Fig. 1: Façade test stand. Left: Solar thermal active glass façade. Right: Solar thermal active metal façade.

For the wind field measurements, nine thermal anemometers (SCHMIDT Technology) were installed over the area of the activated metal façade additionally to the ultrasonic anemometers. The sensors were aligned perpendicular to the façade surface, in order to measure the absolute value of the wind flow velocity in the façade plane. Eight thermal anemometers were distributed evenly within the activated area of the metal façade, while another one was installed as a reference directly next to the central ultrasonic anemometer. In order to record the velocity of the free wind flow in front of the façade without impact of viscous effects near the façade surface, the thermal anemometers were placed at a distance of 6 cm from the façade surface, outside of the boundary layer (estimation of the maximum boundary layer thickness for the façade test stand at a wind speed of 0.1 m/s and an ambient temperature of 30°C: $\delta \approx 4.35$ cm). Fig. 2 shows the exact positions of the anemometers installed on the metal façade as well as the labeling of the individual measuring points used in this article.

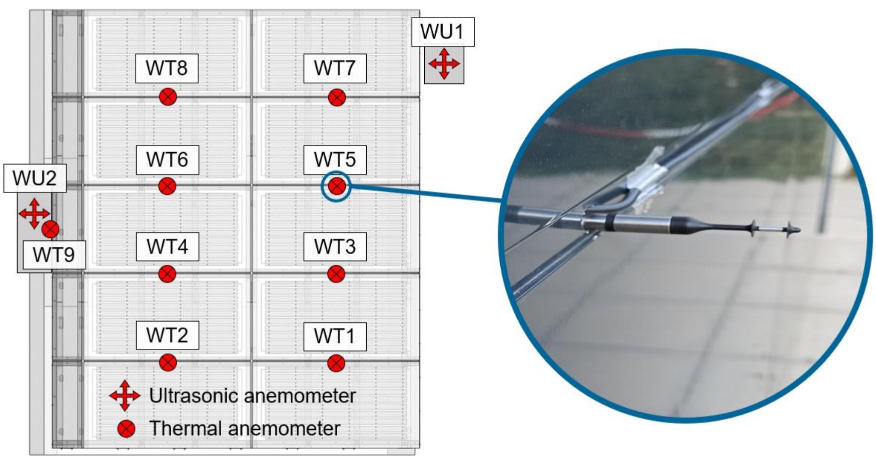

Fig. 2: Left: Positions and labels of the ultrasonic anemometers and thermal anemometers installed on the solar thermally activated metal façade. Right: Thermal anemometer installed on the metal façade with a distance of approximately 6 cm between the façade surface and the measuring probe.

The measured wind speeds are also compared to the data from a nearby freestanding weather station. The weather station is located at a distance of approximately 70 m from the façade and uses an ultrasonic anemometer to record the wind speed as well as the wind direction at a height of about 3 m above the top of the test façade.

3. Evaluation of the wind field measurements

To investigate the correlation between the flow velocities at the individual sensor positions, we carried out a sequence of measurements. To measure the flow velocities caused by the natural wind and to minimize the effects of natural convection due to temperature differences between the façade surface and the ambient air, the fluid temperature inside both test façades was controlled, so that the surface temperature of the façades approached the ambient temperature. A total of approximately 158 hours of data from 18 different days were used for the evaluation of the measurement sequence. The average wind speeds that occurred during these measurements in front of the metal façade range from 0 to 3.5 m/s. The data was recorded with a time step interval of 1 s. For the visualization of the results in the following section, these data points were averaged over 1-minute intervals.

In a first step, we compared the results of the ultrasonic anemometer WU2 to the results of the thermal reference anemometer WT9. This was done to eliminate a systematic measurement error caused by the different measurement methods used for these studies. Additionally, the distance of the thermal reference anemometer to the façade surface was varied between 6 cm and 12 cm in order to analyze the influence of the distance on the measurement results. Fig. 3 shows the comparison between the measured wind speeds of both sensors during the measurement sequence. The flow velocities measured by the thermal anemometer are plotted as data points over the simultaneously measured flow velocities of the ultrasonic anemometer:

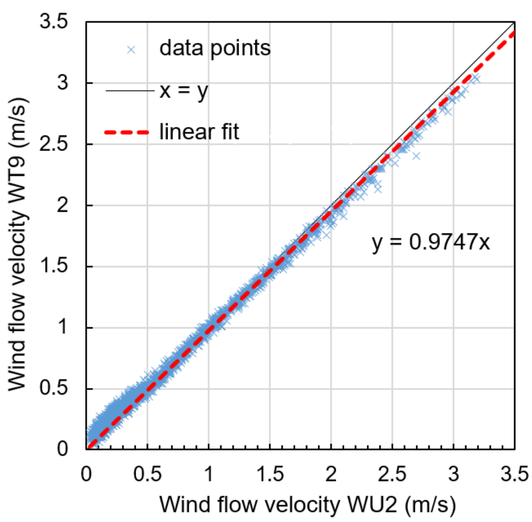

Fig. 3: Comparison between wind flow velocities measured at the ultrasonic anemometer WU2 (x-axis) and the thermal reference anemometer WT9 (y-axis). Measurement points averaged over 1-minute intervals in blue and linear regression of data points in red.

The linear regression of the data points indicates a high correlation between the results of the thermal anemometers and the ultrasonic anemometers of f(x) = 0.975x, with a relative error of approximately -2.5%. The error lies within the manufacturer's information on the measurement accuracy of both sensors, which is given as ± (5% + 0.004 m s^{-1}) for the thermal anemometer and ± 0.1 m s^{-1} for the ultrasonic anemometer. Furthermore, the variation of the thermal anemometer distance from the façade surface shows no noticeable effect on the measurement compared to the ultrasonic anemometer. Therefore, the comparison of measurements from both anemometer types provides valid results.

In a next step, the correlation between wind direction and wind speed measurement on the façade test stand was analyzed. Fig. 4 shows the distribution of wind speeds and wind directions recorded at the weather station during the wind field measurements. The diagram illustrates two dominant wind directions: west direction with wind speeds up to 10 m s^{-1} and south-southeast direction with wind speeds up to 8 m s^{-1}. On the other hand, northwest to east directions only occurred with relatively low wind speeds below 2 m s^{-1}. Similar results were reported during other experiments at ISFH by Lampe et al. (2019). Because of the south orientation of the façade test stand, the majority of the airflow toward the test façades is either parallel to the façade plane (with wind direction west) or perpendicular to the façade plane (with wind direction south).

To analyze the impact of the wind direction on the wind speed measurement in front of the façade, two different data sets filtered by the wind direction are considered separately in the following section (compare Fig. 4a: green - wind direction south-southeast from 95° to 220°, red - wind direction west from 230° to 310°). Fig. 4 b) to d) depict the vertical and horizontal component of the measured wind speed in the façade plane by the ultrasonic anemometers WU1, WU2 and WU3. A data point in the upper left quadrant thus represents an upward flow in the eastern direction. For west direction, the diagrams show a similar distribution of the data points for all three sensors: As expected the measured airflow near the façade surface is mostly towards the eastern direction and airflow in other directions only occurs with low flow velocities. Here, the anemometer WU3 records slightly higher maximum velocities than the other two with up to 3.5 m s^{-1} (WU1: approximately 3 m s^{-1}, WU2: approximately 2 m s^{-1}). This indicates a slight velocity gradient in the vertical direction with wind direction parallel to the façade surface. Furthermore, the sensor WU1 mainly records airflow with an upward component, while the other two sensors also record downward airflow.

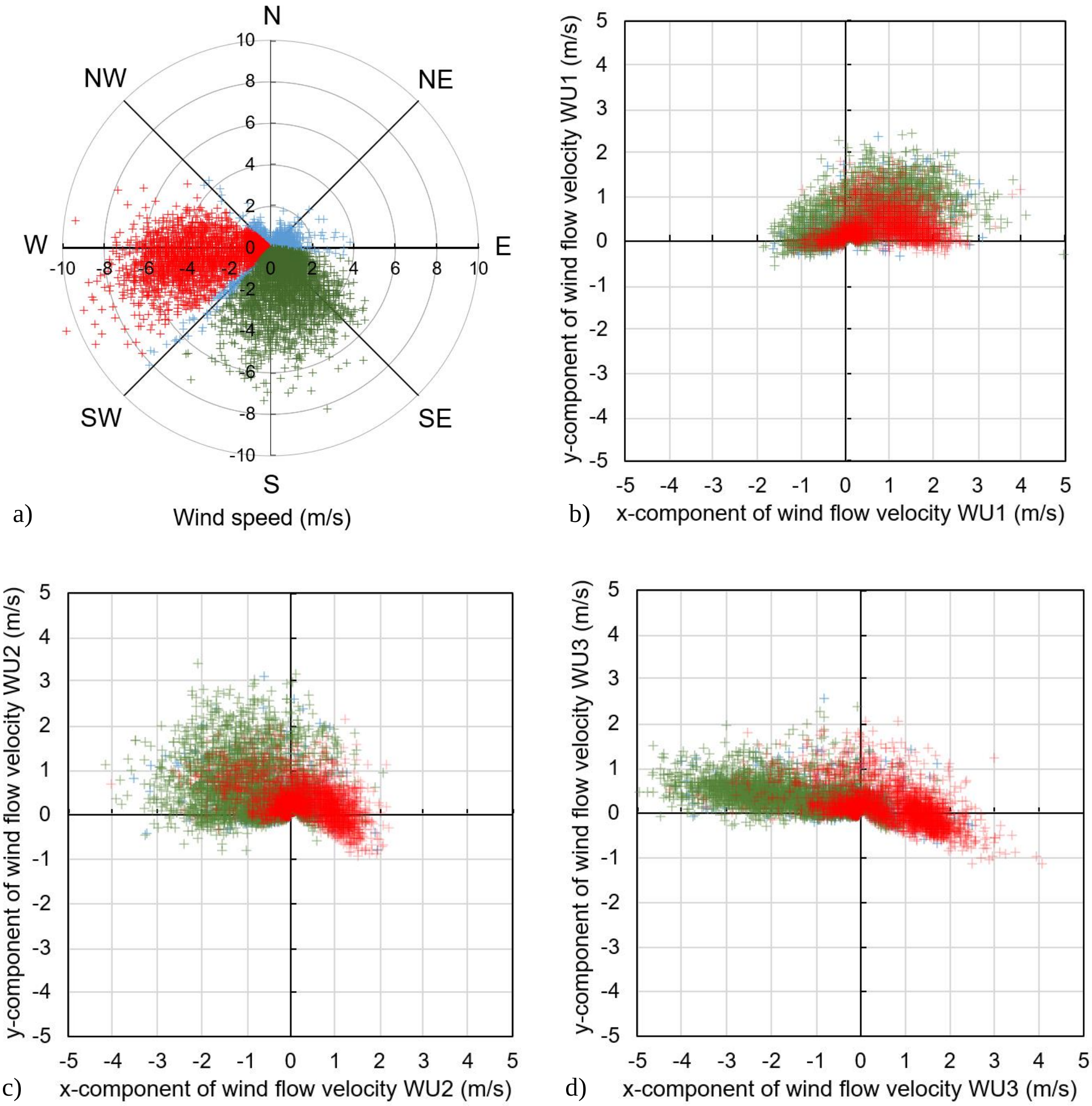

Fig. 4: a) Distribution of measured wind speeds and wind direction at the ISFH weather station during the wind field measurements. b) to d) Vertical (y-axis) and horizontal (x-axis) components of the measured wind flow velocity in the façade plane on the ultrasonic anemometers WU1, WU2, WU3. Red: Data points for west direction (230° to 310°). Green: Data points for south-southeast direction (95° to 220°). Blue: Remaining data points.

For wind direction south-southeast, the distribution of the recorded data points differs significantly from each other: While the anemometer WU1 mainly detects airflow to the eastern direction as in the previous example, WU2 and WU3 show a high tendency for airflow to the western direction. Furthermore, the sensor WU3 also records significantly higher velocities than WU1 and WU2 with up to approximately 4.5 m s^{-1} (WU1 and WU2 both show a maximum of about 3 m s^{-1}, although in different directions). The different behaviour of the airflow at the three positions can be explained by the specific installation of the sensor WU3, which is unobstructed towards the western direction. Wind that comes from southeast can flow in this direction mostly undisturbed, while at sensor WU1 the airflow to the west is restricted by the surface of the façade and thus tends to flow in the eastern direction. For the central sensor WU2 the wind is in this case obstructed in both directions so that airflow with a significant upwards component occurs. Therefore, with wind directions perpendicular to the façade surface, the positioning of the anemometers has a significant effect on the measurement results.

In the next step, the deviation of the flow velocity at the different sensor positions to the mean wind speed in front of the façade was investigated. For this purpose, the mean wind speed was defined as the average value of the measured flow velocities from the thermal anemometers WT1 to WT8, which were distributed evenly over the façade area. Fig. 5 shows an example of the measured data points in the upper (mean value form WT7 and WT8) and in the lower (mean value from WT1 and WT2) area of the façade plotted over the defined mean wind speed over the façade. The mean value was calculated because sensors at the same installed height show a similar behaviour. Again, two different data sets filtered by the wind direction west (red) and south-southeast (green) were considered for the analysis. For a better visualization the data points were averaged over 5-minute intervals.

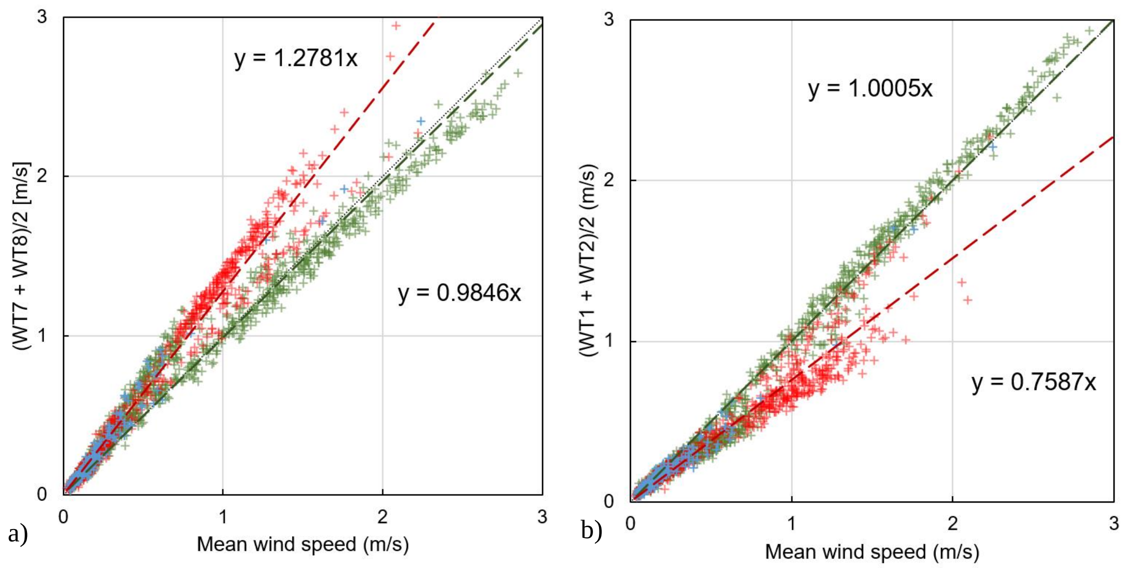

Fig. 5: Correlation between measured wind flow velocities in the upper (a) and lower (b) area of the activated metal façade and the mean wind speed over the façade. Measured data points averaged over 5-minute intervals. Red: West direction. Green: South-southeast direction. Blue Remaining data points.

The diagrams show that the trend of the data points is highly dependent on the considered wind direction. For south-southeast direction, the linear regression of the data points is nearly 1.0. Therefore, the measured flow velocities correspond precisely to the mean wind speed over the façade. In this case, the correlation indicates that there is a homogeneous wind field in front of the façade with only small deviations from the mean wind speed. For west direction, the regression for the flow velocity is approximately 1.28 in the upper façade area and 0.76 in the lower façade area. For a mean wind speed of 1.5 m s^{-1} the difference in the flow velocity between the lower and upper area is therefore about 0.78 m s-1. Tab. 1 lists the scaling factors for the mean wind speed for all installed anemometers on the façade test stand as well as the nearby weather station for the considered wind directions. Furthermore, Fig. 6 shows the scaling factors as a function of the installation height of the respective anemometer on the test façade.

Tab. 1: Scaling factors to the mean wind speed over the façade for the installed anemometers for wind directions west and south-southeast

	WT1	WT2	WT3	WT4	WT5	WT6	WT7	WT8
west	0.74	0.78	0.96	0.91	1.02	1.04	1.28	1.28
south-southeast	0.99	1.00	1.07	1.06	0.93	0.97	0.99	0.97

	(WT1 + WT2)/2	(WT3 + WT4)/2	(WT5 + WT6)/2	(WT7 + WT8)/2
west	0.76	0.93	1.03	1.28
south-southeast	1.00	1.06	0.95	0.98

	WU1	WU2	WU3	Weather station
west	1.29	1.05	1.33	3.49
south-southeast	0.96	1.10	1.45	1.71

The scaling factors of the remaining anemometers and the plot as a function of the installation height confirm the previous statements: In case of wind direction perpendicular to the façade, both the thermal anemometers and the ultrasonic anemometers WU1 and WU2 show scaling factors near 1.0. Therefore, the wind field over the metal façade is homogeneous. The ultrasonic anemometer WU3, that is installed on the glass façade, records considerably higher flow velocities with a scaling factor of around 1.45 due to the unobstructed positioning in the western direction, for the already mentioned reasons. The comparison of the data from the weather station shows that measured wind speeds are approximately 1.71 times higher than in front of the façade.

For wind direction parallel to the façade, the results show a strong correlation between the scaling factors and the installation height of the anemometer on the façade with an almost linear behaviour. The scaling factor increases by approximately 0.142 per meter. Accordingly, at a mean wind speed of around 1.5 m s^{-1} the wind field shows a flow velocity gradient of approximately 0.213 m s^{-1} per meter in the vertical direction. The scaling factors of the ultrasonic anemometers also confirm this behaviour regardless of their positioning relative to the façade test stand. Thus, WU1 and WU3 have similar scaling factors at the same installation height. The weather station records approximately 3.49 times higher velocities compared to the mean wind speed in front of the façade.

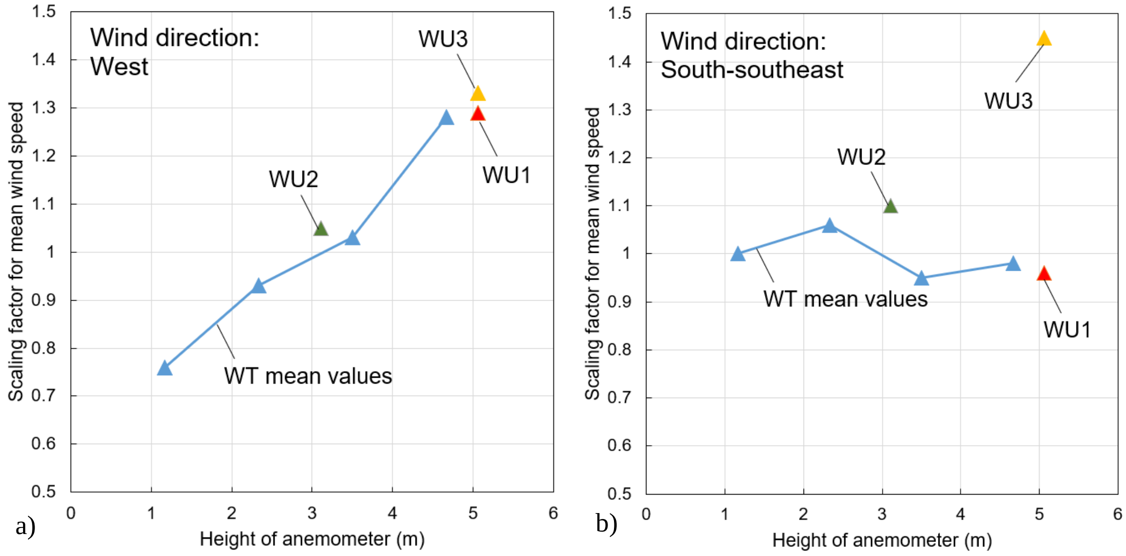

Fig. 6: Dependence of the scaling factor of the installed anemometers to the mean wind speed from the installation height on the test façade. a) Wind direction west. b) Wind direction south-southeast.

4. Performance measurements with adapted wind speed

The results of the wind field measurement were included in the performance measurement of the façade in order to model the influence of the wind speed on the collector performance of the façade more accurately. In the following section, the comparison of the performance characterization with and without adaptation of the reference wind speed is presented.

Frick et al. (2022) demonstrated the performance characterization of the large-scale active metal façade using the quasi-dynamic testing procedure (QDT) as well as a comparison to the steady-state performance measurement (SST) of a single module of the metal façade in the ISFH sun-simulator. It should be noted that the characterization was carried out without the reduction of the wind speed by a constant 3 m s^{-1} according to the DIN EN ISO 9806 (2017), because wind speeds above 3 m s^{-1} rarely occur in front of the façade. A valid evaluation of the parameters a_3 and a_6 is therefore only reasonable without this adjustment. Tab. 2 summarizes the determined collector parameters and compares it to adjusted values that have been calculated by using the adapted wind speed from this study.

Tab. 2: Results of the performance characterization of the solar thermally active metal façade. Indoor steady-state measurement (SST) on a single module as well as outdoor quasi-dynamic measurement (QDT) on the large-scale façade with and without adjustment of the reference wind speed.

Parameter	**$\dot{m}$** kg/hm²	**$\eta_{0,hem}$ / $\eta_{0,b}$**	**K_d** -	**r** -	**a_1** W/m²K	**a_3** J/m³K	**a_4** -	**a_5** J/m²K]	**a_6** s/m
SST-Indoor Single module	60	0.56	-	-	9.86	**1.22**	0.58	-	**0.0386**
QDT-Outdoor Without adapted wind	60	0.59	0.98	0.159	11.33	**0.103**	0.212	22755	**0.0144**
QDT-Outdoor With adapted wind	30	0.55	0.98	0.159	10.96	**1.10**	0.212	22755	**0.0097**

It can be seen that the wind-dependency of the heat loss coefficient a_3 is significantly lower for the outdoor measurement with 0.103 J m^{-3} K^{-1} than for the laboratory measurement with 1.22 J m^{-3} K^{-1}. The comparison to the parameters of common uncovered collectors also shows, that a much higher value for a_3 should be expected than that determined with the outdoor tests. The low a_3 value can be explained by two reasons: First of all, the ultrasonic anemometer WU1 was used for the reference wind speed to evaluate the collector coefficients. As shown in the previous section of the article, during wind direction west, WU1 records flow velocities that are approximately 29% higher than the mean wind speed on the façade.

The effect of the wind speed on the heat losses is thus underestimated in the evaluation. Secondly, the used reference anemometer is located directly next to the investigated façade. This means that with higher façade temperatures the anemometer measures airflow due to the natural convection additionally to the natural wind airflow. The measured velocities at higher absorber temperatures are thus always larger than at low absorber temperatures, which again leads to an underestimation of the effect of the wind speed on the heat losses at higher temperature points. This effect becomes more significant during test periods with generally low wind speeds.

For the adjusted values, the ultrasonic anemometer WU3, that is located near the glass façade, was chosen as the reference wind sensor for the evaluation. During the performance measurements, the temperature of the glass façade was controlled to approach the ambient temperature, to minimize the effect of natural convection on the sensor WU3. During the performance measurements, both wind directions south and west were recorded at the weather station. As shown in section 3, WU3 detects velocities approximately 33% above the mean wind speed in front of the metal façade for wind direction west and 45% higher velocities for wind direction south (Tab. 1). To adjust the measured value at position WU3 to the mean wind speed of the metal façade, the data was scaled by a factor of 0.72 (mean value of 1/.133 and 1/1.45). Wind speeds with a maximum of approximately 3 m s^{-1} were recorded on the metal façade during the adapted performance measurements. For the quasi-dynamic evaluation of the collector coefficients, the recorded data was averaged over 30-second intervals. The incident angle modifiers for direct and diffuse radiation as well as the collector parameters a_4 and a_5, which were determined during the first performance measurement, were not evaluated again to avoid correlations between the coefficients and to be able to focus on the effect on the parameters a_1, a_3 and a_6.

The results show, that the zero-loss efficiency with 0.55 is slightly smaller for the adjusted performance measurements than for the regular performance tests with 0.59. The reason for this deviation is the different fluid mass flow set during the measurements. The regular measurement was carried out with a specific mass flow of 60 kg h^{-1} m^{-2}, which ensures a turbulent flow inside of the heat exchangers over the full temperature range. For the adjusted performance measurement, which was carried out during long-term tests under typical operation conditions, the specific mass flow was set to 30 kg h^{-1} m^{-2}, which leads to a laminar flow and a less efficient heat transfer in the heat exchangers at lower fluid temperatures.

The heat loss coefficient a_3 from the adjusted performance measurement is much closer to the results from the laboratory test and the expected value for an uncovered collector. With the adjusted measurements the correlation between the wind speed and the collector performance is thus estimated more accurately.

To visualize the effect of the higher a_3 value, we calculate the expected thermal output of the façade using the standard collector model from DIN EN ISO 9806 (2017) with the coefficients from Tab. 2. The zero-loss efficiency of the adapted coefficients was set to 0.59 to compensate for the different fluid mass flow during measurements. Fig. 7 a) shows a comparison between the modelled thermal output for the characterization with and without adjusted wind speed measurement at a solar irradiation of G_{Hem} = 1000 W m^{-2} for three different wind speeds.

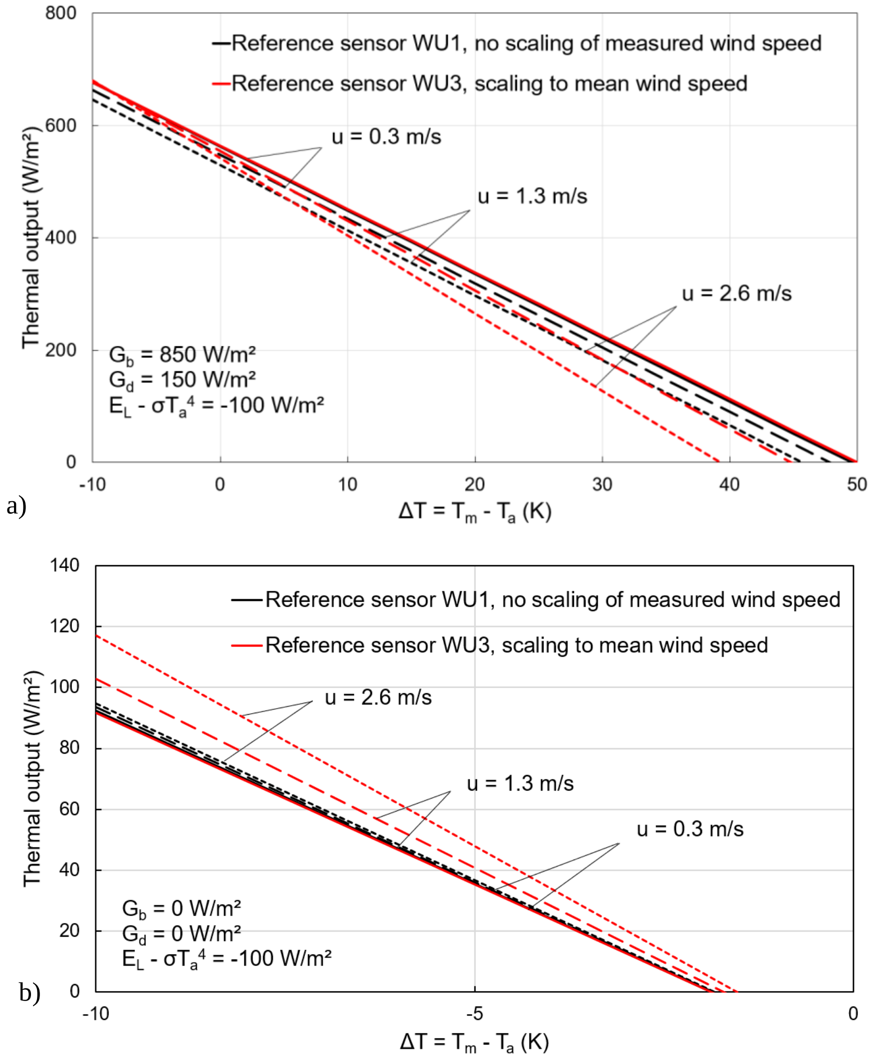

Fig. 7: Comparison of the efficiency curves of the solar thermal active metal façade for performance characterization with and without adjusted wind speed measurement. a) Efficiency curves for solar irradiation G_{Hem} = 1000 W m^{-2}. b) Without solar irradiation.

The diagrams show that, without adjustment of the wind measurement, the wind speed has no significant effect on the collector efficiency apart from a slight parallel shift of the performance curves. Due to the higher a_3 value from the adjusted performance tests, the efficiency curves for different wind speeds diverge significantly with higher temperature differences. Furthermore, the maximum temperatures, at which the metal façade is able to generate heat, differ for both performance characterizations: Without the adjustment, the stagnation temperature drops by approximately 3 K at a wind speed of 2.6 m s^{-1} compared to 0.3 m s^{-1} (49 K to 46 K), while it drops by about 10 K with the adjusted measurement (47 K to 37 K). Fig. 7 b) shows the thermal output for the façade as an environmental heat exchanger without solar irradiation. The comparison shows that the effect of the more accurate a_3 value increases significantly with higher temperature differences.

The different behaviour of the thermal output has an impact on the results of annual yield simulations. To estimate the effect, gross thermal yield calculations were carried out for the active metal façade with the calculation tool ScenoCalc (ESTIF) using both sets of collector coefficients. Fig. 8 shows the results of the yield calculations for a south oriented façade with weather data from Würzburg, Germany as a function of the mean fluid temperature inside the façade. The meteorological wind speeds were scaled with a factor of 0.5 for the calculations. As for the performance measurements, the wind speeds were not reduced by a constant 3 m s^{-1} according to DIN EN ISO 9806 (2017).

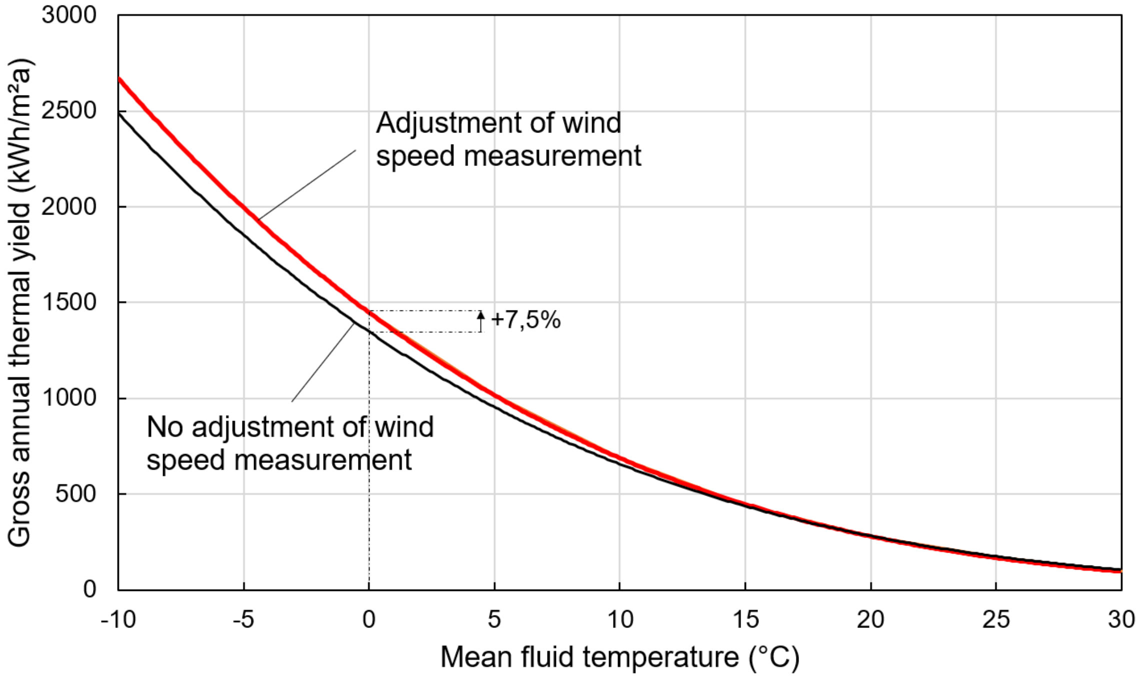

Fig. 8: Comparison of the gross annual thermal yield for the solar thermal active metal façade using the collector coefficients with and without adjusted wind speed measurement. Calculation of the gross thermal yield with ScenoCalc (ESTIF) for a south oriented façade with weather data from Würzburg, Germany.

The diagram illustrates that the main effect of the wind-dependency is noticeable at low temperatures, because the façade mainly operates as an environmental heat exchanger in that temperature range. At a mean fluid temperature of 0°C (e.g. for an application of the façade as a heat pump source or for the regeneration of ice storages) the calculated gross annual thermal yield is approximately 101 kWh m^{-2} a^{-1} higher (relative deviation of 7.5%) when using the coefficients for the accurate wind dependency. At higher temperature both yield curves converge. The effect of the wind speed becomes smaller because the façade operates mainly as a solar absorber and less as an environmental heat exchanger. For applications in temperature ranges above 10°C the relative deviation is below 5% and thus, the impact of the real wind speed is negligible if compared to the results based on performance measurements according to standard procedures.

5. Summary

The paper presents investigations on the effect of the wind speed on the thermal behaviour of solar thermal active façades, which are designed as uncovered collectors. For the investigations, we carried out a wind field measurement on a rear-ventilated metal façade at our façade test stand. For this purpose, a set of thermal anemometers were installed on the test façade in addition to the three already installed ultrasonic anemometers: Eight of the thermal anemometers were distributed evenly within the active area of the metal façade. At the same time, wind data from a nearby weather station was used for the evaluation.

The evaluation of the wind field measurement showed that the two dominant wind directions have a significant influence on the behaviour of the airflow on the façade. With an airflow parallel to the façade surface, a distinctive flow velocity gradient in the vertical direction could be observed. The deviation from the mean wind speed in front of the façade can be approximated as a linear function of the vertical position. The scaling factor for the mean wind speed increases by approximately 0.142 per meter. Also, for this case the positioning of the anemometers inside or outside of the façade area seems to be negligible. For perpendicular airflow on the façade surface the measurements showed that a highly homogeneous wind field in front of the façade is. All the thermal anemometers installed inside the façade area showed similar results. When placing wind sensors outside of the façade area, however, the positioning can affect the measurement results. The comparison to the measured data from the nearby weather station indicate scaling factors of 1.71 to 3.49 depending on the wind direction. These results confirm the adjustment factors of the meteorological wind speeds proposed by Haller et al. (2013) as well as Burch and Casey (2009).

An adjusted performance characterization of the solar thermal active metal façade was carried out with the results from the wind field measurements. The characterization showed that by minimizing the effect of the natural convention of the façade on the reference anemometer and adjusting the measured wind speeds with scaling factors from the wind field measurement, an accurate model for the wind-dependency of the heat losses can be obtained, which is significantly closer to the expected values of uncovered solar collectors and to the values from the laboratory measurements on a single façade module.

The effect of the accurate representation of the wind dependency is most noticeable in yield simulations with generally low fluid temperatures. A comparison of the gross annual thermal yields of the active metal façade shows that with a more accurate model for the wind dependency a 7.5% higher yield is predicted at fluid temperatures around 0°C. This is particularly significant for low-temperature applications such as the regeneration of ice storages or the use of the façade a as heat source for heat pumps.

It should be noted that the results of this work refer to the specific configuration of the façade test stand at the ISFH and are influenced by the surroundings and the microclimate. In order to verify the general applicability of the results to other configurations, a comparison of the results to measurements from other façades and at various locations is necessary.

6. Acknowledgments

The work is based on the results of the project "Solar-VHF", funded by the Lower Saxony Ministry of Science and Culture and by the German Federal Ministry of Economic Affairs and Climate Action (BMWK, reference number 03ETW013A), following a decision of the German Parliament. The investigations are carried out in cooperation with the Fraunhofer-Institut für Bauphysik IBP and the German companies Konvortec GmbH & Co. KG, Systea Pohl GmbH, Gundlach GmbH & Co. KG Wohnungsunternehmen, Pforzheimer Bau und Grund GmbH and Clina Heiz- und Kühlelemente GmbH. The authors are grateful for the support and responsible for the content of the publication.

7. References

Burch J., Casey R., 2009. Wind issues in solar thermal performance ratings. National Renewable Energy Laboratory, Buffalo, New York. Available at https://www.osti.gov/servlets/purl/952890 (Accessed 10 October 2023)

DIN EN 9806:2018-04, 2018. Solar energy – Solar thermal collectors – Test methods (ISO 9806:2017); German version EN ISO 9806:2017. Beuth Verlag GmbH. https://dx.doi.org/10.31030/2681379

ESTIF, 2019. ScenoCalc tool (Solar Collector Energy Output. European Solar Thermal Industry Federation (ESTIF).

Frick E., Büttner C., Kirchner M., Giovannetti F., 2021. Solar thermal, rear-ventilated façades as heat pump sources in multi-storey buildings. *ISES Solar World Congress*, Online Conference, 25-29 October.

Frick E., Kirchner M., Büttner C., Wehmeier T., Giovannetti F., 2022. Dynamische Charakterisierung solarthermisch aktiver Fassaden als Quelle für Wärmepumpensysteme. *32. Symposium Solarthermie und innovative Wärmesysteme*, Bad Staffelstein, 3-5 May.

Hadorn J.-C., 2015. Solar and Heat Pump Systems for Residential Buildings. Ernst & Sohn, Hoboken.

Haller M. Y., Dott R., Ruschenburg J., Ochs F., Bony J., 2013. The Reference Framework for System Simulations of the IEA SHC Task 44 / HPP Annex 38 Part A: General Simulation Boundary Conditions A technical report of subtask C Report C1 Part A. IEA Solar Heating and Cooling Programme. http://dx.doi.org/10.13140/2.1.2221.4727

Hau E., 2017. Windkraftanlagen: Grundlagen. Technik. Einsatz. Wirtschaftlichkeit, 6. Aufl. Springer Berlin Heidelberg, Berlin, Heidelberg.

Lampe C., Kirchner M., Littwin M., Giovannetti F., Asenbeck S., Fischer S., 2019. Experimentelle Untersuchungen an Testfeldern mit SOLINK-photovoltaisch-thermischen Kollektoren. *29. Symposium Solarthermie und innovative Wärmesysteme*, Bad Staffelstein, 21-23 May.

Maurer C., Cappel C., Kuhn T. E., 2017. Progress in building-integrated solar thermal systems. Solar Energy 154, 158-186. https://doi.org/10.1016/j.solener.2017.05.065

MESA Systemtechnik GmbH, 2023. MESA WSWD SONIC Anemometer Datenblatt [Online]. Available at https://mesa-systemtechnik.de/datenblaetter/WSWD_Sonic.pdf (Accessed 10 October 2023)

Munari-Probst M. C., Roecker C., 2007. Towards an improved architectural quality of building integrated solar thermal systems (BIST). Solar Energy 81, 1104-1116. https://doi.org/10.1016/j.solener.2007.02.009

ROCKWOOL GmbH Co. KG, 2023. Fassadendämmplatte Fixrock 035 VS Datenblatt [Online]. Available at https://p-cdn.rockwool.com/syssiteassets/rw-d/datenblatter/fassade-vhf/db-fixrock-035-vs-rockwool.pdf?f=20220801092500 (Accessed 10 October 2023)

SCHMIDT Technology GmbH, 2023. SCHMIDT Strömungssensor SS 20.250 Datenblatt [Online]. Available at https://www.schmidttechnology.de/wp-content/uploads/wpallimport/files/api_files/downloads/SS_20.250_de.pdf (Accessed 10 October 2023)

Simon, H., Bruse M., Cramer L., Sinsel T., 2020. Improving Building Performance Simulation boundary conditions. *PLEA: Passive and Low Energy Architecture*, Coruna, 1-3 September.

Troen I., Lundtang Petersen E., 1989. European Wind Atlas. Risø National Laboratory, Roskilde.

Weiland F., Kracht N., Chhugani B., Pärisch P., 2022. Techno-Economical Assessment of a Solar Regenerated Borehole Heat Exchanger Field with PVT Collectors for District Heating. *EuroSun*, Kassel, 25-29 September.

MULTI-OBJECTIVE OPTIMIZATION OF BUILDING ENVELOPE FOR DAYLIGHT AND ENERGY PERFORMANCE IN HOT AND DRY INDIAN CLIMATE

Pushpendra Chaturvedi, Dr. Nand Kumar, Dr. Ravita Lamba, Pushkar Nachan

Malaviya National Institute of Technology, Jaipur, India

ABSTRACT

The climate-responsive envelope design is the principal component for maintaining the indoor environment. This research presents a multi-objective optimization (MOO) approach to evaluate visual comfort and energy performance. A hypothetical building plan situated in the hot and dry climate of Ahmedabad (23.07° N, 72.63° E), India is chosen as a case study. The optimization was initiated with a Rhinoceros Grasshopper, and the Octopus plugin was used to perform optimization. Spatial Daylight Autonomy (sDA), Spatial Glare Autonomy (sGA), and Energy Use Intensity (EUI) were taken as performance objectives. The design variables such as wall window ratio (WWR), window height, shading configuration, window assembly, wall materials, aspect ratio, building form, and orientation are integrated into the optimization to identify Pareto optimal solutions. This study illustrates that the optimal trade-off solution can reduce the EUI by 31.09% and enhance the sDA and sGA by 93% and 18.58%, respectively, compared to the worst-performing Pareto solutions. The outcomes of this work help building professionals for the designing, and renovation of building envelopes in hot and dry climates and contributing to creating a sustainable built environment.

Keywords: Visual comfort, Energy efficiency, Muli-objective optimization, Envelope design

1. Introduction

The building sector of India is the principal consumer of total primary energy (TPE) supply and it consumed 596 million tons of TPE in 2018 [1-2]. Bureau of energy efficiency (BEE), reported that buildings consumed 33% of total generated electricity in 2018-19, and it may fold by 3 to 5 times by 2031 [3]. The continuous, significant growth in building built fabric and their respective energy demands are responsible for leading to GHG emissions [4]. Indian energy outlook report 2021 states that 160 million tons of CO_2 come from the direct use of fossil fuels in buildings, and 460 million tons of indirect emissions come from the use of electricity [5]. Therefore, high- performance building design becomes the prime concern to achieve energy efficiency in the building sector [6]. There are various iterative challenges in building design that affect the building's energy demand. The challenges include visual comfort from natural lighting, thermal comfort from natural ventilation, indoor air quality, energy demand, and life cycle cost [7-8]. Various building envelope parameters have an iterative correlation with these challenges [9]. Meanwhile, high-performance building design has become an extensive research area in architectural design. Therefore, the computational optimization process provides a plausible design solution by

10.18086/swc.2023.06.04 Available at http://proceedings.ises.org

exploring the wide range of design possibilities [10]. This process provides trade-off solutions by transforming the design problem into a mathematical domain [11]. Past research focused on solving the various challenges of building design. Maintaining visual comfort inside the building space is a crucial task. It enhances occupant productivity, reduces mental stress, and minimizes the use of artificial lighting demand. Besides, achieving thermal comfort is the most challenging task in the hot and dry climate to maintain an indoor thermal environment [12-13]. Approximately 70% of the world's total energy consumption was used to maintain a desirable indoor environment in buildings [14]. It is essential to find a balance between a building's energy needs and the quality of its indoor environment [15]. In this context, C. Marino et al. (2017). optimize the window wall ratio (WWR) in the Italina climate and its significant impact on building energy demand. This research established the relationship between WWR, glazing typology, and energy demand [16]. Fang and Cho (2019) optimized the building geometry including building depth, roof ridge, location of skylight, louvers length, and their significant impact on daylight and operational energy. This work was conducted in three different US climates, and it reveals that robust geometry design reduces the energy demand by 17–20% and enhances the useful daylight illuminance (UDI) by 28–38% [17]. Lee et al. (2013) investigate the potential of window performance in the Asian climate. In this research, the thermophysical properties of glazing, orientation, and WWR were taken into account as design variables to identify the trade-off solution in terms of minimum energy use. It also illustrates the most influential control parameters that affect heating, cooling, and lighting demand by exploring regression analysis [18]. There are various indices available to access and quantify the daylight in terms of quantity of natural light, uniform distribution of daylight, and glare. A number of past studies are available based on two or three objective optimizations including daylight, thermal comfort, and energy [19]. A lack of studies was available that focused on building façade design to reduce disturbing glare, enhance daylight penetration, and reduce energy demand. Therefore, this research presents a multi-objective optimization approach for envelope design, exploring a wide range of design possibilities. Wall window ratio (WWR), window height, shading configuration (horizontal and vertical), window assembly, thermophysical properties of glass, wall materials, aspect ratio, building form, and orientation were taken into account as design variables during optimization. Three objectives, such as Spatial Daylight Autonomy (sDA), Spatial Glare Autonomy (sGA), and Energy Use Intensity (EUI), were investigated by exploring defined design variables in Rhinoceroses Grasshopper with the Octopus plugin. Finally, Pareto optimal solutions were generated, and a trade-off solution was identified that satisfied all objectives. This research illustrates that the optimal trade- off solution reduces the EUI by 31.09% and enhances the sDA and sGA by 93% and 18.58%, respectively, compared to the worst-performing Pareto solutions. The outcomes of this research help building professionals design and renovate building envelopes in hot and dry climates, contributing to creating a sustainable built environment.

2. Methodology

This section presents the methodological approach used for this research. This research work comprises four sequential steps. The first steps include the based model development and selection of input design variables; the second step demonstrates the defined objectives functions; the third step illustrates the multi-objective optimization set-up; and finally, the generation of Pareto solutions. Fig. 1 shows the optimization workflow that is used in this research.

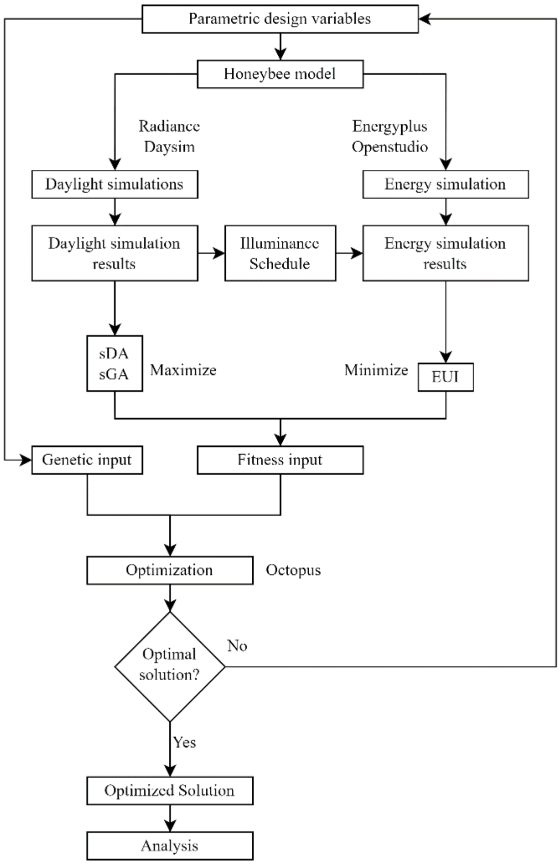

Fig. 1: Methodological flowchart of optimization process.

2.1. Case study

A base model was a hypothetical rectangle-shaped building plan situated in Ahmedabad city, hot and dry climate (Köppen climate classification: BSh) of India was taken into account for the analysis. Ahmedabad heaving extremely hot summer and cold winter climatic conditions. Therefore, envelope design is a complex architectural concept in this region. In this research, the authors considered all envelope parameters as design variables, which are listed in Table 1. The range of design parameters taken is based on typical architectural scenarios in the city. Table 2 reports the wall materials and their thermophysical properties used for optimization. Table 3 reports the conductivity and solar heat gain coefficient (SHGC) value for glass material. Thermophysical properties of glass and wall material were taken from the Indian database and energy conservation building code [20].

Tab. 1: Envelope design variables used for optimization

Design variable	**Ranges**	**Deviation**	**Unit**
V_1: Glass U-value	Shown in Table 2		
V_2: SHGC			

V_3: Wall conductivity (U-value)	Shown in Table 3		
V_{4-7}: WWR- north, south, east west	10 - 70	5	%
V_8: Window height	0 – 2	0.1	meter
V_9: Window sill height	0-1.5	0.1	meter
V_{10-13}: External louver depth – north, south, east, west	0.1-1.5	0.1	meter
V_{14-17}: Louvers count- north, south, east, west	1-5	1	-
V_{18}: Slits angle	0 - 50	5	degree
V_{19-22}: Vertical fins depth-north, south, east, west	0.1 - 1	0.1	meter
V_{23-26}: Vertical fins count-north, south, east, west	1-5	1	-
V_{27}: Orientation	0-360	15	degree
V_{28}: Aspect ratio	1:2.5	0.1	-

Tab. 2: Wall material and their properties used for optimization

Material name	**Thickness (m)**	**Conductivity (W/mK)**	**Density (kg/m^3)**	**Specific heat (J/kgK)**
Compressed stabilized earth brick (CSEB)	0.2	.588	1630	908
Flyash brick	0.23	.802	1844	924
Ariated concreate block (AAC)	.2	.169	608	875
Cellular low weight block (CLWC)	0.23	.193	693	932
Clay brick	0.23	0.969	2119	916.1

Tab. 3: Glass type and their properties used for optimization

Glass type	**U-value ((W/m^{2}K)**	**SHGC (%)**
Glass 1	1.66	0.45
Glass 2	1.43	0.24
Glass 3	2.87	0.55
Glass 4	2.87	0.25

2.2. Performance Objectives

In this work, three building performance objectives were investigated as Spatial Daylight Autonomy (sDA), Spatial Glare Autonomy (sGA) and Energy Use Intensity (EUI).

2.2.1. Spatial Daylight Autonomy (sDA)

It is a metric that assesses the annual sufficiency of ambient daylight level in the interior environment and is defined as the percentage of the analysis area that meets the minimum standard of daylight illumination for a specified portion of the operating hour annually [21]. Example The term "sDA300/50%" refers to the proportion of floor space that receives at least 300 lux for at least 50% of occupied hours per year on the horizontal work plane. It was calculated using Eq. 1.

$$ssssss_{xx/yy\%} = \frac{\sum_{ii}(wwww_{ii} \times DDDD)}{\sum_{ii} pp_{ii}} \in [0, 1] \qquad \text{(eq. 1)}$$

With $$wwww_{ii} = \begin{cases} 1 & iiww \quad ssss \geq ssss_{llillliill} \\ 0 & iiww \quad ssss < ssss_{llillliill} \end{cases}$$

Where x is the reference illuminance level, y is the time fraction, and p_i are the points belonging to the calculation grid.

2.2.2. Spatial Glare Autonomy (sGA)

It is the fraction of occupied time in which daylighting glare probability is less than 40%. Example (sGA40%/5% displays the percentage of a space where the risk of daylight glare exceeds 40% for no more than 5% of the time the space is inhabited. The EN 17037:2018 European Daylight Standard also specifies the 5% level for glare assessments [22].

2.2.3. Energy Use Intensity

It is a metric used to quantify the energy performance of a building. It represents the sum of all electricity, fuel, district heating/cooling, etc. divided by the gross floor area (including both conditioned and unconditioned spaces). In the study, the total load is calculated as the sum of cooling, heating and lighting loads.

2.3. Multi-objective Optimization

In this research, a 3D graphics modeling tool Rhinoceros was used for modeling. An octopus plugin of Grasshopper was used to perform multi-objective optimization. The Honeybee (HB) open studio engine was used for energy simulation and daylight simulation was performed using Radiance engine. Grid is assigned with ‘HB Sensor Grid from Rooms’ component for daylight assessment. The lighting sensors were placed at a grid size of 0.6 m and 0.8 m from the floor. The artificial lighting load was defined as 9.5 W/m^2 as per ECBC. Occupancy and lighting schedule were set as per ASHRAE standard for commercial buildings. The natural ventilation was scheduled as per Indian model of adaptive comfort (IMAC) temperature range for each month of Ahmedabad city. Therefore, the air-conditioning load was calculated based on the IMAC model.

3. Result and discussion

The optimization process was carried out by setting up algorithmic constraints. The strength Pareto evolutionary algorithm (SPEA-2) and hyperreduction algorithm were used to converge the Pareto solutions. Assigned the optimization termination criteria as the maximum generation, and population size is 50 and 50, respectively. Besides, elitism, crossover, mutation rate, and mutation probability are 0.5, 0.8, 0.9, and 0.2, respectively. The Octopus successfully converged all the solutions as shown in Fig. 2. Each point in this figure demonstrates the optimized design solutions.

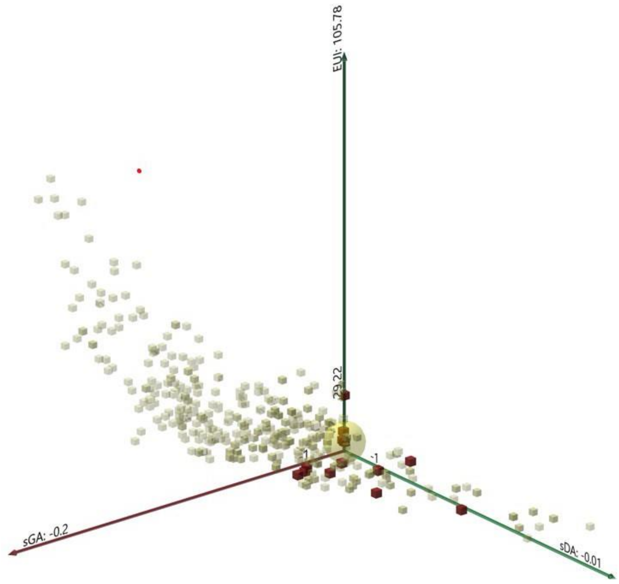

Fig. 2: Tri-objective Pareto solutions during optimization.

The axeview diagram of performance objectives generated by Octopus is presented in Fig. 3. Each line represents a design solution. The lines connect the values for EUI, sGA and sDA. The best trade-off solution that satisfies all the defined performance objectives is shown in the yellow colour line in Fig. 3. Furthermore, the building design parameter values for trade-off solutions are reported in Table 4. It shows that the wall conductivity has a significant impact on the energy demand. Therefore, a lower U-value of wall material reduces heat penetration in the space and reduces cooling energy demand. Besides, WWR plays the major role in balancing daylight and energy demand. The north-south façade building, with a 40% and 50% WWR ratio, provides the best results in energy efficiency and daylight. Window louvers are used to reduce the glare in the space and enhance the natural light in the space. The maximum glare comes from the south-east side. Therefore, increasing the louvers count at a defined angle reduces the glare as well as the heat inside the space due to solar radiation. Moreover, the authors compared the trade-off optimal solutions and the worst-performing Pareto solutions, and their values are reported in Table 5. It reveals that the optimal trade-off solution reduces the EUI by 31.09% and enhances the sDA and sGA by 93% and 18.58%, respectively, compared to the worst-performing Pareto solutions.

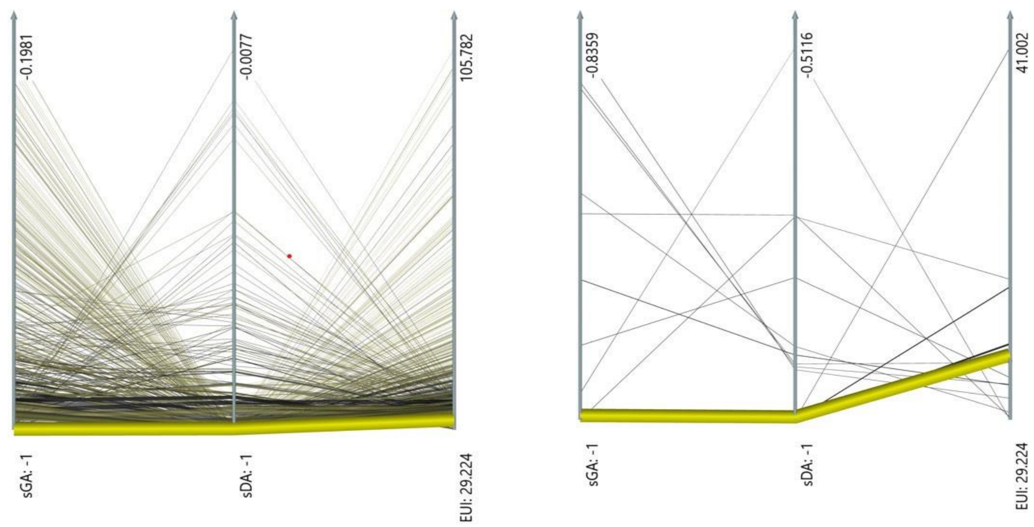

Fig. 3: Axe view diagram of performance objectives and trade-off solution.

Table 5: Best trade-off solution and worst Pareto optimal solutions

EUI (kWh/m²/yr.)		sDA (%)		sGA (%)	
Optimal	Worst	Optimal	Worst	Optimal	Worst
31.292	41.02	99.61	51.35	99.8	84.16

Table 4: Optimal trade-off solution design variable during optimization

Parameter	Optimal trade-off solution	Unit
Aspect ratio	1.28	-
Orientation	N-S	-
WWR N	0.4	%
WWR E	0.6	%
WWR S	0.5	%
WWR W	0.4	%
Height	2	Meter
Horizontal shading devices		
Louver depth N	0.1	Meter
Louver depth E	0.2	Meter
Louver depth S	0.2	Meter
Louver depth W	0.3	Meter
Louver angle (°)	45	Degree
Louver count N	7	-
Louver count E	9	-
Louver count S	8	-

Louver count W	7	-
Vertical shading devices		
Fin depth N	0.15	-
Fin depth S	0.3	-
Fin count N	7	-
Fin count S	4	-
MATERIALS		
U Value for wall material	0.24	W/m^2K
U value for glass	2.87	W/m^2K
SHGC	0.55	-
Trade-off solution		
EUI	31.292	kWh/m^2 /yr.
sDA	99.61	%
sGA	99.8	%

4. Conclusion

This research proposes a multi-objective optimization process for early design stage decision-making of building façade design. The optimization process investigates the daylight and energy performance of a hypothetical commercial building. A Rhinoceroses tool with an Octopus plugin was used to explore the 22-building façade design variable with a wide range of design possibilities and identify the best trade-off solution. This study focused on efficient façade design in hot and dry climatic conditions (Köppen climate classification: BSh) of Ahmedabad, India. The outcomes of this study reveal that the optimal trade-off reduces the EUI by 31.09% and enhances the sDA and sGA by 93% and 18.58%, respectively, compared to the worst-performing Pareto solutions. The outcomes of this research help architects and building professionals to obtain an optimal solution for the early building designing stage in the hot and dry climate of India.

5. References

1. Sen R, Bhattacharya SP, Chattopadhyay S. Are low-income mass housing envelops energy efficient and comfortable? A multi-objective evaluation in warm-humid climate. Energy and Buildings. 2021 Aug 15;245.

2. Khosla R, Agarwal A, Sircar N, Chatterjee D. The what, why, and how of changing cooling energy consumption in India’s urban households. Environmental Research Letters. 2021 Apr 1;16(4).

3. Bureau Of Energy Efficiency Impact of Energy Efficiency Measures: A Report on [Internet]. Available from: www.beeindia.gov.in.

4. Gupta G, Mathur S, Mathur J, Nayak BK. Comparison of energy-efficiency benchmarking methodologies for residential buildings. Energy and Buildings. 2023 Apr 15;285:112920.

5. IEA (2021), India Energy Outlook 2021, IEA, Paris https://www.iea.org/reports/india-energy-outlook-2021, License: CC BY 4.0

6. Chaturvedi PK, Kumar N, Lamba R, Nirwal V. A Parametric Optimization for Decision Making of Building Envelope Design: A Case Study of High-Rise Residential Building in Jaipur (India). InInternational Conference on Advances in Energy Research 2022 Jul 7 (pp. 453-465). Singapore: Springer Nature Singapore.

7. Lan L, Wood KL, Yuen C. A holistic design approach for residential net-zero energy buildings: A case study in Singapore. Sustainable Cities and Society. 2019 Oct 1;50:101672.

8. Cabeza LF, Chàfer M. Technological options and strategies towards zero energy buildings contributing to climate change mitigation: A systematic review. Energy and Buildings. 2020 Jul 15;219:110009.

9. Bano F, Sehgal V. Finding the gaps and methodology of passive features of building envelope optimization and its requirement for office buildings in India. Thermal Science and Engineering Progress. 2019 Mar 1;9:66-93.

10. Wu H, Zhang T. Multi-objective optimization of energy, visual, and thermal performance for building envelopes in China's hot summer and cold winter climate zone. Journal of Building Engineering. 2022 Nov 1;59:105034.

11. Costa-Carrapiço I, Raslan R, González JN. A systematic review of genetic algorithm-based multi-objective optimisation for building retrofitting strategies towards energy efficiency. Energy and Buildings. 2020 Mar 1;210:109690.

12. Bardhan R, Debnath R. Towards daylight inclusive bye-law: Daylight as an energy saving route for affordable housing in India. Energy for sustainable development. 2016 Oct 1;34:1-9.

13. Tabadkani A, Shoubi MV, Soflaei F, Banihashemi S. Integrated parametric design of adaptive facades for user's visual comfort. Automation in Construction. 2019 Oct 1;106:102857.

14. Kumar G, Thakur B, De S. Energy performance of typical large residential apartments in Kolkata: implementing new energy conservation building codes of India. Clean Technologies and Environmental Policy. 2021 May;23:1251-71.

15. Kapoor NR, Kumar A, Alam T, Kumar A, Kulkarni KS, Blecich P. A review on indoor environment quality of Indian school classrooms. Sustainability. 2021 Oct 27;13(21):11855.

16. Marino C, Nucara A, Pietrafesa M. Does window-to-wall ratio have a significant effect on the energy consumption of buildings? A parametric analysis in Italian climate conditions. Journal of Building Engineering. 2017 Sep 1;13:169-83.

17. Fang Y, Cho S. Design optimization of building geometry and fenestration for daylighting and energy performance. Solar Energy. 2019 Oct 1;191:7-18.

18. Lee JW, Jung HJ, Park JY, Lee JB, Yoon Y. Optimization of building window system in Asian regions by analyzing solar heat gain and daylighting elements. Renewable energy. 2013 Feb 1;50:522-31.

19. Carlucci S, Causone F, De Rosa F, Pagliano L. A review of indices for assessing visual comfort with a view to their use in optimization processes to support building integrated design. Renewable and sustainable energy reviews. 2015 Jul 1;47:1016-33.

20. Bureau of Energy Efficiency (BEE) (2018). Eco-Niwas Samhita 2018 (Energy Conservation Building Code for Residential Buildings) Part I: Building Envelope

21. IES I. Standard LM-83-12. Approved method: IES spatial daylight autonomy (sDA) and annual sunlight exposure (ASE). Illuminating Engineering Society of North America. 2012.

22. De Luca F, Sepúlveda A, Varjas T. Multi-performance optimization of static shading devices for glare, daylight, view and energy consideration. Building and Environment. 2022 Jun 1;217:109110.

Performance study of solar water heater integrated with reflectors to enhance the water temperature

Aditya Dave[1], Shubham Prajapati[1] and Zeel Delvadia[1], Nitin Banker[2]

[1]Ahmedabad University, Ahmedabad (India)

[2]National Institute of Technology, Calicut (India)

Abstract

Natural convection-based solar water heater is a widely used system to generate hot water for household as well as industrial applications. With the flat plate collector design, the system can generate a water temperature of around 333 K. Forced circulation or evacuated tube-based solar water heaters are available to generate higher temperatures of about 363-368 K, however, they have higher operating and capital costs. With the objective of generating a higher temperature of water above 363 K, for mainly industrial applications at lower cost, this paper presents an experimental performance study of a basic flat plate collector design integrated with side reflectors. It also includes a performance comparison of solar water heaters with and without reflectors and an evaluation of overall thermal efficiency.

Keywords: Solar water heater, Reflector, Solar energy, Thermal efficiency

1. Introduction

One of the reports states that about 54% of the world's total energy delivered is consumed by the industrial sector mainly in steam generation, air conditioning, and heating application (International Energy Outlook, 2016). Further the global industrial energy consumption is expected to grow by 39% from 2012 to 2040, with an average growth of 1.2% per year; simultaneously, the consumption of renewable energy is also expected to grow at the rate of 1.7% per year from 2012 to 2040 (International Energy Outlook, 2016) with a key role to be played by solar thermal energy based systems due to its favorable conditions in comparison to other renewable resources. Solar Water Heaters (SWH) are one of the widely used solar thermal energy systems to generate hot water for domestic and industrial applications. Fernández (2023) reported that the global solar water heating capacity increased to 522 GWTh (Giga Watts Thermal) in 2021 from 171 GWTh in 2019.

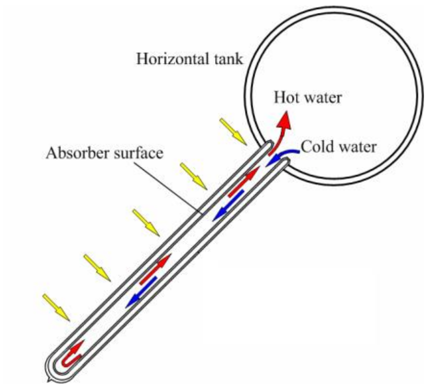

Fig 1: Natural convection process (Budihardjo et al., 2004)

The type of SWH system used for the purpose of this experiment uses natural convection as its working principle. Natural convection is referred to the moment of the fluid caused by the variation in the density due to temperature differences along the fluid body as shown in Figure 1. In the SWH working on this principle, the temperature of water in the solar insolation collecting and absorbing pipes increases relative to the temperature of water in storage tank, this temperature difference is responsible for the natural convection process in the system. The experimental setup has a simple flat plate solar collector design which provides 333-338 K temperature of the water. However, it takes almost complete sunshine hours in a day to achieve such temperatures and this range may not be sufficient for industrial applications. It needs a slightly higher range of hot water temperatures. Other designs such as forced circulation or evacuated tube solar collector-based systems are available to generate a higher temperature of around 363 K at a higher operating and capital cost. In view of this, the efficiency enhancement of natural convection based solar water heater has been selected for the current study.

10.18086/swc.2023.06.01 Available at http://proceedings.ises.org

Enhanced efficiency means a particular solar water heater will be capable of generating more hot water in the terms of temperature, for the same collector design and area for solar insolation collection or a design with some changes, this interprets into lower operating costs over the system's lifetime. Also, as the dependence on conventional fossil fuels decreases, we can avoid the rising costs of energy generation from these fuels by the implementation of such systems.

A case study on the various demonstrated methods that have been studied and employed in the past to enhance the thermal efficiency of flat plate solar collector (FPSC) (Darbari and Rashidi, 2021) includes the use of porous materials, such as conjugated porous blocks placed near the bottom insulator plate to increase collector efficiency by improving heat transfer by effective thermal mixing; similarly, using metal foam for improved thermal mixing; using convective barriers in order to reduce thermal energy loss; using fins to enhance the storage capacity in phase change material with larger values of melting temperature and phase change materials to significantly enhance thermal efficiency. Additionally, the incorporation of nanoparticles, i.e., using enhanced working fluid along with geometrical changes like using converging passages, has been studied, with findings suggesting efficiency improvements as a result of increased convection heat transfer coefficient; the injection of air bubbles into the system has also been explored, resulting in increased outlet temperatures of the working fluid by forming the insulating layer of air on the internal surface of the collector and increasing heat transfer resistance. Also, another method studied was the utilization of rotary pipes to distribute the accumulated heat more efficiently in order to increase convective heat transfer and reduce pressure drop in FPSC. These various techniques collectively contribute to improving the overall performance of FPSCs

The system developed for this experimental study uses reflectors that can be set at different angles to increase the radiation incident on the absorber plate, this constructional improvement helps increase the temperature of the working fluid more effectively, compared to a more conventional SWH without reflectors, for the same ambient temperatures and similar construction. The different constructional requirements include the type of material used for absorbing pipes, the material used for reflectors, the angles at which the reflectors are set, the slope angle, and amount of the water used.

2. Methodology

2.1 Experimental Setup and Components

The complete experiment was carried out in Ahmedabad city (23°01′17.83″ North, 72°34′46.96″ East), Gujarat, India. The experimental setup replicates the conventional parallel tube SWH as shown in Figure 2, consisting of a collector, which is a wooden box with a glass cover and aluminum tubes within it.

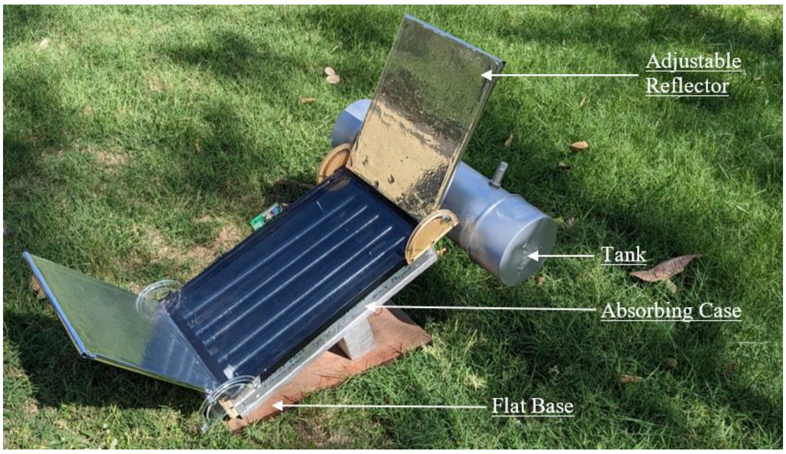

Fig 2: Experiment setup with reflectors and component labels

The collector box is inclined at an angle β, which depends on the latitude of the location (Ali, 2017). The dimensions of the collector box are 560 x 330 x 150 mm, and the interior walls of the collector box are covered with aluminum sheets. The inner base of the collector acts as the absorber, is also covered with an aluminum sheet, and the aluminum tubes are used as thermosyphons (Zohuri, 2020) also painted black. The selection of black paint in the set-up is based on the performed experiments of Tripanagnostopoulos et al. (2000), which evaluated the efficiency and performance of similar collectors with absorbers of different colors, the one with black-colored absorbers yielded maximum efficiency.

The single glass cover is used as a glazing material, of the dimensions 520 x 290 mm with a thickness of 5 mm for optimum SWH efficiency (Bakari et al., 2014). The aluminum tubes are connected to a storage tank externally, which stores as well as supplies the water to be heated. The diameter of the aluminum tubes used is 25 mm with a length of approximately 450 mm within the collector box, such 5 tubes have been used in this setup. The box and the tank are fixed with the supports and are mounted on a base for stability. The exteriors of the collector box and the tank are painted gray, using a light-colored exterior such as gray or white, which helps to keep the tank's exterior temperature lower, reducing the need for adding insulation. The parameters of the setup are given in the Table 1.

Table 1: Experimental setup parameters

Parameters	Values	Definitions
L_1	560 mm	Length of collector box
B_1	330 mm	Breadth of collector box
H_1	150 mm	Height of collector box
L_2	520 mm	Length of glass cover
B_2	290 mm	Breadth of glass cover
H_2	5 mm	Thickness of glass cover
D	25 mm	Diameter of aluminium tube
L_3	450 mm	Length of aluminium tube
L_4	390 mm	Length of reflectors
B_4	270 mm	Breadth of reflectors
Ψ_1	105°	Angle of top reflector, measured from the collector surface
Ψ_2	120°	Angle of bottom reflector, measured form the collector surface
β	23°	Angle of inclination of collector box
γ	180°	Surface azimuth angle, facing due south

There are two equal flat rectangular reflectors integrated into this conventional SWH setup, one at the top and another at the bottom with angles ψ_1 and ψ_2 respectively having the dimensions of 390 x 270 mm. The optimum angles for those reflectors depend on the collector angle β and further on the angle of incidence θ. An experiment conducted by Rachedi et al. (2022) shows the variation in reflector angles as a function of day, for two systems, one with dual-axis tracking, while the other is static, like this experimental setup. For such a system, during summer the optimum angle for the top reflector is more than 70° and for the bottom reflector, the optimum angle is less than 60°. Chrome silver vinyl sheet is used as a reflecting material for the reflectors having reflectivity above 90% which higher than that of polished aluminum foil (Kedar et al., 2021). Another benefit of using chrome silver vinyl sheet is its simplicity in attaching with reflectors and lightweight in compared to mirrors, therefore, unlike mirror, chrome silver vinyl sheet is easier to use as reflectors.

The entire system is integrated with three K type thermocouples with MAX6675 module, controlled by Arduino UNO R3 microcontroller, to obtain real time data of the temperature measurements in different sections of the setup, a micro-SD card module for data collection and a display is also included in order to monitor these temperatures.

2.2 Experimental Procedure

The volume of water used for all the experiments was 15 liters. Total solar insolation is a combination of direct radiation, diffused radiation, and reflected radiation. It depends on the time of the year as well as the time of the day, therefore selection of the time significantly influences the efficiency of the collector. The maximum temperature output in such a system is achieved at noon when the Sun is at its zenith (Proszak-Miąsik and Rabczak, 2017). Therefore, the experiments were performed between 11 a.m. and 3 p.m., in the month of May, when the solar insolation is maximum throughout India, with 90% of the country receiving solar insolation 5 kWh/m^2/day (Ramachandra et al., 2011).

The orientation of the setup is based on the location of the setup. As mentioned earlier, the optimum angle of inclination will depend upon the latitude of the location, and due to which the β has been taken as 23°, which is equal to latitude. The setup is oriented facing due south i.e., γ = 180°, because for the β value less than 40°, optimum solar irradiance is received when γ = 180°, for a static SWH, (Bari. 2001). Any other orientation of the setup or combination of β and γ will result in a decreased incident solar radiation and ultimately, efficiency.

Two configurations were used for the current experimentation, namely, SWH with reflectors and without reflectors. The experiments were conducted for four hours each day of experimentation, from 11:00 a.m. to 3:00 p.m. in the month of May 2023. The temperature data was collected from the different areas of apparatus at a regular interval of one minute. Further, this data was averaged for every 20-minutes to represent it conveniently.

3. Data Analysis and Discussion

3.1 SWH without Reflectors

Figure 3 and Figure 4 show the variation of ambient, storage water and collector box temperature with time for the SWH without reflectors on May 10 and 11, respectively.

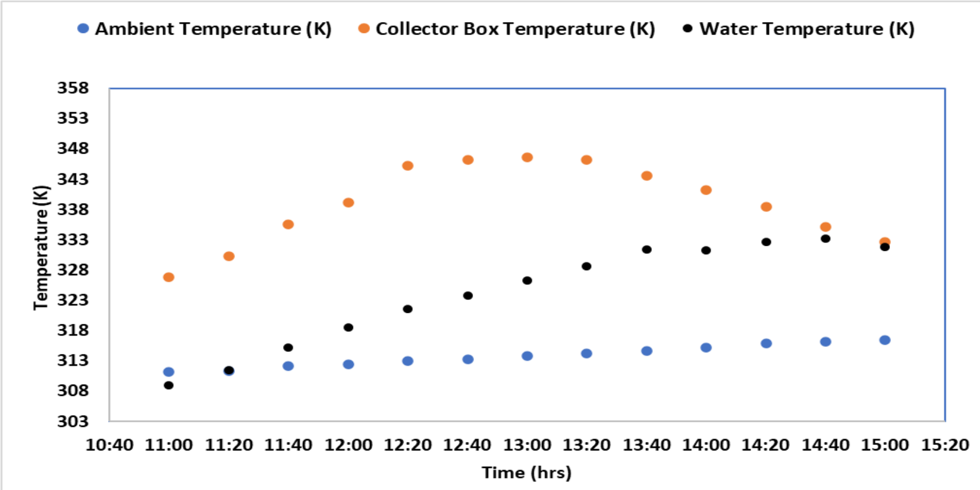

Fig 3: Variation of ambient, water and collector box temperatures with time for SWH without reflectors for May 10

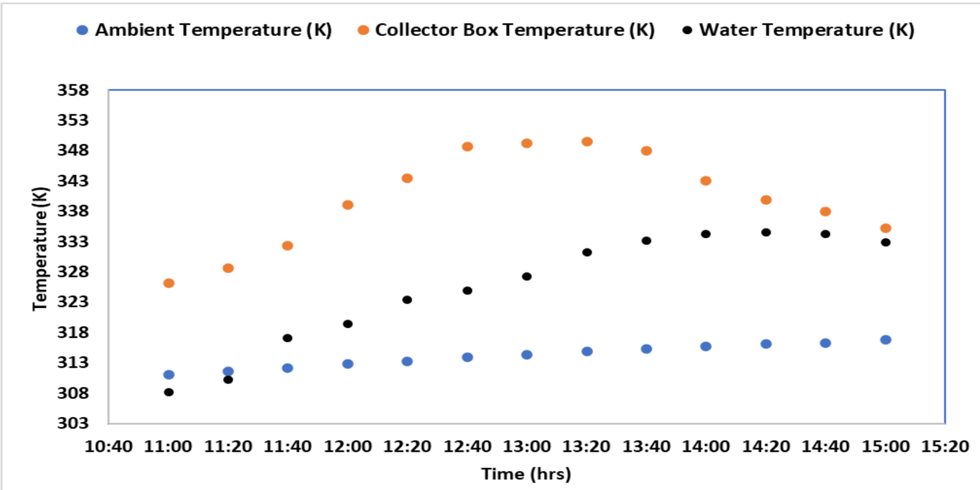

Fig 4: Variation of ambient, water and collector box temperatures with time for SWH without reflectors for May 11

From the figures it is observed that the average rise in the water temperature was about 24 K, the recorded initial temperature of the water on both days was nearly the same that is 308 K which eventually rose to nearly 332 K. Here, the ambient temperature was seen to steadily rising throughout the experiment. However, the temperature inside the collector box sees a high rate of increase till the solar noon and attends almost constant maximum value from 12:30 p.m. to 1:30 p.m. The collector box temperature can be observed to fall after 1:30 p.m. on both days due to a decrease in the solar insolation as mentioned by Mahadi et al. (2014). Also, a similar trend can be observed in the water temperature on both days. Initial recorded water temperature stays below the ambient temperature on both the days which finally attends approximately the same temperature of collector box. A steady rise in the temperature of the water was recorded till the fall in the temperature of the collector box that is approximately 1:30 p.m. and after that it achieves steady value of around 332 K. Interestingly, a subtle drop in the temperature of the water is observed from around 2:30 p.m. on both days. A possible explanation for this observation can be the high rate of decrease in collector box temperature which finally settles below the maximum temperature of the water. In both the scenarios the maximum value of water temperature is achieved couple of readings before the last temperature reading of water (Mahadi et al., 2014).

3.2 SWH with Reflectors

Figures 5 and 6 show the variation of ambient, storage water and collector box temperature with time for the SWH with reflectors on May 12 and 13, respectively.

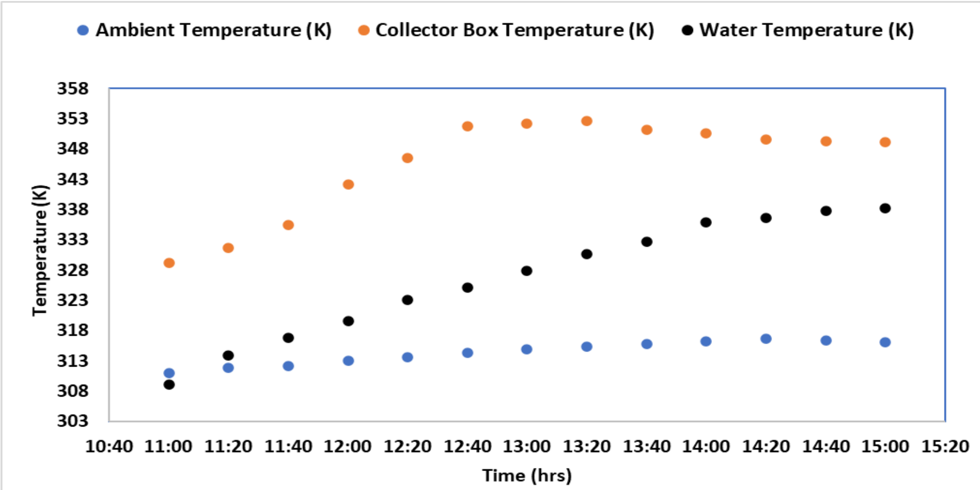

Fig 5: Variation of ambient, water and collector box temperatures with time for SWH with reflectors for May 12, 2023

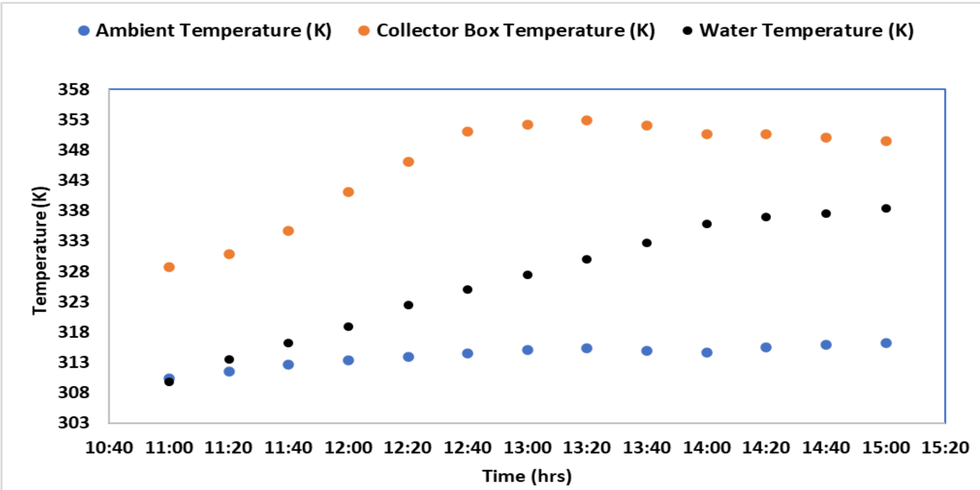

Fig 6: Variation of ambient, water and collector box temperatures with time for SWH with reflectors for May 13, 2023

From the figures it is seen that the rise in water temperature showed nearly the same results for both days, which is about a 30 K rise from 308 K to nearly 338 K. Furthermore, by analyzing Figure 5 and 6 one can deduce a general trend in the rate of temperature increase for all three areas of setup, that is ambient temperature, collector box temperature and water temperature.

The ambient temperature logged on both days displays a steady rise throughout the day. Strikingly similar observation is shown by the collector box temperature in both graphs. Initially, the temperature climbs up the values rapidly, which settles near the maximum value at the solar noon, around 12:30 p.m. Further, the temperature fluctuates at this value till 1:30 p.m. after which it shows a slight deep till the end of the experiment. The third variable, that is water temperature, also followed a similar general trend in both graphs. Initial water temperature was slightly lower than the ambient temperature, it followed a steep increase in the temperature till nearly 2:00 p.m. After which the rate of increase of temperature reduced noticeably till the end of the experiment. This repeating observation can be understood by understanding the collector box temperature which dropped slightly after 1:30 p.m. For both the cases the last recorded value of the water temperature represents the maximum temperature achieved.

In both scenarios, i.e., whether with or without the use of reflectors, we consistently recorded an ambient temperature of approximately 314 K, with individual measurements falling within the range of roughly 311 K to 316 K.

Furthermore, there was a gradual increase in ambient temperature observed throughout each experiment. As for the collector box temperature, a common trend was observed across all data sets. There was a sharp rise in temperature leading up to solar noon, typically around 12:30 p.m., followed by a slight fluctuation around the peak values until approximately 1:30 p.m. Subsequently, there was a subtle decline in temperature for the water heater with reflectors, while the experiment without reflectors exhibited a more significant temperature drop. The best possible explanation for this trend line can be understood from the solar insolation at different times of the day.

However, the most striking and noteworthy distinction between the two cases lies in the maximum water temperature achieved. Without the use of reflectors, the water reached a maximum temperature of approximately 333 K. In contrast, when reflectors were employed, the same setup achieved an astonishing 338 K, representing an increase of 5 K, the results are identical to the results of experiments conducted by Alwan et al.,(2000).

3.3 Water temperature rise

Based on the data analysis, it can be depicted that the approximate average temperature rises for the SWH without and with reflector are 26 K and 29 K respectively. It means the overall enhancement in temperature rise is 14% after incorporating reflectors on the SWH.

This rise in the temperature can be confirmed by understanding the trend line of collector box temperature in both cases. The collector box temperature reached 346 K in the case of without reflectors, while with reflectors it reached approximately 351 K. However, this explains only half the reason for hotter water, the prominent reason for hotter water is the temperature retention quality of the setup when the reflectors are installed. For both the scenarios we observed a drop in collector box temperature at around 1:30 p.m. due to reduced solar insolation, but with the setup without reflector, the collector box temperature recorded a drastic drop, while the setup with reflectors this drop was almost negligible. What the reflectors essentially did was that they prevented the collector box temperature from dropping below the maximum temperature of the water and water continued to heat even at the end of the experiment. This trend is observed due to the increased surface area and ultimately, increased solar insolation by installing the reflectors, which helps the collector box to retain the temperature achieved, at the time of retarding solar insolation.

4. Conclusions

This paper presents an experimental study of SWH with and without reflectors. The experiments clearly showed the maximum temperatures attained by the water in the case of the setup with the integration of reflectors was noticeably on the higher side compared to the setup without reflectors, for the similar conditions of time of the day and duration of the experiment, this was true for the maximum temperatures attained by the collector box as well. The rise in the temperature of the water for the setup with reflectors was 14% higher with respect to the rise in water temperature for the setup with no reflectors.

The observations made and the data recorded suggests that integrating reflectors in a system like the one used for the experiment, i.e., flat plate collector, can enhance the temperature of the water, without any major constructional changes.

5. Acknowledgment

This research did not receive any specific grant from funding agencies in the public, commercial, or not-for-profit sector.

6. References

Ali, F. A. (2017). Evaluation of the Best Slope Angle for a Flat-Plate Solar Collector. Kirkuk University Journal-Scientific Studies, 12(4), 157–178. https://doi.org/10.32894/KUJSS.2017.132393

Alwan, N., Shcheklein, S., Majeed, M., Ali, O., Yaqoob, S., & Khudhur, I. (2022). Assessment of the performance of solar water heater: an experimental and theoretical investigation. *International Journal of Low-Carbon Technologies*, *17*. https://doi.org/10.1093/ijlct/ctac032

Bakari, R., Minja, R., & NJAU, K. (2014). Effect of Glass Thickness on Performance of Flat Plate Solar Collectors for Fruits Drying. *Journal of Energy*, *Hiddawi*, 1–8. https://doi.org/10.1155/2014/247287

Bari, S. (2001). Optimum orientation of domestic solar water heaters for the low latitude countries. *Energy Conversion and Management*, *42*, 1205–1214. https://doi.org/10.1016/S0196-8904(00)00135-7

Budihardjo, I., Morrison, G., & Behnia, M. (2004, January). Performance of single-ended evacuated tube solar water heaters. DOI:10.1016/j.solener.2008.06.010

Chaichana, C., Kiatsiriroat, T., & Nuntaphan, A. (2010). Comparison of Conventional Flat-Plate Solar Collector and Solar Boosted Heat Pump Using Unglazed Collector for Hot Water Production in Small Slaughterhouse. *Heat Transfer Engineering, 31*, 419–429. https://doi.org/10.1080/01457630903375475

Darbari, B., & Rashidi, S. (2021). Thermal efficiency of flat plate thermosyphon solar water heater with nanofluids. *Journal of the Taiwan Institute of Chemical Engineers*, *128*, 276–287. https://doi.org/10.1016/j.jtice.2021.06.027

Energy Information Administration, editor. "Industrial sector energy consumption." *International Energy Outlook 2016*. efaidnbmnnnibpcajpcglclefindmkaj/https://www.eia.gov/outlooks/ieo/pdf/0484(2016).pdf. Accessed 25th September 2023.

Fernández, L. (2023, February 8). *Global solar water heating capacity 2021*. Statista. Retrieved October 3, 2023, from https://www.statista.com/statistics/260688/forecast-capacity-of-csp-plants-worldwide-until-2050/

Kedar, S., Bewoor, A., Murali, G., Kumar, R., Sadeghzadeh, M., & Issakhov, A. (2021). Effect of Reflecting Material on CPC to Improve the Performance of Hybrid Groundwater Solar Desalination System. *International Journal of Photoenergy*, *2021*, 1–13. https://doi.org/10.1155/2021/6675236

Liu, H., Wang, W., Zhao, Y., & Deng, Y. (2015). Field Study of the Performance for a Solar Water Heating System with MHPA-FPCs. *Energy Procedia*, *70*, 79–86. https://doi.org/https://doi.org/10.1016/j.egypro.2015.02.101

Mahadi, Md. S.-U.-R., Hasan, M., Ahammed, A., Kibria, M., & Huque, S. (2014, October). Construction, Fabrication and Performance Analysis of an Indigenously Built Serpentine Type Thermosyphon Solar Water Heater. *Proceedings of 2014 3rd International Conference on the Developments in Renewable Energy Technology, ICDRET 2014*. DOI https://doi.org/10.1109/ICDRET.2014.6861712

Proszak-Miąsik, D., Rabczak, S. (2017). IMPACT OF SOLAR RADIATION CHANGE ON THE COLLECTOR EFFICIENTLY. *Journal of Ecological Engineering*, 18(1), 268-272. https://doi.org/10.12911/22998993/67106

Rachedi, M. Y., Bechki, D., Marif, Y., Boughali, S., & Bouguettaia, H. (2022). A novel model for optimizing tilts of four reflectors on a flat plate thermal collector: Case study in Ouargla region. *Case Studies in Thermal Engineering*, *32*, 101872. https://doi.org/10.1016/j.csite.2022.101872

T. V. Ramachandra, Rishabh Jain and Gautham Krishnadas, 2011. Hotspots of solar potential in India. *Renewable and Sustainable Energy Reviews* 15 (2011) 3178–3186.

Tripanagnostopoulos, Y., Souliotis, M., & Nousia, T. (2000). Solar collectors with colored absorbers. *Solar Energy*, *68*(4), 343–356. https://doi.org/https://doi.org/10.1016/S0038-092X(00)00031-1

Zohuri, B. (2020). Thermodynamic analysis of thermosyphon. *Functionality, Advancements and Industrial Applications of Heat Pipes*, 345–353. https://doi.org/10.1016/B978-0-12-819819-3.00007-9

UNLOCKING ENERGY EFFICIENCY OF BUILDING ENVELOPE THROUGH PASSIVE RETROFITTING

Rahul Verma, Rahul Kumar Sharma and Dibakar Rakshit

Indian Institute of Technology Delhi, New Delhi (India)

Summary

The thermal and visual comfort of occupants is a primary concern in a building when we talk about its optimal performance. HVAC systems are utilized in a building to maintain thermal comfort as per the standards provided by the American Society of Heating, Refrigerating, and Air-Conditioning Engineers (ASHRAE) and health societies. Passive strategies optimize the energy required to provide occupant comfort without relying on mechanical and electrical systems. Passive strategies improve thermal comfort for occupants by maximizing natural ventilation, minimizing thermal fluctuations, and controlling solar heat reflection or absorption. The present study examines the effect of retrofitting different passive techniques on the thermal and visual comfort of a building. The retrofitting techniques considered for the assessment are window layers, window colours, insulation location in walls and roof, infiltration, insulation material and thickness, window local shading, and reflective surface. The integration of these tactics will result in a reduction of total energy consumption by regulating thermal conditions and daylight levels per specific needs. The utilization of passive retrofitting as input parameters is employed to fulfil the objective functions, while a non-sorting genetic algorithm (NSGA2) is utilized to optimize the results. The study illustrates that employing passive strategies in a building can yield energy savings of up to 36% compared to a conventional building.

Keywords: passive techniques, optimization, NSGA2, building energy performance, occupant comfort

1. Introduction

In India, the building industry is experiencing remarkable development, with a forecast of over 40% construction in the upcoming two decades. The building sector alone accounts for more than thirty percent of the total electricity consumption in India. Further, with new constructions, the energy demand would increase, necessitating the urgent optimization of building energy demand in both new and extant buildings (Bureau of Energy Efficiency | A Statutory Body under Ministry of Power, Government of India.). With a growing interest in energy conservation and environmental protection, the effective utilization of various passive strategies in buildings is garnering attention, as it predominantly depends on climate. (Ali et al., 2020) predicted thermal comfort of office rooms in Delhi by varying insulation material types and thicknesses for building envelopes and windows with different glazing materials and blinds. Thermal comfort satisfaction improved by nearly 30% in the environment created by retrofitting passive strategies.(Alsayed & Tayeh, 2019) Determine the optimal insulation thickness based on the life cycle cost analysis for a building situated in Palestine. Investment costs for Polystyrene (I1) and Polyurethane (I2) are 83 and 171.43 \$/m3, respectively. Despite this, (I2), with half the thickness of (I1), can provide the same optimal financial benefits. (Rosti et al., 2020) Analyzed the optimal insulation thickness for Iranian climate zones using a life cycle cost analysis. According to the findings, less than 40 mm of insulation material was required for ACC block walls. (Garg et al., 2016) analyzed the performance of a cool roof, which reduces the surface temperature by reflecting solar radiation, resulting in less heat ingress in building space. The average and maximum reduction in indoor air temperature for the room with a white reflective roof at VNHM School is 2.1°C and 5.0°C, respectively. (G et al., 2018) Different types of window glasses were used to control building cooling and heating burdens through experimental and theoretical research. The effect of grey reflective glass resulted in the most significant annual energy and cost savings across different climates.

For central Italy, (Pisello et al., 2015) analysis of a novel type of green roof that included the benefits of both green and cool roofs found that it decreased the total amount of indoor overheating periods in summertime by 98.2%, with only minimal adverse effects in winter. (He et al., 2020) objective was to measure the variations in the summer and winter thermal energy performance of standard, cool, and green roofs in Shanghai. The results showed that, compared to a typical roof, a cool roof had an average cooling effect of 3.3°C, and a green

10.18086/swc.2023.06.10 Available at http://proceedings.ises.org

roof had an average cooling effect of 2.9°C. According to (Bozonnet et al., 2011), the cool roof reduces the mean exterior surface temperature by over 10°C even in moderate climates, with slight alteration at lower temperatures but a significant effect at higher temperatures. (Androutsopoulos et al., 2017) evaluated the thermal energy performance of a cool roof-incorporated building located in Athens. Summertime demand for energy for ventilation was vividly lowered by 30%, but annual heating energy usage only increased marginally by 12%. In order to assess the efficiency of retrofitting green and cool roofs for lowering the energy burden for offices in Central London (Virk et al., 2015) undertook modelling research. When it comes to preventing summertime overheating, cool roofs have been found to be more beneficial than green roofs. In comparison to cool and green roofs, insulation was perhaps the most efficient energy reduction solution. For numerous boundary conditions determined by optical, thermal, meteorological, and hydrological circumstances, (Kolokotsa et al., 2013) undertook comparative analytical research using the Energy Plus programme on the ability of green roofs and cool roofs to reduce urban heat islands. It has been discovered that cool roofs and green roofs can considerably enhance urban environments and lower energy use.

To optimize the thickness of thermal insulation, (Ozel, 2014) examined how the placement of insulation affects the ever-evolving heat-transfer traits of building outer walls. The cost estimate over a building's 20-year lifespan is employed to pinpoint the optimal insulation thickness. Factors like the yearly mean time lag and decrement are heavily influenced by the insulation's location. However, the insulation's placement doesn't alter the ideal insulation thickness or the annual gearbox loads. (Rosti et al., 2020) investigated the optimal thickness of insulation for both modern and traditional external walls across various Iranian climatic regions. Their findings suggested an insulation thickness requirement of less than 4 cm, which is considerably lower compared to values cited in other countries.

Furthermore, (Yuk et al., 2023) intended to investigate how an old building with an exposed roof structure affects energy efficiency. Instead of standard insulation, a vacuum insulation panel (VIP) retrofit approach is utilized due to the distinctive characteristics of the structure. The potential for passive shading and thermal barriers in multi-story hotel buildings to save energy in the northern hemisphere has been the main focus of the study conducted (Alhuwayil et al., 2023). The outcomes showed that both locations and outdoor weather had a big impact on how much energy could be saved by each choice. A critical review completed on the potential method that enables regulated variation in the heat transfer rate through building envelopes over time is dynamic insulation (Fawaier & Bokor, 2022). According to some research findings, using a dynamic insulating air type could help achieve low heat loss ($U < 0.1$) all the way down to almost zero. Finding insulation for a building envelope is still vital since static, dynamic, and vacuum insulation have challenges with balancing the yearly local environmental conditions and energy components of a building envelope. In addition to the insulating properties and integration techniques, a contradiction occurs in locations with noticeable seasonal variation. As a result, selecting the proper insulation material and inclusion technique for a building's envelope depends greatly on the local climate.

Although significant heat gain or loss occurred through windows in buildings, this had an impact on how comfortable the inhabitants were in terms of temperature. Buildings without windows have the potential to conserve energy, but doing so is not advised, given the advantages of natural light for a comfortable environment in both the visual and biological senses (Hee et al., 2015). An experimental study conducted by (An et al., 2022) focused on seasonal temperature fluctuations and the electricity consumption for cooling and heating in the context of a slim double-skin window (SDSW). Their findings revealed that the energy usage with SDSW was 17.4% lower than double-glazing, 7% lower than double-skin façade, and 2.3% higher than hybrid double-skin façade. To address the imperative of reducing cooling and heating demands across varying climate zones, (G et al., 2018) explored multiple practical and conceptual sun control window solutions in their investigation encompassing eight building orientations and three different climates, grey reflective glass emerged as the most promising option, resulting in substantial annual cost savings for both cooling and heating. The key factor for achieving the greatest net savings was the glass's minimal solar direct transmittance. In a separate analysis, (Valladares-Rendón et al., 2017) evaluated solar-control strategies and optimal building orientations to effectively implement façade shading mechanisms for energy conservation. Their results demonstrated that passive methods significantly reduced solar radiation, leading to remarkable energy savings varying from 4.64% to 76.57%.

For WWR of 40% or above, the latter approach is always the most energy-efficient, even though sun control glass without a shade is the most economical choice overall. (Zeyninejad Movassag & Zamzamian, 2020) investigates double-glazing air flow windows with integrated blinds quantitatively and only takes into account the winter interior mode for future evaluations.(Piffer et al., 2022) analyzed visual qualities of window assemblies with integrated water layers. The findings support earlier research that found that adding water to glazing increases visible light transmittance (VLT) values whilst lowering solar transmittance (ST) rates when compared to glazing without water. Increased water layer thickness in water-based windows (WBWs) reduces direct solar gain but has no effect on VLT values. The optical performance of a WBW is not significantly affected by the number of "glass-water" interfaces on it. Finding glazing for a window system is still important because both static and dynamic glazing have issues with balancing the visual and energy aspects of a window. In places with distinct seasonal fluctuation, contradiction occurs in addition to the glazing properties itself. As a result, the surrounding climate plays a crucial role in choosing the right glass for buildings.

Using the Non-dominated Sorting Genetic Algorithm (NSGA-2), (Lapisa et al., 2018) assessed the effectiveness of passive cooling for low-rise commercial buildings across diverse climates. Their study indicated that, in specific regions, passive cooling techniques could effectively eliminate summertime thermal discomfort without necessitating active cooling systems. The research also identified optimal design criteria for passive approaches such as reflective roofs and nocturnal natural ventilation. In the context of constructing passive buildings in hot and humid regions of Hong Kong, (Chen et al., 2018) introduced a simulation-based optimization approach. By considering equally weighted objectives related to lighting and cooling energy, the final NSGA-2-based solution achieved an energy demand of 35.73 kWh/m^2. A NSGA-2 multi-optimization approach has been developed by (Merlet et al., 2022) for retrofitting solutions designed particularly for windows and building walls. The two main differences were related to the building that was selected for retrofitting, and the improved functionality of each suggested fabric for the retrofit. In order to forecast and improve the energy performance of naturally ventilated buildings in hot and humid regions while considering climate change's consequences(Gonçalves et al., 2024) studied to address a research gap. At the building size, however, climate change significantly impacts thermal performance and might cause a reduction of up to 11% (in 2020) and 39% (in 2050).

The present study aims to reduce energy demand by using passive design strategies in building envelopes by fulfilling the occupant's comfort in space. The current study intends to investigate how the passive techniques will affect buildings in the Indian composite environment in terms of lowering solar heat gain and heat loss. The proposed study looks at the combined impact of different passive methods on the building's visual and thermal performance. The study also discusses the benefits and difficulties of adopting integrated passive techniques for a given climatic zone in a building envelope. A set of passive strategies is applied in the building model with thermal and optical properties variations. A two-story building model is used to optimize energy consumption and determine the appropriate insulation materials and glazing requirements necessary to ensure the well-being of the occupants.

2. Research Approach

The two-story building model located at the DESE IIT Delhi is used to assess passive strategies. The investigation will demonstrate the energy-saving potential of passive strategies in the Indian climate. The rendered view of the model building is depicted in Figure 1. The thermal and optical properties of the base case building model are derived from previous research conducted by the authors (Verma et al., 2023; Verma & Rakshit, 2023). In the present study, the NSGA2 algorithm is used to optimize the objective functions. The Technique for Order Preference by Similarity to an Ideal Solution (TOPSIS) determines the optimal point from the Pareto front. In accordance with the finest optimal point, the energy-saving potential of passive strategies at various locations will be demonstrated.

The methodology was created to investigate buildings' thermal and visual energy performance with passive features such as different types of glazing for windows, insulation, reflecting roofs, etc. A numerical examination is carried out using the Design Builder software to determine the energy performance and optimize energy use.

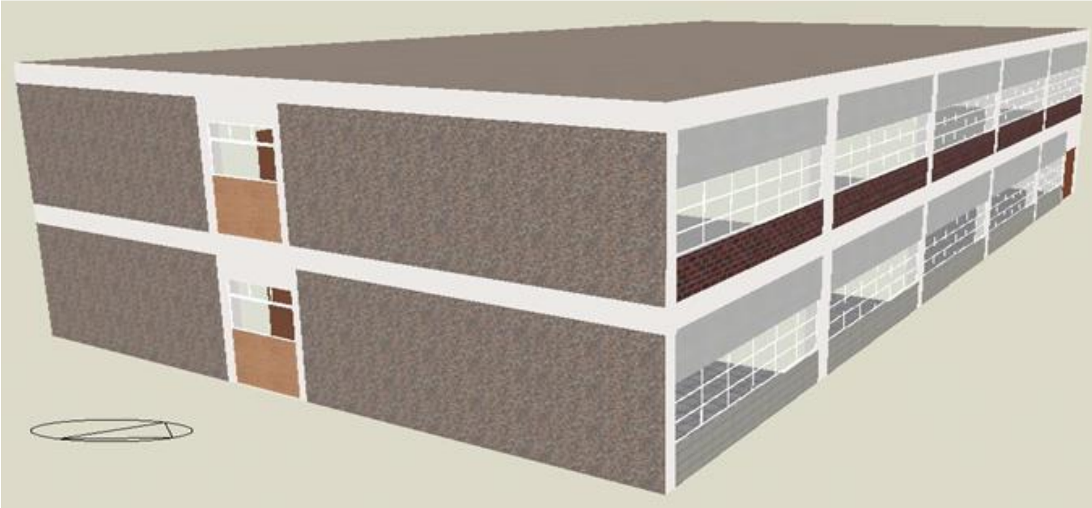

Figure 1:Rendered view of reference building model

The standard weather data of New Delhi, Jaisalmer, Chennai, and Bengaluru, representing composite, hot and dry, warm and humid, and temperate climates, respectively, located in India, is selected for computational study. These climatic regions exhibit the susceptibility and complexity of the Indian climate in passive selection. In order to determine the most effective arrangement of passive techniques for air-conditioned buildings, this study will use these four cities as sample locations for distinct climate zones. The average annual weather characteristics details of sample cities are mentioned in Table 1. The effectiveness of passive strategies largely varies with building climatic zones.

Table 1: Details of annual average weather characteristics of sample cities

Locations	Latitude & Longitude	Alti-tude (m)	Average global horizontal radiation (Wh/m^2)	Average direct normal radiation (Wh/m^2)	Mean -max DBT (°C)	Mean -min DBT (°C)	Mean -max RH (%)	Mean -min RH (%)	Mean -max wind speed (m/s)	Mean -min wind speed (m/s)
New Delhi	28°34'N 77°12'E	216	410	384	30.7	19.9	83	40	1.0	0
Jaisalmer	26°53'N 70°55'E	231	490	535	33.7	22.2	64	32	5	2
Chennai	13°0'N 80°10'E	16	478	412	32.8	25.1	90	49	2	0
Bangalore	12°58'N 77°34'E	921	494	466	28.9	20	92	42	2	0

Building energy retrofit options are introduced in Table 2. The variation in insulation material thermal properties, thickness, and location are mentioned in Table 3, Table 4, and illustrated in Figure 2, respectively. The placement of insulation location in the building envelope does not affect the thermal resistance; however, this may change the energy demand by changing the heat penetration time in the building envelope. The window-to-wall ratio in the building envelope assists in maintaining visual comfort, but it enhances the heat gain through the transparent part of the building envelope. Different window thicknesses and a combination of glasses can reduce heat penetration while maintaining visual comfort. In this study, single-glazing and double-glazing windows with numerous thicknesses were considered to find the optimal window combination for the building envelope. The detailed glazing variation in the building envelope is shown in Table 5. Furthermore, local shading is also selected to reduce the direct radiation falling on the glazing surface in summer. The variation in local shading is described in Table 6. The proposed methodology aims to diagnose and optimize the cooling-heating and cooling-lighting energy demand in buildings, as illustrated in Figure 3.

In the context of multi-objective optimization, these metrics are referred to as decision variables. The choices for each decision variable are provided depending on the various building envelope components, such as the walls, roof, and windows. The passive measures for building envelope: thermal insulation, insulation thickness, insulation location, window glazing type, infiltration, and reflective roof are defined with several variations. Insulation material works as a heat barrier in the building envelope. These materials' thermal conductivity, specific heat, density, and thickness help in the calculation of heat resistance and storage capacity. Variations in material and incorporation in the building envelope give different heat resistance capacities of the building envelope for particular thicknesses. The present study develops a numerous combination of material, thickness, and location of placement in building roofs and walls. The variation in insulation material thermal properties, thickness, and location are mentioned in Table 3, Table 4, and illustrated in Figure 2, respectively. The placement of insulation location in the building envelope does not affect the thermal resistance; however, this may change the energy demand by changing the heat penetration time in the building envelope. The window-to-wall ratio in the building envelope assists in maintaining visual comfort, but it enhances the heat gain through the transparent part of the building envelope. Different window thicknesses and a combination of glasses can reduce heat penetration while maintaining visual comfort. In this study, single-glazing and double-glazing windows with numerous thicknesses were considered to find the optimal window combination for the building envelope. The detailed glazing variation in the building envelope is shown in Table 5. Furthermore, local shading is also selected to reduce the direct radiation falling on the glazing surface in summer. The variation in local shading is described in Table 6. The proposed methodology aims to diagnose and optimize the cooling-heating and cooling-lighting energy demand in buildings, as illustrated in Figure 3.

Table 2: Specifications of retrofitting strategies

<table>
<tr><td>Decision variables</td><td>Examined options</td><td colspan="2">Scenarios</td></tr>
<tr><td>Wall insulation, thickness, and location</td><td>Three types of insulation materials, fibreglass, polyurethane foam, and expanded polystyrene (see Table 3 for properties), incorporated at three locations illustrated in Figure 2 for thickness mentioned in Table 4</td><td rowspan="5">First scenario</td><td rowspan="6">Second scenario
= first scenario
+ RR</td></tr>
<tr><td>Roof insulation, thickness, and location</td><td>Three types of insulation materials, fibreglass, polyurethane foam, and expanded polystyrene (see Table 3 for properties) incorporated at two locations illustrated in Figure 2 for thickness mentioned in Table 4</td></tr>
<tr><td>Window glazing</td><td>Single-layer and double-layer glazing with different thicknesses and colours as noted in Table 5</td></tr>
<tr><td>Infiltration</td><td>Inflitration ranges from 0.2 to 0.4 (ac/h)</td></tr>
<tr><td>Window local shading</td><td></td></tr>
<tr><td>Reflective roof (RR)</td><td>Reflective surface at the roof</td><td></td></tr>
</table>

Table 3: Detailed thermal properties of insulating materials

Insulation material	**Density (kg/m^3)**	**Specific heat (J/kg-K)**	**Thermal conductivity (W/m-K)**
Fiberglass	48	843	0.04
Polyurethane foam (PUF)	30	1800	0.026
Expanded polystyrene (EPS)	15	1300	0.038

Table 4: Selected insulation thickness and material for wall and roof

Structure	**Material constraints**	**Thickness constrains (mm)**

Walls	Polyurethane foam, Fiberglass, Expanded polystyrene	$10 \leq t \leq 110$
Roof		$10 \leq t \leq 150$

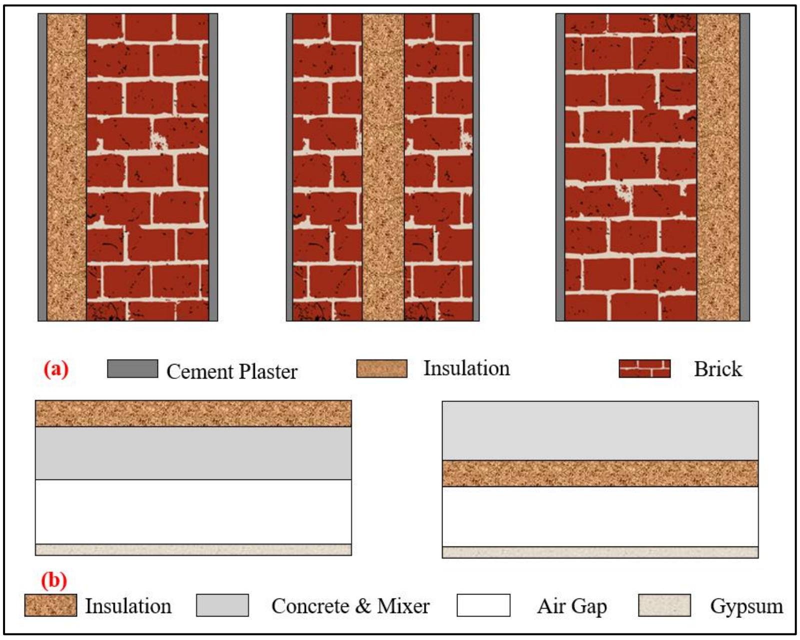

Figure 2: Building retrofitting setup for incorporation of insulation (a) wall (b) Roof

Table 5: Window glazing retrofitting options for optimization.

Glazing type	**Clear**	**Bronze color**	**Green color**	**Grey color**	**Blue color**
Single Layer (Sgl) [glass (mm)]	3 and 6	3 and 6	3 and 6	3 and 6	6
Double layer (Dbl) [(glass -air-glass) (mm)]	3-6-3 6-13-6	3-6-3 3-13-3 6-6-6 6-13-6	3-6-3 3-13-3 6-6-6 6-13-6	3-6-3 3-13-3 6-6-6 6-13-6	6-6-6 6-13-6
Total (Design variable for glazing)					25

Table 6: Window local shading variation to control heat gain and lighting.

Local shading	**Overhangs**	**Louvers**
Length (m)	0, 0.5, 1.0, 1.5, 2.0	0.5, 1.0, 1.5

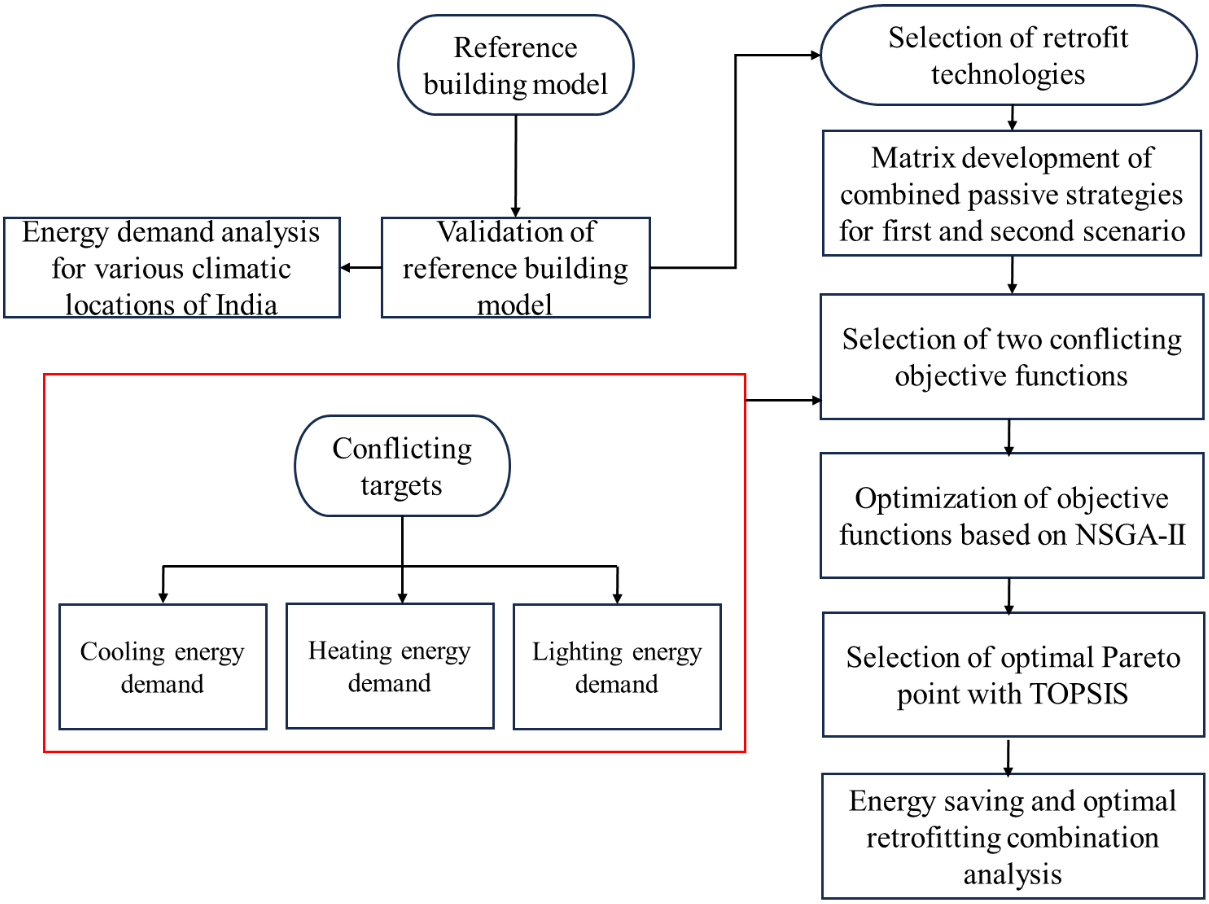

Figure 3: Framework of study

Conduction Transfer Function (CTF) for Inside heat flux

$$q''_{ki}(t) = -Z_o T_{i,t} - \sum_{j=1}^{nz} Z_j T_{i,t-j\,\delta} + Y_o T_{o,t} + \sum_{j=1}^{nz} Y_j\, T_{o,t-j\,\delta} + \sum_{j=1}^{nq} \varphi_j\, q''_{ki,t-j\delta} \qquad \text{(eq. 1)}$$

Conduction Transfer Function for outside heat flux

$$q''_{ko}(t) = -Y_o T_{i,t} - \sum_{j=1}^{nz} Y_j T_{i,t-j\,\delta} + X_o T_{o,t} + \sum_{j=1}^{nz} X_j\, T_{o,t-j\,\delta} + \sum_{j=1}^{nq} \varphi_j\, q''_{ko,t-j\delta} \qquad \text{(eq. 2)}$$

X_j= Outside CTF coefficient, j = 0, 1,…nz. Y_j = Cross CTF coefficient, j = 0, 1,…nz. Z_j = Inside CTF coefficient, j = 0, 1,…nz. φ_j = Flux CTF coefficient, j = 1, 2,…nq. T_i = Inside face temperature T_o = Outside face temperature q''_{ko} = Conduction heat flux on the outside face q''_{ki}= Conduction heat flux on inside face.

3. Results and discussion

To comprehensively gauge the efficiency of passive approaches in air-conditioned (AC) buildings across diverse climatic zones, weighing the energy demand of cooling, lighting, and heating in retrofitted and non-retrofitted structures is essential. This section delves into the Pareto-optimal solution for numerous scenarios indicated in Table 2 within the methodology section. The primary objective, when evaluating passive construction is to diminish the cooling, lighting, and heating loads, along with their corresponding electricity consumption. To ascertain the most favorable energy demands for cooling, lighting, and heating, the TOPSIS decision-making technique is employed. The weight assigned to TOPSIS is determined by the ratio of cooling, lighting, and heating energy demand, as elucidated in Figure 4. The findings of this current investigation aim to provide a comprehensive grasp of how alterations to the building envelope respond to diverse climatic regions. Whether positioned externally or within the walls, insulation in the building envelope proves to be a suitable strategy. Among the three previously discussed insulation materials, polyurethane insulation is superior in enhancing overall building efficiency. In the initial scenario after the execution of TOPSIS on the Pareto front, as illustrated in Figure 5 and Figure 6, it becomes evident that achieving optimal performance for building roof and wall envelopes necessitates insulation thickness ranging from 110 to 150 mm and 70 to 110 mm, respectively, in different cities. Moreover, the evaluation of infiltration rates, ranging from 0.2 to 1.4 air

changes per hour (ACH), was conducted as detailed in Table 2. The calculated results for all climatic locations consistently advocate minimizing infiltration to 0.2 ACH in the present context.
Furthermore, based on the combination highlighted in Table 5, it was established that double-layer green air windows with dimensions of 6 mm/13 mm offer the most suitable solution across all climatic regions. All climatic locations require some amount of local shading. In the current scenario, 0.5 m overhang is preferred for locations except hot and dry climates represented by Jaisalmer. Furthermore, the Pareto points of optimization results of the second scenario are shown in Figure 5 and Figure 6, with the name Pareto Front with CR. The graph clearly shows that after implementing the second scenario, cooling energy demand decreased dramatically, but lighting and heating energy demand increased. In the second scenario, total energy demand was reduced significantly, as the insulation material requirement for the roof case also reached 0 mm for Bengaluru and only 10 mm. for other climates. There is no variation in the remaining passive parameters, which can be considered the optimum values found in the first scenario.
The energy consumption comparison of the first scenario and second scenario with reference case illustrated in Figure 7 for all climatic locations with optimization objective cooling-heating and cooling-lighting. In the first scenario, the cooling-heating objective function was 29.8 %, 30.9%, 34.8%, and 19.4% for New Delhi, Jaisalmer, Chennai, and Bengaluru, respectively. However, for cooling lighting, 23.7%, 27.9%, 33.2%, and 17.1% energy savings were achieved for New Delhi, Jaisalmer, Chennai, and Bengaluru, respectively. After the incorporation of the second scenario, energy savings reached up to 34.6%, 34.7%, 36.1%, and 29.2% for corresponding climatic cities in the cooling-heating objective. However, calculated energy savings for cooling-lighting were achieved up to 31.4%, 32.1%, 34.5%, and 25.8% in New Delhi, Jaisalmer, Chennai, and Bengaluru, representing composite, hot and dry, warm and humid, and temperate climates, respectively.

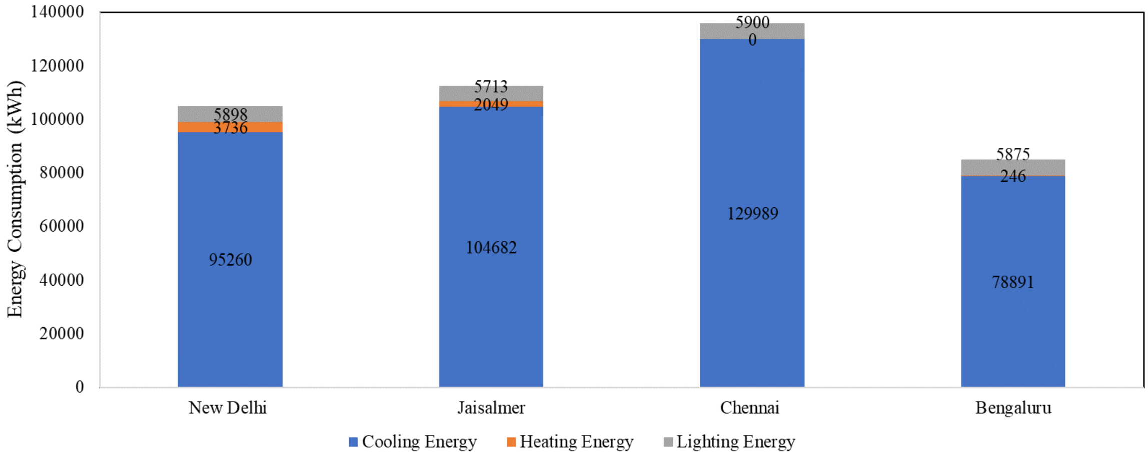

Figure 4: Cooling, heating, and lighting load of reference building for various locations

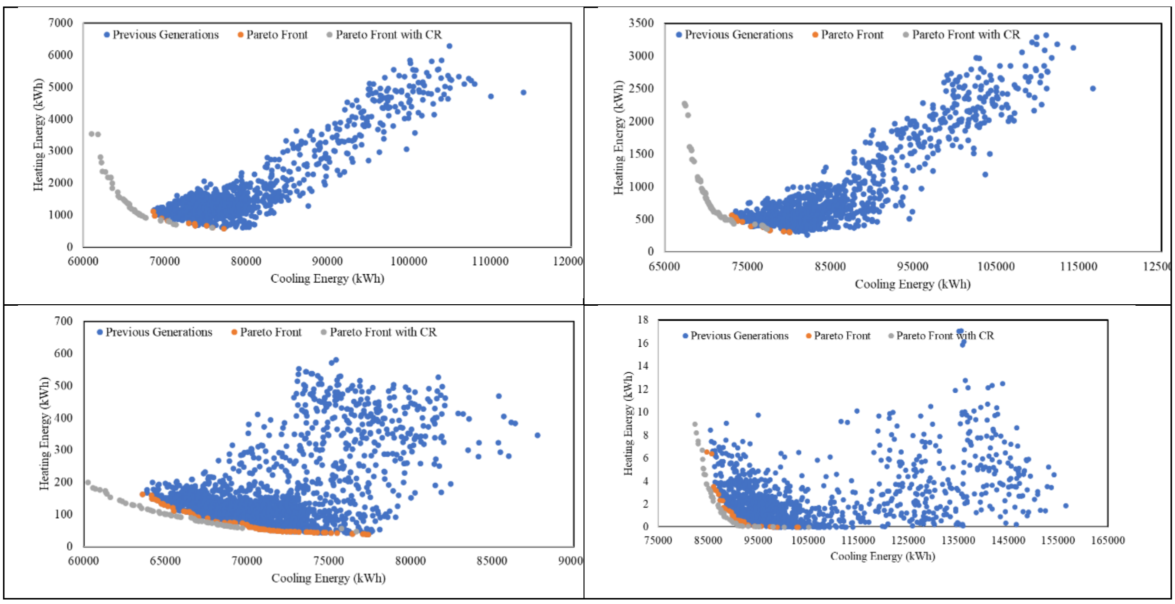

Figure 5: Pareto front of cooling and heating optimization (a) New Delhi (b) Jaisalmer (c) Bengaluru (d) Chennai

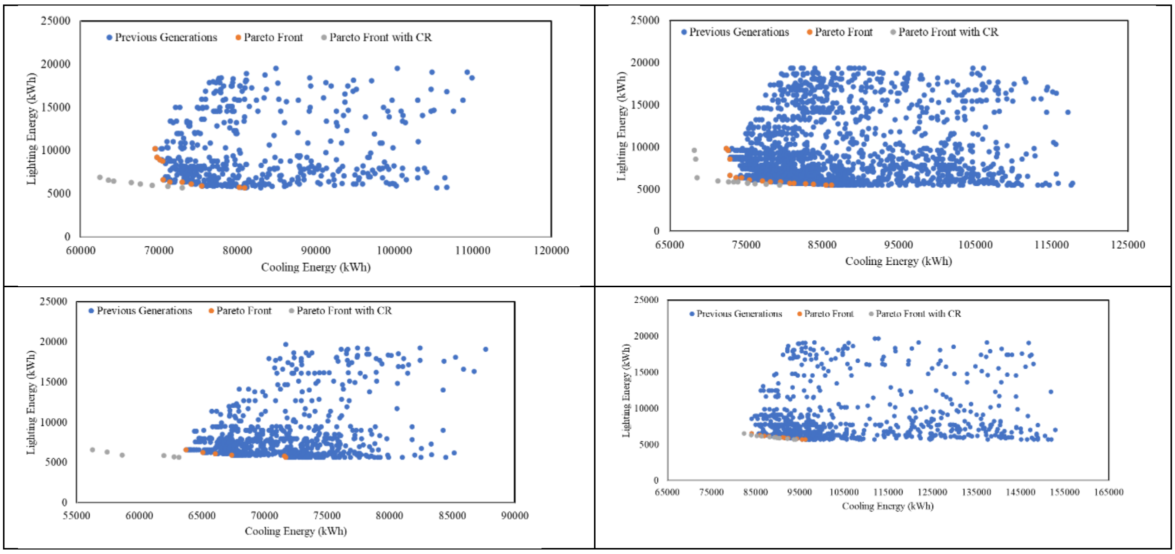

Figure 6: Pareto front of cooling and lighting optimization (a) New Delhi (b) Jaisalmer (c) Bengaluru (d) Chennai

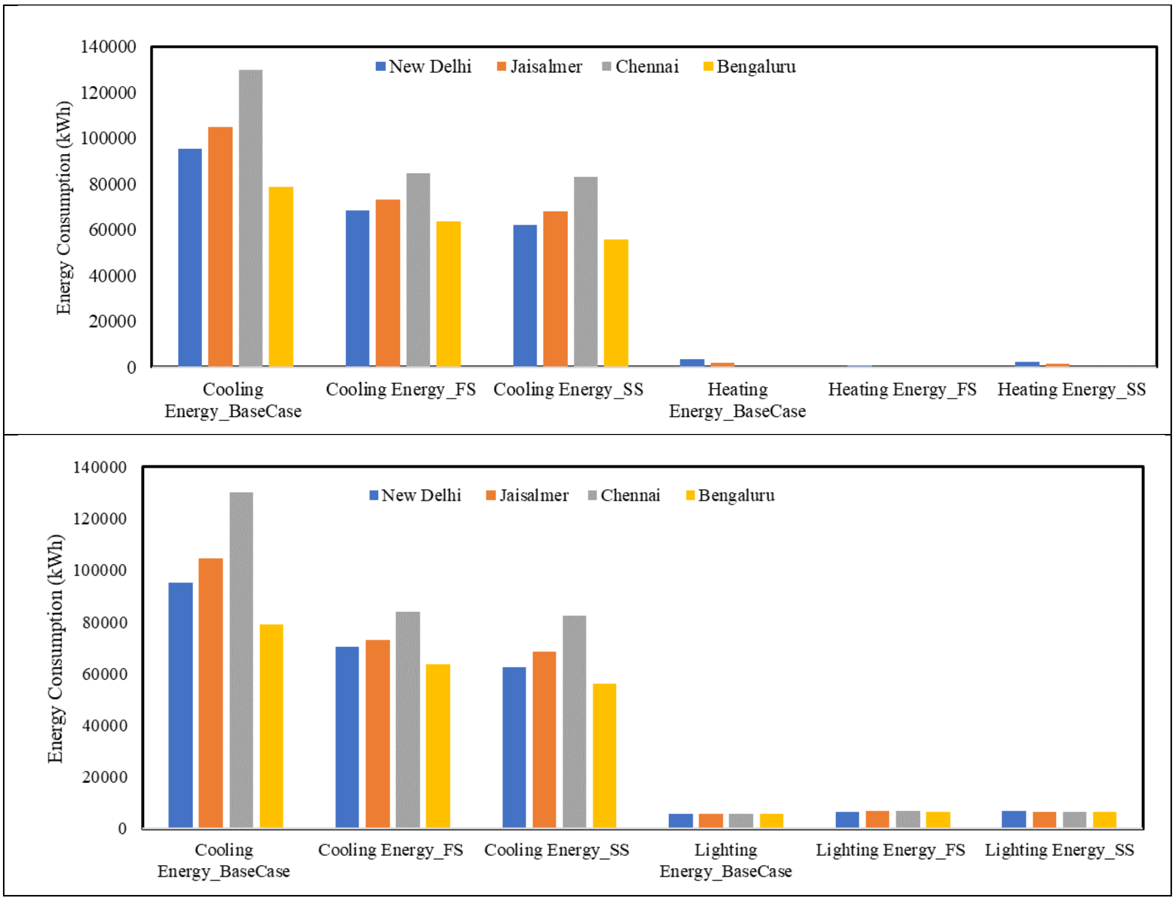

Figure 7: Comparison of energy consumption in (a) cooling-heating (b) cooling-lighting

Conclusions:

This study is innovative in that it uses reflective surfaces to find insulating materials of minimal thickness. Using the simulation program Design Builder, a computational model was created. For the aforementioned scenarios, numerical research was carried out using the verified reference model in various climates. The impact of passive strategies highlighted in the first and second scenarios on lowering the energy demand within buildings in four Indian cities representing different climates. Based on existing findings, the following design requirements for reducing building energy use can be established:

- Existing building design characteristics can be greatly optimized in order to determine the building's sustainability quotient. Total HVAC loads can be lowered by 36% by changing certain aspects of the building envelope.

- Building infiltration needs to be minimized to lower the building energy demand for all four climatic locations.
- It is recommended that green-colored double-paned windows be installed to improve thermal building performance irrespective of climate and thermal resistance.
- The reflective coating on the roof reduces building energy demand and reduces the thickness of the insulation required for optimal performance. Roof insulation thickness requirements for all climatic zones achieved 0 mm for Bengaluru and only 10 mm for other climates.

References

Alhuwayil, W. K., Almaziad, F. A., & Abdul Mujeebu, M. (2023). Energy performance of passive shading and thermal insulation in multistory hotel building under different outdoor climates and geographic locations. Case Studies in Thermal Engineering, 45. https://doi.org/10.1016/j.csite.2023.102940

Ali, S. F., Sharma, L., Rakshit, D., & Bhattacharjee, B. (2020). Influence of Passive Design Parameters on Thermal Comfort of an Office Space in a Building in Delhi. Journal of Architectural Engineering, 26(3). https://doi.org/10.1061/(asce)ae.1943-5568.0000406

Alsayed, M. F., & Tayeh, R. A. (2019). Life cycle cost analysis for determining optimal insulation thickness in Palestinian buildings. Journal of Building Engineering, 22(July 2018), 101–112. https://doi.org/10.1016/j.jobe.2018.11.018

An, Y., Choi, H., Kim, E., & Kim, T. (2022). Experimental analysis of seasonal temperature characteristics and cooling and heating energy consumption of a slim double-skin window. Energy and Buildings, 256, 111681. https://doi.org/10.1016/j.enbuild.2021.111681

Androutsopoulos, A. V., Stavrakakis, G. M., & Damasiotis, M. (2017). Cool Roof Impacts on a School-building Thermal and Energy Performance in Athens, Greece. Procedia Environmental Sciences, 38, 178–186. https://doi.org/10.1016/j.proenv.2017.03.103

Bozonnet, E., Doya, M., & Allard, F. (2011). Cool roofs impact on building thermal response: A French case study. Energy and Buildings, 43(11), 3006–3012. https://doi.org/10.1016/j.enbuild.2011.07.017

Bureau of Energy Efficiency | A staturory body under Ministry of Power, Government of India. (n.d.). Retrieved May 8, 2023, from https://saathee.beeindia.gov.in/Common/BEEContent?MID=2&SMID=44

Chen, X., Yang, H., & Zhang, W. (2018). Simulation-based approach to optimize passively designed buildings : A case study on a typical architectural form in hot and humid climates. Renewable and Sustainable Energy Reviews, 82(June 2017), 1712–1725. https://doi.org/10.1016/j.rser.2017.06.018

Fawaier, M., & Bokor, B. (2022). Dynamic insulation systems of building envelopes: A review. In Energy and Buildings (Vol. 270). Elsevier Ltd. https://doi.org/10.1016/j.enbuild.2022.112268

G, K. K., Saboor, S., Kumar, V., Kim, K. H., & Babu T. P., A. (2018). Experimental and theoretical studies of various solar control window glasses for the reduction of cooling and heating loads in buildings across different climatic regions. Energy and Buildings, 173, 326–336. https://doi.org/10.1016/j.enbuild.2018.05.054

Garg, V., Kotharkar, R., Sathaye, J., Rallapalli, H., & Kulkarni, N. (2016). Assessment of the impact of cool roofs in rural buildings in India. Energy & Buildings, 114, 156–163. https://doi.org/10.1016/j.enbuild.2015.06.043

Gonçalves, E. L. S., Braga, J. L., Sampaio, A. de O., Batista, V. dos S., Menezes, L. J. da R., Eli, L. G., Barata, M. S., Ventura Neto, R. da S., & Zemero, B. R. (2024). Multiscale modeling to optimize thermal performance design for urban social housing: A case study. Applied Thermal Engineering, 236, 121379. https://doi.org/10.1016/j.applthermaleng.2023.121379

He, Y., Yu, H., Ozaki, A., & Dong, N. (2020). Thermal and energy performance of green roof and cool roof: A comparison study in Shanghai area. Journal of Cleaner Production, 267, 122205. https://doi.org/10.1016/j.jclepro.2020.122205

Hee, W. J., Alghoul, M. A., Bakhtyar, B., Elayeb, O., Shameri, M. A., Alrubaih, M. S., & Sopian, K. (2015). The role of window glazing on daylighting and energy saving in buildings. In Renewable and Sustainable Energy Reviews (Vol. 42, pp. 323–343). Elsevier Ltd. https://doi.org/10.1016/j.rser.2014.09.020

Kolokotsa, D., Santamouris, M., & Zerefos, S. C. (2013). Green and cool roofs' urban heat island mitigation potential in European climates for office buildings under free floating conditions. Solar Energy, 95, 118–130. https://doi.org/10.1016/j.solener.2013.06.001

Lapisa, R., Bozonnet, E., Salagnac, P., & Abadie, M. O. (2018). Optimized design of low-rise commercial buildings under various climates – Energy performance and passive cooling strategies. Building and Environment, 132(August 2017), 83–95. https://doi.org/10.1016/j.buildenv.2018.01.029

Merlet, Y., Rouchier, S., Jay, A., Cellier, N., & Woloszyn, M. (2022). Energy & Buildings Integration of phasing on multi-objective optimization of building stock energy retrofit. Energy & Buildings, 257, 111776. https://doi.org/10.1016/j.enbuild.2021.111776

Ozel, M. (2014). Effect of insulation location on dynamic heat-transfer characteristics of building external walls and optimization of insulation thickness. Energy & Buildings, 72, 288–295. https://doi.org/10.1016/j.enbuild.2013.11.015

Piffer, Y., Jonsson, J. C., Güths, S., Silva Machado, R. M., & Lamberts, R. (2022). Development and validation of an optical model for water-based windows with clear glazing: A parametric performance assessment. Building and Environment, 209. https://doi.org/10.1016/j.buildenv.2021.108635

Pisello, A. L., Piselli, C., & Cotana, F. (2015). Thermal-physics and energy performance of an innovative green roof system: The Cool-Green Roof. Solar Energy, 116, 337–356. https://doi.org/10.1016/j.solener.2015.03.049

Rosti, B., Omidvar, A., & Monghasemi, N. (2020). Optimal insulation thickness of common classic and modern exterior walls in different climate zones of Iran. Journal of Building Engineering, 27(May 2019), 100954. https://doi.org/10.1016/j.jobe.2019.100954

Valladares-Rendón, L. G., Schmid, G., & Lo, S. L. (2017). Review on energy savings by solar control techniques and optimal building orientation for the strategic placement of façade shading systems. Energy and Buildings, 140(71), 458–479. https://doi.org/10.1016/j.enbuild.2016.12.073

Verma, R., Kumar, S., Rakshit, D., & Premachandran, B. (2023). Design and Optimization of Energy Consumption for a Low-Rise Building With Seasonal Variations Under Composite Climate of India. Journal of Solar Energy Engineering, 145(1). https://doi.org/10.1115/1.4054831

Verma, R., & Rakshit, D. (2023). Comparison of reflective coating with other passive strategies: A climate based design and optimization study of building envelope. Energy and Buildings, 287, 112973. https://doi.org/10.1016/j.enbuild.2023.112973

Virk, G., Jansz, A., Mavrogianni, A., Mylona, A., Stocker, J., & Davies, M. (2015). Microclimatic effects of green and cool roofs in London and their impacts on energy use for a typical office building. Energy and Buildings, 88, 214–228. https://doi.org/10.1016/j.enbuild.2014.11.039

Yuk, H., Choi, J. Y., Kim, Y. U., Chang, S. J., & Kim, S. (2023). Historic building energy conservation with wooden attic using vacuum insulation panel retrofit technology. Building and Environment, 230. https://doi.org/10.1016/j.buildenv.2023.110004

Zeyninejad Movassag, S., & Zamzamian, K. (2020). Numerical investigation on the thermal performance of double glazing air flow window with integrated blinds. Renewable Energy, 148, 852–863. https://doi.org/10.1016/j.renene.2019.10.170

07. Rural Energy Supply

DESIGN AND DEVELOPMENT OF DOUBLE EXPOSURE SOLAR COOKER WITH FINNED COOKING VESSEL

Abdulkadir Aman Hassen[1] & Mintesinot Yohannes Jorgaa[2]

[1*] School of Mechanical and Industrial Engineeringt, Addis Ababa Institute of Technology, Addis Ababa Univeristy,P.O.Box 385, Addis Ababa, Ethiopia

[2]Mechanical Engineering Department, College of Engineering and Technology, Dilla University, P.O.Box 419, Dilla, Ethiopia

* Corresponding author: abdulkadir.aman@aait.edu.et

Abstract

The main objective of this study is to design, construct and investigate the performance of a modified box type solar cooker supported by parabolic reflector disposed under the cooker. Energy cost for cooking purpose, indoor pollution and the time spent in gathering fuel woods are the main problems that led us to study and develop the cooker. Moreover, the very slow heat up time of box type cookers and their limitation for widespread deployment due to their low operating temperature are motivating factors to design this cooker. The developed cooker under field test gives stagnation plate temperature of 152°C. The "First figure of merit" of the cooker is 0.127 which represents the cooker marked as grade-A solar cooker. A comparative experimental study of double exposure solar cooker with two different cooking vessels (finned and un- finned) was also conducted and results show that under the same climatic conditions; temperature of finned cooking vessel and power are higher.

Keywords: Solar cooker, double exposure, parabolic reflector finned vessel

1. Introduction

Solar box cooker is the simplest type of solar cooker available because it is relatively cheap, low-tech device (Ramaswamy et.al, 1997). The cooking time depends primarily on the materials being used, the amount of sunlight at the time of cooking, and the quantity of food that needs to be cooked. However the low heat rate of most box type solar cookers and the lower working temperature limit are hindering its wide spread use for household cooking. This study is proposed as a remedial to avoid these two problems where both the highest temperature limit and heating rate are improved by a modified design. The double exposure solar cooker (DESC) proposed in this study is a box type solar cooker with support of parabolic reflector disposed under the cooker for additional heat input to the cooking vessel, in which the absorber is exposed to the solar radiation from both sides (at the top of the box from boosters and parabolic flat reflectors placed under the box). A box-part of DESC is single glazed at the top as usual to transmit sun radiation and a double-glass at the bottom allowing the absorber plate to receive maximum solar radiations reflected from parabolic flat reflector on its lower side.

2. Discription of the system

The double-exposure solar cooker used in this investigation consists of a box-part with a double-glass at the bottom allowing the absorber plate to receive solar radiations on its lower side as shown in Fig. 1. The box is equipped with three flat reflectors (one reflector is 50 cm x 60 cm placed at the front rear edge of the box frame) and the two side reflectors are 40cm x 50cm, which are installed upon a wood frame connected with hinges on the upper side of the solar cooker. The walls of solar box are made of a wooden layer (thickness: 2.5 cm), the inner sides of which are covered with an aluminum sheet (thickness: 0.1 - 0.2 cm).

10.18086/swc.2023.07.03 Available at http://proceedings.ises.org

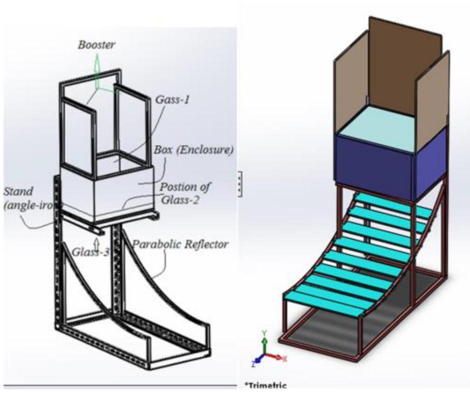

Fig. 1: Schematic diagram of the designed double exposure solar cooker.

The height of the back-side and front-side of the box are equal with 32 cm; the total volume of the box is (50 x 40 x 32 cm). Junction fragments were sealed properly to prevent escaping air from system. At the top of the box part, a glass plate of 4 mm thickness was fixed in position with wooden frame to avoid breakage due to expansion and also to make the cooking space airtight. The parabola is reflecting sun radiation from three different positions which should be adjusted properly to distribute the reflected sun radiation in different part of the absorber plate.

As presented in Fig. 2 below two commercial cooking vessels (finned and unfinned), of 20 cm in diameter and 10 cm in depth, were placed at the center of the box part.

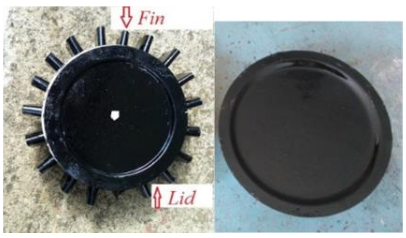

Fig. 2: Finned and un-finned cooking vessel.

The cooking vessels are made of an aluminum sheet of 0.2 cm thickness and the outer surfaces of the cooking vessel are painted black.

3. Methodology

The family size double exposure solar cooker is designed based on the cooking energy requirement for average households for selected food item and or specific site.

3.1 Cooking power.

The power required to cook the food can be obtained as presented in (eq.1) which is then divided by $\Delta t = 600s$ to account for the number of seconds in each 10-minute interval. P is normalized to compare the various cookers in various countries and under various climates. (Funk, 2000) has shown that the power of radiation is standardize to 700 W/m^2.

$$P = \frac{M_w C_{pw} (T_f - T_i)}{\Delta t} \qquad \text{(eq. 1)}$$

3.2 Size of the cooker

Sizing of the cooker can be determined based on the power obtained for cooking using (eq. 2)

$$MC_P \frac{d\theta}{dt} = (\eta_0 I - U\theta)A_C \qquad \text{(eq. 2)}$$

Where □ is the temperature difference between the pot content and the initial temperature in K, η_0 is the optical efficiency, I is the global solar radiation in W/m2, U is the thermal loss coefficient in W/(m2K), $A_C$and is the collector aperture surface in m2.

The parabolic part of system is composed of 9 flat reflectors, 10cm x 46 cm, each parabolic flat reflector is mounted on a parabolic curve placed 2cm apart in order to rotate freely and to set the reflection of sun radiation towards to different part of the absorber plate.

Fig. 3: photographic view of double exposure solar cooker

4. Result and Discussion

Based on the existing international testing standards (Funk, 1998; ASAE, 2003) tests were performed on the solar cooker to obtain stagnation temperature, cooking power, instantaneous and cumulative efficiency (Ibrahim, 2005), and the effect on finned and un-finned cooking vessel.

4.1 Stagnation Test

The result of stagnation temperature under no load condition is shown in fig. 4 and the maximum absorber plate temperature of 152°C was recorded at 12:30pm and at an insolation value of 950 W/m^2 and the ambient temperature 31.9°C. The stagnation temperature without the parabolic temperature has reached 120 °C.

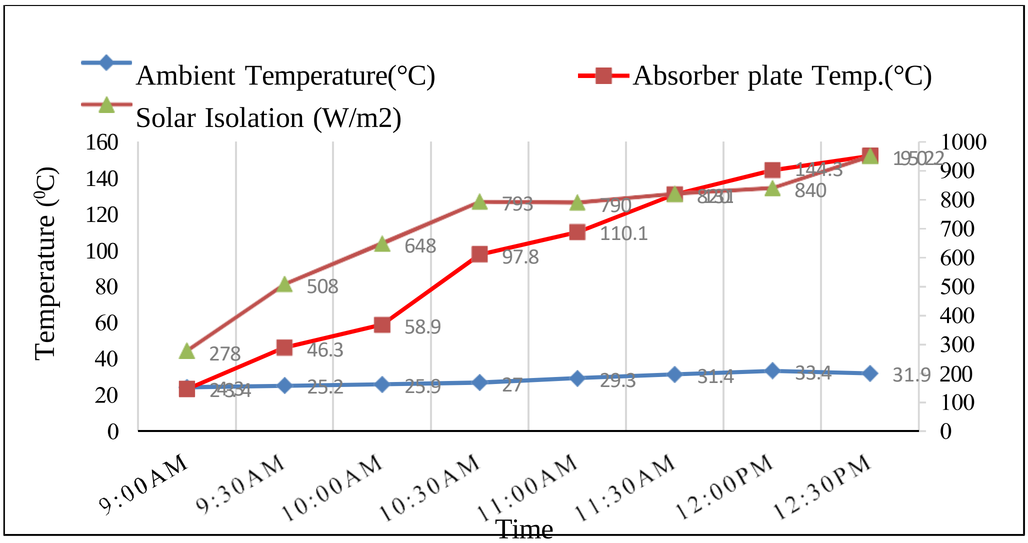

Fig. 4: Thermal performance curve of the double exposure solar cooker under stagnation test condition.

4.2 Loaded Test (Water Heating Test)

Test was conducted by placing a 2kg of water-filled cylindrical pot covered by a lid, for both finned and un- finned cooking vessel. The finned cooking vessel give reached maximum temperature as presented in fig. 5

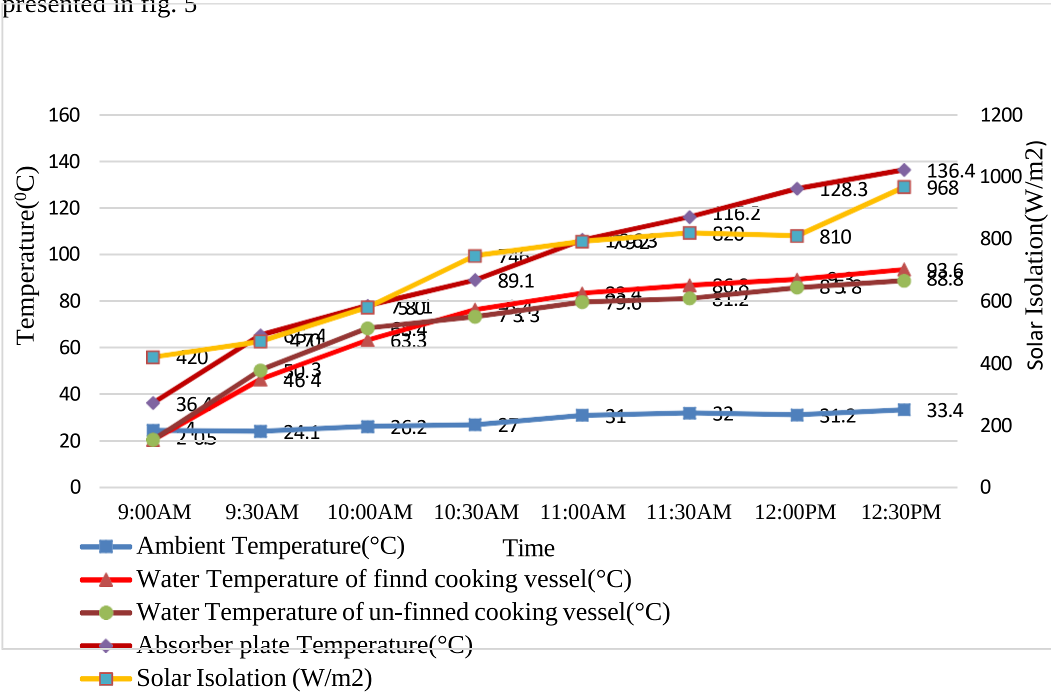

5. Conclusion

The double exposure solar cooker is the best alternative way to improve the performance of the box solar cooker by adding parabolic flat reflector with minimum production cost with better additional heat input to the absorber plate. The presence of parabolic reflector results absorber plate temperature of 152°C, which is additional temperature of 31.9°C compare to the cooker without parabolic reflector. Cooking power and efficiency of the cooker are also improved with an increased thermal efficiency and a cost benefit ration of greater than one.

6. References

ASAE, 2003, ASAE S580: Testing and Reporting of Solar Cooker Performance.

Funk P.A. and D. L. Larson, 1998.Parametric model of solar cooker performance, Solar Energy, vol.62, no.1, pp.63–68, Funk PA., 2000. Evaluating the international standard procedure for testing solar cookers and reporting performance. Solar Energy; 68(1):1–7.

Ibrahim A,2005. Experimental Testing of a Box-Type Solar Cooker Using the Standard Procedure of Cooking Power, Renewable Energy, vol. 30, , pp. 1861-71.

Ramaswamy, T. S., Perumal, K. and Jayaprakash, R., 1997. Thermal performance of low cost solar cooker", Proceedings of The Third International Conference on Solar Cookers-Use and Technology, Coimbatore, India,1997, pp. 157-164.

DEVELOPMENT OF A THERMAL STORAGE SYSTEM FOR SOLAR PV BASED INJERA BAKING APPLICATION

Gashaw G. Birhanu[1, *], Ole J. Nydal[2], Demiss A. Ambie[1], Abdulkadir A. Hassen[1]

[1]School of Mechanical and Industrial Engineering, Addis Ababa Institute of Technology, Addis Ababa, Ethiopia

[2] Department of Energy and Process Engineering, NTNU, Trondheim, Norway

Abstract

This study aims to address energy and energy-related issues in urban and rural communities, as well as institutions that still use biomass for Injera baking, in Ethiopia, by developing an efficient and suitable thermal storage that could serve as a base model for the development of solar PV-based injera baking systems. To achieve this, a three-dimensional model of three storage concepts, each using a solar salt mixture of 60% NaNO3 - 40% KNO3, was developed and compared using COMSOL Multiphysics software to investigate their performance during charging and discharging. The first two concepts comprise phase change material (PCM) filled aluminum cylinders with air or oil as heat transfer fluid. The third concept contains packed PCM in between cylindrical fins, which act as both a containing and conducting wall. The temperature, the percentage of PCM that melted, and the energy stored while charging and discharging were all documented. The performance of the packed PCM (conduction-based) system is 58% higher than that of the oil-based system and 62% higher than that of the air-based system. The result obtained from this simulation will be used to develop a prototype of a PV-based injera baking system. The numerical investigation's results were consistent with the findings of experiments documented in previous literature.

Keywords: Injera, charging and discharging, PV, PCM

1. Introduction

Injera is a staple bread consumed daily in Ethiopia and some parts of eastern African countries. It is mainly made from teff and constitutes 70% of the diet of Ethiopians. Mitad is a traditional plate made of clay used for injera baking. It measures 40-60cm in diameter and 20mm thick. The baking process occurs in the temperature range of 180 ℃ to 220 ℃ at an energy consumption of approximately 0.63MJ per Injera and a baking time of up to 3 minutes. Most of the time, biomass is used for injera baking, though sometimes electricity and other energy sources are used in urban and semi-urban areas. According to studies, cooking consumes 90% of the household energy, and 90% of this is for injera baking. The energy efficiency of electric injera baking pans is 56–60%, according to the Ethiopian Energy Agency, and it has not improved over the past 50 years (Getahun, 2017). Deforestation, frequent power outages, voltage drops, and other issues are caused, among other things, by the injera mitads' low efficiency. With an access rate of roughly 45% of the population (58 million) in 2017, Ethiopia is one of the 20 nations with the highest access deficit. In 2017, Ethiopia's total access to clean cooking technologies and fuels was less than 5% in rural areas and 7-29% in urban areas (SDG7, 2019). A large percentage of urban residents can't afford the electricity tariffs for all residential uses, and for those who can, power outages are the main problem, particularly for high-temperature cooking applications like injera baking. In addition to the households, institutions in Ethiopia (universities, schools, refugee camps, restaurants, etc.) use biomass as a source of energy for cooking.

10.18086/swc.2023.07.01 Available at http://proceedings.ises.org

Fig.1: Injera baking system currently in use at Bahir Dar University

Renewable energy technologies could play a key role in enhancing energy access to rural areas and cities where communities and institutions lack access to energy. However, only lighting and water heating solar energy technologies have been made available in rural areas in contrast to solar cookers. This shows that there hasn't been significant technological progress in using solar energy for high-temperature cooking applications. Various scholars and groups have made efforts to utilize solar energy for injera baking applications (Abdulkadir et al., 2016; Asfafaw et al., 2014a, 2014b; Mesele et al., 2017). The output of these researches and projects shows a promising result on the performance improvement of solar injera baking by employing different techniques, among the efforts, the use of different types of collectors and heat storage media, performance investigation of existing baking systems, and development of new baking pans are some of them. However, the research on the application and feasibility of injera baking with PV and a thermal storage system to solve energy problems in rural and urban communities is limited.

The development of a thermal storage system for solar applications represents a significant advancement in renewable energy technology. Thermal storage systems enable the capture and storage of excess thermal energy generated by solar collectors during periods of peak sunlight. This stored energy can then be utilized during periods of low solar irradiation or at night, allowing for a continuous and reliable energy supply. By integrating thermal storage into solar power systems, we can overcome one of the major limitations of solar energy – its intermittent nature – and enhance its efficiency and reliability.

A numerical investigation is proposed and conducted on a thermal storage system for solar-powered injera baking to address energy availability and sustainability challenges and overcome limitations in existing research. The investigation is conducted on three different concepts for the thermal storage system using a 3D model. Eutectic 40% KNO_3 - 60% $NaNO_3$ is used to store thermal energy due to its demonstrated capability for high-temperature cooking (Asfafaw et al., 2014a, 2014b; Asfafaw et al.,2018; Dejene et al. 2017; Fuente, 2022; Vermachi et al.,2016). The best-performing model from the simulation will be used to develop a PV-based injera baking system.

2. Materials and Methods

In this section, a comprehensive description of the materials used and the methodology followed in conducting the simulation study is presented.

2.1 Physical Model

As the objective is to compare different thermal storage concepts, only a representative physical model is shown, in Fig.2. A PV array is connected with a DC heating element placed on the top of the storage tank. Electric power generated using the PV panels is converted into heat using the heating element. The heat is then transferred to the PCM through different modes of heat transfer depending on the type of the concept. The storage is insulated to minimize heat loss to the surroundings.

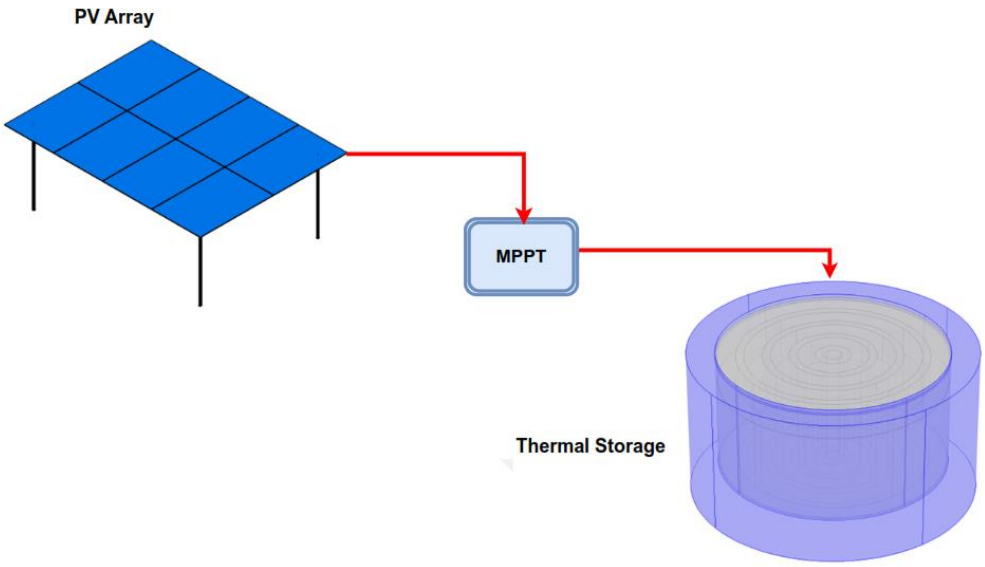

Fig.2: Physical model

2.2 Energy required for baking injera

The first step in designing such a system is determining its energy requirements. The thermal storage and its components can be sized based on knowledge of the required amount of energy. Tab.1 summarizes the energy needed for baking injera including the losses, from previous research.

Tab. 1: Energy required for baking from previous research

No	Reference	Nature of the Study	Energy Consumption
1	Abdulkadir et al., 2016	Experimental	0.630MJ/injera
2	Hiwot et al. 2022	Experimental	0.623MJ/injera
3	Mesele et al., 2017	Experimental	0.454MJ/ injera

According to Tab.1, up to 0.63MJ of energy is required to bake a single injera. For this investigation insulators are used to system can minimize losses on the sides and bottom of the storage. Therefore, assuming 0.6MJ of energy requirement per injera, the system can be sized accordingly.

2.3 Time required for baking injera

The time required for baking is a useful criterion to determine the size of the system. The time required for baking is the sum of the heat-up time (the time to reach baking surface temperature), the total baking time (time to reach boiling temperature of the water in the batter), and the total idle time (time to reach surface baking temperature in between each baking cycle).

$$t_{total} = t_{heatup} + \left(n \times t_{baking}\right) + (n-1) \times t_{idle} \qquad \text{(eq.1)}$$

Where:

t_{total} is the total time for the baking session (s), t_{heatup} is the heat-up time(s), t_{baking} is the baking time for single injera (s), t_{idle} is the idle time (s), n is the number of baking cycle

The heat-up time for the new system is negligible since the baking surface temperature is reached during PCM charging. Tab. 2 shows the total time required for baking a specific number of injeras calculated using eq.1, and taking the average baking and idle time from previous research (Abdulkadir et al., 2011; Asfafaw et al., 2014a).

Tab. 2: Baking time for a specific number of baking cycles

No	No of injeras/baking cycle	Average Baking time(min/injera)	Average Idle time(min/injera)	Total time (min)
1	30	2.5	1.5	118.5
2	40	2.5	1.5	158.5
3	50	2.5	1.5	198.5

2.4 Storage Capacity of the System

Energy storage capacity refers to the ability of a system to store energy for later use. The design and operation of energy systems require careful consideration of storage capacity. The storage capacity of a system depends on several factors, such as the type of storage technology, system size, and energy density of the storage medium. In this case, the system's storage capacity equals the energy needed to bake a specified amount of injera per full charge, including losses. Initially, three storage capacities were proposed, 18MJ, 24MJ, and 30MJ, for baking 30, 40, and 50 injeras, respectively, based on the number of injeras baked in households and institutions in a single baking session. one of the above-proposed systems will be selected after performing the PV power required to charge during the critical month and sizing each system.

2.5 Power required for charging

A detailed sizing of the PV module has been made for charging the proposed storage capacities based on the solar radiation of Addis Ababa. For example, a PV array of 1831W is needed to charge the 18MJ storage during the critical month. This power requirement includes the losses during conversion. The DC heating element converts this power into heat, which is then used to charge the thermal storage. Fig. 3 shows the PV power required for the proposed storage for each month of the year.

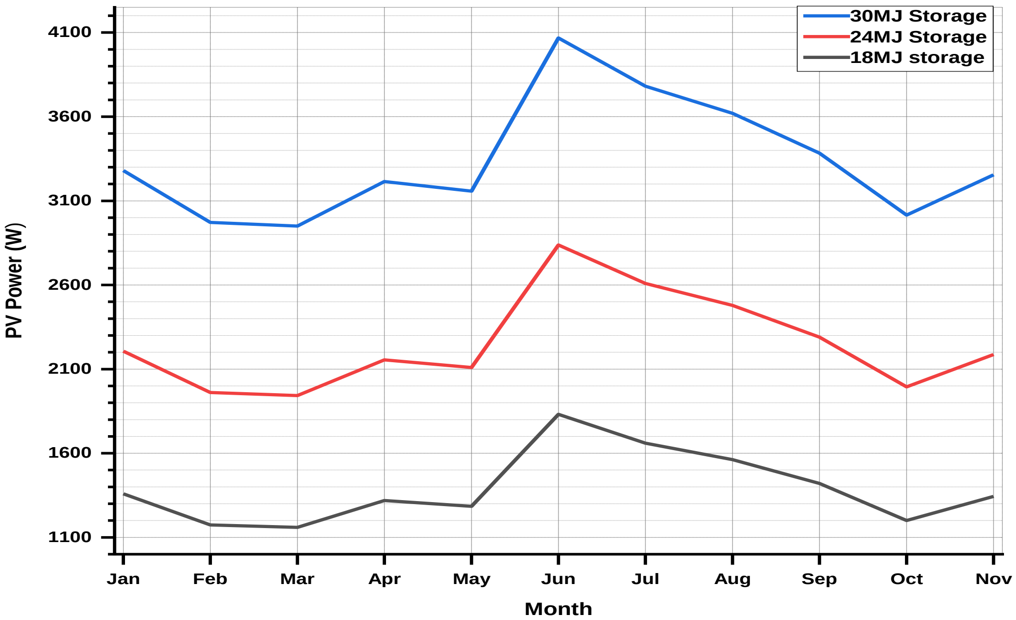

Fig.3: Monthly PV power required for each storage

2.6 Material Selection

2.6.1 PCM Selection

Because of its proven potential for high-temperature cooking (frying), eutectic mixture of 40% KNO_3 and 60% $NaNO_3$ is used as a thermal energy storage system (Asfafaw et al., 2014a, 2014b; Asfafaw et al.,2018; Dejene et al. 2017; Fuente, 2022; Vermachi et al.,2016). Eutectic mixtures are often selected as thermal storage material for cooking applications because they can store large amounts of thermal energy in a compact space and stability. The eutectic mixture of sodium nitrate and potassium nitrate has a melting point of 220°C and can store large amounts of thermal energy at this temperature range. This makes it an ideal storage material for applications such as cooking, where a constant and controlled temperature is required. The mixture is relatively inexpensive and widely available, non-toxic and non-corrosive, making it safe for food-related applications.

2.6.2 Insulation material

The selection of insulation material for cooking applications is an important consideration, as it can affect the efficiency and effectiveness of the cooking process. Different researchers investigate different types of insulation materials for cooking applications. Tab.3 shows some of the insulation materials used for cooking applications.

Tab. 3: List of Insulation materials and their thermal conductivity

No	Material	Thermal conductivity (W/mK)	Max T (^{0}C)	Reference
1	Rock wool	0.033-0.08	750	Ashmore et al., 2013
2	Fiberglass	0.01-0.04	540	Dejene et al., 2017; Watkins et al. 2017
3	Rice hulls	0.05-0.07	440	Watkins et al. 2017
4	Perlite	0.04-0.09	870	Watkins et al. 2017
5	Pyrogel/aerogel	0.015-0.046	650	Musard and O le,2013, Asfafaw et al., 2018

For this application, fiberglass is selected for insulation, because of its availability, lightweight, durability, and excellent insulation properties.

2.6.3 Baking pan material

Replacing the current clay baking pans with metal ones that are better suited for solar application is one of the project’s goals. According to prior studies, the main issue with using metal pans to bake injera is that it is difficult to remove the injera after baking (stickiness). The metal pan used needs to have thermal properties to avoid this issue and produce injera of higher quality. A brief simulation was conducted to select the type of metal pan for the concept development. Based on the simulation result, the 6mm aluminum pan was chosen for this investigation.

3. Concept Development and sizing of the system

3.1 Concept Development

The main objective of the concept development is to identify and develop an efficient and suitable thermal storage system for injera baking applications. This process involves evaluating various arrangements and materials for thermal storage that can increase efficiency and improve performance. We initially developed and evaluated six concepts using various criteria, understanding that the selection and organization of the system's components directly impact its performance and size. Subsequently, we discarded three concepts and further analyzed the remaining three using COMSOL multi-physics software. The concept with the best performance will be employed to build a prototype of a solar PV-based injera baking system. The components within each concept include a storage tank, PCM, heating element, base plate, and baking plate. Then, the difference between the concepts lies in the medium of heat transfer and the arrangement of the components.

Concept 1: Air-based system

Fig.4 (a) shows the basic components of the air-based system. This concept consists of PCM-filled cylinders;

the free space is filled with air.

Concept 2: Oil-based system

Fig.4 (a) shows the oil-based system which is the same as concept 1 except the type of heat transfer fluid used.

Concept 3: PCM-Fins system

Fig.4 (b) shows concept 3 which consists of cylindrical fins integrated with the base plate. The PCM is filled in between the cylindrical fins. In this arrangement, the fins act as a containing wall in addition to conducting heat. Approximately 15% of the storage volume is left for safety.

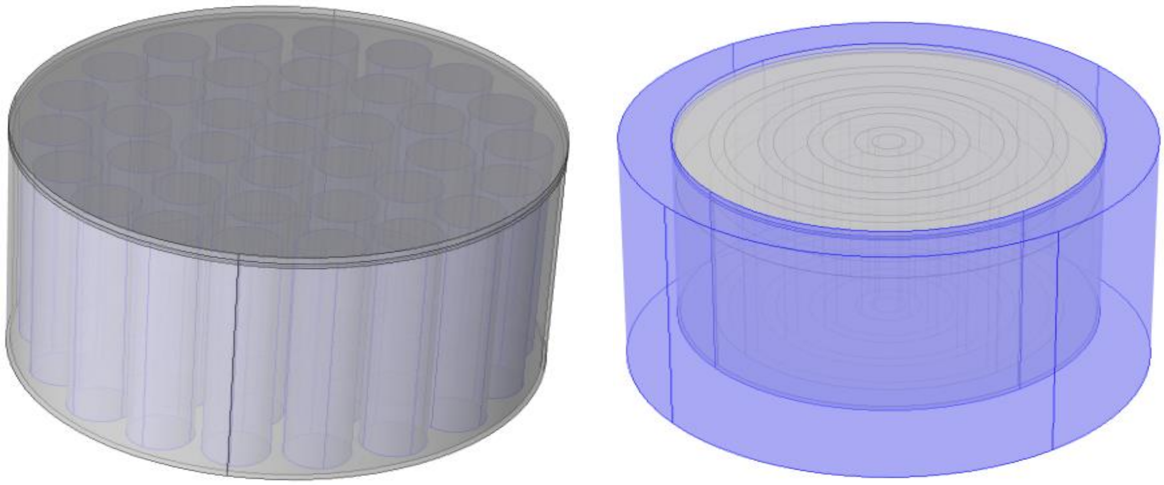

(a) (b)

Fig. 4: Proposed concepts (a) Concepts 1 and 2 (b) Concept 3

Placement of the heater

The placement of the heater has a significant impact on the charging and discharging performance of the system. Placing a heating element at the top or bottom of a thermal storage system can have advantages and disadvantages, depending on the specific application and design. For this case, placing the heating element at the top of the thermal storage between the baking pan and the base plate can allow for more efficient and effective heat transfer. An additional benefit of placing the heating element at the top is baking can be carried out during sunshine hours while charging the PCM.

3.2 Sizing of the different components of the system

3.2.1 Sizing of the Storage

The quantity of injera that needs to be baked will determine how big the storage needs to be. The storage volume for a certain storage capacity can be calculated using eq. (2) by assuming the diameter of the storage to be equal to the diameter of the baking pan:

$$Q_{PCM} = \int_{T_i}^{T_m} m_{PCM} c_{pPCM,S}\, dT + m_{PCM} \Delta h_{fus} + \int_{T_m}^{T_l} m_{PCM} c_{pPCM,L}\, dT \qquad \text{(eq.2)}$$

Where Q_{PCM} is the energy stored in the PCM, T_i is the initial temperature, T_m is the melting temperature,T_l is the liquid PCM temperature, $c_{pPCM,S}$ is the specific heat of solid PCM,$c_{pPCM,L}$ is the specific heat of liquid PCM, and m_{PCM} is mass of PCM.

The mass of PCM is given as

$$m_{PCM} = \rho_{PCM} V_{st} (1 - \xi) \qquad \text{(eq.3)}$$

Where V_{st} is the volume of the storage.

ξ is the fraction of the total volume occupied by fins (ξ_f) or the heat transfer fluid depending on the concept type ($\xi_{air}\ or\ \xi_{oil}$). The porosity value is taken as 0.4 (Dejene et al. 2017).

Table 4 shows the volume of storage for the proposed storage capacities.

Table 4: Mass and Volume of PCM

No	Storage capacity (MJ)	Volume of storage(m^3)	Volume of PCM (m^3)
1	18	0.0256	0.0154
2	24	0.0342	0.0205
3	30	0.0427	0.0256

The height of the storage is calculated using

$$V_{st} = \frac{1}{4}\pi h_{st} d_{st}^2 \quad \text{(eq.4)}$$

The diameter of the storage (diameter of injera pan) is set to be 40cm for the reasons listed below:

- Most institutions are using the 40cm pan.
- The storage system is made of casted aluminum; therefore, it will be easier for machining if the 40cm storage diameter is used.

Now it is time to decide the storage capacity among the proposed storages. Having considered all proposed storage options, the 18MJ (30 injera) capacity emerges as the most suitable solution. Further justification is provided below:

- The cost of the overall system increases as we increase the storage capacity (cost of PV, PCM, etc…).
- 30 injera is commonly the amount of injera baked in most households in a baking session.

Sizing the concepts for 18MJ capacity

In concepts 1 and 2, we calculate the volume of the storage occupied by the fluid by assuming that the void fraction accounts for 40% of the total storage volume. In concept 3, we use the same fraction. However, for safety reasons, only 15% of the total volume is occupied by the air, while the remaining portion is occupied by the fins. The thickness of the fins is then calculated based on this volume. Fig. 5 shows the 2D and 3D views of one of the concepts.

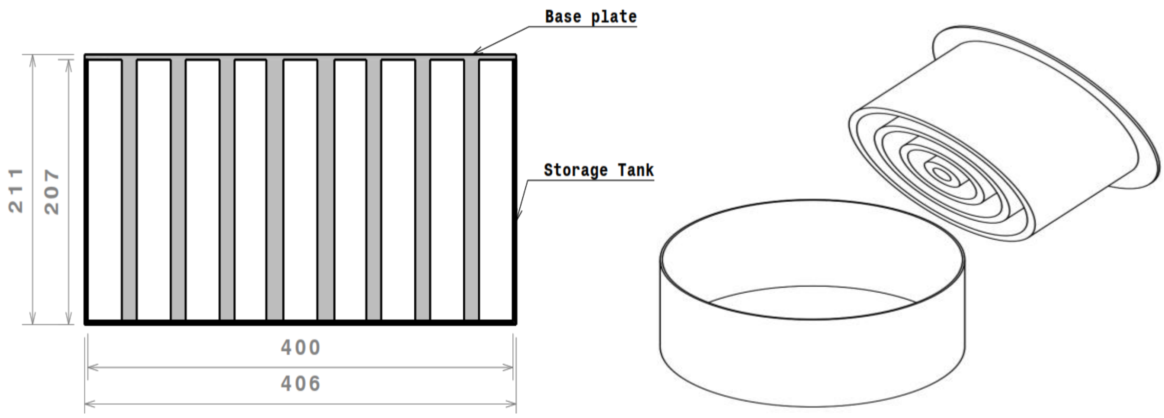

Fig.5: A 2D and 3D view of one of concept 3

Cylindrical encapsulation of the PCM

The PCM is encapsulated in cylindrical tubes made of aluminum to ensure efficient heat exchange between the heat transfer medium and the PCM. The encapsulating cylinders are attached to the bottom of the storage to avoid overheating of the PCM due to the high thermal conductivity of the base plate. A 10% clearance volume is required within each cylinder for safety purposes. The outer and inner diameters of the encapsulating cylinders are 50 mm and 48mm, respectively.

The total volume of the encapsulating cylinder is calculated using:

$$V_{cylinder,total} = V_{PCM} \times 0.10 + V_{PCM} \quad \text{(eq.5)}$$

The number of encapsulating cylinders is calculated from

$$V_{cylinder,total} = n \times V_{cylinder} \quad \text{(eq.6)}$$

Where n is the number of cylinders; $V_{cylinder}$ is the volume of a single cylinder.

4. Mathematical Modeling

The mathematical and numerical models are based on COMSOL multi-physics models for heat transfer in solids, liquids, and phase change materials. The following input boundary conditions are also used in addition to the governing equations:

Boundary conditions during charging:

- Boundary heat source between the baking plate and base plate.
- Natural Convection and radiation boundary conditions on the surface of the insulation.

Boundary conditions during discharging:

- Natural convection and radiation on the surface of the baking plate.
- Natural Convection and radiation boundary conditions on the surface of the insulation.

A 5cm fiber glass insulation is used to minimize loss during charging and discharging. The losses in the system are mainly radiation and convection losses over the surface of the insulation. Other boundary conditions are treated based on COMSOL Multiphysics, depending on the interaction of the mediums. Fig.6 shows the different boundary conditions during charging and discharing.

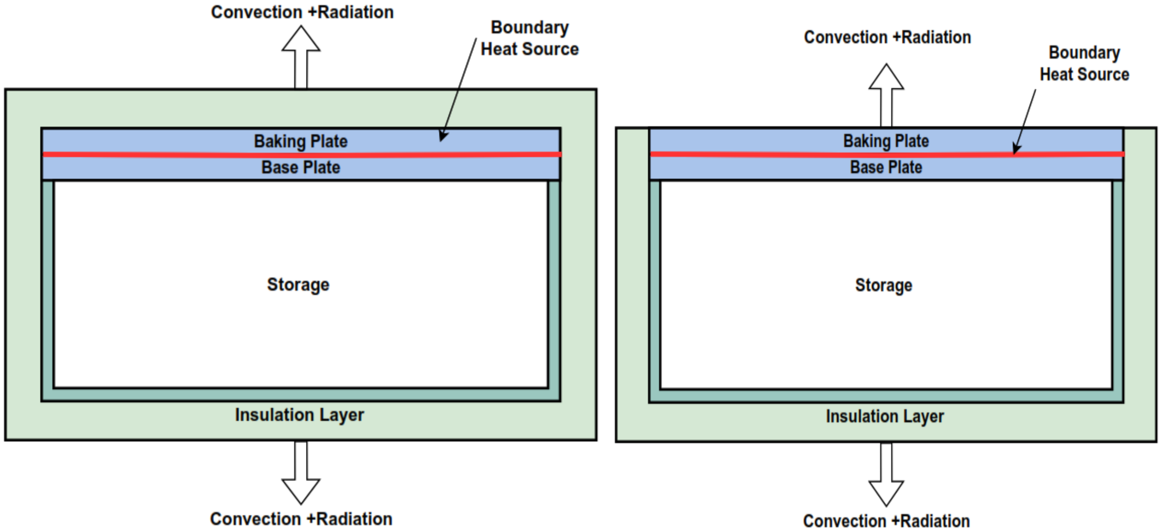

Fig.6: Boundary conditions during charging and discharging

5. Results and Discussion

In this study, three different thermal storage concepts for solar PV-based injera baking applications were developed and compared. The best performing one is selected by conducting a simulation using COMSOL multi-physics software. The three concepts include air-based, oil-based, and PCM-filled storage systems. The concepts were compared in terms of charging efficiency and temperature stability by simulating for a specific charging period (sunshine hours for the critical month) and a constant Power input of 1250W from a PV source during the critical month. The simulation provided results for various parameters, including PCM temperature, melt fraction, pan surface temperature, and energy stored during the charging period. Fig. 7 shows the PCM temperature profile during charging and discharging at three different locations, melt fraction, and insulation surface temperature for concept 1.

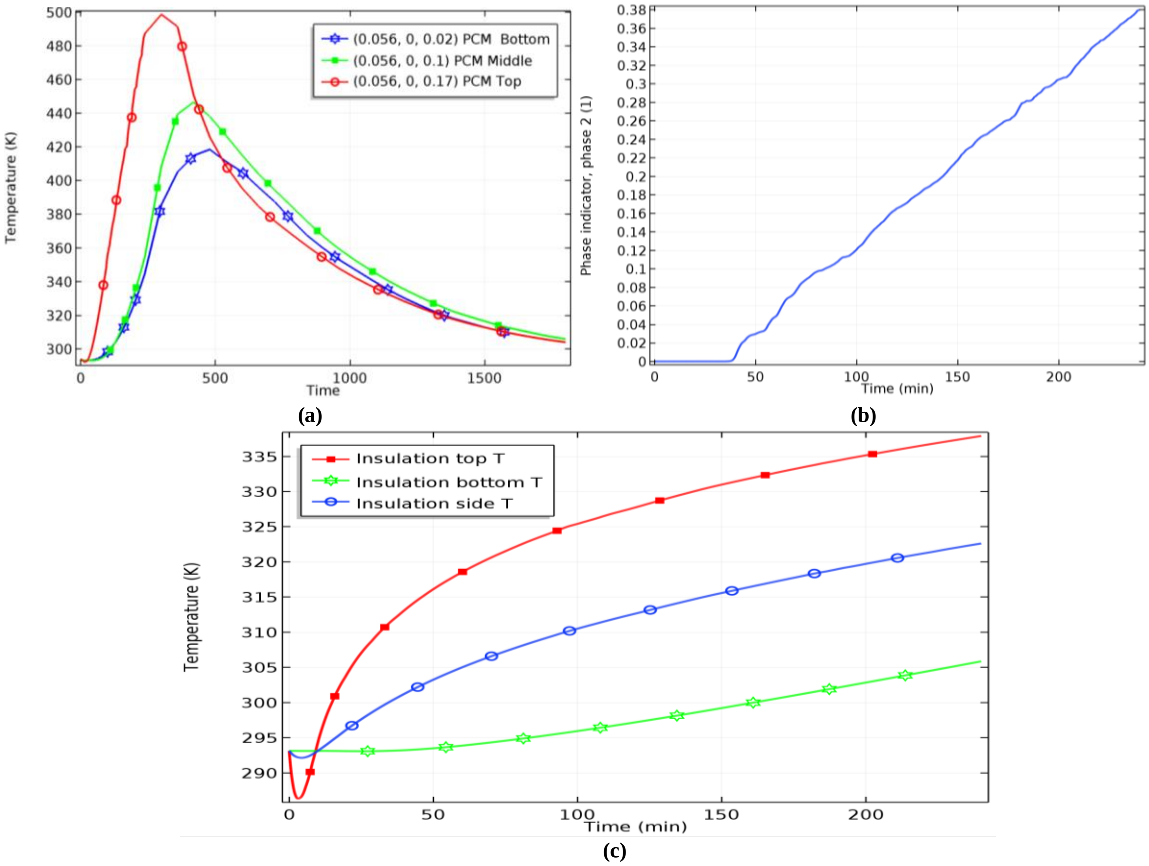

Fig.7: Plots of (a) PCM Temperature profile, (b) melt fraction, and (c) insulation surface T of concept 1

Fig. 8 shows the PCM temperature profile during charging and discharging, melt fraction, and insulation surface temperature for concept 2.

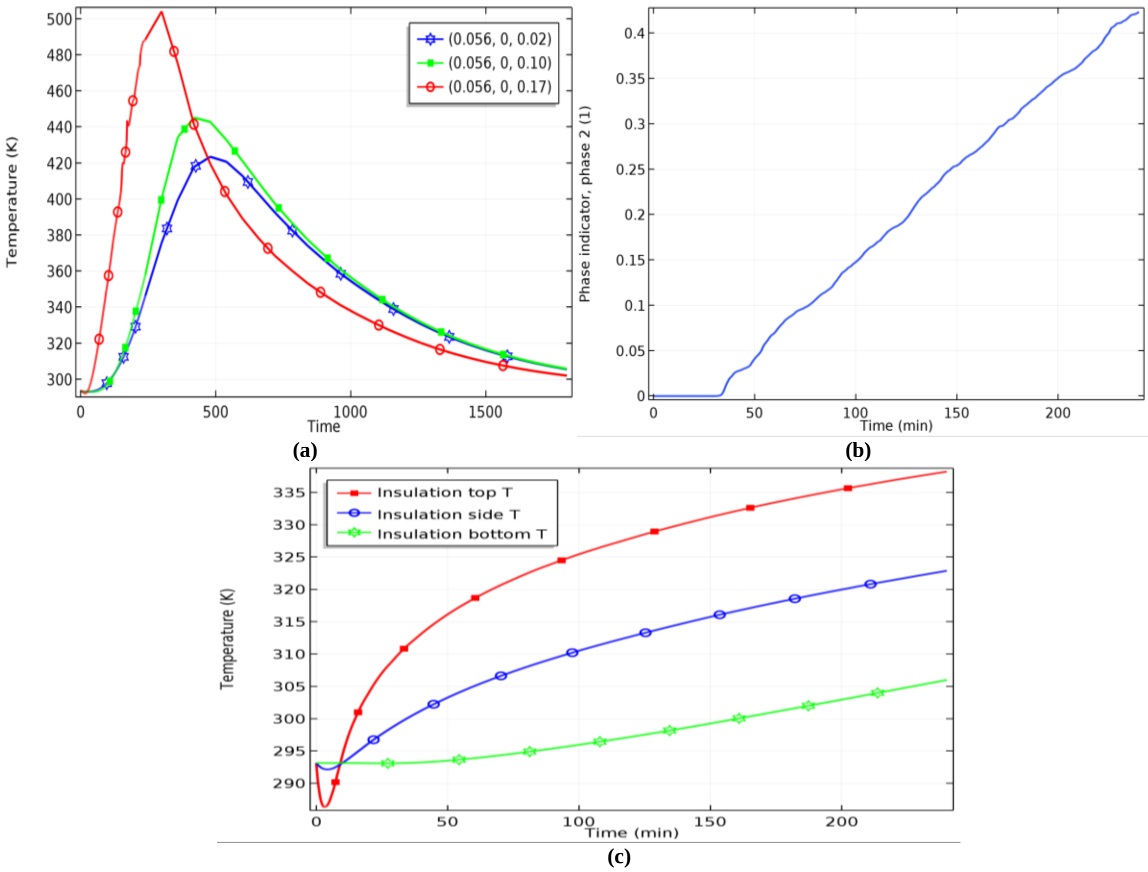

Fig.8: Plots of (a) PCM Temperature profile, (b) melt fraction, and (c) insulation surface T of concept 2

Fig. 9 shows the PCM temperature profile during charging and discharging, melt fraction, insulation surface temperature, and pan surface temperature during charging for concept 3.

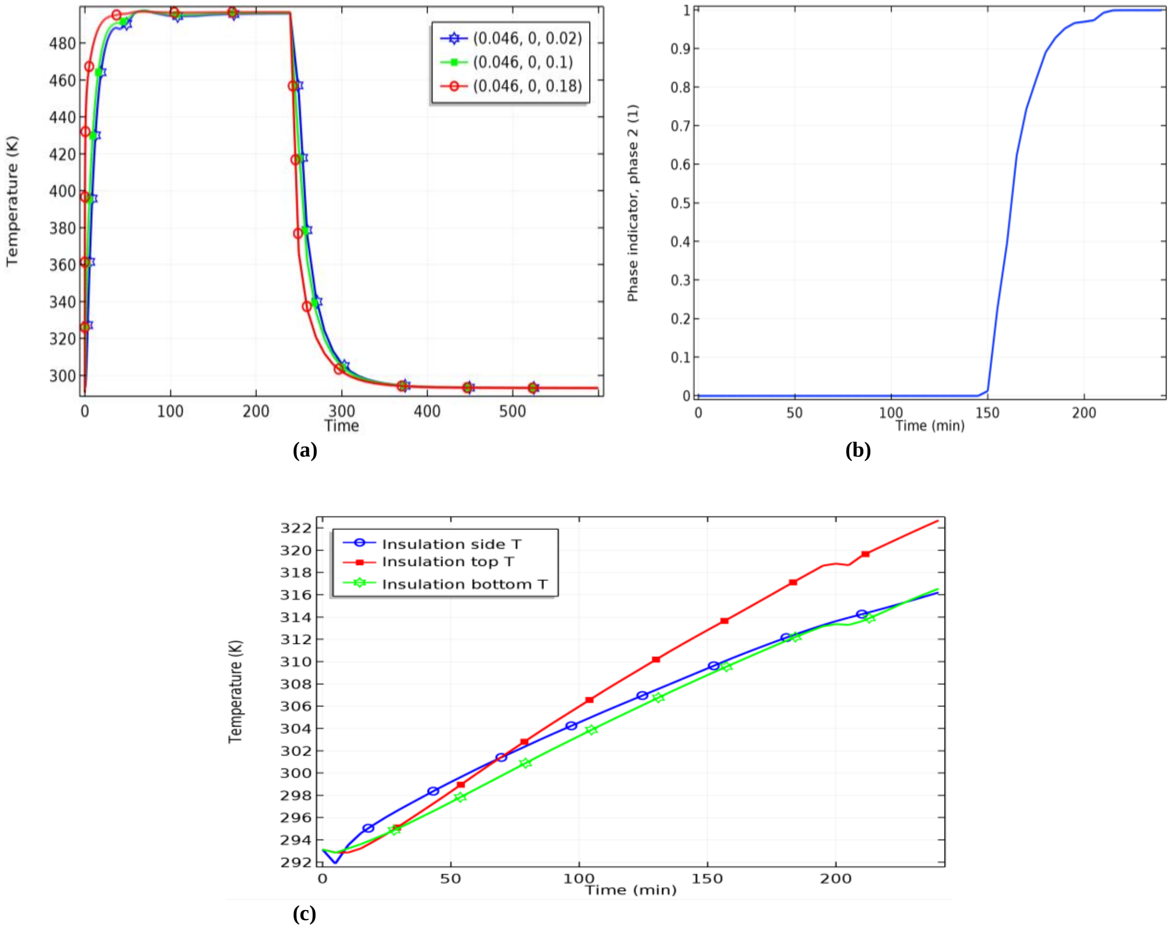

Fig.9: Plots of (a) PCM Temperature profile, (b) melt fraction, and (c) insulation surface T of concept 3

The air-based concept typically exhibits slower charging and discharging rates compared to the oil-based and PCM with fins concept due to the lower thermal conductivity of air (Fig.7a). The oil-based concept allows for efficient heat transfer due to the high thermal conductivity of the fluid, resulting in relatively fast charging and discharging rates compared to the air-based system (Fig. 8a). In the PCM with fins concept, the PCM is combined with fins that enhance heat transfer. During charging, heat is transferred from the base plate to the PCM through the fins, resulting in a relatively fast increase in temperature. The fins increase the surface area available for heat transfer, thereby improving the charging and discharging rate (Fig. 9a).

The air-based storage system exhibited the lowest thermal performance of the three concepts, with a 38% melt fraction, as the air acts as an insulator because of its lower thermal conductivity (Fig.7b). The oil-based storage system displayed a slightly higher melt fraction of 42%. However, there is still a significant portion of the substance that remains in a solid state (Fig. 8b). The PCM-filled storage system showed the highest charging performance, with a melt fraction of 100%, due to the direct contact between the high thermal conductivity aluminum fins and the PCM (Fig. 9b).

Based on the simulation data for insulation top surface temperature (Fig. 7c, 8c, and 9c), Concept 2 has the highest temperature at 338K, followed by Concept 1 at 337K, and Concept 3 has the lowest temperature at 323K. Concept 2 also has the highest temperature at 323 degrees for the side surface, followed by Concept 1 at 322.5K, and Concept 3 has the lowest temperature at 316K. Once again, Concept 3 performs better in maintaining a lower temperature on the side surface. The bottom surface temperature for Concepts 1 and 2 is 306 K, while Concept 3 has a slightly higher temperature of 316 K. In summary, the temperature at the top surface of the insulation in all cases is higher as a result of the placement of the heating element. Concept 3 consistently performs the best among the three concepts in terms of maintaining nearly uniform temperatures on the surfaces of the insulation layer.

In the case of concepts 1 and 2, more heat is transferred through the baking pan instead of charging the PCM, due to the insulating effect of the heat transfer fluid in the storage, resulting in a higher temperature on the surface of the pan. Concept 3 has a relatively lower pan surface temperature since it is in contact with the aluminum base plate and fins at the bottom. Aluminum is known for its high thermal conductivity. As a result, the aluminum absorbs and conducts heat to the PCM away from the pan, leading to a lower temperature for the pan surface.

6 Conclusion

Injera baking is a highly energy-consuming process. To design an efficient injera baking system for solar applications, we should first develop an appropriate storage system suitable for that particular application. The development of a thermal storage system for solar injera baking will play a significant role in the advancement of renewable energy technology. By integrating thermal storage into solar power systems, we can overcome one of the major limitations of solar energy – its intermittent nature – and enhance its efficiency and reliability. In this investigation, three different storage systems (air-based, oil-based, and packed PCM) are proposed and compared numerically by charging them for a specific period and power input. The result of the simulation clearly shows which model has a faster charging period and suitable discharging for injera baking application. The conduction-based model performs best among the three proposed concepts, with a performance of 58% higher than that of the oil-based and 62% higher than the air-based model. All three models demonstrate enough baking surface temperature during discharging, which is more suitable for injera baking. The concepts are also compared based on their pros and cons from different points of view (flexibility, weight, cost, etc.). The result obtained from this investigation will serve as the base model to develop a prototype that incorporates a PV system, thermal storage system, and a metal baking pan.

Further experimental investigation is needed to assess its long-term performance and economic feasibility of implementing these systems at scale. Nonetheless, the results provide a promising starting point for the future development of injera baking systems with thermal storage and demonstrate the potential of these systems to contribute to a more sustainable and energy-efficient injera baking system in rural and urban communities of Ethiopia.

7. Acknowledgment

We sincerely thank the Energy Net Project for funding this effort. The materials that are being presented here are a portion of the entire project and should not be viewed as a project output.

8. References

Abdulkadir A H, Demiss A A, Ole J N. Performance investigation of solar powered Injera baking oven for indoor cooking. ISES solar world congress proceedings, Kassel, Germany; 2011, p. 186-196

Abdulkadir A.H., Sisay B.K., Nigussie M.W., 2016. Design and manufacturing of thermal energy-based Injera baking glass pan. Energy Procedia, 93, 154 – 159.

Asfafaw H. T., Mulu B.K., Ole J. N., 2014a. Solar-powered heat storage for Injera baking in Ethiopia. Energy Procedia 57, 1603 -1612.

Asfafaw H.Tesfaya, Mulu B.K, Ole J. N, 2014b. Design and development of solar thermal Injera baking: steam based direct baking. Energy Procedia 57 (2014) 2946 – 2955.

Asfafaw H. T., Mulu B. K., Ole J. N., 2018. Steam-based Charging- Discharging of a PCM Heat Storage. Momona Ethiopian Journal of Science (MEJS), V10 (1):15-27, 2018

Ashmore M., Simeon H. T., Robert R.J., 2013. Experimental investigation on simultaneous charging and discharging of an oil storage tank. Energy Conversion and Management 65 (2013) 245–254.

Dejene K.K, Demiss A.A, Yilma T.B., 2017. Performance of a Pebble Bed Thermal Storage Integrated with Concentrating Parabolic Solar Collector for Cooking. Hindawi, Journal of Renewable Energy.

Fuente, M.G., Peña, D. G., Tristan, C. A. A Numerical Simulation of an Experimental Melting Process of a Phase-Change Material without Convective Flows. Appl. Sci. 2022, 12, 3640. https://doi.org/10.3390/app12073640.

Getahun M., 2017. Electric Injera Mitad Energy Efficiency Standards & Labeling. Challenges and prospects. Ethiopian Energy Agency (EEA). Vienna energy forum.

Hiwot B., Addisu B., Chandraprabu V., Suyambazhahan S. 2022. Performance improvement of an electric injera baking pan (Mitad) using copper powder as additive material. Energy for Sustainable Development. Volume 68, Pages 242-257.

Mesele H. H., Ole J. N., Mulu B. K., Asfafaw H. T.,2017. A Direct Solar Fryer for Injera Baking Application. ISES Solar World Congress.

Mussard M., Ole J. N., 2013. Charging of a heat storage coupled with a low-cost small-scale solar parabolic trough for cooking purposes. Solar Energy, Volume 95, September 2013, Pages 144-154.

Negash S. M, Omiogbemi I. M.B. and I. M. Dagwa, 2021. Development of a Partially Automated Electric Injera Baking Stove with Improved Efficiency and Production Rate. Materials, Mechanics & Modeling (NCMMM-2020).AIP Conf. Proc. 2341, 030001-1–030001-12; https://doi.org/10.1063/5.0049946.

Watkins T., Arroyo P., Perry R., Wang R., Arriaga O, Fleming M., O'Day C., Stone I., Sekerak J., Mast D., Hayes N., Keller P., Schwartz P., 2017. Insulated Solar Electric Cooking -Tomorrow's healthy affordable stoves? Development Engineering Volume 2, Pages 47-52

Veremachi, A., Cuamba, B., Zia, A., Lovseth, J., Nydal, O.J, 2016. PCM Heat Storage Charged with a Double-Reflector Solar System. Journal of Solar Energy.

PRODUCTIVE USE OF SOLAR WATER PUMPING SYSTEM WITH UNIVERSAL SOLAR PUMP CONTROLLER

Prasun Kumar Das[1], Nilanjan Ghose[1], Anupam Ray[2], PSSSR Murthy[2], Jatin Arora[2]

[1] Deutsche Gesellschaft für Internationale Zusammenarbeit (GIZ) GmbH , Delhi (India)

[2]KPMG Advisory Services Private Limited , Gurugram (India)

Abstract

This paper details the opportunity for additional productive uses of solar water pumping systems (SWPS) by replacing a normal controller with a Universal Solar Pump Controller (USPC). The USPC helps in fulfilling the need for power for running many loads in addition to powering SWPS. Owing to its potential, it is already part of the ongoing PM-KUSUM scheme of India, the largest in irrigation space. It also complements the fact that the utilization of off-grid SWPS is traditionally low. This study intends to assess the existing USPC ecosystem, identify gaps and challenges, and draw out possible strategies and mechanisms for increasing USPC acceptability and its deployment. The paper also entails the details on the assessment of key parameters impacting the adoption of USPC. A tool has been developed to quantify the potential of utilizing the available excess energy generated during non-irrigation hours of SWPs for other applications and analyzed them in 50 districts across different states in India.

Keywords: SWPS, USPC, PM-KUSUM, excess energy, irrigation

1. Introduction

Solar Water Pumps (SWPs) have now become an integral part of the agriculture and irrigation ecosystem in the country. Once a novelty, SWPs are emerging as an effective alternative to traditional options such as diesel and electric pumps. The growth in SWP deployment has seen a great push recently with support from the ambitious national scheme of India, the Pradhan Mantri Kisan Urja Suraksha Evam Utthan Mahabhiyan (PM-KUSUM) scheme. Many research works have been conducted to estimate the performance of SWP along with optimum sizing (Cuadros et al., 2004; Glasnovic and Margeta, 2007; Hamidat and Benyoucef, 2009; Moulay-Idriss and Mohamed, 2013; Kassem, 2012). However, the SWPs deployed at a high upfront cost are currently being utilized only for half of the days in a year (around 150 days per year) on average, which varies to a great extent depending on many factors such as the number of cropping, land size, water table, lack of proper design, etc. As per the study of Anas and Abhishek, 2021 (www.ceew.in), only 27% of the energy generation potential of SWP is utilized in India whereas the remaining 73% of energy just remains unutilized but with a great potential for meeting the energy needs of livelihood applications. It has been observed that increasing utilization of SWPs leads to greater income generation for farmers thereby increasing the financial and commercial viability of the system. The utilization of the SWPs can be increased by broadly two ways: firstly, by aligning the cropping pattern and thus the irrigation requirement as per SWP operation, and secondly by utilizing the excess energy for other income-generating end-use applications. It is challenging to convince farmers to change/ align their cropping patterns since cropping patterns are associated with traditional farming practices passed on from one generation to another. Additionally, many a times, change in cropping is not feasible considering climate, temperature, type of soil, and crop water requirement considerations. A more sustainable method of increasing SWP utilization is thus to explore other applications which can be powered by electricity generated by SWP systems during non-irrigation hours.

10.18086/swc.2023.07.02 Available at http://proceedings.ises.org

In the above context, the Ministry of New and Renewable Energy (MNRE), Govt of India has introduced technical specifications for Universal Solar Pump Controller (USPC), a controller with multiple outputs allowing farmers to utilize the excess energy generation during the non-irrigation hours for operating other applications such as Atta Chakki, Chaff Cutter, etc. It is a unique, multipurpose, variable speed motor controller that replaces a normal controller to run agrarian equipment in addition to a solar pumping system. It converts high voltage, direct current from a photovoltaic (PV) array into highly controlled, three-phase PWM (pulse width modulated) alternating current (VAC) to run standard AC water pump motors. It can also be used to run DC water pumps. As per the specification designed by MNRE, USPC must have at least four numbers of three-phase output cables to feed power to various uses as per the need of the farmer and the farmer should have the option to select the specific application at a time using a keypad or via mobile or remote control connectivity.

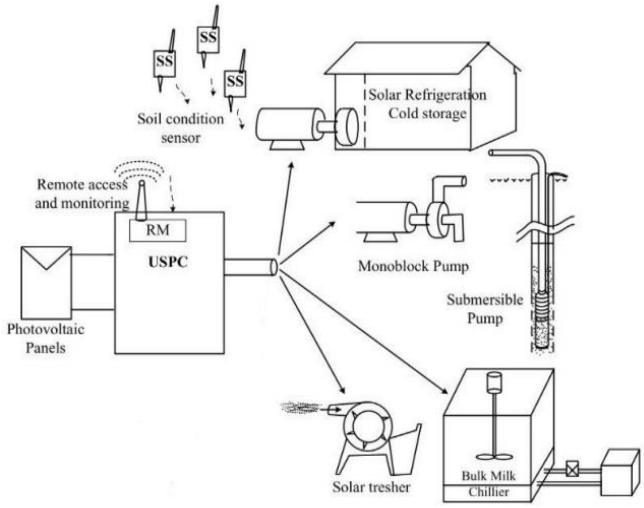

Fig. 1: USPC operation schematic diagram [7]

Even though USPC is part of a national scheme owing to its potential, there are some challenges in adoption and hence, despite encouragement from MNRE to use USPC (by including it in the PM-KUSUM scheme), to date, there are very few installations on the ground across the country. This study has made efforts through primary surveys and stakeholder consultations to understand different aspects of USPC that would aid in identifying the bottlenecks and identify probable solutions and directions for large-scale uptake of USPC.

2. Methodology

To understand the potential and challenges of USPC a two-way approach has been taken. First, the estimation of excess energy available for USPC to run is calculated and analyzed in different scenarios. Secondly, a detailed primary survey was conducted among firsthand users of USPC along with consultation with different stakeholders.

2.1. Excess energy calculation

The Excess Energy Computation Tool (EECT) is an Excel tool based on the Solar Irrigation Pump Sizing (SIPS) Tool developed by the Indian Council of Agricultural Research (ICAR), GIZ, Climate Change, Agriculture and Food Security (CCAFS) and IWMI to estimate the optimal solar pump capacity at a given location in India (https://pmkusum.mnre.gov.in/landing.html). The SIPS tool intends to increase the understanding of factors that drive farmers' irrigation demand, and pumping behavior, and ultimately recommends 'pump size' and monthly irrigation requirement based on various factors, such as location, climate data, irrigation data, etc. Further, an additional layer is added to the tool to estimate the excess energy not utilized by SWP across the selected states and districts. The excess energy is calculated by subtracting the energy consumed by solar water pumps for irrigation purposes from the energy generation by solar panels during a year. The tool aims to allow stakeholders, such as solar developers, policymakers, and financiers, to make informed decisions about SWP installations. The tool provides insights on monthly excess energy available by water pumps across shortlisted districts and can assist stakeholders in identifying areas for improvement and optimization, thereby contributing to the overall effectiveness and enhancing the financial viability of SWP projects.

Selection of states

Estimating excess generation is critical for getting the range of average SWP utilization across various states and districts across the country. Since the surplus energy needs to be estimated across various states and districts, ensuring uniform representation, a framework/methodology for the selection of states and districts based on various parameters/criteria has been created. The methodology for the selection of states and districts has been carried out in two modules (a) Selection of districts from the cluster combination as defined in the IWMI-Tata Policy Paper (https://www.iwmi.cgiar.org) based on high level of farm mechanization, (b) States with higher number of SWP Installations and demand as submitted for Component B of PM KUSUM scheme. The purpose of shortlisting selected districts and states is to ensure that the selected districts represent the varied geographical, geological, and climatic conditions across India. Accordingly, 50 districts in 15 states across the country were selected for the estimation of the excess energy available by SWPs across the country.

The following assumptions have been considered in the base case scenario while estimating the above levels of % of annual excess energy available across the districts:

- 3 times cropping in a year is considered for all the districts.
- Micro-sprinklers were chosen as the irrigation system due to their efficient water distribution, and tube wells were the primary water source employed due to their widespread availability in the studied districts.
- 25 days of irrigation is considered across months.
- The water table depth, crops, and planting months are chosen based on state-specific data available from the respective states' govt. agriculture and irrigation portals.
- Solar irradiation has been considered from the NASA portal for respective districts. (www.power.larc.nasa.gov)

2.2. Primary Survey of USPC users

Currently, the USPC technology is in the nascent phase with very few installations across India. At the time of conducting the survey, Himachal Pradesh is one of the very few states with a relatively higher number of USPC installations. In consultation with MNRE and the Agriculture Department of Himachal Pradesh, 54 farmers across 7 districts (as shown in Fig 2) have been shortlisted for the primary survey. The majority of the SWPs have a capacity of 5 HP. A thorough consultation procedure was designed to facilitate transparent and meaningful interaction with the farmers. During the preparatory phase of the survey, a questionnaire for the farmers was prepared to capture the farmers' motivation for use of USPC, their experience while applying for USPC and using USPC, information on subsidy availed by farmers for purchase of SWP with USPC, key issues (if any) faced while using USPC, typical equipment used with USPC, usage pattern of USPC, etc. The questionnaire was also designed to understand the USPC technology, its cost and benefits, and identify bottlenecks, if any, affecting the USPC adoption by farmers. The questionnaire has a mix of qualitative and quantitative questions to capture relevant information regarding the usage of USPC. The robust and comprehensive questionnaire was intended to capture technical, financial, social, and behavioral aspects related to USPC.

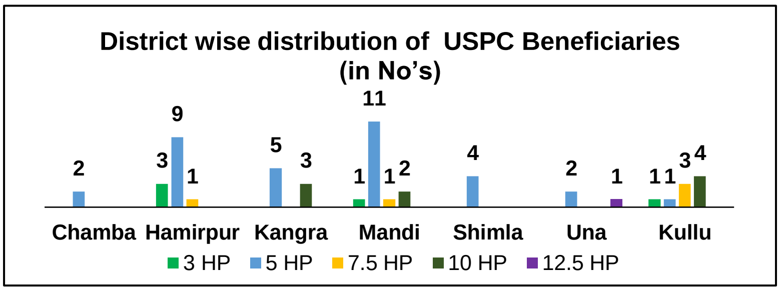

Fig. 2: District Wise USPC Installation to be considered for the primary survey

During the survey conducting phase, a detailed action plan encompassing a meeting agenda, a tentative schedule for consultations, and key points of the discussion were developed. The stakeholders were taken through their respective questionnaires and their responses were documented in a detailed manner.

During the documentation and reporting phase, all the responses from farmers were collected either in pen and paper mode in the local language or in the Survey CTO tool on Electronic Tablets. Both qualitative and quantitative information collected from farmers were analyzed for key insights on USPC penetration, usage, and issues. The responses provided by farmers were corroborated by responses from other farmers to ensure that the insights derived were accurate.

2.3. Stakeholder consultations

The project team conducted consultations with various SWP/USPC/Agri equipment manufacturers, researchers, technical institutes, and SIAs in the country. The discussions were focused on understanding the challenges vis-à-vis technical requirements of the equipment and excess energy produced from SWPs (e.g., electrical compatibility, O&M requirements, etc.) in promoting USPCs.

3. Results and Discussion

3.1. Excess energy availability

As highlighted above, one of the objectives of the study is to estimate the energy available from the solar water pumping system, which can be utilized by farmers for non-irrigation purposes to meet their energy needs. The findings revealed significant variation in the selected 50 districts in the availability of excess energy among these districts as shown in Fig 3. In some districts, annual excess energy available is as high as 85% of the total solar energy highlighting low utilization of SWP for irrigation. In contrast, some of the districts showcased considerably higher utilization, with annual excess energy available as low as 38%. Importantly, this contrast in excess energy utilization is also impacted by optimal SWP capacities for respective locations, which ranged from 1 HP to 10 HP. It is to be noted the tool used for this estimation has the capacity to design a maximum upto 10 HP.

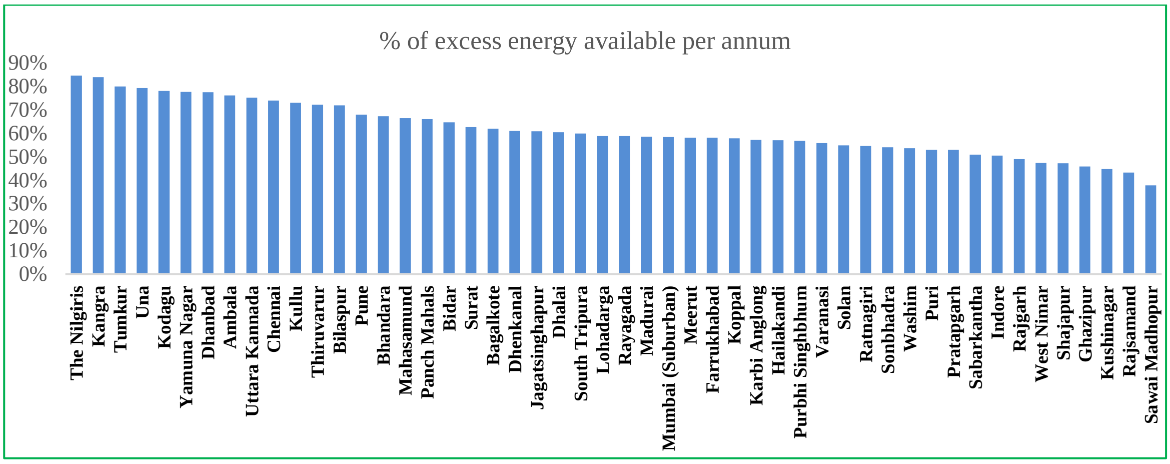

Fig. 3: % of excess energy available per annum across 50 districts

Further, the following sections detail the scenarios that highlight the impact of the number of crops, irrigation system, and water table depth on pump capacity and excess energy generation. The expected outcomes of each scenario, along with the rationale behind them, are discussed in Table 1.

Tab. 1: Expected outcome and rationale of various scenarios

Scenario	Expected Outcome	Rationale
Change in Cropping style	Decreased excess energy availability with a greater number of cropping	The decrease in crop counts within a specific district is likely to result in reduced water demand, subsequently leading to less frequent usage of SWPs. This reduction in usage increases the availability of excess solar energy, which can then be repurposed to meet various agricultural or non-agriculture activities.
Change in Irrigation Style	Shifting from Micro-Sprinklers to Surface irrigation results in higher energy consumption by pumps and may necessitate the need for higher-capacity SWP.	Switching from Micro-Sprinklers to less efficient Surface flooding requires higher capacity SWPs to meet the increased water demand. However, this shift may not correspond to a significant increase in energy unutilized,

Scenario	Expected Outcome	Rationale
		as the energy from added pump capacity is predominantly used for the increased irrigation demand.
Change in Water Table Depth	Increase in requirement of energy for pumping water with an increase in the water table depth.	Pumping water from deeper wells requires more energy, leading to a reduction in the surplus energy of Solar Water Pumps (SWPs) and making the use of higher-capacity pumps necessary for deeper water sources. In such a scenario, for a given amount of non-irrigation hours in a year, more energy will be available for other activities.

For these scenarios, representative districts among the 50 districts were chosen such that the various impacts of each of the parameters on pump capacity, excess energy generation, or both are highlighted clearly.

Scenario 1: Different cropping style

In this scenario, the focus is on assessing the variation of excess energy availability depending on the number of cropping practiced in a year. Keeping all other parameters unaltered i.e., the cropping per year has been reduced from triple to single. As shown in Fig 4, a decrease in cropping number count across districts has either resulted in the need for lesser SWP capacity or higher energy available or both. The graphs below highlight the same across 4 representative districts out of 50 districts.

Fig. 4 (a) illustrates the impact of varying crop patterns in Uttara Kannada, a district in Karnataka, on the percentage (%) of excess energy left unused. It can be observed that a decrease in the number of cropping has marginally decreased the SWP capacity from 2 HP to 1 HP. However, this has resulted in an increase in excess energy available from 75% to 87%. In the Mahasamund district of Chhattisgarh [Fig. 4 (b)], it can be observed that with the decrease in number of cropping from triple to single, the SWP capacity decreased from 10 HP to 2 HP. This has been accompanied by an increase in excess energy from 66% to 82%. Fig. 4 (c) shows the decrease in the number of cropping from triple to single resulting in an increase in SWP capacity from 10 HP to 2 HP and a drop in excess energy from 47% to 80% in the Shajapur district of Haryana. Lastly, in the Kushinagar district of Uttar Pradesh, as shown in Fig. 4 (d), the decrease in the number of cropping didn't alter the SWP capacity but has only resulted in an increase in excess energy (in %) available.

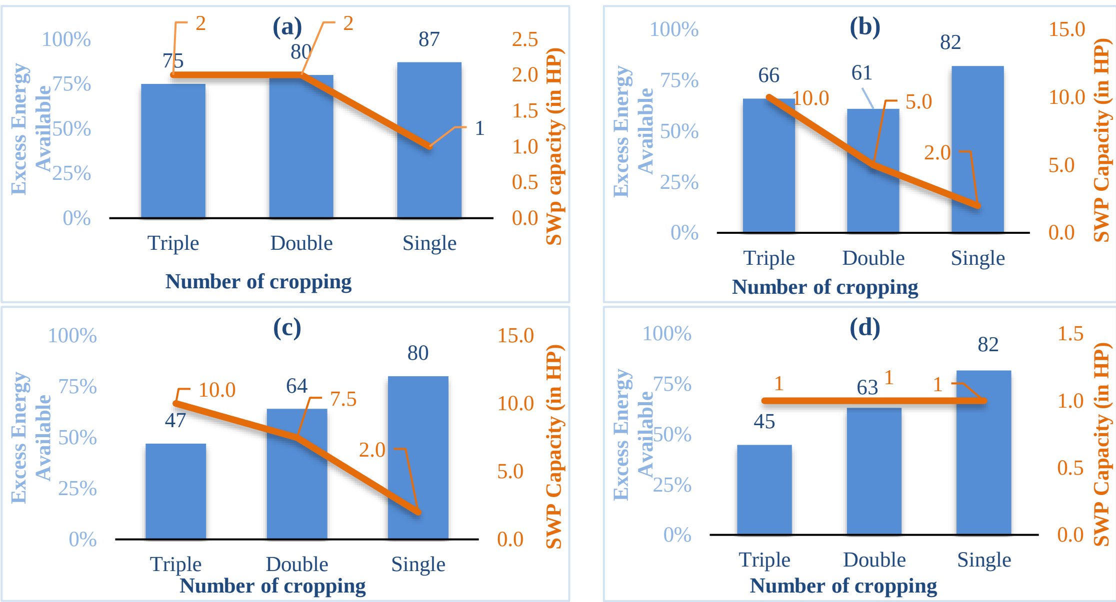

Fig. 4: Impact of Annual Crop Count Change on SWP Capacity and Energy Available (a) - Uttara Kannada District, Karnataka; (b) - Mahasamund district, Chhattisgarh; (c) - Shajapur district, Haryana; (d) - Kushinagar district, Uttar Pradesh

Scenario 2: Different irrigation style

In this scenario, the focus is to understand how the selection of different irrigation systems, viz. Micro-sprinklers, Sprinklers, Drips, or trickle, and Surface/flood can change pump capacity requirements and its utilization time. Fig. 5 shows the impact of change in the irrigation system in 4 representative districts viz. Uttara Kannada District of Karnataka, Kangra District, Himachal Pradesh, Dhanbad District, Jharkhand, and Kushinagar District of Uttar Pradesh.

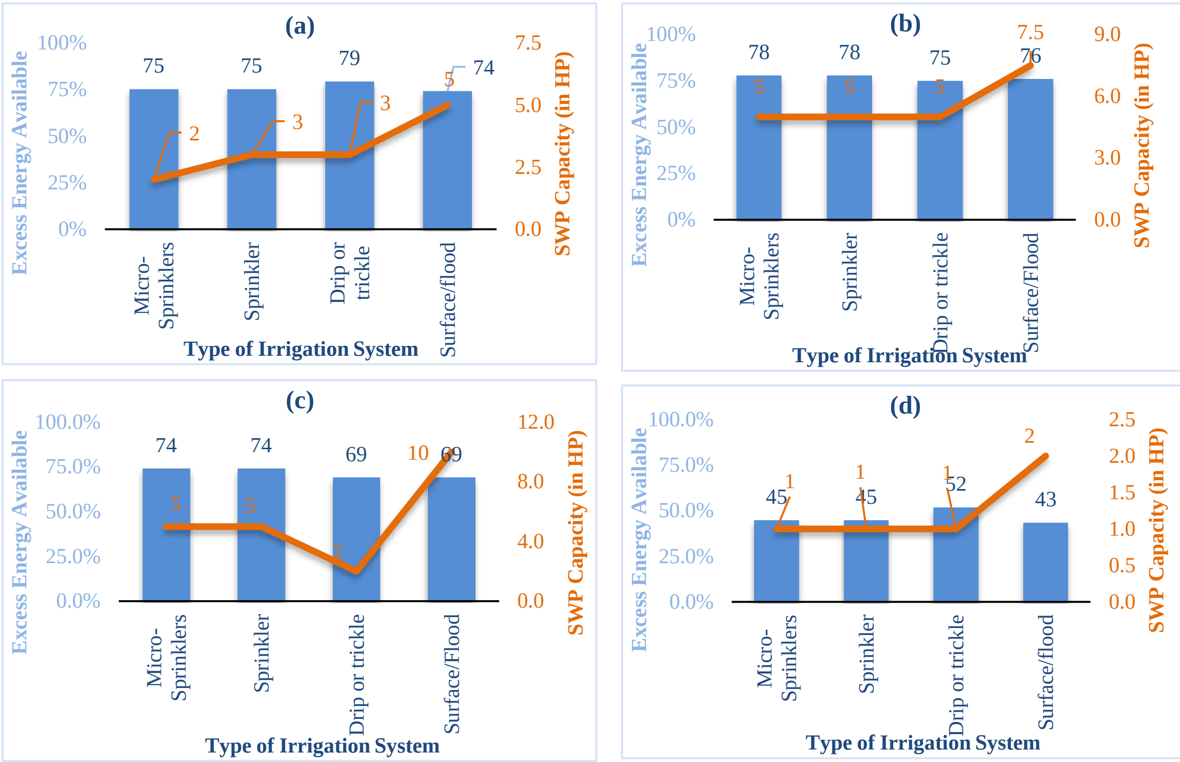

Fig. 5: Impact of change in irrigation system on SWP Capacity and Excess Energy Available (a) - Uttara Kannada, Karnataka; (b) - Kangra district, Himachal Pradesh; (c) - Dhanbad district, Jharkhand; (d) - Kushinagar, Uttar Pradesh

Fig. 5 (a) illustrates the impact of changing irrigation methods employed by farmers in Uttara Kannada district of Karnataka on the SWP capacity (in HP) and the annual percentage of excess energy available. It was observed that transitioning from Micro-Sprinklers to Surface/flood increased the SWP capacity from 2 to 5HP without significant change in excess energy available. Fig. 5 (b) highlights the impact of irrigation systems in the district of Kangra, Himachal Pradesh. With the change in irrigation system from Micro-sprinkler to Surface the SWP capacity increased from 5 to 7.5 HP without significant change in excess energy available. Fig. (c) illustrates the impact of changing irrigation methods in the district of Dhanbad, Jharkhand. With the change in irrigation system from Micro-sprinkler to Surface the SWP capacity increased from 5 to 10 HP and further decrease in excess energy available. As shown in Fig. 5 (d), in Kushinagar district of Uttar Pradesh, transitioning from Micro-Sprinklers to Surface floods increased the SWP capacity from 1 to 2 HP without significant change in excess energy available. It is evident that a significant amount of excess energy is available for all the different irrigation methods across all the locations which concludes the potential of USPC for productive use irrespective of irrigation method preferred by farmers.

Scenario 3: Different water table depth

In this scenario, to understand the impact of changing water table depths, an analysis of the range across 50 districts was conducted, which spanned from 3 m to 40 m. For ease of representation, the analysis was divided into two primary categories: water table depth under 20 m, and water table depth ranging from over 20 m up to 40 m. Further, the impact of water table depth on SWP capacity and % of excess energy available is represented for 5 districts in each of the above-mentioned categories.

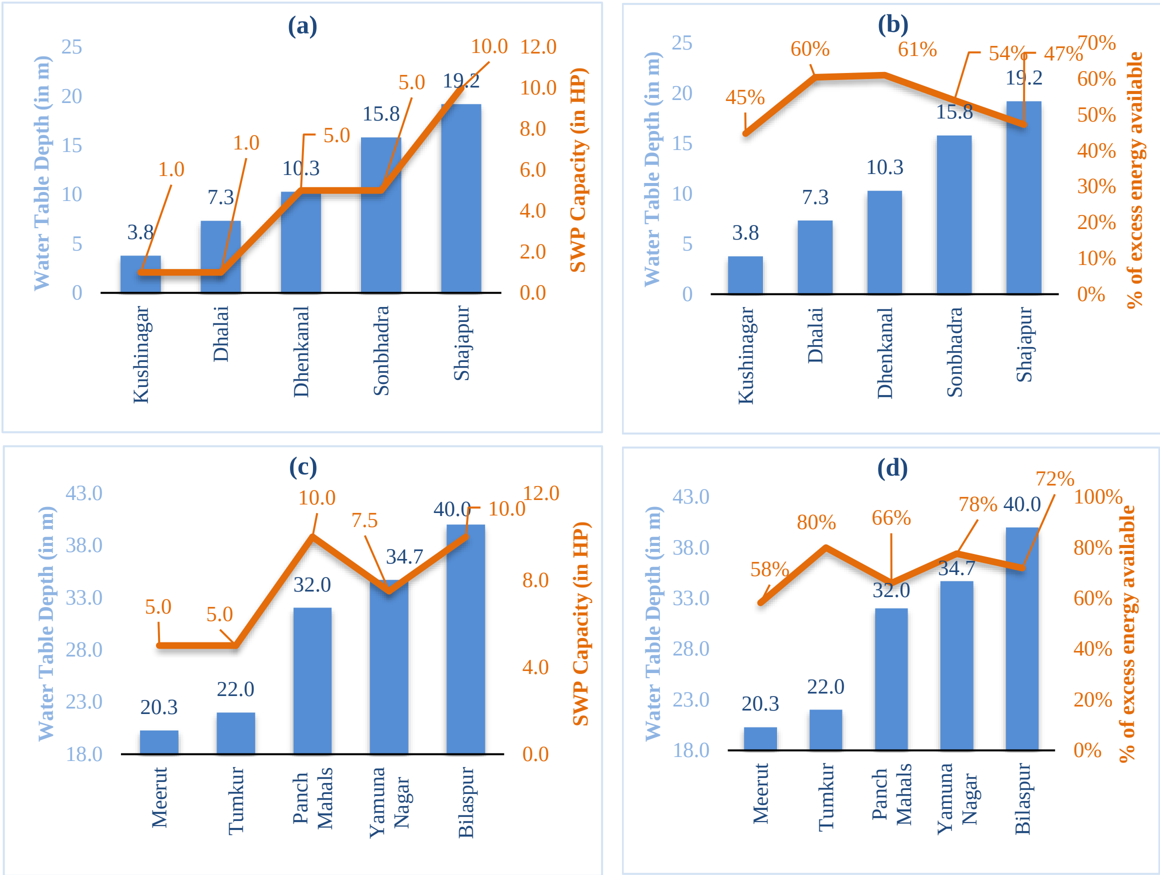

Fig. 6: Impact of change in the water table depth (in m) on SWP Capacity and Excess Energy Available (a) - Water table depth less than 20 m- Change in SWP capacity; (b) - Water table depth less than 20 m- excess energy available (%); (c) - Water table depth 20 to 40 m- Change in SWP capacity; (d) - Water table depth 20 to 40 m- excess energy available (%)

Fig. 6 illustrates the influence of water table depth changes (in m) on SWP Capacity (in HP) and the annual percentage of excess energy that remains unused. This is represented across 10 districts- 5 with a water table depth of less than 20 m and 5 with a water table depth from 20-40 m: As highlighted in the above figures, water table depth is not directly correlated with SWP capacity and % excess energy available. This is attributed to varying rainfall and cropping patterns across different districts of India. Fig. 6(a) illustrates the impact of changes in water table depth (in m) in the districts mentioned above that have a water table depth of less than 20m. It can be observed that as the water table depth increases from ~4 m to ~19 m, the SWP capacity required also increased from 1 HP to 10 HP. Whereas in Fig. 6 (c), while assessing the impact on a district having a water table depth greater than 20 m, it is observed with an increase in water table depth from ~20 m to ~40 m, the SWP capacity increased from 5 HP to 10 HP. However, in all these cases, the absolute value of excess energy available (in kWh) increases with increase in the water table depth.

3.2. Primary Survey

Out of the 54 farmers with whom consultations have been conducted, it was identified that 3 of the farmers were using the normal controller and the rest 51 of the farmers were using USPC. However, based on consultations with 51 USPC beneficiaries, it was revealed that only 1 out of those were utilizing USPC for operating Agri equipment (Chaff Cutter) apart from operating SWP, while the rest of the 50 were utilizing USPC only for SWP operation. Some of the key observations during the survey were highlighted below:

- 15 farmers did not have any agri equipment or any other energy needs to be fulfilled.
- 9 farmers were interested in purchasing the additional Agri equipment for operating it with USPC.
- 8 farmers had stated that the USPC is installed far away from their homes (where agri equipment is installed).
- 8 farmers were interested in connecting the SWP/USPC system with the grid.

- 5 farmers were found to be having single-phase equipment which were incompatible with USPC and 24 had shown interest for single-phase instruments to be connected if possible.
- 10 farmers had witnessed the visual operation of SWP/USPC prior to purchasing the system.

3.3. Key issues and potential solutions

Based on the learning during the primary survey as mentioned above and consultations with different stakeholders, key issues deterring the USPC penetration were identified as shown in Fig 7. The stakeholders include manufacturers of USPC, solar water pumps, agri/food-processing equipment, State Implementation Agencies (SIAs) of the PM-KUSUM scheme, researchers, and testing laboratories. Figure 11 illustrates broad categories of issues identified.

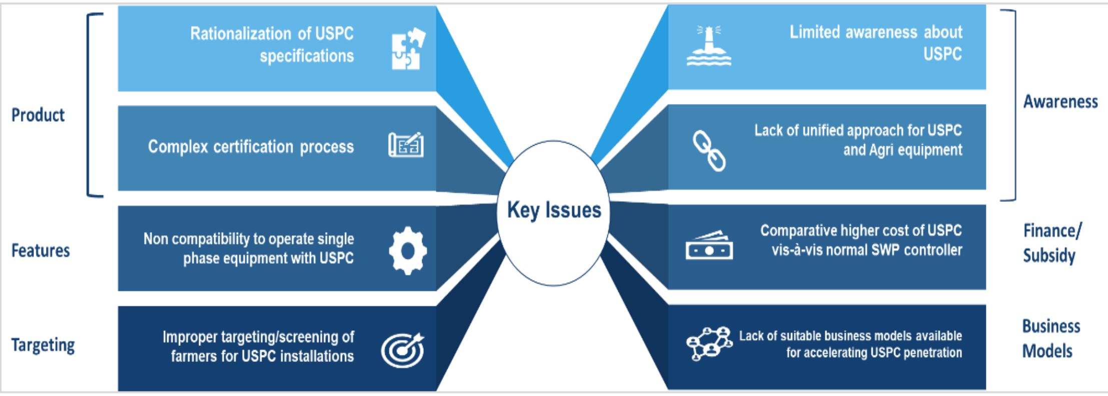

Fig. 7: Key Issues identified for USPC adoption

The following section will explain the different issues under the broad categories mentioned in detail.

- The cost differential between the price of regular controller and USPC is one of the major reasons affecting the USPC adoption. As shown in Fig 8, the cost difference ranges from 8% to 13%. (https://www.hindiyojana.in/wp-content/uploads/2021/02/2021122685-compressed.pdf).

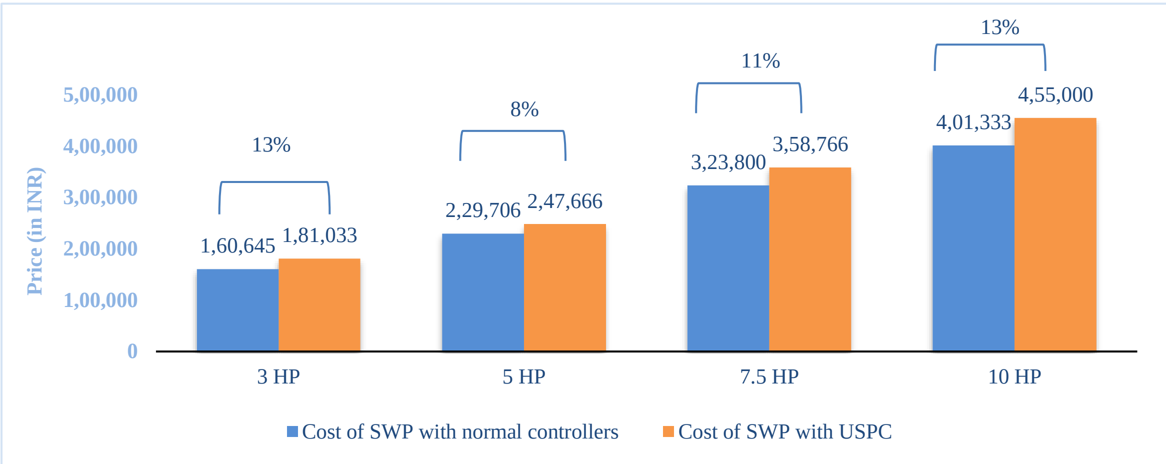

Fig. 8: Cost of USPC Vis-à-vis normal controller

- The current technical specifications of USPC are quite stringent and complex in nature resulting in increasing the cost of USPC. For example, the input voltage range as defined in the specifications may need to be revised based on suitable scientific methodology, since such a surge is not achievable, a change in total harmonics distortion (THD) levels in the range of 3-5% is not practically possible to manage all the time.
- Testing norms of USPC are not standardized by the certification labs across the country. In addition, the current testing procedure requires performing the functional test analysis of USPC by using actual

defined three-phase farm equipment such as Atta Chakki, Chaff Cutter, Bulk Milk Chiller, etc. However, it makes it difficult for vendors to carry the actual farm equipment to the testing centers. Considering the variety of farm equipment, including models and brands, it is impossible to achieve any degree of consistency in results either in the test center or in the field. Further, it would also be logistically difficult for manufacturers to bring the required equipment to the testing centers. In addition, the current technical specifications are detailed about intermediate conditions such as Maximum Power Point Tracker (MPPT) efficiency, number of ports, etc. but are unclear about the 'real' output of the core performance test. Hence, there is a need to simplify the certification process, where the number of equipment to be tested and the testing procedure to be streamlined.

- The current technical specifications permit only the use of three-phase agri equipment with USPC and not single-phase equipment. Primary consultation with USPC beneficiaries across HP revealed that 45% of the farmers had shown interest in using single-phase equipment for their daily needs and indicates an inclination/demand to operate both single-phase and three-phase equipment using USPC. Also, many farmers cited that single-phase agri equipment are easily accessible in the local market in contrast to the three-phase agri equipment, which were stated to be available only in far-off big cities. Further, there might be a high probability of damage/tampering with the equipment/USPC by farmers as farmers due to lack of technical knowledge might connect the single-phase equipment with USPC.
- There is a need for criteria to be adopted for allocating the USPC to farmers (under government-supported programs) to improve the targeting and enhance utilization. It is to be checked in advance whether the USPC can be used for the specific farmer's benefit.
- There is a need for steps to be taken to increase awareness among farmers regarding USPC benefits and the potential list of equipment that can be operated with USPC.
- There is a need to develop suitable business models for both individuals/groups of farmers for better utilization of USPC, better payback period, and maximization of revenue. A suitable delivery model should closely resemble local conditions, often requiring multiple approaches to cater to the needs of the farmers.

In view of the issues highlighted by stakeholders during consultations, the following solutions have been proposed.

- Simplification of specifications and testing procedures: USPC is currently in the nascent stage, hence an adaptive approach is suggested involving gradual simplification/easing up of the testing process, resulting in making the testing procedure more simplified, and streamlined. appropriate feedback may be sought from the various vendors, testing labs, and willing consumers during the process so that a variety of new issues can be identified, recorded, and analyzed to minimize their impact.
- Awareness Campaigns: A comprehensive approach to disseminating information to all stakeholders through awareness campaigns, pilot demonstrations, communication materials, capacity building, and engagement with farmers to educate and address their concerns is required. This would aid in enhancing USPC demand among farmers and would ensure in dissemination of the benefits and applications of USPC among end users and accelerate the adoption of USPC at scale.
- Customized solution: Offering customized solutions to farmers rather than a 'one-size-fits-all' approach will help farmers optimally utilize the excess energy generated for meeting their needs for operating agri equipment using USPC.
- 'Single Window' Information and Support Mechanism (SWISM): Based on the survey conducted with farmers in HP, it was found that the majority of farmers were not aware of the potential list of equipment that can be operated with USPC and also not aware of any financial assistance being provided on purchase of Agri/irrigation equipment. Hence, SWISM can help in providing information for all aspects related to agricultural equipment, solar water pumping systems, and USPC, which shall be beneficial for all the concerned stakeholders.

In addition to these, there is a need for specific criteria for the identification of farmers for USPC installations, so that it can be allocated to the right people in the right way. Some of the criteria suggested for allocating USPC are defined in Table 2.

Tab. 2: Criteria proposed for allocating USPC

Criteria	Details
Availability of diesel pumps	Clear guidelines may be formulated to prioritize farmers using diesel pumps and without agricultural power connections for allocating USPC, with an intention to de-dieselize the farm sector. The absence of such criteria can result in grid-connected farmers cornering subsidy benefits.
Intend/availability to operate Agri equipment:	Implementation agencies of states prioritize farmers having three-phase agri equipment to be operated with USPC or having intentions to operate three-phase agri equipment in the near future, for allocating USPC.
Proximity of Agri equipment with USPC	USPC should be located close to the farm where agri equipment are installed else it is difficult to operate the equipment with USPC
Geographical Location	Farmer is residing in locations where the grid extension is not feasible, or power supply is erratic.

Hence, for allocating USPC to farmers appropriate weightage may be assigned to each parameter discussed above, and depending upon their relative importance, a passing/selection score can be determined for selection of farmers for allocating USPC.

3.4. Case study analysis

While installations of USPC across India are limited in number, they are instrumental in tackling the specific hurdles that two individual farmers from Chikmagalur district of Karnataka and Daulatpura village of Rajasthan are facing.

The first farmer oversees an 8.5-acre organic farm, cultivating a rich array of crops including Robusta coffee, Areca nut, Coconut, and various spices such as Pepper, Ginger, Turmeric, and Cinnamon. However, he does not have a grid power supply which means dependence on manual and diesel-powered solutions for tasks like irrigation and farming.

The second farmer owns a vast 70-acre farm and despite having advanced equipment like a 12.5 HP electric pump and various three-phase equipment that uses Cow Dung as raw material for producing various items such as a Flowerpot-making Machine, he faces challenges due to long-lasting power outages.

Both the farmers resorted to SWP with USPC to meet their irrigation as well as other agricultural needs such as shredding, manuring the crops, etc. The first farmer installed 5 HP SWP with a solar panel capacity of 6.5 kW, USPC, a Battery bank with an inverter, Battery operated spraying machines, and a 5HP shredder to eliminate his dependency on costly diesel fuel and use it for meeting his irrigation needs and operating other Agri equipment. The set of equipment was funded by a combination of a grant and his own equity.

In the case of the second farmer, he initially installed SWP with the normal controller to be independent of unreliable grid power. He also owned multiple agri equipment such as flowerpot making machine, powder machine, sambrani cup-making machine that primarily uses cow dung as its input. This equipment plays a crucial role in recycling animal waste, transforming it into valuable products. In 2021, he contributed approximately INR 21,230, which amounted to 40% of the total cost for the 5 HP USPC installation. The government subsidized the remaining 60% of the capital cost.

We tried to conduct a cost-benefit analysis for both the farmers with usage of USPC as shown in Table 3. For the first farmer, the savings accrued are due to avoided manure costs that were earlier procured from the market and a reduction in labor costs for spraying the pesticides. The equity contribution is apportioned for shredder and battery-operated spraying machines and associated benefits are considered for cost-benefit analysis. For the second farmer, the equity contribution for USPC is apportioned over five agri equipment that he already possesses. The cost-benefit analysis is conducted for one piece of equipment viz. flowerpot making machine.

Tab. 3: Cost-Benefit analysis for USPC

S. No	Parameter	Farmer 1	Farmer 2
A.	SWP capacity (HP)	5	5
B.	USPC capacity (HP)	5	5
C.	Total proportionate equity contribution by farmer (INR)	63,627	4,246
D.	Average annual savings due to USPC (INR)	27,000	4,023
E.	Payback period (Yrs.)	Less than 3	Less than 2

The two cases represented above clearly demonstrate that utilizing their agri equipment is profitable for farmers with a reasonably short payback period. This approach makes sense not only for these farmers but also for similar farmers or agri entrepreneurs who can utilize this excess energy for operating equipment with similar loads/capacity. Despite its advantages, the discussed applications perse have not been widely adopted among many farmers, who often use other comparable equipment for various farming activities. A common example is the ownership of atta chakki machines of similar horsepower that are commonly used by farmers. USPC technology is relatively new and hence its adoption in the agricultural community has been limited. Our study, however, reveals a significant potential for the extensive application of the USPC technology to efficiently harness this energy.

4. Conclusion

SWP remains unused for a considerable period after irrigation demands are met. USPC is a controller with multiple outputs giving farmers the opportunity to utilize the excess energy generation for other applications. The study suggests that the various barriers that contribute to low USPC penetration are majorly due to the high cost of USPC, limited knowledge of the benefits, few technical limitations of USPC, improper targeting and screening of farmers, and lack of supporting ecosystem constraining the demand and thus income generation potential for other end-use applications. As USPC is a relatively new technology compared to SWPs, most stakeholders lack a complete understanding of the technology including its functionality. Focused promotional campaigns may act as a medium to build confidence. It is equally crucial to set up live demonstrations for potential beneficiaries and arrange for exposure visits to view successful USPC systems installed across the districts, which can play a major role in changing their mindsets.

Further, it was revealed that the cost differential between the price of a normal standalone controller and USPC is substantially high from the farmer's perspective. Thus, bridging the price between the two is the need of the hour. Gradually with the increase in demand for USPC, through a targeted program, the production volume will be increased, resulting in a lowering of the cost of USPC. Along with that, USPC technical specifications and testing procedures also need to be evaluated which will aid in bringing down its cost.

5. Acknowledgments

The work described here was conducted under the Promotion of Solar Water Pumps (PSWP) project of Deutsche Gesellschaft für Internationale Zusammenarbeit (GIZ GmbH). The project has been funded by the Federal Ministry of Economic Cooperation and Development (BMZ) and being implemented by GIZ GmbH under the Indo-German Energy Program. The authors would like to thank the Ministry of New and Renewable Energy (MNRE), Government of India, and the Agriculture Department, Himachal Pradesh for their support and input.

6. References

1. Cuadros, F., Lopez-Rodriguez, F., Marcos, A., Coello, J., 2004. A procedure to size solar-powered irrigation (photoirrigation) schemes. Solar Energy 76, 465–473.
2. Glasnovic, Z., Margeta, J., 2007. A model of optimal sizing of photovoltaic pumping system for irrigation. Sol. Energy 81, 904– 916.
3. Hamidat, A., Benyoucef, B., 2009. Systematic procedures for sizing photovoltaic pumping system, using water tank storage. Energy Policy 37, 1489–1501
4. Kassem, M.A., 2012. MPPT control design and performance improvements of a PV generator powered DC motor-pump system based on artificial neural networks. International Journal of Electrical Power & Energy Syst. 43(1), 90–98
5. Moulay-Idriss, C., Mohamed, B., 2013. Application of the DTC control in the photovoltaic pumping system. Energy Convers. Manage. 65, 655– 662
6. https://www.ceew.in/sites/default/files/ceew-study-on-solar-pumps-underutilisation-pattern-in-indias-irrigation.pdf (accessed on 5.9.23).
7. https://pmkusum.mnre.gov.in/pdf/Final%20Specifications%2022.03.2023.pdf (accessed on 14.9.23).
8. Solar Irrigation Pump (SIP) Sizing Tool – User Manual (https://pmkusum.mnre.gov.in/KnowledgeCenter_PMKUSUM.html) (accessed on 5.10.23).
9. https://www.iwmi.cgiar.org/iwmi-tata/PDFs/iwmi_tata_pmksy_policy_paper_june_2016.pdf (accessed on 7.3.23).
10. https://power.larc.nasa.gov/data-access-viewer/ (accessed on 7.3.23)
11. https://www.hindiyojana.in/wp-content/uploads/2021/02/2021122685-compressed.pdf (accessed on 22.1.24)

Socio-economic impacts of solar powered freezers in rural fishing communities: Fiji case study

Alvin Datt[1], Edoardo Santagata[2,3,4], Anna Bruce[2,3,4], Iain MacGill[2,3,5] and Atul Raturi[1,4]

[1] University of the South Pacific (USP), Suva (Fiji)

[2] University of New South Wales (UNSW), Sydney (Australia)

[3] School of Photovoltaic and Renewable Energy Engineering, UNSW

[4] Collaboration on Energy and Environmental Markets, UNSW

[5] School of Electrical Engineering and Telecommunications, UNSW

Abstract

Pacific Island Countries and Territories (PICTs) present significant challenges associated with energy poverty and lack of access to electricity, resulting in limited social mobility and economic development. While providing access to energy services, conventional fossil fuels are very costly and difficult to deliver to remote Pacific communities. Renewable energy sources can provide a cheaper and more reliable solution for these communities if integrated with aspects such as food and water security, health, education, and income-generating activities. This study explores the range of socio-economic impacts that energy access projects of this type can have in remote Pacific communities via a case study approach. Namely, this work presents a solar freezer project installed in 2015 in the small fishing village of Wainika in Fiji. Results show that the project has substantially contributed to food security, wider income opportunities, community infrastructure development, household support, improved education and healthcare, gender equality, and social mobility.

Keywords: Pacific Islands, Energy Poverty, Renewable Energy, PV Systems, Socio-economic Impacts, Remote Communities

1. Introduction

Energy poverty and lack of energy access are particularly acute in many Pacific Island Countries and Territories (PICTs), where geographic isolation and limited resources make it difficult to establish and maintain energy infrastructure. Approximately 70% of the population in the Pacific region lacks access to electricity on average, with countries like Vanuatu, Solomon Islands, and Papua New Guinea having the lowest levels of access (SPREP, 2018; Dornan, 2014). This poses significant obstacles to economic development, education, healthcare, and social mobility (Kanagawa and Nakata, 2007). The majority of the population which lacks access to energy is located in rural and remote locations. Conventional energy sources, such as fossil fuels, can be costly and challenging to transport to these areas, further exacerbating energy poverty and hindering development (Wolf et al., 2016).

Renewable energy sources, such as solar photovoltaic (PV) systems, have the potential to provide reliable and affordable energy services to off-grid communities, where fuel costs and transport logistics to operate traditional generators are problematic and often prohibitive (Weir, 2018; Urmee et al., 2019). Solar PV systems in particular have become a technology of choice for off-grid energy projects in the remote and outer islands of PICTs due to their flexibility and abundant primary resource, easing electrification efforts in challenging resource-constrained contexts and providing a range of socio-economic advantages such as accessing novel income opportunities, strengthening of rural markets, creating new employment opportunities through technical capacity building, improving education through enabling technologies, and accessing improved energy-based essential services such as communication services and lighting (Aklin et al., 2017). In fact, access to energy services and technologies should meet community priorities and have linkages to food, water, health, education, and income-generating applications to be effective and enhance community resilience (To et al., 2021).

10.18086/swc.2023.07.05 Available at http://proceedings.ises.org

Amongst the various services and technologies that off-grid PV systems can enable, refrigeration has been identified as a key service to improve the livelihood of communities (Soboyejo, 2015). In particular, freezers can assist in the storage of perishable and essential items such as food, medicine, and vaccines – with profound implications on food security and safety, income generation through fishing, and healthcare. Because of these crucial linkages, solar powered freezers have been extensively deployed across PICTs (with some systems shown in Figure 1). For example, UNOPS and the India-UN fund delivered and installed 120 chest freezers for household use in the Marshall Islands to improve food security (UNOPS, 2022). As part of a collaboration between WorldFish and the West Are'are Rokotanikeni Association (WARA), 9 solar powered freezers were delivered to various communities in the Solomon Islands to specifically support income generation for women (Eriksson et al., 2019). UNICEF and the government of Japan equipped 234 health clinics in Fiji, Samoa, Solomon Islands, and Vanuatu with cold chain equipment such as chest freezers and portable freezers for vaccine storage and delivery to remote communities (Sharma, 2023).

Fig. 1: Solar powered freezer for vaccines in health clinic (Left) and for fish in community hall (Right), Fiji

Building upon the known benefits of solar powered refrigeration, this study aims to further demonstrate the linkages between energy access and socio-economic outcomes for remote fishing communities in the Pacific. Using a case study approach, this study explores the long-term socio-economic ramifications of a solar freezer project that was designed and installed in a remote fishing community in Fiji in 2015. Through this investigation, a holistic view of the direct and indirect impacts such initiatives can have on rural livelihoods, economic growth, and overall community development will be demonstrated.

2. Context: Wainika Village

Wainika is a small village settlement in Fiji with 23 households and a population of roughly 115 residents. It falls in the province of Cakaudrove near Udu Point and is about 66 km from Labasa, the main urban center in Vanua Levu. Despite being a part of the main island, the settlement is still not connected to the main centres through roads due to the mountainous topography of the area. As shown in Figure 2 (Left), the only means of accessing the village is through sea only via small outboard motor boats due to the lack of proper jetty facilities to accommodate for the anchorage of larger inter-island vessels. Generally, the village can be viewed as an island set due to its isolated nature and maritime character. The livelihood of villagers is heavily dependent on fishing both for subsistence and as a source of income. In fact, the location of the village is not favourable for sufficient levels small-scale subsistence farming, with very few areas of flat land which are still subject to sea water intrusions during high tides, stormy weather, and cyclones. Nonetheless, some locals still choose to farm some cash crops such as *dalo* (taro) and coconut used for local copra production. Women mostly carry out domestic duties and perform various forms of crafts (for instance, pandanus mat weaving), although they are also involved in fishing by collecting *kai* (river mussels) and setting up small fish traps during high tides.

To assess the village's key community aspirations and development priorities, a *Talanoa* (informal discussion session with the whole community) was conducted in 2014 as a culturally-appropriate consultation mechanism (see Figure 2, Right). During this consultation, the villagers mainly expressed their concerns regarding food security and the difficulties of long-term storage for fish and other food items – concluding that supporting fishing is a central priority to improve their livelihood. As such, a solar-powered freezer to store fish was agreed to be an effective solution to respond to these challenges and aspirations. This would enable long-term storage of fish and better means of selling the fish to buyers outside Wainika.

Fig. 2: Travel from Labasa to Wainika (Left) and community consultation in the village's community hall in 2014 (Right)

3. Solar Freezer Project Overview

An initial assessment was carried out to determine the on-site availability of the solar resource using a SunEye Tool. Figure 3 shows the annual sun paths drawn on top of the captured skyline in proximity of the village's community hall – the building selected by the community for installation of the system. The clear path or open sky is shown in yellow and the detected obstructions causing potential shading issues in green – indicating very minimal obstructions caused by the hills surrounding the village, with solar access ranging between 94 and 100%. Average insolation in Wainika is roughly 4.55 kWh/m^2/day.

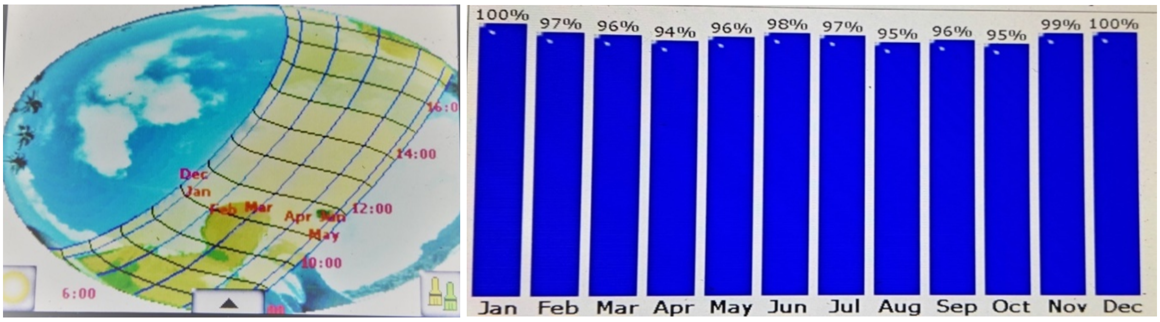

Fig. 3: Sun path diagram (Left) and monthly solar access (Right) at Wainika community hall

A 1.44 kW PV system was installed by the University of the South Pacific (USP) in November 2015, with three 200L freezers added in December 2015, and was funded by the French embassy. An overview of system components can be seen in Figure 4 and Figure 5, while a system wiring diagram of the installation can be seen in Figure 6. Table 1 summarises the system costs and equipment. The installation includes a backup generator (only used twice – once after cyclone Yasa and once during system maintenance in 2018), a battery bank, a data logger, and an inverter to accommodate for AC loads like the freezer. The system was slightly oversized to ensure high levels of availability through periods of bad weather and heavy energy usage. A user manual with simple instructions regarding maintenance and operation of the system was also provided to the village Headman. The village Headman organised a committee to oversee the sale of fish to external middlemen from Labasa, Wainigadru, or Savusavu at a fair price. Individuals in the village were only allowed to access the freezers in the presence of a member of the committee to oversee the intake and dispatch of perishable goods. This arrangement was established to ensure correct system usage and prevent the unnecessary opening of the freezers to save energy. The committee also oversaw the approval of additional system loads.

Fig. 4: Solar panels on community hall roof (Left) and freezers (Right)

Fig. 5: Electrical components (Left) and uncovered battery bank (Right)

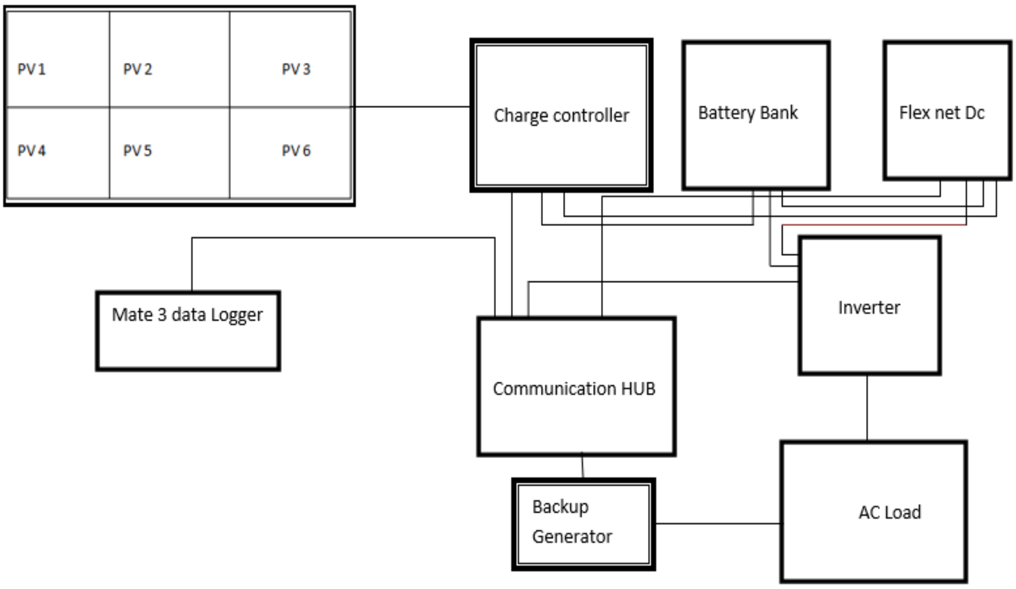

Fig. 6: System wiring diagram

Tab. 1: System costs and equipment (in FJD)

Item	qty	Cost
240W Trina Solar Panel	6	$3,780
3kW 24V Outback Inverter/Charger (24 VDC, 230 VAC @50Hz)	1	$5,902
Outback MPPT charge controller and monitoring system	1	$2,670
600Ah 24V Lead Acid Battery Bank (Deep Cycle)	12	$6,660
2.5kVA Generator (backup)	1	$3,521
Mounting frame for solar panels	/	$420
Wiring and protection materials (solar only)	/	$1,682
Modyl 200L Chest Freezers	3	$2,607
Installation, training, and commissioning	/	$1,080
Transportation, freight, and meals	/	$2,390
TOTAL		$30,712

4. System Performance

PV system performance was monitored using an Outback Flexnet DC coupled with a MATE3 over the course of 9 months (November 2015 – May 2016), requiring minimal community intervention and oversight. Monitoring of the energy into and out of the system battery bank was also implemented to study the energy usage and performance of the freezers under varying load and temperature conditions. Before the installation of the freezers on the 8th of December 2015, the system was only used to power six lights in the community hall and some mobile phone charging. Figures 7-9 respectively show the average daily energy supplied to the battery bank from the solar panels, average daily freezer energy consumption, and the battery bank state of charge (SOC). The average daily energy supplied to the battery bank is 4.62 kWh, with a maximum of 9 kWh. On average, a minimum SOC of 89.53 % was recorded for the battery bank. Throughout the month of December, activities in relation to fishing greatly increased due to community members returning to the village for holidays, although the community was able to effectively coordinate the quick sale of fish to external parties to avoid overloading the freezers. On most occasions, fishermen returned their catch for freezing in the morning, with plentiful hours of sunshine remaining in the day. This practice has greatly helped in maximising energy usage throughout the day.

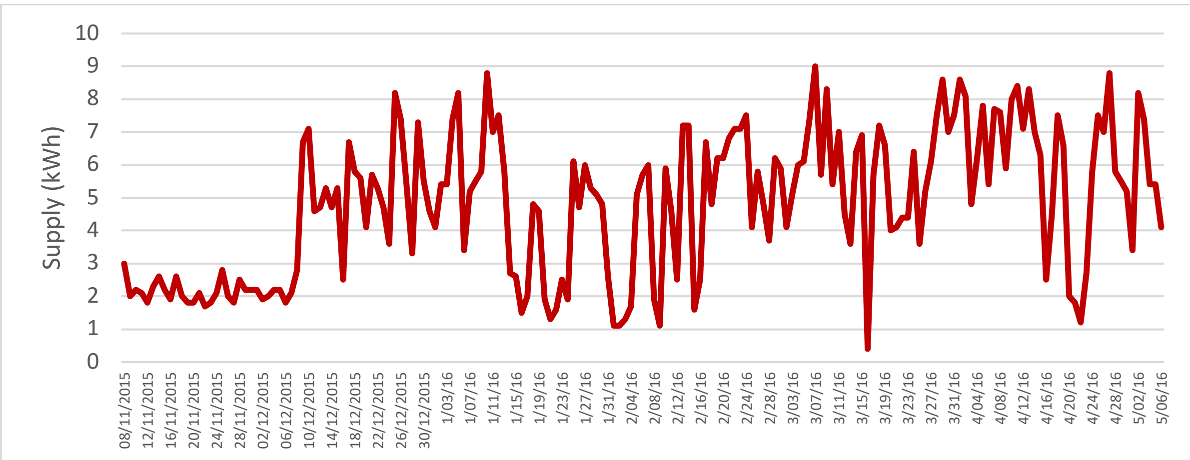

Fig. 7: Average daily energy supplied to battery bank

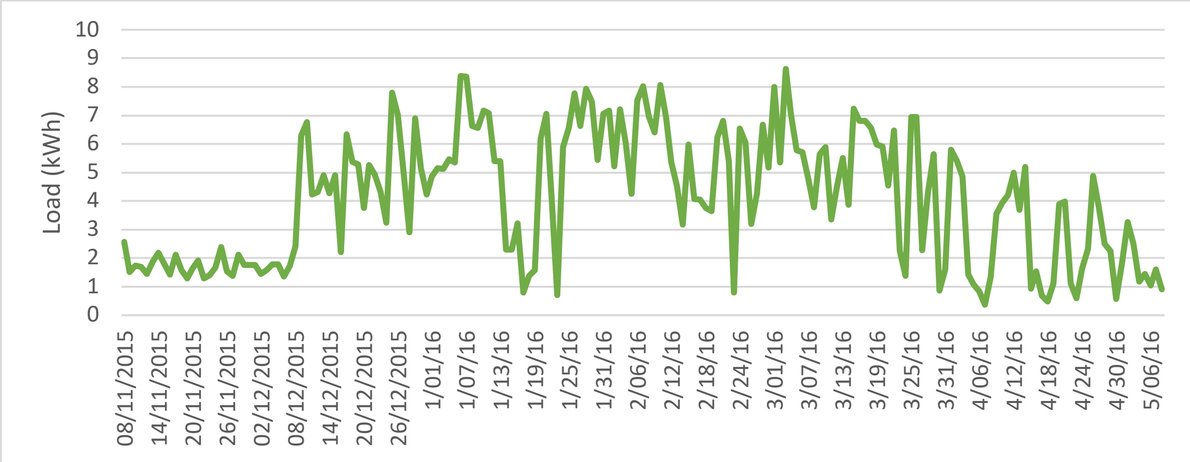

Fig. 8: Average daily energy supplied to the freezers

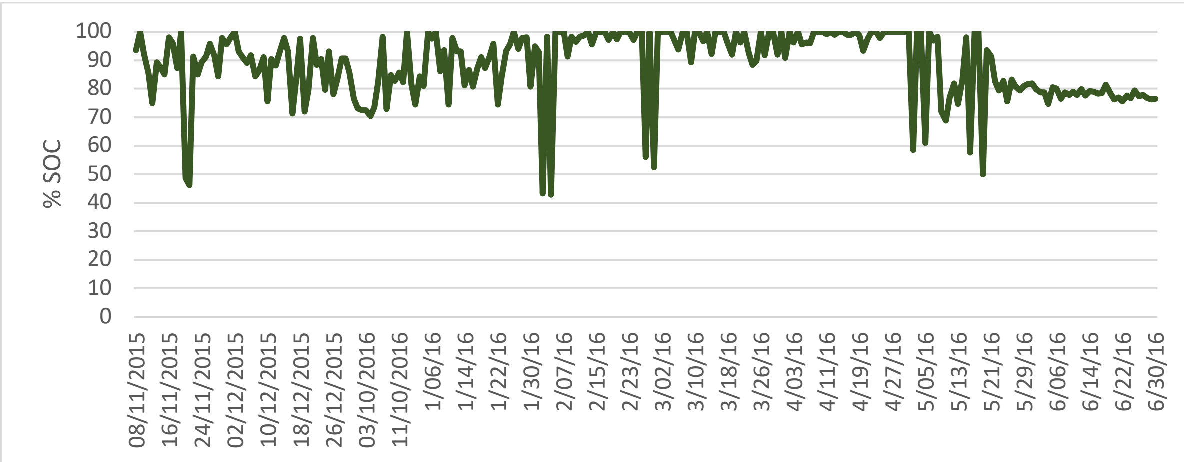

Fig. 9: Battery bank state of charge

5. Socio-economic Impact Assessment

A sample of 20 questionnaires were issued to various community members to assess the social impacts and the economic benefits of the project 6 months after the installation of the freezers, and various consultations were carried out through the years following the installation. Community members that participated in the questionnaire and the ongoing consultations included the village chief, the Headman, fishermen, housewives, farmers, and students. On average, the system generated a profit of roughly $1,300 per month. Given a total system cost of $31,000, this project would have had a payback period of roughly 2 years had the system not been donated to the village. The chief also stated that there are roughly $10,000 saved in a dedicated Village Home Finance Company (HFC) account to cover ongoing maintenance and replacement costs.

Table 2 summarises the socio-economic impacts of the project according to the villagers' questionnaire responses. When asked which impacts have been most beneficial, 30% of the interviewees mentioned income generation, 20% food security, 30% both, and 20% other impacts – demonstrating the strong linkage between energy access, food security, and improved income opportunities. Almost all questionnaire respondents also mentioned that the project itself had contributed to their increased awareness of the benefits of energy for the community's livelihood. Compared to a survey conducted prior to the installation of the system, it was found that many members of the community had shifted towards fishing as their primary role, as shown in Figure 10. Respondents highlighted that they considered fishing to be a more reliable form of income since cold storage had been made available. In particular, many women traditionally busied with domestic duties also started fishing as their primary means of income, suggesting that this type of project has gender equity outcomes as well.

Tab. 2: Socio-economic impacts

Impact	Details
Food Security	Storage for fresh fish and other perishable items over a longer period. Removed need to smoke fish for storage.
Income Opportunities	Income generation through sale of frozen fish to buyers outside Wainika, including a stable buyer from Suva. Buy and resale of fish from other neighbouring villages. Capacity for more community members to engage in fishing as a reliable full-time job. Women enabled to work in crafts.
Infrastructure Development	Refurbishment of community hall including painting, tiling, louvers, ceiling, and roof. Refurbished community church. Construction of health facility and crafts building.
Equipment Upgrade & Safety	Purchase of a fibreglass boat for fishing. Purchase of fishing lines, rods, and life jackets.
Household Support	Ability to purchase more groceries and other essential household items. Reduced household expenses associated with buying ice from Labasa, Wainikoro, and Savusavu to store perishables.
Education	Purchase of exercise books, shoes, and bags for children in preparation of returning to school.
Healthcare	Providing storage space for vaccines and insulin for highly diabetic individuals, removing need to travel to Wainikoro or Labasa for this purpose on regular intervals.
Gender Equality	Purchase of a sewing machine. Additional supply of cotton materials, thread, and needles for sewing and stitching purposes. Working space for women in the crafts building to generate income via sewing. Women involved in fishing.
Social Mobility	Organisation of committee to ensure fish reaches the market at a fair price without residents having to travel themselves to Labasa. Assistance in funding for community gatherings and transportation. Support for church gatherings to perform *Lotu* (prayer).

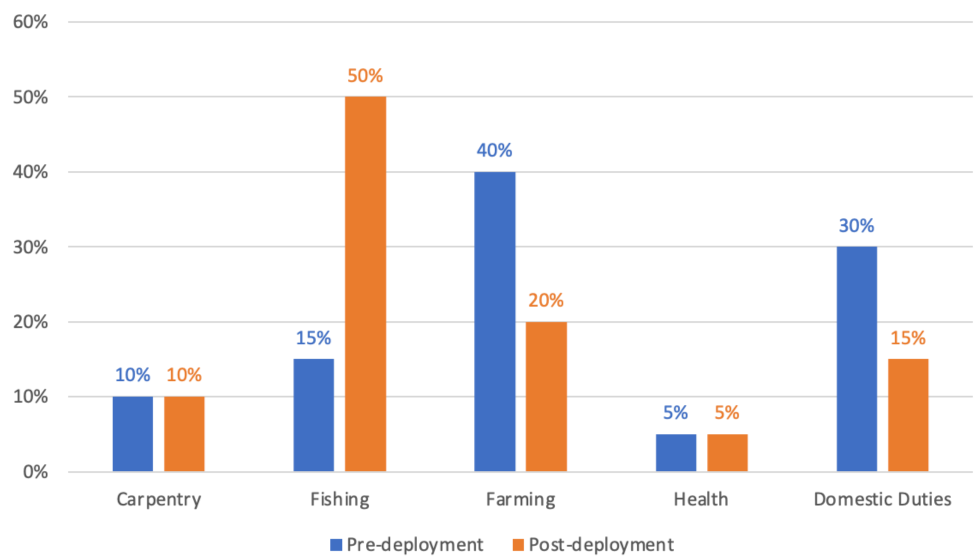

Fig. 10: Comparative analysis of community roles in Wainika

Another community interview conducted by IRENA in October 2019 also confirmed the success of this project in terms of ensuring food security and providing a range of social and economic benefits, with the village chief stating that the project had significantly raised the standard of living for the whole community (IRENA, 2019). The project has also been discussed at regional workshops and is a key example of a successful energy access project in the Pacific (Ravasua, 2019). A more recent visit to the system in September 2023 revealed that the batteries had to be replaced (a process now underway) and that no additional appliances have been run off the system – suggesting the village committee has been very conservative in trying to avoid system misuse or overuse, perhaps missing out on capturing additional benefits but most certainly preserving the system to the fullest extent possible.

6. Conclusions

This solar freezer system has become a primary factor towards improving the general livelihood of individuals in the remote community of Wainika. A suitable technical design and sense of ownership of the project by the village chief and other residents have been major reasons for the success of this project, as it continues to perform effectively in its 8th year of commissioning. This project showcases that energy access projects that meet community priorities and enhance resilience can result in substantial socio-economic benefits. Proper record keeping, village-wide cooperation, and enforcing strict operational guidelines through a village committee have also been identified by the community as some of the key factors for the success of this project. Furthermore, the backup generator for the system has only been used twice since the installation of the project, highlighting the quality of the solar resource and the value of oversizing the system to ensure its availability. With proper maintenance and operation, oversized systems such as this one are very robust and may limit fuel costs only to emergency situations, greatly reducing the financial toll these take on communities. Recommendations for future work include the installation of a larger PV system to enable the implementation of more freezers.

7. References

Aklin, M., Bayer, P., Harish, S.P., Urpelainen, J., 2017. Does basic energy access generate socio-economic benefits? A field experiment with off-grid solar power in India. Science Advances. 3(5), e1602153.

Dornan, M., 2014. Access to electricity in Small Island Developing States of the Pacific: Issues and challenges. Renewable and Sustainable Energy Reviews. 31, 726-735.

Eriksson, H., Cole, S., Van Der Ploeg, J., 2019. Freezing fish in rural Solomon Islands. Available at: https://rethink.earth/freezing-fish-in-rural-solomon-islands/.

IRENA, 2019. Renewable energy transforming sustainable food systems. Available at: https://www.youtube.com/watch?v=d9ZWciXbFe4.

Kanagawa, M., Nakata, T., 2007. Analysis of the energy access improvement and its socio-economic impacts in rural areas of developing countries. Ecological Economics. 62, 319-329.

Ravasua, E., 2019. Community-based solar powered refrigeration: challenges and successes. Pacific Resilience Partnership: Zero Carbon Event.

Sharma, S., 2023. Strengthening cold chain in Pacific Island Countries and Territories. Available at: https://www.unicef.org/pacificislands/stories/strengthening-cold-chain-pacific-island-countries-and-territories.

Soboyejo, W., 2015. Can energy access improve health?. Smart Villages: New Thinking for Off-Grid Communities Worldwide.

SPREP, 2018. SOEC Indicators. Available at: https://pacific-data.sprep.org/system/files/SOEC-Indicator-27.pdf.

To, L.S., Bruce, A., Munro, P., Santagata, E., MacGill, I., Rawali, M., Raturi, A., 2021. A research and innovation agenda for energy resilience in Pacific Island Countries and Territories. Nature Energy. 6, 1098-1103.

UNOPS, 2022. Solar-powered freezer chests improve food security in the Marshall Islands. Available at: https://unsouthsouth.org/2022/11/22/solar-powered-freezer-chests-improve-food-security-in-the-marshall-islands/.

Urmee, T., Harries, D., Schlapfer, A., 2009. Issues related to rural electrification using renewable energy in developing countries of Asia and Pacific. Renewable Energy. 34, 354-357.

Weir, T., 2018. Renewable energy in the Pacific Islands: Its role and status. Renewable and Sustainable Energy Reviews, 94, 762-771.

Wolf, F., Surroop, D., Singh, A., Leal, W., 2016. Energy access and security strategies in Small Island Developing States. Energy Policy. 98, 663-673.

Sustainably Powering Off-grid Schools in Fiji

Ravita D Prasad[1], and Atul Raturi[2]

[1] College of Engineering, Science and Technology, Fiji National University, Suva (Fiji)

[2] The University of the South Pacific, Laucala Bay, Suva (Fiji)

Abstract

Energy poverty is very common in rural areas of developing countries and it is even more pronounced in small island developing states (SIDS). This paper attempts to study the energy requirement of off-grid schools in Fiji and make recommendations on some clean energy supply options to replace heavy dependence on diesel generators for electricity. Of the 173 surveyed schools in Fiji, 17 schools were off-grid schools with an annual average energy consumption of 6,443 kWh (812 L) from diesel fuel, 4,600 kWh from premix fuel (607 L) and 621 kWh (60 L) from kerosene. We have carried out a techno-economic study for these schools and recommend the use of hybrid solar photovoltaics with battery storage where diesel generators will be used only as a backup. This system will replace diesel generators so that schools are supplied with 24/7 electricity and not 3-4 hours every evening as is the case currently. To make these systems resilient to extreme weather conditions such as tropical cyclones, it is suggested that building and installation standards be used and capacity building of community members on ensuring the safety of PV systems during cyclones should be mandatory.

Keywords: off-grid schools, energy consumption, solar photovoltaics, hybrid system, cyclones

1. Introduction

Energy is an enabler for sustainable development in multiple dimensions of any country (Nussbaumer et al., 2012). Being "energy poor" in developing countries means that a certain percentage of the population (rural and poor urban) do not have access to modern energy services that can help communities build socially, economically and environmentally (Sy and Mokaddem, 2022). The uniqueness of Pacific Island countries is that the population is distributed between several dispersed islands within a country and the population on these islands tend to be small and isolated from the main market centres. For such islands and remote villages within large islands, it is economically not viable to extend the electricity grid. Schools in these remote places depend on limited electricity supply produced by expensive and polluting diesel generators. There are many off-grid solutions for such communities; from standalone solar PV systems to hybrid solar systems. However, before the installation of these alternative reliable and sustainable solutions, there needs to be a feasibility study done to determine whether the chosen system can technically, and economically meet the demands of the target community. Researchers have used various tools (Tozzi Jr and Jo, 2017) for analysing the techno-economic feasibility of off-grid renewable energy applications for providing electrical services and the three most commonly used software are ; HOMER, SAM and RETScreen. HOMER makes it possible to optimize hybrid systems that use both renewable and non-renewable energy sources, batteries, and generators. It can also carry out economic and environmental evaluation, as well as sensitivity and uncertainty analysis while RETScreen aids in evaluating the economic viability, efficiency, and overall feasibility of renewable energy systems. The System Advisor Model (SAM) simulates the performance and cost of renewable energy systems, such as solar PV, wind, geothermal and concentrated solar power. The choice of a particular tool will depend on the primary objective of the study and the type of data available.

Giday (2014) used HOMER software to compare the economic viability of a solar photovoltaic/diesel generator/battery hybrid power system with that of a standalone diesel generator only for a hypothetical rural school in Ethiopia. Its results prove that a solar PV system with a backup generator is more affordable and

10.18086/swc.2023.07.04 Available at http://proceedings.ises.org

environmentally beneficial than a standard diesel generator alone system. Apart from the unavailability of quality power supply for off-grid communities, even for the short time (3-4 hours) that electricity is provided, the cost of electricity is massive as (Lozano et al., 2019) report US$1.21/kWh for diesel generator at one of the island communities in Philippines. By using HOMER software, they found that a solar/diesel/battery hybrid is more cost-effective (US$0.3556/kWh) than a solar PV/battery (US$0.3916/kWh) (Lozano et al., 2019). Similar results were also obtained by (Odou et al., 2020) for a rural community in Benin of West Africa where the hybrid (solar/diesel/battery) system has a cost of energy of US$0.207/kWh.

Li and Yu (2016) used RETScreen to assess the feasibility of different off-grid solar PV hybrid systems for households in China and found solar PV/Diesel/battery of one-axis and two-axis tracking systems to give the best performance for GHG reduction. In terms of the cost of energy, hybrid solar/diesel/battery has $1.319/kWh while solar/battery has $1.805/kWh and they further highlight that solar PV fixed axis has lower COE compared to one-axis and two-axis tracking (Li and Yu, 2016). Fathoni et al. (2014) used RETScreen to assess the technical and economic potential of solar photovoltaic grid-connected systems in Indonesia and used pre-tax IRR and simple payback indicators for assessing financial viability. Further, (Bingham et al., 2016) also used RETscreen to assess the potential of solar PV for an island community in the Bahamas.

This paper attempts to assess the energy demand for schools in rural areas and outer maritime islands in Fiji and makes recommendations for solar energy to be used to meet energy needs. RETscreen tool is used to carry out the techno-economic feasibility study for two schools and we also discuss strategies for overcoming barriers to the implementation of solar energy-based solutions.

2. Methodology

This study used a mixed method to assess the school energy consumption in early childhood education (ECE), primary and secondary schools in Fiji. Approval was sought from the Ministry of Education, Heritage and Arts (MEHA) to conduct the research and a multi-mode survey was carried out in 2022. Altogether 173 schools participated in the survey where 17 were off-grid schools while the rest were connected to grid electricity.

According to the questionnaire survey, out of 17 non grid-connected schools, 6 were secondary schools, 10 were primary schools and 1 was ECE school as shown in Fig. 1a. Six schools have their own diesel generator, another 6 schools have solar PV systems, 2 schools have electricity from community-owned diesel generator and 3 schools have solar lights only. Some schools that use diesel generators also have a few solar lights installed. In terms of building structures, 3 off-grid schools have only wooden buildings while 2 schools have concrete building structures and the rest (12 schools) have a mixture of wooden and concrete buildings. 15 schools have single-storey buildings while 2 schools have both single and double-storey buildings. For schools that have diesel generators, the generator is only used to operate a photocopier and also provides 3 hours of electricity in the evenings to teachers' quarters. Some schools mention that electrical appliances are strictly not allowed in schools because the existing solar PV system would not be able to cater for the increased demand. This indicates that a bigger capacity of solar PV system is needed to meet all electrical demand for off-grid schools. None of the off-grid schools have air-conditioners, while three schools have ceiling fans and 7 schools report that they have a couple of stand fans. The number of lights per school varies from 3 to 62;. Water in off-grid schools comes from a range of sources; boreholes, desalination plants, rainwater, springwater or river water. However, all off-grid schools have water tanks for collecting rainwater in case their usual water supply is not working.

Some off-grid schools have recently renovated their buildings that were damaged in recent cyclones. While some schools have bought or received donations of ICT materials – printers, computers, laptops, etc. Some schools have even bought new solar PV systems for their teachers' quarters or bought diesel generators for their schools. Upon asking schools about their plans, 41 % of off-grid schools mentioned that they would like solar PV installed at their schools while 53% of the off-grid schools mentioned that they need their buildings renovated because they are either damaged by tropical cyclones or buildings are old.

The focus of this paper is on typical off-grid schools' energy consumption, hence, a primary and a secondary off-grid school are taken and RETScreen Expert tool version 9 is used to model the school's energy consumption and its generation capacity when the diesel generator is replaced by solar PV system with battery storage or hybrid systems. Data collected during the survey are used as some input parameters into the model while other input data are taken from literature.

RETScreen is selected for this study as it can simulate the financials when incentives such as government grants or subsidies are given. Mirzahosseini and Taheri (2012) present comprehensive advantages of using RETScreen and use it to simulate energy output, GHG emissions reduction, financial analysis and sensitivity and risk analysis.

2.1 Study Site and climate Data

Two schools (one primary and one secondary) were chosen for RETScreen analysis and are marked in Fig. 1. The primary school was established in 1970 with approximately 40 students (4 classrooms) while the secondary school was established in 2002 with approximately 150 students and comprised 5 classrooms. Currently, both schools have diesel generators and some exterior solar lights.

The climate data for the two schools are shown in Fig. 2 with the secondary school being located in a slightly sunnier location than the primary school. The annual average monthly temperature is 26.4°C and 24.6°C for secondary and primary school respectively. The average monthly solar radiation is 5.60 kWh m^{-2} day^{-1} and 4.40 kWh m^{-2} day^{-1} for secondary and primary school respectively.

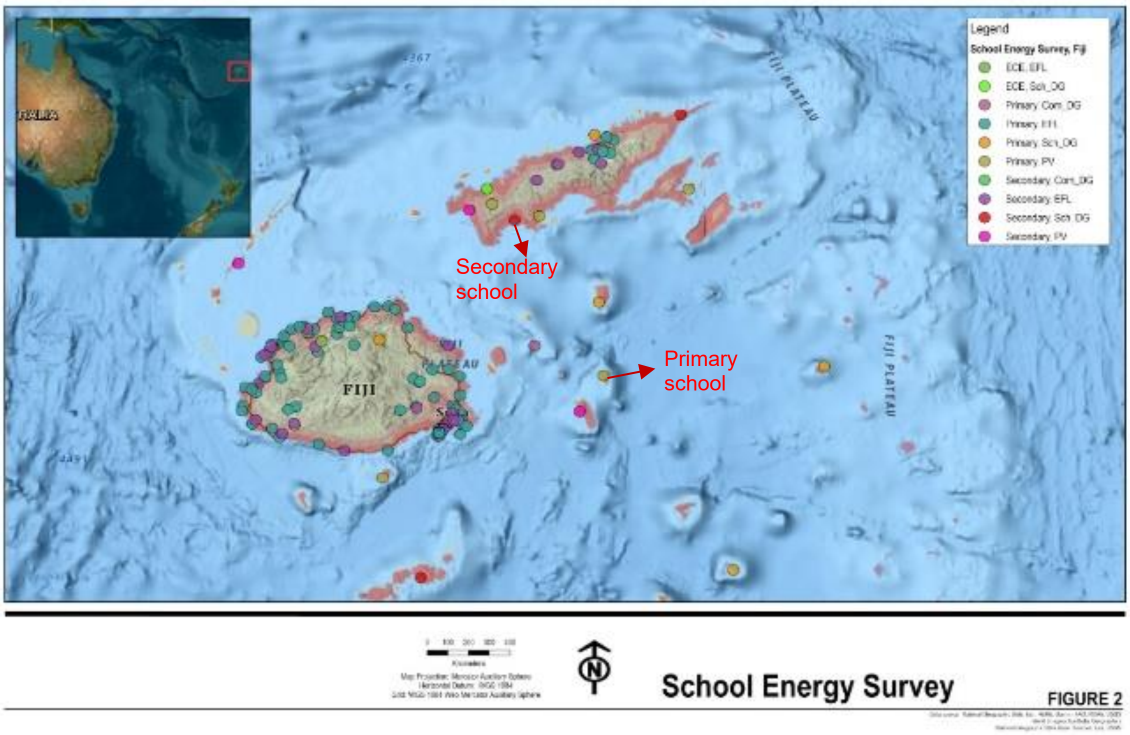

Fig. 1: Map showing the locations of surveyed schools. Note: Sch-DG – school-owned diesel generator, Com_DG -community-owned diesel generator, PV – solar photovoltaic, EFL – Energy Fiji Limited is the grid utility company.

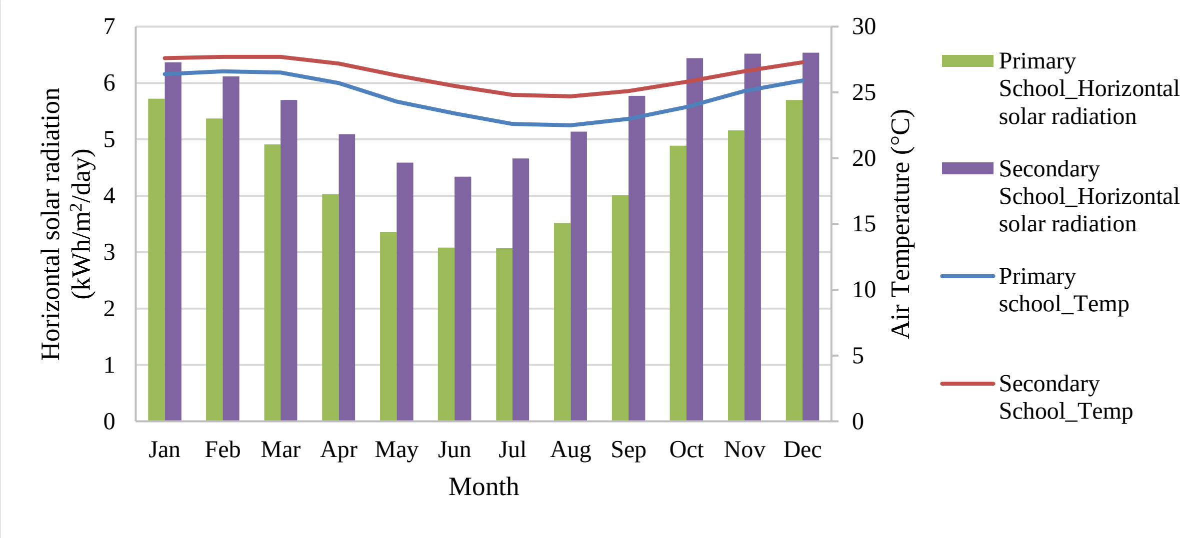

Fig. 2: Horizontal solar radiation and temperature at the two studied schools.

2.2 Scenarios studies in RETScreen

The main purpose of carrying out the RETScreen analysis was to determine the financial viability and potential GHG reduction for the primary and secondary schools. A solar photovoltaic system with battery storage and a hybrid system are modelled to meet the daily energy demand for a primary and secondary school and the summarized results are shown in Tab. 1. For the primary school, average consumption for learning and teaching per day is taken as 11 kWh day^{-1} while for the secondary school, it is taken as 60 kWh day^{-1} based on the average consumption of grid-connected small primary and secondary schools. However, off-grid schools also have teachers' quarters and student hostels, so this demand should also be included. Energy demand for teacher's quarters was not known and hence literature was referred to for assuming the daily demand. (Agrawal et. al., 2020) reports 3.93 kWh/day for rural households in India while (Monyei et al., 2018) report 1.5 kWh/day is usually taken for households in Brazil as the minimum demand for electrification projects. Assuming that one teacher quarter will have a typical rural home consumption of 3 kWh day^{-1} based on the data presented published literature and there are 5 and 13 teachers quarters in primary and secondary school respectively and 0.6 kWh student^{-1} consumption in boarding hostel with 19 and 30 student boarders in primary and secondary school respectively, the total demand for primary and secondary school is taken as 37.4 kWh day^{-1} and 117 kWh day^{-1} respectively as seen in Tab. 1.

Tab. 1: Typical daily load for off-grid schools in Fiji

Description of load	Primary	Secondary
	kWh day^{-1}	kWh day^{-1}
School's learning and teaching activities	11	60
Teachers' quarters	(5 × 3) 15	(13 × 3) 39
Hostel	19 students @ 0.6 kWh day^{-1} =11.4	30 students @ 0.6 kWh day^{-1} = 18
TOTAL	37.4	117

Six cases are studied for each type of school:

Case 1: School power load supplied by solar PV and battery storage – no incentives

Case 2: School power load supplied by hybrid power systems (solar/diesel/battery) – no incentives

Case 3: School power load supplied by solar PV and battery storage – government grant of US$5000 for primary school and US$10,000 for secondary school.

Case 4: School power load supplied by solar PV and battery storage – government grant and carbon credit.

Case 5: School power load supplied by hybrid power systems (solar/diesel/battery) – government grant of US$5000 for primary school and US$10,000 for secondary school.

Case 6: School power load supplied by hybrid power systems (solar/diesel/battery) – government grant and carbon credit.

The input parameters taken in RETScreen are summarized in Tab. 2.

Tab. 2: Input parameters for RETScreen modelling

Parameter	Unit	Primary		Secondary	
INPUT		Solar PV/battery	Hybrid (solar PV/diesel/battery)	Solar PV/battery	Hybrid (solar PV/diesel/battery)
		Nairai Island, Lomaiviti		Ratu Luke School in Bua	
Location					
Latitude		-17.8	-17.8	-16.8	-16.8
Longitude		179.4	179.4	178.6	178.6
Daily electric load	kWh/day	37.4	37.4	117	117
Diesel cost[1]	US$/litre	1.50	1.50	1.50	1.50
Base case					
Diesel generator capacity	kW	5.5	5.5	15	15
Proposed case					
Inverter	kW	20	20	40	40
Inverter efficiency	%	85	85	85	85
Inverter cost	US$/kW	400	400	400	400
Lithium-ion battery					
Days of autonomy		5	1.2	5	1.2
Voltage	V	24	24	96	96
Efficiency	%	80	80	80	80
Nominal battery capacity (calculated using equation 1)	Ah	11,460	2,750	8,962	2,151
Battery cost[2]	US$/kWh	650	650	650	650
Solar PV system					
Tilt angle	°	32	22	32	22
Power capacity	kW	20.13	20.13	43.065	43.065
Number of unit		122	122	261	261
PV cost[3]	US$/kW	2,967	2,967	2,224	2,224
O&M cost[4]	US$/kW-yr	36.94	36.94	25.25	25.25
Financial Parameters					

[1] Diesel price in Fiji in Oct 2023 was FJ$2.83/litre (https://fccc.gov.fj/wp-content/uploads/2023/09/New-Fuel-and-LPG-Prices-for-October-2023-.pdf) which is around US$1.50/litre.
[2] Assumed based on the the pacific report that states "batteries were costed between $200 to $750/kWh in the tenders examined" https://prdrse4all.spc.int/sites/default/files/prif-re-web_2.pdf
[3] Solar PV installed cost has reduced from US$12/W to US$3/W in the Pacific (https://prdrse4all.spc.int/sites/default/files/prif-re-web_2.pdf)
[4] Assumed using RETScreen recommendation

Inflation rate[1]	%	3.1	3.1	3.1	3.1
Discount rate[2]	%	10	10	10	10
Project life	Years	20	20	20	20
Debt ratio[3]	%	70	70	70	70
Government grant	US$ per off-grid school	5,000	5,000	10,000	10,000
Carbon revenue[4]	US$/t$CO_2$/year For first 10 years	16	16	16	16

The battery capacity (Ampere-hour (Ah)) is calculated using eq. (1).

$$Ah\ for\ battery = \frac{AC\ load\ (Wh) \times Number\ \ of\ no\ sun\ days}{\eta_{inverter} \times \eta_{coulomb} \times System\ voltage} \qquad \text{(eq. 1)}$$

Where
$\eta_{inverter}$ is the inverter efficiency.

$\eta_{coulomb}$ is the battery efficiency.

The size of solar PV for off-gris can be estimated by (eq. 2) as suggested by (Ghafoor and Munir, 2015).

$$\text{PV power} = PV\ power = \frac{AC\ load\ (Wh) \times peak\ sun\ (1000\ W\ m^{-2})}{daily\ solar\ radiation\left(\frac{\frac{kWh}{m2}}{day}\right) \times \eta_{inverter} \times \eta_{coulomb} \times temperature\ correction\ factor} \qquad \text{(eq. 2)}$$

Temperature correction factor normally taken as -0.4 to -0.5% per °C for crystalline silicon (Ghafoor and Munir, 2015).

3. Results and discussions

3.1 Energy consumption in off-grid schools

The off-grid schools have no record of the electricity that is generated or consumed by the schools, especially the ones supplied by diesel generators, solar photovoltaic systems or community-owned diesel generators. However, some off-grid schools have records of the quantity of diesel consumed. Apart from using diesel generators to supply electricity, off-grid schools also use premix (mixture of gasoline and 2-stroke oil in a ratio 50:1 (gasoline:oil)) which is used for grass cutting in schools and also in school boats. These schools also use LPG and kerosene for cooking by teachers and student boarders.

Off-grid schools have high diesel and premix use, where on average, 4600 kWh of premix is used annually and 6443 kWh of diesel used annually, as shown in Fig. 3. with an average cost of F$1751/year for diesel and F$1802/year for premix. For schools that have solar PV, only one school reported the size of the system; 6 × 250W panel while some schools reported inverter sizes ranging from 1.5 kW to 10 kW. However, these systems just provide basic lighting to the schools but do not allow the school to expand its learning and teaching tools and methods via the use of ICT so that students in off-grid schools can enjoy the same services as the students in urban settings.

---

[1] Taken from paper https://doi.org/10.1016/j.jclepro.2021.128519
[2] Assumed from paper https://doi.org/10.1016/j.jclepro.2021.128519
[3] Assumed
[4] Assumed based on Bloomberg report https://www.bloomberg.com/professional/blog/long-term-carbon-offsets-outlook-2023/

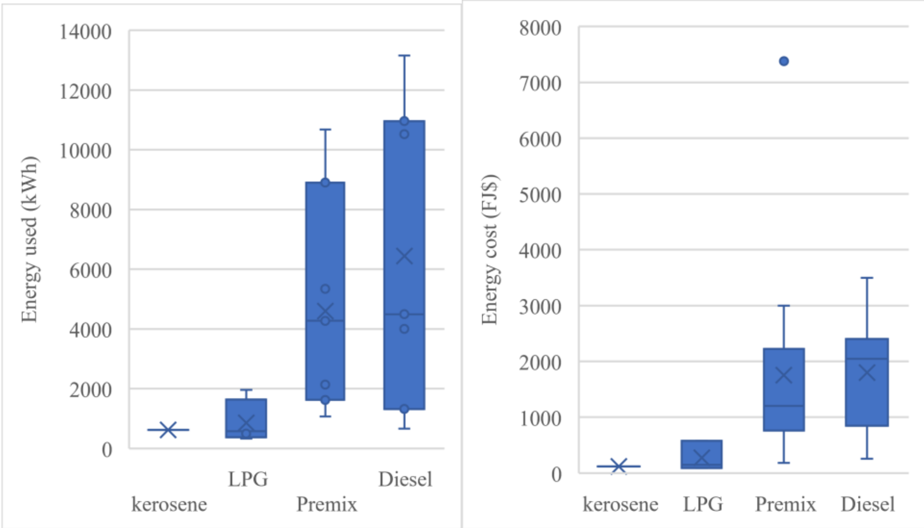

Fig. 3: Box plot of energy used and its cost for different energy sources for off-grid schools.

3.2 Modelling results

3.2.1 Energy output

The annual energy output for primary school is 13,651 kWh for hybrid systems where the PV system meets the load 97% of the time while the rest is met by a diesel generator as shown in Tab. 3. However, for the solar PV system with battery storage, it is seen that only for 0.1% of the time in the year the system is not able to meet the demand. If the system size is increased with battery storage then this deficit will be met but the cost of the system and energy production cost (EPC) will be high.

Similar results are also seen in Tab. 4 for secondary school. For the hybrid system, the annual energy generated is 42,705 kWh where 97.7% of the demand is met by solar PV while the rest is met by diesel generator. Here we see that solar PV has a slightly greater share in generation output compared to the primary school because the location of the secondary school is at a location where the average daily solar radiation is 5.60 kWh m^{-2} day^{-1} while for primary school it is 4.40 kWh m^{-2} day^{-1}.

3.2.2 GHG saving

When solar PV is considered then for primary school 27.3 tCO2-e y^{-1} of GHG emissions is saved while for hybrid system it is 26.7 tCO2-e yr^{-1} which is a 2.2% decrease. This is because as seen earlier, the hybrid system has a diesel generator operating and supplying 3% of the demand. Similarly, for secondary school, only solar PV saves 45 tCO2-e yr^{-1} while hybrid saves 43.9 tCO2-e yr^{-1}.

3.2.3 Financials

From Tab. 3, it is seen that for primary school the solar PV with battery storage has an EPC of $1.61/kWh, the simple payback period is 8.4 years and the net present value (NPV) US$55,723 making it a financially viable system considering that diesel generator is not used to supply the load 24/7. However, the EPC is high, so when a hybrid is considered the EPC reduces to US$1.16/kWh; which is almost a 28% decrease in generation cost. However, for secondary school, because the load is high, and 5 days of storage is taken, the battery cost is very high which makes a completely solar PV system with battery storage not a financially viable solution. When a hybrid system is modelled, it gives a financially viable option. With a solar with battery storage and a diesel generator as backup, it requires less battery storage so makes the system even more financially attractive as shown in Tab. 4.

Tab. 3: Output parameters for RETScreen modelling for primary school

Parameter	**Unit**	**Primary**					
		Nairai Island, Lomaiviti					
System description		Case 1	Case 2	Case 3	Case 4	Case 5	Case 6
Base case		Generator	Generator	Generator	Generator	Generator	Generator
Proposed case		Solar + battery storage	Solar + battery storage + generator	Solar + battery storage	Solar + battery storage	Solar + battery storage + generator	Solar + battery storage + generator
Incentives		None	None	Government grant US$5000	Government grant US$5000 Plus carbon revenue of US$16/$tCO_2$ for the first 10 years	Government grant US$5000	Government grant US$5000 Plus carbon revenue of US$16/$tCO_2$ for the first 10 years
Annual Electricity delivered to load	kWh	13,626 (99.9% of load met)	13,651 (97% solar and 3% diesel)	13,626	13,626	13,651	13,651
Annual GHG emissions saved	tCO_2-e yr^{-1}	27.3	26.7	27.3	27.3	26.7	26.7
Simple Payback Period	Years	8.4	5.8	8.1	7.9	5.5	5.4
Net Present Value (NPV)	US$	55,723	107,321	60,723	63,404	112,321	114,947
Benefit to cost ratio		2.3	4.7	2.4	2.4	4.9	5
GHG reduction cost	US$ tCO_2-e^{-1}	-167	-423	-189	-189	-445	-445
EPC	US$ kWh^{-1}	1.61	1.16	1.56	1.56	1.12	1.12

Tab. 4: Output parameters for RETScreen modelling for secondary school

Parameter	**Unit**	**Secondary**					
		Bua, Vanua Levu					
System description		Case 1	Case 2	Case 3	Case 4	Case 5	Case 6
Base case		Generator	Generator	Generator	Generator	Generator	Generator
Proposed case		Solar + battery storage	Solar + battery storage + generator	Solar + battery storage	Solar + battery storage	Solar + battery storage + generator	Solar + battery storage + generator
Incentives		None	None	Government grant US$10,000	Government grant US$10,000 Plus carbon revenue of US$16/$tCO_2$ for the first 10 years	Government grant US$10,000	Government grant US$10,000 Plus carbon revenue of US$16/$tCO_2$ for the first 10 years
Annual Electricity delivered to load	kWh	42,598 (99.8% of load met)	42,705 (97.7% solar and	42,598 (99.8% of load met)	42,598 (99.8% of load met)	42,705 (97.7% solar and 2.3% diesel)	42,705 (97.7% solar and 2.3% diesel)

			2.3% diesel)				
Annual GHG emissions saved	tCO_2-e yr^{-1}	45	43.9	45	45	43.9	43.9
Simple Payback Period	Years	10.7	6.7	10.3	10.1	6.3	6.1
Net Present Value (NPV)	US$	-220,985	4,341	-210,964	-206,543	14,341	18,653
Benefit to cost ratio		-1.4	1.1	-1.3	-1.2	1.3	1.4
GHG reduction cost	US$ tCO_2-e^{-1}	670	42.06	644	644	15.28	15.28
EPC	US$ kWh^{-1}	1.62	0.999	1.59	1.59	0.971	0.971

With incentives and government grants, the financial viability of the project further improves. The results suggest that by providing government grants to schools, their NPV increases while the simple payback period and energy production cost are reduced. In addition, when receiving carbon-saving revenue from some carbon credit scheme, the schools can further reduce their simple payback period, and increase their NPV but the EPC remains unchanged compared to scenarios when only government grants are given.

For the secondary school just having solar PV with battery storage, even when a government grant of US$10,000 is given with carbon revenue, the project is still a loss for the school and they are not able to recover their investments. The financial viability is not positive. Hence for off-grid secondary schools, it is good to consider a hybrid system (solar/diesel/battery). The main reason is the cost of batteries. For solar PV alone it requires a large battery size to get a reliable power supply which increases the system cost while for the hybrid system, the generator provides the backup power and battery capacity can be reduced. As seen from the cases that are studied, for solar PV alone, the "no sun days" is taken as 5 while for hybrid it is 1.2, so fewer batteries are required in hybrid which makes the system cost relatively cheaper. One option to make only Solar PV with battery storage financially viable is to have some income generation activities at the school such as renting their buildings for functions or external training.

3.3 Climate/weather conditions' impact on Solar PV systems

Extreme weather conditions affect the performance of solar PV and its longevity. In addition, its impacts on the energy infrastructures in small developing economies are devastating (Bundhoo et al., 2018). For small island nations, especially the South Pacific region, it experiences intense tropical cyclones (TC) every year. A Tropical Cyclone, as categorized by the Australian and South Pacific category system is shown Tab. 5 and its mean annual occurrence is more than any other natural climate events in Fiji as seen in Fig. 5. Tropical cyclones usually cause fatalities and substantial economic damage, which has slowed down economic growth and the power sector is not an exception. This section discusses the ways for keeping the power infrastructure safe and resilient to TCs. A resilient energy infrastructure provides reliable power to meet the demand. In addition, the discussion will also be on the impact of salt air breeze on the parts of solar PV systems.

Tab. 5: Categories of tropical cyclones in Fiji and the South Pacific. Source: (FMS, 2017).

Category	**1 (Tropical Cyclone)**	**2 (Tropical Cyclone)**	**3 (Tropical Cyclone)**	**4 (Tropical Cyclone)**	**5 (Tropical Cyclone)**
10-min mean wind (km/hr)	63-87	88-117	118-157	159-200	>200
Max 3-sec gust (km/hr)	<125	125-169	170-224	225-279	>280
Comments	Damaging winds	Destructive winds	Very destructive winds	Very destructive winds	Very destructive winds

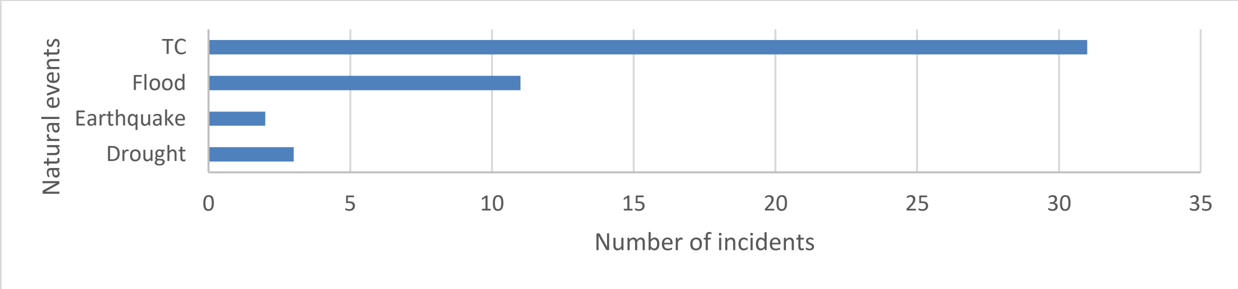

Fig. 5: Number of incidents of natural events between 1980 and 2020. Data Source: (CCKP, 2021).

NREL has developed a set of pre-storm/cyclone checklists to keep solar PV systems either utility-scale or distributed generation (roof-top and ground-based) safe (NREL, 2022). They provide a checklist on the modules, fasteners, racking, electrical (wiring and connectors) and overall system which must be done before the cyclone and during the cyclone it is recommended to power down the PV systems. Further, the Australian PV Association recommend that for the installation of PV systems in cyclone-prone areas the building standards must be enforced when installing PV arrays so that they can withstand the high winds and gusts during cyclones (APVA, 2011). Weir and Kumar (2020) discuss that PV systems can withstand cyclones if they are well-fastened and give an example of Tongan 3 MW of grid-connected PV on the island of Tongatapu, which survived TC Gita in 2018 as it passed right over them. They further observe that, in the Pacific, ground-mounted PV or PV on special poles are able to withstand tropical cyclones much more than rooftop solar PV. It is also recommended that community-based awareness-raising and capacity strengthening should be strengthened to scale up resilient energy infrastructure in climate-vulnerable off-grid islands (Delina et al. 2020; Hills et al. 2018). The communities need to know what impact adverse weather has on the performance of the PV system, what needs to be done when there is a tropical depression warning and what happens during and after cyclones. Moreover, (Castro et al., 2023) recommend hardening the solar PV system such as using sturdier materials in the construction of energy assets or burying powering lines so that it does not get damaged by storms/cyclones/typhoons. They also recommend insuring energy systems against natural disasters. This will ensure that communities would not have the financial burden of maintaining their energy system in times of natural disasters as they will be focusing on other urgent matters in the aftermath of cyclones. Furthermore, most Pacific Island Countries require installations of PV systems that are category 5 cyclone compliant which make the system resilient (PPA and SEIAPI, 2019).

Further, for off-grid applications in the outer remote maritime islands of Fiji where the salt breeze is high, the chances of solar PV components corroding are high, especially the batteries. So, even though the technology may be superior but if it is not installed in a proper manner it will stop working. Installers need to understand the ambient conditions in Fiji and how it will affect different parts of the PV systems. This makes a case for the policymakers to consider proper standards to be established so that quality parts are imported and installation standards ensure that proper housing for batteries and inverters is done and that it is not directly exposed to salty air breeze.

4. Conclusions

This is the first study that considers the energy demand for off-grid schools in Fiji and makes recommendations on some clean energy solutions such as solar PV systems with battery storage that can reduce their dependence on expensive fossil fuels and reduce their carbon footprint. With 4.40 and 5.60 kWh m^{-2} day^{-1} of solar radiation at the sites of primary and secondary schools respectively, the hybrid solar PV system is a favourable renewable energy option that can be used to power off-grid schools, given its relatively low capital cost.

The results show that solar PV system with battery storage and having a diesel generator as backup is a financially viable option for sustainably powering off-grid schools where government grants or incentives make the cost of energy production lower. However, just having solar PV systems with battery storage has significantly higher investment costs which is not financially viable for schools. In addition, to make the system resilient, proper training and awareness must be carried out in communities or solar PV users on how to protect their systems before and during natural disasters, especially tropical cyclones. Providing electricity 24/7 to off-grid schools would mean a higher tier of electricity access for schools that will give opportunities to teachers and students for better teaching and learning techniques. Students in rural or outer smaller islands would enjoy the same services and be able to do research for their learning as students on the main island where grid electricity is taken for granted. The need for concurrent energy efficiency measures cannot be over emphasized.

This study can provide information for potential donors and government departments on the investment needed for off-grid schools and a similar approach can be taken for other schools around Fiji and the region which share most of the characteristics.

5. Acknowledgements

The authors are grateful to the Ministry of Education, Heritage and Arts (MEHA) for giving their approval to carry out the survey in schools and to the Association of Commonwealth Universities for providing the funding for this project work. Special thanks also go to Mr. Metuisela Gauna of MEHA for his advice in reaching out to schools. Finally, authors are thankful to the schools that participated in the survey and provided useful information.

6. References

APVA, 2011. APVA response to James Cook University cyclone testing unit solar panel alert. Australian Photovoltaic Association, https://apvi.org.au/sites/default/files/documents/APVA%20Submissions/PV%20in%20Cyclones.pdf (accessed on 22 September 2023).

Agrawal, S., Harish, S.P., Mahajan, A., Thomas, D. and Urpelainen, J., 2020. Influence of improved supply on household electricity consumption-Evidence from rural India. Energy, *211*, p.118544.

Bingham, R.D., Agelin-Chaab, M., Rosen, M.A., 2016. Feasibility study of a hybrid solar and wind power system for an island community in The Bahamas. Int. J. Renew. Energy Res 6, 951-963.

Bundhoo, Z.M., Shah, K.U., Surroop, D., 2018. Climate proofing island energy infrastructure systems: Framing resilience based policy interventions. Utilities Policy 55, 41-51.

Castro, M.T., Delina, L.L., Esparcia Jr, E.A., Ocon, J.D., 2023. Storm hardening and insuring energy systems in typhoon-prone regions: A techno-economic analysis of hybrid renewable energy systems in the Philippines' Busuanga island cluster. Energy Strategy Reviews 50, 101188.

CCKP, 2021. Fiji: Historical Hazards. Climate Change Knowledge Portal https://climateknowledgeportal.worldbank.org/country/fiji/vulnerability (accessed on 22 September 2023).

Delina, L.L., Ocon, J., Esparcia Jr, E., 2020. What makes energy systems in climate-vulnerable islands resilient? Insights from the Philippines and Thailand. Energy Research & Social Science 69, 101703.

Fathoni, A.M., Utama, N.A., Kristianto, M.A., 2014. A technical and economic potential of solar energy application with feed-in tariff policy in Indonesia. Procedia Environmental Sciences 20, 89-96.

FMS, 2017. 2017/2018 Tropical cyclone season: Summary of alerts and warnings procedures for Fiji. Fiji Meteorological Service, Nadi, Fiji.

Ghafoor, A., Munir, A., 2015. Design and economics analysis of an off-grid PV system for household electrification. Renewable and Sustainable Energy Reviews 42, 496-502.

Giday, Z.G., 2014. Technical and economic assessment of solar PV/diesel hybrid power system for rural school electrification in Ethiopia. International Journal of Renewable Energy Research 3, 735-744.

Hills, J.M., Michalena, E., Chalvatzis, K.J., 2018. Innovative technology in the Pacific: Building resilience for vulnerable communities. Technological Forecasting and Social Change 129, 16-26.

Li, C., Yu, W., 2016. Techno-economic comparative analysis of off-grid hybrid photovoltaic/diesel/battery and photovoltaic/battery power systems for a household in Urumqi, China. Journal of Cleaner Production 124, 258-265.

Lozano, L., Querikiol, E.M., Abundo, M.L.S., Bellotindos, L.M., 2019. Techno-economic analysis of a cost-effective power generation system for off-grid island communities: A case study of Gilutongan Island, Cordova, Cebu, Philippines. Renewable Energy 140, 905-911.

Mirzahosseini, A.H., Taheri, T., 2012. Environmental, technical and financial feasibility study of solar power plants by RETScreen, according to the targeting of energy subsidies in Iran. Renewable and Sustainable Energy Reviews 16, 2806-2811.

Monyei, C.G., Adewumi, A.O. and Jenkins, K.E.H., 2018. Energy (in) justice in off-grid rural electrification policy: South Africa in focus. Energy research & social science, *44*, pp.152-171.

NREL, 2022. Preparing solar photovoltaics systems against storms. National Renewable Energy Laboratory, 15013 Denver West Parkway.

Nussbaumer, P., Bazilian, M., Modi, V., 2012. Measuring energy poverty: Focusing on what matters. Renewable and Sustainable Energy Reviews 16, 231-243.

Odou, O.D.T., Bhandari, R., Adamou, R., 2020. Hybrid off-grid renewable power system for sustainable rural electrification in Benin. Renewable Energy 145, 1266-1279.

PPA, and SEIAPI, 2019. Off grid PV Power Systems: System installation guidelines. https://www.seiapi.com/wp-content/uploads/2022/02/Off-Grid-Install-Guidelines_V3.1-July-2019_compressed.pdf (accessed on 02 February 2024).

Sy, S.A., Mokaddem, L., 2022. Energy poverty in developing countries: A review of the concept and its measurements. Energy Research & Social Science 89, 102562.

Tozzi Jr, P., Jo, J.H., 2017. A comparative analysis of renewable energy simulation tools: Performance simulation model vs. system optimization. Renewable and Sustainable Energy Reviews 80, 390-398.

Weir, T., Kumar, M., 2020. Renewable energy can enhance resilience of small islands. Natural Hazards 104, 2719-2725.

08. System Analysis

CHALLENGES AND CONCEPT FOR AN INTEROPERABLE DIGITAL TWIN ARCHITECTURE FOR PV-INTEGRATED HEATING NETWORKS

Theo Paredes[1,3], Melachroinos Papadimitriou[1,4], Thomas Ohlson Timoudas[2], Zeng Peng[1], Qian Wang[1]

[1] KTH Royal Institute of Technology, Department of Civil and Architectural Engineering, Stockholm (Sweden)

[2] RISE Research Institutes of Sweden, Department of Computer Science, Stockholm (Sweden)

[3] University of Toulouse, IMT Mines Albi, Albi, (France)

[4] University of Thessally, Department of Electrical and Computer Engineering, Volos (Greece)

Abstract

Existing data-driven approaches are not always supported, or only partly implemented, by existing tools, platforms, and services. The study focuses on proposing a novel, theoretical and general model to describe the heating network of buildings. This study will consolidate and abstract access to standardized interfaces, using a transparent interoperability mechanism, the “meta” interface, supporting translation modules to translate from different components or hardware that are commonly used in current heating networks of buildings in Europe. The ICT architecture will be based on state-of-the-art digital twin technologies and methodologies, offering a unified ecosystem for orchestrated deployment of different input/output configurations, and data flow and energy exchanges. This study will further validate the reference ICT architecture using data-driven approaches, applied in a use case that could be considered a typical low-temperature district heating network.

Keywords: building heating network, distributed renewables, data-driven, ontology, interoperability, digital twin, co-simulation

1. Introduction

Building energy networks are currently undergoing a major overhaul. The energy system is becoming increasingly distributed and reliant on intermittent energy sources (e.g. PVs). As the production of solar power is not necessarily correlated with electricity demand, a need for flexibility is emerging. One promising solution is to use renewable energy for heating purposes, considering its costs and benefits (Bloess et al., 2018). Therefore, a strong integration of thermal storages linked with Power-to-heat (P2H) devices in building heating networks, is witnessed. Simultaneously, a trend toward digitization in buildings is underway through increased device connectivity and large-scale data collection. These digital technologies promise increased observability and understanding of the underlying system, processing and optimization (Drgoňa et al., 2020; Weinberg et al., 2022).

Today, most building heating and cooling systems are operated using rule-based control (RBC) techniques. However, these traditional control systems have been proved insufficient in integrating thermal storage solutions, operating in the context of low temperature networks and are energy inefficient. In particular, this method does not take into account the thermal inertia of buildings, which is becoming fundamental in next generation systems. The reduced energy transfer capacity implies a need for longer control horizons (Weinberg et al., 2022). A proposed solution is Model Predictive Control (MPC), a control technique based on constrained optimization. It delivers energy savings of 15 % to 50 %, while improving thermal comfort (Drgoňa et al., 2020). Another advantage lies in the formulation of the cost function. There are several types of orientation for MPC formulation: economic, greenhouse gas emissions, indoor comfort, renewable energy share, integration of multiple storage and generation components, etc. (Cupeiro Figueroa et al., 2018; Figueroa et al., 2020; Weinberg et al., 2022). The objectives can be diverse, considering that the minimization of the cost function can cover anything that can be quantified mathematically in the model (Cupeiro Figueroa et al., 2018).

However, the main bottleneck in the practical implementation of MPC is to address an interface towards the

10.18086/swc.2023.08.04 Available at http://proceedings.ises.org

physical installations in the targeted building, requiring the development of a model. Naturally, the quality of the MPC solution depends on the accuracy of the model, but the overall implementation of MPC is also affected by the chosen modeling approach in several ways (Clausen et al., 2021; Drgoňa et al., 2020; Sutton and Barto, 2018). Various methods have been proposed based on three different approaches: white box, black box and gray box (Zhao and Magoulès, 2012). While the former uses physical principles to determine the energy behavior of a building or a network, the second analyzes large datasets to infer the relationships in the data, while the latter is a hybrid. Physical models can provide accurate results but tend to be complex and very time-consuming (Berthou et al., 2014; Drgoňa et al., 2020; Weinberg et al., 2022; Zhao and Magoulès, 2012). To further improve the system integrations by data-driven methods and existing MPC, interoperability starts to play an essential role for, e.g., co-simulations that hybrids MPC with other machine learning frameworks. However, such approaches require first defining a high-level framework so that the digital representations/descriptions can be initiated, with a clear understanding that the target heating network are described general enough with interoperability to initiate any further modeling and controls.

A digital twin serves as a virtual mirror of a physical object or system, crafted by harnessing real-time data to reflect the physical state of the entity or system. It utilizes technologies such as machine learning to form a dynamic digital simulation model, not only capable of forecasting the current and future states of its physical counterpart but also managing data transmission between the physical and digital worlds (Lu et al., 2020). Moreover, the digital twin has been acknowledged as a strategic technology trend, with its market projected to reach 15 billion dollars by 2023, underscoring its potential impact and relevance in the future across various industries, including construction and building management (Khajavi et al., 2019).

2. Objectives and the digital twinning concept

A building heating network consists of multiple subsystems and components, depending on the size and complexity of the building energy system. Achieving interoperability among the systems and actors involved in future heating networks requires a cost-efficient solution for data harmonization, integration and sharing frameworks that can be generalized. This study develops an automatic process and reference architecture, or framework, for data integration, harmonization, and enrichment based on different data-driven approaches. As the basic layer of the information architecture of the heating network digital twin, the framework will make sure new IoT applications or HVAC components behind-the-meter or operation modeling approaches can be created following a general architecture. The framework will make it easier to connect building heating network-level devices, such as storage tanks, heat pumps, district heating, etc., to aggregation systems and operated safely for the grid and utilities with streamlined information flows.

The objective of this study is to develop a digital twin framework that integrates distributed renewables (in particular PV/T) and energy storage solutions, for modeling and optimizing the system performance in the context of building HVAC systems. This framework is intended to enable the next generation of data-driven modeling and optimization/control approaches that are emerging. The development of such a digital twin framework faces a number of challenges. First, bidirectional data transmission is crucial to ensure a smooth interface between the digital and physical worlds and facilitating not only the integration of data from the physical system in the digital twin but also the dispatch of control signals back to the physical environment. Second, the digital twin should be capable of implementing and utilizing advanced methods, especially machine learning models and algorithms, providing capabilities such as making precise predictions and optimizing control strategies. Third, simulation is inherent to our digital twin, offering a virtual mirror that accurately reflects and simulates the real physical world, thereby enabling analyses of both real-time and future states. Last but not least, we aim to address interoperability issues. Our digital twin should be capable of utilizing existing ontologies and ensure compatibility with various systems to guarantee that different systems can communicate and function synergistically, enhancing the utility and applicability of the digital twin across diverse platforms and use cases. This framework will be elaborated upon in Section 4.

3. Challenges and previous work

A digital twin framework relies on interoperability, as mentioned, which is the ability of multiple entities to communicate and cooperate. In literature many types are described, but the focus is on technical interoperability and semantic interoperability (Motie et al., 2017). This section presents a complete analysis and through literature review about such challenges from previous works.

3.1. Technical interoperability

Addresses systems connectivity (e.g. sensors, actuators), network and device representation. This type of interoperability is no longer a significant challenge thanks to standardized technologies such as BACnet and IEEE standards (Bergmann et al., 2020). For instance, High Level Architecture (HLA) is an IEEE technical architecture that provides a framework for modeling and simulation with a primary goal of facilitating reuse and interoperability among simulations. HLA standard defines run time infrastructure (RTI) allowing to run a set of independent simulators and coordinate them all, thus forming a federation (Lévesque et al., 2014). Each simulator, acting as a federate, implements an interface allowing the synchronization by communicating with a run time infrastructure (RTI). This standard consists in five parts: (1) Framework and Rules, (2) Federate Interface Specification, (3) Object Model Template Specification, (4) Federation Development and Execution Process, (5) Verification, Validation, and Accreditation (VV&A) of a Federation (Falcone and Garro, 2019):

(1) Specifies the rules that a Federate shall follow to interact.

(2) Delineates the functional interfaces between the simulation member applications and the infrastructure that enables the distributed simulation execution. This step covers the capabilities of the software infrastructure of HLA and defines the specifications between the RTI and Federates, which they use to exchange information.

(3) The Object Model Template concerns the mechanisms to specify the format of data, in terms of a hierarchy of both HLA ObjectClasses and HLA InteractionClasses, that are produced and consumed by each Federate participating in a Federation execution

(4) Outlines the procedures that developers must follow to design, develop, and execute an HLA Federation. It provides a framework into which system engineering procedures can be combined and adapted to address specific needs.

(5) Specifies the processes and procedures to design and implement VV&A for HLA Federations. Hence it ensures that the HLA Federation is properly verified, validated, and accredited.

These steps collectively provide the guidelines, specifications, and processes required to set up and execute a distributed simulation using HLA.

Functional Mock-up Interface (FMI) is an open standard designed to solve the problem of technical interoperability, launched in 2010 by a European consortium led by Dassault. FMI provides an interface between master and slaves and addresses data exchange, by ensuring that the definition of types are identical across the whole system. It is nowadays widely adopted for digital twin frameworks. FMI supports different working modes but this study's focus is on FMI for co-simulation since it allows individual Functional Mock-up Units (FMU) to use their own solver engines (Mohseni et al., 2023). In plain terms, FMUs are executables, implementing FMI standard and they consist in a ZIP file containing the required components: FMI model description as an XML-based file, the source code and eventually additional data (Falcone and Garro, 2019). However, the FMI does not include master algorithms for scheduling and execution (Motie et al., 2017; Pedersen et al., 2015). Several approaches have been proposed and will be detailed below. A limitation of the FMI is the definition of inter-model connections which must be done manually in an initialization phase. As described in (Mitterhofer et al., 2017), the correct transmission of data exchanged between simulations and its detection is proving to be a tedious and increasingly complex task, as the number of sub-systems and FMUs increases.

3.2. Semantic interoperability

Addresses the importance of structured metadata, while ensuring that the precise meaning of exchange information is unambiguously interpreted by other systems (Bergmann et al., 2020). Achieving semantic interoperability remains a major challenge and is broadly studied in the literature. Several approaches have been proposed, none of which has yet achieved consensus. In the context of building heating networks with increasingly interdependent heterogeneous systems, it is important to arrive at a structuring of metadata. One of the solutions is making use of semantic taxonomies and standardised ontologies, which act as a common dictionary to map similar contents and data points across various protocols (Bennaceur and Issarny, 2014). In the case of BEM systems, ontology modules can be divided into several layers (Lork et al., 2019):

- **Generic Ontology -** Definitions, terminologies and taxonomies that are common to every building are defined as well as general concepts and sub-concepts for the sensors and equipment.
- **Knowledge Base -** Static and dynamic data are stored in this part. Static data can include the building type (e.g. residential, office), sensor type (e.g. temperature, radiation, humidity) while the dynamic ones can be the sensed values (e.g. temperature, C02, light) or time information (e.g. day of the week, hour).
- **Interface -** Covers the communication between knowledge base and the systems.

Each layer is built on top of the previous one in that it exploits and extends it. Ontology offers semantic integration (mapping and alignment of different data models, protocols, etc.), knowledge representation (concepts, relationships, properties, rules) (D'Elia et al., 2010) and context awareness (building occupancy pattern, environmental conditions, etc.). Several ontology-based approaches have been proposed to solve the problem of semantic interoperability.

One of them consists in creating maps between schema to enable data exchange between information systems (Regueiro et al., 2017). It addresses both syntactic and semantic conflicts. A promising method for BEM systems is the mediator-based approach (Banouar and Raghay, 2016) which makes use of intermediaries (mediators or wrappers). Each of them have specific knowledge linked to a terrain, a mapping or rules. They are independent from one another, and, by receiving requests and distributing them among the heterogenous data sources, bridge the gap between different ontologies and knowledge. Request distribution can be guided by the knowledge of data integration defined in an ontology at the mediator level (Regueiro et al., 2017). The ontology is also used to verify the functional compatibility of the components before mediation (Bennaceur and Issarny, 2014). Therefore, we recognize two types of mediation (Motie et al., 2017):

- Schema mediation such as in (Renner et al., 1996) which aims to connect to schema or ontologies through successive translations.
- Context mediation as described in (Motie et al., 2017).

The manual development of those wrappers is a challenging and time-consuming task, requiring substantial effort and a deep understanding of the application domain. Hence, research efforts are moving in the direction of automation for mediators. Furthermore, automation enables seamless and spontaneous interaction between components in highly dynamic environments (Bennaceur and Issarny, 2014; Regueiro et al., 2017).

4. Proposed digital twin framework

The proposed digital twin framework should support both co-simulation, and (near) real-time control and operation planning. This study emphasizes reusability, modularity, and interoperability to address the requirements of standardization and the incorporation of domain and semantic knowledge (Wiens et al., 2021). The proposed framework solves technical interoperability issues through the FMI standard and semantic interoperability through interoperability with, e.g., Brick Schema ontology. Moreover, by selecting standardized or known tools, it greatly enhances reusability while remaining flexible and efficient. We will provide guidelines to follow for the proper development of such a digital twin starting from the co-simulation aspect and concluding with the control phase.

For the purpose of simulating and controlling the operation of a building heating network, the digital twin should be capable of modeling the flow of energy throughout the building energy system. Therefore, we propose a digital twin architecture comprising the following layers:

1. **Basic system and energy flow representation**: a graph representation of the building HVAC system and relevant parts of the building energy system, containing the key parameters of the system and energy transfer relationships between components, subsystems, and thermal zones;
2. **Ontology framework, semantic interoperability, and data exchange**: the "meta" interface interoperability mechanism for di-directional data exchange between the digital twin model and external systems and hardware components;

3. **Data-driven co-simulation and control**: integration with services and tools developed on top of the information/energy flow layers.

The two first layers are the foundational layers of the digital twin framework, and intended to be very general to further support the development of data-driven models and control algorithms. These layers are explained in more detail in the following subsections.

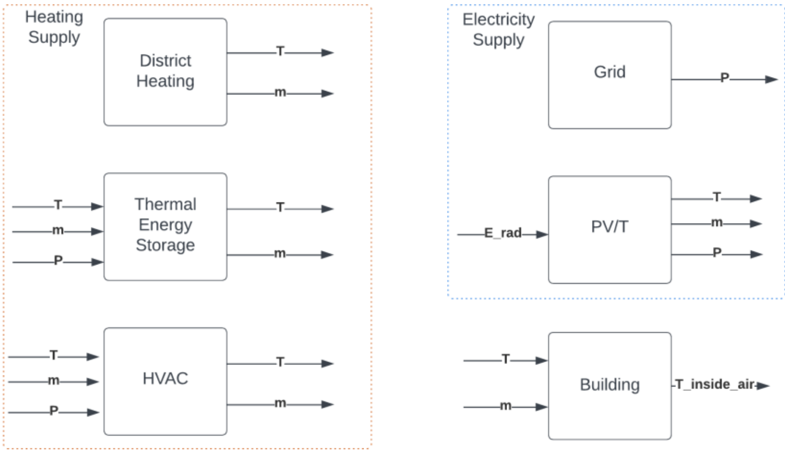

Figure 1. Basic components and inputs/outputs (ports).

4.1. Basic system and energy flow representation

As the framework presented here is intended to be general, a preliminary study has been carried out to determine the system precisely. This involved defining the relevant components and description, as well as the relevant variables and parameters required to support simulation and control of the building HVAC system. The principles of the proposed digital twin concept revolve around two notions: ***components*** and ***ports***. A component takes some *inputs* and produces some *outputs* – these are called ports, and components can be interconnected if they have matching input-output ports. Note that it is not the responsibility of this basic system representation to model the transformation of these components, but rather to model interconnections between components. The upper layers are responsible for modeling the interactions between components.

The basic ports are: 1) temperature (T); 2) mass flow (m); and 3) electric power (P), which model the internal energy flow of the HVAC system. The framework also allows for additional ports, to connect information from external systems to the digital twin – for now we have included the radiation energy. The components may maintain an internal state, which is not the same as a port, for example the temperature of a thermal zone, or other sensor measurements. The basic components are: thermal supply, power supply, and thermal zones. These can be characterized as follow: 1) a thermal supply component is characterized by having a (T, m)-output port, and includes district heating, thermal energy storage, PV/T, and HVAC components; and 2) a power supply is characterized by having a -output port, and includes the power grid, batteries, and PV. A thermal zone is an area with a single temperature setpoint and has a (T, m)-input port.

This methodology adeptly constructs subsystem ontology from an existing comprehensive building ontology, ensuring our digital twin framework is compatible with all buildings and can accurately and effectively represent the physical HVAC systems within them. The connectors represent a connection between two components, whereby some parameter determined by one component influences another component. The physical interfaces of each component have been determined and depicted in Figure 1. However, a clarification needs to be made regarding the storage systems as they are in the meantime feeding their associated aggregator and receiving energy from it. The interfaces presented here aim to be comprehensive and, therefore, by accounting for certain null flows, could represent any configuration. The same applies to Figure 2, which illustrates the isolated physical flows of each component, providing an overview of the possible connections between them.

Our framework, aims to be comprehensive and targets real implementations, to reduce the number of considered parameters without sacrificing precision and gaining computational time, is then of paramount importance. Humidity and solar radiation have joined the outdoor temperature as meteorological factors. Additionally, temporal parameters have been added, as they are inevitable to consider in particular for control perspective (Hao et al., 2023; Maljkovic and Basic, 2020; Roccatello et al., 2022).

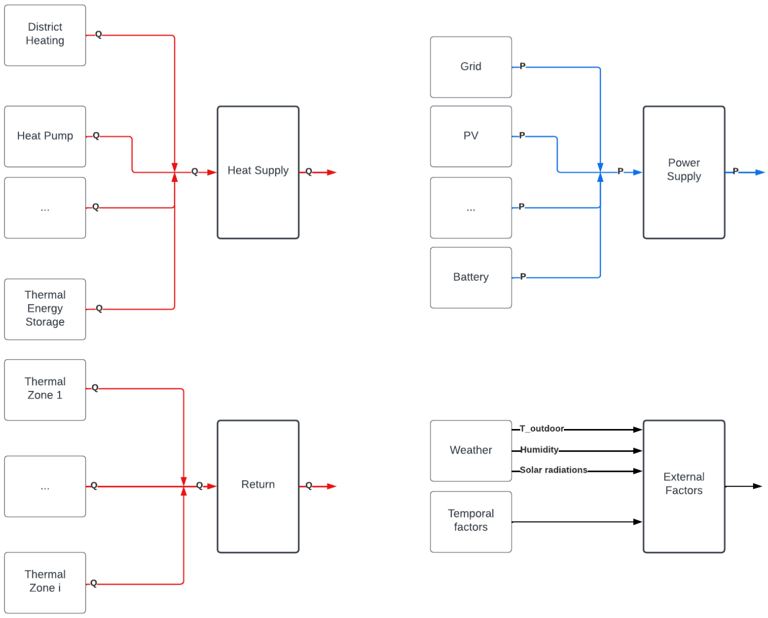

Figure 2. Basic components and inputs/outputs (ports).

4.2. Ontology framework, semantic interoperability, and data exchange

The integration of semantic and domain knowledge occurs through the REC ontology, which serves as a link between digital building representations, their control, and operation facilitated by Internet-of-Things (IoT) technologies. REC can be considered as a standard and modular schema for building knowledge graphs. Among other things, REC is based on ontology reuse, and the consortium is working on increasing the interoperability between well-established ontologies like SSN/SOSA and Brick. Such an ontology then provides a holistic description of building systems from equipment categories to measurable properties, including the integration of the sensor and actuator network. Furthermore, clear process and sampling semantics can be described, through the prism of real-estate.

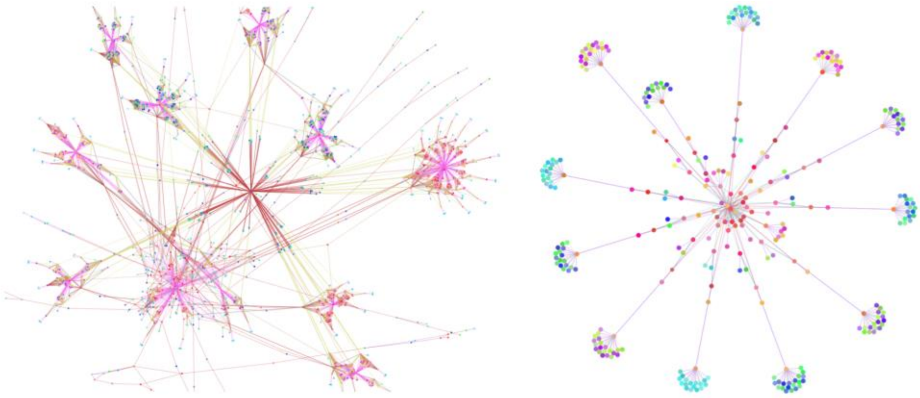

Figure 3. Comprehensive Brick Schema of a Building (left) and AHU (VAV) Subsystems (right).

As the first step, the ontology framework is developed, aiming at providing assurance for digital-twin framework can semantically comprehended and engaged with the intricacies of building systems. Since these ontologies are typically comprehensive and intricate, our approach is focused on distilling only the components that align with the aims of our study. In this section, Brick Schema is used as an example to demonstrate the methodology for extracting a subsystem, such as building heating system (using mechanical ventilation), from a comprehensive existing brick schema. The process encompasses a few strategic steps. Initially, a definitive list of components within the HVAC system, such as AHU, etc., is compiled as these elements form the focal point for the subsequent extraction from the overarching schema. Using Python and SPARQL, we can design specific queries to find and pull out the relevant structure for the listed components from the overall schema, and utilize the CONSTRUCT query in SPARQL to create a new RDF graph, exclusively containing the extracted data. We can visualize or utilize it for validation for further analysis, Figure 3 (left) presents the comprehensive Brick schema from a particular building, while Figure 3 (right) showcases the extracted AHU which using variable air volume (VAV) as subsystems.

4.3. Data-driven co-simulation and control:

According to (Barbierato et al., 2022), a co-simulation framework should include the following parts:

- **a Scenario**: Contains the semantic knowledge of the considered system. It allows for the connection between Simulators and initializes all the relationships that occur between the Model Instances.
- **the Simulators**: Perform calculations based on knowledge provided by Model Instances.
- **the Model Instances**: Represent physical subsystems.
- **an Orchestrator**: Statue of data exchange and time synchronization between simulators.

The simulators and model instances are handled by the FMI standard. Each of the aforementioned components will be modeled through a data-driven approach and exported as FMUs. Consequently, the number of FMUs is not predetermined and is not intended to be so, as the case study will dictate the requirements. This will increase the co-simulation precision and enable better real-world implementation. A pronounced need for a clear and holistic system description is then appearing. Notably, these FMUs must communicate and be connected, and the multiplication of these entities considerably complicates this task. Thus, the reasoning capabilities allowed by the ontology will be harnessed. REC, enabling such a representation, will enable the formulation of SWRL rules to autonomously establish inter-FMU connections. Subsequently, these connections will be semantically valid and mirror the building's reality.

The integration of ontological knowledge into FMUs is achieved by adding an .owl file to the FMU's ZIP file at its creation. For greater flexibility, a layered approach to knowledge incorporation, as described in (Mitterhofer et al., 2017), is preferred. This provides the possibility of using the same FMU types in different contexts. Thus, at this stage, only basic properties are indicated, such as unit or quantity concepts and domain-related information, namely BEM. Thereafter, project-specific knowledge will be added, e.g. spatialization concepts. This final step will be accomplished through reasoning using the SWRL rules and a reasoner.

To address the control aspects, the termination phase of the FMI is equipped with several functions for result extraction. These provide the opportunity to implement control strategies based on the formulation of optimization problems. The constraints and objectives of this problem will depend on the user's needs and the project requirements. It will be essential to keep the objectives in mind for the control during the framework configuration stage.

Control involves providing commands to the identified and defined actuators. With the division of different components into FMUs and thus the developed models, it will be possible to propose adapted and efficient control strategies. Once the predictions and actions are determined, based on the described system, they will be re-injected into the real system. It is then possible to apply different reasoning methods to compare the actual outcomes of the control policies implemented to the expected results.

5. Use case implementation and discussions

The framework has been implemented on a use case based on the heating system of an apartment building in Testbed KTH 3.0 (and neighborhood apartments Testbed EM), located at KTH campus, Stockholm, Sweden. The case consists of a few private rooms with a shared kitchen and common area. The whole apartment is heated by ventilation, supplied by one air-handling unit (AHU) with one heating coil. The supply air can be pre-heated by a ground-source heat pump (HP) with 11 boreholes. The coil in the AHU is heated from a thermal storage unit (TES). The heat pumps also supply another TES, specifically eight domestic hot water (DHW) Tanks. For space heating (SH), the heated air goes directly to the shared spaces by 2 duct openings – one in the living room and one in the kitchen – and to 4 VAVs, one for each private room. Each VAV contains one damper that controls the airflow and one after heater in case more heating of the air is required. Figure 4 presents the schematics of the heating system of the use case. All spaces (each room, the kitchen, the living room and each bathroom) have a Temperature Sensor, a Relative Humidity Sensor, and a CO2 sensor. In addition, over roof temperature sensors, floor temperature sensors etc. are equipped in different rooms. There are also some wall temperature sensors located between rooms and with ambient. Each room has an assigned temperature and CO2 setpoint.

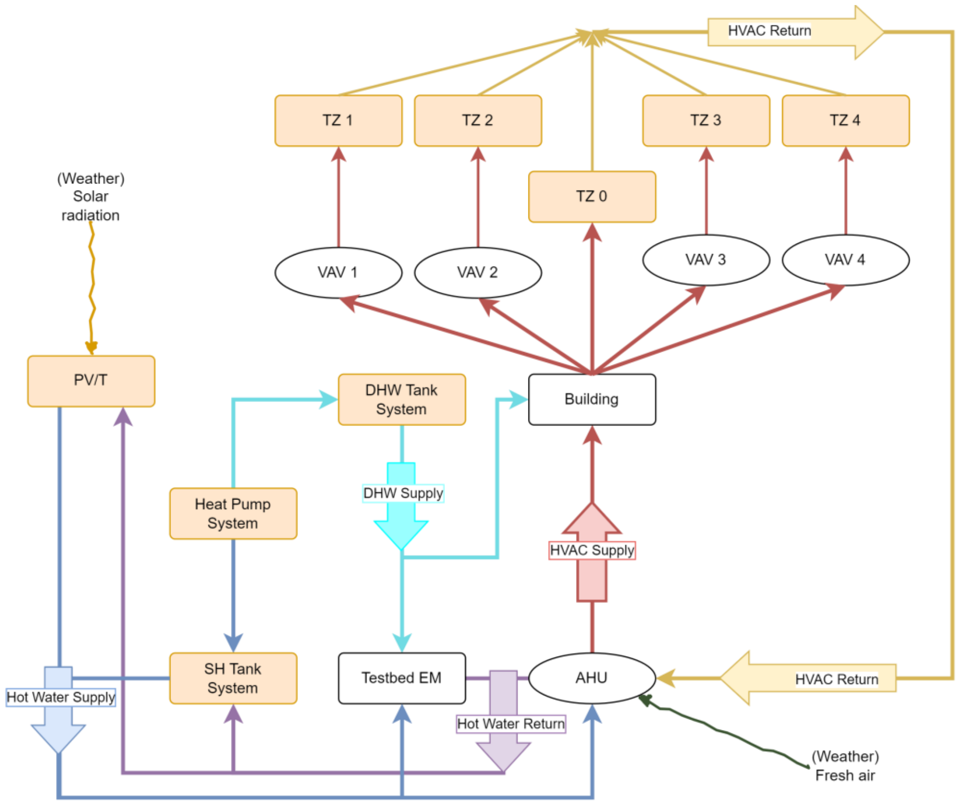

Figure 4. The heating network configuration and energy flow schematics of the suited use case.

Table 1 also presents the components, incl. photovoltaic and thermal (PV/T), that are included in the heating network, and sensing/controllable points.

Table 1: Systems and their Subsystems/Components/Points

	Subsystem	Has Component	Has Point	Is Controlled
PV/T System	Panels			no
	Battery System	Batteries	Storage Capacity	yes
	Ducts	Damper	Damper Setpoint	yes
HVAC	AHU	VAV		
	VAV	Damper	Damper Setpoint	Yes
		After Heater	Setpoint	yes
Space heating Tank System		Tanks (1-3)		
DHW Tank System		Tanks (1-8)		
HP System		Heat Pumps (1-3)		yes

Figure 4 represents the heating network of the selected use case, based on the minimum data and their flow needed in our framework. Red lines represent air supplied to building while the respective ones from heat recovery are represented in yellow lines. Correspondingly blue lines represent water supply while the purple ones water return. In both cases the data are either mass flow and temperature or energy, depending on the available sensors. As is the case with the electricity representation, inputs and outputs are only known to and from each system separately so supplies and returns are aggregated and then split for each system. In Table 2 we see how the data are organized in each case.

Table 2: Inputs and outputs of each system of the electricity network of the use case.

Systems	Inputs	Outputs
PV/T		Electricity Production Thermal Energy Production
Battery System	Unused PV Electricity	
SH TES		Supply Water Temperature Supply Water Flow Rate
DHW TES		Domestic Hot Water Supply
HP System	Total Electricity Used	Condenser Energy For Space Heating Condenser Energy For Domestic Hot Water
AHU	Air Intake Temperature (fresh air) Return Temperature (common) Return Air Flow Rate Supply Air Fan Power Return Air Fan Power	Supply Temperature (common) Supply Temperatures (distribution levels) Supply Air Flow Rate
Grid		Bought Electricity
Testbed KTH	Domestic Hot Water Use Electricity Used	
Other Buildings and Systems		Domestic Hot Water Use Electricity Used

For the electricity network, the building, and by extension the heating system of this study is provided with electric power not only through the grid, but also with locally generated power from PV/Ts located on the roof of neighborhood apartments. Batteries can also be potentially used as storage, where thermal energy produced is used in the preheating of the AHU, see Figure 4. In Figure 5, the electricity system data flow is adapted in the use-case. For clarification, the connections represent every useful data as described in Table 2. Every supply is aggregated and then split based on the knowledge. Dotted lines represent inherited values that are optional/customized, or in the case of the AHU it is because it is a subsystem of HVAC.

Figure 6 presents the framework as an example of how ontology can present the digital twinning of the selected heating network in the use case. Connections represented with dotted lines represent inherited relationships. On the one hand, for the sake of presenting many different interactions, the HVAC system is chosen as it has the most components and connections in our use-case. An example of a relationship that is not presented is the "isComponentOf" inherited connection, which in this case is shown only between the Dampers and HVAC, although this relationship exists between more systems, subsystems and components. Also every relationship described should automatically inherit the inverse relationship, for example every "feeds" creates an inverse direction "isFedBy”.

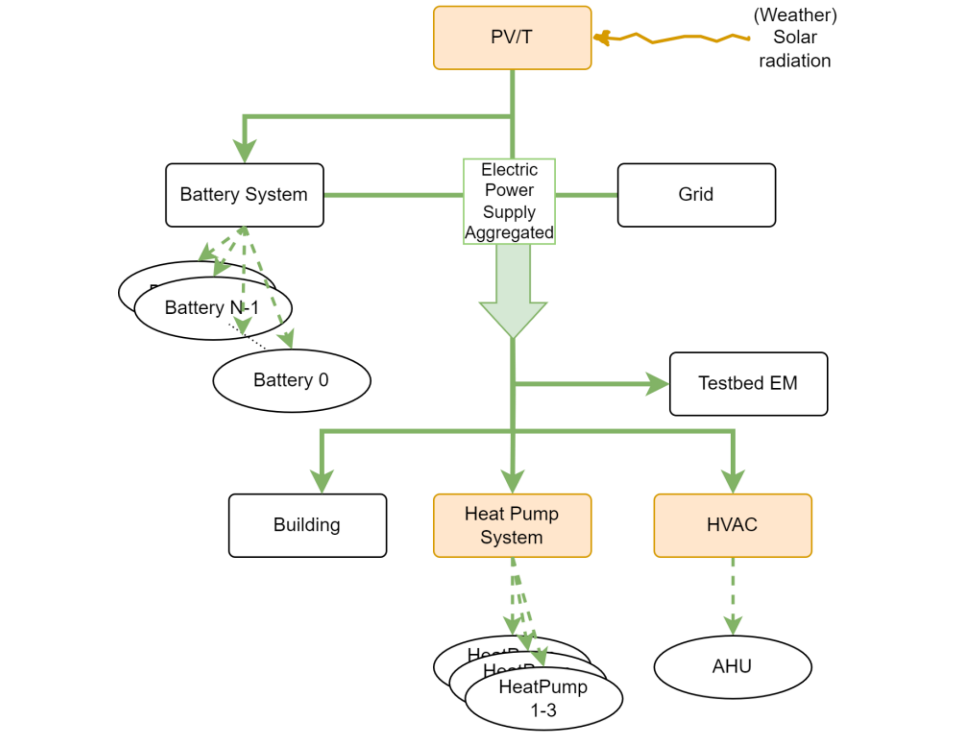

Figure 5: The electricity network configuration and energy flow schematics of the suited use case.

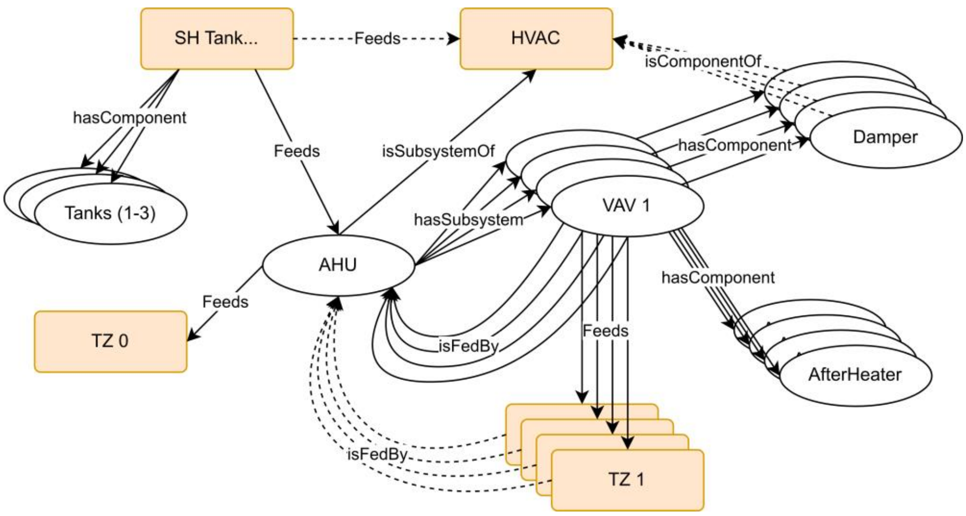

Figure 6: Example of studied ontology of the heating network of the use case.

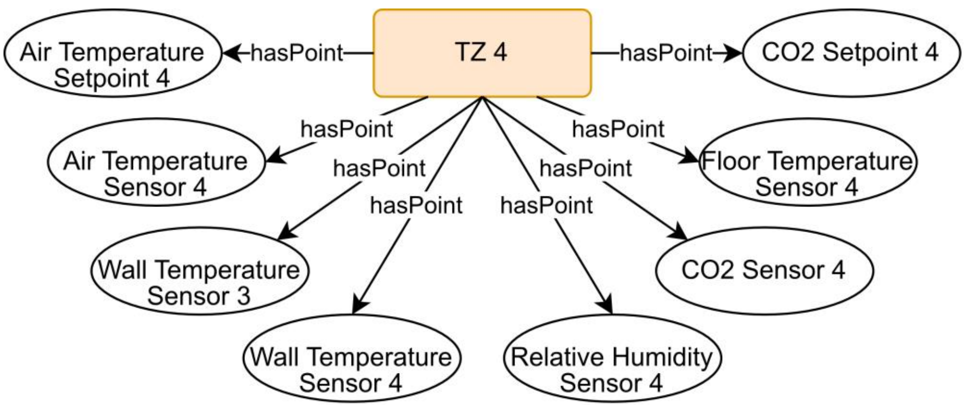

Figure 7: Thermal Zone 4 and its associated points

In this study, thermal Zones are not considered as locations, but abstract spaces/systems affected by parts of the system. Thermal Zones, as well as many other parts of the system, have their own points (sensors or actuators) and are considered through them. Thus, in this case, each room is considered a Thermal Zone because of their actuators and setpoints in the VAV. On the other hand, The shared spaces, although having many sensors have no actuator so they are all considered one Thermal Zone, namely "Thermal Zone 0". Thermal Zone 4 has a wide variety of points and its representation is hereby selected to convey some of the points of the system, as can be seen in Figure 7.

6. Conclusions

This study introduces an interoperability mechanism and a digital twin framework for simulating and controlling building HVAC systems integrating distributed renewables, and especially PV/T, and storage. In particular, it identifies the key components and subsystems, together with their key parameters and interfaces to describe the energy and information flows to support automated, data-driven co-simulation and control. To demonstrate the framework, it has been further adapted to a real building, the live-in-lab testbed at KTH. The interoperability aspects of the framework will be further developed to support IoT and BMS integration.

7. Acknowledgments

This study has been funded by the Swedish Energy Agency (grant number 51544-1) and the European Union’s H2020 programme (grant agreement number 101036656).

8. References

Banouar, O., Raghay, S., 2016. Interoperability of information systems through ontologies: State of art. Int. J. Comput. Sci. Inf. Secur. 14, 392.
Barbierato, L., Rando Mazzarino, P., Montarolo, M., Macii, A., Patti, E., Bottaccioli, L., 2022. A comparison study of co-simulation frameworks for multi-energy systems: the scalability problem. Energy Inform. 5, 1–26.
Bennaceur, A., Issarny, V., 2014. Automated synthesis of mediators to support component interoperability. IEEE Trans. Softw. Eng. 41, 221–240.
Bergmann, H., Mosiman, C., Saha, A., Haile, S., Livingood, W., Bushby, S., Fierro, G., Bender, J., Poplawski, M., Granderson, J., others, 2020. Semantic interoperability to enable smart, grid-interactive efficient buildings.
Berthou, T., Stabat, P., Salvazet, R., Marchio, D., 2014. Development and validation of a gray box model to predict thermal behavior of occupied office buildings. Energy Build. 74, 91–100.
Bloess, A., Schill, W.-P., Zerrahn, A., 2018. Power-to-heat for renewable energy integration: A review of technologies, modeling approaches, and flexibility potentials. Appl. Energy 212, 1611–1626.
Clausen, A., Arendt, K., Johansen, A., Sangogboye, F.C., Kjærgaard, M.B., Veje, C.T., Jørgensen, B.N., 2021. A digital twin framework for improving energy efficiency and occupant comfort in public and commercial buildings. Energy Inform. 4, 1–19.
Cupeiro Figueroa, I., Cigler, J., Helsen, L., 2018. Model Predictive control formulation: a review with focus on hybrid geotabs buildings, in: Proceedings of the REHVA Annual Meeting Conference Low Carbon Technologies in HVAC, ATIC. Proceedings of the REHVA Annual Meeting Conference Low Carbon Technologies …, pp. 1–9.
D’Elia, A., Roffia, L., Zamagni, G., Vergari, F., Bellavista, P., Toninelli, A., Mattarozzi, S., 2010. Smart applications for the maintenance of large buildings: How to achieve ontology-based interoperability at the information level. IEEE Symp. Comput. Commun. 1077–1082. https://doi.org/10.1109/ISCC.2010.5546639
Digital Twin: Vision, Benefits, Boundaries, and Creation for Buildings [WWW Document], n.d. URL https://ieeexplore.ieee.org/document/8863491 (accessed 10.9.23).
Drgoňa, J., Arroyo, J., Figueroa, I.C., Blum, D., Arendt, K., Kim, D., Ollé, E.P., Oravec, J., Wetter, M., Vrabie, D.L., others, 2020. All you need to know about model predictive control for buildings. Annu. Rev. Control 50, 190–232.
Falcone, A., Garro, A., 2019. Distributed co-simulation of complex engineered systems by combining the high level architecture and functional mock-up interface. Simul. Model. Pract. Theory 97, 101967.
Figueroa, I.C., Picard, D., Helsen, L., 2020. Short-term modeling of hybrid geothermal systems for Model Predictive Control. Energy Build. 215, 109884.
Hao, Z., Xie, J., Zhang, X., Liu, J., 2023. Simplified Model of Heat Load Prediction and Its Application in Estimation of Building Envelope Thermal Performance. Buildings 13, 1076.

Lévesque, M., Béchet, C., Suignard, E., Maier, M., Picault, A., Joós, G., 2014. From co-toward multi-simulation of smart grids based on HLA and FMI standards. ArXiv Prepr. ArXiv14125571.
Lork, C., Choudhary, V., Hassan, N.U., Tushar, W., Yuen, C., Ng, B.K.K., Wang, X., Liu, X., 2019. An ontology-based framework for building energy management with IoT. Electronics 8, 485.
Lu, Q., Parlikad, A.K., Woodall, P., Don Ranasinghe, G., Xie, X., Liang, Z., Konstantinou, E., Heaton, J., Schooling, J., 2020. Developing a Digital Twin at Building and City Levels: Case Study of West Cambridge Campus. J. Manag. Eng. 36, 05020004. https://doi.org/10.1061/(ASCE)ME.1943-5479.0000763
Maljkovic, D., Basic, B.D., 2020. Determination of influential parameters for heat consumption in district heating systems using machine learning. Energy 201, 117585.
Mitterhofer, M., Schneider, G.F., Stratbücker, S., Sedlbauer, K., 2017. An FMI-enabled methodology for modular building performance simulation based on Semantic Web Technologies. Build. Environ. 125, 49–59. https://doi.org/10.1016/j.buildenv.2017.08.021
Mohseni, S.-R., Zeitouni, M.J., Parvaresh, A., Abrazeh, S., Gheisarnejad, M., Khooban, M.-H., 2023. FMI real-time co-simulation-based machine deep learning control of HVAC systems in smart buildings: Digital-twins technology. Trans. Inst. Meas. Control 45, 661–673. https://doi.org/10.1177/01423312221119635
Motie, Y., Nketsa, A., Truillet, P., 2017. A co-simulation framework interoperability for Neo-campus project. ESM 2017 31st Eur. Simul. Model. Conf. 7p.
Pedersen, N., Madsen, J., Vejlgaard-Laursen, M., 2015. Co-simulation of distributed engine control system and network model using FMI & SCNSL. IFAC-Pap. 48, 261–266.
Regueiro, M.A., Viqueira, J.R., Stasch, C., Taboada, J.A., 2017. Semantic mediation of observation datasets through sensor observation services. Future Gener. Comput. Syst. 67, 47–56.
Renner, S.A., Rosenthal, A.S., Scarano, J.G., 1996. Data interoperability: standardization or mediation, in: 1st IEEE Metadata Conference.
Roccatello, E., Prada, A., Baggio, P., Baratieri, M., 2022. Analysis of the Influence of Control Strategy and Heating Loads on the Performance of Hybrid Heat Pump Systems for Residential Buildings. Energies 15, 732.
S. H. Khajavi, N. H. Motlagh, A. Jaribion, L. C. Werner and J. Holmström, "Digital Twin: Vision, Benefits, Boundaries, and Creation for Buildings," in IEEE Access, vol. 7, pp. 147406-147419, 2019, doi: 10.1109/ACCESS.2019.2946515.
Sutton, R.S., Barto, A.G., 2018. Reinforcement learning: An introduction. MIT press.
Weinberg, D., Wang, Q., Timoudas, T.O., Fischione, C., 2022. A review of reinforcement learning for controlling Building Energy Systems from a computer science perspective. Sustain. Cities Soc. 104351.
Wiens, M., Meyer, T., Thomas, P., 2021. The Potential of FMI for the Development of Digital Twins for Large Modular Multi-Domain Systems. Model. Conf. 235–240. https://doi.org/10.3384/ecp21181235
Zhao, H., Magoulès, F., 2012. A review on the prediction of building energy consumption. Renew. Sustain. Energy Rev. 16, 3586–3592. https://doi.org/10.1016/j.rser.2012.02.049

Computation of Power Loss in Utility Scale Solar PV Projects due to Power Limitation and Controls

Rajat Sethi, Rashmi Shringi

Amplus Solar, A Member of Petronas Group, Gurugram (India)

Abstract

With more and more renewables being integrated into conventional grids, the grid codes and connectivity requirements are becoming stringent for the distributed sources of generation. As installed solar capacities are increasing, the pressure to overcome the intermittent nature and emphasis to behave like a fixed load power plant is also increasing. This has led to the governing of power from wind and solar plants by various tools and technologies. In the last few years, asset real time performance monitoring has become the norm and organizations have built prediction models to monitor and evaluate their assets' financial returns. This paper covers the common types of controls used in utility scale solar PV projects and various methodologies used for computation of losses due to the controls at Solar Inverters and at grid interconnection point. The current study also compares the methodology used in PVsyst (solar PV energy simulation software used in industry) and real time loss estimations due to these controls. For analysis and evaluation, data from multiple utility scale solar PV assets in India have been considered.

Keywords: Asset monitoring, Performance evaluation, Inverter power control, Clipping loss, Power curtailment losses, Grid limitation losses, Power plant controller, PVsyst, Inverter loss over nominal inverter power, power governance.

1. Introduction

Solar photovoltaic projects work on the principle of conversion of sunlight to electricity. Earth's rotation around the sun makes day and night. During the day, the sun follows a certain path in the sky and if solar modules can track the sun, they will convert this falling radiation into energy. Most of the solar technologies like Solar Photovoltaic (SPV), Concentrated Solar Power (CSP), Solar Thermal Technology, Solar Water Heating Systems, Solar Air Conditioning, Solar Desalination and Solar Powered Vehicles work on the same principle of harnessing sun's energy.

Main components of a grid connected Solar PV system are:

1. PV Modules
2. Module mounting structures (MMS)
3. Solar Inverter Unit (Inverter) for converting DC to AC
4. Switchgear with protection and control circuits
5. Transformers for transformation of energy at different voltage levels
6. Utility Grid
7. DC, AC cables, earthing system and other miscellaneous items

2. Global Renewable Energy Scenario

As per *Statistical review of world energy 2023*, the world has increased its renewable electricity generation at a rate of 14.7% from 2021 to 2022 (page 53 of the report), while the overall electricity generation increased

10.18086/swc.2023.08.07 Available at http://proceedings.ises.org

by 2.26% in 2022 (Fig. 1). The integration of variable sources of energy like wind and solar poses new challenges for grid operators and utilities in terms of demand and supply side forecasting.

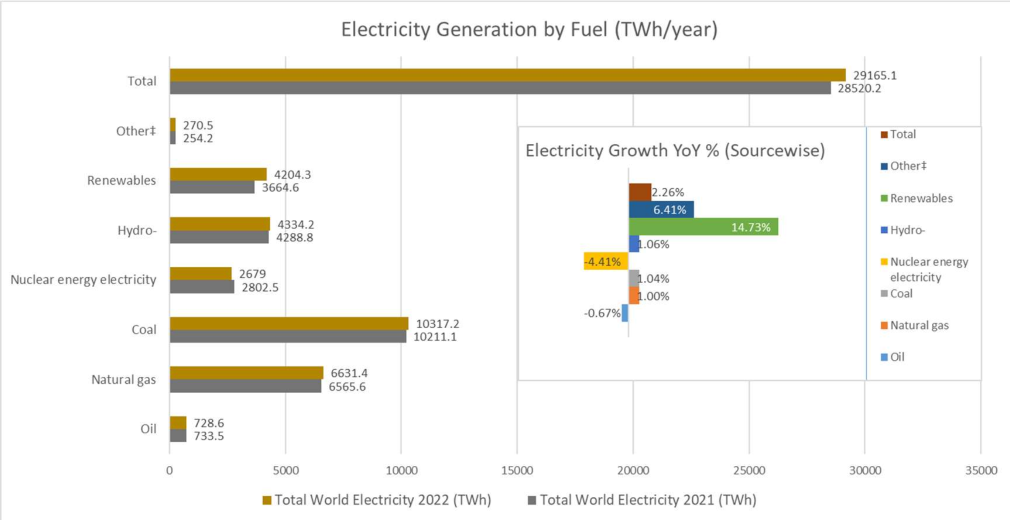

Fig. 1: Electricity Generation across world in Terra Watt Hour/Year in 2021 and 2022. Sub-chart illustrates that renewable sector contribution in energy mix has been growing exponentially YoY in recent years.

With the strong growth in renewable energy sector, the events of power curtailment will also increase in various cases of unbalanced grid and overcapacity in various parts of electric network. *Section 6, Table 1* of this paper covers power governance and control strategies enforced by CEA(Central Electricity Authority), which is the apex body for power sector in India. Utilization of this curtailed energy will be essential for efficient utilization of RE assets. India has started incentivizing new project awards, for round the clock, solar wind hybrid and battery energy storage projects. This will not only help in balancing the grid but also in utilizing this freely available renewable energy in electrifying newer geographies in India.

3. Calculating energy from a Solar Photovoltaic System

Solar system efficiency is dependent on the step efficiency of each system which is a part of the power flow sequence.

$$\mathbf{E_{out} = E_{POA}*(1\text{-}L1)*(1\text{-}L2)*(1\text{-}L3)*(1\text{-}L4)*(1\text{-}L5)*(1\text{-}L6)*(1\text{-}L7)} \qquad \textbf{(eq.1)}$$

The solar energy resource received (E_{POA}) and loss factors (Ln) depend on actual site geography, system design factors (electrical, mechanical, civil) and technology used in various conversion processes.

In the above equation,

E_{out} or Energy Output represents energy generated from a solar PV plant (in kWh)

E_{POA} or Energy Received represents solar irradiation falling on module plane of array (in kWh/m^2).

L1 represents the cumulative percentage loss in irradiation due to shading, reflection, soiling etc. before reaching the collector i.e. solar cells

L2 represents the percentage conversion losses in photovoltaic cells
Energy at end of this stage is also known as E_{array} or array nominal energy.
E_{array} = Irradiation received on collector after L1 losses (in kWh/m^2 area)*collector area(in m^2) *module efficiency (in %)

L3 represents cumulative percentage losses in conversion due to actual site geography, design factors above or below the STC lab conditions. This includes thermal loss, electrical shading loss, light induced degradation, DC ohmic wiring loss etc.

L4 represents cumulative percentage loss at Inverter level. This includes conversion efficiency loss, loss over nominal power, loss due to power threshold, night consumption etc.
L5 represents losses in transformers, AC power cables and transmission infrastructure (in percentage)

L6, **L7** can be any other loss parameter which plays a role in power flow (in percentage). These include imports, transmission line loss, auxiliary consumption, loss against reactive power or voltage support to grid etc.

All the above losses can be estimated with software, like PVsyst, to model the energy output from a certain project having fixed DC and AC capacity. In India, utility scale solar projects are allowed to inject a capped and pre-approved AC power. The cost of renewable energy has significantly decreased from 2010 to 2023, thanks in part to the affordability of modules. (*IRENA renewable power generation costs*).

With low-cost modules, it has become an industry norm to install 30% to 50% higher DC capacity than their pre-approved AC capacity, which means overloading inverters on DC side. This philosophy of overloading is a plus for both generating companies and distribution companies/grid controller, as the former can inject more power during early morning and evening hours and simultaneously the latter can rely more on renewables in overall energy mix.

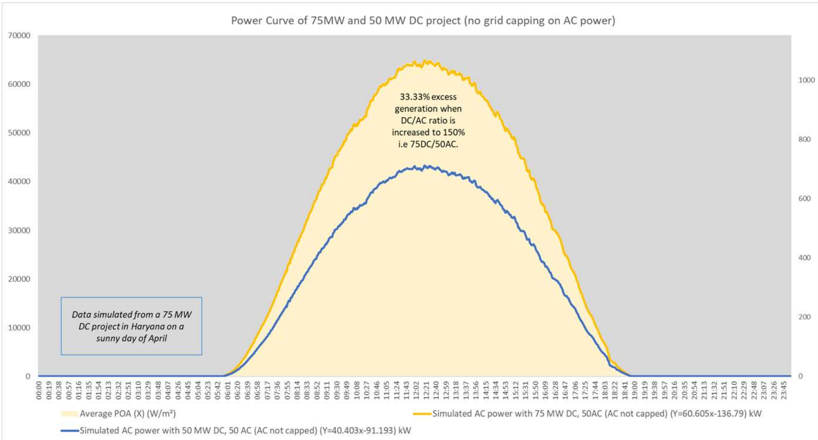

Fig. 2: One day power curve of a 75MW DC and 50 MW DC project without any limitation of evacuation on AC side. The yellow filled area below the line graphs represents Irradiance data on secondary axis.

In an uncapped plant, with higher DC to AC ratio, we can generate up to 33.33% more energy as compared to a system with the same DC to AC rated project. (Fig. 2)

Another key benefit of keeping higher DC to AC ratio can be seen from Fig. 3, where a solar plant with higher DC to AC ratio can pump more power in early hours of the day ($\gamma > \beta > \alpha$). The green curve shows the ideal case, where solar is able to generate at a fixed rated AC capacity from morning till evening. The downward trend in battery prices is resulting in a boosted desirability of the business case of energy storage integration during curtailment hours. (Fig. 3)

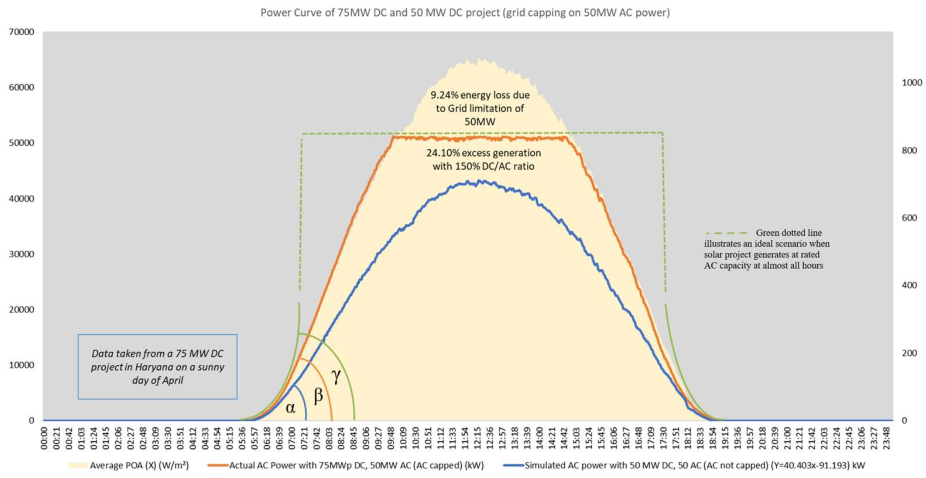

Fig. 3: Power Curve of a fixed 50 MW AC project with 75MW DC (orange curve) and 50 MW DC (blue curve). The yellow filled area below the curves represents Irradiance data.

4. Power governance through Inverters in Solar Projects

In all utility scale grid connected projects, there are stringent requirements to supply power of a desired quality. Power with desired frequency range, voltage range, current range, active-reactive power limits, harmonics and fast dynamic response to various grid events, are few of the requirements as per the grid code of India. These guidelines are enforced by CEA (Central Electricity Authority) through acts or legislation and CERC (Central Electricity Regulatory Commission) through various grid connectivity regulations. Solar Inverter, being the core component of this electricity conversion, is expected to meet all the applicable grid related guidelines.

Typical large scale PV Inverters can operate in three basic operation modes:

a. Voltage control mode: In this mode, the voltage of a reference point is monitored by PPC through inverters and reactive power drawl/ injection is varied accordingly with respect to a voltage set point.

b. Reactive power or Q-control mode: In this mode, the inverter supplies or absorbs a fixed amount of reactive power from the grid.

c. Power Factor control mode: In this mode, the inverters operate at the defined power factors.

There are many inverters which have additional capability to generate and absorb reactive power using a feature known as Night mode or Static VAR generator (SVG) mode. This feature has become a basic requirement in recent times as utilities are becoming increasingly dependent on RE generators for grid stability.

The absorption of reactive power by solar inverters in lean solar period has helped grid operators in reducing requirements of Transmission Line (TL) tripping and TL line isolations at many sub-stations in southern grid of India. As shown in Fig. 4, the PQ (active-reactive) capability curve of inverter showcases the range of reactive power support which can be given by each inverter in case of grid requirement. During the generation period, the energy from PV field is regulated by control algorithms of the inverter to govern the output power.

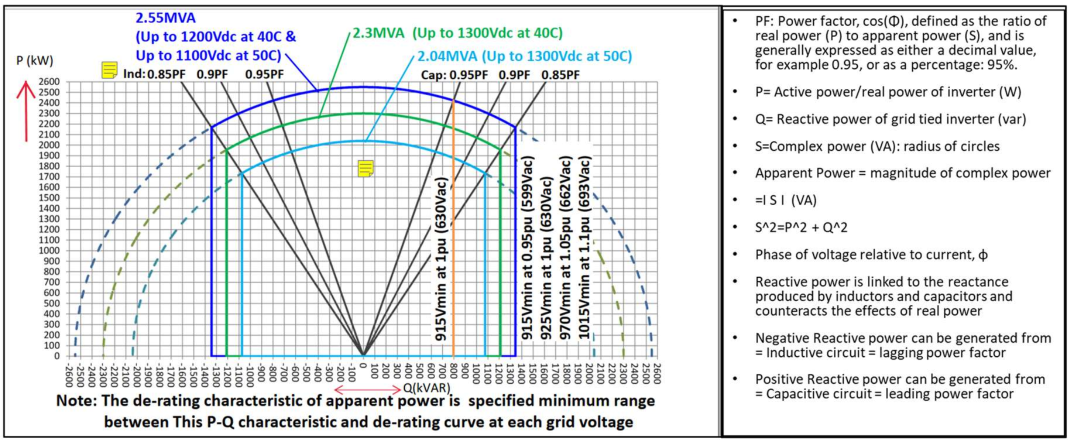

Fig. 4: P-Q curve of 2.55MW TMEIC Solar Inverter with Active/ Reactive power generation capability. The curve shows the various range of operations possible with TMEIC solar central inverter.

In Fig.4, Solar inverter nameplates mention 2.55MVA as its rated power. This rated power can be obtained when the Q value (on x-axis) is zero. With increased reactive power in output, the active power will be reduced by a certain percentage, thereby de-rating the inverter from its peak active power capacity. The above inverter has the capability to generate power with (-0.85) lagging Power Factor (PF) to (+0.85) leading PF, thereby supporting the grid whenever required.

5. Computation of Power loss in Solar PV Projects

For the accurate evaluation of real time energy loss in solar inverters, following parameters must be known:

a. DC capacity of inverter unit

b. Inverter power curve

c. Real time irradiance data

d. Performance Ratio of the inverters or complete power plant

e. AC Set Point conditions at Inverters and real time set point value through Power Plant Controller (PPC)

f. Real time data of inverter power output and grid limitation set point for complete plant

Curtailment at the inverter level can be calculated by evaluating lost irradiation for which solar array was not able to generate electricity. In any utility solar project there are ground based sensors to measure irradiation resource, typically at one minute interval. For electrical equipment, there are metering devices at various levels of solar power flow sequence to measure various parameters for control, monitoring, metering, and protection of equipment and for compliance to grid code.

Methodology of calculating expected power from a solar PV project

The energy generated from a solar PV field can be calculated from measured parameters by the following formula:

$$\mathbf{E_{out} = DC\ capacity * POA * PR} \qquad \textbf{(eq. 2)}$$

where,

E_{out} or Energy Output is the energy generated from a solar PV plant (in kWh)

DC capacity represents the rated capacity of modules installed in the solar project (in kWp)

POA or Plane of array irradiation is the total solar energy received on plane of array per m^2 of area, typically measured by pyranometers (in kWh/m^2).

POA or Peak sun hours (PSH) refers to the equivalent number of hours during a day when the solar irradiance (the amount of sunlight) received at a specific location is equal to an average value known as the "standard solar irradiance of 1000W/m^2." This is a calculated parameter for easy understanding of the irradiation quantum received at any specific location.

PR represents a measure to tell how effectively the power plant can convert sunlight collected by the PV panels into AC energy, which then gets delivered to the grid. It is a relative measure of electricity conversion with respect to what was expected from the plant nameplate rating in DC or kWp. This PR metric quantifies the overall effect of losses due to inverter inefficiency, wiring, cell mismatch, elevated PV module temperature, reflection from the module front surface, soiling, system down-time, shading, and component failures (as per *IEC 61724-1*).

For calculating the curtailment loss, we will utilize the same formula (eq. 2) with certain thresholds and boundary conditions as follows:

In Microsoft Excel data tables, the current methodology calculates curtailed energy with below conditions on DateTime data, Power data and Irradiation data. The power will be considered as curtailed when these conditions (steps 1-3) are qualified.

Step 1. Time shall be >04:00 and < 20:00

Step 2. Inverter power >= 100% or Inverter power >= set maximum power at which inverter is operating

Step 3. Minimum Radiation value threshold at which each inverter reached peak AC power. This is calculated by using relational condition or lookup function of excel. Record and note down each minimum irradiance value (from complete irradiance data of the day) where value of individual inverter active power reached >2500 kW or >set peak power point.

Step 4. Now, compute the Count of instances, where the active power of inverter has reached the peak power. At all these instances, Inverter AC power (kW) >= 2500kW AC.
For e.g. Count the number of instances when the orange data bars of power have hit the flat line as in Fig. 5.

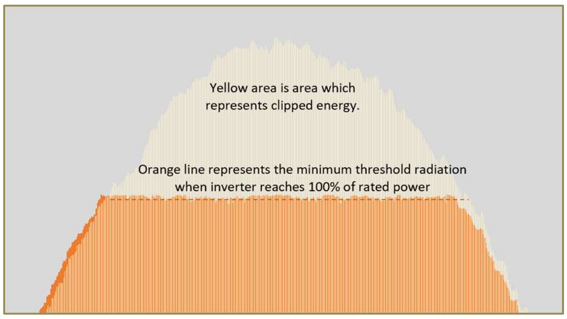

Fig. 5: Bar graph of minute wise Inverter Output Power trend (orange) and Irradiance trend (pale yellow)

Step 5. At all instances captured in step 4, we compute the excess radiation, when all above conditions are met. We do this by subtracting each real time radiation data point from the value calculated in Step 3 above. With this, we will be left with only radiation values which are above the minimum radiation at which clipping starts at each inverter. In other words, we will be left with all the bars which are above the dotted straight orange line as in Fig. 5. This is called as “excess radiation” or “clipped irradiation” which could not be converted into real power.

After computation of excess irradiation, we can replace the POA factor in eq. 2 with cumulative lost radiation (calculated in Step 5) for that day or period of measurement. Inverter level PR for that day or period shall be used in eq. 2 for calculating the clipped energy in that period.
Note: To compute irradiation in kWh/m^2 from irradiance data in W/m^2, one can multiply sum of irradiance values with time interval (1 min in our case) and divide by 1000 to get irradiance value in kW/m^2 and again divide by 60 to get Irradiation in kWh/m^2.

The results from eq. 2 give us the kWh lost due to curtailment. This curtailment can be because of any reason specified in *Section 6 Table 1* below.

Note: For the PV projects which have installed PPC, the data record of set point command values given to each inverter, at every minute interval, shall be used to decide inverter AC set points. In absence of this data, accurately computing the inverter level clipping loss becomes very difficult because minimum irradiance value required at clipping time will vary a lot, with dynamic power set points given by PPC every few minutes. With PPC controlling the inverter AC set points, power curtailment will not be a straight line for all inverters, and one cannot tell with certainty that inverter is generating less power due to any set point/soiling factors/reactive power/voltage control mode or mix of reasons thereof.

6. Power Governance and Control Techniques in Indian context

With the increasing share of non-conventional energy sources, the need for governance of power through integrated resource planning has increased significantly. It includes demand forecasting, generation resource adequacy planning and transmission resource adequacy assessment etc.

In context of Indian grid, RE plants are given must run status by The Indian Electricity Grid Code, 2010 (IEGC) in Regulation 5.2(u), which casts a statutory duty on the SLDC (State Load Dispatch Center)/RLDCs (Regional Load Dispatch Center) to make all efforts to evacuate available solar and wind power. As per IEGC, RE generation is considered as “Must Run”, subject to the grid security, the security of personnel and equipment and ensuring that Curtailment of RE generation is avoided.

As per the grid-code, “Curtailment” means a reduction in the output of a generator from what it could otherwise produce with the given available resources, typically on an involuntary basis. The term curtailment is broadly used to refer to the use of less wind or solar power than is potentially available at that time. Below are a few critical scenarios where power is governed by generators as per the guidelines issued by Central Electricity Bodies (CERC, CEA) or SLDC which is a Government State Electricity Body. In India, as per the working committee of *Forum of Regulators Report* on *“Model Guidelines for Management of RE Curtailment for Wind and Solar Generation November 2022”* and CERC Regulations *“Indian Electricity Grid Code 2023”*, Renewable Energy curtailment can happen in below cases:

Table 1: Curtailment Scenarios of Renewable Energy Projects

Curtailment scenarios of Renewable Power	Power governance and control philosophy
System design overloading: Interconnecting transformer (ICT) loading limits, Solar Inverter Ratings, Turbine ratings etc.	Onsite Curtailment at plant level: Curtailment is done by switching off equipment (wind turbines) or by controlling output power of Solar Inverters through Power Plant Controllers
System Wide Oversupply: Intra-state or Interstate Underdrawal or Over-supply	Underdrawal by State at state periphery outside the range of 250 MW for two or more successive time- blocks will initiate power controls at State transmission Utility/SLDC level. In lean or high renewable seasons, the variation of energy cannot be dynamically absorbed by grid. In such cases, curtailment instructions are executed at generator level to ensure their supply is within the demand band or forecasted power levels.
Transmission constraints: Planned or Unplanned Grid unavailability or Thermal limit of transmission lines as per CEA *(Manual of transmission planning criteria, 2022)*	In cases of grid infrastructure limitations, the RE projects are required to curtail at plant level and not inject scheduled power to grid.

Grid Stability and System security requirements: 1. Guideline of Isolation and Islanding as per CEA guidelines 2. Ramp up or Ramp down of power 3. Install AVR (Automatic Voltage regulator), PSSs (Power system Stabilizers), VAR (Volt amp reactive or Voltage Controller devices), and PPC (Power Plant Controller) 4. Install UFRs (under freq. relays), have frequency controls and reserves. 5. System Protection scheme as finalized by regional power committee or SLDC/RLDC. 6. Operating in steady state voltage range as specified by CEA Grid standards.	In Events of grid voltage issues, frequency disturbances, both demand side management and supply side management controls become effective. For e.g. All Discoms and STUs shall have UFR (under frequency relays) for load shedding in case of frequency decline which could result in grid failure. On supply side, as primary responses, generators shall have ramp up and ramp down capability of +/-5% to +/-10% of their MCR (Max. Continuous Rating), as the case may be. When the frequency falls/rises suddenly, generator can provide this primary response. Voltage Control reserves: Voltage Control reserves shall be deployed for controlling the voltage at a bus or sub-system through reactive power injection or withdrawal.
Operating Frequency band: National Reference Frequency is 50.000 Hz. Allowable operating band: 49.900-50.050 Hz	When average frequency for two or more successive time-blocks exceeds 50.050 Hz or falls below 49.900, then NLDC, RLDC, SLDC shall utilize the controls through various available primary/secondary/tertiary control reserves as specified in *Indian Electricity Grid Code 2023*
Inadequate grid availability or infra-deficit in RE rich states – leading to curtailments	Commands are given to different generators when there is no evacuation infrastructure to cater to the extra generation in peak resource season i.e. high wind or high sun seasons
Commercial interest of discoms (coal power related fixed charges and procuring cheaper electricity) and Maintaining Technical minimum margin for Thermal Power Stations (TPS)	In times of excess renewable energy, discoms cannot purchase all the low cost renewable power as there are minimum plant load factor commitments (55% for intra-state thermal as per state grid code) and fixed price PPAs for conventional power generating projects. In these cases, excess renewable is curtailed.

The above table lists some of the scenarios wherein RE generators can be asked to curtail power. There are other mechanisms like Deviation Settlement Mechanism (DSM), time of day tariffs etc. to discourage generators from supplying excess or infirm power into the grid. *Indian Electricity Grid Code 2023,* related to power sector in India published by CERC captures all mechanisms of governance of conventional and RE power.

7. Utilizing Curtailed Energy

The energy not evacuated into the grid due to reasons attributed to power limitation factors can be utilized in other forms by advanced power management and control systems. The excess generation at the plant level can be utilized in various other applications as below:

- Battery storage and other storage technologies
- Green hydrogen production
- Selling in Real time market (RTM)
- Demand balancing by reducing loads, time of day pricing
- E-mobility sector (charging energy banks)
- Ancillary services and support to grid

All these services will not only improve the returns from the existing assets but will also help the grid in supplying electricity in non-generation hours. The current reverse auctions in Indian solar markets emphasize on providing round the clock energy from renewable sources with integrated storage technologies.

8. Conclusion

With renewable capacities growing at exponential rates across major geographies, the need for advanced energy management systems is also increasing. Energy management systems at project level and grid level along with the help of advanced machine learning models will help in balancing the intricacies of supply and demand side. Government bodies across the globe shall develop policies which support renewable sector by low-cost financing and other policy instruments. Amidst the ever-changing political landscapes, different international bodies shall jointly build a knowledge base of solutions to tackle the new challenges of this sector. The current paper highlights the pace of deployment of RE projects and policies which are also changing with the needs of a stable grid and electric infrastructure as electricity will be the basic right of the next generation. In this paper, computation of losses in RE due to governance of power at various levels have been quantified. The potential commercial advantages of strategies to utilize this unused energy of the system has also been highlighted. This will help policy makers, power plant operators, and the research communities in understanding the nuances of a solar plant and grid related system criteria and developing strategies to tackle new challenges of the RE sector.

9. References

Central Electricity Regulatory Commission (Indian Electricity Grid Code) Regulations, 2023. Central Electricity Regulatory Commission (cercind.gov.in) as accessed on 08 October 2023

IEC 61724-1 Photovoltaic system performance - Part 1: Monitoring, Web: IEC 61724-1:2021 | IEC Webstore as accessed on 08 October 2023.

IRENA Renewable Energy cost trend, Web: Infographic: Renewable Power Generation Costs Continue to Fall Despite Inflation (irena.org) Link: https://infogram.com/1p069jqy1vq15mfeywr5g053xdankexz7jg Last accessed on 08 October 2023

Model Guidelines for Management of RE Curtailment for Wind and Solar Generation November 2022. Web: Forum of Regulators Document: Microsoft Word - Final Model Guidelines for management of RE Curtailment-toupload (forumofregulators.gov.in) as accessed on 08 October 2023

Report on Night Model Operation of PV Inverter Web: srldc.in/UploadFiles/NewsAndUpdate/SRLDC Report on Night Mode Operation (Trial) of PV Inverters at Pavagada Ultra Mega Solar Park.pdf as accessed on 08 October 2023.

Statistical Review of World Energy, Web: Home | Statistical Review of World Energy (energyinst.org) as accessed on 08 October 2023

Impact Analysis of Solar PV Integration and Heating System Retrofit: A District-Level Energy System Model

Ueli Schilt[1,2], Manuel Meyer[1], Sarah Schneeberger[1], and Philipp Schuetz[1]

[1] Competence Centre for Thermal Energy Storage, School of Engineering and Architecture, Lucerne University of Applied Sciences, Horw (Switzerland)

[2] School of Architecture, Civil and Environmental Engineering, École Polytechnique Fédérale de Lausanne (EPFL), Lausanne (Switzerland)

Abstract

The transition from fossil-based to renewable energy systems requires the integration of decentralized energy technologies such as solar photovoltaic (PV). Therefore, it is essential to evaluate multi-energy systems with different spatial and time resolutions. This study presents the first results of a multi-energy system model for the evaluation of district-level energy scenarios in Swiss communities. The model assesses both heat and electricity demand while estimating the potential for integrating decentralized renewables and retrofitting fossil heating systems with low-emission alternatives. Computations are carried out with an hourly resolution and timeframes of one year. The model was applied to a Swiss community, assessing solar PV integration and the effect of replacing fossil heating systems. It was shown that the replacement of fossil-based heating systems poses a significant potential for reducing carbon emissions. The impact of solar PV integration diminishes with increasing share of utilized potential due to a demand-supply mismatch and lack of storage and demand-side flexibility considerations.

Keywords: energy system model, solar PV integration, multi-energy system, decentralized energy, district-level

1. Introduction

The reduction of carbon-based emissions is becoming a growing priority amongst communities. By implementing renewable energy technologies and reducing the share of carbon-emitting infrastructure, progress can be made towards achieving net-zero targets. Orehounig et al. (2014) demonstrate the impact of renewable energy adoption by applying the energy hub approach to analyze the energy system of a Swiss village. The integration of solar photovoltaic (PV) energy systems also plays a key role in replacing carbon-based energy supply, as studied by Pero et al. (2019) in the framework of a multi-energy system of a smart district. Another case study where a model is applied to mixed residential and administrative buildings in Switzerland shows that implementation of solar energy using the energy hub approach is more efficient in contrast to just using standalone operation (Perera et al., 2017). In addition, the replacement of fossil-based heating systems such as oil and gas heaters can drastically reduce carbon emissions in the residential sector, as demonstrated by Wittenburg et al. (2023). To quantify the impact of these measures, a model can be deployed. Many studies of multi-energy system models for districts and communities exist in the literature, such as the one provided by (Heendeniya et al., 2020), focusing on nearly zero-energy districts.

In this study, we developed a district-level multi-energy system model to investigate how PV integration and fossil heating system replacement can contribute to the reduction of carbon-based energy consumption. While most models found in the literature are tailored to one specific district, the objective of this work is to create a model that is applicable to multiple communities. The model examines the impact of integrating solar PV and replacing heating systems on the supply of end-use energy (heat and electricity) for districts. Although model calculations are carried out using absolute values, the objective focuses on demonstrating trends, interrelations, and behavior of the energy demand and supply infrastructure of a community.

2. Methodology

The multi-energy system model discussed in this work represents a simplified description of the energy supply and demand scenario of a district-sized community. The model primarily focuses on Swiss communities, although it can be adapted for use in communities in other countries with just a few modifications. The model is implemented in Python programming language, computed with hourly resolution, and considers a one-year timeframe. A

10.18086/swc.2023.08.06 Available at http://proceedings.ises.org

representative schematic of the model is shown in Fig. 1. The modelling process consists of the following basic steps: (1) data collection for the specific community; (2) estimation of annual and hourly heat and electricity demands; (3) selection of technologies for energy supply, conversion, and storage; (4) parametrization of the model with available data for the specific district or community; (5) solving the energy balance equations for each time step (hour); (6) estimation of potential for additional implementation of renewable energy sources; and (7) application of scenarios with varying degrees of implementation of renewable energies and heating systems refurbishments. Output of the model is an hourly energy supply profile for electricity and heat divided by sources, and generation and conversion technologies, among others.

The model is parametrized using publicly available data containing information about the building stock and heating system types, ambient conditions, currently installed infrastructure, and potential for the implementation of additional energy-related technologies such as solar PV (Federal Statistical Office FSO, 2023). Data on ambient conditions such as temperature and solar irradiation is collected either from nearby weather stations or obtained from interpolated data (Lamprecht, 2023). Hourly weather data for a year is then generated using historic weather data from multiple years, which provides an average profile.

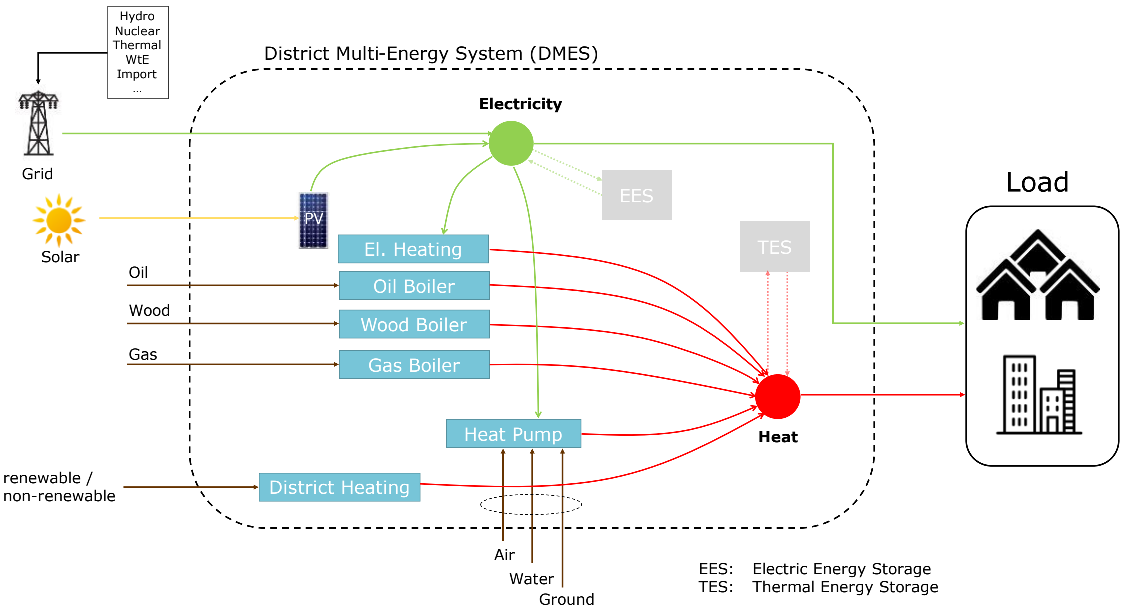

Fig. 1: Schematic of simplified multi-energy system model for districts and communities, including the heat and electricity sectors.

2.1 Electricity demand

In order to capture the intra-day operation, as well as the seasonal behaviour of the various technologies, an hourly electricity demand profile is used for the simulation. The hourly profile is modelled based on the annual electricity demand per community, using data provided by the communities themselves or by the respective utilities. If this data is not available, the annual demand is estimated using piecewise linear regression based on district properties such as the number of buildings, trained on the set of available consumption data from other communities. An hourly load profile is generated using recorded smart meter data across several years, scaling the profile to the respective annual demand. Such smart meter data is for example obtained from Huber et al. (2020). Currently, only residential load profiles are considered, which constitutes a strong simplification. However, in terms of solar PV integration it represents a conservative approach since industrial load profiles are generally more suitable for solar PV integration, as the demand is higher during daylight hours.

2.2 Heat demand

The heat demand in buildings is heavily dependent on ambient conditions and therefore on the time of day, as well as on the season of the year. An hourly demand profile is therefore required. The heat demand of the community is computed using a bottom-up approach: First, the heat demand is estimated for each individual building. Then it is aggregated to the heat demand of the whole community. The demand for an individual building is estimated based on the building properties (e.g. age and size of the building). Information about the building stock is available from the Federal Register of Buildings and Dwellings (Federal Statistical Office FSO, 2023). In combination with ambient temperature data, an hourly heat demand profile for the building is generated for the whole year.

2.3 Electricity supply

The electricity supply is divided into three main categories, namely locally generated PV; nationally generated electricity according to the Swiss electricity mix; and electricity imported from other countries ("cross-border"). Tab. 1 shows the breakdown of the electricity supply. The reason only solar PV was considered for local generation is that the focus of this study was on its integration in the local energy system. Electricity generated by other sources within the district (e.g. CHP) is considered to be shared within the national grid, meaning it is reflected in the national electricity mix. The composition of the nationally generated electricity by sources is based on fixed shares for each source, based on calculations for the year 2021 (Swiss Federal Office of Energy SFOE, 2023a). The share of cross-border imports varies by month, with higher imports in winter and less imports in summer but remains constant within a given month. A time-series of the monthly shares was created using statistical data for the years 2013 to 2022, provided by the SFOE (Swiss Federal Office of Energy SFOE, 2023a). A fixed fraction of the cross-border imported electricity was considered as renewable. Publicly available data on installed solar PV systems within the community provides information about estimated annual yields of the systems. PV yield simulations of individual buildings in various locations in Switzerland are then used to create hourly yield profiles. The profiles are scaled according to the annual yield values to generate an hourly yield profile for the community.

Tab. 1: Breakdown of electricity supply according to source.

Main category	Composition
Locally generated PV	Solar PV generated within the community.
Nationally generated electricity	Electricity generated within Switzerland according to Swiss electricity mix: • Hydro • Nuclear • Conventional CHP • Renewable CHP • Renewable other
Cross-border electricity import	Electricity imported from other countries.

2.4 Heat supply

The carbon-intensity of the heat supply heavily depends on the technologies used for supplying heat to the buildings. For example, supplying heat with an oil or gas boiler will generally have a much higher carbon-intensity as opposed to using other technologies. Therefore, in this model, the energy source used for heating is determined based on the deployed heating system type. It is a parameter that can be adjusted in the various scenarios. In the case of Switzerland, both the information of the heating system type and energy source for each building are available from the Federal Register of Buildings and Dwellings (Federal Statistical Office FSO, 2023). In the model, supplied heat is categorized into six sources: electricity, environment, biomass, fossil, district heating, and other. Tab. 2 shows the allocation of heating system type to heat source and the estimated share of renewable energy for each source.

Tab. 2: Heat sources based on installed heating systems.

Source	Heating system type	Share considered renewable
Electricity	Direct electric heating and electricity supplied to heat pumps	Depending on electricity mix.
Environment	Heat extracted from environment via heat pump (ground, water, air); assumption: fixed heat pump coefficient of performance of 3.	100%
Biomass	Wood burners (including pellets, cuts, and logs)	100%
Fossil	Oil and gas burners	0%
District Heating	Heat source not allocated	50%
Other	Where heating system unknown	50%

2.5 Scenarios

The available potential for additional renewables is identified based on available resources and infrastructure. In the case of solar PV potential, the assessment is based on available surfaces (roof and facades) and data provided by the SFOE (Swiss Federal Office of Energy SFOE, 2023b). Solar PV integration scenarios are generated by utilizing a selected percentage of the identified potential for additional renewables. Similarly, heating system retrofit scenarios are generated by replacing a selected percentage of fossil heating systems by heat pumps, which in turn increases the electricity demand due to increased heat pump capacity. Scenarios can be generated with various combinations of solar PV integration and heating system retrofit. The scenarios can then be compared among each other.

3. Results

The abovementioned energy-model has been applied to multiple municipalities in Switzerland. In this work, we present the results related to a suburban municipality located in the northern part of Switzerland which consists of approximately 6000 buildings and about 19,000 inhabitants. The following four scenarios were investigated (Tab. 3): base scenario (current state) with no additional PV integration or fossil heater replacement (Scenario 0); additional PV integration, no fossil heater replacement (Scenario 1); replacement of fossil heaters, no additional PV integration (Scenario 2); and PV integration and fossil heater replacement (Scenario 3).

Tab. 3: Evaluated scenarios for a Swiss community.

Scenario	Solar PV integration	Heating system retrofit
0	0%	0%
1	0 - 100%	0%
2	0%	0 - 100%
3	0 - 100%	0 - 100%

Fig. 2 to Fig. 4 shows the electricity supply to the community over one year for three selected scenarios, while the daily heat supply for the respective scenarios is shown in Fig. 5 and Fig. 6. While the calculation was done on an hourly basis, the graphs show daily aggregated values. For electricity, the values are split according to source of supply as described in Tab. 1. For heat, the values are split according to heating system type as described in Tab. 2. The annual values of some metrics that are impacted by the share of PV integration and the share of heating system retrofit are presented in Tab. 4, namely locally generated solar PV electricity, locally consumed solar PV energy (i.e. self-consumption), exported solar PV electricity, and cross-border imported electricity.

As a first “as is” scenario, the current state (Scenario 0) was investigated. The daily electricity supply to the community for this scenario is shown in Fig. 2: some electricity is generated locally by solar PV, relatively large shares come from hydro power and nuclear, while there is also a substantial amount of electricity imported from other countries. The share of cross-border imports is larger in winter than in summer. It must be mentioned that this study looks at the imported consumed electricity as opposed to the net imported electricity. Looking at the annual results in Tab. 4 it can be seen that almost all of the locally generated solar PV electricity is also consumed locally, and only a very small share (2 MWh) is exported. The respective daily heat supply for this scenario is presented in Fig. 5: a very large share of the heat demand is covered by oil and gas boilers, while smaller shares are served with heat pumps, district heating, and other technologies. Overall, it can be observed that the heat supply is still largely based on fossil energy sources.

In a “PV only” scenario (Scenario 1) 50% of the solar PV potential was utilized, while no heating system retrofit was considered. Therefore, the heat supply remains the same as in in the “as is” scenario (Fig. 5). The electricity supply, however, is different as can be seen in Fig. 3: the share of locally generated solar PV electricity has increased a lot. While some of the additionally generated solar PV electricity can be consumed (i.e. increased PV consumption), a large share of the generated solar PV electricity is exported due to a mismatch between supply and demand. This can also be seen in the annual values (Tab. 4, “PV only”): while the solar PV self-consumption increased from 6’222 MWh to 31’855 MWh, the solar PV export also increased (from 2 MWh to 30’458 MWh). More solar PV electricity is exported in summer than in winter due to increased generation and decreased overall demand. It can further be observed that the share of cross-border imports has decreased (from 48’186 MWh to 33’200 MWh), due to the increased PV consumption. As in the previous scenario, imports are larger in winter than in summer, but never zero.

In a “PV and heating” scenario, a PV integration rate of 50% and heating system retrofit rate of 50% was investigated (Scenario 3). In this case, the heat supply to the community has changed when compared to the two previous scenarios, as can be seen from the graph of daily heat supply in Fig. 6: while the overall heat demand remains the same, the share of heat supplied by heat pumps has increased, while the share of heat supplied by oil and gas boilers has decreased. The corresponding graph of daily electricity supply is presented in Fig. 4. It can be observed that a large share of the solar PV electricity is still being exported, which can also be seen from the annual values (Tab. 4, “PV and heating”): the solar PV self-consumption only slightly increased (from 31’855 MWh to 33’473 MWh), while the solar PV export slightly decreased (from 30’458 MWH to 28’840 MWh). Again, the reason for the large export is the mismatch between supply and demand. A large difference that can be observed when comparing to the “PV only” scenario is the increase in electricity imported from other countries (from 33’200 MWh to 52’917 MWh). The reason for this large increase of cross-border imports is the increased heat pump activity due to the 50% heating system retrofit.

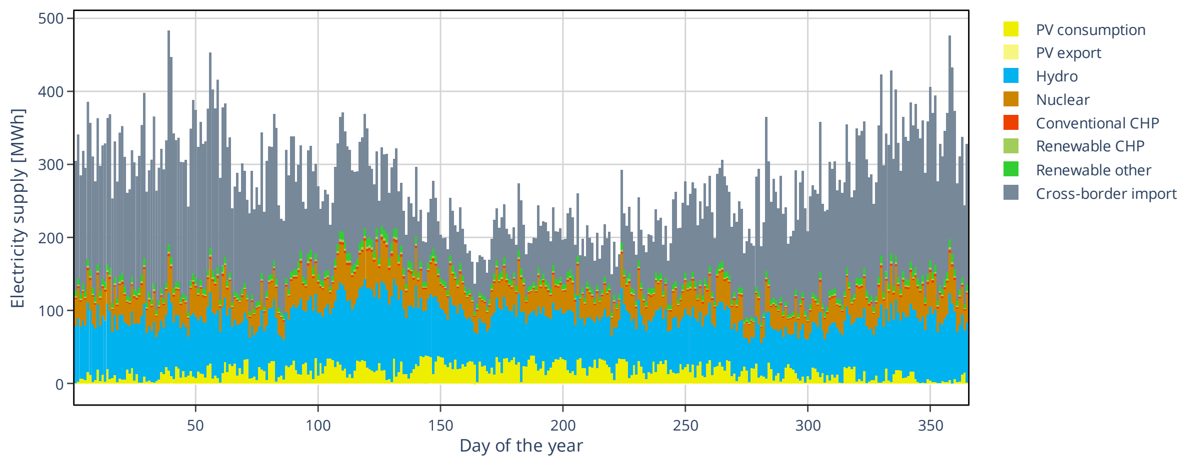

Fig. 2: Daily electricity supply aggregated by source based on hourly data for the “as is” scenario (Scenario 0, current state).

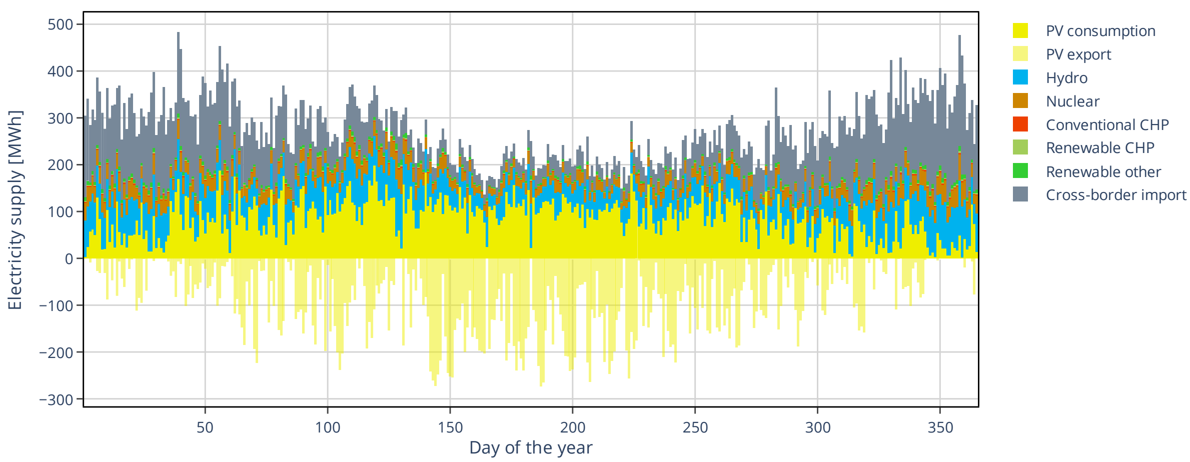

Fig. 3: Daily electricity supply aggregated by source based on hourly data for the “PV only” scenario (Scenario 1 with 50% solar PV integration and 0% heating system retrofit). A large share of the generated solar PV energy is exported due to a mismatch between supply and demand.

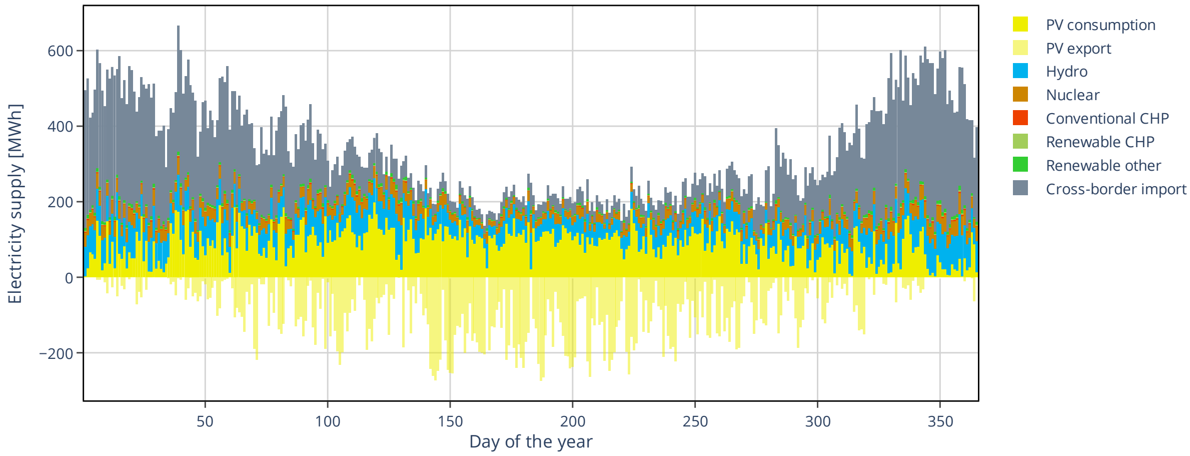

Fig. 4: Daily electricity supply aggregated by source based on hourly data for the "PV and heating" scenario (Scenario 3 with 50% solar PV integration and 50% heating system retrofit). The overall electricity demand has increased due to increased heat pump activity. Sill, a large share of the generated solar PV energy is exported due to a mismatch between supply and demand.

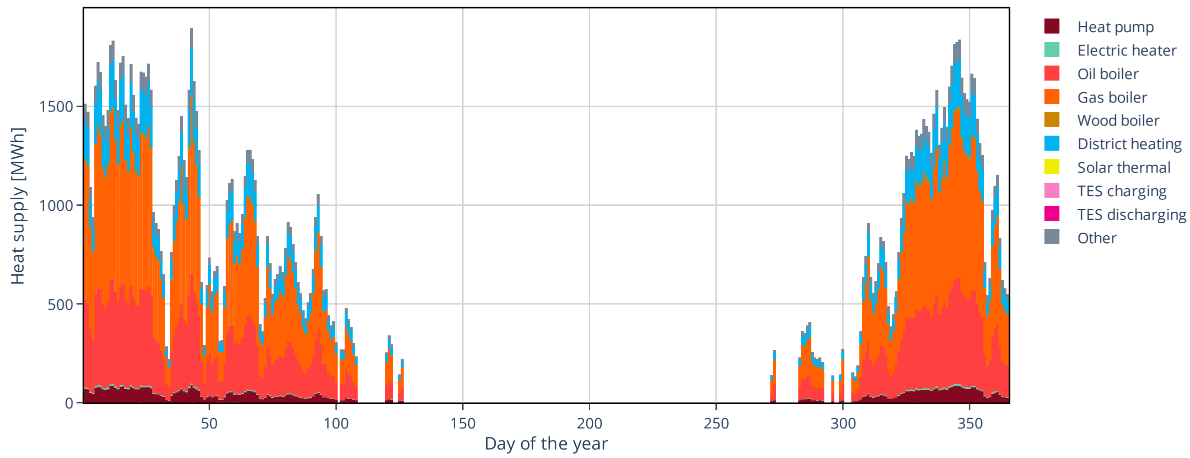

Fig. 5: Daily heat supply aggregated by heating system type based on hourly data for scenarios without heating system retrofit (current state). A large share of the heating demand is supplied by oil and gas boilers.

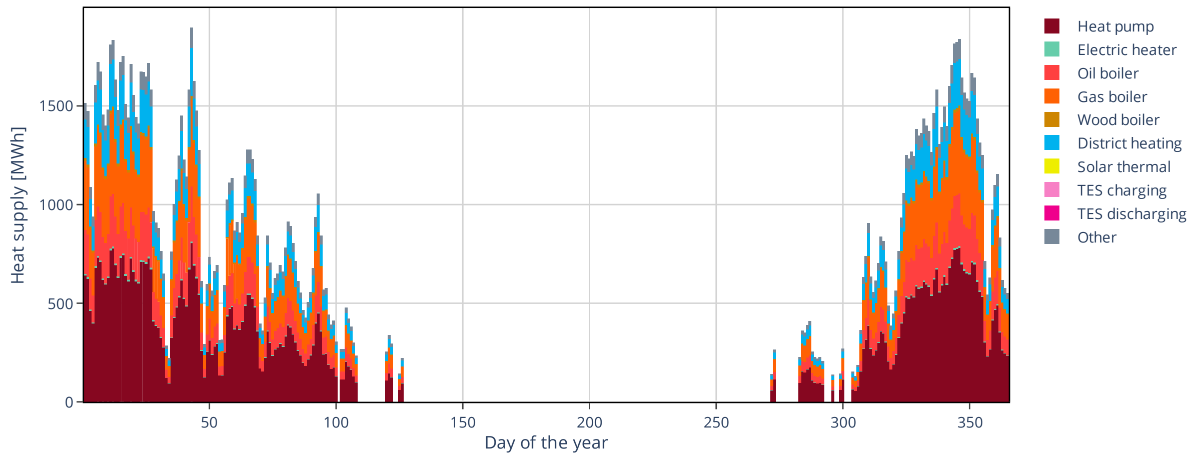

Fig. 6: Daily heat supply aggregated by heating system type based on hourly data for scenarios with a 50% heating system retrofit rate. While the total heating demand remains the same, the share of heating demand supplied by heat pumps has increased.

Tab. 4: Selected annual metrics of electricity supply for various scenarios.

Scenario	PV integration	Heating system retrofit	Annual solar PV generation [MWh]	Annual solar PV self-consumption [MWh]	Annual solar PV export [MWh]	Annual cross-border import [MWh]
"As is"	0%	0%	6'224	6'222	2	48'186
"PV only"	50%	0%	62'312	31'855	30'458	33'200
"PV and heating"	50%	50%	62'312	33'473	28'840	52'917

Fig. 7 shows the results of a parameter study for Scenarios 1 to 3 (see Tab. 3). Each study started with Scenario 0. For Scenario 1, the fraction of PV integration was varied from 0% to 100% (Fig. 7a). Here, it was observed that initial increases of PV integration resulted in notable increases in the share of renewable supply for both electricity and total energy. However, with higher PV integration, this effect diminishes, meaning that additional PV integration has very little effect on the overall share of renewable supply. This is due to the demand and supply mismatch: PV power is produced during hours of the day when demand is already met. For Scenario 2, the fraction of fossil heater replacement was varied from 0% to 100% (Fig. 7b). An increase in replacements results in an almost linear increase in share of renewable supply for both heat and total energy. For Scenario 3, the fraction of PV integration and fossil heater replacement was kept equal, varying from 0% to 100%. A cumulation of the effects from Scenario 1 and 2 can be observed, resulting in a slightly higher total share of renewable supply (Fig. 7c).

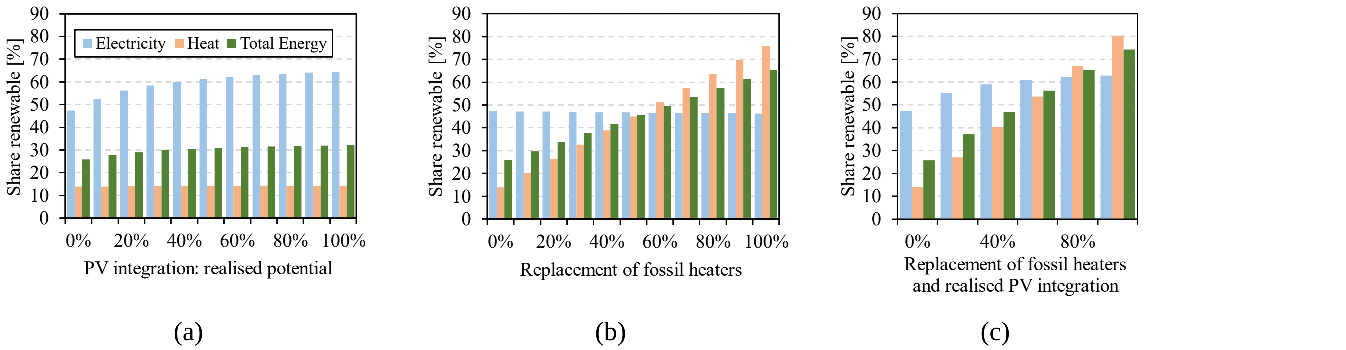

Fig. 7: Renewable share of supply for electricity, heat, and total energy for three scenarios: (a) PV integration, no fossil heater replacement, (b) fossil heater replacement, no PV integration, (c) equal shares of PV integration and fossil heater replacement.

4. Discussion and Conclusions

In this work, a model for the evaluation of energy supply scenarios of communities was introduced and the results of a simulation for a community in Switzerland were presented. The aim of the model is to show the impact of the various scenarios in regard to carbon-based emissions. Increasing the share of renewable energy supply decreases the carbon footprint of a community. The results presented above demonstrate that the replacement of fossil heating systems has a significant impact on the reduction of the overall non-renewable energy supply. This effect can be observed starting from small replacement rates up to a complete replacement of all fossil heaters (100%). For PV integration it is different: while PV integration increases the overall share of renewable supply initially, a 100% PV integration adds little benefit in this case. Even though high PV integration leads to a larger share of PV self-consumption, a large share of the generated solar PV electricity is also exported due to the mismatch between supply and demand. Increasing the share of heating system retrofit in this case increases the PV self-consumption, but only slightly, which is again due to the supply and demand mismatch. This mismatch is present because neither storage nor demand-side flexibility has been considered in the model and therefore excess PV power cannot be utilized. If storage or demand-side flexibility is introduced, this excess power could be shifted to another time on the load profile, where demand is high and renewable supply is low, e.g. during morning and evening hours when considering a daily profile. For example, with the introduction of thermal energy storage, excess PV power could be used to charge the storage via the heat pump. Later, this heat could be used when no PV power is available, reducing the need for cross-border imported electricity. A similar approach can be used for the implementation of demand flexibility: taking into account the thermal mass of the buildings, they could also act as a thermal storage, allowing to shift the heating activity to times of the day when excess solar PV is available. Various approaches to introduce storage and other means of flexibility in the energy system are also discussed in the literature (Connolly and Mathiesen, 2014;

Pleßmann et al., 2014; Solomon et al., 2014). In future work, the presented model can be extended to include storage and flexibility, allowing the investigation of additional scenarios. Further, the model can be coupled to an optimization framework, allowing for optimal control of the heat and electricity supply.

Overall, the results of this study show the benefits of heating system retrofit and PV integration in a community with regards to reducing carbon-based emissions stemming from energy generation. However, it is also shown that PV integration alone cannot generate the desired increase in renewable energy supply if not coupled with storage systems or demand-side flexibility considerations. It is therefore expected that the model presented above will be very useful in exploring this option when extended accordingly.

5. Acknowledgments

The research published in this report was carried out with the support of the Swiss Federal Office of Energy SFOE as part of the SWEET project EDGE. The authors bear sole responsibility for the conclusions and the results presented in this report.

6. References

Connolly, D., Mathiesen, B.V., 2014. A technical and economic analysis of one potential pathway to a 100% renewable energy system. Int. J. Sustain. Energy Plan. Manag. 7-28 Pages. https://doi.org/10.5278/IJSEPM.2014.1.2

Federal Statistical Office FSO, 2023. Federal Register of Buildings and Dwellings [WWW Document]. URL https://www.bfs.admin.ch/bfs/en/home/registers/federal-register-buildings-dwellings.html (accessed 10.8.23).

Heendeniya, C.B., Sumper, A., Eicker, U., 2020. The multi-energy system co-planning of nearly zero-energy districts – Status-quo and future research potential. Appl. Energy 267, 114953. https://doi.org/10.1016/j.apenergy.2020.114953

Huber, P., Ott, M., Friedli, M., Rumsch, A., Paice, A., 2020. Residential Power Traces for Five Houses: The iHomeLab RAPT Dataset. Data 5, 17. https://doi.org/10.3390/data5010017

Lamprecht, C.S., 2023. Meteostat Python [WWW Document]. URL https://github.com/meteostat/meteostat-python/tree/master (accessed 10.10.23).

Orehounig, K., Mavromatidis, G., Evins, R., Dorer, V., Carmeliet, J., 2014. Towards an energy sustainable community: An energy system analysis for a village in Switzerland. Energy Build. 84, 277–286. https://doi.org/10.1016/j.enbuild.2014.08.012

Perera, A.T.D., Mauree, D., Scartezzini, J.-L., 2017. The energy hub concept applied to a case study of mixed residential and administrative buildings in Switzerland. Energy Procedia 122, 181–186. https://doi.org/10.1016/j.egypro.2017.07.342

Pero, C.D., Leonforte, F., Lombardi, F., Stevanato, N., Barbieri, J., Aste, N., Huerto, H., Colombo, E., 2019. Modelling Of An Integrated Multi-Energy System For A Nearly Zero Energy Smart District, in: 2019 International Conference on Clean Electrical Power (ICCEP). Presented at the 2019 International Conference on Clean Electrical Power (ICCEP), IEEE, Otranto, Italy, pp. 246–252. https://doi.org/10.1109/ICCEP.2019.8890129

Pleßmann, G., Erdmann, M., Hlusiak, M., Breyer, C., 2014. Global Energy Storage Demand for a 100% Renewable Electricity Supply. Energy Procedia 46, 22–31. https://doi.org/10.1016/j.egypro.2014.01.154

Solomon, A.A., Kammen, D.M., Callaway, D., 2014. The role of large-scale energy storage design and dispatch in the power grid: A study of very high grid penetration of variable renewable resources. Appl. Energy 134, 75–89. https://doi.org/10.1016/j.apenergy.2014.07.095

Swiss Federal Office of Energy SFOE, 2023a. Electricity statistics [WWW Document]. URL https://www.bfe.admin.ch/bfe/en/home/supply/statistics-and-geodata/energy-statistics/electricity-statistics.html (accessed 10.8.23).

Swiss Federal Office of Energy SFOE, 2023b. Suitability of roofs for use of solar energy [WWW Document]. URL https://www.bfe.admin.ch/bfe/en/home/supply/statistics-and-geodata/geoinformation/geodata/solar-energy/suitability-of-roofs-for-use-of-solar-energy.html (accessed 10.8.23).

Wittenburg, R., Gierow, C., Pötke, R., Müller, K., Holtz, D., 2023. Transition of district heating from fossil to renewable energies – Pathways analysed by dynamic simulation. Renew. Energy Focus 45, 271–286. https://doi.org/10.1016/j.ref.2023.04.008

Influence of decentralization and sector coupling on the load profiles of the remaining grid demand for private household sector in Germany

Rohith Bala Krishnan, Viktor Wesselak, Theresa Reinhardt, Christoph Schmidt

Institut für Regenerativ Energietechnik, Nordhausen University of Applied Sciences, 99734 Nordhausen (Germany)

Abstract

Since Germany has embarked on a journey to transform its energy supply, the share of the renewable energies and decentralized energy supply has been increasing. The proposed German energy market for the year 2030 consists of 29% and 39% share from renewable energies and decentralized supply respectively, which is almost triple the share compared to the year 2010 (KPMG, 2015). The private household sector receive a constant electricity supply according to the standard load profiles developed by German Association of Energy and Water Industries (BDEW, 2018). This paper focuses on the effects of the decentralized energy supply and sector coupling in private households on the standard load profiles. The electricity, heat and e-mobility load profiles are developed for the state of Thuringia in Germany and the effects of decentralized energy supply are analyzed. The prosumer load profiles are published in hourly resolution in the same format as standard load profiles.

Keywords: Energiewende, energy transition, load profiles, grid analysis, decentralized energy supply, photovoltaics, prosumer load profiles, demand, household sector, system analysis

1. Introduction

The German energy transition goals require a drastic change to the existing power supply system. In electricity sector, it is important to achieve affordable and clean electricity (BMWK, 2017). Decentralized energy supply is an increasing trend in private households, due to the high inflation rate on the energy prices. A household can consume up to 30% of energy obtained from the photovoltaic system on rooftop and almost 60-70%, if the system is accompanied with a battery. At the moment, due to high costs of the PV-Battery systems most household have systems without storage, which means the remaining 70% of energy produced by the PV system is fed to the electricity grid. The excess unused energy may have an influence on the constant supply of electricity from energy suppliers. Therefore, the energy suppliers should adjust the standard load profile to prosumer load profile and supply energy to the grid. Standard load profiles (SLPs) are time-resolved representative load profiles and used for power estimation and power gradients, as well as for the simulation of energy systems. A new method proposed to develop the electricity load profiles using bottom-up stochastic model to neglect the disadvantages of SLPs (e.g. constant flow and similar seasonal pattern) (Bala Krishnan, R.K. et al., 2022). This paper shows the way to overcome these disadvantages and analyzing the effects of raising decentralized PV power and storage capacity.

2. Development of load profiles

2.1 Electricity load profile

The load profile for the electrical devices in the household is developed using the open-source tool RAMP. RAMP uses stochastic algorithm to reproduce unpredictable, random consumer behavior (Lombardi, F., 2019). It is necessary to define the users and the appliances in RAMP to generate the desired profiles. The users are classified according to the family type living in a household, as the yearly consumption depends on the no. of person living in a household. The table 1 represents the classification of households according to family type in Thuringia. The state Thuringia is classified into four regions to differentiate the demand.

10.18086/swc.2023.08.03 Available at http://proceedings.ises.org

Tab. 1: Classification of user group according to family type living in a household (TLS, Thüringer Landesamt für Statistik, 2014)

User category	North thuringia	Middle thuringia	East thuringia	Southwest thuringia
EP - Single person	62608	123977	129333	60447
POK - Couple without children	54107	95644	103697	54757
AE - Single parent	17392	29317	28624	18622
PMK - Couple with children	52298	70105	73565	54357
MP - Big family	4090	8679	8694	3504

The common household appliances like indoor/outdoor lighting, television, office materials (PC, Laptop, etc.), refrigerator, deep freezer, washing machine, dishwasher, cooking devices (toaster, induction stove, air fryer, and oven), circulation pump, warm water and miscellaneous devices. The circulation pump is responsible to circulate warm water to the heaters and simulated (not in RAMP) depending on the ambient temperature. The circulation pump is mostly not used during summer season due to less heat demand. Figure 1 represents various information to the simulated electrical devices: i) The inner circle represents the yearly energy consumption (in kWh) for each user category, ii) the pictograms represents the appliances simulated, and iii) The bar plots represents the share of each appliance (in percent) on the total yearly energy consumption for the individual user categories (Stefan Peter, 2013).

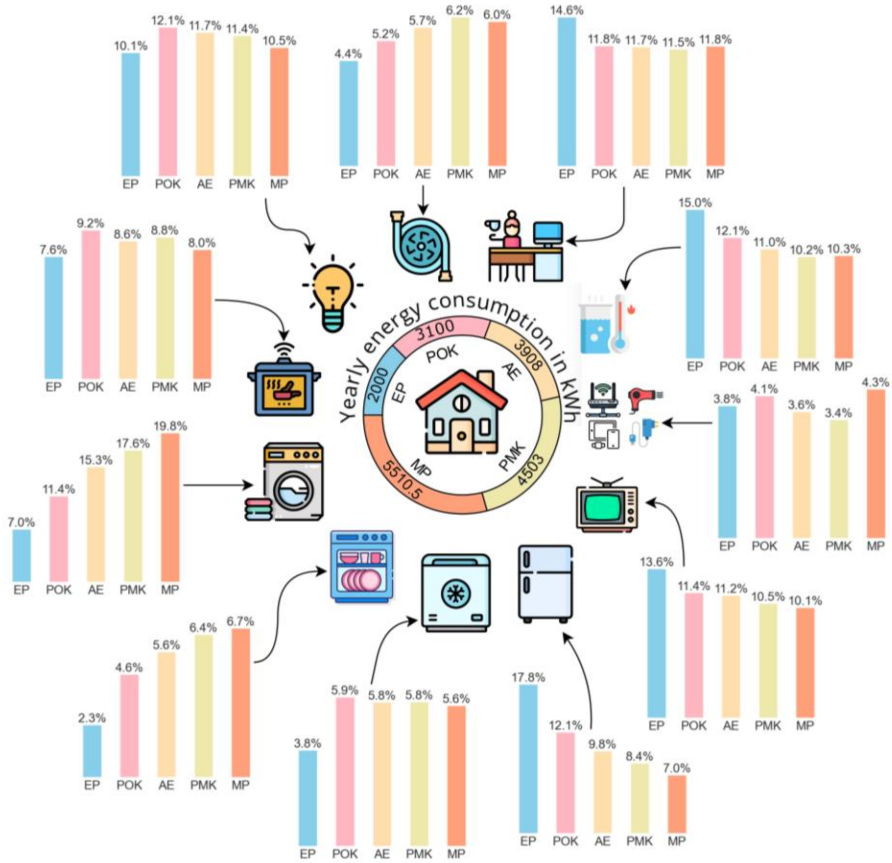

Fig. 1: Defined appliances and their share on the yearly energy consumption

All these devices are simulated with respective total usage time and operating timeframes. The total usage times are obtained from various energy survey reports. Due to insufficient information about the operating timeframes in Germany, the data are more or less obtained from UK energy survey report (EFUS, 2021). The documented total usage time and the operating timeframes are uploaded to the Institute's GitHub profile (in.RET, 2023) profiles are developed and compared with the SLPs for validation. All load profiles are simulated for the calendar year 2050, to have same holiday pattern. To compare, the RAMP profile and the SLP (Household profile - H0) are scaled to a same annual consumption of 1000 kWh/a. Figure 2 shows the comparison of the profiles in daily resolution and clearly represents the RAMP profile overcomes the disadvantages of the SLP and have similar course.

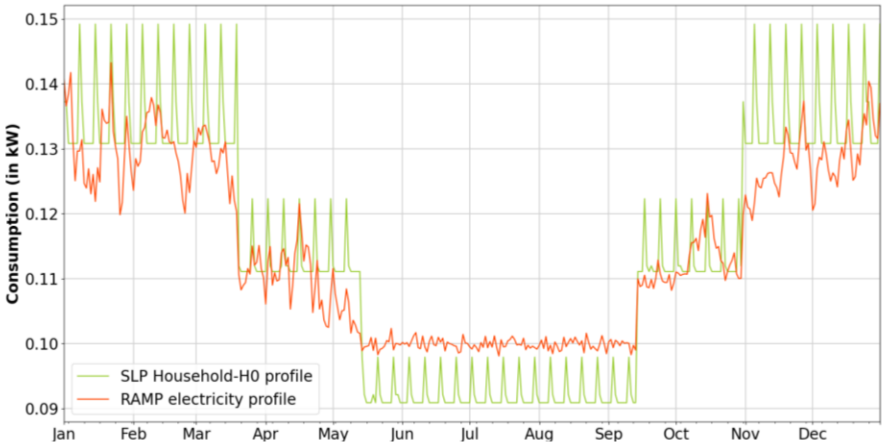

Fig. 2: Comparison between RAMP profile and the SLP in daily resolution

It is necessary to compare the annual load duration curve to make a more sensible comparison. The annual load duration curve represents the course with peak, main, transition and base load periods. Figure 3 shows the comparison between the annual load duration curves between the two profiles and can be clearly interpreted that the RAMP profile load curve has similar course in comparison with the SLP. Henceforth, the dynamic load profile can be substituted for future energy system modelling without interrupting the load course.

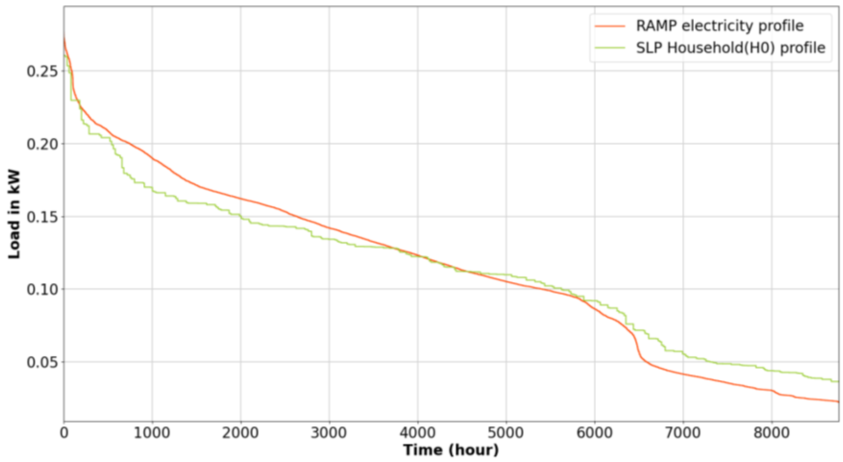

Fig. 3: Comparison of annual load duration curve between RAMP profile and the SLP

2.2 Heating load profile

Heating load profiles are determined by three factors: weather condition, building properties and habitation. The heat load profiles can be either developed using statistical or physical model approach. Due to less availability of data for the Thuringia region, the German statistical measurement methodology (BDEW, 2016) normally used to calculate standard gas load profiles is preferred for further calculations. The standard gas load profile methodology uses sigmoid curve/sigmoid function to calculate the daily heating requirement, which is later scaled up to the calculated annual demand for space heating and domestic warm water. To calculate the annual heat demand, the living area determined by the Thuringia state office for statistics (TLS, 2022) is multiplied with the specific heating requirement (including the demand for warm water) depending on the construction year of the building (Manteuffel B., 2013). Furthermore, it is also necessary to know the share of each building type and the year of construction to calculate the total heating demand for the specific building category. Figure 4 (a) represents the share of the detached houses (EZFH) and apartment buildings (MFH) for the four regions in Thuringia and figure 4 (b) shows the share of the household with respective construction year in Thuringia (TLS, 2022).

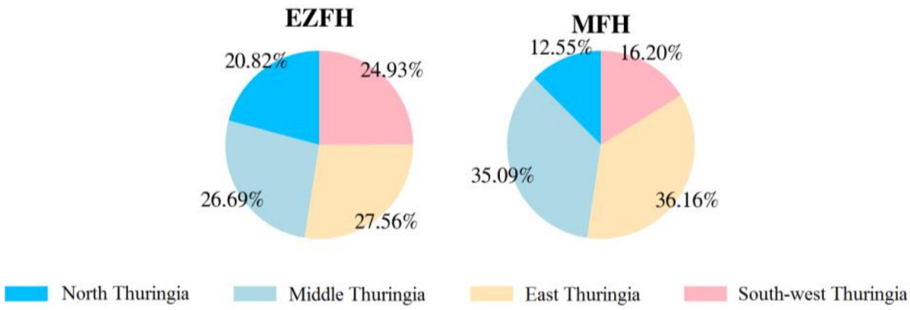

Fig. 4 (a): Share of detached houses and apartment buildings in Thuringia

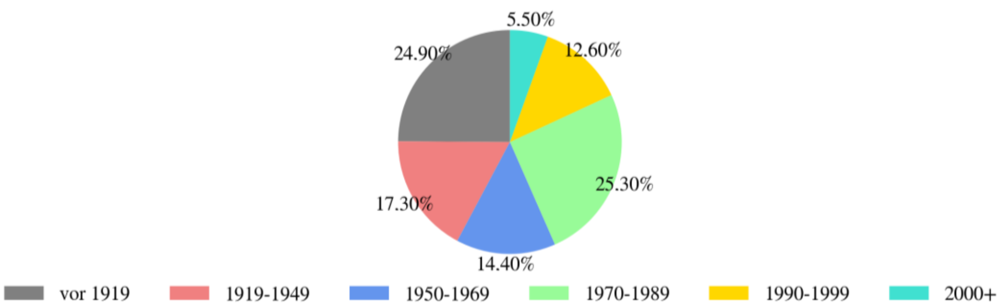

Fig. 4 (b): Share of Household according to the respective construction year in Thuringia

Furthermore, the Federal Association of the German Gas and Water Industry (BGW) presents the hourly demand factors for different building categories and for ten temperature ranges. These factors are multiplied with the respective daily demands to develop daily load curves.

2.3 E-mobility load profile

The expected increase of electric cars in the future will lead to an increased demand for electricity in both residential and commercial sectors. It is assumed that almost 80% of the charging process for electric cars takes place at home, as it can be done more efficiently in the long term and the remaining 20% in public parking's or commercial buildings. In residential building, the peak load is expected to occur in the late afternoon and evening hours when residents returning from work. If the building fails to have the smart charging management installed, the electric vehicles are charged immediately upon arrival and the charging power drops through the night depending on the maximum charging power. Due to lack of information regarding the user charging behavior specifically in private households, presently it is impossible to develop the load profiles stochastically. For the analysis, the e-mobility load profiles for residential building are obtained from a web-based planning tool known as nPro (Wirtz, 2023). Figure 5 shows the e-mobility load profile for residential building according to user behavior during weekday, Saturday and Sunday.

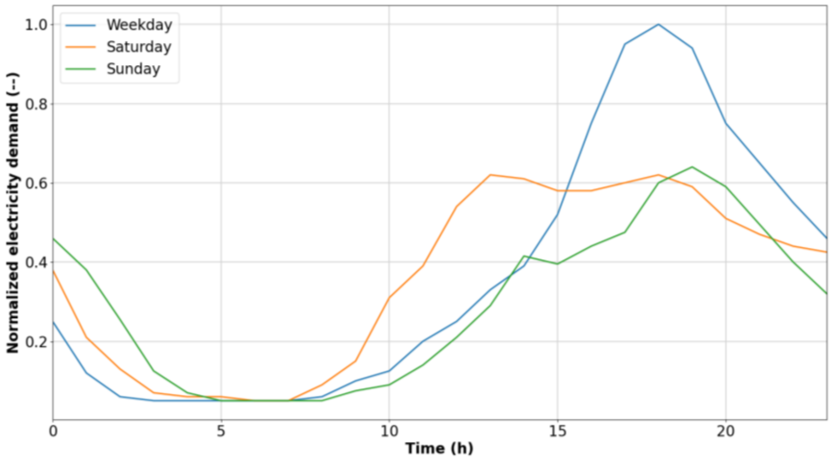

Fig. 5: E-mobility load profiles in the residential buildings according to the day type

2.4 Composition of the load profiles

The above-mentioned load profiles are scaled to the predicted annual electricity consumption (Tab.2) for Thuringia published by the Institute for renewable energies (Wesselak, 2023).

Tab. 2: Predicted final electricity demand for private households in Thuringia until 2045 in TWh

	2030	2040	2045
Electrical devices	2.1	1.9	1.8
Heat pump	0.622	0.85	0.828
Heating rod	0.303	0.234	0.131
E-Mobility	0.924	1.88	1.87
Total electricity demand	3.95	4.86	4.63

3. Energy system modelling

3.1 Predicted PV System Capacity in Thuringia

To analyse the effects of rooftop photovoltaic system on the remaining energy in the grid, it is necessary to predict the installed PV system capacity until 2045. Prognos AG, Öko-Institute e.V., and Wuppertal Institute made an energy system analysis for the whole of Germany and presented the results to achieve the climate-neutral future. The results also show the amount of PV capacity which has to be built by the year 2045 to achieve the energy transition goals (Prognos & Öko-Institut, 2021). The recent report from Fraunhofer Institute for Solar Energy Systems shows the percentage of annual installed capacity by size and the relative share of the federal states in the annual capacity increase in Germany over the past 20 years (Fraunhofer ISE, 2022). It is observed that the small segment PV system on rooftops (<10 kW_p) contributes a relative constant average share of 18.4% over the past ten years. The federal state Thuringia contributes a relative constant share of around 3% on the total installed PV capacity in Germany over the past ten years. It is assumed that the relative shares remain constant in the future and figure 6 represents the predicted capacity of rooftop PV systems (<10 kW_p) (green line) in private household sector in Thuringia.

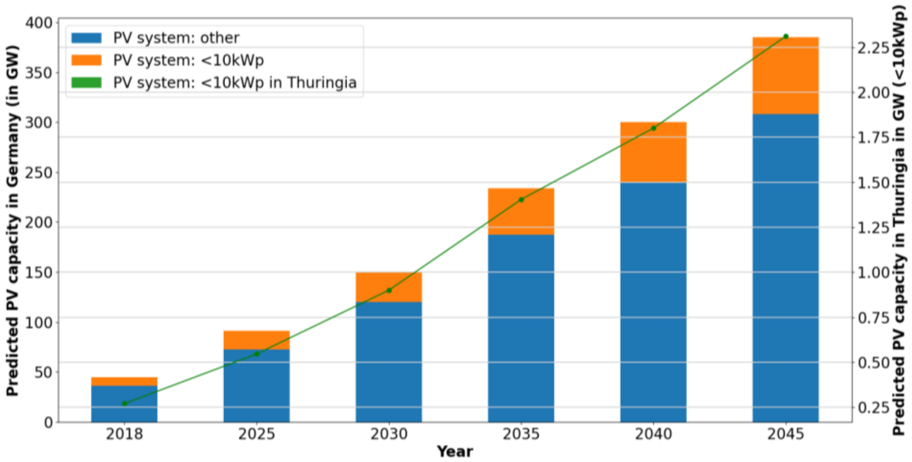

Fig. 6: Predicted capacity of rooftop PV system (<10 kWp) in Thuringia (left y-axis: green line) until 2045

3.2 System Analysis

An average PV feed-in profile is developed for the four planning regions with approx. 1005 kWh/kW_p full load hour. The energy produced by the PV systems significantly reduces the afternoon peak/load, resulting in reducing the utilization of the electricity grid. Before analysing the effects of PV on the electricity grid, it is necessary to compare the theoretically calculated PV capacity (fig. 6) with the optimum PV capacity. A small system is modelled in Open energy modelling framework (oemof) with the following components:

Photovoltaic system (with investment costs), electricity grid (with variable costs of 35 ct/kWh) as source and electricity demand as sink. Oemof.solph translates the energy system into mathematical equation using pyomo and optimizes the system with the help of a mixed-integer linear programming solver (Krien, 2020). The optimizer (cost optimization) suggest having a PV capacity of 2.196 GW by 2045, which is nearly close to our theoretical value (2.31 GW). The electricity demand from the grid is optimized with help of the theoretically predicted PV system capacity.

3.3 Influence of PV system without storage on grid

A self-consumption PV system without storage can consume approximately around 30% of the produced energy and the remaining energy is stored in the grid. People in Germany still prefer to store energy in the grid, as now they receive the feed-in tariff (approx. 8ct/kWh). The feed-in tariff encourages more people to build PV system on rooftops and to relieve the stress on the grid. However, this will change in the future and the feed-in tariff will decrease gradually over time. The people who consume only 30% and store the remaining 70% of the energy produces makes them *Prosumer* (producer + consumer). Hence, it is necessary adjust the SLPs for future energy system analysis or potential estimation and substitute it with the prosumer profile. Figure 7 represents the daily average prosumer demand profile for the year 2030, 2040 and 2045 in comparison with the normal reference load profile (dotted red line). The noticeable peak over the evening course is due to the increasing trend in E-mobility and the afternoon peak reduces significantly due to high PV energy production.

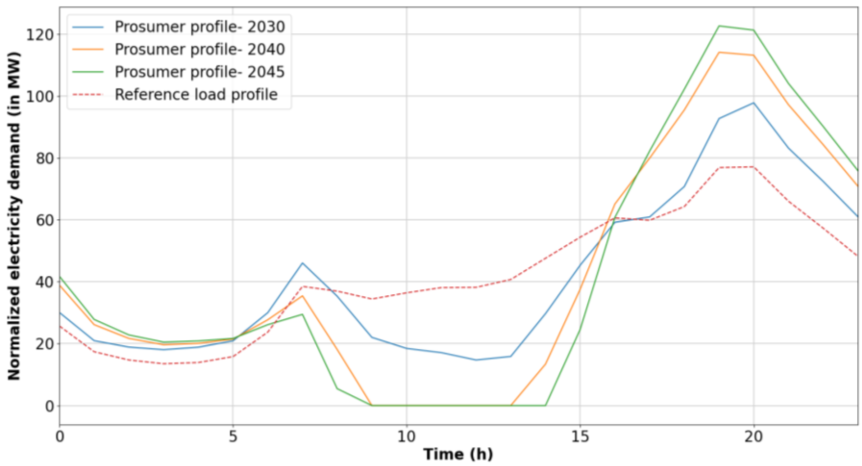

Fig. 7: Average prosumer electricity demand profile for one day in comparison with reference load profile

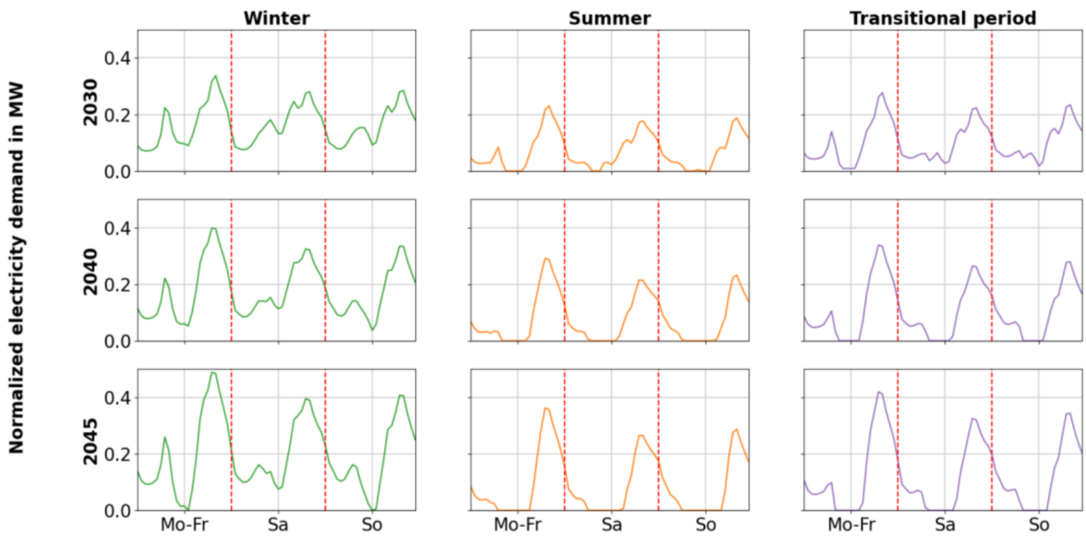

Fig. 8: Average prosumer electricity demand profile (with only PV system) for Weekday (Mo-Fr), Saturday (Sa) and Sunday (So) during winter, summer and transitional period

The yearly electricity demand profile was normalized to 1000 MWh/a and the profile was sorted according to the season and day type (similar to SLP). An average profile is developed for the each sorted profile to show the variation in the prosumer's electricity demand profile depending on the days of the week and season. The figure (Fig. 8) shown above represents a clear comparison between the profiles. In winter, it is noticeable that there is a demand for electricity during daytime due to less power produced by the PV system and in summer, there is almost zero electricity demand.

3.4 Influence of PV system with storage on grid

In contrast to the PV system without storage, the PV systems with battery storage can consume around 65-75% of the energy produced and stores only 35-25% of energy in grid. High electricity prices make the battery storage a more attractive option for the PV system owners, as higher self-consumption rates can be achieved and reduces the dependency on the grid. In Germany, the annual expansion of battery storage has increased significantly in the recent years and has achieved a total installed capacity of 3521 MWh until 2021. In the period 2014 – 2021, the proportion of battery storages installed with low capacity (≤ 5 kWh) continues to decline and lies around 7% of total installed capacity in 2021. On the other hand the storages with a capacity (between 5 -10 kWh) contributes a large share of the total capacity increase and contribute an average share of 40.3% over the past six year (Fraunhofer ISE, 2022). However, it is difficult to predict the total installed battery capacity in Thuringia. The required capacity of the battery can be optimized using oemof with investment model. For the optimization the battery's capex is taken as 80€/kWh. Table 3 shows the optimal battery capacity to be installed to increase the self-consumption rate.

Tab. 3: Optimized battery capacity for the respective predicted PV capacity until 2045 in Thuringia

	2030	2040	2045
Predicted PV capacity	828 MW	1656 MW	2125 MW
Optimized battery capacity	226 MWh	935 MWh	1467 MWh

Figure 9 shows the electricity demand curves from the grid with battery storages combined with PV systems. In comparison with the demand curves only with PV systems, it is noticed that the evening peaks are reduced with the battery system significantly during summer and transition periods. The excess PV energy is stored in the battery and retrieved during the evening's to reduce the grid dependency. It is observed that in 2045, the increase in the installed battery capacity has a significant change in the demand curve. The demand curves during winter looks almost similar in both systems, due to less energy produced and lack of PV excess energy, which can be stored in the battery storage.

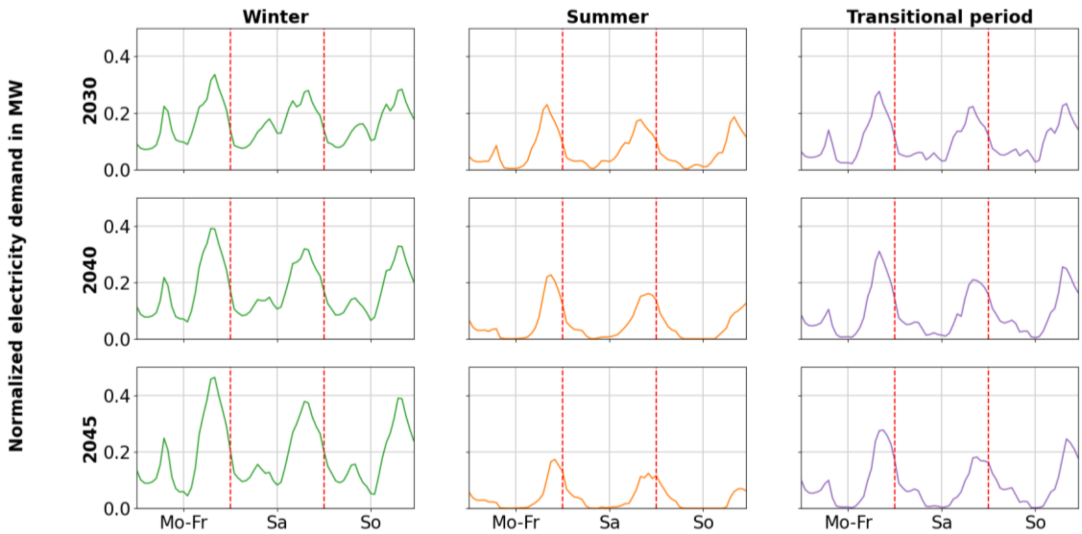

Fig. 9: Average prosumer electricity demand profile (PV + Battery system) for Weekday (Mo-Fr), Saturday (Sa) and Sunday (So) during winter, summer and transitional period

3.5 Annual Load duration curve

The annual load duration curve defines the curve between the load (electricity demand) and time in which the ordinates representing the load, plotted in the order of decreasing magnitude. From the load duration curve (Fig. 10), the total grid usage time (eq.1) and the load factor (eq.2) are calculated using the following equations. The load factor defines the measure of the utilization rate; a high load factor indicates that electricity grid is utilized at a high rate. In addition, the grid usage time represents the total time the electricity grid is used to satisfy the demand.

$$\text{Grid usage time (T)} = \frac{\text{Total energy consumption in a year (MWh)}}{\text{Peak load (MW)}} \qquad \text{(eq.1)}$$

$$\text{Load factor (LF)} = \frac{\text{Average load (MW)}}{\text{Peak load (MW)}} \qquad \text{(eq.2)}$$

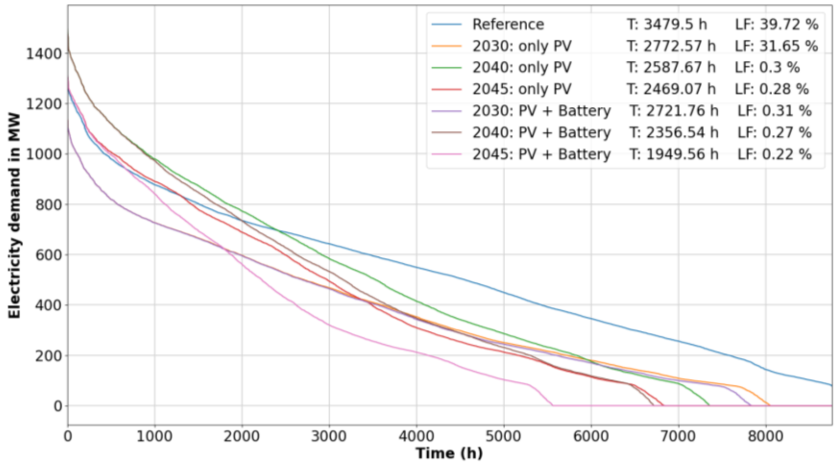

Fig. 10: Load duration curve for different scenarios with respective total electricity grid usage time (T)

The reference curve is the average demand curve of the three simulations (2030, 2040, and 2045). By 2045, the load factor reduces by almost 25% with only PV system and by almost 45% with PV-Battery system and the grid usage time decreases by approx. 29% with only PV system and by approx. 44% with PV-Battery system. The utilization rate can be reduced by almost 20% by complimenting a PV system with a battery storage. The analyses shows that the grid utilization rate is minimized eventually by continuous expansion of the installed capacity of decentralized energy supply system. Therefore, the CO_2 emissions can be minimized by not producing and making the availability of electricity on the grid according to the current SLP used by energy suppliers, and substituting it with the Prosumer load profiles to achieve the estimated political goals.

4. Summary

The effects of the decentralized energy supply on the load profiles were analyzed. As example, the federal state Thuringia in Germany was chosen for analysis, but the similar method can be used for other regions with respective datasets. The PV capacity was predicted until 2045 and the respective battery capacity was optimized using oemof. It was found that increase in the installing of PV system in household sector can significantly reduce the grid utilization rate and the PV system with battery storage can reduce the grid dependency. The prosumer electricity demand profiles were developed and forwarded for analysis. The load factor of electricity grid reduces by almost 25% with PV system and by 45% with PV-Battery systems. The grid dependency decreases largely during summer as well as transition period and slightly during winter, i.e. the grid utilization rate depends on the PV energy produced. Moreover, the excess energy produced from PV system in household sector can also be transferred to other sector (e.g. commercial or industry sector).

The dynamic electricity load profile developed using RAMP is compatible also for other regions in the same time zone. The RAMP profile for each user category is available for scaling to the respective no. of households in the particular region of analysis. The prosumer load profiles are sorted according to similar format as SLP for reference and further analysis. At the moment, the prosumer load profile are available only in hourly resolution but will be updated later with 15-minute resolution. The profiles are uploaded to the Institute's

GitHub handle and can be accessed using the link in the reference section (in.RET, 2023).

5. Acknowledgments

This work was a part of our main project Zero Carbon Cross Emission (ZORRO) and supported by the Thuringian Ministry of Environment, Energy and Nature Conservation.

6. References

Bala Krishnan, R. K., et al., (2022). Auswirkungen dezentraler Energieversorgung auf Standardlastprofil im Stromsektor.Tagnungsband 29th Energy-Symposium REGWA 2022, pg 9-17.

BDEW (Bundesverband der Energie- und Wasserwirtschaft), (2018)., Standardlastprofile. Retrieved from https://www.bdew.de/energie/standardlastprofile-strom/. Date of access: 05.09.2023

BDEW. (2016). Abwicklung von Standardlastprofilen Gas. Berlin: Bundesverband der Energie- und Wasserwirtschaft.

BMWK (Bundesministerium für Wirtschaft und Klimaschutz), (2017). Strom 2030: Langfristige Trends – Aufgaben für die kommenden Jahre.

EFUS. (2021). Lights, appliances, and smart technologies*:* An energy survey report. London: Department for Business, Energy & Industrial Strategy (BEIS).

Fraunhofer ISE. (2022). Photovoltaik- und Batteriespeicherzubau in Deutschland in Zahlen: Auswertung des Markstammdatenregister. Freiburg.

In.RET (Institut für Regenerativ Energietechnik), (2023). Electricity load profile development using RAMP: https://github.com/in-RET/RAMP; Prosumer load profile: https://github.com/in-RET/Prosumer-load-profile Date of Access. 06.10.2023

Krien, U. et al., (2020). oemof.solph- A model generator for linear and mixed-integer linear optimisation of energy system. Software Impacts, Volume 6, https://doi.org/10.1016/j.simpa.2020.100028.

KPMG, 2015. Decentralised energy industry: Opportunity or threat to energy companies?, pg 2. Retrieved from https://assets.kpmg.com/content/dam/kpmg/pdf/2015/06/decentralised-energy-industry.pdf. Date of access: 06.04.2023

Lombardi, F. et al., (2019). Generating high-resolution multi-energy load profiles for remote areas with an open-source stochastic model. Energy, 2019.

Manteuffel B., et al., (2013). Der Gebäudereport Thüringen: Langfassung. Thüringer Ministerium für Wirtschaft, Arbeit und Technologie.

Prognos, & Öko-Institut, W. I. (2021). Towards a Climate-Neutral Germany by 2045. How germany can reach its climate targets before 2050. Executive Summary conducted for Stiftung Klimaneutralität, Agora Energiewende and Agora Verkehrswende.

Stefan Peter, U. (2013). Modellierung einer voll-ständig auf erneuerbaren Energien basierenden Stromerzeugung im Jahr 2050 in autarken, dezentralen Strukturen (Nr. 14/2013). München, Dessau-Roßlau: Umweltbundesamt (UBA), ISSN 1862-4359.

Thüringer Landesamt für Statistik (TLS) (2014). No. of households by household family type in Thuringia. Retrieved from: https://statistik.thueringen.de/datenbank/TabAnzeige.asp?tabelle=gs040001%7C%7C. Date of Access: 15.09.2023

Thüringer Landesamt für Statistik TLS. (2022). Bestand an Wohnungen in Thüringen im Jahr 2021. Erfurt. Retrieved from: https://statistik.thueringen.de/presse/2022/pr_133_22.pdf. Date of Access. 12.09.2023

Wesselak, V. (2023). Entwicklung des Thüringer Energiebedarfs bis 2045. Nordhausen. Retrieved from: https://github.com/in-RET/Prosumer-load-profile. Date of Access. 04.10.2023

Wirtz, M. (2023). nPro: A web-based planning tool for designing district energy system and thermal network. Energy, 126575, 2023. DOI: 10.1016/j.energy.2022.126575.

MOSES – The New Techno-Economic Optimization Modeling Tool for Hybrid Solar Power Plants

Salvatore Guccione[1] and Rafael Guedez[1]

[1] KTH Royal Institute of Technology, Stockholm (Sweden)

Abstract

Techno-economic performance simulations play a crucial role in assessing the feasibility, cost-effectiveness, and overall impact emerging renewable energy system designs. Concentrating Solar Power (CSP) is a promising technology for decarbonizing the electricity grid by integrating cost-effective thermal energy storage (TES). However, their development is hindered by their high levelized cost of electricity compared to other energy sources. Hybrid systems that connect with solar photovoltaic (PV) and battery systems are a viable solution to reduce the cost of these plants while maintaining flexibility and guaranteeing firm production despite the intermittence of solar availability. This paper presents MoSES (Modeling of Solar Energy Systems), an open-source techno-economic modeling tool designed to evaluate the feasibility and cost-effectiveness of hybrid PV-CSP plants. While existing simulation tools perform well with established systems, they face challenges when adapting to new components, configurations, and operating strategies. MoSES addresses this challenge by providing a simulation framework and a versatile library of components and control strategies that can be modified to meet end-users' needs. The tool enables simulation activities to assess the advantages, optimize the design, and benchmark different hybrid PV-CSP plant layouts. This paper outlines the methodology employed to determine system design, costs, and key performance indicators, as well as to estimate operational performance. Furthermore, a case study is presented to illustrate MoSES's effectiveness as a tool for conducting annual simulations despite being in its early stages of development. MoSES provides a valuable contribution to the solar community by enabling the evaluation of the impact of emerging solar-based system designs.

Keywords: Solar Energy, CSP, PV, Hybridization, Simulation Tool, Open-Source, Techno-economic Optimization

1. Introduction

Techno-economic performance simulations play a vital role in evaluating the feasibility, cost-effectiveness, and overall impact of emerging renewable energy system designs. Among renewable energy sources, solar energy stands out as the most abundant worldwide. Solar Photovoltaic (PV) and Concentrating Solar Power (CSP) are two distinct technologies used to harness solar energy for electricity generation. The integration of cost-effective Thermal Energy Storage (TES) has made CSP a promising technology for decarbonizing the electricity grid (IRENA, 2020). However, the heigh levelized cost of electricity associated with CSP plants has limited their development in comparison to alternative renewable energy systems. To enhance the cost competitiveness of CSP systems, various options and pathways have been identified. Hybrid systems that combine CSP with PV and battery systems offer a viable solution to reduce costs while maintaining flexibility and ensuring consistent electricity production despite solar availability fluctuations. Developing efficient and dependable electric heaters becomes crucial to maximize current advantages and enhancing the flexibility of hybrid PV-CSP plants. These heaters serve the purpose of converting PV-generated electricity into heat, subsequently storing it within the TES system of the CSP facility. This endeavor enables an active hybridization that facilitates the exchange of energy flows between the two plants (Guccione & Guedez, 2023). Hybridizing CSP and solar PV can lower costs by up to 25% compared to a CSP-only plant of the same size, depending on the hybridization strategy (Zurita et al., 2018). Additionally, increasing the operating temperature of the system by exploring new Heat Transfer Fluids (HTFs) and power cycles can further improve the economic feasibility of CSP plants. Integrating a compact and efficient supercritical CO_2 (sCO2) power block into CSP plants can increase deployment and overall thermal efficiency, resulting in lower electricity production costs. To determine the most cost-competitive pathway for different locations, scales, meteorological conditions, and electrical markets, robust and customizable techno-economic performance simulations are essential. This study introduces MoSES (Modeling of Solar Energy Systems), an open-source techno-economic modeling tool designed to assess the feasibility and cost-effectiveness of hybrid PV-CSP plants. Among the available tools, the System Advisor Model (SAM) emerges as one of the most extensively used options (National Renewable Energy

10.18086/swc.2023.08.02 Available at http://proceedings.ises.org

Laboratory (NREL), 2022). SAM serves as an open-source instrument primarily designed for assessing the operational and financial feasibility of solar PV and CSP plants. However, it is important to note that SAM's current functionalities do not encompass the simulation of hybrid systems or the incorporation of user-defined components. Another open-source tool catering to the modeling of CSP plants is SolarTherm (Scott et al., 2017). This tool offers a platform for simulating unconventional designs and conducting annual performance simulations of systems, including all main components. SolarTherm's applicability extends beyond CSP systems; it is designed to support various applications such as solar fuels, solar metallurgy, and Concentrated Solar Thermal (CST) industrial process heat. While SAM and other existing simulation tools perform well for established systems, they face challenges when adapting to new components, configurations, and operating strategies. MoSES overcomes this challenge by providing a simulation framework and a versatile library of components and control strategies that can be tailored to meet the specific needs of end-users. The tool facilitates simulation activities to evaluate advantages, optimize designs, and compare different hybrid PV-CSP plant layouts. This paper outlines the methodology employed to determine system design, costs, key performance indicators, and estimated operation. Additionally, a case study is presented to demonstrate the effectiveness of MoSES as a tool for conducting annual simulations, despite being in its early stages of development. MoSES makes a valuable contribution to the solar community by enabling the evaluation of the impact of emerging solar-based system designs.

2. Solar Energy System Description

An illustration of a hybrid PV-CSP plant that can be modeled using MoSES is depicted in Figure 1. This hybrid plant is characterized by a state-of-the-art PV plant and a central tower CSP system that utilizes molten salt as the HTF. It incorporates a two-tank TES and employs a sCO_2 Brayton power block for power generation. The electricity generated by the PV system is converted from DC to AC using an inverter and then transmitted to the grid. Another option is to store the electricity directly into a Battery Energy Storage System (BESS). Alternatively, the excess electric power generated by the PV field can be converted into thermal power by utilizing a molten salt electric heater, which allows for its storage in the TES system. On top of the tower, a tubular molten salt receiver is placed to convert the power collected by the heliostat field into thermal power with operating temperatures ranging between 295 and 565 °C (Turchi et al., 2019). The molten salts are stored in a two-tanks TES that decouples the sCO_2 power block electricity production from the intermittent solar-based heat production. During the TES discharge phase, the molten salts flow in a molten salt-to-sCO_2 heat exchanger, guaranteeing a Turbine Inlet Temperature (TIT) of 550 °C. Likewise, the BESS is discharged when it becomes advantageous to supply electricity to the grid.

3. Modeling Tool

MoSES is a Python-based modeling tool, developed by KTH Royal Institute of Technology to estimate the techno-economic performance of hybrid PV-CSP power plants. A representation of the modeling methodology's flowchart is presented in Figure 2. The thermodynamic performance of the plant is estimated interconnecting the sub-systems quasi-steady-state models and integrating a CoolProp environment (Bell et al., 2014) to estimate the properties of the fluids involved in the plant. Moreover, the NREL-PySAM wrapper for System Advisor Model (SAM) (Gilman et al., 2019) has been integrated into MoSES for designing the solar field and PV plant. The techno-economic performance of the system model is estimated by combining the thermodynamics with an economic model based on a bottom-up estimation method. The resulting system model is customizable in terms of location (meteorological data, grid availability, electricity market, and economics of location), design assumptions, and dispatch strategy.

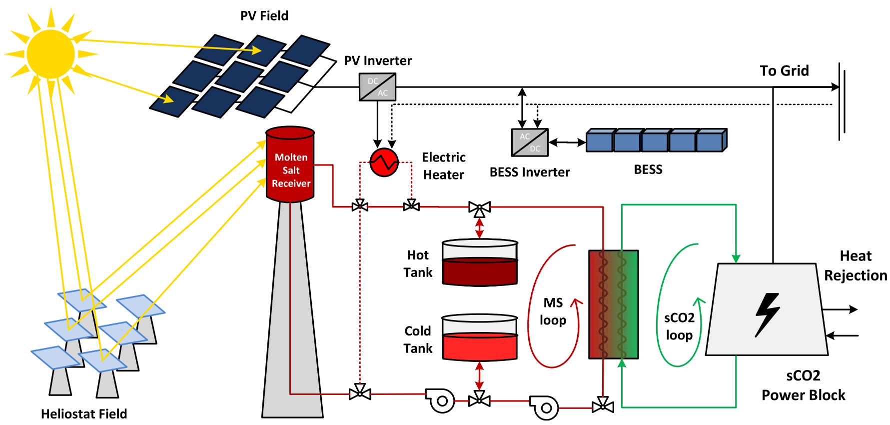

Fig. 1: Hybrid PV-CSP plant schematic layout

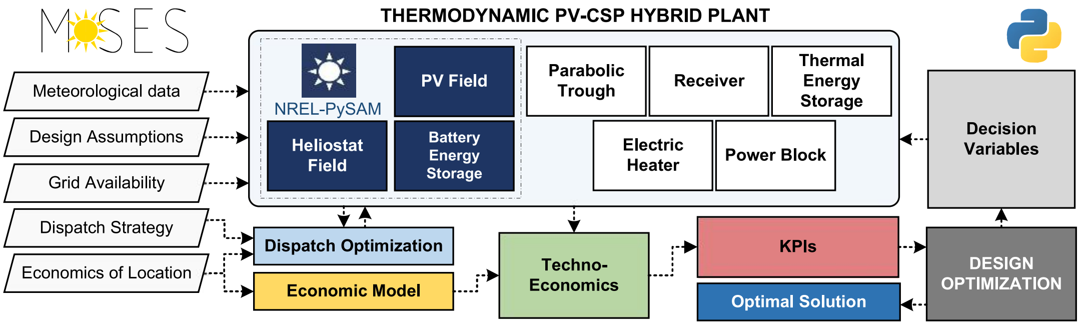

Fig. 2: MoSES modeling methodology flowchart

To identify an optimal design of these hybrid solar plants a multi-objective optimization problem has been implemented so that a set of decision variables can be suggested to minimize/maximize user-selected objective functions such as Levelized Cost of Electricity (LCOE), Hybrid Capacity Factor (H-CF), Capital Expenditure (CAPEX), Annual Energy Yield (AEY), and maximum profit.

3.1 Definition of the system design

Figure 3 presents the outlined approach for defining the design of a specific solar power plant. Initially, the power block design is established by considering various inputs such as gross power, design temperatures and pressures, as well as component efficiencies and effectiveness. Design outputs from the power block model include overall efficiency, required thermal power, mass flow rate, and component size. Simultaneously, the receiver and heliostat field designs are determined. The receiver model takes into account factors such as the heat transfer fluid, design temperatures, and aspect ratio, and based on the solar multiple and thermal power required by the power block, estimates the receiver size, thermal efficiency, and mass flow rate. Subsequently, the heliostat field is designed to ensure the necessary incident power on the receiver, considering user-defined heliostat optical properties. The design of the field impacts the tower height and receiver size, which are iteratively adjusted until convergence. As design outputs for the heliostat field, the solar field area, design optical efficiency, and tower height are provided. Additional inputs are necessary to describe the TES system, including the storage medium, number of TES hours, design temperatures, and tank aspect ratio. The storage model computes the size of the tank(s) capable of storing the maximum amount of energy and determines the thermal losses at the design point. If the CSP plant is integrated with PV or connected to the grid using an electric heater, the electric heater model needs to be customized with specific parameters such as the medium, nominal electric power input, design efficiency, and temperatures. The expected outputs consist of the nominal heat duty, design thermal losses, and mass flow rate. If a PV plant with BESS is co-located or hybridized with the CSP plant, a PV field, an inverter, and a BESS model are incorporated. The PV plant is fully characterized based on the type of PV module, AC nominal power, DC-AC ratio, ground coverage ratio, inverter efficiency, hours of BESS and installed BESS power.

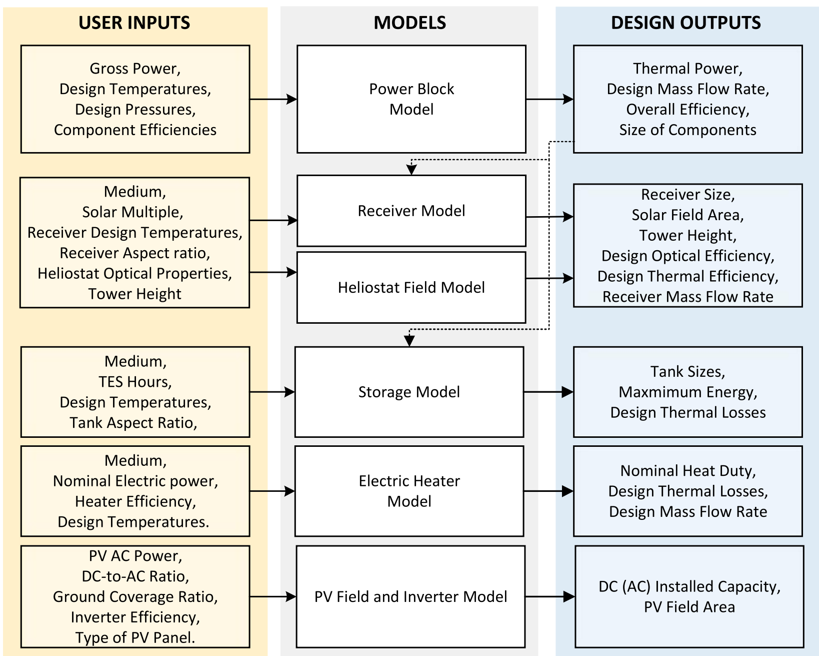

Fig. 3: Schematic representation of the definition of the system design

3.2 Definition of the system costs

In this section, the methodology employed to determine the system costs and the user inputs that can be utilized to tailor the cost model is presented. Specifically, the user can provide component reference costs, as well as financial assumptions including the real discount rate, interest rate, contingency, Engineering Procurement and Construction (EPC) costs, and decommissioning share of the capital cost. Using the design outputs and the specified financial assumptions, the cost model calculates the costs of the subsystems and provides an overall cost estimation, as depicted in Figure 4.

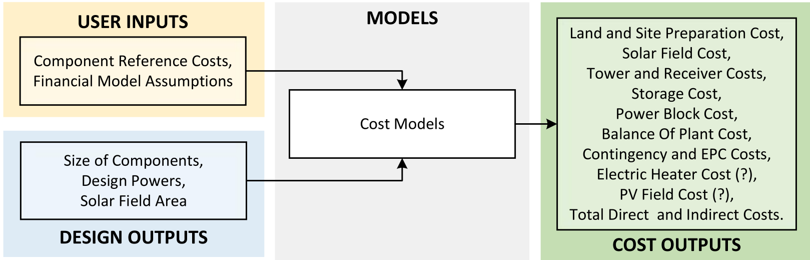

Fig. 4: Schematic representation of the definition of the system costs

3.3 Estimation of the system operating performance

This section presents the methodology employed to estimate the operational outputs of the solar power plant at each time step. For a specific location, the user can choose or supply a weather file, which contains location-specific variables such as irradiance, ambient temperature, and wind speed. These variables are vital in assessing the energy generation potential of both the PV and CSP components, as well as in evaluating the overall performance of the plant. In addition to considering weather-related factors, a dispatch strategy can be selected to determine the plant's operation. If applicable, the strategy can prioritize PV production, align with a user-defined load profile, or be designed to harmonize with a specific tariff scheme. This dispatch strategy selection plays a significant role in optimizing the utilization of the hybrid PV-CSP system based on the prevailing pricing structure or user requirements. The operational performance of the hybrid PV-CSP plant is determined by solving an optimization problem. The objective of this problem is to maximize revenues under a tariff scheme, minimize energy waste, or maximize energy injected into the grid. This problem was solved by adopting a Mixed Integer Linear Programming (MILP) approach. By utilizing the MILP approach, the operational strategy for the plant is derived as an output, providing guidance for its efficient and effective operation. An example of the daily operation of the power plant is presented in Figure 5. The figure showcases key variables, including the raw PV production (black line), the PV production supplied to the grid (yellow area), the State Of Charge (SOC) of the TES (red dashed line), and the CSP production contributed to the grid (blue area). In this case, the objective of the dispatch strategy is to maximize the electricity injected into the grid. The hybrid solar power plant presented in section 2 is characterized by an oversized PV field and a 12h TES. When the PV output exceeds the grid's maximum injectable capacity, surplus electricity is converted into thermal energy via the electric heater and stored in the TES. The CSP plant's power cycle generates electricity to bridge the gap between PV production and the maximum injectable grid power.

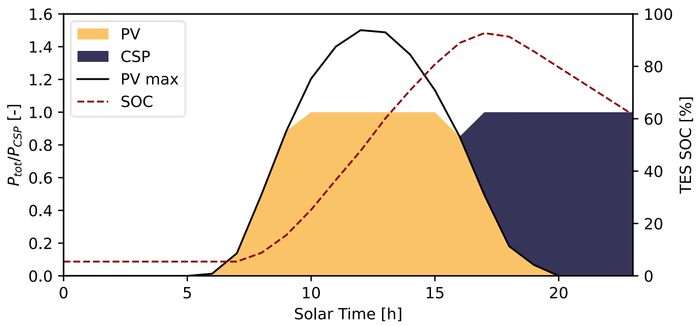

Fig. 5: Schematic representation of the estimation of the system performance

Figure 6 shows that, considering these inputs and based on the design outputs estimated in section 3.1, the subsystem models estimate the operational outputs. Specifically, the sun model extracts Direct Normal Irradiance (DNI), ambient temperature, and wind speed from the weather file and calculates solar angles such as solar elevation and azimuth angles. The user-defined control strategy characterizes the dispatch control model, which takes as inputs the subsystem designs, DNI, solar elevation, SOC of the TES, and PV production (if applicable). It defines the operation of the solar field and determines the mass flow rate of the receiver, electric heater, and power block. Based on the control outputs and DNI values, the heliostat field model estimates the incident power on the receiver, the optical efficiency, and the losses. The receiver model takes the inputs from the controller and the solar field and calculates the thermal power output, operating temperatures, and thermal losses. Similarly, the electric heater estimates the thermal power output, operating temperatures, and thermal losses based on the dispatch control output that interacts with the PV field. Based on the controller outputs and the ambient temperature, the power block model calculates the net electric output, the operating efficiency, and the parasitic losses. The storage model updates the SOC of the TES based on the inlet and outlet mass flow rate, as well as the average temperatures of the tanks and the related thermal losses.

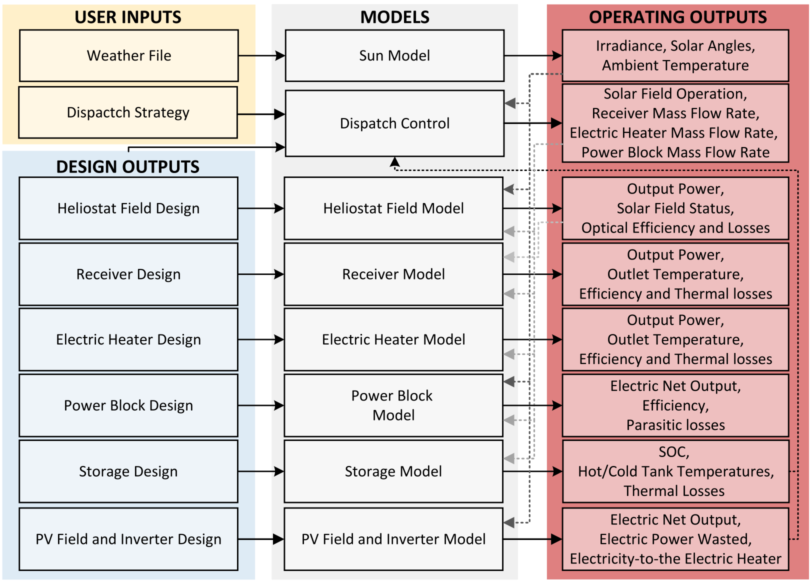

Fig. 6: Schematic representation of the estimation of the system performance

3.4 Definition of the Key Performance Indicators

This section outlines the methodology employed in MoSES to calculate the key performance indicators (KPIs) necessary for benchmarking and comparing different types of CSP plants, including hybrid PV-CSP, PV-CSP with BESS, and various hybridization configurations with the grid. Figure 7 illustrates that, based on specific design, cost, and operational outputs, the model generates the relevant KPIs as outputs for the user's analysis. For independent systems, conventional design variables and performance indicators have been extensively standardized for both CSP (Hirsch & et al., 2017) and PV systems (Stein & et al., 2017). However, these design and performance indicators are insufficient for capturing the complexity and interdependent nature of PV-CSP hybrid systems.

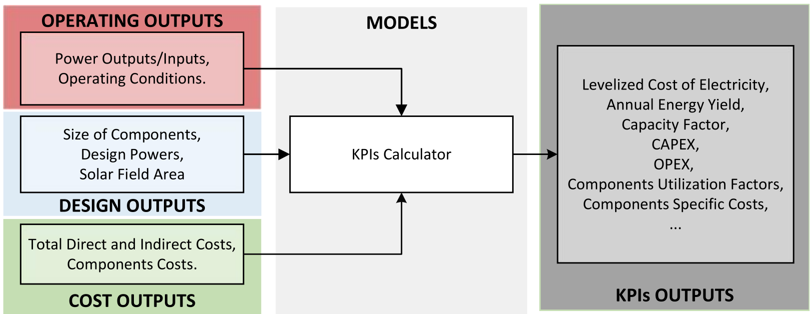

Fig. 7: Schematic representation of the definition of the key performance indicators

Hence, MoSES introduces new Key Design Indicators (KDI) and KPIs specifically tailored for hybrid plants. The newly defined design indicators in MoSES include the Hybrid Solar Multiple (HSM), which compares the total thermal power generated by the solar field (Q_{MSR}^{nom}) and the electric heater (Q_{EH}^{nom}) to the thermal power demand at the power block (P_{PB}^{nom}) as shown in equation (1). Additionally, the Storage Capacity Ratio (SCR), defined in equation (2), represents the ratio between the capacity of the BESS (E_{BESS}) and the equivalent electricity capacity of the TES system ($E_{TES} \cdot \eta_{PB}^{nom}$). To examine the relationship between installed capacities, a Nominal Power Ratio (NPR) is introduced in equation (3), which compares the installed capacity of PV (P_{PV}^{nom}) with the net capacity of CSP ($P_{CSP,net}^{nom}$). Furthermore, the Thermal Production Ratio (TPR), defined in equation (4), measures the ratio between the thermal production through the electric heater ($\dot{Q}_{EH}^{nom}$) and the thermal production of the solar receiver (Q_{MSR}^{nom}). To consider the relative sizes of the PV and BESS in relation to the occupied area of the CSP, the Aperture Ratio (AR) is introduced in equation (5). This metric provides a measure of the footprint of the PV and BESS compared to the area utilized by the CSP component. Additionally, the Irradiance Ratio (IR) is defined as the ratio between the annual Global Horizontal Irradiance (GHI) and the annual Direct Normal Irradiance (DNI) for a specific location. This ratio offers insights into the relative levels of solar irradiance available at the location, providing valuable information for evaluating the energy potential of the system.

$$HSM = (Q_{EH}^{nom} + Q_{MSR}^{nom})/P_{PB}^{nom} \tag{1}$$
$$SCR = E_{BESS}/(E_{TES} \cdot \eta_{PB}^{nom}) \tag{2}$$
$$NPR = P_{PV}^{nom}/P_{CSP,net}^{nom} \tag{3}$$
$$TPR = \dot{Q}_{EH}^{nom}/Q_{MSR}^{nom} \tag{4}$$
$$AR = (A_{PV} + A_{BESS})/A_{CSP} \tag{5}$$
$$IR = \sum_{n=1}^{N} GHI_n \,/ \sum_{n=1}^{N} DNI_n \tag{6}$$

In addition to the aforementioned KDIs, MoSES incorporates several important KPIs. The Annual Energy Yield (AEY) is a key indicator calculated as the cumulative electricity production of the CSP, PV, and BESS components over the course of a year, as represented by equation (7). The Hybrid Capacity Factor (HCF) is another significant metric that measures the ratio between the AEY supplied to the grid and the total annual electric load, which is considered as the maximum injectable energy to the grid. This ratio is derived from equation (8). To assess the contribution of CSP to the total electricity production of the hybrid plant, the Electricity Production Ratio of CSP (EPR_{CSP}) is defined by equation (9). This metric quantifies the impact of CSP production on the overall electricity generation of the hybrid system. Furthermore, the Storage Electricity Fraction (SEF) is introduced as the ratio between the electricity production discharged from the TES and BESS and the AEY, as presented in equation (10). This KPI offers an indication of the portion of electricity production supplied by the storage systems in relation to the total annual energy yield. Lastly, the electric heater utilization factor (UF_{EH}), defined by equation (11), measures the ratio between the annual thermal energy production of the electric heater and the maximum energy that could have been produced if it operated continuously at nominal capacity.

$$AEY = \sum_{n=1}^{N} P_{CSP,n}^{net} + P_{PV,n}^{grid} + P_{BESS,n}^{dis} \tag{7}$$
$$HCF = AEY / \sum_{n=1}^{N} P_{load,n}^{grid} \tag{8}$$
$$EPR_{CSP} = \sum_{n=1}^{N} P_{CSP,n}^{net} / AEY \tag{9}$$
$$SEF = \left(\sum_{n=1}^{N} \dot{Q}_{TES,n}^{dis} \cdot \eta_{PB,n} + P_{BESS,n}^{dis}\right)/AEY \tag{10}$$
$$UF_{EH} = \sum_{n=1}^{N} Q_{EH,n}^{out} \,/ \sum_{n=1}^{N} Q_{EH,n}^{nom} \tag{11}$$

The LCOE serves as an indicator of the hybrid plant's relative profitability and is influenced by the investment cost (CAPEX), operational cost (OPEX), and the AEY.

$$LCOE = (CAPEX \cdot CRF + OPEX)/AEY \tag{12}$$

where CRF is the Capital Recovery Factor, calculated in (13) as a function of the real discount rate (r) and the lifetime of the plant (N). The real discount rate is defined in (14) for a nominal discount (d) and an interest rate (i).

$$CRF = r \cdot (1 + r)^N/((1 + r)^N - 1) \tag{13}$$
$$r = (1 + d)/(1 + i) - 1 \tag{14}$$

3.5 System optimization setup

This section presents the methodology employed for optimizing a hybrid PV-CSP system. Figure 8 illustrates the workflow, where the optimizer receives user-defined inputs such as the ranges of design variables and the objective function(s) to be maximized or minimized. The objective function(s) can be selected from a set of predefined KPIs, including LCOE, HCF, and CAPEX, among others. To solve the single- or multi-objective optimization problem, a Genetic Algorithm is utilized. This algorithm, inspired by natural selection and genetics, employs evolutionary strategies to obtain a set of tradeoff optimal solutions (J.F. et al., 2010). The optimization problem is implemented using either the *scipy.optimize.differential_evolution* algorithm, which is a simple and efficient heuristic for global optimization (Storn & Price, 1997) or the *Pymoo* framework (Blank & Deb, 2020). The algorithm follows a modified survival selection approach based on the general outline of NSGA-II (Deb & Sundar, 2006). The optimizer iterates through a loop, interacting with the system model. It provides a set of single values for the design variables and obtains the corresponding plant design, cost, operating parameters, and KPIs for each input combination. The system model incorporates user-defined financial and design parameters. Based on the user-specified objective function(s), the optimizer delivers the optimal configuration of the hybrid PV-CSP system as the output of the optimization.

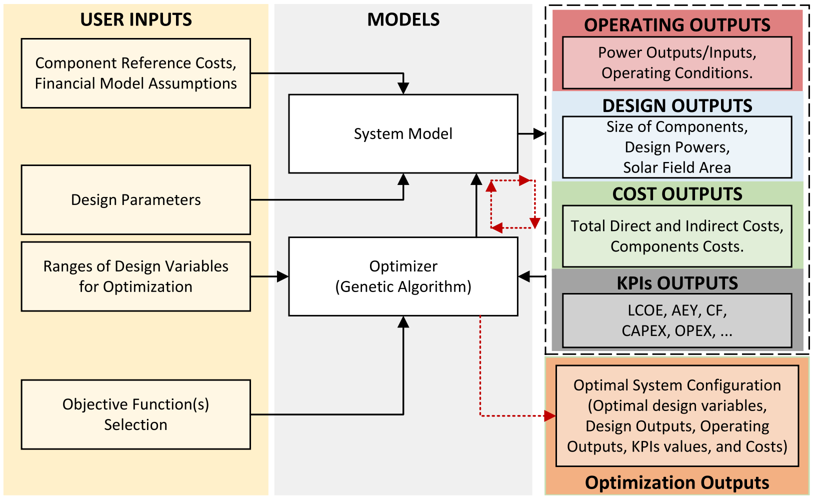

Fig. 8: Schematic representation of the definition of the key performance indicators

4. Techno-economic analysis results - case study

This section presents an example of the results achievable through the utilization of MoSES on the system outlined in Section 2. The design of the molten salt based hybrid PV-CSP plant was identified by solving a multi-objective optimization problem, with the goal of minimizing the LCOE and maximizing the HCF of the plant. To begin with, the hybrid solar plant was optimized adopting as location Evora, Portugal (38.5°N, -8.0°E), with a CSP capacity of 100 MW_e, serving as the base-case scenario. Evora is characterized by an annual DNI of 2000 kWh/m^2/year and an annual Global Horizontal Irradiance (GHI) of 1800 kWh/m^2/year. Then, to explore the scale effect on the techno-economic performance, a CSP capacity of 10 MW_e was implemented at the same location (Evora). This specific size was chosen to emphasize the inherent scalability potential of sCO_2 power blocks and evaluate their ability to enhance the cost competitiveness of CSP, even at smaller scales. Lastly, the impact of location was analyzed for a 100 MW_e plant situated in Likana, Chile (-22.7°N, -68.6°E), with an annual DNI of 3500 kWh/m^2/year and an annual GHI of 2600 kWh/m^2/year.

Figure 9 shows the results of the techno-economic optimization conducted on the hybrid PV-CSP plant for the two different scales and locations. The figure represents the optimal tradeoff between the minimum LCOE and the maximum HCF. The color bar shows the impact of the NPR. The results reveal that higher NPR ratios correspond to greater HCFs, surpassing 70%, albeit with a slight increase in LCOE. Conversely, smaller NPR ratios result in relatively lower HCFs and higher LCOEs. This underscores the significance of hybridizing these technologies: low-cost PV systems enhances the cost-competitiveness of CSP, while the dispatchability of CSP enables achieving high capacity factors and firm electricity production.

For the Portuguese location, the NPR range that minimizes the LCOE of the 100 MWe plant is between 1.9 and 2.1. The optimized configuration achieves a minimum LCOE of 66 EUR/MWh with an HCF of 78%. When considering the smaller scale of 10 MW, the hybrid plant is characterized by a minimum LCOE of 96.6 EUR/MWh (50% higher compared to the larger-scale scenario), alongside a HCF of 70%. This minimum LCOE is obtained at NPR around 2.5, indicating that the integration of PV becomes even more impactful at smaller capacities due to economies of scale. Indeed, despite the reduction in overall plant size, which lowers the total CAPEX, the specific costs associated with central tower CSP rise due to the scale effect and fixed expenses related to non-modular components such as the tower, heliostat field, TES, and power block. These findings underscore the competitive cost of hybrid PV-CSP systems, even at small scales and in a favorable European location. Moreover, at 10 MWe, higher NPR ratios are preferred, signifying a more relevant role of the electric heater in the system.

Regarding the impact of location, Figure 9 illustrates how higher solar resource availability leads to improved system performance, characterized by elevated HCFs and reduced LCOEs. The minimum attainable LCOE reaches 46.5 EUR/MWh, aligning with an 85% HCF. In Likana, owing to enhanced solar availability and a higher DNI/GHI ratio of 1.3, the optimal systems exhibit lower NPRs compared to the base-case scenario situated in Evora. This higher DNI/GHI ratio signifies that in Likana, CSP becomes more efficient than PV in harnessing the solar resource. The NPR ratio that minimizes the LCOE is less than one (0.9), resulting in CSP contributing to 71% of the total production share, without an excess of PV generation. Consequently, the electric heater is not a part of the optimal design. In comparison to the Evora-based plant, CSP assumes a more prominent role in Likana, both in terms of capacity and electricity generation.

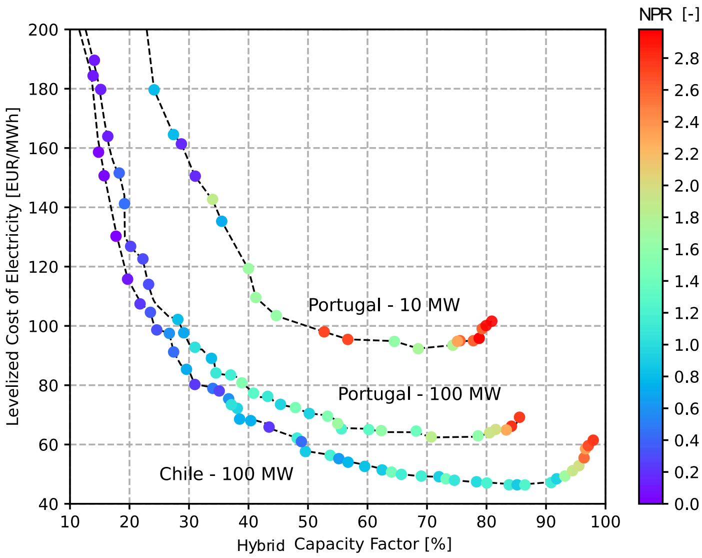

Fig. 9: Techno-economic optimization results for two locations (Portugal - Chile) and scales (10 - 100 MW_e)

5. Conclusions

In this study, a new tool called MoSES (Modeling of Solar Energy Systems) has been introduced. This tool aims to facilitate the evaluation and advancement of innovative solar power plants with energy storage for firm electricity production through simulation activities. MoSES offers a comprehensive platform for designing, optimizing, and benchmarking various solar plant configurations tailored to different locations, sizes, and electricity markets. The tool incorporates pre-defined system models, including sCO_2 power blocks and hybridization with state-of-the-art PV plants and BESS, enabling users to perform techno-economic optimizations, sensitivity analyses, and annual performance simulations. MoSES allows also for the integration and interconnection of existing component models, thereby expanding its capabilities. The modeling approach employed to simulate and optimize the performance of solar hybrid systems has been described, with a specific focus on system design, costs, and expected performance. Furthermore, new KPIs and KDIs specifically designed for hybrid solar power plants have been introduced, providing users with flexibility in selecting objective functions for system optimization. The inputs that can be customized by the user and the expected outputs for the design, operation, cost, and optimization of the system model have been presented.

As a case study, a techno-economic optimization has been conducted using MoSES on a hybrid PV-CSP system layout with molten salt thermal energy storage and a sCO_2 power block. The results demonstrate that integrating sCO_2 power blocks and actively hybridizing with PV can make CSP cost-competitive at both large (<66 EUR/MWh) and small scales (89 EUR/MWh). The study revealed high hybrid capacity factors (>70%), underscoring the role of such hybrid plants in the energy market by providing dispatchable and flexible generation. For European locations with a DNI of 2000 kWh/(m^2-yr), small-scale systems exhibited significant gaps between PV and CSP capacities (NPR > 2.3), allowing for the integration of electric heaters. In locations with abundant solar resources (3500 kWh/(m^2-yr)), electricity production was primarily driven by CSP, with system designs featuring an NPR ratio below 1. Under these conditions, the integration of electric heaters was unnecessary.

The MoSES tool shows to be promising in its early stages of development for simulating hybrid PV-CSP solar power plants. However, to ensure its reliability and effectiveness, there is a need for further refinement and validation efforts. To hinder the accessibility and user friendliness of MoSES, future efforts need to concentrate on the development of a Graphical User Interface (GUI) and the provision of comprehensive documentation. Indeed, the absence of a GUI may discourage some users from engaging with the tool, potentially limiting its adoption and applicability. Moreover, MoSES is slated for additional improvements, including the incorporation of innovative system models designed to evaluate the benefits of next-generation hybrid PV-CSP plants and explore avenues for enhancing CSP's cost-competitiveness. Validation of conventional component models of the hybrid PV-CSP plant has been accomplished through cross-referencing with established models verified against actual power plants. However, emerging technologies such as sCO_2 power block components, high-temperature electric heaters, storage, and receivers still in experimental stages, introduce uncertainties due to the lack of real-world data for validation. To counteract this, correlations derived from inputs provided by industrial partners in different research projects have been formulated and implemented for these low Technology Readiness Level (TRL) components not yet integrated into real power plants. The validation and refinement of these pivotal component models will be executed using real-

world data gathered from demonstrations and research projects that underscore the feasibility of these components. While MoSES boasts accessibility and transparency as an open-source Python-based tool, its necessitates ongoing updates to accommodate new language versions and associated libraries. Neglecting to ensure compatibility with the latest versions of included libraries could result in performance glitches.
In conclusion, the MoSES tool holds promise as a valuable resource for simulating hybrid PV-CSP solar power plants. Addressing these challenges will be instrumental in enhancing the tool's reliability and its ability to provide accurate insights for the advancement of hybrid solar power systems.

6. Acknowledgments

The authors acknowledge the financial support from the European Union’s Horizon 2020 research and innovation program, project No. 952953.

7. References

Bell, I. H., Wronski, J., Quoilin, S., & Lemort, V. (2014). Pure and pseudo-pure fluid thermophysical property evaluation and the open-source thermophysical property library coolprop. *Industrial and Engineering Chemistry Research*, *53*(6), 2498–2508. https://doi.org/10.1021/ie4033999

Blank, J., & Deb, K. (2020). Pymoo: Multi-Objective Optimization in Python. *IEEE Access*, *8*, 89497–89509. https://doi.org/10.1109/ACCESS.2020.2990567

Deb, K., & Sundar, J. (2006). Reference point based multi-objective optimization using evolutionary algorithms. *GECCO 2006 - Genetic and Evolutionary Computation Conference*, *1*, 635–642. https://doi.org/10.1145/1143997.1144112

Gilman, P., Janzou, S., Guittet, D., Freeman, J., DiOrio, N., Blair, N., Boyd, M., Neises, T., Wagner, M., & USDOE Office of Energy Efficiency and Renewable. (2019). *PySAM (Python Wrapper for System Advisor Model ‘SAM’)*. USDOE Office of Energy Efficiency and Renewable Energy (EERE). Renewable Power Office. Solar Energy Technologies Office. https://doi.org/10.11578/dc.20190903.1

Guccione, S., & Guedez, R. (2023). Techno-economic optimization of molten salt based CSP plants through integration of supercritical CO2 cycles and hybridization with PV and electric heaters. *Energy*, *283*, 128528. https://doi.org/https://doi.org/10.1016/j.energy.2023.128528

Hirsch, T., & et al. (2017). SolarPACES Guideline for Bankable STE Yield Assessment. In *IEA Technology Collaboration Programme SolarPACES, Tabernas*.

IRENA. (2020). Renewable Power Generation Costs in 2020. In *International Renewable Energy Agency*.

J.F., K., K., W., C.L., N., & M.J, S. (2010). Genetic Algorithms and Their Application to In Silico Evolution of Genetic Regulatory Networks. In *Computational Biology. Methods in Molecular Biology (Methods and Protocols), vol 673*. Humana Press. https://doi.org/https://doi.org/10.1007/978-1-60761-842-3_19

National Renewable Energy Laboratory (NREL). (2022). *System Advisor Model Version 2022.11.29 (SAM 2022.11.21)*.

Scott, P., Alonso, A. D. L. C., Hinkley, J. T., & Pye, J. (2017). SolarTherm: A flexible Modelica-based simulator for CSP systems. *AIP Conference Proceedings*, *1850*(June 2017). https://doi.org/10.1063/1.4984560

Stein, J. S., & et al. (2017). PV Performance Modeling Methods and Practices. In *Report IEA-PVPS T13-06:2017, IEA Photovoltaic Power Systems Programme*.

Storn, R., & Price, K. (1997). Differential Evolution – A Simple and Efficient Heuristic for global Optimization over Continuous Spaces. *Journal of Global Optimization*, *11*(4), 341–359. https://doi.org/10.1023/A:1008202821328

Turchi, C. S., Boyd, M., Kesseli, D., Kurup, P., Mehos, M., Neises, T., Sharan, P., Wagner, M. J., & Wendelin, T. (2019). CSP Systems Analysis - Final Project. *Nrel/TP-5500-72856, May*.

Zurita, A., Mata-Torres, C., Valenzuela, C., Felbol, C., Cardemil, J. M., Guzmán, A. M., & Escobar, R. A. (2018). Techno-economic evaluation of a hybrid CSP + PV plant integrated with thermal energy storage and a large-scale battery energy storage system for base generation. *Solar Energy*, *173*(July), 1262–1277. https://doi.org/10.1016/j.solener.2018.08.061

A Novel and Holistic Framework For The Selection of Performance Indicators To Appraise Photovoltaic Systems

C. Ramiah, K. Bangarigadu, T. Hookoom and Y. K. Ramgolam

University of Mauritius, Reduit (Mauritius)

Abstract

Most of the countries have targeted to increase the share of renewable energy projects to mitigate the adverse effects of climate change. Among all renewables, the photovoltaic (PV) technology has seen the most remarkable increase in the previous years with a global installed capacity of 1.63 TW in 2022. While expanding the installed capacity of PV technology is commendable, it is also essential to ensure that the PV systems are operating optimally. Such appraisal process not only warrants that the PV systems generation forecasts are met, but also ensures that the ratio of production to investment is as its peak. In this context, a novel and holistic framework for the selection of key performance indicators (KPIs) to assess PV systems is proposed in this study. The approach utilised in this research includes the identification and categorisation of KPIs. The latter were categorised into five groups namely: Intermittent Demand, Performance Assessment, IEC 61724 Standards KPIs, Financial Aspect and Environmental Benefits. In order to conduct a comprehensive evaluation of the financial viability and performance of PV systems, the selected list of KPIs can be computed and evaluated. This process will yield benchmark values that can be used to compare and assess the performance of PV systems to a given extent. In this optic a list of suggestions to guide stakeholders on the utilisation of the selected KPIs is also presented.

Keywords: Photovoltaics, Key performance indicators, Performance assessment

1. Introduction

As per REN 21 (2022), by the end of 2021, 166 countries have committed to increase their share of renewables and are massively investing to achieve the set targets with an aim to mitigate the impacts of climate change. Photovoltaic (PV) is now at the epicentre of the global ecological transition and it is the preferred choice of renewables to meet the renewable energy targets in all countries. The PV sector is expanding at an incredible rate with the global installed capacity increasing from 942 GW_p in 2021 (REN21, 2022) to 1.63 TW_p in 2022 (IRENA, 2023). Installation of photovoltaic energy systems is a commendable initiative, however more important is to ascertain that they are performing to the expected level such that the interest of all parties is not jeopardised. Several guidelines on how to maintain renewable energy and especially photovoltaic systems have been reported and even international standards have been developed by the International Electrotechnical Commission (IEC) for the performance monitoring, measuring, and analysing power and energy production from a PV system. However, there is no reported framework on how to select the key performance indicators (KPIs) and how to interpret the KPIs for assessing the reliability of PV systems. Several authors have used performance appraisal indicators to assess the effectiveness of PV installations in recent literature.

For instance, Seme *et al.* (2019) performed a review of the state-of-the-art PV systems in Slovenia and their performance analysis, which was then compared to other countries worldwide. In their review, the performance ratio was defined as the final yield and reference yield which depends mainly on the intensity of solar radiation and module temperature. These results showed that the performance of the PV systems primarily depended on the proper inclination and azimuth angles of the photovoltaic modules. The reported values for final yield, performance ratio and capacity utilisation factor were 1038 kWh $k^{-1}W_p^{-1}$, 68.84 % and 11.85 % respectively.On the other hand, Klise *et al.* (2017) implemented the standards described in IEC 61724 by means of software to quantify long term performance of PV systems in different climates. The methodology involved data processing, quality control, and the computation of performance metrics as well as the identification of system performance issues found through the analysis. During the investigation, the open-source software packages Pecos and PVLIB were utilised to analyse data collected from the Regional Test Center (RTC) program managed by Sandia National Laboratories (SNL) – a program that collects data across several sites in the United States. The system performance was evaluated at the sites using methods outlined in IEC 61724-4.

10.18086/swc.2023.08.05 Available at http://proceedings.ises.org

Additionally, Ameur *et al.* (2020) conducted an evaluation of the performance of PV systems by comparing the different PV technologies including monocrystalline, polycrystalline, and amorphous silicon (Si) systems. System efficiency, performance ratio, energy output, and capacity factor were computed using data over a period of 5 years. Their analysis revealed that polycrystalline-Si technologies perform better than both monocrystalline-Si and amorphous-Si technologies. The polycrystalline-Si technologies yielded the lowest levelized cost of energy (LCOE) of 0.10 USD $k^{-1}W^{-1}h^{-1}$. Moreover, a software simulated model of the system was developed and the simulated results were measured against the real values. The accuracy of the simulation was validated by means of statistical measures such as root mean square error and mean absolute percentage error. They also analysed and compared the performance of similar PV systems across Morocco using performance indicators including performance ratio (PR), system efficiency (η), and capacity factor (CF). The results showed that monocrystalline-Si has the highest annual average production followed by polycrystalline-Si and amorphous-Si. In 2016, Allouhi *et al.* conducted a performance, economic and environmental assessment of two grid-connected PV systems in Morocco. Reference yield, final yield, performance ratio, energy losses, capacity factor, overall system efficiency, levelized cost of electricity (LCOE) and payback period (PB) and annual avoided CO2 emissions were analysed. They reported that for similar rated systems, polycrystalline-Si modules had a better monthly yield than monocrystalline-Si modules. LCOE and payback period were found to be in the ranges of 0.073-0.082 USD $k^{-1}W^{-1}h^{-1}$ and 11.10-12.7 years, respectively. It was also reported that the installed PV systems could reduce around 5.01 tons of CO_2 emissions per year. Sharma and Goel (2017) monitored the results of a grid-tied 11.2 kW_p PV system between September 2014 and August 2015. PV module efficiency, array yield, final yield, inverter efficiency, performance ratio, capacity utilisation factor and energy losses including capture losses, thermal capture losses and miscellaneous capture losses of the systems were investigated.

In 2021, Anang *et al.* carried out the performance monitoring of a 7.8 kW_p grid-connected rooftop PV system under the feed-in-tariff system. Several performance parameters were assessed using the two-year production data for the period 2018-2019. PVSyst was used to find the optimal orientation and tilt angle of the system. The derating factor of the system was calculated from a two-day data collection which was then used to obtain economic indicators for the estimated system life cycle of 21 years. Performance indicators used included final yield, total energy losses, performance ratio, annual capacity factor and overall system efficiency. LCOE, capital recovery factor, and payback time were used as the economic indicators while the avoided CO_2 emission defined the environmental benefits. The overall system was found to have a payback time of 5-7 years, with a good long-term profit of RM 3,000 per year, while saving 136.5-156.5 tons of CO_2 over the project lifetime. In 2019, Ameur *et al.* performed a comparative analysis of key performance indicators for different photovoltaic technologies namely monocrystalline, polycrystalline, and amorphous silicon (Si) systems. Software solutions like Propre.ma was used in MATLAB to conduct this study. Parameters monitored included AC energy output, performance ratio, system efficiency and capacity factor. An economic analysis was also carried out to evaluate the LCOE of the three technologies. Results show that polycrystalline technology is the most cost-effective technology for the Ifrane region.

Taken together, a holistic PV system performance appraisal comprises several areas such as technical, financial, and environmental characteristics. The synthesis of existing literature revealed that the most used indicators in performance appraisal are efficiency, capacity factor, performance ratio, LCOE, payback time and avoided CO_2 emissions. However, the impact of certain key factors, such as temperature, are often overlooked. This suggests that this field is to be further explored and thus the need for further research. More so, it was also observed that the selection of the KPIs for the assessment of a given PV system mostly stood guided by common practice, rather than a systematic rationale or framework to follow. As such this study endeavours to propose PV stakeholders with a novel and holistic framework which will guide the selection and interpretation of KPIs for the appraisal of PV systems. Identification and categorization of key performance indicators (KPIs) was meticulously undertaken, leading to the development of a concise shortlist of KPIs specifically tailored to comprehensively assess the performance of solar PV systems. These selected KPIs encompass a spectrum of critical factors such as energy production efficiency, system reliability, financial viability, and environmental impact, offering a holistic framework to evaluate and benchmark PV system performance while simultaneously addressing sustainability concerns. This refined set of KPIs serves as a valuable tool for stakeholders in the PV industry, enabling them to make informed decisions, optimize system efficiency, and enhance the bankability of PV projects, thus advancing the adoption of renewable energy solutions. The paper organisation is as follows: Section 2 described the methodology employed, Section 3 presents and discusses the results obtained, and Section 4 provides a conclusion.

2. Methodology

The research has been conducted through a structured methodology encompassing several phases. In the initial phase, the research discusses the different types of PV systems, then focused on identification of KPIs pertinent to the appraisal of solar PV systems. Following this identification process, the KPIs were systematically categorized into five distinct groups. Subsequently, a set of guidelines was developed to aid in the selection of these KPIs. In order to conduct a comprehensive assessment of the overall effectiveness and the bankability of solar PV systems, it is necessary to computationally evaluate the following selected KPIs. In light of this perspective, a compilation of recommendations for the application of the guidelines was produced. This encompassed the identification of relevant PV datasets, along with the utilization of tools and methodologies to facilitate the modelling of solar PV systems. Consequently, the computed KPIs will therefore provide benchmark values which are able to facilitate a comparative analysis and assessment of the performance of PV systems.

2.1 Identification of KPIs

The research methodology for identifying the KPIs related to solar PV systems involved an extensive review of existing literature. This literature review encompassed a comprehensive exploration of scholarly articles, industry reports, international standards and relevant publications to compile a comprehensive list of PV system KPIs. This literature-based approach ensured a well-informed and comprehensive selection of KPIs, laying the foundation for a robust framework for assessing the performance and the bankability of solar PV systems.

2.2 Categorisation of identified KPIs

The identified KPIs were systematically categorized into five distinct groups, including Intermittent Demand, Performance Assessment, IEC 61724 Standards KPIs, Financial KPIs, and Environmental KPIs. This categorisation enhances the clarity and organization of the developed set of guidelines. These categories were established with the purpose of addressing the different aspects of solar PV systems. The Intermittent Demand category focused on metrics related to the variable nature of energy generation from PV systems, addressing issues such as energy demand fluctuations. Performance Assessment explored the KPIs that evaluated the overall efficiency and effectiveness of PV installations, including metrics related to energy production and system reliability. The inclusion of IEC 61724 Standards KPIs ensured adherence to industry standards and regulations, emphasizing the importance of compliance and quality assurance. The financial KPI category delved into metrics associated with the economic viability of PV systems, covering indicators like return on investment and cost analysis. Lastly, the Environmental KPI category considered indicators related to the environmental impact and sustainability of PV systems, acknowledging their role in reducing carbon emissions and promoting renewable energy adoption. This categorization facilitated a comprehensive evaluation of PV systems from various dimensions, enabling a more holistic assessment of their performance and significance.

2.3 Development of a set of guidelines for the selection of KPIs

The list of guidelines for the KPI selection was then developed, taking into account the unique characteristics and considerations of each category. These guidelines aimed to provide a framework for researchers and stakeholders to systematically select and apply KPIs that align with specific objectives and contexts within the realm of solar PV systems, ensuring a comprehensive and standardized approach to performance appraisal.

2.4 Utilisation of the selected KPIs

To effectively utilise the developed set of KPIs for assessing solar PV systems' performance, it is crucial to incorporate relevant solar PV system datasets. These datasets serve as the foundational source of information for evaluating overall system efficiency and productivity. They are essential for understanding how external factors influence solar PV output. The incorporation of performance metrics with actual meteorological data allows for a more precise evaluation of PV system performance under varying conditions. Furthermore, the use of PV system modelling techniques and tools enhances the assessment process by predicting performance, conducting financial analysis, and optimizing system design. A list of suggestions on the types of datasets which can be used along with modelling techniques is provided in the subsequent section.

3. Results and Discussions

3.1 Types of PV Systems

A PV system is a set of electrically interconnected equipment which may reliably convert solar power into electrical power and safely transfer the power to an electrical load in the most efficient and cost-effective manner. PV systems may be broadly categorised into grid connected and off grid systems. The grid connected systems may be further categorised into power optimiser-based systems, micro-inverter based systems, string inverter-based systems and central inverter-based systems. Furthermore, PV systems may be classified into small scale, medium scale and large scale projects. In the context of Mauritius, small scale systems are those with a capacity of less than 50 kW. Medium scale projects range between 50 kW to 2 MW. Large scale projects are those which are above 2 MW. For the sake of this several PV systems were identified in order to assess whether the proposed framework for performance appraisal may be applied to them based on their existing equipment. The performance of a PV systems is impacted by a number of factors such weather conditions, the environment surrounding the PV systems, the way the system has been physically deployed, the type of equipment used, the condition and age of the equipment and also on the way the system is maintained. It must be highlighted that the proposed framework for performance assessment of PV systems is not type specific and may be applicable to any type of PV systems.

3.2 Identification and Categorisation of KPIs

A performance assessment framework consists of detecting low performance in PV systems, investigating the causing factors and help in the setup of maintenance plans to minimise operational costs. The performance assessment of PV power systems is usually carried out by using different types of performance indicators that benchmark the output of these systems against the PV panel output at hypothetical operating conditions. The performance test condition or commonly known the Standard Testing Condition (STC) for the Solar PV systems refers to the reference values of the in-plane irradiance (G_{ref}) of 1000 Wm^{-2}, PV cell junction temperature, T_c of 25°C and air mass (AM) of 1.5 value to be used during the quality testing of any PV device (Ya'acob *et al.* 2014). Additionally, once PV systems are deployed, several other factors impact the expected solar PV performance, the production. Some of these factors include solar irradiance, temperature, and degradation rate (Vidyanandan, 2017). As described by the DOE (2021), PV module output decreases with temperature according to a temperature coefficient, δ, which is the percent reduction in power per degree Celsius above a reference temperature. PV module efficiency unavoidably degrades with age at a rate, of about 0.5% per year. Electrical losses will also occur throughout the balance of the system, which can be estimated. Failure rates are also higher in later years as the equipment ages, increasing downtime. Events such as severe weather can also impact PV system performance in unpredictable ways. A comparison of the system's actual output with the expected output can be used to quantify underperformance.

In this research, the IEC 61724 (2016) standard which outlines terminology, equipment and methods for performance monitoring and analysis of solar PV systems has been used and several research reports have been perused and scrutinised. Following the analysis of literature the KPIs are identified and grouped into several categories. The Intermittent Demand category focuses on metrics related to the variable nature of energy generation from PV systems. Performance ratio is used for evaluating the efficiency of solar PV systems. It can indicate the overall effect of losses on the rated PV capacity due to system inefficiencies such as cell temperature effects, BOS faults, and system downtime (Pless *et al.* 2005). The second KPI in this category is the plant availability factor (PAF). The plant availability factor is used to determine the time duration that PV systems are not operating. This metric is crucial as the availability factor of any PV system cannot be assumed or kept constant. In real time conditions, due to the limitations of system reliability, running interruptions or component failures, the generation ability and generation period are reduced giving a scope for quantifying actual availability time of PV system (Kumar *et al.* 2018).

The performance assessment category includes a set of indicators which broadly assess the electrical performance of a PV system over a period of time. To determine the installed power load factor, average power has to be calculated. It allows comparisons between monthly/quarterly or annual results of the same power plant, or it can be used to compare the generating units' performance within the same power plant. Similarly, the installed power load factor can be calculated on a monthly, quarterly or annually basis and indicates the availability of renewable resources and production capacity of the solar PV system. Also, it can indicate the degree of generating units or equipment's ageing. The installed power load duration can also be calculated as it is able to indicate the according number of operating hours which can be reduced considering only those daytime hours when the PV system is operating (Odeh, 2018). In order to ascertain the value of solar PV systems, the power factor is evaluated. The power factor of a PV system is the ratio between the system's actual power (kW) and apparent power (kVA) (GSES, 2015). When a PV system is producing energy, it mainly produces active power and feeds it directly to the load, hence decreasing the active power demand from the utility. While reactive power needed from the load remains the same. This will result in a reduction in the power factor at the point of grid connection which in turn can lead to penalties that need to be paid to the grid operator. Calculation of the power factor therefore indicates whether measures should be taken to prevent any penalty (Elghobashy, 2020).

The third category depicts the indicators provided in the IEC 61724 standard. Performance Ratio (PR), as defined by IEC61724 and NREL, is the most used metric, however one shortcoming of this indicator is that normal temperature variation influences are not taken into consideration (Odeh, 2018). Unlike the performance ratio, the performance index is not affected by temperature variations and has been considered. In order to use a metric which is more indicative of system condition rather than design or environmental conditions, compensation factors can be added to the basic performance ratio equation. Such a metric as defined by IEC61724 is the temperature compensated ratio (Walker & Desai, 2021). Additionally, yield is one of the most used performance metric for solar PV systems. It is used to compare different locations and to analyse different engineering designs. Rather than performance, yield is a measure of the system value (Tiwari & Sodha, 2006). The normalised efficiency of a solar PV system as a metric allows the monitoring of PV systems on time scales ranging from seconds to days and longer. It also permits an improved qualitative and quantitative comparison of PV systems with different power ratings in graphical displays and numerical calculations (Herteleer *et al.* 2017). One of the shortcomings of both the performance ratio (PR) and the normalised efficiency is that they are sensitive to temperature variations, as the change in temperature leads to a change in efficiency and power, and subsequently energy. The temperature corrected power and efficiency as defined by the IEC 61724 has also been included.

The fourth category is the Environmental KPI category. The details the fundamental KPIs which reflect the positive environmental impact of the installed PV systems. The avoided carbon dioxide emissions represent the amount of CO_2 which has been avoided per unit of electricity generated by the PV system. The equivalent number of trees planted indicates the number of mature trees planted in a tropical environment due to the avoided CO_2 and carbon sequestration in trees.

The last category is the Financial KPI category. It includes the internal rate of return (IRR), the payback period (PBP) and the levelised cost of electricity (LCOE), Net Present Value (NPV) and Return on Investment (ROI) as the main financial indicators. The IRR indicates the discount rate which would result into a zero net present value at the end of the contract period. The pay back period indicates the amount of time required to recover the intial investment. The LCOE is defined as the charge per kilowatt-hour (kWh) that equates the discounted present value of revenues to the discounted present value of costs, including the initial capital investment and annual operating costs as well as any future replacement capital costs incurred over the life of a facility (Tamburini *et al.* 2015). The NPV is used to determine the profitability of the investment over the lifetime of the solar PV project. It is calculated by finding the difference of the present value of cash inflow and the present value of cash outflow, discounted to the present time (Mazumdar and Rajeev, 2015) The return on investment evaluates the profitability and viability of a PV project's investment over its full term (Hoymiles, 2022).

Table 1: Description of Key Performance Indicators

SN	Key Indicator	Symbol	Unit	Formula
A	**Intermittent Demand**			
1	Performance Ratio PR_1 is the ratio between actual electricity production and theoretical production during a reference period where E_{AC} is the total output energy, E_{POA} is the energy per unit area of solar radiation, H_{STC} is the standard test conditions for solar irradiance, typically 1000 Wm^{-2} and P_{DC_STC} is the DC output power under STC (Zenhäusern, 2020)	PR_1	%	$PR_1 = \frac{E_{AC}}{E_{PoA}} \times \frac{H_{STC}}{P_{DC\,STC}}$ (eq. 1)

2	Plant Availability PA is the ratio of plant's Operating Time, OT and the PV plant's Net Available Time, NAT (Klise *et al.* 2016)	PA	%	$PA = \frac{OT}{NAT}$ (eq. 2)
B	**Performance Assessment**			
3	Average Power P_{avg} is the ratio between the produced energy, W and power plant's runtime, (t) depending on the yearly power plant operational time (Pearsall, 2016).	P_{avg}	W s^{-1}	$P_{avg} = \frac{W}{t}$ (eq. 3)
4	Installed Power Load Factor K_u is calculated as the ratio of average power, P_{avg} and installed power, P_i (Oprea and Bâra, 2017)	K_u		$K_u = \frac{P_{avg}}{P_i}$ (eq. 4)
5	Installed Power Load Duration T_i is determined based on installed power load factor, (K_u) multiply by power plant's runtime, (t) (Pearsall, 2016)	T_i	s	$T_i = K_u \times t$ (eq. 5)
6	Maximum Power Load Duration T_{max} is calculated as ratio between generated energy, W and maximum power plant output, P_{max}. (Duffie and Beckman, 2013).	T_{max}	s	$T_{max} = \frac{W}{P_{max}}$ (eq. 6)
7	Performance Index PI is the ratio between the generated energy, W and forecasted energy, W_f (Kalogirou, 2014)	PI		$PI = \frac{W}{W_f}$ (eq. 7)
C	**KPI from IEC 61724 standard (IEC61724, 2016)**			
8	Performance Ratio PR indicates the overall effect of losses on the system output and is the quotient of the system's final yield Y_f to its reference yield Y_r. -Y_f represents the ratio between annual active energy and rated power. -Y_r is the ratio between insolation (kW h m^{-2}) and reference solar irradiance (1 kW m^{-2}).	PR	%	$PR = \frac{Y_f}{Y_r} = \frac{kWh_{AC}}{kW_{DC\,STC}} \times \frac{1\ kW}{kWh_{sun}}$ (eq. 8)
9	Temperature Compensated Performance Ratio, Offsetting factors such as cell temperature (K_{Temp}) can be applied to the PR formulae to adjust the rated power under STC. Where, $K_{Temp} = (T_{Panel} - T_{STC})$, ($T_{STC} = 25^{\circ}C$)	$PR_{TempComp}$	K	$PR_{TempComp} = \frac{PR}{K_{Temp}}$ (eq. 9)
10	Yield Yield is the actual net energy output during a certain period of time divided by the maximum installed power capacity of the PV array and can be measured on various time scales such as daily, monthly or annually	Yield	W h	$Yield = \frac{\sum_{i=1}^{t} kWh_{AC}}{kW_{DC\,STC}}$ (eq. 10)
11	Normalized efficiency η_N is the ratio of the output energy of the PV system to the energy of the incoming irradiation incident on the same PV panels' area	η_N	%	$\eta_N = \frac{P}{P_n} \times \frac{E_{ref}}{E_{PoA}}$ (eq. 11)

12	Temperature Corrected Power Impact of temperature variation is corrected using temperature corrected power	P(T)	K	$P(T) = P_{STC}(1 + \gamma\Delta T_{STC})$ (eq. 12)
13	Temperature Corrected Power	P*	(K)	$P^* = \frac{P(T)}{1+ \gamma\Delta T_{STC}}$ (eq. 13)
14	Temperature Corrected normalized efficiency Seasonal variation of the efficiency is removed by calculating a temperature-corrected efficiency	$\eta_N(T)$	K	$\eta_N = \frac{P^*}{P_n} \times \frac{E_{ref}}{E_{PoA}}$ (eq. 14)
D	**Environmental Benefits**			
15	Avoided CO_2 emissions, The contribution in combating the effect of climate change due to avoided CO_2 emissions with the G_{ef} being the national electrical grid CO_2 equivalent emission factor (NREL, 2012)	$CO_{2\_avoided}$	Kg	$CO_{2\_avoided} = W \times G_{EF}$ (eq. 15)
16	Equivalent trees planted A mature tree can absorb around 48 pounds (or approximately 22 kg) of CO_2 per year. This is equivalent to about 0.022 metric tons of CO_2 per year (Toochi, 2018).	$Trees_{\_eq}$		$Trees_{\_eq} = \frac{CO_{2\_avoided}}{0.022}$ (eq. 16)
E	**Financial Aspects**			
17	Levelized Cost of Electricity LCOE takes into account the time value of money such as capital costs and operation and maintenance costs. It calculates the average cost per unit (Tamburini, Cipollina and Micale, 2021)	LCOE	USD W^{-1}	$LCOE = \frac{I_0+\sum_{t=1}^{n}\frac{A_t}{(1+i)^t}}{\sum_{t=1}^{n}\frac{Q_{el}}{(1+i)^t}}$ (eq. 17)
18	Net Present Value NPV is used to determine the profitability of the investment over the lifetime of the solar PV project. It is calculated by finding the difference of the present value of cash inflow (CF_T) and the present value of cash outflow (CAPEX), discounted to the present time , r. The first indication of the profitability of RE investment is that it shows a positive NPV (Mazumdar and Rajeev, 2015).	NPV	USD	$NPV = \sum_{t=1}^{T}\left[\frac{CF_T}{(1+r)^t}\right] - CAPEX$ (eq. 18)
19	Internal Rate of Return, The IRR represents the discount rate at which the Net Present Value (NPV) of the cash flows from the investment becomes zero (NREL, 2011).	IRR	%	$0 = NPV \sum_{t=0}^{T}\frac{CF_T}{(1+IRR)^t}$ (eq. 19)
20	Payback period PBP indicates the time it takes to recover the initial investment in a PV system. Where CAPEX is the capital expenditure (UNL, 2013).	PBP	Years	$PBP = \frac{CAPEX}{Annual\ cash\ inflow}$ (eq. 20)

21	Return on Investment (ROI) The return on investment evaluates the profitability and viability of a PV project's investment over its full term (Hoymiles, 2022).	ROI	%	$\mathrm{ROI} = \frac{\text{Net income savings}}{\text{CAPEX}} \times 100$ (eq. 21)

3.3 Datasets

To effectively utilise the set of KPIs, it is highly recommended to assess and incorporate relevant solar PV system datasets. The latter serve as the fundamental source of information required for assessing and evaluation the overall performance of solar PV systems. Key types of solar PV datasets include:

3.3.1 Solar PV System Data

The technical details of the PV systems include the location, the date of installation, the details of the inverters, modules, mounting strategy, system rating and details of degradation. In addition to the aforementioned information, it is essential to incorporate financial data into the analysis, including capital costs (CAPEX), operational and maintenance costs (OPEX), discount rates, power purchase agreements (PPA), cash flows, loans, subsidies, relevant taxes, and electricity pricing. Sample description of two PV systems are introduced here. PV System 1 is located at Site 1 with coordinates 20.24° South and 57.50° East, PV System 1 was installed in 2017 and is a Small Scale power optimiser based grid connected PV system rated 20 kW_p with 62 (String 1: 20 Nos; String 2: 21 Nos; String 3: 21 Nos) Yingli 320 W_p (YL320P- 35b 320 W) multi-crystalline PV modules connected to one ABB string inverter (TRIO-27.6-TL-OUTD-S2J-400). The efficiency of the solar panel is 18.5% with a 25-year linear performance warranty and a degradation rate of 0.4825 % per year. PV system 2 was installed in 2019 and is located at Site 2 with coordinates 20.22° South and 57.39° East. It is a Small Scale grid connected string inverter-based PV system rated 50 kW_p. It contains 130 (String 1: 34 Nos; String 2: 32 Nos; String 3: 32 Nos; String 3: 32 Nos) Jinko Solar Eagle 385 W_p (JKM385M-72H-V) monocrystalline PV modules connected to two SolarEdge inverters (SE25K) through 65 SolarEdge Power Optimizer (P850). The efficiency of the solar panel is 19.53 % with a 25-year linear performance warranty and a degradation rate of 0.495 % per year. According to prevailing exchange rates, the cost of PV system 1 amounted to USD 294,106, while PV system 2 costed USD 565,590.

3.3.2 Solar PV production data

Instantaneous, daily, monthly or yearly electrical PV performance data from solar PV systems provide valuable insights into the operating conditions of the PV installations. These data points help in measuring the efficiency and productivity of the PV systems over time. The electrical performance datasets include dc current, voltage and power input at each string of the inverters; ac current, voltage, frequency, power and power factor for each phase of each inverter. These datasets are normally captured by majority of the commercially-available inverters in the market and may be accessed over their web interfaces. However, the sampling rate of the instantaneous data should be configured to be at the minimum intervals. The most recommended sampling rate is 1-minute. However, many of the commercially available inverters may only provide these datasets at either 5, 15, 30 or 60-minute interval.

3.3.3 Weather data

Ground-based or satellite data offer crucial information regarding weather conditions that impact PV system performance. This includes factors such as solar irradiance, temperature, wind speed and direction, humidity and cloud cover. These weather-related datasets are essential for understanding how external factors impact the output of solar PV systems. The requirements of the measuring equipment that may be installed at the PV facilities is well captured in IEC 61724-1. It must be noted that commercially available inverters may display some weather conditions through their web platforms. Satellite based datasets may be procured from recognised data providers such as SolarGIS and Meteonorm amongst others. The utilization of performance metrics and actual meteorological data allows for a more precise evaluation of the performance of PV systems under real weather conditions and during varying durations. The outcome of this process enables decision-making and PV system optimisation. It must be ensured that the measuring equipment are calibrated as per prevailing standards applicable to the equipment in use and that the sampling rate is adjusted to that of the sampling rate of the electrical datasets. The datasets should also be quality control procedures. The reader is referred to Bangarigadu *et al.* (2020) and Ramgolam *et al.* (2020) for more details about the description and justification for the selection of the quality control procedures and techniques.

3.4 Computational tools.

In addition to utilizing relevant PV system datasets, the use of PV system modelling techniques and tools, such as PVsyst and SAM (System Advisor Model), are highly recommended for a comprehensive assessment of PV system performance. The aforementioned modelling tools offer valuable capabilities for the following:

- Performance prediction by providing estimates for energy prediction and system efficiency assessment through the simulation of PV systems under different weather conditions
- Financial analysis by using tools like SAM which can help evaluate the economic viability of PV projects by considering factors such as project costs, incentives, financing options, and return on investment (ROI)
- System design and optimisation by allowing determination of optimal PV panel placement and orientation, as well as the sizing of the system components to maximize energy output and minimize costs.

By incorporating PV system modelling techniques and tools into the assessment process, researchers and stakeholders can gain deeper insights into the expected performance, financial implications, and design considerations of PV systems. This holistic approach, which combines data-driven analysis with predictive modelling, supports more informed decision-making and helps optimize the planning and operation of PV installations. Excel based tools or any other mathematical package may be considered for evaluating the KPIs.

3.5. Guidelines for assessing the performance of PV systems using the KPIs

A set of criteria has been devised to facilitate a comprehensive assessment of solar PV systems. These guidelines have been condensed and presented in the form of a flow chart, as depicted in Figure 1. The first step entails the implementation of a thorough data warehousing to gather technical data, specifically E_{ac}, E_{POA}, H_{STC}, P_{DC_STC}, and P_{ac}, as outlined in Table 1. In a similar vein, this study incorporates weather data obtained from both ground-based measurements and satellite observations, specifically focusing on variables such as temperature,T and plane of array irradiance, POA. Additionally, financial data related to the PV system(s) being examined, including CAPEX, OPEX, electricity price, and price per watt, are also taken into consideration. In order to ensure the accuracy and reliability of the gathered data, a quality control is performed. This includes checking for data completeness, identifying and addressing anomalies, validating sensor and instrument calibration, and assessing data consistency over time.

Additionally, quality control may involve the removal of erroneous or duplicate data points and the application of statistical techniques to detect and rectify any data discrepancies. The goal of this rigorous quality control process is to enhance the integrity of the PV dataset. The subsequent process involves the system modelling of the PV system(s) through the utilization of modelling tools such as PVsyst and simulation techniques. The modelling and simulation of PV systems enable the emulation of system performance in diverse scenarios such as before and after implementation, hence providing valuable information for system optimization. The performance assessment is then conducted by computing the 21 KPIs described in Table 1. The latter facilitates the identification of disparities between the projected and actual performance data, thereby providing guidance to stakeholders on enhancing the operational efficiency of PV system(s).

A comparative analysis of the computed KPIs with respect to benchmark values is also performed. The latter facilitates the identification of disparities between the projected and actual performance data, thereby providing guidance to stakeholders on enhancing the operational efficiency of PV system(s). If the calculated KPIs deviate from the established baseline values, additional examinations such as Root Cause Analysis (RCA) or Fault Tree Analysis (FTA) may be conducted. Consequently, the flawed process will need to be re-executed. On the other hand, once the optimal KPI values are achieved, more optimization measures can be undertaken to improve the efficiency of the PV system(s). Alternatively, a comprehensive report can be prepared to monitor and assess the performance and feasibility of the system(s). The outcome of the report would provide insights into the overall technical, financial and environmental performance detailing whether the intended goals and KPIs are met. Ultimately, the outcome of the report aims to inform on the system's current status and guide future actions to ensure its continued success. By adhering to the guidelines developed in this study, stakeholders can harness the full potential of performance indicators and KPIs for PV systems, fostering informed decision-making, optimizing system performance, and ensuring the sustainability of solar energy endeavors on both environmental and financial fronts.

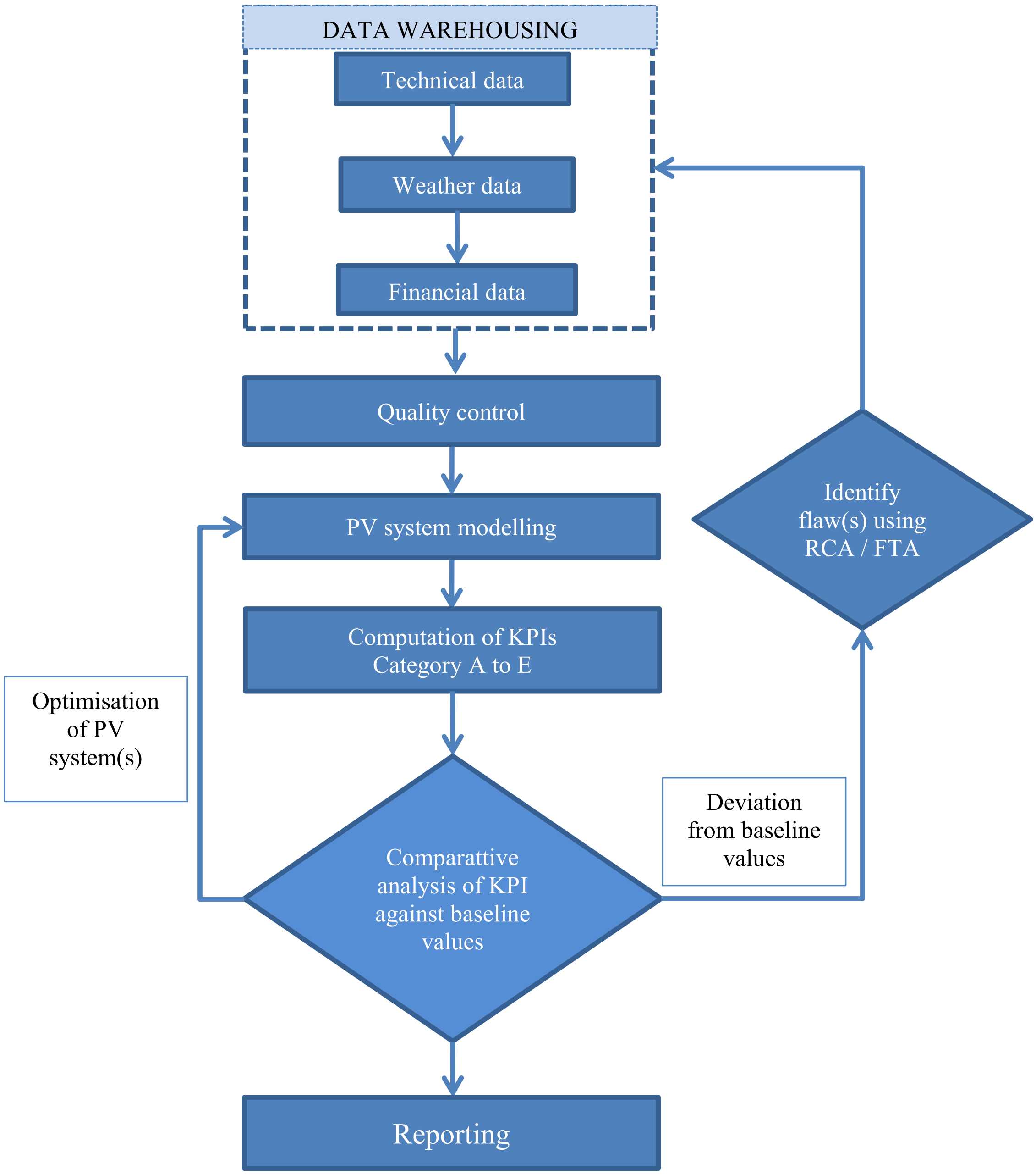

Figure 1: Guidelines for PV performance assessment

4. Conclusion

Solar energy is gaining more and more importance in the contemporary society and is perceived as the future leading source of energy that will revolutionise the global energy mix. PV technology has experienced phenomenal growth over the years due to an incredibly high penetration rate in countries' energy mix. However, it is more crucial for PV systems to perform optimally, rather than just increasing the installed capacity. In a bid to appraise the performance of PV systems, literature provides numerous KPIs. Nevertheless, synthesis of literature revealed that there exists no proper framework to guide the selection of KPIs for a given system. More so, for most KPIs, there are defined benchmarking or recommended values. By meticulously identifying and categorizing the KPIs, this framework provides a comprehensive and tailored approach to evaluate the different aspects of PV system performance. It goes beyond mere energy production metrics, incorporating factors such as reliability, financial viability, and environmental impact. This holistic perspective is crucial in addressing the diverse risks and impacts inherent in solar PV systems. The framework not only facilitates a thorough understanding of PV system performance but also acts as a guide for stakeholders, ranging from investors and policymakers to engineers and project managers, fostering informed decision-making and contributing to the sustainable growth of solar energy initiatives. As the global shift towards renewable energy intensifies, the implementation of this framework is poised to play a pivotal role in ensuring the bankability, efficiency, resilience, and overall success of solar PV systems on a broader scale.

5. Acknowledgments

A heartfelt gratitude goes out to the dedicated team members for their unwavering support and collaborative efforts throughout this research. Additionally, we extend our sincere thanks to Dr Y. K. Ramgolam for his continuous guidance and leadership throughout this journey.

6. References

Allouhi, A. *et al.* (2016). *Grid-connected PV systems installed on institutional buildings: Technology comparison, energy analysis and Economic Performance,* Energy and Buildings, 130, pp. 188–201. Available at: https://doi.org/10.1016/j.enbuild.2016.08.054.

Ameur, A. *et al.* (2019). *Performance evaluation of different photovoltaic technologies in the region of Ifrane, Morocco,* Energy for Sustainable Development, 52, pp. 96–103. Available at: https://doi.org/10.1016/j.esd.2019.07.007.

Ameur, A. *et al.* (2020). *Forecast modelling and Performance Assessment of solar PV systems,* Journal of Cleaner Production, 267, p. 122167. Available at: https://doi.org/10.1016/j.jclepro.2020.122167.

Anang, N. *et al.* (2021). *Performance analysis of a grid-connected rooftop solar PV system in Kuala Terengganu, Malaysia,* Energy and Buildings, 248, p. 111182. Available at: https://doi.org/10.1016/j.enbuild.2021.111182.

Bangarigadu, *et al.* (2020). *Analysis of Solar Power and Energy Variability Through Site Adaptation of Satellite Data With Quality Controlled Measured Solar Radiation Data",* Journal of Solar Energy Engineering, 143 (031008), pp.1-19.

Department of Energy (DOE), (2021). *Understanding solar photovoltaic system performance: An assessment of 75 Federal Photovoltaic Systems*.Energy.gov. Available at: Understanding Solar Photovoltaic System Performance: An Assessment of 75 Federal Photovoltaic Systems | Department of Energy (Accessed: March 12, 2023).

Elghobashy, A. (2020). *Effects of solar installation on the power factor, Solar Project Management*. Available at: Effects of Solar Installation on The Power Factor (Accessed: April 14, 2023).

Herteleer, B. *et al.* (2017). *Normalised efficiency of photovoltaic systems: Going beyond the performance ratio,"* Solar Energy, 157, pp. 408–418. Available at: https://doi.org/10.1016/j.solener.2017.08.037 .

Hoymiles (2022). *How to calculate ROI for a solar system*. Available at: https://www.hoymiles.com/solar-project-contest-2023/ (Accessed: August 23, 2023).

IEC61724, (2016). *Photovoltaic System Performance- Energy Evaluation Method*; International Electrotechnical Commission: Geneva, Switzerland, 2016.

IRENA (2023), Renewable capacity statistics 2023, International Renewable Energy Agency, Abu Dhabi.

Klise, G.T. *et al.* (2016). *PV system "availability" as a reliability metric — improving standards, contract language and Performance Models*, 2016 IEEE 43rd Photovoltaic Specialists Conference (PVSC) [Preprint]. doi:10.1109/pvsc.2016.7749918.

Klise, K.A., Stein, J.S. and Cunningham, J. (2017). *Application of IEC 61724 standards to analyze PV system performance in different climates*, 2017 IEEE 44th Photovoltaic Specialist Conference (PVSC) [Preprint]. Available at: https://doi.org/10.1109/pvsc.2017.8366666.

Kumar, N.M., Dasari, S. and Reddy, J.B. (2018). *Availability factor of a PV power plant: Evaluation based on generation and inverter running periods,* Energy Procedia, 147, pp. 71–77. Available at: https://doi.org/10.1016/j.egypro.2018.07.035

Mazumdar, I. and Rajeev, P.V. (2015). *Financial analysis of rooftop solar photovoltaic power plant for servicing petrol and diesel retail outlets Indexing*. ShivShakti International Journal of in Multidisciplinary and Academic Research (SSIJMAR) (ISSN 2278 – 5973). 4.

National Renewable Energy Laboratory (NREL) *(1999). Photovoltaic Module Energy Ratings Procedure at NREL*. NREL/TP-520-26909, Golden, CO.

National Renewable Energy Laboratory (NREL) (2011). *The Impact of Different Economic Performance Metrics on the Perceived Value of Solar Photovoltaics*. Available at: https://www.nrel.gov/docs/fy12osti/52197.pdf (Accessed: October 10, 2023).

National Renewable Energy Laboratory (NREL) (2012). *Life Cycle Greenhouse Gas Emissions from Solar Photovoltaics*. Available at: https://www.nrel.gov/docs/fy13osti/56487.pdf (Accessed: October 10, 2023).

Odeh, S. (2018). *Analysis of the performance indicators of the PV Power System,* Journal of Power and Energy Engineering, 06(06), pp. 59–75. Available at: https://doi.org/10.4236/jpee.2018.66005

Pless, S. *et al.* (2005). "*Procedure for measuring and reporting the performance of photovoltaic systems in buildings*, *Procedure for Measuring and Reporting the Performance of Photovoltaic Systems in Buildings" (Technical Report)* | *OSTI.GOV*. Available at: https://www.osti.gov/biblio/859414 (Accessed: April 14, 2023).

Ramgolam, *et al.* (2020). *"A Robust Methodology for Assessing the Effectiveness of Site Adaptation Techniques for Calibration of Solar Radiation Data",* Journal of Solar Energy Engineering, 143 (031009), pp.1-15.

REN21. (2022). *Renewables 2022 Global Status Report*, (Paris: REN21 Secretariat), ISBN 978-3-948393-04-5

Seme, S. *et al.* (2019) *"Analysis of the performance of photovoltaic systems in Slovenia,"* Solar Energy, 180, pp. 550–558. Available at: https://doi.org/10.1016/j.solener.2019.01.062.

Sharma, R. and Goel, S. (2017). *Performance analysis of a 11.2 kWP roof top grid-connected PV system in eastern India*, Energy Reports, 3, pp. 76–84. Available at: https://doi.org/10.1016/j.egyr.2017.05.001.

Tamburini, A., Cipollina, A. and Micale, G. (2021). *Salinity Gradient Heat Engines.* Woodhead Publishing

Tiwari, A. and Sodha, M.S. (2006) *Performance evaluation of solar PV/T system: An experimental validation,* Solar Energy, 80(7), pp. 751–759. Available at: https://doi.org/10.1016/j.solener.2005.07.006

Toochi, E.C., (2018). *Carbon sequestration: how much can forestry sequester CO2?*. Forest Res Eng Int J. 2018;2(3):148–150. DOI: 10.15406/freij.2018.02.00040

University of Nebraska-Lincoln Extension (UNL), (2013). *Economics of Solar Photovoltaic Systems* . Available at: https://extensionpublications.unl.edu/assets/pdf/g2182.pdf (Accessed: October 10, 2023).

Vidyanandan, K.V., (2017). *An Overview of Factors Affecting the Performance of Solar PV Systems*. Energy Scan (A house journal of Corporate Planning, NTPC Ltd.). 27. 2-8.

Walker, A. and Desai, J. (2021). *Understanding Solar Photovoltaic System Performance: An Assessment of 75 Federal Photovoltaic Systems*, *(Technical Report)*| *OSTI.GOV*. Available at: https://www.osti.gov/biblio/1838130/ (Accessed: April 15, 2023).

Ya'acob, M.E. *et al.* (2014). *Performance test conditions for direct temperature elements of multiple PV array configurations in Malaysia,* Energy Procedia, 61, pp. 2387–2390. Available at: https://doi.org/10.1016/j.egypro.2014.12.011.

Zenhäusern, D. (2020). *Key performance indicators for PVT systems* [Preprint]. doi:10.18777/ieashc-task60-2020-0007.

Reinforcement Learning for Building Energy System Control in Multi-Family Buildings

Michael Bachseitz, Muhammad Sheryar, David Schmitt, Thorsten Summ, Christoph Trinkl and Wilfried Zörner

Institute of new Energy Systems, Technische Hochschule Ingolstadt, Ingolstadt (Germany)

Abstract

Replacing the widespread use of fossil fuel heating systems in the existing multi-family building stock with systems powered by renewable energy is one of the most important contributions to the energy transition in Germany. Heat pumps can also be a suitable solution for older buildings, especially in combination with photovoltaic systems. Advanced control strategies are needed to optimize the self-consumption rate and reduce the load on the electricity grid. Due to the increase in available computing power, artificial intelligence methods such as reinforcement learning, which can be used to control (energy) systems, have become very popular in the recent years. A literature review was conducted to provide an up-to-date overview of the use of reinforcement learning for building energy system control, with a focus on multi-family buildings. Such a building with an energy system including a heat pump, thermal and electrical storage, and a photovoltaic system was modeled in MATLAB/Simulink. The model is used to investigate typical control strategies as a reference and to develop a heat pump control strategy using the MATLAB Reinforcement Learning Toolbox. Two reinforcement learning agents with different numbers of observations were trained to control the heat pump and studied in annual simulations. Both RL agents provide the required supply water temperature. Adding one observation improves the annual reward by 160 %. Nevertheless, a potential to improve learning the RL agent switching of the heat pump at times of high bottom storage temperatures was identified.

Keywords: multi-family building, energy system, optimization, self-consumption, reinforcement learning

1. Introduction

The decarbonization of the residential building sector is one of the most important contributions to the energy transition in Germany. In addition to reducing the energy consumption, especially for heating, through the energy renovation of existing buildings, the widespread use of fossil fuel heating systems must be replaced by more efficient systems powered by renewable energy. The scenario of a climate-neutral Germany by 2045 introduced in Prognos et a. (2021) shows a need of in total 14 million heat pumps in the building sector.

Heat pumps are a highly efficient solution for supplying heat to buildings based on (partially) on-site renewable energy, such as rooftop photovoltaic (PV) systems. Bongs et al. (2023) investigated low-exergy concepts for multi-family buildings, which account for about 41 % of the living space in Germany (Loga et al., 2015). They developed, analyzed, and demonstrated solutions for the efficient use of heat pumps, heat transfer systems, and ventilation systems for energy renovations of multi-family buildings. Their results show that by replacing only a few radiators in critical rooms (e.g., 2 - 7 % of the existing radiators in their use case), the heat supply temperatures can be reduced to 60 °C or less, and therefore, heat pumps can be a suitable solution for heat supply, especially in combination with PV systems.

In order to use most of the electricity generated on site in the building itself and to reduce the load on the electricity grid, battery storage is often used to better match demand and generation. As battery storage is still expensive, the conversion of electricity into thermal energy via heat pumps and the use of thermal storage can provide an even cheaper alternative or additional flexibility to battery storage (Zator and Skomudek, 2020). A heat pump in combination with a thermal storage is typically operated in an on/off mode, depending on the temperatures in the thermal storage, without considering the PV electricity generation. Sometimes simple rule-

10.18086/swc.2023.08.01 Available at http://proceedings.ises.org

based approaches are used to increase the PV self-consumption rate. They switch on the heat pump and/or increase the set point for the supply water temperature when the PV power exceeds the electricity demand of the households. More advanced control strategies using model predictive control (MPC) have also been developed, e.g., Kuboth et al. (2019). However, they cannot easily be implemented due to the high effort of designing and parameterizing each energy system model required for the variety of existing multi-family buildings (Dounis and Caraiscos, 2009). In recent years, the increase in available computing power has led to an intense development and exploration of artificial intelligence (AI) approaches for a variety of applications. Reinforcement learning (RL) is one of the three types of machine learning that is used for system control (Sutton and Barto, 2018). RL agents learn control strategies by interacting with the environment (building energy system) and can learn preferences, such as comfort requirements, by interacting with users. This method is potentially model-free, meaning that models of the environment are not required, as is the case with mixed integer linear programming (MILP) approaches. Forecasts - for weather and heat/electricity demand - are not required but can be implemented and will improve the results. (Yu et al., 2020, 2021, Vázquez-Canteli and Nagy, 2019) Due to these advantages, RL became attractive for the energy management in residential buildings and has been investigated for the control of a variety of building energy (sub)systems. Wu et al. (2018) write that reinforcement learning algorithms "…could be promising candidates for home energy management…" and Yu et al. (2021) want to "…raise the attention of SBEM [smart building energy management; author's note] research community to explore and exploit DRL, as another alternative or even a better solution for SBEM.". Therefore, this paper investigates an RL approach for controlling the energy system of a conventionally energy renovated multi-family building that includes an air source heat pump, thermal storage, PV system, and optional battery storage. The focus is on controlling the heat pump according to the temperatures in a stratified thermal storage to ensure the required supply water temperatures of the heating system, as a conventional controller does. The development of this RL agent will be the basis for further developments for the implementation of PV optimization.

The novelty of this work is the investigation of a multi-family building using a detailed building energy system model in MATLAB Simulink in combination with RL algorithms provided by the Reinforcement Learning Toolbox of MATLAB (The MathWorks, Inc., 2023) to control heat pump operation.

In Section 2, an overview of the use and development of reinforcement learning approaches for the control of building energy (sub)systems with a focus on residential buildings is given. Section 3 introduces the building energy system model developed in MATLAB/Simulink using the CARNOT toolbox (Solar Institut Jülich, 2022), describes typical control strategies, and shows the development of RL-based heat pump controller using the Reinforcement Learning Toolbox (The MathWorks, Inc., 2023). The results of annual simulations using i) the typical control strategies and ii) the developed RL-based control strategies are presented and discussed in Section 4. A conclusion and outlook are given in Section 5.

2. Literature Review

A literature review was conducted to obtain an up-to-date overview of related scientific work and to investigate the use of RL for energy systems in multi-family buildings. The most popular databases of the scientific journals *Science Direct* and *EIII* were analyzed. Keywords used for the research included machine learning, deep reinforcement learning, building/home energy management, building energy system, system control, building control, smart buildings, smart home, multi-family buildings. The most relevant papers are presented here.

Yu et al. (2021) provide a comprehensive review of publications on deep reinforcement learning (DRL) for smart building energy management (SBEM). They also identify existing open issues and suggest possible future research directions. A distinction is made between studies on single building energy subsystems, multi energy subsystems in buildings, and microgrids. Only six of the 15 publications mentioned for single building energy subsystems deal with residential buildings. Three of them examine electric water heaters and another three examine heating, ventilation, and air conditioning (HVAC) systems. Their primary objective is to reduce energy costs or consumption. Six of the eight publications on multi energy subsystems in buildings deal with residential buildings and have energy costs as an objective. Only one of them (Ye et al., 2020) investigates a system similar to the one described in this paper (Section 3), but with an additional back-up system of a gas boiler.

Vázquez-Canteli and Nagy (2019) reviewed reinforcement learning algorithms and modeling techniques for demand response, ultimately selecting and summarizing 105 articles. Most of the studies were conducted for only one or two (combined) systems, especially for HVAC systems, electric vehicle charging strategies, or distributed generators combined with electric storage. They identified HVAC and domestic hot water (DHW) systems as one of four major groups of energy systems with significant demand response (DR) potential. However, many publications on HVAC systems examine only the reduction of thermal energy demand while maintaining thermal comfort for building occupants. None of the publications cited examine a system like the one described in Section 3.

Langer and Volling (2022) study a system configuration identical to the one used in this paper. They transform a mixed integer linear program (MILP) into a DRL implementation. Through numerical analyses of self-sufficiency, they compare the results of a deep deterministic policy gradient (DDPG) algorithm with a model predictive controller (MPC) under full information (theoretical optimum) and a rule-based approach. Their best DDPG algorithm achieves an overall self-sufficiency of 75 % which outperforms the rule-based approach with 66 % and reaches almost the theoretical optimum of 79 %.

However, the buildings considered in Ye et al. (2020) and Langer and Volling (2022) are very energy efficient single-family homes due to their small system dimensions. The investigations there are based on simplified linear models developed in previous MILP investigations with time step sizes of one hour, where mass flows and temperatures in hydraulic circuits and thermal storages are not considered in detail.

To the best of the author's knowledge, there are no studies on the energy system of an energetically renovated multi-family building that includes an air source heat pump, a thermal storage, a PV system, and optional battery storage that are modeled in detail. In the next two sections, such a model is introduced, the development of RL agents for heat pump control is described and results of annual simulations are shown.

3. Building Energy System Model

For the simulation of typical control strategies and the development of RL-based control strategies in MATLAB/Simulink, a multi-family building was chosen according to the building age category E of the IWU building typology of Germany (Loga et al., 2015). There, the large variety of architecture and construction methods of the German residential building stock is described, analyzed, and classified. The rough classification of the energy quality of the buildings is based on specific parameters. The definition of these parameters, the assignment of the buildings to age categories and to the state of renovation, a summary of the number of buildings as well as the presentation of typical specifications and energy saving potentials of each category are part of this typology. A building in age category E was chosen because it represents 19 % (225 million m²) of the total multi-family buildings living space in Germany (1,168 million m²) and is therefore the largest category for multi-family buildings. Such buildings were built between 1958 and 1968 and typically have 3 to 5 floors with a heated floor area of about 2,850 m² divided into 32 apartments. For each category, three types of energy quality are described: the original unrenovated state, a conventional renovated state, and a future-oriented renovated state with a calculated space heating energy demand of 145.9 $kWh/m^2_{\text{net floor area}}$, 67.3 $kWh/m^2_{\text{net floor area}}$ and 42.0 $kWh/m^2_{\text{net floor area}}$ respectively. According to the results presented in Bongs et al. (2023), the conventionally renovated version of this building was chosen for the investigations because the heat supply temperatures can be reduced to 60 °C or less, which allows the use of heat pumps for the thermal energy supply.

3.1. Building energy system model

The investigated building with its heat and electricity demand and the energy system consisting of an air source heat pump (hp), a thermal storage, a PV system and, in an extended version, a stationary battery storage was modeled in MATLAB/Simulink using the CARNOT toolbox (Solar Institut Jülich, 2022). CARNOT is a toolbox extension that provides an open-source library of models for the calculation and simulation of typical components of building energy systems in MATLAB/Simulink. The models can be individually parametrized or even redesigned due to the open-source code that can be modified.

The system configuration modeled for the investigations is shown in Figure 1.

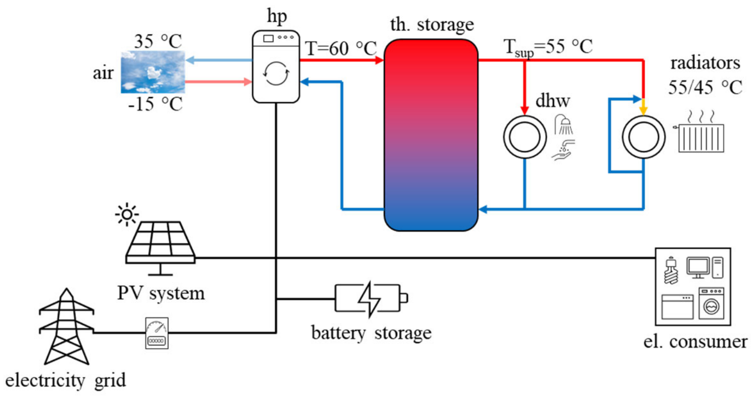

Fig. 1: Investigated building energy system configuration

The multi-family building itself was modeled with the “House simple” block, which uses a single zone building model with radiators as the heat transfer system. The parameters (geometry, U-values, etc.) were defined according to the data given in Loga et al. (2015) and supplementary data.

For the internal heat gains caused by the occupants, the occupancy profile given in SIA (2021) was used and upscaled to 60 persons.

The test reference year (TRY) of *Ingolstadt* provided by the German Weather Service (DWD, 2017) was used as input weather data for the simulations as well as for the load profile generation described below.

The method described in the VDI guideline 4655 (VDI, 2021) was used to generate the household electricity consumption profile, which is also used for internal heat gains caused by electrical appliances, and the domestic hot water (DHW) consumption profile. The guideline defines 12 typical days according to ambient temperature (winter, transition, summer), irradiation (clear or cloudy), and day of the week (workday or Sunday/holiday). For each typical day, normalized daily standard load profiles for electricity, DHW and heat consumption and PV generation are given in hourly time resolution for existing and low-energy buildings. The sequence of typical days and the annual normalized load profiles were determined from the DWD TRY data. The normalized profiles were scaled by an annual consumption of 96,000 kWh/a (3,000 kWh/a per household, VDI, 2021) for electricity consumption and 61,500 kWh/a (approx. 2,000 kWh/a per household, Loga et al., 2015) for DHW consumption.

The DHW hydraulic circuit is modeled in a simplified manner using a freshwater station. The supply water mass flow is controlled to match the given DHW load profile at a fixed return water temperature.

A separate hydraulic circuit is defined for the space heating with radiators. The supply water temperature is calculated by a heating curve according to the ambient temperature. The mass flow is controlled by a thermostatic valve to maintain the room temperature at 21 °C.

The ventilation system is included in the building model and ensures a hygienic air exchange with a ventilation rate of 0.4 1/h and prevents an overheating of the building in summer with additional ventilation at night.

To decouple the thermal energy consumption from the heat production and to provide some flexibility in the operation of the heat pump, a stratified thermal storage tank is modeled as a hydraulic separator between the heat pump hydraulic circuit and the consumer hydraulic circuit. For this purpose, the block “Buffer storage tank - type 1” has been modified to provide two consumer hydraulic circuits. Its volume is 8.5 m³, which corresponds to approximately 50 l/kW of the heat pump’s thermal power.

For the heat supply, an air source heat pump with a thermal capacity of approximately 170 kW was modeled by a modified version of the “Heat pump” block. The modification removes the (unknown) thermal inertia and allows direct control of the supply water temperature. Real data from a heat pump manufacturer was used for the parameter set. To provide the DHW preparation, the setpoint for the supply water temperature of the heat pump was set to 60 °C.

To partially cover the electricity demand of the households and the heat pump, a PV system is modeled on the south-facing roof of the building. The usable roof area was examined from an existing multi-family building in *Ingolstadt* and is about 215 m², which results in a 65 kW_p PV system producing approximately 65,000 kWh_{el}/a.

In an extended version for the simulations, a battery storage with a usable capacity of 65 kWh (1 $kWh_{el}/kW_{el,PV}$) is modeled. It is located between the consumers/producers and the electricity grid. The (dis)charging power is limited according to the specifications of the battery storage. The control strategy (described in Section 3.2) is implemented in the model. The outputs are the state of charge (SOC) and an energy balance showing the electricity consumed from and fed into the grid.

Due to the high complexity of the model described, a variable time step solver was required to solve the problem. As a result, the time steps for the model calculation were much shorter than the hourly time resolution used in the MILP-based approaches.

3.2. Typical control strategies

For the control of the heat pump and the battery storage, typical control strategies have been defined and implemented in the simulation model. They are used as a reference.

Heat pumps in combination with thermal storages are typically operated in an on/off mode depending on the temperatures in the thermal storage (basic control strategy) as shown in Figure 2. In this study 55 °C are used as setpoint for the heat pump control.

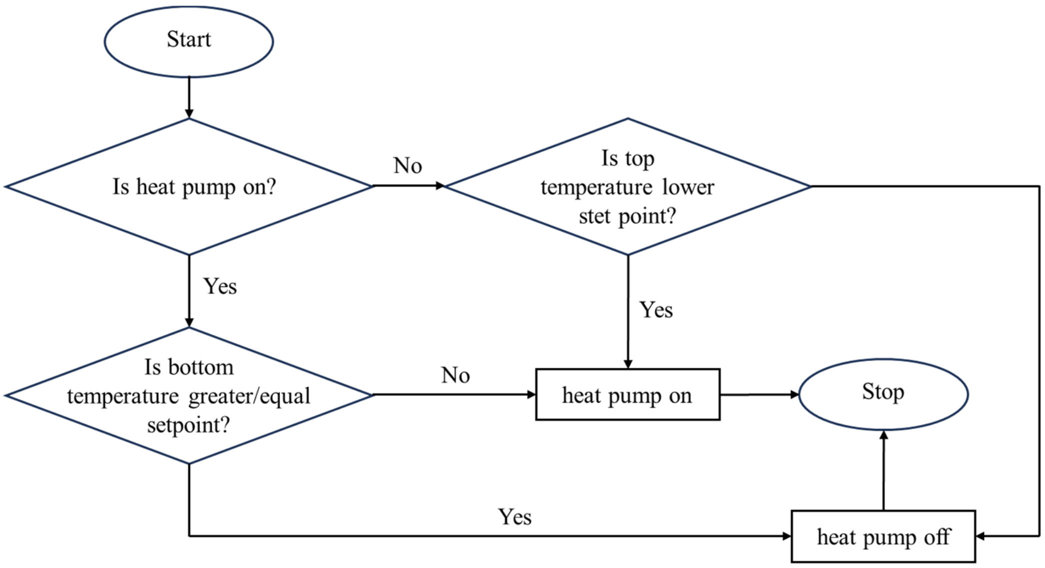

Fig. 2: Typical control strategy of heat pump

Sometimes simple rule-based approaches are used to better match the heat pump electricity consumption and the PV generation. For example, they increase the set point for the heat pump's supply water temperature by 5 K when the PV power exceeds the household's electricity demand (rule-based PV optimized strategy). This results in the heat pump being turned on when it was off, and at the same time, when it is turned on, the electricity demand increases due to the increased temperature difference between the heat source and heat sink. In the case shown here, the supply water temperature set point is increased when the PV surplus exceeds 25 kW_{el}, which is about half of the maximum simulated PV power.

When a battery storage is part of the building energy system, it is typically charged when not all of the electricity generated by the PV system is consumed directly by the households and the heat pump, and is discharged when the electrical loads exceed PV power.

3.3. Development of reinforcement learning based building energy system control

An RL agent learns an optimal policy by interacting with an unknown environment. In the study presented here, the policy is the control strategy for the heat pump to be learned, and the environment is the building energy system modeled in MATLAB/Simulink. Interacting in this case means that at each time step, the agent receives some information from the building energy system (observations) and decides how to operate the heat pump (action) based on the observations and the learned policy. For each action, the RL agent receives a reward depending on the defined reward function that evaluates the chosen action. In the learning phase, the policy is optimized to obtain the maximum reward over a defined period of time (in this case over the total episode length) to optimally perform the required task. The challenge in designing an RL agent is the goal-oriented definition of the reward function, the selection of an appropriate RL agent/method with its policy (e.g., deep neural network) and learning algorithm (policy optimization), and the parameterization of the hyper-parameters e.g., sample time, discount factor or learning rate.

The workflow for setting up an RL-based controller is shown in Figure 3.

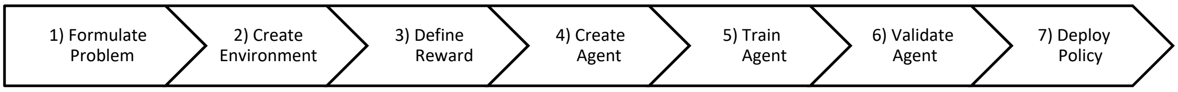

Fig. 3: Workflow of setting up an RL-based controller according to The MathWorks, Inc. (2023)

For steps 3) through 6) the Reinforcement Learning Designer application provided by the Reinforcement Learning Toolbox (The MathWorks, Inc., 2023) was used.

1) Formulate Problem

At the beginning of the RL agent design process, it is necessary to define the task, the way of interaction and the objectives. In this study, the objective of the RL agent is to control the heat pump in such a way that the thermal storage always delivers temperatures of at least 55 °C to the consumers, as the typical controller (Section 3.2) does. The continuous action space (0.2 to 1) is the control signal of the modulating heat pump. It is switched off when the control signal is less than the minimum modulation level of 0.3, or switched on when it is between 0.3 and 1. It is chosen according to the observation of the top T_{top} and bottom storage temperatures T_{bottom} and, in an advanced version, the thermal load for space heating and domestic hot water preparation.

2) Create Environment

The environment the agent interacts with is created as a MATLAB/Simulink subsystem and describes the building energy system shown in Section 3.1. This subsystem is connected to the RL agent block by the input of the control signal for the heat pump and the outputs of the top and bottom temperatures of the thermal storage, the thermal load, and the reward.

3) Define Reward Function

The reward function is based on the temperatures of the thermal storage. It gives a negative reward r i) if the top and bottom temperatures are too low to maintain the heat supply temperature and ii) if the bottom temperature is too high to prevent the thermal storage from overheating. In all other cases, the reward r is zero or positive. The definition of this region-based reward is shown in the following equations.

$$r_1 = -4 \quad \text{if } T_{top} < 55\ °C \qquad \text{(eq. 1)}$$
$$r_2 = 0 \quad \text{if } 55\ °C <= T_{top} < 57\ °C \ \text{ else } 3 \qquad \text{(eq. 2)}$$
$$r_3 = -16 \quad \text{if } T_{bottom} > 58\ °C \qquad \text{(eq. 3)}$$
$$r_4 = -6 \quad \text{if } 58\ °C >= T_{bottom} > 53\ °C \qquad \text{(eq. 4)}$$
$$r_5 = 2 \quad \text{if } 53\ °C >= T_{bottom} >= 45\ °C \ \text{ else } -5 \qquad \text{(eq. 5)}$$

At each time step t the reward r_t is calculated:

$$r_t = r_1+r_2+r_3+r_4+r_5 \qquad \text{(eq. 6)}$$

This reward function is implemented in the MATLAB/Simulink subsystem that contains the building energy system model.

4) Create Agent

An RL agent contains two components: the policy, represented by a function approximator (e.g., artificial neural networks), and a learning algorithm that optimizes the policy based on the chosen actions, observations from the environment, and rewards. Both depend on the type of agent.

The RL Designer application offers six types of agents:

- Deep Q-Network (DQN)
- Deep Deterministic Policy Gradient (DDPG)
- Twin-Delayed Deep Deterministic (TD3)
- Proximal Policy Optimization (PPO)
- Trust Region Policy Optimization (TRPO)
- Soft Actor-Critic (SAC)

When creating an RL agent, the RL Designer application only suggests agent types that are compatible with the environment being created. In this case, the Soft Actor-Critic (SAC) is chosen because it is model-free and can handle continuous action spaces. Values between 0.2 and 1 are defined as the action space for the control signal of the heat pump. In contrast to the time variable step size of the model solver, the RL agent requires a fixed time step size for its actions. As a trade-off between high temporal resolution of the RL agent actions and an acceptable computation time, a sample time of 600 seconds was chosen.

Two agents were created to explore the influence of the number of observations on the performance of the learned policy. The first receives only the two temperatures of the thermal storage as observations, while the second also observes the thermal load for space heating and domestic hot water preparation.

5) Train Agent

The agents were trained for a maximum episode length of three winter days. The rewards are cumulated over a whole episode. The stopping criterion for the leaning process was the average reward of the episodes. So, when the average reward over a defined number of episodes is not improving significantly the training will be stopped.

6) Validate Agent

After training the agent, its learned policy was evaluated in an annual simulation. The results are presented in Section 4.

7) Deploy Policy

As a final step in the RL agent design process, the learned policy can be transferred to real controllers by generating appropriate code. This paper focuses on a simulation-based investigation; therefore, this step was skipped.

4. Results and Discussion

The building energy system model described in Section 3.1 was used to run simulations with different control strategies for the heat pump. The simulation results are presented in the following subsections.

4.1. Simulation of typical control strategies

As a reference, the typical on/off strategy based on the temperatures of the thermal storage described in Section 3.2 (basic control strategy) was simulated with and without stationary battery storage. The calculated annual electricity consumption of the heat pump is 90,250 kWh_{el}/a. It provides 230,500 kWh_{th}/a of heat with an annual coefficient of performance (COP) of 2.555. The monthly distribution for the electricity consumption of the heat pump and households is shown in Figure 4.

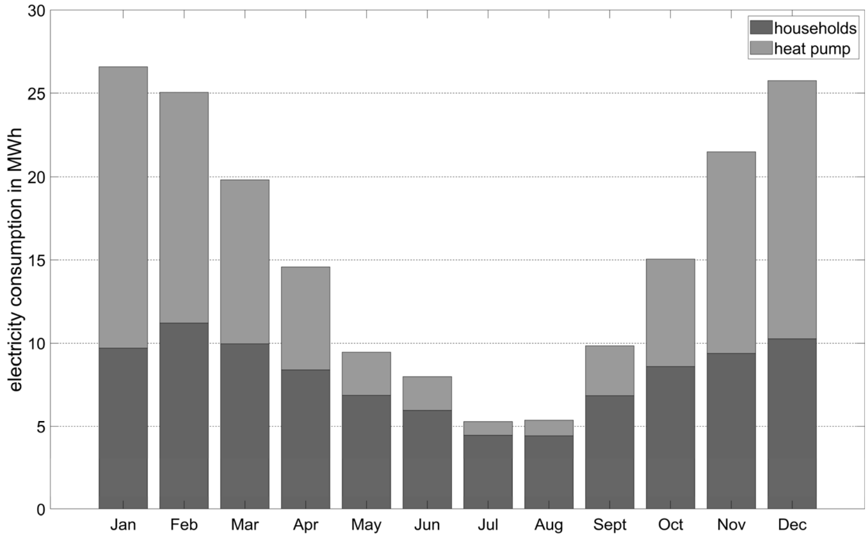

Fig. 4: Monthly distribution of total electricity consumed, broken down by heat pump and households

The monthly over all electricity consumption varies between 5.3 MWh in July and 26.6 MWh in January. Comparing the monthly distribution of the electricity consumption with the PV generation (Figure 5), it is clear that there is a PV surplus in summer and a shortage of self-generated electricity in winter.

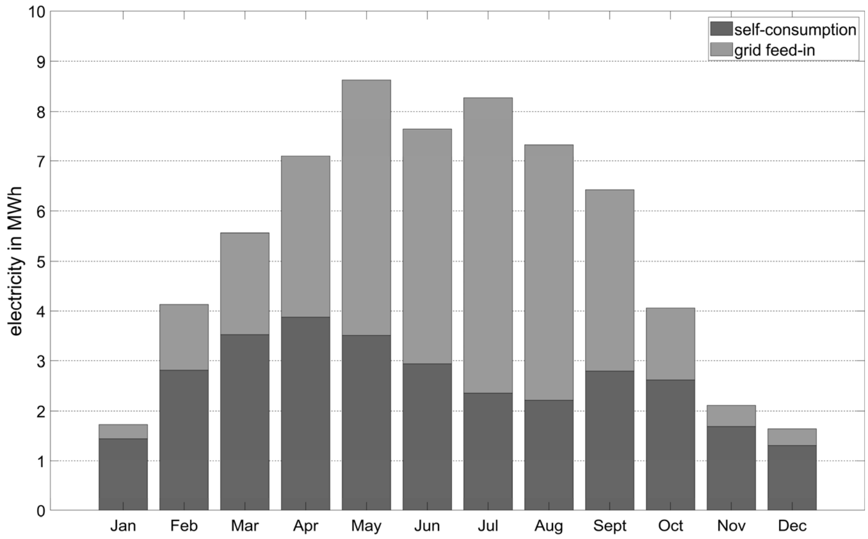

Fig. 5: Monthly distribution of PV electricity generation, broken down by self-consumption and grid feed-in for basic control strategy

For the variant without battery storage, the simulation results (Figure 5 and Table 1) show a higher annual self-consumption rate (48.1 %) and a lower annual self-sufficiency (16.7 %) compared to conventional single-family buildings (Quaschning, 2022) or a net-zero energy single-family building (both approx. 37 %, Milan et al., 2012). This is due to the higher electricity demand compared to the size of the PV system. In the winter months, up to 80 % of the monthly generated PV electricity is self-consumed, while in summer months up to 70 % has to be fed into the grid (Figure 5). Even in an ideal case (infinite capacity of the battery storage), only about 1/3 of the total electricity consumption can be covered by the PV system.

By implementing battery storage, the annual self-consumption rate and self-sufficiency can be increased by a factor of about 1.5, and the grid consumption and feed-in can be reduced. The monthly self-consumption rate can be increased up to 100 % in winter.

Tab. 1: Simulation results

Simulation Variant / Performance Indicator	Basic Control without Battery Storage	Basic Control with Battery Storage	PV Optimized without Battery Storage
Self-consumption rate in %	48.1	72.2	49.3
Self-sufficiency in %	16.7	25.1	17.1
Electricity demand of heat pump in kWh	90,250		90,511
Annual coefficient of performance	2.555		2.547
Electricity consumption from grid in kWh	155,192	139,564	154,620
Electricity feed-in into grid in kWh	33,577	17,949	32,744

Instead of implementing battery storage, the rule-based PV optimized strategy described in Section 3.2 was tested. The simulation shows only very small improvements of about 2.5 % for the self-consumption rate and self-sufficiency compared to the basic control strategy. One reason for this is that, in the on/off mode, the electric power consumed by the heat pump is always higher than the surplus of PV power, which leads to electricity consumption from the grid. Therefore, a modulating operating mode is necessary to improve the match between the surplus and the heat pump's electricity demand and should be considered in the development of RL approaches. The second reason for only very small improvements is that the high PV electricity surplus in summer cannot be shifted to cover the household's electricity consumption in the evening and at night, as a battery storage can do. Therefore, even with more advanced control strategies for the heat pump, battery storage should be used.

The simulation results shown here will be used as a reference for comparison with more advanced RL-based strategies that will be developed based on the RL agent introduced in Sections 4.2 and 4.3.

4.2. Design and training of reinforcement learning based heat pump control

During the initial learning process, high temperatures in the bottom storage tank caused an infinite mass flow between the heat pump and the thermal storage, resulting in a training termination. To ensure that the agent can explore actions that lead to high bottom storage tank temperatures and high negative rewards without terminating the learning process, an additional controller was implemented in the environment. It turns off the heat pump when the bottom storage tank temperature exceeds 58 °C, even if the action chosen by the RL agent is the opposite. This approach allows the agent to learn a policy that avoids too high temperatures in the bottom storage tank.

Two RL agents were trained with different numbers of observations. Figure 6 shows the episode reward (light blue line) and the average of 5 episodes (dark blue line) for both trainings. The increasing rewards from episode to episode show a good improvement of the policy. In both cases, the stopping criterion is met after only eleven episodes with an episode reward of about 1,880. So, the learning process itself is obviously not improved by an additional observation.

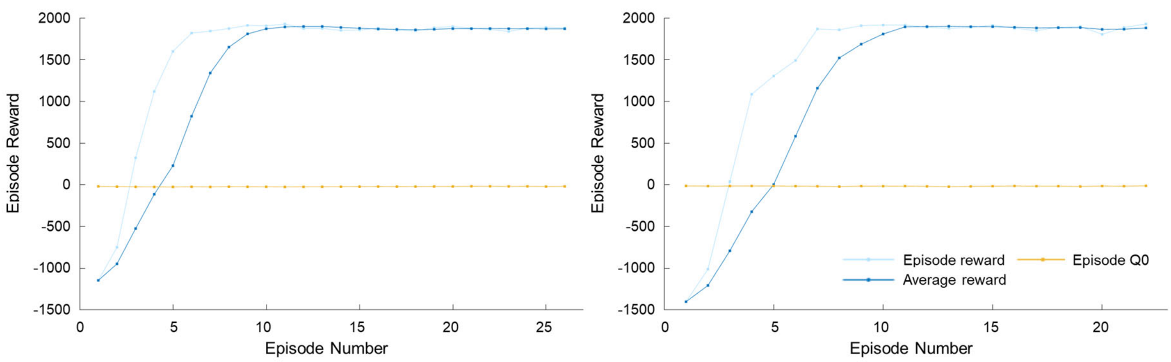

Fig. 6: Episode reward during learning process of RL agent with two observations (left) and three observations (right)

Due to the different thermal loads, especially for space heating, in winter and summer, it was tested to train the RL agent for an additional summer period of three days. However, this resulted in decreasing rewards, so the policy learned for winter only was used for the annual simulations presented in Section 4.3.

4.3. Simulation of reinforcement learning based heat pump control

The annual simulations show similar electricity consumption from and feed-in into the electricity grid compared to the basic control strategy, which was expected since there is no PV optimization implemented yet.

Both RL agents can always provide the required supply water temperatures. However, the analysis of the annual positive and negative rewards earned by the two agents (Table 2) shows that in an identical environment and with an identical reward function, adding one observation can improve the operation of the heat pump to better meet the temperature constraints implemented in the reward function, even though the training itself did not show any improvement.

Tab. 2: Comparison of gained annual rewards

Reward	2 Observations	3 Observations	Improvement absolute	Improvement relative in %
Positive	2,436,545	3,361,755	925,210	38.0
Negative	-1,530,056	-1,011,139	518,917	33.9
Sum	906,489	2,350,616	1,444,127	159.3

Including an additional observation can increase the positive annual reward by 38.0 % and reduce the negative annual reward by 33.9 %. In total the reward increases by 159.3 %.

The intervention of the additional controller, which switches off the heat pump when the bottom storage tank temperature exceeds 58 °C, was also analyzed. The total intervention time of the controller and the number of interventions were calculated for both agents (Table 3).

Tab. 3: Analyses of the intervention of the additional controller

	2 Observations	3 Observations
Total intervention time in h	53.1	74.4
Number of interventions	80	105

The additional controller only needs to intervene for up to approximately 75 hours, or 105 times per year. The average intervention time is less than one hour. Most of the interventions take place in summer when the thermal load is low. This is consistent with the results of the additional summer period training (Section 4.2). Thus, there is a potential for further improvement in learning the agent switching of the heat pump at times of high bottom storage temperatures.

One solution is to modify the heat pump model. The fixed heat pump output temperature of 60 °C used in this simulation causes the infinite mass flow when the thermal storage is fully charged at 60 °C (Section 4.2). Therefore, using a variable output temperature depending on the return water temperature may be a promising approach to allow the RL agent to better learn to switch off the heat pump at high storage temperatures even without the intervention of the additional controller.

5. Conclusions and outlook

A review of the literature showed that most of the publications investigating RL approaches for building energy (sub)systems have been carried out for only one or two (combined) systems and have the reduction of energy costs or consumption as their primary objective. Only two publications use system configurations like the one investigated here. However, the models were developed for energy efficient single-family homes and are based on simplified linear models with time steps of one hour, which is a coarse time resolution for building energy system control and not suitable for detailed models. Also, mass flows and temperatures in hydraulic circuits and thermal storages are not considered in detail. However, it is very important to consider the temperature distribution in the thermal storage because its thermal capacity is highly dependent on it, and the efficiency of the heat pump is influenced by the output temperature. Therefore, the detailed model used here provides more realistic results.

A detailed model of a multi-family building energy system was developed in MATLAB/Simulink using the CARNOT toolbox (Solar Institut Jülich, 2022). Typical control strategies were used for an annual simulation, which will serve as a reference for future RL agent developments implementing PV optimization.

The Reinforcement Learning Designer application of the Reinforcement Learning Toolbox (The MathWorks, Inc., 2023) was used to design and train two RL agents for the heat pump control. One agent receives only two storage tank temperatures as observations, while the other agent also observes the thermal load of the building. The RL agents were trained to provide the required supply water temperature of at least 55 °C to the consumers, as the typical controller does.

Annual simulations show that both RL agents can always provide the required supply water temperature. The annual reward of the RL agent using three observations instead of two increases by about 160 %, so the control strategy can be significantly improved by adding one observation.

The analysis of the additional controller that prevents too high bottom storage temperatures shows that it only intervenes up to 75 hours per year, mostly in summer, which is a satisfactory result. However, there is potential to improve learning the agent switching of the heat pump at times of high bottom storage temperatures e.g., by modifying the heat pump model.

With a well-trained reinforcement learning agent that satisfies the temperature constraints in the thermal storage, the next step is to design an agent that takes into account the PV electricity generation to control the heat pump to increase the self-consumption rate. Therefore, PV electricity generation and household electricity consumption need to be added to the observations, and electricity exchange with the grid needs to be implemented as a criterion in the reward function. The challenge in designing the reward function will be the weighting of the two objectives, the required temperatures in the thermal storage, and the reduced electricity exchange with the grid.

Acknowledgments

The work presented in this paper was funded by the Bavarian Research Foundation within the research network “Energy – Sector Coupling and Micro Grids (STROM)” (Project ID: AZ 1473-20) within subproject 7 “Decentralized Energy Management”. The objective of subproject 7 is to develop forecast and/or AI-based control strategies for energy systems in multi-family buildings that couple the heat, electricity, and e-mobility sectors.

References

Bongs, C., Wapler, W., Dinkel, A. Miara, M., Auerswald, S., Lämmle, M., Hess, S., Kropp, M., Eberle, R., Rodenbücher, B., Schmidt, F., Ruppert, M., Carbonare, N., Wagner, A., 2023. LowEx-Konzepte für die Wärmeversorgung von Mehrfamilien-Bestandsgebäuden, final report. Available online: http://www.lowex-bestand.de/wp-content/uploads/2023/03/Abschlussbericht_LiB.pdf. Accessed 8 August 2023

Dounis, A.I., Caraiscos, C., 2009. Advanced control systems engineering for energy and comfort management in a building environment - A review. Renewable and Sustainable Energy Reviews, vol. 13, pp. 1246-1261. DOI: 10.1016/j.rser.2008.09.015

DWD Deutscher Wetterdienst, 2017. Testreferenzjahre. Available online: https://www.dwd.de/DE/leistungen/testreferenzjahre/testreferenzjahre.html. Accessed 4 September 2023

Kuboth, S., Heberle, F., König-Haagen, A., Brüggemann, D., 2019. Economic model predictive control of combined thermal and electric residential building energy systems. Applied Energy, vol. 240, p. 372-385. DOI: 10.1016/j.apenergy.2019.01.097

Langer, L., Volling, T., 2022. A reinforcement learning approach to home energy management for modulating heat pumps and photovoltaic systems. Applied Energy, vol. 327, p. 120020. DOI: 10.1016/j.apenergy.2022.120020

Loga, T., Stein, B., Diefenbach, N., Born, R., 2015. Deutsche Wohngebäudetypologie: Beispielhafte Maßnahmen zur Verbesserung der Energieeffizienz von typischen Wohngebäuden, 2nd ed. IWU, Darmstadt. ISBN 9783941140479. Available online: http://www.building-typology.eu/downloads/public/docs/brochure/DE_TABULA_TypologyBrochure_IWU.pdf. Accessed 8 August 2023

Milan, C., Bojesen, C., Nielsen, M. P., 2012. A cost optimization model for 100% renewable residential energy supply systems. Energy. vol. 48, pp. 118-127. DOI: 10.1016/j.energy.2012.05.034

Prognos, Öko-Institut., Wuppertal Institut, 2021. Towards a Climate-Neutral Germany by 2045. How Germany can reach its climate targets before 2050. Executive Summary conducted for Stiftung Klimaneutralität, Agora Energiewende and Agora Verkehrswende. Available online: https://www.agora-energiewende.de/en/publications/towards-a-climate-neutral-germany-2045-executive-summary. Accessed 9 October 2023

Quaschning, V., 2022. Regenerative Energiesysteme -Technologie, Berechnung, Klimaschutz, 11th ed. Hanser, München. ISBN: 978-3-446-47163-4

Solar Institut Jülich. CARNOT Toolbox Ver. 7.3, 2022 für Matlab/Simulink R2018b, Available online: https://www.fh-aachen.de/forschung/solar-institut-juelich/carnot. Accessed 8 August 2023

SIA Schweizerischer Ingenieur- und Architektenverein, 2021. SIA 2024 – Raumnutzungsdaten für die Energie- und Gebäudetechnik, Zürich.

Sutton, R. S., Barto, A. G., 2018. Reinforcement Learning : An Introduction, second edition. MIT Press, Cambridge, ISBN 9780262039246

The MathWorks, Inc., 2023. Reinforcement Learning Toolbox™ – User's Guide. The MathWorks, Inc.

Vázquez-Canteli, J. R., Nagy, Z., 2019. Reinforcement learning for demand response: A review of algorithms and modeling techniques. Applied Energy, vol. 235, pp. 1072-1089. DOI: 10.1016/j.apenergy.2018.11.002

VDI Verein Deutscher Ingenieure e.V., 2021. VDI 4655 - Referenzlastprofile von Wohngebäuden für Strom, Heizung und Trinkwarmwasser sowie Referenzerzeugungsprofile für Fotovoltaikanlagen, Düsseldorf.

Wu, D., Rabusseau, G., François-lavet, V., Precup, D., Boulet, B., 2018. Optimizing Home Energy Management and Electric Vehicle Charging with Reinforcement Learning. *ALA 2018: Adaptive Learning Agents Workshop at the Federated AI Meeting 2018*, Stockholm, 14-15 July. Available online: https://ala2018.cs.universityofgalway.ie/papers/ALA_2018_paper_37.pdf. Accessed 30 August 2023

Ye, Y., Qiu, D., Wu, X., Strbac, G., Ward, J., 2020. Model-free real-time autonomous control for a residential multi-energy system using deep reinforcement learning. IEEE Transactions on Smart Grid, vol. 11, no. 4, pp. 3068-3082. DOI: 10.1109/TSG.2020.2976771

Yu, L., Xie, W., Xie, Di, Zou, Y., Zhang, D., Sun, Z., Zhang, L., Zhang, Y., Jiang, T., 2020. Deep reinforcement learning for smart home energy management. IEEE Internet of Things Journal, vol. 7, no. 4, pp. 2751-2762. DOI: 10.1109/JIOT.2019.2957289

Yu, L., Qin, S., Zhang, M., Shen, C, Jiang, T., Guan, X., 2021. A review of deep reinforcement learning for smart building energy management. IEEE Internet of Things Journal, vol. 8, no. 15, pp. 12 046-12 063. DOI: 10.1109/JIOT. 2021.3078462

Zator, S., Skomudek, W., 2020. Impact of DSM on Energy Management in a Single-Family House with a Heat Pump and Photovoltaic Installation. Energies, vol. 13, no. 13, 5476. DOI: 10.3390/en13205476

09. Testing, Certification and Monitoring

SWC 2023

ADHESIVE MATERIALS IN SOLAR-THERMAL COLLECTORS: RESULTS OF SEVEN YEARS FIELD EXPOURE AND ACCELERATED AGING TESTS USED TO SIMULATE 25 YEARS OF OPERATION

Abstract

The aging effects occurring in solar collectors within the adhesive material are by now not well understood. They are determined primarily by the temperature level in the collector. This temperature level has significantly increased during the last years due to the enhancement of the collector efficiency and the trend towards systems with higher solar fractions resulting in an increase in stagnation time and temperature. Furthermore, durability analyses of novel market products are needed, since only little is known about their long-term behavior.

The adhesive joint takes over multiple functions in the solar thermal collector, such as the structural bonding, the absorption of thermal stress of the transparent cover to the collector housing, and the sealing of the collector with respect to humidity, air and particle entry. Thus, it is a central component in a solar thermal collector. The accelerated aging tests represent the measured load in the solar collector at the component adhesive joint to a calculated corresponding period of 25 years.

We found that all test specimens showed a 100% cohesive fracture pattern after these stress tests. Thus, the adhesion between the transparent cover and the collector housing can be assumed to be ensured using the framework with the load depicted in the defined test cycle over 25 years. Compared to the reference value before aging, the tensile strength values change only marginally after being degraded.

The results of the mechanical properties of the small test specimens before and after seven years of exposure in maritime climate were determined and compiled. A nondestructive characterization method at the test specimens with Raman spectroscopy accompanied before the mechanical tensile testing was done.

Keywords: Components for solar collectors, adhesive, accelerated aging, thermal stress, humidity stress, tensile strength

1. Introduction

The objectives of the SpeedColl2 [1] project are the analysis of aging processes and the development of accelerated aging tests for solar thermal collectors and their components. The exposure of collectors and components in extreme climatic conditions enables the verification of these procedures and the development of degradation models.

Depending on their location and prevalent climatic conditions, the components of solar thermal collectors have to bear high climatic and mechanical stresses. High temperatures, UV-light, wind, snow, humidity or saline and corrosive atmospheres can be causes for a rapid degradation of materials and components.

This work focuses on the influence of the stress factors temperature and high humidity on the adhesive material bonding the glass cover with the frame in a solar thermal collector.

Since solar thermal technology is well-established round the globe, there is little information on the longterm behavior of collectors and solar systems. Basic statements on sealings in solar thermal collectors have been made at Sveriges Tekniska Forskningsinstitut (2013). This work was a guidance on how to define requirements on materials for seals and gaskets in solar collectors, mainly of flat plate type, potentially resulting in higher product quality and optionally also lower costs [2]. Additional work discussing the mechanical behaviour of an all-round fully adhesive supported absorber was done by Hermann Riess et al. (2013) [3].

10.18086/swc.2023.09.01 Available at http://proceedings.ises.org

Of recent date are works of Shemelin et al., addressing a novel concept of unglazed solar thermal facade collector based on a commercially available metal cladding facade system. From the architectural point of view, adhesive bonding allows one to attach a hydraulic system to the absorber sheet without any visible injuries to the front of the facade collector (2022) [4]. The component adhesive materials have also appeared more frequently in connection with combining photovoltaics (PV) and solar thermal (T) technology systems in recent times. The work of Huang et al. is mentioned here as an example (2023) [5].

In this project environmental stress data such as humidity and temperature were determined. The data collection varies from tests carried out in alpine, moderate and maritime locations through to measurements in arid and tropical regions. Test stands are installed on the Zugspitze, as well as in Freiburg, Stuttgart, Gran Canaria, the Negev Desert in Israel and Kochi in India. Additionally, the solar collectors and components undergo accelerated aging tests in the laboratory. Using the collected data, we will in future validate the procedures of the aging tests, which will provide information about the collector's thermal performance over its entire lifetime.

2. Methods: Adhesive material durability testing

2.1 Adhesion and mechanical properties

Adhesion and mechanical properties of the adhesive material are determined by the use of small test specimens (H-bar, see figure 2) in tensile tests. Tensile tests are among the most frequently performed test methods in mechanical materials testing. They are used to characterize the strength and deformation behavior under uniaxial loading.

Representative material combinations were selected for this purpose. The collector manufacturers involved in the project provided the frame materials, which were then used as substrates for the H-bar with 2-component silicone in the three variants aluminum raw, aluminum powder coated and aluminum anodized.

2.2 Approach for durability testing

The determination of real load data takes place at various outdoor weathering test stands of the participating research institutes in Freiburg and Stuttgart (moderate climate), on the Zugspitze (alpine) and on Gran Canaria (maritime), as well as in India (tropical) and the Negev desert in Israel (arid). Here, the individual components adhesives, absorbers, reflectors and transparent covers as well as complete collectors are exposed.

The exposure sites are equipped with extensive stress monitoring that continuously records aging-relevant environmental conditions as well as various, microclimatic variables of materials and components. The data are used to investigate the effects of specific stress factors and combinations. The aim is to develop aging models and validated test procedures for components and collectors.

Galvanic isolation between the H-PK and the holding structure is ensured by a specially designed holder made of polytetrafluoroethylene (PTFE). In total a number of 405 test specimens were exposed.

As time transformation model the approach as by Savante Arrhenius was chosen. The derived equation of reaction kinetics, which describes the relationship between the change of a state P and the temperature, is [6]:

$$\Delta P \sim \exp\ [-E_T/RT] \qquad \text{(eq. 1)}$$

where ΔP is the chance of state, E_T is the Arrhenius activation energy expressing the temperature dependence of a thermal reaction of an absorber surface in kJ/mol, R is the ideal gas constant equal to 8.314 J/(K*mol), T is the temperature in K.

The accelerated test duration t_R corresponding to 25 years of real exposure at a constant temperature T_R is thus described by [7]:

$$t_R = 25 years \cdot \exp\left[-\frac{E_T}{R}\cdot\left(\frac{1}{T_{eff}}-\frac{1}{T_R}\right)\right] \qquad \text{(eq. 2)}$$

where t_R is the duration of the experiment in hours, E_T is the Arrhenius activation energy expressing the temperature dependence of a thermal reaction of an absorber surface in kJ/mol, R is the ideal gas constant equal to 8.314 J/(K*mol), T_{eff} is the effective mean temperature in K and T_R is the temperature for accelerated testing in K and a service life of 25 years with 8760 h per year.

2.3 Non-destructive analysis

As a complement to the tensile tests, a non-destructive analytical method was selected. A confocal Raman spectrometer (WITec, alpha 500) was used for the analysis of any molecular changes in the test specimens caused by the exposure. The excitation source is a laser with a wavelength of 532 nm and a maximum power of 75 mW. The spectrometer is equipped with a 600 lines/mm grating and a CCD camera. This analytical method was chosen to try an alternative to the classical standard tensile tests.

3. Outdoor exposure

A set of three different solar thermal collectors and small test specimens (H-bar) were exposed to outdoor weathering in different climatic regions while the climatic conditions (temperature, humidity, wind, precipitation, UV). The absorber and the adhesive joint temperature at different position were monitored continuously (figure 1).


Figure 1 Thermal solar collectors prepared with thermocouple to measure the adhesive joint temperature position top left (left) and position top middle(right) alt maritime exposition

Within the project, small test specimens (H-bar) with representative material combinations were used for the determination of real load data taking place (figure 2).

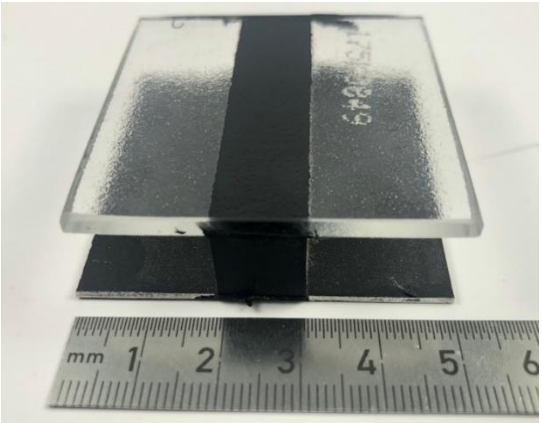

Figure 2 Test specimen (H-bar) for outdoor exposure and indoor testing, Adhesive is 12 x 12 x 50 mm³ (left) and Exposure at the maritime site Gran Canaria (right)

3.1 Quality assurance of meteorological data

A measurement system allowed all sensors read out by every minute and stored as 5-minute average values automatically. A data processing began after archiving the data in a database. The processing of meteorological parameters was done almost automatically. It started with a script-programmed pre-processing step, in which the absolute limits for each meteorological parameter are defined and existing data gaps and grossly erroneous values are identified by a plausibility check. Subsequently, the outliers were eliminated by a parameter-specific moving average and by considering the residuals. In addition, linear interpolation was applied for gaps of up to ten minutes and the data was converted to a suitable format for further manual processing. For larger gaps, data from the partner institutes at the respective sites had to be used. The missing data was then adapted accordingly by transformation using suitable models. Once this process had been completed, the data was checked for plausibility. With the release of the data, the data processing was completed. Figure 3 the shows the schematic diagram of the process [8].

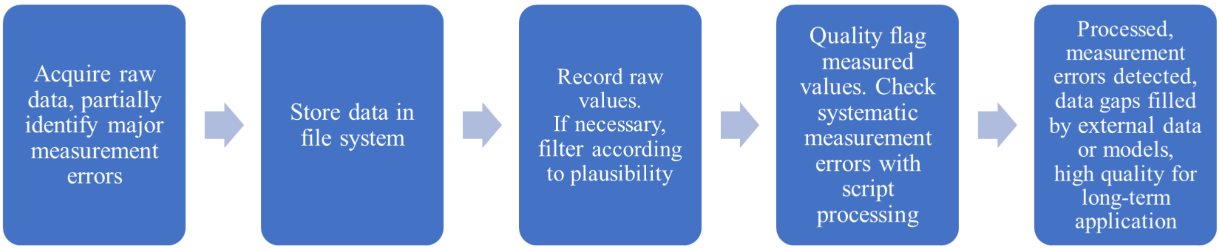

Figure 3 Schematic diagram of the process of measurement and processing of meteorological data.

3.2 Exposure of collectors and test specimens

A set of three collector types of similar collector design were exposed at the test sites. Table 1 documents the specifications of the collectors where η_0 is the optical efficiency [-], a_1 is the heat loss coefficient [W/(m²K)] and a_2 is the heat loss coefficient [W/(m²K²)]. The flat-plate collectors were all vented.

Tab. 1: Specification of the three collector types

type 1	type 2	type 3
solar glass cover	solar glass cover with an anti-reflective coating	solar glass cover
silicone bonding	aluminum cover strip	silicone bonding
PVD coated absorber on aluminum plate	PVD coated absorber on aluminum plate	PVD coated absorber on aluminum plate
harp-shaped copper piping ultrasonically welded	meander-shaped copper piping laser-welded	meander-shaped copper piping laser-welded
mineral wool insulation	melamine epoxy foam insulation	mineral wool insulation
aluminum frame	aluminum frame	aluminum frame
steel bottom plate with an aluminum-zinc coating	steel bottom plate with an aluminum-zinc coating	steel bottom plate with an aluminum-zinc coating
aperture area 1.94 m²	aperture area 2.33 m²	aperture area 2.35 m²
η_0= 0.739, a_1 = 3.98, a_2=0.0096	η_0= 0.793, a_1 = 3.63, a_2=0.0119	η_0= 0.835, a_1 = 3.63, a_2=0.0132

In order to gain also worst-case data, some of the test sites were located in extreme climates with very harsh conditions (Table 2).

Tab. 2: Exposure of collectors and test specimens (H-bar) at locations with extreme climates and the tilt angle

Climates	Location	Tilt angle	collectors	test specimens H-bar
tropical	Kochi, India	25°	yes	yes
alpine	Schneefernerhaus, Zugspitze, Germany	45°	yes	no
arid	Sede Boker, Negev Dessert, Israel	31°	yes	no
maritime	Pozo Izquierdo, Gran Canaria, Spain	23°	yes	yes
moderate	Stuttgart and Freiburg, Germany	45°	yes	yes

Small test specimens (H-bar) with representative material combinations were used for the determination of real load data taking place. The collector manufacturers involved in the project provided the frame materials, which were then used as substrates for the H-bar with 2-component silicone in the three variants aluminum raw, aluminum powder coated and aluminum anodized (Table 3).

Tab. 3: Specification of the three H-bar types

type 1	type 2	type 3
solar glass cover 3 mm thickness	solar glass cover 3 mm thickness	solar glass cover 3 mm thickness
silicone bonding 12 mm thickness	silicone bonding 12 mm thickness	silicone bonding 12 mm thickness
substrate aluminum row 5.0 mm thickness	substrate aluminum powder coated black 1.2 mm thickness	substrate aluminum anodized black 1.8 mm thickness

In Figure 4, the six outdoor exposure test sites are shown. The tilt angle was chosen to maximize the solar gains depending on the latitude of the different locations. All collectors were oriented to the south.

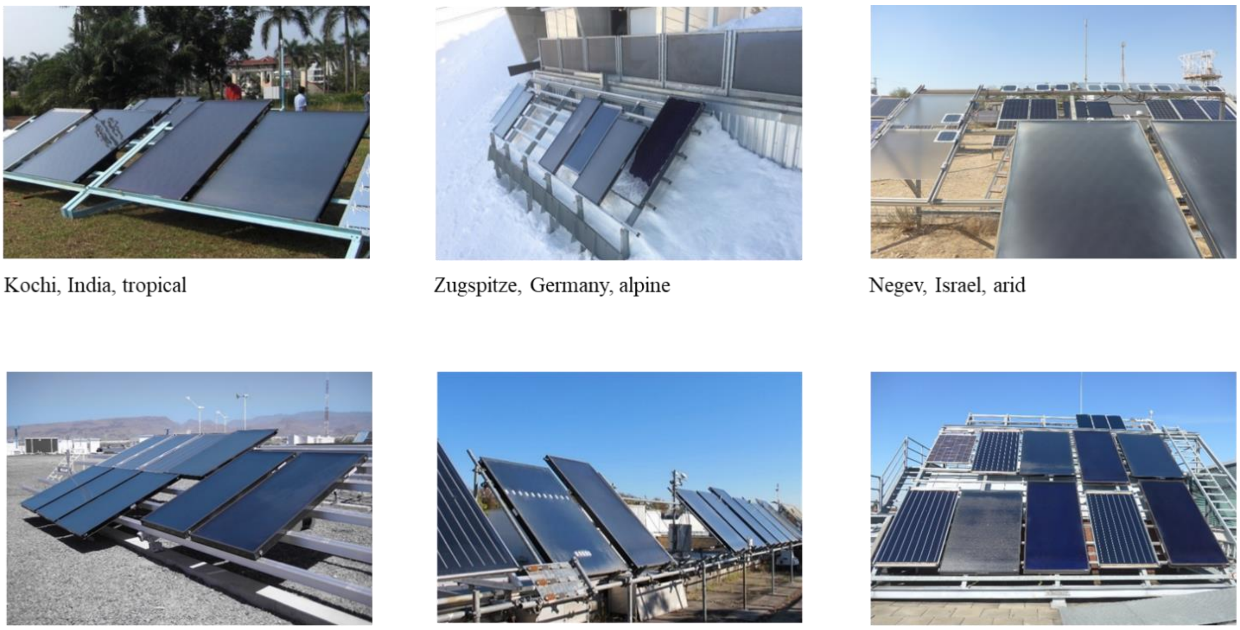

Kochi, India, tropical | Zugspitze, Germany, alpine | Negev, Israel, arid

Gran Canaria, Spain, maritime | Stuttgart, Germany, moderate | Freiburg, Germany, moderate

Figure 4 Exposure sites for solar thermal collectors and test components at different climate conditions tropical, alpine, arid, maritime and moderate

4. Results

4.1 Outdoor exposure of solar thermal collectors and test specimens: thermal stress

A set of three different solar thermal collectors were exposed to outdoor weathering under different climatic conditions while the climatic conditions and the collector microclimate were monitored continuously.

The histogram of the absorber temperature distribution in a solar thermal collector of type 3 is shown for different climates within the project is shown in figure 5. Since the collectors were not connected hydraulically to a domestic hot water system, the operating mode took place under constant stagnation conditions in an air air-filled system. For the different exposure sites, we used the same flat-plate collector type with a transparent cover. The sides and back of the housing were insulated to reduce heat loss to the environment.

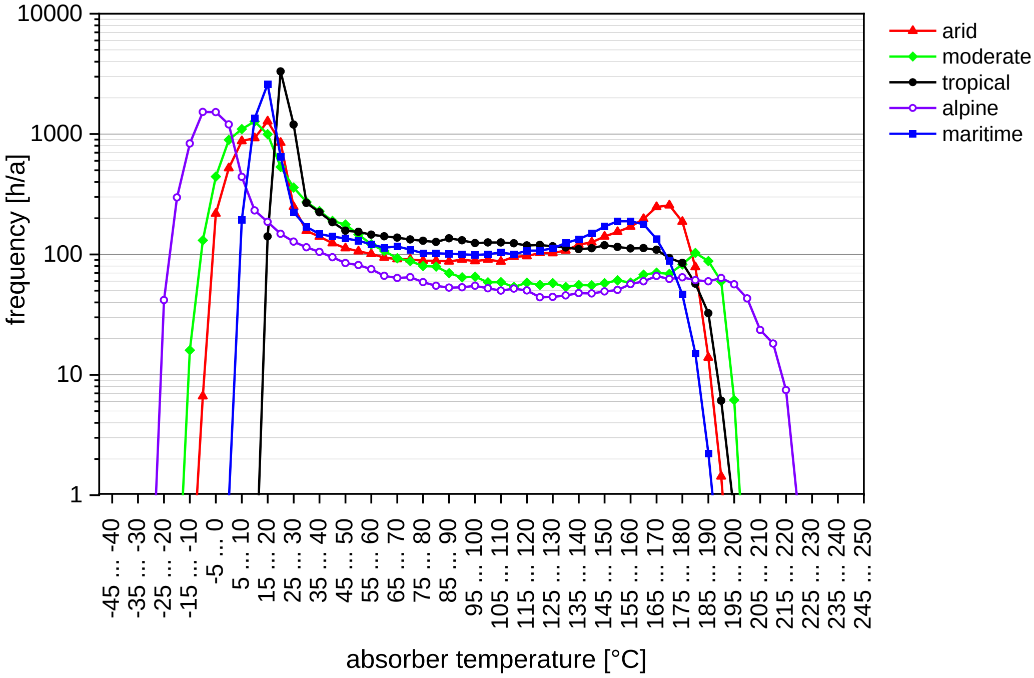

Figure 5 Absorber temperature distribution in a solar thermal collector under stagnation condition for different climates

The highest absorber temperatures, up to 225 °C, were measured at the alpine exposure site. This unexpected result is explained by the albedo effect of reflection from glacier and snow surfaces and by the relatively low pollution levels of the air at the alpine exposure site compared to all other exposure sites [8].

In figure 6 the ambient- and adhesive joint temperature and irradiance in collector plane at the arid exposition site at Negev desert in Israel for one typical day in September is shown.

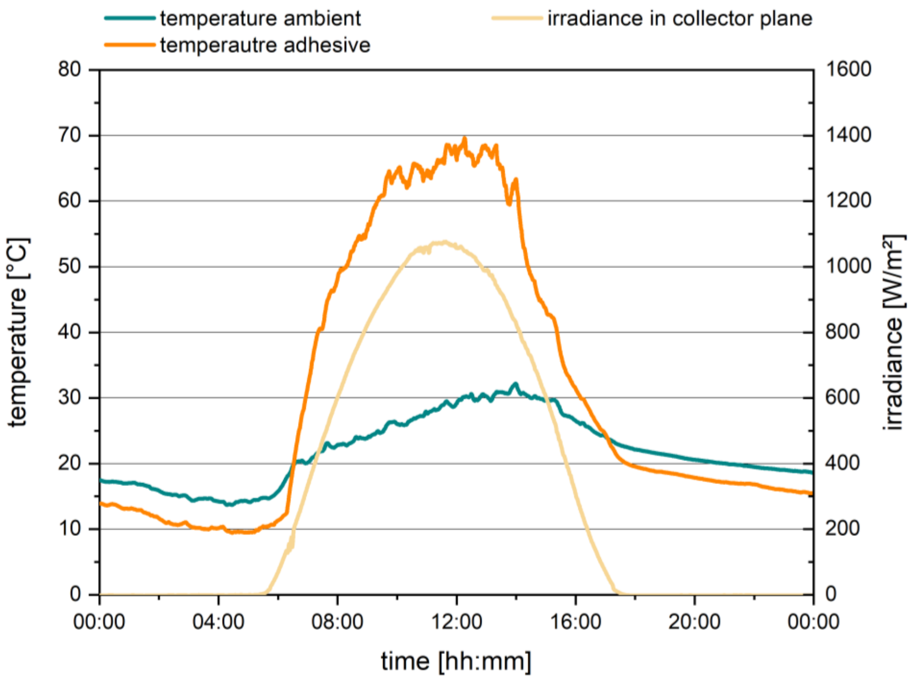

Figure 6 Ambient- and adhesive joint temperature one day in °C and irradiance in collector plane at arid exposition at Negev desert, Israel

In comparison to the other locations the alpine exposure site reaches the highest absorber temperature, which is consequently associated with a higher temperature within the collector and therefore the highest thermal load on the adhesive joint can be assumed in this case. Therefore, the thermal stress load of the alpine exposition site was chosen for the further for deriving the service life modeling. In figure 7 the frequency in hours in the period of one year of the adhesive joint- and ambient temperature at alpine exposition site is shown.

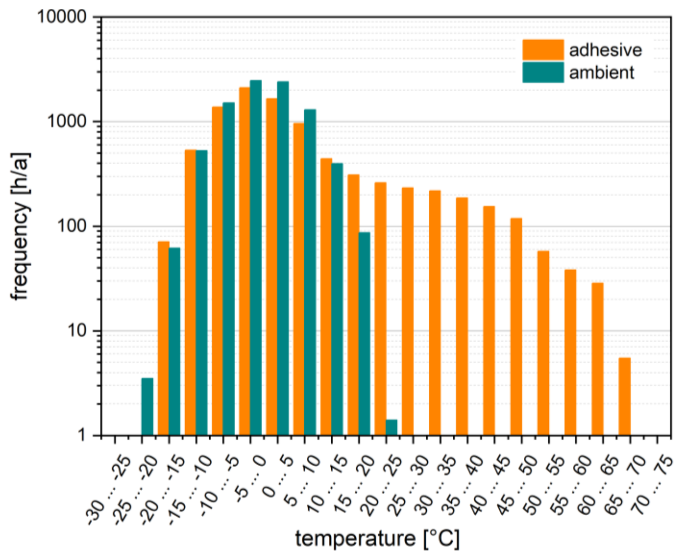

Figure 7 Frequency in hours in the period of one year of adhesive joint- and ambient temperature in °C at alpine exposition at Zugspitze, Germany

The maximum measured temperature of adhesive joint reaches 70 ° C. This value is over 45 K higher than the maximum measured ambient temperature.

4.2 Outdoor exposure of solar thermal collectors and test specimens: humidity stress

In order to answer the question of the combination of temperature and humidity stress regarding the adhesive material, a measurement was carried out on collectors in a cooled operating state at the reference site in Stuttgart. For this purpose, the collectors were hydraulically connected to a corresponding heat sink. The temperature and relative humidity inside the collector in the air gap between the absorber and the transparent cover was measured with a combined temperature and humidity sensor. The sensor was inserted through the back wall of the solar collectors and through their absorbers into the space between the absorber and the transparent cover. The preparation of the collector was done during the production at the solar collector manufacturer. The positioning in the collector plane was centered to the absorber length and width.

In figure 8 the temperature of the adhesive and relative humidity in the collector between absorber and inner glass surface is shown.

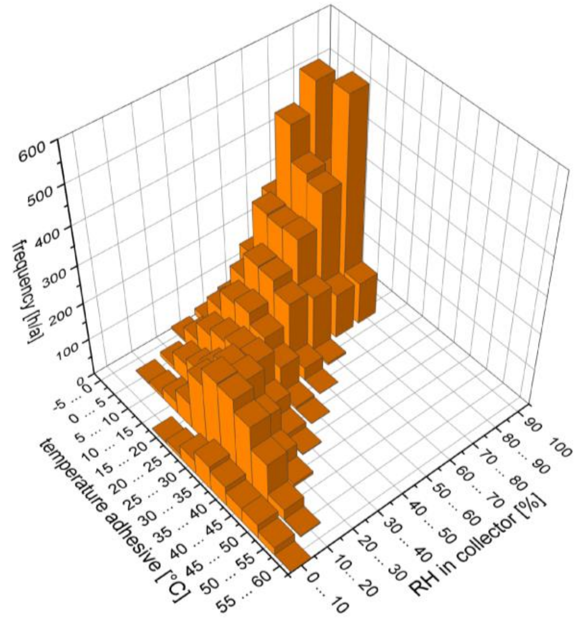

Figure 8 Temperature adhesive and relative humidity in the collector between absorber and inner glass surface at moderate exposition site, Stuttgart, Germany

A simultaneous occurrence of high temperature and relative humidity cannot be observed. in solar collectors during operation conditions. Therefore, a combined test with high temperature and humidity is not considered to be useful, since this stress situation for the adhesive joint in solar collectors does not occur in operation.

4.3 Adhesive material durability testing: Modelling

These measurement data are used to define the test conditions and times. As a model for the kinetics of the degradation processes, the approach of a time transformation according to Arrhenius was chosen (eq. 2). As a corresponding time period for a service life estimation, 25 years were used, corresponding to the expected period of service life for a thermal solar collector. In figure 9 the testing time for adhesive materials for thermal stress equivalent to a lifetime of 25 years with thermal loads taken from the alpine exposition site for three different testing temperature 75 °C, 85 °C and 95 °C, as function of the activation energy are shown.

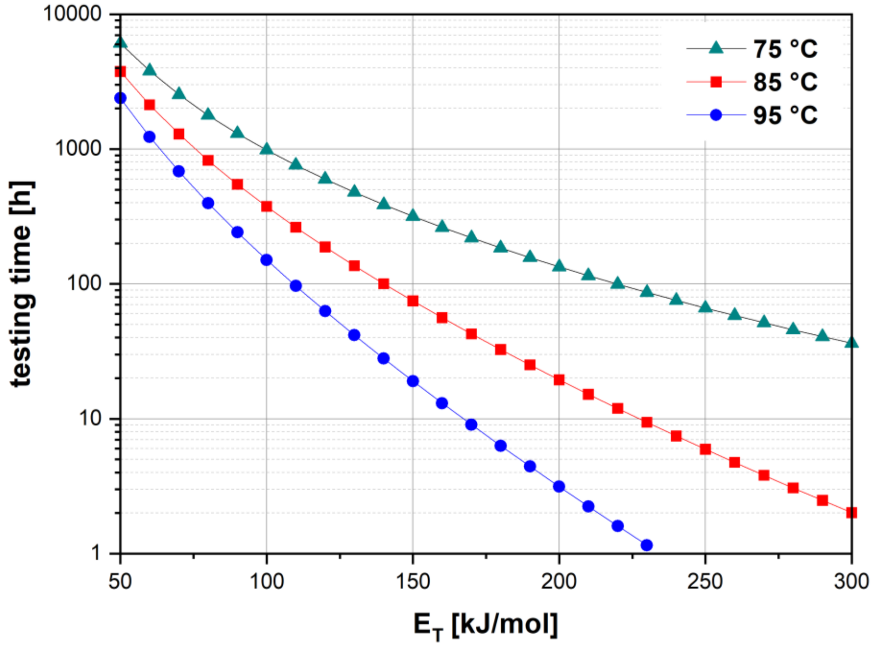

Figure 9 Testing time for adhesive material for thermal stress equivalent to a lifetime of 25 years with thermal loads taken from Zugspitze (alpine) in the German Alps for 75 °C, 85 °C and 95 °C testing temperature, as function of the activation energy

Based on the temperature stresses measured at the site and the accelerated aging model, we propose to perform the following tests on H-test specimens. The relevant stress factors of temperature and humidity will be considered. In addition, the adhesion properties between transparent cover and substrate will be tested. For this purpose, the adhesive joints are statically stretched in tension during aging (figure 10).

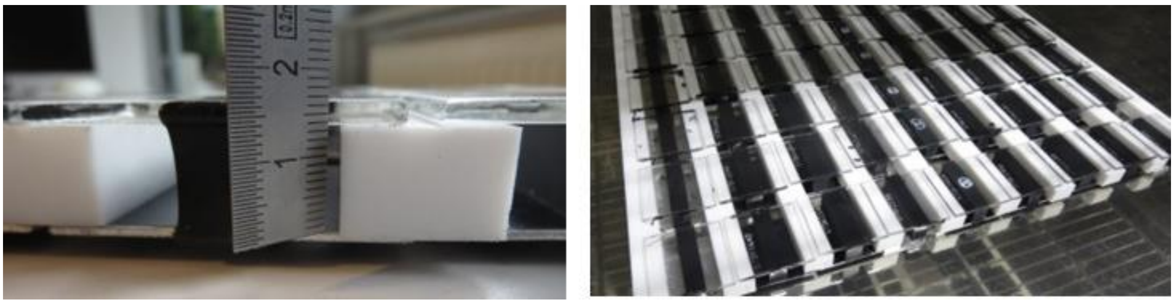

Figure 10 Test specimen (H-bar) for indoor Part C mechanical load via static elongation (12,5%) (left) and set in climate cabinet

The tests represent the measured load in the solar collector at the component adhesive joint to a calculated corresponding period of 25 years. For the activation energy, a value of 90 kJ/mol was assumed, at which the hydrolysis of covalent siloxane bonds takes place [9]. A maximum testing temperature of 85 °C was specified for the service life test. Using the approach described above, a value of approx. 600 h test time can be derived for the temperature stress factor in order to achieve an accelerated aging of 25 years. The test sequence consists of three parts addressing temperature and moisture stability as well as a combination of moisture stability and mechanical load via static elongation shown in table 4.

Tab. 4: Testing Part A, B, C

Testing	**Temperature**	**Humidity**	**Duration**
Part A temperature stability	85 ° C	RH <10%	600 h
Part B moisture stability	40 ° C	RH 95%	600 h
Part C moisture stability and mechanical load via static elongation (12,5%)	40 ° C	RH 95%	600 h

4.4 Adhesive material durability testing: results

In table 5 the results of the test sequence part A, part B and part C for one H-bar test specimen are shown. The results of the mechanical properties of the small test specimens before and after seven years of exposure are being determined and compiled. For statistical reasons, five test specimens were used for each test. The values shown are therefore mean values from a sample of n=5. In order to capture the time dependence of the accelerated aging on the test specimens, the following time steps were chosen: 150 h, 300 h, and 600 h.

Tab. 5: Testing results for Part A, B,

Part A temperature stability				
Mean value from 5 H-bars	tensile strength [N/mm²]	elongation F_{max}. [%]	tensile strength at 10% elongation [N/mm²]	tensile strength at 50% elongation [N/mm²]
Reference	0,58	115	0,12	0,30
150 h	0,62	141	0,11	0,29
300 h	0,52	131	0,10	0,25
600 h	0,52	134	0,09	0,24
fracture pattern	**100% cohesive fracture each (n=20)**			

Part B moisture stability				
Mean value from 5 H-bars	tensile strength [N/mm²]	elongation F_{max}. [%]	tensile strength at 10% elongation [N/mm²]	tensile strength at 50% elongation [N/mm²]
Reference	0,58	115	0,12	0,30
150 h	0,54	133	0,10	0,25
300 h	0,60	149	0,10	0,25
600 h	0,57	154	0,10	0,25
fracture pattern	**100% cohesive fracture each (n=20)**			

Tab. 5: Testing results for Part C

Part C moisture stability and mechanical load via static elongation (12,5%)				
Mean value from 5 H-bars	tensile strength [N/mm²]	elongation $F_{max.}$ [%]	tensile strength at 10% elongation [N/mm²]	tensile strength at 50% elongation [N/mm²]
Reference	0,58	115	0,12	0,30
150 h	0,50	112	0,08	0,26
300 h	0,60	143	0,08	0,25
600 h	0,62	156	0,08	0,24
fracture pattern	**100% cohesive fracture each (n=20)**			

In order to present the changes in mechanical properties more clearly, the results were also presented graphically (table 6).

Tab. 6: Testing results for Part A, B, C

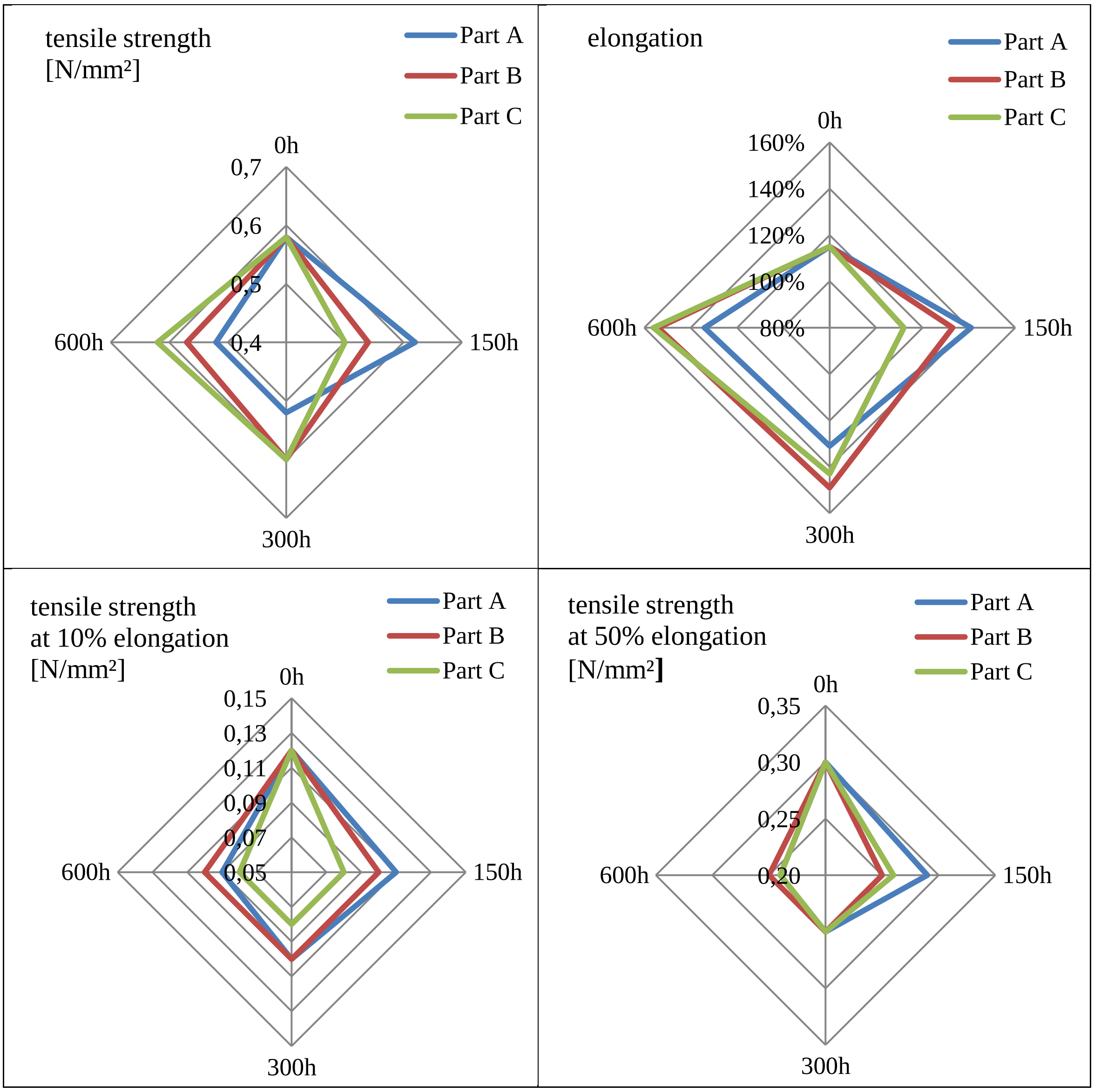

Performed tensile tests after aging according to part A, B or C showed 100% cohesive failure for all samples regardless of the chosen testing period up to 600 h. Therefore, the mechanical properties with respect to the adhesion of the transparent cover to the collector housing can be assumed to be ensured within the scope of the load depicted in the defined test cycle for more than 25 years. Compared to the reference values of the tensile strength, the values change only slightly after the service life test (-14% to 7%).

4.5 Outdoor exposure of test specimens at maritime exposition site

At the maritime site we had the facilities to keep a complete set of test specimens in sum 7.8 years continuously in exposure. In figure 11 an unexposed (reference) and an exposed test specimen are shown.

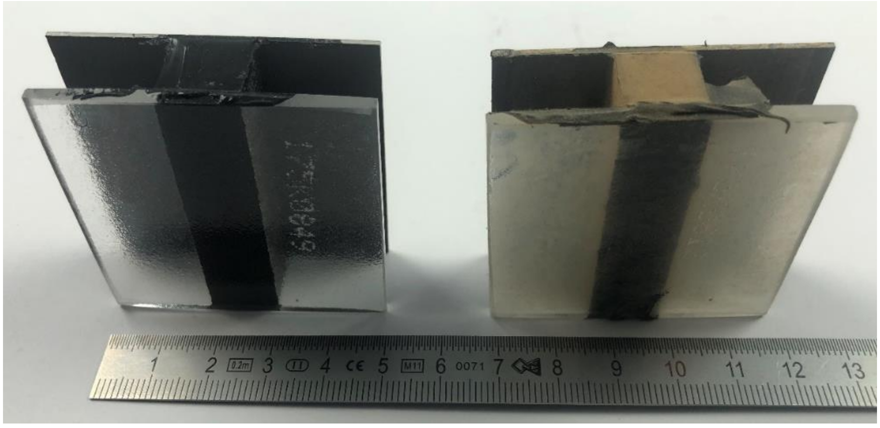

Figure 11 Test specimen (H-bar) Adhesive is 12 x 12 x 50 mm³left: reference, right after 7.8a Gran Canaria

Raman spectra were previously recorded on these test specimens before the mechanical tensile tests. In figure 12 Raman spectra and the associated molecule group vibrations for the reference sample and for the 7.8 years exposed sample at the maritime test site as measured and after a background subtraction are shown.

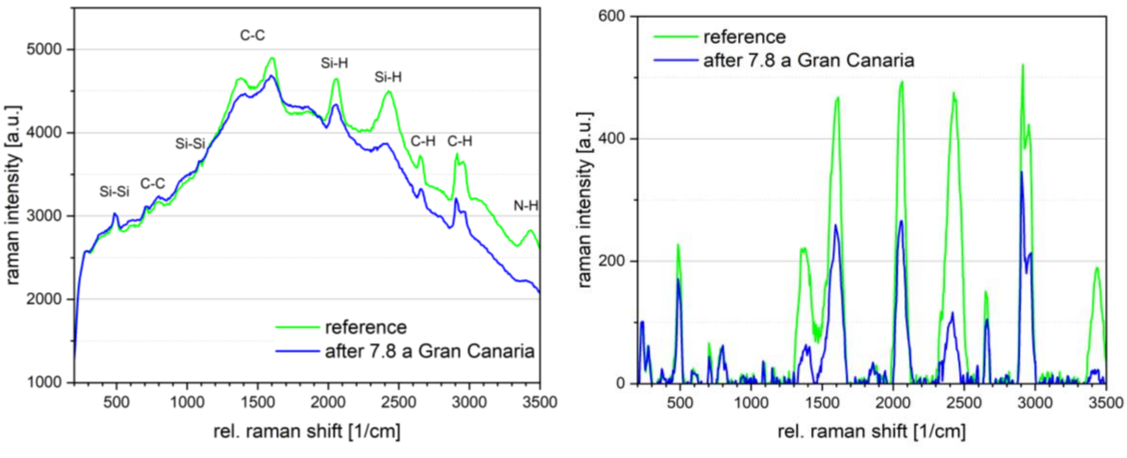

Figure 12 Raman spectra and associated molecule group vibrations reference and after 7.8a Gran Canaria as measured (left), after background subtraction (right)

It remains to be noted that no new Raman bands were caused by the exposure. It can therefore be concluded that the material has probably not changed chemically. The results of the tensile test are summarized in Table 7. A glass breakage was detected on one of the test specimens. Thus, mechanical tensile tests could only be performed on 4 H-bars for the type 1 material combination.

7.8 years exposure at maritime test site, Gran Canaria **H-bars type 1, type 2, type 3**				
Mean value	tensile strength [N/mm²]	elongation F_{max}. [%]	tensile strength at 10% elongation [N/mm²]	tensile strength at 50% elongation [N/mm²]
type 1 **Reference** from 5 H-bars	0,45	101	0,10	0,26
type 1 **7.8a maritime** from 4 H-bars	0,58	50	0,10	0,57
type 2 **Reference** from 5 H-bars	0,76	67	0,25	0,66
type 2 **7.8a maritime** from 5 H-bars	0,58	50	0,20	0,57
type 3 **Reference** from 5 H-bars	0,98	57	0,34	0,91
type 3 **7.8a maritime** from 5 H-bars	0,55	31	0,28	-
fracture pattern	**100% cohesive fracture each (n=29)**			

As a result of the comparison of the values of the tensile strength before and after exposure, changes from -44% to 45% can be observed. For all samples a 100% cohesive failure pattern was found.

5. Conclusion

Different solar thermal collectors and components we exposed in various extreme climates within the speedcoll2 project. Continuously monitoring the outdoor climatic conditions and the micro-climate inside the collector was performed. A complex quality assurance of the measured data was successfully defined and implemented.

The maximum measured temperature of adhesive joint in a solar thermal collector under stagnation conditions reaches 70 °C at the alpine exposition site. This value is over 45 K higher than the maximum measured ambient temperature. Based on the temperature stresses measured and the accelerated aging model, a proposal for service life test with three parts was developed. The relevant stress factors of temperature (Part A) and humidity (Part B) will be considered as well as the adhesion properties between transparent cover and the collector frame. For this purpose, the adhesive joints are statically stretched in tension during the aging tests (Part C).

Performed tensile tests after aging according to part A, B and C showed 100% cohesive fracture pattern for all samples regardless of the chosen testing period up to 600 h. Therefore, the mechanical properties with respect to the adhesion of the transparent cover to the collector housing can be assumed to be ensured within the scope of the load depicted in the defined test cycle for more than 25 years. Compared to the reference values of the tensile strength, the values change only slightly after the service life test (-14% to 7%).

The accelerated aging tests represent the measured load in the solar collector at the component adhesive joint to a calculated corresponding period of 25 years.

At the maritime site we had the facilities to keep a complete set of test specimens in sum 7.8 years continuously in exposure.

Tensile tests of the unexposed and the exposed test samples showed 100% cohesive fracture pattern for all samples. As a result of the comparison of the values of the tensile strength before and after exposure, changes from -44% to 45% and a 100% cohesive failure pattern can be observed.

A confocal Raman spectrometer was used as a non-destructive analytical method as a complement to the tensile tests. This allowed the analysis of any molecular changes in the test specimens caused by the exposure. No new Raman bands were caused by the exposure. It can therefore be concluded that the material has probably not changed chemically. This statement is consistent with the measurement results of the tensile test and the suitability of the method could be proven.

6. Acknowledgements

The authors would like to thank the industrial partners and the German Federal Ministry for Economic Affairs and Energy (FKz. 0325969A) for their support and funding.

7. References

[1] Development of Accelerated Aging Tests for Solar Thermal Collectors and their Components, www.speedcoll2.de

[2] Peter Kovacs, Jenny Johansson and Anna Jansson. “Guideline for sealings in solar thermal collectors.” SP Sveriges Tekniska Forskningsinstitut, (2013)

[3] Hermann Riess, Sebastian Brandmayr, Wilfried Zörner, Richard M. Greenough. “Analysis of the mechanical behaviour of an all-round fully adhesive supported absorber.” SHC 2013, International Conference on Solar Heating and Cooling for Buildings and Industry September 23-25, 2013, Freiburg, Germany

[4] Shemelin, Viacheslav, and Tomas Matuska. "Unglazed solar thermal collector for building facades." Energy Reports 8 (2022): 605-617.

[5] María Herrando, Kai Wang, Gan Huang, Todd Otanicar, Osama Bany Mousa, Rafaela A. Agathokleous, Yulong Ding h, Soteris Kalogirou, Ned Ekins-Daukes,, Robert A. Taylor f, Christos N. Markides, “A review of solar hybrid photovoltaic-thermal (PV-T) collectors and systems”, Progress in Energy and Combustion Science 97 (2023) 101072

[6] Svante Arrhenius, Z. Phys. Chem. 1889, 4, S. 226–248

[7] Köhl, M.; Heck, M.; Brunold, S.; Frei, U.; Carlsson, B.; Möller, K,.”Advanced Procedure for the assessment of the lifetime of solar absorber coatings.” Solar Energy Materials and Solar Cells, Volume 84, Issues 1-4, October 2004, Pages 275-289

[8] Kaltenbach, Thomas, Markus Heck, and Ismail Kaaya. "Standard testing of absorber surface durability according to ISO 22975–3 versus measured thermal and high-humidity stress of absorber surface at extreme test sites." Solar Energy Advances 3 (2023): 100042.

[9] Wolf, A. T., "Effects of Water Immersion on Building and Civil Engineering Joints and the Use of the Arrhenius Method in Predicting Adhesion Lifetime of Water-Immersed Joints," Journal of ASTM International, Vol. 5, No. 8, 2008, pp. 1-17

Reduction in soiling loss of PV module using hydrophobic coating with different water contact angle

Shivam Vishwanath[1], Anand Abhinav[2], Sudhanshu Mallick[2]

[1]Centre for Research in Nanotechnology & Science, Indian Institute of Technology Bombay, Mumbai, India
[2]Department of Metallurgical Engineering and Material Science, Indian Institute of Technology Bombay, Mumbai, India

Abstract

The deposition of dust particles on Photovoltaic (PV) surfaces is a well-known problem affecting solar panels' performance by reducing their efficiency. Dust and other soiling agents hinder the absorption of solar energy by photovoltaic cells. Consequently, this decreases energy generation, resulting in considerable losses to the PV industry. Hydrophobic coatings are known to reduce soil deposition on any surface. The objective of the present study is to compare the soiling loss of PV modules with and without hydrophobic coatings. Hydrophobic coatings with varying water contact angles (WCA) were applied to PV modules. Uncoated and coated mini-modules were kept for dust deposition in a simulated soiling chamber at different tilt angles to mimic real-world conditions. The soil deposition on coated PV mini-module is significantly less than on uncoated mini-module, leading to lower soiling loss. It indicates that applying hydrophobic coatings is an effective way to reduce the impact of soiling.

Keywords: Hydrophobic, Photovoltaic, Water contact angle, and soiling loss.

1. Introduction

The Photovoltaic (PV) module, used to generate electricity from the sun, must be used efficiently to minimize the current global energy crisis. PV modules comprise glass that prevents the solar cell from storms and dust. The wind carries the dust, and dirt settles on the PV cover glass, reducing the optimum solar irradiance that must reach the solar cell. It has been found that 4 g/m^2 of dust layer on the solar panel decreased the output power of the solar panel by 40% [1][2][3]. Hence, frequent cleaning is needed, which adds to the maintenance cost. However, the frequency of such a cleaning process can be reduced significantly by applying anti-soiling coatings on the PV cover glass. The anti-soiling coatings can be categorized as hydrophobic surfaces and super hydrophilic surfaces. However, hydrophobic anti-soiling coatings can also reduce the dust deposition rate on the surface of the PV modules [4][5].

Factors responsible for dust settlement are PV system tilt-angle and orientation, ambient temperature and humidity, site characteristics, dust properties, wind velocity, and glazing characteristics [3]. Different experimental conditions may result in varying dust deposition behaviors [6]. Further investigations are pivotal in unraveling the roles of roughness and surface energy on dust deposition, especially considering complications arising from different environmental conditions. In addition, the correlation between surface wettability and dust deposition remains an unsolved issue.

Several studies have demonstrated the effectiveness of hydrophobic, super hydrophilic, and super hydrophobic coatings for PV application [7][8]. However, none of the studies discussed the desired water contact angle (WCA) of the layer required for solar panels installed at different tilt angles. This study aims to quantify the losses on soiled PV modules at different tilt angles and with different surface wettability of PV modules. This study will help to determine the optimum water contact angle for hydrophobic coating needed to reduce the soiling loss of the solar panel. In addition, the dust coverage on PV modules with different surface wettability is quantified through an image-based method.

10.18086/swc.2023.09.03 Available at http://proceedings.ises.org

2. Experimentation

An artificial soiling chamber is a chamber that is used to accelerate the process of dust deposition, as it can take days in field conditions. The chamber is a 55 x 45 x 45 cm^3 cuboidal box made of 6 mm thick acrylic sheets shown in Figure 1, which creates a cloud of dust, and after some time, dust settles to form a uniform deposition over the exposed surface as shown in Figure 2. The dust used in experiments has been extracted from PV module placed at a real-time outdoor module monitoring station at IIT Bombay, Mumbai, India. The extracted dust was dried in a hot air oven to remove any moisture content before using it [9].

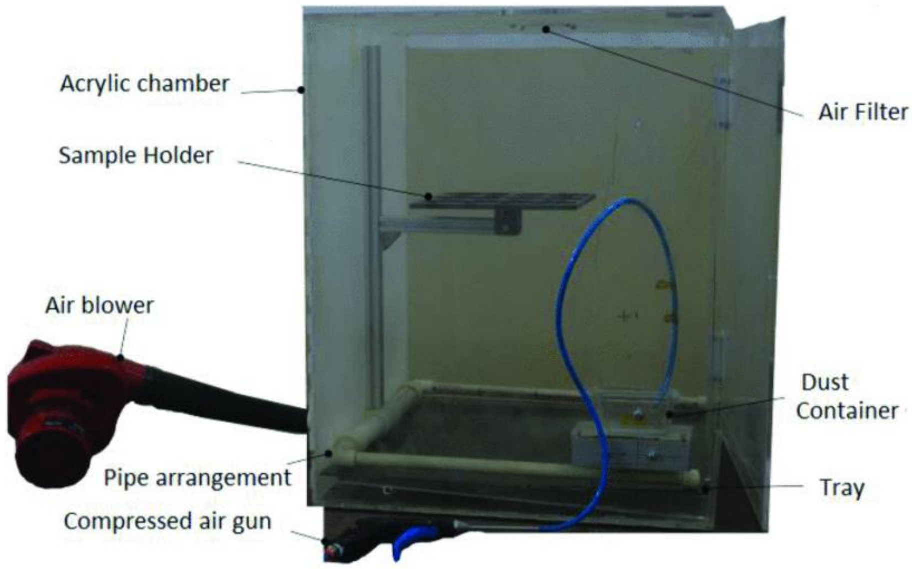

Figure 1. An artificial dry dust deposition system used in the experiment [9]

Hexamethyldisilazane-modified silica coating was developed, and three coating solutions were developed by varying the ratio of HMDS and silica [10]. Three mini-modules were spray-coated with these coating solutions, which resulted in coating with three different water contact angles. Three coated and one uncoated mini-module were kept for soiling in the soiling chamber at two different tilt angles, as shown in Figure 2. I-V characteristics of PV modules were studied before and after soiling. The quantification of dust coverage was studied using optical images and analyzed with ImageJ software.

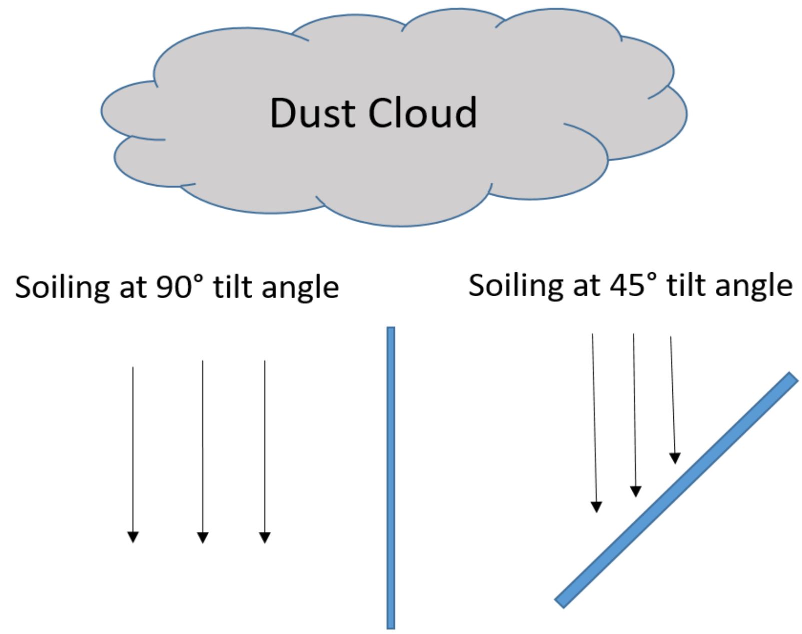

Figure 2. Schematic diagram of soiling setup

3. Results and Discussion

3.1. I-V characteristics of PV mini-module at different conditions

We have analyzed the effect of dust deposition on the output current of coated and not-coated PV mini-modules in indoor conditions. Figure 3 shows the IV curve of the uncoated and coated mini-module before and after soiling at two different tilt conditions at room temperature. When the tilt angle is 90°, the short circuit current (I_{sc}) drop is less than 1% in all cases, as in Table 1. It shows that at 90°, the coating has no significant impact, and very little dust adheres to the surface. At 45° tilt angle, the drop in I_{sc} for an uncoated mini-module is 9.9%, and for a coated mini-module, it is 2.9%, 2.1%, and 1.2% for water contact angles 106°, 114°, and 128° respectively. It shows that at a 45°-soiling condition, more dust adheres to the surface of the uncoated mini-module, i.e., glass, than on the coated mini-module. We can also see that the higher the water contact angle, the lower the drop in I_{sc}.

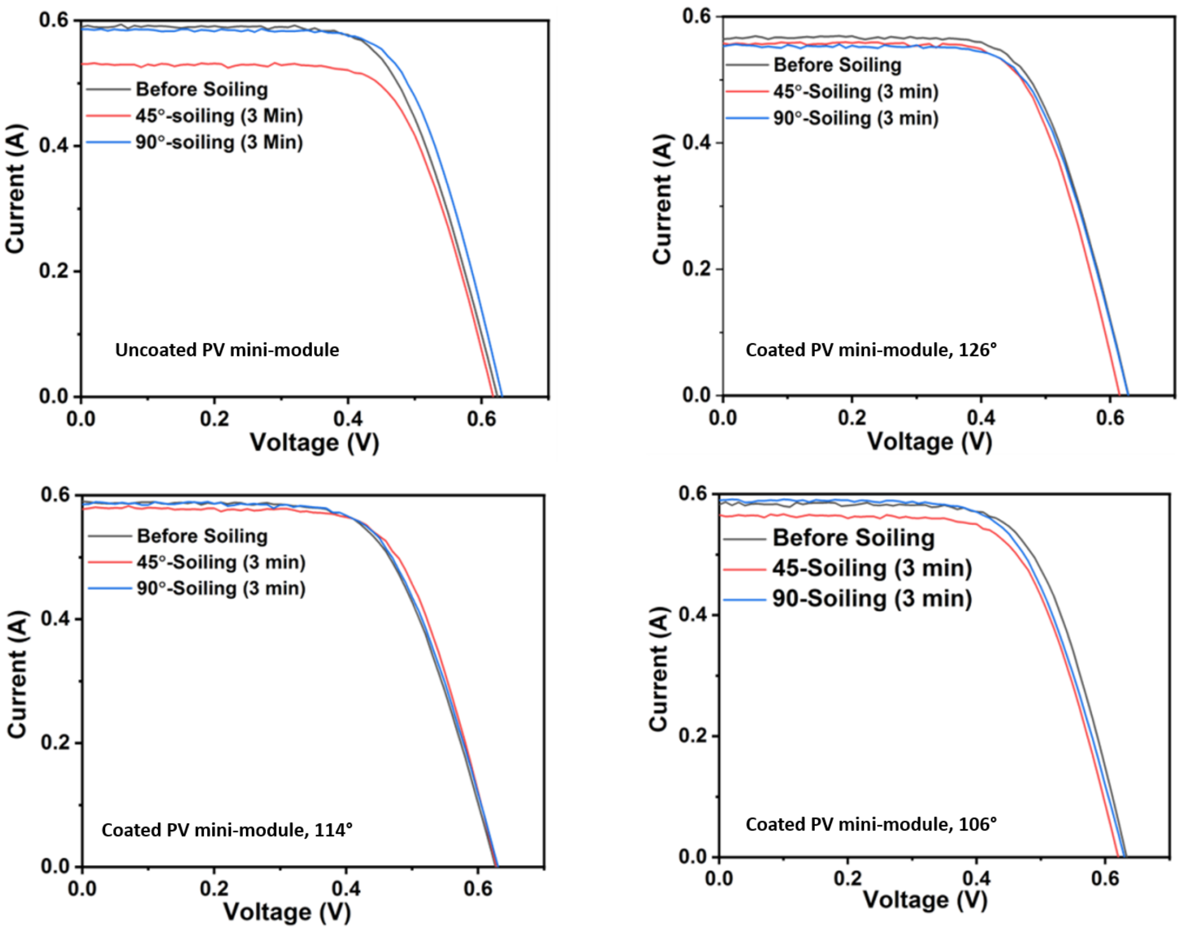

Figure 3. IV curves of the uncoated and coated module before and after soiling at two different tilt conditions at room temperature.

Table 1. Short circuit current of uncoated and coated module before and after soiling and % change

WCA of PV mini-module	Short circuit current (I_{sc}) without soiling	I_{sc} after soiling at 90°	% change after soiling at 90°	I_{sc} after soiling at 45°	% change after soiling at 45°
36°	0.589	0.586	< 1	0.530	9.9
106°	0.582	0.583	< 1	0.565	2.9
114°	0.590	0.585	< 1	0.577	2.1
128°	0.564	0.561	< 1	0.557	1.2

3.2. Quantification of dust coverage area on coated and uncoated PV mini-module

The proposed algorithm is based on four stages: image acquisition, converting the image to 16-bit, setting the threshold, and calculation of area. A digital camera captures the module's image in the visible spectrum, which is then processed to extract the region of interest. Figure 4 shows the soiling surface of coated (106°) and not coated PV mini-modules at a 45° tilt angle. The soiling coverage area was calculated according to the above model, and the effect of the grid was eliminated by subtracting the area of the grid from the total coverage. The area of the grid was measured when the mini-module was clean. It was found that dust particles covered 54% of the area of non-coated surfaces, whereas they covered 19% of the coated surfaces. Even though 54% of the area is covered by dust, it only shows I_{sc} loss of 9.9% because a thin layer of dust is deposited on the surface of the uncoated mini-module, which hinders the light coming to the cell but does not entirely block it. The same observation can be seen in the case of coated mini-module. As discussed, the result complements the I-V characteristic of the coated and not-coated module surfaces.

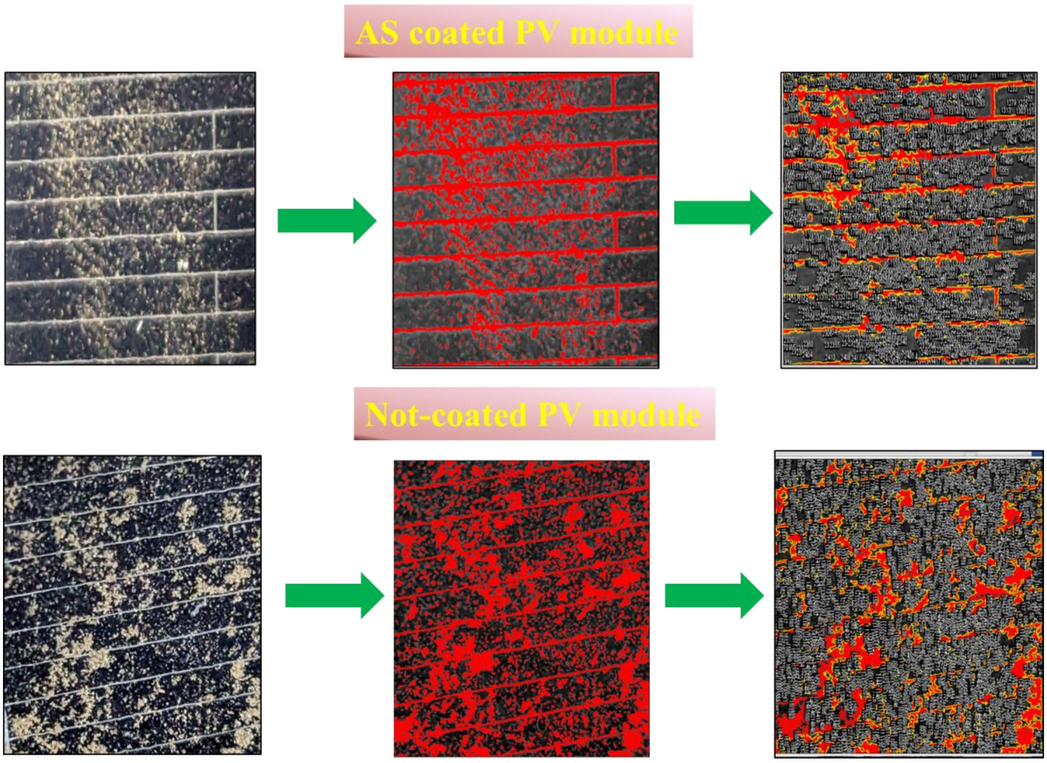

Figure 4. Optical Image of coated and not-coated PV module after soiling and image analysis

4. Conclusion

Coated and uncoated PV modules showed a drop of less than 1% in short circuit current when placed at 90°, which shows negligible soiling of modules. When placed at a 45° tilt angle, the uncoated PV mini-module showed a drop of 9.9%, and the coated PV mini-modules for different WCA of 106°, 114°, and 128° showed a decline of 2.9%, 2.1%, and 1.2% in I_{sc}. It indicates that hydrophobic coating effectively reduces the loss caused by soiling. Higher water contact angle shows lower loss due to soiling by decreasing the adhesion force between dust and surface. An analysis of Optical images of coated and uncoated PV mini-modules also verifies this result.

5. Acknowledgment

The authors acknowledge the NCPRE for soiling studies, the Industrial Research and Consultancy Center for central facilities at IIT Bombay, and the Sophisticated Analytical Instrument Facility and CEN for characterization facilities at IIT Bombay.

6. References

[1] S. A. Sulaiman, A. K. Singh, M. M. M. Mokhtar, and M. A. Bou-Rabee, "Influence of dirt accumulation on performance of PV panels," *Energy Procedia*, vol. 50, pp. 50–56, 2014, doi: 10.1016/j.egypro.2014.06.006.

[2] M. R. Maghami, H. Hizam, C. Gomes, M. A. Radzi, M. I. Rezadad, and S. Hajighorbani, "Power loss due to soiling on solar panel: A review," *Renew. Sustain. Energy Rev.*, vol. 59, pp. 1307–1316, 2016, doi: 10.1016/j.rser.2016.01.044.

[3] M. Mani and R. Pillai, "Impact of dust on solar photovoltaic (PV) performance: Research status, challenges and recommendations," *Renew. Sustain. Energy Rev.*, vol. 14, no. 9, pp. 3124–3131, 2010, doi: 10.1016/j.rser.2010.07.065.

[4] G. He, C. Zhou, and Z. Li, "Review of self-cleaning method for solar cell array," *Procedia Eng.*, vol. 16, pp. 640–645, 2011, doi: 10.1016/j.proeng.2011.08.1135.

[5] J. Zhang, W. Wang, S. Zhou, H. Yang, and C. Chen, "Transparent dust removal coatings for solar cell on mars and its Anti-dust mechanism," *Prog. Org. Coatings*, vol. 134, no. March, pp. 312–322, 2019, doi: 10.1016/j.porgcoat.2019.05.028.

[6] F. M. Zaihidee, S. Mekhilef, M. Seyedmahmoudian, and B. Horan, "Dust as an unalterable deteriorative factor affecting PV panel's efficiency: Why and how," *Renew. Sustain. Energy Rev.*, vol. 65, pp. 1267–1278, 2016, doi: 10.1016/j.rser.2016.06.068.

[7] S. Sutha, S. Suresh, B. Raj, and K. R. Ravi, "Transparent alumina based superhydrophobic self–cleaning coatings for solar cell cover glass applications," *Sol. Energy Mater. Sol. Cells*, vol. 165, no. January, pp. 128–137, 2017, doi: 10.1016/j.solmat.2017.02.027.

[8] Z. S. Huang *et al.*, "Experimental investigation of the anti-soiling performances of different wettability of transparent coatings: Superhydrophilic, hydrophilic, hydrophobic and superhydrophobic coatings," *Sol. Energy Mater. Sol. Cells*, vol. 225, no. March, p. 111053, 2021, doi: 10.1016/j.solmat.2021.111053.

[9] L. Fernandes, S. Bhaduri, A. Alath, N. S. Shiradkar and A. Kottantharayil, "Artificial dust deposition chamber for investigation of soiling loss in photovoltaic modules," *2019 IEEE 46th Photovoltaic Specialists Conference (PVSC)*, pp. 2875-2878, doi: 10.1109/PVSC40753.2019.8981343.

[10] S. D. Wang and S. S. Luo, "Fabrication of transparent superhydrophobic silica-based film on a glass substrate," *Appl Surf Sci*, vol. 258, no. 14, pp. 5443–5450, May 2012, doi: 10.1016/j.apsusc.2012.02.032.

10. Circular Economy, Recycling

Performance analysis of waste to best solar water heater

Dharmesh.J. Chavda[1], Sanjeev.D. Suryawanshi[2]

[1] B Tech Mechanical Engineering, S.S.V.P.S. B.S.D COE, Dhule 424001 (India)

[2] Department of Mechanical Engineering, S.S.V.P.S. B.S.D COE, Dhule 424001 (India)

Abstract

Water heating is an essential aspect in the industrial and domestic purposes. Various methods have been adapted for heating water. Fossil fuels and electricity are widely used for water heating which consumes more high-grade energy and causes pollution. Due to increase in population, consumption of fossil fuels has drastically increased. These precious conventional resources depleting with time. Here the non-conventional resources come in to the picture. Solar water heating is a promising solution for water heating in the both domestic and commercial applications. But the solar water heaters are quite expensive and cannot be afforded by common peoples. In search for affordable solar water heating solution waste water bottles can be used as a glazing, since plastic waste management is serious issue throughout the world. Solar collector is developed and tested using PVC pipes as an absorber and transparent waste bottles as a glazing. Additional removable glazing cover of polyethylene improves performance in acute winter. Bottom part of transparent bottles covered with reflective foil to augment collector's performance. It generates hot water up to the temperature 66^0C, with good structural rigidity of the collector.

Keywords: *PVC pipes, waste bottles as glazing, glazing cover, headers, reflective foil*

---

1. Introduction

Water heating is the crucial part in the industrial and domestic applications. Fossil fuels are widely used in the water heating application. About 8% of all end-use natural gas is used to heat water in commercial and residential buildings [1]. Major energy used for water heating include natural gas, electricity, oil, and liquefied petroleum gas (LPG) [1]. Despite the popularity of wood as an energy source for water heating, its use might have harmful effects on health when rudimentary stoves are used as the burning means; such devices allow the smoke to pollute the household air with ashes [2]. Therefore, use of solar energy for water heating is the promising solution to reduce the use of fossil fuels. The ETC type solar water heater is quite expensive and cannot be afforded by many peoples. Many researchers are working to discover affordable solar water heating solution. A solar water heater prototype was constructed using polyethylene terephthalate bottles to determine its feasibility as a component of the average household in rural areas in Guatemala [3]. A solar water heater design made from plastic bottles of Pepsi or Miranda with plastic pipes run up the center of each row of bottles. These bottles act as glazing, and also hold reflectors made from beverage cartons [4].

Nonbiodegradability of plastics is attributed towards causing waste management problems and choking of the drains in urban cities [5]. Some types of plastic waste like multi layered laminates; EPS, etc. are not easily recyclable by conventional process [5]. So, using of waste bottles can be beneficial for the environment and reduces the cost of the solar water heater. The Indian patent is granted entitled "Solar collector using plastic glazing", Patent number 455451, dated 27/09/2023. Most of the evacuated tubes are imported from China [7], it is decided to have indigenous development of solar water heating system that gives some of the advantages of flat plate collectors (FPC) and some of the ETC. In FPC forced circulation, draining of deposited salts is possible and for ETC no insulation is required for collector.

Mostly water heating from combustion of fossil fuel is the practice in rural areas, the problem is more acute with poor financial background. It is decided to manufacture a cost-effective solar water heater.

Therefore, it is decided to manufacture a setup and to analyze the performance of the collector with PVC pipes as an absorber and the waste bottles as a glazing, with an additional removable glazing that will improve the performance of the solar water heater in acute winter.

10.18086/swc.2023.10.01 Available at http://proceedings.ises.org

2. Materials and methods

Present system of waste to best solar water heater consists of,

1. Matt black painted PVC absorber pies
2. Transparent plastic bottles (polyethylene terephthalate)
3. Mild steel supportive frame
4. PVC plumbing accessories
5. Reflective foil
6. Clear silicon sealant
7. Teflon tape

Present setup is environment friendly, indigenous, safe and low cost since the material used is easily available at low cost in India. In today’s scenario disposal of waste plastic bottles is a big question for ecological researchers. It’s a need of an hour to utilize waste plastic bottles effectively. In conventional FPC solar water heater system the convection losses are more in acute winter compared with present study.

For manufacturing the collector, the bottles are cut from mouth end side and holes are pierced in the base of bottles with predefined dimensions. The bottles after preparation are inserted with interference fit over the absorber pipes. During inserting the bottles over the pipe, the mouth end side should match with base side of next bottle as shown in figure 1. Bottles are inserted from base side over the absorber pipe. This interconnected part of bottle is sealed by some sealant, preferably clear silicon sealant to have air tight connection between two bottles. Clear silicon sealant allows solar radiation to pass through and maintains the aesthetics of collector.

The absorber pipes with bottles are connected with tee at top and bottom to have respective headers of the collector, this will form an array of the pipes which makes the collector. To facilitate effective use of most of solar radiation entering through aperture on the collector, one third arc of outer bottom surface of transparent bottles are covered by reflective foil to reflect solar radiation towards the bottom side of black absorber pipes of the collector.

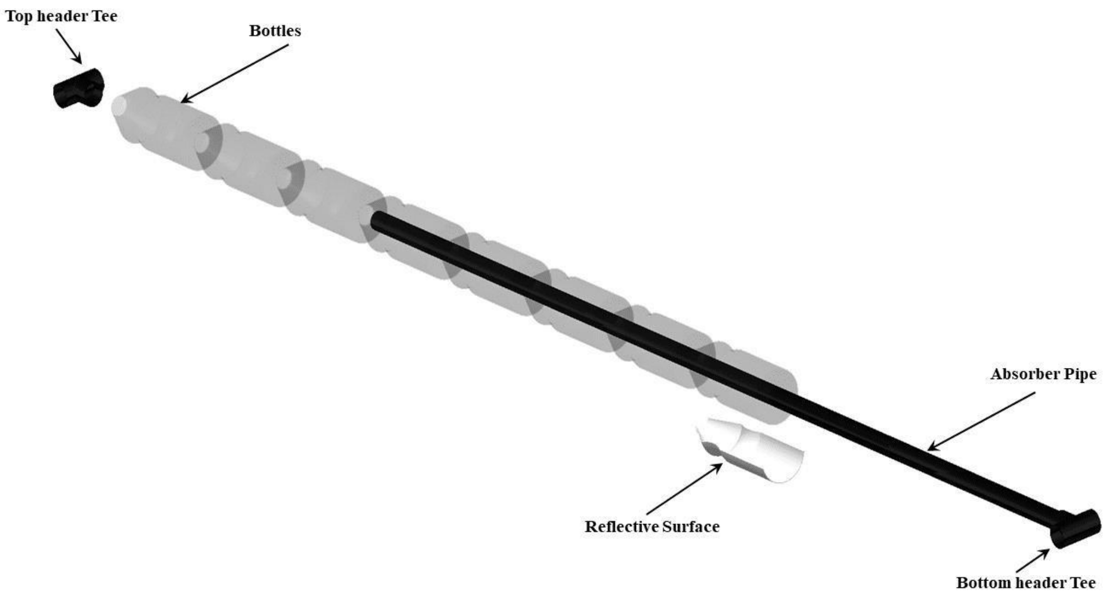

Figure 1: Elements of the collector

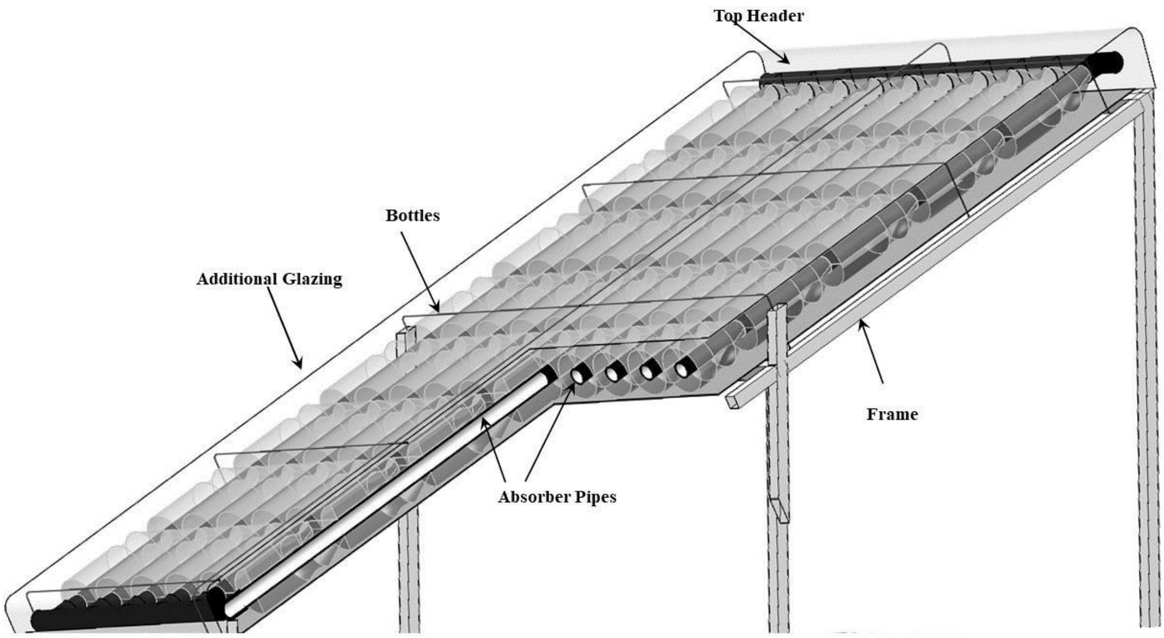

Figure 2: Sectional view of collector, model 1

3. Experimentation

In the present experimental setup, the absorber pipes of collector get heated by absorbing incoming solar radiation, this heats the water, develops a thermosiphon circulation in between the collector and hot water tank. Temperature of the hot water increases until the thermal equilibrium between collector and the surrounding is reached.

The performance of the solar water heater depends on various aspects, one of it is “Dead Volume”, dead volume is the water present in the solar collector apart from the water in the hot water tank. This dead volume directly impacts on the solar water heater performance i.e., if the dead volume is more the time required for heating the water and developing thermos-syphon increases, which reduces efficiency. The performance of the solar water heater system is strong function of this dead volume specifically in monsoon, when *intermittent solar radiations* are available. For lesser dead volume the thermo-syphon circulation is faster, once the water is heated and circulated, it will be stored in hot water tank. Therefore, the main objective of the experimentation is to reduce the time required for the water heating by decreasing the *dead volume*.

It is decided to develop three models for the test setup as follows

1st model is made with array of 32mm diameter pipes as shown in figure 3.

2nd model is made with array of 32mm pipes eccentrically fixed inside 40mm diameter pipes as shown in figure 4.

3rd model is made with array of 40mm pipes eccentrically fixed inside 50mm diameter pipes shown in figure 5.

Eccentrically fixing the pipes as shown in figures 3 to 5 not only improves utilization of incident solar radiation but also decreases dead volume in the collector, intensifies the thermosiphon circulation between the collector and hot water tank. To have eccentric insertion of inner pipe in outer pipe, spacers are sticked on top circumference of inner pipe of proper dimensions at four locations (not shown in figures). Top and bottom ends of inner pipe are sealed with cap and sealant to have air tight connection.

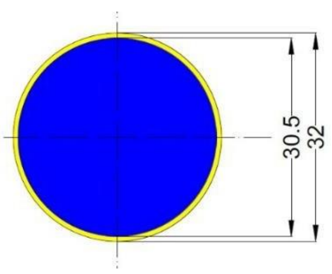

Figure 3: Cross section of pipe of model 1

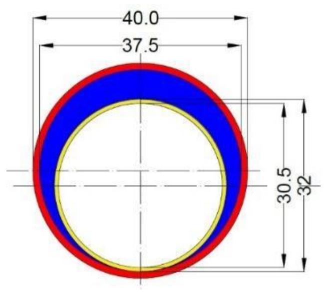

Figure 4: Cross section of pipe of model 2

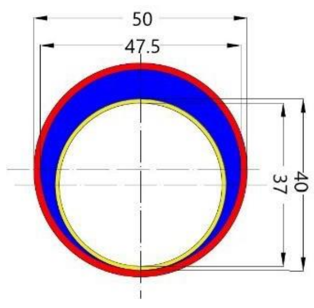

Figure 5: Cross section of pipe of model 3

(Blue shaded part shows the water)

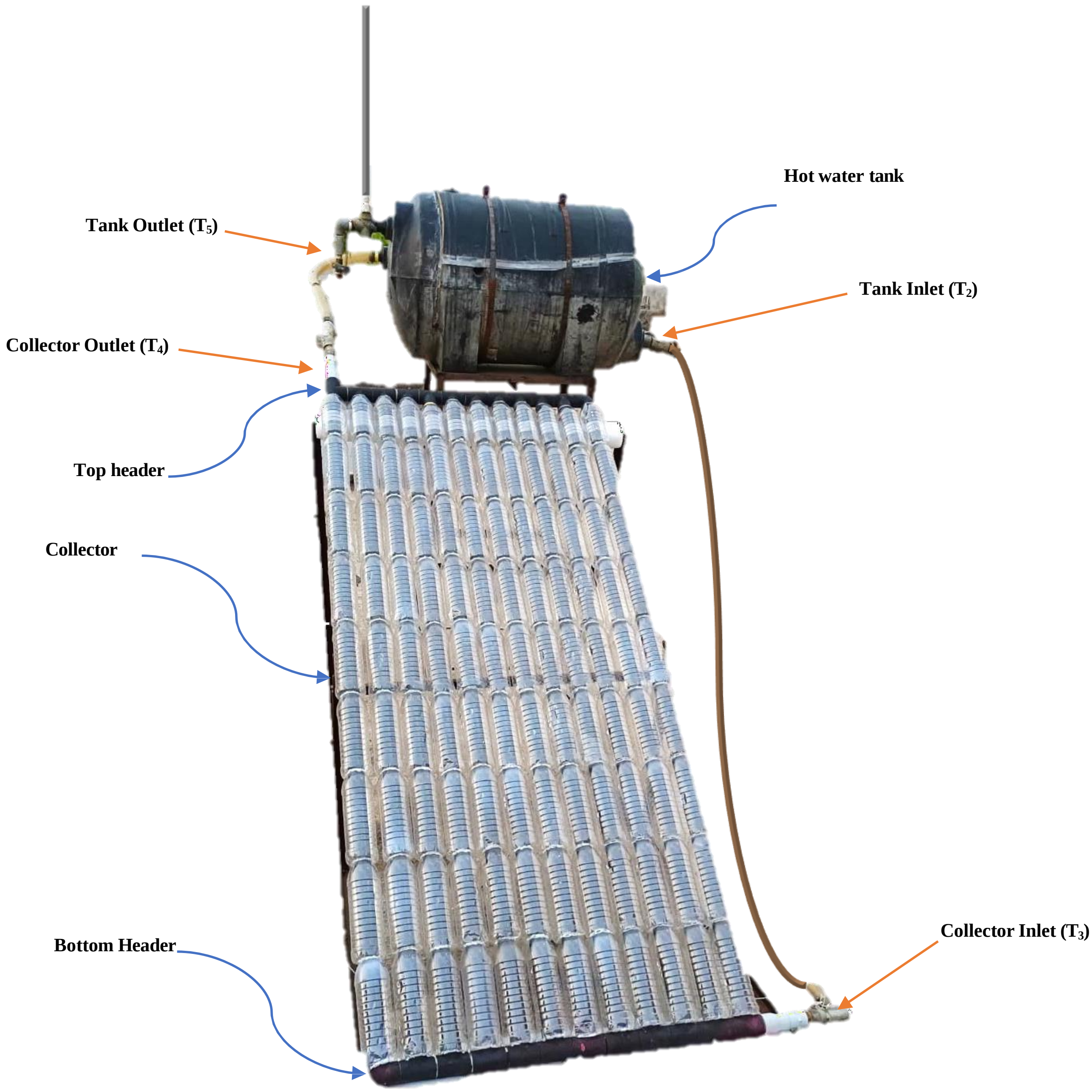

Figure 5: Experimental setup.

4. Results and discussions

In this experiment the test was carried for 2x1m solar collector, the following readings were taken at regular intervals of time of the three models. The observations were taken for three models of present experimentation and compared with ETC collector. All models are of 100-liter capacity.

Tab. 1: Comparison of three Models with ETC

	Model 1	Model 2	Model 3	ETC
Solar Aperture* m^2	0.768	0.96	1.2	0.66
No of pipes/tubes	12	12	12	10
Dead volume liters	13.6	5.5	9.5	19.34
Time taken to reach maximum temperature in hours	6.5	4.5	5.5	5.2
Maximum temperature at collector outlet °C	53	66	58	67

[*Effective aperture which utilizes direct incident solar radiation]

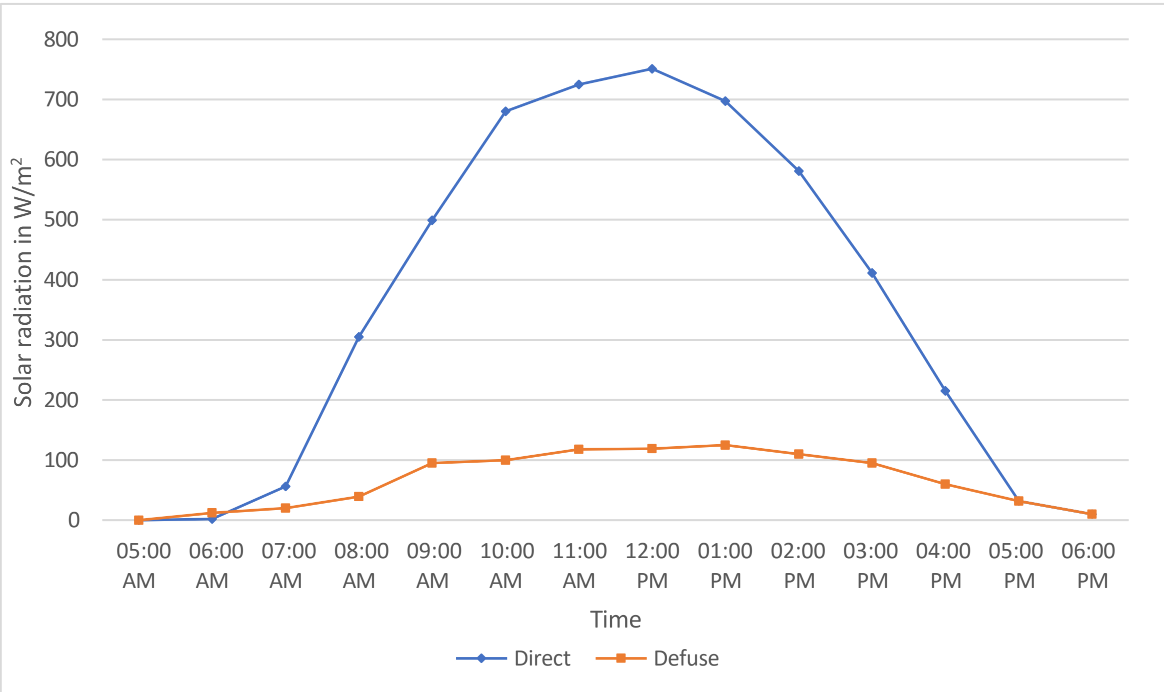

Figure 6: Solar radiation intensity

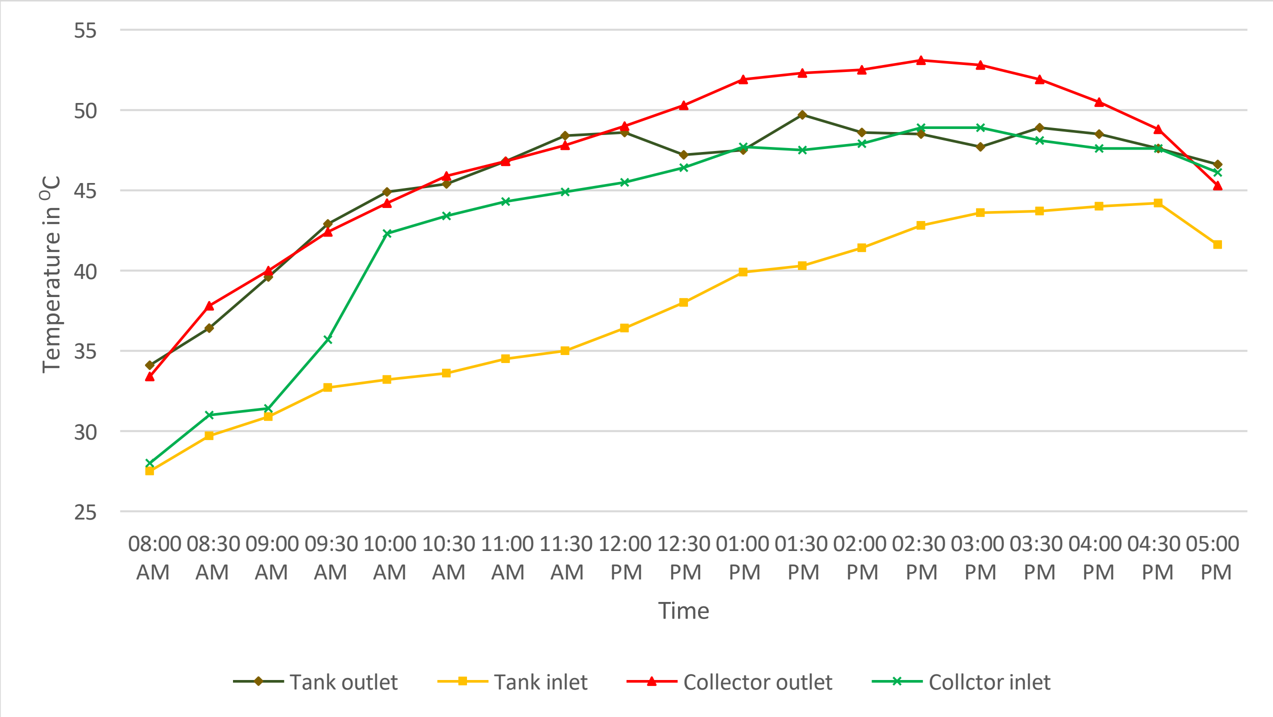

Figure 7: Temperature readings for model 1

4.1. Model 1

Figure 7 shows the performance of model 1 where the collector is constructed with the 32mm pipes. The readings were taken from 8:00 AM with the initial temperature at inlet 26°C. The dead volume in model 1 is 13 liters. Time required for the water to reach maximum temperature is 6.5 hours at 2.30 pm with temperature of 53°C.

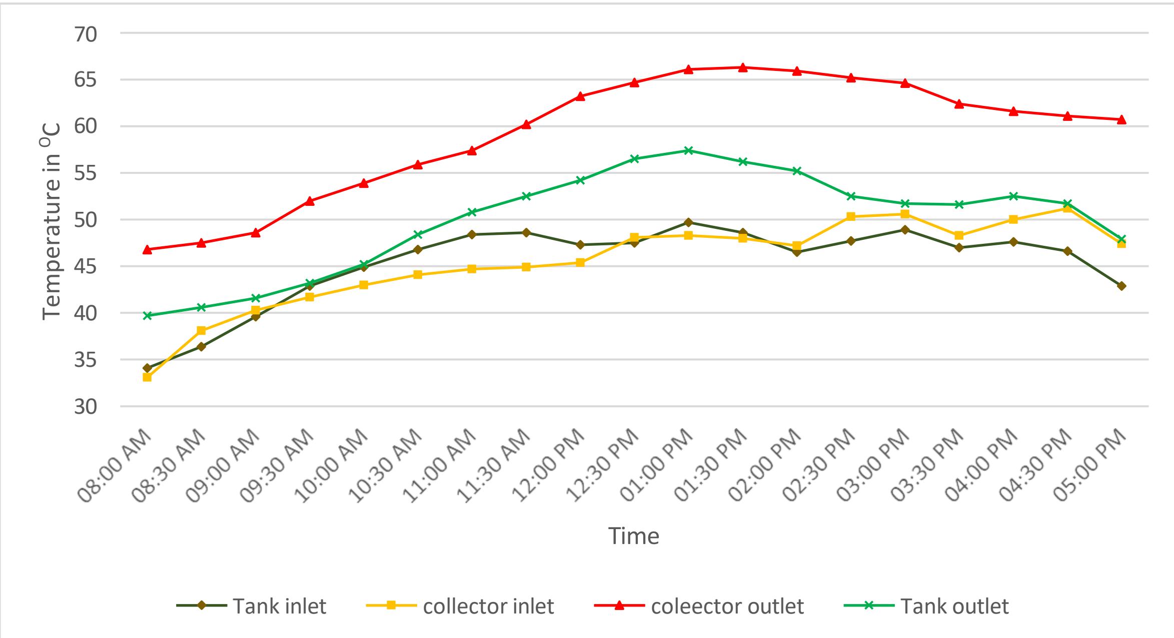

Figure 8: - Temperature readings for Model 2

4.1. Model 2

Figure 8 shows the performance of model 2 where the collector is constructed by 32mm diameter pipes eccentrically fixed inside 40mm diameter pipes. The readings were taken from 8:00 AM with 32°C initial temperature at the inlet. The dead volume in model 2 is 5.5 liters. Time required to reach maximum temperature of 66. 2°C of the water is 4.5 hours this temperature is attained at 1.30 pm. It is observed that due to reduction in dead volume compared with model 1 time required to reach maximum temperature of water outlet from collector is reduced, also the maximum temperature achieved is elevated.

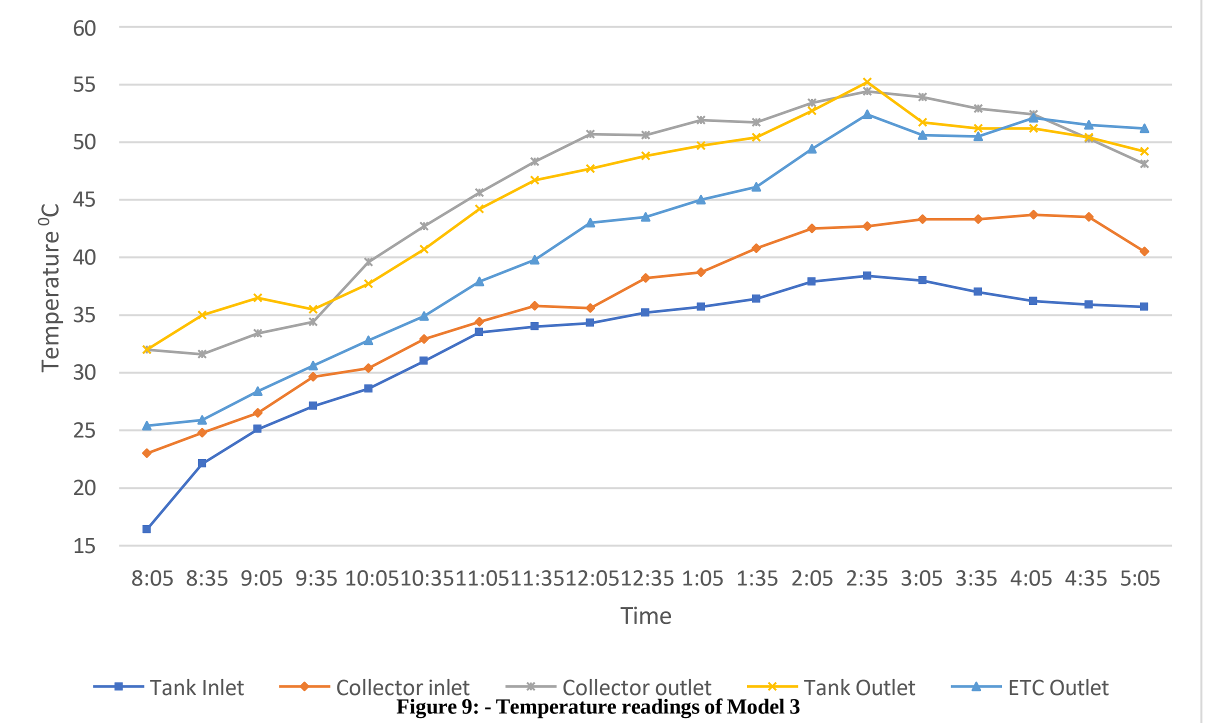

Figure 9: - Temperature readings of Model 3

4.1. Model 3

Figure 9 shows the performance of model 3 where the collector is constructed with the 40mm diameter pipes are eccentrically fixed in 50mm diameter pipes. The readings were taken from 8:00 AM till 5.00PM with the initial temperature of 26°C at inlet with the final temperature of 52°C was reached. The dead volume in model 3 is 9.5 liters. Time required for the water to reach maximum temperature of 58°C is 5.5 hours this temperature is attained at 2:30 PM. It is observed that due to 9.5 liters of dead volume, compared with model 1 and model 2 it is in-between first two models, time required to have maximum temperature of water outlet from collector is also changed. As effective aperture utilization is increased, the time required to heat 100 liters of water is less compared to first two models.

5. Conclusion

Solar heat gain for water heating is considered similar to flat plate collector (FPC)and ETC. In model 1 with the 32mm pipes the dead volume is 13.26 liters, which is quite high and increases the time for thermosyphon, where as the model 2 has an eccentrically fixed 32mm pipes in 40mm pipes with reduced dead volume to 5.5 liters. This reduction in dead volume improves thermos-syphon circulation between collector and hot water tank. Increase in absorber pipe diameter, not only increases solar aperture utilization but also decreases the gap between the array of bottles which reduces the convection loss. With the 3rd model an eccentrically fixed 40 mm pipes in 50mm pipes optimizes the dead volume up to 9.5 liters. With 50mm diameter pipes the solar aperture area for the absorption of solar radiation increases which decreases the time required for heating of water of same capacity.

The waste to best solar water heater can be seen as a combination of ETC and flat plate solar collectors with improved performance with less production cost. Present work gives some of the advantages of flat plate collectors (FPC) and some of the ETC. In FPC forced circulation, draining of deposited salts is possible and for ETC no insulation is required for collector.

Due to optimized cost of collector this type of collector will provide techno commercially viable solution.

6. References

[1] P. Denholm. The Technical Potential of Solar Water Heating to Reduce Fossil Fuel Use and Greenhouse Gas Emissions in the United States, Technical Report NREL/TP-640-41157 March 2007

[2] US Environmental Protection Agency. (2000). Health Effects of Breathing Woodsmoke. Retrieved July 26, 2014, from http://www.epa.gov/burnwise/pdfs/woodsmoke_health_effects_jan07.pdf

[3] Jorge de la Torre. Feasibility overview of a solar water heater made of polyethylene terephthalate bottles for rural areas in Guatemala. Institute of Science and Technology for Development, Rafael Landivar University

[4] Amal. H . Husain. Solar Water Heater From plastic Bottles and Beverage carton. Journal of Engineering and Development, Vol. 16, No.2, June 2012 ISSN 1813- 7822

[5] Javeriya Siddiqui and Govind Pandey. A Review of Plastic Waste Management Strategies. International Research Journal of Environment Sciences ISSN 2319–1414 Vol. 2(12), 84-88, December (2013)

[6] Indian patent applied, Sanjeev D Suryawanshi et.al. “Solar collector using plastic glazing”, Patent number Patent number 455451, dated 27/09/2023

[7] Solar water heater evacuated tube import data, https://www.seair.co.in/solar-water-heater-evacuated-tube-import-data.aspx

Recycling of crystalline silicon (c-Si) photovoltaic (PV) solar module- A review

Krishan Kumar Patel[1,2], Nivedita Iyer[1], Vrishali Madav[1] and Sudhanshu Mallick[1]

[1]Department of Metallurgical Engineering and Materials science, Indian Institute of Technology Bombay Mumbai, Maharashtra, 400076 (India)

[2]Oriental College of technology, Bhopal, Madhya Pradesh 462022 (India)

Abstract

This review is an overview of the step-wise recycling of crystalline silicon (c-Si) PV modules after End-of-life (EOL) using mechanical, thermal, and chemical routes. Aluminium frames, cables & junction boxes were removed from modules mechanically before further recycling. Encapsulated EVA (ethylene vinyl acetate) & backsheet polymers were primarily removed from the module by chemical route or thermal pyrolysis. As reported works of literature, pyrolysis of modules is the most efficient, faster, and less hazardous than chemical processes. After that, they recycled solar cells to recover high-value materials such as Ag, Al, and Si from waste PV cells via a chemical route to facilitate sustainable development for PV industries.

Keywords: Photovoltaic (PV) module, recycling, c-Si, and solar cells

1. Introduction & Literature

Harnessing solar energy through the PV module (Photovoltaic effect) to produce electricity has become the fastest-growing sector in the renewable energy production industry [Dias, P, et. al. 2017]. A Typical PV module (fig. 1) consists of Si solar cells connected in rows and columns by solder and interconnects rails. Generally, solar cells are divided into four broad categories silicon-based solar cells, thin film solar cells, perovskite solar cells, tandem solar cells, etc (figure 2 & Table 1) [Dobra, T. et. al.,2022]. The solar cells are encased in an encapsulant (typically Ethylene Vinyl Acetate, EVA) and fused to glass on the front and with a backsheet [Weckend, S, et. al. 2016]. The entire structure is encased in an Aluminum frame. There is a junction box on the backside for making the electrical connections. Photovoltaic modules work for almost 25-30 years before they are no longer usable due to reduced efficiencies [Ambaryan, G. N, et. al. 2019]. Worldwide estimated solar energy target by 2050- 4500 TW [Kim, S. W et. al. 2016], and the same tonnage estimated Solar Waste will be 78 million tons [Sah, D, et. al. 2022] (Figure 3-4). As the installation of PV modules increases exponentially, the End-Of-Life modules are also expected to rise by the same proportion shortly [Wang, X. Et. al. 2022]. Despite the obvious environmental benefits, it is difficult for PV module recycling to be widely accepted due to economic constraints, namely, the low value of recovered material and high recycling cost [Xu, Y. et. al. 2018]. The lack of PV-specific disposal guidelines, technical know-how, and intense industrial involvement further add to this burden. Thus, decommissioned panels are primarily being dumped in landfills or, at best, sent to glass recyclers.

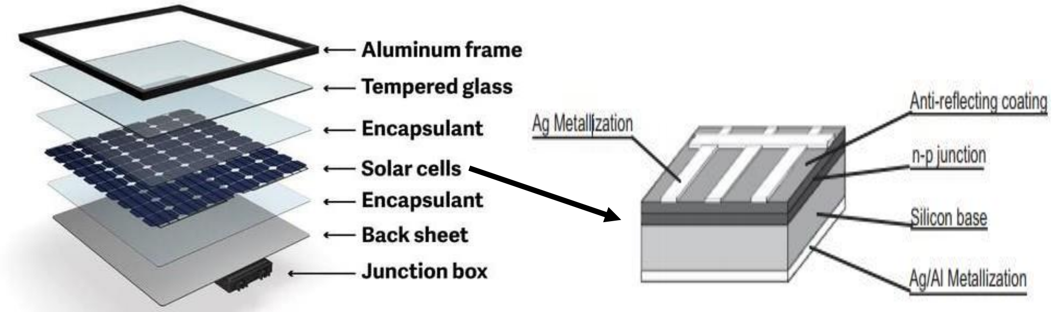

Fig. 1. Solar module basic structure and types of material used in solar cells [Dias, P, et. al. 2017].

10.18086/swc.2023.10.02 Available at http://proceedings.ises.org

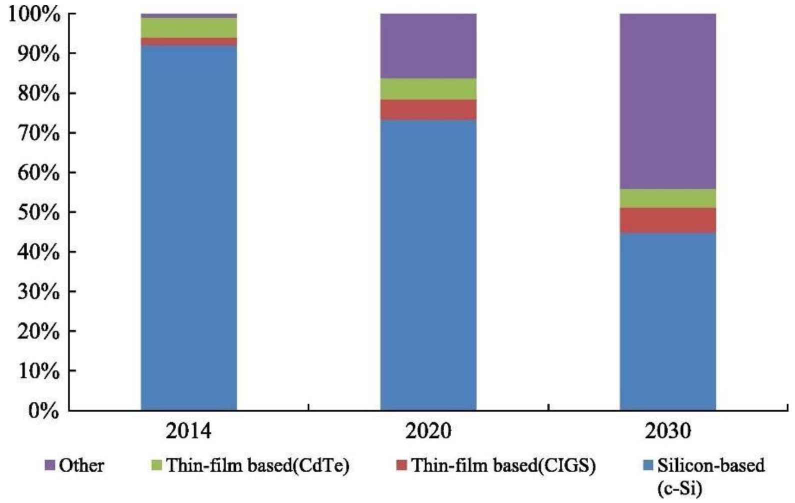

Fig. 2. Market share by different Solar panels [Xu, Y. et. al. 2018]

Table 1. Solar PV panels types

S.No.	Generation of PV panels	Solar PV panel Types
01	1st Generation (c-Si)	Monocrystalline
		Multi-crystalline
02	2nd Generation (Thin Film)	Cadmium telluride (CdTe)
		Copper indium gallium selenide (CIGS)
		Amorphous silicon
03	3rd Generation	Dye-sensitized solar panel
		Organic solar panel
		Hybrid solar panel

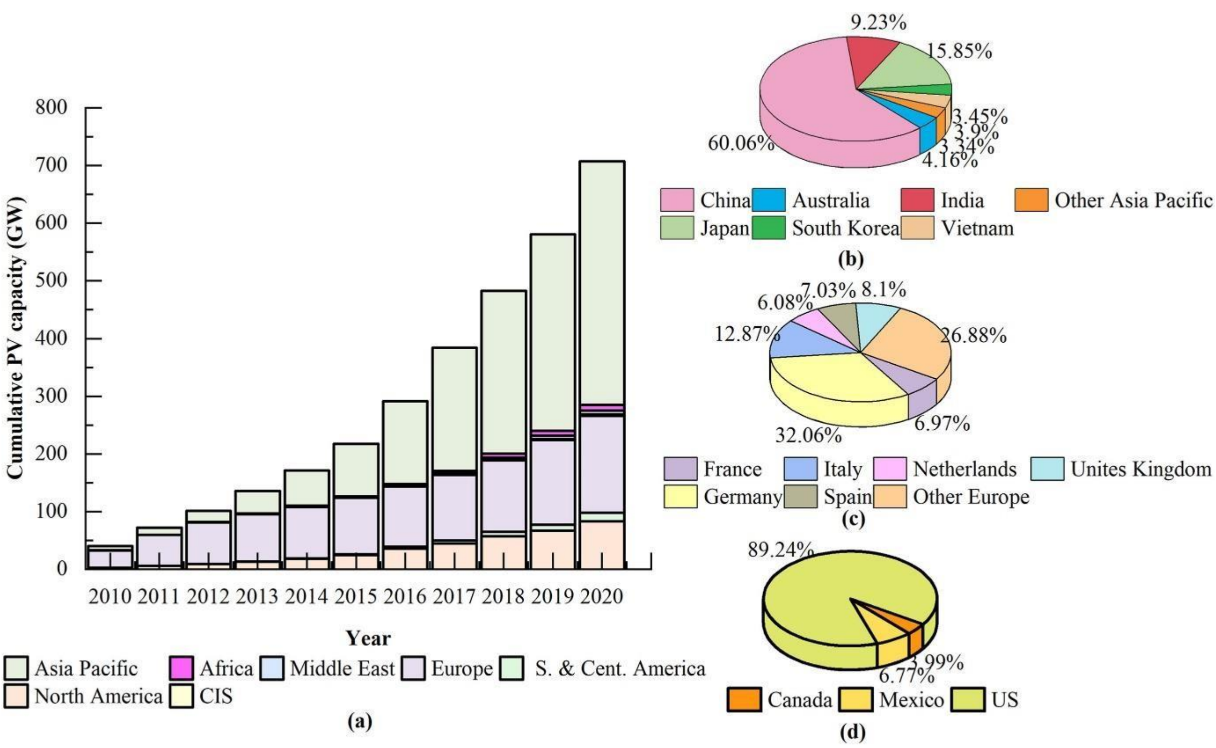

Fig. 3. Globally cumulative installed PV panel capacity (a) Global cumulative installed (b) share in Asia-Pacific in 2020, (c) Share in Europe 2020, (d) Share in North America in 2020 [Wang, X. Et. al. 2022].

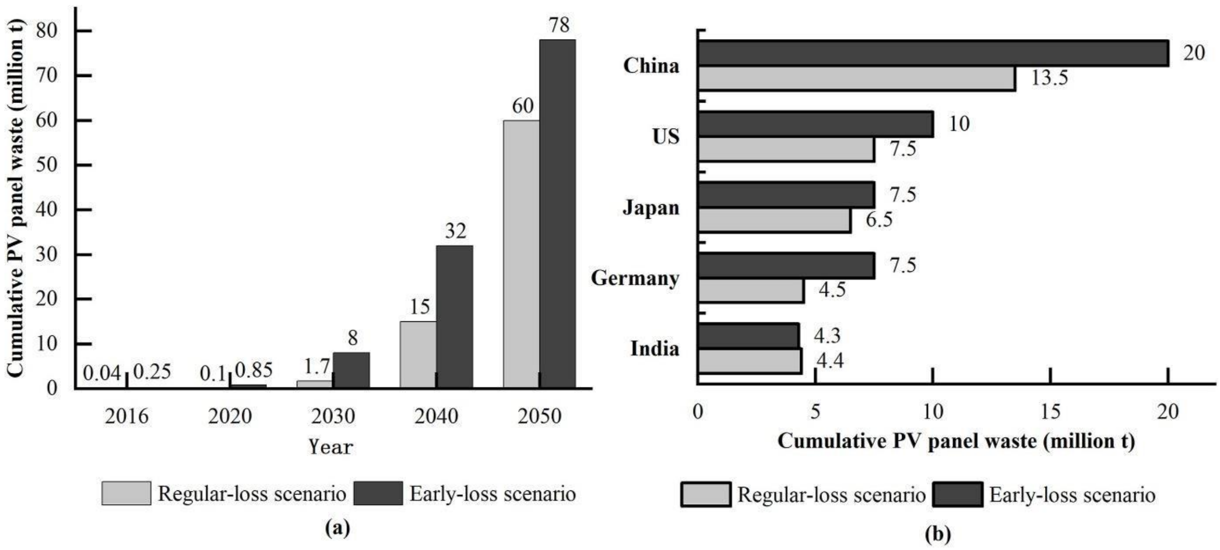

Fig. 4. Estimated cumulative waste of EOL PV panels. (a) Cumulative global waste (million t) of EOL PV panels, (b) Cumulative waste by the top five countries in 2050. Date source: End-of-Life Management: Solar Photovoltaic Panels (IRENA)

During the thermal treatment (pyrolysis) of Silicon PV solar modules, hazardous byproducts could get released into the environment. In a study reported earlier, the PV module is placed inside a closed furnace and heated at 500°C for pyrolysis, and complete degradation of the encapsulant (EVA) is achieved [9]. Later the trapped gases were analyzed to quantify the release of metals, if any. The results indicate the presence of small amounts of dangerous metals like Pb, Si, Cu, and Ag in the gases evolved during pyrolysis [Fiandra, V et. al. 2019]. Usually, the recycling process for the EOL PV module starts with the manual removal of junction boxes and aluminum frames. After that, the removal/delamination of backsheet and encapsulant from the solar cell and glass plate needs to be done, which is a challenging task. Several routes have been tested and employed in the past for removal of the encapsulant by organic solvent, acetic acid, shockwave recycling and thermal decomposition . In the studies by [Farrell C et al. 2019], in-situ pyrolysis of c-Si solar PV module having EVA and PVDF backsheet was performed in a vacuum atmosphere. The evolved gas was tested using TGA-MS and TGA-FTIR with selected molecular fragments ion intensity spectral signals such as m/z= 43, 44, 2, 13, and 18 corresponding to acetic acid, carbon-di-oxide, hydrogen, carbon-13, and water vapour, respectively to identify the gases evolved during decomposition. Researcher [Wang, R et al. 2019] reported removal of EVA encapsulation of the c-Si PV module by pyrolysis at 500°C. At the end of the pyrolysis, undamaged glass and silicon wafers were obtained, which could be recycled further.

FTIR is a rapid well-proven and unique chemical fingerprint technique to identify organic as well as inorganic entities present in the sample. Researchers [Rathore, N. et. al.2022] used FTIR technique to detect EVA encapsulant and PVF backsheet and different functional group present in the gas evolved during pyrolysis of the PV module. They found that the C-H bond stretches at the absorption bond of 3000-2800 cm^{-1}. Several researchers have reported TGA-MS analysis of PV module pyrolysis [Dias, P et. al. 2018]. However, reports on the product of pyrolysis, reaction mechanics, and evolved gas characteristics have not been found deliberated exhaustively.

2. Recycling techaniques

Recycling combines mechanical, Thermal, and Chemical methods [Dias, P, et. al. 2017]. The processes chosen depend on the requirement of the end products (Figure 5 & Table 2).

The Aluminum frames are removed by mechanical means by physically separating them from the modules. The encapsulants are usually unrecoverable. They are typically pyrolyzed by heating to approximately 500°C. The other option is to dissolve it chemically in organic solvents. The key challenge here is either the generation of gaseous exhaust from polymer pyrolysis or the disposal challenge of large quantities of organic solvents [Weckend, S, et. al. 2016]. Glass removal: The glass used in PV modules is low Fe, Tempered, and Textured Glass. It is the primary recoverable material in a module. Most recycling operations crush the module into small pieces of glass with Si and encapsulant stuck to them. Solder is usually removed thermally or chemically. Though Lead-free solders have been developed, the PV modules still use lead-containing solder, especially those expected to come for recycling over the next few decades. Depending on the local legislative requirements, these may need to be recovered. Interconnects are usually quickly recovered once the solder is removed. These can be easily collected and recycled as Al or Cu [Ambaryan, G. N, et. al. 2019].

Silicon recovery: Silicon solar cell recovery depends to a large extent on the preparatory steps as they determine if the cell is recoverable intact or in pieces. If the modules are not crushed, it may be possible to obtain intact Si cells. However, these cells are not reusable because the Ag interconnect grids, a Passivation layer, and Al back contacts will likely have been damaged [Sah, D, et. al. 2022]. Generally, it is observed that the PV panel waste is treated by engaging the Four-R-Principle; R-Reuse (generate a robust secondary market for second-hand use of the panel at lower efficiency and lower power rating below 80%, though), R-Recycle (major components like Aluminium frame, cables, and glass are retrieved intact and are either reused or repurposed), R- Recover (Various physicochemical ways recover valuable materials like Silver, Aluminium, and Silicon) and R-Reduce (the hazardous components from the waste like lead, bismuth, etc. are separated carefully and reduced in volume for further processing).

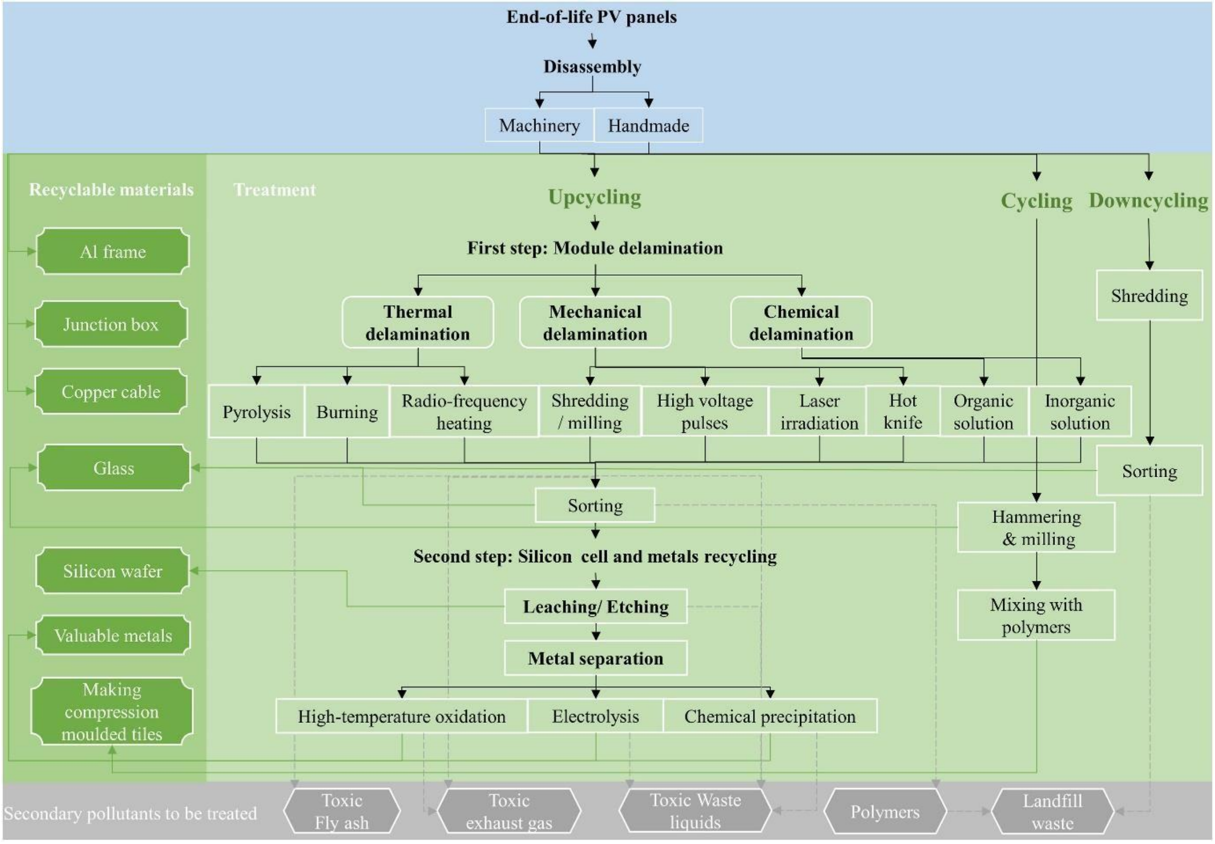

Fig. 5. Possible EOL PV panels recycling strategies and process [7].

Table 2. Various recycling routes of c-Si PV solar modules.

Process	Type of module	Advantage	Disadvantage	Processing time/Scale
Mechanical separation by hot knife/wire cutting [2]	C-Si/ thin film	Cell & glass recover.	Other separation processes required for the complete removal of EVA	2 to 60 min/one by one
Thermal treatment [4]	C-Si/ thin film	Full EVA, Glass & cell removal	Harmful gas emissions	2 to 5 hr/ Bulk
Organic dissolution [5-6]	C-Si/ thin film	EVA/Backsheet removal	Cell defects, harmful emissions, waste solution treatment	6 to 48hr/Bulk

Conclusions: Following conclusions can be summarized point to point below:

1. This work demonstrates that present past and future challenges and opportunity with solar PV modules. It is possible to recover most of the materials in the c-Si PV modules for reuse and recycling.
2. The development of new generation of solar panel to fulfil the energy demand of society. After EOL the modules need to be proper way to recycle to protect our eco-system and environment.
3. Step-wise sequential recycling of PV modules to minimize the minimum environmental impact and maximum material recovery to facilitate the sustainable development to PV industries.

Acknowledgments

All authors declare that no conflict of interest of this research work.

References

1. Dias, P., Javimczik, S., Benevit, M., & Veit, H. (2017). Recycling WEEE: Polymer characterizationand pyrolysis study for waste of crystalline silicon photovoltaic modules. *Waste Management, 60*, 716- 722..
2. Dobra, T., Vollprecht, D., & Pomberger, R. (2022). Thermal delamination of end-of-life crystalline silicon photovoltaic modules. *Waste Management & Research*, *40*(1), 96-103.
3. Weckend, S., Wade, A., & Heath, G. A. (2016). *End of life management: solar photovoltaicpanels* (No. NREL/TP-6A20-73852). National Renewable Energy Lab.(NREL), Golden, CO (United States).
4. Ambaryan, G. N., Vlaskin, M. S., Zhuk, A. Z., & Shkol'nikov, E. I. (2019). Preparation of High- Purity Aluminum Oxide via Mechanochemical Oxidation of Aluminum in a 0.1 M KOH Solution, Followed by Chemical and Heat Treatments. *Inorganic Materials*, *55*, 244-255.
5. Kim, S. W., Chung, H. E., Kwon, J. H., Yoon, H. G., & Kim, W. (2010). Facile synthesis of silver chloride nanocubes and their derivatives. *Bulletin of the Korean Chemical Society*, *31*(10), 2918-2922.
6. Sah, D., Lodhi, K., Kant, C., Srivastava, S. K., & Kumar, S. (2022). Extraction and Analysis of Recovered Silver and Silicon from Laboratory Grade Waste Solar Cells. *Silicon*, *14*(15), 9635-9642.
7. Wang, X., Tian, X., Chen, X., Ren, L., & Geng, C. (2022). A review of end-of-life crystalline siliconsolar photovoltaic panel recycling technology. *Solar Energy Materials and Solar Cells, 248*, 111976.
8. Xu, Y., Li, J., Tan, Q., Peters, A. L., & Yang, C. (2018). Global status of recycling waste solar panels:A review. *Waste management*, *75*, 450-458.
9. Fiandra, V., Sannino, L., Andreozzi, C., & Graditi, G. (2019). End-of-life of silicon PV panels: A sustainable materials recovery process. *Waste management*, *84*, 91-101.
10. Farrell, C., Osman, A. I., Zhang, X., Murphy, A., Doherty, R., Morgan, K., Rooney, D.W., Harrison, J., Coulter, R. and Shen, D. (2019). Assessment of the energy recovery potential of waste Photovoltaic (PV) modules. *Scientific reports,* 9(1), 1-13.
11. Wang, R., Song, E., Zhang, C., Zhuang, X., Ma, E., Bai, J., Yuan, W. and Wang, J. (2019). Pyrolysis-based separation mechanism for waste crystalline silicon photovoltaic modules by a two-stage heating treatment. *RSC advances,* 9(32), 18115-18123.
12. Rathore, N., & Panwar, N. L. (2022). Strategic overview of management of future solar photovoltaic panel waste generation in the Indian context. *Waste Management & Research,* 40(5), 504-518.
13. Dias, P., Schmidt, L., Gomes, L. B., Bettanin, A., Veit, H., & Bernardes, A. M. (2018). Recycling waste crystalline silicon photovoltaic modules by electrostatic separation. *Journal of Sustainable Metallurgy*, 4, 176-186.

11. Solar Resource Assessment and Energy Meteorology

Advancing Solar Energy Potential Assessment Of Urban Landscapes: A Deep Learning And Computer Vision Based Architecture For High-Resolution Topographic Data Incorporating Temporal Shadowing

Medha Sharma[1], Sonam Maheshwari[1]

[1] MESO Constructivist LLP, Raipur (India)

Abstract

Accurately assessing solar energy potential is essential for effective urban planning and successful solar panel installations. While conventional methods consider factors like climate conditions, low-resolution topography, and mean solar radiation, there is a pressing need to incorporate high-resolution topographic data and account for the temporal shadowing effect caused by neighbouring structures and trees. This research aims to address these challenges and develop an algorithmic architecture specifically tailored for densely populated tropical areas like New Delhi in India.

By introducing computer vision techniques, this study pioneers a novel approach to analyzing temporal shadowing effects in urban environments. This integration significantly enhances the accuracy and efficiency of solar energy potential assessment while improving the methodology's scalability and generalizability. This study fills a critical gap by considering the temporal shadowing effect and utilizing high-resolution topographic data.

A key focus of this research is data-driven decision-making in renewable energy planning. This comprehensive approach enables more informed decisions in urban planning, paving the way for sustainable and resilient cities. The findings hold great promise for transforming urban energy planning and fostering the widespread adoption of solar energy systems.

Keywords: Solar Energy Potential, Urban Planning, Temporal Shadowing Effect, Rooftop PV mounting, PV installation, Renewable Energy Planning, Satellite Data, GIS, Computer Vision, Deep Learning, Solar Radiation, Google Earth Engine, Building footprint.

1. Introduction

In light of the intensifying global environmental crises and soaring energy demands, renewable energy sources, notably solar energy, have established a foothold as indispensable alternatives to conventional fossil fuels. Solar energy, with its abundant, pollution-free, and perpetually renewable nature, unfolds a spectrum of possibilities in paving the way towards a sustainable future, minimizing carbon emissions and mitigating climate change implications. Particularly, as metropolitan areas continue to increase, it becomes increasingly important to harvest solar energy efficiently inside these areas in order to fulfil the ever-increasing energy demands of modern cities.

India, according to NREAP (National Renewable Energy Action Plan) 2022, illuminated with an impressive average solar irradiation of 5.4 kWh/m2/day, positions itself as a potential powerhouse for solar energy generation. Despite this, the tangible adoption of solar energy within the nation is crippled by a myriad of barriers such as elevated costs associated with solar panels, a pervasive lack of awareness and knowledge about solar energy as discussed in his paper by Jain, 2020. However, recent advances in governmental backing and policy-driven support promises some social development and awareness to which demand is estimated to soar in near future. But these developmental paces need preparations years ahead. It is against this backdrop that the current research paper aims to carve out an innovative pathway to augment the solar energy potential in urban zones of India and similar landscapes.

In two separate studies by Kumar,2021 and Yuhu Zhang, 2020, it was already pointed out that one pivotal challenge throttling the development and optimization of solar energy in urban landscapes is the temporal shadowing effect, prominently witnessed in densely populated urban environments. This phenomenon refers to the obstruction or blocking of sunlight by neighbouring buildings, infrastructures, and vegetation, which inadvertently diminishes the

10.18086/swc.2023.11.01 Available at http://proceedings.ises.org

volume of solar energy that can be proficiently harnessed. Temporal shadowing does not merely pose a physical barrier but also intricately influences the optimal solar energy yield by clouding photovoltaic systems at varying intervals throughout the day. Given the widespread and towering architecture that characterizes urban areas, particularly in India, the severity of these shadowing effects is notably amplified in such highly dense urban regions, demanding meticulous quantification and strategic circumvention to precisely gauge and enhance urban solar energy potential.

Historically, the assessment of solar energy potential has been rooted in simplified models and lengthy computational approaches, which have consistently fallen short of capturing the multifaceted interactions amongst shadows, terrains, and dynamic urban environments. Yet, as in a paper Siddharth Joshi, 2021 said, the dawn of technological advancements, encompassing remote sensing technology, high-resolution topographic data, deep learning algorithms, and computer vision techniques, heralds a promising horizon in or circumventing these constraints and giving more precise, reliable, and expansive evaluations of solar energy potential assessments.

In the field of Artificial Intelligence, computer vision Computer Vision is a field of AI that simulates Vision processing capabilities of human. Major Tasks are:

- Detection
- Recognition
- Segmentation
- Reconstruction
- Generation

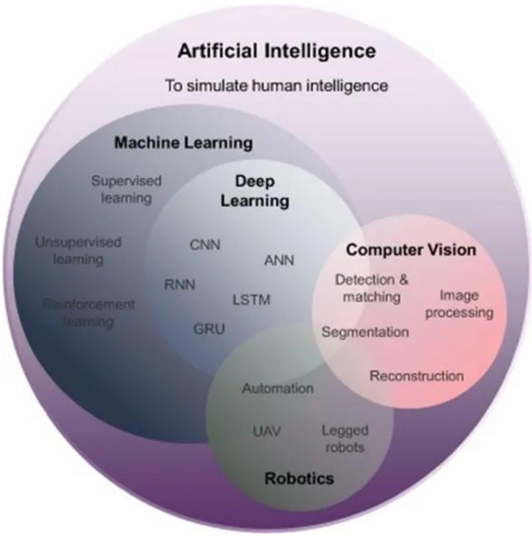

Fig. 1 Artificial Intelligence Venn Diagram (Shravani Upadhyay)

Some Deep Learning architectures are developed to perform these tasks very efficiently. Deep Learning encompasses the area of Artificial Intelligence study working on frameworks with complex neural networks that processes information with nodes and links exactly resembling neural networks in our brain. See Fig. 1 illustrated by Shravani Upadhyay et.al for structured Venn diagram to understand the hierarchical relationship between these terms.

This research paper aims to present a novel approach for assessing solar energy potential in Indian urban regions by incorporating high-resolution topographic data, deep learning algorithms, and computer vision techniques to account for temporal shadowing effects. The proposed methodology considers the specific challenges and characteristics of the Indian context, such as the high population density, diverse urban landscapes, and varying weather patterns, to ensure the accuracy and applicability of the results. The incorporation of technological innovations not only enhances the precision of measurements but also endeavors to surmount the previously insurmountable hurdles presented by temporal shadowing effects.

2. Data Source

In this study, primarily satellite imagery is used. The source for this type of data is combinational from different data collection instruments/missions, the Sentinel-2 MSI mission (Sentinel 2A and 2B) which has high-resolution multispectral data, Sentinel 3 OLCI, DEM/DSM. The images were finally chosen with a resolution is as good as 10 meters in the visible band which is best suitable for studying dense urban landscapes. Another markable dataset is High-Resolution Imagery data, Google Earth Images. In the Data aggregation step, developed by *Gorelick* and his team at Google, this data is collected from Google Earth Engine (Available on the web) and Google Earth Pro Software. The rest of the topographical and meteorological data is acquired from NASA's open GIS database for the last 10 years.

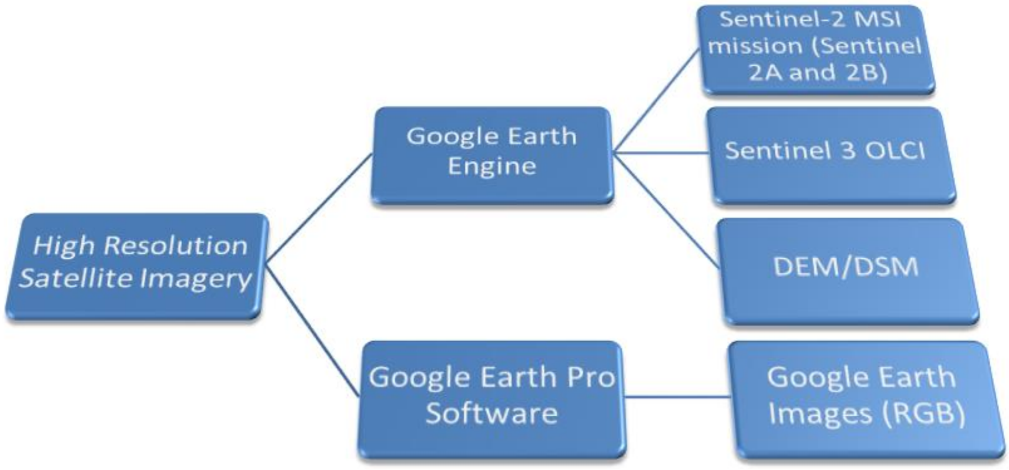

Fig. 2 Different Data sources used in this study

3. Methodology

The primary focus of this study is to recognize precise areas suitable for optimal electricity generation from solar panels, i.e., suitable rooftop area for PV installations, as evidently radiant with sunlight and predict the Solar Energy Potential of the area. To accomplish this, a multi-step methodology is employed, incorporating advanced computer vision techniques and deep learning architecture. An overview of working data flow is given in the Fig 3. The process begins by utilizing satellite data, which is fed into the system for data preprocessing following through the application of semantic segmentation, a powerful computer vision technique, the system extracts the suitable areas that will be subjected to further calculation and analysis. This segmentation process considers several crucial factors, including the Sun's position, seasonal effects like clouds, topological surface and shadowing effects caused by obstacles. Unlike traditional methods that involve tedious and time-consuming image analysis using masking techniques, the integration of deep learning streamlines the process, making it more efficient.

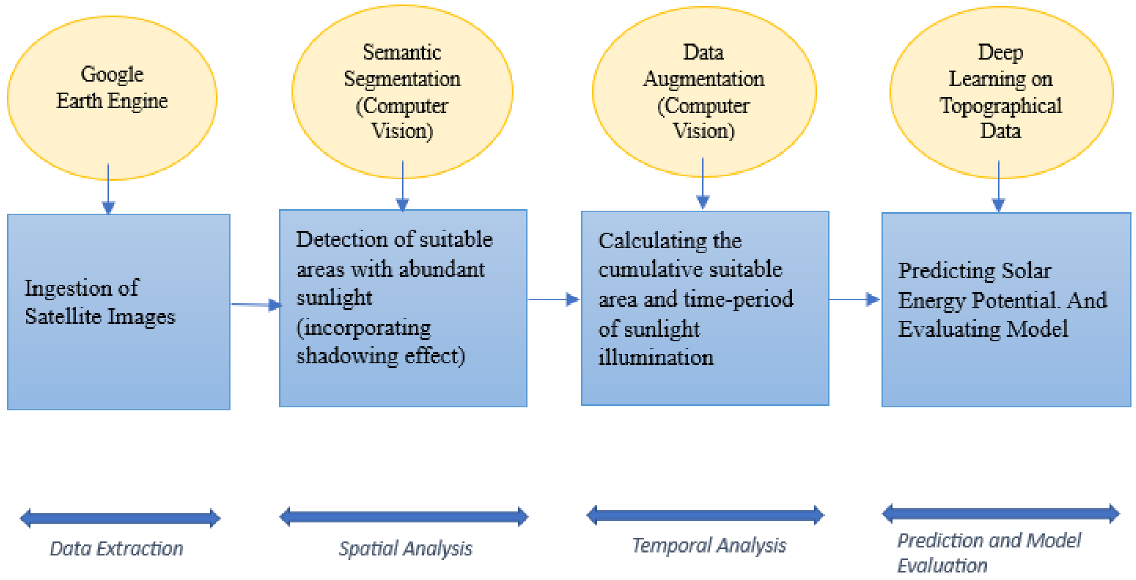

Fig. 3: High-Level Workflow of the proposed architecture for Solar Energy Potential Assessment

We have divide our workflow into two clear agenda. **One**, *detect and segment rooftops from satellite images*.and **second**, *analyze the variation in shadows on these rooftops over time*.

For this purpose we first acquired high-resolution satellite images from different random spots in New Delhi belonging to various types of Urban topography for spatial analysis, over different period of time for temporal analysis. For spatial analysis, the image samples can be more or less divided by the infrastructure style and density into: 1. High posh area, 2. Densely populated uniform high rise infrastructure, 3. Densely populated non-uniform infrastructure, 4. Less densely populated. We made sure that images were taken at roughly the same timestamps of the day across different dates to ensure consistent shadow analysis.

For a proper training dataset, we needed some annotated images which can be done manually by annotating a subset of images one by one, marking rooftops and shadows. And another method was taking some data as ground truth from certain opensource dataset like OpenBuilding (*W. Sirko* et.al), an open source dataset of building footprints which we have utilized as ground truth, which consists of outlines of buildings derived from high-resolution 50 cm satellite imagery. We chose the later approach. Then, split the dataset into training, validation, and test sets. Normalize and resize the images to a consistent size of 256x256. We used keras data augmentation techniques to enhance the dataset with time availability for satellite imagery. For our analysis we experimented with different deep learning frameworks starting from ANN (Artificial Neural Network), CNN (Convolutional Neural Network) to VGG-19 (Visual Geometry Group -19) and Resnet architectures. However, our interest peaked at UNet Architecture. UNet is primarily a CNN characterized by its U-shaped architecture. It consists of two main parts:

a. Contracting/Downsampling Path (Left side of the U):

   It consists of a series of convolutional layers followed by max-pooling layers. Each step involves two consecutive 3x3 convolutions (with ReLU activation), 2x2 max pooling operation with stride 2 for downsampling. At every step, the number of feature channels is doubled. This path aims to capture the context of the input image, reducing the spatial dimensions while increasing the depth (number of feature maps).

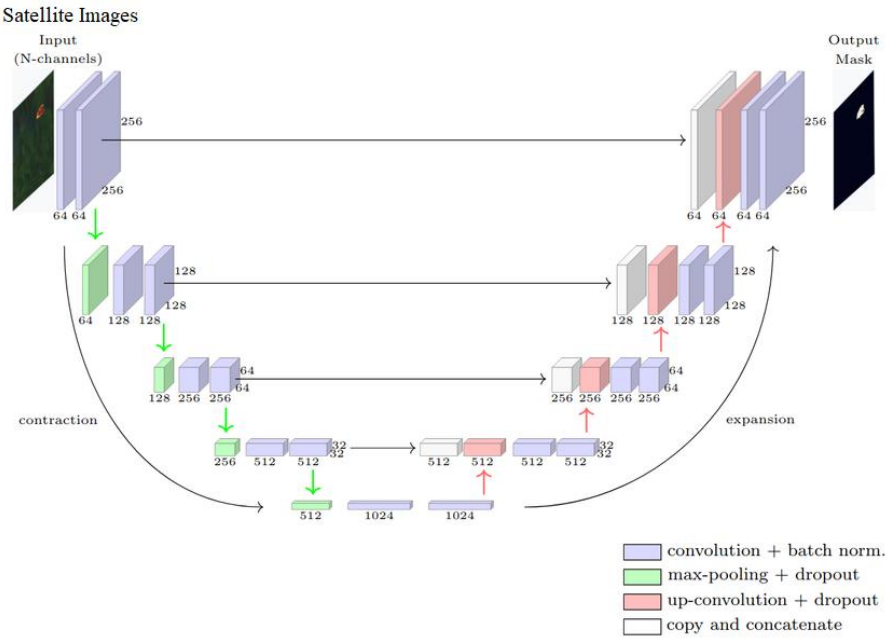

Fig.4. Modified UNet Architecture for Satellite Imagery

b. Expansive/Upsampling Path (Right side of the U):

This path upsamples the feature maps from the contracting path to recover the spatial dimensions. Each step in this path consists of an upsampling of the feature map, a 2x2 up-convolution that halves the number of feature channels, concatenation with the corresponding cropped feature map from the contracting path. This skip connection is crucial as it allows the network to use information from the downsampling phase, and two 3x3 convolutions (with ReLU activation). The expansive path allows the network to use the context captured in the contracting path to make precise localization, yielding a more accurate segmentation map.

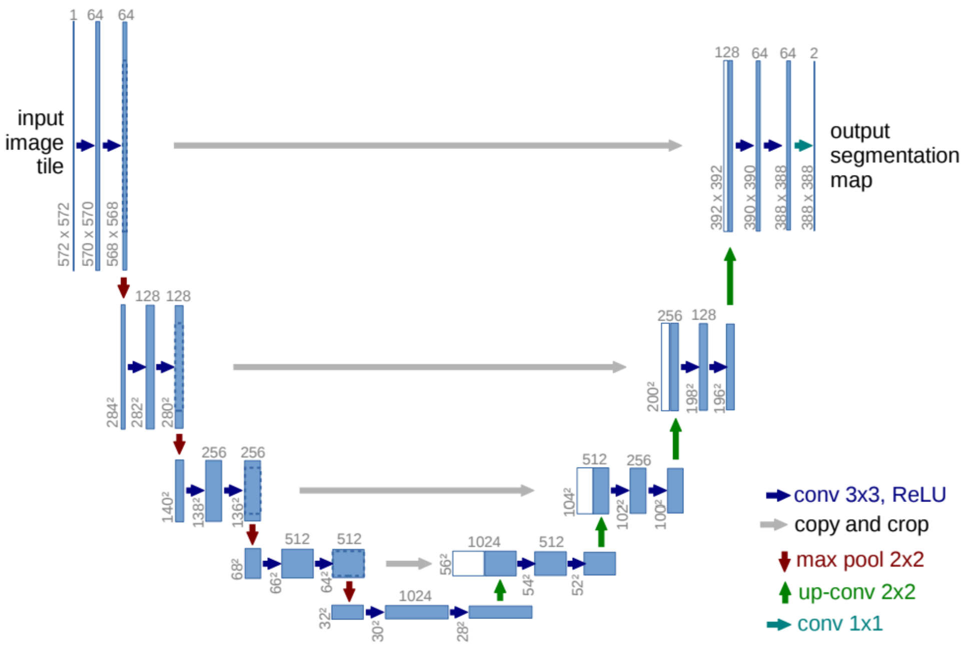

Fig.5. Basic UNet Architecture taken from its original source (Olaf Ronneberger, 2015)

The UNet architecture infamously used in biomedical image analysis, however its capability to understand the context of images and then localizing the features, is what needed for our use case. However, we posed many difficulties of resolution and image quality for this architecture to shine. In order to get the best results we targeted to implement the U-Net architecture tailored for satellite images.

As we moved to the second part of our objective to analyze the shadowing effect, we extracted the segmented rooftops from all temporal images and then analyzed the shadows and area under shadow versus irradiant areas on these extracted rooftops. We calculated total rooftop areas, effective area after removing the area under shadow for each rooftop in each image with each timestamps. We classified the rooftop based on average percentage under shadow using 2 thresholds.

a. The rooftops in green are more than 80% fully irradiant with direct sunlight,

b. The rooftops with yellow colour are the ones with 75-80% radiance, or 20-30% area of these rooftops is mostly in shadow.

c. The rooftops in red are the ones with 75% or less radiance, or more than 25% area of theses rooftops is mostly in shadows.

Further for validation we evaluated the model based on precision, recall and R-score, iteratively using fine-tuning and hyperparameter optimization between Precision and Recall, final model was decided. Precision tells what ratio of all classification was closer or exact match with the ground truth, while recall means what ratio of multiple calls the model is able to classify the same class. Both are considered evaluation metrics for machine learning or deep learning algorithms and models. Precision-Recall curves (Fig. 9 in Results and Discussion section) summarize the trade-off between the true positive rate and the positive predictive value for a predictive model using different probability thresholds.

The Fig. 6 summarizes the steps followed in the adopted methodology of this study.

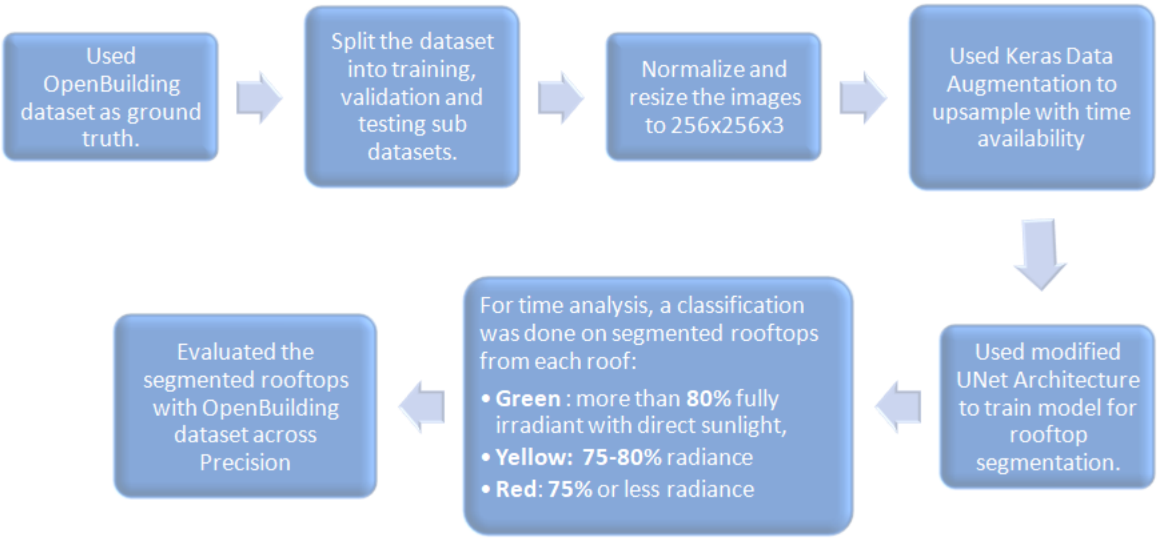

Fig. 6 Summary of steps followed in the adopted methodology

4. Results and Discussion

After data collection of high resolution satellite imagery, some sample images are attached from Fig.7.1-Fig.7.5 which were representative images collected from different data sources and regions in New Delhi with different infrastructure density and style. Fig.7.1 was collected from Posh or highly maintained area in New Delhi. Fig.7.2 was from less densely populated areas, Fig.7.4 belonged to densely populated areas with non-uniform infrastructure.

Fig. 7.1. Collected from Google Earth Image from Posh area in New Delhi

Fig.7.2 Collected from Google Earth Images from less dense urban region

Fig. 7.3 Collected from moderately dense urban region

Fig. 7.4 Satellite Images collected from densely populated areas with non-uniform infrastructure.

After Segmentation with enhanced visualisation, the building rooftops were segmented and were classified into Red, Yellow and Green color based on the percentage of the rooftop area being mostly in shadow. As described in Methodology section, the colors represent:

a. The rooftops in green are more than 80% fully irradiate with direct sunlight,

b. The rooftops with yellow color are the ones with 75-80% radiance, or 20-30% area of these rooftops is mostly in shadow.

c. The rooftops in red are the ones with 75% or less radiance, or more than 25% area of theses rooftops are mostly in shadows.

From the images, although most rooftops seem to be pigmented green, that is most part of the rooftops are usually directly illuminated by sun rays. Some rooftops that are marked red in Fig.8.1. and even fewer are marked as yellow, representing that posh areas have lineated rooftops without much difference in heights and so lesses regions with shadows on roof. While a similar trend is seen densely populated regions but with uniform infrastructure, Fig. 8.2. Fig. 8.4 and Fig 8.5 both are high populated regions with non-uniform infrastructure, but Fig 8.4 shows non-uniformity in heights of towers/buildings while Fig 8.5 shows non-uniformity in distribution of buildings on x-y-plane (or ground). But both have shown higher number of yellow and red coloured segments showing lesser best-suited rooftops for solar panels.

Fig. 8.1. Image segmentation result in High Posh Area

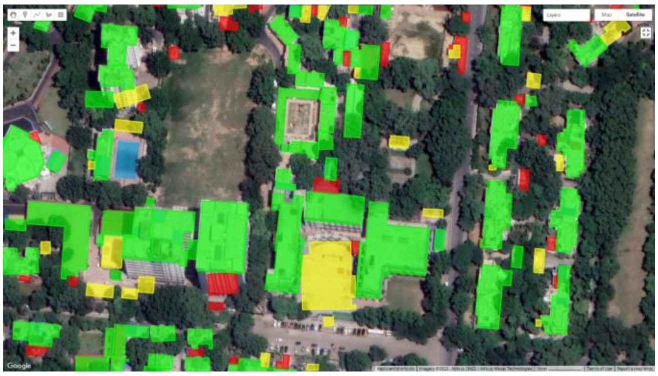

Fig. 8.2 Less densly populated area

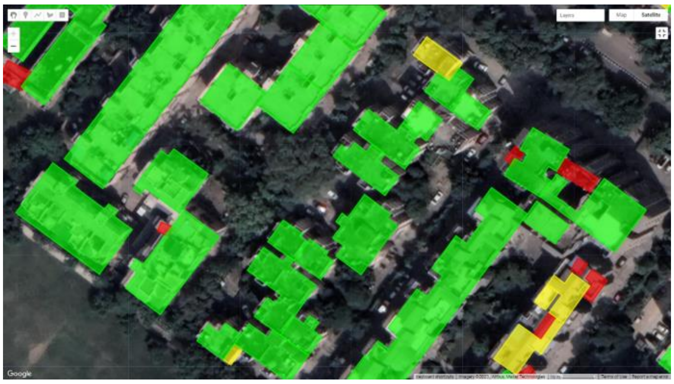

Fig. 8.3. Densely populated uniform high-rise infrastructure

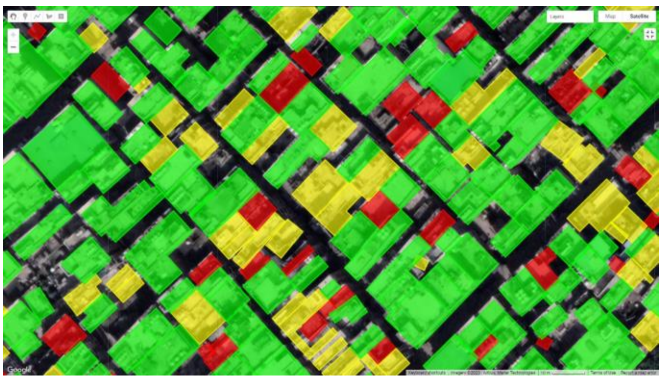

Fig. 8.4. Densely populated non-uniform infrastructure

Fig. 8.5. Densely populated non-uniform infrastructure

While performing model evaluation, we checked the trend of precision vs recall, Fig. 9, based on the ground truth, the building footprint data from OpenBuilding, it showed segmentation and classification confidence was higher in urban regions with high-density infrastructure, and our model also performed better in such regions this was not the case with any other reported algorithms, and it performed especially well in regions with uniform infrastructure which is anyway intuitive.

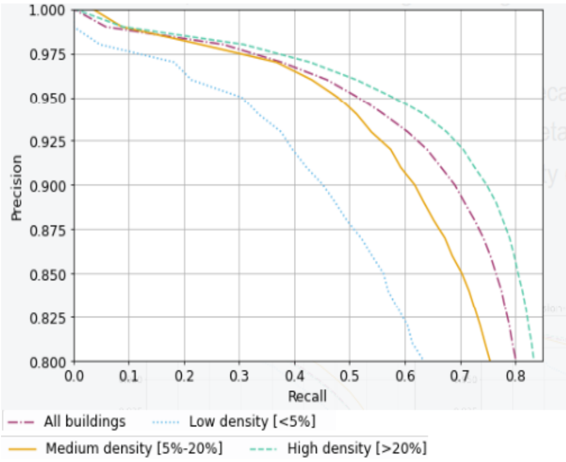

Fig. 9. Evaluation of Precision and Recall based on infrastructure density

5. Conclusion

The algorithm developed in this study leverages the potential of computer vision and deep learning architecture to optimize the best working weights for parameter aggregation from satellite imagery. This optimization process is crucial for accurately determining the suitable rooftop areas for planning the design and installation of photovoltaic (PV) panels. By incorporating deep learning, the algorithm reduces the complexity of the calculation, enabling users to easily assess the most suitable rooftop areas. Furthermore, the calculated areas are utilized to predict the most suitable roofs or buildings for PV installation and estimate the Solar Energy Potential for urban region planning. This prediction helps in making informed decisions about solar panel placement, ensuring maximum energy generation and utilization.

In addition to spatial analysis, this study also examines the temporal dimension of solar potential. By considering the variation of solar radiance available on roof over time, the research aims to incorporate time reference into the calculation by parameterizing shadows on roof. Utilizing the Data Augmentation technique of Computer Vision, the low quality or low data availability can be pushed further as well as the temporal effect can be easily parameterized and added to the analysis. The temporospatial analysis of solar radiation potential in the city is vital for understanding the dynamics of solar energy availability and optimizing its utilization. However, this is also one of the bottleneck for the algorithm as the quality of data is determined by augmentation limitations. In the era of data-driven decision-making, the whole challenge remains at the availability, accessibility and quality of data used in the study.

Further based on infrastructure density as well as style, the suitable rooftop area changes which is adequately exposed to sun rays, affecting precise assessment of solar potential. With proper spatio-temporal analysis can this be achieved to accurately assess solar potential and optimize PV designing for diverse Urban landscapes like India and New Delhi.

To validate the accuracy and effectiveness of the algorithm, the predicted results are compared with previous data labels and analysis results but for future work, we can utilize the ground truths obtained from ArcGIS rooftop detection algorithms, a widely used geographic information system. This comparison will provide a comprehensive assessment of the algorithm's performance, ensuring its reliability for practical applications.

The sustainable future of urban India hinges significantly on the efficient, unbridled harnessing of solar energy, necessitating a synergistic blend of technological advancements and context-specific methodologies. The proposed novel approach transcends traditional barriers and paves the way for accurate, reliable, and optimized solar energy potential assessments amidst the complexities and unique challenges witnessed within the Indian urban landscape. Consequently, this research not only stands to significantly augment the usage of solar energy in India but also charts a pragmatic course towards realizing a sustainable, energy-secure future, underscored by technological innovation and strategic planning.

6. Acknowledgments

We are grateful for ISES for helping us throughout the submission process and giving us this opportunity to delve into this topic of research which has paved new admiration for technology and its applications.

7. References

Energy, M.o. (2022), (NREAP), National Renewable Energy Action Plan. Retrieved from https://mnre.gov.in/national-renewable-energy-action-plan-nreap

Jain, V. P. (2020), Solar potential assessment using machine learning techniques for Indian cities, Solar Energy, 203.

Kumar, P. S. (2021), Estimating rooftop solar potential in Indian cities using deep learning and high-resolution imagery, Applied Energy, 292.

Siddharth Joshi, S. M. (2021), High resolution global spatiotemporal assessment of rooftop solar photovoltaics potential for renewable electricity generation, Nat Commun 12. doi: https://doi.org/10.1038/s41467-021-25720-2

Yuhu Zhang, J. R. (2020). Solar energy potential assessment: A framework to integrate geographic, technological, and economic indices for a potential analysis, Renewable Energy, Volume 149, Retrieved from https://doi.org/10.1016/j.renene.2019.12.071

Google Earth Pro, Available on the web: https://www.google.com/intl/en_in/earth/about/versions/#earth-pro

Google Earth Engine, Available on the web: https://developers.google.com/earth-engine/datasets/

Teng Zhong, Zhixin Zhang, Min Chen, Kai Zhang, Zixuan Zhou, Rui Zhu, Yijie Wang, Guonian Lü, Jinyue Yan, A city-scale estimation of rooftop solar photovoltaic potential based on deep learning, Applied Energy, Volume 298, 2021, 117132, ISSN 0306-2619, DOI: https://doi.org/10.1016/j.apenergy.2021.117132.

Gorelick, N., Hancher, M., Dixon, M., Ilyushchenko, S., Thau, D., & Moore, R. (2017). Google Earth Engine: Planetary-scale geospatial analysis for everyone.

C.Donlon et al. L. A. Brown, J. Dash, A. L. Lidón, E. Lopez-Baeza and S., The Global Monitoring for Environment and Security (GMES) SENTINEL-3 mission.

U.S. Geological Survey, 2019, 3D Elevation Program 1-Meter Resolution Digital Elevation Model (published 20200606), accessed October 23, 2019 at URL https://www.usgs.gov/the-national-map-data-delivery

Olaf Ronneberger, Philipp Fischer, and Thomas Brox, U-Net: Convolutional Networks for Biomedical Image Segmentation, 2015.

Shravani Upadhyay,Kaavya Shree, Padigi Reddy Sangeetha, Computer Vision in Space Science Technology : Advancements and Applications.

W. Sirko, S. Kashubin, M. Ritter, A. Annkah, Y.S.E. Bouchareb, Y. Dauphin, D. Keysers, M. Neumann, M. Cisse, J.A. Quinn. Continental-scale building detection from high resolution satellite imagery. arXiv:2107.12283, 2021.

12. Perspectives for a 100% Renewable Energy World

Impact of global warming on the potential for passive solar heating and overheating of buildings in Montenegro

Luka Pajek[1] and Mitja Košir[1]

[1] Faculty of Civil and Geodetic Engineering, University of Ljubljana, Ljubljana (Slovenia)

Abstract

Montenegrin building stock is highly energy inefficient, while the country has a high potential for using solar energy. Therefore, the potential for implementing passive solar heating and overheating in residential buildings was assessed in four locations among the country's three climate zones, namely the Coastal zone, the Continental zone and the Mountain zone, for the current climate and two different climate change scenarios (SSP2-4.5 and SSP5-8.5). Besides, the need for overheating prevention measures was assessed as well. The results demonstrated a relatively high potential for applying passive solar heating in Montenegrin buildings in current and future climate conditions, especially in the Mountain zone. At the same time, the need for overheating prevention measures is projected to increase under global warming the most in the Continental climate zone. The locations in this zone are the most vulnerable to overheating because they will potentially shift from heating-dominated to cooling-dominated, depending on the climate change scenario. Therefore, because of the high climate variability in Montenegro, building design approaches and policies should be addressed accordingly.

Keywords: passive solar heating, overheating, buildings, global warming, Montenegro. energy efficiency

1. Introduction

Montenegro is located in the western Balkans and has been among Europe's most inefficient energy consumers. Its process of negotiations for EU accession is open. Thus, energy efficiency improvement is considered a strategic goal at the national level. Improving the energy efficiency of building stock will have political and economic implications for Montenegro, given that about 2/3 of thermal energy use in households is covered by electricity, and 1/3 of all electricity is provided by imports. Detached houses in Montenegro represent 83.7 per cent of building stock. At the same time, their average annual heating demand is 276.50 kWh/m^2, the average annual domestic hot water demand is 31.9 kWh/m^2, and the annual cooling demand is 74.0 kWh/m^2 (Navikova et al., 2015). The average number of yearly heating degree days (HDD) in Montenegro is 2386 Kdays (Ministry of Economy, 2013). Unlike many other countries in the region, Montenegro does not have a district heating system or gas network and residential buildings are primarily heated using solid fuels or electricity. On the other hand, Bajat et al. (2020) stated that Montenegro is one of the European countries with the highest potential for the development, production, and consumption of solar energy, with an average annual potential insolation of 1800 kWh/m² and more than 2000 annual hours of sun. Therefore, implementing passive solar architecture and solar collectors for heating buildings or photovoltaics for electricity production should have excellent potential. Due to the country's concurrent high energy inefficiency and a high potential for using solar energy, the study aimed to assess the potential for implementing passive solar heating (PSH) in residential buildings, which was assessed for two different climate change scenarios.

2. Methods

2.1. Locations and climate

According to Navikova et al. (2015), Montenegro is divided into three climate zones: Zone 1: Coastal zone (Mediterranean climate, average annual HDD = 1623 Kdays, Bar, Budva, Danilograd, Herceg Novi, Kotor, Podgorica, Tivat, and Ulcinj), Zone 2: Continental zone (temperate climate, average annual HDD = 2528

10.18086/swc.2023.12.03 Available at http://proceedings.ises.org

Kdays, Nikšić and Cetinje) and Zone 3: Mountain zone (continental climate with cold winters, average annual HDD = 3388 Kdays, Andrijevica, Berane, Bijelo Polje, Žabljak, Kolašin, Mojkovac, Plav, Plužine, Pljevlja, Rožaje, Šavnik). However, a significant part of the country has a mild Mediterranean climate, while concurrently, the mountainous part is less populated. In particular, about 2/3 of residential buildings are located in Zone 1, with more than 30 per cent of the country's population in Podgorica alone. Roughly 25 per cent of the population lives in Zone 3, and only about 11 per cent in Zone 2 (Navikova et al., 2015). Therefore, the study included four locations, namely Podgorica and Ulcinj (Zone 1), Nikšić (Zone 2) and Žabljak (Zone 3) (see Table 1 and Figure 1). The selected locations' climate files (EPW based on TMY 2004–2018) were collected from the Repository of free climate data for building performance simulation (Climate.OneBuilding, 2023). Furthermore, future climate files considering global warming were morphed using the Future Weather Generator (Rodrigues et al., 2023). The future climate files were morphed per the IPCC's Shared Socioeconomic Pathways (SSP) scenarios SSP2-4.5 (intermediate greenhouse gas – GHG emissions) and SSP5-8.5 (very high GHG emissions) and 2036–2065 and 2066–2095 timeframes.

Tab. 1: Analysed locations (also see Figure 1)

Climate zone	Location	ASHRAE climate zone	Köppen-Geiger climate	Latitude	Longitude	Elevation
Zone 1	Ulcinj	3A	Cfa	41°55' N	19° 14' E	29 m
Zone 1	Podgorica	3A	Cfa	42° 26' N	19° 17' E	50 m
Zone 2	Nikšić	4A	Cfa	42° 46' N	18° 57' E	647 m
Zone 3	Žabljak	6A	Dfb	43° 9' N	19° 38' E	1450 m

Fig. 1: Climate zones of Montenegro with the analysed locations

2.2. Potential for passive solar heating

The potential for PSH was assessed using the BcChart v2.3 tool (Košir and Pajek, 2021). The tool uses the upgraded Olgyay's bioclimatic chart, considering the outdoor air temperature, relative humidity and solar radiation intensity to determine if human thermal comfort in a generic building may be achieved at certain outdoor conditions. Besides, potential passive building design measures are proposed when human thermal comfort is unmet. In particular, for this study, the comfort achieved by solar radiation utilisation (C_{sn}) and the potential for PSH (R) values were considered, which were summed up to represent the cumulative PSH potential (P_{PSH}) of a location and expressed as the number of days per year. Additionally, the number of days when shading is needed (S_h) and the number of days when thermal comfort is achieved by solar control (C_z), either shading or solar utilisation, was determined for each location. All the above-stated values were determined using the average, maximum and minimum daily outdoor temperature, relative humidity and solar irradiance for each month. The exact methodology used by the BcChart tool is presented in the paper by Košir and Pajek (2017).

2.3. Implications for energy-efficient building design

In the last step, the results were evaluated in the context of implications for energy-efficient building design using degree hours as a generic proxy for building energy performance. Although the use of degree hours (or degree days) for estimating the energy efficiency of a large and averaged sample of buildings is a well-established top-down method, it has limitations due to being based solely on the external temperature and a presumed building base temperature (Košir, 2019). Nevertheless, the degree hours method can be used to approximate the impact of climate and climate change on the average building's energy use for heating and cooling (Dirks et al., 2015; Clarke et al., 2018). For this reason, yearly values of heating degree hours (HDH) and cooling degree hours (CDH) were calculated using equations 1 and 2.

$$\mathrm{HDH} = \sum_{i=1}^{8760}\left(T_{b,H} - T_{o,i}\right)^{+} \quad \text{if } \mathrm{T_{b,H}} - \mathrm{T_{o,i}} > 0 \qquad \text{(eq. 1)}$$

$$\mathrm{CDH} = \sum_{i=1}^{8760}\left(T_{b,C} - T_{o,i}\right)^{+} \quad \text{if } \mathrm{T_{o,i}} - \mathrm{T_{b,C}} > 0 \qquad \text{(eq. 2)}$$

$T_{b,H}$ is the heating base temperature equal to 10 °C and $T_{b,C}$ is the cooling base temperature equal to 23 °C. $T_{o,i}$ represents the outdoor air temperature at the i-th hour of the year. Only the positive differences between T_b and $T_{o,i}$ are considered. The corresponding heating and cooling base temperatures were defined so that the results of HDH and CDH are representative for newly built or recently energy-renovated buildings.

3. Results and Discussion

3.1. Potential for passive solar heating

Figure 2 shows the P_{PSH} in days per year at each studied location, indicating the annual occurrence of environmental conditions allowing for PSH. Namely, the number of days when solar radiation is adequate to ensure passive solar heating is given. At current climate conditions (i.e. 2004–2018), the location with the highest P_{PSH} of 194 days annually is Žabljak (Zone 3 – i.e. cold climate), which was expected. On the other hand, Podgorica (Zone 1 – i.e. Mediterranean climate) has the lowest P_{PSH} at only 145 days annually. Nevertheless, all the analysed locations show a relatively high $P_{PSH,}$ and solar energy may be utilised up to 50 per cent of the year to provide indoor thermal conditions. In particular, in Žabljak, the highest P_{PSH} is achieved between April and October, while solar radiation is insufficient between November and March. Thus, heat retention and conventional heating are necessary during the specified period. In Žabljak, global warming is projected to decrease the P_{PSH}, mainly between June and September (due to overheating occurrence), especially in the SSP5-8.5 emission scenario. In the latter's case, the P_{PSH} would be reduced by 36 days (18.5 per cent relative to 2004–2018). Similar behaviour, although less pronounced, may be observed for Nikšić. In contrast, under global warming (SSP5-8.5), P_{PSH} is projected to decrease and later increase (due to increased winter temperatures) even above the current values in Ulcinj and Podgorica. In Ulcinj, P_{PSH} values are projected to increase to the extent that they would be even higher than in Žabljak and Nikšić until the end of the century. The range of the projected P_{PSH} at the analysed locations would be 137–184 days in the SSP2-4.5 scenario and 149–164 days in the SSP5-8.5 scenario.

Although the potential for passive solar heating is not expected to change under global warming in the analysed locations significantly, the effects of global warming need to be evaluated in the context of overheating occurrence. Therefore, the number of days when shading is needed was assessed at all the locations. Observing data in Figure 3, it can be seen that the importance of shading (i.e. overheating prevention) is projected to increase significantly. At current climate conditions, locations in Zone 1 have the highest shading need, with 135 days in Podgorica and 121 days in Ulcinj. The intermediate shading need of 54 days is observed in Nikšić

(Zone 2). At the same time, Zone 3 (Žabljak) has the lowest shading need at 0 days annually. As expected, the need for shading is expected to increase over time due to the effects of global warming, with the highest projected increase of 86 days in Nikšić (SSP5-8.5) at the end of the century. Therefore, the results highlight the increased importance of overheating prevention (i.e. shading) even if the P_{PSA} is not projected to change significantly.

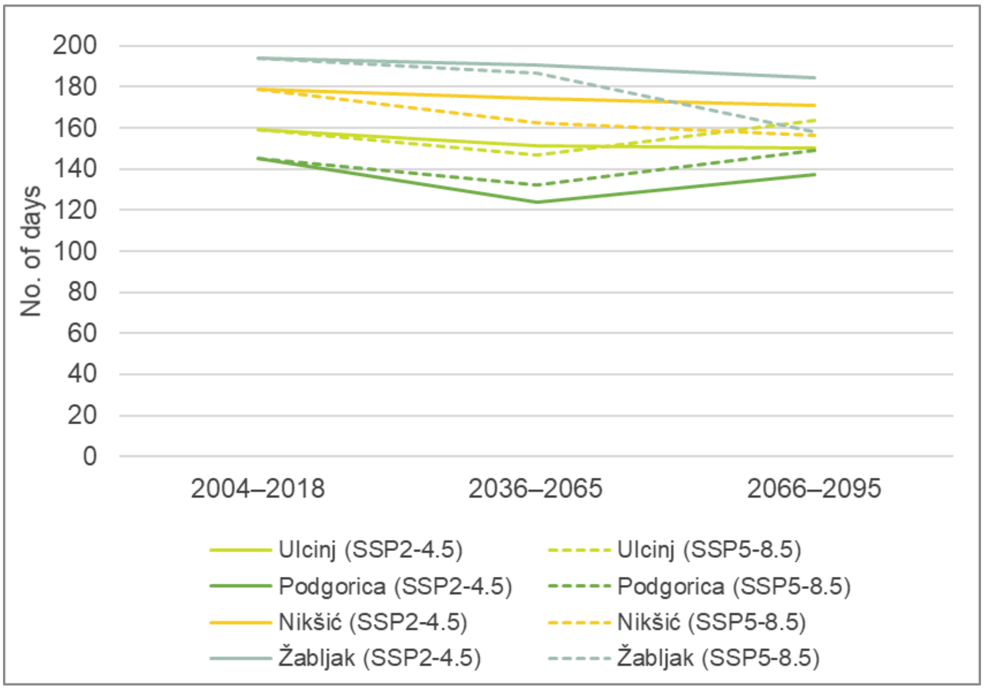

Fig. 2: Potential for passive solar heating in the analysed locations for current and two future periods. The potential is expressed in the number of days when solar radiation is adequate to ensure passive solar heating

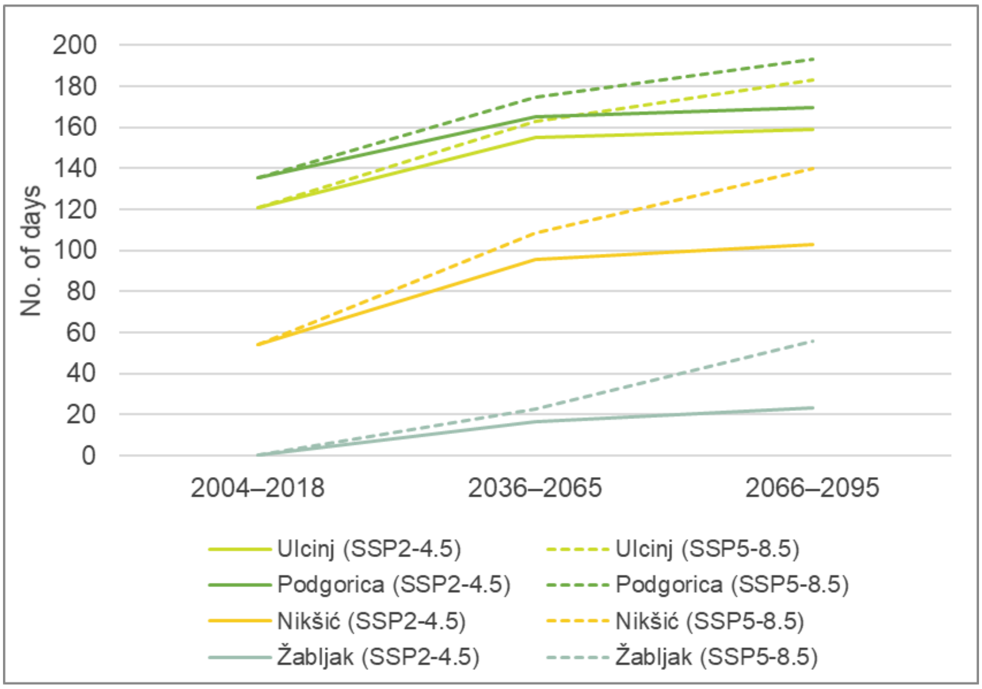

Fig. 3: Shading potential in the analysed locations for current and two future periods. The potential is expressed in the number of days when shading is needed to ensure thermal comfort

Moreover, the thermal comfort potential was assessed when comfort could be assured by solar energy control, either shading or solar harvesting, to understand how global warming affects the time when no additional passive measures are needed (i.e. free-run operation of buildings). Figure 4 shows that in Zone 1, the number of days when free-run comfort is achieved is projected to decrease significantly, especially in Ulcinj (i.e. by 35 days for SSP5-8.5 compared to the 2004–2018 period). On the other hand, Nikšič (Zone 2) and Žabljak (Zone 3) exhibit an increase in free-run comfort potential, with the highest increase of 51 days for SSP5-8.5 relative to 2004–2018 in Žabljak.

The projected changes in the bioclimatic potential of the analysed locations indicate that building design in the three Montenegrin climatic zones should focus on implementing overheating prevention measures while preserving passive solar heating actions. The latter's importance will remain high, which, in conjunction with the increased importance of overheating prevention, represents a challenge for the passive design of buildings under the future projected climates. The results align with the findings of the study by Pajek and Košir (2022) conducted for Podgorica under RCP4.5 and RCP8.5 climate change scenarios. Building designers should consider climate adaptation to minimise energy use and increase occupant thermal comfort. Therefore, in section 3.2, implications for energy-efficient building design are discussed.

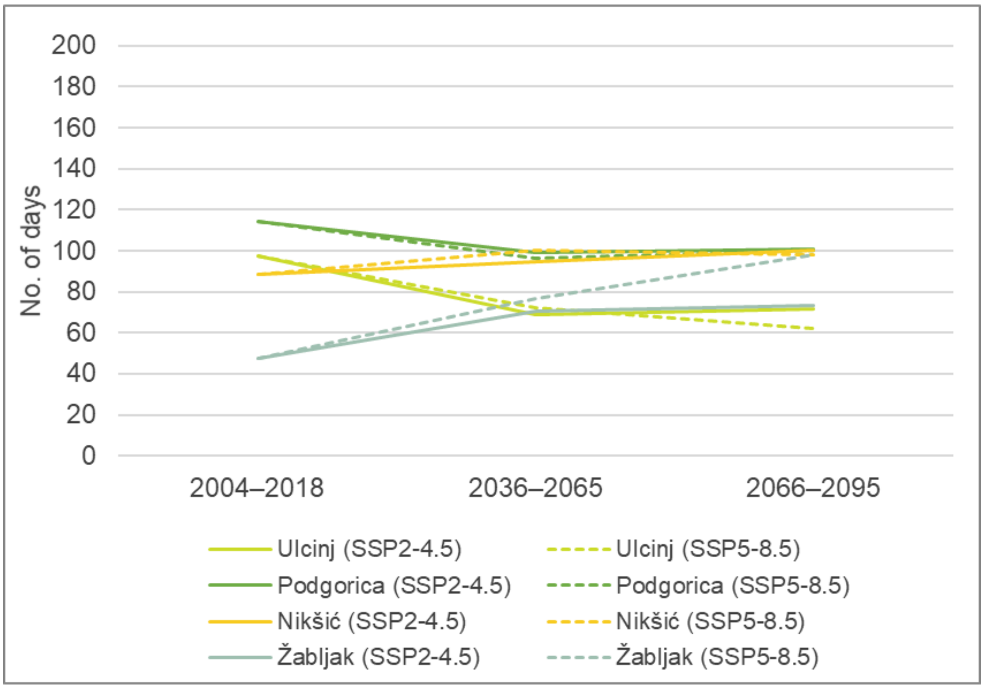

Fig. 4: Comfort potential in the analysed locations for current and two future periods. The potential is expressed in the number of days when comfort can be assured by solar energy control (either shading or solar harvesting)

3.2. Implications for energy-efficient building design

Concurrently with the bioclimatic analysis presented in the previous chapter, the evaluation of climate change impacts on energy use in the analysed locations and zones was evaluated. HDH and CDH were calculated using the original (i.e. 2004–2018) and morphed climate files for both climate change scenarios. The results presented in Figures 5 (SSP2–4.5) and 6 (SSP5–8.5) underscore the conclusions of the bioclimatic analysis. Furthermore, the calculated values of HDH and CHD more clearly illustrate the projected changes for energy use in average buildings of the analysed locations.

The analysis shows a similar trend for both climate change scenarios, which is a general reduction in annual HDH for all locations and an increase in the annual value of CDH (Fig. 5 and 6.). The presented data also clearly indicates the difference between climate Zone 1 and Zones 2 and 3, as the locations of Podgorica and Ulcinj will exhibit a disproportionate increase in CDH compared to a decrease in HDH. In general, this means that the cumulative value of HDH and CDH is expected to increase in Zone 1 and decrease in Zones 2 and 3. In particular, the most considerable impact of climate change is projected for Podgorica as by the end of the century the CDH is expected to increase by 11131 Kh (91 per cent increase) for SSP2–4.5 and 22559 Kh (185 per cent increase) for SSP5–8.5 scenario relative to 2004–2018. Simultaneously, the HDH will decrease by 55 and 85 per cent for SSP2–4.5 and SSP5–8.5 scenarios, respectively, resulting in an overall increase of energy needed for cooling and heating (Fig. 5. and 6.). The same trend is also actual for Ulcinj, although with a more minor overall expected energy use for cooling.

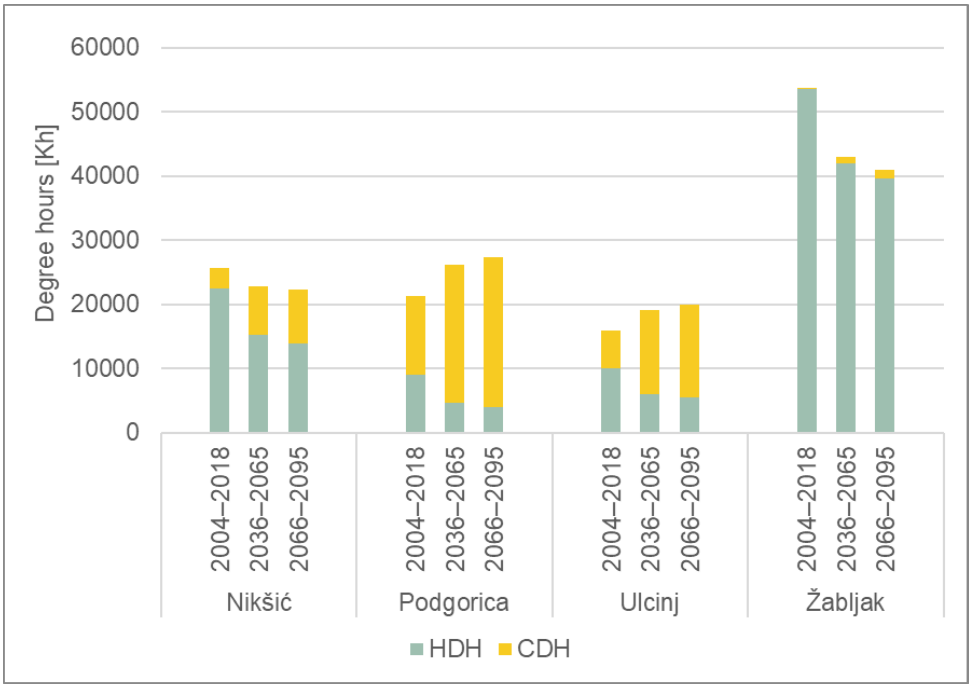

Fig. 5: Heating (HDH) and cooling degree hours (CDH) under current and SSP2–4.5 climate change scenario

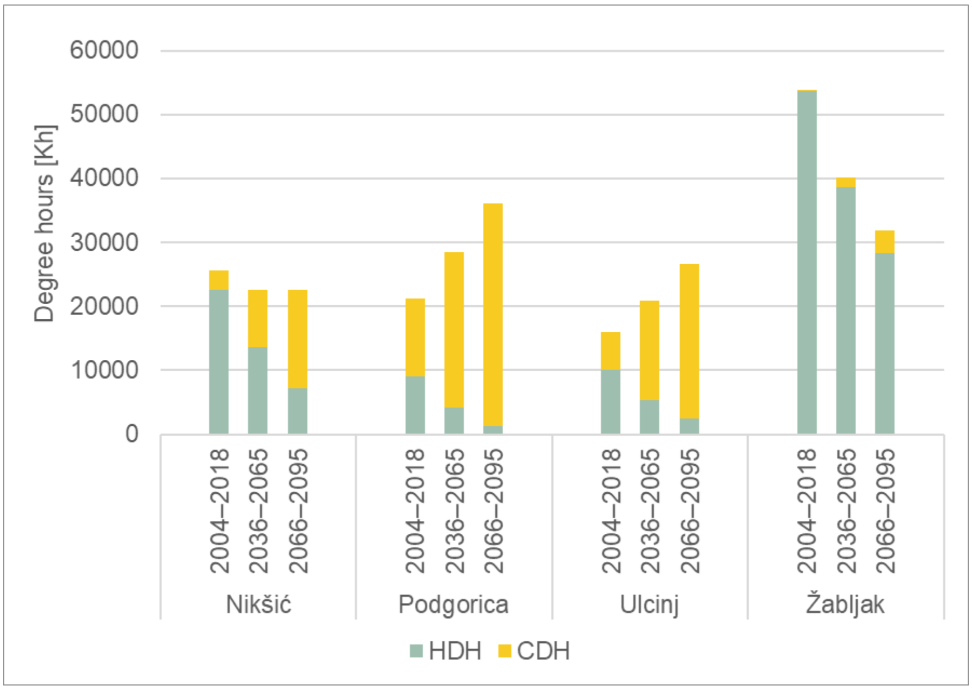

Fig. 6: Heating (HDH) and cooling degree hours (CDH) under current and SSP5–8.5 climate change scenario

Contrasting the impact of global warming in Zone 1 are the outcomes for Nikšić and Žabjak. As illustrated in Figures 5 and 6, these locations will generally benefit from projected climate change as the cumulative value of HDH and CDH is projected to decrease under both scenarios. Particularly for Žabjak, the projected impact is substantial as the HDH is expected to decrease by 13969 Kh (26 per cent decrease) for SSP2–4.5 and 25217 Kh (47 per cent decrease) for SSP5–8.5, with relatively small increases in CDH. The case of Nikšić is less straightforward as the increase in the cooling need is substantially conditioned by the climate change scenario in question. This means that under the SSP2–4.5 scenario, the location of Nikšić will remain heating-dominated (i.e. HDH > CDH, see Fig 5.) at the end of the century, while under the SSP5–8.5, it will become cooling-dominated (i.e. HDH < CDH, see Fig. 6). However, regardless of the considered scenario the overall sum of HDH and CDH for Nikšić is projected to decline and remain comparable among considered climate change scenarios up to the end of the 21st century.

4. Conclusions

The potential for passive solar heating in Montenegro is projected to be affected by global warming. In particular, the locations in the Continental and Mountain climate zones (i.e. Zones 2 and 3, respectively) might face a reduction of the potential because of higher spring–autumn air temperatures and solar radiation. On the contrary, the locations in the Coastal climate zone (i.e. Zone 1) would face a less significant potential reduction, while in specific scenarios, the potential for passive solar heating would even increase. On the other hand, locations in the Coastal zone have the highest and ever-increasing need for overheating prevention measures, while the need is projected to increase under global warming the most in the Continental zone. Overall, it may be concluded that passive solar heating has a relatively high potential for application in buildings in Montenegro, which is, on the country's average, not expected to decrease significantly due to global warming. However, in the context of energy-efficient building design and overheating vulnerability, the implications of global warming need to be addressed. In this manner, the locations in Continental zone are the most vulnerable to overheating because buildings in this zone will potentially shift from heating-dominated to cooling-dominated, depending on the climate change scenario.

Furthermore, the results of the presented analysis point to the fact that although Montenegro is geographically a small country, it is exceptionally climatically varied. Consequentially, such variability should be addressed at the level of building design approaches and legislative regulation, as is underscored by the differences between the Coastal and Mountain zones. Furthermore, the projected climate change will represent an additional challenge for energy-efficient and climate-adapted building design, particularly for Continental climate zone locations like Nikšić. At such locations, depending on the climate change scenario, buildings might become cooling-dominated in the second half of the century, necessitating a substantial shift in the design approaches. This is especially important because occupants have limited awareness about the potential of passive measures when summer thermal discomfort is the dominant issue (Pajek et al., 2023).

5. Acknowledgements

The research presented in this paper results from bilateral cooperation funded by the Slovenian Research Agency and the Ministry of Science and Technological Development of Montenegro (project No. BI-ME/23-24-002). The Slovenian authors further acknowledge the financial support from the Slovenian Research Agency (research core funding No. P2 – 0158).

6. References

Bajat, B., Antonijevic, O., Kilibarda, M., Sekulic, A., Lukovic, J., Doljak, D., Buric, D., 2020. Space-time high-resolution data of the potential insolation and solar duration for Montenegro. Spatium 45–52. https://doi.org/10.2298/SPAT2044045B

Clarke, L., Eom, J., Marten, E.H., Horowitz, R., Kyle, P., Link, R., Mignone, B.K., Mundra, A., Zhou, Y., 2018. Effects of long-term climate change on global building energy expenditures. Energy Econ. 72, 667–677. https://doi.org/10.1016/j.eneco.2018.01.003

Climate.OneBuilding, 2023. Repository of free climate data for building performance simulation from the Creators of the EPW [WWW Document]. URL https://climate.onebuilding.org/ (accessed 4.20.23).

Dirks, J.A., Gorrissen, W.J., Hathaway, J.H., Skorski, D.C., Scott, M.J., Pulsipher, T.C., Huang, M., Liu, Y., Rice, J.S., 2015. Impacts of climate change on energy consumption and peak demand in buildings: A detailed regional approach. Energy 79, 20–32. https://doi.org/10.1016/j.energy.2014.08.081

Košir, M., 2019. Climate Adaptability of Buildings: Bioclimatic Design in the Light of Climate Change. Springer International Publishing, Cham. https://doi.org/10.1007/978-3-030-18456-8

Košir, M., Pajek, L., 2021. BcChart v2.3 – A tool for bioclimatic potential analysis [WWW Document]. URL https://kske.fgg.uni-lj.si/en/research/ (accessed 4.14.23).

Košir, M., Pajek, L., 2017. BcChart v2.0 – A Tool for Bioclimatic Potential Evaluation, in: Proceedings of SWC2017/SHC2017. Presented at the ISES Solar World Conference 2017 and the IEA SHC Solar Heating and Cooling Conference for Buildings and Industry 2017, International Solar Energy Society, Abu Dhabi, pp. 1–10. https://doi.org/10.18086/swc.2017.21.04

Ministry of Economy, 2013. Energy Efficiency Action Plan of Montenegro 2013–2015.

Navikova, A., Csoknyai, T., Miljanić, Z., Gligorić, B., Vušanović, I., Szalay, Z., 2015. The typology of the residential building stock of Montenegro and modelling its low-carbon transformation. Regional environmental center, Montenegro.

Pajek, L., Jevrić, M., Ćipranić, I., Košir, M., 2023. A multi-aspect approach to energy retrofitting under global warming: A case of a multi-apartment building in Montenegro. J. Build. Eng. 63, 105462. https://doi.org/10.1016/j.jobe.2022.105462

Pajek, L., Košir, M., 2022. Implications of projected RCP4.5 and RCP8.5 climate change scenarios for the bioclimatic potential of Podgorica, in: Rakočević, M., Šćepanović, B. (Eds.), GNP 2022 Proceedings. Presented at the GNP 2022: The Eight International Conference Civil Engineering Science & Practice, University of Montenegro Faculty of Civil Engineering, Kolašin, Montenegro, pp. 747–754.

Rodrigues, E., Fernandes, M.S., Carvalho, D., 2023. Future weather generator for building performance research: An open-source morphing tool and an application. Build. Environ. 110104. https://doi.org/10.1016/j.buildenv.2023.110104

REVIEW OF SOLAR PV POLICY INCENTIVES AND REGULATIONS RELATED TO METERING AND BILLING OF GRID-CONNECTED ROOFTOP PV SYSTEMS IN INDIAN STATES

Pratik Joshi[1], Anand B. Rao[1,2] and Rangan Banerjee[1,3,4]

[1] **Ashank Desai Centre for Policy Studies (ADCPS), Indian Institute of Technology Bombay, Mumbai (India)**

[2] **Centre for Technology Alternatives for Rural Areas (CTARA), Indian Institute of Technology Bombay, Mumbai (India)**

[3] **Department of Energy Science and Engineering (DESE), Indian Institute of Technology Bombay, Mumbai (India)**

[4] **Department of Energy Science and Engineering (DESE), Indian Institute of Technology Delhi, New Delhi (India)**

Abstract

The share of rooftop photovoltaic (PV) capacity in India to total PV capacity has been marginal as the rooftop PV sector is falling short of its targeted capacity of 40 GW. This paper reviews solar PV policy incentives and contemporary regulations related to the metering and billing of grid-connected rooftop PV systems in Indian states and Union Territories (UTs) to understand their historical trend and present status. The policy incentive's deployment order and its effect on the PV capacity addition are presented using the National Renewable Energy Laboratory's (NREL) policy stacking framework. The review of policy documents shows that the states with the highest PV capacity published more policies between 2002 and 2022 than their counterparts. The Indian states and UTs significantly used market-expansion incentives over market-creation incentives to develop the domestic PV market. The prevailing metering and billing-related regulations in states and UTs are reviewed to understand the regulatory landscape of the country's grid-connected rooftop PV systems. It is observed that the choice of metering and billing mechanism employed differs across states and UTs, with net metering being the most commonly adopted mechanism.

Keywords: rooftop solar, policy incentives, policy stacking framework, solar energy, net metering,

1. Introduction

In 2015, India had targeted to install 100 GW of solar photovoltaic (PV) capacity by 2022 under the Jawaharlal Nehru National Solar Mission (JNNSM), comprising 60 GW for ground-mounted large-scale PV and 40 GW from rooftop solar. (Press Information Bureau, 2015) As of August 2023, India installed 71.61 GW of total solar PV, of which ground-mounted large-scale installations comprise 53.8 GW. The grid-connected rooftop PV contributes 11.08 GW of capacity (MNRE, 2023). The Prime Minister of India announced installing 500 GW of non-fossil energy capacity by 2030 at the 26th Conference of Parties (COP26) in Glasgow in November 2021. (Press Information Bureau, 2021) A policy document on a national program on high-efficiency solar PV modules published by the Ministry of New and Renewable Energy (MNRE) indicates that up to 280 GW of solar capacity is required for the optimum energy mix by 2029-30. (Production Linked Incentive Scheme "National Programme on High Efficiency Solar PV Modules," 2021)

It is evident that the PV installations are falling short of their targeted capacity despite having the potential to play a significant role in meeting India's electricity demand. Over the years, the PV sector has created a skilled workforce, thriving installation businesses, and a working supply chain in the domestic market. In order to promote the deployment, the Indian government has been supporting the installation of PV generation systems through various schemes under JNNSM. In addition, states and Union Territories (UTs) adopted numerous policy incentives to promote the uptake of PV systems. Despite government efforts, the share of PV generation in total electricity generation has been marginal and necessitates significant growth in the future.

The present status of deployment and future targets make it imperative to review the PV policies and regulations in the country. This paper reviews solar PV policy incentives and contemporary regulations related to metering and billing of grid-connected rooftop PV systems in Indian states and UTs to understand their historical trend and present status. The study aims to understand the state-specific policy strategies and their relationship with PV deployment to

10.18086/swc.2023.12.01 Available at http://proceedings.ises.org

enhance and coordinate the country's deployment efforts in the grid-connected rooftop PV segment.

2. Methodology

The state and UT-level PV policy documents and PV-related metering and billing regulations were obtained from government department websites, state electricity regulatory commissions, and joint electricity regulatory commissions. The 25 Indian states and five UTs published 66 policies from 2002 till 2022. Of the 66 policies, 33 were related to solar PV from 21 states, and 23 were related to nonconventional and renewable energy from 15 states. Five states, namely Jharkhand, Manipur, Punjab, Sikkim, and Uttar Pradesh, and a union territory of Jammu and Kashmir, published dedicated policies for rooftop solar systems. In addition, Gujarat and Madhya Pradesh published dedicated policies for small-scale distributed solar and decentralized solar, respectively. The other two policies target solar–wind hybrid projects.

The policy incentive’s deployment order and its effect on the PV capacity addition were studied using the National Renewable Energy Laboratory's (NREL) policy stacking framework (Doris, 2012). The framework was applied to study the solar market development in different state contexts in the USA. (Steward et al., 2014) The framework states that the solar PV market must undergo three stages of development: market preparation, market creation, and market expansion, to achieve responsible market saturation. It demonstrates how policy incentives should be deployed by focusing on the optimal deployment sequence. A study performed to understand the effectiveness of policy incentives in the US states using the policy stacking framework indicated that market expansion policies will be more successful once the market preparation policies are in place. (Ryan et al., 2019) The application of the policy stacking framework and grouping of policy incentives based on stages for the present study is shown in Fig. 1.

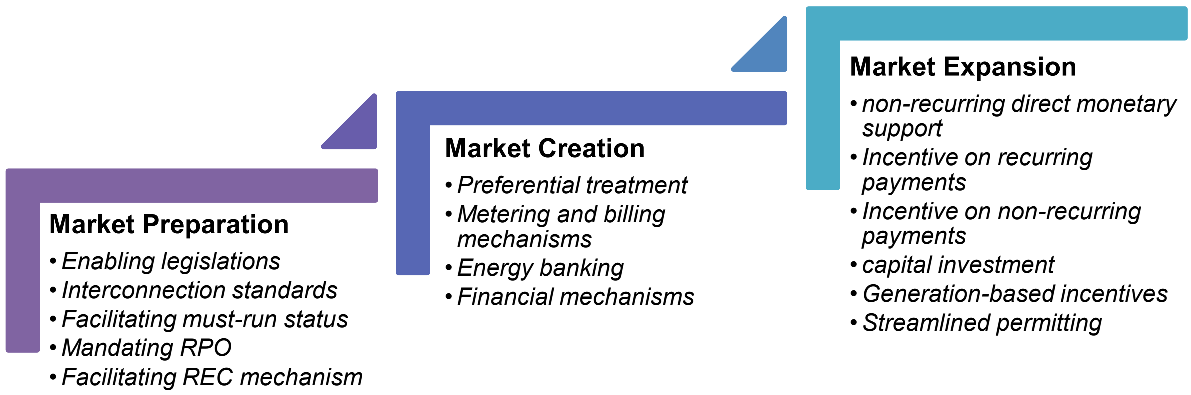

Figure 1 Application of policy stacking framework in Indian states and UTs (Author’s work based on NREL’s policy stacking framework)

The framework identifies incentives that remove legacy or institutional barriers to legally allow market players to use the technology as market preparation incentives. (Doris, 2012) The enabling legislation, interconnection standard, must-run status, Renewable Portfolio Obligation (RPO), and renewable energy certificate (REC) were labeled as market preparation incentives. The Electricity Act 2003 fulfills the requirement of market preparation incentives, as discussed in detail in the results section.

Market creation incentives are known as incentives that allow a motivated consumer to access the market and services and assure investors of long-term policy certainty without directly altering the project's economics. (Doris, 2012) The market creation incentives were grouped into preferential treatment (during grid access, project allotment, power dispatch, and land allocation), metering and billing mechanisms, energy banking, and financial mechanisms (interest subvention on loans).

A metering and billing mechanism facilitates the commercial settlement of the electricity bill the distribution utility raises to a prosumer with a grid-connected PV system. Five types of metering and billing mechanisms, namely net metering, group net metering, virtual net metering, net billing, and gross metering, were discussed in the present study. In the case of a net metering arrangement, solar units exported to the grid from a prosumer's grid-connected solar PV system are deducted from units (kWh) imported from the grid to arrive at the net imported or exported electricity. The net electricity import or export is billed, credited, or carried over by the distribution utility based on the applicable retail tariff (Tamil Nadu Electricity Regulatory Commission (Grid Interactive Solar PV Energy Generating Systems) Regulations, 2021). Group and virtual net metering are extended versions of net metering arrangement, facilitating demand aggregation benefits. In group net metering, a prosumer can offset the import and export of units for multiple service connections against a single grid-connected PV plant. In virtual net metering, multiple prosumers can offset the import and export of units for their respective service connections against a single grid-connected PV plant (Delhi Electricity Regulatory Commission (Group Net Metering and Virtual Net Metering for Renewable Energy) Guidelines, 2019).

In net billing, the units imported by the prosumer from the grid and solar units exported are recorded independently at the interconnection point. The monetary value of units imported by the prosumer is calculated based on the retail tariff, and the monetary value of solar units exported is calculated using a feed-in tariff to arrive at the net billing amount. The criterion of offsetting the import and export of electricity differs in net metering and net billing. The units directly offset each other in net metering as their monetary value equals the applicable retail tariff. In net billing, offsetting is calculated based on the different monetary values of the imported and exported units.

In the case of gross metering arrangement, solar units (kWh) generated from a prosumer's grid-connected solar PV system and units (kWh) imported from the grid are measured. The monetary value of units imported by the prosumer is calculated based on the retail tariff, and the monetary value of solar units generated is calculated using a special tariff to arrive at the final billing amount.

Market expansion incentives target the development of individual projects by directly altering the project economics. (Doris, 2012) The market expansion incentives comprise non-recurring direct monetary support (grant/ capital subsidy/ viability gap funding), incentives on recurring payments (exemption/ deduction/ rebate/ credit/ abatement/ holiday/value-added tax), incentives on non-recurring payments (charge/ duty/ cess/ surcharge), capital investment, generation-based incentive, and streamlined permitting. The incentives were mapped over time to understand the state-specific policy strategies.

The regulatory landscape was examined with the help of 29 regulatory documents related to grid-interactive rooftop solar PV systems. The observations pertaining to the acceptance of metering and billing mechanism, permissible system size per consumer connection, and limit on utilization of distribution transformer capacity to integrate rooftop PV systems on the Low Tension (LT) side are discussed in the subsequent section with the help of maps.

3. Results

India's electricity sector is governed by the Electricity Act of 2003, which sets the foundation for the rules and regulations related to generation, transmission, distribution, trading, and electricity use. Section 9(2) of the Electricity Act 2003 empowers an individual or agency to set up a captive power generation plant and facilitates access to transmission facilities. Section 61(h) and section 86(1)(e) of the act entrust electricity regulatory commissions to promote cogeneration and generation of electricity from renewable energy sources. Section 86(1)(e) further suggests to adopt mechanisms such as renewable purchase obligation. Section 3(1) of the act directs the central government to prepare national electricity policy and tariff policy in consultation with state governments and the central electricity authority. (The Electricity Act, 2003) The act legislated fundamental prerequisites for completing the market preparation stage by removing the legacy barriers related to the uptake of solar PV systems.

The patterns in the use of policy incentives were assessed by splitting policies into three time periods: policies published before 2010 (before the announcement of Jawaharlal Nehru National Solar Mission), policies published between 2010 and 2015 (before the announcement of revised targets under the mission), and policies published after 2015 (after the announcement of revised targets under the mission).

Before 2010, nine states published policies promoting the use of renewable energy sources, whereas only one state published a policy promoting solar PV as an electricity source. Gujarat was the first Indian state to publish a dedicated policy for solar PV in 2009. (Gujarat Solar Power Policy 2009, 2009) With the announcement of the Jawaharlal Nehru National Solar Mission in 2010, fourteen more states published independent PV policy documents by 2015. Four states and two UTs announced dedicated policies for solar PV between 2016 and 2022.

The adoption of market-creation and market-expansion incentives in Indian states and union territories between 2002 and 2022 is shown in Fig. 2 and Fig.3, respectively. States and UTs are arranged in decreasing order of cumulative PV capacity as of August 2023. According to the data from the Ministry of New and Renewable Energy, Rajasthan installed the highest PV capacity, whereas Nagaland has the least capacity addition as of August 2023. (MNRE, 2023) It is evident from the graphs that the state with the most PV installations announced more PV incentives than that of the other states. The states with significant PV capacity were typically characterized by higher geographical areas and published more dedicated policies than their counterparts.

The number of state/UT policies published between 2002 and 2022 throws light on their outlook toward PV technology. The average number of policies published by the states with a geographical area above the national mean value was around 3, whereas the average number of policies published by the rest of the states and UTs was 1.4. The States with larger geographical areas envisaged PV as a potential solution for diversifying their energy needs. It was noted that states like Uttarakhand, Punjab, Haryana, Kerala, and UT of Delhi ranked better in terms of PV deployment despite having a geographical area below the national mean.

Among the ten states with the highest PV deployment as of 2023, Gujarat, Karnataka, and Punjab published their first policy before 2010. The policy document analysis indicated that two of the three states allowed a reduction in contract demand for consumers installing PV systems and provided a single window facility for project approval. The rest of the states and UTs published dedicated PV policies by 2015, except Maharashtra and Punjab, which announced PV incentives through renewable energy policies.

States with the highest PV capacity increasingly extended the benefits of state-level industrial policy to solar PV projects after 2010. Moreover, the exemption from paying electricity duty and relaxing the requirement of environmental clearance was widely mentioned in the policy documents of leading states. In addition, four out of ten leading states provided single window clearance facilities and authorized the use of government wasteland for PV projects. Many states and UTs revised their policies after 2015 as the capacity addition target of the Jawaharlal Nehru National Solar Mission, renamed National Solar Mission, increased from 20 GW to 100 GW. In addition to extending the benefits of state industrial policy, leading states exempted PV projects from paying the wheeling and transmission charges and cross-subsidy surcharge, and facilitated the banking of surplus energy into the grid.

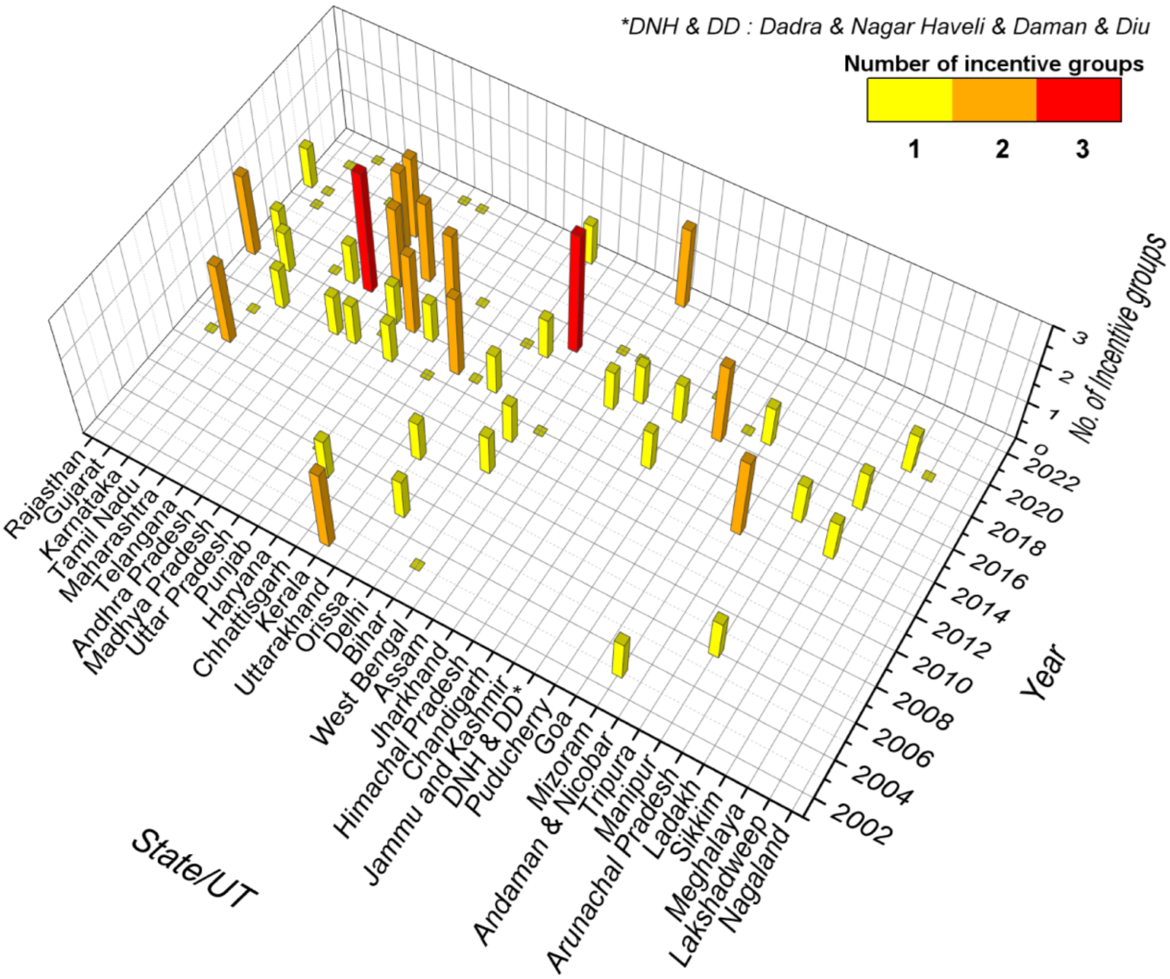

Fig. 2 Adoption of market-creation incentives in Indian states and UTs (Author's work based on the data from respective state/UT's policy documents)

The Indian states and UTs significantly used market-expansion incentives over market-creation incentives to develop the domestic PV market. Streamlined permitting and incentives on recurring and non-recurring payments were the most used market expansion incentives. Streamlined permitting comprises extending the benefits of state industrial policy, authorizing the use of government wasteland, relaxing the requirement of environmental clearance, relaxing the rules of using agricultural land to install PV systems, allowing a reduction in contract demand to consumers installing PV systems, and providing single window clearance facility. The incentives on recurring payments include exemption from paying electricity duty, wheeling and transmission charge, cross subsidy surcharge, and electricity cess. The incentives on non-recurring payments include an exemption from entry tax, a refund of stamp duty, and a refund of the value-added tax (VAT). The widely used market-creation incentives include facilitating the banking of surplus energy and providing access to various metering and billing mechanisms.

Our analysis of Policy documents reveals that financing mechanisms (such as interest subvention on loans) and announcing preferential treatment to PV projects were the least-used market-creation incentives. The incentives related to preferential treatment include preference during offtake of power if a manufacturer develops a power plant within the state, preference for renewable energy-based manufacturing industry within the state in existing and upcoming special economic zones and industrial parks, priority to a PV manufacturer during a government land allotment process, and price preference for setting up the plant within the state in competitive bidding. The least used market-expansion incentives were generation-based incentives, capital investment by the state government and UTs, and extending non-recurring direct monetary support (such as additional capital subsidy from the state/UT). While the use of generation-based incentives was limited, the states and UTs implemented net and gross metering mechanisms. The central government extended non-recurring direct monetary support (such as viability gap funding, grants, and capital subsidy) through various schemes under the National Solar Mission.

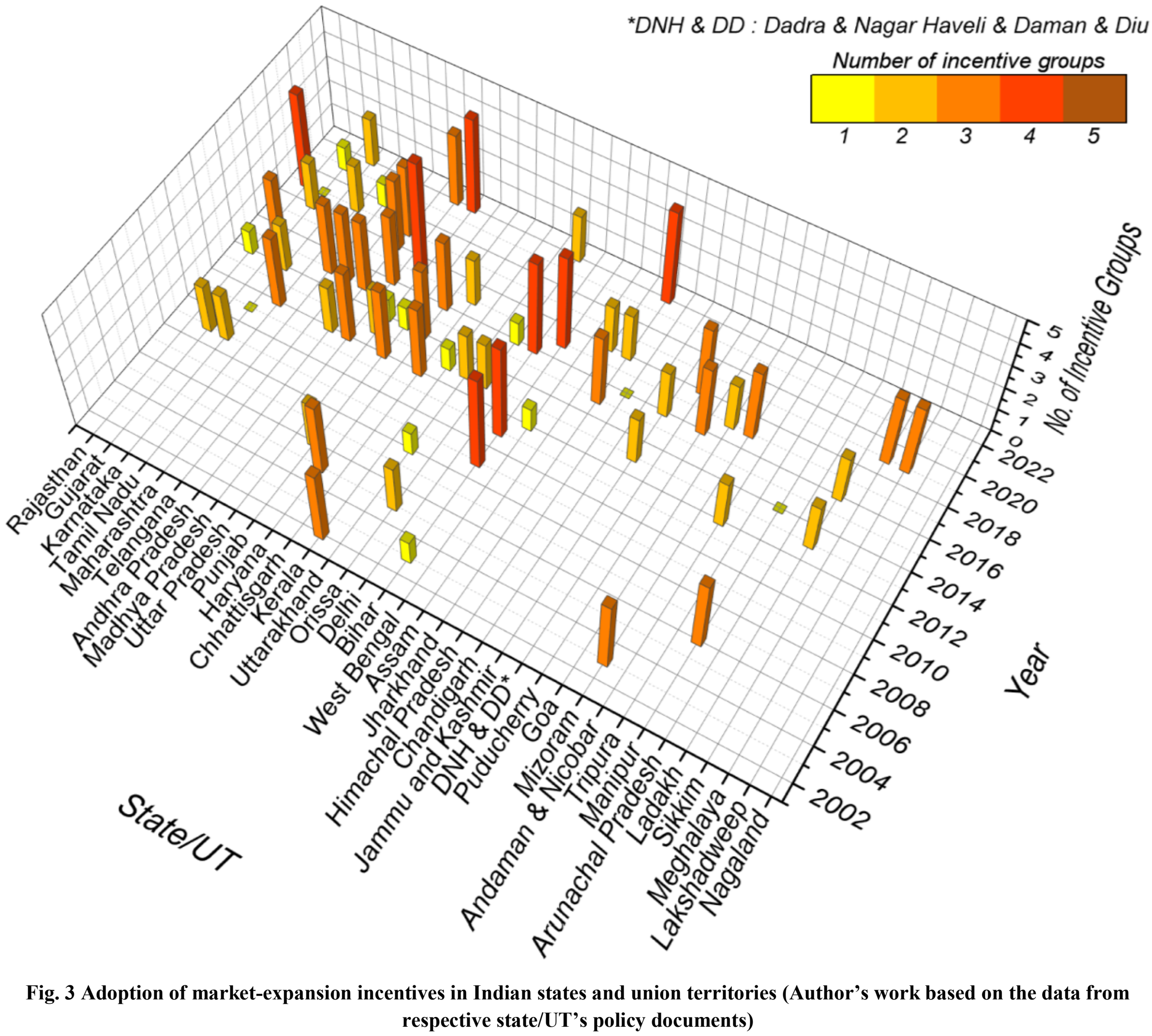

Fig. 3 Adoption of market-expansion incentives in Indian states and union territories (Author's work based on the data from respective state/UT's policy documents)

Indian states and UTs use metering and billing mechanisms such as net metering, net billing, and gross metering as critical public policy tools to increase the uptake of grid-connected rooftop PV systems. The acceptance of metering and billing mechanisms varied with the state. Fig. 4 shows the adoption of metering and billing mechanisms in Indian states and union territories. Net metering was adopted nationwide, whereas gross metering was adopted in 16 states and two union territories. Three states and two UTs published regulations related to the net billing mechanism. Three states and seven UTs adopted virtual net metering and group net metering.

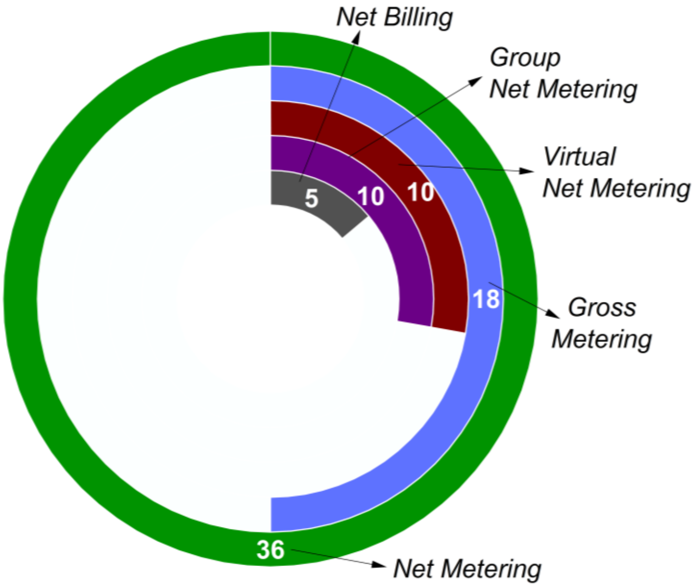

Fig. 4. Adoption of metering and billing mechanisms in Indian states and union territories (Author's work)

The acceptance of metering and billing mechanisms in Indian states and union territories as of August 2023, presented in Fig. 5, shows that the combination of net metering and gross metering was India's most widely used mechanism. The use of gross metering, in addition to net metering, has increased in the past five years. As of August 2023, 12 states published regulations allowing consumers to use net or gross metering for their grid-connected rooftop PV systems. Eight out of ten states that adopted only net metering mechanisms had cumulative rooftop PV installed capacity of less than 800 MW as of August 2023. The use of virtual net metering and group net metering increased after 2016. As of August 2023, three states and seven UTs adopted the regulation related to virtual net metering and group net metering. The adoption of virtual and group net metering regulations is anticipated to rise due to their demand aggregation benefits.

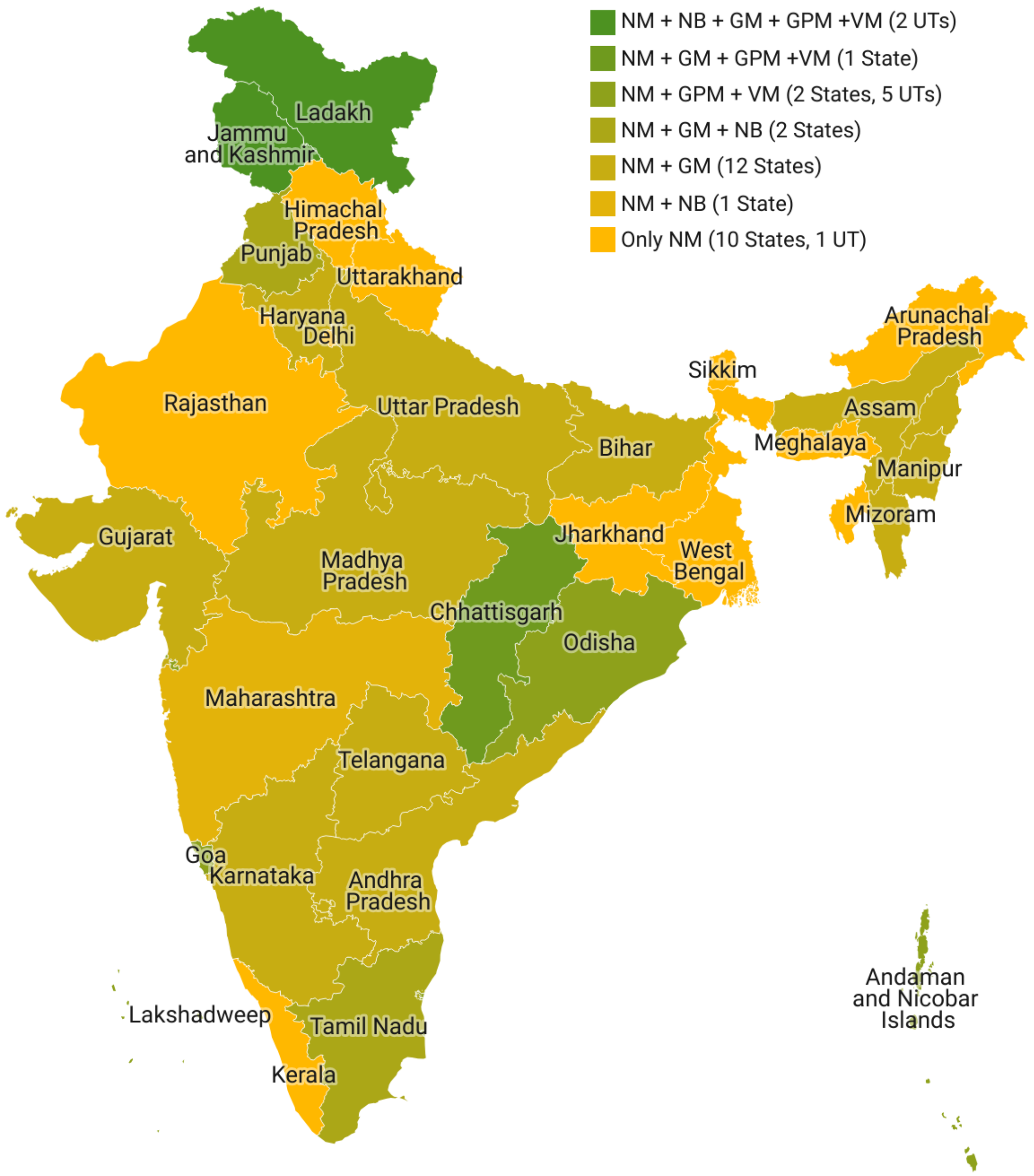

NM: Net Metering, NB: Net Billing, GM: Gross Metering, GPM: Group Metering, VM: Virtual Metering

Fig. 5. Acceptance of metering and billing mechanisms in Indian states and union territories (Author's work based on the data from respective SERC/JERC regulations on grid interactive rooftop PV systems)

Fig. 6 shows the limit on permissible system size per consumer connection in Indian states and union territories for residential net metering mechanisms. Most states and UTs granted permission to install a rooftop PV system having a capacity equal to the consumer's sanctioned load/contract demand. States like Gujarat and Uttarakhand adopted a liberal approach by imposing no limit for residential consumers. In the case of Gujarat, the provision of not capping the system size was further extended to Micro, Small, and Medium Enterprises (MSME) consumers and non-residential consumers with captive use.

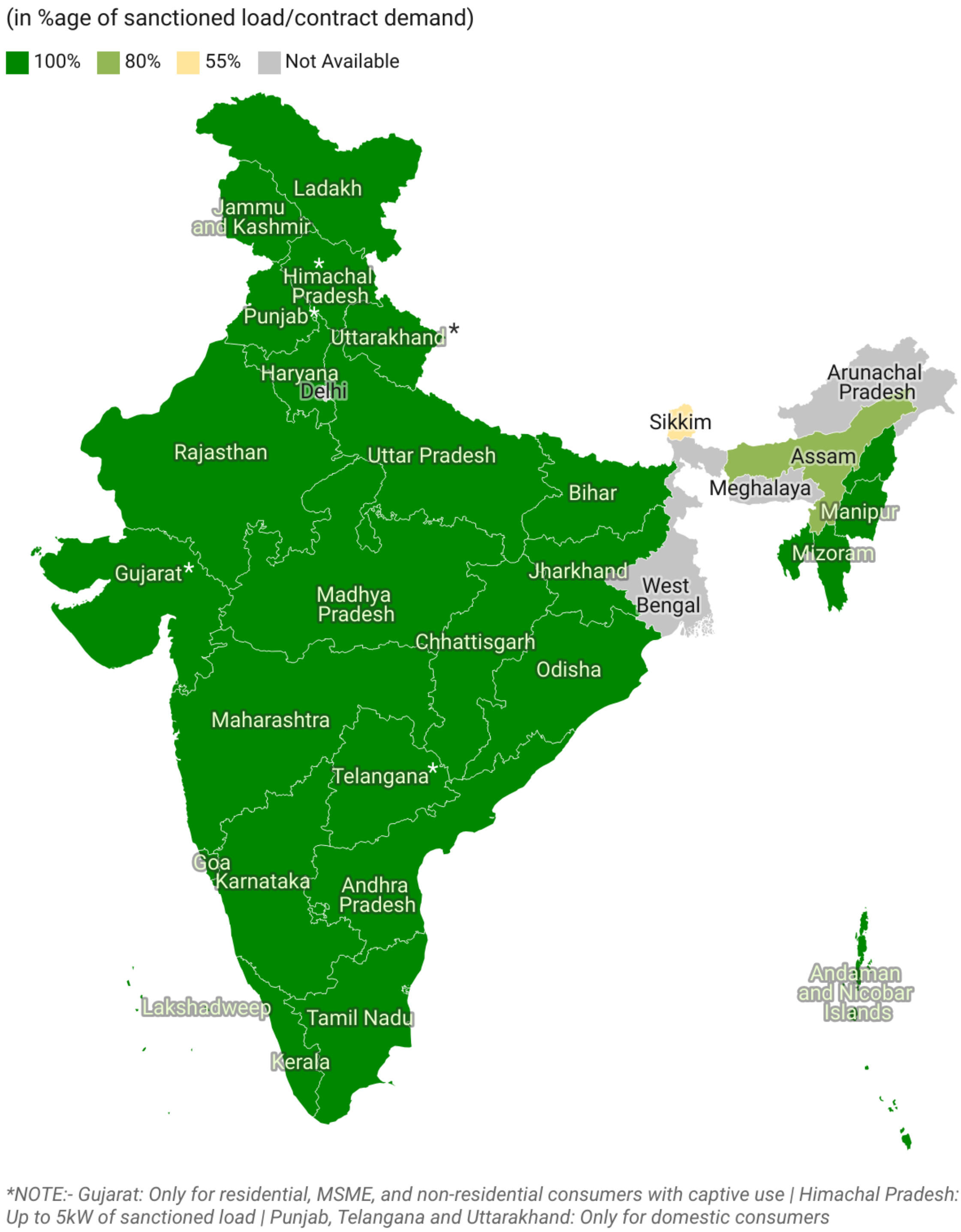

Fig. 6. Limit on permissible system size per consumer connection in Indian states and union territories for residential net metering mechanism in % age of sanctioned load/contract demand (Author's work based on respective SERC/JERC regulations on grid interactive rooftop PV systems)

Fig 7 shows the limit on the hosting capacity of the distribution transformer (DT) in Indian states and union territories in terms of the percentage of DT capacity. The allocation of distribution transformer capacity exhibited significant interstate variation. Only six states and two UTs allowed 100% utilization of distribution transformer capacity to integrate rooftop PV systems on the LT side. Eight states and one UT prohibited consumers from installing more than 50% of the distribution transformer's hosting capacity, thereby limiting the penetration of rooftop PV systems in the distribution grid. The present scenario indicates the potential to improve provisions related to the hosting capacity and calls for further investigation.

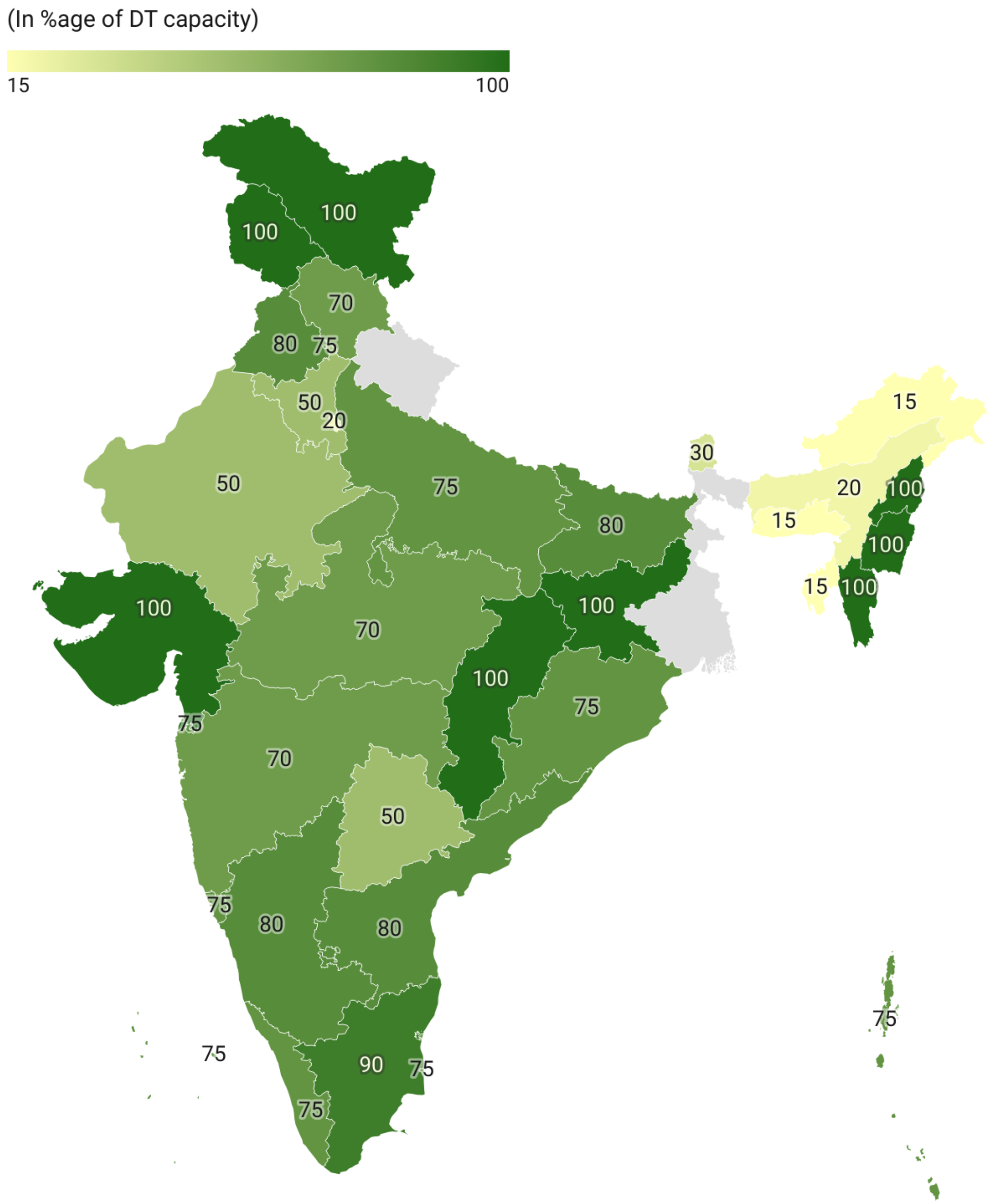

Fig. 7. Limit on hosting capacity of distribution transformer in Indian states and union territories in %age of DT capacity (Author's work based on the respective SERC/JERC regulations on grid interactive rooftop PV systems)

4. Conclusion

The solar PV policy incentives and contemporary regulations related to the metering and billing of grid-connected rooftop PV systems in Indian states and union territories are reviewed. The state-specific policy strategies and their relationship with PV deployment are presented to enhance and coordinate the country's efforts to accelerate the deployment. Applying policy stacking framework on data collected from 66 policy documents indicated that Indian states and UTs significantly used market-expansion incentives over market-creation incentives to develop the domestic PV market. The following are the noteworthy takeaways from the study:

- The states with significant PV capacity were typically characterized by higher geographical areas and published more policies than their counterparts.
- The state with the most PV installations announced more PV incentives than the other states.
- The least-used market-creation incentives were financing mechanisms (such as interest subvention on loans) and announcing preferential treatment to PV projects.

- The least-used market-expansion incentives were generation-based incentives, capital investment by the state government or UT, and provision of non-recurring direct monetary support (such as additional capital subsidy from the state/UT).

The central government used capital subsidy as a policy tool and offered non-recurring direct monetary support through grants, viability gap funding, and central finance assistance. The underutilization of these incentives by states and UTs indicates their commitment to avoiding redundancy in policy incentives.

The list of policy incentives offered by states and UTs with significant PV capacity is as follows;

- Before 2010: reduction in contract demand for consumers installing PV systems, and single window facility for project approval
- Between 2010 and 2015: exemption from paying electricity duty, and relaxing the requirement of environmental clearance
- After 2015: exemption for PV projects from paying the wheeling and transmission charge, cross-subsidy surcharge, and facility of banking of surplus energy into the grid

The study of 29 regulatory documents indicated that the number of metering and billing mechanisms offered by distribution utilities varied across states and UTs, highlighting the necessity of implementing additional mechanisms to expand the array of choices available to end consumers. The following are the noteworthy takeaways from the study;

- Net metering was adopted nationwide, whereas net and gross metering were the most widely used mechanisms by distribution utilities in India.
- Most states granted permission to install a rooftop PV system having a capacity equal to the consumer's sanctioned load/contract demand.
- The allocation of distribution transformer capacity exhibited significant interstate variation.

5. References

Delhi Electricity Regulatory Commission (Group Net Metering and Virtual Net Metering for Renewable Energy) Guidelines, 7 (2019).

Doris, E. (2012). Policy building blocks: Helping policymakers determine policy staging for the development of distributed PV markets. *World Renewable Energy Forum, WREF 2012, Including World Renewable Energy Congress XII and Colorado Renewable Energy Society (CRES) Annual Conference*, *5*(April), 3437–3442.

Gujarat Solar Power Policy 2009, Pub. L. No. SLR-11-2008-2176B (2009). https://geda.gujarat.gov.in/Gallery/Media_Gallery/Solar_Power_policy_2009.pdf

The Electricity Act, Pub. L. No. 36 of 2003, 1 (2003). https://www.indiacode.nic.in/bitstream/123456789/2058/1/A2003-36.pdf

Production Linked Incentive Scheme "National Programme on High Efficiency Solar PV Modules," Pub. L. No. F. No. 283/62/2020-GRID SOLAR, 1 (2021). https://mnre.gov.in/img/documents/uploads/file_f-1619672166750.pdf

MNRE. (2023). *State-wise installed capacity of grid interactive renewable power as on 31/03/2023*. https://mnre.gov.in/the-ministry/physical-progress

Press Information Bureau. (2015, June 17). Revision of cumulative targets under National Solar Mission. *Press Information Bureau*. https://pib.gov.in/newsite/PrintRelease.aspx?relid=122567

Press Information Bureau. (2021, November 1). National Statement by Prime Minister Shri Narendra Modi at COP26 Summit in Glasgow. *Press Information Bureau, Government of India*, 2. https://pib.gov.in/PressReleasePage.aspx?PRID=1768712

Ryan, A. J., Donou-Adonsou, F., & Calkins, L. N. (2019). Subsidizing the sun: The impact of state policies on electricity generated from solar photovoltaic. *Economic Analysis and Policy*, *63*, 1–10. https://doi.org/10.1016/j.eap.2019.04.012

Steward, D., Doris, E., Krasko, V., Hillman, D., Steward, D., Doris, E., Krasko, V., & Hillman, D. (2014). *The Effectiveness of State-Level Policies on Solar Market Development in Different State Contexts* (Issue February). https://www.nrel.gov/docs/fy14osti/61029.pdf

Tamil Nadu Electricity Regulatory Commission (Grid Interactive Solar PV Energy Generating Systems) Regulations, Pub. L. No. TNERC/GISS Regn.23-1/Dated 07. 1 0.2021, 3 Government of Tamil Nadu 20 (2021).

SOLAR PV INTEGRATION INTO THE GRID: A TECHNO-ECONOMIC ANALYSIS IN THREE CLIMATE ZONES OF BURKINA FASO

Sami Florent Palm[1], Sebastian Waita[1], Thomas Nyangonda[1] and Ahmed Chebak[2]

[1] Condensed Matter Research Group, Department of Physics, University of Nairobi, Nairobi, Kenya

[2] Green Tech Institute, Mohammed VI Polytechnic University, Benguerir, Morocco

Abstract

Grid-Connected Solar Photovoltaic Systems (GCSPS) have emerged as effective means of decarbonizing the electricity sector and hastening the energy transition. The goal of this study is to investigate the feasibility of installing GCSPS in Burkina Faso's three climate zones, which are the Sahelian zone represented by Dori, the Sudan-Sahelian zone represented by Ouagadougou (Ouaga), and the Sudanese zone represented by Bobo-Dioulasso (Bobo). This study was carried out using the PV Syst software for design and Python for modelling the economic aspects of a 50MW GCPS in each climatic zone. The obtained results allowed for the comparison of annual production, Levelized Cost of Energy (LCOE), Net Present Value (NPV), Internal Rate of Return (IRR) and Pay Back Period (PBP). These comparisons show that the GCPS from Dori is more economically viable than those of Ouaga and Bobo-Dioulasso. This study will provide policymakers and private investors with information about the potential for investment in the installation of GCPS in the Sahel regions.

Keywords: Solar photovoltaic, Grid-connected, Techno-economic, Burkina Faso

1. Introduction

The combined effects of climate change, COVID19, and the Ukrainian crisis have significantly increased the cost of energy around the world (IRENA, 2022). Despite the various crises, the development of renewable energies, particularly solar Photovoltaic (PV), has continued to grow. For example, the world's installed solar PV capacity increased from 855162 MW in 2021 to 1046614 MW in 2022; a 22.4 % increase (Renewable Energy Agency, 2023).Thus, solar PV continues to be essential for accelerating the energy transition.

Burkina Faso, located in the heart of West Africa, continues to face significant challenges in increasing access to electricity in order to boost economic growth. Burkina Faso is the second most expensive ECOWAS country in terms of electricity costs after Guinea-Bissau (Moner-Girona et al., 2017) despite the country being well endowed with significant solar potential(Global, 2020). According to the 2020 National Electricity Society report, the Burkina Faso national grid's energy mix consists of only 3% solar PV injection, with thermal energy production based on fossil fuels accounting for more than half of national energy production(SONABEL, 2020). The contribution of mix energy in Burkina Faso in 2020 is depicted in Figure 1 below.

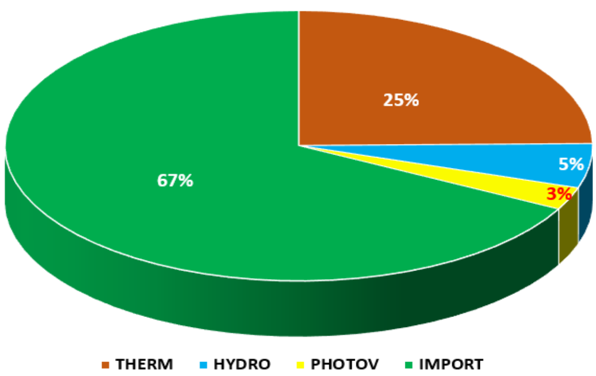

Fig. 1:Energy distribution in Burkina Faso in 2020 [5]

10.18086/swc.2023.12.04 Available at http://proceedings.ises.org

Techno-economic assessment of Energy system is one of the best ways to know the benefit of a solar PV system. Various researchers around the world have tried to carry out solar PV studies using different approaches. Kazem et al., (2017) used numerical simulation to conduct a technical-economic feasibility study of a 1MW grid-connected PV power plant in Adam City, Oman, and discovered that the appropriate inverter size is 800kWh with 250Wp PV modules. The cost of producing electricity is $0.2258/kWh, with a 10-year payback period. These findings indicate that the construction of a 10MW PV plant in Adam is feasible. Garni & Awasthi, (2017) investigated the techno-economic feasibility of a grid-connected PV system with different tracking using HOMER in Saudi Arabia's Makkah region. Solar irradiation, ambient temperature, load profile, and electricity cost were all used in this study. This study found that optimal tracking significantly lowers the cost of electricity in this area, so tilting and orienting the PV modules at specific times could make grid-connected PV energy production more profitable. Liet al., (2018) used HOMER software to conduct an objective analysis of the technical-economic feasibility study of grid-connected PV systems in five Chinese climatic zones: Beijing, Harbin, Shanghai, Guangzhou, and Kunming. According to the findings of this study, grid-connected PV systems in these five zones are economically, technically, and environmentally feasible. Using the HOMER software, Das et al., (2021) investigated the technical-economical and environmental feasibility of a stand-alone and grid-connected hybrid system in five climatic zones of Bangladesh. HOMER software was used by Mohand Kaci et al., (2022) to assess the technical and economic feasibility of two different PV system configurations (grid/PV and grid/PV/battery) in five different areas of Algeria. The grid/PV system was the most feasible, according to the findings. Battery cost subsidization and the development of a regional pricing system should aid in the effective implementation of the grid/PV/battery system.. Mohamed& Maghrabie, (2022) used the Feed-in-Tariff (FIT) mechanism to carry out a technical and financial feasibility study of the 1600 MW Benban solar park in Egypt. The findings revealed a 12% interest rate with a 10.1-year payback period. The advantages of implementing the FIT are amply supported by this study. Boddapati et al., (2021) have carried out a technical and economic study of a 50MW PV power plant in India, taking into account the effect of power evacuation curtailment, using measured data and simulation using PVsyst software. This study showed firstly that the measured results and the simulated results were very close, and secondly that the payback period of the PV power plant increased with the effect of power evacuation curtailment. The results obtained differ depending on the specificity of each zone. Nonetheless, the grid-connected hybrid system configuration produces the best results in each climatic zone. Ouedraogo & Yamegueu, (2019) evaluated the integration of solar PV into the Burkina Faso electricity grid using the Levelized Cost of Energy (LCOE) technique based on the estimated capacity of electricity consumption. According to the findings of this study, injecting large amounts of PV energy into Burkina Faso's electricity grid was both economically and environmentally feasible. Burkina Faso's electricity costs would be reduced as a result. This study did not consider the technical aspects of integrating PV energy into the power grid.

Until now, not much work has been done on the techno-economic feasibility study of grid-connected PV power plants in different climatic zones of Burkina Faso using actual site data. This paper will focus on the techno-economic analysis of PV integration into the grid in different climatic zones of Burkina Faso, a comparison study that we have not come across evidence that it has been done for the three zones. The rest of this paper is divided in four parts. First, the study area; then the methodology, Results and discussions and conclusion.

2. Methodology

2.1 The three climatic zones of Burkina Faso

Burkina Faso is composed of three different climatic zones: the sudanese zone in the south, the sudano-sahelian zone at the centre and the sahelian zone in the north. Figure 2 shows these different climatic zone. For this study, the cities of Bobo-Dioulasso, Ouagadougou and Dori were used to represent these three climatic zones respectively.

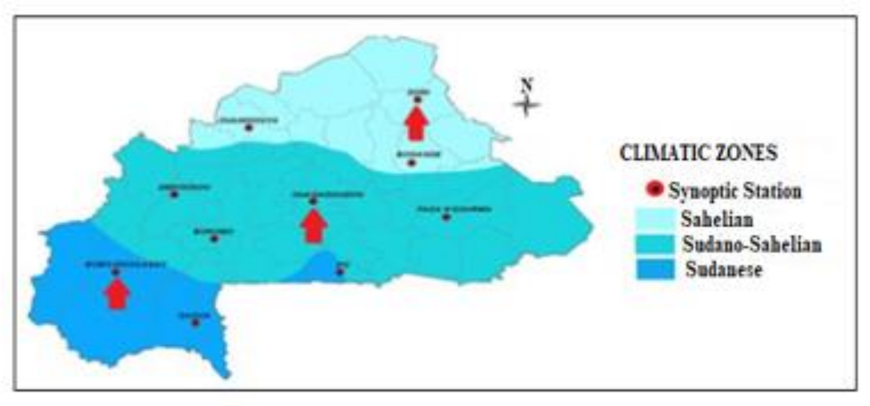

Fig. 2:Burkina Faso Climatic zones(Sanou et al., 2023)

2.2 Meteorological parameters

Data on insolation, ambient temperature, wind speed and humidity was collected at the Agence Nationale de la Meteorologie (ANAM) of Burkina Faso for the period of 2010 to 2020.

Figure 3 depicts the monthly variation of daily insolation for the cities of Ouaga, Bobo, and Dori from 2010 to 2020, with a general insolation value greater than 5h for these three regions. The lowest values are observed in August due to the very cloudy skies during this time of year, while the highest values are obtained in November-January, and this is attributed to a much clearer sky. It is also observed that insolation is more in Dori, then Ouaga, and finally Bobo in that order.

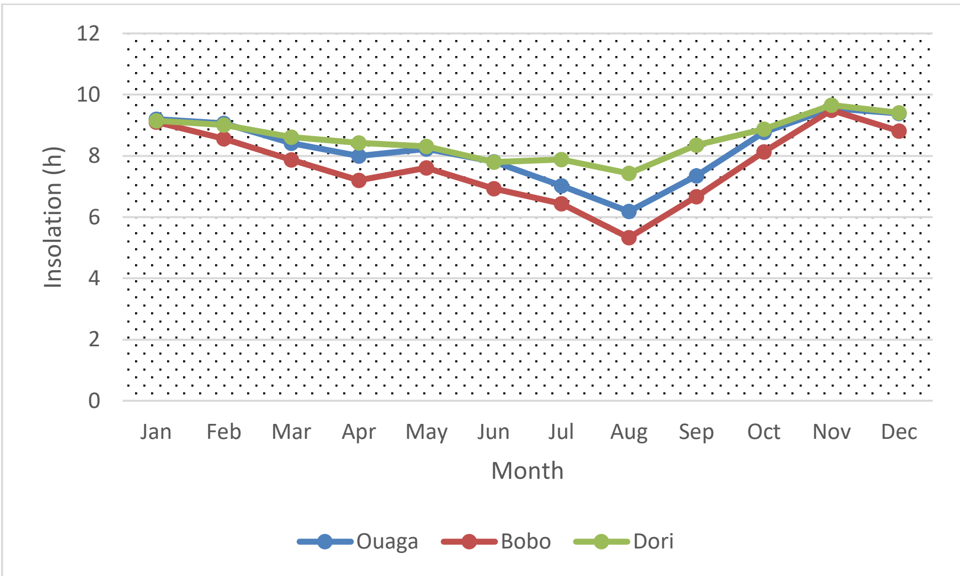

Fig. 3:Monthly Insolation(ANAM Burkina Faso, 2021)

Figure 4 depicts the monthly evolution of the daily temperature in Ouaga, Bobo, and Dori from 2010 to 2020. These curves clearly show that the average temperature in each of these three regions is above 24 degrees Celsius. Dori is warmer than the other two cities, with minimum temperatures in January and August in Ouaga and Bobo, and maximum temperatures in April and May in Ouaga and Bobo, respectively. High temperatures during these months have a negative impact on the yield of solar photovoltaic plants.

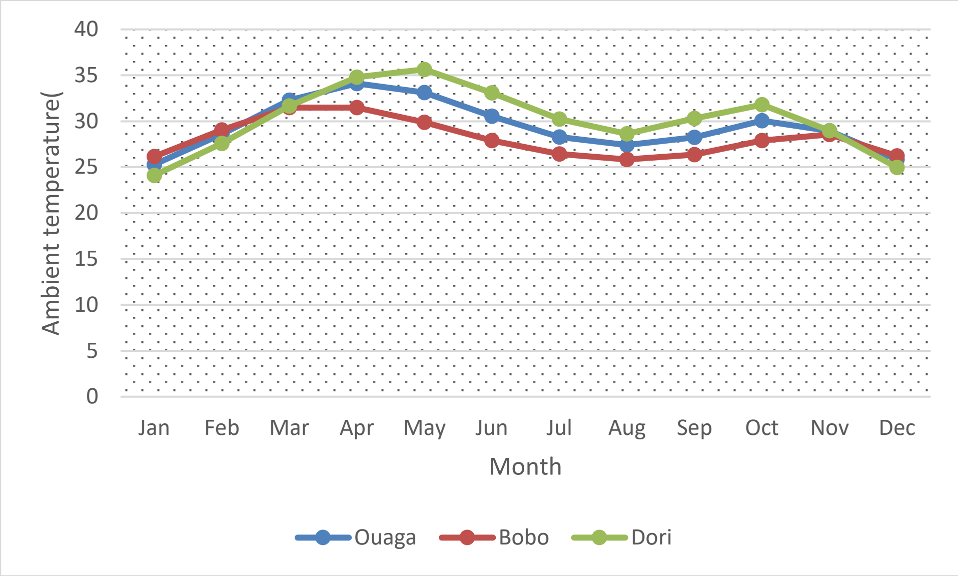

Fig. 4:Monthly Ambient temperature(ANAM Burkina Faso, 2021)

Figure 5 shows the monthly behavior of the daily wind speed from 2010 to 2020, which is clearly less than 5 m/s. This explains why wind speeds are lower in these three areas. Nonetheless, wind speeds in Bobo are higher than in the other two cities, Ouagadougou, and Dori, with average wind speeds ranging from 1.88 m/s in November to 3.22 m/s in May in Ouagadougou, 2.88 m/s in October to 4.7 m/s in February in Bobo, and a minimum of 0.7 m/s in November to 0.7 m/s in February in Dori. In general, wind speed varies continuously throughout the measurement period. Low wind speeds will have less of an impact on solar PV systems in Burkina Faso, but given their variability, the impact may be noticeable at times when instantaneous wind speeds are very high Putting dust on solar PV modules.

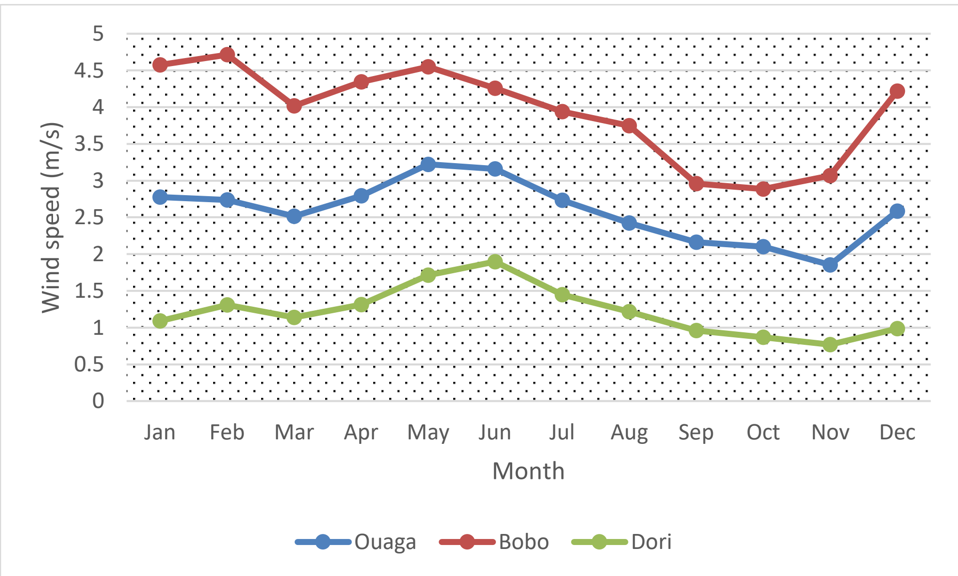

Fig. 5:Monthly wind speed(ANAM Burkina Faso, 2021)

Figure 6 represents the monthly evolution of daily relative humidity for Ouaga, Bobo, and Dori, displaying a bell-shaped curve with high relative humidity values observed from June to October. Between February and March, the minimums are around 20%, and the maximums are around 80% in August. Humidity is a factor that affects the efficiency of a solar PV system by dropping the power output (Mekhilef et al., 2012).

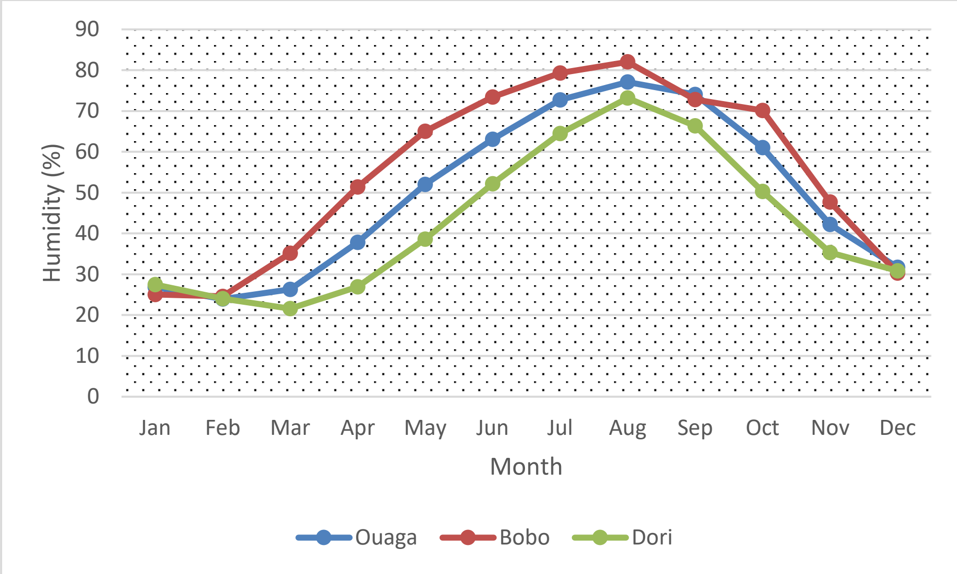

Fig. 6:Monthly relative humidity(ANAM Burkina Faso, 2021)

2.3 Energy production and solar PV plants design

Using the PVGIS solar irradiation database, PVsyst software was used to design a 50 MW PV system to be installed in each of the three climatic zones. Jinko Solar 585Wp modules and Ingeteam inverters were used for this purpose.

2,4 Economic assessments

The LCOE, NPV, IRR, and DPBP were used as economic evaluation parameters. The project was estimated to last 25 years, and the discount rate in Burkina Faso was 4.25% (indexmundi, 2020). Table 1 shows the details of the investment cost (CAPEX), equipment replacement cost, operation and maintenance costs(O&M).

Tab. 1:Economic parameters

Designation	Cost ($/KWp)	Total cost ($)
Modules	540	27,000,000
Inverters	400	20,000,000
Installation	145	7,250,000
Structure	158	7,900,000
DC and AC cables	75	3,750,000
Insurance	10	500,000
Study & Control	90	4,500,000
Land cost(12m^2/kWp) in Burkina $20/m^2	240	12,000,000
Total Capital cost	1718	82,900,000
O&M (1.5% CAPEX)	……..	……..
Inflation rate (2%)	………	……..
Inverters replacement (each 10 year)	400	20,000,000

- Net Present Value (NPV)

The NPV is used to assess the profitability of long-term projects (Mohand Kaci et al., 2022). The higher the NPV value, the more economical the investment. The NPV is the difference between the present values of all cash inflows and cash outflows over the course of an investment project. The NPV expression is given as in equation 1(Kebede, 2015):

$$NPV = -C_o + \sum_{t=1}^{n} \frac{NCF_t}{(1+i)^t} \quad \text{(eq. 1)}$$

Where C_o is the initial investment in year 0, NCF_t is the net cash flow in year t (which is the revenue minus expenses in year t), i is the discount rate in % and n is the project lifetime. From monetary benefit viewpoint, the NPV needs to have a positive value (NPV >0)(Oloya et al., 2021).

$$NCF_t = Revenue_t - (C_{i,t} + C_{O\&M,t}) \quad \text{(eq. 2)}$$

$$Revenue_t = E_t \times Energy\ cost \quad \text{(eq. 3)}$$

$$E_t = (0.99)^{(t-1)}.\ E_1 \quad \text{(eq. 4)}$$

- The Internal Rate of Return (IRR)

The IRR is a financial parameter used to assess the attractiveness of an investment opportunity. It can be calculated by setting the NPV of the total investment to zero, it should be greater than the discount rate for an investment to be viable. The IRR is useful when comparing projects with the same initial investment costs. It can be determined as (Oloya et al., 2021)(Bouacha et al., 2020) (Ilse et al., 2019).

$$NPV = -C_o + \sum_{t=1}^{n} \frac{NCF_t}{(1+IRR)^t} = 0 \quad \text{(eq. 5)}$$

- Levelzied Cost of Energy (LCOE)

The LCOE is the cost of per unit(kWh) produced from the solar plant over a specified time (Ahmed et al., 2021) **.** It is an economic assessment of the total cost to building and operating a solar PV installation over its lifetime divided by the total energy output of the asset over that lifetime. It can also be expressed as the minimum price at which electricity must be sold to break-even over the project's lifetime. (Oloya et al., 2021).The LCOE can be expressed by:

$$LCOE = \frac{Lifetime\ cost}{Lifetime\ Energy\ Produced} \quad \text{(eq. 6)}$$

or

$$LCOE = \frac{C_0 + \sum_1^n \frac{C_{i,t} + C_{O\&M}}{(1+i)^t}}{\sum_1^n \frac{E_t}{(1+i)^t}} \quad \text{(eq. 7)}$$

Where $C_{i,t}$,$C_{O\&M}$ and E_t are the investment cost (such as replacement cost),operation and maintenance cost and electricity generated at year t respectively.

- Discounted Payback Period (DPBP)

The DPBP represents the time required to recoup the PV power plant initial investment. It is commonly used to assess the level of risk in long-term investments [Rawat R et al]. A DPBP of less than the lifetime of the projects indicates that the investment is favorable (Mohand Kaci et al., 2022).By comparing projects with the same initial investment cost, smaller is DPBP, more the project is viable. The DPBP can be given by the following equation:

$$\sum_{t=1}^{DPBP} \frac{NCF_t - C_{O\&M}}{(1+i)^t} = C_0 \qquad \text{(eq. 8)}$$

3. Results and discussions

For each of the 50MWp solar power plants, 85468 modules of 585Wp and 14 centralized inverters of 2876 KVA are used. To ensure the operation of the panels in the voltage range of each inverter (873-1300V), 23 modules are placed in series. This results in a total of 3716 strings of 23 modules in series. PVsyst allows us to obtain this design as can be seen in figure 7.

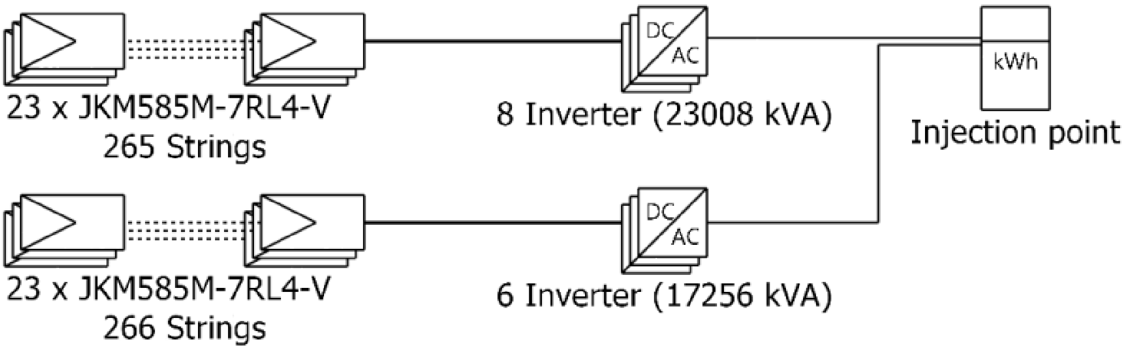

Fig. 7:50 MWp solar park design by PVsyst

Figure 8 below show all the different losses involved in converting the energy collected from the sun into electrical energy that can be fed into the grid, depending on the efficiency of the PV module chosen, in this case the module has an efficiency of 21.4%. The significant losses are due to temperature. These losses are higher in the hottest areas such as Dori which represents -12.6% followed by Ouaga -11.8% and finally Bobo -11.6% Soiling comes second in terms of losses, the soiling margin is between 2% and 5% according to the literature our study, we choose 3% for each region by considering that the difference in soiling effect is negligible. consequently, the performance ratio values in Ouaga, Bobo and Dori are respectively 79.45%;79.7% and 78.4%. To significantly reduce the effect of temperature and soiling, constant cleaning of the PV modules should be considered, which could generate huge costs and make the modules more fragile in the long term. The effect of mismatch should be considered as an important factor in degrading the efficiency of grid-connected PV systems. The modules chosen should have very similar characteristics to avoid the mismatch effect as much as possible. The efficiency of the inverter is also determinant for the energy production at its output. In our case the inverter has an efficiency of 98.6%. It is also noticed that the inverter loss due to voltage threshold is high in Dori than the others region because of the temperature influence in voltage. The final energy at the output of the inverter is $9.1\text{x}10^7$Kwh; $9.0\text{x}10^7$kWh and 9.4 $\text{x}10^7$kWh respectively in Ouaga, Bobo and Dori after all losses. Dori's production is the highest, followed by Ouaga and Bobo due to the higher sunshine in Dori. Nevertheless, an experimental study on these 3 sites should be considered to evaluate the difference on the effect of soiling.

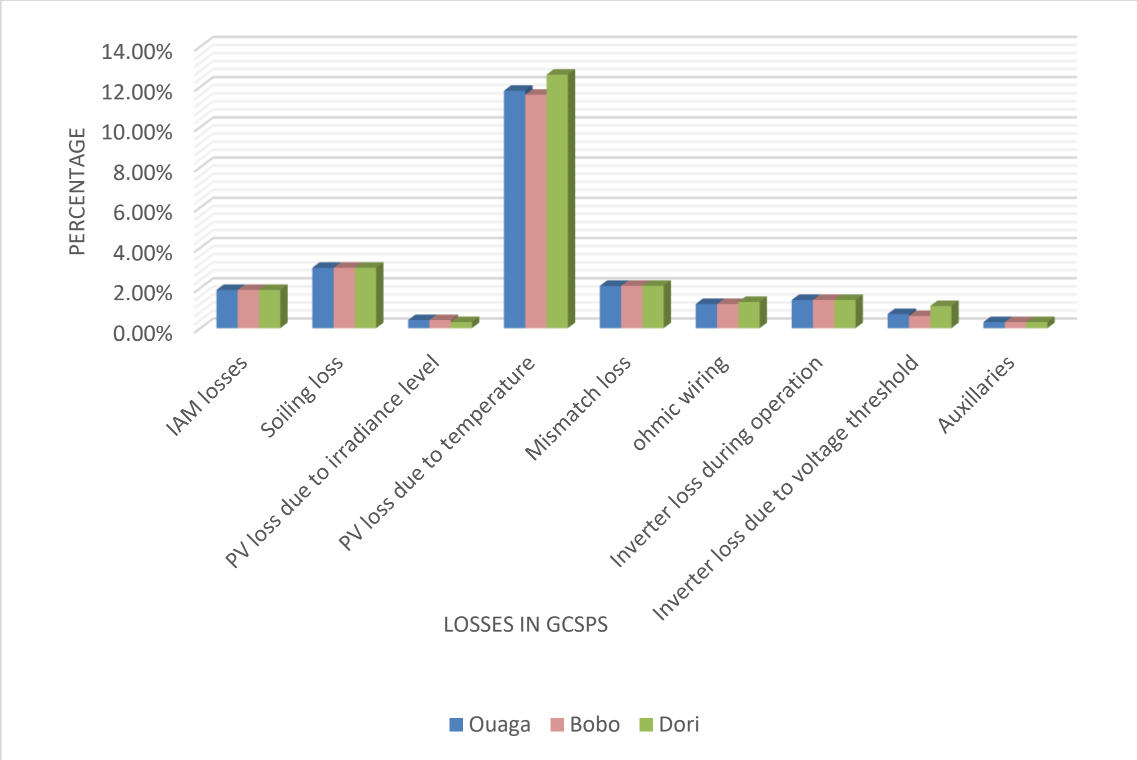

Fig. 8:Losses diagram in the three different locations

Tables 2 and 3 show respectively the electrical parameters of the PV array and inverter as determined by simulation with PVSyst.

Tab. 2:PV array electrical parameters

Manufacturer	Jinkosolar
Model	JKM585M-7RL4-V
Nominal Power	585 Wp
Number of modules	85468 Units
Pmpp at 50°C	45.61 MWp
Umpp at 50°C	926 V
Impp at 50°C	49242 A
Total PV Power	49999 Kwp
Module area	233676 m^2

Tab. 3:Inverter electrical parameters

Manufacturer	Ingeteam
Model	Ingecon Sun 3600TLC615 Preliminary
Nominal Power	2876 kWac
Number of inverter	14 Units
Total power	40264 kWac
Operating voltage	873-1300 V
Maximum Power	44744 kWac
Pnom ratio (DC:AC)	1.24

Figure 9 below shows the LCOE and NPV for each area. It can be seen that the NPV and LCOE As can be seen, the highest NPV is that of Dori, followed by that of Ouaga and finally that of Bobo. This result clearly shows that the PV installation in Dori is more beneficial than in the other two regions, because the LCOE is lower in Dori.

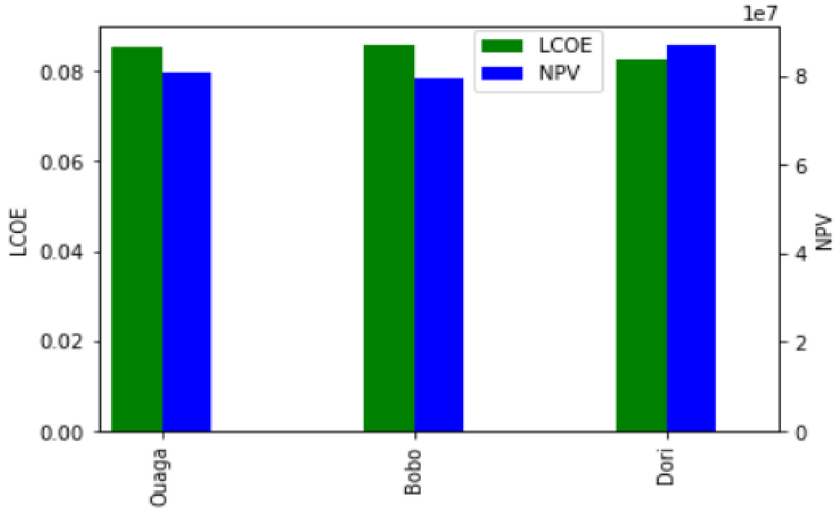

Fig. 9:LCOE & NPV for each climatic zone

Figure 10 shows the evolution of the NPV as a function of the discount rate in the three regions. It can be seen that when the discount rate increases, the NPV decreases, which explains why the uncontrolled inflation rate could make the PV system installation project less viable. Also, the limit of the discount rate that should not be exceeded depends on each region. For Ouaga and Bobo, the maximum discount rate that should not be exceeded is around 12%, and the maximum discount rate for Dori is around 13%, with the cost of the kWh being fixed at $0.15. This clearly explains why, if the discount rate is high, the installation of solar PV plants remains more feasible in Dori than in the other two cities. Figure 11 shows the cumulative NPV over the lifetime of the grid-connected PV project in each of the three regions, with a payback period of between 5 and 10 years for an estimated electricity cost of $0.15/kWh. However, the payback period is quickly reached in Dori, then in Ouaga and finally in Bobo. This period could be the same for all these regions if different electricity costs are applied, which means that PV electricity would be more expensive in Bobo than in the other two regions. There is also a decrease in NPV in years 10 and 20 due to the cost of replacing equipment such as the inverter which has a life span of 10 years. The results for each of the three climate zones are summarized in table 4. These results clearly show the advantage of installing GCSPS in the three locations,

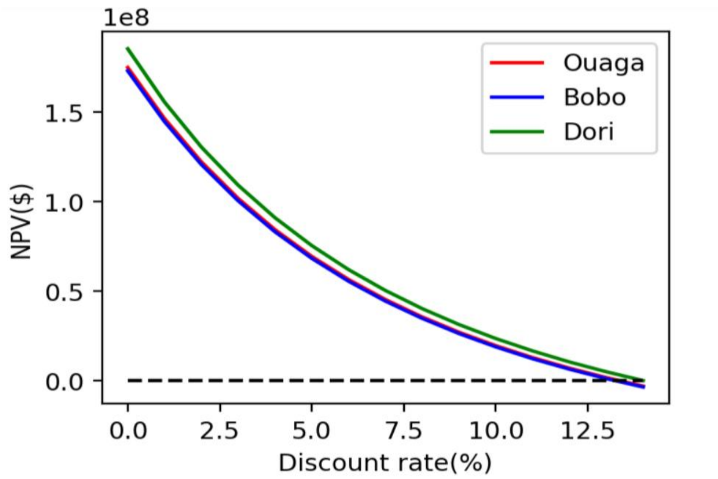

Fig. 10:NPV with different discount rate

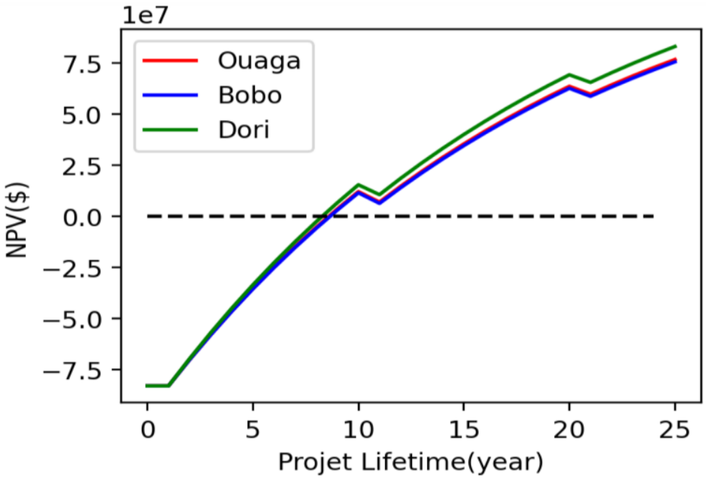

Fig. 11:NPV with project implementation time

Tab. 4:Economic results in the three different climatic zones

City	PV capacity (MWp)	LCOE ($/kwh)	NPV ($)	Discount rate(%)	Energy produced(kWh/year)	Actual LCOE ($/kwh)
Ouaga	50	0.0853	80512952	4.25	9.1 x10^7	0.25
Bobo	50	0.0859	79353487	4.25	9.0 x10^7	
Dori	50	0.0825	87017962	4.25	9.4 x10^7	

4. Conclusion

.This study determined the technical and economic feasibility of a 50 MW GCSPS in each of Burkina Faso's three climate zones, considering each zone's unique characteristics. PVsyst software was used to design a 50 MW GCSPS, and Python software was used to model the system's economics in each climate zone. The results showed that energy production in Ouaga, Bobo, and Dori was 9.1x10^7 kWh, 9.0 x10^7 kWh, and 9.4 x10^7 kWh, respectively. In comparison to the other two zones, this result clearly confirms that Dori is the most privileged zone for the implementation of a PV plant. The LCOE in each zone is approximately $0.08/kWh, which is significantly lower than the current cost of producing electricity in Burkina Faso, which is $0.25/kWh. Finally, the payback period in each zone is less than ten years, implying that the installation of PV power plants is highly viable in Burkina Faso. However, the initial investment cost remains very high due to taxes, transportation costs, land costs, and a lack of subsistence subsidies.With the continued decline in the cost of modules and the advancement of more efficient PV technology, the prospects for the development of GCSPS are bright.

.

5. Acknowledgments

The authors would like to thank Burkina Faso National Meteorological Agency (ANAM) for their support.

6. Reference

Ahmed, N., Naveed Khan, A., Ahmed, N., Aslam, A., Imran, K., Sajid, M. B., & Waqas, A. (2021). Techno-economic potential assessment of mega scale grid-connected PV power plant in five climate zones of Pakistan. *Energy Conversion and Management*, *237*. https://doi.org/10.1016/j.enconman.2021.114097

ANAM Burkina Faso. (2021). *Meteorological data for Ouaga, Bobo and Dori*.

Boddapati, V., Nandikatti, A. S. R., & Daniel, S. A. (2021). Techno-economic performance assessment and the effect of power evacuation curtailment of a 50 MWp grid-interactive solar power park. *Energy for Sustainable Development*, *62*, 16–28. https://doi.org/10.1016/j.esd.2021.03.005

Bouacha, S., Malek, A., Benkraouda, O., Arab, A. H., Razagui, A., Boulahchiche, S., & Semaoui, S. (2020). Performance analysis of the first photovoltaic grid-connected system in Algeria. *Energy for Sustainable Development*, *57*, 1–11. https://doi.org/10.1016/j.esd.2020.04.002

Das, B. K., Alotaibi, M. A., Das, P., Islam, M. S., & Das, S. K. (2021). Feasibility and techno-economic analysis of stand-alone and grid-connected PV / Wind / Diesel / Batt hybrid energy system : A case study. *Energy Strategy Reviews*, *37*(December 2020), 100673. https://doi.org/10.1016/j.esr.2021.100673

Garni, H. Al, & Awasthi, A. (2017). *Techno-Economic Feasibility Analysis of a Solar PV Grid-Connected System with Different Tracking Using HOMER Software*.

Global Photovoltaic Power Potential by Country (Issue June). (2020).

Ilse, K., Micheli, L., Figgis, B. W., Lange, K., Daßler, D., Hanifi, H., Wolfertstetter, F., Naumann, V., Hagendorf, C., Gottschalg, R., & Bagdahn, J. (2019). Techno-Economic Assessment of Soiling Losses and Mitigation Strategies for Solar Power Generation. In *Joule* (Vol. 3, Issue 10, pp. 2303–2321). Cell Press. https://doi.org/10.1016/j.joule.2019.08.019

indexmundi. (2020, November 27). *Burkina Faso Central bank discount rate*. https://www.indexmundi.com/burkina_faso/central_bank_discount_rate.html

IRENA. (2022, May 9). *https://www.irena.org/Digital-Report/World-Energy-Transitions-Outlook-2022*. IRENA.

Kazem, H. A., Albadi, M. H., Al-Waeli, A. H. A., Al-Busaidi, A. H., & Chaichan, M. T. (2017). Techno-economic feasibility analysis of 1MW photovoltaic grid connected system in Oman. *Case Studies in Thermal Engineering*, *10*(April), 131–141. https://doi.org/10.1016/j.csite.2017.05.008

Kebede, K. Y. (2015). Viability study of grid-connected solar PV system in Ethiopia. *Sustainable Energy Technologies and Assessments*, *10*, 63–70. https://doi.org/10.1016/j.seta.2015.02.003

Li, C., Zhou, D., & Zheng, Y. (2018). Techno-economic comparative study of grid-connected PV power systems in five climate zones, China. *Energy*, *165*, 1352–1369. https://doi.org/10.1016/j.energy.2018.10.062

Mekhilef, S., Saidur, R., & Kamalisarvestani, M. (2012). Effect of dust, humidity and air velocity on efficiency of photovoltaic cells. In *Renewable and Sustainable Energy Reviews* (Vol. 16, Issue 5, pp. 2920–2925). https://doi.org/10.1016/j.rser.2012.02.012

Mohamed, A. S. A., & Maghrabie, H. M. (2022). Techno-economic feasibility analysis of Benban solar Park. *Alexandria Engineering Journal*, *61*(12), 12593–12607. https://doi.org/10.1016/j.aej.2022.06.034

Mohand Kaci, G., Mahrane, A., Ghedamsi, K., & Chikh, M. (2022). Techno-economic feasibility analysis of grid-connected residential PV systems in Algeria. *Energy & Environment*, 0958305X2211469. https://doi.org/10.1177/0958305X221146953

Moner-Girona, M., Bódis, K., Korgo, B., & Huld, T. (2017). *Mapping the least-cost option for rural electrification in Burkina Faso. Scaling-up renewable energies PERFORMANCE-A science base on photovoltaics performance for increased market transparency and customer confidence View project*. https://doi.org/10.2760/900097

Oloya, I. T., Gutu, T. J. L., & Adaramola, M. S. (2021). Techno-economic assessment of 10 MW centralised grid-tied solar photovoltaic system in Uganda. *Case Studies in Thermal Engineering*, *25*. https://doi.org/10.1016/j.csite.2021.100928

Ouedraogo, B. I., & Yamegueu, D. (2019). Techno-economic assessment of solar photovoltaic integration into national grids: A case study of Burkina Faso. *Energy Science and Engineering*, *7*(5), 1458–1468. https://doi.org/10.1002/ese3.364

Renewable Energy Agency, I. (2023). *RENEWABLE CAPACITY STATISTICS 2023 STATISTIQUES DE CAPACITÉ RENOUVELABLE 2023 ESTADÍSTICAS DE CAPACIDAD RENOVABLE 2023 About IRENA*. www.irena.org

Sanou, C. L., Neya, O., Agodzo, S. K., Antwi-Agyei, P., Bessah, E., Belem, M., & Balima, L. H. (2023). Trends and impacts of climate change on crop production in Burkina Faso. *Journal of Water and Climate Change*, *14*(8), 2773–2787. https://doi.org/10.2166/wcc.2023.137

SONABEL. (2020). *Rapport d’activités 2020*.

THIRTY FIVE YEARS OF RESEARCH AND USE WITH MY FAVORITE HYBRID SOLAR CUM ELECTRIC OVEN IN COSTA RICA.

Shyam S. Nandwani

Retired Professor, Researcher, Promotor and User of Solar Energy, Heredia, Costa Rica.

Abstract

Author designed, constructed, and used solar food warmer first time in the house 1979. Looking into success, various models of cookers/ovens like conventional solar oven, hybrid solar electric oven, and also including dryer, were designed and used for next 35 years. Got a patent on Solar Oven for Costa Rica in 1984 and also published a practical book on Solar oven in Spanish, in 1992 and 2004. Also with the collaboration of Solar Cookers International, based at Sacramento, USA, organised a world conference on Solar Cooking in Costa Rica in July 1994.

These ovens were/are used for cooking, warming meal and other uses, when the climate permits, about 7-8 months for cooking and about 11 months per year for low temperature applications, like warming meals, pasteurizing water and drying domestic products. In this presentation only Hybrid Solar Electric Oven will be mentioned.

*Keywords**: S**olar oven, Solar electric hybrid Oven, Solar pasteurizer, Solar oven cum dryer, Smart switch, Energy saving.*

Introduction

Due to electric rationing imposed by National electric company, author constructed and studied solar food warmer for family use in April 1979. Looking into success, various models of cookers/ovens (Nandwani, 2012) like conventional solar oven (Nandwani, 1988), hybrid solar AC (Nandwani, 1989) electric oven, Solar Electric Microwave oven (Currin et.al.,1994). two compartments oven for research (Nandwani et.al, 1997), Multipurpose Solar Electric oven including dryer (Nandwani, 2007) etc. were designed, studied and published during 44 years of research. Got a patent on Solar Oven for Costa Rica (Nandwani, 1984) and also published a practical book on Solar oven in Spanish, in 1992 and 2004 (Nandwani, 2003).

These ovens were/are used for cooking, warming meal and other uses, when the climate permits, about 7-8 months for cooking and about 11 months per year for warming meals, pasteurising water and drying domestic agricultural products. etc.

Photo 1 shows some of the ovens designed and used by author and family at home.

10.18086/swc.2023.12.02 Available at http://proceedings.ises.org

Photo 1. Some of the solar ovens designed and used by author at home since 1980.

In this presentation I will be mentioning only Hybrid Solar Electric Oven, and some practical devices added, during last ten years to make the hybrid oven more friendly.

Solar Oven

Although Hot box oven is well known however we can mention in brief (Nandwani, 1988). As shown in Figure 2A and Photo 2B, it is a box having metal sheet, painted black on the top to receive the maximum -solar radiation, glass wool as heat insulation on four sides and below the metal plate,

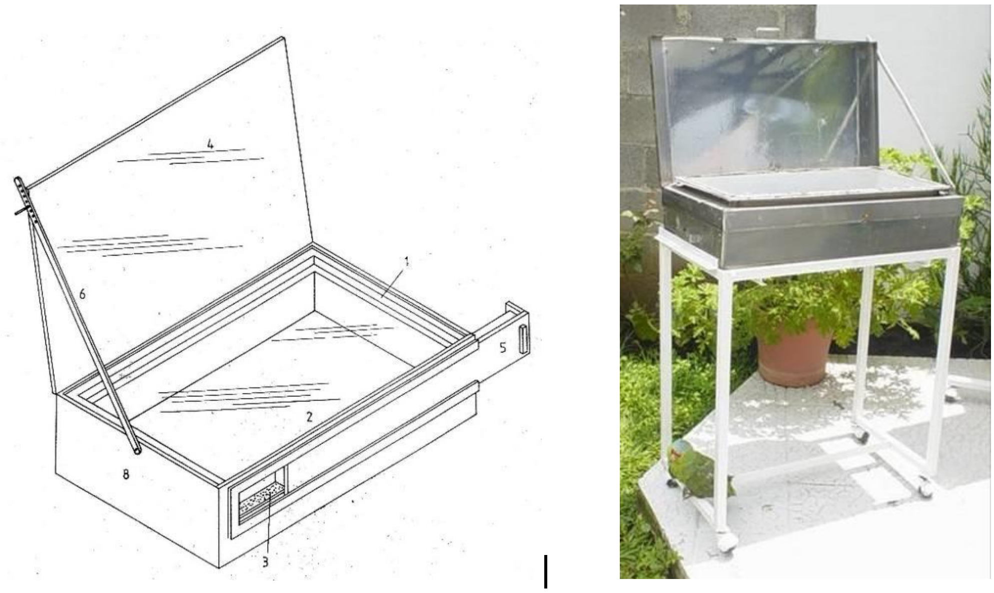

A B

1.Two transparent window glasses, 2. metallic plate, 3. heat insulating material, 4. reflecting sheet, 5. door to keep and take out cooking pots, 6. rod with some holes to adjust reflector angle, 8. outer box.

Fig. 2. Conventional Hot box, drawing (A) and Oven (B) at author house.

On the top of the box there are two transparent window glasses to allow the entrance of low wavelength solar radiation coming from sun and impedes the exit of high wavelength emitted from the hot metal plate. On the top of the box there is also one reflector (although could be more) to increase the solar radiation and thus increase oven temperature. In this way the box becomes very hot. On sunny day the oven temperature could reach up to 150 ℃ (without any meal) to cook meal and pasteurize water etc.

Hybrid solar electric oven.

The advantages of Solar ovens are well known, like free, clean and abundant solar energy, no smoke, reduction of deforestation, cooking even in absence of cook etc. (Nandwani, 1996). However, has the limitation like absence of solar energy, not only at night, but also during cloudy/rainy period. More than that, the fluctuating/ unpredictable climate even during sunny day, especially in Central American countries including in Costa Rica, mainly due to sea on both eastern and western coasts. Figure 10 will show the solar radiation drop on one particular sunny day at beginning. This is sufficient reason to frustrate most of the women when meal is not cooked, including my wife. Thus (fortunately) I was forced to find some solution. In 1986, I made, studied and published Electric cum Solar Oven (Nandwani, 1989).

As shown in Figure and Photo 3, The Hybrid Solar Oven is in fact similar to conventional Solar oven but with two changes, the normal metallic plate is replaced by electric grill plate (1000-1200Watts) and thermostat for fixing plate temperature. In this way, one put the meal in the box to be cooked and fix the plate temperature say about 100 ℃. Depending on the climate/ solar intensity, in case oven temperature is maintained, no electrical energy will be used, however in case the solar intensity falls, electricity will be used and again in case clouds disappear, no more electrical energy etc. In this way switching from Solar to Electrical energy and vice versa is automatic. More results can be seen in the original paper presented firstly at 1987 ISES Conference held at Hamburg/ Germany and published in the journal (Nandwani, 1989). The user is sure to get the meal cooked. but with the minimum use of electric energy. In other words, it can be used for cooking, baking and pasteurizing water even in cloudy climate. Thus, this is my favourite model.

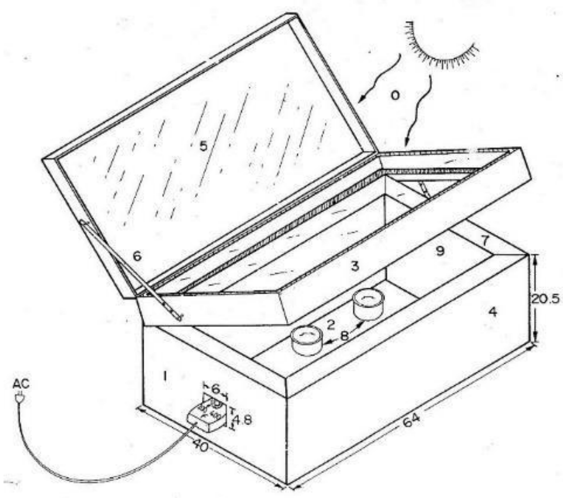

0 Solar Radiation AC Alternating Current 1. Thermostat 2. Electric Black Plate 3. Two Transparent Glass Covers 4. Outer Wooden Box. 5. Reflector 6. Arrangement to adjust the angle of reflector 7. Glass Wool 8. Cooking Pots 9. Inner Wooden Box. All dimensions are in cm.

Fig. 3 and photo 3. Hybrid Electric cum Solar Oven at authors house and in working mode at exhibition in Costa Rica

.

Hybrid multipurpose solar electric oven

In the hybrid Solar Electric oven mentioned already and made in 1986 at my university the outer box was made of wood, due to budget limitation. Later on I made the similar one for the house but with stainless steel, for better durability, as well with some changes like including Solar dryer as shown in Photo 4. Dryer is very useful for drying some domestic products, and require less temperature, like coriander and other herbs etc. (Nandwani, 2007).

Photo 4. Multipurpose and Hybrid Solar electric Oven designed and used at authors home since 1988.

Energy measuring and controlling device.

During last 35 years of use, I have found this as useful oven. Then I decided to add some additional devices to make this favourite Hybrid oven more practical for safety and measurements, like oven thermometer, Watt meter to measure electricity consumed, switching ON and OFF oven remotely, and measurement of oven temperature and solar intensity remotely with smart switch and cell phone etc. Some recent experimental data will also be informed.

a. Oven Thermometer.

In conventional solar oven its good to have oven thermometer (photo 5) to know the air temperature while cooking meal but in the case of Hybrid solar oven its very much necessary also for the safety reasons. May be due some problem with thermostat the oven temperature can increase too much and it can burn your hand while taking meal.

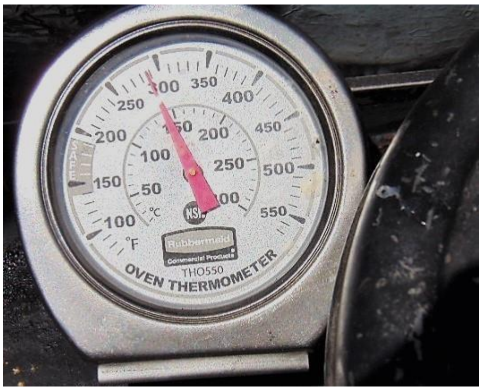

Photo 5. Oven thermometer to measure temperature.

b. Energy Measuring Device.

Although the meal can be cooked in any climate, with minimum use of electrical energy, however the researcher and user may want to know the electrical energy used/saved. The simplest way could be observing the time LED light ON Time, in the thermostat. Adding this light time (hr.) and multiplying with average wattage of electrical plate (1.2 kW), one can calculate the total electrical energy used (kWh) for cooking. Now I use Kill a Watt meter (Photo 6a) connected in series to Hybrid solar device (Photo 6b) to know the electricity used and also for public demonstration etc. In case any researcher/cook wants to know total energy consumed, he/she can use portable solar meter.

Photo 6. One of the commercial Energy Meter, KILL A WATT (a) Oven and connection to oven (b) for measuring electric energy used.

c.Smart Switch

Solar Oven, in addition to save conventional fuel also has another BIG advantage, it can cook unattended, it means, user can keep the meal and go for shopping and even to office, The SUN will be doing his job to cook the food. The food will not burn as solar oven is slow cooking device. and does not attain very high temperature (about 100 °C, with meal inside). But with Hybrid Oven, it cannot be done always, especially when you are not at home. May be the user has to disconnect electricity after 2-3 hours depending on climate and quantity of meal etc. Although some programable timers are available for switching off the devices after particular time, commonly used for Electric water heater, TV or other appliances etc. However around 8-9 months ago I found Smart Switch (Photo 7) which combined with Smart Cell phone can switch the Hybrid Solar/Electric oven whenever you want, even you are in the office, market in or out of country, (Nandwani, 2022).

Photo 7. Smart Switch (left) and Smart Cell phone (right), to control Hybrid Solar Oven, via Wi-Fi.

d. Data reading remotely.

So far everything is OK. Being a retired person, I continue doing some research at home with solar thermal and photovoltaic devices. At home I do not have data logger to record data. While doing measurements manually, some time I have to leave home say for 1 to 2 hours and do not want to miss data, like solar intensity and oven temperature. Fortunately, recently I could find a smart DC camera (Photo 8). Through this camara and corresponding application in smart cell phone, one can see the data through Cell phone, even you are on the road or at some coffee shop etc. One can either note the data or take screen shot to note down later.

Photo 8. Smart Wi-Fi camara with Cell Phone to measure some variables remotely.

Some experimental results

Although in the earlier papers (Nandwani, 1989 and Nandwani, 2007) on this subject. many experimental results are informed; however I will add only one more experimental data measured recently, where by chance climate change occurred.

On October 4, 2023, two solar ovens, one conventional and another hybrid Oven were used to cook same quantity of meal. At 8 am both ovens were kept in patio without any meal. Solar radiation and oven temperatures were measured each 15 to 30 minutes. At 11 am, the oven temperature was about 105-110 °C, in each oven (Fig. 10). Now we put vegetables (260 g of potatoes) in both ovens (Photos 9).

(a)

(b)

Photo 9. Solar (a) and Hybrid Oven (b), with the same quantity of meals kept at 11 am.

Unfortunately for cooking (but fortunately for study) the solar radiation started reducing, due to clouds.

I connected the hybrid oven with electricity and Energy meter (kill a Watt). From the Figure 10, one can see very clearly the drop of oven temperature in conventional solar oven and the housewife has the sufficient reason to get frustrated. At 12:30 pm, meals in both ovens were checked and the meal in solar oven was not cooked whereas the meal in hybrid oven was cooked, consuming only 0.16 kWh of electrical energy.

To the best of my knowledge, at least hybrid electric Solar ovens are sold commercially at least in India and USA, but without additional accessories mentioned here..

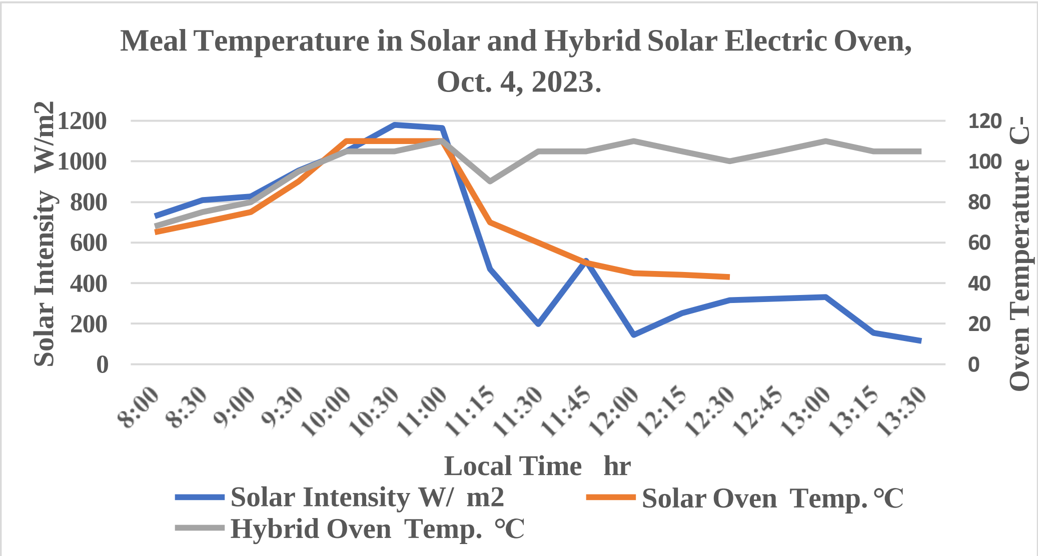

Fig. 10. Variation of Meal temperature with solar intensity, in Solar and Hybrid Oven.

Conclusions

With this hybrid gadget, which can be used mainly in electrified areas, with electricity generated from fossil fuel or from Renewable sources, one can heat, cook bake and roast meal, pasteurize water and dry spices etc., using mainly solar and electricity if required). Thus we can consider the device with accessories mentioned above as a practical device for user as well for researcher etc. In the case of rural area, the other fuel could be firewood or electricity from PV panels. This will help in reducing conventional fuel and cool the only planet we have (Nandwani, 1996).

Acknowledgement

Author is thankful to all ex collaborators, Eliecer Madrigal, Marvin Alpizar, Carlos Delgado and Guillermo Torres etc. for the help in construction and measurements.

References

Nandwani, S., 1984. El Horno Solar. Patent No. 2367. *National Register, Costa Rica.*

Nandwani, S., 1988. Experimental and theoretical analysis of simple solar oven in the climate of Costa Rica,
Solar and Wind Technology, Pergamon Press, 5 (2), pp.159-170.

Nandwani, S., 1989. Design, Construction and Experimental Study of Electric Cum Solar Oven-II, *Solar and Wind Technology*, Pergamon Press, 6 (2), pp.149-158.

Currin, Ced., Nandwani, S., Alpizar, Marvin., 1994. Preliminary study of Solar Powered Microwave Oven. *Second world Conference on Solar Cookers, Use and Technology,* Costa Rica, 12-15 July 1994. Published in Proceedings., April 1995, pp. 149-158.

Nandwani, S., 1996. Solar cookers – cheap technology with high ecological benefits.
Ecological Economics, Vol. 17, pp. 73- 81, 1996.

Nandwani, S., Steinfart, J., Henning., H.M., Rommel, M., Wittwer, V., 1997.Experimental study of Multipurpose Hot box at Freiburg, Germany*, Renewable Energy, an International Journal*. Pergamon Press, Vol. 12, pp. 1-20.

Nandwani, S., 2003. Book: La Cocina /Horno Solar, *Editor, Fundacion Universidad Nacional Costa Rica*, pp. 1-126. ISBN, 9977-906-39-4.

Nandwani, S., 2007. Design, construction and study of a hybrid solar food processor in the climate of Costa Rica, *Renewable Energy- An International Journal* (Elsevier Ltd). 32 (3), pp. 427-441.

Nandwani, S., 2012. Solar Cookers and Dryers to conserve Human and Planet Health, Invited article. Published in
Encyclopedia of Sustainability Science and Technology, Robert A. Meyers (Ed.) Springer Verlag, pp. 9486-9509.

.

Nandwani, S., 2022. Hybrid Solar/electric Oven with Smart Switch and Smart Phone, *Acta Scientific Computer Sciences*, 4(8),
pp. 10-14.

13. Solar Photocatalysis and Solar Fuel Production

GREEN HYDROGEN AS A TOOL TO COMPLETELY DECARBONIZE OFF-GRID AMAZONIAN COMMUNITIES

Daniel Odilio dos Santos[1], Aline Kirsten Vidal de Oliveira[1], Helena F. Naspolini[1] and Ricardo Rüther[1]

[1] Fotovoltaica/UFSC, Universidade Federal de Santa Catarina, Florianópolis (Brazil)

Abstract

This paper explores the feasibility of utilizing green hydrogen (H2) for decarbonizing an isolated community in the Brazilian Amazon, focusing on the off-grid system of Oiapoque-AP. It assesses the optimal sizing of equipment required for this solution, considering the current energy supply that is given by a diesel plant and a PV system, as well as the planned addition of a hydroelectric plant. Findings indicate that a combination of lithium-ion batteries and green H2 fuel cell system is well-suited to comply with the short- and long-term storage needs to decarbonize the system. Simulations and sensitivity analysis determined the optimal sizing of components, including a PV system expansion of 25 MW, an electrolyzer of 3 MW and a tank of 2.5 M Nm³. A sensitivity analysis of electrolyzer and the additional PV system sizes revealed optimized combinations that can meet the H2 gas demand in the system. A system with additional 25 MWp in PV generation combined with a 3 MW. The study highlights the potential of H2 storage as a sustainable solution for off-grid communities and the results provide valuable insights into the integration of H2 technology and its advantages for decarbonization efforts in remote regions. The operational analysis shows the optimum sized electrolyzer operates on 51% of the year's days, with consistent hydrogen production from February to September. This suggests high component operation, which is important given its high system cost. For the studied community, a 4.2 MW fuel cell is projected to operate from September to January, indicating potential system inefficiency.

Keywords: Amazon region, green hydrogen, off-grid communities.

Introduction

Brazil hosts a vast interconnected electric grid controlled by a centralized operator, but due to technical and geopolitical challenges in constructing energy-related infrastructure, isolated microgrid systems have been adopted (Carvalho, 2006). These microgrids, primarily concentrated in the Brazilian Amazon Region, have traditionally relied on diesel generators for their energy needs due to low-capital costs, ease of installation, and portability (Ribeiro et al., 2012). However, as global efforts to address climate change intensify and renewable technology costs decline, off-grid renewable energy systems are emerging as a more sustainable alternative.

While the region experiences relatively low wind speeds and faces concerns of illegal deforestation associated with increased biomass demand, solar photovoltaic (PV) systems are considered the most suitable energy source for off-grid solutions. The abundant rainfall combined with an equivalent global horizontal irradiation to sunniest European countries make solar PV feasible (Pereira et al., 2017). However, to overcome the intermittent nature of solar energy, an energy storage system is required, either in the form of traditional battery technology or a hydrogen (H2) storage system (Suleman, Dincer and Agelin-Chaab, 2015).

Lithium-ion battery storage systems and hydrogen storage systems represent two crucial technologies for the storage of renewable energy. Each possesses its own set of advantages and disadvantages when considering factors such as utility, cost-effectiveness, efficiency, reliability, and safety (Sterner and Stadler, 2019). Lithium-ion battery systems offer notable advantages, particularly in terms of efficiency, that range from 85% to 95%. Furthermore, these systems exhibit a high energy density, enabling them to store significant energy quantities within compact spaces (Alshahrani et al., 2019).

In contrast, hydrogen serves as a high-energy-density fuel and also serves as a viable energy storage medium. Hydrogen demonstrates remarkable versatility, finding application as a fuel for vehicles, as a means for generating electricity via fuel cells, as a source of emissions-free heat generation, and in various chemical industry processes

Selection and/or peer review under responsibility of Scientific Committee
10.18086/swc.2023.13.02 Available at http://proceedings.ises.org

(Møller et al., 2017). Nevertheless, the storage of electrical energy using hydrogen involves more processes, producing an efficiency from 20 to 50%. Despite its low efficiency, hydrogen has the advantage of very small self-discharge ratio, so it is suitable for a long storage period. Lithium-ion batteries, on the other hand, have a medium self-discharge ratio and are suitable for a storage period not longer than tens of days (Chen et al., 2009). Given that, even with the financial barriers, a combination of green H2 and lithium ion batteries can be used to supply stored energy in communities where there is a mismatch between energy demand and supply (Oliveira et al., 2023).

This study investigates the viability of utilizing green H2 to decarbonize an isolated community in the Brazilian Amazon. The analysis evaluates the optimal sizing of the equipment necessary for this solution, assessing its technical feasibility. While the focus is on an extreme case of an off-grid community in the Amazon, the findings can be extrapolated to more conventional communities, particularly in terms of understanding the potential of long-term H2 storage and its advantages and trade-offs compared to conventional battery storage.

Methods

This analysis is focused on the off-grid system of Oiapoque. Oiapoque is a city in the state of Amapá, located about 550 km from the capital Macapá, bordering French Guiana. The system is currently supplied by an Independent Electric Energy Producer, contracted through an auction held in 2014, effective until November 2030. The electric energy is supplied by a 12.83 MW thermoelectric diesel plant and a PV system of 4.3 MWp. The first one is intended to be deactivated upon the construction of the run-of-river hydroelectric plant Salto Cafesoca (7.5 MW), scheduled to be finalized in 2024. However, the decarbonization of the energy production of this community is a complex problem, which requires the addition of energy storage systems in addition to non-dispatchable energy sources.

To solve this problem, lithium-ion batteries and H2 storage are two prominent technologies for storing renewable energy, each with their own advantages and disadvantages in terms of use, cost, efficiency, reliability, and safety (Sterner and Stadler, 2019). For short-term energy storage, lithium-ion batteries are well suited, given their high efficiency and high energy density. However, given their self-discharge, for long-term energy storage, the use of green H2 is a better fit. Given the mismatch of the load profile and of the hydroelectric generation potential (as shown in Fig. 1), a mix of both types of storage is recommended (Due to information limitations, data available in the public domain on the locality's load, provided on an hourly basis, and the estimated monthly production energy from the hydroelectric plant will be used). To optimize the appropriate size of both storage systems, data on energy demand and estimated generation of the hydroelectric and PV plants were analyzed (Empresa de Pesquisa Energética (EPE) and Ministério de Minas e Energia (MME/SPE), 2018).

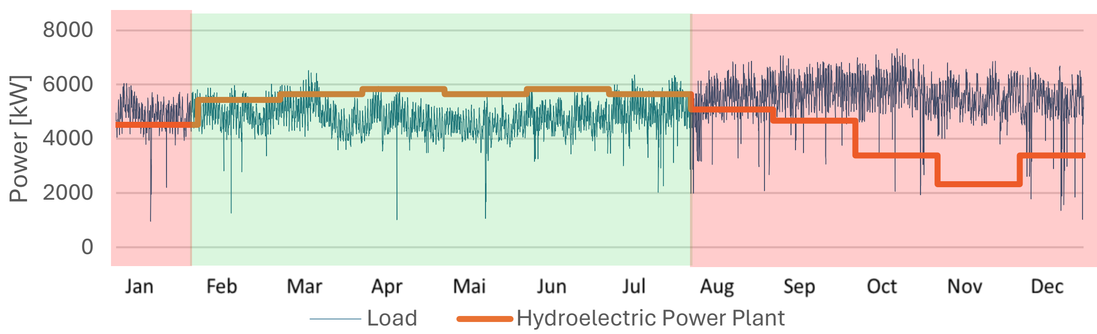

Fig. 1: Mismatch between load and Hydroelectric power plant generation.

To fully meet the energy demands of Oiapoque through a renewable system, it is necessary to combine a rapid response storage system to meet load variations and intermittent generation, with a storage system capable of storing large volumes of energy without self-degradation. According to Sterner M. and Stadler I. (2019), the battery storage system must be employed to compensate the daily load fluctuations, while the H2 storage system should address the annual variation in generation from the small hydropower plant. Therefore, in this study, for the sizing of the H2 system, it was considered that the surplus of hydro and solar energy produced is used for gas production. This generated gas is then used in the remaining months for the production of electric power. The sizing of the battery storage system was carried out to ensure the daily energy supply to the community, from February to July, bearing in mind that during this period, the use of H2 as an electricity source would not be required. For the evaluation of the calculated sizing, the amount of energy used to produce green H2 and the energy dispatch in the fuel cell was calculated in each timestep (1 hour) in a period of one year. For moments when there is an excess of renewable energy generation, the energy dedicated to H2 producing in the eletrolyzer (E_{el}) is determined by Eq. 1.

$$E_{el} = E_{PV} + E_{Hydro} - L - E_{Bat_{Charge}} \quad \text{(eq. 1)}$$

In the equation, E_{PV} represents the amount of PV energy produced and E_{Hydro} represents the production of energy of the hydropower plant. The energy demand of the community is represented by L and $E_{Bat_{Charge}}$ corresponds to the energy that is feed into the battery, respecting its capacity and inverter limits. On the other hand, the energy supplied by the fuel cell (E_{FC}) when there is not enough renewable energy available, and the limits of the battery are achieved is given by Eq. 2.

$$E_{FC} = L - E_{PV} - E_{Hydro} - E_{Bat_{Discharge}} \quad \text{(eq. 2)}$$

Here, the coefficients for energy production and energy demand remain the same as the Eq. 1, with the addition of $\boldsymbol{E_{Bat_{Discharge}}}$, which represents the energy that is provided by the battery to the system.

The expansion of the PV system was also considered as a possibility. A sensibility analysis of different combinations of sizing of the equipment was carried out, based on supplying the demand of the community in terms of power and energy, attempting to optimize renewable energy availability.

The operation of the electrolyzer must be carefully evaluated, especially with regard to its operating behavior over different periods and conditions. Given its position as the most expensive component within the energy system under analysis, the ideal goal is for the electrolyzer to be used for the longest possible period of time, thus maximizing its efficiency and return on investment.

Optimizing the operating regime of this device not only extends its usefulness within the system as a whole, but also contributes to the overall effectiveness of the configuration, directly impacting on metrics such as energy autonomy, sustainability and economic viability. Such considerations are fundamental to both the design phase and the execution and management of the system and should be incorporated into any subsequent technical analysis and strategic decision.

Table 1 shows the parameters used for the simulation and sizing of equipments to fully meet the energy requirements of the community. The parameters of the efficiency of the equipment are based in analysis of datasheets of commercial products. The sizing of power and capacity of the systems are variable and calculated during the simulations.

Table 1- Technical premises used for the simulation of the system.

Battery Storage System	Type	Li-ion	
	Round-trip efficiency	98%	
	Capacity	Variable	
	PCS	Variable	
	Time response	milliseconds	
PV system	Global Horizontal irradiation (year average)	4,94 kWh/m²/day	
	Performance ratio (PR)	0,78	
	Installation type	Fixed	
	Azimuth	0°	
	Tilt	10°	
	Size	Variable (0MWp -30MWp)	
Electrolyzer	Operational Power Range	PEM	(20%-100%)
		Alkaline	(80%-100%)
	Efficiency	5 kWh/Nm³	
	Size	Variable (0MW -10MW)	
Fuel Cell	Consumption	70g/kWh	
	Size	Variable	
Gas storage	Size	Variable	

Results

The battery storage system was designed to ensure the daily supply of electricity to the community. The system is used to store PV energy produced during the day to feed the grid when the hydro generation is not sufficient. To meet the community's energy needs during this time, a system capacity of 16 MWh, coupled with a 2 MW Power Conversion System (PCS) was estimated to be a minimum necessary. Fig 2 illustrates the storage system State of Charge (SOC) along the year using the minimum possible sizing. It can be noted during the months of February and July, there is practically no need to dispatch the storage system, as the hydroelectric generation system and the solar PV generation system are enough for the microgrid to function correctly.

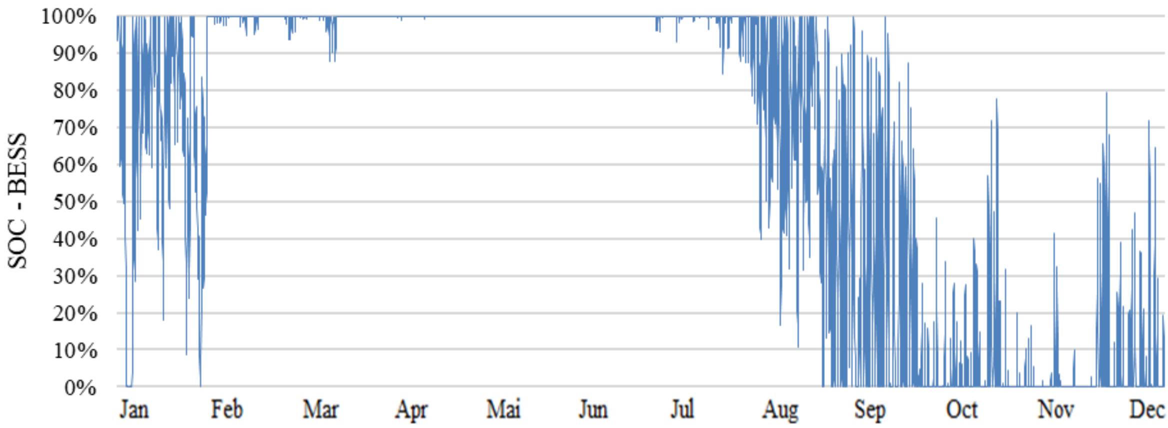

Fig. 2– Battery SOC that controls short variations in charge.

Simulations were performed using different strategies for the sizing of the components, which resulted in different full load hours of the eletrolyzer, the most expensive equipment in the analysis. The different sizing scenarios had a direct influence on the volumetric requirements of the hydrogen storage tanks. In the evaluated scenario, the optimally calculated system requires a storage capacity of approximately 2.5 x 10^6 Nm³ (224.7 tons of H2), with the target of completing the full load by mid-September. The sized tank is extremely large and would require a tank of 8,3 x 10^3 m³ at 300 bars. Therefore, the best option to optimize space would be a cryogenic solution. Fig. 3 shows the impact of different electrolyzer sizes on the proper operation of the hydrogen storage infrastructure.

The orange line shows a system with optimal sizing between the electrolyzer and the energy sources. This is seen when the hydrogen storage tank starts the year empty, reaches its maximum capacity at the end of September and subsequently discharges through the fuel cell in the following months, leaving no surplus hydrogen. When the electrolyzer is oversized, as indicated in blue, a premature filling of the tank occurs, observed in point A. In addition, excess hydrogen remains at the end of the year, leading to further underutilization of the electrolyzer in the following year, as shown in point B. On the contrary, an undersized electrolyzer results in premature emptying of the tank, as shown in point C, thus inducing an energy deficit in the system.

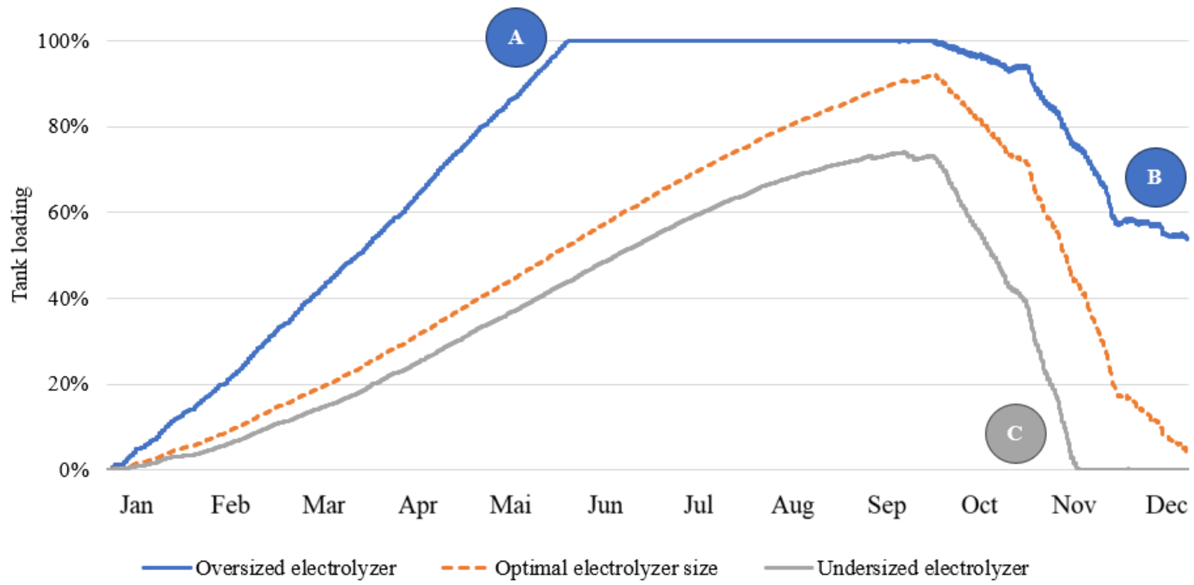

Fig. 3 - The Impact of Electrolyzer Sizing on the Hydrogen Storage System.

In order to assess the feasibility of incorporating green H2 production and consumption in the community, it is essential to carry out a sensitivity analysis of the size of the electrolyzer and PV system to be added to the 4.5 MWp system already installed in the community. Table 2 shows the annual energy deficit produced by each combination of systems considering an electrolyzer with PEM technology. In the table, the optimized combinations are highlighted in bold, and the best scenarios, which are cheaper, are highlighted in red.

Table 2- Maximum power shortage at each combination of PEM electrolyzer size and additional PV power (MWh).

		Additional PV Power plant						
		0MWp	5MWp	10MWp	15MWp	20MWp	25MWp	30MWp
Electrolyzer size	1 MW	3.35	1.96	1.48	1.26	1.12	1.02	0.96
	2 MW	3.06	1.53	0.98	0.71	0.55	0.44	0.36
	3 MW	2.95	1.26	0.60	0.28	0.08	**0.00**	**0.00**
	4 MW	2.93	1.09	0.31	**0.00**	**0.00**	0.00	0.00
	5 MW	2.98	1.01	0.10	0.00	0.00	0.00	0.00
	6 MW	3.05	0.97	**0.00**	0.00	0.00	0.00	0.00
	7 MW	3.11	0.97	0.00	0.00	0.00	0.00	0.00
	8 MW	3.18	1.00	0.00	0.00	0.00	0.00	0.00
	9 MW	3.23	1.03	0.00	0.00	0.00	0.00	0.00
	10 MW	3.29	1.08	0.00	0.00	0.00	0.00	0.00

For any size of electrolyzer, it is unfeasible to ensure total fulfillment of the community's energy demand without integrating additional energy production. It is necessary to integration an additional capacity of at least 10 MWp of

PV systems to fully meet the demand. For an electrolyzer with a capacity of 6 MW, it is essential to incorporate at least 10 MWp of PV generation. For a 4 MW electrolyzer, the requirement increases to a minimum addition of 15 MWp in PV capacity. Similarly, a 3 MW electrolyzer requires a minimum increase of 25 MWp in PV generation for effective operation. It can be concluded that electrolyzers with a capacity of less than 3 MW are undersized for this system, resulting in a lack of energy to suit the community.

The previously mentioned evaluations were carried out using PEM (Proton Electrolyte Membrane) type electrolyzers, which have a wide operating range, varying between 20% and 100% of their capacity. For comparison purposes and to improve the analytical scope, electrolyzers operating with alkaline technology were also investigated, whose operating range is notably narrower, oscillating between 80% and 100%. The energy deficit resulting from these technological variations is presented in Table 3, providing a more comprehensive and rigorous view of the limitations inherent in each type of electrolization technology.

Table 3- Power Shortage at each combination of Alkaline electrolyzer size and additional PV power (MWh).

		Additional PV Power plant						
		0MWp	5MWp	10MWp	15MWp	20MWp	25MWp	30MWp
Electrolyzer size	1 MW	3.45	2.05	1.57	1.34	1.20	1.11	1.04
	2 MW	3.41	1.85	1.28	0.99	0.82	0.69	0.60
	3 MW	3.49	1.74	1.00	0.65	0.43	0.27	0.16
	4 MW	3.62	1.74	0.85	0.36	0.09	**0.00**	**0.00**
	5 MW	3.78	1.81	0.77	0.18	**0.00**	0.00	0.00
	6 MW	3.90	1.90	0.76	0.06	0.00	0.00	0.00
	7 MW	3.93	2.05	0.79	**0.00**	0.00	0.00	0.00
	8 MW	3.94	2.19	0.91	0.00	0.00	0.00	0.00
	9 MW	3.94	2.37	1.05	0.00	0.00	0.00	0.00
	10 MW	3.94	2.51	1.23	0.07	0.00	0.00	0.00

With regard to the alkaline electrolyzer, its restricted operating range means that a larger PV generation system is needed to fully satisfy the community's energy demands. It can be seen that, in this specific scenario, it is not possible to guarantee the community's complete energy supply without the inclusion of an additional minimum of 15 MWp of PV generation. Furthermore, in order to achieve this goal with an additional 15 MWp of PV capacity, an electrolyzer with a capacity of 7 MW is required, which represents an increase of 75% compared to PEM electrolyzers. This comparative analysis serves not only to elucidate the differential performance metrics between the different electrolyzer technologies, but also provides a robust empirical substrate for making strategic decisions and evaluating operational efficiency.

In addition, Tables 4 and 5 show the amount of surplus energy generated in the system for each combination of electrolyzer and PV capacity, for the PEM and alkaline technologies, respectively.

Table 4 - Energy surplus for each combination of PEM electrolyzer size and additional PV power (MWh/year).

				Additional PV Power plant				
		0MWp	5MWp	10MWp	15MWp	20MWp	25MWp	30MWp
Electrolyzer size	1 MW	3.46	8.42	14.63	21.21	28	34.83	41.966
	2 MW	1.63	5.71	11.43	17.77	24.35	31.068	37.842
	3 MW	0.89	3.94	8.98	14.98	21.34	27.89	34.54
	4 MW	0.82	2.9	7.15	12.669	18.762	25.113	31.88
	5 MW	1.12	2.32	5.78	11.34	18.76	24.549	31.29
	6 MW	1.54	2.1	5.02	11.034	17.87	24.049	30.74
	7 MW	1.95	2.1	4.96	10.77	17.083	23.59	30.23
	8 MW	2.36	2.26	4.94	10.588	16.759	23.178	29.76
	9 MW	2.74	2.5	4.94	10.44	16.468	22.82	29.316
	10 MW	3.122	2.81	4.96	10.35	16.221	22.48	28.918

The values marked in red in the tables show combinations that result in the system being oversized, resulting in surplus gas stored in the H2 tank at the end of the annual cycle. It should also be noted that a residual amount of energy will always be present in the system. This is because the instantaneous remaining PV generation is not always fully absorbed by the electrolyzer in operation. This characteristic implies the need for refined control of the Maximum Power Point (MPPT) of the PV inverter, in order to prevent this excess generation from being translated into an unwanted variation in the frequency of the electricity grid. This observation highlights the importance of effective management and a rigorous control strategy to guarantee the stability and efficiency of the integrated system.

In addition, due to the limited operating range of alkaline electrolyzers, the implementation of this technology results in a greater accumulation of surplus energy in the system.

Table 5 - Energy surplus for each combination of Alkaline electrolyzer size and additional PV power (MWh/year).

				Additional PV Power plant				
		0MWp	5MWp	10MWp	15MWp	20MWp	25MWp	30MWp
Electrolyzer size	1 MW	4.12	9.05	15.24	21.82	28.55	35.377	42.239
	2 MW	3.878	7.77	13.32	19.56	26.06	32.68	39.4
	3 MW	4.38	7.04	11.54	17.34	23.58	29.97	36.56
	4 MW	5.21	7.02	10.57	15.521	21.39	27.52	33.909
	5 MW	6.25	7.47	10.09	14.36	19.57	25.5	31.57
	6 MW	6.98	8.08	9.99	13.56	18.336	24.4	31.11
	7 MW	7.23	9.04	10.204	13.089	17.751	24.1	30.724
	8 MW	7.25	9.94	10.94	12.91	17.634	23.8	30.39
	9 MW	7.27	11.01	11.89	12.98	17.53	23.7	30.16
	10 MW	7.28	12	13.03	13.64	17.5	23.64	29.84

Consequently, the application of PEM-type electrolyzers appears to be the most advantageous alternative. Specifically, the configuration that includes an increase of 25 MWp in PV generation combined with a 3 MW electrolyzer emerges as the most effective option. This finding is particularly justified by the fact that the electrolyzer is the most expensive component in the integrated system.

Fig. 4 outlines the annual behavior of the system in the scenario that incorporates a 3 MW electrolyzer. This graph is instrumental in elucidating the system's operating profile and efficiency over an annual cycle.

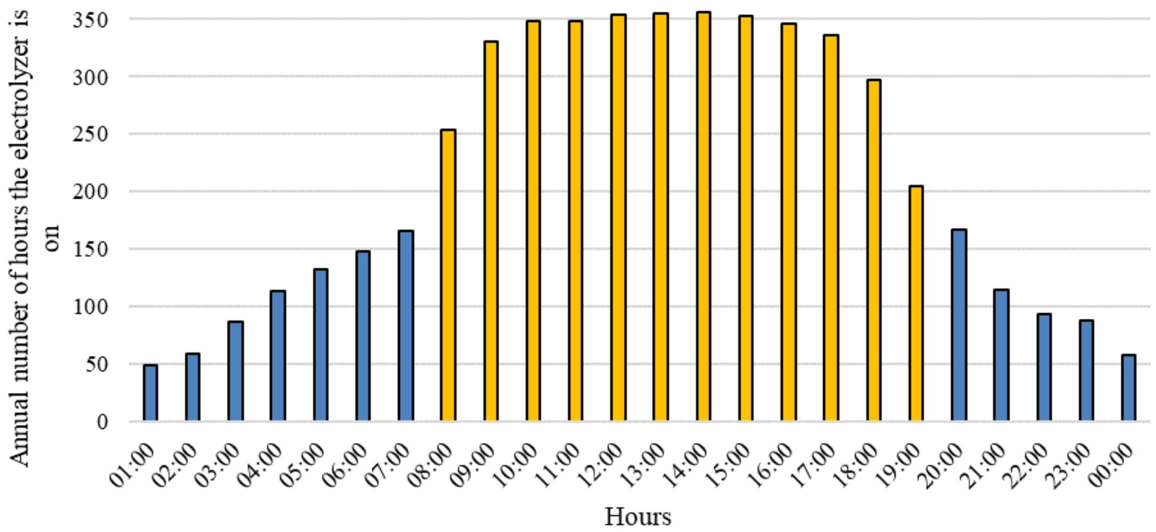

Fig. 4 – Electrolyzer annual operation.

This specific configuration results in an operating regime in which the electrolyzer is active for approximately 51% of the annual cycle. The columns highlighted in yellow denote the number of hours in which the electrolyzer is active, essentially due to the surplus of PV energy. In these moments of the day, there is a significant number of days of the year that the device operates, being practically active on more than 350 days throughout the year, specifically in the time interval between 10am and 4pm. The bars colored in blue are indicative of the periods that the electrolyzer operates because of a surplus in hydroelectric generation.

An analysis of Fig. 5 shows the annual operational profile of the optimized electrolyzer. It can be seen that, during the period from February to August, the device is in operation almost 100% of the time. Even in the months from September to January, when hydroelectric generation capacity is reduced, the electrolyzer is still activated, primarily to take advantage of the surplus of PV solar energy. However, it is crucial to point out that even in the months when the electrolyzer operates all the time, it is not necessarily working at full capacity. During these periods, it is common for the electrolyzer to operate at a load level of around 40%, as shown in the example of Fig. 6, that shows the electrolyzer load in May. This finding highlights the need for precise operational control in order to maximize the system's efficiency while maintaining the stability of the energy network.

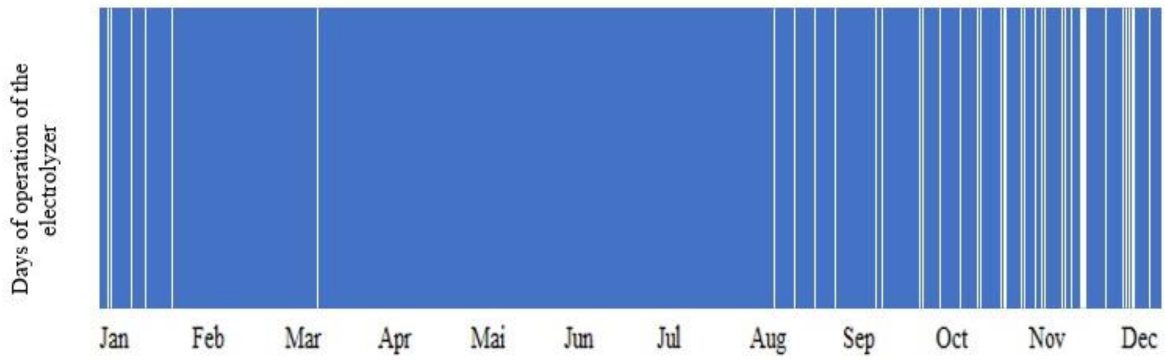

Fig. 5 - Days of operation of the electrolyzer during the year.

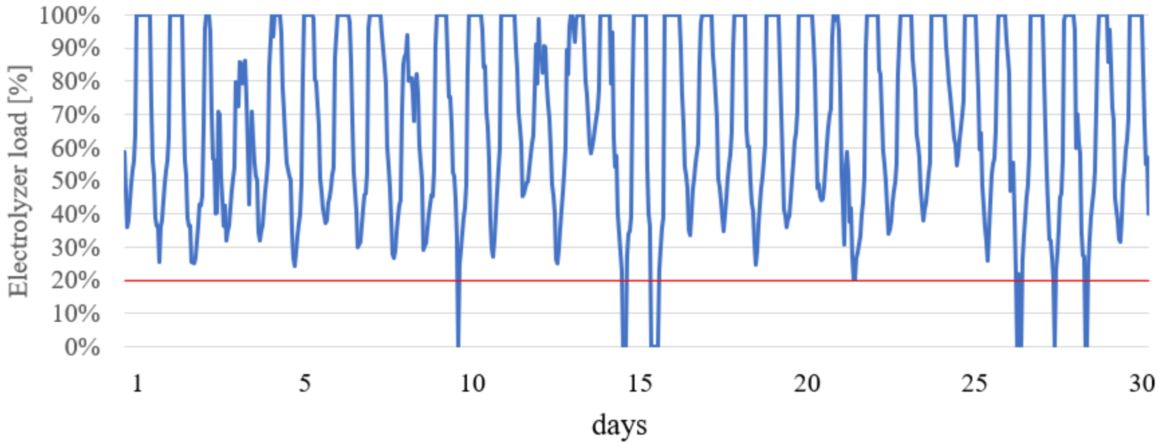

Fig. 6 – Electrolyzer load during the month of May.

Fig. 7 illustrates the fuel cell dispatch profile. The fuel cell is only required to operate between September and January. Its power peaks predominantly at the end of November, reaching values of around 4.2 MW. Given this scenario, it is imperative that the system has a fuel cell with a minimum capacity of 4.2 MW in order to fully meet the community demand. However, it is crucial to note that this component remains idle for a large part of the annual cycle.

The process of converting electrical energy into hydrogen, and subsequently hydrogen into electrical energy, presents an efficiency of approximately 25%. Although this figure is lower when compared to other energy storage methods, it is imperative to recognize the industrial value intrinsic to hydrogen. This aspect allows for an alternative sizing approach for the system, aiming for both energy autonomy and the promotion of sustainable local industrialization, thus contributing to the economic strengthening of the region in an ecologically responsible manner.

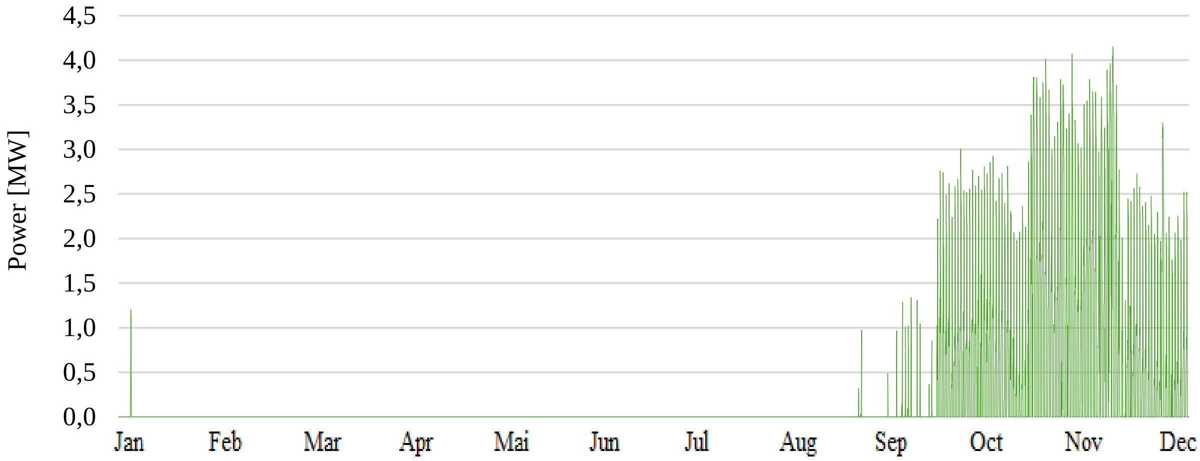

Fig. 7 - Fuel cell dispatch profile during the year.

In addition, it is worth noting that the PV generation system does not need to be centralized, which makes it possible to implement a distributed network for PV energy generation. This configuration is especially advantageous for the production of green hydrogen, since this element acts as a positive charge within the energy system. This panorama suggests an operational flexibility that can be exploited to optimize both the energy efficiency and the industrial and environmental impact of the integrated system.

Conclusions

The study provides insights into the potential of long-term H2 storage, and its advantages compared to conventional battery storage for off-grid communities, focusing on the case of an isolated community in the Brazilian Amazon. The findings of this study indicate that a combination of storage system is recommended to optimize energy supply, with lithium-ion batteries compensating for daily load fluctuations and the H2 storage system addressing annual variations in generation. Simulations and sensitivity analysis were performed to determine the optimal sizing of components, also considering the expansion of the PV system installed in the community. The results show that a battery storage system with a capacity of 16 MWh and a 2 MW Power Conversion System is necessary to meet the community's daily energy needs during high-usage months. It was also demonstrated the importance of the correct sizing of the H2 tank, in order to avoid energy losses and energy deficits. A tank of 2.5 M Nm^3 was calculated to be the optimal size for the analyzed system.

A sensitivity analysis of electrolyzer and the additional PV system sizes revealed optimized combinations that can meet the H2 gas demand in the system. A system with additional 25 MWp in PV generation combined with a 3 MW alkaline electrolyzer resulted in the most effective option. The operational analysis of this optimum sizing indicates that the electrolyzer is in operation on approximately 51% of the days of the year, with an almost constant production of hydrogen during the period from February to September. This behavior suggests a relatively high efficiency of this component, especially when we consider that it is the most expensive element in the energy system in question.

For the community under study, the projection is that the fuel cell will need to have a capacity of 4.2 MW and that its operation will be restricted to the months of September to January. The need for a 4.2 MW fuel cell to operate only in certain months of the year reveals a possible gap in the overall efficiency of the system, considering that the component remains inactive for a significant portion of the year. The results also indicate that a different system-sizing strategy that aspires to achieve not only energy autonomy, but also sustainable local industrialization can be beneficial, bolstering the region's economy in an environmentally responsible way.

The present study was limited to technically evaluating the incorporation of storage systems for the total decarbonization of Oiapoque. Given this, considerations to be evaluated for future work include the financial assessment, considering all the peculiarities of initial cost, logistical problems, financial incentives, and the local development of specialized labor. Furthermore, it is important that a future study also evaluates the prerogatives of greenhouse gas emissions in the complete energy production cycle in the locality, from the manufacturing process of the components to the disposal and recycling process, aiming for a comparison of greenhouse gas emissions in the project's lifecycle.

Acknowledgements

This publication was made possible by the project in partnership between UFSC and the H2Brasil project. The H2Brasil project is part of the Brazil-Germany Cooperation for Sustainable Development and is implemented by the Deutsche Gesellschaft für Internationale Zusammenarbeit (GIZ) GmbH and the Ministry of Mines and Energy (MME) and financed by the Federal Ministry of Economic Cooperation and Development (BMZ) of Germany. DOS acknowledges the National Council for Scientific and Technological Development (CNPq) for a doctoral scholarship.

References

Alshahrani, A., Omer, S., Su, Y., Mohamed, E. and Alotaibi, S., 2019. The technical challenges facing the integration of small-scale and large-scale PV systems into the grid: A critical review. *Electronics (Switzerland)*, 8(12). https://doi.org/10.3390/electronics8121443.

Carvalho, G.O., 2006. Environmental Resistance and the Politics of Energy Development in the Brazilian Amazon. *The Journal of Environment & Development*, 15(3), pp.245–268. https://doi.org/10.1177/1070496506291575.

Chen, H., Cong, T.N., Yang, W., Tan, C., Li, Y. and Ding, Y., 2009. Progress in electrical energy storage system: A critical review. *Progress in Natural Science*, 19(3), pp.291–312. https://doi.org/10.1016/j.pnsc.2008.07.014.

Empresa de Pesquisa Energética (EPE) and Ministério de Minas e Energia (MME/SPE), 2018. *Sistemas Isolados: Estudo de alternativas para suprimento de energia elétrica ao Oiapoque pelo Sistema Interligado Nacional*. [online]

Available at: <http://www.epe.gov.br>.

Møller, K.T., Jensen, T.R., Akiba, E. and Li, H. wen, 2017. Hydrogen - A sustainable energy carrier. *Progress in Natural Science: Materials International*, 27(1), pp.34–40. https://doi.org/10.1016/j.pnsc.2016.12.014.

Oliveira, A.K.V.D., Azevedo, K.L.R.D., Santos, D.O.D., Aghaei, M., Rüther, R., Orabona, R. and Naspolini, H., 2023. Assessing the Potential of Green Hydrogen in Decarbonizing Off-Grid Amazonian Communities. In: *2023 International Conference on Future Energy Solutions (FES)*. [online] 2023 International Conference on Future Energy Solutions (FES). Vaasa, Finland: IEEE. pp.1–6. https://doi.org/10.1109/FES57669.2023.10182925.

Pereira, E.B., Martins, F.R., Gonçalves, A.R., Costa, R.S., Lima, F.J.L. de, Rüther, R., Abreu, S.L. de, Tiepolo, G.M., Pereira, S.S.V. and Souza, J.G. de, 2017. *Atlas brasileiro de energia solar*. [online] São José dos Campos: Universidade Federal de São Paulo. https://doi.org/10.34024/978851700089.

Ribeiro, L.A. de S., Saavedra, O.R., Lima, Shigeaki.L., de Matos, J.G. and Bonan, G., 2012. Making isolated renewable energy systems more reliable. *Renewable Energy*, 45, pp.221–231. https://doi.org/10.1016/j.renene.2012.02.014.

Sterner, M. and Stadler, I. eds., 2019. *Handbook of Energy Storage*. [online] Berlin, Heidelberg: Springer Berlin Heidelberg. https://doi.org/10.1007/978-3-662-55504-0.

Suleman, F., Dincer, I. and Agelin-Chaab, M., 2015. Environmental impact assessment and comparison of some hydrogen production options. *International Journal of Hydrogen Energy*, 40(21), pp.6976–6987. https://doi.org/10.1016/j.ijhydene.2015.03.123.

Performance of mixed phase TiO_2 film samples immobilized on a 2-D flat plate surface in photo catalytic applications and reusability

Tripurari Kumar Harsh[1, 2,3], S K Samdarshi[1, 2,3*], Uday Deshpande[3], Bhola Kumar[1], Md. Rahbar Jamal[1,2], Rahul Kumar Rajak[1], and A.S Bhattacharya[2]

[1] Department of Energy Engineering, Central University of Jharkhand, Ranchi (India)

[2] Centre of Excellence in Green and Efficient Energy Technology, CUJ, Ranchi, Jharkhand (India)

[3] UGC-DAE CSR, Indore 452001,MP (India)

Abstract

TiO_2 is well known photocatalyst for environmental remediation technology with a green approach of oxidation and reduction using solar irradiation. In this study three TiO_2 samples were successfully synthesized using sol-gel method and then calcined at 550°C, 650°C and 750°C(termed as Ti-550, Ti-650, and Ti-750, respectively). The prepared nano-powder samples were immobilized as two dimension (2-D) thin film over glass plate surface using doctor-blade method. The characterization of the prepared photocatalysts was done using X-Ray diffractometer (XRD), UV-Vis diffuse reflectance spectroscopy (DRS) and photoluminescence (PL) spectroscopy. The resultant samples were nanoscale systems of pure anatase, and anatase-rutile mixed phase. The band gap of the nano-catalyst samples Ti-550, Ti-650, and Ti-750 were found to be 3.04 eV, 2.97 eV, and 2.92 eV, respectively. The theoretical modeling and analysis of the samples was done by Materials Studio® software and the optical characterization was done with its CASTEP module using DFT. The performance of the samples was studied by methylene blue (MB) dye degradation kinetics under solar radiation (avg. 955 W/m^2) outdoors. We conducted reusability tests on the coated samples for three cycles, with the Ti-650 sample exhibiting the highest rate constant in each degradation cycle. This may be attributed to the suitable band gap, phase ratio, and the resultant reduction in recombination of the photo-generated charge-carriers of the nano-samples. The rate constants of three continuous cycle of Ti-650 thin flim samples were calculated to be 0.00809, 0.00511 and 0.00508 per minute wherein a stabilization in performance is seen after second cycle.

Keywords: Titania, Mixed phase, Thin flim, Phase ratio, Reusability, Theoretical analysis

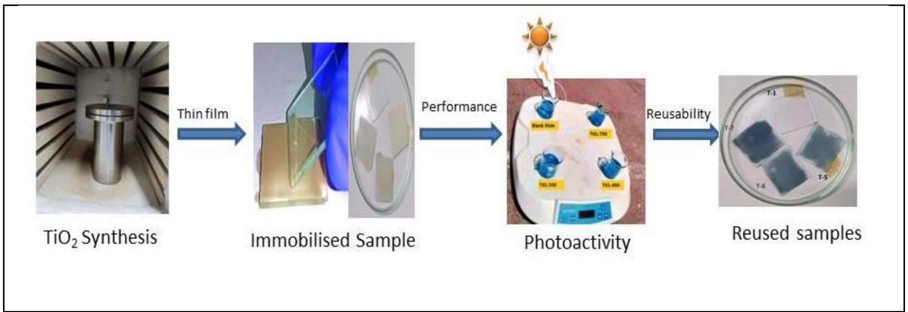

1. Introduction

As energy and environmental concerns and the need for sustainable solutions continue to grow, the utilization of titanium dioxide (TiO_2) thin films for the degradation of organic pollutants under outdoor solar irradiation has emerged as a promising and eco-friendly approach. TiO_2 thin films have garnered significant attention due to their abundance, exceptional photocatalytic properties, durability, and reusability, making them a valuable and versatile semiconductor material with a wide range of applications in various fields of photocatalytic hydrogen production, carbon valorization, including environment remediation [1-3].

TiO_2 exists in several crystalline phases, with the three most common ones being anatase, rutile, and brookite

10.18086/swc.2023.13.01 Available at http://proceedings.ises.org

phase. Each of these phases possesses distinct structural and electronic characteristics that influence their catalytic performance under solar irradiation. The bandgap of anatase and brookite TiO_2 falls within the ultraviolet (UV) region of the electromagnetic spectrum, and are highly effective in utilizing UV solar radiation for photocatalytic reactions. Anatase TiO_2 has been extensively employed in applications such as water splitting, pollutant degradation, and hydrogen production due to its exceptional photoactivity. The rutile phase of TiO_2 is another important crystalline form, known for its exceptional stability and relatively narrower bandgap compared to anatase. Rutile TiO_2 is less active under UV light but becomes increasingly efficient under visible light irradiation. The mixed phase of TiO_2 is the least common among the three major phases but is gaining attention for its unique photocatalytic properties. Understanding the unique properties and capabilities of each of the TiO_2 phase is essential for harnessing their full potential in sustainable and energy-efficient photocatalytic processes, contributing to a cleaner and more sustainable future [3-14].

The utilization of titanium dioxide (TiO_2) immobilized onto a substrate in the form of thin films has emerged as a promising and eco-friendly approach due to their exceptional durability, reusability, and insignificant loss of the catalyst, making it a valuable system. TiO_2 thin films are engineered structures that consist of a thin layer of TiO_2 deposited onto a multidimensional substrate. These films possess several advantages for photocatalytic applications under outdoor conditions. Furthermore, the thin film format allows for easy integration into various outdoor settings, for some specific applications such as wastewater treatment plants, polluted air purification systems, and self-cleaning surfaces on buildings and infrastructure including others [15-21].

As indicated, one of the most remarkable features of TiO_2 thin films is their reusability. Unlike some traditional catalysts that degrade or require regeneration after a single use, TiO_2 thin films can be employed repeatedly without significant loss of catalyst material and catalytic activity. This property is of utmost importance for cost-effectiveness and sustainability. By simply exposing the thin films to natural outdoor sunlight, any absorbed/adsorbed organic pollutants or other reactive species are degraded, and the catalyst is regenerated, and is ready for reuse. The reusability of TiO_2 thin films not only reduces operational costs but also minimizes the environmental footprint of pollution remediation and energy conversion processes. This approach aligns with the principles of green chemistry and sustainable development, contributing to a cleaner and healthier environment. Moreover, the ability to deploy these thin films in outdoor settings means that they can address pollution at its source, preventing the accumulation of harmful substances in our ecosystems [22, 23].

2. Experimental details

2.1. Synthesis of nanoparticles

The synthesis of mixed phase TiO_2 nanoparticles using the sol gel method of synthesis of titanium dioxide is a well-known technique. Titanium tetra isopropoxide (TTIP) was purchased from Sigma-Aldrich, and isopropyl alcohol from Merck, India. The triton X solvent (LR grade) was from Sigma-Aldrich, India. In all of the experiments, double-distilled water was used, and all of the chemicals employed in the synthesis were of analytical grade. TTIP and 2-propanol were taken in 1:10 ratio. After 15 minutes, 0.5 mL of DI water was added in the sol while being constantly stirred for 16 hours. The produced gel was aged for 12 hours and then dried at 80^{o}C for 12 hours. To obtain crystalline nanoparticles, the final product was calcined in air for two hours at 550, 650, and 750^{o}C with a ramping rate of 5^{o}C. Henceforth, these samples are referred to as Ti-550 , Ti-650 and Ti-750 respectively.

2.2. Characterization

The structural properties of titanium dioxide samples prepared at different temperatures were analyzed by X-ray diffractometer (Proto AXRD Benchtop, Canada). The spectral response was assessed using UV–Vis–NIR spectrophotometer with DRS (UV 3600 Plus, Shimadzu, Japan). The trap states of the samples were identified using photoluminescence (PL) spectrum obtained from photoluminescence spectrometer (Fluromax-4, Horiba Scientific, USA).

2.3 Thin film deposition

The glass substrate we thoroughly cleaned using acetone, water, and sonication; and then dried. The photocatalyst material was formed into slurry for this to create the binder solution; the photocatalyst nano particles (20 mg), triton X solvent (2 drops), and acetic acid (2 drops) were progressively mixed. Using the doctor blade approach, the photocatalyst slurry of was applied to the substrate surface. After deposition, the layer was kept at 60°C on a hot plate for two hours before cooling in the open to form a stable film on the substrate [Fig.1].

2.4 Photocatalytic activity test:

The activity of the immobilized catalyst was evaluated by the degradation kinetics of aqueous methylene blue as probe pollutant over it under outdoor solar irradiation. The degradation kinetics was assessed under a catalyst loading of 0.5 g/l. To ensure adsorption-desorption equilibrium the system was initially kept in dark for 30 min. Then, the system was exposed to outdoor solar irradiation and sampling was done at an interval of 30 min. Finally, the collected sample was centrifuged before conducting photometric studies on the resultant solution for degradation analysis.

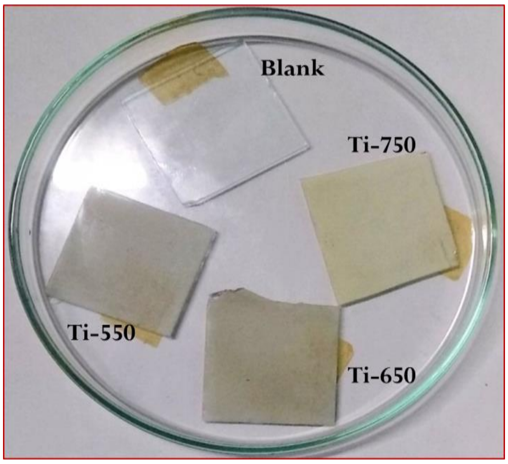

Fig.1: Different TiO_2 samples coated on plate surface

3. Result & discussion:

3.1. XRD analysis

Fig.2 shows the XRD spectra of TiO_2 nanoparticles samples. From XRD pattern it is revealed that the Ti-550 corresponds to pure anatase phase (JCPDS File No.894203). The samples Ti-650 and Ti-750 both correspond to anatase-rutile mixed phase (JCPDS File No.894203 and 894920). The crystallite sizes of the particles were calculated using Scherrer's formula, $D=k\lambda/\beta\cos\theta$; where D is the average crystallite size and k is the shape factor taken as 0.9, λ is the wavelength of X-ray radiation (Cu Kα =1.5406 Å), β is the full width at half-maximum intensity (in radian) and θ is the diffraction angle. The anatase and rutile mass fraction and anatase to rutile (A/R) ratio were calculated using Spurr's equation: $fa= (1+1.26Ir/Ia)^{-1}$, fr= (1-fa) and A/R= (fa/fr); where fa and fr are anatase and rutile mass fraction, and Ia and Ir are the most intense anatase and rutile peak, respectively [9-11]. The crystallite size and phase composition of each TiO_2 nanoparticles at different temperatures are given in Table.1. XRD spectra reveal that at temperature 550°C pure anatase phase was formed. The mixed phase transition was identified at 650°C which could be seen to continue up to 750°C in the form of anatase and rutile. The crystallite size as well as rutile ratio of the samples increased with the increase in the temperature.

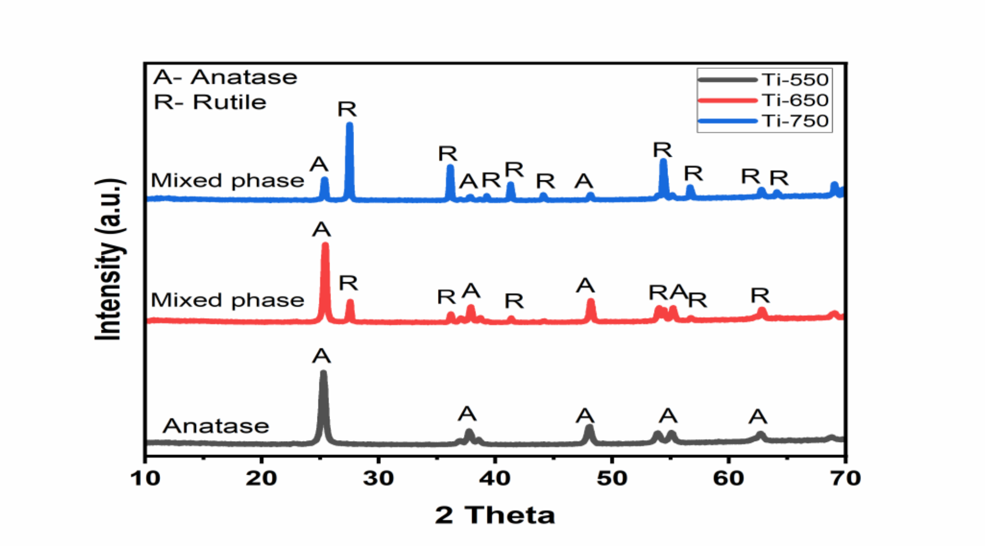

Fig.2. XRD pattern of titanium dioxide catalyst calcined at different temperatures

Tab 1: Shows the crystallite size and phase composition of TiO_2 nanoparticles at different temperatures

Sample	Calcination temp (^oC)	Crystallite size (nm)		Fraction (%)		A/R ratio
		Anatase (A)	Rutile (R)	Anatase	Rutile	
Ti-550	550	20.56	0	100	0	∞
Ti-650	650	28.18	36.29	72.82	27.18	2.68
Ti-750	750	35.40	40.22	19.47	80.53	0.24

3.2. UV-VIS DRS analysis

The optical characteristics of the samples were examined using the UV-VIS DRS spectra. In Fig. 3(a) and (b), samples that were calcined at a higher temperature exhibit a red shift in the wavelength. As the calcination temperature rises, the samples band gap gradually narrows. Absorbance was obtained from the diffuse reflectance using Kubelka-Munk transformation. Bandgap was calculated from the Kubelka-Munk absorbance using Tauc plot shown in Fig. 3(b). The band gap variations between the samples can be attributed to thermally induced defects in the red-shifted samples and changes in the crystallite phases of the individual samples. It is evident from the bandgap (i.e. 2.9eV-3.1 eV) that the samples absorb in UV-Vis range of solar spectrum so it would be interesting to study the photoactivity in the outdoor solar spectra.

(a) (b)

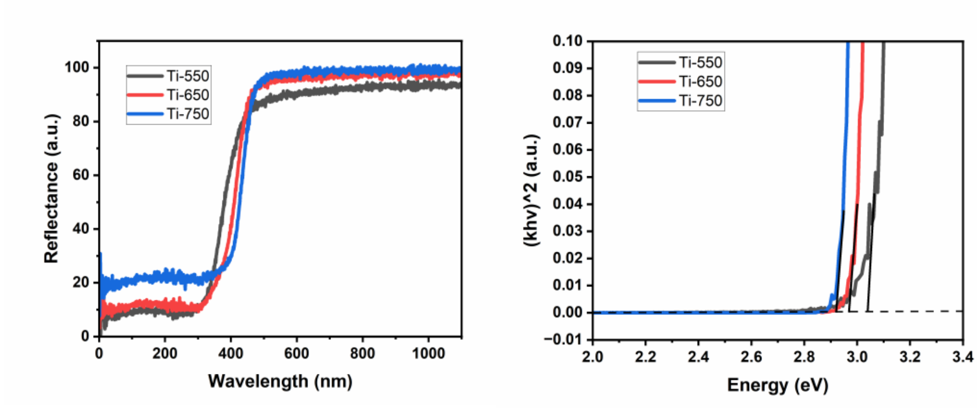

Fig.3: (a) UV–Vis diffuse reflectance spectra of samples (b) Bandgap of the prepared samples

3.3. PL spectra analysis

The photoluminescence spectra of the samples were recorded at the six different excitation wavelengths starting from 325 nm to 425 nm in the progressive interval of 25 nm and at 500 nm. Fig 3(a) shows that at high energy photon excitation the rutile dominant mixed phase has high quenching and hence least carrier recombination. Fig 3(b) also has similar results but, in this case, the emission wavelength peaks at the lower wavelengths 405 nm, 440 nm and 450 nm correspond to the band gap of the Ti-550, Ti-650 and Ti-750 samples, respectively, which may be attributed to the close proximity of the excitation wavelength to the band gap.. Figs 3(c) and (d) provide identical conclusion with poor resolution attributable to the excitation wavelength. Interestingly, with excitation wavelength in or close to visible range the quenching pattern shows a reversal with Ti-750 (mixed phase) showing least quenching with high intensity emission and, hence, high recombination (Fig 3(e) and (f)). Thus, the low temperature samples are expected to show more photocatalytic activity. But high quenching in Ti-550 may be because of low emission due to decreased absorption of low energy excitation wavelength. Ti-650, however, shows genuine non-zero quenching attributatble to decreased recombination. Ti-750 shows high quenching in spite of high conductivity which may because resonance of the excitation wavelength with the system trap level/band gap as shown in fig (a-d). The broad peaks between 400 nm to 650 nm may be attributed to the presence of the defects state and oxygen vacancies at higher temperature. It is evident from the PL spectra that recombination in the sample treated at higher temperature is lowered as compared to the samples treated at lower temperatures, This may be due to higher oxygen vacancies created in the high temperature samples due to induced defect levels and change in the crystallite phases.

(a) (b) (c)

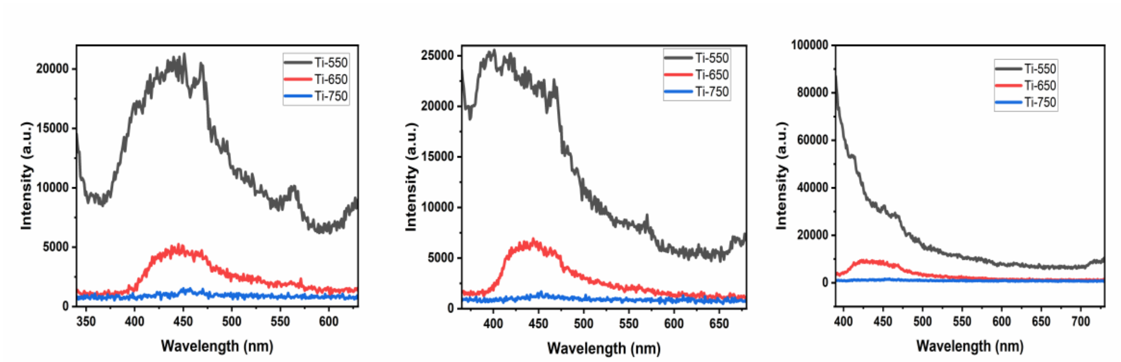

(d) (e) (f)

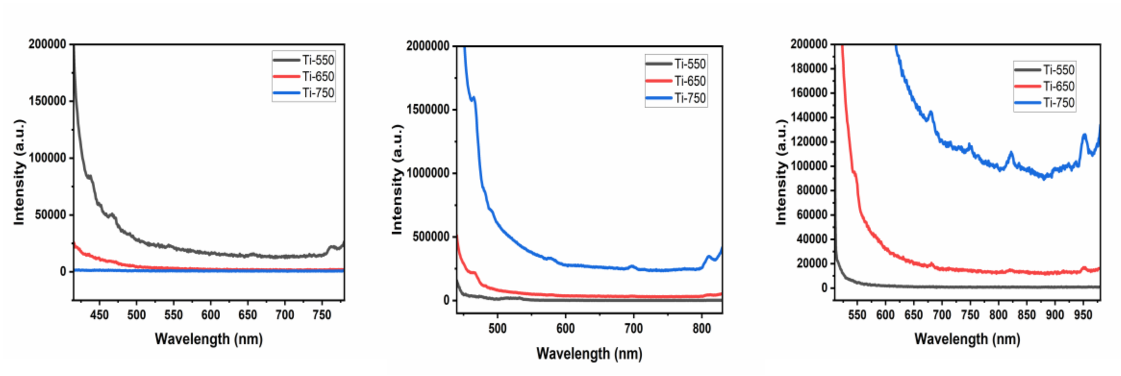

Fig. 4: Photoluminescence excitation spectra of samples at high energy (UV) wavelength of (a) 325nm (b) 350nm (c) 375 nm (d) 400nm and at low energy (Visible) wavelength of (e) 425 nm and (f) 500nm.

3.4. Computational modeling and analysis:

This theoretical analysis has been conducted using the Perdew-Burke-Ernzerhof module programme in BIOVIA Materials Studio version 2017 R2 (Dassault Systems). It was combined with an ultra-soft pseudo potential and a plane wave basis set with a kinetic energy cut-off of 380 eV. For the theoretical investigation, the anatase and rutile phases of the titanium crystal structure were used. Electronic band structures of the crystals were calculated using Koelling-Harmon grid settings on the optimized geometry crystal with 3×3×2 k-points sampling. Atomic coordinates and cell parameters were optimized during the iterative optimization process. The CASTEP computation calculation and analysis were performed on the optimized crystal band. The band gap of a anatase structure was larger than a rutile structure. The band gap (E_g) and density of states (DOS) of anatase(101) and rutile(110) phase layer were 2.078, and 1.879eV respectively as shown in the fig.5 its prediction is always less than the experimental analysis and supports the order of the bandgap of phases of the samples [24,25].

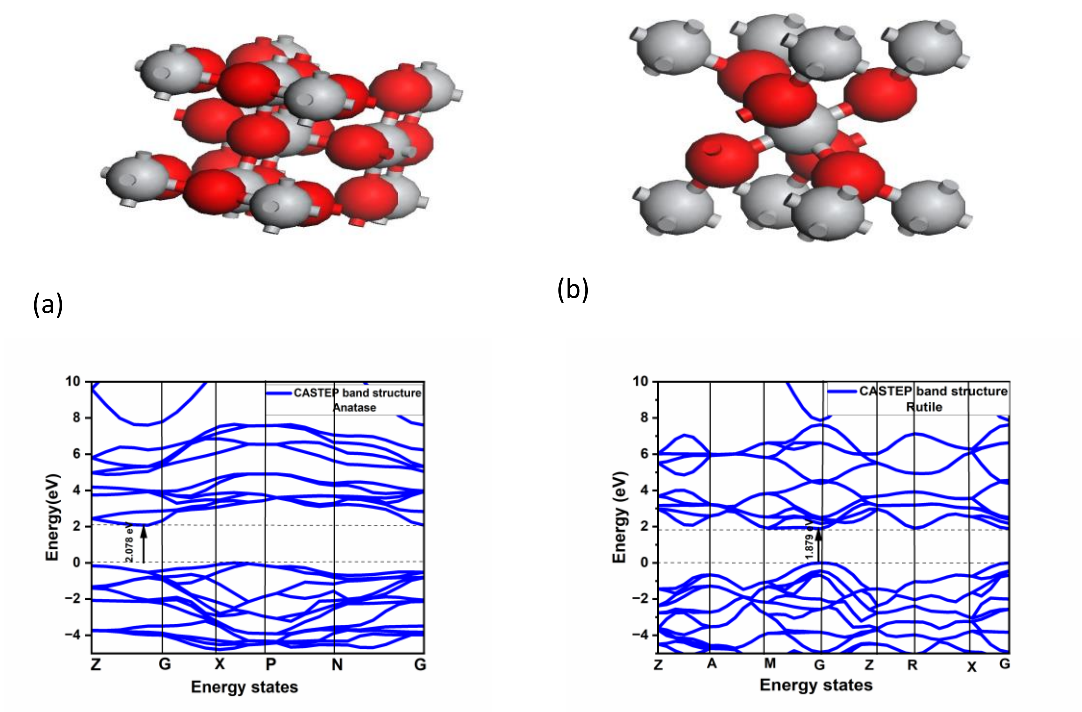

(c)

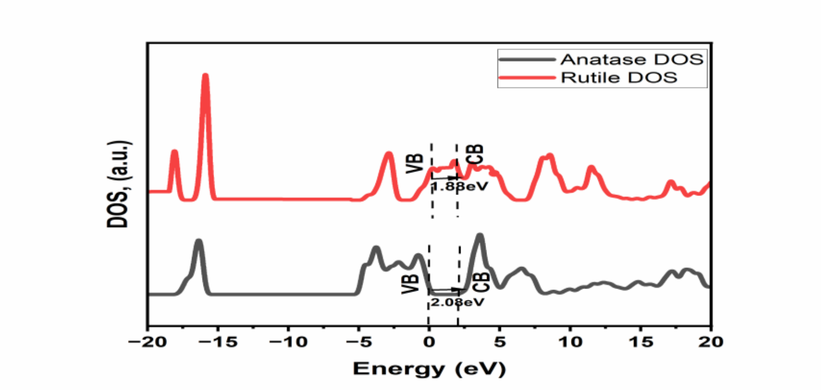

Fig.5: Crystal structure and bandgap of (a) anatase and (b) rutile, respectively; Crystal (Note: Red and white sphere represent oxygen and titanium, respectively (c) Density of states of anatase and rutile

4. Photo-activity analysis

The photoactivity test of the photocatalyst was performed under available outdoor solar irradiation during solar noon (900-970 W/m^2, Table 2) using methylene blue dye degradation. The dye degradation rate of each sample is calculated using pseudo-first order kinetics. The calculated band gap and rate constant is given in the Table 3 The rate constant value discloses that the mixed phase samples are more active in outdoor solar irradiation. The kinetics of degradation of rate constant of reusability activity of three cycles is shown in fig.6. The photocatalytic rate constant for Ti-650 sample is the highest in each cycle. The catalyst weight loss after each cycle activity is shown in the table 4. The catalyst weight loss is more in the first cycle activity and then becomes stable and very less catalyst loss of each sample afterwards cycle. This may be as a result of the creation of higher oxygen vacancies induced trap states as well as band offset at the rutile-anatase interface.

Tab 2: Outdoor solar radiation data

Activity time	10:30 am	11:00 am	11:30 am	12:00 pm	12:30 pm	01:00 pm
Direct Solar Irradiation(W/m^2)	Dark	955	970	965	970	900

Tab. 3: Calcined temperature, Band gap and rate constant in outdoor irradiation for different samples.

Sample	Calcined temperature(^{o}C)	Bandgap (eV)	Rate constant (K) in outdoor solar irradiation (min^{-1})		
			Test 1	Test 2	Test 3
Blank	--	--	0.00349	0.00336	0.00359
Ti-550	550	3.04	0.00636	0.00425	0.00400
Ti-650	650	2.97	0.00809	0.00511	0.00508
Ti-750	750	2.92	0.00723	0.00453	0.00418

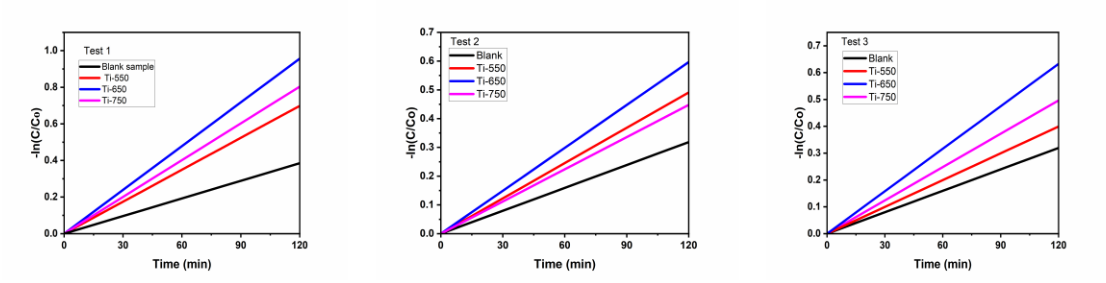

Fig.6: Kinetics of degradation for calculation of rate constant of reusability activity (a) cycle test 1 (b) cycle test 2 and (c) cycle test 3.

Tab:4 Catalyst weight loss after each cycle of degradation activity

Sample	Blank slide weight (mg)	Coated weight (mg)	Weight after reusability (mg)	Weight after second reusability(mg)	Weight after third reusability(mg)
Blank slide	2144.80	2144.80	2144.80	2144.80	2144.80
Ti- 550	2149.77	2163.10	2159.05	2157.70	2757.05
Ti- 650	2179.12	2192.82	2189.40	2187.62	2187.25
Ti- 750	2064.05	2077.42	2074.00	2072.21	2071.77

(a) **(b)**

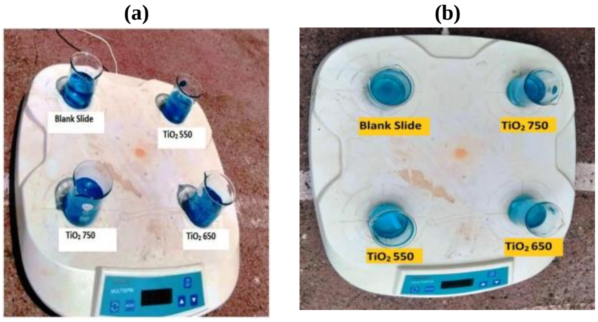

.

Fig.7: photoactivity test (a) before and (b) after

5. Mechanism

The high photo activity under outdoor solar irradiation may be ascribed to the interfacial behavior of the band offset and oxygen vacancies in mixed phase titania nanoparticles. The band gap and carrier recombination are both significantly reduced when there are defects at the junction, which raises the photocatalytic activity. The mechanism shown in Fig 9(a) and (b) has been framed based on the behavior of PL spectra of the samples at different excitation wavelength, wherein, there is a reversal of quenching after an excitation wavelength of 400nm, i.e in the visible range [9]. The movement of the carriers under UV and visible irradiation, respectively, are shown in Fig 9(a) and 9(b).

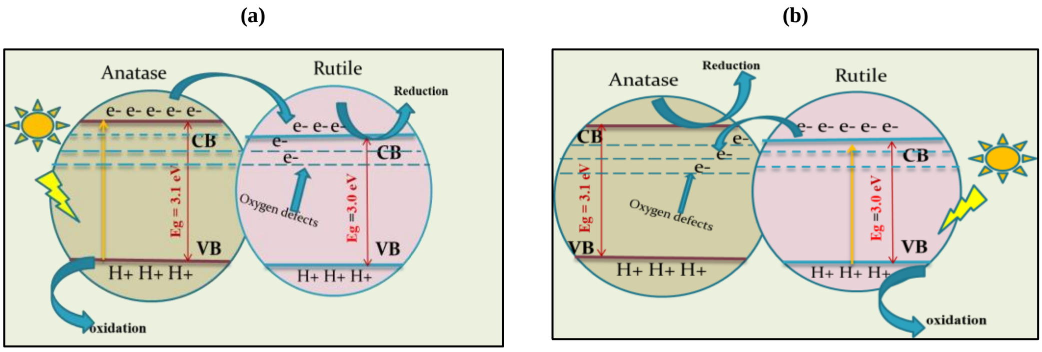

Fig.9: highly active mixed phase junction of anatase and rutile for (a) wavelength < 400nm (b) wavelength > 400nm.

6. Conclusion

TiO_2 thin films represent a remarkable and sustainable solution for the degradation of organic pollutants under outdoor solar irradiation. Mixed phase Ti-650 samples shows highest rate constant which may be attributed to their suitable bandgap, anatase-rutile phase ratio, defect states, band offset and the crystallite size. The ability of mixed phase thin films to harness solar radiation, together with their reusability, places them as a vital technology in the quest for environmental remediation and other energy applications.. The reusable application of TiO_2 thin films holds great promise for a more sustainable and cleaner future.

7. Acknowledgments

1) This work was carried out using the facilities of Centre of Excellence in Green and Efficient Energy Technology (CoE-GEET), DEE, Central University of Jharkhand, Ranchi-835205
2) “This work was partially carried out using the facilities of UGC-DAE CSR. The authors acknowledge the financial support from UGC-DAE CSR through a Collaborative Research Scheme (CRS) project number CRS/2021-22/01/403”

8. References

1) Athanasekou, Chrysoula P., Vlassis Likodimos, and Polycarpos Falaras. "Recent developments of TiO2 photocatalysis involving advanced oxidation and reduction reactions in water." Journal of environmental chemical engineering 6.6 (2018): 7386-7394.

2) Wei, Yaqing, Marina V. Tokina, Alexander V. Benderskii, Zhaohui Zhou, Run Long, and Oleg V. Prezhdo. "Quantum dynamics origin of high photocatalytic activity of mixed-phase anatase/rutile TiO_2." *The Journal of Chemical Physics* 153, no. 4 (2020).

3) Liu, Hongli, Yaping Ma, Jiangyao Chen, Meicheng Wen, Guiying Li, and Taicheng An. "Highly efficient visible-light-driven photocatalytic degradation of VOCs by CO_2-assisted synthesized mesoporous carbon confined mixed-phase TiO_2 nanocomposites derived from MOFs." *Applied Catalysis B: Environmental* 250 (2019): 337-346.

4) Lin, Xiaojing, Mingxuan Sun, Bowen Gao, Wen Ding, Zihan Zhang, Sambandam Anandan, and Ahmad Umar. "Hydrothermally regulating phase composition of TiO_2 nanocrystals toward high photocatalytic activity." *Journal of Alloys and Compounds* 850 (2021): 156653.

5) Paumo, Hugues Kamdem, Sadou Dalhatou, Lebogang Maureen Katata-Seru, Boniface Pone Kamdem, Jimoh Oladejo Tijani, Venkataraman Vishwanathan, Abdoulaye Kane, and Indra

Bahadur. "TiO_2 assisted photocatalysts for degradation of emerging organic pollutants in water and wastewater." *Journal of Molecular Liquids* 331 (2021): 115458.

6) Lal, Manmohan, Praveen Sharma, and Chhotu Ram. "Calcination temperature effect on titanium oxide (TiO_2) nanoparticles synthesis." *Optik* 241 (2021): 166934.

7) Kim, Min Gu, Jeong Min Kang, Ji Eun Lee, Kang Seok Kim, Kwang Ho Kim, Min Cho, and Seung Geol Lee. "Effects of calcination temperature on the phase composition, photocatalytic degradation, and virucidal activities of TiO_2 nanoparticles." *ACS omega* 6, no. 16 (2021): 10668-10678.

8) Assayehegn, Elias, Ananthakumar Solaiappan, Yonas Chebude, and Esayas Alemayehu. "Fabrication of tunable anatase/rutile heterojunction N/TiO2 nanophotocatalyst for enhanced visible light degradation activity." *Applied Surface Science* 515 (2020): 145966.

9) Verma, Ranjana, and S. K. Samdarshi. "Correlating oxygen vacancies and phase ratio/interface with efficient photocatalytic activity in mixed phase TiO2." *Journal of Alloys and Compounds* 629 (2015): 105-112.

10) Nair, Ranjith G., Samrat Paul, and S. K. Samdarshi. "High UV/visible light activity of mixed phase titania: A generic mechanism." *Solar energy materials and solar cells* 95, no. 7 (2011): 1901-1907.

11) Verma, Ranjana, S. K. Samdarshi, Kalpana Sagar, and B. K. Konwar. "Nanostructured bi-phasic TiO2 nanoparticles grown on reduced graphene oxide with high visible light photocatalytic detoxification." *Materials Chemistry and Physics* 186 (2017): 202-211.

12) Ramchiary, Anjalu, S. K. Samdarshi, and T. Shripathi. "Hydrogenated mixed phase Ag/TiO2 nanoparticle–A super-active photocatalyst under visible radiation with multi-cyclic stability." *Solar Energy Materials and Solar Cells* 155 (2016): 117-127.

13) Ali, Imran, Gi-Beom Han, and Jong-Oh Kim. "Reusability and photocatalytic activity of bismuth-TiO2 nanocomposites for industrial wastewater treatment." *Environmental research* 170 (2019): 222-229.

14) Lin, Xiaojing, Mingxuan Sun, Bowen Gao, Wen Ding, Zihan Zhang, Sambandam Anandan, and Ahmad Umar. "Hydrothermally regulating phase composition of TiO2 nanocrystals toward high photocatalytic activity." *Journal of Alloys and Compounds* 850 (2021): 156653.

15) Samy, Mahmoud, Mona G. Ibrahim, Mohamed Gar Alalm, Manabu Fujii, Shinichi Ookawara, and Teruhisa Ohno. "Photocatalytic degradation of trimethoprim using S-TiO2 and Ru/WO3/ZrO2 immobilized on reusable fixed plates." *Journal of Water Process Engineering* 33 (2020): 101023.

16) Mahmood, Asad, and Jae-Woo Park. "TiO2/CdS nanocomposite stabilized on a magnetic-cored dendrimer for enhanced photocatalytic activity and reusability." *Journal of colloid and interface science* 555 (2019): 801-809.

17) Shen, Yinghua, Xiang Yu, Weitian Lin, Yi Zhu, and Yuanming Zhang. "A facile preparation of immobilized BiOCl nanosheets/TiO2 arrays on FTO with enhanced photocatalytic activity and reusability." *Applied Surface Science* 399 (2017): 67-76.

18) Moma, John, and Jeffrey Baloyi. "Modified titanium dioxide for photocatalytic applications." Photocatalysts-Applications and Attributes 18 (2019): 10-5772.

19) Kocijan, Martina, Lidija Ćurković, Igor Bdikin, Gonzalo Otero-Irurueta, María J. Hortigüela, Gil Gonçalves, Tina Radošević, Damjan Vengust, and Matejka Podlogar. "Immobilised rGO/TiO2 nanocomposite for multi-cycle removal of methylene blue dye from an aqueous medium." Applied Sciences 12, no. 1 (2022): 385.

20) Raza, N., Raza, W., Gul, H., Azam, M., Lee, J., Vikrant, K., & Kim, K. H. (2020). Solar-light-active silver phosphate/titanium dioxide/silica heterostructures for photocatalytic removal of

organic dye. Journal of Cleaner Production, 254, 120031.

21) Ali, I., Han, G.B. and Kim, J.O., 2019. Reusability and photocatalytic activity of bismuth-TiO2 nanocomposites for industrial wastewater treatment. Environmental research, 170, pp.222-229.

22) Bento, Rodrigo T., Olandir V. Correa, and Marina F. Pillis. "On the surface chemistry and the reuse of sulfur-doped TiO2 films as photocatalysts." Materials Chemistry and Physics 261 (2021): 124231.

23) Malakootian, Mohammad, Alireza Nasiri, and Majid Amiri Gharaghani. "Photocatalytic degradation of ciprofloxacin antibiotic by TiO2 nanoparticles immobilized on a glass plate." Chemical Engineering Communications 207, no. 1 (2020): 56-72.

24) Xing, Jiahui, Yuzheng Wang, Yusheng Wu, Laishi Li, and Pengwei Liu. "Influence of calcination temperature on the microstructure and photocatalysis performance of B/Sm-TiO2 nanomaterials." *Vacuum* 212 (2023): 112063.

25) Ibrahim, Qusai, Rokhsareh Akbarzadeh, and Salem Gharbia. "The electronic properties and water desalination performance of a photocatalytic TiO2/MoS2 nanocomposites bilayer membrane: A molecular dynamic simulation." *Journal of Molecular Modeling* 28, no. 3 (2022): 61.

14. Solar Energy Advances: SWC 2023 Select Papers

Analysis of the performance and operation of a photovoltaic-battery heat pump system based on field measurement data

Baraskar, S., Günther, D., Wapler, J., Lämmle, M.

Abstract

Photovoltaic-heat pump (PV-HP) combinations with battery and energy management systems are becoming increasingly popular due to their ability to increase the autarchy and utilization of self-generated PV electricity. This trend is driven by the ongoing electrification of the heating sector and the growing disparity between growing electricity costs and reducing feed-in tariffs in Germany. Smart control strategies can be employed to control and optimize the heat pump operation to achieve higher self-consumption of PV electricity. This work presents the evaluation results of a smart-grid ready controlled PV-HP-battery system in a single-family household in Germany, using 1-minute-high-resolution field measurement data. Within 12 months evaluation period, a self-consumption of 43 % was determined. The solar fraction of the HP amounts to 36 %, enabled also due to higher set temperatures for space heating and domestic hot water production. Accordingly, the SPF decreases by 4.0 % the space heating and by 5.7 % in the domestic hot water mode. The combined seasonal performance factor for the heat pump system increases from 4.2 to 6.7, when only considering the electricity taken from the grid and disregarding the locally generated electricity supplied from photovoltaic and battery units.

Keywords: Heat pump, Photovoltaic, Battery, Energy-efficienc, Monitoring, Self-consumption, Sg-ready

The paper was published in Solar Energy Advances as part of the SWC2023 select papers.

10.1016/j.seja.2023.100047

10.1016/j.seja.2023.100047 Available at http://proceedings.ises.org

Categorizing Indian states based on operating condition of photovoltaic system

Pareek, A., Niyaz, H.M., Kumar, M.

Abstract

Electricity generation of a photovoltaic (PV) module is primarily affected by local weather conditions, which vary significantly across vast geographic areas. This work introduces an approach to categorize Indian states based on outdoor operating conditions of PV modules that influence performance and reliability. Module temperature and irradiance are the two most important parameters which affect PV performance. Relative humidity (RH), module temperature, and global horizontal irradiance (GHI) are the three most important parameters that affect PV reliability. In this work, the PV module's most frequent operating condition (MFOC) of temperature and irradiance corresponding to maximum energy production has been analyzed for dominant PV technology (multi-crystalline silicon). Data from various sites across India were analyzed and subsequently grouped by state as PV installation decisions are generally based on state-level factors, such as state business policies, incentives, availability of local human resources, state power policies, etc. The MFOC method used in this work was supported by experimental results. Based on estimated states' MFOC, PV module output power has been obtained and compared with its rated power. Further in this work, major stressors affecting PV modules namely average RH, module temperature, and total annual GHI have been analyzed for different Indian states. Based on these specific stressors, states with similar stressor patterns have been grouped by the k-means clustering method. Results of MFOC estimation show potential for additional standardization methods to estimate PV system performance accurately. Statistical analysis of stressors highlights the importance of selecting PV technology modules carefully.

Keywords: Pv module, India, MFOC, k-means

The paper was published in Solar Energy Advances as part of the SWC2023 select papers.

10.1016/j.seja.2024.100052

10.1016/j.seja.2024.100052 Available at http://proceedings.ises.org

Comfort in cold: A novel approach to sustainable building energy efficiency

Mehta, K., Zörner, W.

Abstract

Kyrgyzstan's high-altitude rural housing sector consumes 3–5 times more energy than European buildings due to ageing infrastructure, lack of insulation, and reliance on non-sustainable resources. One potential solution is the implementation of thermal insulation. However, due to limited public awareness of energy efficiency, inadequate government policies, insufficient technology, and challenging geography, people in rural areas rely on non-sustainable resources such as coal, cow dung, and firewood for heating, which creates a negative impact on the local ecosystems. To close the energy efficiency gap, the paper proposes a sustainable and holistic approach that integrates thermal insulation with effective energy efficiency planning using a staged-renovation approach by utilising locally available insulation materials / resources. The feasibility study presented in the paper was conducted with a simulation-based parametric study to recognise the potential of novel and sustainable insulation structures on building heat demand. This innovative approach can potentially reduce heat demand in high-altitude houses by as much as 70 %, offering a transformative solution. Furthermore, its adaptability makes it transferable to similar high-altitude communities, thus advancing sustainable energy practices for climate change mitigation and contributing to broader sustainable development goals.

Keywords: High-altitude, Cold climate, Building energy, Building renovation, Local insulation materials, Sustainable building energy efficiency

---

The paper was published in Solar Energy Advances as part of the SWC2023 select papers.

10.1016/j.seja.2024.100055

10.1016/j.seja.2024.100055 Available at http://proceedings.ises.org

Comparison of Solar District Heating and Renovation of Buildings as Measures for Decarbonization of Heat Supply in Rural Areas

Kelch, J., Kusvy, O., Zipplies, J., Orozaliev, J., Vajen, K.

Abstract

In this study two different decarbonization strategies for rural heat supply are compared on the example of 180 buildings located in a small village in Germany with about 860 inhabitants and typically mainly old buildings, partly in half-timbered construction. The comparison shows that erection of a solar district heating system with solar fraction of about 67 % leads to similar heating costs as an energy efficient renovation followed by installation of decentralized air source heat pumps for most of the buildings. Both concepts aim to achieve a heat supply that is free from the local use of fossil fuels. While the solar district heating system can probably be realized within a few years and therefore achieves the full CO2 savings promptly, this would take decades for the implementation of energy efficient renovation and heat pumps due to low renovation rate. Reaching climate-neutrality for the heat supply could thus be accelerated significantly by the construction of a solar district heating system. Moreover, the two decarbonization approaches do not appear to be fundamentally mutually exclusive: subsequent steady renovation of connected buildings will either increase solar share in heat supply or enable connection of new consumers at similar solar coverage rate. However, it should be also noted that with solar district heating alone, not always the same thermal comfort as with reinforced building renovation is achieved.

Keywords: Decarbonization, Energy efficient renovation, Existing buildings, Rural heating, Solar district heating

The paper was published in Solar Energy Advances as part of the SWC2023 select papers.

10.1016/j.seja.2024.100060

Experimental assessment of a solar photovoltaic-thermal system in a livestock farm in Italy

Murali, D., Murai, D., Acosta-Pazmiño, I.P., Loris, A., Garcia, A.C., Benni, S., Tinti, F., Gomes, J.

Abstract

This paper presents an experimental evaluation of the performance of a solar photovoltaic-thermal (PVT) system in a swine farm at Mirandola in Italy. In this project named RES4LIVE, funded by the EU's Horizon 2020 program, a PVT system is installed to replace fossil fuel consumption in one of the barns on the farm. The electrical energy from the collectors is utilized to operate the heat pump and provide electricity to the barn, whereas the thermal energy from the collector is stored in a borehole thermal energy storage (BTES) for further use by a 35 kW heat pump. The hybrid solar field consists of 24 covered PVT flat plate collectors (7.68 kW and 25 kW) with a total aperture area of 39.3 m , which can increase the temperature of the heat transfer fluid (HTF) to up to 40 °C. The PVT system is connected to a modular solar central (SC) with a standardized design that can also be used for other similar applications. The hybrid solar system complemented by energy storage is expected to save approximately 20,850 kg CO /year. The data collected from the PVT system, SC, and BTES are rigorously analyzed to evaluate its overall performance. A comprehensive performance assessment reveals the capability of the solar system to reduce carbon emissions and effectively replace fossil fuel consumption in the agricultural sector.

Keywords: Renewable energy source (RES), Livestock farm, Photovoltaic-thermal (PVT), RES4LIVE, Borehole thermal energy storage (BTES)

The paper was published in Solar Energy Advances as part of the SWC2023 select papers.

10.1016/j.seja.2024.100051

Performance evaluation of artificial neural network and hybrid artificial neural network based genetic algorithm models for global horizontal irradiance forecasting

Wahidna, A., Sookia, N., Ramgolam, Y.K.

Abstract

The output of photovoltaic (PV) systems is highly dependent on Global Horizontal Irradiance (GHI). Thus, accurate prediction of GHI is essential to meet increasing energy demands, stabilise the electric grid system and mitigate climate change. The main objective of this study is to accurately model and forecast GHI at Albion, Mauritius for a time step of every 15 min using the Artificial Neural Network (ANN) and hybrid Artificial Neural Network based Genetic Algorithm (ANN-GA) techniques. Ground-based measurement (GBM) data, collected every 15 min for a winter month was checked for stationarity and normalised to enhance its quality. Only strongly correlated input variables were selected to minimise uncertainties in forecasts. Special emphasis is given to short-term forecasting with a relatively small dataset size. This work is repeated for 30 min and 1 h time scales. The study is further validated using satellite data for a different location (Curepipe) in Mauritius. The performance evaluation over different statistical metrics indicated that the ANN model has the best capabilities for GHI forecasting, regardless of the location. The highest quality forecasts from the ANN technique resulted in values of 0.9999 for correlation coefficient (r), 0.9999 for coefficient of determination (R2), 0.1537 W/m2 for Mean Absolute Error (MAE), 0.0641 W/m2 for Mean Square Error (MSE) and 0.2532 W/m2 for Root Mean Square Error (RMSE). The best ANN technique outperformed the strongest hybrid ANN-GA technique for every measured performance indicator.

Keywords: Solar energy, Global horizontal irradiance, Forecas, Artificial neural network, Genetic algorithm

The paper was published in Solar Energy Advances as part of the SWC2023 select papers.

10.1016/j.seja.2024.100054

Solar photovoltaic/thermal (PVT) technology collectors and free cooling in ground source heat pump systems

Beltran, F., Pourier, C., Sommerfeldt, N.

Abstract

Ground source heat pump (GSHP) systems offer a low carbon heating and cooling solution for the decarbonization of buildings. As global temperatures rise, the cooling requirements of buildings will grow, even in regions where cooling systems have been historically uncommon due to their colder climate, such as Sweden. The combination of free cooling (FC) with GSHPs seems like a natural way to meet the increasing cooling needs, since the heat extracted from the building during the summer months can be injected into the ground to potentially regenerate the borehole field and enhance heat pump performance. However, a technology that is generally integrated with GSHP systems for borehole regeneration are photovoltaic/thermal collectors. This study investigates the performance of a ground source heat pump system with free cooling for a multi-family building in Stockholm, Sweden, and the interference on the free cooling capabilities of the system when photovoltaic/thermal collectors are present. The results demonstrate that the integration of PVT and FC not only maintains the cooling supply but also enhances heat pump performance, all the while reducing borehole length and land area requirements.

Keywords: Passive cooling, Solar hybrid, Solar PVT, Heat pumps, Low energy buildings

The paper was published in Solar Energy Advances as part of the SWC2023 select papers.

10.1016/j.seja.2023.100050

Testing solar cookers for cooking efficiency

Bigelow, A., Tabatchnick, J., Hughes, C.

Abstract

Solar Cookers International (SCI) staff developed and implemented a calculation to measure the cooking efficiency of solar thermal cookers. The calculation complements and enhances SCI's existing performance evaluation process (PEP), which can now be used for determining both the standard cooking power and the cooking efficiency for solar thermal cookers. The standard cooking power value is a single measure of solar cooker performance taken when the temperature of the test water load is specifically 50 °C greater than ambient temperature. Cooking efficiency values extend the perspective of solar cooker performance, as they are applicable to a continuum of load temperature measurements made during a heating cycle. Cooking efficiency is the ratio of energy absorbed by the solar cooking load divided by the input solar energy intercepted by the device during a test interval. Examples of cooking efficiency calculations using water loads during three days of testing for an anonymous group of different types of solar cookers are: solar box oven (18.9 %), reflective-panel solar cooker (28.5 %), parabolic reflector (35.2 %), and evacuated-tube solar cooker (34.6 %).

Keywords: Efficiency, Testing standards, Solar cookers, Solar thermal cooking

---

The paper was published in Solar Energy Advances as part of the SWC2023 select papers.

10.1016/j.seja.2024.100053

10.1016/j.seja.2024.100053 Available at http://proceedings.ises.org

Unveiling the Potential of Infrared Thermography in Quantitative Investigation of Potential-Induced Degradation in Crystalline Silicon PV Module

Gupta, R., Puranik, V.E.

Abstract

Potential-induced degradation-shunting (PID-s) is a severe degradation mechanism in photovoltaic (PV) cells that significantly impacts module performance. Regular monitoring and quantitative assessment of PID-s are crucial for ensuring long-term reliability of PV systems. Current-voltage (I-V) characteristics and electroluminescence (EL) imaging are commonly used for quantitative performance evaluation of PID-s affected PV modules. However, conducting I-V measurements is time-consuming when performed across large PV installations, while EL imaging has limitations for severely PID-s affected cells with no EL emission. This article proposes the use of inverse infrared (IRINV) thermography as an alternative investigation technique for PID-s in a PV module. IRINV imaging is fast and also effectively maps the severely PID-s affected cells in a PV module. This article unveils the potential of IRINV thermography in quantitative investigation of PID-s in crystalline silicon PV modules. The module level investigations present insights into the correlations between cell temperature and power output under different imaging conditions using Pearson correlation. Results indicate that steady-state operation with medium input current provides the most suitable condition for quantitative PID-s investigation. Furthermore, cell level analysis of temperature distribution and its variation with PID-s progression has been investigated using histogram and kernel density estimation (KDE) statistical tools, revealing distinct patterns as PID-s progresses. A PID-s severity index is proposed based on KDE, providing a quantitative measure of PID-s severity in cells within a PV module. This work provides valuable insights into the use of IRINV thermography as an alternative technique for assessment of PID-s in PV module inspection.

Keywords: Potential-Induced Degradation (PID), Infrared (IR) Imaging, Photovoltaic (PV) Module, Cell Power

The paper was published in Solar Energy Advances as part of the SWC2023 select papers.

10.1016/j.seja.2023.100049

11. Solar Resource Assessment and Energy Meteorology

Forecasting global horizontal and direct normal irradiation in the Arabian Peninsula: Sensitivity to the explicit treatment of aerosols

Vineeth Krishnan valappil[1], Luis Martin-Pomares[1], Michael Weston[1]

[1]Dubai Electricity and Water Authority, Dubai, UAE

Abstract

Global horizontal (GHI) and Direct Normal Irradiation (DNI) predicted using an operational three-dimensional atmospheric meteorology-chemistry model and a triple-nesting configuration over the Middle East with a focus on the hot desert climate of UAE is presented. The model runs every day, providing solar radiation components and air quality variables with a temporal step of one hour and a horizon of 72 hours. The model performance was assessed with measurement data of solar radiation from a ground monitoring station in Dubai (UAE) collected over one year, from January to December 2022, of representative and distinct meteorological regimes. We have examined the ability of the model to forecast GHI and DNI values under the RRTM (Rapid Radiative Transfer Model) and different shortwave downward radiation parameterizations. On an annual scale, the GHI and DNI displayed a mean rMBD of 0.51% and 18.7% and rRMSD of 21.6% and 69.7% respectively. The introduction of advanced treatment of aerosols dramatically improves the model performance in predicting GHI and DNI.

Keywords: solar radiation; desert dust; NWP model; Middle East, WRF-Chem, RRTM, aerosol

1. Introduction

The Middle East and North Africa (MENA) region has abundant solar resources and is implementing plans for renewable energy (Nematollahi, Hoghooghi, Rasti, & Sedaghat, 2016, Sgouridis, S. et al, 2016). The demand for electricity keeps rising in large urban environments of MENA, and the need for diversification from conventional energy production is now pushing for methods to reduce carbon emissions towards more sustainable development (Munawwar & Ghedira, 2014). Several solar resource assessment and feasibility studies for concentrated solar power plants (CSP) and photovoltaic plants (PV) have recently been carried out in the Middle East (Charabi & Gastli, 2010; Liqreina & Qoaider, 2014; Mokri, Aal Ali, & Emziane, 2013; Zell et al., 2015). Several research studies over the Middle East have shown that PV systems offer the most reliable and stable solution for primarily hot and humid environments (Pomares, 2017;). Therefore, accurate predictions of Global Titled Irradiance (GTI) derived from solar components of GHI, DNI and Diffuse Horizontal Irradiation (DHI) and local ground albedo in the region are of fundamental importance for efficient grid-connected PV establishments.

Accuracy in determining the expected solar irradiance and electricity production from solar power plants is essential for reducing grid integration costs and for more effective electricity grid management. Unlike wind power, solar radiation predictive capabilities are still nascent. GHI and DNI forecasting are traditionally conducted using various modeling approaches, including statistical models, models based on satellite data and sky cameras, and numerical weather prediction (NWP) models. The forecasting target horizon and spatial and temporal resolution determine the optimum modeling approach. For forecasts over the first minutes up to approximately 1-2 hours ahead of time (nowcasting), time series of solar irradiance can be provided by statistical approaches based on measured solar radiation data and sky cameras at a specific location (Hugo T.C.PedroCarlos F.M.Coimbra & Hugo T.C.Pedro, 2012; Mellit & Pavan, 2010). For forecasts from ~2 hours up to ~5 hours ahead (short-term forecasting), approaches based on the detection of cloud motion derived from satellite remote sensing are used to infer intra-hour solar irradiance with often high spatial and temporal resolution (Chow et al., 2011). The most valuable tool for GHI and DNI forecasting from 6 hours up to several days ahead is a Numerical Weather Prediction (NWP) model.

NWP models inherently include a radiative transfer model that is used to predict GHI and DNI through dynamic modeling of the troposphere. (R. J. Zamora, 2003; Robert J. Zamora et al., 2005) evaluated the hourly GHI predictions of the Fifth-Generation Penn State/NCAR Mesoscale Model (MM5) (Grell, Jimy, & David, 1994) and the National Center for Environmental Prediction (NCEP) Eta Model in certain locations in the USA and

10.18086/swc.2023.11.02 Available at http://proceedings.ises.org

reported model errors on the order of 100 Wm-2 for high aerosol loadings. The ability of MM5 to predict hourly solar irradiance was also studied by (Heinemann, Lorenz, Girodo, & University, 2006), who found a relative root mean square error (rRMSD) of about 50% in Germany. (Perez, Moore, Wilcox, Renne, & Zelenka, 2007) showed an rRMSD of 38% after applying a correction function estimating the hourly-averaged GHI by the National Digital Forecast Database (NDFD) as published by NCEP (Lorenz et al., 2009; Perez et al., 2013). (Mathiesen & Kleissl, 2011) conducted a comprehensive analysis of hourly GHI forecasts from three NWP models (NAM, GFS, and ECMWF) over the continental USA and found biases of up to 150 Wm-2. The capability of the Weather Research and Forecasting (WRF) model to predict hourly averaged solar irradiance in Andalusia, Spain, was examined by (Lara-Fanego, Ruiz-Arias, Pozo-Vázquez, Santos-Alamillos, & Tovar-Pescador, 2012) who found an rRMSD ranging between 10% (for clear-skies) and 50% (for cloudy conditions). (Ruiz-Arias, Dudhia, Santos-Alamillos, & Pozo-Vázquez, 2013), using WRF, validated various shortwave radiation parameterizations in the US and found a superiority of the RRTMG scheme (Rapid Radiative Transfer Model for Global climate models), if reliable aerosol data are provided as input to the model. More recently, (Zempila, Giannaros, Bais, Melas, & Kazantzidis, 2016) focused on the sensitivity of WRF to shortwave irradiance schemes while following a simple approach for investigating the impact of aerosol variations. They found that hourly averaged GHI over Greece is overestimated with all schemes (by 40-70% in terms of relative bias) for all-sky conditions while for clear skies an RMSD ranging between 90 and 110 Wm-2 was found. (Gleeson, Toll, Pagh Nielsen, Rontu, & Mašek, 2016) studied the effect of aerosols on clear sky solar radiation predictions using the Aire Limitee Adaptation dynamique Developpement InterNational – High Resolution Limited Area Model (ALADIN-HIRLAM) numerical weather prediction system for the August 2010 Russian wildfire case while testing three shortwave radiation schemes. They showed a reduction of error in global shortwave irradiance from 15 % at midday to 10% when standard climatological aerosols were used.

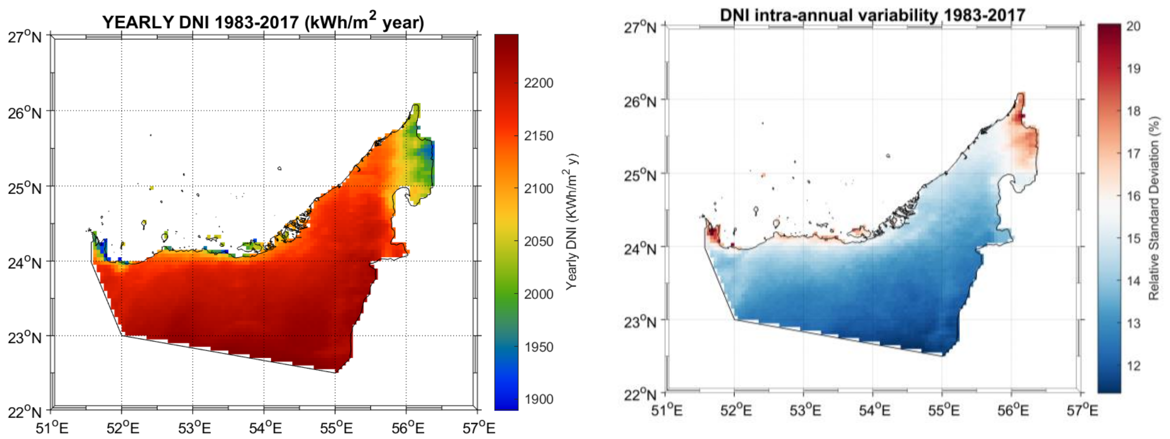

Fig 1: Yearly DNI and intra-annual variability from SARAH2 database. Year period 1983-2017.

One of the advantages of mesoscale NWP models is that they can cover a limited (urban to regional) geographical area and thus can be computationally inexpensive. At the same time, their physics can include additional details compared to global large-scale NWP models. Furthermore, NWP models are well-suited for solar irradiance predictions as they have advanced shortwave solar radiation parameterizations (Ruiz-Arias et al., 2013). However, the fluctuating nature of solar irradiance reaching the surface, caused by highly variable weather and air pollution patterns, is a significant challenge in the cost-effective management, operation, and integration of solar energy into existing electricity supply systems. More specifically, the subgrid-scale variability of clouds and the high temporal and spatial variability of atmospheric aerosol concentrations are the primary sources of uncertainty in predicting GHI and DNI (direct normal irradiance). Complex cloud microphysics (e.g., calculation of total cloud water content) and non-deterministic aerosol patterns are not well represented by NWP models (Heinemann et al., 2006). Traditionally, NWP models either neglect the presence of particles in the atmosphere or (more often) include a simplified aerosol approach (e.g., use of climatological data) while often miscalculating the location and lifetime of clouds resulting in significant biases in solar irradiance forecasting (Lara-Fanego et al., 2012; Thompson et al., 2016; R. J. Zamora, 2003; Robert J. Zamora et al., 2005; Zempila et al., 2016).

In the MENA region, high temperatures during most of the year often result in cloud-free atmospheric conditions due to rapid cloud dissipation. Aerosol concentrations, on the other hand, are high throughout the year due to frequent dust events and other emission sources in urban centers (Kalenderski, Stenchikov, & Zhao, 2013; Rakesh, Singh, & Joshi, 2009; Tsiouri, Kakosimos, & Kumar, 2015). Therefore, consideration of the effect of aerosols in radiation models is crucial to reduce solar irradiance prediction errors in this region. Contrary to ozone, carbon dioxide, and water vapor, aerosols' temporal and spatial variability is larger and more challenging to predict. In this work, we predict GHI and DNI in UAE and the Middle East using a three-dimensional meteorology-chemistry model, including a state-of-the-art prognostic treatment of aerosols.

2. Methodology

The following sections explain the WRF-chem model, the observational datasets, and the model evaluation diagnostics adopted in this study.

2.1. Observational datasets

The solar radiation measurements used in this study were recorded using the Dubai Electricity and Water Authority's (DEWA) high-precision monitoring station in Outdoor Test Facility (OTF) near MBR solar park (Dubai) (Latitude 24.76°N, longitude 55.36°E, altitude 30 meters). DEWA's OTF monitoring station (Fig. 1) is equipped with EKO thermoelectric radiometer, each mounted on an EKO STR-22G sun tracker, which also has a sun sensor kit for improved tracking accuracy. Two EKO MS80 ISO9060:2018 Class A pyranometers are used for measuring GHI and DHI, and one ISO 9060:2018 Class A EKO MS-57 pyrheliometer is used for DNI measurements. A shading ball assembly is also mounted on the tracker for measuring DHI. All data from the station are sampled every second and registered as one-minute averages in Wm-2. Quality checks and routine maintenance are conducted at high frequency (daily or every other day) and involve detailed cleaning of all sensor domes/windows, replacement of the desiccant of sensors when needed, and checking of the sensor shading, sensor tracking, and level/alignment, as well as offline data validation. Additionally, DEWA's air quality monitoring station, located next to the solar radiation station, is equipped with a Thermo-hygrometer (DMA867-875) and an Anemometer (DNA827) and continuously measures (every 1 min) ambient relative humidity, the temperature at 2m, wind velocity and wind direction at 10 meters altitude.

Fig 2: DEWA R&D OTF radiometric station.

2.2. WRF model

The three-dimensional meteorology-chemistry model WRF-Chem version 4.1.1 (Weather Research Forecasting with Chemistry) (Fast et al., 2006; Grell et al., 2005) was employed over the Arabian Peninsula region with an enhanced grid resolution over UAE. The orography of the area and modeling domain is shown in Fig. 3. The topography of the Arabian Peninsula is characterized by flatlands on the eastern side and highlands on the western side. The terrain of UAE is low-lying flat, and barren desert covered with loose sand and gravel. The Al Hajar mountain dominates in the northeastern part, and the rural type of land cover prevails in the western part of the UAE. An urban land cover predominates in the emirates of Abu Dhabi and Dubai, with thick shrublands to the east of Dubai. The WRF-chem model was applied over the Middle Eastern Area using a two-way nested domain (Figure 3). Each domain communicates with its inner/parent domain, and all three run simultaneously. The parent domain is configured to a 50 km × 50 km grid spacing while the intermediate nested domain (focused on the Arabian Desert) to a 10 km × 10 km spacing. The third domain was configured over the region of Dubai (at 2 km × 2 km).

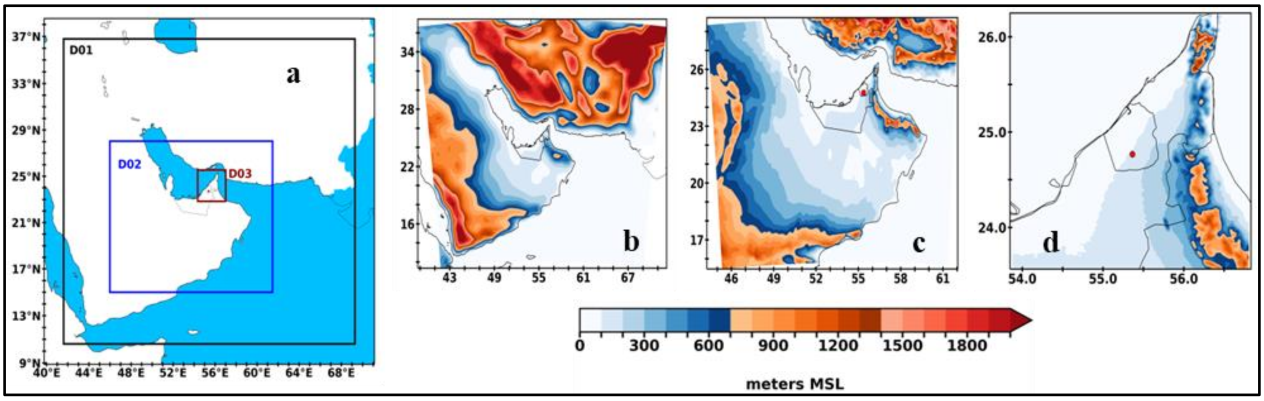

Fig 3: (a) WRF Model domains and orography (m) of (b) D01 (50 km), (c) D02 (10 km), and (d) D03 (2 km) WRF domains.

The physics part of the WRF-Chem stems from the WRF model, a non-hydrostatic meteorological mesoscale model that includes parameterizations of the land surface, planetary boundary layer, and cloud processes. The reference simulations for this work used the Grell 3D cumulus parameterization (Grell & Dévényi, 2002), the Lin microphysics scheme (CHEN & SUN, 2004), the 5-layer thermal diffusion Land Surface Model, the revised MM5 Monin–Obukhov surface layer scheme, the Goddard shortwave radiation scheme, the Rapid Radiative Transfer Model longwave radiation scheme (Mlawer, Taubman, Brown, Iacono, & Clough, 1997) and the Yonsei University boundary layer scheme (Hong, Noh, & Dudhia, 2006). This set of choices has been widely used when applying WRF (e.g. (Lara-Fanego et al., 2012; Ruiz-Arias et al., 2013; Zempila et al., 2016). Information concerning species concentrations propagates into and out of each computational area during model integrations. The WRF-Chem model simulates three essential components: emissions of atmospheric constituents (gases and aerosol particles), transport and the physicochemical transformations of atmospheric species. This grid nesting capability of WRF-Chem allows for a computationally efficient modeling setup capable of spanning large areas in which regional transport of pollutants (e.g., dust) is essential while providing fine resolution in select regions to address small-scale features. The altitude coordinate was discretized into 28 vertical layers in all three computational domains, extending from the surface to approximately 20 km. A Lambert map projection was employed in all the WRF-Chem runs. Dynamic meteorological data were obtained from the Global Forecast System (GFS; ftp://nomads.ncdc.noaa.gov/GFS/) and used to initialize WRF-Chem simulations.

2.3. Model verification

The uncertainty of the numerical predictions was calculated against ground measurements through uncertainty parameters based on data dispersion frequently used in the solar resource community (Espinar et al., 2009; Gueymard, 2014). The dispersion parameters were calculated using relativized versions of the mean bias deviation (MBD), and root mean square deviation (RMSD), as shown in equations (1) and (2), where Yexp and Ymod are the measured and predicted values of the variable, respectively, and N is the total number of points.

$$rMBD = 100\frac{1}{N}\sum_{i=1}^{N}\frac{(Y_{exp}-Y_{mod})}{\overline{Y_{exp}}} \quad (1)$$

$$rRMSD = 100\frac{1}{\overline{Y_{exp}}}\sqrt{\frac{1}{N}\sum_{i=1}^{N}\left(Y_{exp}-Y_{mod}\right)^2} \quad (2)$$

3. Results

This section explains the accuracy of WRF-chem forecasts with ground station measurements. Annual mean GHI and DNI forecast over the study region for day one, day two and day 3 for domain three are shown in Figures 2 and 3, respectively. The annual mean GHI and DNI vary between 200 to 300 Whm−2 and 100 to 400 Whm−2, respectively. The forecasts are also available as time series for single locations accessible through SQL, FTP and web services for operators of solar power plants.

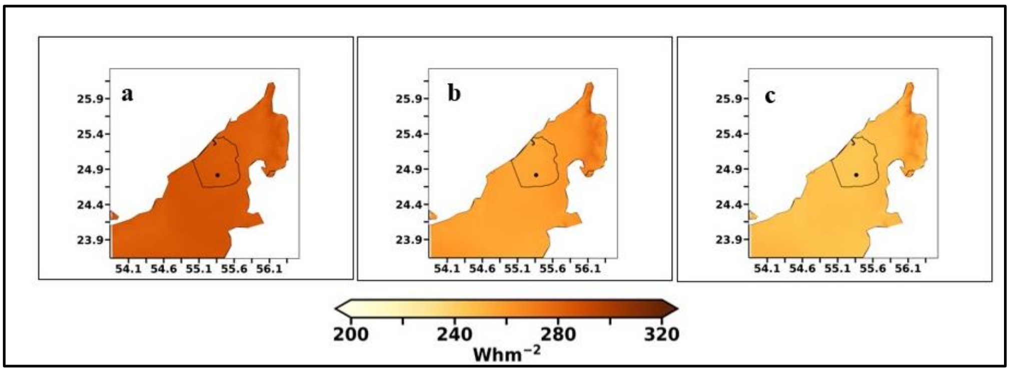

Fig 2: Annual mean GHI (Whm−2) predicted by WRF/Chem (with aerosols) for (a) day1, (b) day 2, (c) day 3 horizon of the forecast over the domain 3.

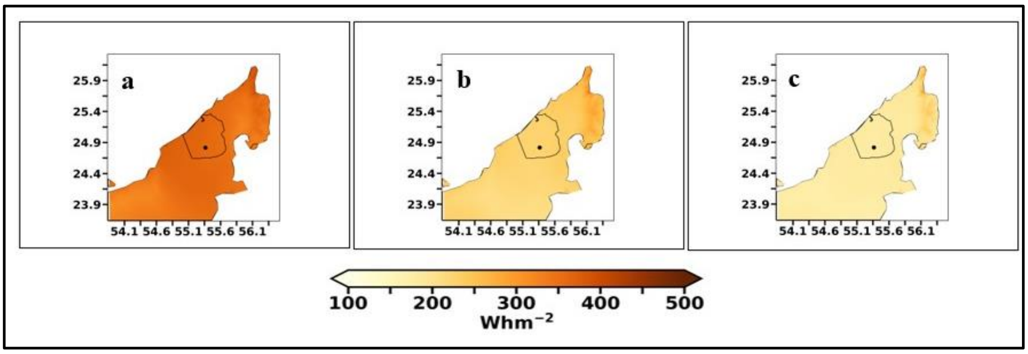

Fig 3: Annual mean DNI (Whm−2) predicted by WRF/Chem (with aerosols) for (a) day1, (b) day 2, (c) day 3 horizon of the forecast over domain 3.

The prediction skill of the WRF-Chem model was quantified using the root mean square deviation (RMSD), the relative RMSD (rRMSD), the mean bias deviation (MBD) and its relative magnitude (rMBD) using the mean value of the measurements for the period analyzed. Table 1 to Table 5 present the validation of the GHI and DNI forecast at the OTF facility. The period of validation for the data from the operational WRF-Chem model and ground radiometric measurements goes from the 1st of January 2022 to the 31st of Dec 2022. The accuracy of GHI and DNI from the WRF-chem model is summarized in Table 1 annually. Overall, the GHI showed a mean bias of 0.60 Wm−2 and mean rMBD of 0.51%, whereas the DNI displayed a mean bias of 69.1 Wm−2 and rMBD of 18.7%. The corresponding RMSD and rRMSD for GHI and DNI are 71.5 Whm−2, 21.6% and

222.2 Whm−2, 69.7%, respectively. The results are further divided into each of the three days of forecast, and the total error for the three days for each season separately is displayed in Table 2 to Table 5.

Tab. 1: WRF/Chem-DEWA Analysis against observations of Global Horizontal Irradiance (GHI) and Direct Normal Irradiance (DNI) at the DEWA monitoring station in OTF (Outdoor Test Facility), Dubai, UAE, for JAN – DEC 2022.

	MBD (Whm−2)	rMBD (%)	RMSD (Whm−2)	rRMSD (%)
GHI	-0.60	0.51	71.5	21.6
DNI	69.1	18.7	222.2	69.7

Tab. 2: Prediction skill metrics of WRF/Chem against observations of Global Horizontal Irradiance (GHI) and Direct Normal Irradiance (DNI) at the DEWA monitoring station in Dubai for the Winter season (DJF) 2022.

	MBD (Whm−2)		rMBD (%)		RMSD (Whm−2)		rRMSD (%)	
	GHI	DNI	GHI	DNI	GHI	DNI	GHI	DNI
0-23 hours	39.6	260.1	9.8	55.7	100.8	332.9	24.3	69.6
24-47 hours	8.3	70.1	1.8	15.1	110.7	292.4	26.4	58.1
48-71 hours	-7.9	-25.3	-2.2	-3.8	24.8	53.7	24.9	53.8
TOTAL (0-71 hours)	13.3	101.6	3.2	22.3	78.7	226.3	25.2	60.5

Tab. 3: Prediction skill metrics of WRF/Chem against observations of Global Horizontal Irradiance (GHI) and Direct Normal Irradiance (DNI) at the DEWA monitoring station in Dubai for the Spring season (MAM), 2022.

	MBD (Whm−2)		rMBD (%)		RMSD (Whm−2)		rRMSD (%)	
	GHI	DNI	GHI	DNI	GHI	DNI	GHI	DNI
0-23 hours	64.4	341.2	13.1	79.4	90.7	382.7	18.2	88.7
24-47 hours	14.4	75.4	2.1	17.3	91.1	267.2	17.6	59.7
48-71 hours	-18.5	-76.2	-4.3	-15.5	18.3	52.1	18.32	52.1
TOTAL (0-71 hours)	20.1	113.4	3.6	27.1	66.7	234.0	18.06	66.9

Tab. 4: Prediction skill metrics of WRF/Chem against observations of Global Horizontal Irradiance (GHI) and Direct Normal Irradiance (DNI) at the DEWA monitoring station in Dubai for Summer (JJA), 2022.

	MBD (Whm−2)		rMBD (%)		RMSD (Whm−2)		rRMSD (%)	
	GHI	DNI	GHI	DNI	GHI	DNI	GHI	DNI
0-23 hours	48.4	263.1	11.6	94.1	113.4	357.5	24.2	128.9
24-47 hours	-51.8	-114.1	-8.1	-25.3	139.1	272.1	27.6	82.3
48-71 hours	-84.6	-170.3	-14.6	-45.4	30.8	78.9	30.7	78.9
TOTAL (0-71 hours)	-29.4	-7.1	-3.7	7.7	94.4	236.1	27.5	96.7

Tab. 5: Prediction skill metrics of WRF/Chem against observations of Global Horizontal Irradiance (GHI) Global Horizontal Irradiance (GHI) and Direct Normal Irradiance (DNI) at the DEWA monitoring station in Dubai for Fall (SON), 2022.

	MBD (Whm−2)		rMBD (%)		RMSD (Whm−2)		rRMSD (%)	
	GHI	DNI	GHI	DNI	GHI	DNI	GHI	DNI
0-23 hours	25.9	257.8	5.6	59.8	52.9	288.7	13.2	65.7
24-47 hours	-12.6	35.2	-2.4	11.2	66.4	242.8	15.4	51.8
48-71 hours	-32.8	-87.8	-6.5	-18.1	18.5	44.6	18.5	44.2
TOTAL (0-71 hours)	-6.5	68.4	-1.1	17.6	45.9	192.1	15.7	54.8

In Comparison with observations, the model generally overestimates the GHI for each simulation period, with an RMSD ranging between 18.5 and 139.1Whm−2 and a relative RMSD ranging from 13.2 to 26.4%. Similarly, DNI showed an overestimation of 44.6 and 382.7 Whm−2 and 44.2 and 88.7% for RMSD and relative RMSD, respectively, for different seasons. The winter and Fall seasons displayed better accuracy than the summer or spring seasons. These errors are within the lower end of GHI and DNI errors found in other parts of the world. Interestingly the 48-71 hours (day 3) forecast shows better accuracy than 0-23 hours (day 1) and 24-48 hours (day 2), which could be due to the WRF-chem model's capability to accommodate the aerosol direct and indirect effect.

4. Conclusions

Clouds have, in general, a substantial effect on solar insolation but the mostly cloud-free conditions throughout the year in UAE and its position within the sunbelt favor solar PV adoption as a renewable energy production method. However, high atmospheric aerosol concentrations in this location attenuate solar radiation considerably. This study concentrates on validating operational predictions of global horizontal and direct average irradiation in the Middle East with a particular focus on the UAE using a regional meteorology-chemistry model combined with ground measurements from the continuous operation of a monitoring station in Dubai, UAE.

We have presented the maps to the users and validated the predictions of GHI and DNI. The WRF-Chem model has been running operationally since Jan 2022 providing daily hourly forecasts over UAE and the Arabian Peninsula with a temporal horizon of 72 hours.

Results show that the numerical weather prediction model WRF-Chem systematically over-predicts global horizontal irradiance and Direct Normal Irradiance in Dubai. The WRF chem model overestimates the aerosol direct and indirect effects, leading to increased scattering or absorption of solar radiation reaching the ground. The major source of error can be attributed to inaccuracies in the input emissions utilized for the simulations. In addition, the parameterizations used in the WRF model for aerosols may not be detailed enough to represent the diverse and dynamic nature of aerosol properties and their impact on irradiance. This can lead to inaccuracies in forecasting solar irradiance. This configuration serves as our baseline setup, which will be the foundation for our ongoing refinements and improvements in the model configuration.

Modeling aerosols is especially crucial for fast-changing urban environments like Dubai, which has experienced recent land conversion and rapid urbanization. Over the greater region of the Arabian Peninsula, we already know from a previous publication (Fountoukis, Martín-Pomares, Perez-Astudillo, Bachour, & Gladich, 2018) that the impact of accurate aerosol concentrations on the predicted GHI is considerable (15–20% on average). A previous study (Fountoukis, Martín-Pomares, Perez-Astudillo, Bachour, & Gladich, 2018) also show a prognostic treatment of aerosols in a numerical weather prediction model is essential in regions with high aerosol concentrations. Further improving the anthropogenic emissions inventory, refining model parameterization schemes, and better maintenance of the radiometers are expected to eliminate errors in irradiance forecasts.

5. Acknowledgments

The authors wish to acknowledge the continuous dedication of DEWA R&D infra team on the maintenance and operation of DEWA OTF station.

The authors wish to acknowledge the Photovoltaic Power Systems (PVPS) Programme within the International Energy Agency (IEA) and all the experts who participate in the IEA Task 16 (Solar resource for high penetration and large-scale applications). The development of this work was partly motivated by participation in Task 16 Expert Meetings.

6. References

Charabi, Y., & Gastli, A. (2010). GIS assessment of large CSP plant in Duqum, Oman. Renewable and Sustainable Energy Reviews, 14(2), 835–841. https://doi.org/10.1016/j.rser.2009.08.019

CHEN, S.-H., & SUN, W.-Y. (2004). A One-dimensional Time Dependent Cloud Model. Journal of the Meteorological Society of Japan. Ser. II. https://doi.org/10.2151/jmsj.80.99

Chow, C. W., Urquhart, B., Lave, M., Dominguez, A., Kleissl, J., Shields, J., & Washom, B. (2011). Intra-hour forecasting with a total sky imager at the UC San Diego solar energy testbed. Solar Energy, 85(11), 2881–2893. https://doi.org/http://dx.doi.org/10.1016/j.solener.2011.08.025

Espinar, B., Ramírez, L., Drews, A., Beyer, H. G., Zarzalejo, L. F., Polo, J., & Martín, L. (2009). Analysis of different comparison parameters applied to solar radiation data from satellite and German radiometric stations. Solar Energy, 83(1), 118–125. https://doi.org/doi: DOI: 10.1016/j.solener.2008.07.009

Fast, J. D., Gustafson, W. I., Easter, R. C., Zaveri, R. A., Barnard, J. C., Chapman, E. G., … Peckham, S. E. (2006). Evolution of ozone, particulates, and aerosol direct radiative forcing in the vicinity of Houston using a fully coupled meteorology-chemistry-aerosol model. Journal of Geophysical Research Atmospheres. https://doi.org/10.1029/2005JD006721

Fountoukis, C., Ackermann, L., Ayoub, M. A., Gladich, I., Hoehn, R. D., & Skillern, A. (2016). Impact of atmospheric dust emission schemes on dust production and concentration over the Arabian Peninsula. Modeling Earth Systems and Environment, 2(3), 115. https://doi.org/10.1007/s40808-016-0181-z

Fountoukis, C., Martín-pomares, L., Perez-astudillo, D., Bachour, D., & Gladich, I. (2018). Simulating global horizontal irradiance in the Arabian Peninsula : Sensitivity to explicit treatment of aerosols. Solar Energy, 163(February), 347–355. https://doi.org/10.1016/j.solener.2018.02.001

Fountoukis, C., Martín-Pomares, L., Perez-Astudillo, D., Bachour, D., & Gladich, I. (2018). Simulating global horizontal irradiance in the Arabian Peninsula: Sensitivity to explicit treatment of aerosols. Solar Energy. https://doi.org/10.1016/j.solener.2018.02.001

Gleeson, E., Toll, V., Pagh Nielsen, K., Rontu, L., & Mašek, J. (2016). Effects of aerosols on clear-sky solar radiation in the ALADIN-HIRLAM NWP system. Atmospheric Chemistry and Physics. https://doi.org/10.5194/acp-16-5933-2016

Grell, G. A., & Dévényi, D. (2002). A generalized approach to parameterizing convection combining ensemble and data assimilation techniques. Geophysical Research Letters. https://doi.org/10.1029/2002gl015311

Grell, G. A., Jimy, D., & David, R. S. (1994). A description of the fifth-generation Penn State/NCAR Mesoscale Model (MM5). NCAR Technical Note NCAR/TN-398+STR. https://doi.org/10.5065/D60Z716B

Grell, G. A., Peckham, S. E., Schmitz, R., McKeen, S. A., Frost, G., Skamarock, W. C., & Eder, B. (2005). Fully coupled “online” chemistry within the WRF model. Atmospheric Environment. https://doi.org/10.1016/j.atmosenv.2005.04.027

Gueymard, C. a. (2014). A review of validation methodologies and statistical performance indicators for modeled solar radiation data: Towards a better bankability of solar projects. Renewable and Sustainable Energy Reviews, 39(0), 1024–1034. https://doi.org/10.1016/j.rser.2014.07.117.

Heinemann, D., Lorenz, E., Girodo, M., & University, O. (2006). Forecasting of solar radiation. Oldenburg (Alemania). Retrieved from n:%5CTesis_USB%5CReferencias_Biblio%5CLuis_M%5CRadiacion Prediccion%5Cestado del arte%5CHeinemann-P (Chapter 7, Part II).doc

Hong, S.-Y., Noh, Y., & Dudhia, J. (2006). A New Vertical Diffusion Package with an Explicit Treatment of Entrainment Processes. Monthly Weather Review. https://doi.org/10.1175/mwr3199.1

Hugo T.C.PedroCarlos F.M.Coimbra, & Hugo T.C.Pedro, C. F. M. C. (2012). Assessment of forecasting techniques for solar power production with no exogenous inputs. Solar Energy. https://doi.org/10.1016/J.SOLENER.2012.04.004

Kalenderski, S., Stenchikov, G., & Zhao, C. (2013). Modeling a typical winter-time dust event over the Arabian Peninsula and the Red Sea. Atmospheric Chemistry and Physics. https://doi.org/10.5194/acp-13-1999-2013

Lara-Fanego, V., Ruiz-Arias, J. A., Pozo-Vázquez, D., Santos-Alamillos, F. J., & Tovar-Pescador, J. (2012). Evaluation of the WRF model solar irradiance forecasts in Andalusia (southern Spain). Solar Energy, 86(8), 2200–2217. https://doi.org/10.1016/j.solener.2011.02.014

Liqreina, A., & Qoaider, L. (2014). Dry cooling of concentrating solar power (CSP) plants, an economic competitive option for the desert regions of the MENA region. Solar Energy, 103(0), 417–424.

Lorenz, E., Remund, J., Müller, S. C., Traunmüller, W., Steinmaurer, G., Pozo, D., … Romeo, M. G. (2009). Benchmarking of different approaches to forecast solar irradiance. Proceedings of the 24th European Photovoltaic Solar Energy Conference.

Mathiesen, P., & Kleissl, J. (2011). Evaluation of numerical weather prediction for intra-day solar forecasting in the continental United States. Solar Energy. https://doi.org/10.1016/j.solener.2011.02.013

Mellit, A., & Pavan, A. M. (2010). A 24-h forecast of solar irradiance using artificial neural network: Application for performance prediction of a grid-connected PV plant at Trieste, Italy. Solar Energy. https://doi.org/10.1016/j.solener.2010.02.006

Mlawer, E. J., Taubman, S. J., Brown, P. D., Iacono, M. J., & Clough, S. A. (1997). Radiative transfer for inhomogeneous atmospheres: RRTM, a validated correlated-k model for the longwave. Journal of Geophysical Research: Atmospheres. https://doi.org/10.1029/97jd00237

Mokri, A., Aal Ali, M., & Emziane, M. (2013). Solar energy in the United Arab Emirates: A review. Renewable and Sustainable Energy Reviews, 28(0), 340–375. https://doi.org/http://dx.doi.org/10.1016/j.rser.2013.07.038

Munawwar, S., & Ghedira, H. (2014). A review of Renewable Energy and Solar Industry Growth in the GCC Region. Energy Procedia, 57, 3191–3202. https://doi.org/10.1016/j.egypro.2015.06.069

Nematollahi, O., Hoghooghi, H., Rasti, M., & Sedaghat, A. (2016). Energy demands and renewable energy resources in the Middle East. Renewable and Sustainable Energy Reviews, 54, 1172–1181. https://doi.org/10.1016/j.rser.2015.10.058

Perez, R., Lorenz, E., Pelland, S., Beauharnois, M., Van Knowe, G., Hemker, K., … Pomares, L. M. (2013). Comparison of numerical weather prediction solar irradiance forecasts in the US, Canada and Europe. Solar Energy. https://doi.org/10.1016/j.solener.2013.05.005

Perez, R., Moore, K., Wilcox, S., Renne, D., & Zelenka, A. (2007). Forecasting solar radiation - Preliminary evaluation of an approach based upon the national forecast database. Solar Energy, 81(6), 809–812. http://www.sciencedirect.com/science/article/B6V50-4MH2KN8-1/1/c8d5d462390cb9b1b469b00411a2fdbb

Pomares, L. M., & Sanfilippo, A. (2017). Analysis of the long-term solar potential for electricity generation in Qatar Analysis of the long-term solar potential for electricity generation in Qatar. Renewable and Sustainable Energy Reviews, 73(June), 1231–1246. https://doi.org/10.1016/j.rser.2017.01.125

Rakesh, V., Singh, R., & Joshi, P. C. (2009). Intercomparison of the performance of MM5/WRF with and without satellite data assimilation in short-range forecast applications over the Indian region. Meteorology and Atmospheric Physics. https://doi.org/10.1007/s00703-009-0038-3

Ruiz-Arias, J. A., Dudhia, J., Santos-Alamillos, F. J., & Pozo-Vázquez, D. (2013). Surface clear-sky shortwave radiative closure intercomparisons in the Weather Research and Forecasting model. Journal of Geophysical Research Atmospheres. https://doi.org/10.1002/jgrd.50778

Sanfilippo, A., Martin-Pomares, L., Mohandes, N., Perez-Astudillo, D., & Bachour, D. (2016). An adaptive multi-modeling approach to solar nowcasting. Solar Energy, 125, 77–85. https://doi.org/10.1016/j.solener.2015.11.041

Thompson, G., Tewari, M., Ikeda, K., Tessendorf, S., Weeks, C., Otkin, J., & Kong, F. (2016). Explicitly-coupled cloud physics and radiation parameterizations and subsequent evaluation in WRF high-resolution convective forecasts. Atmospheric Research. https://doi.org/10.1016/j.atmosres.2015.09.005

Tsiouri, V., Kakosimos, K. E., & Kumar, P. (2015). Concentrations, sources and exposure risks associated with particulate matter in the Middle East Area—a review. Air Quality, Atmosphere and Health. https://doi.org/10.1007/s11869-014-0277-4

Zamora, R. J. (2003). Comparing MM5 radiative fluxes with observations gathered during the 1995 and 1999 Nashville southern oxidants studies. Journal of Geophysical Research. https://doi.org/10.1029/2002jd002122

Zamora, Robert J., Dutton, E. G., Trainer, M., McKeen, S. A., Wilczak, J. M., & Hou, Y.-T. (2005). The Accuracy of Solar Irradiance Calculations Used in Mesoscale Numerical Weather Prediction. Monthly Weather Review. https://doi.org/10.1175/MWR2886.1

Zell, E., Gasim, S., Wilcox, S., Katamoura, S., Stoffel, T., Shibli, H., … Subie, M. Al. (2015). Assessment of solar radiation resources in Saudi Arabia. Solar Energy, 119, 422–438. https://doi.org/10.1016/j.solener.2015.06.031

Zempila, M. M., Giannaros, T. M., Bais, A., Melas, D., & Kazantzidis, A. (2016). Evaluation of WRF shortwave radiation parameterizations in predicting Global Horizontal Irradiance in Greece. Renewable Energy. https://doi.org/10.1016/j.renene.2015.08.057

12. Perspectives for a 100% Renewable Energy World

A preliminary scenario modelling tool to investigate resilience, renewable energy integration, and multi-sectoral decarbonization in Pacific energy supply chains: Fiji case study

Edoardo Santagata[1,2,3], Anna Bruce[1,2,3] and Iain MacGill[1,3,4]

[1] University of New South Wales (UNSW), Sydney (Australia)

[2] School of Photovoltaic and Renewable Energy Engineering, UNSW

[3] Collaboration on Energy and Environmental Markets, UNSW

[4] School of Electrical Engineering and Telecommunications, UNSW

Abstract

Pacific Island Countries and Territories (PICTs) are heavily reliant on fossil fuel imports to fulfill their energy needs, resulting in high and volatile energy costs. As a result, most PICTs have ambitious renewable energy targets as a means of reducing reliance on imported fuels, lowering energy costs, and mitigating the emissions associated with energy production, and there is increasing interest in electrification of transport and other sectors to advance decarbonisation objectives. However, the adoption of renewable energy and broader decarbonisation efforts have been limited, amongst other factors, by a lack of appropriate tools to support energy planning across these economic sectors. This study presents the development of a preliminary open-source scenario modelling tool – the *Energy Transition and Resilience Planning Tool* (ETARP) – to investigate energy resilience as well as the impacts and requirements of transitioning to renewable energy and electrifying various economic sectors to meet strategic energy and emissions targets in PICTs. To demonstrate the capabilities of the tool, Fiji is adopted as a case study for the Pacific. In particular, scenarios for its net-zero and 100% renewable energy targets are parametrised and investigated in terms of resilience, fuel imports, energy supply and consumption, and emissions.

Keywords: Pacific, Renewable Energy, Fuel Imports, Scenario Modelling, Sectors, Tool, Planning, Resilience

1. Introduction

Pacific Island Countries and Territories (PICTs) face a unique set of challenges relating to climate change and energy (Aleksandrova et al., 2021). They are constituted by small islands and low-lying atolls with few local resources and limited land availability. As such, PICTs are placed downstream in the global energy supply chain, being for the most part energy consumers who rely on fossil fuel imports to fulfill their energy needs (Figure 1, left) (Raghoo et al., 2018; Wolf et al., 2016). This greatly exposes PICTs to high and volatile fuel prices, often resulting in comparatively high electricity prices for consumers and overall high national expenditure on fuel (Figure 1, right) (Atteridge and Savvidou, 2019).

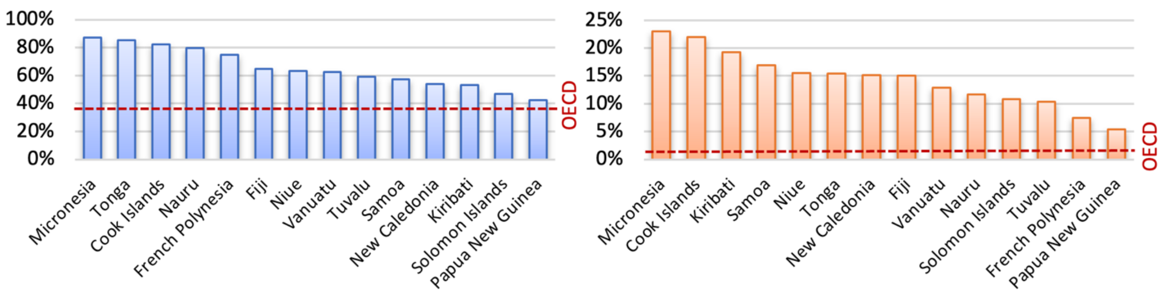

Fig. 1: Fuel consumption as percentage of total energy (Left) and GDP (Right) in 2018. Data: UN (2021), SPC (2019), OEC (2020)

10.18086/swc.2023.12.05 Available at http://proceedings.ises.org

To overcome the challenges posed by fossil fuel dependence, PICTs have set ambitious targets for increasing the share of renewable energy in their electricity mix (Weir, 2018). Furthermore, many PICTs have also committed to significant emissions reductions as part of international agreements (UN, 2023). To understand pathways to, and implications of, transitioning to clean energy sources and reducing sectoral emissions, analysis of energy consumption across various economic sectors is required (Gargiulo and Gallachoir, 2013). While several sector-coupling modelling tools do exist to investigate the interdependencies between energy production and sectoral consumption (Groissböck, 2019), research has highlighted that there is a lack of tools and data that specifically support energy planning and decision-making in PICTs (Lucas et al., 2017; Michalena et al, 2018; To et al., 2021). Namely, PICTs need specific tools that incorporate energy resilience, enable scenario modelling for specific Pacific economic sectors, have integrated energy data from a variety of sources, and help identify strategies relevant to key Pacific policy objectives (e.g. fossil fuel import reduction).

2. Scenario Modelling Tool Development

To accommodate these specific needs, a preliminary open-source scenario modelling tool has been developed to investigate energy resilience and assess the impacts of increasing renewable energy capacity and electrifying various economic sectors in PICTs – the *Energy Transition and Resilience Planning Tool* (ETARP). The tool has been developed in Excel such that it requires minimal training, provides adaptable outputs, and presents ease in integrating the tool's model structures with other tool or interfaces in use by energy planners, policy makers, and engineers. Table 1 summarises the various sheets available in the tool along with their respective functions. Figure 2 shows a screenshot of the main page user interface. The left section of the main page provides a range of input parameters, as well as various forecasting methods. The central section of the main page displays an adaptable dashboard with the main graphical outputs the tool delivers, subdivided across key categories such as 'Renewable Energy', 'Emissions', and 'Resilience'. The right section of the main page displays raw annual data for key model variables of energy supply chain, such as oil imports, electricity supply, and sectoral consumptions. Users can access more detailed graphs, raw data, and modelling options in the several sheets associated with different sections of the energy supply chain, as shown in Figure 3.

Tab. 1: Tool sheet index and functions

#	Name	Function
1	info	Tool description, sheet index, user manual, and distribution licence
2	MAIN	Main inputs to generate transition scenarios, including goal setting and model parameters
3	Imports, Exports, Bunkering	Annual balancing for fuel imports, exports, and bunkering
4	Supply	Annual balancing for primary energy supply
5	Capacity	Capacity estimation based on selected energy mix
6	Transformations	Annual balancing for transformations
7	Consumption	Annual balancing for sectoral consumption
8	Energy Access	Access to electricity and clean cooking
9	EV	Electric vehicle penetration in land transport fleet using vehicle registrations
10	Hydrogen	Use of hydrogen in energy supply chain
11	Emissions	Sectoral emissions
12	Costs	Cost calculation

13	RE Potentials	Technical potential for each country based on external studies
14	Resilience Indicators	Indicators assessing energy resilience
15	Chevron Profiles	Supply and demand profiles for hourly matching
16	Hourly Matching	Hourly matching for every year of simulation
17	PICTs Data	Database of Pacific Island Countries and Territories

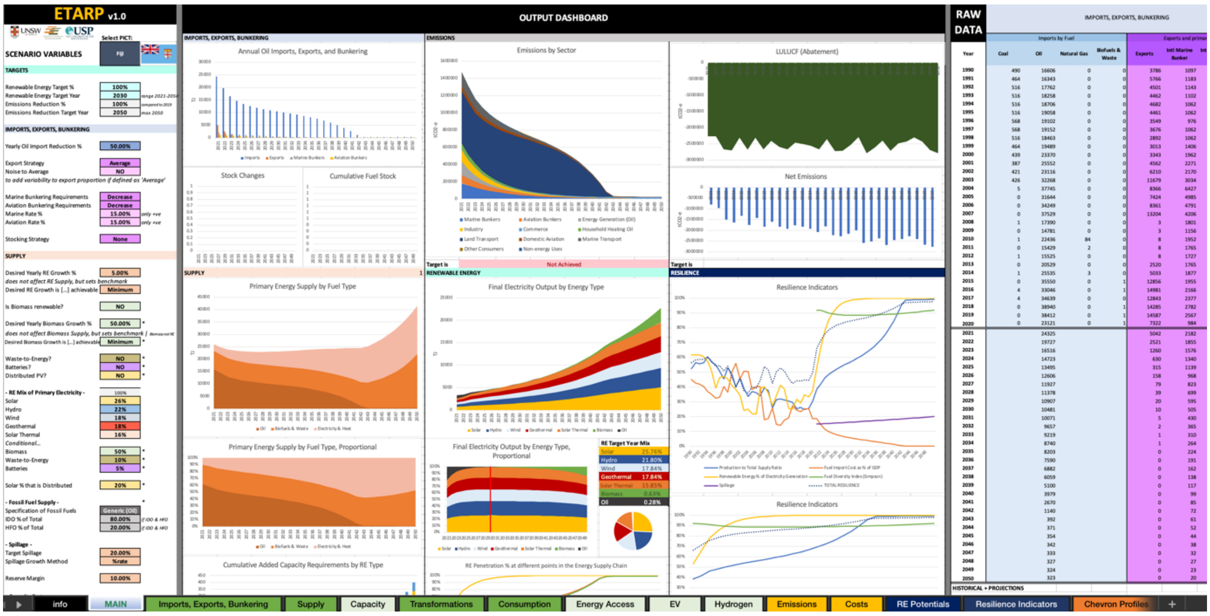

Fig. 2: Screenshot of 'MAIN' sheet

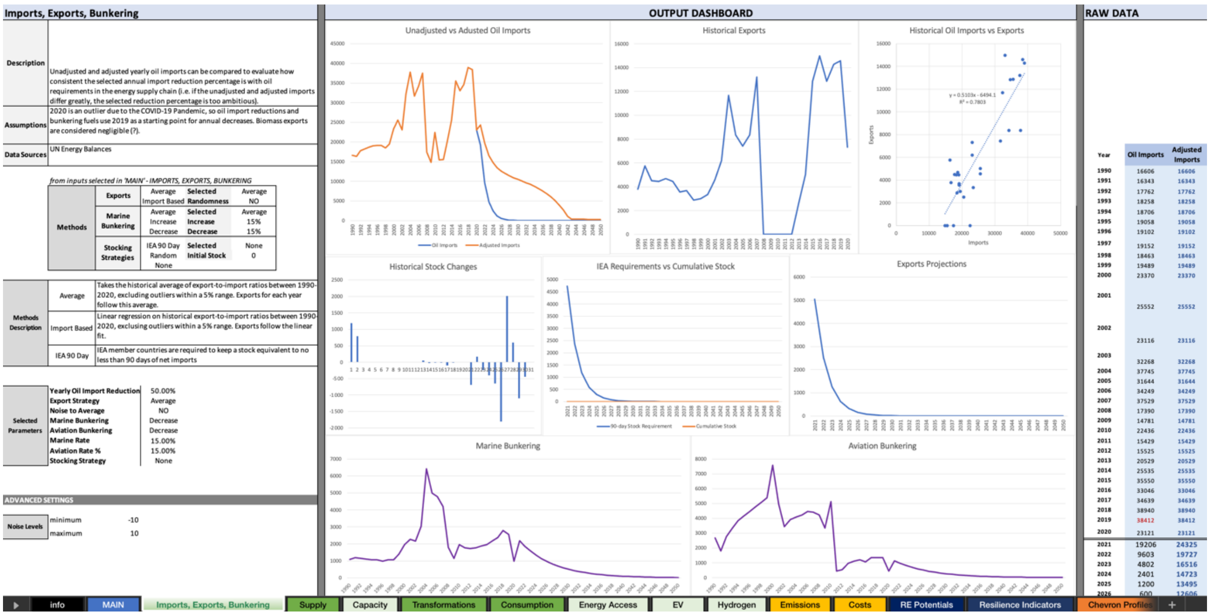

Fig. 3: Screenshot of 'Imports, Exports, Bunkering' sheet

Figure 4 features a flowchart presenting the tool's model structures and variables, input parameters, outputs, data sources, and assumptions. The energy supply chain is subdivided in 4 key categories: imports, exports, and bunkering; primary energy supply; transformations; and consumption – capturing all key energy flows. Input parameters for all types of energy imports, production, and consumption are specified as an annual percentage increase or decrease, in alignment with typical energy policy prescriptions for the region. The model forecasts results for the specified model variables for the period 2021-2050 (with exception of electric vehicle penetration, which starts from 2023 due to recently available data regarding vehicle registrations), and determines whether the inputted targets in terms of renewable energy and emissions have been met. Depending on the user's selection, model variables related to sectoral consumption for each fuel type (i.e. oil, electricity, biomass) are forecasted using one of two methods: linear regression between related variables using historical data (e.g. commerce electricity consumptions vs GDP), or annual percentage changes (increase or decrease). By modelling sectoral consumption in a variety of ways, users can determine how particular economic sectors might change their energy consumption through time to ensure national energy and emissions targets are met.

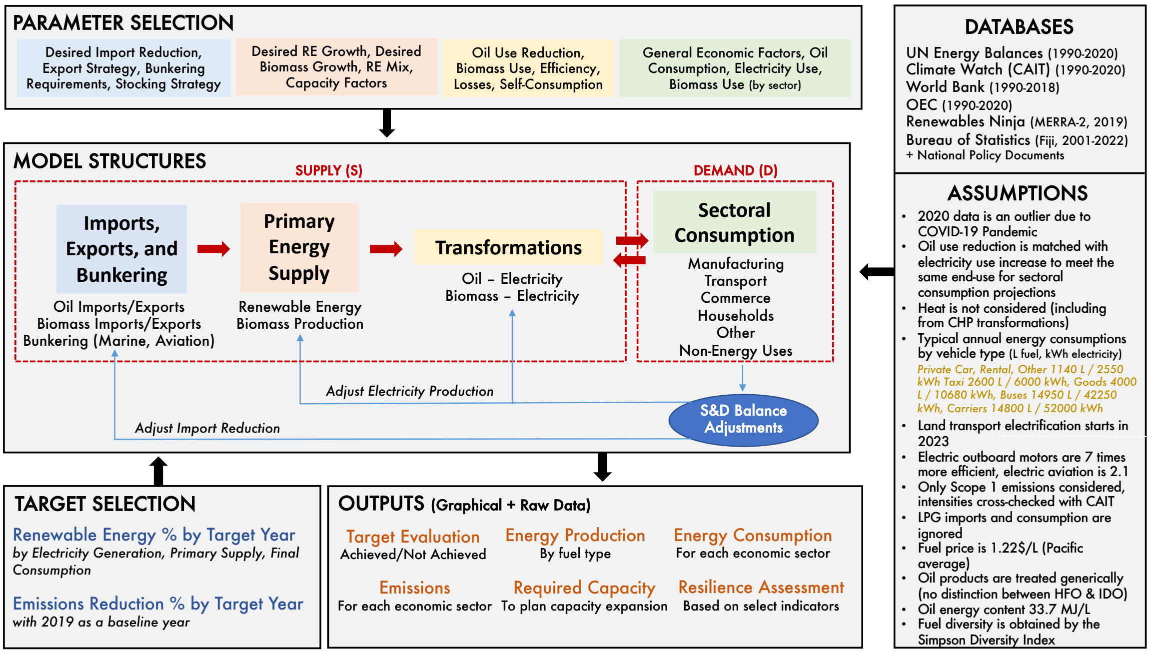

Fig. 4: Scenario modelling tool input parameters, model structures, data sources, assumptions, and outputs

This preliminary version of the tool implements an annual energy supply and demand balancing approach, ensuring that input parameters do not result in an insufficient energy supply to match the forecasted annual demand. Equation 1 is used to determine the required adjustment for each fuel type to balance supply and demand, with $E_{consumption}$ and E_{supply} being determined by the first pass of the model with the initially selected parameters. Equation 2 is used to balance supply and demand based on the required adjustment.

$$\Delta E = E_{consumption} - E_{supply} \qquad \text{(eq. 1)}$$

$$E_{supply} + \Delta E = E_{supply,adjusted} \qquad \text{(eq. 2)}$$

The tool provides several key indicators that can be used to track energy resilience, drawn from key policy documents and literature (Kruyt et al., 2009; Sovacool, 2013; SPC, 2021). These include: production to total energy supply ratio; fuel import costs as a percentage of GDP: fuel diversity index (Equation 3, with n indicating energy units produced by each fuel type and N the total); and renewable energy percentage of total electricity generation.

$$\mathrm{D}_{fuel} = 1 - \sum \frac{n(n-1)}{N(N-1)} \qquad \text{(eq. 3)}$$

3. Methods

This short study adopts Fiji as a case study to test the tool's outputs. Model input parameters were adjusted through various iterations to generate 2 key scenarios related to Fiji's strategic energy and emissions targets: 100% renewable energy by 2030 ('RE100') and economy-wide carbon neutrality by 2050 ('C-0') (Fiji Ministry of Economy, 2018b). Parametrisation of both scenarios is described as follows. Fuel stocking strategies were not considered in either scenario, and bunkering requirements were set to decrease at 2% for RE100 and 15% for C-

0. The specific renewable energy mix for both scenarios is based on the *Low Emission Development Strategy (LEDS) 2018-2050*, with proportions of 26% solar, 17% wind, 22% hydro, 18% biomass, and 17% geothermal in the 'Very High Ambition' scenario (Fiji Ministry of Economy, 2018a). The LEDS was also used to determine annual sectoral electricity consumption increases, averaging around 2%. Capacity factors for solar (18° tilt, 10% system losses) and wind (80m hub height) are adopted from the *Renewables Ninja* database (Pfenninger and Staffell, 2016), while data from NREL was used for other technologies (NREL, 2022). Oil to electricity transformations were set at 34.9% for RE100 and 14% for C-0. Land transport saw 15% and 10% electrification rates for RE100 and C-0 respectively (with goods and carrier vehicles only electrified under C-0), aviation 2% and 10%, and navigation 5% and 10%. Sectoral oil consumption reductions were set at 10% for RE100 and 15% for C-0.

4. Results & Discussion

Results for the two parametrised scenarios are primarily shown in terms of key model variables as well as selected resilience indicators in Figure 5. Key model variables include final oil consumption and import costs to assess fuel dependence, renewable energy growth and emissions reductions (from a baseline) to assess broad energy transition and decarbonisation annual requirements, and renewable electricity percentage to assess target feasibility. Figures 6-13 display more detailed default graphs for a few select output categories, namely fuel imports and energy supply, sectoral consumption, and emissions.

4.1. Overview & Resilience Indicators

Figure 5 shows results for the selected resilience indicators in both scenarios. Annual fuel import reductions average 9.6% for RE100 and 23.73% for C-0, with more significant import reductions under RE100 earlier in the transition. Renewable energy growth averages 4.96% for RE100 and 4.01% for C-0. RE100 is met in terms of electricity generation, but falls 38% short on average to be met in terms of final energy consumption – a target achieved in C-0 through widespread electrification across all sectors. In fact, the final oil consumption ratio for RE100 remains at around 30% in 2050. Emissions reductions under RE100 taper off from 2040 onwards due to limitations in electrifying heavy vehicles, highlighting the need for advanced electrification options to achieve carbon neutrality. Total resilience, obtained by equally weighing all resilience indicators, increases faster under RE100 but reaches higher values in C-0, suggesting that sustained renewable energy growth and sectoral electrification are more effective for overall resilience.

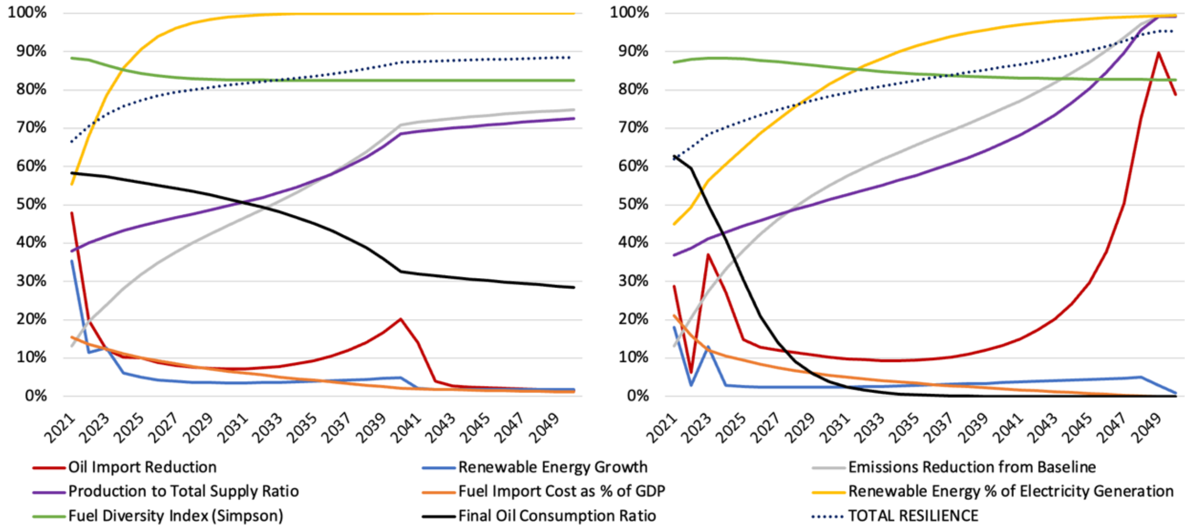

Fig. 5: RE100 (Left) and C-0 (Right), annual percentage changes of key model variables and resilience indicators

4.2. Fuel Imports & Energy Supply

Figure 6 shows the annual oil imports, exports, and bunkering requirements for both scenarios. Differing annual import profiles are due to variations in oil demand across various sectors, with bunkering contributing negligible amounts in the future granted that shipping decarbonisation efforts validate the assumed yearly reduction. Figure

7 shows primary energy supply by broad fuel type – suggesting a greater reduction in overall energy requirements under C-0. Figure 8 shows final electricity outputs by specific fuel type – with biomass growing the slowest due to its primary use in the food and tobacco industry and household cooking.

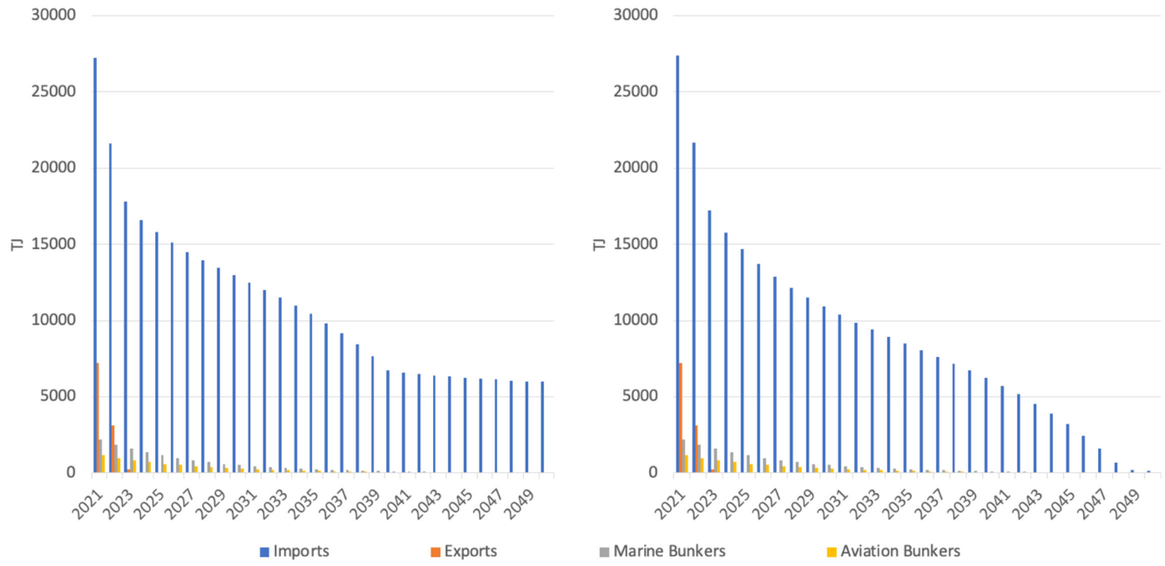

Fig. 6: RE100 (Left) and C-0 (Right), annual oil imports, exports, and bunkering

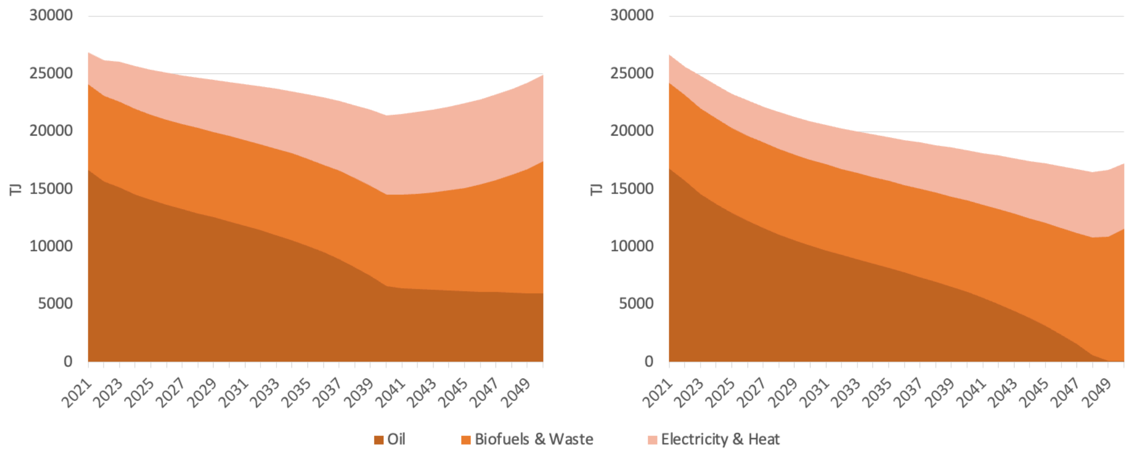

Fig. 7: RE100 (Left) and C-0 (Right), primary energy supply by fuel type

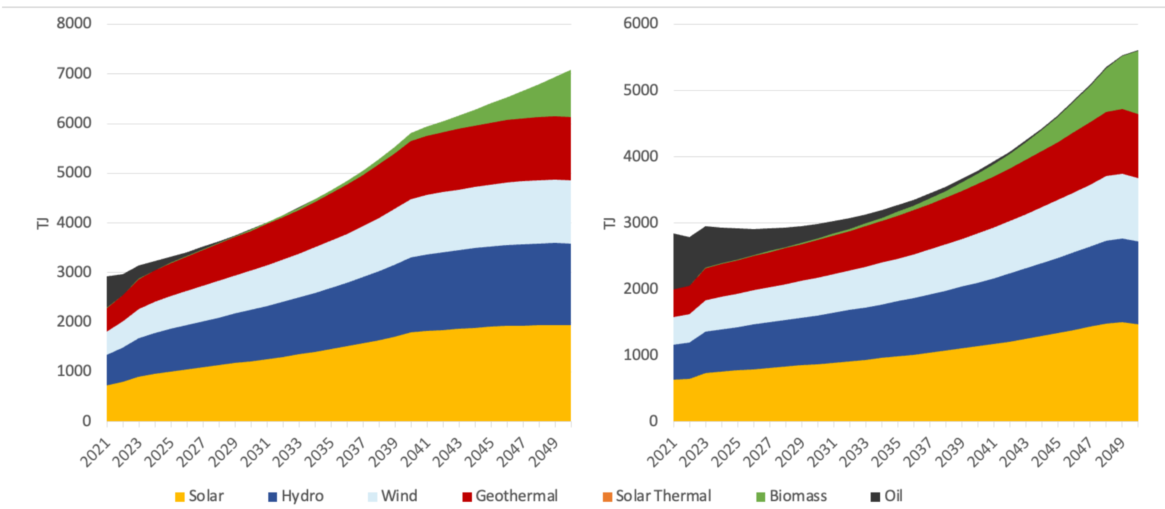

Fig. 8: RE100 (Left) and C-0 (Right), final electricity output by energy type

4.3. Sectoral Consumption

Figure 9 shows final oil consumption for each sector – with land transport dominating both scenarios and requiring a stark and steady decrease in C-0. Figure 10 shows final electricity consumption for each sector. Consistently with the required oil consumption reduction efforts, land transport dominates electricity consumption in 2050 under C-0 – suggesting that electric vehicle integration requires particular attention for long-term decarbonisation. Figure 11 shows final biomass consumption for each sector – confirming that its use is limited to fewer industries. Figure 12 shows electricity consumption for land transport, with goods vehicles requiring the largest amount of electricity due to their prominence and overall vehicle weight.

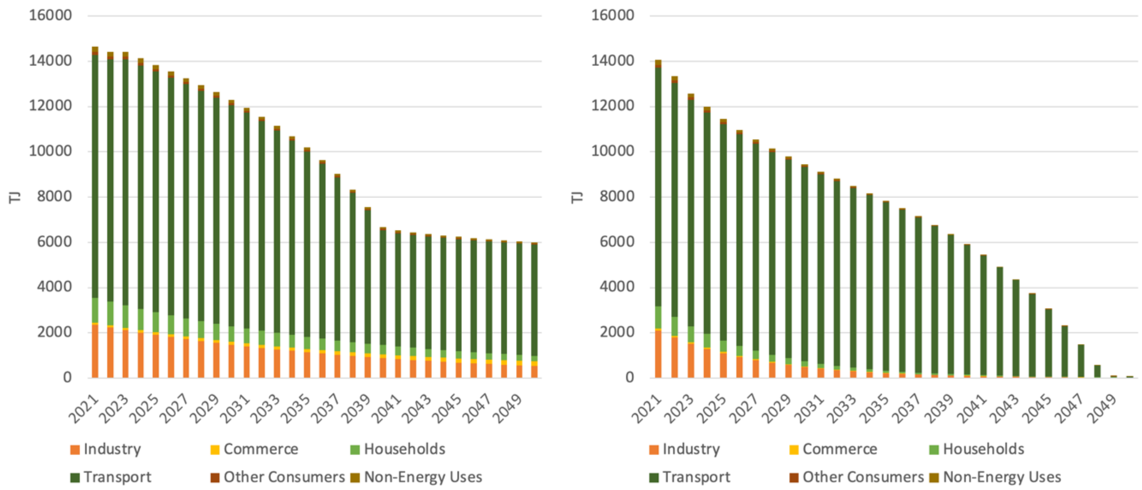

Fig. 9: RE100 (Left) and C-0 (Right), final oil consumption by sector

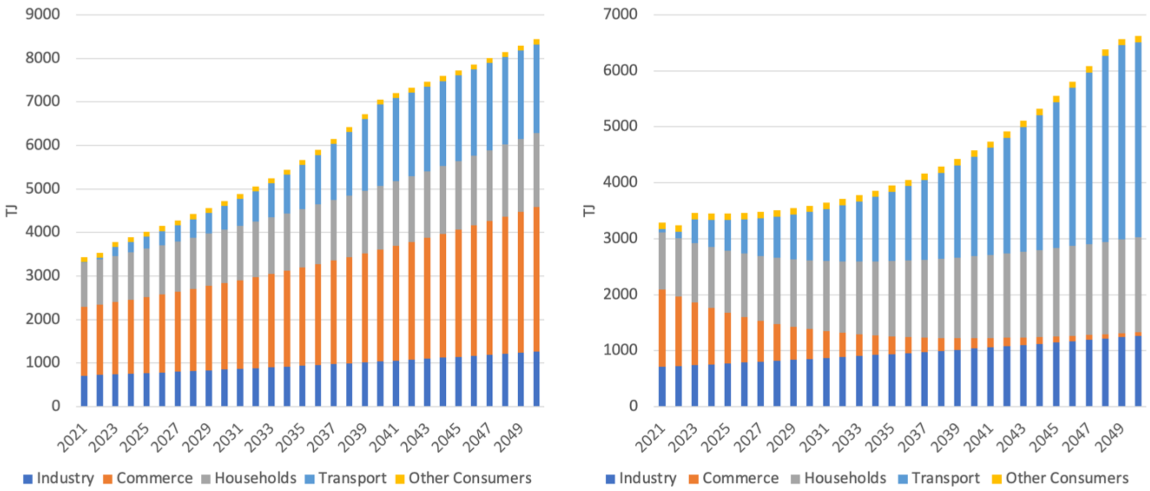

Fig. 10: RE100 (Left) and C-0 (Right), final electricity consumption by sector

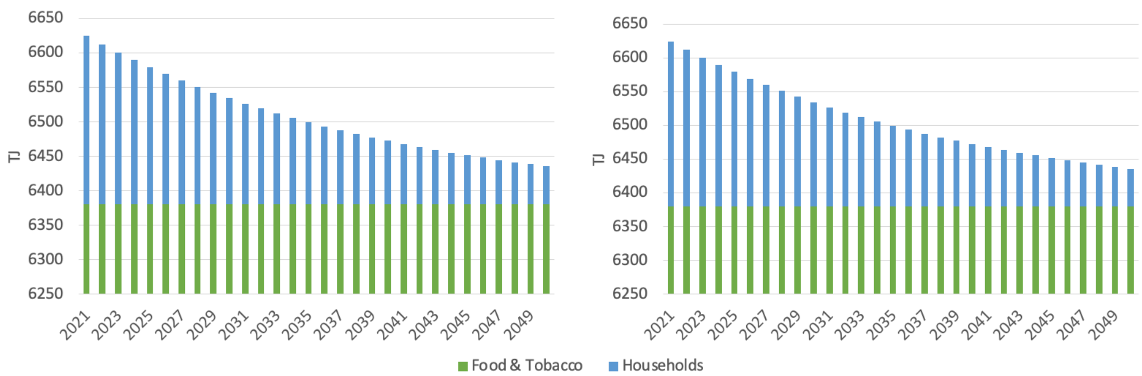

Fig. 11: RE100 (Left) and C-0 (Right), final biomass consumption by sector

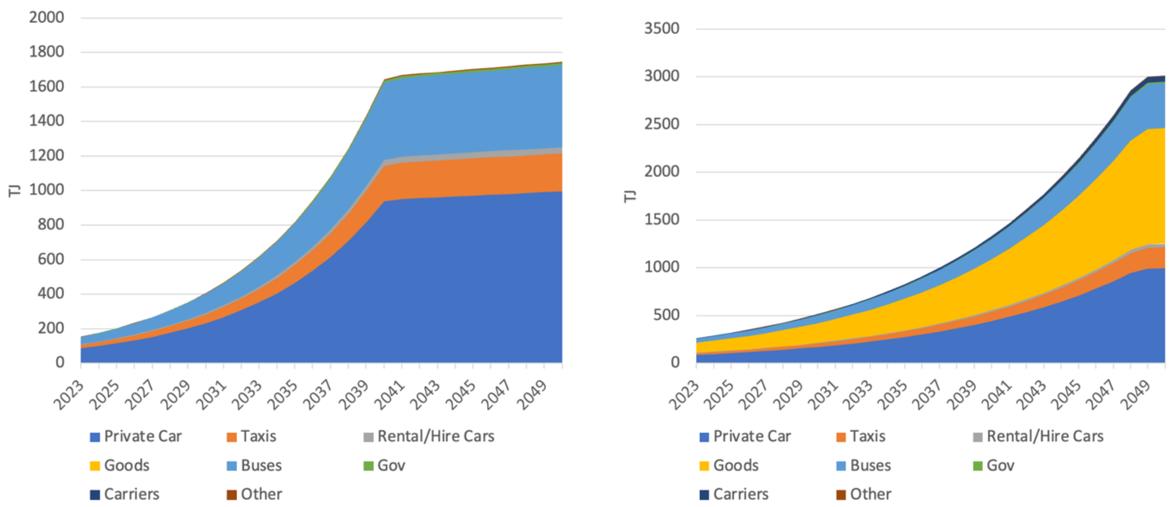

Fig. 12: RE100 (Left) and C-0 (Right), electricity consumption by vehicle type in land transport

4.4. Emissions

Figure 13 shows sectoral emissions for both scenarios – suggesting that decarbonisation efforts should primarily focus on land transport to achieve net-zero targets. In RE100, industry, household heating oil, marine transport, and domestic aviation still contribute to a noticeable portion of emissions in 2050.

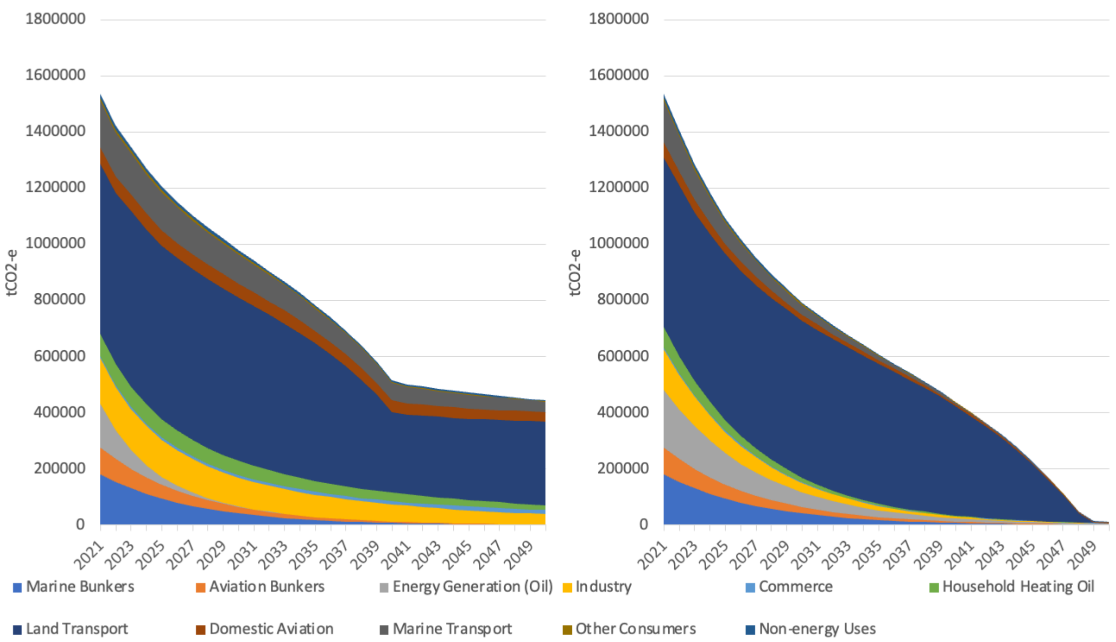

Fig. 13: Fig. 13: RE100 (Left) and C-0 (Right), sectoral emissions

4.5. Interpreting other key outputs for PICTs

As seen in Table 1, this tool also provides outputs regarding other key agendas for PICTs, such as energy access. In both explored scenarios household electricity consumption remains steady, although in countries with lower electricity access levels than Fiji, which sits at roughly 96% (ITA, 2022), selected options for energy access affect overall household consumption. These options include urban and rural population increase/decrease (with the key assumption that urban population is connected to the grid), as well as electrification rates for household cooking (typically done with mostly biomass). Furthermore, the tool also enables the user to select emission abatement rates via land use, land use change, and forestry (LULUCF) – to reflect afforestation and blue carbon management initiatives coupled with national decarbonisation plans – as well as the option to consider biomass "non-renewable" in circumstances where limited land availability may compromise its overall viability as an energy source.

5. Conclusions & Future Work

This study shows that modelling the interdependencies between energy and various economic sectors can provide insights for planning energy transitions to achieve specific targets and enhance resilience. To further develop the accuracy and applicability of the tool, additional parameters should be included or refined to better reflect sectoral transition models (e.g. electric vehicle adoption represented by electric vehicle sales and conventional vehicle decommissioning rather than replacement). Moreover, this study demonstrates the importance of developing extensive national and sectoral energy databases, as well as selecting appropriate input parameters in the development of electrification and decarbonisation plans. Scenario parametrisation should fully capture technical and market developments for various technologies that can reduce emissions (e.g. e-mobility, clean shipping).

Country-specific hourly electricity demand for every sector should also be integrated to enable hourly supply and demand matching, which can better determine capacity requirements and the implications of different renewable energy mixes. Figure 14 shows a preliminary version of this hourly matching for a random scenario – indicating experienced levels of curtailment (with equal curtailment across all energy sources), unmet demand, and overall utility battery requirements (including expected charge/discharge periods). Other planned improvements include capacity factor calculations, cost estimations for renewable technologies, efficiency options for different technology types associated with electrification across sectors, integration of renewable spillage for better capacity estimates, creation of further supply classes that better reflect the Pacific energy supply chain (e.g. on-grid solar and off-grid solar for better capturing energy access), and flexibility modelling (e.g. batteries, demand-side management).

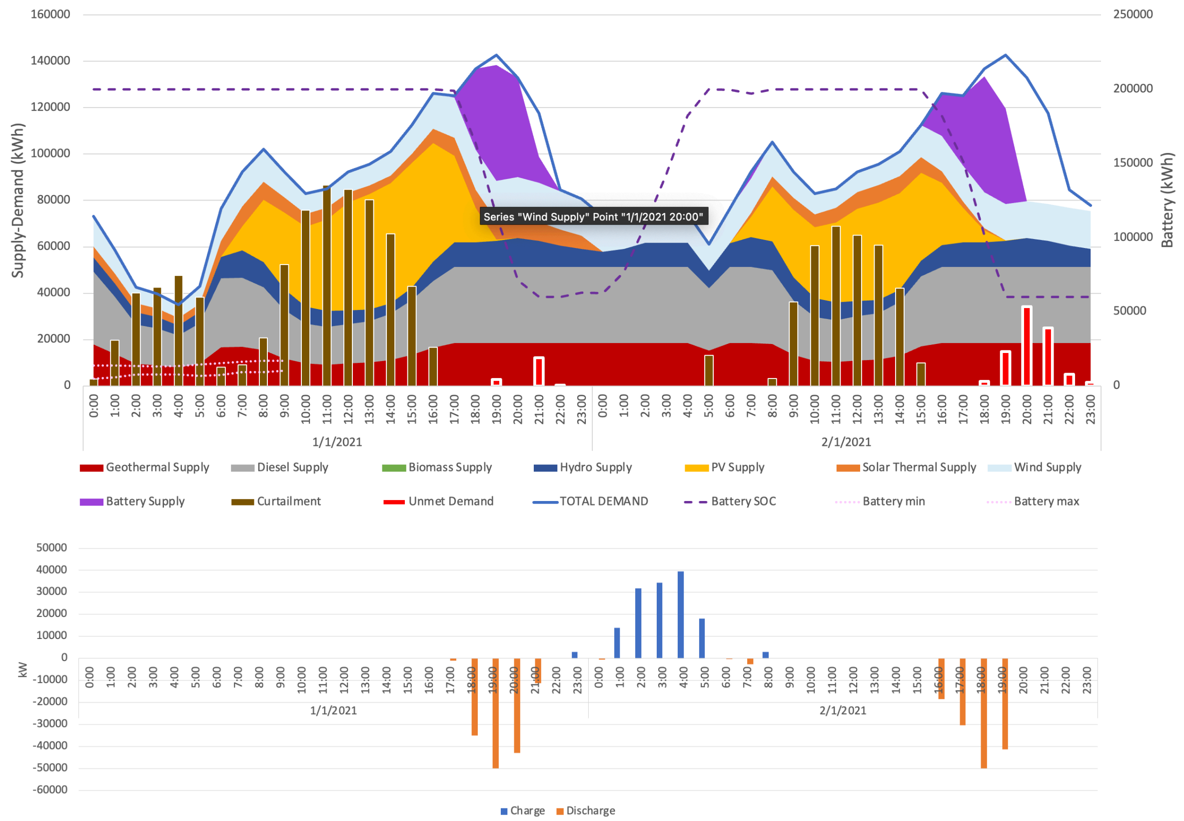

Fig. 14: Hourly supply and demand matching (Top) and overall utility storage behaviour (Bottom) for 2 days (random scenario)

6. Acknowledgements

The authors would like to acknowledge Shayan Naderi for his work on the assessment of technical renewable energy potentials across various Pacific Island Countries and Territories, included in his tool *Pacific Islands Energy Balance*.

7. References

Aleksandrova, M., Balasko, S., Kaltenborn, M., Malerba, D., Mucke, P., Neuschäfer, O., Radtke, K., Prütz, R., Strupat, C., Weller, D., Wiebe, N., 2021. World Risk Report.

Atteridge, A., Savvidou, G., 2019. Development aid for energy in Small Island Developing States. Energy, Sustainability and Society. 9, 10.

Fiji Bureau of Statistics, 2023. Distribution of Vehicles registered in Fiji.

Fiji Ministry of Economy, 2018a. Low Emission Development Strategy 2018-2050.

Fiji Ministry of Economy, 2018b. National Climate Change Policy.

Gargiulo, M., Gallachoir, B.O., 2013. Long-term energy models: Principles, characteristics, focus, and limitations. Wiley Interdisciplinary Reviews: Energy and Environment. 2, 158-177.

Groissböck, M., 2019. Are open source energy system optimization tools mature enough for serious use? Renewable and Sustainable Energy Reviews. 102, 234-248.

ITA, 2022. Fiji – Country Commercial Guide. Available at: https://www.trade.gov/country-commercial-guides/fiji-renewable-energy.

Kruyt, B., van Vuuren, D.P., de Vries, H.J., Groenenberg, H., 2009. Indicators for energy security. Energy policy. 37, 2166-2181.

Lucas, H., Fifita, S., Talab, I., Marschel, C., Cabeza, L.F. 2017. Critical challenges and capacity building needs for renewable energy deployment in Pacific Small Island Developing States (Pacific SIDS). Renewable Energy. 107, 42-52.

Michalena, E., Kouloumpis, V., Hills, J.M., 2018. Challenges for Pacific Small Island Developing States in achieving their Nationally Determined Contributions (NDC). Energy Policy. 114, 508-518.

NREL, 2022. Annual Technology Baseline.

OEC, 2020. Crude Petroleum Imports.

Pfenninger, S., Staffell, I., 2016. Renewables Ninja.

Raghoo, P., Surroop, D., Wolf, F., Leal Filho, W., Jeetah, P., Delakowitz, B., 2018. Dimensions of energy security in Small Island Developing States. Utilities Policy. 53, 94-101.

Sovacool, B.K., 2013. Assessing energy security performance in the Asia Pacific, 1990–2010. Renewable and Sustainable Energy Reviews. 17, 228-247.

SPC, 2019. Pacific Fuel Price Monitor: Covering 1st Quarter 2019 (January-March).

SPC, 2021. Framework for Energy Security and Resilience in the Pacific (FESRIP). Noumea, New Caledonia.

To, L.S., Bruce, A., Munro, P., Santagata, E., MacGill, I., Rawali, M., Raturi, A., 2021. A research and innovation agenda for energy resilience in Pacific Island Countries and Territories. Nature Energy. 6, 1098-1103.

UN, 2021. Energy Balances.

UN, 2023. Nationally Determined Contributions Registry.

Weir, T., 2018. Renewable energy in the Pacific Islands: Its role and status. Renewable and Sustainable Energy Reviews, 94, 762-771.

Wolf, F., Surroop, D., Singh, A., Leal, W., 2016. Energy access and security strategies in Small Island Developing States. Energy Policy. 98, 663-673.

World Bank, 2018. World Bank Open Data.

World Resources Institute, 2022. Climate Watch (CAIT).

A

B

D

E

F

G

J

K

L

M

N

O

P

R

S

Zörner, W.